

C.T. Russell
Editor

The STEREO Mission

C.T. Russell
Editor

The STEREO Mission

Previously published in *Space Science Reviews* Volume 136,
Issues 1–4, 2008



Springer

C.T. Russell
Institute of Geophysics & Planetary Physics
University of California
Los Angeles, CA 3845, USA

Cover illustration: STEREO performing stereoscopic observations.

All rights reserved.

Library of Congress Control Number: 2008930096

ISBN-978-0-387-09648-3

e-ISBN-978-0-387-09649-0

Printed on acid-free paper.

© 2008 Springer Science+Business Media, BV

No part of this work may be reproduced, stored in a retrieval system, or transmitted in any form or by any means, electronic, mechanical, photocopying, microfilming, recording or otherwise, without the written permission from the Publisher, with the exception of any material supplied specifically for the purpose of being entered and executed on a computer system, for the exclusive use by the purchaser of the work.

Contents

Foreword

C.T. Russell **1**

The STEREO Mission: An Introduction

M.L. Kaiser · T.A. Kucera · J.M. Davila · O.C. St. Cyr · M. Guhathakurta ·
E. Christian **5**

The STEREO Observatory

A. Driesman · S. Hynes · G. Cancro **17**

STEREO Space Weather and the Space Weather Beacon

D.A. Biesecker · D.F. Webb · O.C. St. Cyr **45**

Sun Earth Connection Coronal and Heliospheric Investigation (SECCHI)

R.A. Howard · J.D. Moses · A. Vourlidas · J.S. Newmark · D.G. Socker · S.P. Plunkett ·
C.M. Korendyke · J.W. Cook · A. Hurley · J.M. Davila · W.T. Thompson · O.C. St Cyr ·
E. Mentzell · K. Mehalick · J.R. Lemen · J.P. Wuelser · D.W. Duncan · T.D. Tarbell ·
C.J. Wolfson · A. Moore · R.A. Harrison · N.R. Waltham · J. Lang · C.J. Davis ·
C.J. Eyles · H. Mapson-Menard · G.M. Simnett · J.P. Halain · J.M. Defise · E. Mazy ·
P. Rochus · R. Mercier · M.F. Ravet · F. Delmotte · F. Auchere · J.P. Delaboudiniere ·
V. Bothmer · W. Deutsch · D. Wang · N. Rich · S. Cooper · V. Stephens · G. Maahs ·
R. Baugh · D. McMullin · T. Carter **67**

STEREO IMPACT Investigation Goals, Measurements, and Data Products Overview

J.G. Luhmann · D.W. Curtis · P. Schroeder · J. McCauley · R.P. Lin · D.E. Larson ·
S.D. Bale · J.-A. Sauvaud · C. Aoustin · R.A. Mewaldt · A.C. Cummings · E.C. Stone ·
A.J. Davis · W.R. Cook · B. Kecman · M.E. Wiedenbeck · T. von Rosenvinge ·
M.H. Acuna · L.S. Reichenthal · S. Shuman · K.A. Wortman · D.V. Reames ·
R. Mueller-Mellin · H. Kunow · G.M. Mason · P. Walpole · A. Korth · T.R. Sanderson ·
C.T. Russell · J.T. Gosling **117**

The STEREO IMPACT Boom

R. Ullrich · J. McCauley · P. Turin · K. McKee · B. Donokowski **185**

The STEREO/IMPACT Magnetic Field Experiment

M.H. Acuña · D. Curtis · J.L. Scheifele · C.T. Russell · P. Schroeder · A. Szabo ·
J.G. Luhmann **203**

The IMPACT Solar Wind Electron Analyzer (SWEA)

J.-A. Sauvaud · D. Larson · C. Aoustin · D. Curtis · J.-L. Médale · A. Fedorov ·
J. Rouzaud · J. Luhmann · T. Moreau · P. Schröder · P. Louarn · I. Dandouras ·
E. Penou **227**

The STEREO IMPACT Suprathermal Electron (STE) Instrument

R.P. Lin · D.W. Curtis · D.E. Larson · J.G. Luhmann · S.E. McBride · M.R. Maier ·
T. Moreau · C.S. Tindall · P. Turin · L. Wang **241**

The Suprathermal Ion Telescope (SIT) for the IMPACT/SEP Investigation

G.M. Mason · A. Korth · P.H. Walpole · M.I. Desai · T.T. Von Rosenvinge ·
S.A. Shuman **257**

The Low-Energy Telescope (LET) and SEP Central Electronics for the STEREO Mission

R.A. Mewaldt · C.M.S. Cohen · W.R. Cook · A.C. Cummings · A.J. Davis · S. Geier ·
B. Kecman · J. Klemic · A.W. Labrador · R.A. Leske · H. Miyasaka · V. Nguyen ·
R.C. Ogliore · E.C. Stone · R.G. Radocinski · M.E. Wiedenbeck · J. Hawk · S. Shuman ·
T.T. von Rosenvinge · K. Wortman **285**

The Solar Electron and Proton Telescope for the STEREO Mission

R. Müller-Mellin · S. Böttcher · J. Falenski · E. Rode · L. Duvet · T. Sanderson ·
B. Butler · B. Johlander · H. Smit **363**

The High Energy Telescope for STEREO

T.T. von Rosenvinge · D.V. Reames · R. Baker · J. Hawk · J.T. Nolan · L. Ryan ·
S. Shuman · K.A. Wortman · R.A. Mewaldt · A.C. Cummings · W.R. Cook ·
A.W. Labrador · R.A. Leske · M.E. Wiedenbeck **391**

The Plasma and Suprathermal Ion Composition (PLASTIC) Investigation on the STEREO Observatories

A.B. Galvin · L.M. Kistler · M.A. Popecki · C.J. Farrugia · K.D.C. Simunac · L. Ellis ·
E. Möbius · M.A. Lee · M. Boehm · J. Carroll · A. Crawshaw · M. Conti · P. Demaine ·
S. Ellis · J.A. Gaidos · J. Googins · M. Granoff · A. Gustafson · D. Heirtzler · B. King ·
U. Knauss · J. Levasseur · S. Longworth · K. Singer · S. Turco · P. Vachon ·
M. Vosbury · M. Widholm · L.M. Blush · R. Karrer · P. Bochsler · H. Daoudi · A. Etter ·
J. Fischer · J. Jost · A. Opitz · M. Sigrist · P. Wurz · B. Klecker · M. Ertl ·
E. Seidenschwang · R.F. Wimmer-Schweingruber · M. Koeten · B. Thompson ·
D. Steinfeld **437**

S/WAVES: The Radio and Plasma Wave Investigation on the STEREO Mission

J.L. Bougeret · K. Goetz · M.L. Kaiser · S.D. Bale · P.J. Kellogg · M. Maksimovic ·
N. Monge · S.J. Monson · P.L. Astier · S. Davy · M. Dekkali · J.J. Hinze ·
R.E. Manning · E. Aguiar-Rodriguez · X. Bonnin · C. Briand · I.H. Cairns ·
C.A. Cattell · B. Cecconi · J. Eastwood · R.E. Ergun · J. Fainberg · S. Hoang ·
K.E.J. Huttunen · S. Krucker · A. Lecacheux · R.J. MacDowall · W. Macher ·
A. Mangeney · C.A. Meetre · X. Moussas · Q.N. Nguyen · T.H. Oswald · M. Pulupa ·
M.J. Reiner · P.A. Robinson · H. Rucker · C. Salem · O. Santolik · J.M. Silvis ·
R. Ullrich · P. Zarka · I. Zouganelis **487**

The Electric Antennas for the STEREO/WAVES Experiment

S.D. Bale · R. Ullrich · K. Goetz · N. Alster · B. Cecconi · M. Dekkali · N.R. Lingner ·
W. Macher · R.E. Manning · J. McCauley · S.J. Monson · T.H. Oswald · M. Pulupa **529**

STEREO/Waves Goniopolarimetry

B. Cecconi · X. Bonnin · S. Hoang · M. Maksimovic · S.D. Bale · J.-L. Bougeret ·
K. Goetz · A. Lecacheux · M.J. Reiner · H.O. Rucker · P. Zarka **549**

Theoretical Modeling for the STEREO Mission

M.J. Aschwanden · L.F. Burlaga · M.L. Kaiser · C.K. Ng · D.V. Reames · M.J. Reiner ·
T.I. Gombosi · N. Lugaz · W. Manchester IV · I.I. Roussev · T.H. Zurbuchen ·
C.J. Farrugia · A.B. Galvin · M.A. Lee · J.A. Linker · Z. Mikič · P. Riley ·
D. Alexander · A.W. Sandman · J.W. Cook · R.A. Howard · D. Odstrčil · V.J. Pizzo ·
J. Kóta · P.C. Liewer · J.G. Luhmann · B. Inhester · R.W. Schwenn · S.K. Solanki ·
V.M. Vasylunas · T. Wiegemann · L. Blush · P. Bochsler · I.H. Cairns · P.A. Robinson ·
V. Bothmer · K. Kecskemeti · A. Llebaria · M. Maksimovic · M. Scholer ·
R.F. Wimmer-Schweingruber **565**

STEREO Ground Segment, Science Operations, and Data Archive

J. Eichstedt · W.T. Thompson · O.C. St. Cyr **605**

**The Solar Terrestrial Relations Observatory (STEREO) Education and Outreach
(E/PO) Program**

L.M. Peticolas · N. Craig · T. Kucera · D.J. Michels · J. Gerulskis · R.J. MacDowall ·
K. Beisser · C. Chrissotimos · J.G. Luhmann · A.B. Galvin · L. Ratta · E. Drobnes ·
B.J. Méndez · S. Hill · K. Marren · R. Howard **627**

Foreword

C.T. Russell

Originally published in the journal Space Science Reviews, Volume 136, Nos 1–4.
DOI: [10.1007/s11214-008-9344-1](https://doi.org/10.1007/s11214-008-9344-1) © Springer Science+Business Media B.V. 2008

The Sun-Earth Connection is now an accepted fact. It has a significant impact on our daily lives, and its underpinnings are being pursued vigorously with missions such as the Solar TErrestrial RElations Observatory, commonly known as STEREO. This was not always so. It was not until the middle of the nineteenth century that Edward Sabine connected the 11-year geomagnetic cycle with Heinrich Schwabe's deduction of a like periodicity in the sunspot record. The clincher for many was Richard Carrington's sighting of a great white-light flare on the Sun, on September 1, 1859, followed by a great geomagnetic storm 18 hours later. But was the Sun-Earth Connection significant to terrestrial denizens? Perhaps in 1859 it was not, but a century later it became so. Beginning in the 1930's, as electrical power grids grew in size, power companies began to realize that they occasionally had power blackouts during periods of intense geomagnetic activity. This correlation did not appear to be sufficiently significant to bring to the attention of the public but during the International Geophysical Year (IGY), when geomagnetic activity was being scrutinized intensely, the occurrence of a large North American power blackout during a great magnetic storm was impossible to ignore. By this time it was also known that ionospheric storms could disrupt communications, and late in the IGY the first orbiting spacecraft were launched and the radiation belts were discovered. The Sun, the magnetosphere, solar wind, and coronal mass ejections became the topic of news articles of interest to the public as well as to the scientific community.

Space, or at least near-Earth space, was no longer a frontier, it became a terrestrial workplace. Astronauts occupied it. Communication satellites, weather satellites, and navigation satellites depended on it, but these space systems proved to be sensitive to solar variability. Further our power grids continued to prove to be fragile. We learned quickly what the Sun was doing but we learned only slowly why and how the Sun behaved that way. Early missions such as Skylab, Solwind and later SOHO showed us the tremendous ejections from the Sun. HELIOS, ISEE and Ulysses revealed the interior structure of these ejections once they

C.T. Russell (✉)
University of California, Los Angeles, USA
e-mail: ctrussel@igpp.ucla.edu

left the vicinity of the Sun. Unfortunately, as valuable as these missions were they provided only either projections on the plane of the sky or single cuts through the structure. A stereoscopic view of the Sun was needed, as was a multipoint in situ measurement of the material ejected from the Sun. Thus was born the concept of the STEREO mission, twin spacecraft, separated at launch, that slowly drift further and further ahead and behind the Earth near 1 AU, both triangulating with an optical suite of instruments on solar disturbances, and sounding these same disturbances when they reach the STEREO spacecraft and their suites of in situ devices.

This collection of articles describes the STEREO mission, its spacecraft, instrument and operations. The paper by M.L. Kaiser and colleagues describes the history of the project and its objectives and the article by A. Driesman and colleagues the observatory itself. A unique feature of this space-weather mission is its beacon mode that transmits a low rate data stream comprised of both in situ samples and solar image snapshots to Earth continually to help geomagnetic forecasters. The operation of this system is described by D.A. Biesecker, D.F. Webb and O.C. St. Cyr. The largest investment of the scientific payload is in the Sun-earth Connection Coronal and Heliospheric Investigation (SECCHI) whose acronym invokes the memory of a pioneering solar scientist. This suite of optical instruments includes coronagraphs and heliospheric imagers that can follow disturbances from the Sun until they pass 1 AU. This article is followed by a series of papers covering the elements of the payload that measure the plasma, energetic particles and magnetic and electric fields at the spacecraft. In many senses the radio system too is a remote sensor with direction finding capability that follows the solar disturbances. The first nine of these papers are devoted to the IMPACT investigation, starting with a detailed overview by J.G. Luhmann et al. and followed by discussions of the boom by Ullrich et al., of the magnetometer by M.H. Acuña et al., of the solar wind electron analyzer by J.-A. Sauvage et al., of the suprathermal electron detector by R.P. Lin et al., of the suprathermal ion detector by G.M. Mason et al., of the low-energy telescope by R.A. Mewaldt et al., of the solar electron and proton telescope by R. Müller-Mellin et al., and the high energy telescope by T.T. von Rosenvinge et al.

The solar wind ion instrument is separate from the IMPACT suite as is the plasma waves investigation. The former instrument named the Plasma and Suprathermal Ion Composition Investigation (PLASTIC) is described by A.B. Galvin et al. The radio and plasma waves investigation has been dubbed the STEREO/Waves or S/WAVES investigation. It is described in an overview article by J.L. Bougeret et al., followed by articles on the electric antennas by S.D. Bale et al. and the direction finding mode by B. Cecconi et al.

The collection of articles closes with topics that cross all discipline areas. The first of these articles by M.J. Aschwanden et al. describes the theory and modeling effort supporting the STEREO mission. The next by J. Eichstedt, W.T. Thompson and O.C. St. Cyr describes the operations and data archive and the last led by L.M. Peticolas describes the education and public outreach program.

The success of this volume is due to the efforts of many people. The editor is extremely grateful for the assistance he received in assembling this volume. First of all he is grateful to the authors themselves who responded well to the comments of the referees. He is also grateful to the many referees who assisted by spending their time improving the contents of this volume. These referees include J.-L. Bougeret, S.R. Cranmer, A. Cummings, A. Davis, W. Farrell, J. Gosling, E. Grayzeck, S. Gulkis, S.R. Habbal, D. Haggerty, R.C. Harten, T. Horbury, R. Howard, M.-B. Kallenrode, W.S. Kurth, P. Lamy, L.J. Lanzerotti, J.G. Luhmann, W. Magnes, G. Mason, J. McCarthy, L.A. McFadden, B. McKibben, R. Mewaldt, R. Mueller-Mellin, M. Neugebauer, D. Reames, B. Reinisch, H.O. Rucker, R. Schwenn, A.C. Stewart, J. Wise, T. Zurbuchen. The editor also wishes to thank Markus J. Aschwanden

who acted as editor where there were conflicts of interest; the staff at Springer, especially Fiona Routley and Randy Cruz for all their assistance in assembling this volume; as well as Marjorie Sowmendran at the University of California, Los Angeles, who skillfully assisted us by acting as the interface between the editors, the authors, the referees and the publisher.

March 24, 2008

The STEREO Mission: An Introduction

M.L. Kaiser · T.A. Kucera · J.M. Davila · O.C. St. Cyr ·
M. Guhathakurta · E. Christian

Originally published in the journal Space Science Reviews, Volume 136, Nos 1–4.
DOI: [10.1007/s11214-007-9277-0](https://doi.org/10.1007/s11214-007-9277-0) © Springer Science+Business Media B.V. 2007

Abstract The twin STEREO spacecraft were launched on October 26, 2006, at 00:52 UT from Kennedy Space Center aboard a Delta 7925 launch vehicle. After a series of highly eccentric Earth orbits with apogees beyond the moon, each spacecraft used close flybys of the moon to escape into orbits about the Sun near 1 AU. Once in heliospheric orbit, one spacecraft trails Earth while the other leads. As viewed from the Sun, the two spacecraft separate at approximately 44 to 45 degrees per year. The purposes of the STEREO Mission are to understand the causes and mechanisms of coronal mass ejection (CME) initiation and to follow the propagation of CMEs through the inner heliosphere to Earth. Researchers will use STEREO measurements to study the mechanisms and sites of energetic particle acceleration and to develop three-dimensional (3-D) time-dependent models of the magnetic topology, temperature, density and velocity of the solar wind between the Sun and Earth. To accomplish these goals, each STEREO spacecraft is equipped with an almost identical set of optical, radio and in situ particles and fields instruments provided by U.S. and European investigators. The SECCHI suite of instruments includes two white light coronagraphs, an extreme ultraviolet imager and two heliospheric white light imagers which track CMEs out to 1 AU. The IMPACT suite of instruments measures in situ solar wind electrons, energetic electrons, protons and heavier ions. IMPACT also includes a magnetometer to measure the in situ magnetic field strength and direction. The PLASTIC instrument measures the composition of heavy ions in the ambient plasma as well as protons and alpha particles. The S/WAVES instrument uses radio waves to track the location of CME-driven shocks and the 3-D topology of open field lines along which flow particles produced by solar flares. Each of the four instrument packages produce a small real-time stream of selected data for purposes of predicting space weather events at Earth. NOAA forecasters at the Space Environment Center and others will use these data in their space weather forecasting and their resultant products will be widely used throughout the world. In addition to the four instrument teams,

M.L. Kaiser (✉) · T.A. Kucera · J.M. Davila · O.C. St. Cyr
NASA/Goddard Space Flight Center, Greenbelt, MD 20771, USA
e-mail: Michael.Kaiser@nasa.gov

M. Guhathakurta · E. Christian
NASA Headquarters, Washington, DC 20024, USA

there is substantial participation by modeling and theory oriented teams. All STEREO data are freely available through individual Web sites at the four Principal Investigator institutions as well as at the STEREO Science Center located at NASA Goddard Space Flight Center.

Keywords CME · Solar · Three-dimensional

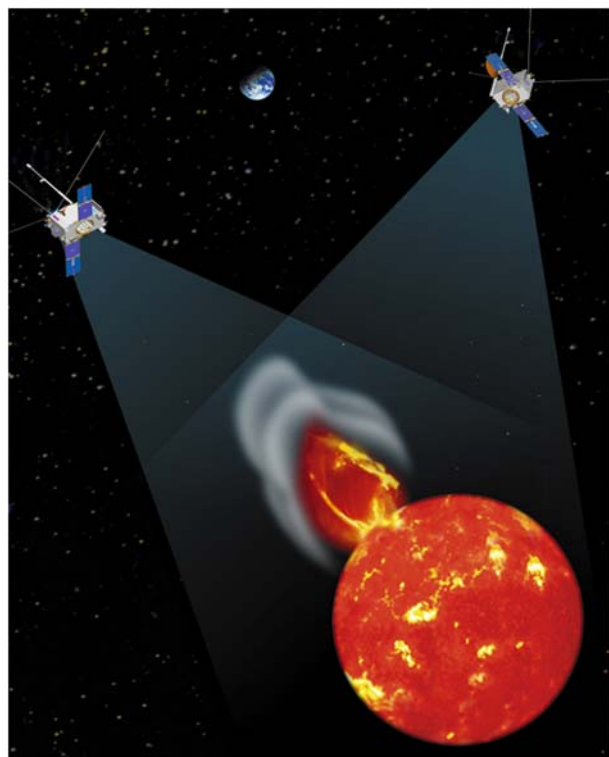
1 Preface: “Heliophysics: The New Science of the Sun–Solar System Connection”

These are the words from the recent strategic plan of the Heliophysics Division within NASA’s Science Mission Directorate. An integral part of exploration, Heliophysics is the system science that unites all of the linked phenomena in regions of the cosmos influenced by magnetically variable stars like our Sun.

That same roadmap also describes the evolving Heliophysics Great Observatory composed of the present fleet of spacecraft which act as a distributed network, providing multi-point measurements of the components. The STEREO mission, depicted in Fig. 1, represents the most significant upgrade and expansion to the Great Observatory in the past decade. In fact, this mission represents more of a “revolutionary” addition than “evolutionary”, as it will provide not only a rich package of upgraded sensors, it will travel to new vantage points.

The vastness of the inner solar system means we can obtain only sparse and infrequent measurements—at least as compared to other applied sciences like meteorology and

Fig. 1 An artist’s conception of the STEREO mission. Two nearly identical spacecraft situated well off the Earth–Sun line, making simultaneous measurements of the Sun



oceanography. A long-term goal of Heliophysics is to emphasize understanding of the underlying physics of this complex, coupled dynamic system by extending measurements and predicting the system behavior as it affects Earth and other remote locations. STEREO will provide unique insight into the physics of coronal mass ejections (CMEs) and provide an ideal opportunity to improve and to test current physics-based models and their predictions in the inner solar system.

As you read the papers in this issue describing the technical details of this rich payload, try to envision the sailing ships of the past, on their voyages of exploration and discovery. The STEREO mission has the potential to be one of those memorable voyages, changing our scientific understanding of how our magnetically variable star affects Earth and all other bodies in our solar system.

2 Introduction

Over a period of two to three decades, solar physicists have come to realize that the extremely energetic solar storms known as coronal mass ejections (CMEs) are the form of solar activity most forcefully felt at Earth. CMEs impacting Earth's environment are the primary cause of major geomagnetic storms and they are associated with nearly all of the largest solar proton events. The growth in society's reliance on technology has led to an increased vulnerability to impacts from the space environment and, hence, to an importance in understanding the multifaceted influence of the Sun and CMEs on Earth. More recently, an initiative to return human and robotic explorers to the Moon and to extend a human presence to Mars has been undertaken, making protection of the space travelers from the harmful effects of radiation storms an important goal in "space weather" research and prediction. Unfortunately, to date we cannot predict reliably when a CME will occur or what its effects will be.

Many current and past space missions and ground-based observations have studied CME disturbances from their initial lift-off at the Sun and through their propagation in the region near the Sun, 10–15% of their way to Earth. Other spacecraft have measured the effects of CMEs *in situ* near Earth. However, there have not been missions to follow CMEs continuously from Sun to Earth. The evolution of CMEs in the vast space between Sun and Earth has been mostly predicted by empirical and theoretical models, and the estimating CME arrival times at Earth have been disappointing.

The report of the science definition team for the STEREO Mission (Rust et al. 1997) lists a number of fundamental questions about the physical causes of CME eruptions that remain to be answered, such as:

- Are CMEs driven primarily by magnetic or nonmagnetic forces?
- What is the geometry and magnetic topology of CMEs?
- What key coronal phenomena accompany CME onset?
- What initiates CMEs?
- What is the role of magnetic reconnection?
- What is the role of evolving surface features?

Since the corona is optically thin at most wavelengths, all previous single spacecraft observations have suffered from line-of-sight integration effects which cause ambiguities and confusion. None of these questions can be satisfactorily addressed with additional single vantage point observations of the type available prior to STEREO. However, with the range of view angles accessible to the STEREO telescopes, CMEs and coronal structures

and even the underlying preeruption features can be reconstructed in three dimensions. Early in the mission, STEREO extreme ultraviolet observations of the underlying active regions will reveal the three-dimensional nature of coronal loops, including their exact cross-sectional shape and their interactions with each other, key to understanding the initiation of CMEs. These same STEREO extreme ultraviolet observations should resolve the three-dimensional nature of the enigmatic waves seen in extreme ultraviolet traveling across the “surface” of the Sun immediately following a CME lift-off. These waves appear not to be “blast waves”, but they are intimately involved with CMEs. With the stereoscopic capabilities of STEREO and the rapid cadence of its extreme ultraviolet instrument, the exact relationship to CMEs and the trigger for these waves should be discovered.

The surface features underlying CMEs are best observed near disk center, whereas with prior single vantage point missions, CMEs themselves were best observed near the solar limb where plane-of-sky projection effects are minimal. When the STEREO spacecraft are far apart so that their plane of the sky encompasses Earth, they can detect CMEs that originate above surface locations that are at disk center (when viewed from Earth).

Compounding the problem of incomplete observations of CMEs, the CMEs that most affect Earth are also the least likely to be detected and measured by ground-based or Earth-orbiting coronagraphs because they are viewed only as an expanding “halo” around the Sun, inhibiting measurement of their speed, morphology and even exact direction toward the observer. Arrival times of significant space weather events at Earth have typically only been accurate to about ± 12 hours in the past. However, with the STEREO spacecraft measuring Earth-directed CMEs from well off the Earth–Sun line, a CME’s speed and direction can be determined via triangulation and should greatly improve Earth impact prediction times. Furthermore, STEREO’s complete observational coverage of CMEs from lift-off to arrival at 1 AU and beyond will allow a determination of the instantaneous distribution of matter in the inner heliosphere. This is currently not possible.

The principal mission objective for STEREO is to understand the origin and consequences of CMEs, the most energetic eruptions on the Sun and the cause of the most severe nonrecurrent geomagnetic storms at Earth. Specific science objectives are to:

- Understand the causes and mechanisms of CME initiation.
- Characterize the propagation of CMEs through the heliosphere.
- Discover the mechanisms and sites of solar energetic particle acceleration in the low corona and the interplanetary medium.
- Develop a three-dimensional, time-dependent model of the magnetic topology, temperature, density and velocity structure of the ambient solar wind.

These four rather generic science goals imply more specific measurements as shown in Table 1. These are the STEREO Level 1 science requirements. Minimum success for STEREO was defined as being able to make the measurements in the table with both spacecraft for a period of 150 days after achieving heliocentric orbit, followed by at least one of the spacecraft continuing to make the full suite of measurements for the remainder of the two year prime mission. The minimum success 150-day interval was reached on June 21, 2007. Full success of the mission requires the measurements to be made by both spacecraft for the entire two-year interval of the prime mission, again after reaching heliocentric orbit. Full success will be reached on January 23, 2009.

For each of the Level 1 science requirement measurements in Table 1, several combinations of instruments from the twin spacecraft contribute so that loss of any one instrument

Table 1 STEREO Level 1 science requirements

Scientific objective	Measurement requirement
Understand the causes and mechanisms of CME initiation	A Determine CME initiation time to within 10 minutes B Determine location of initiation to within five degrees of solar latitude and longitude
Characterize the propagation of CMEs through the heliosphere	C Determine the evolution of CME mass distribution and the longitudinal extent to within five degrees as it propagates D Determine the CME and MHD shock speeds to within 10% as it propagates E Determine the direction of the CME and MHD shock propagation to within five degrees
Discover the mechanisms and site of energetic particle acceleration in the low corona and interplanetary medium	F Develop distribution functions to an accuracy of 10% for electrons and/or ions with energies typical of solar energetic particle populations G Locate regions of particle acceleration in the low corona to within 300,000 km in radius and in interplanetary space to within 20 degrees in longitude
Develop a 3-D time-dependent model of the magnetic topology, temperature, density and velocity of the ambient solar wind	H Obtain a time series of the solar wind temperature to within 10% accuracy at two points separated in solar longitude I Obtain a time series of solar wind density to within 10% accuracy at two points separated in solar longitude J Obtain a time series of solar wind speed to within 10% accuracy at two points separated in solar longitude K Measure global magnetic field topology near the ecliptic by determining the magnetic field direction to within 10 degrees

does not result in STEREO's inability to satisfy a science requirement. Also, the nominal two-year STEREO mission scientific goals do not depend on acquiring these measurements during any particular phase of the solar cycle because CMEs and other phenomena to be studied are common to all phases of the cycle. Although the CME rate varies from about 0.5 per day at solar minimum to several per day at solar maximum, assuming a CME rate consistent with the minimum of the solar magnetic activity cycle, we expect that STEREO will observe at least 60 CMEs in remote sensing instruments and at least 24 interplanetary events *in situ*. In fact, the SECCHI coronagraphs have already recorded >60 CMEs during the initial 150 days of the mission.

STEREO is managed by NASA's Goddard Space Flight Center (GSFC) in Greenbelt, MD. GSFC provided science instrument management, systems engineering, mission assurance and reliability during the design and build phase, as well as science and data analysis, data archiving and coordination of Education and Public Outreach (EPO) efforts after launch. The Johns Hopkins University Applied Physics Laboratory (JHU/APL) in Laurel, MD, was responsible for the design, construction, integration and testing of the space-

craft and conducts the mission operations of the observatories during the post-launch period.

3 History

The first appearance of a multi-spacecraft mission to observe the Sun within NASA strategic planning documents (Space Physics Missions Handbook and Space Physics Strategy-Implementation Study) was the appearance of the Global Solar Mission in 1991. These documents were the result of a planning session convened in Baltimore, MD, by Stan Shawhan to develop missions for the new Sun–Earth Connection division. The Global Solar Mission envisioned a large number of spacecraft to observe the Sun from around the ecliptic and with polar orbiting spacecraft.

On June 11, 1992, at the 23rd meeting of the Solar Physics Division (SPD) of the American Astronomical Society in Columbus, OH, an open evening town hall session was organized to discuss future solar physics mission concepts. At this session two mission concepts were presented for the first time, which eventually were united to become the STEREO mission.

The Solar Tomography Mission, presented by one of us (JMD), envisioned a set of two to four spacecraft in heliocentric orbit, providing simultaneous images of the corona. From these images, the three-dimensional structure of active regions, streamers, coronal holes and other solar features would be deduced. Subsequently, at the 24th meeting of the SPD in Stanford, CA, in July 1993, Davila presented a paper reporting the results of an informal mission feasibility study conducted at Goddard Space Flight Center, and preliminary results of tomographic reconstruction simulations, which were eventually published (Davila 1994a, 1994b).

In the same SPD session (23rd), Ernie Hildner of the NOAA Space Environment Laboratory (now the SEC-Space Environment Center) outlined a mission called Global Understanding of the Sun (GUS), which later evolved into Special Perspectives Investigations (SPINS; Pizzo 1994). In this concept, a coronagraph similar to SOHO/LASCO-C2 is placed in heliocentric orbit, at roughly 90 degrees from the Sun–Earth line to observe Earth-directed CMEs from the Sun. The 90-degree position was selected to provide the optimum visibility of a CME in the occulted field of view of the coronagraph. Studies of the SPINS concept were conducted at Ball Aerospace.

It was soon recognized that these missions had elements in common, and a workshop was organized at SEL in Boulder, CO, by Vic Pizzo and David Sime in November 1993 to discuss a possible mission that would combine the goals of the Tomography Mission and SPINS. Approximately 30 interested scientists attended the two-day workshop. On August 5–6, 1996, a second workshop was held to further refine the combined mission concept in preparation for the initial Sun–Earth Connection Roadmap. A name was chosen, the Solar Terrestrial Relations Observatory (STEREO), and a conceptual mission very similar to the current version of STEREO was agreed upon (Davila et al. 1996). The objectives were to understand the initiation and propagation of CMEs and their effect on the near-Earth environment. To accomplish these goals, it was agreed that the three-dimensional nature of the corona must be observed, i.e., multiple spacecraft were required. Subsequently, the NASA Headquarters selected STEREO as the second mission (after TIMED) in the newly formed Solar Terrestrial Probe (STP) mission line.

In 1996, a Science and Technology Definition Team (STDT) was formed with David Rust (APL) as the chair, and Joseph Davila (GSFC) as the Study Scientist. After several

meetings, intermediate studies, and vigorous discussion among the committee members, the straw man payload was defined and instrument priorities were established. The report of the STDT formed the basis for the NASA Announcement of Opportunity soliciting instrument proposals in 1999. Additional mission architecture studies provided the technical information needed for the release of the STEREO mission AO (Watzin and Davila 1997; Rowley 1997; Galloway 1998).

A mission similar to STEREO, but much larger in scope was studied at JPL in 1982 (Schmidt and Bothmer 1995). Other multi-spacecraft missions to observe the Sun were proposed in Russia (Grigoryev 1993; Grigoryev et al. 1996; Chebotarev et al. 1997), in Europe (Schmidt et al. 1993), Canada (Timothy et al. 1996) and the United States (Liewer et al. 1998). Workshops provided the opportunity for the Heliophysics community to provide input into the ongoing studies (Bothmer and Foing 1996). Two missions were proposed in the Explorer proposal opportunity of 1995 that used a single spacecraft in heliocentric orbit combined with near-Earth observatories like SOHO to obtain multiple views of the solar corona, and multipoint measurements of the heliosphere (Brueckner et al. 1995; Davila et al. 1996). The NRL mission provided the acronym STEREO, though it represented a slightly different underlying title.

In this paper, we provide an introduction to the STEREO mission. Each of the areas described below receives in-depth treatment in the other papers in this issue. Some aspects of the history of the mission and some of the important trade-studies that define the final mission design will be described here.

4 The Science Investigations

The STEREO science payload consists of four measurement packages, each of which has several components totaling at least 18 individual sensors. Together, this suite of instruments will characterize the CME plasma from the solar corona to Earth's orbit. The instrument packages are described in detail in the other papers in this issue, but here we provide a brief introduction.

- Sun–Earth Connection Coronal and Heliospheric Investigation (SECCHI). SECCHI encompasses a suite of remote sensing instruments including two white-light coronagraphs, an extreme ultraviolet imager and two white-light heliospheric imagers all designed to study the three-dimensional evolution of CMEs from the Sun's surface through the corona and interplanetary medium to their eventual impact at Earth. Russell Howard of the Naval Research Laboratory of Washington, DC, leads this investigation. A comprehensive description of the SECCHI suite of instruments is given by Howard et al. (2007).
- In situ Measurements of PArticles and CME Transients (IMPACT) was designed, built and tested by an international team led by Janet Luhmann of the University of California, Berkeley. It measures the interplanetary magnetic field, thermal and suprathermal solar wind electrons, and energetic electrons and ions. IMPACT is a suite of seven instruments, three of which—the solar wind electron analyzer (SWEA), the suprathermal electron instrument (STE) and the magnetic field experiment (MAG)—are located on a six-meter deployable boom deployed anti-sunward. The remaining IMPACT instruments—the low-energy telescope (LET), the high-energy telescope (HET), the suprathermal ion telescope (SIT) and the solar electron and proton telescope (SEPT)—are all located on the main body of the spacecraft and are dedicated to measuring solar energetic particles (SEPs). The IMPACT suite is described in a series of papers in this issue. Luhmann et al. (2007) provides an overview. The boom suite of instruments are described by Sauvaud et al.

Table 2 STEREO instruments

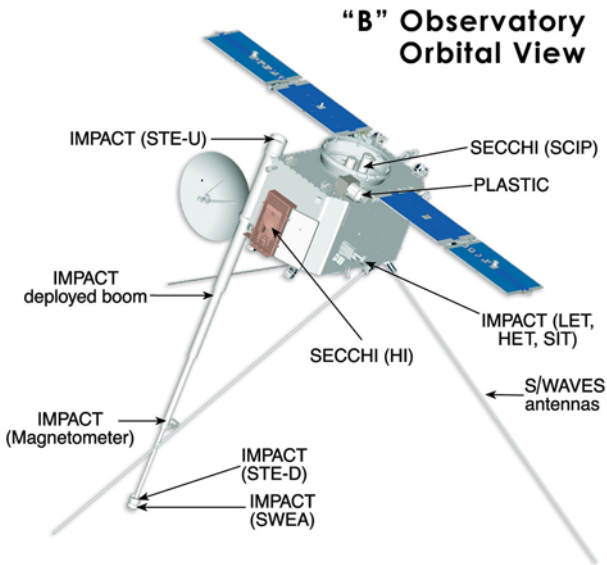
Instrument	Acronym	Purpose
SECCHI	COR1	Coronagraph 1.4–4.0 solar radii
	COR2	Coronagraph 2–15 solar radii
	EUVI	Extreme ultraviolet imager
	HI	Heliospheric imager 12 → 215 solar radii
IMPACT	SWEA	Solar wind electrons to 3 keV
	STE	Suprathermal electrons 2–100 keV
	SEPT	Electrons 20–400 keV; protons 60–7,000 keV
	SIT	Composition He–Fe 300–2,000 keV/nucleon
	LET	Protons, He, heavy ions to 40 MeV/nuc
	HET	Protons, He to 100 MeV; electrons to 8 MeV
PLASTIC	MAG	Vector magnetic field to 65,536 nT
	SWS	Protons, alpha dist. functions to 100 keV Heavy ions to 100 keV
	WAP	Wide angle heavy ions to 100 keV
S/WAVES	HFR	Electric field 125 kHz–16 MHz
	LFR	Electric field 2.5–160 kHz
	FFR	Fixed frequency 32 or 34 MHz
	TDS	Time domain to 250 k sample/sec

(2007) (SWEA), Lin et al. (2007) (STE), Acuña et al. (2007) (MAG) and Ulrich et al. (2007) (the boom itself). Mewaldt et al. (2007) describe the LET instrument and the computer system that controls all the SEP instruments, known as SEP central. The HET instrument is described by Von Rosenvinge et al. (2007), the SIT by Mason et al. (2007) and the SEPT by Müller-Mellin et al. (2007)

- PLASma and SupraThermal Ion Composition (PLASTIC), built by an international consortium led by Antoinette Galvin of the University of New Hampshire, provides in situ plasma characteristics of protons, alpha particles and heavy ions. It supplies key diagnostic measurements of the mass and charge state composition of heavy ions and characterizes the CME plasma from ambient coronal plasma. The PLASTIC instrument is described by Galvin et al. (2007).
- STEREO/WAVES (S/WAVES) was built by a team led by Jean-Louis Bougeret of the Observatoire de Paris. S/WAVES is an interplanetary radio burst tracker that observes the generation and evolution of traveling radio disturbances from the Sun to the orbit of Earth. As its primary sensors, S/WAVES uses three mutually orthogonal monopole antenna elements, each six meters in length. The three monopoles were deployed anti-sunward so that they remain out of the fields of view of Sun-facing instruments. The S/WAVES instrument is described by Bougeret et al. (2007) There are two companion papers describing the S/WAVES antennas (Bale et al. 2007) and the radio direction finding technique (Cecconi et al. 2007)

Table 2 gives more details about these instrument suites and Fig. 2 shows the “behind” spacecraft with the instrument locations indicated. The spacecraft themselves are relatively small, with a combined mass of about 1,280 kg, including maneuvering fuel (see Dreisman et al. 2007).

Fig. 2 An artist's conception of the Behind spacecraft with the locations of the instruments shown. The SECCHI instruments point at the Sun and the IMPACT boom and S/WAVES antennas are on the opposite end. There are very slight differences between the Ahead and Behind spacecraft, mainly due to the fact that the spacecraft fly upside down relative to one another so that their high-gain antenna is always on the Earth-facing side of the spacecraft. This means that some of the particle instruments which need to point into the solar wind magnetic field direction have different placements on the two spacecraft



In addition to these four instrument teams, there are several groups devoted to global modeling (see Aschwanden et al. 2007) with the goal of understanding the connection between the solar activity observed near the sun by SECCHI and S/WAVES and the in situ measurements taken by IMPACT, PLASTIC and S/WAVES when the disturbances finally reach the STEREO spacecraft. Modeling includes the coronal plasma and the solar wind and its expansion outwards from the Sun. Modeling of dynamic phenomena associated with the initiation and propagation of coronal mass ejections (CMEs) will be given particular emphasis. The modeling of the CME initiation includes magnetic shearing, kink instability, filament eruption and magnetic reconnection in the flaring lower corona. The modeling of CME propagation entails interplanetary shocks, interplanetary particle beams, solar energetic particles (SEPs), geoeffective connections and space weather.

5 The STEREO Orbits and Mission Phases

During the formulation stage of STEREO, scientists from the instrument teams and mission analysts discussed several different mission designs, including drift rates and formations (e.g., both ahead of Earth, both behind, or ahead/behind) for the two spacecraft. Although valid arguments existed for other formations, the selected mission design featured one spacecraft leading the Sun–Earth line while the other lagged. Likewise, scientific arguments for “slow” drift rates (e.g., a few degrees separation per year) and for “fast” drift rates (e.g., >45 degrees per year) were considered, and an optimum mean rate of ± 22 degrees per year (with an uncertainty of ± 2 degrees per year) was selected as the requirement. An additional goal was to minimize the eccentricity of the heliocentric orbits in order to minimize the variation in solar diameter as viewed from the spacecraft, an important consideration for the SECCHI coronagraph occulters. The STEREO orbits are described in detail by Dreisman et al. (2007).

There is no single angular spacing that is best for all STEREO instruments and science goals. The SECCHI coronagraphs best detect coronal features when they are relatively near the plane of the sky as viewed from each spacecraft. This would imply that an overall angle

of at least 60° would be best. On the other hand, stereoscopic measurements of small features like loops visible in the SECCHI extreme ultraviolet imager can only be made with small angular separations between the spacecraft, approximately 3–4° to perhaps 20°. Triangulation on radio emissions from Earth-directed CME-driven shock fronts would be most accurate in the 60–90° separation range. The in situ instruments have a scientific interest in having both spacecraft at different positions inside the same magnetic cloud, which would argue for separation angles less than 50°.

Because of these scientific considerations and the final orbit selections where the spacecraft are continually separating, the mission has four distinct phases. Phase 1 occurs approximately the first year when the spacecraft are less than 50° apart when the configuration is optimum for making high cadence 3-D images of coronal structures. Stereoscopic image pairs and sequences will capture the 3-D of the corona before, during and after CMEs. It is also during phase 1 that intercalibrations between like instruments on the two spacecraft are possible.

Phase 2 is centered on quadrature between the two spacecraft with separations between 50° and about 110°, corresponding to days 400 to 800. During this interval, triangulation on CMEs is optimal. It is also quite likely that one spacecraft will be able to observe a CME in the plane of the sky that actually impacts the other spacecraft, thereby linking characteristics of a CME (composition, magnetic field orientation density and velocity at 1 AU) with its launch and propagation parameters (size, velocity and source region characteristics).

Phase 3 (and 4) corresponding to days 800 to 1,100 would occur during an extended mission period, since the STEREO prime mission is only two years after reaching heliocentric orbit. During phase 3, the spacecraft are at angles from 110 to 180 degrees and are both able to view Earth-directed CMEs in the plane of the sky. The two spacecraft will also have a nearly complete view of the sun, allowing the longitudinal extent of CMEs and other activity to be measured.

Beyond the 180° point (phase 4), events on the far side of the sun that launch particles toward Earth will be visible for the first time. Active regions can be tracked and studied for their eruptive potential from their emergence, wherever it occurs on the Sun. The results will have a tremendous impact on our ability to anticipate changes in solar activity and to predict changes in space weather conditions. Such predictive capability is vital if we are to build permanent lunar bases or send astronauts to Mars.

6 STEREO Data and the STEREO Science Center

Transmission of the complete data stream to ground is conducted via NASA's Deep Space Network (DSN). The data are then sent to the Mission Operations Center at APL which distributes it to the instrument teams and STEREO Science Center (see below). Each instrument has an allocated telemetry rate during DSN real-time contacts, which occur for each spacecraft once daily during regular operations. When the spacecraft are out of contact, instrument telemetry is written to a solid state recorder and down linked during subsequent contact period.

Launched in late 1995, SOHO, a joint ESA/NASA science mission, demonstrated that the onset of Earth-directed CMEs could be detected routinely from a space-based platform. An informal channel between NOAA's Space Environment Center and the SOHO science operations team at GSFC was opened in 1996 for the purpose of communicating activity seen in EIT (Delaboudiniere et al. 1995) and in the LASCO coronagraphs (Brueckner et al. 1995). With the passage of time and the efforts of researchers, the utility of these observations was clearly demonstrated, and the space weather forecasting community embraced

the idea that eruptions at the Sun could be detected and their initial journey into the interplanetary medium tracked. Because of this success with SOHO, the two STEREO spacecraft augment their daily full-resolution data downloads with the broadcast continuously a low rate (~ 600 bps) set of data consisting of typically one-minute summaries (or several minute in the case of SECCHI) to be used for space weather forecasting (see Biesecker et al. 2007). Several participating NOAA and international ground-tracking stations will collect the data and send it electronically to the STEREO Science Center (see below) where they are processed into useful physical quantities and placed on the public and scientific STEREO Web pages.

The STEREO Science Center (SSC) serves as the central facility responsible for telemetry distribution and archiving and other central functions, such as long-term science planning and coordination with the science teams (see Eichstedt et al. 2007) and the central node for education and public outreach activities (see Peticolas et al. 2007). The SSC is also responsible for the receipt and processing of the real-time Space Weather data. The SSC is the principal interface with the scientific community and the public at large. Two Web sites are maintained. For the general public, the site is:

<http://stereo.gsfc.nasa.gov>.

For the scientific research community, the site is:

<http://stereo-ssc.nascom.nasa.gov>.

Additionally, NASA Headquarters hosts a site

<http://www.nasa.gov/stereo>

that contains the press releases and other announcements and graphics of wide interest.

It is the policy on the STEREO Project that all data be available within as short a time as possible. The space weather data will be available from the SSC in near real time and the daily instrument data files should start becoming available within 24 hours of ground receipt and finalized with about one month of ground receipt. Higher level data products will be made available as they are produced.

7 Summary

The STEREO mission will move space-based observations of the Sun to the next logical step, the ability to make 3-D measurements. During the early portion of the STEREO mission, many existing spacecraft near Earth—such as SOHO, Wind and ACE—should also still be operating as well as the Hinode spacecraft, launched the same year as STEREO (2006). Also in geospace, there are new additions to the existing fleet such as the recently launched THEMIS to study effects in Earth’s magnetosphere. Thus, there is an impressive fleet of spacecraft dedicated to solar observations and we predict that this era will become an extremely productive period in our understanding of our Sun and its connections to Earth.

References

- M.H. Acuña et al., Space Sci. Rev. (2007, this issue). doi:[10.1007/s11214-007-9259-2](https://doi.org/10.1007/s11214-007-9259-2)
- M. Aschwanden et al., Space Sci. Rev. (2007, this issue). doi:[10.1007/s11214-007-9224-0](https://doi.org/10.1007/s11214-007-9224-0)
- S.D. Bale et al., Space Sci. Rev. (2007, this issue). doi:[10.1007/s11214-007-9251-x](https://doi.org/10.1007/s11214-007-9251-x)
- D. Biesecker, D. Webb, O.C. St. Cyr, Space Sci. Rev. (2007, this issue). doi:[10.1007/s11214-007-9165-7](https://doi.org/10.1007/s11214-007-9165-7)

- V. Bothmer, B.H. Foing (Conveners), European Geophysical Soc. Symp. ST 8A, The Hague, Netherlands, 1996
- J.-L. Bougeret et al., Space Sci. Rev. (2007, this issue)
- G.E. Brueckner et al., Sol. Phys. **162**, 357–402 (1995)
- B. Cecconi et al., Space Sci. Rev. (2007, this issue). doi:[10.1007/s11214-007-9255-6](https://doi.org/10.1007/s11214-007-9255-6)
- B.E. Chebotarev, V.M. Grigoryev, V.S. Konovalov, P.G. Papushev, G.R. Uspensky, Phys. Chem. Earth **22**, 445–449 (1997)
- J.M. Davila, Goddard Space Flight Center Report, 1994a
- J.M. Davila, Astrophys. J. **423**, 871 (1994b)
- J.M. Davila, D.M. Rust, V. Pizzo, P.C. Liewer, Missions to the Sun. SPIE Proceedings, 2804 (1996)
- J.P. Delaboudiniere et al., Sol. Phys. **162**, 291–312 (1995)
- A. Dreisman, S. Hynes, G. Cancro, Space Sci. Rev. (2007, this issue)
- J. Eichstedt, W. Thompson, O.C. St. Cyr, Space Sci. Rev. (2007, this issue). doi:[10.1007/s11214-007-9249-4](https://doi.org/10.1007/s11214-007-9249-4)
- V.M. Grigoryev, Sol. Phys. **148**, 386–391 (1993)
- A.B. Galvin et al., Space Sci. Rev. (2007, this issue)
- J. Galloway, Mission study report, Goddard Space Flight Center, Greenbelt, MD, 1998
- V. Grigoryev, P. Papushev, V. Chebatorev, V. Kosenko, G. Uspensky, V. Konovalov, SPIE Proc. **2804**, 90–94 (1996)
- R.A. Howard et al., Space Sci. Rev. (2007, this issue)
- P.C. Liewer et al., *Stereo X-Ray Corona Imager Mission* (Jet Propulsion Lab, Pasadena, 1998)
- R.P. Lin et al., Space Sci. Rev. (2007, this issue)
- J.G. Luhmann et al., Space Sci. Rev. (2007, this issue). doi:[10.1007/s11214-007-9170-x](https://doi.org/10.1007/s11214-007-9170-x)
- G.M. Mason et al., Space Sci. Rev. (2007, this issue). doi:[10.1007/s11214-006-9087-9](https://doi.org/10.1007/s11214-006-9087-9)
- R.A. Mewaldt et al., Space Sci. Rev. (2007, this issue)
- R. Müller-Mellin, S. Böttcher, J. Falenski, E. Rode, Space Sci. Rev. (2007, this issue). doi:[10.1007/s11214-007-9204-4](https://doi.org/10.1007/s11214-007-9204-4)
- L.M. Peticolas et al., Space Sci. Rev. (2007, this issue)
- V. Pizzo (ed.), SPINS—Special Perspective Investigations. SEL Workshop Report, NOAA Space Env. Lab. Boulder, CO, 1994
- B. Rowley, Solar STEREO (Solar Terrestrial Relations Observatory), Team X Rept., Jet Propulsion Lab, Pasadena, CA, 1997
- D. Rust et al., The Heliosphere in Three Dimensions. Report of the Science Definition Team, Johns Hopkins Applied Physics Lab, Laurel, MD, 1997
- J.-A. Sauvaud et al., Space Sci. Rev. (2007, this issue). doi:[10.1007/s11214-007-9174-6](https://doi.org/10.1007/s11214-007-9174-6)
- W.K.H. Schmidt et al., LEGRANGE—The Sun and Inner Heliosphere in Three Dimensions. A proposal to ESA, Lindau, Germany, 1993
- W.K.H. Schmidt, V. Bothmer, Adv. Space Res. **17**, 369 (1995)
- J.G. Timothy, A.M. Hamza, L. Mayer, D. Knudsen, J.S. Murphree, E.J. Llwelllyn, R.P. Lowe, I.C. McDade, R.W. Nicholls, J.M. Davila, R.B. Hoover, M.C.E. Huber, G. Tondello, A.B.C. Walker, Tomography of Solar and Auroral Plasmas. Proposal to Canadian Space Agency, 1996
- R. Ulrich et al., Space Sci. Rev. (2007, this issue)
- T.T. Von Rosenvinge et al., Space Sci. Rev. (2007, this issue)
- J. Watzin, J. Davila, *Solar Terrestrial Relations Observatory (STEREO) Mission Concept* (Goddard Space Flight Center, Greenbelt, 1997)

The STEREO Observatory

Andrew Driesman · Shane Hynes · George Cancro

Originally published in the journal Space Science Reviews, Volume 136, Nos 1–4.
DOI: [10.1007/s11214-007-9286-z](https://doi.org/10.1007/s11214-007-9286-z) © Springer Science+Business Media B.V. 2007

Abstract The Solar Terrestrial Relations Observatory (STEREO) is the third mission in NASA’s Solar Terrestrial Probes program. The mission is managed by the Goddard Space Flight Center (GSFC) and implemented by The Johns Hopkins University Applied Physics Laboratory (JHU/APL). This two-year mission provides a unique and revolutionary view of the Sun–Earth system. Consisting of two nearly identical observatories, one ahead of Earth in its orbit around the Sun and the other trailing behind the Earth, the spacecraft trace the flow of energy and matter from the Sun to Earth and reveal the three-dimensional structure of coronal mass ejections (CMEs) to help explain their genesis and propagation. From its unique side-viewing vantage point, STEREO also provides alerts for Earth-directed solar ejections. These alerts are broadcast at all times and received either by NASA’s Deep Space Network (DSN) or by various space-weather partners.

Keywords STEREO · Coronal mass ejections · Solar-terrestrial relations · Heliocentric orbit · Heliospheric science

1 Introduction

The two Solar Terrestrial Relations Observatories (STEREO) were launched on a Boeing Delta II 7925-10L launch vehicle from the Cape Canaveral Air Force Station on October 26, 2006, at 00:52 UTC. Shown in the launch vehicle fairing in Fig. 1, the spacecraft were designated “Ahead” (A) and “Behind” (B) based on their relative position to the Earth while in their heliocentric orbits. To achieve their mission, observatory A, shown in Fig. 2 at the launch site integration facility, has a shorter orbital period than the Earth

A. Driesman (✉) · G. Cancro
The Johns Hopkins University Applied Physics Laboratory, 11100 Johns Hopkins Road, Laurel,
MD 20723-6099, USA
e-mail: andrew.driesman@jhuapl.edu

S. Hynes
Stellar Solutions, Inc., 250 Cambridge Avenue, Suite 204, Palo Alto, CA 94306, USA

Fig. 1 The twin observatories stacked for launch on a Delta II 7925-10L launch vehicle. One fairing half is installed



and hence drifts ahead of the Earth at an average rate of approximately 22° per year. Correspondingly, observatory B has a longer orbital period than the Earth and thus lags the Earth with a similar drift rate. The actual drift rates achieved were $+21.650^\circ$ per year for Ahead and -21.999° per year for Behind. These drift rates were chosen as a compromise between in situ instrument science team members who desired both spacecraft to spend time within a single coronal mass ejection (CME) and imaging instrument science team members who wanted to quickly achieve the separation necessary to produce three-dimensional images.

To meet full mission success, each STEREO observatory is required to meet performance requirements for two years after both observatories reach heliocentric orbit. To achieve minimum mission success, both STEREO observatories are required to meet performance requirements for 150 days (after reaching heliocentric orbit), with either observatory meeting performance requirements for an additional 530 days. Each spacecraft bus is required to carry sufficient propellant to last five years.

2 Orbital Characteristics

The heliocentric orbit of the two STEREO observatories is shown in an inertial frame of reference in Fig. 3a; the geocentric solar ecliptic (GSE) frame is shown in Fig. 3b. These two views of the orbital dynamics of the spacecraft illustrate their relative motion within the

Fig. 2 Observatory A at Astrotech in Titusville, FL, shown prior to its final blanketing. The observatory's battery is shown at the top center of the image, and the star tracker aperture is shown at the bottom



Earth–Sun system that allows them to achieve the stereoscopic view of the Sun and CMEs at various scales and geometries. Specifically, the inertial frame shows the size differences of the semimajor axes that result in the relative movement of the two observatories with respect to the Earth and each other. The perihelion of observatory B is equivalent to the Earth's radius, whereas conversely the aphelion of observatory A is equivalent to the Earth's radius. This, combined with the eccentricity of the Earth's orbit, results in the variations in the drift rate throughout the year, as shown in the GSE coordinate system of Fig. 4. Also clearly illustrated by the GSE coordinate system view of the spacecraft in Fig. 3b is the relative location of the spacecraft with respect to the Earth while viewing the Sun. Figure 4 details the integrated Sun–Earth–Probe angle through the life of the mission based on the nominal prelaunch 22° per year drift rate for the spacecraft.

2.1 Phasing Orbit Characteristics

The mission design team at The Johns Hopkins University Applied Physics Laboratory (JHU/APL) developed an innovative orbit design with multiple lunar gravity assists to place

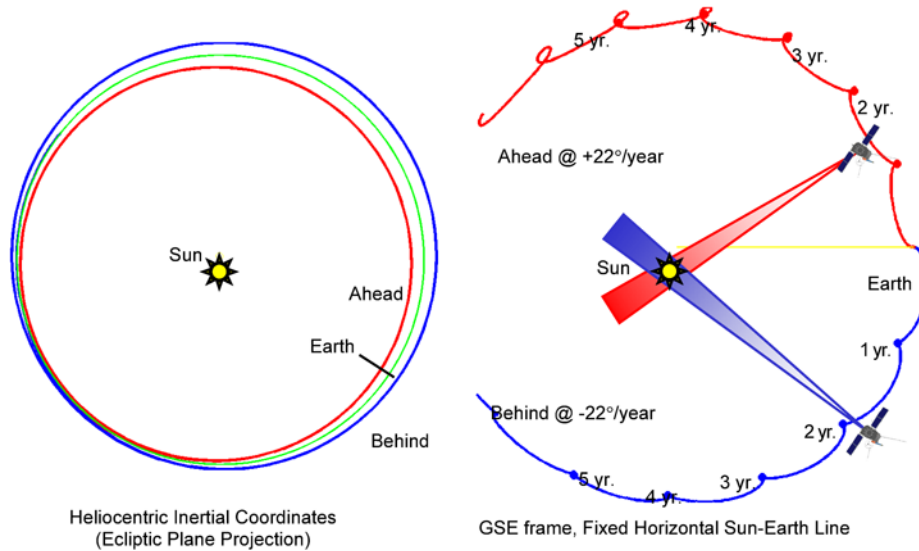


Fig. 3 (a) The two observatory orbits projected onto the ecliptic plane. The projection shows the relative eccentricities of the orbits. (b) The same projection is shown but with a fixed Earth–Sun line. This figure shows the evolution of the relative geometries over the life of the mission

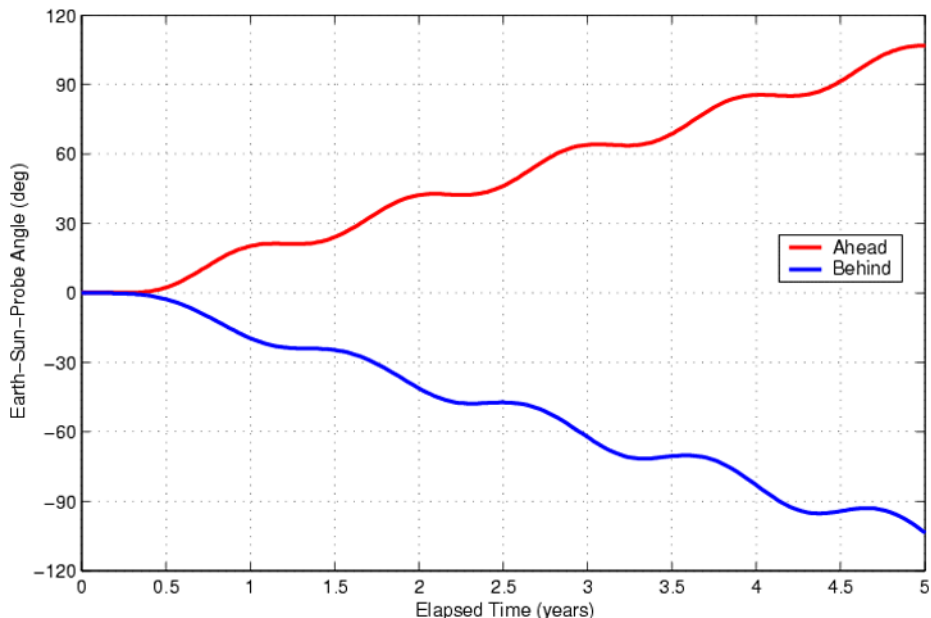


Fig. 4 The graph shows the relative drift rates of the two observatories based on the prelaunch drift rates of 22° per year for observatory A and -22° per year for observatory B

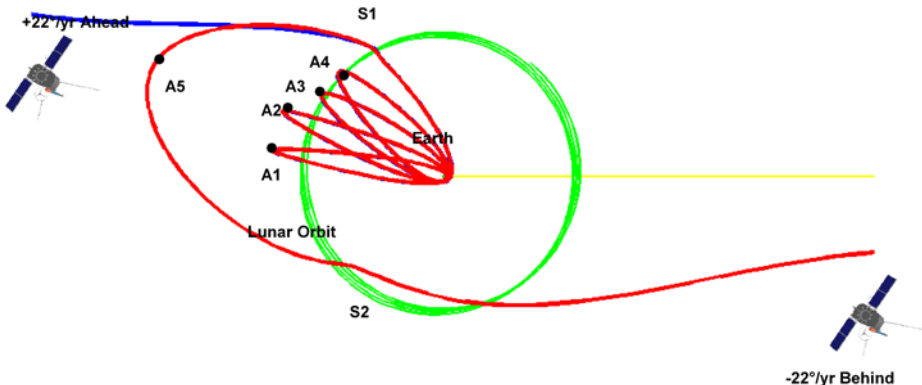


Fig. 5 Illustrated are the phasing orbits of the two observatories. Observatory A was ejected into heliocentric orbit after spending 52 days in Earth orbit. Observatory B re-encountered the Moon 38 days later and was ejected into a trailing orbit

both spacecraft in their respective heliocentric orbits. This unique design allowed the two observatories, which had drastically different orbital requirements, to be launched on a single launch vehicle. Figure 5 shows a series of phasing orbits in the GSE frame with apogees denoted as $A1$ – $A4$. A series of propulsive maneuvers at events $A1$, $P1$, $A2$, $P2$, $A4$, $S1+$, and $A5+$ were used to adjust the trajectories to achieve the required lunar swing-by distances. These phasing orbits provided time to position the two observatories on slightly different trajectories at the first lunar swing-by (denoted as $S1$ in Fig. 5). By virtue of the lunar swing-by, observatory A gained sufficient energy to be ejected from the Earth–Moon system and to achieve the required heliocentric orbit. The $S1$ event imparted enough energy to observatory B to place it in a higher elliptical orbit, thus re-encountering the Moon for a second lunar swing-by (denoted as $S2$ in Fig. 5) approximately 40 days after the $S1$ event. The $S2$ event ejected observatory B into a heliocentric orbit with a larger semimajor axis and therefore a drift rate lagging the Earth. A further propulsive maneuver was added after launch to refine the trajectory when it was realized that the Behind observatory trajectory could be positioned such that a lunar transit would occur on February 25, 2007. The lunar transit is used by the Extreme Ultra-Violet Imager (EUVI) in the Sun–Earth Connection Coronal and Heliospheric Investigation (SECCHI) suite as a means of understanding the stray-light performance of the instrument. The Moon essentially blocks out all light from the Sun, thus any UV light appearing on the area of the EUVI charge-coupled device that is occulted by the Moon is stray light. This knowledge is used to update the EUVI calibration data.

To support the various maneuvers needed to properly position the spacecraft, an initial estimate of 180 m/s delta velocity (ΔV), equivalent to approximately 62 kg of hydrazine propellant, was used to determine the size of the propulsion system on each observatory. Driving the ΔV requirement was the need to support a monthly launch window of two weeks and a daily launch window of 15 minutes per day. Accommodating these launch windows and supporting the 3σ launch dispersions associated with the Delta II sized the ΔV requirement. The actual launch time occurred in the middle of the monthly launch window and at the end of the daily window. The launch vehicle dispersions were very low, thus each observatory achieved their heliocentric orbits with 43 kg of propellant.

2.2 Instrument Accommodations

The STEREO instrument suite initially was challenging to accommodate because it encompassed optical, particle, and electromagnetic wave instruments, each with their own set of unique requirements. For example, the optical instruments required very low jitter and extreme cleanliness, whereas the particle instruments required large unobstructed fields of view and electrostatic cleanliness, and the STEREO/Waves (SWAVES) instrument required extreme electromagnetic cleanliness. This section provides details on the primary drivers that the instruments imposed on the overall observatory design.

The instrument integration challenge is further illustrated by Table 1, which shows the fields of view and boresight of the various instruments. The final spacecraft and instrument payload design was a result of extensive technical trades. With the exception of some minor compromises, all field-of-view requirements were satisfied. An early instrument accommodation study resulted in dividing the Supra-Thermal Electron (STE) instrument into two: STE-Upstream (STE-U) mounted on the $+X$ (Sun-pointing) end of the boom and a STE-Downstream (STE-D) mounted toward the end of the boom. The High-Energy Telescope (HET), Low-Energy Telescope (LET), and Solar Electron Proton Telescope (SEPT) instruments are mounted in different orientations on the two spacecraft to allow their respective boresights to point in the direction of the Parker spiral. See Fig. 6 for illustration of the instrument configuration of spacecraft B.

The SECCHI Sun-Centered Imaging Package (SCIP) instruments have stringent pointing and jitter requirements. A detailed discussion of these requirements can be found in Sect. 4.2. The In-situ Measurements of Particles and CME Transients (IMPACT) booms, SWAVES antennae, and solar arrays all have fundamental frequencies that could affect the pointing and jitter requirements.

The combination of the particulate requirements from the coronagraphs and the condensable and hydrocarbon requirements from the EUVI instrument levied stringent contamination requirements on all the instruments, spacecraft, and processing facilities. The observatories' external surfaces had a specification of 300A at the time of launch, where "300" refers to the number of allowable particles of a given size per square foot and "A" refers to the amount of allowable nonvolatile residue deposited on a surface, with "A" being equal to one $\mu\text{g}/\text{cm}^2$ of deposition (Department of Defense 1994). The internal surfaces of the instruments had requirements ranging from 200A/3 to 100A/5. A contamination committee consisting of members from JHU/APL, the Naval Research Laboratory, University of California–Berkeley, University of New Hampshire, and the University of Minnesota met repeatedly throughout the program to plan and implement the contamination control plan. All of the spacecraft bus and instrument fabrication facilities were class 10,000, and any time the coronagraphs were opened to the environment was class 1,000. The facilities at JHU/APL, Goddard Space Flight Center (GSFC), Astrotech, and launch complex 17 were cleaned thoroughly and repeatedly during the integration and testing program. At the time of launch, the spacecraft external surfaces and internal surfaces had achieved their cleanliness requirements.

The Solar Wind Electron Analyzer (SWEA) instrument necessitated a requirement to have the spacecraft body at a uniform and low electrical potential with respect to the plasma. To meet this requirement, all observatory surfaces, with the exception of the solar arrays, were required to be conductive, less than $10^{-8} \Omega/\text{square}$. The Sun-facing surfaces of the spacecraft were covered with indium-tin-oxide (ITO)-coated silver Teflon thermal blankets. ITO has a surface conductivity of approximately $10^{-5} \Omega/\text{square}$, and its surface is perforated with small ITO-plated through-holes to the silver backing material. This design provided a robust connection between the delicate ITO on the front surface and the backing

Table 1 Instrument field-of-view accommodations

STEREO Science Instrument	Field of View (FOV)	Component boresight orientation
SECCHI		
SCIP	8° Cone (w/180° Clear FOV)	Sun-Pointing
HI*	85° Cone (w/183° Clear FOV Tilted 1.5° Along –Z Axis)	90° to Sun–Earth Line
IMPACT		
SWEA	130° × 360° Annular Shape	Boom-Mounted, Anti-Sun
STE	80° × 80° Fan Shape into Ecliptic (East & West)	Boom-Mounted, Anti-Sun
MAG	N/A	Boom-Mounted, Anti-Sun
SEP		
LET		
Earth Behind Observatory	100° × 30° Fan Shape into Ecliptic (East & West)	50° to Sun–Spacecraft Line
	130° × 30° Fan Shape into Ecliptic (East & West) Goal	
Earth Ahead Observatory	100° × 30° Fan Shape into Ecliptic (East & West)	50° to Sun–Spacecraft Line
	130° × 30° Fan Shape into Ecliptic (East & West) Goal	
HET		
Earth Behind Observatory	50° Full Cone into Ecliptic (East & West)	45° to Sun–Spacecraft Line
	60° Full Cone into Ecliptic (East & West) Goal	
Earth Ahead Observatory	50° Full Cone into Ecliptic (East & West)	45° to Sun–Spacecraft Line
	60° Cone into Ecliptic (East & West) Goal	
SEPT-E		
Earth Behind Observatory	45° Full Cone in Ecliptic (East & West)	45° to Sun–Spacecraft Line
	52° Cone into Ecliptic (East & West) Goal	
Earth Ahead Observatory	45° Full Cone in Ecliptic (East & West)	45° to Sun–Spacecraft Line
	52° Cone into Ecliptic (East & West) Goal	
SEPT-NS		
Earth Behind Observatory	52° Cone Perpendicular to Ecliptic (North & South)	90° to Sun–Spacecraft Line
Earth Ahead Observatory	52° Cone Perpendicular to Ecliptic (North & South)	90° to Sun–Spacecraft Line
SIT		
Earth Behind Observatory	44° × 17° Rectangular Shape into Ecliptic (West)	45° to Sun–Spacecraft Line
Earth Ahead Observatory	44° × 17° Rectangular Shape into Ecliptic (West)	45° to Sun–Spacecraft Line

Table 1 (Continued)

STEREO Science Instrument	Field of View (FOV)	Component boresight orientation
PLASTIC		
Solar Wind Sector Main	$55^\circ \times \pm 20^\circ$ Fan Shape (clear FOV)	Sun-Pointing
Solar Wind Sector Proton	$55^\circ \times \pm 20^\circ$ Fan Shape	Sun-Pointing
Wide-Angle Partition	$250^\circ \times \pm 7^\circ$ Fan Shape	In Ecliptic Non-Sunward
SWAVES	Three Mutually Orthogonal Antenna Elements	Anti-Sun

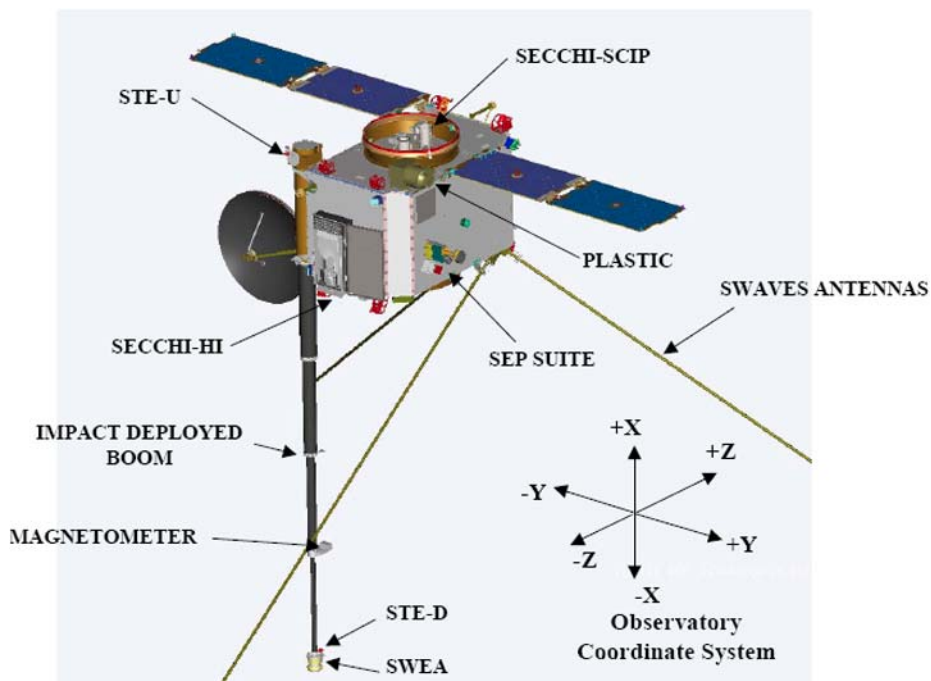


Fig. 6 Illustration of spacecraft B in its deployed configuration. For scale, the large vertical boom (IMPACT boom) is approximately 6 m long

material, which is connected to the spacecraft structure with redundant wires. After a design analysis, it was determined that the solar array cover-glass did not need to be conductive. The electrostatics of the observatory, including the solar array, were modeled. It was found that, due to the deposition of photoelectrons and the distance of the most sensitive electron instruments, the buildup of charge on the solar array was acceptable. With small exceptions (optical apertures and star tracker lens), the remainder of the spacecraft's outer surface was covered with conductive black Kapton thermal blanket, with a conductivity of less than $10^8 \Omega/\text{square}$. Special attention was paid to shaded surfaces, which could not be discharged by photoelectrons. For example, with the exception of apertures, no nonconducting surfaces were allowed on shaded portions of the spacecraft.

The SWAVES instrument drove the observatory electromagnetic compatibility (EMC) requirements. An EMC committee with members from all the critical institutions was chartered early in the program to generate design and test requirements for all flight hardware. The approach to controlling electromagnetic emissions had several facets, including shielding, twisted-pair wiring, use of differential circuits, and control of primary and secondary grounds. Even with stringent controls, it was understood early that the largest source of noise on the observatories would be the switching power supplies found in almost every electronics box. Rather than try to (overly) control the conducted and radiated noise from these supplies (a costly effort), control instead was placed over the switching frequency. Power supplies were required to switch at a frequency of 50 kHz (± 1 part in 10,000) or a harmonic thereof. This novel approach limited the bulk of the electromagnetic noise to narrow bands, which allowed the SWAVES instrument to tune its receiver bands (starting at 100 kHz) in between the “noisy” bands. In addition to control, a stringent test program was put in place that ensured compliance with the radiated and conducted emissions requirements, which in some places were 20 dB below MIL-STD-461 requirements (Department of Defense 1999). All observatory hardware was screened individually. Once the hardware was integrated into an observatory, each observatory went through radiated and conducted compatibility testing. Compatibility testing was used rather than standard emissions testing because the SWAVES instruments were, in general, more sensitive than the receivers used to conduct the emissions testing.

2.3 Instrument Data Volume

Each observatory has five imaging instruments: EUVI, Coronagraph 1 (COR1), Coronagraph 2 (COR2), Heliospheric Imager 1 (HI-1), and Heliospheric Imager 2 (HI-2). These imagers are capable of producing images at a rate that would be impossible to bring to the ground, which when coupled with the Earth–observatory distances approaching 0.8 AU generated a series of early trade studies aimed at maximizing the data volume brought down to the ground via the Deep Space Network (DSN). The trade studies were used to size the spacecraft’s communications system, the level of image compression, the size of ground antennas used, the duration of ground tracks, the size of the onboard solid-state recorder (SSR), the interfaces between the imagers and the spacecraft bus, and the software used to communicate between the two. The resulting requirement was to bring down 5 Gbits of data per day averaged over a 12-month period. To account for normal outage (e.g., DSN station outages), the system was designed to bring down 6.2 Gbits per day. Table 2 shows the baseline design.

Table 2 Instrument downlink data rates and resulting average daily volumes

Instrument	Average data rate (kbps) ^a			Average daily data volume (Mbits)		
	Months 0–14	Months 15–18	Months 19–24	Months 0–14	Months 15–18	Months 19–24
SECCHI	54.888	50.727	46.239	4,742	4,383	3,995
IMPACT	3.274	3.590	3.274	283	310	283
SWAVES	2.074	2.272	2.074	179	196	179
PLASTIC	3.274	3.590	3.274	283	310	283

^aIncluding space-weather data and packet primary and secondary header overhead

3 Spacecraft Bus Overview

The development of the twin STEREO spacecraft commenced in 1999 and culminated with its launch on October 26, 2006. Because of cost constraints, the observatories were designed from initial concept to be as identical as possible. The only significant differences were in the positioning of some of the IMPACT instruments (to allow better view angles of the Parker spiral), primary structure (the bottom spacecraft structure was more robust to support the weight of the top spacecraft), guidance and control parameters (e.g., as a result of different mass properties), and thermal design (radiators on Observatory B were smaller). All other subsystems, including flight software and their interrelations, were identical.

Each observatory is a three-axis-stabilized platform that, with the exception of propulsive maneuvers, operates with the fixed solar arrays and pointing at the Sun. Each observatory has 16 distinct instruments, each with its own set of diverse requirements. The wet mass at launch of Observatory A was 623 kg, Observatory B weighed 658 kg. Of this mass, approximately 62.4 kg was expendable (hydrazine and GHe₂). The power subsystem of each spacecraft is capable of producing 716 W of power, beginning of (solar array) life at a worst-case distance of 1.089 AU from the Sun. Each observatory uses a maximum of 641 W during maneuvers, with normal science operations consuming about 400 W. The system is capable of transmitting 720 kbps of data, resulting in a maximum science data capture capability of 6.2 Gbits per day.

3.1 Observatory Architecture

The STEREO spacecraft architecture was originally conceived at JHU/APL as a build-to-print follow-on of the Thermosphere, Ionosphere, Mesosphere, Energetics and Dynamics (TIMED) spacecraft (Driesman et al. 2001). Because the cost-capped STEREO mission required two observatories, it had been planned that a single side of the redundant TIMED spacecraft would serve as the avionics for the single-string STEREO observatory. However, because of the long STEREO phase A/B, it became clear that the TIMED designs would be difficult to support, so a decision was made to abandon the TIMED designs in favor of the Mercury Surface, Space Environment, Geochemistry, and Ranging (MESSENGER) spacecraft designs.

It was well understood that simply using a single side of the redundant MESSENGER spacecraft would create numerous potential single-point failures within STEREO. As the STEREO observatory designers studied this MESSENGER extraction, it was noted that it would be possible to parse functionality (rather than physicality) while maintaining the MESSENGER hardware, thus making it more robust and providing limited redundancy, while still maintaining build-to-print designs. To this end, the STEREO design reallocated functionality among two processors, resulting in some processor redundancy, where the safing functionality was moved from the guidance and control processor into the command and data handling (C&DH) processor. In addition to reparsing functionality, redundancy was evaluated on a component-by-component basis. The results of the numerous architecture trades and redundancy evaluations generated the hardware architecture shown in Fig. 7, with fully redundant hardware shaded in green and partially redundant hardware shaded in gray.

The primary housekeeping and control functions of each observatory reside in two modules, the observatory's integrated electronics module (IEM) and power distribution unit (PDU). The IEM provides the C&DH and guidance and control functions, while the PDU provides power-switching functions and single-event services (e.g., pyro-actuation) as well

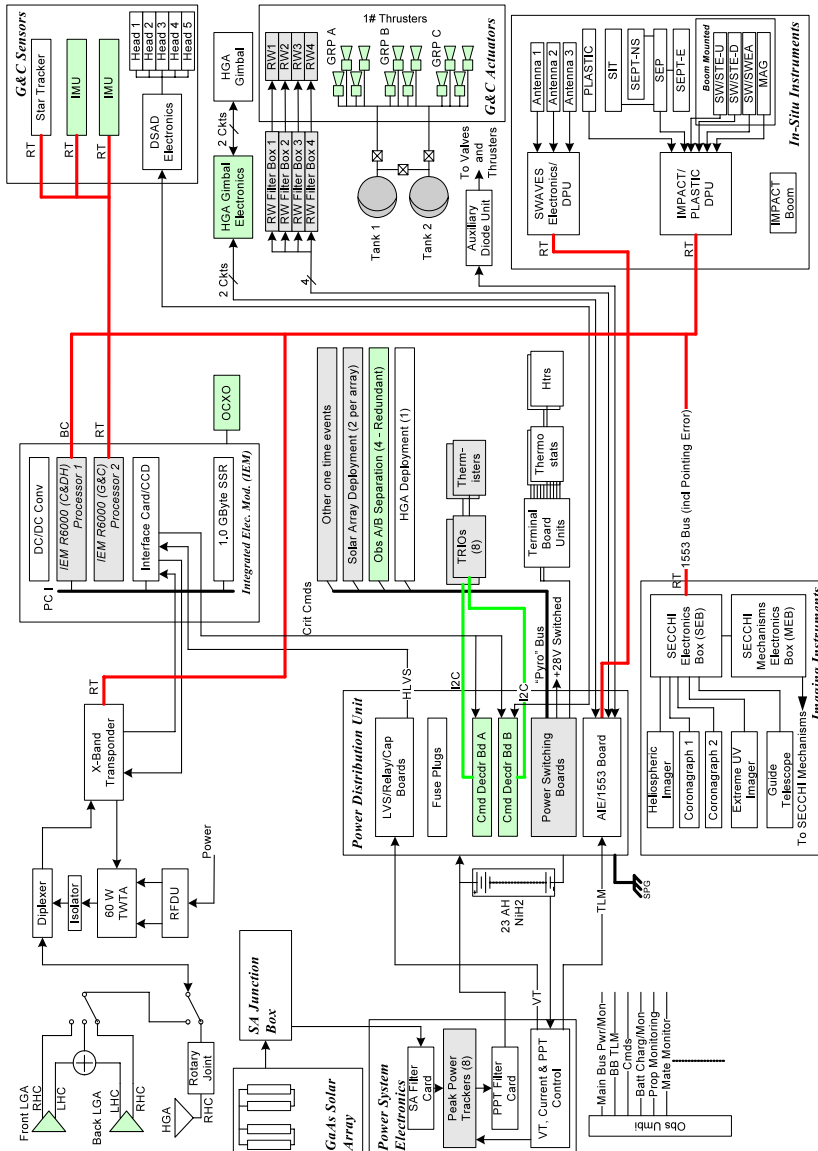


Fig. 7 System block diagram. Fully redundant hardware is shaded in green and partially redundant hardware is shaded in gray

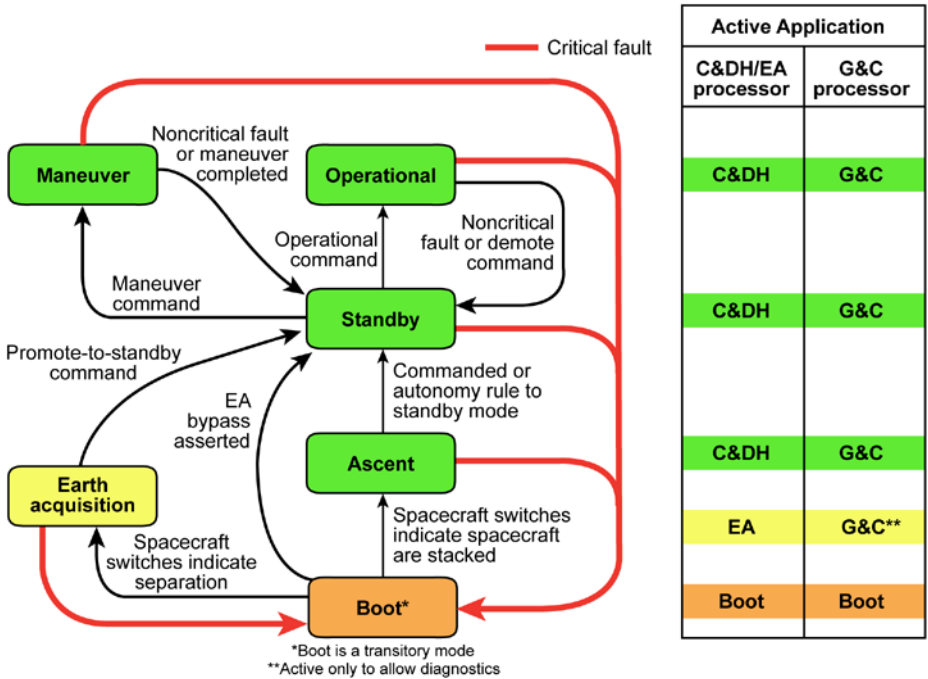


Fig. 8 Observatory mode transition diagram and software applications active during each mode. G&C, guidance and control

as serving as an interface hub for all non-MIL-STD-1553 bus guidance and control sensors and actuators.

The IEM contains two 32-bit RAD6000 processors, each operating at 25 MHz. The C&DH/Earth acquisition (EA) processor board communicates within the IEM through a peripheral component interconnect (PCI) bus. It communicates with the guidance and control processor through the MIL-STD-1553 bus (Department of Defense 1978). The primary function of the CDH/EA is handling commands/telemetry and power management. It also serves all functions, inclusive of guidance and control, when the observatory is in EA mode (safe mode). When the observatory is not in safe mode, the guidance and control processor controls the observatory's attitude, points the high-gain antenna (HGA), and handles observatory maneuvers.

The software architecture as it relates to observatory state is shown in Fig. 8. Only in EA mode is the observatory flying on a single processor. Note, in EA mode, the guidance and control processor is active purely in a self-diagnostic mode of operation. In higher modes, functionality is split between the two processors, which was necessary to meet the computationally intensive guidance and control requirements.

In addition to the processors, the IEM houses an interface card and a 1-GB Solid State Recorder (SSR). The interface card, developed at JHU/APL, provides miscellaneous interfaces (e.g., up- and down-link interface to transponder) that do not come standard with the off-the-shelf processors and SSR. In addition, the interface card houses a critical command decoder (CCD) and command loss timer (CLT). The CCD's primary function is to allow power-switching commands to be sent directly from the transponder to the power subsystem without processor intervention, which permits a subset of "critical" commands

to go through without a functioning processor. The CLT monitors command traffic from the ground and expires if the observatory has not received a command in 72 hours. Both the CLT and the hard low-voltage sense have software equivalents that are set with less stringent trip points.

3.2 Instrument Operations

An additional driver for the system that is not revealed by the previous figures is the concept of operations associated with spacecraft bus-instrument interfaces (Ossing 2001). In an effort to keep interfaces simple and straightforward, the STEREO observatory was designed around a “decoupled operations” concept. The intent of the design was to provide enough resources and degrees of freedom such that each instrument team could operate independent of spacecraft bus operations and the operations of any other instrument suite within pre-described limits. This concept drove the data system (telemetry and command) architecture into what is essentially a bent-pipe system (Fig. 9). Each payload operations center (POC) develops command sequences independent of each other. These command sequences are sent to the mission operations center (MOC), where they are relayed to the C&DH subsystem aboard each spacecraft bus, which in turn sends them on to the particular instrument suite. Likewise, science and instrument housekeeping data are relayed back to the POCs through the reverse path. With this system, neither the MOC nor the C&DH subsystem requires any knowledge of the content of the commands or the telemetry. The MOC and

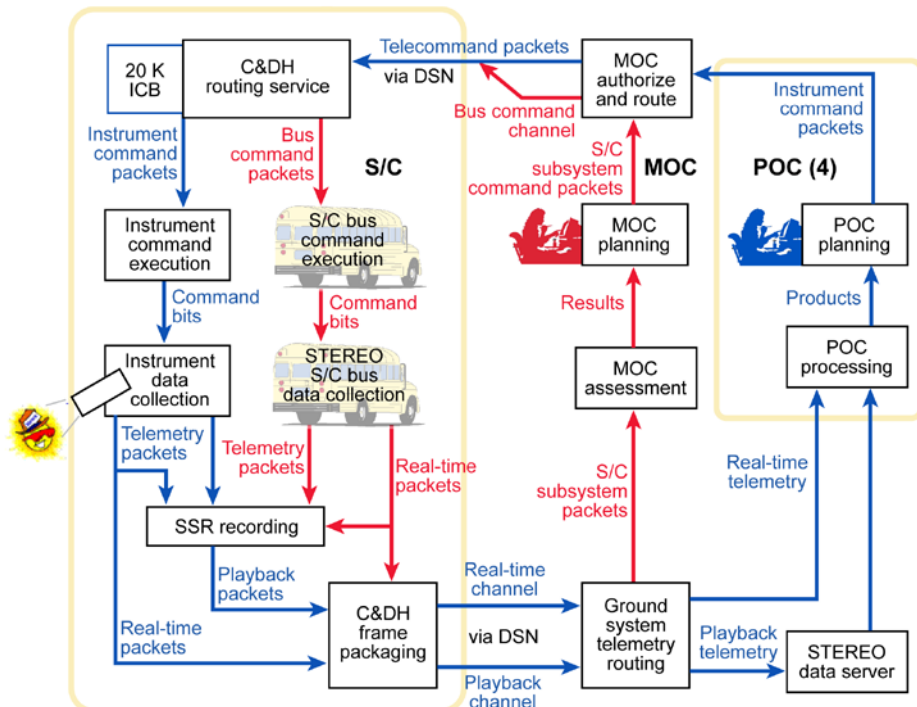


Fig. 9 Graphical representation of decoupled instrument operations. The inside loop (*in red*) shows command processing, and the external loop (*in blue*) shows telemetry processing. *S/C*, spacecraft; *ICB*, instrument command buffer.

C&DH do some validity checks on commands prior to routing them to the specific instrument. Combined instrument operations are coordinated by the STEREO Science Center and discussed with the larger team during weekly teleconferences.

From a fault-protection perspective, engineers designed (and tested) each instrument in such a way that it could not cause harm to any other instrument or the spacecraft bus. All couplings between the instruments and the spacecraft bus are handled through status data that are passed from the spacecraft bus to the instruments, and vice versa, once per second. These data include such information as pending thruster use, warnings of instrument power shutdowns, SSR% full, etc. Similarly, the instrument provides the spacecraft bus with status/request information (e.g., requests to have a power service shutdown). The STEREO-specific operational ground elements are the STEREO MOC, instrument POCs, and the STEREO Science Center. There is at least one POC for each STEREO investigation.

The POCs are responsible for the following operational tasks for all instruments:

- Planning, scheduling, and generating instrument commands
- Instrument health
- Calibration
- Synchronization of instrument operations between spacecraft.

The POCs assemble instrument command loads and transfer them to the MOC prior to a scheduled DSN track. Separate command messages are required for each spacecraft. Included as part of the command packet transfer to the MOC are certain identifying data that are used by the MOC to verify that an authorized source has generated and transferred the data. The POCs attach data that specify both the earliest and latest times that the attached command packet may be uplinked to the instrument. The MOC is responsible for the delivery of the content of the packet(s) to the addressed instrument but assumes no responsibility regarding the actual command content.

On each observatory, the shared MIL-STD-1553 data bus provides all data interfaces between the spacecraft bus and the instruments. The C&DH processor is the bus controller of this bus, and each instrument is a remote terminal, with the exception of the Plasma and Supra-Thermal Ion and Composition (PLASTIC) instrument, which shares a data-processing unit (DPU) with IMPACT. The C&DH subsystem reports in telemetry the status of both the receipt (from the ground) and delivery (to the onboard instrument or subsystem) of these commands. The POC is responsible for the verification and validation of its instrument response based on the uplinked command load.

The spacecraft bus can also store command packets for distribution to the instruments at a later time. The aggregate size of memory available to all instruments for stored commands is 20 KB. Stored command packets can be time-tagged individually with one-second granularity. To keep the instruments informed of spacecraft bus activity, an unpacketized broadcast message is distributed to all instruments once per second. This message contains the following:

- Time (in UTC)
- Warning flags
 - Observatory coarse pointing
 - Observatory fine pointing
 - Thruster firing
 - HGA movement
 - Instrument power service off
- SSR partition fill status

Likewise, each instrument provides a status message to the spacecraft bus containing the following:

- A request to be powered down, by power service
- Status of SECCHI recloseable doors (SECCHI only)
- Status of HI ontine door (SECCHI only).

The spacecraft bus polls the instruments for data via the MIL-STD-1553 bus according to a fixed bus schedule. All science data are recorded on the SSR and may be downlinked in real time during instrument commissioning and contingency operations.

The spacecraft bus does not process instrument data before recording or downlinking; any processing or data compression is the responsibility of the instruments. The instruments have no direct access to the onboard recorder and are not able to retrieve data stored on it. The instruments generate each science data packet according to the full Consultative Committee for Space Data Systems (CCSDS) telemetry packet format, including primary and secondary headers, checksums, etc.

Housekeeping data from each instrument are collected every second. The spacecraft bus does not monitor this data, rather it monitors the instrument status message for needed fault protection responses. For example, one bit in the instrument status message is designated as a request by the instrument for the spacecraft bus to turn off its power. Other than this monitoring, the instruments cannot depend on the spacecraft bus to perform any processing of their housekeeping data. Each instrument includes housekeeping data in its science data packets if needed for science evaluation.

A small amount of space-weather data, which is both stored and telemetered, is collected from each instrument every second. Space-weather packets are collected from each instrument. When the observatory is not in contact with a DSN ground station, it transmits the space-weather data at a low rate (633 bps). The data are received by National Oceanic and Atmospheric Administration (NOAA)-affiliated sites around the world. The space-weather data also are recorded and downlinked as part of the normal science data.

3.3 STEREO Fault Protection (Cancro and Driesman 2004)

System fault protection is defined as “the use of cooperative design of flight and ground elements to detect and respond to perceived spacecraft faults” (NASA Preferred Reliability Practices 1995). As stated previously, each STEREO spacecraft bus is a single-string bus with redundancy added in selected areas to increase reliability. NASA standard PD-EC-1243 (NASA Preferred Reliability Practices Number PD-EC-1243) discusses the trade-offs that led to the current system design described by the block diagram in Fig. 7 (Driesman et al. 2001). The fault-protection system exists as hardware and software in the two spacecraft bus processors and as hardware and firmware in the interface card within the IEM. Fault protection also exists as firmware in two command decoder boards (within the PDU), hardware in the low-voltage sense (LVS) boards (in the battery), and hardware and firmware in the power-switching boards within the PDU. Not shown are the fault-protection functions that exist within individual procured devices such as the transponder and the star tracker. These embedded functions are not discussed in detail.

Examining the STEREO mission reveals that the majority of the spacecraft’s time is spent Sun-pointing. STEREO launched two observatories together, and both observatories needed to transition from super-geostationary transfer orbits (GTO) to Earth-leading and Earth-lagging orbits by using multiple maneuvers and phasing orbits. The STEREO mission

design is fault tolerant, providing many opportunities to adjust the orbits to place the spacecraft at the proper lunar fly-by distance, which limited critical sequences to observatory-to-observatory separation and detumble/initial acquisition. Thus a decision was made to make the initiation hardware for this time-critical sequence completely redundant, while allowing other hardware, not involved with the critical sequences, to be single-string. Thus the mission is tolerant to soft failures in nonredundant hardware. The plan for separation was to perform the event as soon as possible after the Delta II third-stage separation; all available redundancy was used at one time. STEREO accomplished the critical separation sequence by using complete redundancy in the power subsystem to provide two separate paths that detected third-stage separation and initiated the release of the observatory-to-observatory clamp band system. Redundancy also was inertial measurement units (IMUs, historically failure-prone) and a fourth reaction wheel (moveable parts).

The STEREO architecture includes five modes of operation: Operational, Maneuver, Standby, Ascent, and Earth Acquisition (EA). Figure 8 shows the system modes for each of the STEREO observatories. The observatory modes were developed by using two tiers of fault-protection intervention. The first tier, transition from Operational mode to Standby mode, is designed to correct known system faults and transition back to Operational mode with minimal sacrifice to ongoing science. The second tier, transition to EA mode, is designed to save the observatory from the occurrence of any known or unknown fault. Demotion from any mode into EA mode follows the same path of system-wide reset (or “system reset”). During every system reset, all critical hardware and software are reset, noncritical hardware is shut off, and the observatory points to the Sun and rolls about the Sun line to maximize antenna coverage. System reset coordinates all hardware and software fault protection into a single response and places the system in a known, well-understood configuration. Having a single path and one end state allows for testing and operations to be more easily accomplished. For example, from only the system state telemetry, mission operations immediately understands the state of all hardware and software on board the observatory.

4 Observatory Subsystems

4.1 Power Subsystem

The power subsystem for each STEREO observatory consists of two gallium-arsenide (GaAs) solar array wings with two panels per wing (Fig. 10), one 23-amp-hour NiH₂ battery, one solar array junction box (SAJB), one power supply electronics (PSE) box, and a PDU. A block diagram of the STEREO power subsystem is shown in Fig. 11. The system is designed to support each observatory with power throughout its two-year mission and through the eclipses that occurred during the first three perigees. Each eclipse was approximately 25 minutes long.

The STEREO power subsystem is a peak power-tracking battery on the bus topology. Eight converters in the PSE provide sufficient power to the observatory to support loads. The PSE controls battery charge current and solar array operating point. The bus voltage sits at whatever the battery voltage is, lower during discharge cycles and higher when the battery is fully charged.

The battery consists of 11 common pressure vessels (CPVs) connected in series, each of which contain two battery cells. The specified operating bus voltage for the system, assuming no failed CPVs, is 24–35 V. The bus is unregulated, thus the regulation function falls to individual components. The battery was used to support the observatory from about



Fig. 10 Observatory B during testing with a single solar array wing deployed

15 minutes before launch through observatory detumble, about 68 minutes after liftoff. The battery also supported the observatory through three eclipses, reaching a depth of discharge of about 12%.

Each STEREO observatory has four triple-junction GaAs solar panels covering 3.2 m^2 . On orbit, testing of the arrays showed power production of 795 W (BOL) at worst-case perihelion (1.022 AU) for Observatory A and greater than 716 W (BOL) at worst-case perihelion (1.089 AU) for Observatory B. The perihelion distances listed here are not those achieved but rather the design specifications.

Power is supplied to the PSE through the SAJB, which contains solar array string-isolation diodes, wing current monitor shunts, and fuses that protect the input of the PSE. Power conditioned through the PSE is distributed to the observatory through the PDU. The PDU is responsible for supplying power for all switched and unswitched loads, and it contains fusing for all noncritical loads. Critical loads are not fused. The PDU also is responsible for supplying current to pulse loads such as one-time events (e.g., A/B Observatory separation pyro firings). Table 3 details the loads supported.

Besides the power distribution function, the PDU serves as the interface for all attitude control sensors and actuators that were not on the MIL-STD-1553 bus. These include propulsion, reaction wheels, HGA gimbal, and Sun sensors. The PDU also is the location of some of the limited spacecraft bus redundancy. The PDU provides redundancy for critical events such as A/B Observatory separation, solar array deployment, and all observatory switched loads.

4.2 Guidance and Control Subsystem Description

The STEREO observatory is a three-axis-stabilized platform that relies on a guide telescope (part of the SECCHI instrument suite), a star tracker, digital solar aspect detectors (DSADs),

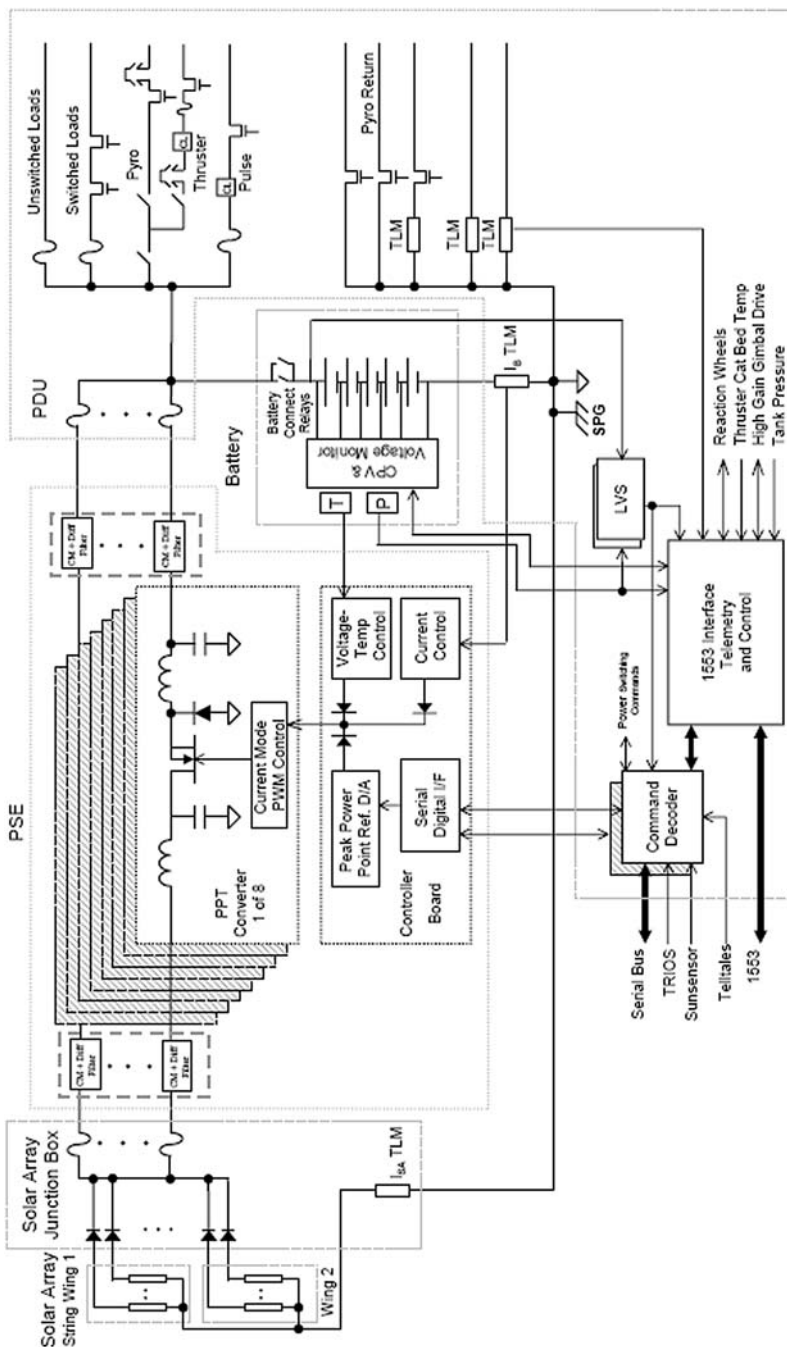


Fig. 11 STEREO power subsystem block diagram (Butler 2003)

Table 3 PDU loads including spares (Butler 2003)

Load	Switched	Unswitched	Pulse	Ordnance	Actuators ^a	Thruster
Propulsion	12	2	20			24
Communications	3	1	18			
Guidance and Control	7	1	16			
Instruments	13			6	8	
Power	3	5	30			
IEM	1	1				
Thermal	18					
Deployment			8	22		
Spare	3	5	36	4	2	6
Total	60	15	128	32	10	30

^aActuators are nonredundant commands

and an IMU for attitude determination. The star tracker is used for ascertaining the observatory's attitude with respect to J2000 inertial coordinates. The DSADs consist of five separate sensing heads and are used primarily as safing sensors. The five heads are used to sense the Sun's location and cover almost 4π steradians. The IMU provides observatory angular rate information.

The guide telescope is used to determine the observatory's attitude with respect to the solar disk. To meet the pitch and yaw pointing requirements (± 7 arcsec with respect to the guide telescope's error signal, 3σ control) for the mission, the guide telescope provides an error signal to the guidance and control processor at 250 Hz over the MIL-STD-1553 bus.

Attitude control of the observatory is accomplished through use of four reaction-wheel assemblies mounted along the axes of a pyramid. The observatory is configured as a zero-momentum system. The primary force generating adverse torque is solar pressure acting at the observatory's center of pressure (C_p). The generated torque is proportional to the offset between the observatory's C_p and center of mass (C_m). This offset changes with the position of the HGA. Once the system has reached a predetermined momentum, it is dumped using the propulsion system, which allows the reaction-wheel assemblies to de-spin.

Processing for the attitude control system occurs in the guidance and control processor. The primary tasks for this computer are processing all of the sensor data, running the control loops (computationally at 50 Hz) that manage the actuators, autonomously controlling system momentum, and steering the HGA.

4.2.1 Pointing Accuracy, Jitter, and Windowed Stability

One of the largest drivers for design of the system was control of observatory pointing accuracy, jitter, and windowed stability. Their requirements are shown in Table 4. The accuracy, jitter, and windowed-stability specifications are driven by the imaging instruments within the SCIP. Specifically, accuracy is driven by the EUVI, which is concerned about smearing images caused by relatively low-frequency off-pointing. The jitter and windowed-stability specifications are driven by the coronagraphs. Coronagraph images are reconstructed from multiple images with different polarizations. The jitter specification addresses spacecraft

Table 4 SCIP pointing, jitter, and windowed stability requirements

	Pitch and yaw performance each axis (arcsec)	Roll performance (arcmin)	Window times (seconds)
Accuracy	$3\sigma a \leq 7.25$	$3\sigma a \leq 35$	–
jitter	$\sigma j \leq 1.53$	$\sigma j \leq 3.4$	$T_j = 15$ (30 as a goal)
Windowed stability	$\sigma sw \leq 1.90$ $\sigma sw \leq 3.75$	$\sigma sw \leq 6.70$ $\sigma sw \leq 6.70$	$0.1 \leq T_j \leq 1.0$ $T_{S1} = T_j + 2.3T_{S2} = 2T_{S1}$ $T_{S3} = T_j + 4.6T_{S4} = 2T_{S3}$ $1.0 \leq T_j \leq 8.0$ $T_{S1} = T_j + 2.3T_{S2} = 2T_{S1}$ $T_{S3} = T_j + 4.6T_{S4} = 2T_{S3}$

body motion during the integration time over a single polarization image. The windowed-stability specification addresses spacecraft body motion from one image to the next. Essentially, the windowed-stability specification allows the spacecraft body to “do what it wants” between taking polarization images as long as it ends up within 3.75 arcsec (pitch and yaw) of where it was when the last image was taken. The accuracy, jitter, and windowed-stability specifications and metrics were developed specifically for the STEREO mission. For a more detailed discussion, please see the work by Pittelkau (2002).

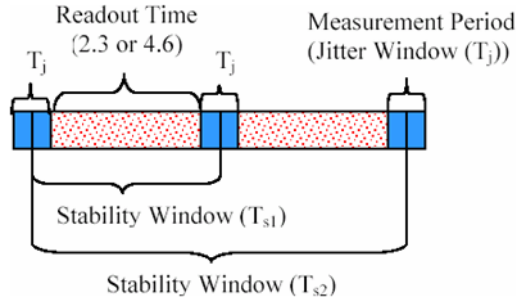
For a more complete understanding of the derivations of these specifications along with the time-domain representation, please consult the work by Pittelkau (2002).

The following definitions apply:

- *Accuracy* is the root-mean-square (RMS) pointing error σa of the line of sight (LOS) over any interval of time (window width $T \rightarrow \infty$).
- *Jitter* is the RMS pointing error σj of the LOS *within* an interval of T_j seconds. The jitter window T_j is defined by the integration or measurement time for a single-instrument observation. The range of T_j is different for each SCIP instrument, and the value for each instrument can change during normal operations.
- *Windowed stability* is the RMS change in the LOS from the centroid time of one measurement to the centroid time of another measurement. The stability window (T_S) is referenced from the centroid of the first measurement to the centroid of the second window and from the centroid of the first measurement to the centroid of the third measurement. Each measurement is separated by a readout time. For STEREO, these readout times can be either 2.3 or 4.6 seconds in duration. The stability window is graphically illustrated in Fig. 12, which shows its relationship to jitter.

On orbit, the system currently is performing well, meeting or exceeding specifications for long periods of time. Pointing issues induced by zero-speed wheel crossings and excitation of observatory structural modes (though very minimal) are being dealt with primarily through the use of a wheel-speed-avoidance algorithm (Kantsiper et al. 2007), developed within the Mission Design, Guidance, and Control Group at JHU/APL. This algorithm allows the guidance and control system to avoid a designated band around problematic wheel speeds (e.g., zero). The algorithm forces any wheel within these bands to speed quickly through it. This significantly reduces the time during which the system is excited by any given wheel frequency, and momentum is redistributed among the wheels.

Fig. 12 Graphical illustration of jitter and stability windows



4.3 Radio Frequency Telecommunications Subsystem

The primary function of the radio frequency (RF) telecommunications subsystem (Von-Mehlem 2003) is to provide the interface between the DSN ground stations and the two STEREO observatories, including support for uplink commands, downlink telemetry, and ranging. The RF system on each observatory consists of one small deep space transponder (SDST), one 60-W (RF) traveling wave tube amplifier (TWTA), one isolator, two RF switches, one diplexer, two low-gain antennas (LGA), one combiner/divider, and one 1.2-m HGA mounted with a single-axis rotary actuator. Figure 13 shows a block diagram of the RF subsystem.

The RF subsystem is designed to operate at the uplink bit rates designated in Table 5 and the downlink bit rates designated in Table 6. The subsystem can provide numerous downlink encoding options. Only the turbo-coding option is shown because it is the only one currently being used. Primary rates are shown in bold.

Currently the RF subsystem is meeting or exceeding specifications. During the first 19 months in heliocentric orbit, each observatory will downlink data at 720 kbps during a four-hour DSN pass. During the following 10 months, because of increasing observatory–Earth distance, the data rate will drop to 480 kbps and the DSN pass duration will increase to five hours. Figure 14 shows how the downlink rate through the HGA falls off over time. As data levels fall off, each instrument’s data allocation is reduced proportionally.

During all periods when the observatories are not in contact with the DSN, each observatory broadcasts a highly reduced set of data that is transmitted to Earth at 633 bps. These data are geared toward providing space-weather information and providing the Earth with data from unique vantage points. These data provide the recipients, the primary one being NOAA, with up to three days’ warning of solar activity that could impact terrestrial systems.

4.4 Thermal Control Subsystem

The thermal control subsystem for each observatory is a passive system, relying on blanketing, thermostatically controlled heaters, and radiators to maintain energy balance. The subsystem for each observatory is nearly identical, with differences extending only to the sizing of radiator surfaces; Observatory B has a slightly smaller radiator area because of its greater Sun distance.

In order to keep the subsystem relatively simple, a requirement to support large temperature ranges was levied on all conductively coupled components. Isolated components, by definition, are required to maintain their own thermal environment and therefore could set

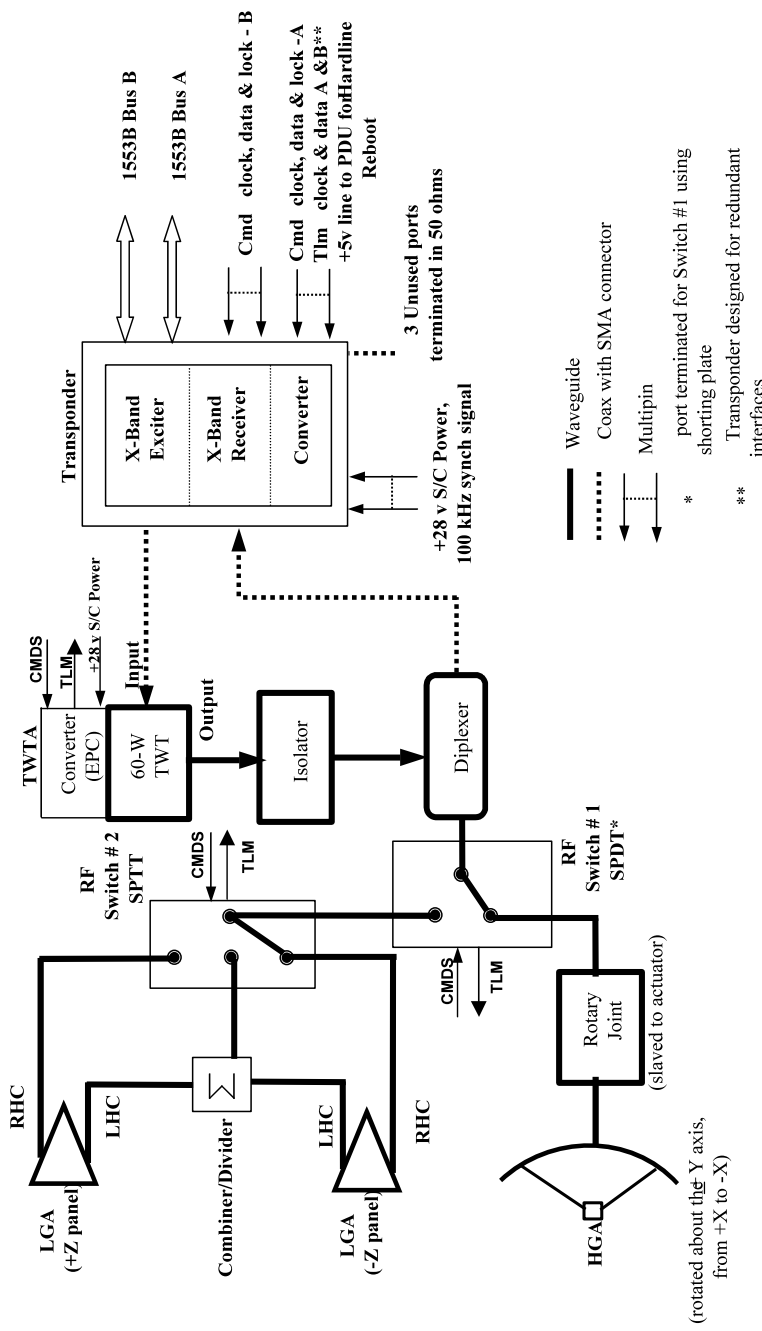


Fig. 13 STEREO RF subsystem block diagram

Table 5 Uplink command rates

Data rate (bps)	Purpose
7.8125	Emergency Command Rate with LGA
125	Normal Required Command Rate with HGA and LGA During Phasing Orbits
500	Software Upload Rate with HGA (When Link Supports Rate)
1000	Software Upload Rate with HGA (When Link Supports Rate)
2000	Software Upload Rate with HGA

Primary rates are shown in bold

Table 6 Downlink telemetry rates

Bit rate (bps)	Data format	Turbo coding rate	Symbol rate (ksp/s)	Purpose
720,000	NRZ-L	$r = 1/2$	1,440	Mission Orbit Science, Required Bit Rate
480,000	NRZ-L	$r = 1/4$	1,920	Mission Orbit Science, Required Bit Rate
360,000	NRZ-L	$r = 1/4$	1,440	Mission Orbit Science, Required Bit Rate
360,000	NRZ-L	$r = 1/2$	720	Backup
160,000	Bi-Phase-L	$r = 1/6$	960	Backup
96,000	Bi-Phase-L	$r = 1/6$	576	Backup
30,000	Bi-Phase-L	$r = 1/6$	180	Phasing Orbits, Required Bit Rate
10,000	Bi-Phase-L	$r = 1/6$	60	Backup
6000	Bi-Phase-L	$r = 1/6$	36	Backup
3000	Bi-Phase-L	$r = 1/6$	18	Backup
1000	Bi-Phase-L	$r = 1/6$	6	Backup
633	Bi-Phase-L	Turbo $r = 1/6$	3.798	Space-Weather, Required Bit Rate
35.1365	NRZ-L	Turbo $r = 1/6$	0.2108	Emergency, Spacecraft Roll Stopped
11.712	NRZ-L	Turbo $r = 1/6$	0.0703	Emergency, Spacecraft Roll

Primary rates are shown in bold

their own thermal requirements. Table 7 shows the thermal operational and survival requirements for all observatory bus components and instruments. The thermal isolation requirement that was levied on all components was $>20^{\circ}\text{C/W}$. In most cases this requirement was met, with a few components falling between 10 and 20°C/W . Heat density requirements also were levied, thus removing the need for active heat transfer. The requirement was to keep power densities below 465 W/m^2 .

The thermal subsystem is performing well on-orbit. All observatory components are being maintained within their operational requirements.

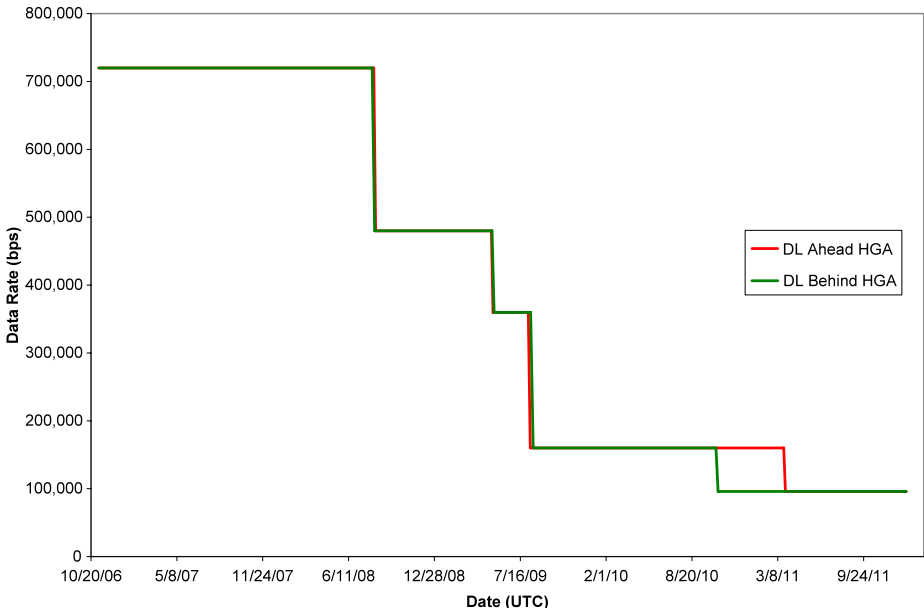


Fig. 14 Observatory A and B downlink rates versus time

4.5 Propulsion Subsystem

The prime function of the propulsion subsystem is to provide ΔV to adjust the observatory's orbit such that it arrives at the correct lunar fly-by geometry. It also is used approximately every 30 days to desaturate the reaction-wheel assemblies. The STEREO propulsion subsystem is a mono-propellant blow-down system that uses hydrazine as the propellant and GHe₂ as the pressurant. When loaded for flight, the subsystem is capable of changing the observatory's velocity by approximately 180 m/s. The subsystem schematic is shown in Fig. 15.

Each observatory was loaded with approximately 62 kg of hydrazine prior to launch. Table 8 shows the number of maneuvers and the quantity of propellant used to achieve each observatory's final orbit. The last two maneuvers on Observatory B were used to target a lunar transit of the Sun, not to achieve final orbit. Final orbits were reached by using only deterministic maneuvers.

Each observatory has approximately 43 kg of propellant left. Because no maneuvers are necessary once the observatories are in heliocentric orbit, this propellant is needed solely for managing system momentum. The quantity of propellant left allows for many tens of years of operations.

The propulsion system itself consists of two titanium propellant tanks, each equally loaded. The tanks feed two manifolds that can be isolated from each other in the event of a tank leak. The latch valves are used in the event of a leak to isolate the tanks from each other, and/or the tanks from the thrusters, otherwise they are left open. There are 12 4.4-N ($\sim 1\text{-lbf}$) thrusters located in two sets of four. Sets are located on the $-x$ deck, the $+z$ deck, and the $+x$ deck. Each thruster is canted 15° off the observatory axes. The engineering team dictated the quantity of thrusters onboard by constraining the system to perform maneuvers with the solar arrays within 45° of the Sun. The $-x$ set of thrusters is the chosen set for

Table 7 Thermal survival and operational requirements (JHU/APL 2005)

Component (no. of units per spacecraft)	Interface type	Component survival (°C)	Component operational (°C)
Guidance and Control Subsystem:			
Sun Sensor Optical Heads (5)	Coupled	−55 to +75	−40 to +75
Sun Sensor Electronics (1)	Coupled	−28 to +60	−23 to +55
Star Tracker (1)	Coupled	−28 to +60	−23 to +55
Reaction Wheels (4)	Coupled	−28 to +60	−23 to +55
Inertial Measurement Units (2)	Coupled	−28 to +60	−23 to +55
Propulsion Subsystem:			
Rocket Engine Assemblies (12) (Nonoperational)	Isolated	+5 to +50	+10 to +50
Hydrazine Storage Tanks (1)	Isolated	+5 to +50	+10 to +50
Pressure Transducers (2)	Isolated	+5 to +50	+10 to +50
Lines (Away from Components)	Isolated	+5 to +50	+10 to +50
Valves and Plumbing (Considered Part of Subsystem and Not Individual Components)	Isolated	+5 to +100	+5 to +100
Avionics:			
IEM (1)	Coupled	−28 to +60	−23 to +55
Oscillator (1)	Coupled	−28 to +60	−23 to +55
RF Communications Subsystem:			
TWT (1)	Coupled	−30 to +90	−25 to +80
Electrical Power Converter (1)	Coupled	−30 to +75	−25 to +65
Transponder (1)	Coupled	−28 to +60	−23 to +55
RF Component Assembly (1)	Coupled	−28 to +60	−23 to +55
Diplexer (1)	Coupled	−28 to +60	−23 to +55
Wave Guide Switches (2)	Coupled	−28 to +60	−23 to +55
Combiner (1)	Coupled	−28 to +60	−23 to +55
Isolator (1)	Coupled	−28 to +60	−23 to +55
Parabolic Dish HGA (1)		−130 to +90	−130 to +90
HGA Rotary Actuator	Coupled	−45 to +60	−45 to +60
HGA Rotary Actuator Electronics	Coupled	−28 to +60	−23 to +55
RF Rotary Joint	Coupled	−50 to +75	
LGA (2)	Coupled	−90 to +90	−90 to +90
Power Subsystem:			
Solar Panels (2) (Including Solar Panel Hardware)		−90 to +110	−90 to +110
SAJB (1)	Coupled	−28 to +60	−23 to +55
Power Subsystem Electronics (1)	Coupled	−28 to +60	−23 to +55
PDU (1)	Coupled	−28 to +60	−23 to +55
NiH ₂ Battery (1) ^a	Isolated	−10 to +20	−10 to +20
Harness			
Auxiliary Diode Unit (1)	Coupled	−28 to +60	−23 to +55
RF Diode Unit (1)	Coupled	−28 to +60	−23 to +55
Terminal Board Unit (6)	Coupled	−28 to +60	−23 to +55
Thermal			
TRIOS (8)	Coupled	−28 to +60	−23 to +55

Table 7 (Continued)

Component (no. of units per spacecraft)	Interface type	Component survival (°C)	Component operational (°C)
Instruments			
SECCHI			
SCIP Assembly	Isolated ^b	−15 to +35	−20 to +40
SEB	Coupled	−23 to +55	−28 to +55
HI	Isolated ^b	−15 to +45	−20 to +50
IMPACT			
SEP Main (with HET and LET)	Isolated ^b	−15 to +45	−20 to +50
SEPT-E	Isolated ^b	−15 to +45	−20 to +50
SEPT-NS	Isolated ^b	−15 to +45	−20 to +50
Instrument DPU	Coupled	−23 to +55	−28 to +60
MAG			
STE-D	Isolated ^b	No Interface	No Interface
STE-U	Isolated ^b	No Interface	No Interface
SWEA	Isolated ^b	No Interface	No Interface
BOOM	Isolated ^b	−23 to +55	−28 to +60
SWAVES			
DPU	Coupled	−23 to +55	−28 to +60
Antenna Housing	Coupled	−23 to +45	−28 to +45
Antenna Element	Isolated ^b	No Interface	No Interface
PLASTIC	Isolated ^b	−15 to +45	−20 to +50

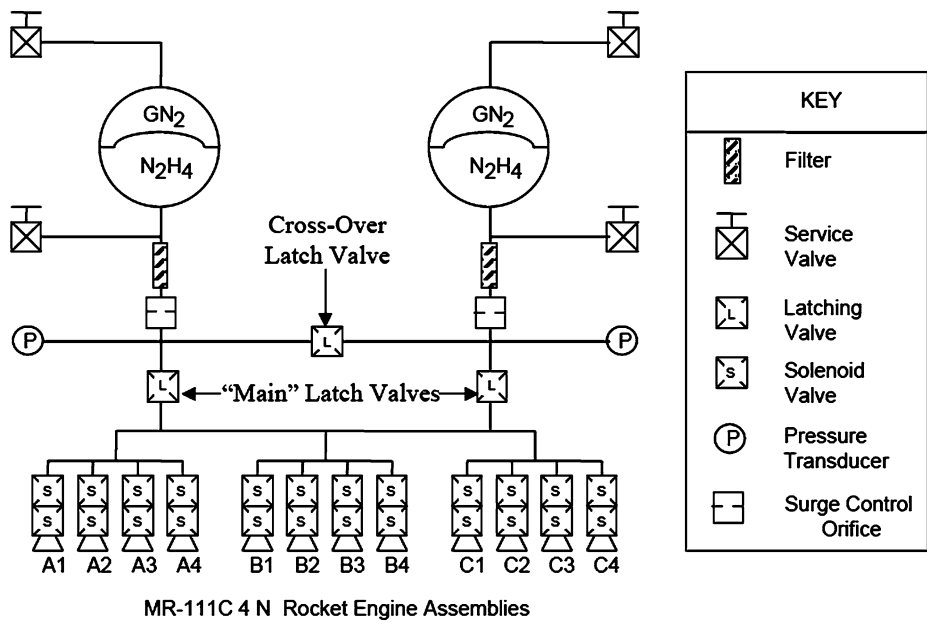
**Fig. 15** Propulsion subsystem schematic

Table 8 ΔV summary

Event (estimation method)	Observatory A		Observatory B	
	ΔV (m/s)	Propellant used (kg)	ΔV (m/s)	Propellant used (kg)
Initial Propellant Load		62.38		62.42
<i>EBl</i> (Counts)	0.2	0.07	0.2	0.07
<i>AJ</i> (PVT)	11.7	3.50	11.7	3.64
<i>EB2</i> (Counts)	0.2	0.07	0.2	0.07
<i>A2+</i> (PVT)	46.1	13.58	28.4	8.46
<i>P2</i> (PVT)	2.7	0.79	4.9	1.62
<i>A4</i> (Counts)	Not Needed	0.000	0.2	0.07
<i>SI+</i> (PVT)	Not Needed	0.000	10.0	3.35
<i>A5+</i> (Counts)	Not Needed	0.000	0.8	0.20
Propellant Expended				
(PVT)		18.02		17.48
Uncertainty		0.41		0.41

PVT, pressure, volume, and temperature

wheel desaturation so as to minimize contamination of the sensitive optical surfaces and instrument apertures pointing in the $+x$ direction.

Acknowledgements The continuing success of the STEREO mission is the result of the hard work and sacrifices by many staff members at JHU/APL, GSFC, and scientific institutions from around the world. Any attempt to list names would invariably result in the omission of a staff member who has made a critical contribution to the STEREO project. The authors acknowledge these engineers, scientists, managers, and administrative staff who have made the development of the STEREO mission successful, providing many enjoyable memories. We acknowledge Dr. Patrick Stader, who provided last-minute editorial support with regard to the writing of this paper.

References

- M.B. Butler, STEREO critical design review, power subsystem presentation, 18–21 February 2003
- G.J. Cancro, A.S. Driesman, Fault protection system development process for the STEREO spacecraft, in *55th International Astronautical Congress of the International Astronautical Federation, the International Academy of Astronautics, and the International Institute of Space Law*, Vancouver, Canada, 4–8 October 2004, IAC-04-IAF-U.3b.08
- Department of Defense, Aircraft internal time division command/response multiplex data bus. Institute of Environmental Sciences, Mount Prospect, Illinois, 21 September 1978, MIL-STD-1553B
- Department of Defense, Product cleanliness levels and contamination control program. Institute of Environmental Sciences, Mount Prospect, Illinois, 11 April 1994, MIL-STD-1246C
- Department of Defense, Requirements for the control of electromagnetic interference characteristics of subsystems and equipment. Institute of Environmental Sciences, Mount Prospect, Illinois, 20 August 1999, MIL-STD-461E
- A. Driesman, B.W. Ballard, D.E. Rodriguez, S.J. Offenbacher, STEREO observatory trade studies and resulting architecture, in *2001 IEEE Aerospace Conference Proceedings*, vol. 1, March 2001, pp. 1/63–1/80. doi:[10.1109/AERO.2001.931696](https://doi.org/10.1109/AERO.2001.931696)
- JHU/APL, STEREO environmental definition, observatory, component, and instrument test requirements. JHU/APL, Laurel, Maryland, 2005, Document 7381-9003C
- B. Kantsiper, J.C. Ray, J. Hunt, T. Strikwerda, Autonomous avoidance of structural resonances on the STEREO mission. American Institute of Aeronautics and Astronautics Guidance, Navigation, and Control Conference 2007, Hilton Head, South Carolina, 20–23 August 2007, AIAA-2007-6549

-
- NASA Preferred Reliability Practices, Fault protection. NASA, Washington, DC, October 1995, Number PD-EC-1243
- D.A. Ossing, JHU/APL STEREO mission operations concept. JHU/APL, Laurel, Maryland, 2001, Document 7381-9020
- M.E. Pittelkau, Pointing definitions and pointing error metrics. JHU/APL, Laurel, Maryland, 21 November 2002, SRM-02-072
- U.I. VonMehlem, STEREO RF telecommunications subsystem performance specification. JHU/APL, Laurel, Maryland, 21 February 2003, Document 7381-9350

STEREO Space Weather and the Space Weather Beacon

D.A. Biesecker · D.F. Webb · O.C. St. Cyr

Originally published in the journal *Space Science Reviews*, Volume 136, Nos 1–4.
DOI: [10.1007/s11214-007-9165-7](https://doi.org/10.1007/s11214-007-9165-7) © Springer Science+Business Media, Inc. 2007

Abstract The Solar Terrestrial Relations Observatory (STEREO) is primarily a solar and interplanetary research mission, with one of the natural applications being in the area of space weather. The obvious potential for space weather applications is so great that NOAA has worked to incorporate the real-time data into their forecast center as much as possible. A subset of the STEREO data will be continuously downlinked in a real-time broadcast mode, called the Space Weather Beacon. Within the research community there has been considerable interest in conducting space weather related research with STEREO. Some of this research is geared towards making an immediate impact while other work is still very much in the research domain. There are many areas where STEREO might contribute and we cannot predict where all the successes will come. Here we discuss how STEREO will contribute to space weather and many of the specific research projects proposed to address STEREO space weather issues. The data which will be telemetered down in the Space Weather Beacon is also summarized here. Some of the lessons learned from integrating other NASA missions into the forecast center are presented. We also discuss some specific uses of the STEREO data in the NOAA Space Environment Center.

Keywords STEREO · Space weather · Coronal mass ejection · Solar wind · Forecasting

D.A. Biesecker (✉)
NOAA/Space Environment Center, 325 Broadway, Boulder, CO 80305, USA
e-mail: doug.biesecker@noaa.gov

D.F. Webb
Institute for Scientific Research, Boston College, Chestnut Hill, MA 02467, USA

O.C. St. Cyr
NASA/Goddard Space Flight Center, Greenbelt, MD 20771, USA

1 Introduction

1.1 Background on Space Weather

As society becomes increasingly reliant on technologically advanced systems for many of its day-to-day functions, our ability to predict and respond to the impacts of space weather gains greater importance. Among the systems most susceptible to geomagnetic disturbances are power grids, satellites, and aviation communications—systems upon which our reliance increases dramatically every year. The use of pagers and mobile phones has become almost ubiquitous. The global positioning system (GPS) is used heavily by the military, commercial airlines, the construction and extraction industries, and the shipping and boating industry, and is being introduced into automobiles. As the use of these systems, which are vulnerable to space weather, becomes more widespread, space weather disturbances will impact a wider array of people and human activities. A comprehensive text on telecommunications and the susceptibility of such systems to space weather is that of Goodman (2005). Also, summaries on the impact of space weather on technological systems are available in Lanzerotti et al. (1999) and Lanzerotti (2001).

One example of a space weather impact was the apparent loss of a communications satellite and associated widespread loss of services due to a space weather disturbance, which was described by Baker et al. (1998). They found that the combination of coronal mass ejections (CMEs), solar flares, and high speed solar wind streams led to a prolonged period of geomagnetically disturbed conditions during which the Galaxy 4 communications satellite was subjected to an intense population of highly energetic, relativistic electrons just prior to its loss. The Galaxy 4 satellite outage affected CBS, NPR, Reuters, ATM networks and many pagers. Since our society is becoming more dependent on advanced technological systems, we are increasingly vulnerable to malfunctions in those systems. A single civilian communications satellite can cost several hundred million dollars. There are now over 300 commercial spacecraft in geosynchronous orbit and entire new constellations of satellites are being placed into a variety of Earth orbits. If even a small percentage of these satellites exhibit severe problems due to the space environment, the costs will be significant (Odenwald et al. 2006).

The need to study, forecast and mitigate space weather effects is gaining increased attention at the national level. Specifically, the need to develop a coordinated plan to improve present capabilities in specifying and forecasting conditions in the space environment has led to the formation of national programs such as the U.S. National Space Weather Program (<http://www.nswp.gov>), NASA's Living With a Star (<http://lws.gsfc.nasa.gov/>), and ESA's Space Weather Programme (<http://www.esa-spaceweather.net/>). As a scientific pursuit, space weather is considered analogous to atmospheric weather, having both research and forecasting elements. In some sense, our knowledge and ability to build predictive models of space weather is equivalent to, yet distinctly different from, the early stages of atmospheric weather studies (Siscoe 2006; Siscoe and Solomon 2006). For a comprehensive overview of the recent state of the art in space weather research, readers are directed to the AGU Monograph *Space Weather* (Song et al. 2001) and to the text *Space Weather: The Physics Behind a Slogan* (Scherer et al. 2005).

The ultimate source for most space weather effects is the Sun and its activity. The NOAA Space Environment Center categorizes space weather in three convenient scales which are each related to the type of solar event driving them (Poppe 2000). All three scales rate space weather disturbances on a scale from one (1) to five (5), with one being considered ‘minor’ and five ‘extreme’. The G (Geomagnetic Storm) scale is discussed in the next section. The

R (Radio Blackout) scale is based on the GOES X-ray flux measurement. High levels of X-ray flux result in significant enhancements of ionization of the ionosphere on the sunlit side of Earth, causing sudden ionospheric disturbances (SIDs) and communication problems. Note that extreme ultraviolet and radio emissions also contribute to ionospheric effects, but the X-ray flux serves as a useful proxy in their place. The S (Solar Radiation Storm) scale is measured against the flux of solar energetic particles (SEPs). These SEPs are accelerated in eruptive solar events. The most energetic SEPs (>1 GeV) arrive at Earth within tens of minutes, for magnetically well-connected events on the Sun's western hemisphere. The bulk of the particles in SEP events have lower energies (10–100 MeV) and begin to arrive tens of minutes to hours after solar onset. Eruptive events originating on the Sun's eastern hemisphere have delayed onsets relative to well connected events (Cane et al. 1988 and Fig. 2). These events cause ionospheric-related communications and navigation problems. The proton flux can remain elevated for days and can cause state changes or latch ups in electronic devices on satellites and hazardous conditions for astronauts and even airline crew and passengers.

In addition to the space weather scales, from which many alerts and warnings to customers are derived, there are many other products issued by the SEC. It is clear that there is room to improve many, if not all, of the existing products and there is a need for yet new products. There are numerous space weather products which one can imagine. The NOAA Space Environment Center maintains a list of those products which the forecast center has identified as the most needed. These are separated into two categories; high priority and highest priority. These are broad, subjective, categories with the placement of particular items in each category determined by the forecasters. Table 1 shows these high and highest priority items. Some of these can obviously be addressed by the STEREO mission. Since it would be presumptuous to identify which items could be addressed by the STEREO mission, we do not do so here. The applicability of STEREO to any need is limited only by the imagination of researchers.

1.2 CMEs and Space Weather

As mentioned previously, the third space weather scale is the G (Geomagnetic Storm) scale. Most of the energy imparted to the solar wind by a solar event is associated with the ejected plasma and magnetic fields that collectively are called a coronal mass ejection and usually take several days to reach Earth. However, the fastest CMEs travel from the Sun to the Earth in less than one day. Note that high speed wind streams also cause geomagnetic storms, but rarely do they produce very strong storms (e.g. Richardson et al. 2006). CMEs cause space weather disturbances, including the largest geomagnetic storms, in a number of ways. First, strong southward magnetic fields in the CME can reconnect with the predominately northward fields of the Sun-facing magnetosphere, producing strong induced fields and electric currents in the magnetosphere, the ionosphere, and at Earth's surface (Fig. 1). These southward field regions can occur both in the compressed plasma between the shock and CME and in the CME itself, which often contains magnetic field structures called magnetic clouds. Second, the impact of the CME compresses Earth's day side magnetosphere, which can leave high altitude geostationary satellites directly exposed to the solar wind. The third way CMEs drive space weather is through the production of SEP events, as discussed in the previous section.

Although recent strides have been made in our understanding of the relationship between CMEs and space weather, our current ability to forecast space weather disturbances caused by CMEs is still relatively poor. Improvements are needed both in our ability to predict if

Table 1 A list of the products and observations that NOAA Space Environment Center forecasters consider to be most needed

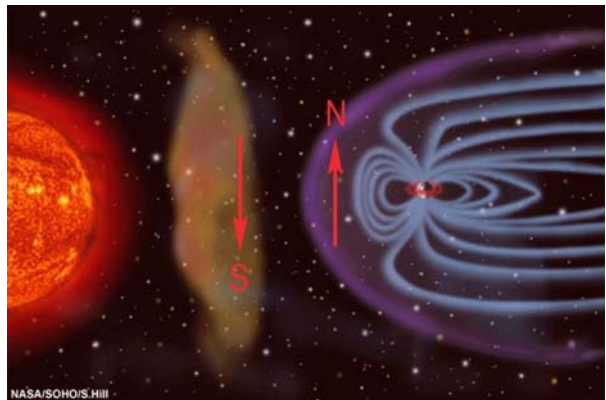
SEC highest priority needs ^{1,2,3}	SEC high priority needs ^{1,2,3}
SEP event forecasts, including start and end time, peak flux, time of peak, spectrum, fluence and probability of occurrence	Visualization of disturbances in interplanetary space
Solar wind data from L1 or further upstream	Geomagnetic activity predictions (1–7 days)
Solar coronagraph data	Geomagnetic storm end time forecast
Energetic e ⁻ flux prediction for the International Space Station	Real-time estimates of geomagnetic indices
Regional geomagnetic activity nowcasts and forecasts	Real-time quality diagnostics (verification) of all warning/watch/forecast products
Ionospheric maps of Total Electron Content and scintillation (nowcast and forecast)	Statistical/numerical guidance for all forecast quantities
Geomagnetic indices (Ap, Kp, Dst) and probability forecasts	Magnetopause crossing forecasts based on L1 data
Solar particle degradation of polar HF radio propagation (nowcast and forecast)	Short-term (days) F10.7 and X-ray flare forecasts
Background solar wind prediction	Improved image analysis capability
	EUV index

¹Items in each column are not necessarily in any priority order

²Required product lead times range from hours to days depending on the user and product

³Needed product quality (e.g. skill, accuracy) is user specific and remains to be determined in most cases

Fig. 1 A cartoon illustrating a CME in interplanetary space, with the southward component of magnetic field indicated. This is in contrast to the northward field of the Earth



and when a CME will impact Earth as well as in prediction of the magnitude and duration of the anticipated impact. The Large Angle Spectrometric Coronagraph (LASCO) and Extreme

Ultraviolet Imaging Telescope (EIT) observations from the Solar and Heliospheric Observatory (SOHO) have demonstrated an advancement in this prediction capability by reliably detecting halo CMEs—events that are directed along the Earth–Sun line and are visible as expanding ‘halos’ around the coronagraph occulting disk. Halo CMEs were first identified with the Naval Research Laboratory SOLWIND coronagraph (Howard et al. 1982) but only a handful were seen. With the increased sensitivity of the LASCO coronagraphs, however, it is now possible to detect almost all of these events. In addition, observations of the origin of the CME on the disk by EIT, GOES Soft X-Ray Imager (SXI), H-alpha, radio, etc., can be used to determine whether the CME is headed toward or away from Earth.

The associated surface activity of “frontside” halo CMEs can be well observed and, days later, when the CME passes near-Earth spacecraft, the physical structure of CMEs can be analyzed. Initial studies using LASCO data showed that frontside halo CMEs were associated with flaring active regions and filament eruptions within half a solar radius of Sun center and often accompanied at coronal wavelengths by circular, expanding fronts, or waves, and areas of dimming (e.g. Moses et al. 1997; Thompson et al. 1998).

The geoeffectiveness of halo CMEs has been examined in several studies by comparing the timings of the CME onsets with WIND and Advanced Composition Explorer (ACE) spacecraft data at 1 AU and with geomagnetic activity. Brueckner et al. (1998), St. Cyr et al. (2000) and Webb et al. (2000) found good correlations between frontside halo CMEs and moderate geomagnetic storms with a lag time of 2–5 days dependent on the phase of the cycle. Magnetic clouds preceded by interplanetary shocks usually signified the arrival at Earth of the CME structure.

Great strides have been made in theoretical modeling and simulations of CMEs (see Aschwanden 2006 for a recent review). Current models generally fall into the classes of dynamos, mass loading, tether release and tether straining. There are two kinds of CME simulations: analytical time-dependent MHD models, which provide insight into the physical mechanisms, and numerical time-dependent MHD simulations, which can reasonably reproduce observations given sufficiently accurate initial and boundary conditions.

The lesson from the SOHO data that pertains to the STEREO mission is that even moderately energetic CMEs, such as observed by LASCO near solar minimum, can be very geoeffective because they often contain coherent magnetic structures and move faster than the ambient solar wind. One dramatic example of this occurred in January, 1997 when an unremarkable halo CME, as seen by LASCO, was possibly associated with the failure of the Telstar 401 satellite (Webb et al. 1998; Reeves et al. 1998). The failure of Telstar 401 cannot be absolutely attributed to the geomagnetic storm, as Lanzerotti et al. (1999) showed in data from charge plate sensors on a nearby satellite (Telstar4), that the environment during “the interval of failure could be considered geomagnetically benign as compared to the disturbed levels of the previous day.” The Telstar 401 failure occurred at just after 11 UT on January 11, more than a day after the extreme geomagnetic conditions ended at the Telstar4 satellite. According to the official failure report, the loss was attributed to “shoddy workmanship” (Lanzerotti et al. 1999). From the space weather viewpoint, one key element is to determine whether the CME is aimed toward Earth or not. With STEREO we also anticipate significant improvements in our ability to predict the timing and impact of CME-induced geomagnetic disturbances.

One key area where STEREO will not necessarily help with predicting CME related geomagnetic storms is the inability to predict, or even determine via remote sensing, the direction of the magnetic field in the CME or interplanetary CME. As mentioned at the outset of this section, it is primarily the existence of southward magnetic field which will determine the strength of a geomagnetic storm.

2 Use of the STEREO Instruments for Space Weather

At different periods during the STEREO mission the forecasting utility will emphasize different portions of the payload. Early in the mission, while the two spacecraft are still relatively close to Earth, the in situ instruments, the In Situ Measurements of Particles and CME Transients (IMPACT) Experiment (Luhmann et al. 2007) and the Plasma and Suprathermal Ion and Composition (PLASTIC) Experiment (Galvin et al. 2007), will likely be more useful to space weather as they will detect large scale structures in the solar wind. For example, either spacecraft may encounter interplanetary CME (ICME) shocks prior to their arrival at Earth. Also, solar energetic particles from activity east of about 45° west heliographic longitude will travel along interplanetary magnetic field lines and be detected by the lagging spacecraft minutes to hours before their arrival at Earth. Further, corotating interaction regions can be geoeffective, and these will be detected by the lagging spacecraft prior to their passage by Earth. Identification of potentially geoeffective features in the plasma electron, magnetic field, and energetic particle data from IMPACT should be straightforward. The ion compositional content from PLASTIC will be useful for identifying ICMEs and other structures in the solar wind.

As the STEREO spacecraft drift farther away from Earth, the SECCHI imaging instrument suite will become more important for space weather forecasting by providing observations that are not available from the Sun–Earth line. The eruption of Earth-directed CMEs will be detected by the Sun Earth Connection Coronal and Heliospheric Investigation (SECCHI) EUVI, COR1, and COR2 experiments (Howard et al. 2007). Early in the mission, when the STEREO spacecraft are near the orbit of Earth, COR1 and COR2 will record halo CMEs produced by front-side sources detected with EUVI. This is currently done with the LASCO coronagraphs and EIT instrument on SOHO and these instruments will continue to provide data during the early phases of the STEREO mission. As the separation of the STEREO spacecraft increases, the different vantage points will allow determination of the velocity vector of the CME, as well as the material that will directly impact Earth. The velocity vector and its rate of change will be determined by triangulation techniques involving simultaneous stereo image pairs. Also, images from EUVI on the lagging spacecraft will show newly formed active regions prior to their appearance at the Sun’s east limb (as seen from Earth). EUVI will also image other potentially geoeffective structures such as coronal holes and filament channels.

The strongest geomagnetic storms are caused by CMEs and it is clear that significant improvements still need to be made in forecasting these storms. This is expected to be a main area of focus for space weather research with STEREO, as it has been with SOHO. Accurate prediction of whether or not a CME will occur is a highly desired goal. There is significant activity in this area, as this is a goal of the NASA Solar Dynamics Observatory mission. Also NASA’s Living With a Star Targeted Research and Technology program lists the forecasting of CME events prior to their eruption as a research priority (Gosling et al. 2003). When a CME does occur, there are still many parameters of a geomagnetic storm which need to be forecast. In particular, the first parameter to determine is the impact angle of the CME on the Earth. Will it hit Earth directly along its central axis or will it graze or miss Earth completely? In the case where the CME will hit Earth, the next parameters to forecast are the arrival time, geomagnetic storm strength, and geomagnetic storm duration. Much work has been done on the first two of these parameters during the past solar cycle, utilizing data from the SOHO mission. Many authors have examined the ability to predict CME arrival time based on available data, particularly the CME speed as measured by SOHO/LASCO. The typical error in arrival time has been found to be of order ± 11 hours (Gopalswamy et

al. 2000; Michalek et al. 2004). Less work has been done on predicting geomagnetic storm intensity, though Moon et al. (2005) has shown from a limited data set that a simple measure of CME impact parameter does correlate with geomagnetic storm strength.

STEREO Waves (SWAVES) will be used as a remote sensing instrument to produce radio dynamic spectra (Bougeret et al. 2007). These spectra will be used to track the propagation of shocks associated with Type II interplanetary radio bursts through the heliosphere (e.g. Kaiser et al. 1988). The comparison of dynamic spectra from the two spacecraft will give an estimate of the true location of the emission, and hence of the shock, by calculating the time delay between the observations.

The occurrence rate of CMEs follows the solar sunspot cycle in phase and amplitude. The rate of CMEs at solar minimum is about 0.5 per day and peaks at almost 6 per day at solar maximum (St. Cyr et al. 1999; Yashiro et al. 2004; Gopalswamy 2006). The primary STEREO mission will extend from late 2006 to late 2008, during the solar minimum activity phase. However, important geomagnetic storms can occur during any phase of the solar cycle and there will be plenty of CMEs to provide data of interest to researchers.

The global solar magnetic field and its extension into space will simplify during the approach to solar minimum and consequently the identification and tracking of individual CME events from the new STEREO viewpoint should be relatively straightforward. This simplicity, in turn, should aid our ability to investigate the origins of CMEs, their propagation through the solar wind, and their coupling to Earth's environment.

A real advance in our ability to predict the arrival of CMEs at Earth should be provided by the Heliospheric Imagers (HIs) on both STEREO spacecraft, which will track CMEs throughout their trajectory to Earth. This is an important new component of our space weather prediction capability, because of the straightforward ability to accurately predict the arrival of a CME at Earth. Though it is not yet known what the errors in estimated arrival times will be, the HIs should provide significantly smaller errors than current prediction techniques. Since the HIs will view CMEs traveling along the Sun–Earth line, image reconstruction will allow us to determine, for each Earth-directed CME, the direction of its central axis, its overall geometry and size, its mass and its velocity. Detection and limited tracking of CMEs between the Sun and Earth has already been demonstrated by the Solar Mass Ejection Imager (SMEI), an all-sky imager launched in January 2003 into Earth orbit (Howard et al. 2006; Webb et al. 2006). Although data latency limits its use in realtime forecasting, preliminary analyses of SMEI data suggest that such an instrument can detect most geoeffective CMEs and should decrease the errors in estimated arrival times.

The next step in advancing our understanding of this aspect of space weather lies in predicting the geoeffectiveness of CMEs, which is strongly governed by the southward component of its magnetic field, B_z . For at least some events, constraining the geometry of an embedded magnetic flux rope through the morphological appearance of the CME, may allow one to predict the magnetic field orientation, at least in the large scale (Cremades and Bothmer 2004). One area where advances might be expected is in predicting B_z resulting from pileup of the heliospheric plasma sheet in front of a CME. Odstrcil et al. (2005) was able to show that with good modeling of the background heliospheric structure and with a crude parameterization of a CME's initial properties in the low corona, the piled up field could be reasonably modeled. With the improved determination of CME properties that STEREO will provide, models can be better constrained and thereby produce better results.

The twin STEREO spacecraft will provide valuable platforms for detecting and studying SEP events. SEPs are known to be well associated with fast and wide CMEs and their attendant interplanetary shocks (Reames 1997). High energy (1 to hundreds of MeV) particles in an SEP event are thought to be accelerated in the shock near and ahead of a fast CME.

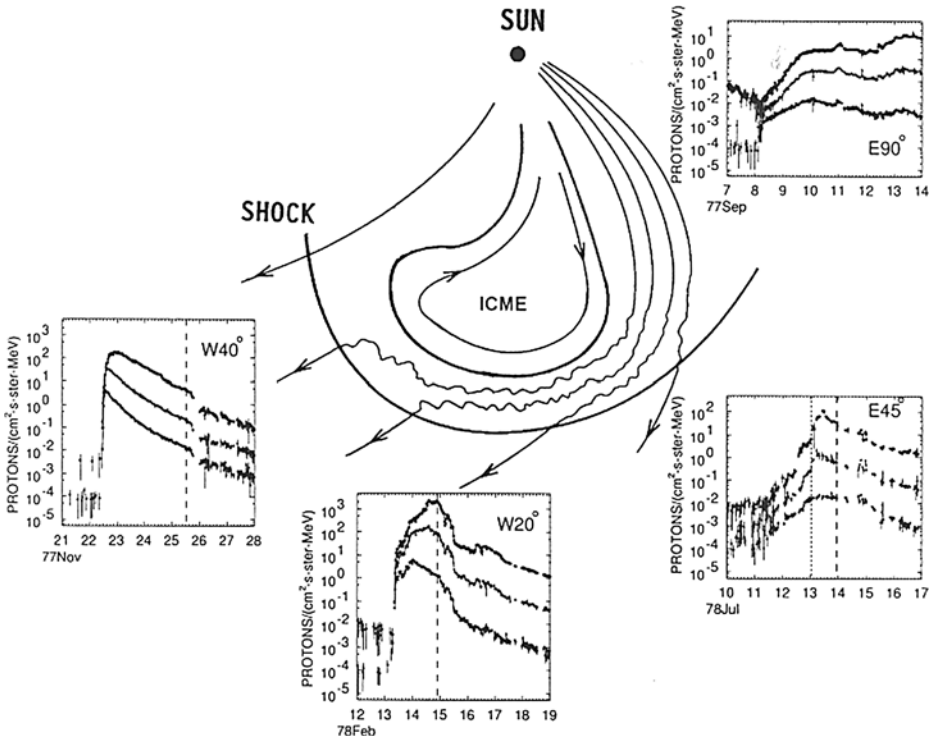


Fig. 2 A view of the ecliptic plane of the heliosphere with 4 inset images showing the SEP event profile expected for each of 4 observer locations relative to the ICME location. Representative *magnetic field* lines illustrate the interplanetary magnetic field and the ICME. For the well connected, W40° case, the SEP onset is prompt and the rise to the peak is rapid. As the observer moves towards the West (moving the ICME source location Eastward), the onset of the SEP event is delayed and the rise time to the event peak lengthens. Figure courtesy of Cane and Lario (2006; Fig. 2)

When the particles gain access to open field lines ahead of the shock, they can propagate into the heliosphere far from the acceleration site. The open field lines emanating from the Sun form an Archimedean spiral and the particles are forced to travel along this curved path (see Fig. 2). Thus, SEPs will have the most direct access and will arrive earliest at a point in space which is east of the SEP source longitude. Therefore, a particle detector on a spacecraft near Earth will be “well-connected” to SEP source regions at western solar longitudes (i.e. W40 degrees), and will see a prompt rise in particle flux (within tens of minutes). Therefore, the STEREO spacecraft lagging Earth (STEREO-B) will be well connected to field lines which are near Sun center as viewed from Earth. Its particle detectors can be used to predict the onset and size of a prompt SEP, as well as the onset of the CME associated with the SEP, at Earth. These are among the most important reasons to have a real-time Beacon available for the STEREO mission.

3 The Space Weather Beacon

The STEREO Space Weather Beacon mode is a continuous, real-time, low data-rate (633 bps) broadcast of the data from the STEREO instruments. The Beacon mode (e.g. St. Cyr

Table 2 The NOAA and NOAA partner ground stations that have agreed, as of January, 2007, to support the Space Weather Broadcast from STEREO

Site	Agency/Institute	Latitude, Longitude
Koganei, Japan	National Institute of Information and Communications Technology (NICT)	35.7N, 139.5E
Toulouse, France	Centre National d'Études Spatiales (CNES)	43.4N, 1.5E
Chilbolton, UK	Rutherford Appleton Laboratory (RAL)	51.1N, 1.4W
Wallop Island, VA	National Oceanic and Atmospheric Administration (NOAA)	37.9N, 75.5W
Boulder, CO	NOAA	40.1N, 105.2W
Fairbanks, AK	NOAA	65.0N, 147.5W

and Davila 2001) is desired for use by both civilian and military agencies for enhancing and providing continuity for space weather products. NASA will provide coverage through the Deep Space Network for about 6 hours per day for each of the STEREO spacecraft. Because of the value of the STEREO data, the NOAA Space Environment Center (SEC) has taken on the responsibility to establish a ground station network to ensure the Space Weather Beacon broadcast from both satellites is received continuously.

The ground stations enlisted to support the STEREO Beacon, as of the start of the prime science mission are given in Table 2. Due to the need to observe two spacecraft simultaneously, and continuously, it is clear that additional ground stations are needed to ensure complete tracking with a high reliability.

Upon receipt of the data at each ground station, each telemetry packet is transferred, as soon as it is received (approximately every 14 seconds), to the STEREO Science Center (SSC) via a socket connection over the internet. A complete discussion of the flow of data and Space Weather Beacon data from the spacecraft to the SSC is covered by Eichstadt et al. (2007). The SSC will make the Level 0 and higher level products available to the scientific community and to NOAA/SEC forecasters in near real-time, with a latency of about 5 minutes from the time the data are received at the ground stations. The data and products desired by NOAA will be fetched automatically from the SSC for integration into forecast specific tools.

The beacon data rate is 633.245 bits per second. This very low data rate necessitates careful choices of the data to be telemetered, as it is clear the full STEREO data set cannot be downlinked in the beacon. In general, the data that will be available in the beacon will be a subset of the full science data set, and will be averaged, binned, and/or compressed to maximize the number of observations which can be returned in real-time. Care has been taken to work with the instrument teams to ensure the resulting data will still be of value to the NOAA space weather forecasters. Some of the tools that are envisioned for use by the NOAA forecasters are described in Sect. 5. The beacon data is described more fully in each of the instrument papers in this volume, but we present here a centralized summary of the data. The data from PLASTIC, IMPACT, and SWAVES are, mostly, fixed and are summarized in Table 3. The beacon imagery content from SECCHI can be reprogrammed in-flight and is almost certain to change throughout the mission. It is expected the relative value of imaging data sets will change with the changing separation angle of the spacecraft,

Table 3 The data available in the Space Weather Broadcast from the PLASTIC, IMPACT, and SWAVES instruments. The Space Weather Broadcast is a low data rate (633 bps) continuous transmission of a subset of the full science data. The SECCHI instrument Space Weather Broadcast is described in the text

Instrument	Observable	Frequency	Units
IMPACT	Instrument status	1 per min	
IMPACT Magnetometer	B vectors	6 per min	nT
IMPACT Suprathermal Electron Telescope – U	Solar e ⁻ flux at 5E [†] , ¹	1 per min	#/cm ² /s
	Non-solar e ⁻ flux at 5E		
IMPACT Suprathermal Electron Telescope – D	e ⁻ flux at 5E	1 per min	#/cm ² /s
IMPACT Solar Wind Electron Analyzer	e ⁻ density	1 per min	cnts/cm ³
	e ⁻ bulk velocity	(computed from 2 second integration)	km/s
	e ⁻ pressure tensor		eV/cm ³
	e ⁻ heat flux		eV/cm ² /s
	PAD [‡] at 2E [†] in 12 look directions		cnts/cm ² /s
IMPACT	Solar Energetic Particle Instrument Suite Status	1 per min	
IMPACT Solar Electron Proton Telescope	e ⁻ flux at 2E in 4 look angles	1 per min, 1 min average	/cm ² /s/sr/MeV
	e ⁻ flux at 2E summed over look angles		
	ion flux at 2E in 4 look angles		
	ion flux at 2E summed over look angles		/cm ² /s/sr/nucleon
IMPACT Low Energy Telescope	Proton flux at 1E in 2 look angles	1 per min, 1 min average	/cm ² /s/sr/nucleon
	Proton flux at 2E summed over look angles		
	He flux at 2E in 2 look angles		
	He flux at 1E summed over look angles		
	³ He flux at 2E summed over look angles		
	CNO flux at 3E summed over look angles		
	Fe flux at 4E summed over look angles		
IMPACT High Energy Telescope	e ⁻ flux at 1E	1 per min,	/cm ² /s/sr/MeV
	Proton flux at 3E	1 min average	/cm ² /s/sr/nucleon
	He flux at 3E		
	CNO flux at 2E		
	Fe flux at 1E		

Table 3 (*Continue*)

Instrument	Observable	Frequency	Units
IMPACT Suprathermal Ion Telescope	He flux at 4E	1 per min,	/cm ² /s/sr/nucleon
	CNO flux at 4E	1 min average	
	Fe flux at 4E		
PLASTIC	Solar Wind H density	1 per min, 1 min average	1/cm ³
PLASTIC	Solar Wind bulk H velocity (v _x , v _y , v _z)	1 per min, 1 min average	km/s
PLASTIC	Solar Wind H ⁺ temperature tensor	1 per min, 1 min average	K
PLASTIC	Solar Wind H ⁺ heat flux tensor	1 per min, 1 min average	J/m ² /s
PLASTIC	Solar Wind He ⁺⁺ peak distribution	1 per min, 1 min average	counts
PLASTIC	Solar Wind He ⁺⁺ peak energy step	1 per min, 1 min average	Step number
PLASTIC	Solar Wind He ⁺⁺ peak deflection step	1 per min, 1 min average	Step number
PLASTIC	Solar Wind He ⁺⁺ peak position	1 per min, 1 min average	Bin number
PLASTIC	Representative Solar Wind charge states	1 per 5 min, 5 min average	counts
PLASTIC	Suprathermal rates	1 per 5 min, 5 min average	counts
PLASTIC	Post Acceleration Field Value	1 per min, 1 min average	kV
	Microchannel Plate Value		
SWAVES	every 100 kHz from 0.125 to 16.025 MHz	1 per min	

[†]Indicates items which can be changed in flight

[‡]PAD – Pitch Angle Distribution, with respect to B field

¹E – Energy channel

as well as when advances are made in key areas of research. The number of SECCHI images to be included in the beacon has not yet been determined. The allocation for the SECCHI space weather data is 500 bits/second. The amount of image compression and binning applied will determine the number of images per hour which can be downlinked. Nominally 7 images can be downlinked if a lossy compression of a factor of 5 is applied and images are binned down to 256 × 256 pixels (8× binning). The amount of compression and binning are programmable on board and testing during the early stages of the mission will determine

the optimal tradeoff of compression, binning, image cadence, and instrument. The SECCHI beacon images are taken from the regular science data sequence. There are no images taken in addition to a normal SECCHI image sequence, so the maximum cadence of images which can be included in the beacon is the regular sequence cadence. At the start of the mission, the highest priority is being given to the COR2 coronagraph data, as experience with SOHO (Sect. 5) shows that its expected value to forecasting geomagnetic storms is high. The data from the HI instruments are also being given high priority, as the ability to track CME's through the heliosphere and update forecasts in real-time is also valuable. Highly binned EUVI images can serve as an irradiance/flare monitor. The forecasting value of COR1 is less clear, so it is given a lower priority for inclusion in the beacon. However, if during the mission, the COR1 data are shown to be useful for forecasting, its priority can be raised. Another possibility is to include automated event detection bits.

4 Space Weather Tools and Projects

The STEREO Space Weather Group was formed in 2002 for the purpose of promoting the scientific community's involvement in preparing, well in advance of the launch of STEREO, to use STEREO data for space weather. More specifically, the Space Weather group has led in organizing the various efforts in software development, modeling efforts and research studies in preparation for using the STEREO observations as a tool for Space Weather. The public internet site for the group is available through the "Science: Space Weather" link on the home page of the STEREO Science Center at: <http://stereo.gsfc.nasa.gov/>. Any interested scientist, whether or not they are a member of the STEREO consortium, is invited to join in the group's efforts, as described on the website.

All pertinent details and information related to the STEREO Space Weather Group efforts are coordinated at the group's website and its activities are closely coordinated with those of the SSC, where the STEREO data, including the Beacon data, will be available. The purpose of the Space Weather Group is to help coordinate space weather efforts involving the STEREO mission and its instruments, including that of individual team members, and to help coordinate those efforts that lead to tools and products that can be tested and used before and after the STEREO launch. Other activities of the group include incorporating and interfacing STEREO data and space weather activities with: (1) Both imaging and in situ data from other existing space missions such as ACE, WIND, SOHO, Ulysses, the Transition Region and Coronal Explorer (TRACE), SMEI, Hinode, the GOES Soft X-ray Imagers (SXI); ground-based observations such as interplanetary scintillation (IPS), optical line and broadband emission, and radio; and future missions planned for the STEREO timeframe, such as the Solar Dynamics Observatory (SDO); (2) The Geospace community to understand the coupling of and geospace responses to CMEs and other transient disturbances by encouraging and participating in space weather campaigns; (3) The Community Coordinated Modeling Center (CCMC) and other simulation and modeling groups to use STEREO data as input to space weather models; (4) The SECCHI 3D Reconstruction and Visualization Team to develop models that have a space weather context; (5) The various virtual observatories that are being developed; (6) The International Heliophysical Year (IHY) program in 2007; (7) Meetings and workshops involving space weather; and (8) NASA's EP/O and PAO and other outreach activities.

Some of the tools and projects currently being developed for use with the STEREO observations for space weather applications are briefly described next, with references where available. These have been grouped into categories of Space Weather Tools, including those

for CME Detection and CME-related Features Detection, Space Weather-Enabling Projects, and Data Browsers and Viewers. Each project description contains a title, the names of the main coordinators and their affiliations, and a brief description. Such projects are continually evolving, so this list should be considered only as an indication of the projects that will be available at the start of the mission. Undoubtedly, after launch, and as the STEREO data accumulates, the concepts of how to use these data for space weather purposes will evolve and new projects will be added.

SPACE WEATHER TOOLS:

Geometric Localization of STEREO CMEs (*V. Pizzo, D. Biesecker – NOAA; Pizzo and Biesecker 2004*)

A tool utilizing a series of lines of sight from two views to define the location, shape, size and velocity of a CME. This is to be automated and used to decide whether and when a CME will impact Earth.

WSA Model Predictions (*N. Arge – Air Force Research Laboratory; J. Luhmann – Univ. of California-Berkeley; D. Biesecker – NOAA; Arge and Pizzo 2000*)

The Wang-Sheeley-Arge and ENLIL 3D MHD solar wind models will be integrated. The combined model will provide routine predictions of vector solar wind velocity, density, temperature and magnetic polarity anywhere desired in the inner heliosphere. This model will be driven by ground-based magnetograph data.

CME Detection:

CACTUS – Computer Aided CME Tracking (*E. Robbrecht, D. Berghmans; Royal Observatory of Belgium; Robbrecht and Berghmans 2005*)

A near real-time tool for detecting CMEs in SECCHI images. The output is a quicklook CME catalog with measurements of time, width, speed, and near real-time CME warnings. It has been successfully tested on LASCO data and the tool is available at <http://sidc.oma.be/cactus>.

SEEDS – Solar Eruptive Event Detection System (*J. Zhang; George Mason Univ.*)

A tool for detecting, classifying and analyzing CMEs in SECCHI images. The output is an automatically generated CME catalog with measurements of time, width, speed, and near real-time CME warnings. It is being tested on LASCO data.

On-board Automatic CME Detection Algorithm (*E. De Jong, P. Liewer, J. Hall, J. Lorre, NASA/Jet Propulsion Laboratory; R. Howard, Naval Research Laboratory*)

An algorithm based on feature tracking which uses two successive images to determine whether or not a CME has occurred. The algorithm is intended to be run on-board the spacecraft.

CME-Related Features Detection:

Computer Aided EUVI Wave and Dimming Detection (*O. Podladchikova, D. Berghmans, A. Zhukov – Royal Observatory Belgium; Podladchikova and Berghmans 2005*)

A near real-time tool for detecting EUV waves and dimming regions. It is being tested on SOHO EIT images.

Velocity Map Construction (*J. Hochedez, S. Gissot – Royal Observatory Belgium*)

A program to analyze velocity flows on SECCHI images and to detect CME onsets & EUV waves. Also produces near-realtime warnings of fast CMEs and reconstructs 3D velocity maps of CMEs from 2D maps from each STEREO spacecraft.

Automatic Solar Feature Classification (*D. Rust, P. Bernasconi – Johns Hopkins University/Applied Physics Laboratory*)

A tool for detecting and characterizing solar filaments and sigmoids using recognition and classification in solar images. The goal is to measure magnetic helicity parameters and forecast eruptions using filaments and sigmoids.

SPACE WEATHER – ENABLING PROJECTS:

Identifying and Tracking CMEs with the Heliospheric Imagers (*R. Harrison, C. Davis – Rutherford Appleton Laboratory*)

A tool that uses triangulation to measure the speed and direction of CMEs in order to forecast their arrival at Earth. Simulations will be used to show how model CMEs can be identified and tracked with the HIs.

Structural Context of the Heliosphere Using SMEI Data (*D. Webb – Boston College/Air Force Research Laboratory; B. Jackson – Univ. of California-San Diego; e.g. Jackson et al. 2006*)

A tool that uses analyses of SMEI images to provide structural context of the heliosphere, especially for the HIs. It will also provide complementary observations of transient disturbances, especially those that are Earth-directed.

Interplanetary Acceleration of ICMEs (*M. Owens – Boston University*)

A program to construct acceleration profiles of fast ICMEs over a large heliocentric range using multi-point HI measurements to understand the forces acting on ejecta. This tool will aid in improved prediction of ICME arrival times at Earth.

Relationship Between CMEs and Magnetic Clouds (*S. Matthews – Mullard Space Science Lab.*)

A project to assess the potential geoeffectiveness of CMEs based on their association with magnetic clouds. This project is intended to determine which particular characteristics lead to the production of a magnetic cloud.

3-dimensional Structure of CMEs (*V. Bothmer, H. Cremades – University of Goettingen; D. Tripathi – Cambridge University; Cremades and Bothmer 2004*)

A program to compare analysis of SECCHI images on the internal magnetic field configuration and near-Sun evolution of CMEs with models based on SOHO observations. The goal is to forecast flux rope structure and make 3-dimensional visualizations of CMEs.

DATA BROWSERS AND VIEWERS:

STEREO Science Center Real-Time Data Pages (*W. Thompson – GSFC*)

The main public website for viewing real-time STEREO data. Available at the following URL: http://stereo-ssc.nascom.nasa.gov/mockup/latest_mockup.shtml.

Solar Weather Browser (*B. Nicula, D. Berghmans, R. Van der Linden – Royal Observatory Belgium*)

A user-friendly browser tool for finding and displaying solar data and related context information. The tool is available at <http://sdc.oma.be/SWB/>.

STEREO Key Parameter Browser (*C. Russell & IMPACT, PLASTIC & SWAVES teams; UCLA*)

An easily browsable merged key parameter data display including the in situ and SWAVES radio data.

Carrington Rotation In situ Browser (*J. Luhmann, P. Schroeder – Univ. of California-Berkeley*)

A browser for identifying in situ events and their solar sources over Carrington Rotation time scales. It includes near-Earth (ACE) data sets for third point views and image movies from SECCHI and SOHO (near-Earth). See: http://sprg.ssl.berkeley.edu/impact/data_browser.html.

JAVA-3D Synoptic Information Viewer (*J. Luhmann, P. Schroeder – Univ. of California-Berkeley*)

A JAVA applet for viewing 3-dimensional Sun and solar wind data based on synoptic solar maps and potential field models of the coronal magnetic field.

Radio and CME Data Pages (*M. Pick, M. Maksimovic, J.L. Bougeret, A. Lecacheux, R. Romagan, A. Bouteille – Observatoire de Paris-Meudon*)

A collection of ground radio imaging, spectra and movies, as well as SWAVES and SECCHI summary data on CMEs. Available at <http://secchirh.obspm.fr/>.

5 Space Weather Tools for the SEC Forecast Center

5.1 Lessons from the SOHO and ACE Missions

In the recent past and continuing, two non-NOAA missions, SOHO and ACE, were successfully utilized in the forecast center. Each of these missions followed a different path into the forecast center, and thus, are illustrative for bringing STEREO into the forecast center.

In the case of the SOHO mission, there were few, if any, expectations of the mission being used for space weather forecasting. However, one dramatic event in January, 1997, the effects of which were described in Sect. 1.1, quickly changed that. The event was a halo CME observed by SOHO/LASCO on January 6th (Burlaga et al. 1998) which was reported by D. Michels of the Naval Research Laboratory to a meeting of the International Solar Terrestrial Physics (ISTP) project, while the event was still in progress. It was predicted the event would arrive at Earth on January 10th, a remarkably good real-time prediction. This illustrated the ability to use the mission in a real-time way. The time for a typical CME to transit 1 AU (~ 3 days) implies that a latency of a few hours still allows time for a forecast to be made. This event, and subsequent halo CMEs, resulted in NOAA and the SOHO/LASCO team working together to make the data available to NOAA as quickly as possible.

However, it took more than just having available data, to do the forecasting. During normal business hours, the LASCO team examines the data and issues a report on all halo events, which includes a detailed description, including the speed of the event. The NOAA forecast center operates 24 hours a day, and can't always wait for a report from the LASCO team. Thus, the same tools used by the LASCO team to plot height-time curves and derive speed estimates for the events were installed at the forecast center, with direct assistance and training from the LASCO team. Since then, the SOHO/LASCO data have been on prominent display in the forecast center, where they are used to help forecast geomagnetic storms. One

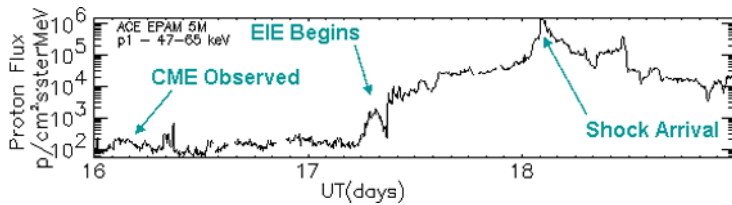


Fig. 3 An example of an energetic ion enhancement (EIE) with arrows indicating events of interest to forecasters. Plotted are 5 minute averages of 47–65 keV proton fluxes

lesson learned is that it was non-NOAA scientists who not only learned the value of the data for forecasting, but also demonstrated it. The close cooperation between the scientists and the forecast center, which included training on relevant tools, was also a key component.

In the case of the ACE mission, it was recognized from the start that its data would be important for forecasting. As is being done now for STEREO, NOAA organized a network of ground stations to receive ACE data in real-time. Because ACE, which monitors the solar wind, orbits the L1 Lagrange point, there is typically only about 1 hour of warning between when an event passes L1 and arrives at Earth, and extreme events arrive much more quickly. Thus, the data must be available in the forecast center within minutes of being acquired or it becomes less useful to forecasters. To meet this requirement, ACE broadcasts real-time data continuously and ground station processing gets the data to forecasters quickly.

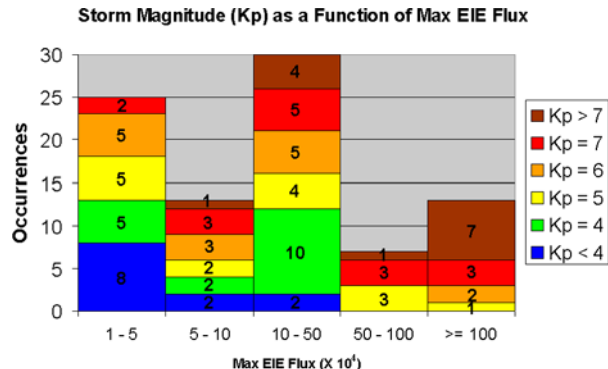
The ACE data from the magnetometers and solar wind measurements were expected to be and are used daily by forecasters to monitor the state of the solar wind and to watch for arriving ICMEs. It was also recognized that the low energy proton channels of ACE/EPAM (Gold et al. 1998) would be useful for warning of approaching interplanetary shocks (Zwickl et al. 1998). An annotated example of an energetic ion enhancement (EIE) is shown in Fig. 3. Other than a study by Smith and Zwickl (1999) utilizing WIND data, there were no quantitative studies of these events from which forecasters could derive information to use in producing a forecast. Even the Smith and Zwickl study only discussed typical signatures that were needed to be certain a shock was on-coming, without providing specific values which could be used by forecasters to produce a product for customers. Thus, the forecast center undertook a study to provide themselves with the data necessary for forecasting shock arrival and subsequent geomagnetic storms (Smith et al. 2004).

Key elements of the Smith et al. study relevant to forecasting were: the use of the geomagnetic index K_p , which is a forecast center product; the establishment of a relationship between the intensity of energetic ion enhancements (EIE) and the resulting K_p ; establishing thresholds of EIE flux above which forecasters could be confident of distinguishing an ICME source from a high speed stream source; looking specifically at overlapping events; and the role of B_z . Shown in Fig. 4 is a chart which shows quite a lot of information to the forecasters. If the flux of the EIE is seen to exceed $50 \times 10^4 \text{ p cm}^{-2} \text{ s}^{-1} \text{ sr}^{-1} \text{ MeV}^{-1}$ then a storm reaching a level of at least G1 ($K_p = 5$) will result. What is also clear is that EIE fluxes an order of magnitude smaller still have a slight chance of producing a severe geomagnetic storm.

5.2 Bringing STEREO into the Forecast Center

In this section, we describe some of the STEREO mission related tools which SEC has identified as desirable. Some of these tools will be developed in time for the start of the mission, while others may never be developed, depending on whether our preconceptions of

Fig. 4 An example from an internal forecast center document showing the number of geomagnetic storms as a function of the peak flux of the corresponding shock-associated EIE

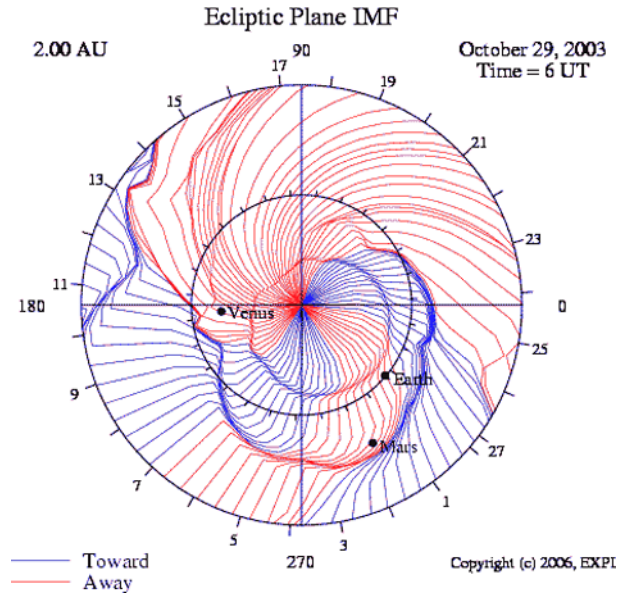


the utility of the data turn out to be true and are commensurate with the resources needed for development. There are several important points to make about integrating STEREO data into the SEC forecast center. With the addition of so many data sets, it will be difficult for forecasters to inspect all of the relevant basic time series data or raw imagery from STEREO in addition to all of the data already used in the forecast center. Thus, algorithms which can aid in at least some simple interpretations of the data will be valuable. In addition, without tools to take advantage of the three-dimensional view provided by STEREO data, the full value of the STEREO data to forecasters will not be realized. It is hoped and expected that many of the projects described in Sect. 4 will be successful and will produce tools and products which can be transitioned to the SEC forecast center.

It is worth mentioning that there are substantial hurdles to be overcome for a tool to be useful for forecasters. First, the overall benefit the tool provides to forecasters must be clear. However, even when the benefits of a tool or model are clear, unless the forecasters have confidence that the tool is providing a good prediction at a certain time or for a specific event, they are unlikely to use the tool. Thus, it is vital for validation studies to have been performed, illustrating under what conditions a tool does or does not work.

The STEREO PLASTIC and IMPACT instruments provide a suite of observations which complement the NASA ACE mission (Stone et al. 1998; Garrard et al. 1998) data currently in use by NOAA forecasters. Thus, the only additional knowledge required for interpretation of the in situ data from these instruments will be recognizing how to account for the displaced location of the STEREO spacecraft relative to ACE. One obvious way to do this is to use the lagging STEREO-B spacecraft as a monitor of co-rotating structures. Whether it is a sector crossing or a high speed wind stream, the lagging spacecraft will encounter these structures before they sweep past Earth. One year into the mission, the lead time for corotating structures will be about 40 hours. There will be an obvious trade-off between the forecast lead time and the confidence in the forecast, as longer lead times mean greater time for a structure to evolve. Even given a temporally stable structure, small changes in spatial location can lead to significant observed differences, as was clearly shown by results from the HELIOS mission (e.g. Schwenn et al. 1981). Any temporal changes can be mitigated to some extent by ensuring the forecasters also have access to models of the solar wind. Thus, for forecasters, we envision a standard data display, similar to what forecasters use for ACE/SWEPAM data, showing solar wind density, speed and temperature (see http://www.sec.noaa.gov/ace/ACErtsw_data.html). Appended to this would be the same parameters from STEREO-B, with the lead time clearly identified on the horizontal axis. Overlaid on this would be the solar wind speed derived from the Wang-Sheeley model (Wang

Fig. 5 The interplanetary magnetic field as computed with the HAFv2 model. A series of ICMEs are evident, in particular, one with a leading edge just beyond Mars and another just inside the orbit of Earth. Figure courtesy of Exploration Physics International, Inc. (EXPI), Huntsville, Alabama



and Sheeley 1990). Returning to a point made in the previous paragraph, adding the Wang-Sheeley solar wind model to this display aides the forecaster, as a variation on this model is currently used in the forecast center (Arge and Pizzo 1999). Note, the predictions from both STEREO-B and Wang-Sheeley are valid only for co-rotating structures and any interplanetary ejecta will invalidate the output of these models. Clearly forecasters will need something integrated into the tool, or good situational awareness, to identify times when the model output will be invalid due to the presence of ICMEs.

Another potential product would involve utilizing the STEREO-B solar wind data to provide a longer lead time for predicted K_p from models such as the Costello Geomagnetic Activity Index (e.g. Detman and Joselyn 1999; <http://www.sec.noaa.gov/rpc/costello/index.html>) and that of Wing et al. (2005). Because these models rely on data from the ACE spacecraft, they can only be used for short term warnings. It is obvious that adding STEREO-B data to these models would provide a longer lead time.

STEREO will provide important validation data both for the Wang-Sheeley model and the Hakamada-Akasofu-Fry version 2 (HAFv2) solar wind model (Fry et al. 2003). While the HAF model is not an official SEC forecast product, it is used by forecasters, and it has recently been adopted by the USAF Air Force Weather Agency. Both models can provide an ecliptic plane view of the heliosphere out to large heliocentric distances (see Fig. 5). The HAFv2 model output is available out to 10 AU, encompassing the orbits of Mars, Jupiter and Saturn. Currently, validations for each model can only be based on comparisons to ACE data. One data point of comparison for a model of the whole ecliptic plane is obviously inadequate. The addition of data from both STEREO spacecraft is still woefully inadequate, but will be a significant improvement over the current situation. This will be particularly true for Mars forecasts when Mars is not in conjunction with Earth but may be in conjunction with either of the STEREO spacecraft.

Improvements to SEC's SEP event prediction is consistently identified as a high priority need by the forecasters (see Table 1). Given the clear relationship between the shape and relative timing of SEP light curves and the longitude difference between the source region

and Earth (Cane et al. 1988), adding the STEREO spacecraft SEP data should provide some of the desired improvement. Determining what needs to be done to create a tool which takes the real-time STEREO data and produces an improved SEP prediction at Earth has not yet been done.

Turning now to the remote sensing data, it is obvious that the three-dimensional information about ICMEs that STEREO will provide can be of great benefit for forecasters. However, there are currently a myriad of ideas on how the three-dimensional reconstructions can be done and how they can be displayed. Here, we outline one simple example that would be beneficial to forecasters. From a display perspective, rather than giving the forecaster complete control and the ability to view an event from any angle, the basic information needed can be reduced to three displays. First, the same ecliptic plane view, as illustrated in Fig. 5, is an obvious choice. This gives the forecaster the ability to see the relative location of the event and Earth, along with a way to see how it is evolving and accelerating. The display would also show the longitudinal extent of the ICME and its distribution of mass. Second, a view from perpendicular to the Sun–Earth line, in the ecliptic plane, would illustrate the latitudinal extent of the event and the distribution of mass. Third, and finally, the ability to also see a view from the perspective of an observer on Earth, looking in the direction of the Sun will be important. This would give the forecaster the information they need about whether the event will strike Earth. The same information could be derived from the first two views, however, this particular view would make it obvious from just a single picture.

Pictures and movies are always good to have, partly because they give forecasters a quick overview of the situation, but also because they are a quick way to validate the output of any model or tool. A tool that SEC researchers envision for the forecast center would be one which provides all of the desired parameters about CME-related geomagnetic storms in one place. As described in earlier sections, efforts are underway or planned on forecasting CME arrival time, CME impact angle and the resulting storm magnitude, and even on the basic question of whether the interplanetary CME will strike Earth. Asking a forecaster to perform all the image processing necessary to derive such information, even given acceptable models, would be too time consuming. Thus, automation of CME detection, CME speed determination, CME impact angle, and potentially other parameters will be needed. Much work has been done in this area (e.g. Robbrecht and Berghmans 2005) but much more work is needed. Automated tools which have a high rate of false positive results may be sufficient for a researcher, but are of little or no use for forecasters, who must act in real-time. Given an automated tool meeting forecaster needs, its output can then be fed into models which predict if the CME will hit Earth, and if so when, how strong the resulting storm will be and how long the storm will last. Putting these predictions into a single display for forecasters with the associated errors would be a significant benefit. By constantly updating the forecasted parameters, utilizing data from the SWAVES and SECCHI/HI instruments, it is hoped that forecasters would be provided with the best possible predictions throughout the entire transit of an ejection. As stated earlier, the imagery would be available to validate and check any of the parameters being predicted.

6 Summary

The NOAA Space Environment Center believes the STEREO mission will be a significant benefit for forecasters and has invested the effort to put together a ground station network to receive the STEREO data in real-time. But, the promise of the STEREO mission and the expected return from the mission is just that, a promise. When the data finally become

available and the performance of the instruments is verified, then we will have a better idea of whether the promise will be realized. It is difficult to predict which elements of the program will be successful and ultimately beneficial to forecasters, either immediately or in the long term. In this paper, we focused primarily on the promise of projects and illustrated some of the features which are necessary for a successful product; primarily utility, ease of use, and validation. One thing to keep in mind is that with the changing elongation angles, the relative utility of STEREO will constantly evolve. This may also necessitate changes in the way data are interpreted as the mission progresses. However, there are no technical hurdles to the STEREO mission extending beyond its 2-year design life and, if the mission proves successful, the research advances made during the first one-half orbit of STEREO to the far-side of the Sun could be applied as each STEREO spacecraft completes its orbit, coming back towards Earth.

References

- C.N. Arge, V.J. Pizzo, in *Proceedings of the 9 International Solar Wind Conference*, ed. by S.R. Habbal, R. Esser, J.V. Hollweg, P.A. Isenberg (1999), p. 569
- C.N. Arge, V.J. Pizzo, *J. Geophys. Res.* **105**(A5), 10465 (2000). doi:[10.1029/1999JA900262](https://doi.org/10.1029/1999JA900262)
- M.J. Aschwanden, *Physics of the Solar Corona* (Springer, Praxis, 2006), Chap. 17
- D.N. Baker, J.H. Allen, S.G. Kanekal, G.D. Reeves, *EOS* **79**(40), 477 (1998)
- Bougeret et al., this volume (2007)
- G.E. Brueckner, J.-P. Delabouminiere, R.A. Howard, S.E. Paswaters, O.C. St. Cyr, R. Schwenn, P. Lamy, G.M. Simnett, B. Thompson, D. Wang, *Geophys. Res. Lett.* **25**, 3019 (1998)
- L. Burlaga, R. Fitzenreiter, R. Lepping, K. Ogilvie, A. Szabo, A. Lazarus, J. Steinberg, G. Gloeckler, R. Howard, D. Michels, C. Farrugia, R.P. Lin, D.E. Larson, *J. Geophys. Res.* **103**(A1), 277 (1998)
- H.V. Cane, D. Lario, *Space Sci. Rev.* (2006). doi:[10.1007/s11214-006-9011-3](https://doi.org/10.1007/s11214-006-9011-3)
- H.V. Cane, D.V. Reames, T.T. von Rosenvinge, *J. Geophys. Res.* **93**, 9555 (1988)
- H. Cremades, V. Bothmer, *Astrophys. Astron.* **422**, 307–322 (2004). doi:[10.1051/0004-6361:20035776](https://doi.org/10.1051/0004-6361:20035776)
- T. Detman, J. Joselyn, in *Proceedings of the Ninth International Solar Wind Conference*, ed. by S.R. Habbal, R. Esser, J.V. Hollweg, P.A. Isenberg (1999), p. 729
- J. Eichstadt, W.T. Thompson, J.B. Gurman, P. Schroeder, this volume (2007)
- C.D. Fry, M. Dryer, Z. Smith, W. Sun, C.S. Deehr, S.-I. Akasofu, *J. Geophys. Res.* **108**(A2), 1070 (2003). doi:[10.1029/2002JA00947](https://doi.org/10.1029/2002JA00947)
- A. Galvin et al., this volume (2007)
- T.L. Garrard, A.J. Davis, J.S. Hammond, S.R. Sears, *Space Sci. Rev.* **86**, 649 (1998)
- R.E. Gold, S.M. Krimigis, S.E. Hawkins, III, D.K. Haggerty, D.A. Lohr, E. Fiore, T.P. Armstrong, G. Holland, L.J. Lanzerotti, *Space Sci. Rev.* **86**, 541 (1998)
- Goodman, J.M. *Space Weather & Telecommunications*. Kluwer International Series in Engineering and Computer Science, vol. 782 (Springer, 2005)
- N. Gopalswamy, A. Lara, R.P. Lepping, M.L. Kaiser, D. Berdichevsky, O.C. St. Cyr, *Geophys. Res. Lett.* **27**, 145 (2000)
- N.J. Gopalswamy, *Astrophys. Astron.* **27**(2–3), 243–254 (2006)
- J. Gosling, S. Antiochos, K. Baker, P. Bellaire, B. Blake, G. Crowley, J. Eddy, C. Goodrich, N. Gopalswamy, M. Hesse, N. Hurlburt, C. Jackman, J. Kozyra, B. Labonte, J. Lean, J. Linker, J. Mazur, T. Onsager, D. Sibeck, Targeted research and technology within NASA's living with a Star Program – Report of the Science Definition Team. NASA Document FP-2003-11586-GSFC, November 2003
- R.A. Howard, D.J. Michels, N.R. Sheeley Jr., M.J. Koomen, *Astrophys. J.* **263**, L101 (1982)
- R.A. Howard et al., this volume (2007)
- T.A. Howard, D.F. Webb, S.J. Tappin, D.R. Mizuno, J.C. Johnston, *J. Geophys. Res.* **111**, A04105 (2006). doi:[10.1029/2005JA011349](https://doi.org/10.1029/2005JA011349).
- B.V. Jackson, A. Buffington, P.P. Hick, X. Wang, D. Webb, *J. Geophys. Res.* **111**, A4 (2006). doi:[10.1029/2004JA010942](https://doi.org/10.1029/2004JA010942)
- M.L. Kaiser, M.J. Reiner, N. Gopalswamy, R.A. Howard, O.C. St. Cyr, B.J. Thompson, J.-L. Bougeret, *Geophys. Res. Lett.* **25**, 2501 (1998). doi:[10.1029/98GL00706](https://doi.org/10.1029/98GL00706)
- L.J. Lanzerotti, D.J. Thomson, C.G. Maclennan, in *Modern Radio Science*, ed. by M.A. Stuchly (Oxford, University Press, Oxford 1999), pp. 25–50.

- L.J. Lanzerotti, in *Space Weather*, ed. by P. Song, H.J. Singer, G.L. Siscoe. AGU Monograph, vol. 125, (2001), pp. 11–22
- J. Luhmann et al., this volume (2007). doi: [10.1007/s11214-007-9170-x](https://doi.org/10.1007/s11214-007-9170-x)
- G. Michalek, N. Gopalswamy, A. Lara, P.K. Manoharan, Astron. Astrophys. **423**, 729 (2004). doi: [10.1051/0004-6361:20047184](https://doi.org/10.1051/0004-6361:20047184)
- Y.-J. Moon, K.-S. Cho, M. Dryer, Y.-H. Kim, S.-C. Bong, J. Chae, Y.D. Park, Astrophys. J. **624**, 414 (2005). doi: [10.1086/428880](https://doi.org/10.1086/428880)
- D. Moses, F. Clette, J.-P. Delaboudinière, G.E. Artzner, M. Bougnet, J. Brunaud, C. Carabetian, A.H. Gabriel, J.F. Hochedez, F. Millier, X.Y. Song, B. Au, K.P. Dere, R.A. Howard, R. Kreplin, D.J. Michels, J.M. Defise, C. Jamar, P. Rochus, J.P. Chaunineau, J.P. Marioge, R.C. Catura, J.R. Lemen, L. Shing, R.A. Stern, J.B. Gurman, W.M. Neupert, J. Newmark, B. Thompson, A. Maucherat, F. Portier-Fozzani, D. Berghmans, P. Cugnon, E.L. Van Dessel, J.R. Gabryl, Solar Phys. **175**, 571 (1997). doi: [10.1023/A:1004902913117](https://doi.org/10.1023/A:1004902913117)
- S. Odenwald, J. Green, W. Taylor, Adv. Space Res. **38**, 280 (2006). doi: [10.1016/j.asr.2005.10.046](https://doi.org/10.1016/j.asr.2005.10.046)
- D. Odstrcil, V.J. Pizzo, C.N. Arge, J. Geophys. Res. **110**, A02106 (2005). doi: [10.1029/2004JA010745](https://doi.org/10.1029/2004JA010745)
- V.J. Pizzo, D.A. Biesecker, Geophys. Res. Lett. **31**, L21802 (2004). doi: [10.1029/2004GL021141](https://doi.org/10.1029/2004GL021141)
- O. Podladchikova, D. Berghmans, Solar Phys. **228**, 265 (2005). doi: [10.1007/s11207-005-5373-z](https://doi.org/10.1007/s11207-005-5373-z)
- B.B. Poppe, EOS **81**(29), 322 (2000)
- D.V. Reames, in *Coronal Mass Ejections*, ed. by N. Crooker, J.A. Joselyn, J. Feynman, AGU Geophysical Monograph, vol. 99 (1997), p. 217
- G.D. Reeves, R.H.W. Friedel, R.D. Belian, M.M. Meier, M.G. Henderson, T. Onsager, H.J. Singer, D.N. Baker, X. Li, J.B. Blake, J. Geophys. Res. **103**(A8), 17559 (1998). doi: [10.1029/97JA03236](https://doi.org/10.1029/97JA03236)
- I.G. Richardson, D.F. Webb, J. Zhang, D.B. Berdichevsky, D.A. Biesecker, J.C. Kasper, R. Kataoka, J.T. Steinberg, B.J. Thompson, C.-C. Wu, A.N. Zhukov, J. Geophys. Res. **111**(A7), A07S09 (2006). doi: [10.1029/2005JA011476](https://doi.org/10.1029/2005JA011476)
- E. Robbrecht, D. Berghmans, Solar Phys. **228**, 239 (2005). doi: [10.1007/s11207-005-5004-8](https://doi.org/10.1007/s11207-005-5004-8)
- O.C. St. Cyr, J.T. Burkepile, A.J. Hundhausen, A.R. Lecinski, J. Geophys. Res. **104**(A6), 12493 (1999)
- O.C. St. Cyr, R.A. Howard, N.R. Sheeley, S.P. Plunkett, D.J. Michels, S.E. Paswaters, M.J. Koomen, G.M. Simnett, B.J. Thompson, J.B. Gurman, R. Schwenn, D.F. Webb, E. Hildner, P.L. Lamy, J. Geophys. Res. **105**(A8), 18169 (2000)
- O.C. St. Cyr, J.M. Davila, in *Space Weather*, ed. by P. Song, H. Singer, G. Siscoe, AGU Geophysical Monograph, vol. 125 (Washington DC, 2001), p. 205
- K. Scherer, H. Fichtner, B. Heber, U. Mall, *Space Weather: The Physics Behind a Slogan*. Lecture Notes in Physics, vol. 656 (Springer, Berlin 2005). doi: [10.1007/b1000037](https://doi.org/10.1007/b1000037)
- R. Schwenn, K.-H. Mühlhäuser, H. Rosenbauer, in *Solar Wind 4*, ed. by H. Rosenbauer (1981), p. 118
- G. Siscoe, Space Weather **4**, S01003 (2006). doi: [10.1029/2005SW000178](https://doi.org/10.1029/2005SW000178)
- G. Siscoe, S.C. Solomon, Space Weather **4**, S04002 (2006). doi: [10.1029/2005SW000205](https://doi.org/10.1029/2005SW000205)
- Z. Smith, W. Murtagh, C. Smithtro, J. Geophys. Res. **109**, A01110 (2004). doi: [10.1029/2003JA010044](https://doi.org/10.1029/2003JA010044)
- Z. Smith, R. Zwickl, in *Solar Wind Nine*, ed. by S.R. Habbal, R. Esser, J.V. Hollweg, P.A. Isenberg (1999), p. 577
- P. Song, H.J. Singer, G.L. Siscoe, *Space Weather*. AGU Monograph, vol. 125 (2001)
- E.C. Stone, A.M. Frandsen, R.A. Mewaldt, E.R. Christian, D. Margolies, J.F. Ormes, F. Snow, Space Sci. Rev. **86**, 1 (1998)
- B.J. Thompson, S.P. Plunkett, J.B. Gurman, J.S. Newmark, O.C. St. Cyr, D.J. Michels, Geophys. Res. Lett. **25**, 2465 (1998). doi: [10.1029/98GL50429](https://doi.org/10.1029/98GL50429)
- Y.-M. Wang, N.R. Sheeley Jr., Astrophys. J. **355**, 726 (1990). doi: [10.1086/168805](https://doi.org/10.1086/168805)
- D.F. Webb, E.W. Cliver, N.U. Crooker, O.C. St. Cyr, B.J. Thompson, J. Geophys. Res. **105**(A4), 7491 (2000). doi: [10.1029/1999JA000275](https://doi.org/10.1029/1999JA000275)
- D.F. Webb, E.W. Cliver, N. Gopalswamy, H.S. Hudson, O.C. St. Cyr, Geophys. Res. Lett. **25**, 2469 (1998). doi: [10.1029/98GL00493](https://doi.org/10.1029/98GL00493)
- D.F. Webb, D.R. Mizuno, A. Buffington, M.P. Cooke, C.J. Eyles, C.D. Fry, L.C. Gentile, P.P. Hick, P.E. Holladay, T.A. Howard, J.G. Hewitt, B.V. Jackson, J.C. Johnston, T.A. Kuchar, J.B. Mozer, S. Price, R.R. Radick, G.M. Simnett, S.J. Tappin, J. Geophys. Res. **111**, A12101 (2006). doi: [10.1029/2006JA011655](https://doi.org/10.1029/2006JA011655)
- S. Wing, J.R. Johnson, J. Jen, C.-I. Meng, D.G. Sibeck, K. Bechtold, J. Freeman, K. Costello, M. Balikhin, K. Takahashi, J. Geophys. Res. **110**(A4) (2005). doi: [10.1029/2004JA010500](https://doi.org/10.1029/2004JA010500)
- S. Yashiro, N. Gopalswamy, G. Michalek, O.C. St. Cyr, S.P. Plunkett, N.B. Rich, R.A. Howard, J. Geophys. Res. **109**, A07105 (2004). doi: [10.1029/2003JA010282](https://doi.org/10.1029/2003JA010282)
- R.D. Zwickl, K.A. Doggett, S. Sahm, W.P. Barrett, R.N. Grubb, T.R. Detman, V.J. Raben, C.W. Smith, P. Riley, R.E. Gold, R.A. Mewaldt, T. Maruyama, Space Sci. Rev. **86**, 633 (1998)

Sun Earth Connection Coronal and Heliospheric Investigation (SECCHI)

**R.A. Howard · J.D. Moses · A. Vourlidas · J.S. Newmark · D.G. Socker ·
S.P. Plunkett · C.M. Korendyke · J.W. Cook · A. Hurley · J.M. Davila ·
W.T. Thompson · O.C. St Cyr · E. Mentzell · K. Mehalick · J.R. Lemen ·
J.P. Wuelser · D.W. Duncan · T.D. Tarbell · C.J. Wolfson · A. Moore · R.A. Harrison ·
N.R. Waltham · J. Lang · C.J. Davis · C.J. Eyles · H. Mapson-Menard ·
G.M. Simnett · J.P. Halain · J.M. Defise · E. Mazy · P. Rochus · R. Mercier ·
M.F. Ravet · F. Delmotte · F. Auchere · J.P. Delaboudiniere · V. Bothmer ·
W. Deutsch · D. Wang · N. Rich · S. Cooper · V. Stephens · G. Maahs · R. Baugh ·
D. McMullin · T. Carter**

Originally published in the journal Space Science Reviews, Volume 136, Nos 1–4.
DOI: [10.1007/s11214-008-9341-4](https://doi.org/10.1007/s11214-008-9341-4) © Springer Science+Business Media B.V. 2008

R.A. Howard (✉) · J.D. Moses · A. Vourlidas · J.S. Newmark · D.G. Socker · S.P. Plunkett ·
C.M. Korendyke · J.W. Cook · A. Hurley
E.O. Hulbert Center for Space Research, Naval Research Laboratory, Washington, DC 20375, USA
e-mail: russ.howard@nrl.navy.mil

J.M. Davila · W.T. Thompson · O.C. St Cyr · E. Mentzell · K. Mehalick
NASA Goddard Space Flight Center, Greenbelt, MD 20742, USA

J.R. Lemen · J.P. Wuelser · D.W. Duncan · T.D. Tarbell · C.J. Wolfson · A. Moore
Lockheed Martin Solar and Astrophysics Lab., Palo Alto, CA 94304, USA

R.A. Harrison · N.R. Waltham · J. Lang · C.J. Davis
Space Science and Technology Dept., Rutherford Appleton Laboratory, Chilton, Didcot,
Oxfordshire OX11 0QX, UK

C.J. Eyles · H. Mapson-Menard · G.M. Simnett
Astrophysics and Space Research Group, University of Birmingham, Edgbaston, Birmingham B15 2TT,
UK

J.P. Halain · J.M. Defise · E. Mazy · P. Rochus
Centre Spatial de Liège, Université de Liège, Avenue du Pré-Aily, 4031 Angleur, Belgium

R. Mercier · M.F. Ravet · F. Delmotte
Laboratoire Charles-Fabry de l'Institut d'Optique (IOTA), Campus Polytechnique, RD 128-91227,
Palaiseau Cedex, France

F. Auchere · J.P. Delaboudiniere
Institut d'Astrophysique Spatiale, Centre universitaire d'Orsay, Bât 120-121, 91405 Orsay Cedex,
France

V. Bothmer
Max-Planck-Institute for Solar System Research, Institute for Astrophysics, University of Göttingen,
37077 Göttingen, Germany

Abstract The Sun Earth Connection Coronal and Heliospheric Investigation (SECCHI) is a five telescope package, which has been developed for the Solar Terrestrial Relation Observatory (STEREO) mission by the Naval Research Laboratory (USA), the Lockheed Solar and Astrophysics Laboratory (USA), the Goddard Space Flight Center (USA), the University of Birmingham (UK), the Rutherford Appleton Laboratory (UK), the Max Planck Institute for Solar System Research (Germany), the Centre Spatiale de Leige (Belgium), the Institut d'Optique (France) and the Institut d'Astrophysique Spatiale (France). SECCHI comprises five telescopes, which together image the solar corona from the solar disk to beyond 1 AU. These telescopes are: an extreme ultraviolet imager (EUVI: 1–1.7 R_{\odot}), two traditional Lyot coronagraphs (COR1: 1.5–4 R_{\odot} and COR2: 2.5–15 R_{\odot}) and two new designs of heliospheric imagers (HI-1: 15–84 R_{\odot} and HI-2: 66–318 R_{\odot}). All the instruments use 2048 × 2048 pixel CCD arrays in a backside-in mode. The EUVI backside surface has been specially processed for EUV sensitivity, while the others have an anti-reflection coating applied. A multi-tasking operating system, running on a PowerPC CPU, receives commands from the spacecraft, controls the instrument operations, acquires the images and compresses them for downlink through the main science channel (at compression factors typically up to 20×) and also through a low bandwidth channel to be used for space weather forecasting (at compression factors up to 200×). An image compression factor of about 10× enable the collection of images at the rate of about one every 2–3 minutes. Identical instruments, except for different sizes of occulters, are included on the STEREO-A and STEREO-B spacecraft.

Keywords Solar corona · Lyot coronagraph · XUV heliograph · Heliospheric imager · Coronal loops · Coronal mass ejections · Stereo · Heliosphere

1 Introduction

The Sun-Earth-Connection Coronal and Heliospheric Investigation (SECCHI; see Howard et al. 2000) for the NASA Solar Terrestrial Relations Observatory (STEREO) mission is a suite of optical telescopes that will, for the first time, observe the entire inner heliosphere from the solar surface out to the vicinity of Earth. By combining this very large field of view with the radio and *in-situ* measurements from STEREO as well as from other space- and earth-based assets, we expect to answer some important questions of the physics of Coronal Mass Ejections (CMEs). The instrument acronym is also a reference to Angelo Secchi (1818–1878) a pioneering Italian astrophysicist who was one of the first to apply the new technology of photography to recording eclipses. In a similar way we anticipate that SECCHI will provide pioneering observations of CMEs as well as other structures, such as loops, plumes, streamers, comets, etc., using stereo reconstruction techniques.

W. Deutsch
Max-Planck-Institut for Solar System Research, Katlenburg-Lindau, Germany

D. Wang · N. Rich
Interferometrics, Inc., 13454 Sunrise Valley Drive, Herndon, VA 20171, USA

S. Cooper · V. Stephens · G. Maahs
HYTEC Inc., 110 Eastgate Drive, Los Alamos, NM 87544, USA

R. Baugh · D. McMullin · T. Carter
Praxis, Inc., 2550 Huntington Ave. Suite 300, Alexandria, VA 22303, USA

The primary objective of the STEREO mission is to understand the CME phenomenon, a phenomenon that was discovered in 1971 and has been observed by coronagraphic instruments on five missions, most recently the ESA/NASA Solar and Heliospheric Mission (SOHO) (see Howard 2006 and references therein). But, this is the first mission whose primary objective is to elucidate the CME itself. The primary objectives of SECCHI are:

- What is the timing of physical properties involved in CME initiation? What are the structures involved in the CME initiation?
- What is the 3-dimensional structure and kinematic properties of CMEs?
- What is the 3-dimensional structure of active regions, coronal loops, helmet streamers, etc.?
- What are the critical forces controlling the propagation of CMEs in the corona and interplanetary medium?

The SECCHI instrument suite consists of five telescopes covering a broad range of fields of view, starting at the solar surface and extending all the way to the interplanetary space between the Sun and Earth. The five telescopes are of three types. The first is an extreme ultraviolet (EUV) imager, EUVI that will image the solar chromosphere and low corona in four emission lines out to $1.7 R_{\odot}$. The COR1 and COR2 telescopes are the second type and are visible light Lyot coronagraphs with nested fields of view. These two telescopes will image the inner and outer corona from 1.4 to $15 R_{\odot}$ and were split into two telescopes because of the large radial gradient of coronal brightness in this height range. The third type of telescope extends the coronal imaging from $15 R_{\odot}$ out to the radius of Earth at $215 R_{\odot}$. To satisfy the stray light requirement over this field, the task was divided into two wide field heliospheric imagers (HI1 and HI2). Figure 1 gives a summary of the science objectives and how each telescope in the SECCHI suite will contribute. EUVI and the CORs are instruments that have flown on previous missions, but the HI is a new concept.

STEREO provides us with several important new opportunities for CME research, including the following:

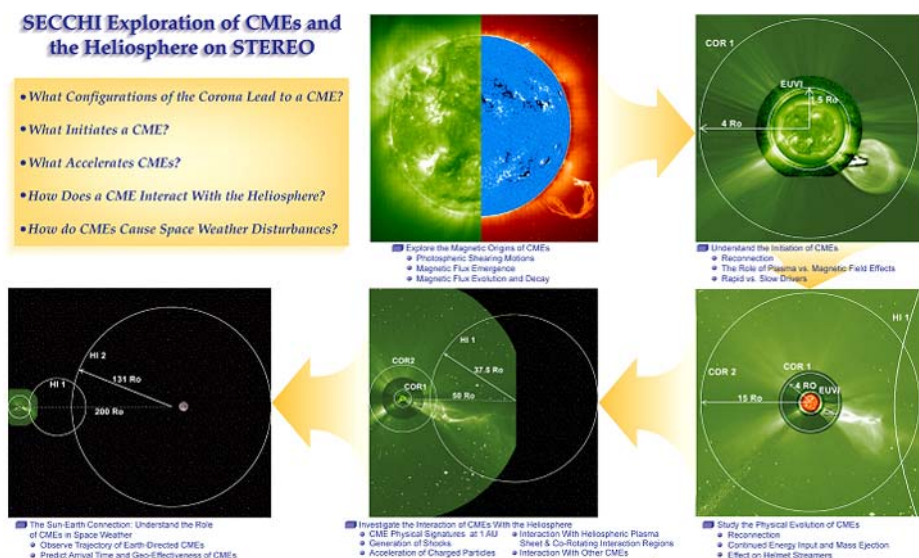


Fig. 1 Summary of SECCHI science objectives

- The first opportunity to obtain stereographic views of CMEs;
- The first opportunity to observe a CME in interplanetary space at the same time that *in-situ* measurements are made;
- The first opportunity to make simultaneous optical and radio observations of CMEs and shocks;
- The first opportunity to observe geo-effective CMEs along the Sun-Earth line in interplanetary space;
- The first opportunity to detect CMEs in a field of view that includes the Earth.

In this paper we present an overview of the SECCHI instrument—the five main telescopes, the guide telescope (GT), the optical bench for the sun-pointed instruments, the mechanisms, the SECCHI electronics, the CCD detector, housing and control electronics, the flight software and the concept of operations. The hardware is assembled into three packages: (1) the Sun-Centered-Instrument Package (SCIP) which has the EUVI, COR1, COR2, GT and the SCIP camera electronics box (CEB), (2) the Heliospheric Imager (HI), which contains both the HI-1 and HI-2 and the HI-CEB, and (3) the SECCHI electronics box (SEB). The SCIP is located within the spacecraft cylinder at the center of the spacecraft; the HI is located on the earthward-pointing spacecraft face and the SEB is located within the spacecraft.

2 Extreme UltraViolet Imager (EUVI)

2.1 EUVI Telescope Overview

The EUVI (see Wülser et al. 2003) observes the chromosphere and low corona in four different EUV emission lines between 17.1 and 30.4 nm. It is a small, normal-incidence telescope with thin metal filters, multilayer coated mirrors, and a back-thinned CCD detector. Figure 2 shows one of the EUVIs during integration at LMSAL. Figure 3 is a cross section through the telescope.

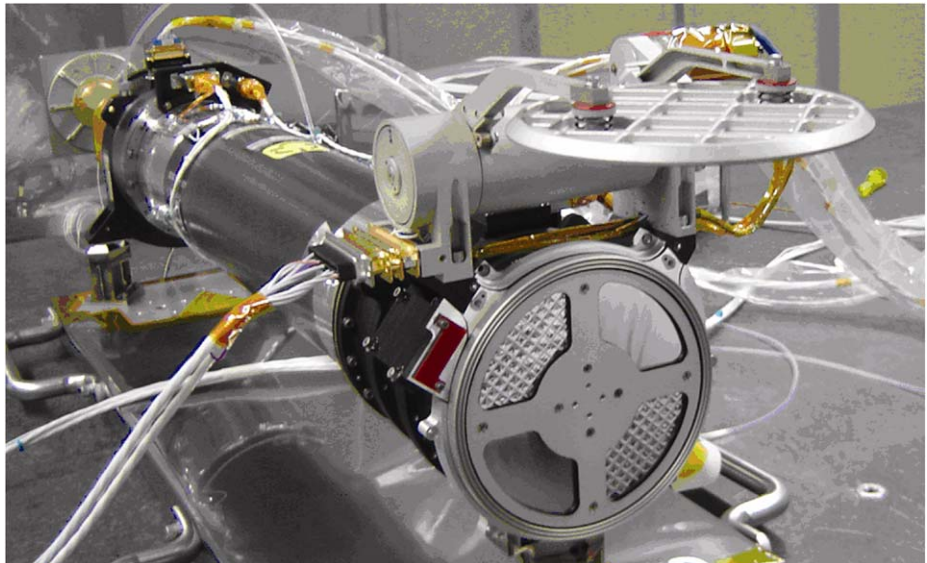


Fig. 2 The EUVI telescope prior to integration into the SECCHI suite. The door is open and reveals the thin Al entrance filters. The *bottom left* and *top right* filters are mesh based filters, the others are polyimide backed supported on a coarse grid

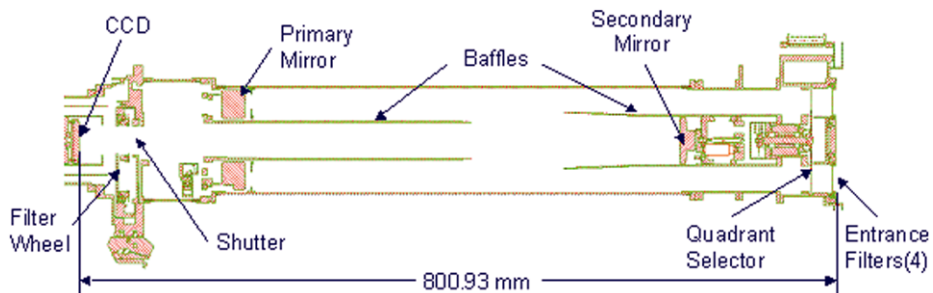


Fig. 3 EUVI telescope cross section

Table 1 EUVI telescope properties

Instrument type	Normal incidence EUV telescope (Ritchey-Chrétien)
Wavelengths	He II 30.4 nm, Fe IX 17.1 nm, Fe XII 19.5 nm, Fe XV 28.4 nm
IR/visible/UV rejection	$>10^{13}$ using thin metal film filters
Aperture	98 mm at primary mirror
Effective focal length	1750 mm
Field of view	Circular full sun field of view to ± 1.7 solar radii
Spatial scale	1.6'' pixels
Detector	Backside illuminated CCD (e2v CCD42-40), 2048 \times 2048 pixels
Mechanisms	Aperture door, Quadrant selector, Filter wheel, Focal plane shutter
Image Stabilization	Active secondary mirror (tip/tilt) Range: $\pm 7''$, jitter attenuation: factor 3 at 10 Hz

EUV radiation enters the telescope through a thin metal film filter of 150 nm of aluminum. This filter suppresses most of the UV, visible, and IR radiation and keeps the solar heat out of the telescope. During launch, the filter is protected by the front door. The radiation then passes through the quadrant selector to one of the four quadrants of the optics. Each quadrant of the primary and secondary mirror is coated with a narrow-band, multilayer reflective coating, optimized for one of four EUV lines. After bouncing off the primary and secondary mirror, the radiation continues through a filter wheel that has redundant thin-film aluminum filters to remove the remainder of the visible and IR radiation. A rotating blade shutter controls the exposure time. The image is formed on a CCD detector. The main parameters for the EUVI telescope are summarized in Table 1.

2.2 Optics

2.2.1 Optical Design

The EUVI telescope is a Ritchey-Chrétien system with a secondary mirror magnification of 2.42. This system provides pixel limited resolution across the entire field of view in all four quadrants. The low secondary mirror magnification reduces the telescope's sensitivity to shifts in the mirror separation and eliminates the need for a focus mechanism. The telescope is fully baffled to prevent charged particles entering the front aperture from reaching the CCD. The telescope pupil is located just in front of the primary mirror and is defined by an aperture mask. The baffles and aperture mask have been designed for an unvignetted

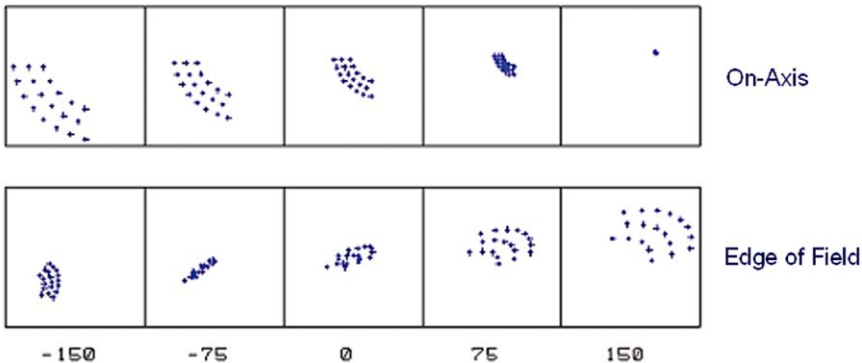


Fig. 4 Ray trace results for a single quadrant and two field angles (0 and 27 arcmin) at nominal focus, and up to 150 μm inside (-150) and outside (150) of nominal focus. The boxes indicate the size of one CCD pixel

Table 2 Properties of the multilayer coatings

Quadrant/channel	17.1	19.5	28.4	30.4
Center wavelength (two mirror system)	17.3 nm	19.6 nm	28.5 nm	30.7 nm
Bandwidth (measured FWHM for single reflection)	1.4 nm	1.6 nm	1.9 nm	3.0 nm
Peak reflectivity (measured, for single reflection)	39%	35%	15%	23%
Coating materials	MoSi	MoSi	MoSi, var. spacing	MoSi

field of view to ± 1.7 solar radii. Figure 4 shows ray trace results for a single quadrant, both on-axis and at the edge of the field, and up to 0.15 mm inside and outside of nominal focus. The system has a minor amount of field curvature; the nominal focus location is chosen to minimize the aberrations across the field.

2.2.2 Mirrors

The EUVI mirrors were figured, polished, and multilayer coated at the Institut d’Optique in Orsay, who also made the mirrors for SOHO/EIT. The Zerodur mirror substrates were first polished to a sphere and superpolished to the required surface roughness. They were then aspherized using an ion beam etching technique that preserves the superpolished properties of the surface. Finally, each quadrant of each mirror was coated with a narrow passband reflective multilayer, optimized for the specific EUV emission to be observed in that quadrant. All coatings consist of MoSi layer pairs using constant layer spacing. The coating for the 28.4 nm quadrant has a variable Mo/Si thickness ratio for optimum suppression of the nearby 30.4 nm He II emission line. The other coatings use constant layer spacings. Table 2 summarizes the properties of the coatings (Ravet et al. 2003).

2.2.3 Filters

The EUVI uses thin metal film filters at both the entrance aperture and near the focal plane to suppress undesired UV, visible, and IR radiation. Two types of filters are at the entrance of the telescope (Fig. 2): an aluminum-on-polyimide foil on a coarse nickel grid for the short wavelength quadrants (17.1 and 19.5 nm), and a single layer aluminum foil on a fine nickel mesh for the long wavelength quadrants (28.4 and 30.4 nm). Both types of filters use a 150 nm thick layer of aluminum to reject visible light. The grid-supported aluminum filter is backed with a 70 nm thick layer of polyimide for strength. The polyimide layer allows the filter to be supported by a coarse grid with 5 mm line spacing that causes only minimal diffraction at EUV wavelengths. The polyimide transmits only about 50% of the EUV radiation at the observing wavelengths, but this is not a major concern for the strong lines at 17.1 and 19.5 nm.

The mesh supported filter avoids the absorbing polyimide layer, whose transmission is too low at longer wavelengths, especially for the somewhat weaker line at 28.4 nm. However, the fine mesh, with 0.36 mm line spacing, causes a noticeable amount of diffraction. Both types of filters have been flown on highly successful experiments: EIT used a plastic reinforced aluminum foil on a nearly identical coarse grid for all wavelengths and TRACE (Handy et al. 1999; Strong et al. 1994) used fine mesh supported filters nearly identical to the ones on the EUVI.

Near the focal plane, a final filter reduces the visible light transmitted by the first filter and by any pinholes that form in the front filter. This final filter is in a filter wheel with four positions, to provide additional protection against pinholes. A third filter wheel position contains two filters in series to mitigate against any catastrophic damage to the entrance filters. The fourth filter slot is left open, which enabled visible light testing on the ground. All filters were manufactured by LUXEL Corporation.

2.2.4 Aliveness Source

The EUVI telescope contains blue and violet light emitting diodes (LEDs) for testing and calibration purposes. One set of LEDs is mounted in the spider and illuminates the detector through reflection off the two telescope mirrors. A second set is mounted near the CCD. Photons from the blue LED at 470 nm have a similar penetration depth in silicon as EUV photons, while photons from the violet LED at 400 nm, which have a shallower penetration depth, provide a diagnostic that is sensitive to CCD surface effects.

2.3 Mechanical Design

2.3.1 Metering Structure

The EUVI uses a Graphite/Cyanate Ester metering tube as the main telescope structure. The tube stiffness maintains proper alignment of the optical system through launch. The low coefficient of thermal expansion (CTE) in the axial direction minimizes changes in the mirror separation and keeps the telescope in focus throughout the operational temperature range. This eliminates the need for a focus mechanism. The metering tube is lined with an aluminum foil on the inside that acts as a vapor and contamination barrier.

Attached to the front of the metering tube are the secondary mirror spider, the quadrant selector spider, and the entrance chamber with the entrance filters and the interfaces to the aperture door and the forward mount. The spider arms are hollow and incorporate separate vent paths for the secondary mirror tip-tilt mechanism and for the quadrant selector motor.

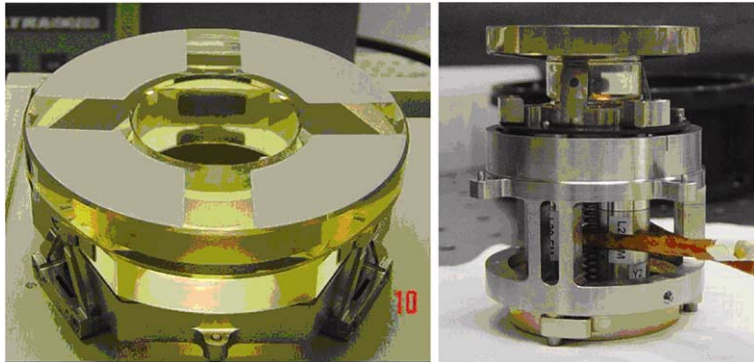


Fig. 5 *Left*—EUVI primary mirror, coated and mounted. The mirror diameter is 105 mm. The regions between the quadrants are deliberately left uncoated. *Right*—EUVI secondary mirror and tip-tilt mechanism. The mirror diameter is 48 mm. One of the three PZTs (marked “L2...M”) is visible inside the housing

Attached to the aft end of the metering tube are the primary mirror mount and the aft metering structure with the shutter and filter wheel mechanisms, as well as the interfaces to the focal plane assembly and the aft mounts. The aft structure again incorporates separate vent paths for its mechanisms to minimize potential sources of contaminants inside the optical cavity.

2.3.2 Mirror Mounts

The EUVI primary mirror and mount are shown in Fig. 5. The mount consists of a hexagonal Titanium ring that interfaces to the mirror substrate via three bi-pod flexures. This arrangement is semi-kinematic: each bi-pod strongly constrains two degrees of freedom, but is relatively flexible in the other four, thus isolating the mirror from thermal stresses in the mount. Interferometric tests showed that temperature changes of up to 22°C cause no measurable deformation of the mirror figure. The bi-pods are made of Invar and attach to the Zerodur mirror through bonded Invar mounting pads. This mirror mount is very compact to fit the tight envelope constraints of the EUVI telescope.

The secondary mirror mount with its tip-tilt mechanism is shown in Fig. 5. The mount is a single piece of Invar with three machined fingers that are bonded to the cylindrical base of the Zerodur mirror substrate. The tip-tilt mechanism is very similar to the one on the TRACE telescope. It uses three piezoelectric (PZT) actuators that push against the Invar mount of the mirror. Software in the SECCHI flight electronics processes fine pointing signals from the SECCHI guide telescope and drives the PZT actuators open loop via a simple digital-to-analog converter and low voltage drivers. The tip-tilt range in the EUVI image space is ± 7 arcseconds, sufficient to accommodate worst case spacecraft jitter.

2.4 Instrument Response and Calibration

2.4.1 Calibration Results

The EUVI mirrors were calibrated as pairs at the synchrotron of the Institut d’Astrophysique Spatiale in Orsay. The mirrors were arranged in the same geometry as in the EUVI telescope,

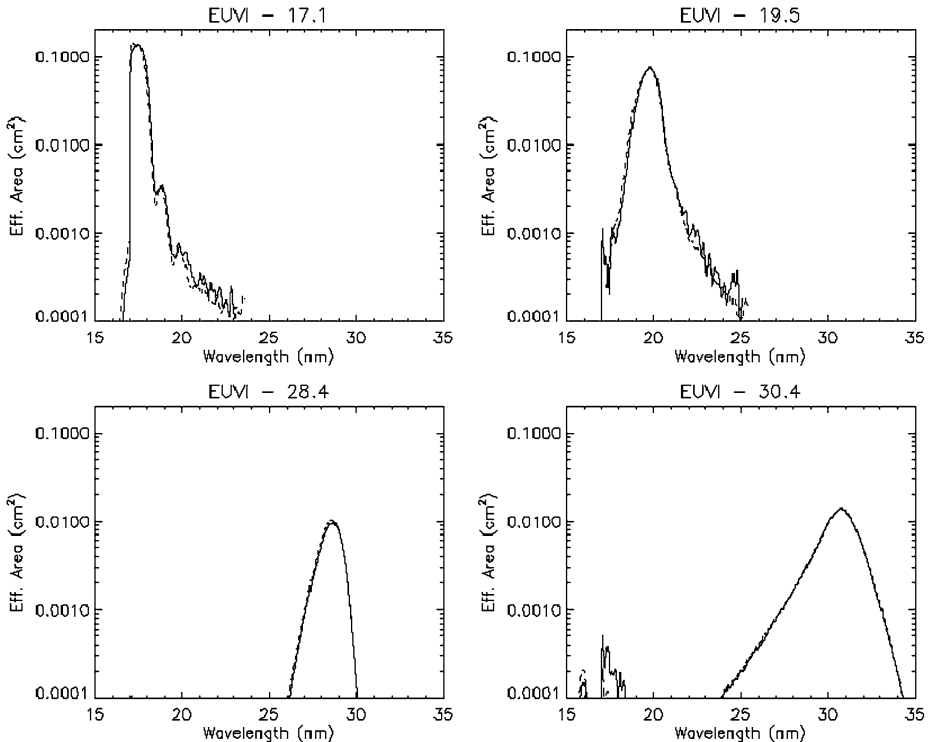


Fig. 6 EUVI effective area. The *solid lines* are for the EUVI-A, the *dashed lines* for the EUVI-B

and illuminated with a nearly collimated beam from a monochromator attached to the synchrotron. Each telescope quadrant was measured individually. Wavelength scans were performed with and without the telescope in the beam; the measured ratio provides the absolute total reflectivity of the mirror pairs. Single reflection coating properties are reported in Table 2. All coatings perform well, both in terms of high reflectivity and proper wavelength of peak reflectivity. The coating for 28.4 nm is optimized for rejecting the strong He II line at 30.4 nm, which results in a somewhat lower peak reflectivity as expected.

CCDs were calibrated on the NRL beamline at Brookhaven synchrotron and at the LMSAL XUV calibration facility. The entrance and focal plane filters were also calibrated at the LMSAL XUV calibration facility (Windt and Catura 1988). The results of those measurements were used to fit CCD and filter response models. The calibration curves of the individual components were combined to obtain the EUVI effective area as a function of wavelength. The results are shown in Fig. 6. The two telescopes (EUVI-A and EUVI-B) have very similar responses.

2.4.2 Predicted Response to Solar Phenomena

Using the calibration results we predict the response of the EUVI to typical solar plasmas. We take typical differential emission measure distributions (DEMs) reported in the literature, predict the resulting solar spectral line emission using the CHIANTI software (Dere et al. 1997; Young et al. 2003), and combine the result with our calibration data. Table 3 summarizes the pixel count rates for selected solar features in the different EUVI channels.

Table 3 Photon count rates (photons/pixel/second) for some solar features predicted with the CHIANTI code. The numbers for the 30.4 nm channel have been tripled to adjust for the fact that CHIANTI typically underestimates the He II flux. The first number in each box is for the EUVI-A, the second for the EUVI-B

Photons/s/pixel	Quiet Sun	Active region	M class flare
17.1 nm	92/98	954/976	25700/26700
19.5 nm	40/41	784/792	92200/101500
28.4 nm	4/4	118/130	5540/6110
30.4 nm	30/30	428/419	18100/17800

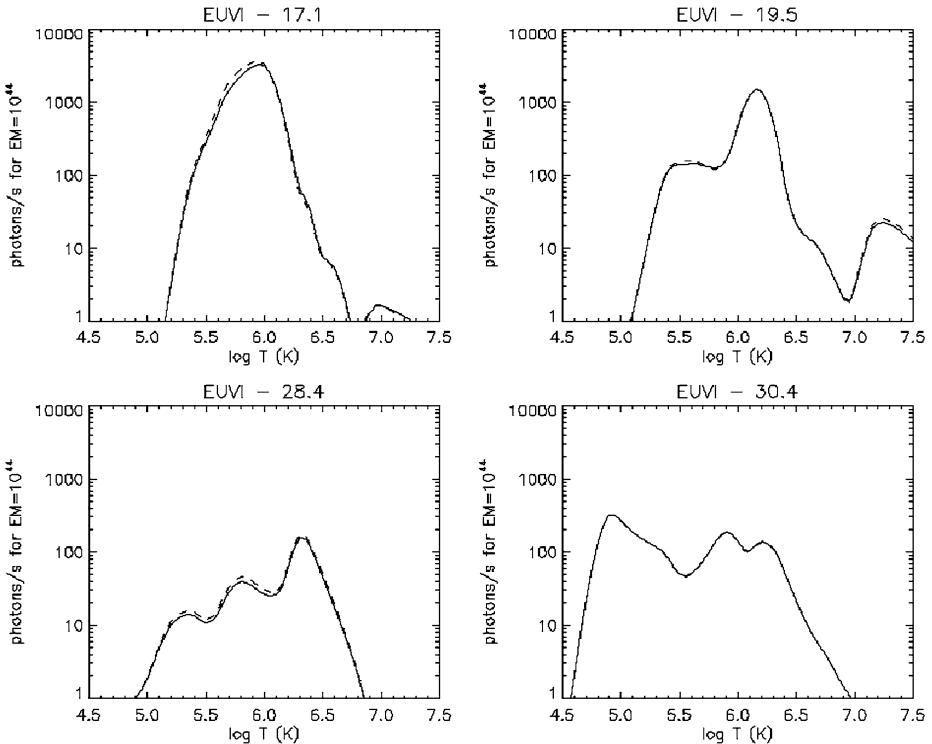


Fig. 7 The response of the EUVI as a function of solar plasma temperature. The *solid lines* are for the EUVI-A, the *dashed lines* for the EUVI-B

Note that CHIANTI underestimates the He II flux by typically a factor of three so we have multiplied the prediction by a factor of 3. Figure 7 shows count rates (in photons/pixel/s) predicted for isothermal plasmas (for an EM of 10^{11} cm^{-5}) as a function of plasma temperature.

3 Inner Coronagraph (COR1)

3.1 COR1 Overview

Like all coronagraphs, COR1 is designed to measure the weak light from the solar corona in the presence of scattered light from the much brighter solar photosphere. It is a classic

Lyot internally occulting refractive coronagraph (Lyot 1939) which will observe the white light corona from 1.4 to 4 R_{\odot} . The COR1 design is the first space-borne internally occulted refractive coronagraph in contrast to the LASCO/C1 (Brueckner et al. 1995), which was an internally occulted *reflective* design. The optical design, described in the next section, uses the principles articulated by Lyot to eliminate some of the sources of stray light. The internal occultation enables better spatial resolution closer to the limb than an externally occulted design.

The COR1 signal will be dominated by instrumentally scattered light, which must be removed to measure the underlying coronal signal. This stray light cannot be removed by the Lyot principles but is largely unpolarized and therefore can be eliminated or at least greatly reduced by making polarized observations in three states of linear polarization and calculating the polarized brightness (pB). To achieve this separation, we must have a high enough signal to noise ratio, even in the presence of the large scattered light noise. This is partly achieved by performing on-board binning of the pixels.

3.2 Optical Layout

Figure 8 shows the opto-mechanical layout of the COR1 instrument. Sunlight enters through the front aperture, where the objective lens focuses the solar image onto the occulter. To keep scattering to a minimum, a singlet lens is used for the objective, made of radiation hardened BK7-G18 glass.

The occulter is mounted on a stem mounted at the center of the field lens (Fig. 9). The tip of the occulter is cone shaped, to direct the sunlight into a light trap, which surrounds the occulter. The radius was chosen to block all wavelengths (350–1100 nm) out to a radius of 1.1 R_{\odot} at orbital perigee. At the design wavelength of 656 nm, the solar image is completely occulted out to 1.30 R_{\odot} , and partially vignetted out to 1.64 R_{\odot} . (When combined with the

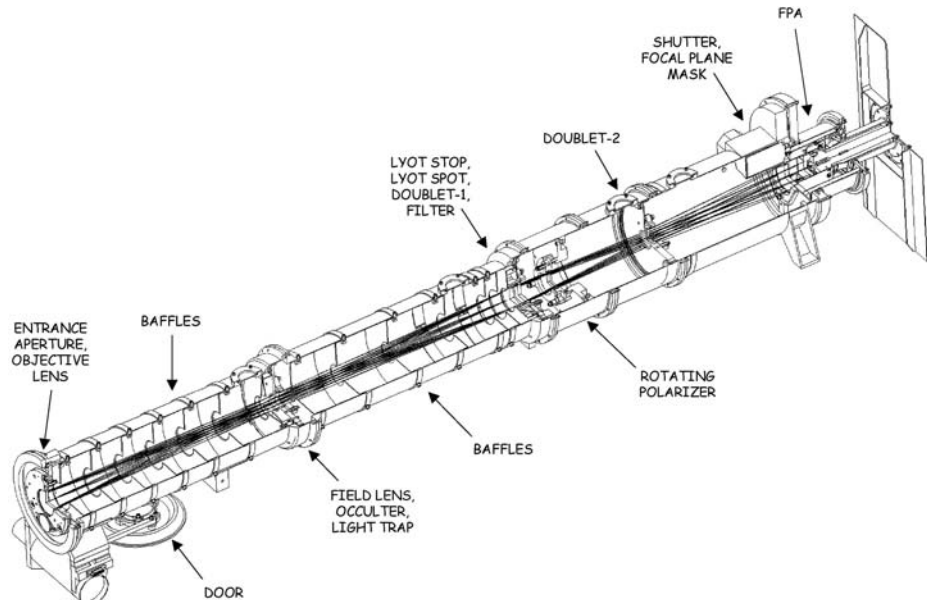


Fig. 8 Layout of the COR1 instrument package

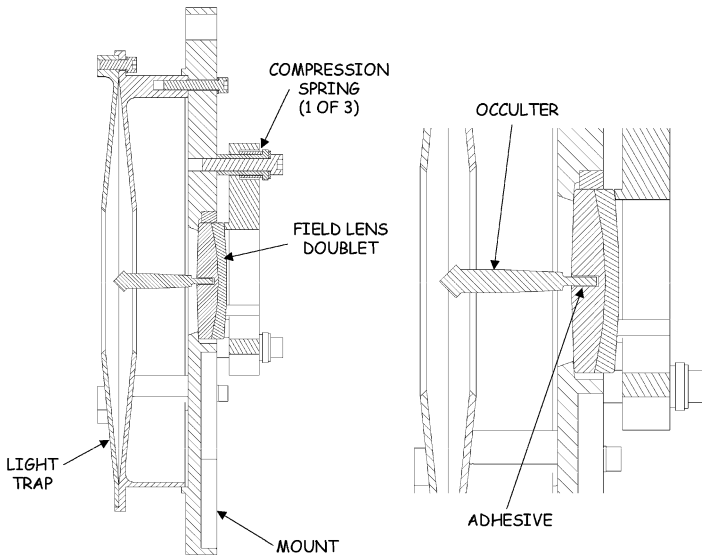


Fig. 9 The conical occulter mounted at the center of the field lens, and surrounded by the light trap. Hatched regions show the presence of material at the central plane in this cutaway view

focal plane mask discussed below, these numbers become 1.4 and $1.9 R_{\odot}$ respectively.) The wedge-shaped design of the light trap ensures that any ray entering it must reflect many times, so that the light will be absorbed before it can find its way out again.

Two doublet lenses are used to focus the coronal image onto the CCD detector. The first, a positive power achromat, is placed immediately behind the Lyot stop, while the second, a negative power achromat, is placed further down the optical path. Together, these act as a telephoto-lens system, focusing the coronal image onto the detector plane, while maintaining diffraction-limited resolution. A bandpass filter 22.5 nm wide, centered on the $H\alpha$ line at 656 nm, is placed just behind the first doublet. Thus, the Lyot stop, spot, first doublet, and bandpass filter form a single optical assembly.

A linear polarizer on a hollow core motor rotational stage is located between the two doublets. The polarizing material is Corning's Polarcor, chosen for its uniformity. The placement of the polarizer was chosen to be as close to the first doublet as possible within the dimension constraints of the largest diameter piece of Polarcor that can be obtained (33 mm clear aperture). Normal operations call for three sequential images to be taken with polarizations of 0 degrees and ± 60 degrees, to extract the polarized brightness.

3.3 Stray Light Suppression

The primary photospheric light suppression mechanisms in COR1 are those described by Lyot (1939)—(1) the objective lens to occulter imaging system, (2) the aperture stop to field lens to Lyot stop imaging system and (3) a Lyot spot. A final stray light suppression technique is the inclusion of a focal plane mask.

The singlet objective lens only focuses the solar image accurately at a single wavelength. Thus only a single wavelength of the photosphere is blocked by the internal occulter. A narrow band filter defines the passband of the instrument, which matches the wavelength at the primary focus of the objective lens. Rather than relying on the out-of-band rejection of

the filter, the primary suppression mechanisms are designed to work over the full sensitivity wavelength band of the instrument.

The solar image from the objective will be chromatically aberrated, so the occulter must be sized to block all the solar photospheric light from the near UV to infrared (350–1100 nm). The cut-on at 350 nm is set by the transmission of the BK7-G18 glass in the objective lens, and the cut-off at 1100 nm is set by the band gap of the silicon detector. Subsequent lenses in the optical train balance the chromatic aberration from the objective. The narrow bandpass of the instrument also minimizes the effect of chromatic aberration in the final image.

Diffracted light from the edge of the front entrance aperture is focused onto a Lyot stop by the field lens and removed. This eliminates the largest source of stray light in the system. Additional stray light rejection is accomplished by placing baffles at various points between the front aperture and Lyot stop. A Lyot spot is also glued to the front surface of the doublet lens immediately behind the Lyot stop, to remove ghosting from the objective lens.

A focal plane mask is located between the shutter and the focal plane detector, and is used to remove diffracted light from the edge of the occulter. This circular mask, mounted on a plane of BK7 glass, is sized to be slightly larger than the occulter image at that location. Without the mask, the image on the detector would be dominated by bright rings at the umbral and penumbral edges of the occulter shadow. The addition of the focal plane mask removes these bright rings. The focal plane assembly is discussed in Sect. 9.

3.4 Mechanical and Thermal Design

The COR1 mechanical structure is designed as a series of tube sections (Fig. 8), which are bolted and pinned together for stability. The individual optics are aligned, mounted, and pinned within these tube sections. COR1 assembly starts from the front tube section, with the objective, occulter, light trap, and field lens, and then each subsequent section is added, together with its associated optical or mechanical components. Because the individual tube sections are pinned together, sections can be taken off and back on again without changing the optical alignment.

Three mechanisms are included in the COR1 instrument package. At the front of the instrument is a door, to protect the instrument before and during launch, and during spacecraft maneuvers. On the front of this door is a diffuser so that the operation of the instrument can be tested when the door is closed, and to provide a flat-field calibration signal. The diffuser is sized to completely illuminate the objective over all angles within the field-of-view.

The other two mechanisms are the hollow core motor to rotate the linear polarizer, and a rotating blade shutter mounted just in front of the focal plane detector assembly, both supplied by Lockheed Martin. All the mechanisms, together with the focal plane CCD detector, will be operated from a centralized control system for all the SECCHI instruments.

Because the two STEREO spacecraft are in elliptical orbits about the Sun, the COR1 instruments will experience considerable variation in solar load, from 1264–1769 and 1068–1482 W/m² for the Ahead and Behind spacecraft respectively. When these loads are combined with the modeled changes in the material thermal properties from beginning to end of life, and with the most extreme differences in the thermal loads from the surrounding structure, the worst-case temperature variation in the COR1 instrument is from 2.5 to 30°C. There's also an axial gradient in temperature from the front to the back of the instrument, varying from 3°C in the cold case, to 7°C in the hot case. Strategically placed software controlled proportional heaters with programmable set points, are used to keep the instrument

within the 0–40°C operational temperature range. There are also survival heaters on mechanical thermostat control to keep the instrument within the –20 to +55°C non-operational range.

Specialized composite coatings of oxides over silver are used to help manage the intense solar fluxes which COR1 will be experiencing. The oxide coatings are deposited onto many of the exposed surfaces around the aperture area, such as the objective lens holder assembly and door assemblies. This coating exhibits very low solar absorbtivities, is very stable, and has relatively high IR emissivity values depending on the thickness of the deposited oxide layers. Silver teflon is used for the front layer of the multilayer insulation. The majority of the solar load collected by the front objective is concentrated on the occulter tip (Fig. 9). In the worst-case analysis, the tip can reach a temperature of 125°C. This tip is made of titanium, and is diamond-turned to direct the sunlight into the light trap. It is coated with a Goddard composite silver coating for high reflectivity. The occulter shaft is coated with black nickel to radiate away the heat. A thin cross-section titanium shaft is used to thermally isolate the occulter from the field lens.

3.4.1 Calibration and Performance Results

Before building the COR1 flight units, an extensive test program was carried out on a series of breadboards and engineering test units, using the Vacuum Tunnel Facility at the National Center for Atmospheric Research in Boulder, Colorado (Thompson et al. 2003). These tests were used to demonstrate the instrument concept, and to improve the design for flight. One result of this testing was the addition of a focal plane mask to remove diffracted light from the edge of the occulter.

Characterization of the COR1 flight units was carried out in a similar vacuum tank facility at the Naval Research Laboratory in Washington, DC. The instrument was installed in a large vacuum chamber within a class 10,000 cleanroom. A long vacuum tunnel extended out from one end of the vacuum chamber to a window, where an entrance aperture was mounted to simulate the size of the Sun at perigee. The total distance between the source aperture and the COR1 front aperture was 11 meters. A partially collimated Xenon arc lamp was used to illuminate the source aperture, with the degree of collimation chosen to direct the light onto the COR1 objective and heat shield. Different aperture sizes were used for the Ahead and Behind instruments, because of the different orbital perigees of the two spacecraft.

As well as stray light, this vacuum tunnel facility was also used to measure other performance characteristics, such as resolution, polarization, and photometric response. The photometric calibration of the instrument was measured by illuminating the aperture at the end of the tank with a diffuse unpolarized light source of known intensity. Placing a sheet polarizer in front of this source allowed us to test the polarization response. Focus was tested by projecting an Air Force 1951 resolution test target through a collimator onto the instrument. The instrumental flat field was tested using both the diffuser mounted in the door, and with an external double-opal source mounted in front of the instrument, with identical results.

The vignetting function and flat field response of the instrument is demonstrated in Fig. 10. The field is unvignetted except for a small area around the edge of the occulter, and near the field stop in the corners of the image. (The dim spot in the center of the occulter shadow is caused by scattering within the instrument.) Only the Ahead data are shown—the Behind response is virtually identical.

Figure 11 shows the measured COR1 scattered light performance for the Ahead and Behind instruments. The average radial profile is well below $10^{-6} B/B_\odot$ for both instruments.

Fig. 10 Flat field response of the COR1 Ahead instrument

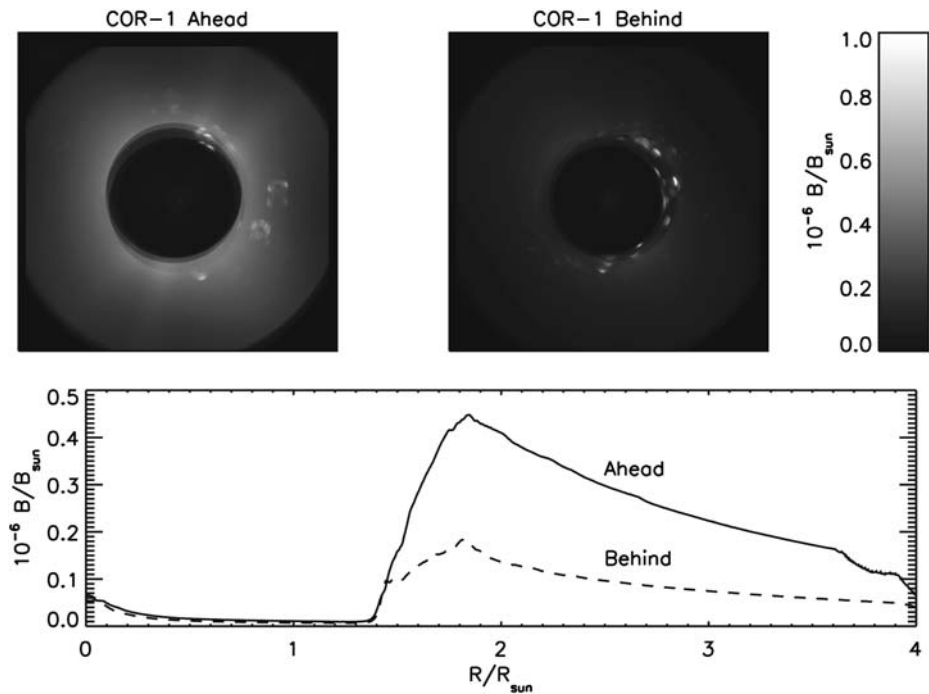


Fig. 11 Measured scattered light images and average radial profiles for the COR1 Ahead (*solid*) and Behind (*dashed*) instruments

There are discrete ring-shaped areas of increased brightness, which can climb to as high as $1.4 \times 10^{-6} B/B_{\odot}$ for the Behind instrument. It has been determined that these are caused by features on the front surface of the field lens.

Some contamination was found on the COR1 Behind objective lens after thermal vacuum testing of the STEREO spacecraft. The objective has been cleaned and re-installed, and may no longer have the performance shown in Fig. 11.

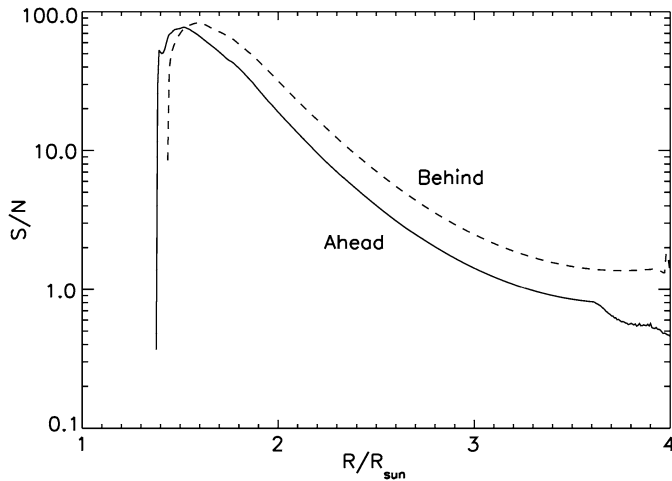


Fig. 12 Estimated signal-to-noise ratios for a modeled K-corona for an exposure time of 1 s, with 2×2 pixel binning

Table 4 COR1 performance characteristics

Parameter	Units	Ahead	Behind
Pixel size, full resolution	arcsec	3.75	3.75
Pixel size, 2×2 binned	arcsec	7.5	7.5
RMS spot size (design)	arcsec	4.17	4.17
Planned exposure time	s	1	1
Polarizer attenuation	—	10^{-4}	10^{-4}
Photometric response	B_\odot/DN	7.1×10^{-11}	5.95×10^{-11}
Time to complete pB sequence	s	11	11
Image sequence cadence	min	8	8

Combining the data from Figs. 10 and 11, together with a model of the K corona polarized brightness, allows one to estimate the signal-to-noise ratios that will be seen during flight. The results are shown in Fig. 12 for an exposure time of 1 second. The coronal model used is based on Gibson (1973), is valid between 1.4 and 4 solar radii and has the functional form:

$$\log_{10}(pB) = -2.65682 - 3.55169 (R/R_\odot) + 0.459870 (R/R_\odot)^2.$$

The overall performance characteristics of the COR1 instruments are summarized in Table 4. In order to increase the Signal to Noise Ratio, the 3.75 arcsec square pixels will be summed together into 2×2 bins, to form larger pixels 7.5 arcsec on a side. The design goal for the root-mean-square spot size on the detector was chosen to be 15 μm (4.17 arcsec), somewhat larger than the 13.5 μm size of a single CCD pixel, but well within the 27 μm size of a 2×2 binned pixel. The largest contribution to the optical error budget comes from thermal changes on orbit, which can be as large as 12 μm .

The three images in a polarization sequence will be taken as quickly as possible, within 10 s, so that changes due to evolution of the corona will be minimized. Each set of three im-

ages makes up a complete observation, and the cadence of observations is the time between one three-image set and the next.

4 Outer Coronagraph (COR2)

Like the COR1, the SECCHI outer coronagraph, COR2, observes the weak coronal signal in visible light. It is an externally occulted Lyot coronagraph and derives its heritage from the highly successful LASCO C2 and C3 coronagraphs aboard SOHO (Brueckner et al. 1995). The externally occulted design shields the objective lens from direct sunlight, enabling a lower stray light level than COR1 thus achieving observations to further distances from the Sun. It is very complementary to COR1, which observes closer to the Sun.

The primary requirement on the COR2 was to observe CMEs in polarization brightness (pB) with a 15 arc second per pixel spatial resolution. To obtain pB images, a sequence of 3 linearly polarized images is taken. In order to minimize the smear caused by the CME motion during the polarization image sequence, the sequence of 3 images need to be acquired in a short time. A moderately fast CME moving at the speed of 750 km/s would traverse a COR2 pixel (15 arcsec) in 15 seconds. This was the time criterion that was established. CMEs moving faster than this can still be accommodated, by binning the image down (on the ground) until the motion is within one pixel.

4.1 Optical Design

Solar coronal radiation enters the coronagraph through the A0 aperture (see Fig. 13). A three-disk external occulter shades the objective lens from direct solar radiation and creates a deep shadow at the objective lens aperture (A1). A heat rejection mirror reflects incident solar radiation back through the entrance aperture.

The optical design uses three lens groups, a spectral filter, and a polarizer. The objective lens group (O1) images the external occulter onto the internal occulter and the field lens group (O2) images the A1 aperture onto the A3 aperture (Lyot stop). The O1 also creates an image of the A0 onto A2 (the A0 image stop). The interior occulter and aperture stops capture the brightly illuminated edges of the external occulter and the A0 and A1 apertures. The internal occulter is sized to be slightly larger than the image of the third disk of the external occulter, and the Lyot stop is sized to be slightly smaller than the image of the A1 aperture. These two elements define the inner edge of the coronagraph field of view at a field angle corresponding to an altitude of $2.5 R_{\odot}$ in the corona at the nominal perihelion distance of each of the STEREO spacecraft. The outer limit of the field of view is determined by the field stop, which is located in the plane of the coronal image formed by the O1 lens group. The field of view of COR2 is $\pm 4^{\circ}$, corresponding to a height of $15 R_{\odot}$ in the corona at 1 AU. The third lens group (O3) forms an image of the coronal scene in the focal plane. The optical materials used in the lenses are BK7, LAK10, and SF10. All of these materials have extensive space flight heritage. The spectral filter transmits from 650 nm to 750 nm (FWHM). This bandpass optimizes instrument throughput and image quality. The Polarcor polarizer is mounted in a hollow-core motor mechanism (see Sect. 8.5) that rotates the polarizer to various angles.

Adequate K-corona signal detection in the faint outer portion of the field of view requires high exposure and minimal scattered light production at O1 and O2. High levels of diffracted light originating at the external occulter and localized in the final image near the $2.5 R_{\odot}$

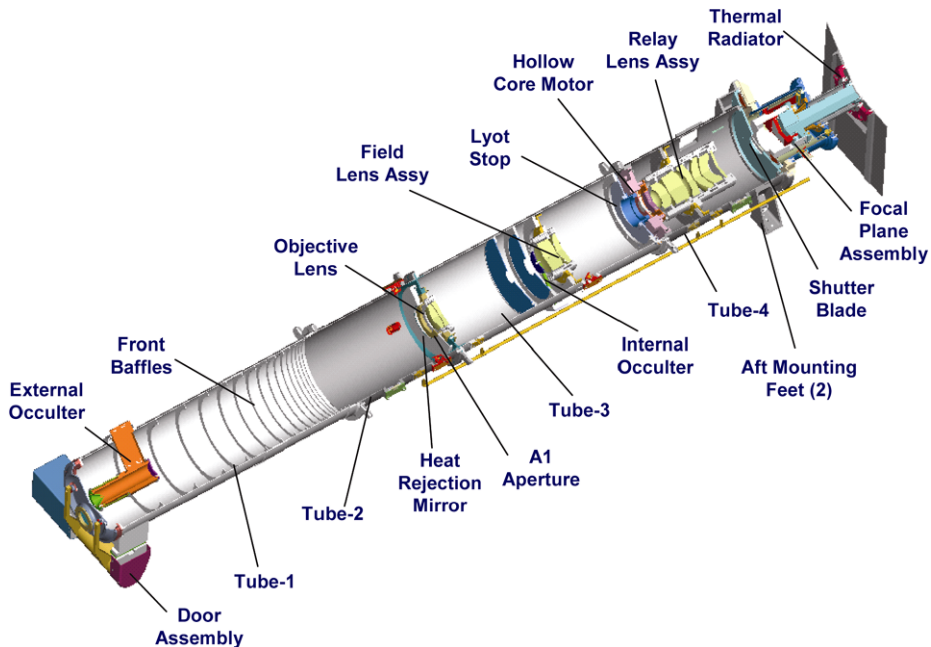


Fig. 13 COR2 mechanical layout

inner field of view cut off would both saturate the CCD before an adequately high exposure is achieved and increase scattered light production by O1 and O2. A related concern is the need to accommodate the expected COR1/COR2 bore sight offset and spacecraft jitter. We addressed these issues by paying particular attention to external occulter diffraction. Two diffraction models were developed and validated with laboratory tests. The models allow diffracted light level to be calculated accurately and minimized for a given inner field of view cutoff by adjustment of the diameters of the first two disks of a three-disk occulter system.

In addition to the diffraction modeling and testing, we also paid close attention to another source of instrumental background in the design phase: ghost images of the bright diffraction sourcing at the external occulter. Ghost images are formed by internal reflections of light from the bright edge of the final external occulter disk in the coronagraph, primarily in the O1 lens and secondarily by reflections from the CCD back toward the lens system. By selecting specific lens surface radii in the optical design phase, we were able to achieve an optical design that confined all significant ghost images present at the focal plane to regions outside the CCD photosensitive area.

The requirement of obtaining a polarization sequence within 15 seconds demanded an optical design that had high light gathering power in comparison to LASCO. Three techniques were used: (1) a shorter exposure time was achieved by using a CCD with a higher quantum efficiency (80% vs. 36%) (2) the light gathering power was increased by using a 34 mm A1 aperture rather than 20 mm (C2) or 9 mm (C3) apertures, and (3) Polarcor polarizing glass was substituted for Polaroid plastic sheet in the linear polarization analyzer which provides better matching of the solar spectral distribution peak to the CCD spectral responsivity.

The need for C2-like spatial resolution in combination with the $15 R_{\odot}$ field of view (C2 field limit was $7 R_{\odot}$) was accomplished in part with a $2k \times 2k$ CCD. The *f*-ratio was set to $f/5.6$ to avoid a substantial increase in instrument length that would be required to accommodate the larger A1 at the same *f*-ratios used for C3 ($f/9.3$) and C2 ($f/20$). Because the large A1 aperture, wide field angle and high spatial resolution placed a burden on the design of the lens system, particularly the O2 lens group, the assembly of the lens systems had tight tolerances, which was accomplished by precision potting techniques.

4.2 Mechanical and Thermal Design

The COR2 mechanical layout is shown in Fig. 13. The mechanical structure consists of a series of circular cross-section tubes. The tubes are mechanically aligned, machined, drilled, and pinned to allow for repeatability in assembly. There are a total of four primary tubes for mounting the optics and the FPA (see Sect. 9.2) tube section. The tubes are fabricated from 6061-T6 aluminum. The COR2 instrument interfaces with the SCIP optical bench via a kinematic mount system comprising of three titanium flexures. The fundamental frequency of the structure with the kinematic mounts is 92 Hz. The COR2 instrument weighs approximately 11 kg and is 1.4 m long.

The first tube section, Tube 1, supports the door assembly, the A0 aperture, and the external occulter subassembly. Tube 1 is machined with internal baffles to reduce stray light entering A1. The tube incorporates a stiffening ring locally where it interfaces the front flexure for additional stiffness. The external occulter subassembly is cantilevered off the tube wall with a single pylon to reduce diffraction. The occulter system consists of three highly precision-machined disks mounted on a spool. Tube 2 serves as additional metering length for the coronagraph. The objective lens assembly is integrated at the interface between Tubes 2 and 3. The assembly consists of the heat rejection mirror, the A1 stop, and the objective lens set. Tube 3 supports two additional apertures, namely the coronal image and A0 image stops, and the field lens assembly. The internal occulter and the Lyot stop is also mounted to Tube 3.

Tube 4 supports the hollow core motor, the relay lens set, the shutter mechanism, and the FPA. The mechanisms are described in Sect. 7 and the FPA and CCD in Sect. 9.

The COR2 thermal design is similar to COR1 in that it uses a slightly cold biased design. A mirror attached to the bulkhead between Tubes 2 and 3 reflects the solar disk radiation coming through the A0 entrance aperture back through the A0. MLI (multi-layer insulation) blankets from the SCIP closeout insulate the instrument from its surroundings. The instrument temperature is maintained using a combination of thermostatically controlled survival heaters and software controlled operational heaters. The structural tube surfaces are treated with an inorganic black anodize. This surface finish provides an optical black and increases thermal coupling within the instrument, reducing thermal gradients.

When the aperture door opens, some of the components comprising the front end of the instrument are exposed to the solar environment. Structural surfaces exposed to direct sunlight are coated with a silver composite coating (CCAG) to prevent overheating. All other surfaces are black anodized to minimize scattered light. The heat rejection mirror, mounted in front of the objective lens, reflects the incident solar radiation back through the A0 aperture and into space.

4.3 Calibration and Performance Results

The COR2 calibration plan involved testing at both the component and telescope levels. The properties of the linear polarizers were measured in the lab and the two best polarizers were chosen for the flight instruments. The bandpass filters were manufactured and measured by Andover. The bandpass response was verified at NRL and again the best filters were used in the flight instruments. The most extensive component-level testing was performed on the various lens sets of the COR2 optical train. A breadboard version of the instrument was constructed to mount the 3 lens groups and to allow us to verify the optical prescription. With the aid of an Air Force resolution target, we were able to measure the MTF at various field angles and choose the lens group combinations with the best imaging performance.

The flight unit performance was measured at NRL's Solar Coronagraph Optical Test Chamber (SCOTCH) facility (Morrill et al. 2006). The same facility was used in a similar configuration for the COR1 calibration (Sect. 3.4.1). The instrument vignetting function and spectral response were measured in air. The stray light levels, image quality and absolute photometric calibration were measured under vacuum. The tests were based on similar tests for the SOHO/LASCO coronagraphs.

The COR2 vignetting pattern for the Ahead telescope is shown in Fig. 14. The image is vignetted throughout the field of view reaching a minimum of 20% at about $10 R_{\odot}$ before increasing again towards the edge. The vignetting around the occulter pylon is only about 40–50%, which does not impede imaging and therefore the pylon will be invisible in the images similarly to LASCO/C2.

The stray light tests (Fig. 15) showed that the instrument performance exceeds the design requirements and will allow us very detailed imaging of the extended corona. The image on the left of Fig. 15 was taken during the stray light test and shows back-reflections onto baffles in the chamber. The plot on the right is the intensity from the center outward to the lower right corner of the image. It passes through one of the low-scatter surfaces (vel-black). The effectiveness of the vel-black is seen immediately in the contrast to the neighboring region which is light being reflected onto the end of the chamber. On the plot is shown the intensity scan of the COR2 as the dot-dash curve, which is below the Saito et al. (1977) (SPM) model of the K-corona as a dotted curve and the curve of the K- and F-coronae and stray light as

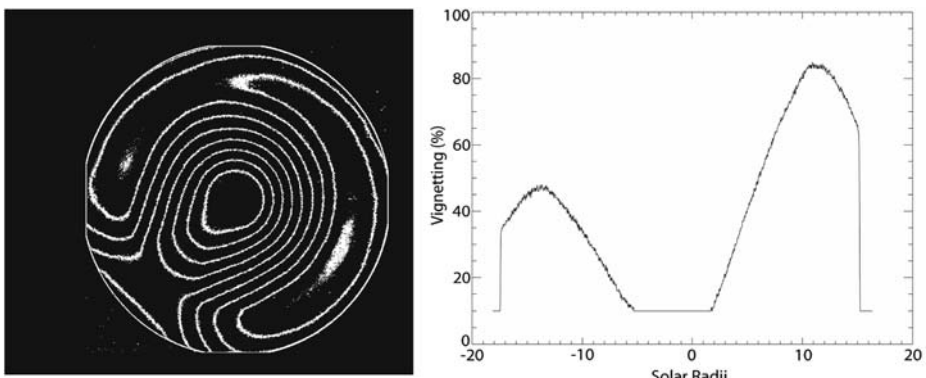


Fig. 14 Flat field response of the COR2 Ahead instrument. The plot on the *right* is an intensity cut diagonally from the lower left to the upper right, through the pylon

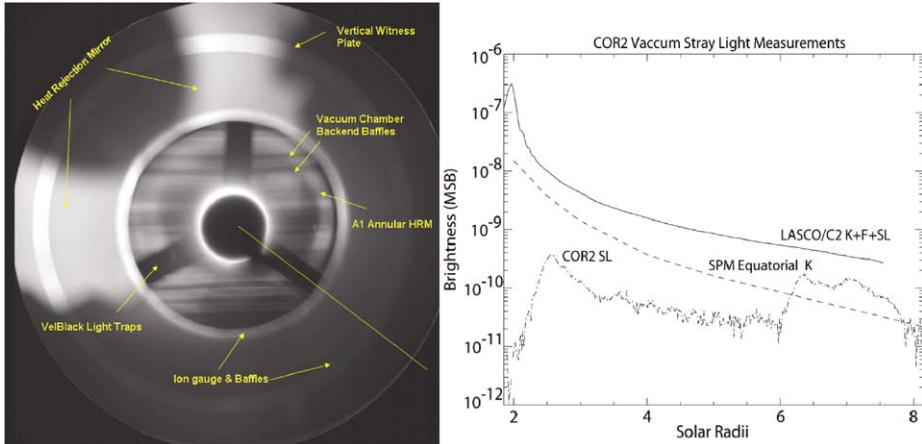


Fig. 15 Stray light performance of the COR2 Ahead instrument. The image on the *left* is an image taken during the stray light test. The plot on the *right* shows the intensity along the radial track along the line in the *lower right* of the image as a *dot-dash*. The brightness is given in units of Mean Solar Brightness

Table 5 COR2 performance requirements

Parameter	Units	Ahead	Behind
Field of view (half-angle)	Degrees	4	4
Inner limit of field of view	R_{\odot}	2.5	2.5
Pixel size, full resolution	arcsec	14.7	14.7
RMS spot size (design)	arcsec	15	15
Planned exposure time	sec	<4	<4
Polarizer attenuation	—	10^{-4}	10^{-4}
Photometric response	B_{\odot}/DN	1.35×10^{-12}	1.25×10^{-12}
Time to complete pB sequence	sec	11	11
Image sequence cadence	min	15	15

recorded by the LASCO/C2. Note that the COR2 curve is an upper limit to the true stray light (which must be determined on-orbit) and is about one order of magnitude less than the K-coronal model.

The overall performance characteristics of the COR2 instruments are shown in Table 5.

4.4 Operations

The COR2 instruments will acquire only polarized images of the corona since the polarizer is always in the beam. The standard sequence will be three images at -60° , 0° , and $+60^{\circ}$, similar to COR1. All three images will be transmitted to the ground and then combined to produce total and polarized brightness images for further analysis. A low resolution, total brightness image created by the summation of the three polarized images will also be calculated onboard and transmitted through the space weather beacon channel. An alternative observation mode is to take two images at 0° and 90° in rapid succession without reading out the CCD in between exposures. This so-called “double” exposure corresponds to a total

brightness image and is transmitted to the ground as a single image. This is useful way to save telemetry and increase image cadence for special observations. More details about the instrument operations are given in Sect. 11.

5 The Heliospheric Imagers (HI)

5.1 Instrument Concept

The HI objectives, like the rest of the SECCHI suite, are to make visible light observations of CMEs and other structures as they transit from the corona and into the heliosphere. The HI package consists of two small, wide-angle telescope systems (HI-1 and HI-2) mounted on the side of each STEREO spacecraft, which together view the region between the Sun and Earth. HI has no mechanisms, other than a one-shot door that protects the instrument from contamination during ground operations and launch. Thus, an image is collected in the shutterless mode, in which the intensity at each pixel is an accumulation of the static scene and a smearing of the image during readout. This smearing can be removed on the ground.

The HI instrument concept was derived from the laboratory measurements of Buffington et al. (1996) who determined the scattering rejection as functions of the number of occulters and the angle below the occulting edge. The concept is not unlike observing the night sky after the Sun has gone below the horizon.

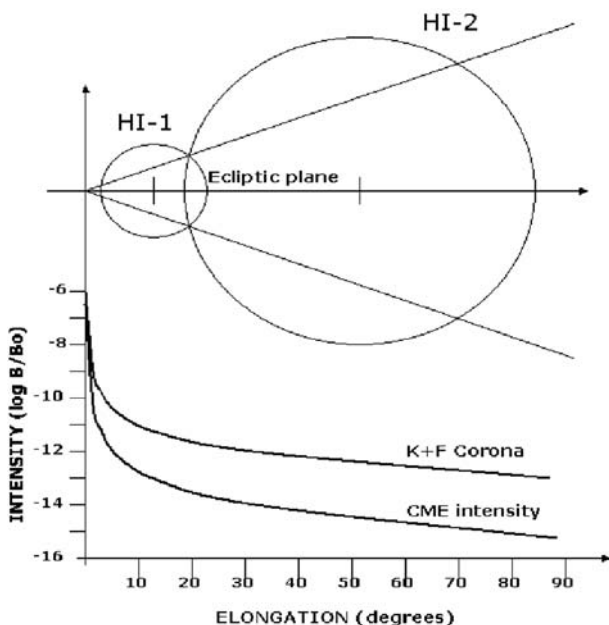
While the specific concept used here has not been flown before, two other instruments have flown which have validated the ability to measure the electron scattered component against the strong zodiacal light and stellar background. The Zodiacial Light Photometer (Pitz et al. 1976) on the Helios spacecraft, launched in 1974, and from the Solar Mass Ejection Imager (SMEI) instrument (Eyles et al. 2003), on the Coriolis spacecraft, launched in 2003 have demonstrated that a properly baffled instrument can detect CMEs (Tappin et al. 2003).

The performance specifications for HI are listed in Table 6. The HI-1 and HI-2 telescopes are directed to angles of about 13 degrees and 53 degrees from the principal axis of the instrument, which in turn is tilted upwards by 0.33 degrees to ensure that the Sun is sufficiently below the baffle horizon. Thus, the two fields of view are nominally set to about

Table 6 Performance specifications of the HI telescopes

	HI-1	HI-2	Units
Direction of centre of FOV	13.98	53.68	Degrees
Angular field of view	20	70	Degrees
Angular range	3.98–23.98	18.68–88.68	Degrees
Image array (2×2 binning)	1024×1024	1024×1024	Pixels
Image pixel size	70 arcsec	4 arcmin	arcsec
Spectral bandpass	630–730 nm	400–1000 nm	nm
Nominal exposure time	12–20 s	60–90 s	sec
Typical exposures per image	150	100	
Nominal image cadence	60 min	120 min	min
Brightness sensitivity	3×10^{-15}	3×10^{-16}	B_{\odot}
Straylight rejection (outer edge)	3×10^{-13}	10^{-14}	B_{\odot}

Fig. 16 The geometrical layout of the HI fields of view and the major intensity contributions (based on a figure from Socker et al. 2000)



14 and 54 degrees from the Sun, along the ecliptic line, with fields of view of 20 and 70 degrees, respectively. This provides an overlap of about 5 degrees.

The geometrical layout of the fields of view of the SECCHI instruments is shown in the top half of Fig. 16. The HI-1 and HI-2 fields provide an opening angle from the solar equator at 45° , chosen to match the average size of a CME. This configuration provides a view of the Sun-Earth line extending from the COR2 outer limit to Earth. Since these observations are done from both spacecraft a stereographic view of an Earth-directed CME is obtained as it propagates through the inner heliosphere. In the bottom half of Fig. 16 are shown the major contributions to the observed intensities: the sum of the F-corona (zodiacal light) and K-corona (electron scattering), and the anticipated CME intensities. Note that the F + K-coronal intensity is about two orders of magnitude brighter than the CME signal.

The anticipated instrument stray light level must be at least an order of magnitude less than the F-coronal signal which can be seen, from Fig. 16, to require levels of better than $\sim 3 \times 10^{-13} B_\odot$ for HI-1 and $\sim 10^{-14} B_\odot$ for HI-2, where B_\odot is the mean intensity of the solar disk. In contrast, the brightness sensitivity requirement is based on the need to extract the CME signal from the other signal sources, which demands the detection of CME intensities down to $3 \times 10^{-15} B_\odot$ and $3 \times 10^{-16} B_\odot$.

5.2 Baffle Design

The baffle design is the key to the HI concept. As shown in Fig. 17, the baffle sub-systems consist of a forward baffle, a perimeter baffle along the sides and rear and the internal baffle system. The forward baffle is designed to reject the solar disk intensity, reducing straylight to the required levels. The perimeter baffle is principally aimed at rejecting straylight from the spacecraft, and the internal baffle system is aimed at rejecting light from the Earth and stars.

The forward baffle protects the HI-1 and HI-2 optical systems from solar light using a knife-edge cascade system, as demonstrated in Fig. 18. The five-vane system allows the re-

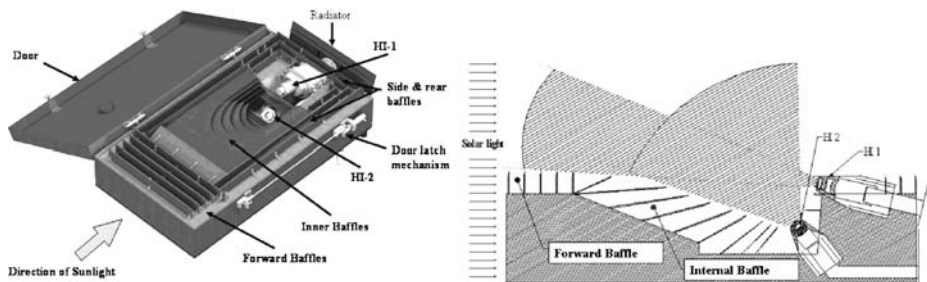


Fig. 17 *Left:* The Heliospheric Imager structural concept. *Right:* A schematic side view of the optical configuration, demonstrating the two fields of view of the two telescopes and the orientation of the interior baffles

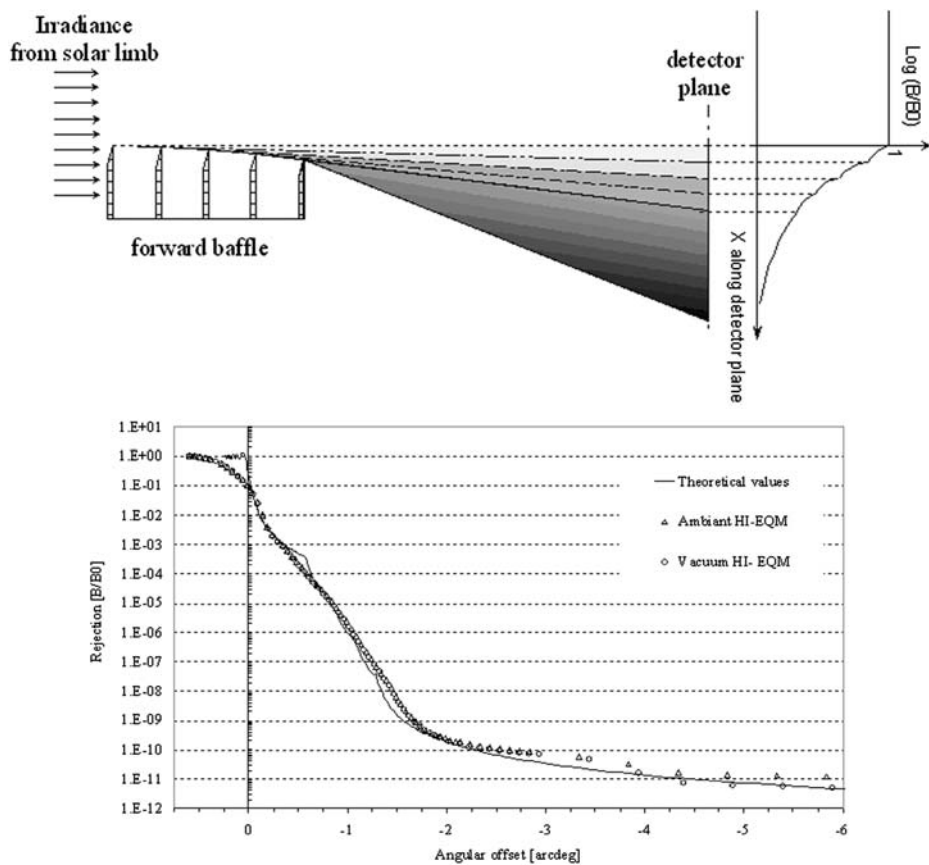


Fig. 18 Comparison of observations of the diffraction from the cascade knife-edge system of the forward baffle system with the theoretical prediction

quired rejection to be achieved, as computed using Fresnel's second order approximation of the Fresnel-Kirchhoff diffraction integral for a semi-infinite half-screen. The schematic plot in the top panel of Fig. 18 shows the nature of the function $\log (B/B_\odot)$, where B_\odot is the solar brightness, plotted with distance below the horizon. The heights and separations of

the five vanes have been optimized to form an arc ensuring that the $(n + 1)$ th vane is in the shadow of the $(n - 1)$ th vane. The computed global rejection curve for this system is plotted in Fig. 18 (bottom panel), together with measurements made using a full 5-vane mock up baffle in ambient and vacuum conditions which show good adherence to the predicted rejection levels (Defise et al. 2003).

The perimeter baffle (sides and rear vane systems) protects the HI optical systems from reflection of sunlight off spacecraft elements lying below the horizon defined by the baffles, including the High Gain Antenna, door mechanisms etc. However, one spacecraft element does rise above the baffles, namely the 6 m long monopole antenna of the SWAVES instrument, although it is not in the field of view of the telescopes. However, from the measured reflection measurements provided by the SWAVES team and calculations, the level of reflected light from the monopole entering the entrance aperture will be insignificant.

The internal baffle system consists of layers of vanes which attenuate unwanted light from multiple reflections into the HI-1 and HI-2 optical systems, mainly from stars, planets the Earth, zodiacal light and the SWAVES monopole. Although the Earth, stars and planets may be within the HI fields, the internal baffle system limits the uniform background scattered into the optical systems.

5.3 Optical Systems

Figure 17 shows the locations of the HI-1 and HI-2 optical units. The optical configurations for these are shown in Fig. 19. These systems have been designed to cater for wide-angle optics, with 20° and 70° diameter fields of view, respectively, with good ghost rejection, using radiation tolerant glasses (as indicated by the notation for each lens). The HI-1 lens system has a focal length of 78 mm and aperture of 16 mm and the HI-2 system has a 20 mm focal length and a 7 mm aperture. The design is optimized to minimize the RMS spot diameter and anticipates an extended thermal range from -20°C to $+30^\circ\text{C}$. The detector system at the focus in each case is a 2048×2048 pixel 13.5 micron CCD.

The lens assemblies have undergone detailed design and test procedures and one of the key requirements is on the stray light rejection; the lens systems are mounted in blackened barrels. For HI-1 and HI-2 stray light rejection is measured to be at 10^{-3} or lower. This combined with the stray light measurement of the front baffle, shown in Fig. 18, provides an overall light rejection level of $10^{-11}\text{--}10^{-14}$ for HI-1 and 3×10^{-15} for HI-2. These values are better than the straylight requirements (Table 6).

5.4 Mechanical Structure

The basic design concept for HI can be seen in Fig. 17. The instrument is a $720 (L) \times 420 (W) \times 240 (H)$ mm box. A door covers the optical and baffle systems during launch and the initial cruise phase activities. The door is designed for single-use operation and will be opened after all contamination generating spacecraft propulsion events have occurred prior to insertion into heliocentric orbit.

The HI structure has 6 components: (1) a five-sided box with stiffening braces, (2) the linear baffle assembly, (3) the perimeter baffle assembly, (4) an interior baffle assembly, (5) telescope trunion mounts and (6) the FPAs. The box is an aluminum honeycomb structure with carbon-fiber (CFRP) face sheets. The face sheets were either 3 or 6 layers in which the layers were oriented at 60 degrees to each other to create pseudo-isotropic thermal characteristics. The 3 layer layups were used in non-load bearing areas. The temperature

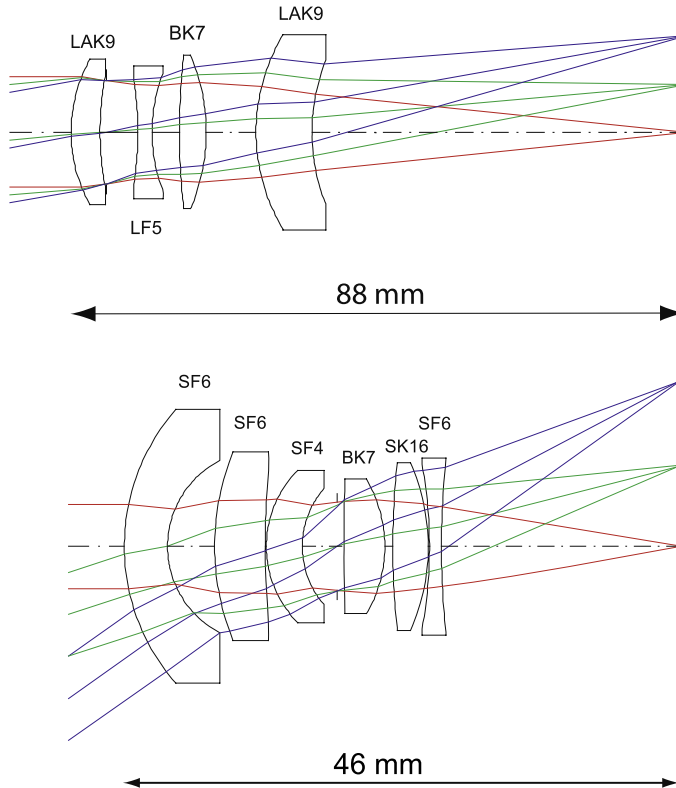


Fig. 19 The optical configurations of the HI-1 (*upper*) and HI-2 (*lower*) lens assemblies

extremes in the instrument are expected to be on the order of 100°C and the relationship between the front baffle assembly to the HI-1 and HI-2 optical axes must be held to within 125 and 240 arcsec (respectively). The baffles are made with 6–8 layers of face sheet layups. The exposed CFRP surfaces were painted with Chemglaze Z307 black paint. The structure met the requirement to have the first natural frequency resonance at or above 50 Hz. The spacecraft mounts were similar to those described in Sect. 7.1.

5.5 Operations

In order to extract the CME signal from the much more intense background of Zodiacal light and stellar background, the SNR must be increased over a single exposure. This is accomplished by summing individual exposures on-board. This requires that the individual images be scrubbed for cosmic rays, prior to summing and also prior to being 2×2 pixel binned. This 2×2 binning results in angular sizes of 70 arcsec (HI-1) and 4 arcmin (HI-2) per pixel. The combination of summing 50 images and 2×2 binning results in an increase in the SNR of about 14 \times . For each telescope, Table 6 lists a nominal exposure time range and typical number of exposures per summed image. Since there is no shutter, a smearing will occur during the readout. Software to remove this effect was applied to images taken during thermal-vacuum testing with excellent results.

A simulation of the instrument performance has been reported in Harrison et al. (2005). In that study the scene was simulated by adding the contributions from the F-corona,

K-corona, stars, planets, and the instrumental characteristics such as point spread function, stray light, photon noise and the shutterless operation. In this background a simulated CME was launched and shown to be detectable.

6 Guide Telescope

The SECCHI Guide Telescope (GT) is mounted on the SCIP and serves two main purposes:

1. The GT acts as the spacecraft fine sun sensor.
2. The GT provides the error signal for the EUVI fine pointing system (FPS).

The GT images the Sun onto an occulter, which is sized to block most of the solar disk and to pass only the solar limb. The intensity of the limb is measured in 4 sections by photodiodes, placed 90° apart. The concept is based on the guide telescope for the TRACE Small Explorer mission.

The optical system consists of an achromatic refractor with bandpass entrance filter and a Barlow lens (Fig. 20). A set of 4 redundant photodiodes behind an occulter measure the location of the solar limb (Fig. 21). The signals from the photodiodes are amplified and passed to the SECCHI Electronics Box. Table 7 lists key parameters of the GT. In contrast to the TRACE GT, the SECCHI GT has no provisions for off-pointing the GT relative to the science telescopes. The focal length of the GT for SECCHI is shorter than for TRACE, and is different for the Ahead and the Behind observatories. This extends the range of apparent solar diameters that the GT can accommodate, and allows the GT to operate throughout the elliptical orbit of each STEREO observatory.

The analog photodiode signals from the GT pre-amplifier are sampled every 4 ms by a 12-bit analog-to-digital converter in the SECCHI Electronics Box. The SECCHI flight software converts the four diode voltages into pitch and yaw pointing error signals, and a set of four sun presence flags (one flag for each photodiode). Those signals are sent to the spacecraft. If all four photodiodes are illuminated, then the sun is within the linear range of the GT, all four sun presence flags are set, and the error signals are valid. If only one, two, or three photodiodes are illuminated, then the sun is within the acquisition range of the GT, and the STEREO spacecraft uses the sun presence flags to acquire the sun. The SECCHI flight software further processes the GT error signals to generate the drive voltages for the active secondary mirror of the EUVI Fine Pointing System.

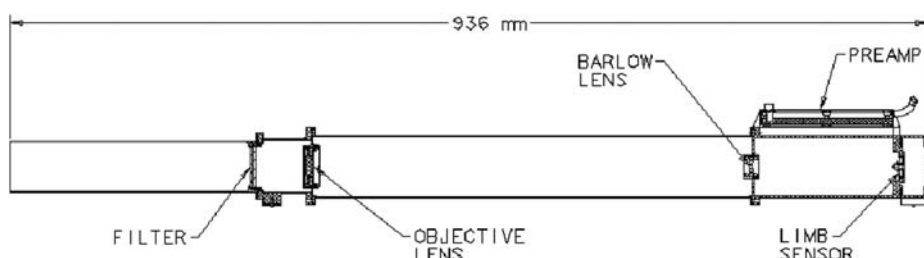


Fig. 20 Schematic cross section of the SECCHI Guide Telescope

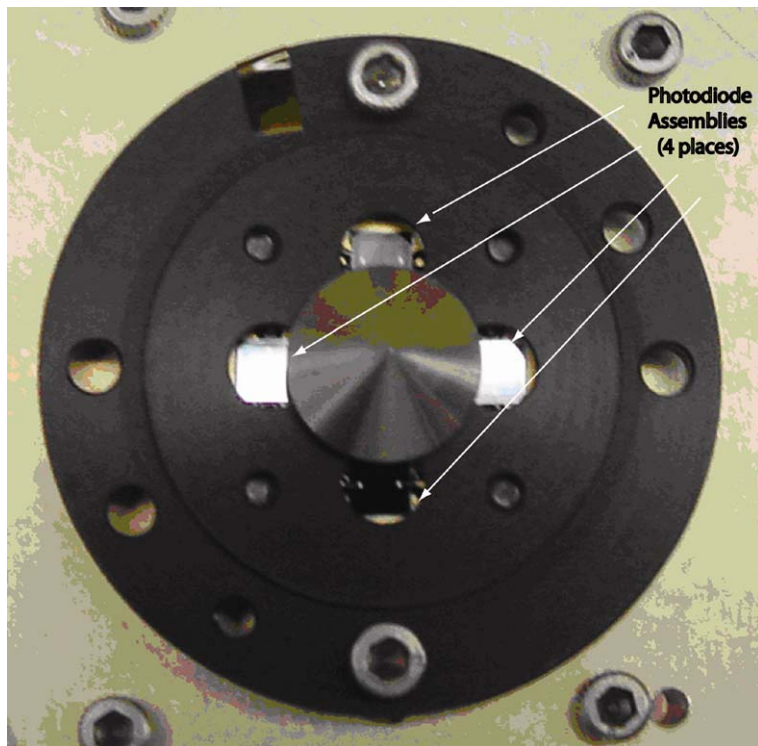


Fig. 21 Guide Telescope sensor head with occulter and photodiodes

Table 7 Key Guide Telescope parameters

Optics	Achromatic refractor with Barlow lens
Lens materials	Radiation hardened glass
Aperture	27 mm (aperture stop at objective lens)
Focal length	Ahead: 1454 mm, Behind: 1562 mm
Bandpass filter	Center wavelength: 570 nm, bandwidth: 50 nm (FWHM)
Limb sensor	4 (+4 redundant) photodiodes
Telescope structure	Aluminum
Acquisition range	> \pm 20 arcmin (worst case)
Linear range	> \pm 70 arcsec (worst case Aphelion)
Pre-amplifier	Two selectable gains: sun/stimulus telescope (artificial sun)
Noise	<0.4 arcsec (3σ , single sample)
Sample frequency	250 Hz (digital sampling in SEB)

7 SCIP Bench

The SCIP (Sun Centered Instrument Package) structure supports the four SCIP telescopes (COR1, COR2, EUVI, and GT), the two SCIP electronics boxes (SCIP CEB and MEB), and the associated harnesses and thermal blankets. The design of the SCIP structure is driven by several requirements. The structure must (1) provide easy mounting and accessibility

for component and spacecraft integration, (2) preserve the unobstructed field of view requirements of each telescope, (3) facilitate co-alignment activities and preserve telescope co-alignment on-orbit, (4) be sufficiently stiff to avoid coupling with spacecraft and launch vehicle modes, and (5) meet a stringent mass budget while surviving test and launch loads.

The SCIP structure is a simple optical bench. The four telescopes are mounted on one side of the bench while the electronics boxes are mounted on the opposite side. Several holes through the bench allow harnessing to pass between the telescopes and the electronics. The SCIP bench is a 6.3 cm thick aluminum honeycomb panel (112 cm × 70 cm) with high modulus graphite/cyanate ester face sheets. Face sheet layup is biased for high shear stiffness and a resulting higher torsional stiffness of the optical bench. The design provides sufficient stiffness to meet the 50 Hz SCIP assembly first natural frequency requirement (measured a 54 Hz first mode, bench torsion, during assembly vibration testing).

An additional thermal tent structure is attached to the bench to support an enclosure of thermal blankets over the telescopes. The thermal tent structure is comprised of 0.5 cm honeycomb panels at the sun and anti-sun ends of the bench with tubular stringers connecting the panels. Thermal blankets are draped over the structure to control the thermal and contamination environments inside the enclosure and provide insulation from the spacecraft cylinder. This generates a very uniform thermal environment for the SCIP telescopes.

7.1 SCIP Flexure Mounts

A key requirement of the SCIP structure is its ability to facilitate instrument co-alignment and maintain it throughout the test program and instrument life on-orbit. The key to meeting this challenging requirement is the development of a flexure-based near-kinematic mounting scheme. The scheme incorporates a set of three flexure mounts for each telescope. Each mount is very stiff in the normal and lateral directions and much less stiff in the axial direction and in the three directions of rotation. Acting as a set of three, the mounts provide a fully constrained, but not over-constrained, mounting scheme. The design of the flexure mounts has several distinct advantages: (1) The ratio of modulus in the “stiff” directions to the modulus in the “released” degrees of freedom provides an essentially kinematic mounting system. (2) The kinematic nature of the mounts minimizes thermal stress in the telescopes, preserves co-alignment on-orbit and allows shimming of the telescopes without inducing stress in the telescope tube structure. Shimming of the telescopes was performed with 5 arcsec resolution. (3) The mounts utilize snug fitting pins at each interface to prevent shifts after integration and assure co-alignment repeatability when a telescope is removed and re-installed. (4) The titanium alloy provides high strength and stiffness with low mass, and large thermal isolation.

7.2 Analysis and Testing

The primary analysis tool for the SCIP structure was a MSC/NASTRAN finite element model. The SCIP optical bench was modeled in detail, including models of each telescope and of the electronics box, with a 189,000 degree-of-freedom model. Due to the developmental effort on the flexure mounts, a highly detailed (140,000 degree-of-freedom) model was constructed to analyze high stress areas and predict mount stiffness. Based on the detailed model, a simplified model of the mount was constructed for use in the assembly-level model. The full assembly-level model was used to predict assembly first frequency, assess stress levels in the structure, derive component test spectrums and interface loads, and predict on-orbit telescope alignment shifts due to thermal loads.

Significant testing was performed to correlate the finite element results and load test the flight structures. The flexure mounts went through two rounds of prototype testing before the flight design was finalized. A monolithic telescope simulator facilitated testing of the mount system to determine its mounting stiffness. After the flight hardware was manufactured, other simulators were constructed to be used in static and dynamic load testing of the flight article. The test results were used to validate the component test spectra that were used to qualify the telescopes before they were integrated with the flight optical bench.

8 Mechanisms

The SECCHI SCIP telescope suite contains a total of 10 mechanisms of 6 distinct designs. EUVI has a focal plane shutter, filter wheel, and a quadrant selector. The COR1 and COR2 telescopes each have a focal plane shutter and polarizer mechanism. All three of the SCIP telescopes have a door mechanism. The HI telescopes have one mechanism, a door, which was discussed in Sect. 4.

All mechanisms have heritage from previous flight programs. The SCIP door mechanisms are based on a SOHO-LASCO design. The EUVI quadrant selector is an evolution from the mechanism used in the TRACE quadrant selector, in that there are no restrictions in the frequency of changes between telescope quadrants. The EUVI filter wheel, COR2 and COR2 polarizer wheels and shutter mechanisms are nearly identical to the ones used on GOES SXI-N (Stern 2003).

8.1 SCIP Aperture Doors

The re-closable doors of the EUVI, COR1 and COR2 telescopes are referred to as the SESAMES (SECCHI Experiment Sun Aperture Mechanisms). In total there are two sets of SESAMES, one for each SCIP assembly (Fig. 22). The prime objectives of the re-closable doors are to protect the sensitive optics of the telescopes from damage due to contamination during ground operations, but also at critical times during flight operations. The launch of

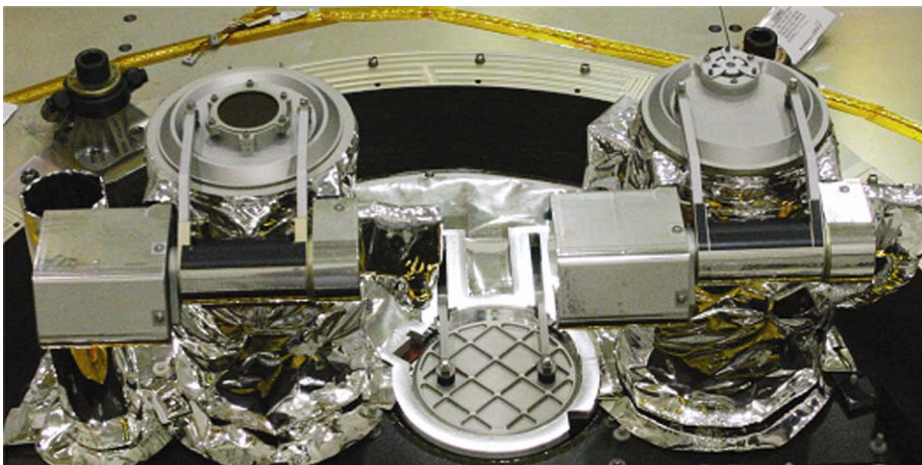


Fig. 22 Top front view onto the SCIP-B assembly after integration into observatory B. From *left to right*: COR 1, EUVI and COR 2 doors. The SCIP-A doors are identical

the Delta rocket generates large acoustic vibrations requiring the door lids to be pressed tightly against the telescope entrance apertures without generating particles. The EUVI is especially sensitive because the lid has to protect the thin optical filters lying directly behind it. The doors also help to maintain the cleanliness of the optical systems from external contaminants that may be caused during thruster firings to control the orbit of the STEREO spacecraft. Because of momentum desaturation the thrusters will be fired about every 6 days on average, implying that the COR doors will be cycled about 120 times during the two-year nominal operations period. Re-closable doors are also required because the optical systems must open and close during ground testing and calibration of the optical systems.

All three doors have a similar baseline design. Each is operated by a stepper motor which drives a special screw-ball bearing mechanism to open and close the lids. In case of the malfunction of the motor a paraffin actuator acts as the failsafe device to open the door permanently. The command to “fire” the paraffin actuation is controlled by the spacecraft. The doors can be driven by the motors into different positions: superclosed, closed, cracked and open. The superclosed position presses the door lid against the aperture to withstand the launch environment, which could cause the lid to vibrate against the telescope tube. This vibration would create particles. The closed position is the normal closed position without the launch pre-load. The cracked position is an intermediate position between closed and open to permit outgassing to occur after launch. The open position is the normal position for science operations. The lid designs of EUVI, COR1 and COR2 have different sizes and structures, with calibration windows being integrated into the COR lids. The opening angle of the EUVI door is 90 degrees, that of the COR doors is 270 degrees.

8.2 Shutters

The EUVI, COR1 and COR2 shutter designs are based on shutters that have successfully flown on SOHO/MDI, TRACE (Akin et al. 1993), and Solar-B/FPP and will be flown on GOES-N/SXI. Both consist of a brushless DC motor with an optical encoder to which is attached a thin circular blade with a 120° opening that is positioned in front of the telescope’s focal plane. The motor rotates the blade to open the shutter, exposing the CCD. The blade is rotated in the same direction to close the shutter. The SECCHI shutters are capable of exposures from 40 ms to 67 seconds in a programmable mode that are repeatable to better than 15 µs and uniform across the CCD to 50 µs. The exposure length can be indefinite when open and close motions are controlled directly by the SEB.

8.3 Quadrant Selector

The EUVI quadrant selector is nearly identical in design to the coronagraph shutters. The motor rotates a blade with a 90° opening just behind the telescope’s thin-film entrance filters. The mechanism is commanded to rotate in 90° increments in approximately 45 ms to mask off all but one of the telescope’s four EUV channels.

8.4 EUVI Filter Wheel

EUVI also incorporates a four position filter wheel just behind the telescope’s shutter. The filter wheel consists of a 101 mm diameter brushless DC motor surrounding a rotor with four 32 mm diameter through holes. The mechanism will be launched with the filter wheel in the open position, leaving the telescope beam-path open and protecting the three-filter position within the mechanism housing. Operation time between two adjacent filter positions is approximately 300 ms. Like the SECCHI shutters, the filter wheel has heritage from TRACE, MDI, SXI, and FPP.

8.5 Polarizer Wheel

The coronagraph polarizer mechanism, also known as the hollow-core motor (HCM), is the most unique of the SECCHI mechanisms. Its design is derived from a similar mechanism used with success in MDI. It has a 144 step brushless DC motor similar to that used for the EUVI filter wheel. A large-diameter, thin-section bearing supports a stainless steel rotor with Teflon toroid separators. The space inside the bearing is left open, providing a 48 mm clear aperture for the coronagraph light bundle. With the 144 step motor design, the polarizing optic that is mounted to the rotor can be positioned in 2.5° increments. During normal observing operations, the polarizer mechanism will rotate 120° with an angular repeatability of better than 30 arcseconds. It makes this move in approximately 400 ms.

8.6 Lifetime Requirements

The lifetime requirements for each of the SECCHI mechanisms are 2.1 million operations for the EUVI quadrant selector, filter wheel, and shutter and 0.6 million operations for the COR polarizer mechanisms and shutters. Comprehensive life testing was completed to prove the designs of the EUVI quadrant selector, coronagraph shutter, and HCM. These mechanisms underwent vibration to levels greater than for flight, thermal functional testing, and flight like operation in vacuum to three times their design lifetime. The quadrant selector was qualified to 8 million operations, the coronagraph shutter qualified to 2.8 million operations, and the polarizer mechanism qualified to 3.5 million operations with no degradation in performance. The designs for the EUVI filter wheel and shutter were previously proven to be capable of more than 32 million operations.

9 SECCHI Electronics

SECCHI contains three types of electronics arranged into 4 different boxes. The main electronics is contained within the SECCHI electronics box (SEB) and is described in Sect. 9.1. The SCIP mechanisms are driven from a remote electronics box, described in Sect. 9.2. The SCIP and HI cameras are driven from remote electronics boxes, called the Camera Electronics Box (CEB) and described in Sect. 10.3.

9.1 The SECCHI Electronics Box (SEB)

The SEB (SECCHI Electronics Box) is the payload controller for the SECCHI Instrument Package on the STEREO spacecraft, controlling and monitoring all SECCHI hardware. A block diagram of the SEB is shown in Fig. 23. The SEB provides the instrument's interface to the spacecraft via the MIL-STD-1553 and power interfaces. It receives and distributes commands from the spacecraft and collects and converts state of health telemetry data before providing it to the spacecraft. Image data from the telescopes (2 channels, 100 MB/s) is received over two SpaceWire ports and is then processed, compressed, and transmitted across the 1553 interface to the spacecraft for downlink. The SEB had to be designed to meet stringent program EMI requirements, as will be discussed briefly below. An Engineering Development Model (EDM) was designed and built before the flight hardware as a pathfinder for the designs. This EDM is now part of the software testbed that will be maintained during the life of the mission. The flight hardware underwent EMI/EMC, vibration and thermal-vacuum testing before integration with the SECCHI instrument packages.

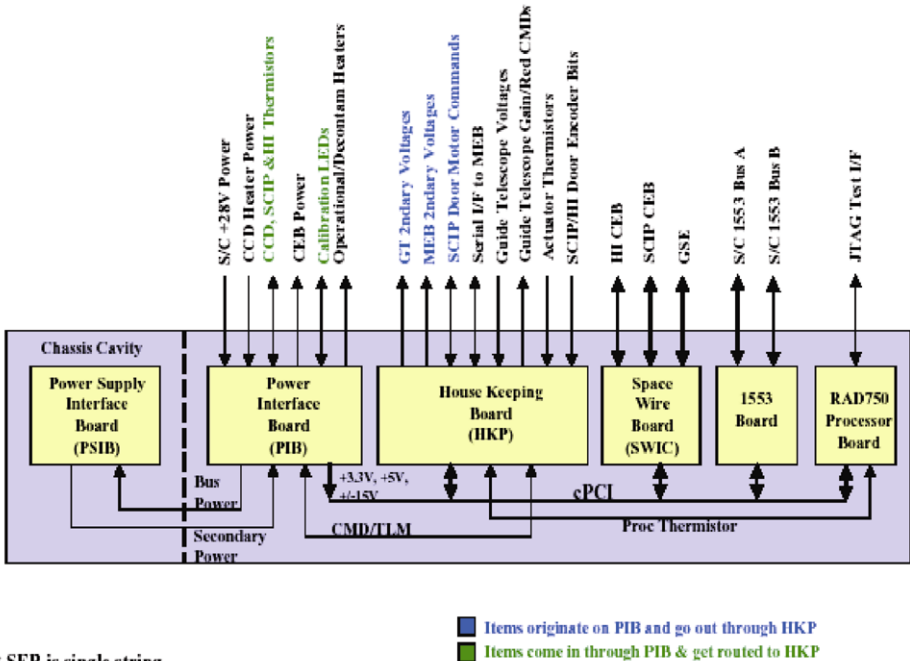


Fig. 23 SECCHI Electronics Box (SEB) functional block diagram

9.1.1 Motherboard

The SEB Motherboard provides electrical connectivity between all cards housed within the SEB enclosure. It is a customized, cPCI compliant, five (5) slot, 6U back plane. The first four (4) cPCI slots which utilize the PCI signaling strictly adhere to the cPCI specification. The fifth slot which does not use the PCI signaling has been customized for communications on the user defined connectors, P3/P4/P5. Unused cPCI connectors were eliminated from the design.

9.1.2 Electrical Power

The SEB must interface to the spacecraft's unregulated power bus. The electrical power system provides this interface as well as power conversion, control and distribution. Due to EMI requirements, the electrical power system was divided into two (2) functional assemblies—the DC/DC converters and related circuitry (PSIB) and the power interface and distribution functions (PIB).

The PIB interfaces to the primary spacecraft power bus through a front panel connector and routes this power off the motherboard and through the EMI cavity line filter panel, to the DC/DC converters in the small EMI cavity. Regulated secondary power is then routed back from the DC/DC converters to be distributed throughout the SEB and SECCHI system by the PIB card. Internal secondary SEB power is distributed across the motherboard as required. External SECCHI power is routed through PIB I/O connectors and, in some cases, across the motherboard and out through the HKP I/O connectors due to front panel limitations. Power control signals are generated from gate arrays resident on the HKP card,

as commanded by the RAD750 processor card. The HKP card determines the proper commands to send to the PIB and uses a serial interface across the motherboard to transfer the information. The PIB also provides motor drive power from control signals generated on the HKP. Voltage and current monitoring circuits on board provide state of health telemetry to the HKP for conversion and, ultimately, downlinking. This card also houses the operational heater drive circuits with appropriate switching for thermal control of the instrument package. The heaters are again controlled via the HKP card since the PIB has no interfaces with the processor for real estate and design simplification reasons. A second power bus from the spacecraft is distributed to SECCHI decontamination heaters through latching relays on this card.

The PSIB assembly resides in the small EMI cavity and includes three (3) DC/DC converters that provide all secondary power for the SEB and SECCHI system, as well as all necessary filtering and protection. A single converter provides +3.3 Vdc power for internal logic. A triple output converter provides +5 VDC for internal and external legacy logic and +/−15 Vdc power for analog functions. The third converter provides +15 Vdc dedicated for “noisy” motors and mechanisms. Primary and secondary power interfaces, to the main cavity, are through an EMI filter panel.

9.1.3 RAD750 Processor

The SEB RAD750 processor, procured from BAE Systems, provides all processing required for the SECCHI system and the control of all SEB circuitry via the cPCI backplane. At the core is a custom Power PCI Bridge chip providing the interface between the PowerPC 750 and the cPCI bus. The primary computing resource is the radiation hardened PowerPC 750. The RAD750 card provides for 256 kbytes of EEPROM StartUp ROM (SUROM) and 128 Mbytes of SDRAM. SDRAM EDAC can correct nibble errors and detect double nibble errors. The card provides a self-refresh mode and scrubbing for the SDRAM. The RAD750 is capable of 120MIPS and is being run at 116 MHz in the SECCHI application. This card is the only 3U card in the SEB.

9.1.4 MIL-STD-1553 Interface Card (1553)

The 1553 card provides a fully compliant MIL-STD-1553 Remote Terminal (RT) bus interface to the spacecraft and 3 Mbytes of EEPROM storage for software application code. The 1553 interface is the only communications interface with the host spacecraft. All commands, data uploads and telemetry are communicated across this bus. Full redundancy makes this a very robust interface. The EEPROM is arranged as two (2) banks of 1.5 Mbytes × 16 bits wide. This storage is fully accessible across the cPCI bus and provides for redundant flight software storage.

9.1.5 SpaceWire Interface Card (SWIC)

The SWIC provides two (2) 100 Mb/s, simultaneous SpaceWire compatible links to the SCIP and HI instruments respectively. All image data and camera setup commands are transferred using these interfaces. The TSS901E ASIC, from Atmel, provides these SpaceWire links. 256 Mbytes of SDRAM allows for temporary image storage while awaiting retrieval and processing by the RAD750, and can also be used by the processor for data storage or program execution. The SDRAM is complete with programmable refresh, scrubbing and EDAC. To efficiently move large amounts data, the PCI interface can be configured for DMA transfers, on to or off of the SWIC.

9.1.6 Housekeeping Card (HKP)

The HKP is the bridge between the analog interfaces and the digital cPCI bus for the SEB. It controls serial data transfers with the SCIP mechanisms controller (Mechanisms Electronics Box—MEB hardware) for shutter control and other commands. All SECCHI door status is monitored and made available by the HKP. A regulated current source provides selectable drive for SECCHI calibration LED illumination. Analog Guide Telescope signals are received and digitized by the HKP at a 250 Hz rate for delivery to the processor for transfer to the spacecraft’s Attitude Control System (ACS). Sixty three analog telemetry points, including voltage, current and temperature sensors, for both SEB internal and SECCHI external, are digitized (0 to +10 V range, 12 bit conversions) and made available to the system processor for use in fault detection and isolation and general state of health monitoring.

9.1.7 Enclosure

The enclosure was machined from a single block of aluminum. It includes 2 compartments allowing EMI isolation of the internal DC/DC converters. The bottom and one side have removable covers with labyrinth seals. Individual cards are installed from the top, with each card having a connector bracket that provides additional EMI protection and structural tie points. One final top cover, with clearance for each connector, completes the EMI seal. The DC/DC converters reside in a separate “EMI cavity” isolated from the main cavity. The interface between the 2 cavities is achieved with an EMI-tight, filter capacitor panel. The overall dimensions are $198 \times 292 \times 267$ mm ($H \times W \times L$), weighing 9.4 kg.

9.2 Mechanism Electronics Box (MEB)

All of the SECCHI SCIP mechanisms, with the exception of the telescope doors, are controlled by the SECCHI Mechanisms Electronics Box (MEB), which is mounted on the underside of the SCIP optical bench. Physically, the MEB is a $210 \times 56 \times 171$ mm box with a mass of approximately 1.4 kg with connectors dedicated to power and commands from the SEB and each of the telescopes. The MEB inputs are a Low-Voltage Differential Signal (LVDS) from the SECCHI SEB, 5 V power for the MEB and mechanism encoders, ± 15 V power to drive mechanism motors. The three LVDS inputs to the MEB from the SEB include a strobe, clock signal, and a serial command signal. A single return LVDS signal is sent back to the SEB. The MEB contains two boards and each has two Field Programmable Gate Arrays (FPGAs). The FPGAs on the first board control the EUVI shutter, quadrant selector, and filterwheel, and drive the EUVI Fine Pointing System (FPS). The two FPGAs on the second board each control a shutter and polarizer mechanism on each of the coronagraphs.

The MEB accepts low level commands such as “load target position,” “move clockwise” to that position, and “read current encoder position.” These commands are sequenced by the SEB and there is no command buffer in the MEB. Table 8 provides a partial listing of commands accepted by the MEB in the order in which they are typically employed. MEB commands are 16-bit and consist of an 8-bit command word and an 8-bit variable word such as exposure time for a shutter or target position for the HCM.

The mechanism motors are driven by a 15 V, three-phase signal generated by the MEB in response to the signal provided by the optical encoders in each of the SECCHI mechanisms. The SECCHI MEB also drives the EUVI FPS, the design of which is discussed in a separate section. The MEB accepts commands from the SECCHI SEB to derive three analog voltages from 0–10 V to drive the ISS PZTs. There is no PZT or mirror position feedback to the MEB.

Table 8 MEB commands

Command	Action
RESET	<ul style="list-style-type: none"> – HCM and filter wheel target and encoder reading cleared – Shutters rotate to “ready for exposure” position, exposure time cleared – Quadrant selector rotates to 284 Å quadrant, target cleared
LOAD TARGET	HCM, filter wheel, and quadrant selector desired position saved
MOVE CW	Mechanism moves to saved target
LOAD EXPOSURE	Shutter desired exposure time saved
CW EXPOSURE	Shutter makes a 120° clockwise move to open position, waits for desired saved exposure time, and makes a 240° clockwise move to closed/ready position
READ ENCODER	MEB returns to the SEB the current position of the mechanism
READ STATUS	MEB returns to the SEB the current status of the mechanism

10 Charge Couple Device (CCD) Cameras

10.1 CCD Detectors

Each of the scientific instruments on SECCHI uses a three-phase, back-illuminated, non-inverted mode (to ensure good full well capacity, 150k to 200k electrons), CCD model CCD42-40 manufactured by E2V in the United Kingdom. There are $2048 (H) \times 2052 (V)$ image pixels, each measuring 13.5 micron on a side and providing a total imaging area of 27.6 mm square. The total readout is 2148×2052 pixels, providing 100 columns of non-imaging over and under-scan region for camera calibration and engineering purposes. Two readout ports on the left and right side of the imaging area are available. In principle the device may be fully read through either port, or through both ports to double the readout speed. To save mass the SECCHI instruments use only one port, which is hard wired through the harness in our flight configuration, although non-flight harnesses were developed to test from either port. The CCDs used for visible light detection (COR-1, COR-2, HI-1 and HI-2) have an anti-reflective coating on their backside (illuminated side). Quantum efficiency (QE) of these devices is roughly 80% at 500 nm, 88% at 650 nm, 64% at 800 nm, and 34% at 900 nm. The backside of the EUVI CCD has no coating in order to provide sensitivity at shorter wavelengths, with a quantum efficiency of 74% at 17.1 nm, 70% at 30.3 nm, and 46% at 58.4 nm. CCDs are operated at a temperature design point of $<-65^{\circ}\text{C}$.

The CCD is mounted on a custom ceramic carrier, which is precision mounted on an invar chip carrier. Electrical connections are made through a flex-print cable secured to the carrier, and a 25-pin micro-D connector. Figure 24 shows the SECCHI CCD in its flight package. The CCDs have excellent vertical and horizontal charge transfer efficiencies—better than 99.999%. The dark current generation rate is better than $2 \text{ nA/cm}^2/\text{s}$ at 20°C , which is equivalent to 24,000 electrons per pixel/s.

10.2 Focal Plane Assembly (FPA)

The SECCHI Focal Plane Assembly (FPA) provides the SECCHI CCDs with physical mounting, optical positioning, electrical connection, and thermal cooling. The basic FPA

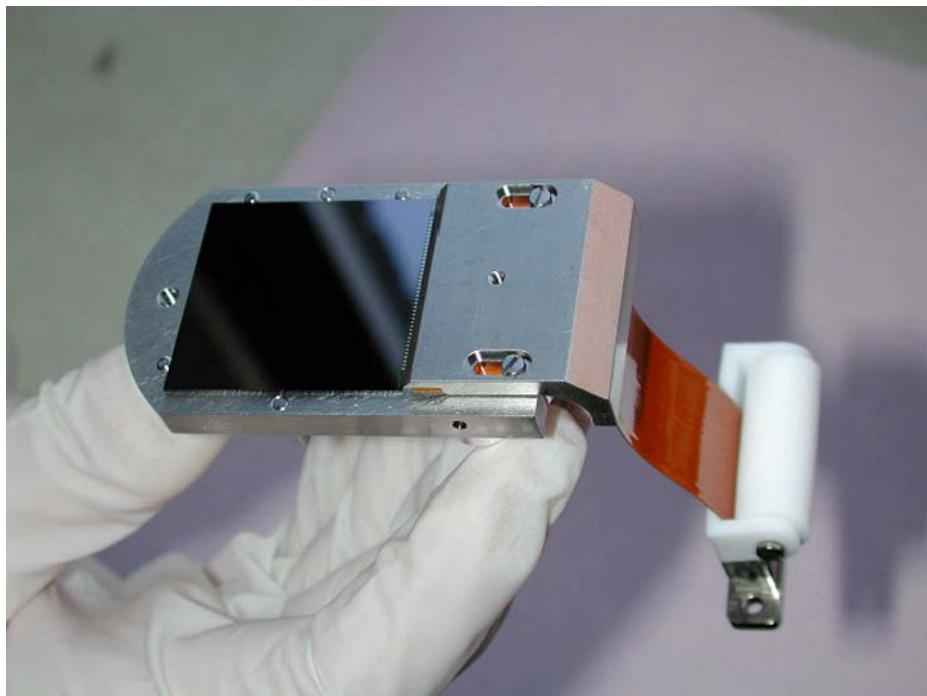


Fig. 24 SECCHI CCD in its package with flexprint harness attached. The CCD size is 28.1 mm × 30.3 mm

design for SECCHI was used on all five telescopes. All five assemblies are nearly identical except for differences in the length and shape of the cold finger, radiator size and shape and focal plane masks.

The requirements for the design of the FPA were: (1) Cool the CCD using passive radiation techniques to $<-65^{\circ}\text{C}$ using an aluminum cold finger coupled to a surface radiating to deep space; (2) Position the CCD at the focal plane of the telescope, perpendicular to the optical axis and aligned to the optical axis; (3) Keep the CCD positioned at room and operating temperatures; (4) Provide a capability to add a spacer in between the FPA and telescope mounting flange to account for different focal plane positions of the various telescopes and to account for any focal plane shift between room and operating temperatures; (5) Provide a capability to heat the CCD to at least 30°C to drive off contaminants and to “anneal” the CCD after radiation damage; (6) Provide a cold cup at a temperature slightly colder than the CCD to act as a contamination shield for the CCD.

Figure 25 shows a cutaway of an FPA assembly as viewed from the front/side and also in the lower right as viewed from the rear/side. At operating temperatures, the CCD will be below -60°C and the mounting flange will be about 20°C . The CCD is cooled to this low temperature by conducting away the heat from the CCD through an aluminum “cold finger” which then is attached at the back end to an aluminum thermal radiator plate that has a clear view to deep space. The CCD chip carrier is first bolted onto an invar block which has a heater coil in between the carrier and the block. The heater coil can heat the CCDs to above 50°C . The invar block is attached to the cold finger, which runs inside an outer support tube and attaches to the thermal radiator. The interior of the outer support tube and the cold finger are gold plated to reduce the heat transmission between the two. At the mechanical interfaces

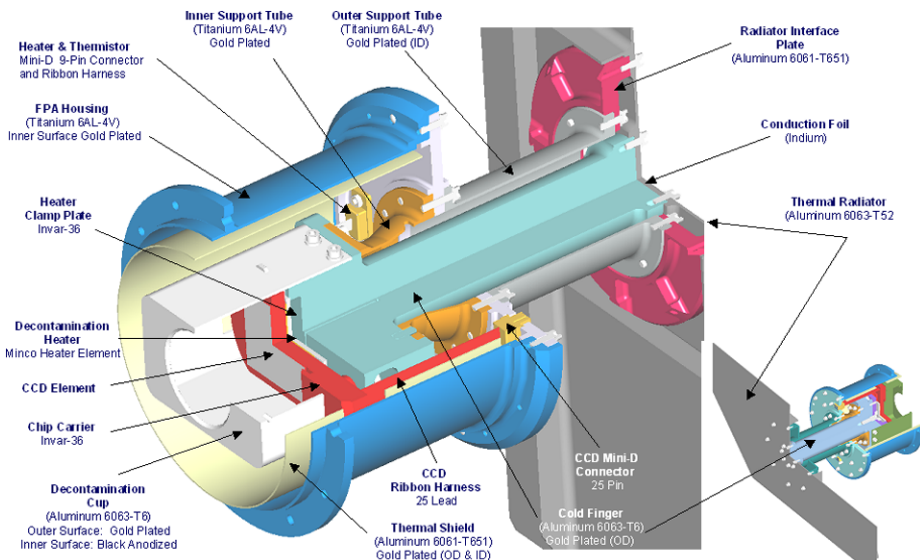


Fig. 25 Focal plane assembly

on either end of the cold finger an indium foil is sandwiched in the joint to minimize the heat conduction loss across the joint. A titanium inner support tube is attached to the cold finger on one end and the FPA housing, made of titanium. Using titanium minimizes heat conduction from the instrument to the cold finger. The front of the FPA housing attaches to the rear of the telescope housing. Attached directly to the cold finger is a cylinder that surrounds the CCD and is colder than the CCD since it has fewer mechanical interfaces and does not have the heat generated by the CCD. This cylinder (decontamination cup) collects any volatiles that are driven off the CCD during the “bake-out” process.

10.3 Camera Electronics Box (CEB)

The CEB must provide the appropriate control signals to each of the telescope CCDs, accept the analog signal out, digitize the signal to 14 bits and send the image data to the SEB. The CEB will collect housekeeping information to be sent to the SEB. The camera requirement calls for a CCD pixel readout rate of 1 Mpixels/s, yet also dictates very challenging low mass and low power budgets. ASIC and surface-mount packaging technologies help minimize the size, mass, and power requirements of the cameras. Controlling three CCDs from the SCIP box, and two CCDs from the HI box minimizes the overhead arising from the spacecraft interfaces and the power converters, and thus the overall size, mass, and power of the camera controllers.

Figure 26 is a schematic of the CCD Camera Electronics Box (CEB). It comprises (1) Two (HI) or three (SCIP) CCD Driver Cards; one dedicated to each of the CCDs. A block diagram of the CCD Driver Card is shown in Fig. 27. (2) A Camera Interface Card that provides a common interface between the three CCD Driver Cards and the SECCHI instrument computer. (3) A DC-DC Power Converter mounted in an internal screened housing in the base of the electronics box. (4) A backplane interface for inter-connection of the daughter PCBs.

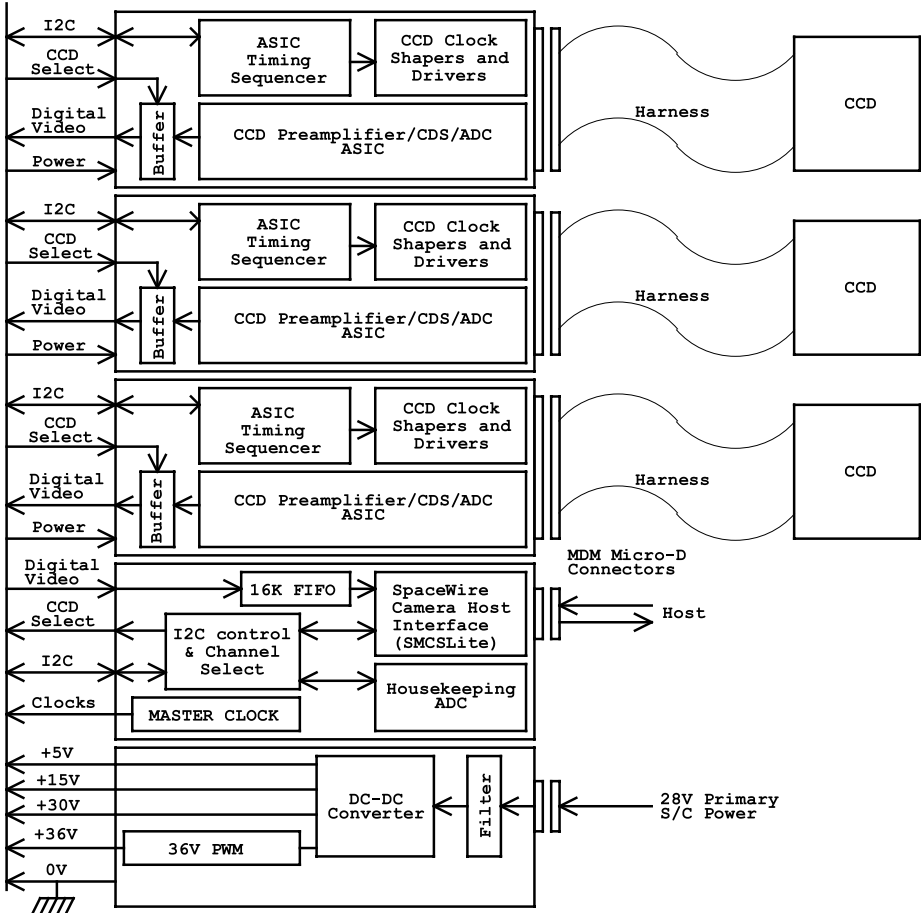


Fig. 26 CEB architecture

Each CCD Driver Card (Fig. 27) accommodates a dedicated waveform generator and sequencer ASIC, CCD clock drivers, low noise DC bias supply generators, a CCD video preamplifier, correlated double sampler (CDS), and 14 bit analog to digital converter (ADC) system.

The camera electronics exploits the same basic waveform generator ASIC and CCD clock driver circuit topologies designed for the SMEI CCD cameras (Eyles et al. 2003), but updated for faster pixel readout rate for SECCHI. Each CCD is clocked from its own dedicated sequencer and clock drivers, and is read out through its own 14 bit CDS/ADC video processor. The 14 bit CDS/ADC video processor is implemented in an ASIC which is a special purpose designed, radiation tolerant chip developed at RAL.

Each camera communicates with the SECCHI instrument computer via an IEEE1355/SpaceWire link, enabling camera programming, camera command, gathering of housekeeping data, and the transmission of digitized CCD video data. The data transmission rate is up to 100 Mbits/s, employing the SpaceWire LVDS hardware interface standard. Exposure timing for each CCD is controlled directly from the SECCHI instrument computer. Appropriate programming and control of the camera waveform generator ASICs enables updating

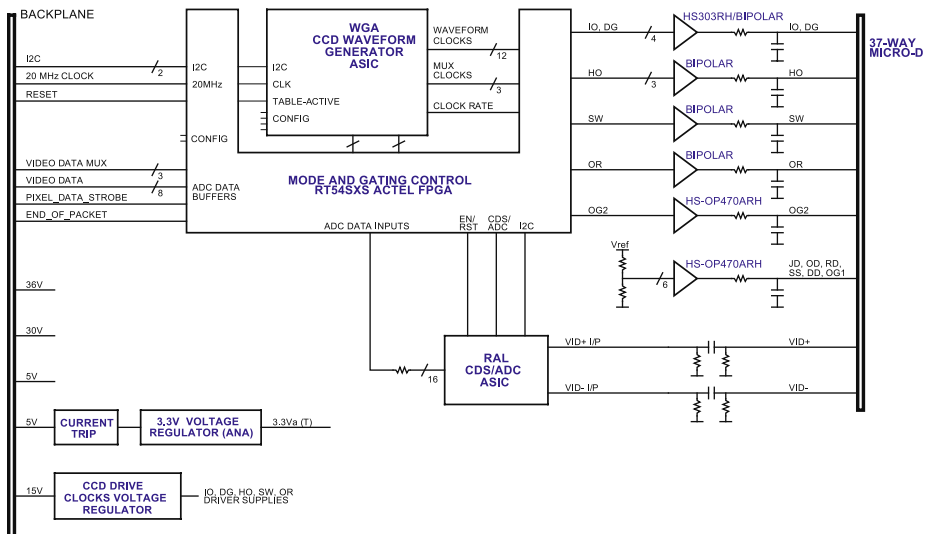


Fig. 27 CCD driver card

of CCD readout waveform patterns and readout tables, and the initiation of various readout modes e.g. clearing, exposure, full-frame, windowed, or continuous readout. Pixel binning, programmable video gain, and programmable video DC offset level are also supported.

Each camera contains a DC-DC power converter that converts the incoming 28 V space-craft primary power to the required +5 V, +15 V, +30 V, and +36 V secondary supplies. The camera's 28 V power supply input is in-rush current limited, and current-trip protected. The converter's output supply rails are also filtered to minimize any noise and/or current-switching transitions on the supply rails to the CCD drive circuitry. The complete power converter system is screened from the CCD drive electronics within its own, shielded sub-housing within the CEB.

The survival power and decontamination heater power supplies for the CCDs are not routed through the camera boxes, but go directly from the SECCHI instrument computer to the CCD heads. Similarly, the temperatures of the CCDs are monitored directly from the SECCHI instrument computer and not through the camera electronics units. Housekeeping telemetry from the camera electronics enables the controller's secondary power supply voltage rails and internal temperature to be monitored.

The SCIP camera electronics enclosure is 195 mm × 126 mm × 85 mm, including all mounting feet, connector, and fixing screw protrusions. The HI camera electronics enclosure is slightly smaller (195 mm × 126 mm × 70 mm) to conserve volume and mass.

Operationally, the camera will respond to the following modes:

Clear Clearing of the CCD will take advantage of the CCD's 'dump-drain' running adjacent to the serial output register. Appropriate programming of the ASIC waveform generator will allow the entire array to be cleared any number of times prior to integration.

Integration During integration, the CCD's parallel register clocks will be held at appropriate voltage levels. The serial register clocks can be individually programmed to be high, low, or clocking. Dither clocking of the parallel register clocks will be possible to help minimize dark current generation, and to allow some degree of testing at room temperature.

Readout Appropriate programming of the ASIC waveform generator will allow any number of readout modes including:

- (1) full-frame readout of n lines,
- (2) windowed readout of at least two windows (dump n lines, read x lines, dump m lines, read y lines, etc.),
- (3) full-frame, or windowed readout with $n \times m$ pixel binning (pixel binning parameters can be different between windows provided that the windows are not overlapping),
- (4) continuous clocking.

The size of the readout area (or image format) is programmable without restrictions. Multiple windowed readout is possible up to the memory limits of the ASIC's internal 'readout table' memory. Window co-ordinates are programmable within CCD 'readout tables', but must be specified from the control computer. Any variety of camera operating cycles will be possible by appropriate programming of the waveform generator ASIC. Cycles may be implemented as a series of short 'readout tables', individually initiated from the control computer; or alternatively as one long 'readout table' initiated only at the beginning.

11 Flight Software

11.1 Flight Software Overview

The SECCHI flight software runs within a real-time, multi-tasking operating system, Vx-Works, that provides all of the software services needed by the instruments. This includes handling commands from the spacecraft, housekeeping and science telemetry to the spacecraft, heater control, guide telescope control, instrument control, image scheduling and image processing. The code is derived from code used in NASA's Small Explorer (SMEX) series of satellites and from the SOHO/LASCO experiment which was then modified for the SECCHI instrument.

The VxWorks operating system provides the infrastructure for running multiple tasks and each of the major functions listed above are run as separate tasks that can be started, stopped or reloaded independently. This made modifying the heritage code easy since the code is naturally modular. VxWorks also provides inter-task communications, which have been developed into a software bus library, shared by all tasks. The heritage software provided a large amount of useful code which reduced our task to modifying the telemetry and command tasks for SECCHI hardware and STEREO spacecraft protocols, developing new tables, telemetry and commands within the SMEX framework and developing new SECCHI code for image scheduling, image processing and control of the SECCHI hardware, specifically cameras, mechanisms, heaters, power, housekeeping board. The SECCHI flight software contains about 250,000 lines of code.

11.2 Instrument Scheduling

The STEREO spacecraft will use the NASA Deep Space Missions System for commanding and telemetry downlink. Only one or two 4-hour contacts per day per spacecraft are planned. During the contact time the uplink rate is 2 kbits/s shared between all instruments and the spacecraft, which means limited daily commanding and a need for handling large blocks of schedule. The distance of the spacecraft from Earth and the resulting light travel time curtails interactive operations so that the instrument must perform most operations by programmed sequences on-board the instrument.

The SECCHI concept of operations leads to the following characteristics for image scheduling:

- (1) Provide for an autonomous operation for long periods of time (1 week or more)
- (2) Synchronize image taking between spacecraft in which every image is scheduled
- (3) Handle some non-image taking operations in timeline (doors and script tasks)
- (4) Manage timeline of image taking and events to 1 second resolution
- (5) Accept relative time schedules e.g. take COR1 image at 1 hour, 1 minute and 10 seconds from the current time
- (6) Accept absolute time schedules e.g. take COR1 image at 12:01:10 A.M. Nov 15, 2007
- (7) Compact the image schedule of commands to reduce the uplink load
- (8) Use on-board tables to minimize the amount of information uplinked daily
- (9) Provide blocks of schedule commands that may be reused and called from a daily schedule
- (10) Provide the planned schedules as a simple text file with embedded comments to facilitate ground operations and communication via email with co-investigators.

The image scheduling software maintains a single timeline of observations for all five telescopes. The uplinked schedules are parsed and entered into the timeline either manually or automatically at midnight each day from a RAM disk file. Normally the automatic load is used. If the expected schedule is not found then a default schedule is loaded.

A normal image acquisition sequence consists of the following steps: set up the instrument mechanism configuration, clear the CCD, open the shutter for a specified time, read out the CCD and transmit the digitized signal to a buffer in the SEB, process the image for downlink. One CCD from the SCIP and one CCD from the HI can be read out at the same time. With a readout time of about 4 seconds, this is not a severe restriction. Exposures may overlap on all of the telescopes.

Schedules are designed on the ground using a software planning tool that uses the flight software tables as input. The planning tool is able to add, delete and insert images into its timeline, manage on-board resources such as RAM buffer space, downlink telemetry, computer usage, spacecraft solid state recorder (SSR) usage, times of image exposure and image readout. The tool can merge blocks of schedule to form daily schedules. One common use is to merge a special observing program with a synoptic schedule. The planning tool also schedules door operations in anticipation of spacecraft thruster firings and script tasks used for guide telescope calibration and mechanism calibration.

11.3 Image Processing

Once an image is taken, the image is moved from the camera buffer memory to the computer for image processing. The image processing task is a background task that processes one image at a time and produces an image file ready to downlink. Since there are 27 camera buffers it is possible for image taking to take data faster than it can be processed, so the task maintains a queue of images to be processed in the order they are taken.

There are 120 image processing functions including three major types of image compression, event detection and reporting, two types of cosmic ray scrubbing, automatic exposure control, automatic compression control, occulter and region of interest masks, adding and subtracting images and the ability to send images down any of four channels (real-time, space weather, solid state recorder 1, solid state recorder 2). When the image is scheduled, image processing is selected by specifying a row from an image processing table where each row is a list of functions to be done in sequential order. There are 100 rows in the image processing table. New image processing tables can be uploaded in flight as needed.

Image compression is the most important feature of the image processing. Four types are provided including no compression. The Rice method is a lossless compression providing about a factor of 2.2 times compression. H-Compress is a lossy wavelet image compression with a variable image compression. ICER is a lossy wavelet image compression, which has the advantage of being able to specify the desired output size. ICER is predicted to produce useful images with a compression factor of up to 20. Rice and H-compress were used to compress the LASCO and EIT images and ICER was used on the Mars Exploration Rover (MER) mission.

In order to achieve the desired signal to noise ratio, the HI images require longer exposure times (about 30 minutes) than the SCIP images. To eliminate the dark current the long exposures are obtained by exposing the CCDs for short times (up to 1 minute) and then summing the desired number of images in the on-board computer. The summing involves the following steps: remove the electronic offset, scrub the images of cosmic ray impacts, perform a 2×2 pixel sum to create a 1024×1024 image and then add the binned image to the image sum. The cosmic ray impacts (about 45 pixels/s) must be removed prior to summing. Two types of cosmic ray scrubbing are provided. The first does a two-image compare of each pixel of the current image to the previous image. If the current pixel is within the photon noise range of the last pixel it is accepted otherwise it is replaced with the older pixel. The second method does a three-image compare and chooses the median value. The images are then summed and added to $1024 \times 1024 \times 32$ bit image buffers. Successive HI images, typically tens of images, are added to the image buffer until the 32 bit image buffer is sent down using Rice image compression. The cosmic ray scrubbing and image summing for HI is the single most demanding task for the on-board computer.

After image processing is done, the completed files are put on a 52 MB RAM disk for the telemetry task to send the file to the spacecraft over the MIL-STD 1553 spacecraft bus. The bus transfers roughly 1 MB per minute to the spacecraft. A full sized SECCHI uncompressed image is 8 MB in size. Using an image compression factor of $20\times$ means that a full sized image will downlink to the spacecraft in just 24 seconds and that the RAM buffer can hold about 120 images.

12 SECCHI Concept of Operations

12.1 Overview

The SECCHI Payload Operations Center (POC) will be located at NRL for all normal operations, except for critical instrument debugging when it will be located at the Johns Hopkins University Applied Physics Laboratory (APL). The POC sends commands to and receives telemetry from the instrument via the Mission Operations Center (MOC), located at APL. SECCHI uses the Integrated Test and Operations System (ITOS) software hosted on Sun Blade workstations running Solaris (one for each spacecraft) for commanding and telemetry processing. Commands to be transmitted to the instrument are sent to the MOC. The MOC performs simple verification tests and then queues the commands for transmission to the spacecraft via the Deep Space Mission System (DSMS). Finally, the Command and Data Handling (C&DH) process on the spacecraft forwards the commands to SECCHI over the 1553 bus. During normal operations, commands will be sent to the MOC at least 8 hours in advance of a daily track that lasts from 3.5 to 5 hours, depending on the phase of the mission. The daily tracks are nominally centered every 24 hours for each observatory.

Most housekeeping and science data are recorded on the onboard solid-state recorder (SSR) for later transmission to the ground during the daily track. The nominal SECCHI

real-time data rate is 3.6 kilobits per second (kbps), and will be used predominantly for critical housekeeping data. Real-time telemetry is forwarded immediately to the MOC, and is made available to the POC via a TCP/IP connection. All real-time and SSR playback telemetry is forwarded from the DSMS to the MOC after completion of each track. The MOC maintains an archive of all instrument telemetry for 30 days. The SECCHI POC will retrieve the telemetry daily, after the MOC has produced cleaned and merged Level-0 files. The MOC will split the daily telemetry into 6 files, each containing four hours of SECCHI telemetry. Because data for a given day may require more than one track to be completely transmitted to the ground, the Level-0 files are regenerated each day for the two preceding days. The final Level-0 files are generated by the MOC after 30 days. The SECCHI POC will download those files also. The pipeline processing will be applied daily to the quick-look Level-0 files and again after the final Level-0 files are prepared.

12.2 SECCHI Data Allocation and SSR utilization

Table 9 shows the peak data rate at which the C&DH collects telemetry data from SECCHI over the 1553 bus, and the SSR volume and downlink bandwidth allocated to SECCHI at various stages during the nominal two-year mission. Note that the allocations in this table are based on the average data volume guaranteed by the MOC to be downlinked during each daily track. The actual daily data volumes achieved during the mission may be higher than the nominal SSR allocations. The SECCHI SSR allocation of 6553 Mbits includes margin to account for cases where the daily tracks are separated by more than the nominal 24 hours, and is sufficient to hold up to 36 hours of data at an average SSR write rate of 50 kbps.

The SSR allocation is divided into two partitions for science data and one for space weather data. The SSR1 partition is nominally 80% of the total allocation for science data. When SSR1 partition is full, no further data may be written to it until all data on the partition has been transmitted to the ground. The SSR2 partition is nominally 20% of the total allocation for science data. The SSR2 partition functions like a circular buffer, and will overwrite the oldest data when full. The flight SW controls which packets get sent to the SSR2 and can stop writing if it detects an event trigger for example.

It is anticipated that SSR1 will be used for a synoptic program that will maintain synchronized observations on both spacecraft, and that will remain unchanged for extended periods of time throughout the mission. A sample synoptic program that fits within the nominal SSR1 allocation in the first 14 months on heliocentric orbit is shown in Table 10. The program shown in Table 10 is only for illustration of the type of observations that might be taken. The exact program will be decided after launch and the commissioning period and can change throughout the mission. SSR2 will be used for special observing programs, for

Table 9 SECCHI data rates and SSR allocations

1553 bus TM peak data rate	152 kbps
SSR partitions	
SSR1	5162 Mbits
SSR2	1291 Mbits
Downlink data volume	
Mission time ¹	
Months 0–14	54 kbps
Months 14–18	50 kbps
Months 18–24	45 kbps

¹ Months after entering heliocentric orbit

Table 10 Sample daily synoptic program for the first 14 months on heliocentric orbit

Telescope	# Images and size (pixels)	Cadence (minutes)	Total images/day	Compression factor	Total Mbits/day
EUVI	2 2k × 2k	4	576	40.0	845.6
	4 2k × 2k	20	288	10.0	1691.1
COR1	3 1k × 1k	8	540	10.0	792.7
COR2	3 1k × 1k	15	216	10.0	317.1
	3 2k × 2k	60	72	10.0	422.8
HI1	1 1k × 1k	60	24	2.5	211.4
HI2	1 1k × 1k	120	12	2.5	105.7
Total			1728		4386.4

example those that require high-cadence observations with one or more telescopes for a short period of time. These may or may not be duplicated on the other spacecraft. For example, if the trigger to stop recording is based on an on-board CME detection, there is no guarantee that both spacecraft will see the same event at the same time.

12.3 Observation Planning

The SECCHI flight software has enabled a very flexible program and supports the acquisition of over 5000 images each day for each spacecraft. The relative cadence of the various image types is the main variation that affects the planning. The basic observing philosophy for SECCHI consists of two observing programs that run simultaneously on both observatories. The first (“synoptic”) program schedules every observation by time, is identical on both observatories, and occupies about 80% of the available telemetry. The second (“campaign”) program is more flexible, allowing higher data rates for limited periods of time. It writes to SSR2, the overwriting telemetry buffer. Simultaneous observations from both observatories are still desirable in this mode, but are not a requirement. The lower cadence data from the synoptic program from both observatories remains undisturbed.

It is important to keep in mind that the scientific emphasis of the STEREO mission is constantly changing as the two observatories drift apart. Since observations at a specific spacecraft separation angle can't be repeated, observations must be carefully planned in advance. We will favor the EUVI observations early in the mission, when the separation angle between the observatories is small enough for stereoscopic imaging in the classical sense, and when the STEREO telemetry rate is highest due to the proximity to Earth. During that time, the EUVI will focus on CME initiation studies using high cadence imaging.

Planning for SECCHI observations will occur in multiple stages in coordination with other STEREO instruments and the MOC, with more detailed plans established at each stage. Broad science plans and priorities will be established at quarterly meetings of the STEREO Science Working Group (SWG) and at the SECCHI team meetings. The plans will be posted on the web and will be refined during monthly meetings of the Science Operations Working Group (SOWG), after which a schedule of observations will be generated. The detailed plans will be finalized at weekly teleconferences, with participation from the spacecraft, all instrument teams and the SSC. The SECCHI observing plans for one day up

to a week will be generated using the SECCHI Planning Tool. This tool is a set of Interactive Data Language (IDL) procedures that provides a graphical user interface to allow the operator to generate a file of schedule commands for both spacecraft to be sent to the MOC via the ITOS software. The planning tool performs constraint checking (for example, a warning is generated if simultaneous readouts from two CCDs controlled from the same CEB are scheduled), and monitors both internal buffer space and telemetry usage for each telescope. It is based on a similar tool that has been used in planning LASCO and EIT observations on the SOHO mission for over 10 years. The planned schedule can be displayed on the Web both in graphical format and as a text file.

12.4 Beacon Mode

SECCHI space weather data will be broadcast continuously at a rate of 504 bps over the beacon channel. These data will consist of a subset of images from each telescope. In order to fit within the low bandwidth, the images need to be highly compressed, probably binned to a low spatial resolution, as well as a subset of event messages that can be used to monitor instrument status outside of the regular track periods. The exact compression techniques will be determined after launch. The SSC is responsible for collecting these data from the various ground stations that receive them, processing the data and serving them on the Web.

12.5 SECCHI Campaigns

For two or more periods totaling four weeks during the mission, there will be an additional track, beginning 12 hours after the start of the normal daily track. The effect of this additional track is to double the amount of telemetry that SECCHI is able to downlink each day. These ‘SECCHI Campaigns’ will enable high-cadence observations targeted to specific science objectives.

12.6 Routine Processing and Data Products

Routine processing of SECCHI data will take place at the POC (for real-time and socket playback data) and at the SECCHI Data Processing Facility (DPF, for Level-0 packet files) at NRL. Science data will be processed into FITS files, consisting of a binary data array preceded by a header, with one file per image. No calibrations will be applied to the data during routine processing, and the resulting FITS file will be referred to as Level-0.5. FITS files generated from real-time data are referred to as ‘quick-look’. FITS files generated from socket playback or Level-0 files will be referred to as ‘preliminary’. When the final Level-0 files are available from the MOC after 30 days, the resulting FITS files will be referred to as ‘final’. All final Level-0.5 FITS files will be archived at NRL, and will also be delivered electronically to the SSC and to Co-Investigator institutions. Processing of data to Level-1 and higher levels will be done by individual users, using IDL routines and auxiliary data that will be freely distributed as part of the SolarSoft software library and database. Some higher level data products, such as polarized brightness images from COR1 and COR2, and Carrington maps, will be generated routinely by the DPF. Additional data products, including browse images, movies, lists of events such as CMEs and comets, housekeeping tables and long-term trending plots of key instrument performance parameters will also be generated routinely and made available electronically.

12.7 SECCHI Data Policy

The SECCHI data policy is to have completely open access to all data, including the calibration data and procedures necessary to calibrate and process the data to higher levels. SECCHI images will be available as soon as the routine processing steps have been completed. This is estimated to be within 30 minutes of receipt of all data necessary to form an image. The image data will be accessible via the Web using a searchable database. It will be possible to generate queries to select and download data of interest using FITS header keywords as parameters. Temperatures, voltages, and other housekeeping parameters will also be accessible through database queries.

Acknowledgements We gratefully acknowledge the hard work and dedication of the literally hundreds of people who contributed to the SECCHI program. The SECCHI instrument was constructed by a consortium of institutions: the Naval Research Laboratory (NRL, Washington, DC, USA), the Lockheed Martin Solar and Astrophysical Laboratory (LMSAL, Palo Alto, CA, USA), the NASA Goddard Space Flight Center (GSFC, Greenbelt, MD, USA), the Max Planck Institut für Sonnensystemforschung (MPS, Lindau, Germany), the Centre Spatial de Liege (CSL, Angleur, Belgium), the University of Birmingham (UB, Birmingham, UK), the Rutherford Appleton Laboratory (RAL, Didcot, UK), the Institut d'Optique (IOTA, Orsay, France), the Institute d'Astrophysique Spatiale (IAS, Orsay, France).

NRL is the lead institution in the consortium and was responsible for the supplying the COR2 coronagraph, the experiment electronics, the CCDs and focal plane assemblies, the flight and ground software, the integration and testing of the instrument and the overall program management. LMSAL was responsible for providing the EUVI telescope, the GT, the mechanism electronics box and mechanisms for the COR1, COR2 and EUVI shutters and wheels. The GSFC was responsible for providing the COR1 telescope.

The USA effort was supported by the NASA Solar Terrestrial Physics STEREO Program under DPR S-13631-Y. The program managers at GSFC were Abby Harper, Haydee Moldanado and for the last 3 years of the program, Nicholas Chriessimos. The program manager for instruments was Michael Delmont and the SECCHI instrument manager was Bernie Klein. We are indebted to their efforts and to those of the other members of the STEREO project. The NRL effort was also supported by the USAF Space Test Program and the Office of Naval Research.

At NRL, the COR2 subsystem design, fabrication and testing was done by Dennis Socker, Simon Plunkett, Angelos Vourlidas, Clarence Korendyke, Edward Shepler, Jeff Morrill of NRL, Qian Gong, Robert Haggard, Paul Nikulla and Pete Patterson of Swales, Inc., Martin Koomen of Sachs-Freeman, Robert Moye, David Roberts, Arnaud Thernisien and Robin Colaninno of Artec and Marc Westcott of Tropel. The FPA was designed and tested by Benjamin Au of Praxis, Dan Moses, Jeffrey Newmark of NRL, and Paul Nikulla and Miles Newman of Swales. The FPAs were fabricated at the University of Birmingham by Chris Eyles, Clive Longstaff, and John Bryant. The CCDs were procured from e2V and were calibrated by Richard Kroeger of NRL. The SEB hardware was designed and tested by Sean Lynch, Robert Skalitzky and Amy Hurley of NRL, Drew Roberts, Greg Clifford, and Dennis Silver of Silver Engineering, Inc., and Dale Bankus of OSC. The SEB flight software was designed and developed by Dennis Wang of Interferometrics, Inc., and Ladd Wheeler and Joel Chiralo of the Hammers Company and Matthew Hayden of NRL. The harness was designed and built by Susie LaCava, James (Chris) Garner, and Richard Cooksey of NRL and Ralph Hopkins of Honeywell. The SCIP door design and testing was supported by Stephen Koss and Paul Oppenheimer of NRL. The SECCHI environmental testing was performed by Michael VanHerpe, Robert Haynes and Michael Obara of NRL. Contamination control support was provided by Therese Errigo, Radford Perry and Andrew Uhl of Swales Inc. Configuration management was provided by John Tota, Nick Virmani, Ken Slocum, Stu Schweitzer of Swales. SECCHI project management was provided by Rebecca Baugh, Donald McMullin and Dale Harris of Praxis, Inc. System engineering was provided by Timothy Carter and Benjamin Au of Praxis and James Garner of NRL. The SCIP thermal design was performed by Miles Newman of Swales.

At LMSAL, the EUVI and GT telescopes were designed, fabricated, and tested by James Lemlen, Jean-Pierre Wuelser, Jacob Wolfson, Glenn Gradwohl, Theodore Tarbell, Joseph Cannon, Noah Katz, Dunagan Pearson. The mechanisms were designed and built by Augustus Moore and David Akin. The MEB and GT electronics were designed by Larry Springer, George Rossi and Russell Lindgren. Contamination support was provided by Syndie Meyers and thermal support by Rose Deguzman. Program management was done by Dexter Duncan, Larry Springer and Frank Friedlaender. Configuration management and system engineering support was performed by Brock Carpenter and Claude Kam.

At GSFC, the COR1 was designed, fabricated and tested by Joseph Davila, Eric Mentzell, Kim Mehalik, Julie Crooke, Rebecca Derro, Chris St Cyr, William Thompson of GSFC and Michael Hersh and Miles

Newman of Swales. Program management was performed by Lawrence Orwig and system engineering by Richard Wiesenbergs.

The German science and hardware contributions to SECCHI—the project STEREO/Corona—is supported by the German “Bundesministerium für Bildung und Forschung” through the “Deutsche Zentrum für Luft- und Raumfahrt e.V.” (DLR, German Space Agency). The Max-Planck-Institute für Sonnensystemforschung supplied the aperture doors for the SCIP telescopes.

The UK contribution to STEREO was funded by the Particle Physics and Astronomy Research Council (PPARC) and we also acknowledge significant support for the Heliosphere Imager from the School of Physics and Astronomy, University of Birmingham. The HI and CEB program management was led by Richard Harrison and James Lang at RAL. At the University of Birmingham, the HI design, fabrication and testing was performed by Christopher Eyles, CEB hardware was designed by Nick Waltham, James King, Andrew Marshall and Matthew Clapp. The CEB software was developed by Duncan Drummond and John Rannnie. The CEBs were fabricated and tested at the University of Birmingham by Chris Eyles, John Bryant and David Smith. The HI thermal design was performed by Helen Mapson-Menard initially and completed by Bryan Shaughnessy of RAL.

The French teams were supported by the Centre National d’Etudes Spatiales and the Centre National de la Recherche Scientifique. At IOTA, the design and fabrication of the EUVI multilayers was performed by Marie-Françoise Ravet, Françoise Bridou, Franck Delmotte and Arnaud Jerome and the polishing/figuring of the EUVI mirrors was performed by Jean-Yves Clotaire, Gilles Colas, Michel Lamare, Raymond Mercier and Michel Mullot. The testing and calibration of the multilayer mirror performance was performed at IAS by Jean-Pierre Delaboudinie, Frederic Auchere, Philippe Bouyries and Xueyan Song.

The Belgian effort was supported by the Belgian Science Policy Office. The HI optical design, environmental testing and calibration (stray-light and photometric) was performed at Centre Spatial de Liege by Jean-Marc Defise, Jean-Philippe Halain, Emmanuel Mazy, Philippe Ronchain and Pierre Rochus.

References

- D. Akin, R. Horber, C.J. Wolfson, Three high duty cycle, space-qualified mechanisms, in *NASA Conf. Pub.*, vol. 3205 (1993)
- G.E. Brueckner, R.A. Howard, M.J. Koomen, C.M. Korendyke, D.J. Michels, J.D. Moses, D.G. Socker, K.P. Dere, P.L. Lamy, A. Llebaria, M.V. Bout, R. Schwenn, G.M. Simnett, D.K. Bedford, C.J. Eyles, *Solar Phys.* **162**, 357–402 (1995)
- A. Buffington, B.V. Jackson, C.M. Korendyke, *Appl. Opt.* **35**, 6669–6673 (1996)
- K.P. Dere, E. Landi, H.E. Mason, B.C. Monsignori Fossi, P.R. Young, CHIANTI—an atomic database for emission lines. *Astron. Astrophys. Suppl. Ser.* **125**, 149 (1997)
- J.M. Defise, J.P. Halain, E. Mazy, P. Rochus, R.A. Howard, J.D. Moses, D.G. Socker, R.A. Harrison, G.M. Simnett, Design and tests for the heliospheric imager of the STEREO mission, in *Innovative Telescopes and Instrumentation for Solar Astrophysics*, ed. by S.L. Keil, S.V. Avakyan. Proc. SPIE, vol. 4853 (SPIE, Bellington, 2003), pp. 12–22
- J.P. Delaboudinière et al., EIT: extreme-ultraviolet imaging telescope for the SOHO mission. *Sol. Phys.* **162**, 291–312 (1995)
- C.J. Eyles, G.M. Simnett, M.P. Cooke, B.V. Jackson, A. Buffington, P.P. Hick, N.R. Waltham, J.M. King, P.A. Anderson, P.E. Holladay, *Sol. Phys.* **217**, 319–347 (2003)
- E.G. Gibson, *The Quiet Sun*, SP-303, National Aeronautics and Space Administration (1973)
- B.N. Handy et al., The transition region and coronal explorer. *Sol. Phys.* **187**, 229–260 (1999)
- R.A. Harrison, C.J. Davis, C.J. Eyles, The STEREO heliospheric imager: how to detect CMEs in the heliosphere. *Adv. Space Res.* **36**, 1512–1523 (2005)
- R.A. Howard, Historical perspective on coronal mass ejections, in *Solar Eruptions and Energetic Particles*, ed. by N. Gopalswamy. Geophysical Monograph Series, vol. 165 (American Geophysical Union, Washington, 2006), pp. 7–13
- R.A. Howard, J.D. Moses, D.G. Socker, the SECCHI consortium, Sun-Earth connection coronal and heliospheric investigation (SECCHI), in *Instrumentation for UV/EUV Astronomy and Solar Missions*, vol. 4139, ed. by S. Fineschi, C.M. Korendyke, O.H. Siegmund, B.E. Woodgate (SPIE, Bellingham, 2000), pp. 259–283
- B. Lyot, The study of the solar corona and prominences without eclipses (George Darwin Lecture, 1939). *Mon. Not. R. Astron. Soc.* **99**, 580–594 (1939)
- J.S. Morrill et al., Calibration of the SOHO/LASCO C3 white light coronagraph. *Sol. Phys.* **233**, 331–372 (2006)

- E. Pitz, C. Leinert, H. Link, N. Salm, HELIOS zodiacal light experiment, in *Interplanetary Dust and Zodiacal Light*. IAU Colloq., vol. 31 (Cambridge University Press, Cambridge, 1976), pp. 19–23
- M.F. Ravet, F. Bridou, X. Zhang-Song, A. Jerome, F. Delmotte, M. Bougnet, J.P. Delaboudinière, Ion beam deposited Mo/Si multilayers for EUV imaging applications in astrophysics. Proc. SPIE **5250** (2003)
- K. Saito, A.I. Poland, R.H. Munro, A study of the background corona near solar minimum. Sol. Phys. **55**, 121–134 (1977)
- D.G. Socker, R.A. Howard, C.M. Korendyke, G.M. Simnett, D.F. Webb, The NASA solar terrestrial relations observatory (STEREO) mission heliospheric imager, in *Instrumentation for UV/EUV Astronomy and Solar Missions*, vol. 4139, ed. by S. Fineschi, C.M. Korendyke, O.H. Siegmund, B.E. Woodgate (SPIE, Bellingham, 2000), pp. 284–293
- R.A. Stern, the SXI Team, Solar X-ray imager for GOES. Proc. SPIE **5171** (2003)
- K. Strong, T. Bruner, M. Tarbell, A. Title, C. Wolfson, TRACE—the transition region and coronal explorer. Space Sci. Rev. **70**, 119 (1994)
- S.J. Tappin, A. Buffington, M.P. Cooke, C.J. Eyles, P.P. Hick, P.E. Holladay, B.V. Jackson, J.C. Johnston, T. Kuchar, D. Mizuno, J.B. Mozer, S. Price, R.R. Radick, G.M. Simnett, D. Sinclair, N.R. Waltham, D.F. Webb, Geophys. Res. Lett. **31**, L02802 (2003). doi:[10.1029/2003GL018766](https://doi.org/10.1029/2003GL018766)
- W.T. Thompson, J.M. Davila, R.R. Fisher, L.E. Orwig, J.E. Mentzell, S.E. Hetherington, R.J. Derro, R.E. Fed erline, D.C. Clark, P.T.C. Chen, J.L. Tveekrem, A.J. Martino, J. Novello, R.P. Wesenberg, O.C. St Cyr, N.L. Reginald, R.A. Howard, K.I. Mehalick, M.J. Hersh, M.D. Newman, D.L. Thomas, G.L. Card, D.F. Elmore, COR1 inner coronagraph for STEREO-SECCHI, in *Innovative Telescopes and Instrumentation for Solar Astrophysics*, ed. by S.L. Keil, S.V. Avakyan. Proc. SPIE, vol. 4853 (SPIE, Bellingham, 2003), pp. 1–11
- D.L. Windt, R.C. Catura, Multilayer characterization at LPARL. Proc. SPIE **984**, 132–139 (1988)
- J.-P. Wülser et al., EUVI: the STEREO-SECCHI extreme ultraviolet imager. Proc. SPIE **5171** (2003)
- P.R. Young, G. Del Zanna, E. Landi, K.P. Dere, H.E. Mason, M. Landini, CHIANTI—an atomic database for emission lines. Astrophys. J. Suppl. Ser. **144**, 135–152 (2003)

STEREO IMPACT Investigation Goals, Measurements, and Data Products Overview

J.G. Luhmann · D.W. Curtis · P. Schroeder · J. McCauley · R.P. Lin · D.E. Larson · S.D. Bale · J.-A. Sauvaud · C. Aoustin · R.A. Mewaldt · A.C. Cummings · E.C. Stone · A.J. Davis · W.R. Cook · B. Kecman · M.E. Wiedenbeck · T. von Rosenvinge · M.H. Acuna · L.S. Reichenthal · S. Shuman · K.A. Wortman · D.V. Reames · R. Mueller-Mellin · H. Kunow · G.M. Mason · P. Walpole · A. Korth · T.R. Sanderson · C.T. Russell · J.T. Gosling

Originally published in the journal Space Science Reviews, Volume 136, Nos 1–4.
DOI: [10.1007/s11214-007-9170-x](https://doi.org/10.1007/s11214-007-9170-x) © Springer Science+Business Media, Inc. 2007

Abstract The IMPACT (In situ Measurements of Particles And CME Transients) investigation on the STEREO mission was designed and developed to provide multipoint solar wind and suprathermal electron, interplanetary magnetic field, and solar energetic particle information required to unravel the nature of coronal mass ejections and their heliospheric consequences. IMPACT consists of seven individual sensors which are packaged into a boom suite, and a SEP suite. This review summarizes the science objectives of IMPACT, the instruments that comprise the IMPACT investigation, the accommodation of IMPACT on the STEREO twin spacecraft, and the overall data products that will flow from the IMPACT measurements. Accompanying papers in this volume of Space Science Reviews highlight the individual sensor technical details and capabilities, STEREO project plans for the use of IMPACT data, and modeling activities for IMPACT (and other STEREO) data interpretation.

Keywords STEREO · Coronal mass ejection · Solar energetic particles · Suprathermal electrons · Solar wind electrons · Interplanetary magnetic field · Multipoint heliospheric measurements

J.G. Luhmann (✉) · D.W. Curtis · P. Schroeder · J. McCauley · R.P. Lin · D.E. Larson · S.D. Bale
Space Sciences Laboratory, University of California, Berkeley, CA 94720, USA
e-mail: jgluhman@ssl.berkeley.edu

J.-A. Sauvaud · C. Aoustin
CESR, BP 4346, 31028 Toulouse Cédex 4, France

R.A. Mewaldt · A.C. Cummings · E.C. Stone · A.J. Davis · W.R. Cook · B. Kecman
California Institute of Technology, Pasadena, CA 91125, USA

M.E. Wiedenbeck
Jet Propulsion Laboratory, Pasadena, CA 91109, USA

T. von Rosenvinge · M.H. Acuna · L.S. Reichenthal · S. Shuman · K.A. Wortman · D.V. Reames
NASA/Goddard Space Flight Center, Greenbelt, MD 20771, USA

List of acronyms

ACR	Anomalous Cosmic Rays
CIR	Corotating Interaction Region
CME	Coronal Mass Ejection
GCR	Galactic Cosmic Rays
ICME	Interplanetary Coronal Mass Ejection
IDPU	Instrument Data Processing Unit
IMF	Interplanetary Magnetic Field
HET	High Energy Telescope
LET	Low Energy Telescope
MAG	Magnetometer
SEP	Solar Energetic Particles
SEPT	Solar Electron and Proton Telescope
SIT	Suprathermal Ion Telescope
STE	Suprathermal Electron Telescope
STEREO	Solar Terrestrial Observatory
SWEA	Solar Wind Electron Analyzer

1 Introduction to the IMPACT Investigation

The primary mission of the STEREO (Solar TERrestrial RElations Observatory) twin space-craft is to understand the 3-dimensional nature of the Sun's corona, including the eruptions known as coronal mass ejections (CMEs), from their birth in the corona to their impact at the Earth. The IMPACT (In situ Measurements of Particles and CME Transients) investigation focuses on the invisible particles and fields that affect Earth's space weather by contributing solar wind and suprathermal electron, interplanetary magnetic field, and solar energetic particle (SEP) measurements toward this goal. IMPACT measurements are also essential for other STEREO objectives, especially for relating the 3D corona and solar wind structure, for advancing knowledge of the sources and physics controlling solar energetic particle acceleration and propagation, and for unraveling the relationship between CMEs

R. Mueller-Mellin · H. Kunow
University of Kiel, 24118 Kiel, Germany

G.M. Mason
Applied Physics Laboratory, Johns Hopkins University, Laurel, MD 20723, USA

P. Walpole
University of Maryland, College Park, MD 20742, USA

A. Korth
Max-Planck-Institut für Sonnensystemforschung, Lindau, Germany

T.R. Sanderson
Research and Scientific Support Division, ESA, Noorwijk, The Netherlands

C.T. Russell
Institute of Geophysics and Planetary Physics, UCLA, Los Angeles, CA 90095, USA

J.T. Gosling
Laboratory for Atmospheric and Space Physics, University of Colorado, Boulder, CO 80309, USA

and the solar magnetic cycle (see the overall STEREO mission goals described by Kaiser et al., [this volume, 2007](#)).

IMPACT includes seven scientifically related in situ sensors on each spacecraft, a telescoping boom, and an instrument data processing unit that provides the primary interface between the sensors and the spacecraft. Detailed descriptions of the different IMPACT sensors can be found in companion papers by Mewaldt et al. ([this volume, 2007](#)), Mueller-Mellin et al. ([this volume, 2007](#)), von Rosenvinge et al. ([this volume, 2007](#)), Mason et al. ([this volume, 2007](#)), Acuna et al. ([this volume, 2007](#)), Sauvaud et al. ([this volume, 2007](#)), and Lin et al. ([this volume, 2007](#)), and the novel boom design is described by Ullrich et al. ([this volume, 2007](#)). A previous brief summary of the complete IMPACT investigation can be found in Luhmann et al. ([2005](#)). In this paper we provide more details about the overall makeup and science goals of IMPACT including its data plans and products. The IMPACT team is committed to the regular integration of IMPACT data with the other STEREO observations to take full advantage of the information obtained by the observatories. Complementary PLASTIC investigation ion composition measurements, and SWAVES plasma wave measurements are described in accompanying papers by Galvin et al. and Bougeret et al., respectively. Joint observing and data analysis plans involve these other in situ measurements, as well as the SECCHI investigation imaging (Howard et al., [this volume, 2007](#)) and SWAVES radio remote sensing results (Bougeret et al., [this volume, 2007](#)).

The IMPACT investigation was designed to fulfill many of the in situ measurement requirements for STEREO, illustrated by Fig. 1. The strength and orientation of the in-

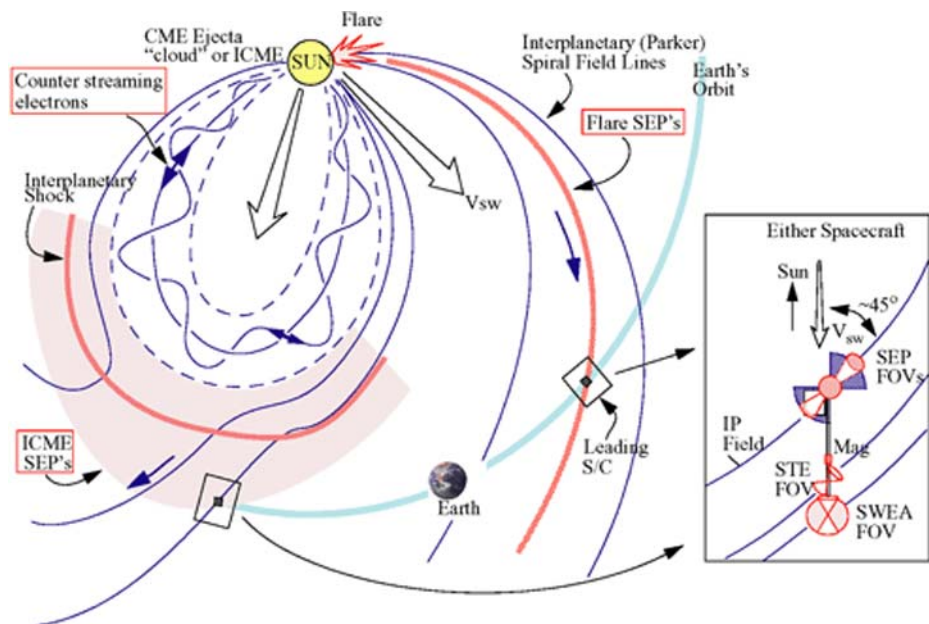


Fig. 1 Illustration of the interaction of a flux rope-like interplanetary CME (ICME) structure inferred from pre-STEREO measurements with the ambient solar wind. Counterstreaming suprathermal electron beams within the ejecta have been used to deduce its structure and size. An interplanetary shock is formed when the ejected mass of plasma and field moves sufficiently fast with respect to the ambient solar wind ahead. This shock often is a source of solar energetic particles that race ahead of it along the spiral interplanetary field lines to arrive at 1 AU well before the ICME and shock. The *inset* shows how the instruments of the IMPACT investigation on STEREO, described later in the text, are configured to make in situ measurements of the structures and particle populations in this picture at each spacecraft location

terplanetary magnetic field at the two different STEREO spacecraft, combined with the suprathermal (several 100 s of eV) electron measurements help determine whether the local magnetic fields of the interplanetary CME, the ICME, are rooted at the Sun at one or both ends or disconnected. Such magnetic topology information tells us about the coronal origins of the CME/ICME and also about the role of processes such as reconnection at the Sun and in the interplanetary medium. Higher energy electron, and also ion, detectors provide information on whether the local field connects to a flaring active region. Detection of SEP events at the two locations, with high time resolution and directional information over the energy range from 10 s of keV to \sim 100 MeV, allow remote sensing of the CME-initiated shock location and strength as it travels into the heliosphere. SEP ion composition measurements make it possible to distinguish between electron and heavy ion-rich flare-accelerated particles and solar wind particles accelerated at the interplanetary shock. The lowest energy SEP ions also provide information on the ambient suprathermal ion “seed” populations that may feed the higher energy SEP production at the CME related shocks. With the radio and plasma waves investigation, opportunities exist for in situ plasma microphysics diagnostics on local shock structures and waves, as well as comparisons of radio remote sensing and SEP remote sensing of coronal shocks. The in situ data integration with images and ground based images and magnetograph observations through Sun-to-Earth modeling (e.g. Aschwanden et al., [this volume, 2006](#)) enables a STEREO era of regular cradle-to-grave analyses of the CME phenomenon (e.g. Fox et al. 1998; Webb et al. 2000). In particular, details of the conditions on the Sun that lead to specific 1 AU consequences can be investigated, and used to refine observational strategies for future space weather missions such as Solar Dynamics Observatory, SDO, and the Heliospheric Sentinels, and for formulating updated science questions for Solar Orbiter and Solar Probe.

Most solar wind structures can be categorized as either corotating or transient, with examples being long-lived high-speed streams and ICMEs, respectively. In both cases, identical measurements of the same structures at the two STEREO locations flanking the Earth test ideas about their size and uniformity and help characterize the features causing magnetic storms and SEP events at 1 AU. The spacecraft separation increases at \sim 45 deg/year, providing the opportunity to watch the two sets of in situ observations increasingly differ. Invaluable additions to STEREO in such multipoint studies are the corresponding in situ observations upstream of Earth on the ACE and WIND spacecraft, creating regular third-point measurements of conditions at 1 AU with separation rates (from STEREO spacecraft) of \sim 22 deg/year. The nominal angular width of ICMEs has been inferred to be \sim 90° although shocks preceding their ejecta “drivers” may produce much wider (\sim 180°) disturbances at 1 AU. At the end of the second year of STEREO heliocentric orbit observations, the Ahead and Behind spacecraft will be \sim 90° apart. Single STEREO spacecraft ICME detections will become the norm, with ACE and WIND extending the period of possible multipoint ICME measurements. Quadrature observations, in which one spacecraft measures the 1 AU disturbances from CMEs observed on the limb of the Sun by the SECCHI coronagraphs on the other spacecraft, will then become the primary mode of measurement. In particular, the SECCHI Heliospheric Imager (HI) is expected to track ICME density perturbations to the Earth, where they can be detected by the L1 in situ instruments. The quadrature observations are the most valuable for investigating how particular events and structures imaged near the Sun evolve into the plasma and field structures observed at 1 AU. They will also test the concept of a space weather forecasting system located at a heliographic longitude removed from the Sun–Earth line.

As part of the STEREO Space Weather Beacon, IMPACT supplies real-time plasma electron, magnetic field, and SEP key parameters analogous to those currently available

from the ACE RTSW system (Garrard et al. 1998; Zwickl et al. 1998), with corresponding plasma ion quantities from PLASTIC (see Galvin et al., [this volume, 2007](#)). ACE real time solar wind plasma, magnetic field, and SEP data are currently being used to drive space weather models that forecast the Earth's radiation environment, ionospheric dynamics, and general geomagnetic activity levels \sim 30–45 min ahead of their occurrence (see http://www.srl.caltech.edu/ACE/ASC/related_sites.html). Because STEREO Beacon measurements come from two spacecraft flanking the Earth at increasing distances, their potential applications differ from those using an L1 monitor. A challenge for forecasters is how to take advantage of these data sets. In this respect, STEREO complements efforts within NASA's Living With a Star program whose goal is a time-dependent, predictive global model of the solar wind.

The ultimate success of IMPACT in its role on STEREO depends on obtaining comprehensive observations of a sufficient number of CME-related events to allow multipoint structural diagnosis, and when the spacecraft are near quadrature (\sim 90 degrees apart), to allow detailed comparisons between coronal and heliospheric imager images and in situ measurements. The timing of the two-year STEREO prime mission near solar activity minimum is advantageous for minimizing the ambiguity in identifying solar cause and interplanetary effect, but also reduces the number of events that will be detected in situ. Only one or two clearly flux rope-like ICME ejecta per month were observed on the WIND spacecraft during a similar period between cycles 22 and 23. Continuous operation is necessary to collect several events that are well-sampled and simple enough in structure to constrain complete Sun-to-Earth CME event interpretations and reach the STEREO primary mission goal. Continuation of mission operations into the next solar maximum in \sim 2010 can greatly increase the number and variety of observed events available for analysis.

The success of both IMPACT and STEREO also depends on dedicated modeling activities (see Achwanden et al., [this volume](#)) that can describe the physical and geometrical connections between what is seen in both the SECCHI images and the in situ measurements. Correlative data analysis by itself generally cannot provide the complex and coupled 3D descriptions available from state-of-the-art realistic simulations of the global corona, solar wind, CMEs, ICMEs and SEPs. The SAIC 3D MHD corona model coupled with the University of Colorado/SEC solar wind model (Riley et al. 2003; Odstrcil et al. 2002), and the University of Michigan 3D MHD adaptive grid solar wind and ICME transport model (Manchester et al. 2005; Roussev et al. 2003), will be brought to bear on the interpretation of IMPACT observations. Overlap between the IMPACT and other STEREO modeling efforts enables the treatment of the CME problem in its entirety.

This overview of IMPACT begins with brief descriptions of specific science issues targeted by the investigation. We next describe the instruments that provide the measurements needed to address them. We conclude with a summary of the data and data analysis plans. The latter provides the potential user of IMPACT data with a guide to products, tools, and access information.

2 IMPACT Science Objectives

2.1 Reconstructing 3D Pictures of CMEs and Their Interplanetary Consequences

2.1.1 Coronal Connections

Years of CME observations with coronagraphs on Skylab, Solwind, SMM and SOHO-LASCO, as well as with ground-based coronagraphs, have yielded no generally accepted

paradigm for CME generation. Nonetheless, this substantial observational background provides the starting point for STEREO. Key solar imaging results include the observed association of CMEs with the coronal helmet streamer belt (Hundhausen 1993), their solar cycle dependence (Webb and Howard 1994), their frequent 3-part (core, cavity, loop) structure on the limb and association with filament or prominence activations or disruptions (Webb et al. 2000), their apparent temporal and spatial coincidence with soft X-ray sigmoidal structures and post-eruption arcades (Canfield et al. 1999), and waves propagating across the solar surface observed in the EUV (Thompson et al. 2000). Another important observation from coronagraphs is the distribution of apparent CME speeds, which peaks at velocities well below the average solar wind velocity, but extends up to over 1,000 km/s (Gosling et al. 1976; Hundhausen et al. 1994). A few events observed by SOHO LASCO appeared to be traveling at speeds \sim 2500 km/s (Yashiro et al. 2005). What causes such a range of CME speeds is unknown, but it is clear that the speed of a CME has important heliospheric and geomagnetic consequences.

The ICME signatures measured by IMPACT and PLASTIC provide a test of the canonical pre-STEREO picture in Fig. 1. Figure 2 shows an example of in situ plasma, field, and suprathermal electron measurements from the WIND spacecraft during the passage of an isolated ICME (from Larson et al. 1997). Shocks form ahead of the faster ICMEs so that the disturbance associated with a fast ICME generally consists of a leading shock, a compressed ambient solar wind sheath, and the ICME itself that is energized in the eruption. Flux rope models have been a standard way of interpreting the magnetic fields of ICMEs, though they only fit \sim 30% of the observations at 1 AU (Gosling 1990). The essential question of what feature or structure in the corona actually becomes the ICME (e.g., Kumar and Rust 1996; Leamon et al. 2004) is one of the major issues STEREO hopes to resolve. Some ejecta can be fit with flux ropes that have leading edge field orientations consistent with the prevailing large scale coronal streamer belt field orientation, and inferred axes roughly parallel to the heliospheric current sheet (Mulligan et al. 1998; Li et al. 2001) as suggested by Fig. 3a. The solar magnetic cycle dependence of the inferred flux rope polarity, defined by the leading northward or southward magnetic fields in the ejecta, is illustrated in Fig. 3b (from Li and Luhmann 2004). This striking evidence of the ejecta relationship to the large scale coronal magnetic fields and the solar dynamo is not yet understood. It appears that the handedness of the flux rope field rotations can often be related to the local photospheric field geometry around CME-associated erupting filaments (Bothmer and Schwenn 1998; Kumar and Rust 1996). It thus appears that both small scale fields and the overlying large scale coronal fields may contribute to ICME topology.

Bidirectional or counterstreaming suprathermal electron anisotropies within many ICME ejecta are commonly interpreted (e.g., Gosling et al. 1987) as meaning at least partial connection of ICME fields to the Sun at both ends (see Fig. 1)—a picture consistent with the expanding loop structures in coronagraph images (e.g., Crooker et al. 1993). But ICMEs also often contain unidirectionally streaming electrons (e.g., Shodhan et al. 2000), suggesting that 3-dimensional reconnection within the magnetic legs of CMEs alters their magnetic topology as they propagate out from the Sun (Gosling et al. 1995a). The fact that ICME ejecta often do not fit the flux rope model leaves open the question of whether the flux rope is sometimes not intercepted, or simply does not describe most ejecta field structures. Energetic particle flux anisotropies and high charge state Fe ions occasionally indicate the involvement of flaring active regions near the solar-connected foot-points of the ICME field lines or in the surrounding corona (Kahler and Reames 1991; Larson et al. 1997; Popecki et al. 2000), a feature that may help to identify ICME source regions in STEREO data. In fact major, high-speed ICMEs tend to be preceded by a combination of a flare or

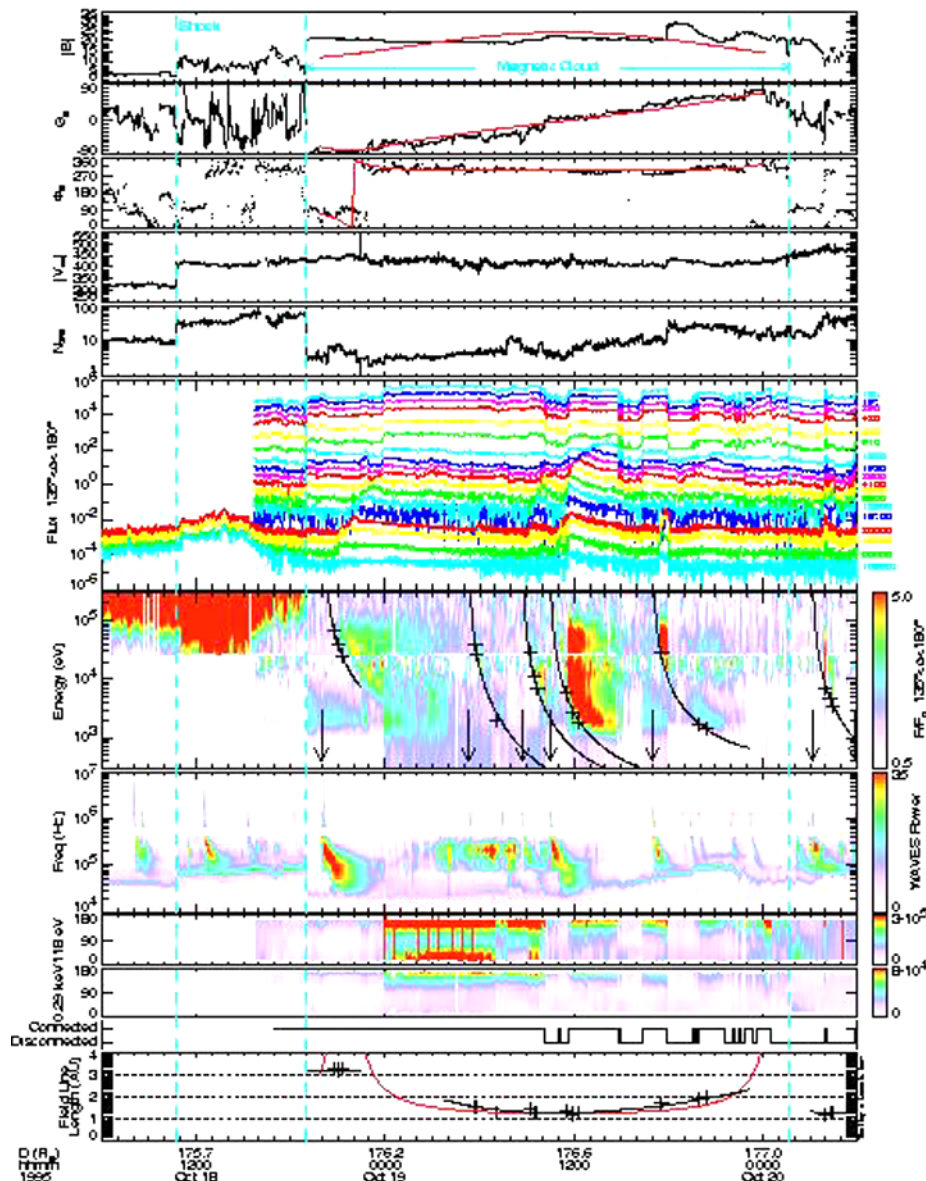
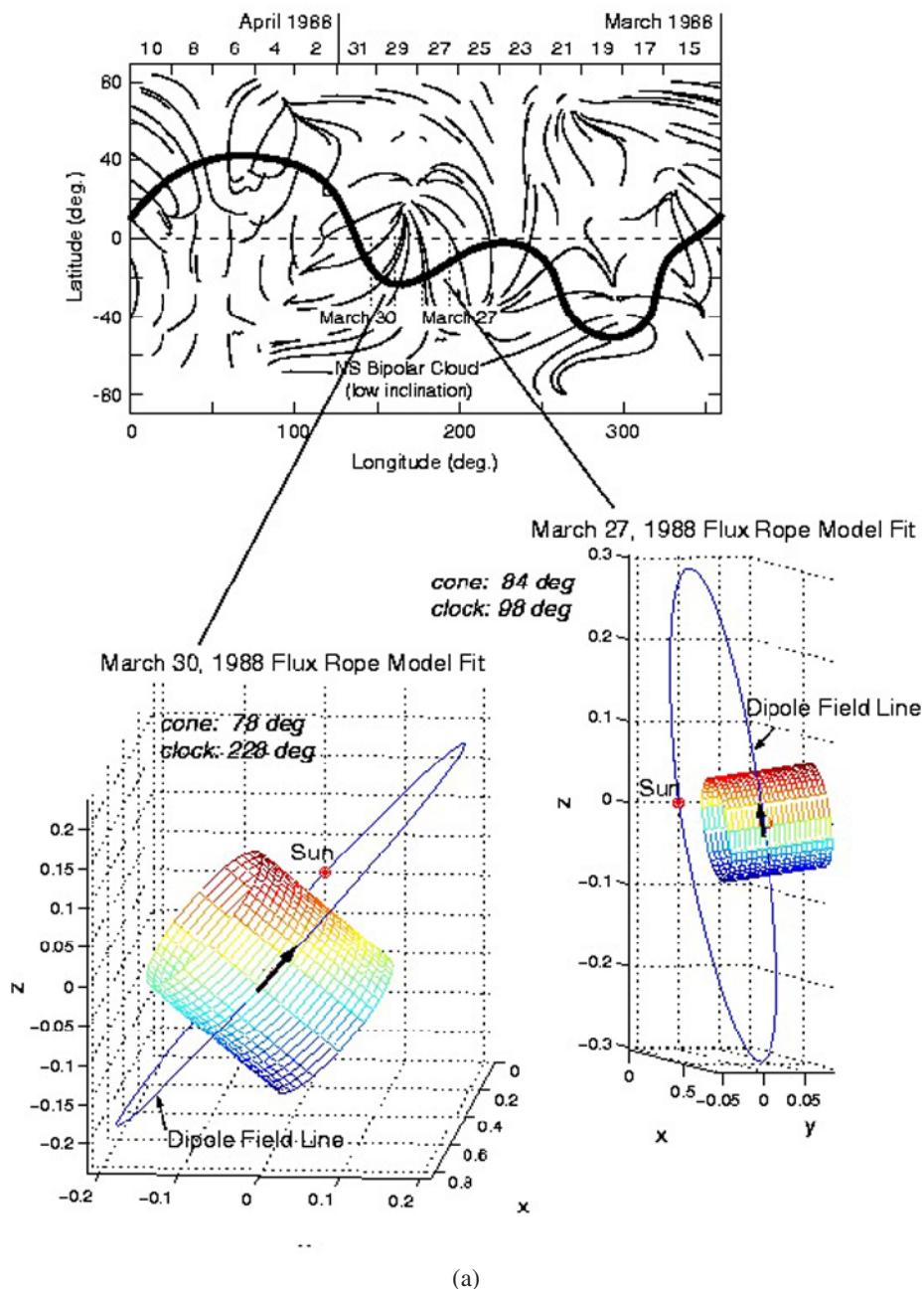


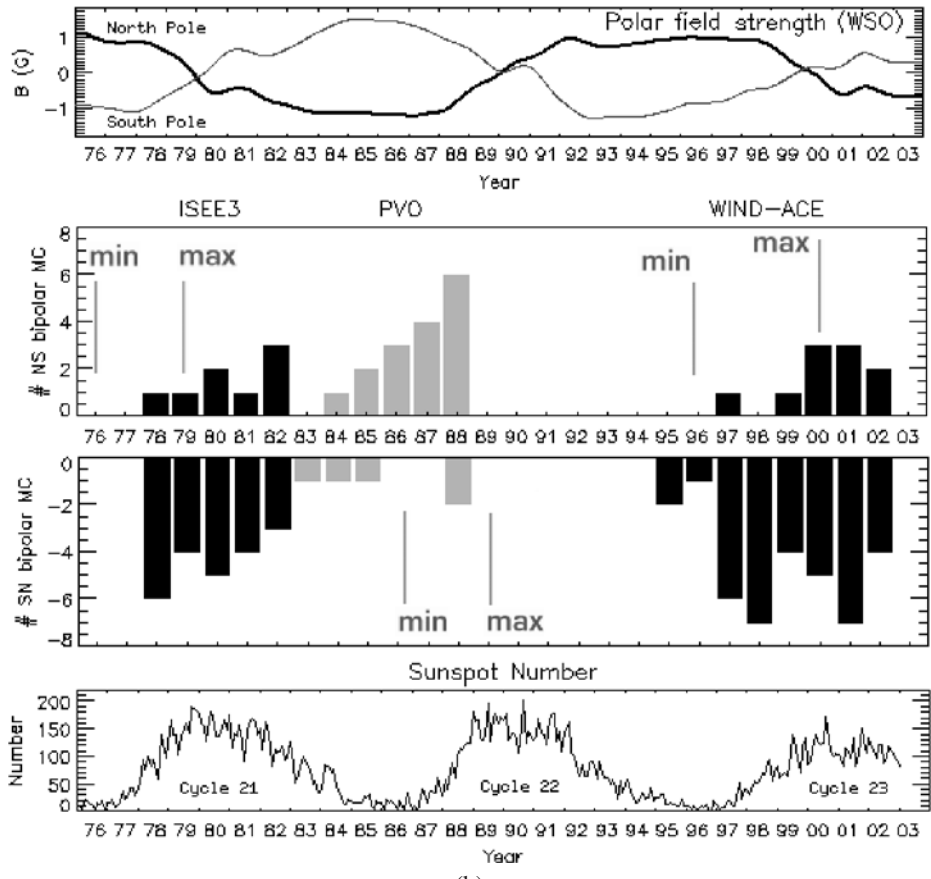
Fig. 2 Example of in situ plasma and field measurements for an isolated ICME observed on WIND by Larson et al. (1997). The top three panels show magnetic field magnitude and direction, with the red line showing a fit to the data of a standard flux rope model. The next panels show solar wind speed and density, and the fluxes of suprathermal electrons of various energies. An electron energy spectrogram, radio spectrogram, and two electron angular spectrograms for suprathermal electrons follow. At the bottom is the field line length inferred from the time of arrival of electrons of various energies, and the curve expected from the flux rope fit at the top

flares and a CME at the Sun (Feynman and Hundhausen 1994), perhaps an indication of the complex coronal conditions that can give rise to those events.



(a)

Fig. 3 **a** Illustration of the relationship between the coronal streamer belt magnetic field and inferred ICME flux rope ejecta fields (Mulligan 1999, personal communication). **b** Figure from Li and Luhmann (2004) showing the updated analysis of ICME flux rope polarities compared to the solar cycle and global solar magnetic field. “MC” stands for “magnetic cloud”, and “NS” and “SN” for north-south and south-north bipolar signatures in the out-of-ecliptic field component. The gray part of the histogram is derived from PVO measurements, obtained at 0.73 AU



(b)

Fig. 3 (Continued)

Other provocative findings have come from groundbased observations and models. In particular, certain flux emergence patterns in the photosphere have been linked to filament disappearances, and by inference, to CMEs (Feynman and Martin 1995). The solar cycle variability of CME occurrence resembles the rate of increase of open solar flux at the source surface of potential coronal field models based on photospheric magnetograms (Luhmann et al. 1998). These results complement what is known from the observations described above, especially in their suggestion that CMEs are linked to the evolution of the large scale coronal magnetic field (Harrison et al. 1990). They also pave the way for STEREO investigations of the influence of active region emergence on CME genesis during the rise of cycle 24.

IMPACT observations can constrain our interpretations of CME initiation mechanisms through a number of ICME magnetic field topology diagnostic measurements. In particular, the energy range and wide angular coverage of IMPACT electron measurements allow the suprathermal electron anisotropy measurements that indicate local field connections to the Sun, including connections to active regions. The magnetic field measurements allow single or multipoint flux rope or other topological modeling of the ICME fields for comparisons with the electron diagnostics and structures observed in the SECCHI images. The IMPACT

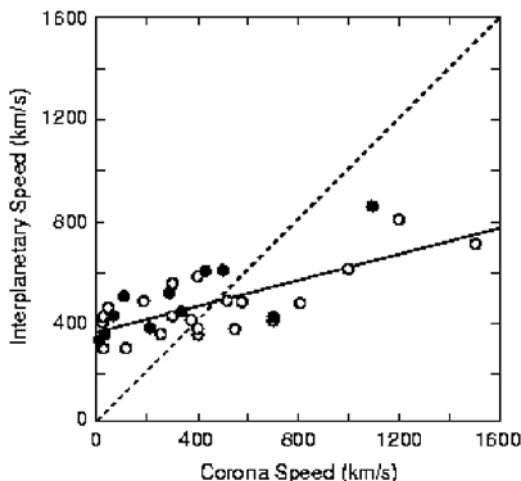
SEP measurements help identify the CME source region when energetic particles from either the ICME shock or an associated flare are detected on interplanetary field lines connected to that region. Moreover, SEP ion composition time profiles and fluxes can be used to analyze the CME–flare relationship (e.g., by assuming Fe ion-rich intervals within the larger event are a signature of flare contributions). In all of these cases the availability of multiple site measurements, including any corresponding parameters observed on ACE and WIND, allow us to better infer the location in the corona where the CME initiation occurs.

IMPACT investigation team modelers have shown that it is possible to simulate the formation and eruption of large flux-ropes in the corona in several ways. One approach (Manchester et al. 2005) embeds pre-defined out-of-equilibrium structures in coronal helmet streamers, which then undergo energetic expansion into the heliosphere. Others produce flux rope-like eruptions by energizing existing coronal structures via footpoint shearing followed by canceling or reducing the magnetic flux at the solar boundary (Linker and Mikić 1995). These structures and others from different initiation schemes can be realistically transported to 1 AU using solar wind simulation codes (e.g. Odstrcil et al. 2002; Riley et al. 1997, 2003; Roussev et al. 2003), and then compared with the in situ measurements from IMPACT and PLASTIC. Only comprehensive, sophisticated analyses of this kind can definitively test how ICMEs from various CME generation mechanisms differ, and which, if any, have been confirmed by STEREO observations.

2.1.2 Interplanetary Consequences

Not since the days of the Helios spacecraft and the SOLWIND coronagraph on P78-1 have observational comparisons of coronagraph images of CMEs observed on the limb with in situ measurements of ICMEs been regularly possible. These observations (Sheeley et al. 1985) as well as those obtained using Pioneer Venus Orbiter in situ measurements (Lindsay et al. 1999a) showed that ejecta moving slower than the ambient solar wind are accelerated up to the solar wind speed; while ejecta moving faster than the ambient solar wind are decelerated. This result, illustrated in Fig. 4, is supported by the statistics of coronagraph-derived CME speeds and in situ measured ICME speeds (Gosling 1997a). Ulysses measurements at high heliographic latitudes showed that ICMEs in the high-speed polar coronal hole flows

Fig. 4 Lindsay et al. (1999a) result from a quadrature study of CME speeds versus ICME speeds. Other investigations have also derived similar results showing that ICME speeds increase when they are slower than the solar wind, and decelerate when they are faster. Here the open circles represent the highest confidence cases



typically have speeds comparable to that of the ambient solar wind speed, but also highlighted the role of expansion in ICME evolution (Gosling et al. 1994a, 1994b; Gosling and Riley 1996). Comparisons between observations of the same ICME at high and low heliographic latitudes illustrate that expansion tends to dominate the ICME interaction with the solar wind at high latitudes, while at lower latitudes relative bulk speed tends to dominate the interaction (Gosling et al. 1995b). Upstream of Earth, ICMEs typically show aspects of both expansion and compression, depending on their location within the ambient solar wind stream structure. They are often found at either the leading or trailing edge of a high-speed stream, consistent with the CME connection with the helmet streamer belt and with the frequent ICME association with the heliospheric current sheet (Crooker et al. 1998).

The interpretation of the in situ observations of ICMEs including their preceding shocks, solar wind compressions or sheaths, and ejecta drivers, is not necessarily straight-forward even if a fairly simple magnetic flux rope structure ejecta is involved. Figure 2 showed an example of a well-studied event from the WIND spacecraft including electron and magnetic field measurements similar to those that IMPACT will obtain. The problem is that what reaches 1 AU is a combination of what is ejected from the Sun and how the related disturbance evolves in transit in the structured solar wind. In the simplest cases the sheath region ahead of a fast ICME is characterized by increased plasma speed, density, temperature, and magnetic field strength that may or may not be preceded by a shock. The ambient magnetic field within the region of compression is reoriented and drapes about the ejecta as illustrated in Fig. 1 (e.g., Hundhausen 1972; Gosling and McComas 1987). The ICME slows as a result of the interaction, while the ambient wind accelerates. If the ICME originally moves faster than the trailing solar wind as well, a rarefaction forms behind the disturbance. In such cases pressure gradients associated with the rarefaction cause both an expansion and a deceleration of the rear portion of the ICME (e.g., Gosling 1996). Compressions from behind by a trailing high speed solar wind stream are also evident in some events, as are compositional signs that a filament of originally colder, denser coronal material forms a part of the observed ICME structures (e.g., Schwenn et al. 1980; Gosling et al. 1980; Skoug et al. 1999). On the other hand, many ICMEs are characterized by ions of high charges states, indicating probable flare origins to some ICME material (e.g., Bame et al. 1979; Lepri et al. 2001).

Because the ambient solar wind is far from homogeneous, particularly at low heliographic latitudes, ICMEs and the shocks they drive must become highly distorted as they propagate outward through the heliosphere (e.g., Riley et al. 1997; Odstrcil and Pizzo 1999a, 1999b, 1999c). It is thus somewhat surprising that about a third of observed ICMEs have magnetic field structures that can locally be fit to simple flux rope models (e.g. Lepping et al. 1990). It is likely that our simplistic cartoons of ICMEs between the Sun and Earth (e.g., Fig. 1) are inadequate. Sophisticated numerical modeling of individual CME initiation and transport cases is required to make substantial progress, as noted above. The combination of 3D reconstructions of the ejections from SECCHI images, and the multipoint perspective on both the ICMEs and surrounding solar wind structure provided by STEREO IMPACT electron and magnetic field measurements and PLASTIC ion measurements, will allow realistic modeling of their complex interplanetary evolution.

A challenge related to the above questions is how best to identify the coronal ejecta portion of ICME disturbances using in situ observations. A variety of signatures (anomalously low plasma ion temperatures, counterstreaming suprathermal electrons, magnetic field rotations, low proton beta, unusually low-variance magnetic fields, anomalous compositions, energetic particle counterstreaming or flux decreases, some of which can be seen in Fig. 2), have proven useful for identifying the ejected material in the solar

wind, but that identification remains more of an art than a science (e.g., Gosling 1990; Neugebauer and Goldstein 1997). These various signatures often poorly overlap within ejecta, varying from one event to the next or even within a given ICME. For example, the counterstreaming suprathermal electrons in Fig. 2 occur sporadically within the time interval when the smoothly varying magnetic field of the inferred flux rope is observed, suggesting a mixture of open and closed field lines in that event. Recent 2-point magnetometer measurements using NEAR and WIND suggest that the flux rope signature can vary significantly for longitudinal separations as small as 15 degrees (Mulligan and Russell, 2001). The two-point measurements provided by STEREO using identical IMPACT measurements with increasing separation can reveal the spatial extent of various signatures, including the flux rope-like magnetic topology and electron anisotropies, within ejecta passing over both spacecraft. Combined with PLASTIC plasma ion measurements, IMPACT measurements will provide improved ways to characterize ejecta and their boundaries.

STEREO CME/ICME shock tracking and diagnosis (of radial speed profile, strength, extent, structure) from the Sun to 1 AU depends on IMPACT multipoint suprathermal and energetic electron measurements together with SWAVES radio remote sensing data. The directionality and timing of the shock-accelerated electrons serve as probes of the shock surface as it travels Earthward. Analysis of WIND observations using this technique suggests the surface of an ICME-driven shock can be highly corrugated, giving rise to multiple radio emission sites (Bale et al. 1999). Anticipated stereoscopic sounding of shocks using IMPACT electron measurements with SWAVES radio data adds the possibility of obtaining multidimensional information about the shock structures and particle populations corresponding to Type II sources. The IMPACT SEP data and SWAVES observations each provide diagnostics of the radial profile of the ICME shock strength, and in particular a measure of the shock strength in the corona, where it is inferred to be its strongest during major events. The comparison of inferred shock properties at widely separated sites is of particular value because only part of the shock is expected to be a strong SEP source. SWAVES observations can identify that location, filling the gaps between places on the shock for which SEP remote sensing is available.

Many questions related to CME/ICME evolution in the solar wind are closely connected to the questions of CME origins. While most CMEs appear to expand as they propagate out through the heliosphere, there is not yet a consensus on what drives these expansions (e.g., Osherovich and Burlaga 1997; Gosling 1997a). Like ion temperatures, the electron temperatures in ICMEs can be extremely cold (Montgomery et al. 1974; Larson et al. 2000), implying that some ICMEs expand adiabatically. Other issues relate to the role of reconnection in creating the magnetic topologies observed within ICMEs near 1 AU. Does the flux rope topology in some ICMEs result from the solar source directly (e.g., Gibson and Low 1998), or is it created in the corona by reconnection during and after CME lift off (e.g., Gosling 1990; Antiochos et al. 1999)? How does reconnection produce the various mixtures of closed, open, and (sometimes) disconnected magnetic topologies inferred to be present within ICMEs based on suprathermal electron anisotropy measurements (e.g., Gosling et al. 1995a; Shodhan et al. 2000)?

As mentioned earlier, some ICMEs move faster than the highest speed solar wind. How are such extreme speeds (up to \sim 2500 km/s) produced? In general, how does the dynamic interaction of an ICME with the surrounding solar wind affect its observed speed at 1 AU (e.g., Cargill et al. 1996; Gosling and Riley 1996)? Is the flare and/or filament association of CMEs simply incidental or is there a causal relationship and, if so, exactly what is that relationship? How much solar magnetic flux and helicity does the typical ICME contain? What is the origin of observed magnetic polarity changes of ICMEs, in which

the sequence of the field rotation changes from north-south to south-north or the reverse with the advance of the solar cycle (e.g., Bothmer and Rust 1997; Mulligan et al. 1998; Li and Luhmann 2004)? These and other questions about ICME nature and evolution opened by earlier observations of CMEs and ICMEs, can be addressed anew with STEREO and IMPACT multipoint observations of electron anisotropies and magnetic fields together with interpretive modeling. For example, the increasingly possible numerical simulation of realistic coronal eruptions, propagated through a realistically structured solar wind, can be compared to both the CME images and the IMPACT *in situ* plasma and field measurements. If they compare favorably, one can probe the geometries and force balances in the simulation results in detail to more fully understand what determines the speed and geometry of the structure that STEREO observed.

2.2 The Relationship of the 3D Corona to Solar Wind Structure

The dichotomous high speed and low speed nature of the solar wind was made especially clear by Ulysses in its polar orbit about the Sun (Phillips et al. 1995; McComas et al. 2003). While the high speed wind connection to large polar coronal holes is relatively well-established (e.g., Krieger et al. 1973; Neugebauer et al. 1998), the nature of the slow wind remains under debate. Much of the slow solar wind appears to originate from either the cusps of closed field regions making up the coronal streamers, or the edges of coronal holes. This origin accounts for its association with the heliospheric current sheet. The slow solar wind has a highly variable density and ion composition near Earth (e.g., Gosling 1997b) that may result from spatial inhomogeneities or temporal variability in its source regions. The slow solar wind also has different characteristic suprathermal electron anisotropies than the fast solar wind, including less intense heat flux electron beams (Pilipp et al. 1987; Ogilvie et al. 1999), and sometimes sunward directed anisotropies that indicate magnetic fields folded back toward the Sun (Kahler et al. 1984) as well as heat flux dropouts (McComas et al. 1989). One suggestion is that the slow wind at least in part consists of transient events from magnetic reconnection at the coronal hole boundaries or the cusps of streamers (e.g., Crooker and Intriligator 1996; Wang et al. 1998). The bright blobs observed by SOHO-LASCO emanating from coronal streamers (Sheeley et al. 1997) may be visible evidence of this process, but they have proven difficult to identify with *in situ* measurements. The twin STEREO spacecraft offer the possibility of relating features seen by the coronagraph on one spacecraft with structure in the slow solar wind detected on the other by IMPACT. IMPACT electron measurements, far from the contaminating influence of Earth's bow shock, also provide especially good opportunities for definitive analyses of the slow solar wind magnetic field topology.

During the STEREO mission, knowledge of the prevailing ambient 3-dimensional coronal and solar wind structure is needed for providing the context of both CME origins in the corona and their propagation in the solar wind. IMPACT's continuous 2-point measurements of the solar wind plasma and magnetic field, together with the imaging data, will allow the use of coupled corona/solar wind 3D models (e.g. Aschwanden et al., *this volume*, 2006) to infer global from local or multipoint behavior. It is expected that the L1 monitors ACE and WIND will continue to operate throughout the STEREO mission, in which case 3 or 4-point measurements are routinely available for analysis. Moreover, the Mercury-bound MESSENGER spacecraft is in its cruise phase, Venus Express is in orbit at Venus, and MGS and Mars Express are orbiting Mars, giving the possibility of providing *in situ* particle and field information over a wide heliolongitude and radial range. Ulysses provides special opportunities for out-of-ecliptic sampling, for more distant quadrature observations, and for coalignments

allowing observations of the radial evolution of structures. Taking advantage of these other missions makes an effective inner heliosphere constellation for further constraining the 3D solar wind structure deduced from STEREO in situ observations.

2.3 SEP Acceleration and Propagation

Major solar energetic particle events (SEPs) usually are closely associated with CMEs and are a key STEREO measurement objective. The duration and intensity of these large gradual events are in contrast to the impulsive, generally weaker, flare-generated events, an example of which is shown next to a gradual event example in Fig. 5. Peak fluxes of the particles in these events are strongly correlated with maximum CME speeds close to the Sun (Kahler et al. 1984). By comparing height-time profiles of CMEs with particle intensities at 1 AU, Kahler (1994) inferred that acceleration peaks when the shock is at 5–10 solar radii for protons with energies up to \sim 21 GeV. However, acceleration of protons and other ions to \sim 1 GeV sometimes continues out to 1 AU and beyond (Reames 1999). Many gradual SEP events have a local maximum in intensity near shock passage. Such intensifications are known as ESP (Energetic Storm Particle) events. Sometimes the ESP increase at shock passage contains the largest flux measured in a SEP event. These intensifications are thought to result from shock-accelerated particles trapped by the shock and related upstream and downstream field fluctuations. The earlier, more anisotropic parts of gradual events are produced by leakage from this region, the leaked particles racing well ahead of the shock source. The relationship between the ESP events and the prompt parts of the gradual events are still a subject of research, with particle anisotropies (e.g. Reames 1999) and shock-associated waves (e.g. Sanderson et al. 1985) an important element of the data interpretation. Major SEP events are observed in most years of the 11-year solar cycle, except near solar minimum (e.g., Shea and Smart 2002).

Investigations of the heliolongitude extent of SEP events with respect to their source locations indicate they can span over 180 degrees (Cane et al. 1988). However, the intensity-time

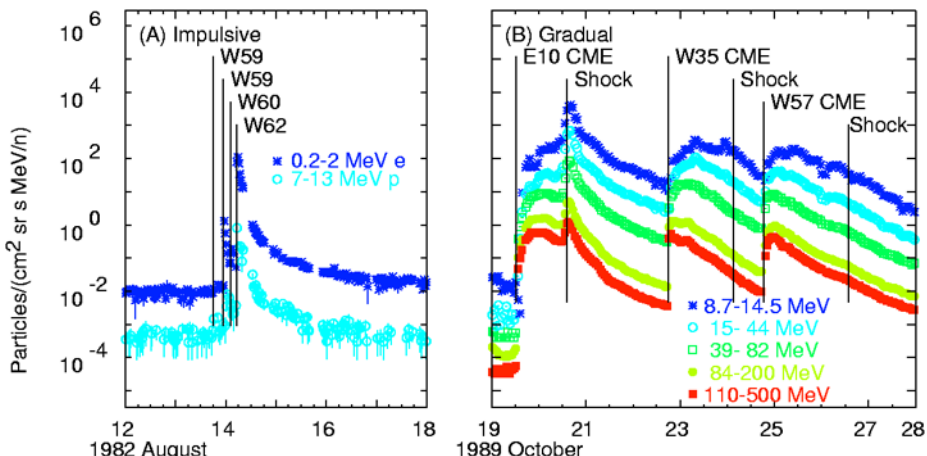


Fig. 5 Illustrations of impulsive (flare-generated) and gradual (interplanetary shock-generated) SEP events observed on the WIND spacecraft. The flare and CME times and locations on the solar disk with respect to the central meridian are indicated in these time series. The impulsive event on the left lasts several hours while the gradual events, here a sequence of three, last several days each. Note the shock arrival ESP event in the first gradual event in near coincidence with shock passage

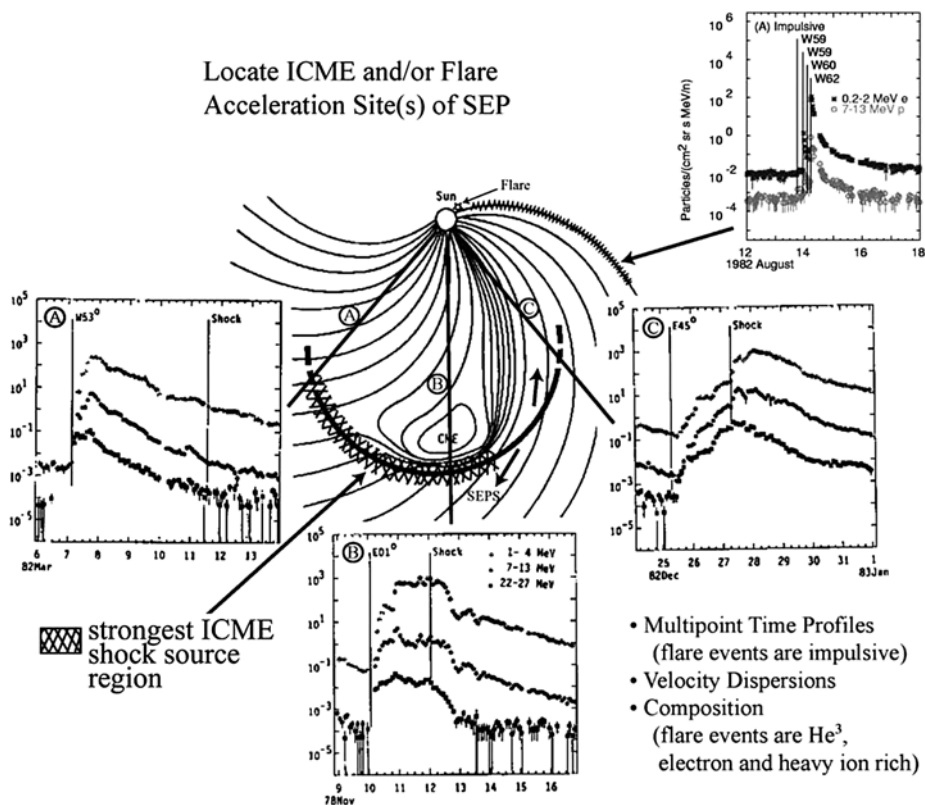
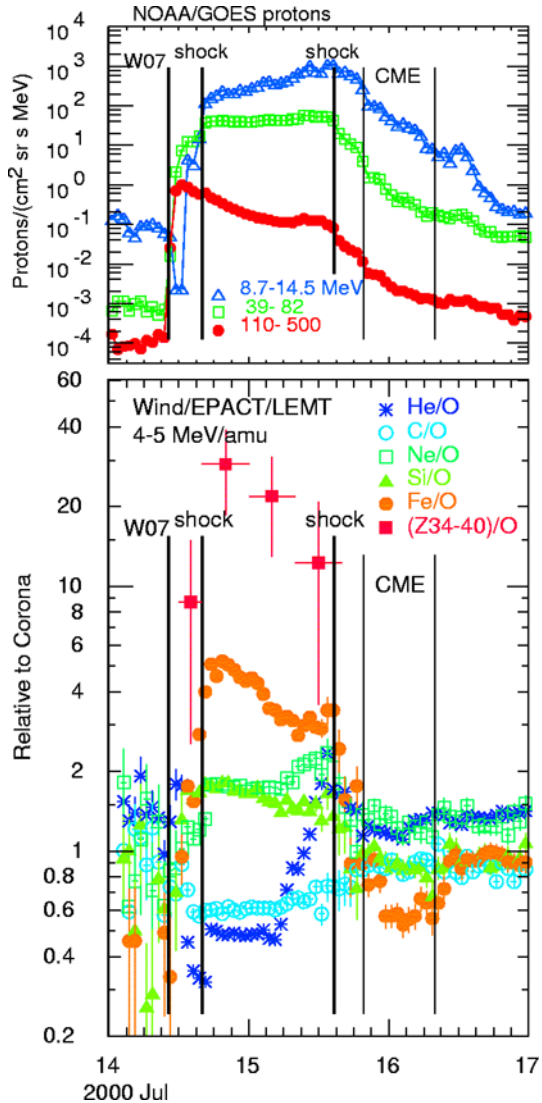


Fig. 6 A classic picture adapted from Cane et al. (1988) showing the spatial organization of time profiles of SEP events with respect to a CME location. STEREO observations will regularly test this picture, and refine it, with multipoint and ion composition observations

profiles of the particles depend on the longitude of the associated solar event as illustrated in Fig. 6. This paradigm-defining result was investigated with earlier multi-spacecraft observations, primarily using data from IMP-8 and the two Helios spacecraft. The interpretation is that particle intensities peak near the nose of the shock and decline on the flanks (Reames et al. 1996). Because of the generally spiral nature of the interplanetary magnetic field, an observer's connection point to a shock swings eastward with time across the face of the outward-moving shock through an angle of $\sim 50\text{--}60$ degrees. The observer remotely senses the particle acceleration when it magnetically connects to the shock. With IMPACT on the two STEREO spacecraft, two different points along the shock can routinely be sampled simultaneously, allowing separation of these spatial and temporal effects as the shock travels outward.

The primary tool for understanding the SEP acceleration physics in recent years has been measurements of the abundances of elements and charge states in SEP ions and their variation in space and time. Systematic variations in abundance patterns, for events with different source longitudes were first reported by Breneman and Stone (1985). An illustration of the evolution of the ion composition in one gradual event is shown in Fig. 7. Events at western longitudes peak early and are initially Fe-rich, the ion composition presumably having been affected by flare-like processes in the hot corona (e.g. Cane et al. 2003). In contrast,

Fig. 7 Illustration of the variation of ion composition through a gradual SEP event detected by both GOES and WIND



central disk and eastern events are relatively Fe-poor, peak later, and contain larger contributions of particles with solar wind-like composition. Adequate abundance measurements were not available on Helios to allow multipoint ion composition studies. Nevertheless, theoretical analyses suggest that as protons stream away from the shock they generate Alfvén waves that trap the particles that follow, causing efficient acceleration to higher energies (Lee 1983, 2005). The spectrum of these self-generated waves is related to the proton energy spectrum and varies with space and time, throttling the flow of SEP ions away from the shock. Ions of the same velocity, but with different charge-to-mass ratios, Q/M , resonate with waves of different wave number, k . Thus, the relative abundances of different ions that leak away from the shock probe the wave spectrum in the vicinity of the shock. Recent measurements have made it possible to analyze the time dependence of the ion abundance

variations (Tylka et al. 1999; Reames and Ng 1998), and to develop time-dependent theoretical models of the acceleration and transport of SEPs (Ng et al. 1999) that explain these variations. The initial abundance variations depend strongly on the (unseen) spectrum and intensity of high-energy protons back at the shock when it is still near the Sun. With IMPACT instruments, the quantitative relationship between shock parameters, proton spectra, and abundance variations can be sorted out. It may also be possible to use SEP abundance observations to remotely sense the properties of an oncoming shock and forecast its subsequent behavior. STEREO IMPACT, with its SEP composition measurements, provides the opportunity to study abundances on spatially separated spacecraft, allowing us to infer the spatial distribution of the wave spectrum along the surface of a remote shock and its evolution with time. Large spacecraft separations (20–180 degrees) are best for such analyses given the extensive spatial structure of the gradual SEP events.

The leakage of particles from the shock acceleration region produces a spectral “knee” as acceleration becomes less efficient. In some events the energy of this knee can be at 15 MeV, in others it is over 100 MeV. Understanding the relationship between the knee energy and the properties of the CME-driven shock is essential for determining how rare, extreme SEP events are produced. IMPACT data are expected to reveal new aspects of the physics of particle acceleration that can help us better understand the origin of the SEP spectral knees, at least up to the \sim 100 MeV energy limit of IMPACT HET measurements. In general, the ability to measure the energy spectra arising from different locations on the same shock on two spacecraft is ideal for testing previously held ideas about the origins of different spectral features.

Although most major SEP ion events are a result of CME-driven shock acceleration, the electron-rich impulsive SEPs arise from flares and yield unique information about the flare process. Flare-heated electrons above 20 keV produce hard X-ray bursts when they interact with the solar atmosphere. Other accelerated electrons stream outward on open coronal field lines to produce type III radio bursts. Current theory suggests that electron beams produce waves between the gyrofrequencies of H and ^4He that are resonantly absorbed by the rare isotope ^3He so as to enhance the $^3\text{He}/^4\text{He}$ ratio by factors of \sim 1,000 in the impulsive events (e.g., Roth and Temerin 1997). Ten-fold enhancements are also produced in the abundance of heavy elements such as Fe. The IMPACT investigation will enable coordinated SEP composition and SWAVES radio burst measurements, allowing in-depth analysis of flare acceleration processes that can be contrasted with the processes which accelerate particles at ICME-driven shocks. Recent work using energetic electron events and Type III radio bursts from WIND and ACE show that there is often a large temporal offset between a Type III burst, and the associated electron event (Krucker et al. 1999; Haggerty and Roelof 2002). The origin of this offset is still being debated. With IMPACT and SWAVES investigations on the two spatially-separated STEREO spacecraft, SEP electrons and Type III radio bursts can be compared at two points. Mapping the onset times back to the Sun, we can remotely probe the source(s) at the injection site(s).

Energetic particles streaming out from the Sun can also be used to map the topology of magnetic field lines in the solar wind (Kahler and Reames 1991; Bothmer and Schwenn 1996; Larson et al. 1997) The high and low energy suprathermal electron observations often have different anisotropy signatures (Lin and Kahler 1992; Kahler and Reames 1991) and thus provide complementary information on magnetic field topology. Large decreases in energetic ion intensity are often observed during passage of ICMEs (e.g., Mazur et al. 1998; Cane 2000), probably indicating the inability of the shock-accelerated particles to penetrate significantly into the closed field regions of the ICMEs. The separation of the two STEREO

spacecraft allows us to determine if the topological and source properties inferred from the particle anisotropies and ion composition are consistent with current paradigms (e.g. as summarized in Reames 1999; Kahler 2001).

It has been argued, based on available observations, (e.g. Kahler 2001; Desai et al. 2006) that the presence of a significant prior background of suprathermal ions from previous CMEs or flares generally increases the intensity of gradual SEP events. While this idea is still under debate, it is intuitively clear that preacceleration should enhance any subsequent acceleration by a statistical process at the shock. Several of IMPACT's detectors, especially SIT, are designed to address the seed population problem observationally. In particular the multipoint sampling on STEREO will reveal how uniform or nonuniform such populations can be, and whether the shock portions with seed populations are more SEP-productive. Observations often show particle spectra of the same intensity and shape over large spatial regions (Reames et al. 1997), from which it has been inferred that particles may be effectively trapped behind shocks. There is some evidence that these trapped particles can form a seed population for SEP generation by a second fast CME near the sun. Later SEP events in a series of SEP events often have higher intensities than the first, suggesting that extreme events may be more easily generated when multiple CMEs occur (e.g. Gopalswamy et al. 2003). An understanding of seed populations in general is a high priority for IMPACT measurement analyses.

Like CME simulations, SEP event models are coming of age as a natural extension of the progress in developing sophisticated coronal and heliospheric numerical models. Several efforts described in the literature (e.g. Lario et al. 1998; Li et al. 2003) make use of MHD model simulations of interplanetary shocks as the basis for SEP spatial distribution and time profile descriptions that can be compared to multipoint or single spacecraft observations. The existence of the IMPACT modeling efforts and others are expected to lead to realistic and detailed SEP event descriptions that are consistent with both the SEP observations on STEREO and the related CME and ICME measurements and models.

2.4 The Solar Origins of Geoeffectiveness

Magnetic indices based on ground magnetic perturbations, levels of ionospheric disturbance, relativistic electron and other radiation belt enhancements, and auroral activity are just a few of the commonly used measures of the geoeffectiveness of solar wind events. The parameters from solar wind monitors most widely associated with disturbed conditions include one or more of high bulk speed, high ion density (or dynamic pressure), and strong magnetic field, particularly when the field contains a southward component in GSM coordinates (e.g. see Luhmann 1997; Webb et al. 2000, and references therein). While solar wind stream interaction regions contain enhanced values of the geoeffective parameters, the largest and longest-lived enhancements are from ICMEs (Lindsay et al. 1995) or combinations of stream interaction regions and ICMEs (Tsurutani et al. 1992). In particular, fast ICMEs preceded by interplanetary shocks produce the major geomagnetic storms (Gosling et al. 1990, 1991; Gosling 1993) because of the high dynamic pressures and strong magnetic fields, often with strong southward components, commonly associated with such disturbances, all of which are made more geoeffective by accompanying high bulk speeds. Thus the primary questions raised above about the physics behind the CME speed, and its solar wind stream structure context, are highly relevant to the geoeffectiveness issue.

The basic physics of geoeffectiveness is well known from the viewpoint of solar wind-magnetosphere interaction physics (e.g., Kivelson and Russell 1995), but it is not clear how

geoeffective structures at 1 AU relate to the transients seen at the Sun. In particular, the coronal conditions leading to eruptions with high speed ejecta carrying intense southward magnetic fields, the recipe for geoeffective ICMEs, is not understood. For example, sometimes an apparent fast halo event in LASCO images, thought to portend an important Earth-bound ICME, is not followed by a significant solar wind event at 1 AU. An ICME may change speed and character as it propagates to Earth, rendering it less locally impressive than inferred from coronagraph images, or it may miss the Earth altogether. Similarly, an event may lead to an impressive L1 disturbance in which the bulk of the large out-of-ecliptic fields are northward. Geoeffectiveness thus depends on the heliolongitude dependence as well as the intrinsic nature of ICME properties and those of the ambient wind into which it propagates. IMPACT measurements combined with L1 measurements will provide 2- and 3-point information on the geoeffective extent of specific events observed by the imagers on STEREO. For example, proxy calculations of geomagnetic indices such as Dst (Lindsay et al. 1999b) and Kp (Detman and Joselyn 1999) based on solar wind parameters for each spacecraft can give a measure of the potential geoeffectiveness of a particular event along a significant segment of Earth’s orbit. IMPACT team modeling of specific events can help to establish the observational and physical basis for relating geoeffectiveness to solar observations.

Monitors at L1 and other upstream locations do not always give a good indication of the solar wind control of the magnetosphere because they are generally not on the stagnation streamline that reaches the magnetopause. Multispacecraft studies upstream of the bow shock suggest that the coherence length of solar wind structures is sometimes smaller than the separation of the monitors (Paularena et al. 1999), and studies of structure orientations show that they often do not move in planar fronts perpendicular to the Earth–Sun line. Structures strongly influenced by the corotating solar wind streams tend to align themselves along the Parker Spiral direction (Richardson and Paularena 1998), while high speed transients with large internal pressures often give the impression that the incident structure is perpendicular to the Sun–Earth line (e.g. Lindsay et al. 1994). Numerical simulations of the magnetosphere-solar wind interaction show that the angle of incidence of interplanetary structures affects the magnetosphere’s response, while simulations of ICME propagation in a structured solar wind show how complicated they can become in the course of their interplanetary evolution (as discussed above). IMPACT observations in the STEREO configuration with an ever-widening baseline between spacecraft provide a controlled experiment for measurements of coherence scale lengths of solar wind structures, including ICMEs and solar wind stream interaction regions. They also form the basis for determining the normals and curvatures of shocks and the changes in the appearance of ICMEs over the varying baseline, allowing reassessment of needs for positioning solar wind monitors and future interplanetary constellation spacecraft. IMPACT 3D heliospheric models consistent with the observed solar wind and ICMEs, used to drive 3D MHD magnetosphere models, are expected to provide insights into the Earth’s response not possible with L1 observations alone.

2.5 The Solar Magnetic Cycle

The photospheric magnetic field is dominated by the cycle of emergence and decay of active regions that somehow participate in the periodic reversals of the global solar field. During the course of this dynamo-driven cycle, the amount of flux threading the photosphere changes by a factor of ~ 5 in the present epoch (e.g., Schrijver and Harvey 1994). Eclipse and coronagraph observations and coronal models based on photospheric field observations show that the corona responds to changes in the photospheric field, but it is not always

obvious how such changes affect the heliospheric magnetic field (McComas et al. 1992; McComas 1995). Some studies suggest a factor of two change in the total interplanetary magnetic flux over the cycle (e.g. Luhmann et al. 1998). Both the loop-like appearance of CMEs and the measurements of counterstreaming electrons in ICMEs indicate that new solar magnetic flux opens into interplanetary space during transients, but on the average, newly opened solar flux must be counterbalanced by newly closed flux as the solar magnetic field does not become increasingly open over time. Yet direct interplanetary signatures of magnetic flux closing down at the Sun, which would produce heliospheric field lines disconnected from the Sun, have been elusive. If magnetic flux tubes are completely disconnected from the Sun, electron heat flux dropouts would be expected and are observed during disconnection events that occur well away from the Sun at the heliospheric current sheet (Gosling et al. 2005b), but these do not appear to be present in equal numbers with counterstreaming electron intervals (indicators of closed field lines), or are masked by some other process. Those dropouts that have been detected are concentrated in the vicinity of the heliospheric current sheet in the slow solar wind (McComas et al. 1989).

STEREO IMPACT will provide sensitive measurements of suprathermal electron angular distributions over broad angle and energy ranges, together with interplanetary magnetic field measurements, at two low-heliolatitude sites. These measurements will not, in general, be contaminated by suprathermal electrons originating from Earth's bow shock, as is often the case at L1. Thus IMPACT provides the best opportunity to date to utilize suprathermal electron observations in determining the overall evolving topology of the heliospheric magnetic field and to study the opening and closing of magnetic flux in the solar environment. Coordination with the SWAVES experiment allows assessment of the effects of scattering on suprathermal electron distribution at locations where the electron heat flux drops out. The dual-site measurements and imaging that STEREO affords make it possible to compare suprathermal electron distributions and anisotropies at different spacecraft separations and to compare those distributions with prevailing conditions at the Sun and in the corona.

The solar dynamo transforms poloidal field to toroidal field and also results in polar field reversals. Eruption of the active region fields must eventually lead to a loss or relaxation of the toroidal fields, with CMEs playing a part in this process (e.g., Rust 1994). Above it was pointed out that the magnetic structures of those ICMEs that can be described as flux ropes are related to the global solar magnetic polarity, with their leading edge fields sometimes corresponding to the orientation of the prevailing helmet streamer belt field. However, the handedness or twists of these structures is not clearly related to the magnetic cycle. In contrast, the magnetic fields observed around active region and polar crown filaments, whose eruptions often accompany CMEs, appear to have a definite organization of handedness. Right-handed fields seem to prevail in the southern hemisphere, while left-handed fields prevail in the north (Bothmer and Schwenn 1994). The relationship between the magnetic field of a filament and its surroundings, and the magnetic field that is observed in an ICME, remains an open question (e.g. Leamon et al. 2004). Some regard the filament and its local overlying fields as the source of the ICME flux ropes, while others consider the former is a small part of a much larger erupting coronal structure that supplies most of the interplanetary flux rope via coronal reconnection. IMPACT field and electron measurements, coupled with PLASTIC measurements of the plasma ion composition, can be used to distinguish the magnetic fields in the filamentary material from those of other parts of the ICME structure, and examine their relationship, an important step toward resolving the source region question (e.g. Gloeckler et al. 1999).

Additional insights into the solar magnetic cycle come from comparing the characteristics of both ICMEs and solar wind structure for different cycles given the behavior of the

photospheric field (e.g. Wang and Sheeley 1990a; Luhmann et al. 2002; Li and Luhmann 2006). Fairly continuous interplanetary data sets from L1 exist from ISEE-3 (1978–1987), WIND (1996–present) and ACE (1998–present) missions. Although the STEREO mission will have a lifetime limited by resources and orbital evolution, it will observe the rise to the cycle 24 maximum for comparison with the rise to cycle 21 maximum observed by ISEE-3 and the rise to cycle 23 maximum observed by WIND and ACE. The observed properties of the active regions can be compared with the number and nature of the ICMEs detected by IMPACT. While this study could also be carried out with an L1 monitor, the availability of the STEREO multipoint view provides the basis for a clearer interpretation in terms of quantities such as the size and flux content of ICMEs that can then be used in retrospective studies of the earlier data. IMPACT will extend the records of information on features such as ICME flux rope occurrence, polarity, orientation and handedness, providing an improved basis for comparisons with solar dynamo models and their coronal counterparts.

2.6 Complementary Science Objectives

2.6.1 Space Plasma Microphysics

After decades of effort, uncertainty remains regarding the physics of thermalization of solar wind electrons at collisionless shocks. As the electrons encounter the shock, they are thought to move adiabatically through the layer under the influence of the cross-shock potential, leaving an inaccessible region of phase space downstream (e.g., Feldman et al. 1982; Goodrich and Scudder 1984). It has been suggested that this form of the downstream distribution function is unstable to the two-stream instability (Gedalin 1999). Furthermore, intense nonlinear electrostatic waves and phase space holes have been observed near the overshoot of collisionless shocks (Bale et al. 1998a), a possible signature of nonlinear evolution in a two-stream instability. As a shock passes over each STEREO spacecraft, IMPACT and SWAVES operating together in the burst mode can capture detailed distribution functions and plasma wave waveforms, allowing us to systematically study the evolution of both the waves and electrons in the shock layer.

The radio emission observed during an IP Type II or III radio burst is generated at $1 f_{pe}$ and/or $2 f_{pe}$ by a process known as plasma emission. The microphysics of the plasma emission process underwent a paradigm shift due to WIND observations of elliptically polarized plasma waves at $1 f_{pe}$ in the source of these bursts, where longitudinally polarized Langmuir waves were expected (Bale et al. 1998b; Kellogg et al. 1999). This observation implies strong scattering or possibly wave trapping. The SWAVES experiment on STEREO measures all 3 electric field components of these waves, while IMPACT provides essential detailed information on the electron beams driving this process. Other related observations indicate that the Type II source can be probed in situ (Bale et al. 1999). The radio emission comes from near quasi-perpendicular connections to the ICME-driven shock, while the shock-accelerated electrons show the shock surface is highly structured, as mentioned earlier, giving rise to multiple emission sites. Together, SWAVES and IMPACT can further resolve the Type II source nature, allowing improved inference of the shock structure from remote energetic particle and radio measurements.

2.6.2 CIRs and SIRs

From WIND experience, we know that CIRs (Corotating Interaction Regions) (and sometimes non-repeating SIRs, Stream Interaction Regions) are the source of much of the lower

energy interplanetary energetic particle population during periods of low solar activity (Reames 1999; Desai et al. 2006). While they are not ICMEs, CIRs and SIRs give us valuable information about shock acceleration processes. CIRs and SIRs are formed when high-speed solar-wind streams overtake low-speed solar wind emitted earlier in a solar rotation. A pair of shock waves forms around these regions, the forward shock propagating outward into the slow wind and a reverse shock propagating backward into the high-speed stream (e.g., Gosling and Pizzo 1999). The shocks generally form beyond 1 AU, but a good fraction of L1 stream interaction regions exhibit them as well. The strongest particle acceleration in CIRs and SIRs occurs at the reverse shock. Observations on the WIND spacecraft show distinctive features in these energetic particles, with C/O abundances that depend upon stream speed (e.g., Mason et al. 1997); evidence of cross-field particle transport in intense events (Dwyer et al. 1997), and spatial distributions of 1–10 MeV/amu particles extending over 226° in solar longitude (Reames et al. 1997). The CIR and SIR particles may also be an important source of suprathermal seed populations for subsequent ICME shock acceleration. STEREO IMPACT provides a unique opportunity for multi-point composition measurements of the CIR and SIR-associated ions as these enormous 3D structures rotate past the spacecraft.

2.6.3 ACRs

ACRs (Anomalous Cosmic Rays) are believed to be produced when interstellar pickup ions are carried out by the solar wind and accelerated at the heliospheric termination shock (Fisk et al. 1974). Subsequently they make their way back into the inner heliosphere against the flow of the solar wind. Because pickup ions are selectively accelerated by the termination shock primarily due to their high injection speeds, ACRs provide information on the role of the injection process in determining the maximum particle intensities of SEPs from CME/ICME-driven shocks. IMPACT provides sensitive coverage of the low-energy (1–30 MeV/nucleon) ACR ions at a time in the solar cycle when their spectrum is least modified by transient interplanetary structures, giving a truer picture of their source spectrum at two heliospheric locations.

2.6.4 Reconnection Physics

It has recently been demonstrated (Gosling et al. 2005a, 2005b, 2006; Phan et al. 2006) that local, quasi-stationary reconnection occurs relatively frequently in the solar wind and produces pairs of Petschek-type exhausts i.e., exhausts bounded by Alfvén or slow mode waves emanating from reconnection sites. These exhausts occur as brief (typically minutes) intervals of roughly Alfvénic accelerated or decelerated plasma flow confined to magnetic field reversal regions that usually take the form of bifurcated current sheets. The overall transitions from outside to inside the exhausts typically, but not always, are slow-mode-like on both sides. Multi-spacecraft observations by ACE, Wind, and Cluster at 1 AU demonstrate that the exhausts result from local quasi-stationary reconnection at extended X-lines, in one case persisting for at least 2.5 hours along an X-line that extended for at least 2.5×10^6 km (Phan et al. 2006). These are lower limit estimates based on the limited spatial separations available for the spacecraft. In order to extend these estimates to larger scale sizes and longer times, larger spacecraft separations are required. Observations by IMPACT and PLASTIC on the dual STEREO spacecraft will allow us to determine the overall spatial and temporal scale of reconnection in the solar wind. Such determinations will have important implications for models of the reconnection process in other environments such as the solar atmosphere and Earth's magnetosphere.

2.6.5 Space Weather Applications

In support of STEREO's space weather beacon activity (see Thompson et al., and Biesecker et al., [this volume, 2007](#)), IMPACT supplies 1 min averaged basic solar wind plasma and suprathermal electron, magnetic field, and SEP ion and electron information processed onboard (in the IDPU) to conform to the designated telemetry allocation. The IMPACT beacon data contents are summarized in Table 2. Synchronized PLASTIC plasma ion beacon data are also produced in the IMPACT IDPU. IMPACT team members experienced in supplying data to the ACE RTSW system (see Garrard et al. 1998), an effective prototype for the STEREO beacon system, has led to an active IMPACT role in the organization of the in situ beacon data at the STEREO Science Center. IMPACT also includes team members from the NOAA Space Environment Center (SEC) who act as interfaces between our investigation and their operations, enabling forecaster use of STEREO IMPACT beacon data (also see Biesecker et al., [this volume, 2007](#)).

The plasma and magnetic field information from the trailing spacecraft can be used by forecasters to anticipate the arrival at Earth of corotating structures. In particular, if a high speed solar wind stream is detected, a forecast can be made of an imminent magnetospheric relative electron increase and a modest magnetic storm from the associated stream interaction region. The SEP beacon data also allow forecasts of the arrival of an interplanetary shock and its ICME driver. If both leading and trailing spacecraft detect a gradual SEP event, the probability of the shock and ICME impacting Earth's magnetosphere squarely is high. Moreover, if the SEP event observed at the leading spacecraft has a rapid rise-time, it is likely that the shock nose is between the two STEREO spacecraft-a situation favoring a local gradual SEP event including an ESP component on shock arrival at Earth, plus geomagnetic storm consequences of the ICME. Any SEP information from upstream of Earth could be combined with this information to further diagnose the shock strength and nose position with respect to the Sun-Earth line.

A forward-looking issue for NASA is concern over radiation safety during interplanetary human spaceflight, in particular to the Moon and Mars. Reports dealing with the potential hazards to astronauts (e.g., Zeitlin et al. 2004) point out the need to monitor solar activity from many viewpoints to ensure adequate warnings of potential large SEP fluxes. LRO (Lunar Reconnaissance Orbiter), the first vision for Space Exploration mission launching in 2008, carries an energetic particle telescope that will measure the SEP events STEREO IMPACT will detect from other perspectives. Together, these measurements will provide a demonstration of the sensitivity of the local SEP environment to heliospheric location. IMPACT also provides an occasional upstream solar wind monitor for Mars missions. Mars Express includes some in situ particle instrumentation, making coordinated studies of Mars space weather with STEREO possible.

2.6.6 Relationships to Other Missions and Ground-Based Observations

STEREO represents part of NASA's evolutionary sequence of solar/interplanetary missions in the SEC Roadmap that targets the 3D Sun and inner heliosphere, and space weather's underlying causes. STEREO IMPACT investigation measurements build on the information gained primarily from IMP-8, Helios 1/2, ISEE-3, PVO, Ulysses, WIND, and ACE, the latter three of which are still operating. IMP-8 observations led to the first work on the magnetic flux rope models of ICMEs (Lepping et al. 1990 and references therein), ISEE-3 provided long-term detailed in situ measurements at L1 from which solar cycle variations of ICME occurrence and internal information on ICMEs including electron anisotropies were

derived (Gosling et al. 1987). Helios 1/2 enabled the first in situ look at solar wind character and transients into 0.3 AU (Bothmer and Schwenn 1998). PVO provided an effective 0.7 AU outpost to measure solar wind behavior at Venus, allowing both evaluation solar wind monitor for space weather purposes closer to the Sun than L1 (Lindsay et al. 1999a), and study of CME/ICME relationships in a quadrature configuration with SMM and Solwind coronagraphs at Earth (Lindsay et al. 1999b). Ulysses explored the high latitude heliosphere, first during low solar activity conditions (e.g., Phillips et al. 1995) and then during high solar activity conditions (e.g., McComas et al. 2003), revolutionizing our in situ perspective of the 3D heliosphere. Ulysses in situ data and SOHO images were also used in efforts to match solar signatures of CMEs with ICMEs (Funsten et al. 1999). However, combined ACE, WIND and SOHO studies (e.g. Webb et al. 2000) provide what are perhaps the best examples of what can be accomplished with the planned STEREO imaging, SWAVES, PLASTIC, and IMPACT measurements in combination. The GOES spacecraft is of course another reliable source of near-Earth information on SEP protons and solar X-rays with a long history, though its SEP measurements are limited by its magnetospheric location.

On the complementary imaging side, SOHO, TRACE and RHESSI continue to provide solar EUV and X-ray imaging of the corona for use in interpretive studies (e.g. Klein et al. 2005). Earthward-directed CMEs are observed as halo events on SOHO. SMEI on Coriolis (Jackson et al. 2004) provides wide-field coronagraph images from an Earth-orbiting Air Force satellite platform, and is ideally suited for STEREO HI comparisons and in situ comparisons. SXI on NOAA's GOES-M approximates Yohkoh soft X-ray images at a 1-minute cadence in a softer, more sensitive, X-ray band geared toward coronal studies (Pizzo et al. 2005). Both these imagers complement STEREO imaging, and enhance IMPACT science by providing a more complete description of the coronal events preceding detected ICMEs. Solar-B, to be launched around the same time as STEREO, adds a unique coordination capability in that it allows detailed looks at the active regions giving rise to the CME events STEREO will observe. For example, the vector magnetic field measurements obtained with Solar-B can be used to assess the nonpotentiality, polarity, and twist of the magnetic fields in the active regions giving rise to detected ICME structures. Planned campaigns are required (e.g. see Thompson et al., [this volume](#), 2007) given Solar-B's smaller high resolution imaging field of view. However, Solar-B also has a full-disk Yohkoh-like soft X-ray imaging capability that can enhance STEREO data interpretation more generally. Solar Dynamics Observatory (SDO) may launch before the STEREO mission is over. SDO would provide full disk vector magnetograms that could add significantly to the solar connections analyses and IMPACT interpretive modeling. The SDO images are also expected to be returned at a higher rate than those from SOHO, showing more details of time-dependent solar and coronal features.

Opportunities also exist for organizing opportunistic inner heliosphere constellations by combining interplanetary plasma, magnetic field, and SEP observations from several planetary missions. MESSENGER, destined to reach Mercury in 2015 obtains limited in situ particle and field measurements during its cruise phase. However, in Mercury orbit MESSENGER provides an inner heliosphere outpost for space weather measurements. Venus Express and Mars Express respectively provide in situ measurement outposts at Venus and Mars, as mentioned earlier. There is already a plan in place at CESR to combine the data sets from the SWEA-like instruments on Mars Express and Venus Express with STEREO IMPACT SWEA measurements on a regular basis. The possibilities for exploiting the heliosphere-wide models of observed STEREO events to interpret these widely distributed measurements are potentially ground-breaking in terms of future Heliospheric Sentinels mission

planning. The planetary missions also benefit from STEREO's physically separated measurements given their own needs to interpret solar wind interaction effects.

The importance of ground-based instruments to STEREO, especially those providing information on solar magnetic fields, cannot be overstated. Two particular ground-based resources that deserve highlighting because of their importance to STEREO-related modeling are the SOLIS full-disk vector magnetograph installations, and the GONG near-24 hr solar field monitoring network. Together with MDI on SOHO, these observatories provide the synoptic maps and local magnetograms that make possible unifying coronal, heliospheric and SEP event modeling (see Aschwanden et al., [this volume, 2006](#)). Photospheric field maps are already used at NOAA SEC to make predictions of the solar wind speed and interplanetary field polarity based on the Wang/Sheeley/Arge semi-empirical approach (Arge and Pizzo 2000; at <http://sec.noaa.gov/wsa/>), at the LMSAL Solar Soft site for coronal holes and solar wind source mapping (http://www.lmsal.com/solarsoft/latest_events/, also see Thompson et al., [this volume, 2007](#)), and at CCMC as boundary conditions for 3D MHD models of the corona and solar wind (<http://ccmc.gsfc.nasa.gov>). The SOLIS full-disk vector magnetograms and maps are expected to revolutionize the capabilities of models to describe CME initiation and propagation more accurately. GONG magnetograph data currently provide the best possibilities for continuous and high cadence magnetogram coverage from the ground. KPNO, MWO and WSO magnetograms, MLSO coronagraph images, H-alpha and other measurements from NSO, ISOON and other active solar optical and radio observatories linked to some of the above websites contribute further information toward interpreting what is deduced from the combined STEREO imaging and in situ observations.

3 IMPACT Instruments Overview

3.1 Overview and Spacecraft Accommodation

The IMPACT investigation involves engineers, technicians and scientists in 19 institutions. Table 1a provides a list of the team members and their affiliations. Responsibilities for the instrumentation are summarized in Table 1b. IMPACT includes hardware contributions from both university and NASA centers, as well as from international partners. Its overall development was guided by technical Project Manager D.W. Curtis at UCB-SSL. The nature of the instruments and team organization made it advantageous to carry out the development as the two instrument suites shown in Fig. 8a. IMPACT's Boom suite includes the SWEA, STE and MAG sensors, while the SEP suite includes SIT, SEPT, LET and HET sensors. DPU (data processing unit) functions are handled in both a SEP-suite-specific "SEP central" box, and an all-IMPACT IDPU box that provides the single IMPACT interface to the spacecraft commanding and data system. Caltech team member A.C. Cummings adopted day-to-day responsibility for the SEP suite technical oversight.

STEREO spacecraft are non-spinning, so that the particle sensor providers had to take that into account in their designs and spacecraft accommodation plans. The Boom Suite instruments are mounted on a ~5.8 m telescoping carbon fiber epoxy boom, shown in a stowed configuration in Fig. 8b. The boom is mounted along one corner of each spacecraft in a position that minimizes interference with the high gain and SWAVES antennas, and is deployed antisunward. The instruments at its end are usually in the spacecraft shadow. Boom suite development work was centered at UCB-SSL with other IMPACT institutions providing the SWEA and MAG sensors. The detectors in the SEP suite are mounted in several boxes on the body of the spacecraft as shown in Fig. 8c, with different locations on the Ahead and Behind spacecraft to maintain the desired fields of view with respect to the

Table 1a IMPACT team

Institution	Members
UC Berkeley	J.G. Luhmann, D.W. Curtis, P. Schroeder, R. Lin, D. Larson, S. Bale, J. McCauley, R. Ullrich, P. Turin, P. Berg, S. McBride, N. Craig, L. Peticolas, M. Hashii
CESR	J.-A. Sauvaud, C. Aoustin, J. Dandouras, P. Louarn
Caltech	E.C. Stone, R.A. Mewaldt, A.C. Cummings, W.R. Cook, B. Kecman, R. Leske, A.J. Davis, C.M.S. Cohen, V. Nguyen, H. Miyasaka
GSFC	T.T. von Rosenvinge, M.H. Acuna, L.S. Reichenthal, K. Ogilvie, A. Szabo, D.V. Reames, C.K. Ng, S. Shuman, J. Hawk, K. Wortman
JPL	M.E. Wiedenbeck, R.G. Radocinski
Univ. of Kiel	R. Mueller-Mellin, H. Kunow, S. Boettcher, B. Heber
Research and Scientific Support Division, ESA	T.R. Sanderson, R.G. Marsden
JHUAPL	G.M. Mason
Univ. of Maryland	P. Walpole
MPS	A. Korth, V. Vasiliunas
UCLA	C.T. Russell, A. Lam
LASP, Univ. of Colorado	J.T. Gosling
SWRI	D.J. McComas
LANL	H. Funsten
DESPA/Meudon	J.-L. Bougeret
Univ. of Michigan	T. Gombosi, D. DeZeeuw
SAIC	J.A. Linker, P. Riley, Z. Mikic
NOAA-SEC	V. Pizzo, D. Odstrcil
Univ. of Goettingen	V. Bothmer
KFKI	K. Kecskemeti

nominal Parker Spiral magnetic field orientation in the ecliptic. Figure 9 summarizes the IMPACT particle detectors' fields of view described in the instrument summaries below.

3.2 Boom Suite

3.2.1 SWEA (*Solar Wind Electron Analyzer*)

Solar wind electron measurements are essential for investigating the topology and solar connections of solar wind and ICME magnetic fields. SWEA, the IMPACT Solar Wind Electron Analyzer, was provided by the CESR and is described in detail by Sauvaud et al. (this volume, 2007). Its main purpose is to obtain close to 4π steradian measurements of solar wind thermal and suprathermal (halo) electrons with sufficient angular and time resolution to allow use of the highly anisotropic heat flux electrons (energies \sim 300–800 eV) to characterize the local magnetic field topology and its solar connections.

To accomplish its goals, SWEA measures the distribution function of the solar wind thermal and suprathermal electrons from \sim 0 to \sim 3000 eV with the instrument shown in Fig. 10. SWEA's top-hat (\sim 90° symmetric quadrangular) electrostatic analyzer (ESA), with 360° acceptance angle in a plane, uses electrostatic deflectors to provide \pm 65 degree coverage in elevation out of the plane. Electrons entering the SWEA ESA at different azimuthal angles are focused onto stacked microchannel plate (MCP) detectors at 16 angular locations.

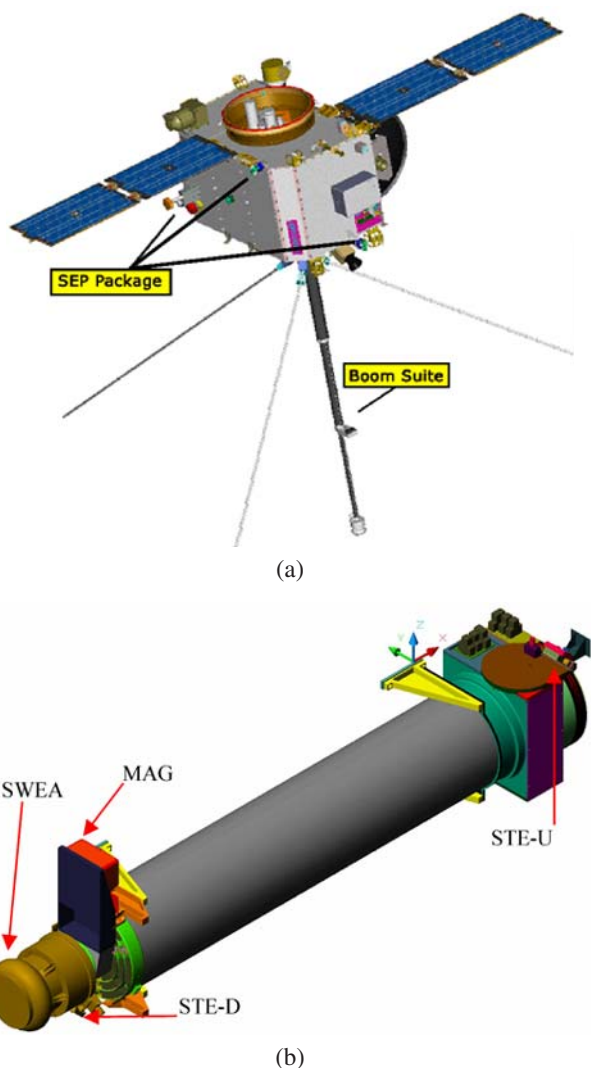
Table 1b Summary of IMPACT instruments and their basic measurements

Experiment	Instrument	Measurement	Energy or mag. field range	Time res.	Instrument provider
SW	STE	Electron flux and anisotropy	2–100 keV	10 s	UCB
	SWEA	3D electron distrib., core & halo density, temp. & anisotropy	~0–3 keV	3D = 30 s 2D = 8 s Moment. 2 s	CESR + UCB
MAG	MAG	Vector field	±500 nT, ±65536 nT	1/8 s	GSFC
SEP	SIT	He to Fe ions ^3He	0.03–5 MeV/nuc 0.3–0.8 MeV/nuc	30 s 30 s	U. of Md. + MPS + GSFC
SEP	SEPT	Diff. electron flux Diff. proton flux Anistropies of e, p	30–400 keV 60–7000 keV As above	1 min 1 min 1 min	U. of Kiel + ESA
	LET	Ion mass numbers 2–28 & anisotropy ^3He ions flux & anisotropy H ions flux & anisotropy	2–40 MeV/nuc 2–15 MeV/nuc 2–13 MeV	1 min 1 min 1 min	Caltech + GSFC + JPL
	HET	Electrons flux H He ^3He	1–6 MeV 13–100 MeV 13–100 MeV 15–60 MeV/nuc	1 min 1 min 1 min 1 min	GSFC + Caltech + JPL
IMPACT Common	IDPU (+Mag Analog)	—	—	—	Caltech + GSFC UCB

The output provides \sim 22.5 degree resolution in azimuth and elevation. This type of detector system has been successfully flown on both WIND and FAST.

SWEA is mounted at the end of the \sim 5.8 m IMPACT boom, with the magnetometer sensor mounted \sim 1 m inboard. This provides a SWEA open field of view over $>\sim$ 91% of the sky; with the spacecraft plus solar panels blocking \sim 3.5% of the remaining 9%. The wide SWEA field of view is illustrated in Fig. 9. With this capability, the directionality of the suprathermal electrons can be determined even when the interplanetary magnetic field rotates far out of the ecliptic, as is often observed in ICMEs. SWEA also measures the thermal solar wind plasma, or core, electrons, allowing determination of the core/halo relationships and the calculation of bulk solar wind properties from the electron 3D distribution moments. The nominal time resolution for full 3D distributions, and hence moments, from SWEA is 30 s.

Fig. 8 **a** STEREO Behind spacecraft, showing the two IMPACT instrument suites. **b** The IMPACT Boom Suite, including SWEA, STE and MAG instruments. **c** The IMPACT SEP suite on the body of the Ahead and Behind spacecraft, including SEPT, SIT, LET and HET



Measurements of the electron distribution at low energies are affected by the spacecraft potential. An illuminated spacecraft emits photoelectrons and charges up to a few volts positive potential for typical solar wind conditions. The potential of a spacecraft adjusts itself so that the flux of escaping photoelectrons approximately equals the flux of ambient electrons that hit the spacecraft surface. The STEREO spacecraft exterior surfaces are conductive to avoid the related development of large potentials that can strongly distort the incoming electron trajectories. Nevertheless, the low energy portion of the ambient distribution function may not be accurately resolved. IMPACT's design allows the potential of the SWEA instrument to be set to the spacecraft potential so that measurements can be made with full spectral resolution of the analyzer over the entire electron distribution. Such biasing has been successfully implemented on the UCB electron sensor on the Mars Global Surveyor spacecraft. To ensure a minimal impact of spacecraft charging on the SWEA measurements, a NASCAP analysis was performed by Mandell et al. at SAIC (personal communication,

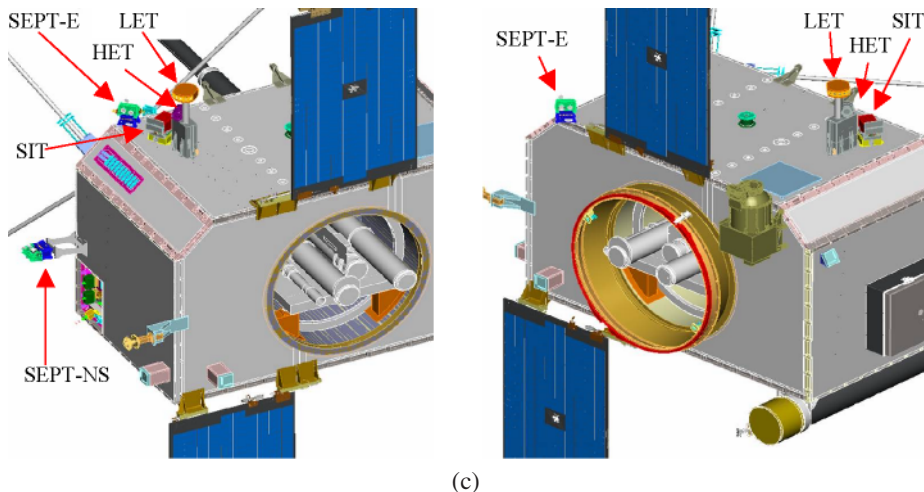


Fig. 8 (Continued)

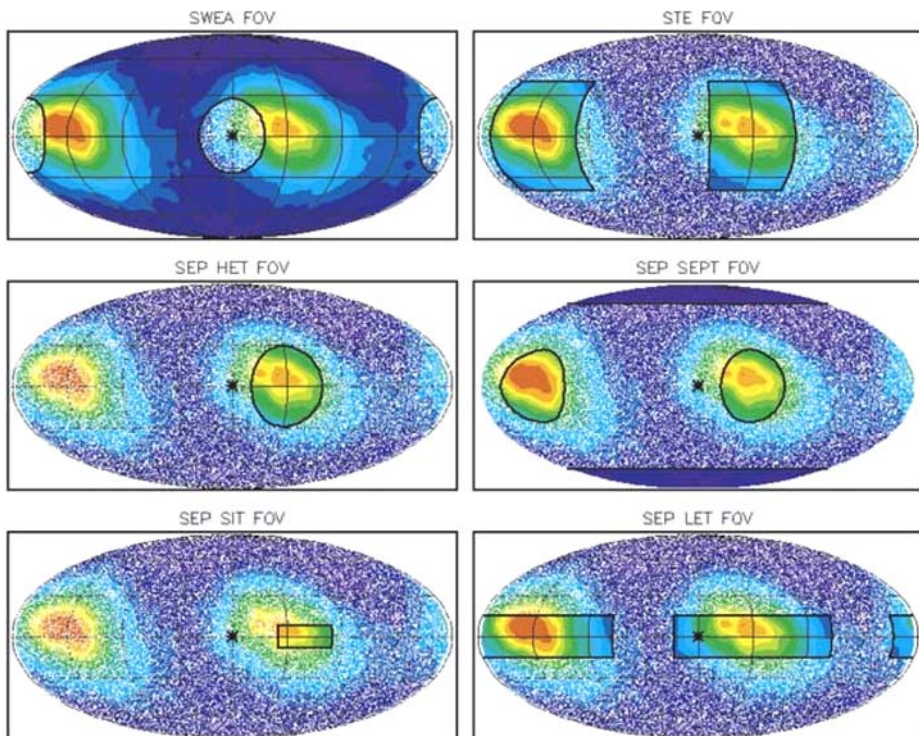


Fig. 9 IMPACT particle sensors fields of view (Reproduced from Luhmann et al. 2005). The color contours show the statistics of the interplanetary field on a mercator projection with the center of the plot toward the Sun. The speckled regions are outside of the field of view. Many of the SEP instruments focus on the nominal Parker Spiral field direction, while the SWEA instrument nearly covers the entire directional sphere

Fig. 10 Photograph of a SWEA/STE-D flight unit



2002). That analysis provided recommendations for materials to use on the spacecraft surfaces. These included black kapton blankets or ITO silver teflon. The notable exception is the solar array front surface (which is non-conductive but always sunlit and so will not charge much). These electrostatic cleanliness measures were regarded as sufficient to preserve the low energy electron measurements given the length of the IMPACT boom.

While the PLASTIC ion analyzer measures the solar wind plasma ion moments that are typically used to characterize solar wind density, bulk velocity, and dynamic pressure, SWEA thermal plasma electron measurements provide a reliable confirmation of the ion moments together with the (anisotropic) electron temperature in different solar wind and CME-related interplanetary structures. Figures 11a,b use analogous WIND 3DP electron data (Larson et al. 1997) to illustrate that accurate electron-based solar wind moments can usually be obtained with a SWEA-like instrument.

Once it is commissioned, SWEA requires only minimum commanding to reset the potential bias mentioned above, if desired. SWEA participates with STE and MAG in an IMPACT burst mode of operation, described below, which allows brief periods of 2 s full 3D distributions to be obtained for periods of 10 min around a specified triggering event.

3.2.2 STE (*Suprathermal Electron Telescope*)

STE, the University of California, Berkeley, suprathermal electron telescope, is a new instrument that measures \sim 2–100 keV electrons moving in the sunward and antisunward directions along the local Parker Spiral interplanetary fields with some angular resolution in the ecliptic plane. Lin et al. (this volume, 2007) describe STE in detail. STE is included in IMPACT to cover solar electrons in the energy range above SWEA that generate type III radio bursts, shock accelerated electrons that produce type II radio emission, and the super-

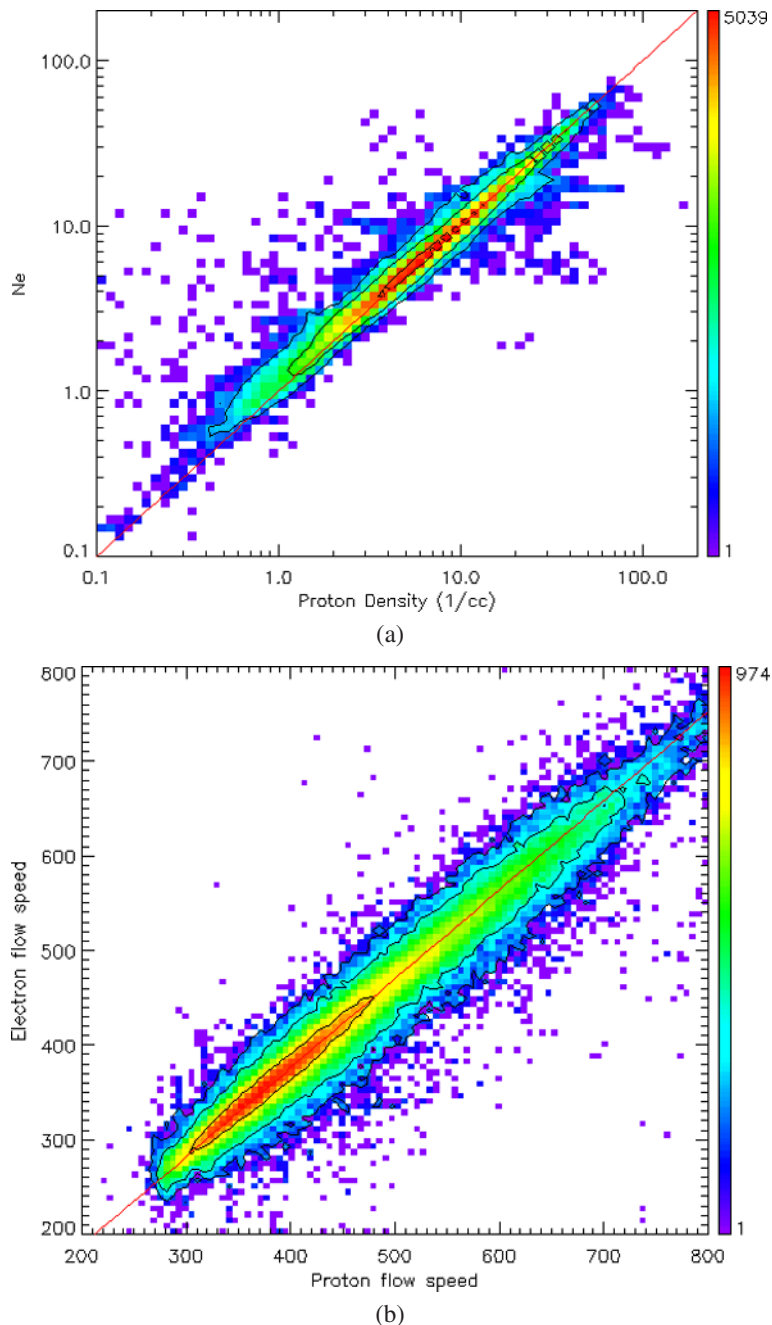
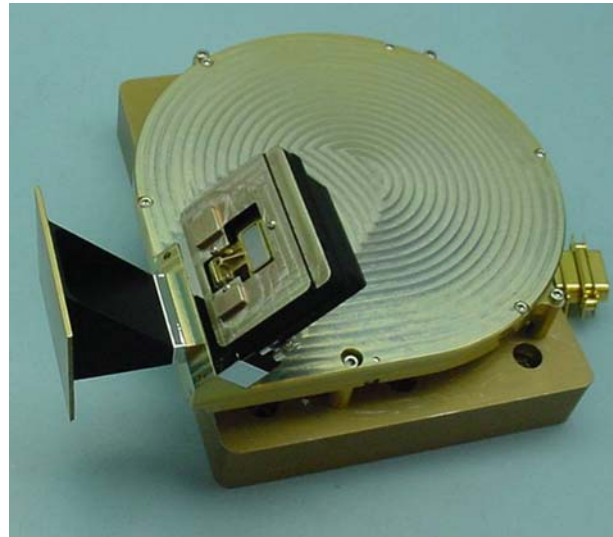


Fig. 11 **a** Plasma proton density measured on WIND with 3DP compared with the plasma electron density measurements. 3DP electron measurement techniques are similar to those used for SWEA. **b** Comparison of plasma bulk speed derived from WIND 3DP proton and electron data. The electrons provide accurate alternate measures of solar wind density and speed under most conditions

Fig. 12 Photograph of a STE-U flight unit



halo electrons (whose origin is unknown) during quiet times. The superhalo was discovered by the high sensitivity electron measurements on WIND using a very large geometric factor electrostatic analyzer, EESA-H. Even so, the count rate above ~ 2 keV at quiet times was dominated by intrinsic background counts of the very large microchannel plate detector. Thus, weak impulsive electron events could not be detected on wind, and the superhalo observations could not be carried out without long integrations.

The STE sensors provide high sensitivity with low background by using small, low capacitance, low leakage current, passively cooled silicon semiconductor detectors configured in arrays on a wafer, together with low power, low noise electronic chains. Laboratory tests show that electrons down to ~ 1.5 keV energy can be detected. The overall energy range for stopping electrons is ~ 1.5 to ~ 100 keV. STE's intrinsic energy resolution is about 1 keV; its telemetered data resolution varies from $\sim 7\%$ to $\sim 20\%$ (ΔE over E). The STE design uses two arrays consisting of four SSDs in a row. Each array looks through a rectangular opening that provides a $\sim 20 \times \sim 80$ deg. field of view for each SSD (~ 1 steradian solid angle); adjacent fields of view are offset from each other by ~ 20 degrees. The custom-designed low power preamp-shaping electronics are mounted next to the SSDs to minimize noise pickup.

A picture of one of the upstream units of STE (STE-U) is shown in Fig. 12. The downstream units (see Fig. 6b) of STE (STE-D) are located at the end of the boom, where they share an electronics box and harness with SWEA. The upstream units of STE (STE-U) are at the boom's sunward end, pointing along the Parker Spiral interplanetary field, while STE-D points in the opposite direction. This requires different arrangements on the two observatories. Figure 9 shows the two-part STE's combined field of view. The STE units include doors to protect the detectors from exposure to sunlight during spacecraft commissioning and reorientations, and from possible contamination during thruster firings. The doors also contain thin film radiation sources that are available for calibrating the STE sensors throughout the STEREO mission.

Although STE uses a new detector design, the previous measurements in this electron energy range made with the less sensitive traditional solid state detector telescopes on the WIND spacecraft demonstrated the concept and the value of the measurement. Figure 2

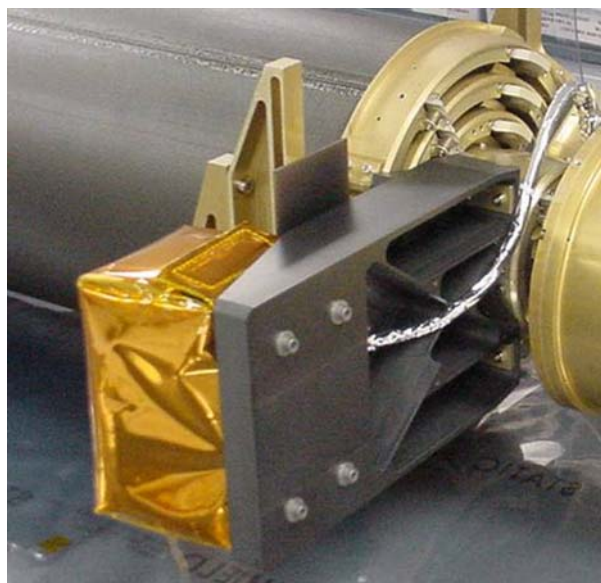
showed in situ measurements of an ICME from Larson et al. (1997) in which electrons in the STE energy range are detected within the ejecta identified with the other plasma and magnetic field measurements. These were interpreted as resulting from local magnetic field connections to a flaring active region at the time of the ejecta arrival at the WIND spacecraft. The velocity dispersion of these electrons was used to estimate the length of the field lines in the ejecta. STE measurements are intended to allow such magnetic topology and connectivity analyses routinely.

STE requires on-orbit commanding only to open and close its doors as desired. These doors are generally expected to remain open after commissioning, except perhaps during times of STEREO off-axis pointing maneuvers and major thruster firings. STE's nominal time resolution for electron fluxes and spectra is 10 s. Like SWEA and MAG, STE participates in the IMPACT burst mode operations described below, providing 2 s resolution data for 10 min periods around triggering events.

3.2.3 MAG (*Magnetometer*)

Figure 13 shows the IMPACT magnetometer, MAG. MAG is a triaxial fluxgate Magnetometer built at Goddard Space Flight Center to measure the vector magnetic field in two ranges up to 65,536 nT and up to 500 nT with 0.1 nT accuracy. It is a high-heritage instrument, with updated features based on the MESSENGER magnetometer design. The location of the magnetometer near the end of the ~5.8 m IMPACT boom (see Fig. 8a) minimizes the contribution of any spacecraft fields to the measurements. In addition, a magnetics cleanliness program was enforced from the beginning of the project in order to provide a minimum cost, intrinsically clean spacecraft from a magnetics perspective. This was achieved by sensitizing instrument and spacecraft providers to materials uses and design and construction practices, by screening particularly troublesome parts such as reaction wheels, and by magnetically “sniffing” the instruments from all investigations prior to their delivery as well as the spacecraft and the integrated system. In addition, magnetic

Fig. 13 Photograph of an IMPACT MAG flight unit on its boom tray



field data were obtained during integration and test phases to keep track of and characterize unavoidable signatures in the MAG data from permanent instrument and spacecraft features, and during spacecraft and instrument commissioning operations. The MAG design, calibration and operation is described in detail in a companion paper by Acuna et al. ([this volume, 2007](#)).

The digital resolution of the 500 nT range of the IMPACT MAG is 16 pT. Signals from the fluxgate sensor are processed by the analog electronics and then fed to the IDPU for interfacing to the spacecraft. These magnetometer raw data are low pass filtered, digitized, averaged, and then formatted into a MAG telemetry packet. The magnetometer has sufficient sensitivity and dynamic range to study the magnetic fields associated with all the phases and regions of interest in the mission. For example, the lower sensitivity range permits MAG operation in the Earth's field without special shields or field cancellation equipment. The limitation of the measurements is the amount of magnetic noise introduced by the spacecraft and its instruments. The nominal accuracy of ± 0.1 nT is adequate to achieve the STEREO mission science objectives for the magnetometer. The nominal time resolution of the MAG data is 8 vectors/s, though 32 Hz (~ 0.03 s) vector data are available during the IMPACT burst mode periods described below.

The IMPACT magnetometer is one of a long and successful line of instruments provided by GSFC for planetary, earth observing and space physics missions. The sensors and analog electronics are high performance, low noise, wide dynamic range off-the-shelf designs that have been or are being flown on numerous NASA, ESA and ISAS missions (e.g. Voyager, AMPTE, MAGSAT, GIOTTO, DMSP, WIND, CLUSTER, MGS, GEOTAIL, Lunar Prospector, Messenger). Virtually every in situ instrument on STEREO uses the MAG data (some on-board) to support their own data interpretation. Planned spacecraft rolls throughout the mission allow checks on the MAG sensor offsets and calibrations. No regular commanding is needed for MAG.

3.3 SEP Suite

IMPACT's SEP (Solar Energetic Particle) suite (Fig. 8c) is made up of SIT, the Suprathermal Ion Telescope, SEPT, the Solar Electron and Proton Telescope, LET, the Low Energy Telescope, and HET, the High Energy Telescope. Together, the SEP suite covers measurements of heliospheric electrons from 0.03–6 MeV, protons from 0.06–100 MeV, Helium ions from 0.12–100 MeV/nucleon, and heavier ions from 0.03–40 MeV/nucleon. It represents the next step in state-of-the-art measurements of SEPs carried out on ACE and WIND, which began to reveal the physics of SEP sources, acceleration, and transport through comprehensive energy range and composition measurements. A SEP-central Data Processing Unit is included as part of the LET/HET electronics box. Many of the SEP suite data handling functions are performed within SEP central, although there are also dedicated processors in SIT, and LET/HET, and the spacecraft telemetry interface is via the IMPACT IDPU-as it is for the Boom suite.

3.3.1 SEPT (Solar Electron and Proton Telescope)

The University of Kiel and ESA provided the SEPT (Solar Electron and Proton) telescopes to detect the dominant proton and helium ions, and the energetic electrons, of the SEP population using a two-part double-ended solid state detector design. Details on the SEPT instrument can be found in the paper by Mueller-Mellin et al. ([this volume, 2007](#)). Two double-ended telescopes in each unit, illustrated in Fig. 14, provide oppositely directed measure-

Fig. 14 Photograph of the SEPT telescope pairs (SEPT-E and SEPT-NS) for both spacecraft, showing their aperture doors open on the *left*, and closed on the *right*



ments of both protons and alphas (fully ionized Helium ions) in the energy range 0.06–7.0 MeV and electrons in the energy range 30–400 keV. Separate units of double ended telescopes are mounted on the spacecraft in locations where one obtains information on particles traveling both ways along the local Parker Spiral magnetic field (SEPT-E), while the other provides the same measurements looking up and down from the ecliptic, or North and South (SEPT-NS). Their combined fields of view on each spacecraft can be seen in Fig. 9.

SEPT employs ion-implanted planar silicon detectors (PIPS) to obtain high sensitivity measurements of the particle energy while broom magnets and foils are used to separate electrons and ions. The double-ended magnet/foil design allows detection of electrons incident from the foil side with an essentially unaltered spectrum. Ions are registered when incident from the magnet side. A rare earth permanent magnet (NdFeB) sweeps away electrons below 400 keV, but leaves ions unaffected. Using a magnet system with one magnet serving two telescopes by way of two air gaps minimizes the weight, and together with the use of low noise, high performance analog electronics allows anisotropy measurements otherwise impossible within the weight constraints. Particle anisotropy information on the nonspinning spacecraft is obtained from the observations in four look directions. The geometry factor for each of the four magnet telescopes is $0.17 \text{ cm}^2 \text{ sr}$ and for each of the four foil telescopes $0.13 \text{ cm}^2 \text{ sr}$. Unobstructed view for four viewing directions along and perpendicular to the interplanetary magnetic field necessitated different locations on the Ahead and Behind STEREO spacecraft (see Fig. 8c).

The SEPT design is based on techniques for which long-standing experience exists at the University of Kiel, ESA's Research and Scientific Support Division, and the University of California, Berkeley. On SOHO, rare-earth magnets were also successfully implemented. ESA and University of California, Berkeley, designed and built the Solid State Telescope (SST) onboard the WIND spacecraft that is still in operation. SST included many elements of the SEPT design. In the area of new technologies, SEPT uses miniaturized electronics based on a Mixed Analogue/Digital Application Specific Integrated Circuit (ASIC) which has been developed for the Space Science Dept. of the European Space Agency (ESA). This circuit contains almost all of the circuitry required to process the signal coming from

a solid state detector. A simple logarithmic compression algorithm run in the SEP Central DPU is used to reduce the telemetry bitrate requirement to 72 bps. There are no SEPT requirements on the IMPACT IDPU other than receipt of commands (less than 20) and collecting telemetry data.

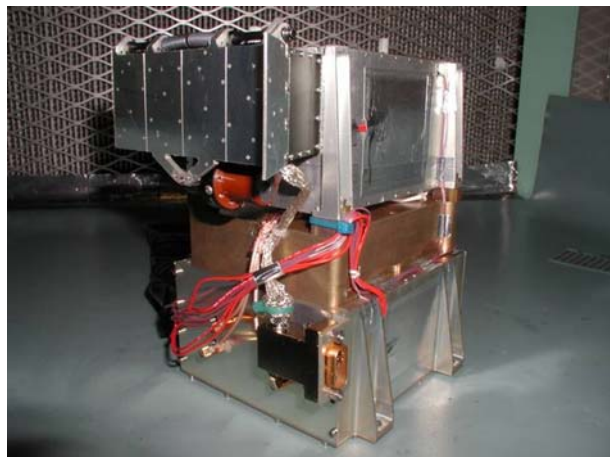
SEPT provides what may be considered the most basic STEREO SEP measurements in both the STEREO beacon and research data sets. Its observations of both electrons and major ions in the primary energy ranges of SEPs provide time profiles of both impulsive and gradual events, and anisotropies indicating the approach and recession of the ICME shock source of SEPs, as well as isotropization at the ICME shock passage. The interpretations of the SEP ion composition data from SIT and LET will depend on comparative analysis with SEPT observations.

3.3.2 SIT (*Suprathermal Ion Telescope*)

SIT is a time-of-flight (TOF) ion mass spectrometer included in IMPACT to measure ion composition in the SEP low energy (suprathermal) range. Details about SIT's design, construction and calibration at the University of Maryland, Max-Planck Institute for Solar System studies in Lindau, and Goddard Space Flight Center are given in the accompanying paper by Mason et al. ([this volume, 2007](#)). SIT measures the elemental composition of He–Fe ions from \sim 30 keV/nucleon to 2 MeV/nucleon, thus covering the energy range between the PLASTIC Plasma Ion Analyzer (see Galvin et al., [this volume, 2007](#)) and the IMPACT Low Energy Telescope (LET). The isotopes ^3He and ^4He are well resolved by SIT, allowing clear identification of ^3He -rich impulsive solar particle events, critical for distinguishing between flare and interplanetary shock sources. One of the SIT instruments is shown in Fig. 15, where the telescope box (aperture cover closed) is visible on top of the amber high voltage power supply box and the electronics box at the bottom.

Ions enter the SIT telescope through two thin entrance foils (1000 Å Ni) and stop in the solid state detector. Secondary electrons from the entrance foil are accelerated, and deflected so as to strike chevron microchannel plates (MCPs), providing a START signal for the time-of-flight measurement. The STOP signal is obtained from secondary electrons emitted when the ion strikes the solid state detector. The solid state detector signal also provides a measurement of the kinetic energy of the ion. The time-of-flight T , the energy E , and the known path length in the telescope L are then combined to derive the mass of the ion: $M = 2E(T/L)^2$.

Fig. 15 Photograph of the SIT flight unit for the Ahead spacecraft



The incident energy is obtained by correcting for the energy losses in the entrance foil and detector window. The MCP and detector areas are each 6.0 cm^2 ; the solid state detector is a silicon ion implant detector with 500 micron active thickness.

The SIT geometry factor is $0.29\text{ cm}^2\text{ sr}$, and thus large enough to allow study of even small impulsive solar particle events. For each ion triggering the telescope, time-of-flight and energy information are obtained. Full information on selected events is telemetered, and all events are classified into mass and energy bins which are summed on-board to allow rapid accumulation of intensities and spectra. The on-board analysis is done within SIT using a MISC processor. SIT uses the common SEP low-voltage power supply, obtains detector bias from the SEP Central DPU element, and generates its own high voltage ($\sim 3.5\text{ kV}$) for the microchannel plate/secondary electron assembly. The SIT telescope and electronics are located on the spacecraft body near the LET, HET and SEP Central boxes (see Fig. 8c). The $\sim 44^\circ$ field of view of the telescope, illustrated in Fig. 9, is pointed at a small angle to the nominal interplanetary field direction, with its center at about 60° to the solar direction. A sunshade prevents solar UV from striking the telescope entrance foil. A mechanical door protected the foil from acoustic damage during launch.

The SIT plays a key role in the IMPACT SEP Suite. Many impulsive solar particle events produce enhancements in the sub-MeV/nucleon range that identify connection to active regions at the Sun. During ICME passages, ${}^3\text{He}$ -rich flare events have been observed along with impulsive suprathermal electrons, implying that at least one foot of the local magnetic field remains at least intermittently attached to the corona on those occasions (Mazur et al. 1998). SIT also provides important information in the interpretation of observations by the IMPACT Solar Electron Proton Telescope (SEPT, described above). Because SEPT counts all ions, protons usually dominate the signal, but in instances of steep energy spectra, He and heavier ions can dominate. SIT will allow the proper interpretation. Moreover, by measuring low energy ion spectra and composition at two points along a shock with STEREO, SIT provides insights into the role of suprathermal seed particles in the shock acceleration of SEPs.

Forerunners of SIT include the LICA instrument on SAMPEX, the EPACT/STEP instrument on WIND, and the ULEIS instrument on ACE. Each of these sensors was developed and constructed at the University of Maryland. The SIT telescope design is identical to EPACT/STEP. The TOF digitizing circuit was newly developed by MPS for IMPACT. GSFC collaborated on many aspects of SIT development and testing including mechanical and thermal design, assembly and integration.

SIT was calibrated with laboratory alpha-sources, and the engineering model telescope and flight electronics were tested with heavy ion beams at the Brookhaven Tandem van de Graaff accelerator facility. Post launch, instrument calibration is easily monitored from the appearance of the time-of-flight vs. energy data. If drifts do occur, the instrument's internal mass binning tables can be modified by ground command. After initial turn-on, the SIT aperture cover was opened, but SIT requires no subsequent routine commanding other than occasional (every few months) adjustment of microchannel plate bias voltages.

3.3.3 LET (Low Energy Telescope)

Caltech and the Jet Propulsion Laboratory provided IMPACT's LET (Low Energy Telescope) to obtain high time-resolution measurements of the composition and energy spectra of heavy ions in solar energetic particle events and in interplanetary space. LET is a novel dual directional fan-like solid state detector telescope, with ion composition capability in

the energy range above that of SIT. It uses a dE/dx vs. E telescope configuration to provide measurements of elements from He to Ni ($2 \leq Z \leq 28$) over the energy from ~ 2.0 to ~ 40 MeV/n (depending on species) and H over a limited range from ~ 2 to ~ 13 MeV. LET also measures trans-iron nuclei with $30 < Z < 83$. A more detailed description of LET can be found in the accompanying paper by Mewaldt et al. (this volume, 2007).

Previous SEP studies have demonstrated that both the elemental and isotopic composition of SEPs vary significantly from event to event and composition signatures such as ${}^3\text{He}/{}^4\text{He}$, He/H, Fe/O, Ne/O and e^-/p have become the most common way in which the flare-related impulsive events and CME-driven shock acceleration events are identified. LET will make accurate composition measurements in the critical 2 to 40 MeV/nuc energy range. This energy interval is also low enough to include a large number of solar events, but not so low that velocity dispersion washes out the time structure of acceleration effects near the Sun. The combination of SIT (described above) and LET, and also HET (described below) give complete coverage from ~ 0.05 to ~ 100 MeV/n of many species, providing important tests of acceleration models. Real-time space-weather data from LET are of special interest for identifying heavy-ion rich solar events that extend to high energy (> 50 MeV/nuc) because Fe and other highly ionizing nuclei are capable of creating single-event upsets (SEUs) in critical spacecraft hardware. During solar active periods fluxes and energy spectra of more than a dozen species are available from LET on a continuous basis.

The LET, shown in Fig. 16, uses a fan-like array of 10 thin devices in combination with a four-detector central stack. All detectors are ion-implanted devices for high reliability and

Fig. 16 Photograph of a LET and HET flight unit, together with a SEP Central box. LET has the wide-field telescope head at the *top* of the picture. HET is the smaller cylindrical telescope in the *middle left of the LET platform column*



low leakage current. The symmetry axis of the telescope is aligned along the average Parker spiral ($\sim 45^\circ$ from the solar direction). Five detectors arrayed at each end combine to cover ~ 150 deg in each direction in the ecliptic plane looking sunward and antisunward. LET is mounted on the spacecraft so that the array of detectors has an unobstructed field of view, illustrated in Fig. 9. The multi-element double-ended front end achieves a geometric factor of $\sim 4.0 \text{ cm}^2\text{-sr}$, while providing particle anisotropy measurements over ~ 260 deg of the ecliptic plane.

During large solar particle events the detection rate can approach 1000 nuclei per second, far more than can be handled by the bit-rate allocation to LET if all measured pulse heights were telemetered. However, on-board processing algorithms enable the atomic number and energy of each of these events to be identified and accumulated in a Z (mass) $\times E$ (energy) matrix that is telemetered every minute. This approach, which has been successfully employed in the LEMT instrument on WIND, makes it possible to achieve excellent statistical accuracy for studying time variations of SEP ion spectra and composition.

The particle detection and instrumentation approaches are based on a long series of successful energetic particle experiments flown on OGO, IMP, Pioneer, Helios, Voyager, ISEE-3, SAMPEX, WIND, and ACE by the Goddard and Caltech groups and their collaborators. LET uses detector designs derived from experience on ISEE-3 and WIND, and low-power front-end electronics based on designs developed for three instruments on ACE (Stone et al. 1998a, 1998b). LET also exploits designs and on-board particle identification techniques developed for WIND/LEMT (von Rosenvinge et al. 1995).

LET requires only infrequent commanding to update on-board algorithms and possibly adjust thresholds. An average data rate of 577 bps includes 1-minute average count rates of 16 species in ~ 12 energy intervals, pitch angle distributions for key species, count rates of individual detectors, and housekeeping data.

3.3.4 HET (High Energy Telescope)

The High-Energy Telescope (HET) provided by GSFC and Caltech is designed to make key measurements of the intensity and energy spectra of the higher energy H and He ions, and electrons accelerated in solar energetic particle events. Together with SEPT, SIT, and LET, HET will provide IMPACT solar particle energy spectra over three decades of energy. In addition, HET provides measurements of the elemental composition of $Z > 2$ nuclei with energies $> 30 \text{ MeV/n}$, thereby extending the energy range of LET for key species. HET uses an all-solid-state design, and low-power electronics to achieve its objectives with minimal weight and power resources. On-board analysis algorithms provide real-time fluxes of key species important to the STEREO beacon applications, including protons and He with energies of ~ 13 to $\sim 100 \text{ MeV/n}$, and electrons with energies from 1 to 6 MeV. Further details about HET can be found in the companion paper by von Rosenvinge et al. (this volume, 2007).

HET, shown together with LET in Fig. 16, includes two thick detectors on one end of a traditional telescope design to define the geometry of incident particles. The subsequent elements of the detector stack are made by combining thinner devices. Particles incident on the aperture which stop are identified using standard dE/dx total energy analysis. This includes protons and He with ~ 13 to $\sim 50 \text{ MeV/n}$. Higher energy H and He that penetrate can be identified using multiple dE/dx measurements up to $\sim 100 \text{ MeV/n}$. Measurements of ${}^3\text{He}$ extend from ~ 15 to $\sim 60 \text{ MeV/n}$. Although HET's response to electrons is more complex than its response to ions because of the effects of electron scattering, experience with similar telescopes (flown on IMP-7,8, Pioneer 10,11, Voyager 1,2 and SAMPEX) has

shown that HET will provide accurate measurements of the intensity and energy spectra of ~ 1 to ~ 6 MeV electrons during both solar particle events and at quiet times dominated by interplanetary Jovian electrons.

During SEP events the telemetry allocation to HET allows transmission of pulse-height data for only a small fraction of the particles triggering HET. As for LET, on-board processing algorithms are used to identify the charge and energy of the detected particles which are accumulated in a species vs. energy matrix that is telemetered once per minute. The design and operating principles of HET draw extensively on previous instruments of similar design flown by the Caltech and Goddard groups on missions that include IMP, Pioneer, Voyager, ISEE, SAMPEX and WIND. HET's detector designs are derived from these experiences and its low-power front-end electronics are based on designs developed for three instruments on ACE (Stone et al. 1998a, 1998b). Like LET, HET utilizes the on-board particle identification approaches developed for WIND (von Rosenvinge et al. 1995).

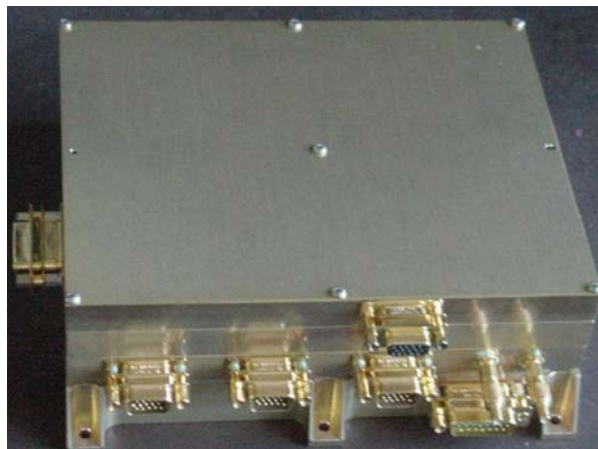
HET is mounted with its axis in the plane of the ecliptic, pointed upstream along the average Parker spiral interplanetary field (see Fig. 8c). Its field of view is compared with those of the other IMPACT SEP instruments in Fig. 9. The gain, offset, and energy conversion factors (MeV/channel) of all HET detectors were calibrated on the bench prior to launch. The response tracks of H, He, and other nuclei were also calculated using the measured detector thicknesses. As for LET and SIT, the final calibrations are performed in-flight by observing the response tracks of quiet-time and SEP particles. All parameters in the on-board identification scheme can be adjusted by command.

Like LET, HET is only infrequently commanded to update on-board algorithms and possibly adjust thresholds. The HET instrument requires an average data rate of 209 bps. This includes 1-minute average count rates of protons, He, and electrons in several energy intervals, samples of the pulse height data from individual events, once per minute dumps of the $Z \times E$ matrix, coincidence count rates, singles rates of individual detectors, and house-keeping data. HET also contributes 1-minute average fluxes of the most energetic SEP H, He, CNO, Fe ions and electrons, calculated on-board, to the real-time STEREO beacon data stream described below.

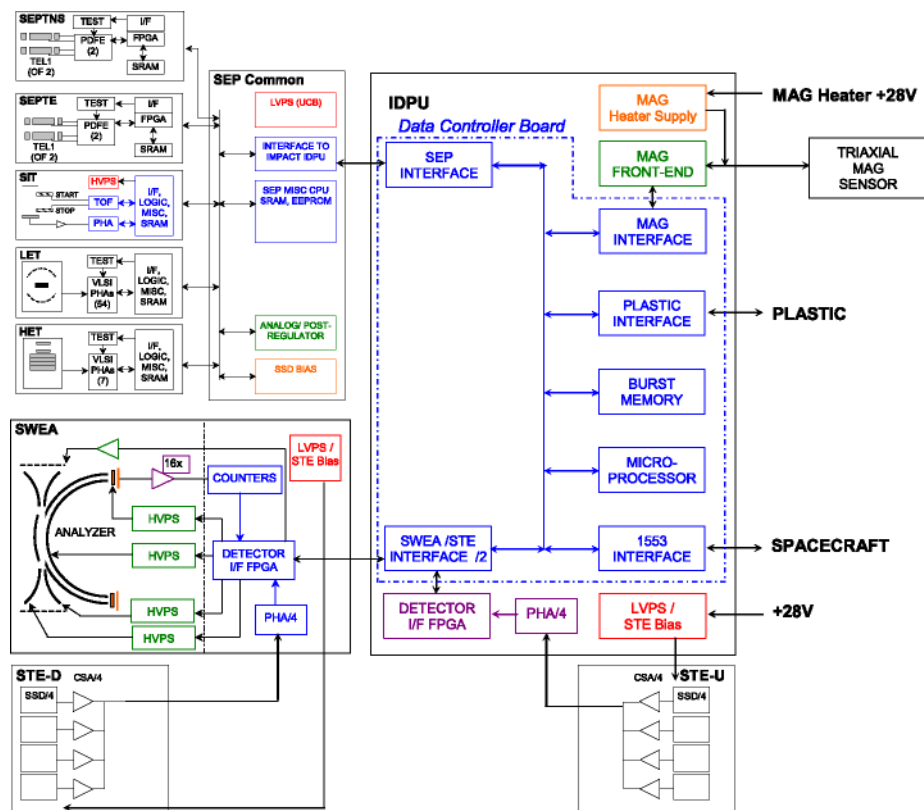
3.4 IDPU

IMPACT's Instrument Data Processing Unit or IDPU, shown in Fig. 17a, provides a single point digital interface to the spacecraft for all of the IMPACT instruments. It also serves the PLASTIC investigation with data processing and packaging services, and shares data with the SWAVES investigation to allow synchronized high data rate burst-mode operations (described below) following on-board identification of predefined triggering events in the IMPACT data. The IDPU is designed to manage instrument control and monitoring, the instrument timing clock, and instrument data collection, compression, and packetization for telemetry. MAG and STE-U analog interfaces also reside in the IDPU box while the other IMPACT instruments have their front-end electronics co-located with the instrument. Figure 17b shows a flow diagram of the IMPACT IDPU interfaces. Note that the SEP Suite instruments (SEPT, SIT, HET, and LET) interface with a SEP Common electronics box (SEP Central) that provides the IDPU with a single interface to the SEP suite. The IDPU is mounted inside the spacecraft body.

The IDPU occupies a small box that contains a low voltage power supply (LVPS), a MAG heater power supply, the MAG analog electronics board, a STE-U Interface board, and the Data Controller Board (DCB). The DCB contains an 80CRH196KD microprocessor, 3 Mbyte RAM, 256 Kbyte EEPROM and 8 Kbyte PROM memory, 1553 interface, and five



(a)



(b)

Fig. 17 **a** Photograph of an IDPU flight unit. The IDPU is mounted inside of the spacecraft. **b** Flow diagram showing the IDPU interfaces with the IMPACT instruments

identical serial instrument interfaces. The 1553 interface connects to the Spacecraft bus for commands and telemetry. Serial instrument interfaces connect the IDPU to the IMPACT instrument suite (MAG, SEP, SWEA/STE-D, STE-U), and to PLASTIC, providing commands, timing, and telemetry. The DCB PROM contains boot code which can load flight code from either the EEPROM or from the spacecraft interface (in the event of EEPROM failure or corruption). The EEPROM contains 4 copies of the flight code. The RAM is used for code, variables, and buffers. The majority of the DCB RAM is used for a burst memory to save high time resolution interval snapshots from MAG, SWEA, and STE, which are then played out slowly via telemetry. The Burst System captures interesting events based on criteria extracted from the IMPACT instrument data streams, plus SWAVES and PLASTIC instruments. Ten minute segments of high time resolution data are monitored onboard for the “best” event of interest within three hour intervals. SWAVES and IMPACT exchange burst criteria via the 1553 bus so that burst data capture can be coordinated on board. The telemetered burst data for every three hours is then the saved high resolution data in the 10 minutes centered on the best triggering event. The triggering criteria can be changed by commanding from the ground.

The IDPU LVPS provides power to the DCB, MAG, and STE-U. The other instruments are powered separately by the spacecraft. In addition to analog and digital supply voltages, the IDPU LVPS provides a programmable bias supply (0–150 V) for the STE-U detectors. The MAG heater supply provides AC power to the MAG sensor heater to maintain its temperature. AC power is required to avoid DC magnetic fields at the MAG sensor. The supply provides a 50 kHz pulse-width modulated supply controlled by a feedback loop using a temperature sensor in the MAG sensor. The MAG heater supply is independently powered by the spacecraft and functions independent of instrument power.

The IDPU was designed and constructed at the University of California, Berkeley, with the exception of the magnetometer front-end electronics, which were designed and fabricated by GSFC. It is conceptually identical to similar units successfully flown by UCB on previous spacecraft, such as the FAST SMEX mission. As on FAST, the system provides interfaces to diverse instrument types. Bringing all instruments to a common IDPU saves both instrument and spacecraft bus resources and complexity (only a single interface to the instrument complement). It also allows a more flexible sharing of instrument resources such as bit-rate, and enables collaborative science such as the coordinated burst data acquisition and shared/synchronized IMPACT and PLASTIC data sets. The common part of the IDPU was designed to be especially reliable and robust, with individual subsystems electrically isolated so that a failure in one does not impact the remainder.

Table 2 summarizes the properties and spacecraft resource requirements for the IMPACT investigation, including the IDPU, while Figs. 18a–c illustrate the overall scope of the IMPACT investigation particles measurements.

IMPACT, together with the PLASTIC ion composition and SWAVES plasma waves investigations, satisfies STEREO in situ measurement goals. The basic IMPACT data products, including the real time beacon data, are covered in a later section together with details about the IMPACT operations.

4 IMPACT Operations and Data Plans

4.1 IMPACT Payload Operations Center

STEREO mission operations are conducted from the MOC (Mission Operations Center) at APL (see Kaiser et al. and Thompson et al., [this volume, 2007](#)). However, the MOC receives

Table 2 IMPACT instrument resource requirements

Instrument	Mass	Power	Data rate
SEP:			
LET	1.32 kg ^e	1.18 W	577 bps ^g
HET	0.60 kg	0.36 W	218 bps ^g
SEP central	2.19 kg	4.06 W	9 bps ^h
SIT	1.63 kg	1.65 W	424 bps ^g
SEPT-E	0.80 kg	0.60 W	40 bps ^g
SEPT-NS	1.18 kg ^f	0.60 W	40 bps ^g
Boom:			
Boom	11.25 kg		
MAG sensor	0.27 kg	0 W	398 bps ^a
SWEA/STE-D	1.97 kg	3.81 W	534 bps ^b + 230 bps ^c
STE-U	0.40 kg	0.21 W ^a	
IDPU:	1.90 kg	5.67 W	697 bps ^d
Harness:			
Operational heaters:		5.30 W	
Blankets:	2.40 kg		
Total	27 kg	23 W	3200 bps

^aExcluding electronics in IDPU^bSWEA^cSTE-U + STE-D^dBitrate includes Housekeeping + Burst + Beacon^eIncludes 0.46 kg for LET mounting bracket^fIncludes 0.38 kg for SEPT-NS mounting bracket^gBitrate for Science + Housekeeping + Beacon, without CCSDS packet header^hBitrate for Housekeeping + Beacon, without CCSDS packet header

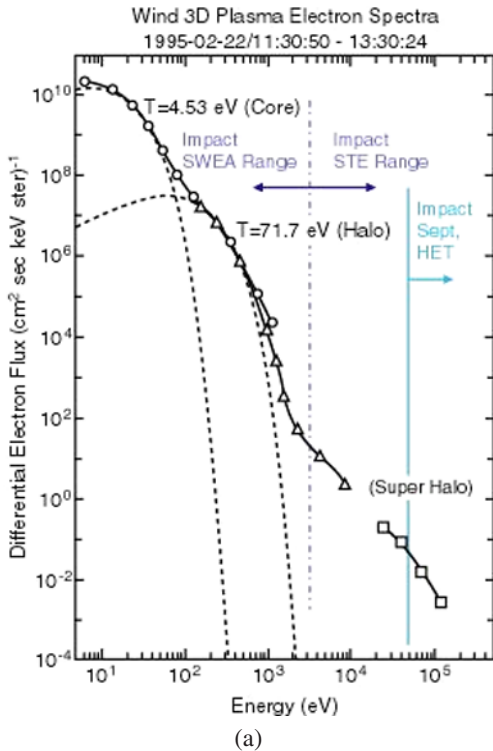
instrument commands from distributed investigation POCs (Payload Operation Centers) for upload to the spacecraft, and also distributes the Level Zero spacecraft data obtained from the Deep Space Network to the SSC (STEREO Science Center, discussed in this volume by Thompson et al., [this volume, 2007](#)) and the POCs. The IMPACT Payload Operations Center (POC) is located at the Space Sciences Laboratory at UCB. A second backup POC is located at the APL MOC in the event of a network failure at UCB.

4.1.1 Security

Both the UCB and APL IMPACT POCs are located in secure locations and are heavily firewalled to prevent misuse or accidental interference. The UCB POC is located in SSL's Mission Operations Center which currently supports secure operations for several missions including RHESSI and FAST.

The UCB Mission Operations Center has a dedicated backup generator in the event of a power failure. The diesel generator system delivers power to the Center within 10 seconds of power loss. Each IMPACT POC computer is connected to an uninterruptible power supply

Fig. 18 **a** Nominal interplanetary electron spectrum, showing how IMPACT measurements cover a large energy range, including thermal, suprathermal and energetic components. **b** Energy and species coverage of all of the in situ particle instruments on STEREO, showing the IMPACT contributions to both ion and electron coverage. Colors indicate protons (blue), electrons (red) and heavier ions (green). The PLASTIC investigation is only roughly indicated by the blue line (solar wind proton and alpha spectrum) and blue bar at plasma energies. Details of its broader energy and ion composition coverage are described by Galvin et al. (this volume, 2007). **c** IMPACT SEP suite instrument coverage of suprathermal and energetic ion composition. Here the colors indicate the instrument: SIT (black), LET (blue) and HET (red). SEPT (green) measures protons and alphas only



(a)

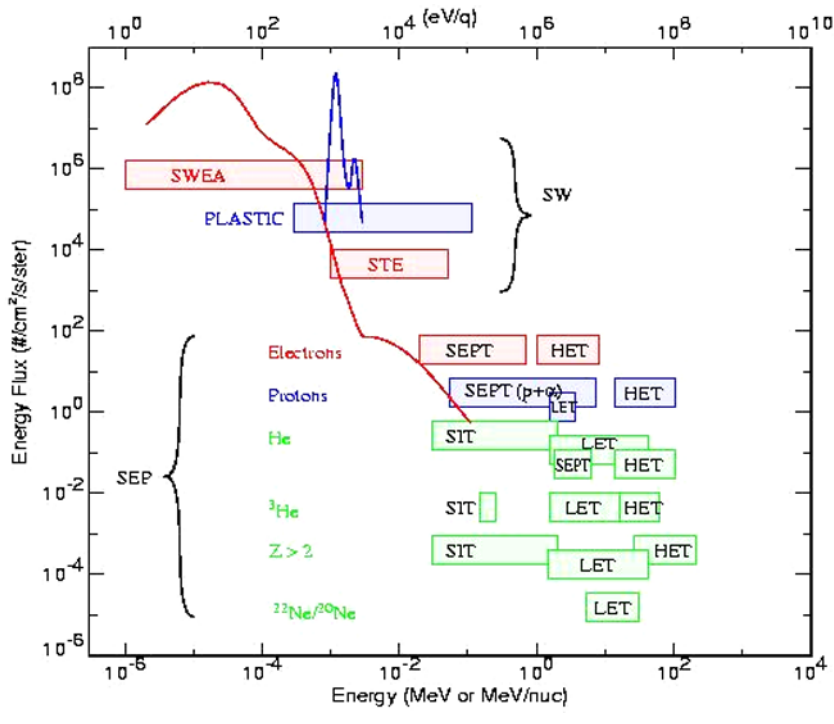
(UPS) to provide power during the potential 10 second gap in power. The diesel generator and UPS systems are tested twice monthly. Enough fuel for 24 hours of diesel generator operation is located onsite at all times.

4.1.2 Design of POC System

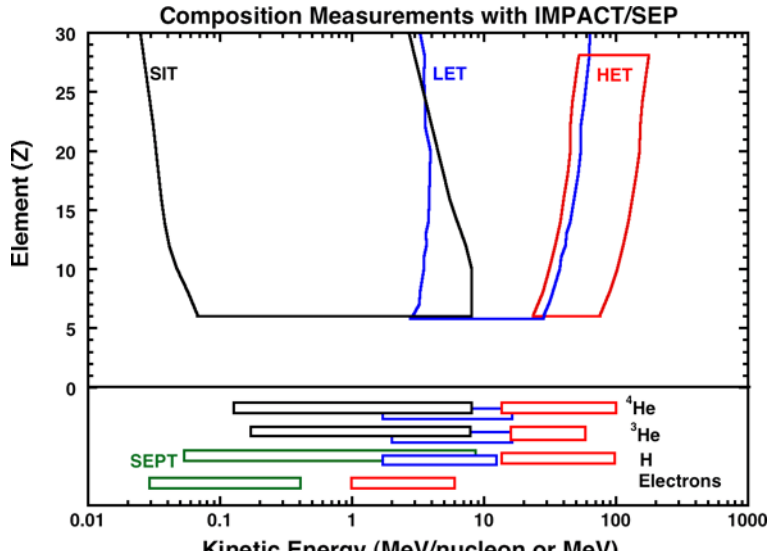
POC Operations System The IMPACT POC is an enhanced version of the existing IMPACT Command and Telemetry GSE which was used extensively in instrument testing and in Observatory I&T. The POC consists of two Windows XP, PC-based systems, one for each spacecraft, connected to the MOC over a TCP/IP network connection through secure shell (SSH) tunneling. It is capable of generating IMPACT commands and monitoring IMPACT's state of health using the real-time telemetry stream provided by the MOC.

The POC uses a system of command mnemonics that are translated into Supplemented Command Messages (SCMs) and forwarded to the MOC for uplink. The software is capable of encoding time-tagged commands and can run command scripts written in a subset of STOL. SCMs developed by the SEP team can be saved and forwarded to the MOC after being filtered for potentially hazardous commands and approved by the local operator at the POC. The software uses a closed-loop system for verifying command receipt by the IMPACT IDPU. Commands are verified by the IDPU via instrument housekeeping and noted by the POC software. A log of all commands sent to the MOC is maintained by the software.

The POC software collects, decodes, displays and performs limit checks on the instrument state of health telemetry. The POC automatically notifies the POC operator if it detects a limit violation or other error. A log of these limit violations and errors is also maintained.



(b)



(c)

Fig. 18 (Continued)

Real-time telemetry is saved to a local archive. The POC can generate trend plots of selected telemetry points and can display periodic instrument parameter table dumps. Separate software modules for display of IMPACT science data are provided to the IMPACT team. These modules have the ability to connect to the IMPACT POC in real time over a TCP/IP connection. In this way, team members at their home institutions can both verify instrument state of health and monitor science data in real time.

POC Data System The data processing plan is designed to minimize cost, optimize data quality and enable efficient dissemination with one point of contact, the Operations/Data Manager (ODM) at UCB. P. Schroeder is the current IMPACT ODM. The instrument providers deliver specialized software to the ODM for the routine processing of the raw spacecraft data, as well as updates based on ongoing evaluations of the received data and software performance. The ODM maintains a secure website for data and software exchange, tracks versions and anomalies, and works with the STEREO project and the IMPACT team to optimize the data sets and enable their use. The main portals to the IMPACT comprehensive data set are at UCB-SSL and the SSC. SSL maintains a website with browse and download capabilities. SSL is also responsible for delivering the archive of processed IMPACT data to the SSC. Higher level, science-quality, key parameter data that includes merged 1-min resolution subsets of IMPACT, PLASTIC and SWAVES key parameter data, together with selected event data identifications and characterizations, are made available through another data server at UCLA.

Figure 19 summarizes the data flow from receipt from the STEREO MOC through to the data archive. The Level zero data are unpacked, time sorted, and distributed to the STEREO teams by the MOC. The IMPACT Level zero data are downloaded to SSL, catalogued, and distributed by the ODM to the individual IMPACT instrument teams. The instrument provider is responsible for quality checking their data and informing the ODM of any irregularities. The ODM analyzes and reports any such irregularities in either the instrument or IDPU level zero data and records them in a database to be archived with Level 1 data. The Level zero archive includes the space weather beacon data.

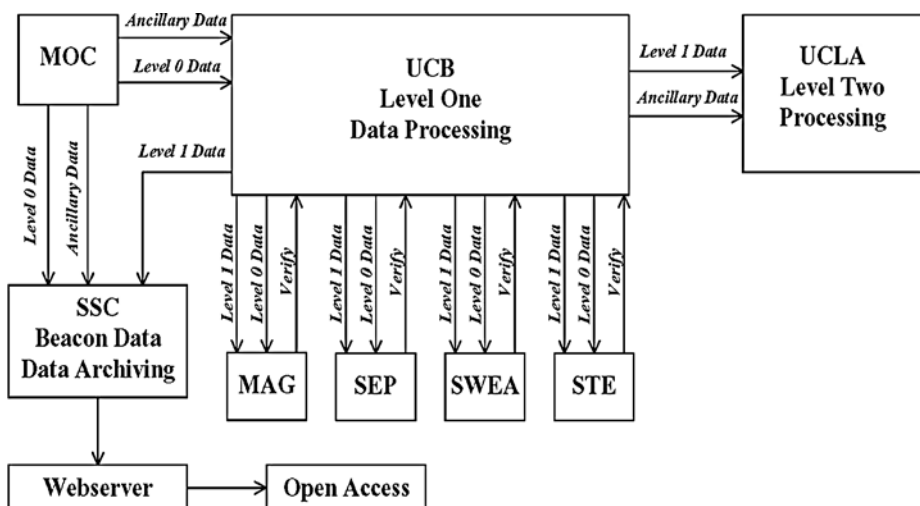


Fig. 19 Diagram of the IMPACT data processing and products flow

Level 1 data are obtained by running the Level zero data through the calibration and IMPACT data processing software at UCB. Original versions collected by the ODM from each instrument provider prior to launch are updated as necessary by the developer. Both the Level zero and Level 1 data, together with calibration and basic processing software for the full investigation, are regularly submitted to the designated project archives at the SSC by the IMPACT ODM. These Level 1 data are also referred to as high (time) resolution data, and contain all of the measurement results available from the IMPACT instruments in physical units.

The second stage of IMPACT data processing, at an in situ STEREO data access site at UCLA, generates Level 2 and 3 products for serving and archiving. The Level 2 or key parameter data consist of synchronized one-minute summary data sets containing the most often used quantities from IMPACT, PLASTIC and SWAVES, such as plasma moments and magnetic fields. Level 3 products result from basic analyses of the in situ data that identify and characterize events such as shocks, ICMEs and SEP events.

The Level 2 processing software creates the merged, averaged data useful for much of the research involving combinations of STEREO in situ data. These summary data include all of the IMPACT and PLASTIC Beacon data contents in final, calibrated form (see IMPACT's list of Beacon data below). They also include additional derived products. Web access is provided to the Level 2 summary data through the on-line UCLA solar wind data server (<http://www-ssc.igpp.ucla.edu>), while specialized data products and displays can be accessed through hyperlinked instrument contributor Web sites.

The Level 3 data products are available for users interested in specific types of in situ events. Team members review the database to identify and characterize features and events of interest. These Level 3 data are also made available for the STEREO project archival database. The overall timeline for the complete data processing chain is shown in Table 3.

While the routine processing steps are centralized to minimize costs, we emphasize that each cognizant CoI develops the calibration factors and software for the individual data sets, performs quality checks, calculates moments as appropriate and compares these with the real-time space weather data that are transmitted separately. This critical validation process is placed under cognizant CoInvestigator control, both to minimize the possibility of errors, and to maximize the utilization of experience and existing software. As soon as the data have passed the data quality checks, the ODM is notified and the data are documented and submitted to the archive. Software is included with any level of archived IMPACT data for access and display, making the IMPACT data readily usable by the scientific community.

Some minor Level 1 processing is desirable for the space weather Beacon data from IMPACT, for example the calculation of the magnetic field in various coordinate systems such as GSM and GSE, or the calculation of SEP fluxes using improved geometric factors and updated efficiencies. For this purpose, the IMPACT team supplies the necessary software to the SSC which is the distribution point for the real-time STEREO Beacon data.

Table 3 Nominal process time from release of Level zero data (location)

Check and verify Level 0, catalogue (location)	<3 hours (UCB)
Run calibration on Level 0 and Level 1	24 hours (UCB)
Level 0 and 1 data + software to SSC archive	1–2 months (UCB)
Process Level 2 (summary database)	2.5 months (UCLA)
Level 2 products to SSC and archive	2.5 months (UCLA)
Create Level 3 value-added products	3 months (UCLA)
Level 3 products to SSC archive	3 months (UCLA)

4.1.3 Configuration Management

Rewrites to the POC operations software and hardware replacements require approval by a committee composed of the technical Project Manager, the Operations/Data Manager, any affected instrument leads and CoInvestigators as designated. Such changes to the operations system are tested and verified by this committee before implementation. A version numbering system tracks each change. Hardware configuration changes are similarly recorded in a web-accessible database.

As noted above, the IMPACT instrument teams provide software to the SSC to produce corrected Beacon data, and to UCB-SSL to process the Level 1 data and submit to the archive. Each data processing routine provided by the instrument teams to process Beacon, Level 1 Data, or Level 2 Data is associated with a software version number. Each time that a routine is revised, that routine's software version number is incremented. All original routines have a software version number of 1. Every data product created by one of these routines includes a field for the software version number which indicates the number of the software revision used to create that product. The Level 2 Data products also include the software revision number that created the Level 1 Data product from which they are derived.

When an instrument team revises a Beacon Data, Level 1 Data, or Level 2 Data processing routine, the revised routine undergoes a review process to demonstrate that the revised routine performs correctly. During the review of a revision of Beacon Data or Level 1 Data processing software, the ODM uses the revised routine to produce data products for at least three days of data. During the revision of Level 2 processing software, UCLA personnel similarly use the revised routine to produce data products for at least three days of data. The dates that are processed are chosen for their differing characteristics (i.e. One date during an ICME event, one date during which no events occur, one date within the Earth's magnetosphere, etc.). A committee consisting of the ODM, the Co-Investigator in charge of the instrument, and ad hoc members chosen by the ODM and Co-Investigator such as instrument engineers and software developers determine the dates to be tested and whether the data products created with the revised routine are correct. If the products created are not correct, the revision is rejected. If the committee determines that the routine is functioning correctly, the ODM archives the previous version of the routine, keeping it available for retrieval by team members and the public by a web interface from UCB-SSL. The new routine replaces the previous routine in the data processing stream. Data products created by the routine are reprocessed from the beginning of the mission to the present. These data products replace the products created by the old routine. If a Level 1 processing routine is modified and new Level 1 data produced, UCLA is notified of the updated data products so that new Level 2 Data are generated.

Each IMPACT instrument calibration data file provided by the developer is also associated with a calibration version number. Every data product created using one of these calibration data files includes a field for the calibration version number which indicates the number of the calibration revision used to create that product. When an instrument team revises a calibration data file, the revised calibration data file must undergo a review process identical to that of a processing software version. The ODM, the Co-Investigator in charge of the instrument, and others chosen by the ODM and Co-Investigator such as instrument engineers and software developers will approve the revised calibration data file after testing its use on at least three days of data. A publicly accessible web page maintained at UCB by the ODM contains a history of calibration revisions. The web page indicates the latest calibration version number for each calibration data file, the dates that revisions, past and present, were approved, and notes on the revisions made to the calibration data files.

4.2 Phasing Orbit Operations

During the phasing orbits (see Thompson et al., [this volume, 2007](#)), the IMPACT technical Project Manager who was responsible for the instrument development and delivery phase was in charge of IMPACT's operations with the assistance of the ODM. Routine operations were conducted from the UCB POC. During instrument commissioning, web-accessible displays were available to team members to monitor events remotely. The UCB POC was connected to the STEREO MOC's voicenet during critical IMPACT operations and events. Critical operations during the phasing orbits included:

- Day 3: Powering up of the IMPACT IDPU, SEP Central, and the MAG and SWEA instruments. The SWEA cover was opened on Day 3. These systems were then checked out for the following few days.
- Day 9: Deployment of the IMPACT boom.
- Day 19: Powering up and checking out of STE and the SEP instruments.
- Day 25: The first MAG calibration roll manoeuvre. The spacecraft was rotated to calibrate MAG post-launch.

Release of the first IMPACT data products from the phasing orbits occurred approximately 2 months after launch.

4.3 Normal Operations

Once the STEREO spacecraft entered heliocentric orbit, the ODM became responsible for IMPACT operations. Transition of control from the Project Manager to ODM began in the late stages of the phasing orbits. The ODM has an alternate who is able to conduct IMPACT operations when the ODM is unavailable.

The ODM is responsible for the creation of IMPACT command sequences for all IMPACT instruments except the SEP suite. When commands are needed for SWEA, STE or MAG, the ODM uses the POC operations console to assemble, test, and submit commands to the MOC. When SEP commands are required, the SEP instrument providers send the ODM a full Supplemented Command Message. The ODM tests and submits these commands to the MOC. The IMPACT suite requires very few commands, on the order of three per spacecraft per day. These generally consist of minor threshold adjustments and small changes to the burst mode criteria to better catch important events.

The POC system is capable of monitoring real time telemetry without user intervention. During these unattended periods, the POC system monitors for limit violations and other errors. If a limit violation or error is detected, the ODM receives an automatically produced text page through an automated email/pager system with information about the error condition. The ODM maintains a list of responses including contact information for subsystem personnel for each error condition. If the designated subsystem personnel are unavailable when an anomaly occurs, the ODM performs a backup action that was agreed upon before launch. This list of contingency responses and contact information is also available to the ODM's alternate and is regularly updated.

As noted above, under normal operations, processed Level 1 data are expected to appear on the IMPACT data server website within \sim 30 days of receipt on the ground. Users who are interested in plasma microphysics may be particularly interested in the special Burst Mode observations.

Burst Mode The IMPACT burst mode is used to capture high time resolution data during “events”, and play it back slowly as part of the IMPACT telemetry system. Instrument modules provide a continuous stream of high time resolution data to the Burst System, which is in a circular RAM buffer. A criterion function based on IMPACT, PLASTIC and SWAVES data indicates when an event occurs and the event size. The best event over each consecutive three-hour interval is then sent as the next burst. This involves three buffers; one for the transmitting burst event, one for the current best burst event, and one for the current data while looking for a better burst event. Most of the 3 Mbyte RAM is used for these Burst buffers. The buffered burst data include data from 5 min before to 5 min after the sample satisfying the preprogrammed burst criteria. The time resolution of the IMPACT burst mode data is 2 s for SWEA and STE, and 32 Hz (~ 0.03 s) for MAG. Saved burst data are passed to the Burst System by the instrument modules in the form of CCSDS telemetry packets. Burst data are processed in the IDPU in parallel with the normal SWEA, STE and MAG data, so there is no interruption to the normal Level Zero data stream from IMPACT.

The data are subjected to the burst event criteria computation that is part of the Instrument software. The burst criteria are passed to the Burst System, which uses them to decide what data are kept for transmission. At the time of launch, the burst criteria were set to be a weighted sum of individual burst criteria from MAG, SWEA, STE, PLASTIC, and SWAVES:

- The MAG criteria requires sudden changes in the MAG field vector.
- The SWEA criteria requires sudden changes in the SWEA count rates around 400 eV.
- The STE criteria requires increases in the STE count rate, integrated over energy and direction.
- The PLASTIC criteria requires sudden changes in the computed solar wind velocity vector.
- The SWAVES criteria requires increases in electric field fluctuation power in selected frequency bands.

These criteria can be reprogrammed after experience is gained with the data.

5 Data Products, Access, and Analysis Plans

5.1 Data Product Descriptions and Content

5.1.1 *Level Zero*

Level Zero data from the spacecraft via DSN are provided by the STEREO MOC to the IMPACT POC via a secure ftp interface. These data consist of raw telemetry frames in a format defined by the STEREO MOC/POC/SSC ICD. The telemetry provided in Level Zero files are cleaned, merged and time-ordered by the MOC before they are sent to the POC and the SSC.

5.1.2 *Level 1*

As mentioned above, Level One data are produced at UCB-SSL with software and calibration data provided by the IMPACT instrument teams. Each IMPACT instrument has a designated individual responsible for ensuring the delivery of Level 1 processing software

and for validating the Level 1 data products. Level 1 data are divided into instrument products and consist of all science data at highest time resolution in scientific units and, in the case of MAG data, rotated into heliographic-radial-tangent-normal coordinates (HGRTN). The Level 1 data are stored in ISTP-compliant CDF files whose structure and content as of launch are given below. Separate data files for burst mode data are produced. A web-accessible database is available to indicate burst mode time intervals. Table 4 summarize the content of IMPACT Level 1 data files.

Table 4 IMPACT Level 1 data

Instrument	Quantities in Level 1 data
MAG	Bx, By, Bz, B (all in nanoteslas) Coordinate system: Spacecraft coordinates, STEREO Solar Orbital Coordinates, HGRTN Time resolution: 0.1 s
SWEA	Pitch angle distributions in flux units ($1/\text{cm}^2/\text{s}/\text{ster}/\text{eV}$) including: Look angles [NA] in degrees Energy steps [NE] in eV Time resolution: 10 s 3D electron distributions in flux units ($1/\text{cm}^2/\text{s}/\text{ster}/\text{eV}$) including: Look angles [NA] in degrees Energy steps [NE] in eV NE = 16, NA = 80 Time resolution: 30 s Electron moments: Density in $\#/ \text{cm}^3$ Velocity in km/s Pressure tensor in eV/cm^3 Heat flux in $\text{eV}/\text{cm}^2/\text{s}$ SC potential in volts Time resolution: 2 s Coordinate systems: STEREO Solar Orbital Coordinates, HGRTN
STE	Electron flux [NE, NA] in units of flux ($1/\text{cm}^2/\text{s}/\text{eV}$) Look angles [NA] in degrees Energy steps [NE] in eV NE = 32, NA = 8 Coordinate systems: STEREO Solar Orbital Coordinates, HGRTN Time resolution: 10 s
SEPT	Electron count rates (counts/s) in two look directions at 32 energies Ion count rates (counts/s) in two look directions at 32 energies Time resolution: 1 min

Table 4 (*Continued*)

Instrument	Quantities in Level 1 data
LET (all intensities given both in units of flux (#/cm ² /s/ster/MeV/nucleon) and in counts for statistics)	Unsectored data: Proton intensities at 12 energies ³ He intensities at 11 energies ⁴ He intensities at 12 energies C intensities at 12 energies N intensities at 12 energies O intensities at 12 energies Ne intensities at 13 energies Na intensities at 8 energies Mg intensities at 14 energies Al intensities at 9 energies Si intensities at 14 energies S intensities at 13 energies Ar intensities at 13 energies Ca intensities at 13 energies Fe intensities at 16 energies Ni intensities at 9 energies Sectored data (all in 16 look directions): Proton intensity at 1 energy ³ He intensity at 1 energy ⁴ He intensities at 2 energies CNO intensities at 2 energies NeMgSi intensities at 2 energies Fe intensities at 2 energies Time resolution: 1 min
HET	Much like the LET set with unsectored, high energy resolution data and sectored, low energy resolution data. Intensities for H, ³ He, ⁴ He, C, O, Ne, Mg, Si and Fe—exact numbers of energy bins still being determined as of this writing. Same units as LET Time resolution: 1 min
SIT	Intensities for H, ³ He, ⁴ He, C, O, NeS (range Ne through S), and Fe Exact energy ranges TBD Units: #/cm ² /s/ster/MeV/nucleon Time resolution: 1 min

5.1.3 Level 2

Level 2 data are produced at the STEREO in situ data access site at UCLA. These in situ summary or “key parameter” data consist of a subset of IMPACT’s measured quantities averaged to a synchronized one minute cadence. For several reasons, the content of the

Beacon data, described below, was chosen as the baseline for the Level 2 data set. Quantities from the PLASTIC and SWAVES instruments are also included as well as derived quantities such as solar wind dynamic, thermal and magnetic pressures and plasma beta. The key parameter data are available in ASCII and binary flatfile formats and are calibrated, verified and publishable data products.

The beacon data quantities were selected by the STEREO IMPACT, PLASTIC and WAVES teams as concise, representative subsets of their most widely and generally used measurements. Together with the derived parameters that often depend on the results from several instruments, they are intended for wide use, statistical studies, and beacon data retrospective validations.

5.1.4 *Level 3*

Level 3 data are also produced at UCLA with assistance from various IMPACT, PLASTIC and SWAVES team members. These data include feature and event lists of scientific interest. Shock identifications are accompanied by an estimate of their properties such as strength, shock normal angle, and angle of incidence. ICME start and stop times are recorded together with any derived flux rope or other model fit parameters. SEP event start and stop times and peak fluxes are noted together with related flares and CMEs based on STEREO and other available information. They are provided in ASCII table format.

5.1.5 *Beacon Data*

Beacon data are produced at the STEREO Science Center (SSC) where final processing and correction steps are made using software provided by, and updated by, the IMPACT team. These data provide access to near realtime solar wind electron, interplanetary magnetic field, and SEP quantities particularly useful for space weather predictions and predictive modeling. The 1-min averaged IMPACT beacon data are listed in Table 2 and in more detail in Table 5. These data will reside natively in the CDF format but will be available in other formats such as ASCII.

5.1.6 *Complementary L1 In Situ Data Sets*

Complementary data sets from spacecraft located at L1 are made available in parallel with the IMPACT data at SSL. In situ products from the ACE and Wind spacecraft can be browsed and downloaded through the SSL web interfaces described below. As much as possible, data from the L1 spacecraft are tightly integrated with IMPACT's data services to enable immediate comparison and analysis of analogous data quantities.

5.2 Data Access and Browsers

5.2.1 *STEREO Science Center Beacon and Archive Access*

The STEREO Science Center provides access to the IMPACT Beacon data set. It also archives all IMPACT science products (see Thompson et al., [this volume, 2007](#)). Users interested in beacon data history and performance can access the IMPACT beacon data at the usual IMPACT data access sites and compare it to the IMPACT key parameter (Level 2) data at UCLA, or they can compare the two in the archived IMPACT data.

Table 5 IMPACT Beacon Data

Beacon Data from IMPACT include the following:

MAG:

B vectors in nT, 6 samples/minute in spacecraft coordinates. Beacon Data Processing software transforms the data into other coordinate systems as well (e.g. STEREO Solar Orbital and HGRTN).

STE:

For STE-U:

Solar electron fluxes at 5 (modifiable) energies at 1 sample/minute.

Non-solar electron fluxes at 5 energies at 1 sample/minute.

For STE-D:

Electron fluxes at 5 energies at 1 sample/minute.

Units #/cm²/s

SWEA:

Moments calculated from 2 second integration once per minute. Moments include:

Electron density in cnts/cm³

Electron bulk velocity in km/s (in STEREO Solar Orbital and HGRTN)

Electron pressure tensor in eV/cm³

Electron heat flux vector in eV/cm²/s (in STEREO Solar Orbital and HGRTN)

Pitch Angle Distributions (with respect to B field) at 2 (modifiable) energies in 12 look directions once per minute, units cnts/cm²/s

SEP:

SEP status

Note: For all SEP fluxes, units are 1/cm²-s-ster-MeV or 1/cm²-s-ster-MeV-nucleon.

In addition all SEP quantities given in raw counts for statistical analysis

SEP-SEPT:

Electron flux at 2 energies in 4 look directions averaged over 1 minute.

Electron flux at 2 energies summed over 4 look directions averaged over 1 minute.

Ion flux at 2 energies in 4 look directions averaged over 1 minute.

Ion flux at 2 energies summed over 4 look directions averaged over 1 minute.

SEP-LET:

Proton flux at 1 energy in 2 look directions averaged over 1 minute.

Proton flux at 2 energies summed over all look angles averaged over 1 minute.

He flux at 2 energies in 2 look directions averaged over 1 minute.

He flux at 1 energy summed over all look angles averaged over 1 minute.

³He flux at 2 energies summed over all look angles averaged over 1 minute.

CNO flux at 3 energies summed over all look angles averaged over 1 minute.

Fe flux at 4 energies summed over all look angles averaged over 1 minute.

SEP-HET:

Electron flux at 1 energy averaged over 1 minute.

Proton flux at 3 energies averaged over 1 minute.

He flux at 3 energies averaged over 1 minute.

Table 5 (*Continued*)

CNO flux at 2 energies averaged over 1 minute.

Fe flux at 1 energy averaged over 1 minute.

SEP-SIT:

HE flux at 4 energies averaged over 1 minute.

CNO flux at 4 energies averaged over 1 minute.

Fe flux at 4 energies averaged over 1 minute.

IMPACT (in general):

Instrument status.

As an element of the overall STEREO beacon resources, UCB also hosts a browser for visualization of the in situ Beacon data, linked from the SSC website <http://stereo-SSC.nascom.nasa.gov>. This browser is highly customizable allowing users to plot desired quantities for a given time period. It includes Beacon data from IMPACT, PLASTIC and SWAVES.

5.2.2 UCB Data Portal

UCB provides several ways for visualizing and accessing IMPACT data. Routine static plots are created from a fixed subset of IMPACT, PLASTIC and SWAVES quantities in IMPACT Level 1 data and its equivalents for the other instruments. These plots are available for 1-day, 7-day, and Carrington rotation time intervals at the site <http://sprg.ssl.berkeley.edu/impact/>. These are not customizable by the user, and are intended as quick-look resources. Orbit plots are provided to indicate the STEREO spacecraft locations for each browse period.

UCB also provides a highly flexible interface to IMPACT Level 1 data and data from PLASTIC and SWAVES based on the CDAWeb model at <http://cdaweb.gsfc.nasa.gov>. This interface allows the user to specify quantities and time intervals for plotting. It also gives the user the ability to customize a plot's layout and look. Once a user has created a plot layout, the user is able to save that layout for use in future sessions. The web interface at <http://sprg.ssl.berkeley.edu/impact/> is also seamlessly connected with a Level 1 data server. This server provides direct access to the Level 1 data and performs on-the-fly translation to formats other than CDF such as ASCII, HDF, and FITS. Wind and ACE data are also served through this interface for easy comparisons with their similar STEREO counterparts.

A SOAP-based application programming interface (API) is available as well. This API allows for the creation of custom applications by the user community, supporting such activities as advanced data queries by spacecraft separation and by specific content criteria.

5.2.3 UCLA Data Portal

UCLA provides a web portal for the Level 2 and Level 3 data sets. The UCLA digital service allows users to choose quantities for plotting and enables access to data in ASCII and binary flatfile formats. Users can go to this site at http://www_ssc.igpp.ucla.edu to obtain the synchronized 1 min key parameters from PLASTIC and SWAVES merged with IMPACT key parameter data, as well as Level 3 information such as ICME identifications and SEP event lists (see previous discussion of Level 2 and Level 3 data products).

5.3 Data Analysis Plans

As noted earlier, the Helios twin spacecraft mission, a cooperative venture led by the Federal Republic of Germany during portions of solar cycle 21, is the most direct forerunner of STEREO. The timing of the Helios mission was such that images from the SMM and Solwind mission coronagraphs could be exploited to study the solar sources of the detected shocks and ICMEs. In the same spirit as STEREO and ACE, IMP-8 provided regular, complementary near-Earth measurements for comparisons.

Many of the results from the Helios observations are described in a two volume book: Physics of the Inner Heliosphere (eds. R. Schwenn and E. Marsch, Springer-Verlag, Berlin, 1990). Helios measurements were used to investigate the structure of the undisturbed inner heliosphere (e.g. Rhodes and Smith 1975; Behannon et al. 1989), as well as its disturbed state. Especially relevant to STEREO are the results on the speeds and heliolongitude extents of interplanetary shocks resulting from imaged Solwind CMEs (e.g., Sheeley et al. 1985), and the confirmation of the interplanetary shock origins and heliolongitude distribution of CME-related solar energetic particles (e.g., Beeck et al. 1987). A number of these and other seminal studies were carried out on the Helios data set as recently as the nineties (e.g., Kallenrode 1993, 1995; Reames et al. 1996; Richardson 1994; Bothmer and Schwenn 1998). The radial sampling afforded by the Helios elliptical orbits, reaching inward to within 0.3 AU of the Sun and out to 1 AU, provided a further dimension to Helios-based studies of solar wind structure, ICMEs and SEPs that will continue to distinguish these observations, even from those obtained with STEREO.

However, while Sheeley et al. (1985) and Bothmer and Schwenn (1996) made use of the Solwind coronagraph images of CMEs in their studies of Helios interplanetary shock sources and ICME sources, they could only obtain suggestive results on solar causes and interplanetary effects, rather than detailed interpretations connecting specific solar structures with in situ events. The STEREO project has the great advantage of state-of-the-art stereoscopic imaging from SECCHI, of updated analysis capabilities and knowledge of both the solar wind and CMEs/ICMEs from Yohkoh, SOHO, ACE and WIND, and of the involvement of sophisticated, realistic modeling efforts.

Some instrument-specific data analysis tools based on decades of team experience are available at the individual hardware provider sites (see the accompanying papers on SWEA, STE, MAG, SIT, SEPT, LET and HET by Sauvaud et al., Lin et al., Acuna et al., Mason et al., Mewaldt et al., von Rosenvinge et al., Mueller-Mellin et al., all in this volume). In contrast, IMPACT's main data portal is a gateway to the combined investigation designed to take advantage of all of the complementary in situ measurements on STEREO plus connections to the imaging and radio remote sensing results. Our first step toward enabling IMPACT data interpretation beyond the provision of the browse plots and the Level 1 data access and plotting capability (described in the previous section) is the routine merging of key STEREO in situ data in the Level 2 data files described above. Our second step is to provide an easy interface to complementary near-Earth in situ measurements from ACE and WIND to add additional multipoint perspectives and better connect STEREO events to geoeffects. Our third step is to provide links to selected SECCHI and other imaging results and additional complementary information (e.g. archived solar magnetograms and magnetogram-derived synoptic maps). Our ultimate step will be to merge the in situ results with the results from the realistic solar wind and CME/ICME modeling efforts. Toward this end, the Level 3 event and feature lists will provide a useful catalogue from which to select desirable periods.

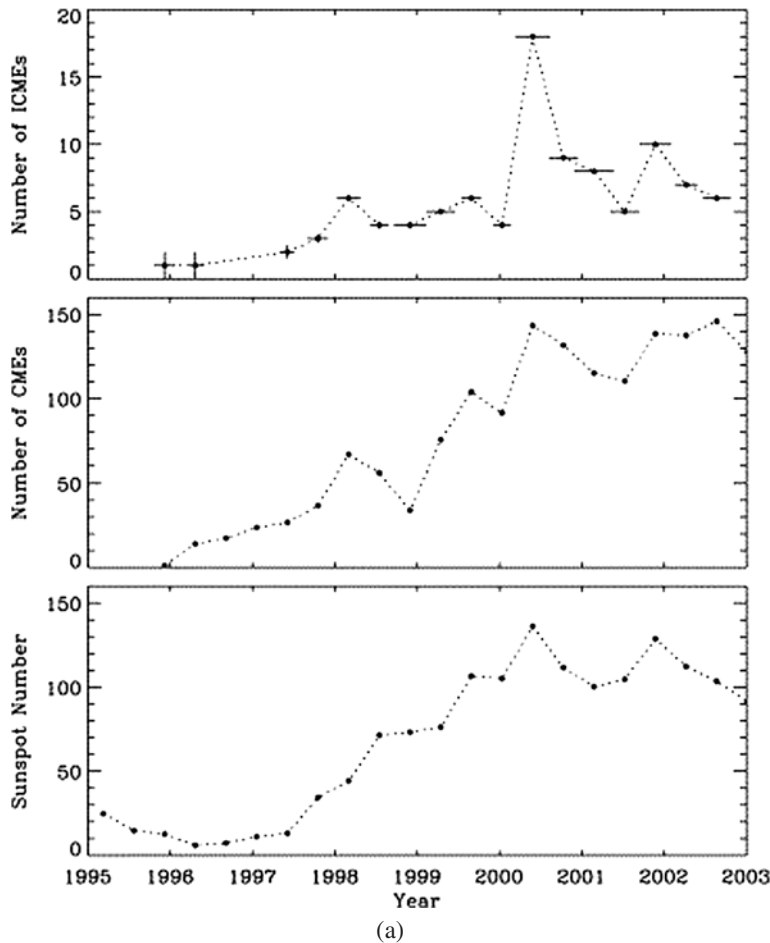
The ability to analyze in situ space weather events in detail depends on the uninterrupted availability of all of the basic measurements: solar wind plasma density, ion and

elemental composition, bulk velocity, ion and electron temperatures, the vector magnetic field, and energetic particle fluxes. The set browse plots of Carrington Rotation-size intervals, mentioned earlier, provide a natural starting point for scanning for events and large scale structures. Week-long and daily set plots allow examination of further detail, including transient events. The spacecraft locations are displayed for each plot interval. Although the slowly separating motion of the STEREO spacecraft will generally not matter for the few-day or longer periods of interest in CME case studies, their separation is a critical piece of information. The science quality (as distinguished from Beacon) plasma moments, magnetic fields, and basic SEP data available from IMPACT and PLASTIC as 1-min averages in the Level 2 data are the next natural point of contact. Note that these data, in contrast to their predecessors, include the heat flux (>100 eV) electron angular distributions and ion composition. Counterstreaming heat flux electrons, like low ion temperatures and large magnitude, low variance, smoothly rotating magnetic fields, have become widely accepted diagnostics of ICME ejecta (e.g., Neugebauer and Goldstein 1997; Shodhan et al. 2000). Similarly, the suprathermal electron anisotropy is used to infer the topology of the interplanetary magnetic field, including the field near the heliospheric current sheet (e.g., Kahler et al. 1996; Crooker et al. 1993, 1998). In the past, it was usual to exclude these data from routine displays of interplanetary plasma and field moments in online browsers, but advancements in interactive plotting allow this to be routine for IMPACT data access sites, and SWEA's nearly 4π coverage of the heat flux electron distribution allows a more accurate interpretation of the electron anisotropies. Level 1 data can be used for even more detail. Recently Gosling et al. (2006b) searched the multipoint plasma and magnetic field measurements from Helios for signatures of extended magnetic reconnection X-lines in the solar wind. IMPACT data contents and displays make such studies easily possible.

SEPs are considered the number one priority for space weather prediction at NOAA SEC (T. Onsager, NOAA SEC, personal communication, 2002), and are another way to remotely sense events and structures in the corona. On Helios, SEP observation studies made the most use of the multipoint sampling. However, many of these early Helios SEP event analyses did not use the context provided by the solar wind and interplanetary magnetic field observations, with the exception of confirming the timing of shock passages (e.g. Kahler et al. 1984; Beeck et al. 1987). In more recent studies using Helios data (e.g. Reames et al. 1996) the advantage of co-analyzing these measurements is clearly demonstrated. IMPACT data include SEP fluxes, compositions, and anisotropies as part of the in situ merged data sets to enable analyses of their heliospheric context at the two STEREO locations at all times.

It is anticipated that by the end of the STEREO 2-year prime mission in 2009, we will have accumulated a significant sample of well-observed events for analysis. Figure 20 contains information on previous solar cycle frequencies of observed CMEs, ICMEs, and SEP enhancements. As STEREO's prime mission is on the leading edge of the rising phase of cycle 24, extending observations for only a few years will more than double the available library of events for study.

Near-Earth Data for Comparisons Schwenn et al. (1978), Burlaga et al. (1978) and Reames et al. (1996) demonstrated the value of comparisons between near-Earth data sets and the Helios plasma, field, and SEP observations. The near Earth data offer both an additional multipoint measurement location and ground-truth for the potential geospace effects of an event seen by other spacecraft. The most complementary data sets from ACE and WIND for STEREO comparisons are listed in Table 6. ACE and WIND observations are

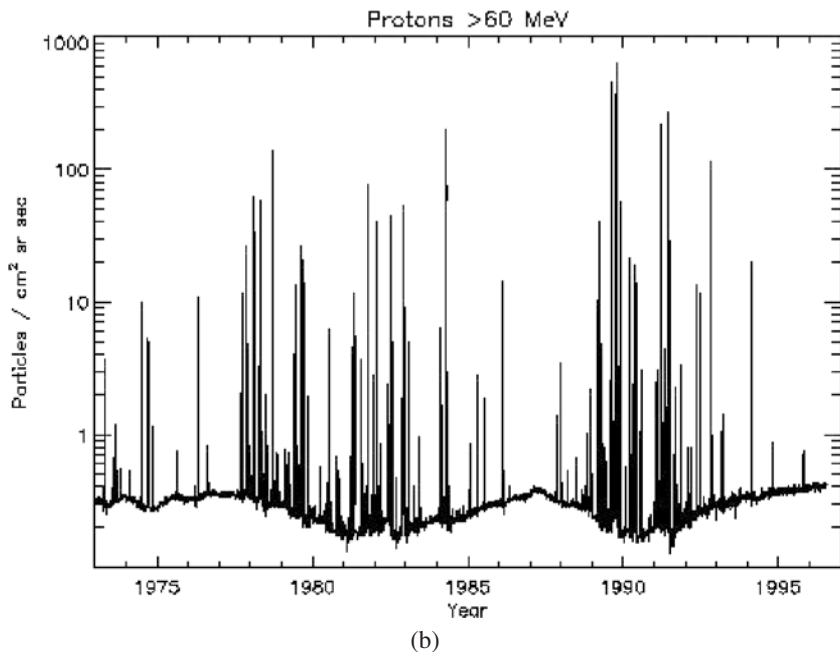


(a)

Fig. 20 **a** CME and ICME rate survey statistics from Liu et al. (2005) for a large portion of the previous solar cycle. **b** SEP event statistics (from Mewaldt, personal communication 2005)

available through the IMPACT Level 1 and Level 2 data access sites to provide the in situ Earth-location perspective throughout the STEREO mission. GOES proton data links are provided as a reminder of these complementary magnetospheric measurements which are a measure of the geospace consequences of solar events.

Integration with Coronagraph and Other Imaging Observations As mentioned earlier, Sheeley et al. (1985) and Bothmer and Schwenn (1994) used available coronagraph observations to interpret the solar sources of the Helios in situ events, including shocks, ICMEs and SEPs. The SMM Coronagraph imaged a quadrant of the Sun between 1.6 and 4.1 solar radii, with full Sun images obtained by pasting four sequential quadrant images together (Burkepile and St. Cyr 1993). Unfortunately, SMM experienced a period of non-operation during the years 1981–mid 1984, losing a large fraction of its potential common observing period with Helios. However, the full-Sun, but lower spatial resolution, Solwind Coronagraph covered the Helios period during the greater part of Cycle 21, including the

**Fig. 20** (Continued)**Table 6** IMPACT instrument/measurement counterparts on ACE and WIND

Measurement	IMPACT	ACE	WIND
Magnetic field	MAG	MAG	MFI
Solar wind plasma	SWEA, PLASTIC	SWEPAM, SWICS	SWE, 3DP
Suprathermal e-	SWEA, STE	SWEPAM	SWE, 3DP
Suprathermal ions	SIT	ULEIS	EPACT/STEP
Energetic electrons	SEPT, HET	EPAM	
Energetic ions	SEPT, SIT, LET, HET	ULEIS, CRIS, SIS, EPAM	EPACT/STEP

solar maximum which was observed in part by SMM. The state-of-the-art SECCHI data, including SOHO EIT-like EUV images, represent major advances in high-quality, multi-spectral coronal imaging over the Helios era observations. The IMPACT data access sites take advantage of this by providing links to relevant SECCHI (and SOHO) images. Sites where RHESSI data, TRACE and SXI EUV solar images, and Solar-B soft X-ray images can be obtained are also linked to the IMPACT data server site, with potential for closer integrations and event studies.

Tools for Connecting Multipoint In Situ Data and Solar Data A sample page from our preliminary web interface to the IMPACT browse plots is shown in Fig. 21. Spacecraft orbit locations for the period of the time series plot (here using Helios data) are included at the bottom. These plots are all clickable for magnification and printing or downloading. In

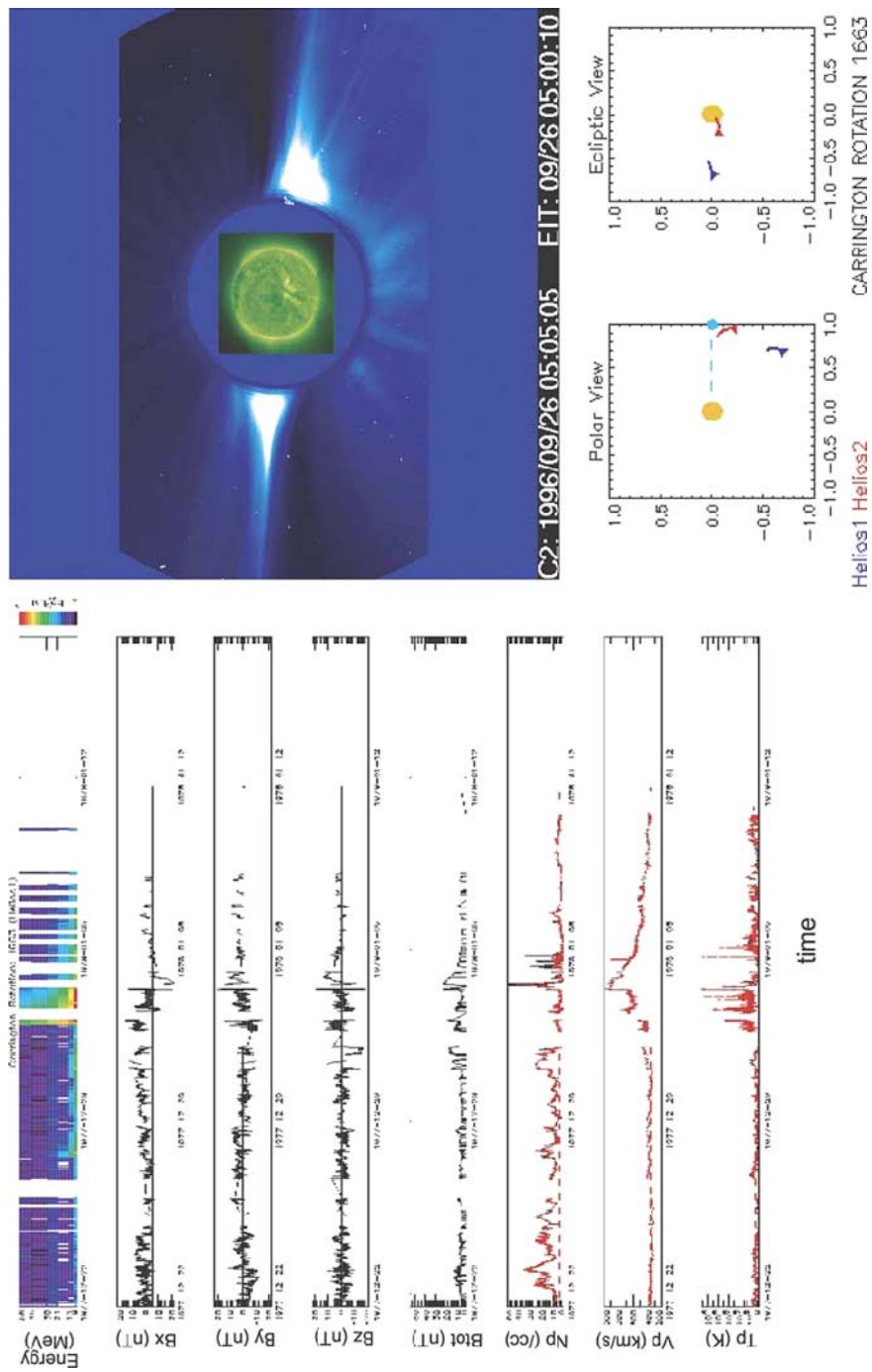
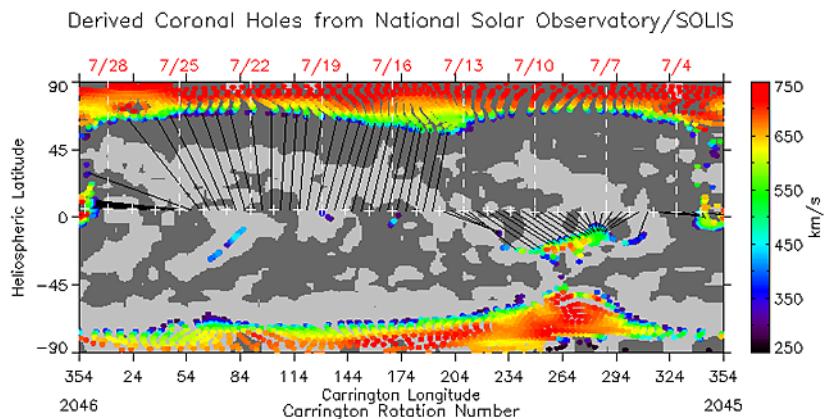


Fig. 21. Sample from an IMPACT browse plot display page, using Helios and SOHO data for demonstration purposes prior to STEREO data integration

addition, toggling between displays for the two spacecraft or adjacent Carrington Rotations (CRs) is possible as a means of scanning for features and patterns. Note that we display the SEP data as time vs. energy vs. flux spectrograms as well as time series. Suprathermal electron pitch angle distributions are also included in similar spectrogram form as time vs. angle vs. flux panels. IMPACT's more customizable plot generating tool was described in the previous section on Data Products. That tool also allows timeline data overlays including lags and leads of the timeline for each data set plotted—a useful capability for testing corotation and other timing delays.

Our challenge has been the design of additional displays that allow the solar connection to be made in an insightful way. While it is a simple matter to link the events that correspond to each browse plot interval (allowing for 4–5 days quiet solar wind transit times and minutes to days for transient events), it is not as obvious how to allow the user to tell, for example, where on the Sun the spacecraft map to along the interplanetary field at a given time, and how a mapped field line relates to the inferred location of a CME seen in a coronagraph image.

The standard and well-tested approach for first-order connection of the corona to points in the inner heliosphere is the potential field source surface model of the coronal magnetic field, mapped kinematically or quasi-kinematically outward. A version of such a model developed by Arge and Pizzo (2000), based on Sheeley and Wang's (1991) empirical relationship between coronal open field divergence and solar wind speed, is currently used to predict solar wind sources, solar wind velocities, and interplanetary field polarity at L1 at the NOAA SEC Rapid Prototyping Center (<http://solar.sec.noaa.gov/ws/>). Figure 22 shows sample products from this model, which is based on synoptic maps of the photospheric field available from a number of ground based observatories. The model can be applied to take



(a)

Fig. 22 Sample plots of WSA (Wang-Sheeley-Arge) solar wind model results from the NOAA SEC website. **a** Coronal hole areas (colored) superposed on a synoptic map of the photospheric magnetic field. The *color code* indicates the model solar wind velocity arising from a particular open coronal field location. The *black lines* indicate what maps to the ecliptic plane and thus affects the Earth. **b** The L1 time series of velocity inferred from the model results in **a**. The various *color points* are from models based on the magnetic field maps from different solar observatories. The *black line* shows the ACE measurements. **b** The interplanetary magnetic field polarity inferred from the results in **a**

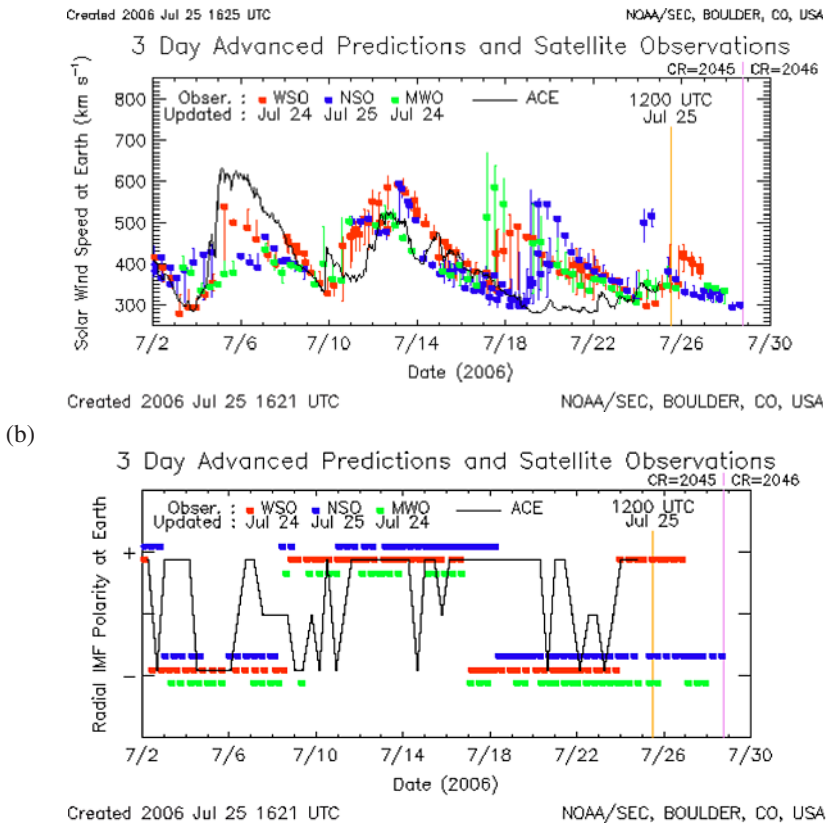


Fig. 22 (Continued)

advantage both of distributed in situ measurements for assessing conditions near Earth, and for relating a coronagraph image and EUV maps of coronal holes to the multipoint in situ solar wind and interplanetary magnetic field time series.

Analysis of solar wind structure and transient events The analysis of 3D solar wind structure, especially before solar activity increases toward the next cycle maximum, is greatly enhanced by access to the combination of SECCHI and SOHO EUV images of coronal holes and 3D models of the solar wind structure such as the Wang/Sheeley/Arge (WSA) model discussed above. The WSA model is now available at the CCMC (Community Coordinated Modeling Center) for general use, along with several other IMPACT team coronal and heliospheric models. Routine STEREO spacecraft data comparisons with this model, in parallel with the ACE and WIND in situ data comparisons (of solar wind speed and interplanetary field polarity) are expected to be added to the SEC WSA model displays shown earlier (N. Arge, personal communication). These model applications and others can be used to trace sources of solar wind streams and boundaries with different attributes, such as those displaying counterstreaming or sunward streaming suprathermal electron features, or exhibiting unusual densities, composition, velocities, or magnetic fields seen by IMPACT and PLASTIC. They can also give insight into the STEREO spacecraft magnetic connectivity to the vicinity of active regions. The great advantage of using the models is that they provide

a physics-based global framework for co-analyzing and integrating the multipoint data sets from STEREO, ACE and WIND (and other available spacecraft).

Armed with the on-disk solar signatures from SECCHI of the coronal morphology of the CME, and the potential field source surface or MHD models of the prevailing large scale coronal magnetic field and related solar wind structure, one can examine the relationship between the involved active region, the overlying larger scale magnetic fields, and the orientation of the fields in the ejecta structure observed at both spacecraft locations. The inward extensions of these models allow us to analyze the spacecraft magnetic connections to the coronal eruption site for the purpose of remotely probing the coronal shock with SEPs. While the possibilities provided by the models are promising, we have not yet developed concepts for their routine application to STEREO transient events.

Special considerations apply to quadrature studies when what is imaged by one SECCHI coronagraph at the limb is detected by the other STEREO spacecraft (or ACE or WIND). The STEREO spacecraft will be 90 degrees apart at the end of the prime mission (see Kaiser et al., [this volume, 2007](#)). If an extended mission occurs, each STEREO spacecraft will be in quadrature with ACE, WIND and SOHO in \sim 2,010, the approximate time of the next solar maximum. Sheeley et al. (1985) created a list of 56 matches of Solwind CMEs and interplanetary shocks observed by either Helios spacecraft when it was within 30 degrees of a limb. They also noted H-alpha flares and GOES X-ray events occurring before the Helios shocks. Bothmer and Schwenn (1996) selected a subset of these when ICME ejecta were also detected, and a smaller subset where solar observations of an erupting polar crown filament preceded detection of a magnetic cloud flux rope. Similar event and feature tables are being collected for STEREO as part of the SSC activities (Thompson et al., [this volume, 2007](#)) and IMPACT Level 3 data sets (see previous section).

Development of potential operational schemes One of the outstanding questions for STEREO mission planning is how best to use in situ multipoint measurements to enhance space weather forecasting capabilities. The most obvious application is the monitoring of corotating solar wind structure on the Behind spacecraft that trails Earth in its orbit structure that may survive until that part of the solar wind corotates to Earth (e.g., Burlaga et al. 1987). Toward this application, and also as a test of solar wind structure steadiness, and hence predictability, we provide for time-shifted time series plots at both IMPACT Level 1 and Level 2 data server sites. The WSA model described above will provide a useful framework for organizing and interpreting corotated and translated features.

Another possible application of the IMPACT data is the deduction from its multipoint SEP measurements of the likelihood that the ICME shock nose will either magnetically connect to or impact Earth, implying maximum SEP fluxes and a storm sudden commencement with its associated geospace effects. Reames et al. (1996) showed that SEP time profiles at spaced locations in the heliosphere follow a pattern that depends on relative shock nose location. Observation-based versions of their classic picture, reproduced in Fig. 4, can be used to qualitatively estimate the SEP and storm impact of events at Earth from what is seen at the STEREO locations. We also use corotational shifts to monitor whether SEP events observed on the Behind spacecraft, like solar wind structure, provide some prediction of SEP behavior when that particular interplanetary flux channel connects to Earth. As SEP events are typically several days long, this may prove most useful for separations of \sim 30 deg or less. On the other hand, the prompt SEPs observed at the Behind spacecraft when the separation is greater may provide warning of the approach to Earth of a strong shock with its associated ESP increase, given the fact that the spiral interplanetary field lines threading it sample the corona at low altitude in the subsolar region.

Finally, applications of IMPACT data to studies of the solar wind interactions with the planets are enabled both by plots of the STEREO spacecraft locations relative to the planets available at SSC (Thompson et al.), and merged SWEA-type data sets from Mars Express and Venus Express available at the IMPACT SWEA site at CESR.

5.4 Expected Impact and Relevance to Heliophysics

The STEREO mission was initiated explicitly for improving our understanding of the origin, propagation, and 1 AU consequences of CMEs, as well as the origins of other solar wind structures.

As a result of the IMPACT investigation, a new, more comprehensive 1 AU in situ data set is available for several heliolongitudes. In particular, it includes the information on suprathermal electron angular distributions often used in the analysis of solar wind structure and CME/ICME events, together with solar wind electron, magnetic field and SEP data. Coordinations with PLASTIC and SWAVES provide subsets of the complete STEREO in situ data on a routine basis. The corresponding near-Earth data from ACE and WIND are moreover made easily accessible through IMPACT data access sites for coordinated analyses. Complementary coronagraph images from SECCHI and SOHO, and solar magnetograph information important for mapping the interplanetary medium to the Sun, are also linked from the IMPACT data access site and displayed in ways that encourage analyses of the physical connections. This resource is made available to the heliophysics community for the lifetime of the STEREO mission and is also integrated into the developing Virtual Heliospheric Observatory for long-term exploitation. STEREO is the testbed for future Heliospheric Constellations as well as space weather monitoring missions. Should it survive its \sim 2013–2015 transit of the farside of the Sun, IMPACT can again become an active participant in providing widespread heliospheric observations for the new rising phase of solar cycle 25. Coordinations with SDO and ESA's Solar Orbiter missions, and a supporting role for any ongoing human exploration activities, will be among its future objectives and goals.

Acknowledgements The IMPACT team is grateful for the support provided by many colleagues in many capacities, including: M. Mandell, G. Ginett, J.B. Blake, J. Fennell, H. Maldonado, H. Culver, A. Harper, M. Delmont, N. Chrissotimos, E. Reynolds, A. Driesman, W. Thompson, E. Christian, B. Anderson, M. Kaiser, R. Jackson, S. McBride, M. Colby, P. Berg, S. Heavner, R. Ullrich (Boom Designer), P. Turin, K. Harps, P. Dobson, S. Lam, M. Hashii, H. Yuan, C. Ingraham, I. Sircar, L. Guhathakurta, R. Fisher. IMPACT is supported by NASA contract NAS5-00133.

References

- Acuna et al. (this volume, 2007)
- S.K. Antiochos, C.R. DeVore, J.A. Klimchuk, *Astrophys. J.* **510**, 485 (1999)
- C.N. Arge, V. Pizzo, *J. Geophys. Res.* **105**, 10465 (2000)
- Aschwanden et al. (this volume, 2006). doi: [10.1007/s11214-006-9027-8](https://doi.org/10.1007/s11214-006-9027-8)
- C.C. Balch, *Radiat. Meas.* **30**, 231 (1999)
- S.D. Bale, P.J. Kellogg, D.E. Larson, R.P. Lin, K. Goetz, R.P. Lepping, *Geophys. Res. Lett.* **25**, 2929 (1998a)
- S.D. Bale, P.J. Kellogg, K. Goetz, S.J. Monson, *Geophys. Res. Lett.* **25**, 9 (1998b)
- S.D. Bale, M.J. Reiner, J.-L. Bougeret, M.L. Kaiser, S. Krucker, D.E. Larson, R.P. Lin, *Geophys. Res. Lett.* **26**, 1573 (1999)
- S.J. Bame, J.R. Asbridge, W.C. Feldman, E.E. Fenimore, J.T. Gosling, *Solar Phys.* **62**, 179 (1979)
- J. Beeck et al., *Astrophys. J.* **322**, 1052 (1987)
- K.W. Behannon, L.F. Burlaga, J.T. Hoeksema, L.W. Klein, *J. Geophys. Res.* **94**, 1245 (1989)
- Biesecker et al. (this volume, 2007). doi: [10.1007/s11214-007-9165-7](https://doi.org/10.1007/s11214-007-9165-7)
- V. Bothmer, R. Schwenn, *Space Sci. Rev.* **70**, 215 (1994)

- V. Bothmer, D.M. Rust, in *Coronal Mass Ejections*, ed. by N. Crooker, J. Joselyn, J. Feynman (AGU, 1997), p. 139
- V. Bothmer, R. Schwenn, *Adv. Space Res.* **17**, 322 (1996)
- V. Bothmer, R. Schwenn, *Annales Geophysicae* **16**, 1 (1998)
- Bougeret et al. (this volume, 2007)
- H.H. Breneman, E.C. Stone, *Astrophys. J. Lett.* **299**, L57 (1985)
- J.T. Burkepile, O.C. St. Cyr, A revised and expanded catalogue of mass ejections observed by the solar maximum mission coronagraph. NCAR Tech. Note NCAR/TN-369+STR, January 1993
- L.F. Burlaga et al., *J. Geophys. Res.* **83**, 5167 (1978)
- L.F. Burlaga, K.W. Behannon, L.W. Klein, *J. Geophys. Res.* **92**, 5725 (1987)
- H.V. Cane, *Space Sci. Rev.* **93**, 55 (2000)
- H.V. Cane, D.V. Reames, T.T. Rosenvinge, *J. Geophys. Res.* **93**, 9555 (1988)
- H.V. Cane, T.T. von Rosenvinge, C.M.S. Cohen, R.A. Mewaldt, *Geophys. Res. Lett.* **30** (2003). doi:[2002GL016580](https://doi.org/10.1029/2002GL016580)
- R.C. Canfield, H.S. Hudson, D.E. McKenzie, *Geophys. Res. Lett.* **26**, 627–630 (1999)
- P.J. Cargill, J. Chen, D.S. Spicer, S.T. Zalesak, *J. Geophys. Res.* **101**, 4855 (1996)
- N.U. Crooker, G.L. Siscoe, S. Shodhan, D.F. Webb, J.T. Gosling, E.J. Smith, *J. Geophys. Res.* **98**, 9371 (1993)
- N.U. Crooker, D.S. Intriligator, *J. Geophys. Res.* **101**, 24343 (1996)
- N.U. Crooker, A.H. McAllister, R.J. Fitzenreiter, J.A. Linker, D.E. Larson, R.P. Lepping, A. Szabo, J.T. Steinberg, A.J. Lazarus, Z. Mikic, R.P. Lin, *J. Geophys. Res.* **103**, 26,859 (1998)
- M.I. Desai, G.M. Mason, J.E. Mazur, J.R. Dwyer, *Astrophys. J.* **645**, L81 (2006)
- T. Detman, J. Joselyn, in *Solar Wind Nine*, ed. by S. Habbal, R. Esser, J. Hollweg, P. Isenburg. AIP Conference Proceedings, vol. 471 (1999), p. 729
- J.R. Dwyer, G.M. Mason, J.E. Mazur, J.R. Jokipii, T.T. von Rosenvinge, R.P. Lepping, *Astrophys. J. (Lett.)* **490**, L115 (1997)
- W.C. Feldman et al., *Phys. Rev. Lett.* **49**, 199 (1982)
- J. Feynman, A.J. Hundhausen, *J. Geophys. Res.* **99**, 8451 (1994)
- J. Feynman, S.F. Martin, *J. Geophys. Res.* **100**, 3355 (1995)
- L.A. Fisk, B. Kozlovsky, R. Ramaty, *Astrophys. J.* **190**, L35 (1974)
- N.J. Fox, M. Peredo, B.J. Thompson, *Geophys. Res. Lett.* **25**, 2461 (1998)
- H.O. Funsten, J.T. Gosling, P. Riley, O.C. St. Cyr, R. Forsyth, R.A. Howard, R. Schwenn, *J. Geophys. Res.* **104**, 6679 (1999)
- Galvin et al. (this volume, 2007)
- T.L. Garrard, A.J. Davis, J.S. Hammond, S.R. Sears, *Space Sci. Rev.* **86**, 649 (1998)
- M. Gedalin, *Geophys. Res. Lett.* **26**, 1239 (1999)
- S.E. Gibson, B.C. Low, *Astrophys. J.* **493**, 460 (1998)
- G. Gloeckler, L.A. Fisk, S. Hefti, N.A. Schwadron, T.H. Zurbuchen, F.M. Ipavich, J. Geiss, P. Bochsler, R.F. Wimmer-Schweingruber, *Geophys. Res. Lett.* **26**, 157 (1999)
- C.C. Goodrich, J.D. Scudder, *J. Geophys. Res.* **89**, 6654 (1984)
- N. Gopalswamy, S. Yashiro, G. Michalek, M.L. Kaiser, R.A. Howard, R. Leske, T. von Rosenvinge, D.V. Reames, in *Solar Wind Ten*, ed. by M. Velli, R. Bruno, F. Malara, Wind Conference, AIP Conference Proceedings, vol. 679 (2003), pp. 608
- J.T. Gosling, E. Hildner, R.M. MacQueen, R.H. Munro, A.I. Poland, C.L. Ross, *Solar Phys.* **48**, 389 (1976)
- J.T. Gosling, J.R. Asbridge, S.J. Bame, W.C. Feldman, R.D. Zwickl, *J. Geophys. Res.* **85**, 3431 (1980)
- J.T. Gosling, D.N. Baker, S.J. Bame, W.C. Feldman, R.D. Zwickl, E.J. Smith, *J. Geophys. Res.* **92**, 8519 (1987)
- J.T. Gosling, D.J. McComas, *Geophys. Res. Lett.* **14**, 355 (1987)
- J.T. Gosling, in *Physics of Magnetic Flux Ropes*, ed. by C.T. Russell, E.R. Priest, L.C. Lee, Geophysical Monograph, vol. 58 (AGU, 1990), pp. 343–364
- J.T. Gosling, S.J. Bame, D.J. McComas, J.L. Phillips, *Geophys. Res. Lett.* **17**, 901 (1990)
- J.T. Gosling, D.J. McComas, J.L. Phillips, S.J. Bame, *J. Geophys. Res.* **96**, 7831 (1991)
- J.T. Gosling, D.J. McComas, J.L. Phillips, S.J. Bame, *J. Geophys. Res.* **97**, 6531 (1992)
- J.T. Gosling, *J. Geophys. Res.* **98**, 18,937–18,949 (1993)
- J.T. Gosling, S.J. Bame, D.J. McComas, J.L. Phillips, B.E. Goldstein, M. Neugebauer, *Geophys. Res. Lett.* **21**, 1105 (1994a)
- J.T. Gosling, D.J. McComas, J.L. Phillips, L.A. Weiss, V.J. Pizzo, B.E. Goldstein, R.J. Forsyth, *Geophys. Res. Lett.* **21**, 2271 (1994b)
- J.T. Gosling, J. Birn, M. Hesse, *Geophys. Res. Lett.* **22**, 869–872 (1995a)
- J.T. Gosling, D.J. McComas, J.L. Phillips, V.J. Pizzo, B.E. Goldstein, R.J. Forsyth, R.P. Lepping, *Geophys. Res. Lett.* **22**, 1753 (1995b)

- J.T. Gosling, Annu. Rev. Astron. Astrophys. **34**, 35 (1996)
- J.T. Gosling, P. Riley, Geophys. Res. Lett. **23**, 2867–2870 (1996)
- J.T. Gosling, in *Coronal Mass Ejections*, ed. by N.U. Crooker, J.A. Joselyn, J. Feynman, Geophysical Monograph, vol. 99 (AGU, 1997a), pp. 9–16
- J.T. Gosling, in *Robotic Exploration Close to the Sun: Scientific Basis*, ed. by S. Habbal, AIP Conf. Proc., vol. 385 (Woodbury, New York, 1997b), p. 17
- J.T. Gosling, V.J. Pizzo, Space Sci. Rev. **89**, 21 (1999)
- J.T. Gosling, R.M. Skoug, D.J. McComas, C.W. Smith, J. Geophys. Res. **110**, A01107 (2005a). doi:[10.1029/2004JA010809](https://doi.org/10.1029/2004JA010809)
- J.T. Gosling, R.M. Skoug, D.J. McComas, C.W. Smith, Geophys. Res. Lett. **32**, L05105 (2005b). doi:[10.1029/2005GL022406](https://doi.org/10.1029/2005GL022406)
- J.T. Gosling, S. Eriksson, R.M. Skoug, D.J. McComas, R.J. Forsyth, Astrophys. J. **644**, 613 (2006a)
- J.T. Gosling, S. Eriksson, R. Schwenn, J. Geophys. Res. **111**, A10102 (2006b). doi: [10.1029/2006JA011863](https://doi.org/10.1029/2006JA011863)
- D.K. Haggerty, E.C. Roelof, Astrophys. J. **579**, 841 (2002)
- R.A. Harrison, E. Hildner, A.J. Hundhausen, D.G. Sime, G.M. Simnett, J. Geophys. Res. **95**, 917 (1990)
- Howard et al. (this volume, 2007)
- A.J. Hundhausen, in *Solar Wind*, ed. by C.P. Sonnett, P.J. Coleman, J.M. Wilcox, NASA SP-308 (Washington, 1972), p. 393
- A.J. Hundhausen, J. Geophys. Res. **98**, 13,177 (1993)
- A.J. Hundhausen, J. Burkepile, O.C. St. Cyr, J. Geophys. Res. **99**, 6543 (1994)
- B.V. Jackson et al., Solar Phys. **225**, 177 (2004)
- S.W. Kahler, D.V. Reames, J. Geophys. Res. **96**, 9419 (1991)
- S.W. Kahler et al., J. Geophys. Res. **89**, 9683 (1984)
- S.W. Kahler, in *Proc. of the Third SOHO Workshop*, ESA SP-373, December 1994, p. 253
- S.W. Kahler, N.U. Crooker, J.T. Gosling, J. Geophys. Res. **101**, 24373–24382 (1996)
- S.W. Kahler, in *Space Weather*, ed. by P. Song et al., AGU Monograph, vol. 125 (American Geophysical Union, 2001), p. 109
- Kaiser et al. (this volume, 2007)
- M.-B. Kallenrode, Adv. Space Res. **13**, 341 (1993)
- M.-B. Kallenrode, Adv. Space Res. **15**, 375 (1995)
- P.J. Kellogg, K. Goetz, S.J. Monson, S.D. Bale, J. Geophys. Res. **104**, 17069 (1999)
- M.G. Kivelson, C.T. Russell, *Introduction to Space Physics* (Cambridge University Press, Cambridge, 1995)
- K.-L. Klein, S. Krucker, G. Tottet, S. Hoang, Astron. Astrophys. **1047** (2005)
- A.S. Krieger, A.F. Timothy, E.C. Roelof, Solar Phys. **29**, 505 (1973)
- S. Krucker, D.E. Larson, R.P. Lin, B.J. Thompson, Astrophys. J. **519**, 864 (1999)
- A. Kumar, D. Rust, J. Geophys. Res. **101**, 15667 (1996)
- D. Lario, B. Sanahuja, A.M. Heras, Astrophys. J. **509**, 415 (1998)
- D.E. Larson et al., Geophys. Res. Lett. **24**, 1911 (1997)
- D. Larson, R.P. Lin, J. Steinberg, Geophys. Res. Lett. **27**, 157 (2000)
- R.J. Leamon, R.C. Canfield, S.L. Jones, K. Lambkin, B.J. Lundberg, A.A. Pevstov, J. Geophys. Res. **109** (2004). doi:[10.1029/2003JA010324](https://doi.org/10.1029/2003JA010324)
- M.A. Lee, J. Geophys. Res. **88**, 6109 (1983)
- M.A. Lee, Astrophys. J. (Suppl.) **158**, 38 (2005)
- R.P. Lepping et al., J. Geophys. Res. **95**, 11957 (1990)
- S. Lepri, T. Zurbuchen, L. Fisk, I. Richardson, H. Cane, G. Gloeckler, J. Geophys. Res. **106**, 29231 (2001)
- G. Li, G.P. Zank, W.K.M. Rice, J. Geophys. Res. **108** (2003). doi:[10.1029/2002JA009666](https://doi.org/10.1029/2002JA009666)
- Y. Li, J. Luhmann, J. Atmos. Terr. Phys. **66**, 323 (2004)
- Y. Li, J.G. Luhmann, Astrophys. J. **648**, 732 (2006)
- Y. Li, J.G. Luhmann, T. Mulligan, J.T. Hoeksema, C.N. Arge, S.P. Plunkett, O.C. St. Cyr, J. Geophys. Res. **106**, 25,103 (2001)
- R.P. Lin, S.W. Kahler, J. Geophys. Res. **97**, 8203 (1992)
- Lin et al. (this volume, 2007)
- G.M. Lindsay, C.T. Russell, J.G. Luhmann, P. Gazis, J. Geophys. Res. **99**, 11–17 (1994)
- G.M. Lindsay, C.T. Russell, J.G. Luhmann, J. Geophys. Res. **100**, 16999–17013 (1995)
- G.M. Lindsay, J.G. Luhmann, C.T. Russell, J.T. Gosling, J. Geophys. Res. **104**, 12,515 (1999a)
- G.M. Lindsay, C.T. Russell, J.G. Luhmann, J. Geophys. Res. **104**, 10335–10344 (1999b)
- J.A. Linker, Z. Mikic, Astrophys. J. **438**, L45 (1995)
- Y. Liu, J.D. Richardson, Planet. Space Sci. **53**, 3 (2005)
- Y. Liu, J.D. Richardson, J.W. Belcher, Planet. Space Sci. **53**, 3–17 (2005)
- J.G. Luhmann, in *Coronal Mass Ejections*, Geophysical Monograph, vol. 99 (American Geophysical Union, 1997), pp. 291–299

- J.G. Luhmann, J.T. Gosling, J.T. Hoeksema, X. Zhao, *J. Geophys. Res.* **103**, 6585–6593 (1998)
- J.G. Luhmann, Y.Li, C.N. Arge, P.R. Gazis, R. Ulrich, *J. Geophys. Res.* **107** (2002). doi:[2001JA007550](https://doi.org/10.1029/2001JA007550)
- J.G. Luhmann et al., *Adv. Space Res.* **36**, 1534 (2005)
- W.B. Manchester, T.I. Gombosi, D.L. De Zeeuw, I.V. Sokolov, I.I. Roussev, K.G. Powell, J. Kóta, G. Tóth, T.H. Zurbuchen, *Astrophys. J.* **622**, 1225 (2005)
- G.M. Mason, J.E. Mazur, J.R. Dwyer, D.V. Reames, T.T. von Rosenvinge, *Astrophys. J. Lett.* **486**, L149 (1997)
- Mason et al. (this volume, 2007). doi: [10.1007/s11214-006-9087-9](https://doi.org/10.1007/s11214-006-9087-9)
- J.E. Mazur, G.M. Mason, J.R. Dwyer, T.T. von Rosenvinge, *Geophys. Res. Lett.* **25**, 2521 (1998)
- D.J. McComas et al., *J. Geophys. Res.* **94**, 6907 (1989)
- D.J. McComas et al., *J. Geophys. Res.* **97**, 171 (1992)
- D.J. McComas, *Rev. Geophys.*, Suppl. **603** (1995)
- D.J. McComas, in *Solar Wind Ten*, ed. by M. Velli, R. Bruno, F. Malara. AIP Conference Proceedings, vol. 679 (2003), p. 33
- D.J. McComas, H.A. Elliott, N.A. Schwadron, J.T. Gosling, R.M. Skoug, B.E. Goldstein, *Geophys. Res. Lett.* **301910** (2003). doi:[10.1029/2003GL017135](https://doi.org/10.1029/2003GL017135)
- Mewaldt et al. (this volume, 2007)
- M.D. Montgomery, J.R. Asbridge, S.J. Bame, W.C. Feldman, *J. Geophys. Res.* **79**, 3103 (1974)
- Mueller-Mellin et al. (this volume, 2007). doi: [10.1007/s11214-007-9204-4](https://doi.org/10.1007/s11214-007-9204-4)
- T. Mulligan, C.T. Russell, J.G. Luhmann, *Geophys. Res. Lett.* **25**, 2959–2962 (1998)
- T. Mulligan, C.T. Russell, *J. Geophys. Res.*, 10,581 (2001)
- M. Neugebauer, R. Goldstein, in *Coronal Mass Ejections*, ed. by N.U. Crooker, J.A. Joselyn, J. Feynman. Geophysical Monograph, vol. 99 (AGU, 1997), pp. 245–251
- M. Neugebauer et al., *J. Geophys. Res.* **103**, 14,587 (1998)
- C.K. Ng, D.V. Reames, A.J. Tylka, *Geophys. Res. Lett.* **26**, 2145–2148 (1999)
- D. Odstrcil, V.J. Pizzo, *J. Geophys. Res.* **104**, 28,225 (1999a)
- D. Odstrcil, V.J. Pizzo, *J. Geophys. Res.* **104**, 483 (1999b)
- D. Odstrcil, V.J. Pizzo, *J. Geophys. Res.* **104**, 493 (1999c)
- D. Odstrcil, J.A. Linker, R. Lionello, Z. Mikic, P. Riley, V.J. Pizzo, J.G. Luhmann, *J. Geophys. Res.* **107** (2002). doi:[10.1029/2002JA009334](https://doi.org/10.1029/2002JA009334)
- K.O. Ogilvie, L.F. Burlaga, D.J. Chornay, R.J. Fitzenreiter, *J. Geophys. Res.* **104**, 22389 (1999)
- V. Osherovich, L.F. Burlaga, in *Coronal Mass Ejections*, ed. by N. Crooker, J.A. Joselyn, J. Feynman. Geophysical Monogr. Ser., vol. 99 (AGU, 1997), pp. 157–168
- K.I. Paularena, J.D. Richardson, G.N. Zastenker, P.A. Dalin, in *Solar Wind Nine*, ed. by S. Habbal, R. Esser, J. Hollweg, P. Isenberg (AIP, 1999), p. 585
- Phan et al., *Nature* **439**, 175 (2006)
- Phillips et al., *Geophys. Res. Lett.* **22**, 3301 (1995)
- W.G. Philipp, H. Migenrieder, K.-H. Muhlhauser, H. Rosenbauer, R. Schwenn, F.M. Neubauer, *J. Geophys. Res.* **92**, 1103 (1987)
- V.J. Pizzo et al., *Solar Phys.* **226**, 283 (2005)
- M. Popecki, E. Moebius, B. Klecker, A.B. Galvin, L.M. Kistler, A.T. Bogdanov, in *Acceleration and Transport of Energetic Particles Observed in the Heliosphere*, ed. by R.A. Mewaldt, J.R. Jokipii, M.A. Lee, E. Moebius, T.H. Zurbuchen. AIP Conference Proceedings, vol. 528 (American Inst. of Physics, New York 2000), pp. 139–142
- D.V. Reames, L.M. Barbier, C.K. Ng, *Astrophys. J.* **466**, 473 (1996)
- D.V. Reames, S.W. Kahler, C.K. Ng, *Astrophys. J.* **491**, 414 (1997)
- D.V. Reames, C.K. Ng, *Astrophys. J.* **504**, 1002 (1998)
- D.V. Reames, *Space Sci. Rev.* **90**, 413 (1999)
- D.J. Rhodes Jr., E.J. Smith, *J. Geophys. Res.* **80**, 917 (1975)
- I.G. Richardson, *Astrophys. J.* **420**, 926 (1994)
- J.D. Richardson, K.I. Paularena, *Geophys. Res. Lett.* **25**, 2097 (1998)
- J.D. Richardson, F. Dashevskiy, K.I. Paularena, *J. Geophys. Res.* **103**, 14619 (1998)
- P. Riley, J.T. Gosling, V.J. Pizzo, *J. Geophys. Res.* **102**, 14,677 (1997)
- P. Riley, J.A. Linker, Z. Mikic, D. Odstrcil, T.H. Zurbuchen, D. Lario, R.P. Lepping, *J. Geophys. Res.* **108** (2003). doi:[10.1029/2002JA009760](https://doi.org/10.1029/2002JA009760)
- I. Roth, M. Temerin, *Astrophys. J.* **477**, 940 (1997)
- I. Roussev, T.I. Gombosi, I.V. Sokolov, M. Velli, W. Manchester, DeZeeuw, P. Liewer, G. Toth, J.G. Luhmann, *Astrophys. J.* **595**, L57 (2003)
- D.M. Rust, *Geophys. Res. Lett.* **21**, 241 (1994)
- T.R. Sanderson, R. Reinhard, P. Van Nes, K.-P. Wenzel, E.J. Smith, B.T. Tsurutani, *J. Geophys. Res.* **90**, 973 (1985)

- Sauvaud et al. (this volume, 2007). doi: [10.1007/s11214-007-9174-6](https://doi.org/10.1007/s11214-007-9174-6)
- C.J. Schrijver, K. Harvey, *Solar Phys.* **150**, 1 (1994)
- R. Schwenn, M. Montgomery, H. Rosenbauer, H. Migenrieder, K.H. Muhlhauser, S.J. Bame, W.C. Feldman, R.T. Hansen, *J. Geophys. Res.* **83**, 1011 (1978)
- R. Schwenn, H. Rosenbauer, K.-H. Muhlhauser, *Geophys. Res. Lett.* **7**, 201 (1980)
- M.A. Shea, D. Smart, *Adv. Space Res.* **29**, 325 (2002)
- N.R. Sheeley Jr., et al., *J. Geophys. Res.* **90**, 163 (1985)
- N.R. Sheeley, Y.M. Wang, *Solar Phys.* **131**, 165 (1991)
- N.R. Sheeley Jr., et al., *Astrophys. J.* **484**, 472–478 (1997)
- S. Shodhan et al., *J. Geophys. Res.* **105**, 27,261 (2000)
- R.M. Skoug et al., *Geophys. Res. Lett.* **26**, 161 (1999)
- Stone et al., *Space Sci. Rev.* **86**, 357 (1998a)
- Stone et al., *Space Sci. Rev.* **86**, 285 (1998b)
- B.J. Thompson, E.W. Cliver, N. Nitta, C. Delannée, J.-P. Delaboudinière, *Geophys. Res. Lett.* **27**, 1431 (2000)
- Thompson et al. (this volume, 2007)
- B.T. Tsurutani, Y.T. Lee, W.D. Gonzalez, F. Tang, *Geophys. Res. Lett.* **19**, 73 (1992)
- A.J. Tylka, D.V. Reames, C.K. Ng, *Geophys. Res. Lett.* **26**, 2141 (1999)
- Ullrich et al. (this volume, 2007)
- T.T. von Rosenvinge, L.M. Barbier, J. Karsch, R. Liberman, M.P. Madden, T. Nolan, D.V. Reames, L. Ryan, S. Singh, H. Trexel, G. Winkert, G.M. Mason, D.C. Hamilton, P.H. Walpole, *Space Sci. Rev.* **71**, 155–206 (1995)
- von Rosenvinge et al. (this volume, 2007)
- Y.-M. Wang Jr., N.R. Sheeley, *Astrophys. J.* **365**, 372 (1990a)
- Y.-M. Wang, N.R. Sheeley, *Astrophys. J.* **355**, 726 (1990b)
- Y.M. Wang et al., *Astrophys. J.* **498**, L165–L168 (1998)
- D.F. Webb, R.A. Howard, *J. Geophys. Res.* **99**, 4201 (1994)
- D.F. Webb, E.W. Cliver, N.U. Crooker, O.C. St. Cyr, B.J. Thompson, *J. Geophys. Res.* **105**, 7491 (2000)
- S. Yashiro, N. Gopalswamy, S. Akiyama, G. Michalek, R.A. Howard, *J. Geophys. Res.* **110** (2005). doi: [10.1029/2005JA011151](https://doi.org/10.1029/2005JA011151)
- C.J. Zeitlin, T. Cleghorn, F. Cuccinotta, P. Saganti, V. Anderson, K. Lee, L. Pinsky, W. Atwell, R. Turner, G. Badhwar, *Adv. Space Res.* **33**, 2204 (2004)
- R.D. Zwickl, K.A. Doggett, S. Sahm, W.P. Barrett, R.N. Grubb, T.R. Detman, V.J. Raben, C.W. Smith, P. Riley, R.E. Gold, R.A. Mewaldt, T. Maruyama, *Space Sci. Rev.* **86**, 633 (1998)

The STEREO IMPACT Boom

Robert Ullrich · Jeremy McCauley · Paul Turin ·
Ken McKee · Bill Donokowski

Originally published in the journal Space Science Reviews, Volume 136, Nos 1–4.
DOI: [10.1007/s11214-008-9334-3](https://doi.org/10.1007/s11214-008-9334-3) © Springer Science+Business Media B.V. 2008

Abstract An essential component of the STEREO IMPACT investigation is its nearly 6 m long boom that provides several of the instruments with a sufficiently clean magnetic environment and minimally restricted fields of view, while having the required rigidity to ensure the spacecraft pointing accuracy for the STEREO imaging investigations. Details of the customized telescoping IMPACT Boom design, construction and testing are described in this review. The successful completion and verification of the IMPACT Booms represents a demonstration of the use of Stacers as motive forces for rigid boom deployment.

Keywords Magnetometer · Spacecraft boom · STEREO mission

1 Introduction

The IMPACT¹ Boom carries 3 of the IMPACT Boom Suite Instruments on the NASA STEREO² satellite. When stowed for launch, the boom is 1.54 m in length, when deployed the boom extends to 5.80 m (see Fig. 18). The boom consists of 5 concentric graphite epoxy (Gr/E) tubes extended by the spring force of a Stacer. The Stacer is fabricated from a flat strip of Elgiloy® spring material, rolled with a constant diameter and fixed helix angle. It supplies the motive force for deployment, and requires no external power once released. The deployed boom exhibits the high rigidity required by the STEREO SECCHI imaging package, the natural frequency first mode occurring at 1.96 Hz. A summary of boom performance is included at the end of this paper, please see Table 1.

¹In-situ Measurements of Particles And Coronal mass ejection Transients.

²Solar-TERrestrial RElations Observatory.

R. Ullrich (✉) · J. McCauley · P. Turin · K. McKee · B. Donokowski
Space Sciences Laboratory, University of California, Berkeley, CA, USA
e-mail: tripleu@uclink.berkeley.edu

Table 1 IMPACT Boom summary of performance

Property	Value	Units/notes
Frequency stowed/deployed	>120/1.96	Hz
Stowed volume	F250 × 1595 L	mm
Maximum length	5.8	m
Deployment force (net)	33	N (Average)
Temperature range	25–348 (75°C)	°K
Deployment accuracy	+/-0.11° (7 arcmin)	@ 4 m
Release power requirements	1A @ 28VDC 50 ms	Minimum

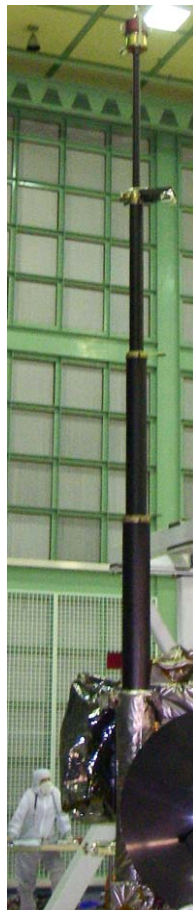
2 Instruments on the IMPACT Boom

The requirements for the STEREO IMPACT Boom were based on the measurement needs of both the IMPACT instruments mounted to it: the Magnetometer (MAG), the Solar Wind Electron Analyzer (SWEA), and the Supra-Thermal Electron (STE) detector; and the rigidity needed by the SECCHI imaging investigation. The general appearance of the boom and its location on the spacecraft are illustrated in Fig. 1. The SECCHI imaging system drove the high rigidity requirement as well as materials selection, which had to satisfy the observatory contamination standards. Overviews of the IMPACT and SECCHI investigations on STEREO can be found in the accompanying papers by Luhmann et al. (2008) and Howard et al. (2008).

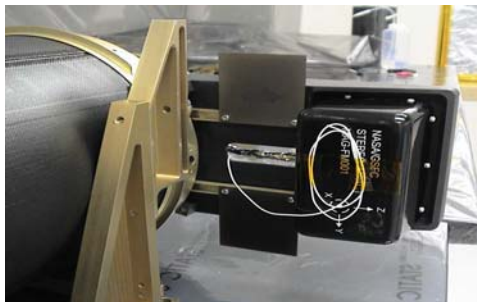
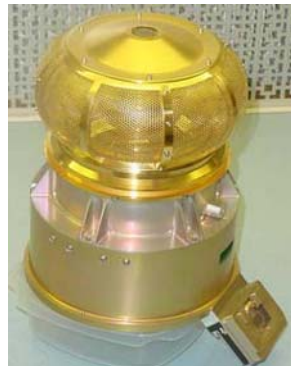
Details of its design relevant to the IMPACT Boom Suite instruments, shown in Fig. 2, are given here. The IMPACT magnetometer's (see Fig. 3) sensitivity was the driver for the EMI/EMC (Electromagnetic Interference and Contamination) design for the spacecraft and the devices near it. To avoid detecting the spacecraft magnetic fields, the magnetometer (built at Goddard Space Flight Center) needed to be 3 m away from it. This requirement set the minimum boom length. To ensure a low magnetic signature from the boom assembly, no ferritic alloys were allowed for its construction.

Titanium screws were used to mount the magnetometer to its tray on the 4th tube element and the tray itself is made of carbon impregnated PEEK, a high strength, conductive engineering plastic. To lower MAG exposure to any eddy currents present in the harness or structure of the boom, the mounting tray offset the MAG 200 mm from the nearest metal in the boom. Additionally there were not to be any other instruments closer than 1 m to the MAG. To provide accurate inter-experiment correlation of data, the angular alignment accuracy and repeatability requirement allowed a deviation of <0.88° (52.5 arcmin) between the IMPACT Boom mounting feet and the magnetometer housing, from the stowed condition to the deployed state. This requirement was for both axes that form the mounting plane of the MAG. Further information about the MAG experiment can be found in the paper by Acuna et al. (2008).

The second instrument mounted on the IMPACT Boom is the Solar Wind Electron Analyzer (SWEA, supplied by CESR, Toulouse, described in detail in the accompanying paper by Sauvad et al. 2008). The SWEA, shown in Fig. 4, has 2 variably charged hemispheric surfaces that attract electrons into an anode assembly which counts them upon impact at the microchannel plates. The SWEA would have a limited field of view if mounted directly to the spacecraft deck, hampering its ability to characterize the full distribution of interplanetary electrons. Proximity to the spacecraft also causes deflections of electrons due to the almost unavoidable static fields that develop near the spacecraft surface. Since this effect

Fig. 1 Deployed boom**Fig. 2** MAG, SWEA and STE-D mounted on the end of the stowed boom

is difficult to model, the boom presents a much better solution. The accommodation of the SWEA on the STEREO spacecraft is extremely good: it is mounted on the extreme end of the boom, allowing a full 2π radians \times 135° field of view (FOV). The demands of the SWEA for mounting to the boom are not complex: power lines, command lines routed to it, data

Fig. 3 IMPACT magnetometer**Fig. 4** SWEA/STE

return lines from it. Figure 5 shows some details of the boom construction in cross-section, with the power and data cables threading through the Stacer and inner boom cylinder.

The final instrument on the boom is the STE, a Supra-Thermal Electron detector (supplied by UCB-SSL and described in Lin et al. 2008). To satisfy its field of view needs, the STE on each spacecraft consists of two parts, one on the sunward side of the spacecraft, called STE-U (U for upstream), on the base of the boom; and STE-D (D for downstream) on the end of the boom (see Fig. 1). STE-D, shown in Fig. 4, is mounted on the side of the SWEA pedestal. It needs a clear $80^\circ \times 80^\circ$ field of view looking along the plane of the ecliptic at a 45° angle (aligned with the Parker spiral), and to stay at $\sim -40^\circ\text{C}$.

The fixed base of the IMPACT Boom is pointed towards the Sun for all science activities, and the only changes in orientation scheduled are for momentum dumping required for spacecraft control. The boom deploys away from the Sun (see Fig. 1), so there is minimal solar radiation incident on the boom suite, giving very low operational temperatures for the instruments. Thermal control was a large concern for the instruments.

3 IMPACT Boom Mechanism

The IMPACT Boom consists of 5 concentric Gr/E Tubes (see Fig. 5), ranging from 50 mm to 210 mm in diameter, with a pair of aluminum rings bonded to each end. Each ring pair contains 3 lock pins, pointing outward at the Sun-ward end, and pointing inward at the deployment end, and 3 sockets, in their corresponding orientations. The pins are spring loaded, and have rollers mounted in their tips. When released, the Stacer spring extends the tubes until the end of travel where the pins drop into sockets, locking the assembly



Fig. 5 Solid model section view of stowed IMPACT Boom

rigid. The mounting feet are integral to the outermost rings on the Ø210 mm tube. The boom incorporates a spool for the electrical harness while stowed, a flyweight brake to control the deployment speed, a shape memory alloy release mechanism with pretensioning adjustment, deployment assist rods and kick springs. Combs at each end hold the tubes in alignment prior to deployment and during launch. A provision for individually adjusting the combs to remove any play in the stowed tubes due to fabrication tolerances is also included. The design was performed in Solidworks™, utilizing its 3 dimensional solid modeling and multiple configuration capabilities.

3.1 Tube Details

The use of telescoping concentric tubes is not a new idea; however, each telescoping application brings its own set of challenges. For the IMPACT Boom, the tubes needed loose tolerances on their cylindricity to allow for simple tube manufacture. The deployment/locking scheme required compliance regarding the inter-tube fit since there is a relatively low force available from the Stacer. The boom needed to be very rigid when deployed, so locking pins were utilized at end of travel, rather than relying on spring force to hold them in place. The tubes have 3 longitudinal concave grooves equispaced about their circumference, running their length, with a precise profile that prevents the rollers from jamming. These grooves keep the pins aligned with the sockets at the far end of the tube. The tubes are five layers of 0.12 mm woven, epoxy pre-impregnated, carbon fiber composite material (Fiberite Hy-E 1034C prepreg) designed to be quasi-isotropic: three 0°–90° layers interleaved with two 45° layers. The tubes were fabricated by Vision Composites of Signal Hill, California on internal mandrels, with a slight taper (<1 mm in 1100 mm) to enhance ease of extraction after cure. The cure regimen was specified to be ‘dry’: the ratio of epoxy to carbon filament was held to a minimum to ensure low surface resistance. This was achieved by using higher autoclave pressure with a slower ‘warm up to cure’ temperature ramp and a thick layer of absorbent over the bleeder sheet. The process determination was somewhat lengthly; however, the final result met requirements. Figure 6 shows the IMPACT telescoping boom cylinders at an early, partial deployment stage.

At both ends of each tube are inner and outer concentric aluminum rings (see Fig. 7) that ‘sandwich’, and are bonded to the Gr/E. After an extensive search, Loctite Hysol 9309NA was used to form the bond. The thermal environment for the boom is rather severe: it will be in the shadow of the spacecraft for all science activity; thermal analysis estimates put the operating low temperature at 30°K. There is very little data for epoxies at this temperature, so we performed a finite element analysis (see Fig. 8) for the bond between the aluminum and the Gr/E to establish what parameters minimized the stresses in the glue, the weakest part. Several parameters for the glue design were examined: thickness of the bond, edge conditions of the bond and effects of the aluminum ring thickness (internal and external) on the joint stresses. The optimized glue line was chosen to be ~0.4 mm thick, with a fillet onto

Fig. 6 Partially deployed tubes



Fig. 7 50 mm tube end: lock pins (EM)

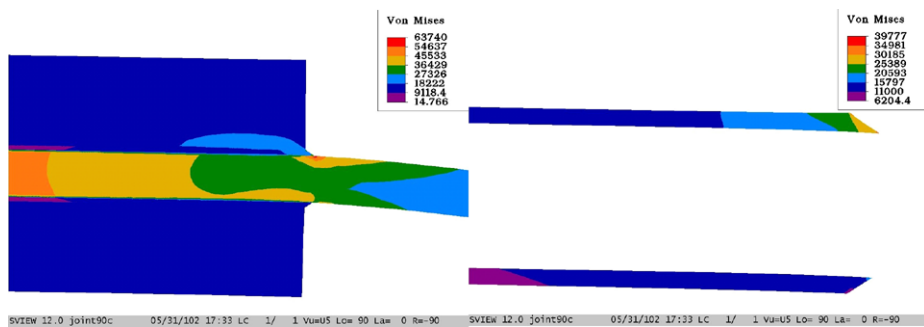


Fig. 8 Analysis of aluminum ring–glue line–Gr/E–glue line–aluminum ring

a tapered aluminum ring edge. This best case predicted a stress value of 110 MPa (16 ksi),¹ which exceeded the glue published maximum stress value of 38 MPa (5.5 ksi).²

There was concern that the joint would not be sound after exposure to the thermal gradient, so a test was needed. A test GR/E tube/aluminum ring assembly was fabricated, with a large cantilever mass attached at the extremity providing $\sim 2X$ expected loads for the tube/ring joint. This test assembly was installed in a cryogenic liquid helium chamber, which

¹Besuner Consulting, Madera, CA 93638.

²Loctite Hysol Applications Note, April/01, Loctite Aerospace, Bay Point, CA 94565.

Fig. 9 Epoxy thermal test chamber



was then installed into a cryogenic liquid nitrogen chamber placed inside of a refrigerated chest (see Fig. 9). A multiple cycle thermal test (in a dry air environment), utilizing 4 candidate glues, was performed. The cold temperature was set to 25°K (-248°C), and warm was 150°K (-123°C). The 9309 performed nominally, with no crazing or cracking and was accepted for use. As a side note, only one of the tested epoxies exhibited any signs of thermal distress. As a hedge against exceeding our thermal predictions, small solar absorbers were attached to the 2 joints in the mid boom. These small flag-like appendages project into sunlight, and raise the expected temperature by ~ 5 degrees, buying some margin for the assembly (see Fig. 6).

3.2 Lock Pin Details

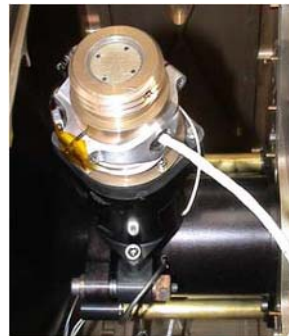
Once the rings are bonded to the tubes, the locking pins/rollers are installed into precision radial bores in these inner and outer rings. When a segment locks, the pins are pushed into the sockets by custom torsion springs, 2 for each pin. The ‘arms’ of the springs also provide alignment for the pins, keeping the roller aligned in the groove. The pin/roller combination accommodates slight tube dimensional changes during deployment, as the spring compliance takes up any bumps or dips. When the tube section reaches end of travel, the pins are pushed into tapered holes, locking the tubes rigidly with respect to each other. Guide ramps are provided at the end of travel to ensure that the pins are aligned with the sockets. Each locking pin has a taper (a 20° included angle) that fits into the corresponding tapered socket. This gives a self-locking feature to the pin, offering increased rigidity and prevents the pins from backing out during vibration. With 6 lock pins engaged per joint, 3 inward acting, 3 outward, the boom exhibits great rigidity, and offers redundancy in the event that one pin does not lock (or more, up to 3 maximum, as long as they all are not in same ring).

Rollers are fitted to the tips of the locking pins to minimize deployment drag when rolling in the tube’s grooves. Repeated deployments have shown no visible signs of wear to the tube or the rollers. To provide conductivity, the tapered portion of the pins and sockets were Alodined, while the sliding cylindrical parts were Type III black anodized to give good wear and low friction sliding properties. The Gr/E exhibits a low surface resistance too, enabling the boom to easily meet the surface resistance requirement of $<10e8$ ohms per square throughout its stroke. The drag was measured to be 3.1 N on average ($+/-0.5$ N) for the assemblies. The main function of the rollers is to keep the tubes aligned during deployment, so that the pin engagement is virtually guaranteed at the end of stroke.

3.3 Shape Memory Alloy Release (SMAR) Details

The SMAR uses the interesting phase change properties of a 45% titanium–55% nickel alloy (trade named Nitinol initially) to provide the actuation of the IMPACT Boom. This device,

Fig. 10 Shape memory alloy release assembly



shown in Fig. 10, was pioneered by TiNi Aerospace³ in cooperation with UCB-SSL. It takes advantage of the $\sim 4\%$ dimensional change in the drawn alloy wire when heated above its transformation temperature to let a ball detent assembly release a large spring loaded retracting pin. Since there was a large design load (50 Gs), $> 2.5 \text{ kN}$ retraction force was needed. A force amplifier was added to the TiNi standard P50 ($\sim 200 \text{ N}$ (50 lb) pin puller). The force amplifier contains a stack of Belleville washers, preloaded and held by the P50 pin in another ball detent assembly, providing a final pull force exceeding 3 kN, and able to withstand a side load of 800 N at the guide bushing—boom tail piece interface. When an electric current is passed through the Ti–Ni wire, it changes phase, elongates, releasing the primary pin, which then retracts and releases the main pin, which retracts with great force, allowing the Stacer to deploy. The main benefit of using a SMAR, aside from increased safety as no explosives are used, is that the flight unit can be tested over and over again (hundreds of cycles), and is simply resetable with a hand tool, with no temperature or time dependant constraints.

3.4 Flyweight Brake

After the SMAR has been triggered, kick springs push the tubes out of the combs ($\sim 20 \text{ N}$ force) and the deployment assist device pushes the Stacer out of the canister with a force of $\sim 90 \text{ N}$, giving the assembly a good initial velocity. The Stacer provides force throughout the extension, so the deployment velocity would increase until a balance between drag and push is achieved. This balance is never reached by the boom, so the deployment velocity would reach a ‘run-away’ condition rapidly, with the possible lock pin shearing, ring-tube separation or other damage as consequences. As with every Stacer, a means to limit deployment velocity is incorporated. For the IMPACT Boom, a flyweight brake mechanism (see Fig. 11) is attached to the Stacer via a woven Dacron (parachute shock) cord. Similar to the device found on rotary dial telephones which prevented the dial from being rotated faster than an old telephone exchange could count, the flyweight brake supplies braking force proportional to the rotational speed of its ‘flying-weight’ assembly. If the force (speed) increases, the brake shoes are centripetally accelerated against the brake drum, increasing the braking force and slowing the rotational velocity. Over a wide range of forces, the brake typically can control the speed to $+/- 10\%$. For the Boom, a deployment velocity of $\sim 0.5 \text{ m/s}$ was chosen. This allows a certain momentum to build, but is slow enough to avoid shearing damage to the lock pins at the end of travel.

³TiNi Aerospace, San Leandro, CA 94577.

Fig. 11 Flyweight brake, harness spool assembly

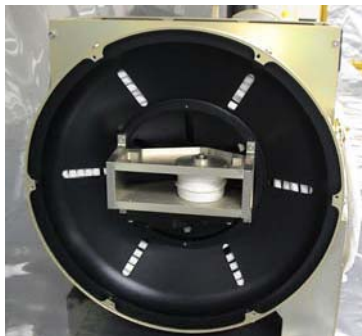


Fig. 12 A length of Stacer

3.5 Harness and Spool

The power and electrical signals between the IMPACT instrument data processing unit (IDPU) and the instruments are carried by a cable routed down the center of the tubes (see Figs. 5 and 11), and is stowed on a spool for launch. This harness is a custom fabricated conductor assembly consisting of 7 coaxial cables and 5 twisted shielded pairs. Built of silver plated copper with Gortex® dielectric, the harness is wound onto a bobbin when stowed and is pulled off when the boom deploys. This ‘straight through’ design provides greater signal bandwidth, higher reliability and allows longer harness lengths as there are no slip rings or other connections between the data processing unit and the instruments. Care is taken to pre-twist the harness to avoid kinking when stowing.

3.6 The Stacer

The Stacer is a rolled, constant helical pitch, fixed diameter flat spring (see Fig. 12). The strip width, thickness, roll diameter, and helical pitch are selectable for each application, allowing each Stacer to be tailored for optimum properties. Stacers range in size from <1 m to >10 m in length, from 4 mm to 55 mm in diameter at the tip, and can provide extensive force from almost nothing to 200 N. Trade studies can balance mass versus length, force, etc. In the last 30 years, more than 650 units have been utilized in aerospace applications, from sounding rocket sensors to gravity gradient booms with large masses on the end. What makes the IMPACT Boom unique is the use of the Stacer as a spring ‘motor’ without using it as the structure or sensor surface. Most applications have the Stacer with the sensor(s) mounted directly on it, or the Stacer as the sensor, for example as an antenna (a total of six 6 m long beryllium copper Stacers are used on STEREO for the SWAVES experiment in this manner; see Bougeret et al. 2008).

To accommodate the MAG requirement of low magnetic signature for the boom, Elgiloy® was selected as the spring material over the more traditional beryllium copper (Be–Cu). This alloy was chosen to minimize any eddy currents that could be developed between

the SWEA/STE and the spacecraft. Originally invented in the late 1940s for use in watches, it has been used for exacting Stacer applications several times. Its internal resistance is higher than copper, and cuts down the eddy currents accordingly. It has a higher modulus (E), and can provide greater force in the same physical volume as the Be–Cu. Elgiloy is a cobalt ‘super-alloy’, having an $E \sim 190$ GPa and a yield strength (S_y) of ~ 1600 MPa.⁴

At deployment, the formation of the Stacer begins with the initial coil winding out of the storage canister onto a cylindrical tip piece, which is slightly larger than the free-coil diameter of the Stacer. Thus the Stacer grabs the tip piece tightly, and the subsequent coils ‘stack’ up on the prior, producing the characteristic spiral appearance. The typical helix angle provides for significant overlap, such that a section taken at any point along the Stacer would yield at least 2 thicknesses of strip material. The outer layer of strip is rolled to the same diameter as the inner layer, so the outer grips the inner with a force normal to the surface. As a result, between layers, significant inter-coil friction exists and prevents inter-coil slipping for small disturbances. This gives the Stacer one of its more useful properties: it behaves as a thin walled tube for small displacements, with similar bending strength and stiffness. If a larger displacement occurs, the coils slip, dissipating the strain energy, serving as a friction damper. The damping ratio value is typically 5–15% for the non-slipping regime, and can reach 30–40% with the slipping. This damping stops the Stacer from “ringing”, and dissipates vibration. Of course, the displacement limit is buckling, as any tube would experience when taken beyond its yielding strength.

As described, the motive force for the deployment is a Stacer. When compressed (stowed) it is a very compact package: it fits in a cylinder $\varnothing 50 \times 130$ mm long. When the Stacer is stowed, the strip is flexed into the canister, laying each coil inside its predecessor, and wound tightly to inner surface of the can. When released, this stored strain energy is reclaimed, giving the motive effort needed to move the tubes along their path. The Stacer generates a higher force at the beginning of stroke, ~ 46 N for this design, and the force curve dropped to 31 N at the end of stroke (there was an isolated minimum value of 18 N obtained from one force test out of 20). The measured force that the Stacer provides is shown in the polynomial fit curve in Fig. 13.

For the purposes of torque (force) margin analysis, the initial push is 45 N, final thrust 18 N (the lowest value obtained). This lower value was used to bound the design force available for deployment. The Torque (force) Ratio (τ_R) requirement from GEVS SE (Sect. 2.4.5.3) for systems dominated by resistive torques due to friction is:

$$\tau_R = \tau_{\text{avail}} / \tau_{\text{required}} \geq 3.0 \quad (1)$$

and the Torque (force) Margin (τ_M) requirement from GEVS is:

$$\tau_M = \tau_{\text{avail}} / \tau_{\text{required}} - 1 \geq 2.0 \quad (2)$$

This assumes worst case for the boom, taking the lowest force for the Stacer and applying it to the entire stroke. There is additional margin, as there is a significant mass at the end of the boom (2.2 kg: SWEA/STE-D + electronics) which contributes momentum towards full deployment stroke. Using the given values it can be shown that the force available: minimum Stacer force of 18 N, divided by the force required, the tube drag of 3.1 N yields a torque ratio of 5.8, and a torque margin of 4.8. The Stacer satisfies the force requirements

⁴Matweb, <http://www.matweb.com/search/SpecificMaterial.asp?Mat=Elgiloy>.

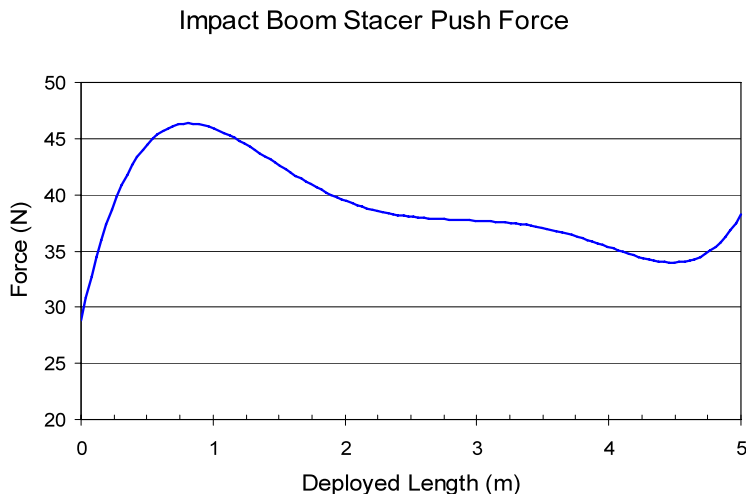


Fig. 13 Graph showing Stacer force

by analysis. Still, the device must show functionality to prove that manufacturing has been in accordance with design.

The graph shows the need for a deployment initiator. The stowed Stacer is in a ‘metastable’ condition. If left by itself, it would partially deploy in either direction, therefore a back plate on the canister is required. To ensure that the Stacer’s first few coils are well-formed, a deployment assist device (DAD) is incorporated. The final upturn in the force curve is an artifact of how the force was measured. The Stacer in this case is 5 m long, and when it is fully deployed, the coils have tightened onto themselves. The force value was taken at the moment the Stacer began to slip back into the canister when axially loaded. For this case, the coil needs to be expanded significantly, and requires greater effort.

There was an additional use for the Stacer after deployment: as the secondary EMI/EMC shield. While each of the conductors in the harness is shielded, the mission’s low noise requirement demanded a second, ‘over-shield’ for all conductors. Since the harness runs down the center of the Stacer, the Stacer was tied to ground, and serves this purpose.

4 Deployment Sequence

Deployment is initiated when the shape memory alloy release device (SMAR) is triggered causing the restraint pin to pull out of the tail of the Stacer tip piece. To give the Stacer and tube deployment an initial ‘kick’, the deployment assist device (DAD) was incorporated between the SMAR mount plate and the 50 mm tube base. The DAD consists of three 150 mm long coil springs, compressed when stowed, and when released provide ~ 90 N of push at the very beginning of the stroke. After the 100 mm of travel the DAD has completed its stroke, the initial coils of the Stacer are fully formed around the tip piece, and the flyweight brake has been spun up to speed. The Stacer is attached to the base of the 50 mm tube via a swivel, allowing the Stacer to wind down while extending, recapturing the strain energy stored when the Stacer was wound ‘out’ against the canister. At the end of the 50 mm tube travel, the 6 lock pins pop into their sockets, and transfer the Stacer push force, as well as momentum from the first tube and the SWEA/STE + electronics, to the 90 mm tube, pulling

it along until it latches with the 130 mm tube; then the assembly extends and latches with the 170 mm tube, and finally the entire 4 tube rigid assembly locks onto the 210 mm tube, which is fixed to the spacecraft. While the actual sequence follows this description fairly closely, occasionally the tube drag would cause one or another tube to partially extend. There was no provision or requirement for the boom to deploy in any set sequence. To control the velocity of the tubes during deployment, the flyweight brake is attached to the 50 mm tube via a lanyard, limiting the speed of deployment to ~ 0.5 m/s, giving a total deployment time of ~ 8 s. There are position alignment blocks (combs) for the stowed (launch) condition holding the tubes aligned relative to each other, and carrying the vibration loads. These also incorporate kick springs to aid in the deployment, and to alleviate any possible “stiction” from the blocks.

The boom is not retractable once deployed. Re-stowing is achieved by removal from the spacecraft, and hand retraction of each set of pins followed by each tube segment being (de) telescoped; after which the Stacer is compressed into its canister; and the harness and flyweight brake are rewound. Finally, the SMAR is reset, reinstalled, and the launch preload is set.

5 Verification

The IMPACT Boom’s verification activities were based on GEVS SE, as modified by JHU-APL for mission specific needs. The test regime selected for the STEREO mission was “Protoflight”, meaning new (unflown or non-heritage) hardware was tested at prototype at levels (i.e. higher temperature or vibration levels) representing significant margin over launch or flight-like conditions while test durations were set by actual flight predictions. This method is typically used to shorten development times by eliminating the engineering/qualification model (EM) fabrication and test period. The IMPACT Team built an engineering model (EM) and 2 flight models (FMs), and tested all 3 assemblies to the protoflight levels. Additional STEREO mission requirements for these tests included Level 300 cleanliness, UV + Visible light inspection; no silicones used for fabrication; and screening for silicone residuals. Vibration levels were taken from the Delta II user’s manual⁵ modified by APL analysis for the stacked satellite configuration. Stringent EMI/EMC levels were also levied due to the extremely sensitive radio receiver (Swaves) and magnetometer on board.

Testing procedures met standard NASA mission requirements. The main tasks to be performed included: demonstration of sufficient force (torque) margin for extension of telescoping sections throughout the Boom’s stroke; thermal design validation at 25°K (discussed previously); and thermal vacuum cycling and deployment verification at hot and cold operational temperatures.

As the team worked on the testing it became clear that Stacer thrust force is not easy to measure accurately or repeatably. The deployment of a Stacer is a ‘stick-slip’ affair: and once stopped, it sticks, then when released slips, giving a wide range of force values due to the hysteresis built into the inter-coil friction. For consistency, the force value used at any point was the force needed to start the Stacer being pushed back into the canister, after overcoming the ‘stick-tion’. This does not accurately convey the sliding force, but is as close as can be statically measured. Attempts to measure Stacer force dynamically were fruitless. Another difficulty lay in measuring the drag from rollers and harness. Each tube

⁵Delta II Payload Planner’s Guide, The Boeing Company, Huntington Beach, CA 92647.

Fig. 14 Thermal vacuum chamber



has a 1.1 m stroke, and pulling steadily for that distance vertically while monitoring force is a challenge. The weight of the tube assembly was subtracted from the pull out force, giving the drag value.

Finally it was seen that proving force margin analytically was not conclusive as the uncertainties in each measurement, when combined, exceeded the margin requirements. A different path was chosen: show that the boom deploys while using 1/3 of the available Stacer force. By definition, there is sufficient margin. This is how the boom force margin was verified.

When testing deployables, the desire is to prove beyond doubt that the mechanism will deploy in space, however, it must be tested here on the ground first. The number of test deployments is a major question, as it brings up wear margin: the design must show that it is sufficiently robust to survive testing and flight without degradation. The EM served this purpose, getting many deployments more than the flight units did (>20). After solidifying the quantity and manner of tests, the test plan was developed, reviewed and implemented.

Testing large deployables in a simulated space environment is difficult, and ensuring that the test actually verifies functionality is critical. Deploying the boom horizontally was initially considered since it is relatively easy to develop a 6 m long test rig that rests on the floor. After a few small efforts in this orientation, it was realized that the only way to ensure

Fig. 15 Gantry detail



that roller drag on the tubes was representative of actual orbital deployment would be to deploy the boom vertically. While several interim off load pulley systems were used, all the verification deployments were performed on the thermal vacuum gantry test rig.

To this end, a tall vacuum chamber was designed and built to allow the tests to be performed (see Fig. 4). Inside the chamber ‘chimney’ a gantry that allowed a counterbalance pulley system to provide G negation was installed (see Figs. 14, 15 and 16). The distance from the top of the boom to the pulley was maximized to provide the least possible restorative (centering) force to the sections of the boom during deployment. Figures 15 and 16 show the boom after a deployment test in the chamber.

5.1 Counterweight Description

To demonstrate the force (torque) margin, the masses to be used for the counterbalance force had to be chosen to show that the Stacer would be energetic enough to deploy the boom. The mass of each of the tubes (in flight configuration) was added to give neutral balance, plus the Stacer neutralization mass (determined by bare Stacer vertical deployments to be 164 gr). This mass (5214 gr) was decreased to 2/3 of the Stacer average minimum force ($31 \text{ N} \times 0.67 = 20.7 \text{ N}$, converted to kgs: $20.7 \text{ N}/9.81 \text{ kg m/s}^2 = 2.07 \text{ kg}$) and subtracted from the counterweights. All 10 verification deployments were ‘force margin’ deployments and were successful. After deployment, each boom was inspected for wear, with no signs of degradation of rollers or Gr/E. The EM has been deployed $\gg 20$ times, and is still in good condition.

Initially, the counterweights far exceed the G negation requirements for deployment as only one tube is being deployed, while it is being pulled by the counter weight for 4 tubes. This was not invalid for our testing needs, as the flyweight brake dissipates the extra force, keeping the velocity in correct range. The area of interest is the very end of travel, where the Stacer force is lowest, and the full mass is being acted on. It was this point that the gantry design addressed.

Fig. 16 IMPACT Boom after a thermal vacuum deployment



5.2 Magnetometer Alignment Verification

After deployment, the alignment of the MAG needed to be measured to determine compliance with the mission requirements. A very accurate digital level (resolution: $0.01^\circ \pm 0.02$) was used for this activity. The measurements were taken relative to the reference coordinate system established in the Interface Control Document (ICD) for the boom. The relative angles for the mounting feet for the $X - Z$ and $X - Y$ planes were recorded. The angles for the same planes (translated to the MAG tray—see Fig. 2) were then measured before and after deployment. The difference was taken, yielding the deviation of the MAG tray from the respective mounting plane. Figure 17 shows the measured differences of the deviations for the flight units for each plane.

For the final determination of pointing error, the root of the sum of the squares (RSS) was calculated to give the magnitude of the deviation (the direction was not of interest as long as the magnitude did not exceed specification). Flight Model 1 measured deviation used 0.10° of its allowable 0.88° error budget, while Flight Model 2 required 0.11° . The IMPACT Boom deploys accurately, repeatably, and exceeds requirements by a large margin.

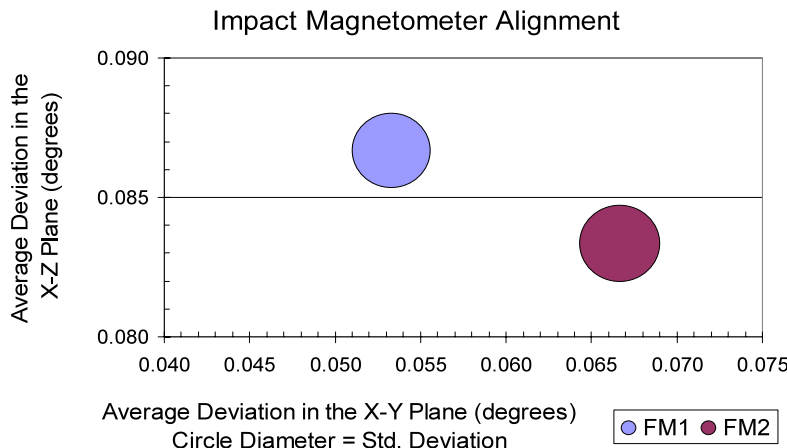


Fig. 17 Magnetometer alignment error

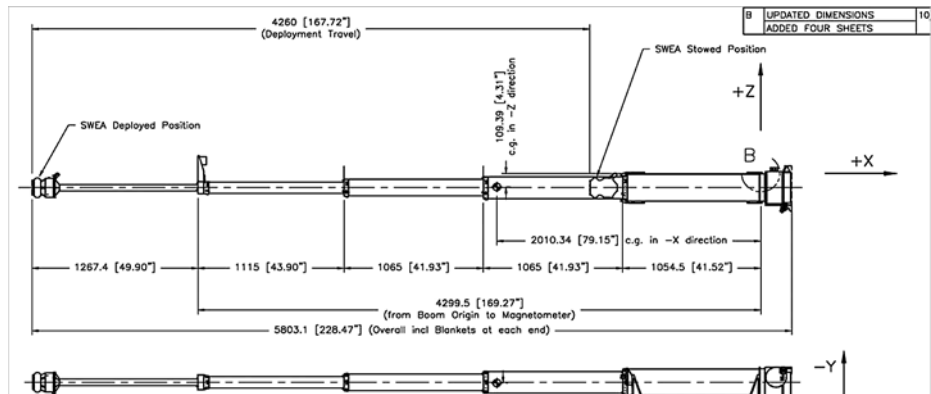


Fig. 18 IMPACT Boom "B" deployed detail

6 Summary

Following deployment tests on the integrated spacecraft at Goddard Space Flight Center, the IMPACT Boom had completed acceptance verification for use in flight on the NASA STEREO mission. This application has demonstrated the use of a Stacer spring as a motive force for a major deployable structure, not only as a sensor or sensor support. This represents a major cost savings from traditional motor driven deployables, with their associated (expensive) electronics. Currently, the STEREO launch is planned for mid-to-late 2006, with deployment of the boom occurring within a 3–30 day window after launch. (Note: both booms deployed nominally and are operating as designed.)

Acknowledgements Thanks go to Dr. Janet Luhmann, principal investigator for the IMPACT Suite, and the entire IMPACT Boom Team at the University of California Berkeley, Space Sciences Laboratory. Thanks also to NASA Goddard Space Flight Center for working with us to get this new hardware off the ground, and to all the reviewers whose inputs and criticisms helped make the boom robust enough to survive qualification. Finally, we are grateful to the STEREO crew at APL for their continued support for the program.

References

- Acuna et al., Space Sci. Rev. (2008, this issue). doi:[10.1007/s11214-007-9259-2](https://doi.org/10.1007/s11214-007-9259-2)
- Bougeret et al., Space Sci. Rev. (2008, this issue). doi:[10.1007/s11214-007-9298-8](https://doi.org/10.1007/s11214-007-9298-8)
- Howard et al., Space Sci. Rev. (2008, this issue). doi:[10.1007/s11214-008-9341-4](https://doi.org/10.1007/s11214-008-9341-4)
- Lin et al., Space Sci. Rev. (2008, this issue). doi:[10.1007/s11214-008-9330-7](https://doi.org/10.1007/s11214-008-9330-7)
- Luhmann et al., Space Sci. Rev. (2008, this issue). doi:[10.1007/s11214-007-9170-x](https://doi.org/10.1007/s11214-007-9170-x)
- Sauvaud et al., Space Sci. Rev. (2008, this issue). doi:[10.1007/s11214-007-9174-6](https://doi.org/10.1007/s11214-007-9174-6)
- Space System Reliability and Safety Office, Code 302; *General Environmental Verification Specification for STS and ELV*, Rev. A (June 1996), National Aeronautics and Space Administration, Goddard Space Flight Center, Greenbelt, MD 20771, Sects. 2.4.5.3–2.4.6.2

The STEREO/IMPACT Magnetic Field Experiment

M.H. Acuña · D. Curtis · J.L. Scheifele · C.T. Russell ·
P. Schroeder · A. Szabo · J.G. Luhmann

Originally published in the journal Space Science Reviews, Volume 136, Nos 1–4.
DOI: [10.1007/s11214-007-9259-2](https://doi.org/10.1007/s11214-007-9259-2) © Springer Science+Business Media B.V. 2007

Abstract The magnetometer on the STEREO mission is one of the sensors in the IMPACT instrument suite. A single, triaxial, wide-range, low-power and noise fluxgate magnetometer of traditional design—and reduced volume configuration—has been implemented in each spacecraft. The sensors are mounted on the IMPACT telescoping booms at a distance of ~ 3 m from the spacecraft body to reduce magnetic contamination. The electronics have been designed as an integral part of the IMPACT Data Processing Unit, sharing a common power converter and data/command interfaces. The instruments cover the range $\pm 65,536$ nT in two intervals controlled by the IDPU (± 512 nT; $\pm 65,536$ nT). This very wide range allows operation of the instruments during all phases of the mission, including Earth flybys as well as during spacecraft test and integration in the geomagnetic field. The primary STEREO/IMPACT science objectives addressed by the magnetometer are the study of the interplanetary magnetic field (IMF), its response to solar activity, and its relationship to solar wind structure. The instruments were powered on and the booms deployed on November 1, 2006, seven days after the spacecraft were launched, and are operating nominally. A magnetic cleanliness program was implemented to minimize variable spacecraft fields and to ensure that the static spacecraft-generated magnetic field does not interfere with the measurements.

Keywords STEREO mission · IMPACT · Space weather · Interplanetary medium · Solar physics

PACS 96.50.Ry · 96.50.Qx · 96.50.sh · 96.50.Xy · 96.60.Ly · 96.60.-j

M.H. Acuña (✉) · J.L. Scheifele · A. Szabo
NASA Goddard Space Flight Center, Greenbelt, MD, USA
e-mail: mario.acuna@nasa.gov

D. Curtis · P. Schroeder · J.G. Luhmann
Space Sciences Laboratory, University of California, Berkeley, CA, USA

C.T. Russell
Institute of Geophysics and Planetary Physics, University of California, Los Angeles, CA, USA

1 Introduction

The STEREO IMPACT investigation incorporates a suite of instruments designed to address important elements of the primary science objectives of the mission (see Luhmann et al. 2007). The interplanetary magnetic field (IMF) structure and dynamics represent an extension of the solar magnetic field as carried out from the Sun by the supersonic solar wind. The IMPACT magnetometer experiment will continuously measure the time-variable, large-scale structure of the IMF at both locations of the STEREO spacecraft in their orbits and in particular the gradients between them indicative of small-scale structures possibly associated with transient events. These measurements will allow us to interpret solar wind parameters, particle distribution functions, the paths followed by energetic particles detected at the spacecraft. We will also be able to analyze local sources for in-situ acceleration mechanisms such as shocks and discontinuities. The experiment incorporates fast measurement capabilities that will allow the characterization of IMF fluctuations over a wide range of frequencies spanning multi-year solar cycle variations to proton gyrofrequencies; this allows the study of microscale phenomena in the solar wind. The magnetic field measurements provide a fundamental frame of reference for defining the background on which multiple interplanetary physics phenomena take place. Of particular interest to the twin spacecraft STEREO mission are those associated with solar transient events that affect the Earth's immediate environment.

The magnetometer provides continuous measurements of the local IMF at both spacecraft locations, with an intrinsic sample rate of 32 samples/s. Raw data at this sampling rate are delivered to the IMPACT suite Digital Processing Unit (IDPU) for processing, packetization and transmission to the ground as well as for use by other IMPACT experiments onboard. The measurements are precise (16-bit A/D converter or 0.003% of full scale) and sensitive (0.015 nT), with an absolute accuracy goal of ~ 0.1 nT. The intrinsic noise level of the magnetometer has the typical $1/f$ spectrum associated with fluxgate sensors (Acuña 2002) and references therein) with a baseline value of 10^{-5} nT 2 /Hz at 1 Hz. At ~ 10 Hz the spectrum flattens out to a value of $\sim 10^{-6}$ nT 2 /Hz. The integrated RMS noise in the 0.001–1 Hz frequency range is typically < 0.01 nT so instrument noise, and its effect on the measurements, is minimal.

The instrument configuration aboard each spacecraft consists of a single triaxial sensor mounted approximately two-thirds of the way along a four-meter deployable boom, or three meters from the edge of the spacecraft bus. This boom is shared with other IMPACT suite instruments, as illustrated in Figs. 1a and 1b. The sensor location represents a reasonable compromise among many conflicting requirements. The telescoping boom (Luhmann et al. 2007) includes a 25-cm tray attached perpendicular to the boom axis on which the magnetometer sensor is mounted. This tray is necessary to place the sensor away from possible interference from magnetic fields created by the signals and currents flowing in the boom harness that supplies power and signals to other experiments on the boom. The triaxial sensor assembly is shown in Fig. 2 and measures $10.8 \times 6.4 \times 6.4$ cm. Boom deployment for both spacecraft took place on November 1, 2006, seven days after launch while the spacecraft were in a low magnetic field environment. Both magnetometer instruments have remained on since their activation on that date. The signal processing portion of the magnetometer electronics was implemented within the IMPACT instrument data processing unit (IDPU), on a $19.6 \times 15.6 \times 2.0$ cm frame that supports the main board and three 16-bit sigma-delta analog to digital converters. The complete assembly is shown in Fig. 3. A common power converter is shared between the IDPU and magnetometer electronics, whose power consumption is ~ 0.5 watts (not including heater power). The thermal environment

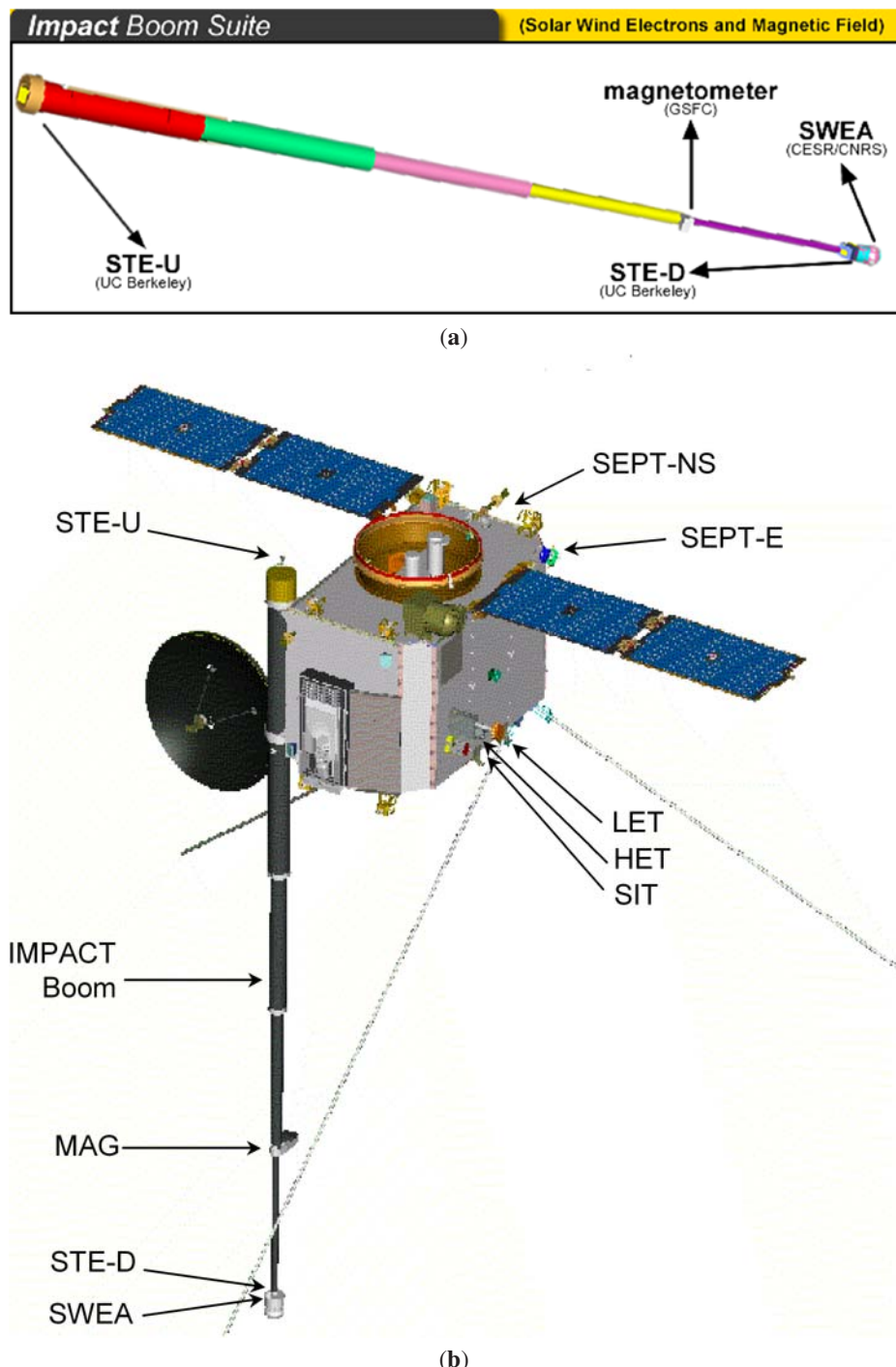


Fig. 1 (a) The STEREO deployable boom and the location of IMPACT suite sensors. The MAG sensor is approximately 1.5 m inboard from the SWEA/STE-D sensors. (b) Relative placement of the IMPACT boom on the STEREO spacecraft. Other IMPACT suite sensors are also shown for reference

Fig. 2 The triaxial MAG sensor assembly, cover and baseplate. The sensor is thermally isolated from the mounting surface by four acetal legs. A foil heater used to adjust the assembly temperature is also visible on the underside of the sensor base. In the final configuration the sensor is wrapped with a 20-layer, grounded thermal blanket that also acts as an electrostatic shield



Fig. 3 The IMPACT/MAG electronics assembly. This “slice” or frame is incorporated within the IDPU assembly that provides interfaces and power. It weighs 232 grams and requires 0.48 watts of power. A combination of surface mount and through-hole components are used to meet stringent performance and quality requirements



of the magnetometer sensor assembly is controlled by the use of thermal blankets and a thermofoil heater that supplies up to 1.2 watts of power at 50 kHz, controlled by a dedicated pulse-width-modulation (PWM) circuit. This AC power system is required to avoid the introduction of stray magnetic fields that a DC heater can generate and its operating frequency is crystal controlled to avoid interference with the SWAVES experiment onboard.

The performance of the IMPACT/magnetometer sensors is typical of that of low-noise, ring-core magnetometers that have been widely used in space missions (Acuña 2002). The zero levels including spacecraft contributions are estimated by means of periodic roll maneuvers about the Earth-pointed spacecraft axis and use of the statistical properties of the interplanetary magnetic field (Schwarzl and Russell 2007). Maneuvers about a second axis, perpendicular to the roll axis, are not allowed by spacecraft safety constraints. As mentioned earlier the instrument incorporates two dynamic ranges (low and high) that can be switched by automatic or manual control. Since the low range upper limit is 512 nT, frequent range changes are not expected when the spacecraft are in their final orbits in the solar wind. However, this wide-range measurement capability is extremely useful during the early part of the

mission when the “phasing” orbits required to inject the spacecraft into their final orbits place them in regions of strong fields.

2 Science Objectives

The overall science objectives of the STEREO mission are: understanding the causes and mechanisms of Coronal Mass Ejection (CME) initiation; characterizing the propagation and evolution of CMEs through the heliosphere; discovering the mechanisms and sites of energetic particle acceleration in the low corona and interplanetary medium; and developing a 3-D time-dependent model of the magnetic topology, temperature, density and velocity structure of the ambient solar wind. The IMPACT investigation addresses these objectives through synergistic measurements of plasma parameters, energetic charged particles and in-situ magnetic fields. The IMPACT fluxgate magnetometer makes significant contributions to all of these objectives.

2.1 CME Identification and Structure

Various parameters are used to identify the boundaries of the interplanetary manifestation of CMEs (ICMEs) often yielding significantly different results for the same event (Zwickl et al. 1983; Neugebauer and Goldstein 1997; Mulligan et al. 1999; and Burlaga et al. 2001). Easiest to identify are magnetic clouds that have slowly rotating strong magnetic fields with a suppressed level of field fluctuations (e.g., Burlaga 1995). In-situ vector magnetic field observations have been used with great success to model these structures as force-free magnetic flux ropes (e.g., Lepping et al. 2006 and references within; also see Fig. 4). Burlaga et al. (1990) used measurements from four spacecraft—Helios I and II, IMP 8 and Voyager (see Fig. 5)—to determine the global shape or geometry of the magnetic clouds. Mulligan et al. (1999) and Mulligan and Russel (2001) used data from the WIND, NEAR and ACE spacecraft to study CME’s and associated IMF structures for selected events. With the two STEREO spacecraft and near Earth observations, this will be routinely accomplished. Current MHD models simulating the evolution of magnetic clouds in the heliosphere predict significant deviation from cylindrical symmetry by 1 AU (e.g., Odstrcil et al. 2004) or even indentations at streamer belt latitudes as the faster moving high-latitude portions of the cloud leave the low-latitude segments behind (Kasper and Manchester 2007). With fortuitous orientation of magnetic clouds, STEREO multi-point magnetic field and plasma observations will be able to determine the validity of these predictions.

The internal structure of magnetic clouds is often very complex. Counterstreaming halo electron measurements have demonstrated that often both foot points of a flux rope are still connected to the Sun when the cloud passes 1 AU (Gosling 1990). However, WIND observations revealed intermittent time periods when some internal field lines disconnected at one or both foot points from the Sun (Larson et al. 1997). Since most magnetic clouds will not pass exactly half way in between the two STEREO spacecraft, thus providing ICME cross-sections at different times, the IMPACT observations will give a glimpse into the time evolution of the internal field line structure of magnetic clouds by comparing the time periods of solar disconnections.

Magnetic clouds represent only 30% to 50% of the total ICMEs observed at 1 AU (Gosling 1990) with possible solar cycle dependence (Richardson and Cane 2004). The physical reasons for the existence of these complex ejecta is not established at this time, but they are due to either interaction between colliding ICMEs or they reflect

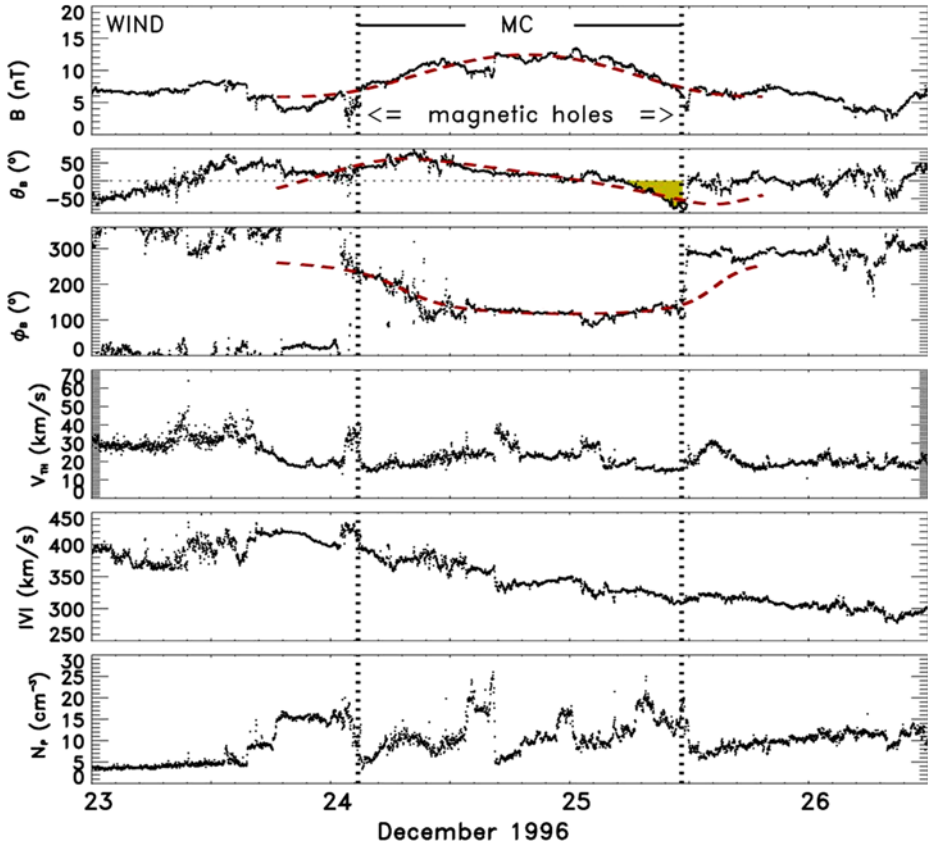


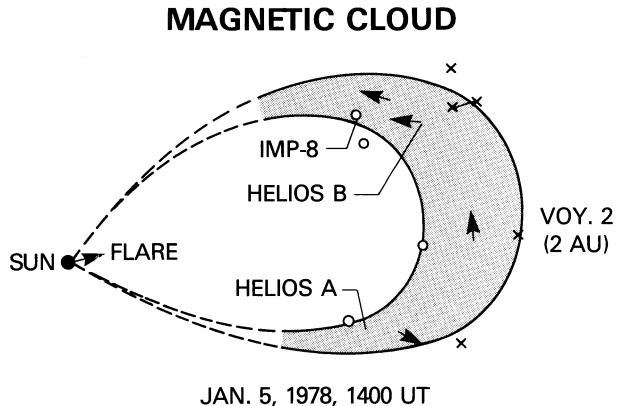
Fig. 4 A magnetic cloud observed by WIND on December 24–25, 1996. The panels are, top to bottom, magnetic field strength, elevation and azimuth angle of the magnetic field direction, solar wind proton thermal speed, proton speed and density. The dotted vertical lines indicate the magnetic cloud boundaries identified based on field signatures. The dashed curves are the result of a constant alpha force-free flux rope fit to the observations (based on Lepping et al. 2006)

a more dynamic coronal magnetic structure during their initiation (Burlaga et al. 2001; Richardson and Cane 2004); or the magnetic cloud forms only part of the ICME structure and is not penetrated on most encounters. In either case, in situ observations of the internal fields and plasma properties at longitudinally widely separated locations of the same complex ICME will provide hints concerning their genesis.

2.2 CME-Driven Interplanetary Shocks

Coronagraph and radio observations show that fast ICMEs often drive interplanetary shocks in front of them. Moreover, statistical studies have established that these interplanetary shocks tend to be the strongest in front of the nose of the driving ICME (Cane 1988; Richardson and Cane 1993). However, it has not been determined how much wider the longitudinal extent of the driven shock is and indeed whether all interplanetary shocks observed at 1 AU are due to fast ICMEs. Observing the same shock at significantly different longitudinal positions will provide this information. High time resolution magnetic field

Fig. 5 The global shape of a magnetic cloud deduced from the four spacecraft observation of the January 5, 1978 event. Helios 1 and 2, IMP 8 and Voyager 2 measurements were used by Burlaga et al. (1990)



observations provided by the magnetometer will be essential to identify the shocks and to differentiate them from more gradually increasing pressure pulses.

The ICMEs do not propagate into a uniform interplanetary medium. Hence the driven shock surfaces are not expected to have a simple slowly changing curved geometry. In fact, near-Earth multi-spacecraft analysis of the same interplanetary shocks have found significant deviation from planarity (Russell et al. 1983; Szabo et al. 2001; Szabo 2005) indicating ripples on the shock surface with a ~ 100 Earth radii scale length. Specifically, Szabo et al. (2001) found—analyzing a few ACE, WIND and IMP 8 observed interplanetary shocks—that with larger inter-spacecraft separation, perpendicular to the solar wind flow direction, larger angular deviation between individually determined shock normals was likely. Supporting this result, WIND electron observations reveal cases where backstreaming electrons at nearly perpendicular shocks imply local shock surface bays of similar scale (Bale et al. 1999). The two STEREO spacecraft will provide much larger longitudinal separations than past near-Earth spacecraft, allowing the full characterization of both local and global geometry of interplanetary shock surfaces.

Interplanetary shocks are not simple step functions in solar wind parameters but have complex, non-MHD or kinetic internal structure composed of the shock foot. The shock foot is characterized by a small but systematic increase in the magnetic field over the steady solar wind values, immediately upstream. It is generally attributed to the presence of reflected ions from the shock (e.g., Paschmann et al. 1982). After the foot, the magnetic field increases sharply in the ramp, reaching values well above the steady downstream conditions thus producing the overshoot. After the peak of the overshoot, a strongly damped oscillation occurs until conditions stabilize on the downstream side. The thicknesses of the various microstructure features and the size and gradient of the ramp have strong impact on the ability of shocks to accelerate particles. The detailed mechanism behind this is still not clear. The STEREO magnetometer will provide the necessary high time resolution (~ 100 ms) magnetic field observations to resolve the various internal shock structures allowing the correlation of locally observed energetic particle characteristics to shock microstructure details.

2.3 Acceleration of Particles at Interplanetary Shocks

Interplanetary shocks are very effective in accelerating charged particles to very high energies. Thus, a large fraction of Solar Energetic Particles (SEPs) are thought to be generated by shocks driven by fast-moving CMEs. The seed particles are energized as

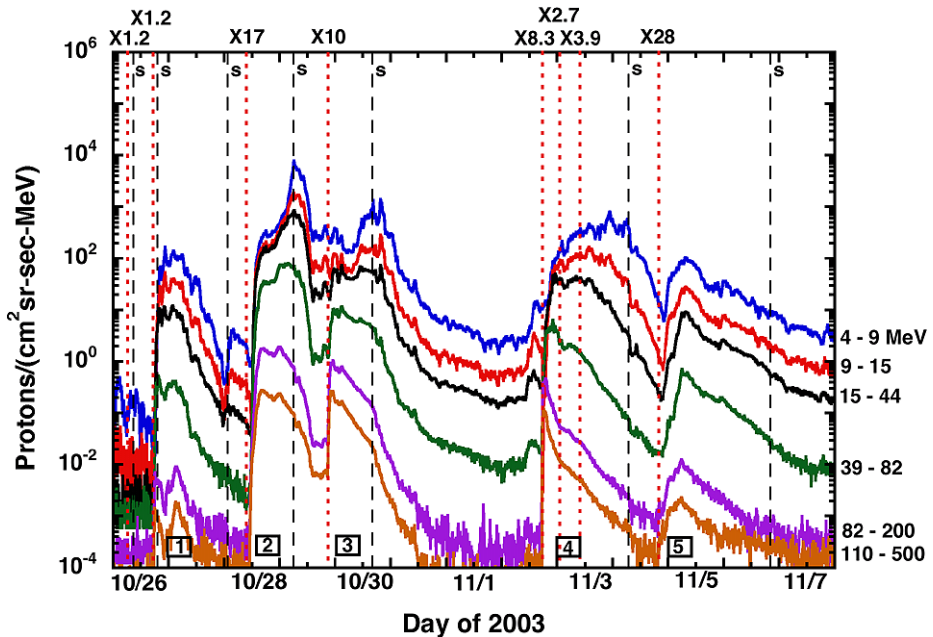


Fig. 6 Proton data measured by GOES-11 in six different energy intervals during the October–November 2003 events. Vertical dashed lines indicate the occurrence of X-class flares and the dotted lines, marked by an “s”, label the passage of interplanetary shocks at 1 AU. Note the additional particle enhancements at the time of shock crossings (after Mewaldt et al. 2005)

they cross back and forth the shock numerous times. This process of diffusive or first-order Fermi acceleration leads to a power-law spectrum of the accelerated particles that is typically observed in interplanetary space (e.g., Zank et al. 2005). The detailed characteristics of the shock, such as the shock strength and the angle between the shock normal and the upstream magnetic field, determine the effectiveness of the acceleration process. Though the highest energy particles are generated very close to the Sun, interplanetary shocks at 1 AU still accelerate particles allowing an insight into the details of the energization process (see Fig. 6). The magnetometer will provide the necessary high time resolution vector measurements of the local magnetic field that is required as input for current state-of-the-art shock-fitting methods (e.g., Viñas and Scudder 1985; Szabo 1994) yielding shock speeds, normal directions and detailed characteristics required to compare theoretical predictions to in-situ observations.

For diffusive shock acceleration to work, a certain degree of magnetic field turbulence upstream and downstream of the shock is necessary to scatter the particles. In turn, the accelerated particles themselves generate turbulence resulting in a complex relationship between the shock properties, the acceleration mechanism and turbulence wave intensity (e.g., Lee 1983; Gordon et al. 1999; Li et al. 2005). In situ particle spectra and magnetic field fluctuation levels observed by ISEE 3 (Sanderson et al. 1985) and more recently by SOHO and ACE (Bamert et al. 2004) have shown correlation between the energetic particle intensity and the wave power density near the shock front. However, these studies were limited to a single point along the shock surface. The STEREO mission, in conjunction with near Earth space-craft, allows the observation of particle intensities and magnetic turbulence levels at three points with increasing separation, thus allowing the separation of local and global processes.

Fig. 7 Composite image of the corona at the time of the eclipse on August 11, 1999 (Koutchmy et al. 2004). The fine-scale structure of the corona is clearly visible in the inner heliosphere, though it might be completely washed out by 1 AU



The STEREO magnetometer will provide high time resolution magnetic field observations that can be used to compute the required power spectral densities to above 10 Hz. This rate is sufficient to resolve ion kinetic phenomena at an interplanetary traveling shock.

2.4 Global Structure of the IMF

An important scientific objective of the STEREO mission is to determine the ambient solar wind structure. The two spacecraft will provide a lengthening baseline for measuring the geometry of interplanetary wave fronts and discontinuities—including the heliospheric current sheet (e.g., Szabo et al. 1999)—on multiple spatial scales. This type of study has been performed using, for example, IMP 8 and WIND observations (Richardson and Paularena 1998) on a limited, near-Earth scale. The STEREO observations will greatly extend the range of the transverse scales accessible.

The spectrum of the magnetic and to some extent other solar wind fluctuations as a function of wave vector is required for understanding the heliospheric turbulent cascade and thus the heating due to these processes; for determining the interaction of the fluctuations with energetic particles and thus the modulation of cosmic ray fluxes; and, by extrapolation back to the Sun, for elucidating the wave-generation mechanisms (e.g., Roberts et al., 1987, 1992). By making measurements at varying spatial scales (different frequency bands in the time series analysis) and at different spacecraft separations, the time scale of persistent features on the Sun that lead to interplanetary disturbances can be determined. It is known that stream structure is due to persistent features, but it is unclear the extent to which “microstreams”—narrow streams within larger streams—are of solar origin (as suggested by modern high-resolution coronagraph images such as Fig. 7) or are generated in transit. STEREO observations will provide the opportunity to resolve this issue.

2.5 Space Weather

The STEREO real-time telemetry capability will enable a number of different space weather forecasting techniques based on CME and flare remote sensing or field line tracing with

energetic particles. Moreover, the slowly increasing longitudinal separation between the two STEREO spacecraft will allow the determination of the typical angular width of ICMEs and high-energy particle beams. Real-time in situ magnetic field data will be essential for the forecasting of geomagnetic events caused by high-speed streams. As the Sun spins, the spacecraft lagging behind Earth will encounter the compressed fields at the leading edge of high speed streams many hours to days in advance of where they impinge on the Earth's magnetosphere causing sudden commencements and possibly geomagnetic storms (StCyr and Davila 2001). Since recurring high-speed streams have a relatively simple and well-known structure, the low cadence real time telemetry mode of STEREO will be sufficient for this purpose.

3 IMPACT/MAGNETOMETER Performance Requirements

The magnetometer performance capabilities were optimized to address the scientific objectives and to make synergistic use of limited spacecraft resources. To support measurements over the range of expected fields, both in the final and phasing orbits as well as during test and integration in Earth's field, the instruments provide a low or fine range covering ± 512 nT for each of three orthogonal axes and a high or coarse range covering $\pm 65,536$ nT. The desired absolute accuracy in the low range to meet the science objectives is ~ 0.1 nT and this goal requires that the spacecraft magnetic field at the magnetometer sensor vary by less than ~ 0.03 nT and that the sensor orientation be known to $\pm 0.5^\circ$ with respect to inertial coordinates. To achieve the magnetic cleanliness goals, a Magnetics Control Plan was implemented; this is described in more detail in Sect. 6. The onboard magnetic measurements must be digitized to a resolution of 16-bits internally for digital processing to provide a resolution of 2.0 nT in the high or coarse range and 0.015 nT resolution in the low or fine range. The scale factors and alignments must be known such that an overall accuracy better than $\sim 1\%$ of the ambient field and ~ 1 degree in alignment is achieved. These values need to be determined in a high field environment such as the Earth's field and extrapolated by laboratory measurements to the low field levels of the IMF (Merayo et al. 2000).

Table 1 shows a summary of the goals and relevant technical performance parameters required for the IMPACT/magnetometer. The availability of flight-qualified, high-resolution sigma-delta analog-to-digital converters allowed the simplification of the multi-range designs used in earlier missions to the one described for STEREO using only two dynamic ranges without loss of performance. Automatic range switching is a requirement and must be controlled automatically by commands from the IDPU in response to the intensity of the ambient field or manually commanded from the ground. The need for increased sampling

Table 1 IMPACT MAG performance characteristics

Description	Goal	Requirement
Noise level	0.01 nT	0.05 nT
Absolute accuracy	± 0.1 nT	± 0.1 nT
Range	± 512 nT, $\pm 65,536$ nT	± 512 nT
Drift	± 0.2 nT/yr	± 0.2 nT/yr
Time resolution	1/8 s (Normal) 1/32 s (Burst) 10 s (Beacon)	1 s

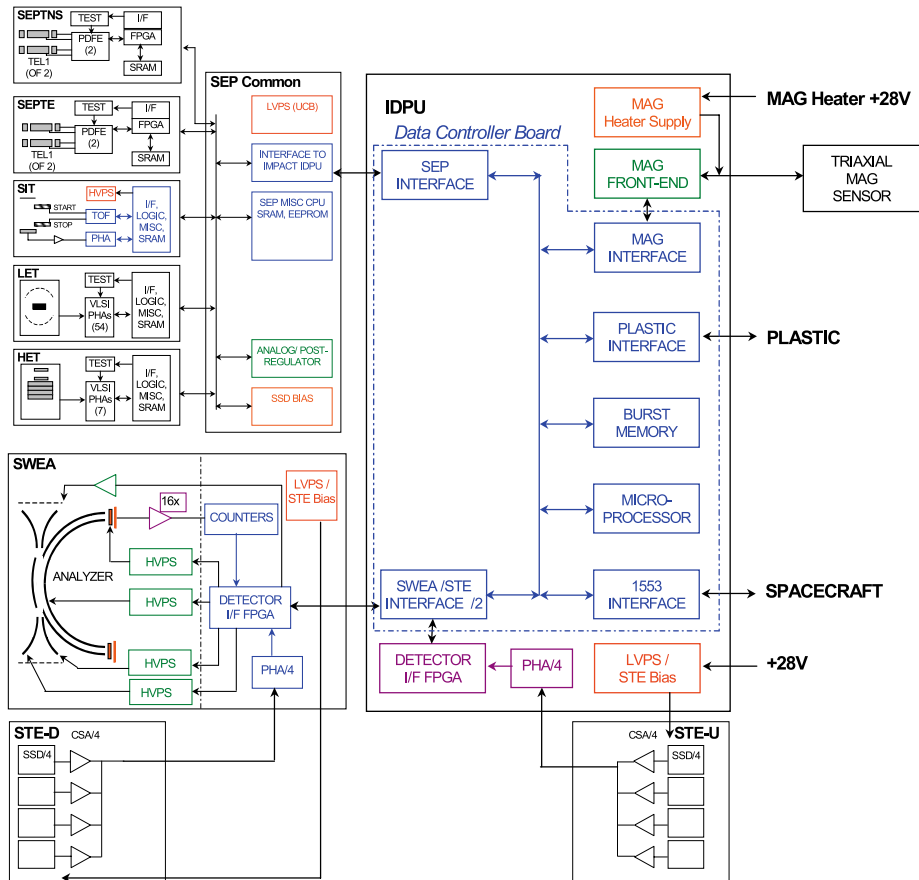


Fig. 8 Block diagram of the IMPACT instrument suite and IDPU illustrating the components associated with the MAG signal and data processing electronics. A separate MAG sensor heater PWM controller operating at a crystal controlled frequency of 50 kHz is also shown

rates in high time resolution modes required that the magnetic data be sampled internally at a constant rate of 32 samples/s. The IDPU must process these “raw” data in one of several formats to deliver the final data structure to the spacecraft packetized telemetry system and for distribution to other users. The IDPU as implemented for STEREO contains two general-purpose processors, a 1553 spacecraft interface, memory, and the necessary interface logic to connect to the magnetometer system. For reference, Fig. 8 shows a block diagram of the IDPU. This architecture defined the requirements for the magnetometer electronics interfaces. Mounting the sensor on a boom, coupled with a cost-effective, end-to-end spacecraft magnetic cleanliness program provides excellent overall performance and was the baseline chosen to satisfy all STEREO magnetic field measurement objectives. To achieve the desired measurement accuracy, STEREO required that a magnetic cleanliness program be implemented. The requirements formulated for the STEREO program included associated laboratory test instrumentation, training sessions and easy access by spacecraft subsystems builders and scientific experimenters to test and consulting resources. This approach has been pioneered by several space magnetic field measurements groups in the U.S.,

Europe and Japan and have been applied successfully to numerous space missions in the past (WIND/POLAR, Galileo, Cassini, Ulysses, CLUSTER II, Giotto, Geotail, ACE, MGS, LP, etc.). The IMPACT/magnetometer inflight instrument performance requirements include a self-calibration capability that can inject a known step-bias current in the sensor, corresponding to a magnetic field offset of approximately one-quarter of full scale along each axis. The IDPU is required to control this self-calibration function by means of commands programmed from the ground. The IMPACT/magnetometer instrument test and calibration requirements included laboratory calibrations and verification at the Goddard Space Flight Center and/or Wallops Island Magnetic Test Facilities, and finally at the system level after spacecraft integration. At this level two basic tests are required: (a) A “static” test to verify that the DC magnetic field generated by the spacecraft (unpowered) is below the required level (typically 1–3 nT), and (b) a “dynamic” test to verify that time-variable fields generated by spacecraft currents, motors, relays, etc. are below the ~ 0.03 nT goal. The system level magnetic compatibility test requirements validate the effectiveness of the magnetics control plan implemented during the design, manufacturing and integration of the spacecraft subsystems. Finally, the magnetometer sensor requires that its temperature remain within an acceptable range and this must be achieved by an active temperature-control system. The heating element is typically a thermofoil heater attached to the magnetometer sensor assembly itself. DC current cannot be used to power this heater since small deviations from its non-inductive design introduce undesirable magnetic fields. A crystal-controlled pulse-width-modulator control circuit running at 50 kHz was chosen to provide AC power to the heater and maintain the sensor temperature in the range of $-25^\circ < T < 65^\circ\text{C}$.

4 Hardware Description

The STEREO IMPACT/magnetometer is a conventional three-axis fluxgate magnetometer design with extensive flight heritage derived from more than 50 space missions (Acuña 1974; Behannon et al. 1977; Potemra et al. 1985; Neubauer et al. 1987; Zanetti et al. 1994; Lohr et al. 1997; Acuña et al. 1992, 1997; Acuña 2002), implemented through a collaboration of NASA’s Goddard Space Flight Center and the Space Sciences Laboratory of the University of California Berkeley. It also benefits significantly from the relevant experience gained through previous collaborations including Firewheel, Giotto, WIND, Mars Global Surveyor and Lunar Prospector. In the case of STEREO the conventional magnetometer design was updated with contemporary elements such as high-resolution sigma-delta analog-to-digital converters, surface mount devices and advanced microelectronics to minimize mass, volume and power resources. As mentioned previously, the basic instrument consists of an electronics board and frame mounted within the IMPACT IDPU enclosure and a triaxial sensor assembly mounted on the deployable IMPACT boom. These were illustrated in Figs. 2 and 3. The sensor assembly uses three orthogonally mounted ring core fluxgate sensors to derive vector components of the ambient field along the three directions. Small mechanical deviations from true orthogonality are corrected in ground processing using an “alignment matrix” determined in preflight calibration.

4.1 Analog Electronics

Figure 9 shows schematically a one-axis block diagram of the magnetometer analog signal processing electronics. The triaxial ring-core sensors are driven at 15.625 kHz (f_0) by a high-efficiency, nonlinear energy storage circuit that ensures that the cores are saturated

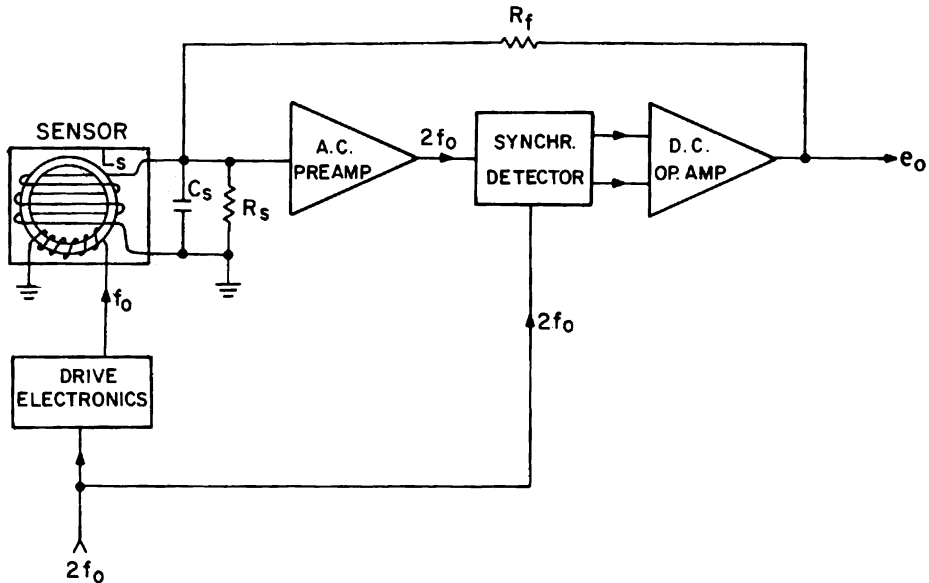


Fig. 9 Schematic block diagram of a one-axis fluxgate magnetometer. A ring core sensor is driven to saturation at frequency f_0 and the resulting signal at $2f_0$ (when a magnetic field is present) processed by the AC preamplifier, phase detector and DC amplifier (integrator) to generate a feedback current (e_0/R_f) that through the sense winding cancels the magnetic field sensed by the core

to more than 100 times their coercive force each cycle, eliminating memory effects (Acuña 1974). This drive signal is derived from a 125 kHz clock provided by the IDPU to control the analog-to-digital converters and interface logic. A related signal at twice the magnetometer excitation frequency (31.25 kHz) is also used as a reference to synchronously detect the amplified signals from the fluxgate sensors. In the absence of a magnetic field, the ring core sensors are balanced and no signal appears at the input of the AC preamplifier. When an external field is applied the sensor balance is disturbed and a signal containing only even harmonics of the excitation frequency appears at the input of the AC amplifier and is applied to the synchronous detector. The output from the synchronous detector is applied to a high gain DC integrator whose output voltage, through the resistor R_f , supplies enough current to null the field seen by the sensor and thus complete the feedback loop. The output voltage of the integrator is directly proportional to the magnitude and direction of the field with respect to each sensor axis orientation so three ring cores mounted orthogonal to each other provide full vector measurement capability. As mentioned earlier the intrinsic noise of the fluxgate sensors is <0.01 nT RMS (0.001–1 Hz). This level of noise is orders of magnitude smaller than that associated with IMF fluctuations and is adequate to detect all magnetic phenomena of interest to STEREO. Dynamic range changes are implemented by changing the parameters (by command) of the feedback resistor and the open loop gain of the AC input preamplifier while maintaining overall feedback loop stability. As already mentioned, the instrument has two dynamic ranges providing full-scale capabilities of ± 512 nT and $\pm 65,536$ nT per axis. All three axes operate in the same range and range changes are synchronized with telemetry packet timing boundaries to allow unambiguous identification of range change events. The scale factor self-calibration function for the magnetometer is im-

plemented by introducing an offset step function into the voltage-to-current converter under IDPU control. The sensor heater AC controller is powered independently from the rest of the magnetometer electronics to allow temperature control when the IDPU is powered off. This high efficiency (>90%) controller includes a foldback current limiter that protects the spacecraft against catastrophic faults in the heater. The sensor assembly and foil heater are covered by a 20-layer thermal blanket to reduce radiative losses to a minimum. The maximum power that the heater controller can deliver is limited by design to <1.2 W.

4.2 Sigma-Delta A/D Conversion

The analog outputs of the magnetometer corresponding to the three orthogonal axes are sampled simultaneously with three independent 16-bit sigma-delta analog-to-digital (A/D) converters (Cirrus Logic CS5507) at a rate of 32 conversions per second. Monotonic time sampling is ensured by the use of a hardware-derived clock synchronized to the IDPU timing functions. A single-pole 16 Hz anti-alias low-pass filter is used on each channel to limit the input bandwidth to the A/D converters. The latter introduce additional poles at 20 Hz and above due to the decimation filters intrinsic to the converters. Detailed measurements of the magnetometer time response characteristics were acquired by activating the magnetometer calibration step function under IDPU control and monitoring the digital response. A self-calibration feature is integral to typical sigma-delta A/D converter features and updates the conversion scale factor and zero offset against a precision voltage reference. The IDPU initializes the A/D converters upon turn-on and can invoke the self-calibration feature by ground command. Periodic in-flight A/D calibrations are planned to correct any long-term drifts associated with the converter scale factors and offsets. The three A/D converters are triggered simultaneously every 31.25 ms to ensure simultaneous sampling and the resulting digital data are serially shifted into the IDPU under the logic control described below.

4.3 Control Logic and Interface to the IDPU

All logic, interface and command functions associated with the magnetometer electronics are implemented within a small gate-count, radiation-hard FPGA (Actel 1020). The automatic range-change algorithm implemented within the IDPU examines the digital values associated with each axis and if they exceed a predetermined threshold the instrument is commanded to the high range. Conversely, if the digital values are below a lower threshold the instrument is commanded to the low range. Manual commands can override the automatic function at any time. Range changes can take place only at defined packet time boundaries to eliminate ambiguities when the data are highly variable. The digitized data corresponding to the three magnetometer axes are shifted serially to the IDPU and stored in memory for further processing. Correspondingly, magnetometer commands, including calibration sequences, are delivered by the spacecraft to the IDPU, processed and shifted serially into the magnetometer control logic for execution.

5 IDPU Magnetometer Software

The IDPU magnetometer software manages data and command interface between the IDPU and magnetometer, performs several data-processing tasks and controls instrument operation. The command and interface functions include reception of commands from the spacecraft and implementation of these actions in the instrument. Data processing functions include reception of digital data from the magnetometer, time tagging, averaging, decimation

and formatting. The software also handles transmission of the instrument status, including housekeeping and safety data. The telemetry data structure consists of three formats and associated time series. The highest time resolution or “burst” data are made up of the high rate samples (32/s) without further processing. Burst data are collected continuously but only the “best data” are sent based on an onboard burst selection criteria extracted from the IMPACT instrument suite (see Luhmann et al. 2007). About 10 minutes of selected burst data are sent to the ground every three hours. The “normal” or continuous MAG data stream is generated by averaging the raw magnetometer data of 32 samples/s over four samples to generate 8 samples/s. A third format is associated with real time data sent to the ground continuously to monitor solar activity. This “beacon” format is a low rate, real time data stream consisting of 10-second averages of the ambient field. Magnetometer data are also used onboard for sorting SWEA electron data into pitch angle distributions. The data are averaged over two seconds (corresponding to the SWEA data collection time). Magnetometer offsets uploaded from the ground are subtracted and the field direction angles (azimuth and elevation) are computed in SWEA coordinates.

5.1 Range Control Strategy

The instrument range can be controlled in automatic or manual mode. In manual mode, the instrument range is set by command. In automatic range mode, the software compares the largest absolute value of the signed count values against the current range’s full scale and adjusts the range if needed to maximize resolution while keeping the readings on scale. On startup, the range is controlled in automatic mode and the default range is low (± 512 nT full scale). The range control strategy must take into account the possibility of indefinite toggling between the two ranges for certain values of the field. To reduce this problem a hysteresis or “guard band” of digital values is used to avoid extended periods of saturation or conversely, low digital resolution data. All decisions associated with the range control function are based on the 32 samples/s data.

5.2 Internal Calibration

As described earlier, the magnetometer includes provisions for two types of internal calibrations that are exercised by ground command. The first is an analog magnetometer scale factor calibration capability that is implemented by injecting a known current into each of the fluxgate sensors equivalent to an external magnetic field of 1/4 full scale amplitude. This function is controlled on and off by setting a control bit in the FPGA logic by ground command. Typically a series of commands are sent to turn the calibration step generator on and off and the resulting step amplitudes in the outputs are analyzed to monitor any scale factor variations. The second calibration function is associated with the capability of sigma-delta A/D converters to self-calibrate scale factors and offset. This function is invoked by setting the proper control bits “high” in the control register and it lasts two conversion cycles (~ 62 ms) during which time the A/D outputs no data (see CS5507 data sheet for additional details). The A/D self-calibration function is turned off automatically after the cycle is complete. During initial turn on the IDPU initializes the A/D by commanding a self-calibration to be executed. Further A/D calibrations can be invoked by ground command only to avoid affecting primary data during periods of high scientific interest.

6 Preflight Calibration and Testing

6.1 Scale Factors, Offsets and Alignment

The magnetometer electronics were initially adjusted for zero offset and approximate scale factor using a multilayer magnetic shield and calibration solenoids in the laboratory. These adjustments are generally sufficient to define these parameters to within $\sim 2\%$ of their final values. Absolute scale factor calibration and relative sensor alignment measurements were conducted at the Goddard Space Flight Center and its Magnetics Test Facility. The absolute scale factor and relative alignment tests were derived using a modified version of the multiposition calibration technique described by Merayo et al. (2000). This technique yields extremely accurate values of alignment and scale factors but its application is restricted to the high range. The derived scale factors in this range were then transferred to a laboratory setup where the ambient magnetic field noise is minimal and small fields can be applied using a calibration solenoid. The zero field offsets were estimated by sensor rotations inside a magnetic shield where the residual field was less than 0.5 nT.

The scale factor and relative axis alignment technique consists of rotating the triaxial sensor assembly through 24 or more angular positions in a constant background field that is measured by means of a proton precession magnetometer. The measured field components (in digital counts or voltages) corresponding to each position and vector measurement are recorded and fitted to the model described later to minimize the residual error between the ambient and calculated total field. Precise angular positioning of the sensor is not required with this technique. However, the resulting alignment determination is relative to an arbitrarily chosen reference magnetic axis and not to a mechanical reference axis. Normally, the Earth's field can be used to establish the scale factor and relative alignment quickly and with acceptably small errors. This approach was used for the magnetometer calibration, and the ambient field used was that present at the 12 m GSFC magnetics test facility. If a reliable magnetics test facility is available, the procedure can be repeated for the low range to establish linearity. However, ambient magnetic noise limits the accuracy achievable. If we assume that the magnetometer linearity is of the order of 10^{-4} and the ambient field magnitude is constant for all sensor positions one can pose a linear least squares minimization problem to estimate the desired parameters (Merayo et al. 2000). Denoting the readings (counts) in the X , Y and Z axes by c_x , c_y and c_z and the fixed offsets as c_{x0} , c_{y0} and c_{z0} , one writes the magnetic field in sensor coordinates as

$$\begin{aligned} B_x &= k_x(c_x - c_{x0}), \\ B_y &= \alpha k_x(c_x - c_{x0}) + k_y(c_y - c_{y0}), \\ B_z &= \beta k_x(c_x - c_{x0}) + \gamma k_y(c_y - c_{y0}) + k_z(c_z - c_{z0}), \end{aligned} \quad (1)$$

where k_x , k_y and k_z are the scale factors for each axis and α , β and γ measure the contributions of X to the Y axis (α), X to the Z axis (β), and Y to the Z axis (γ), respectively, as off-diagonal elements of an alignment correction matrix (M)

$$[M] = \begin{bmatrix} 1 & 0 & 0 \\ \alpha & 1 & 0 \\ \beta & \gamma & 1 \end{bmatrix}. \quad (2)$$

In this case we have chosen the X -axis as the reference axis against which all misalignments are measured. Because the applied external field, B_{appl} , is the same for all orientations of the

sensor one can pose a least squares minimization problem defined by

$$\Delta^2 = \frac{1}{N} \sum_i (B_{x,i}^2 + B_{y,i}^2 + B_{z,i}^2) - B_{\text{appl}}^2, \quad (3)$$

where Δ is the residual to be minimized. Ideally one can also obtain an estimate of the zero-field offsets corresponding to each axis, c_{iO} , but convergence of the least squares solution is obtained much more rapidly if these offsets are determined independently such as from measurements in a magnetic shield or from “flipping” the sensor 180° in a weak ambient field. The low-range scale factors were determined by measuring the ratio of the responses in the high range to the low range in the laboratory once the high-range parameters had been established as described. The overall accuracy of the solutions is estimated at better than 0.1%.

The absolute alignment of the triaxial sensor assembly with respect to reference space-craft coordinates after boom deployment is determined by means of spacecraft rolls in a moderate ambient field. Clearly, perfect alignment would imply no modulation along the axis parallel to the S/C roll axis and once more a least squares problem can be posed that estimates the alignment corrections that need to be implemented to achieve this result.

6.2 Frequency Response and Timing

The overall frequency response of the magnetometer is determined by several contributors along the signal path, from the analog electronics to the digital output of the A/D converter. The first contributor is the intrinsic closed loop frequency response of the negative feedback system described in Sect. 4.1 for each axis. Typically the magnetometer is designed to have an intrinsic 3 dB cutoff frequency well above the desired signal roll-off characteristics and in the STEREO case the typical value is >60 Hz. A first-order output low-pass filter is then added at the output with a 16 Hz cutoff frequency to limit the analog bandpass and aliasing power present at the analog-to-digital converter input. This intrinsic frequency response is axis and range-dependent but the output low-pass filter normalizes the output bandwidth to a nominal range of 0 to 16 Hz within acceptable error limits. The typically steep f^{-n} characteristics of IMF fluctuations imply that the aliasing power contributed outside of the Nyquist frequency is small and a first-order low-pass filter is sufficient to ensure a reasonable and minimally aliased overall response. In addition, a first-order low-pass filter has minimal phase shift and the magnetometer amplitude and phase response can be easily inverted for spectral studies of the fluctuations of the IMF.

The sigma-delta A/D converter decimation output filter contributes additional amplitude and phase delays that can be represented as a Gaussian filter response or approximately constant time delay (~ 6 ms). For additional details please refer to the CS5507 specification data sheet. All of these characteristics must be taken into account when spectral studies of the interplanetary magnetic field fluctuations at the highest time resolution of the magnetometer are carried out or when time correlations with other STEREO instrument data are desired.

6.3 Environmental Testing

The sensor assembly and electronics were environmentally tested at GSFC prior to space-craft integration. Since high voltages and vacuum-sensitive components are not present in the magnetometer, initial thermal qualification testing was carried out in ambient air to reduce costs. Electrical performance as a function of temperature was tested over the range of

$-25^{\circ}\text{C} < T < +65^{\circ}\text{C}$; thermal cycling and survival tests were carried out over a temperature range 20°C wider at each extreme. Instrument performance was monitored exercising the analog step-calibration feature calibration and the A/D self-calibration capability. Determination of zero drifts with temperature is a time-consuming and difficult task because of the time variability of the typical laboratory magnetic environment (including that inside of multilayer magnetic shields) and historic in-flight performance must be used against comparative laboratory test data to estimate ultimate performance. For example, the Voyager magnetic field instruments (Behannon et al. 1977) provided almost 30 years of historical performance for this type of magnetic field instrument and show that under nominal conditions zero drifts are $<0.2\text{ nT/year}$. Thermal vacuum and final vibration testing were performed at the integrated IMPACT IDPU level at the Space Sciences Laboratory of the University of California Berkeley.

7 Spacecraft Magnetics Control Program

The success of weak interplanetary magnetic field measurements is intimately tied to the ability of the development team to control the magnetic fields generated by the spacecraft itself at the location of the MAG sensor (see Acuña 2002). Scientific measurements contaminated by spacecraft fields lead to controversy and inefficient use of limited resources in attempts to “clean up” the data. The STEREO project implemented a goal-oriented magnetics control program based on close cooperation among the experimenters and spacecraft builders. The objectives were to reduce as much as possible the static and dynamic fields generated by the spacecraft and experiments that introduce errors in the magnetic field measurements. For the static contribution, all components of the spacecraft employing magnetic materials (motors, actuators, relays, valves, RF isolators, etc.) were screened for magnetic signatures and compensation or reduction solutions developed where appropriate. The large contributions associated with the propulsion system valves and the communication system traveling wave tube amplifiers (TWTA) were canceled by adding permanent magnets mounted on the S/C bus. The dynamic (time variable) contribution is the most important since it is largely associated with variable currents circulating in the spacecraft, and its impact on the measurements cannot be easily eliminated by subtraction, spacecraft maneuvers, or modeling. Hence a set of “best engineering” practices must be followed to reduce their effect. For example, current loops associated with the power subsystem (battery, solar array, thermal control, power distribution system and spacecraft harnesses) were minimized using balanced twisted pairs for each major load and motors and actuators associated with the SECCHI instrument were magnetically shielded. The solar array layout and wiring was analytically optimized to reduce the associated magnetic field to a minimum while maintaining desirable electrostatic characteristics. Where “heritage” systems are involved and redesign or modification are not possible, artificial cancellation loops were used within the power distribution electronics as well and the battery cells were wired in a figure eight pattern and the orientations of the cells optimized to minimize the total magnetic moment of the battery.

To verify the success of the magnetics control program two system-level tests were conducted once the spacecraft were fully integrated: (a) a static magnetic moment assessment by measuring the dependence with distance of the spacecraft generated magnetic field, and (b) a magnetic compatibility test where all spacecraft subsystems are energized in a controlled sequence and the resulting magnetic field monitored with external test magnetometers.

8 Flight Checkout and Performance

The STEREO spacecraft were launched on October 25, 2006, and seven days later the IMPACT booms were deployed following the MAG activation. Figure 10 illustrates the magnetic field data acquired during the deployment of the “B” spacecraft boom. The data are not converted to physical units but are shown in counts to illustrate the automatic range control function. Prior to boom deployment the magnetometer sensor is close to the spacecraft bus and the highly magnetic TWTA and hence is in the HIGH range registering an elevated magnetic field value. When the boom deploys the measured field decreases rapidly to the lower digital threshold where the IDPU range control algorithm causes the magnetometer to switch to the low range increasing the sensitivity of the instrument. The behavior of the measured field after the range change is dictated by the sequence of boom segment deployments with respect to the sensor position.

To estimate the effective values of the IMPACT/MAG zero offsets, a number of spacecraft roll maneuvers have been executed under a variety of ambient field conditions. Higher

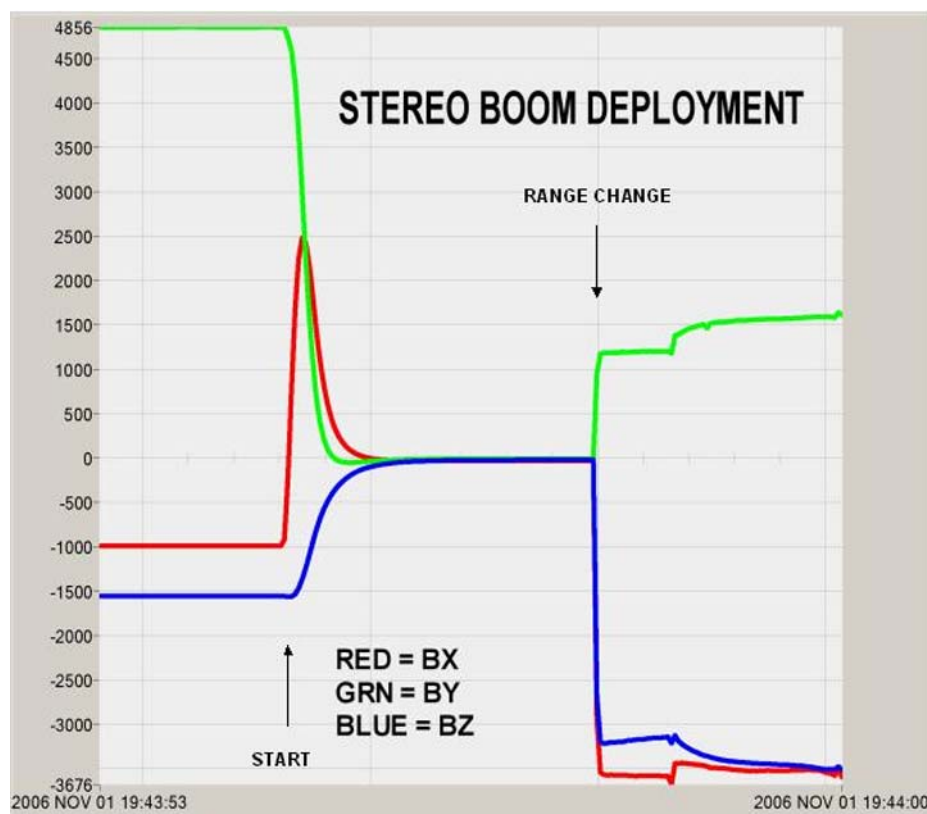


Fig. 10 MAG data acquired during the “B” spacecraft boom deployment. The data are shown in raw digital counts ($\pm 32,768$) versus time. The magnetometer is initially in the HIGH field status ($\pm 65,536$ nT) reading a relatively strong field associated primarily with the proximity to the TWTA magnets. As the boom deploys the readings decrease rapidly to zero until the automatic range change algorithm drives the magnetometer to the LOW range (± 512 nT) causing the digital readings to increase. As the boom settles slowly into its fully deployed position the readings approach the sum of the ambient magnetic field plus spacecraft induced offsets

than expected zero offset values have been noted on both spacecraft and are attributed to the accidental magnetization of structural fasteners used to attach the MAG tray to the boom. Fortunately, these offsets can be successfully removed by spacecraft maneuvers and analytical techniques that take advantage of the statistical properties of the IMF (Acuña 2002; Schwarzl and Russell 2007). The analysis of the roll data also follows in general the strategy described by Acuña (2002). Since the spacecraft motion is known and the ambient field is approximately constant for very short periods of time, a least squares minimization problem can be posed as follows. The scalar product of the measured field (including offsets) times the change in the field due to the spacecraft motion can be written as a two-dimensional vector expression,

$$\mathbf{B}_m \cdot \Delta\mathbf{B} = (\mathbf{B}_e \cdot \Delta\mathbf{B}) + (\mathbf{Z} \cdot \Delta\mathbf{B}), \quad (4)$$

where \mathbf{B}_m is the measured field, $\Delta\mathbf{B}$ the instantaneous change in field due to rotation, \mathbf{B}_e the external field in the plane of the roll and \mathbf{Z} is the unknown offset vector. It is clear that if the amplitude of the field does not change instantaneously between samples $\mathbf{B}_e \cdot \Delta\mathbf{B} = 0$ and if we select a time series of sequential, two-dimensional vectors (bold) during the time that the spacecraft is rolling,

$$(\mathbf{B}_m)_i \cdot (\Delta\mathbf{B})_i = \mathbf{Z} \cdot (\Delta\mathbf{B})_i \quad \text{for } i = 1, 2, 3, \dots, n \text{ vectors} \quad (5)$$

we can obtain an estimate for \mathbf{Z} as a solution to the least squares problem,

$$\mathbf{Z} = ((\mathbf{B}_m)_i \cdot (\Delta\mathbf{B})_i)((\Delta\mathbf{B})_i)^{-1}, \quad (6)$$

where $((\Delta\mathbf{B})_i)^{-1}$ denotes the pseudo-inverse of the $((\Delta\mathbf{B})_i)$ matrix.

This technique is particularly useful in cases where the ambient field is changing “adiabatically” (i.e., the field amplitude varies slowly with time without significant changes in direction) during a spacecraft roll as shown in Fig. 11 for the roll executed by spacecraft B on day 333 of 2006. The vertical and horizontal lines through the center of the spiral illustrate the solution obtained by the method described earlier. Significant advantages are the fact that sampling time information is not necessary and the ambient field need not be constant. The only knowledge required is that the spacecraft is rolling and the field is changing adiabatically. Note also that if we assume that all IMF fluctuations are changes in direction rather than amplitude, the technique described earlier can be used to estimate zero levels along all three magnetometer axes if the distribution of fluctuations is nearly isotropic during the interval of time considered (Acuña 2002; Schwarzl and Russell 2007).

9 Magnetometer Ground Data Processing

Magnetometer raw data records are produced at the University of California, Berkeley (UCB) and stored as Common Data Format (CDF) files. These data are sampled continuously at 8 Hz with occasional burst mode data (see Luhmann et al. 2007) obtained at 32 Hz. The data are then transferred to UCLA where one-second averages are produced of the raw data for use in the offset determination program (Schwarzl and Russell 2007). When offsets are changing slowly, less than about 0.3 nT/day the program can follow these changes to usually better than 0.1 nT. After the offsets are determined, Level-1 magnetometer records are made with all known corrections applied. The 8-Hz data (125 ms) are then averaged to one second resolution using overlapped averages of two seconds in length, and one-minute

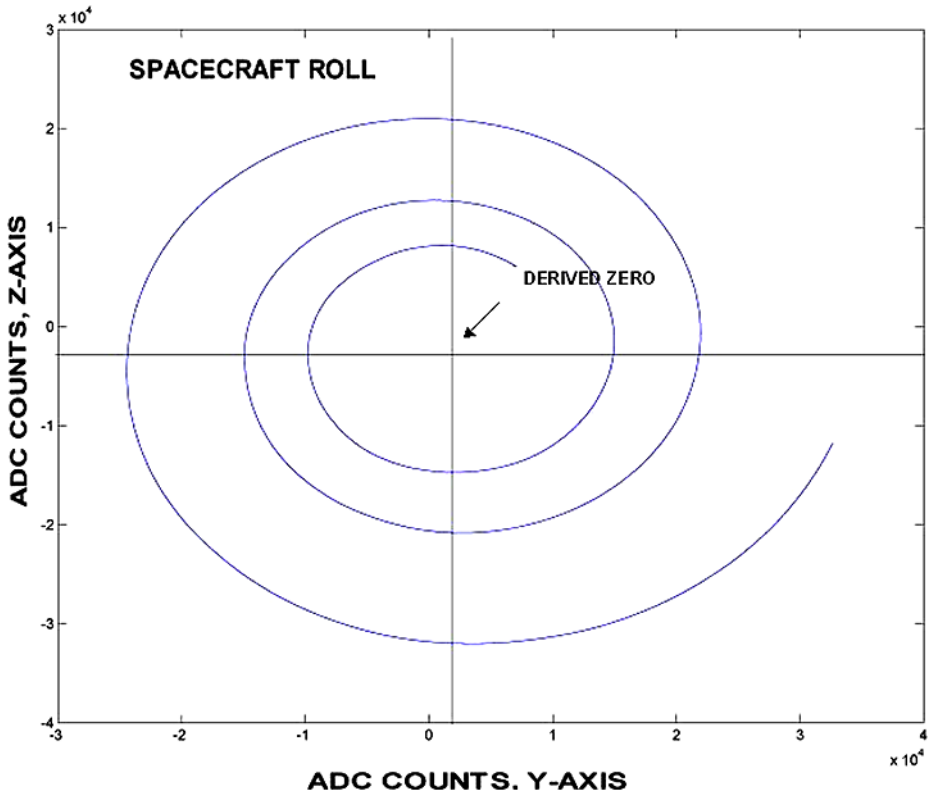


Fig. 11 A plot of Y -axis vs Z -axis digital readings during a spacecraft roll maneuver. A slowly varying ambient results in the spiral shown in the figure. The intersection of the *horizontal* and *vertical lines* illustrate the solution obtained by the method described in the text for estimating the zero level offsets in the roll plane

resolution data prepared with overlapped two-minute averages. These data are returned to UCB where CDF files are prepared. At UCLA the three data products (125 ms, 1 s, and 1 min) are rotated to RTN coordinates and stored in a Web-based data server with the original spacecraft coordinate data. Those using the data in geophysical studies will principally use the RTN system. Those using the magnetometer to reduce particle data will principally use the data in the spacecraft frame. The RTN (radial, tangential north) is defined so that R is radially outward with its origin at the Sun. The RN plane contains the rotation axis of the Sun and the T axis is in the direction of the cross product of the solar rotation axis and the Sun–spacecraft vector which is roughly in the direction of planetary motion. The spacecraft coordinates have X toward the Sun along the optical axis of the spacecraft. The Y and Z orientations about that direction are chosen to optimize communication with the Earth. Offset corrections are also made available, for use with UCLA-provided coordinate transformation software, to process STEREO beacon magnetometer data at the STEREO Science Center.

The processed magnetometer data are available both through the main IMPACT investigation data servers (see Luhmann et al. 2007) and the STEREO data archive at Goddard Space Flight Center. The near-real-time beacon data stream is available through the STEREO Science Center (see Thompson et al. 2007) and is also part of the archive. A descriptive example of fully processed data products is shown in Fig. 12 where we have plotted one-second averages of MAG data from both spacecraft in RTN coordinates for a period of

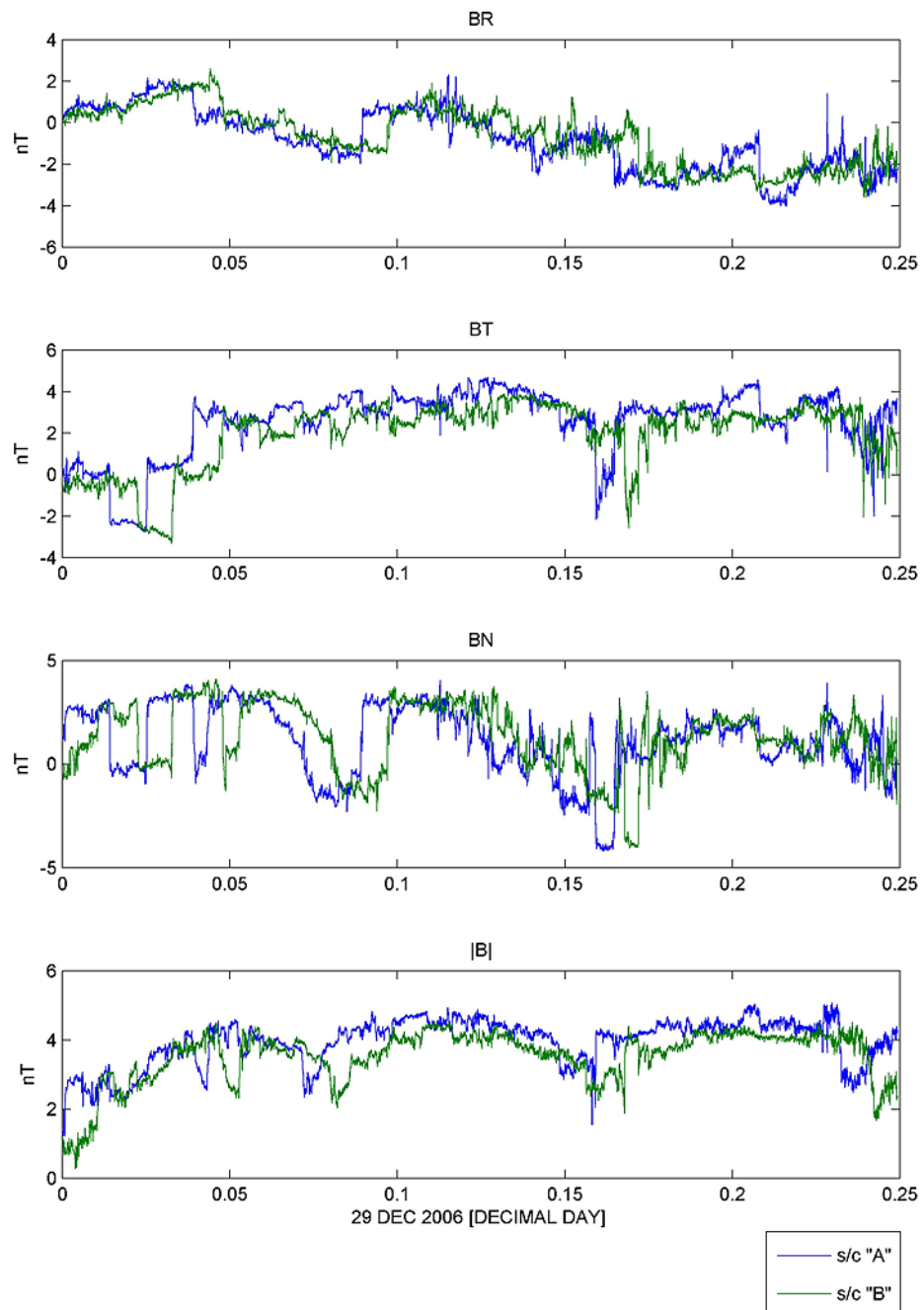


Fig. 12 A plot of IMPACT/MAG fully processed flight data from spacecraft “A” (blue lines) and spacecraft “B” (green lines) for a period of six hours on December 29, 2006. The *top three panels* correspond to the BR, BT and BN components while the bottom panel illustrates the magnitude of the field. Note that the IMF structures (mostly discontinuities) observed in spacecraft “A” lead in time the corresponding ones observed by spacecraft “B” as expected from the position of the spacecraft and co-rotation

six hours on December 29, 2006. Note that IMF structures are observed first by the “A” or ahead spacecraft and later by the “B” or behind spacecraft. This reflects both the radial position of the STEREO spacecraft as well as the effects of solar rotation on these structures.

Acknowledgements The authors thank the STEREO Project and the numerous individuals at Goddard Space Flight Center and JHU Applied Physics Laboratory who helped to ensure the quality of the STEREO magnetometer measurements. This work was supported as a Center-led portion of the STEREO IMPACT investigation.

References

- M.H. Acuña, IEEE Trans. Magnetics **MAG-10**, 519 (1974)
- M.H. Acuña et al., J. Geophys. Res. **97**(E5), 7799–7814 (1992)
- M.H. Acuña, C.T. Russell, L.J. Zanetti, B.J. Anderson, J. Geophys. Res. **102**(E10), 23,751–23,760 (1997)
- M.H. Acuña, Space-based magnetometers. Rev. Sci. Instrum. **73**(11), 3717–3736 (2002)
- S.D. Bale, M.J. Reiner, J.-L. Bougeret, M.L. Kaiser, S. Krucker, D.E. Larson, R.P. Lin, Geophys. Res. Lett. **26**, 1573–1576 (1999)
- K. Bamert, R. Kallenbach, N.F. Ness, C.W. Smith, T. Terasawa, M. Hilchenbach, R.F. Wimmer-Schweingruber, B. Klecker, Astrophys. J. **601**, L99–L102 (2004)
- K.W. Behannon, M.H. Acuña, L.F. Burlaga, R.P. Lepping, N.F. Ness, F.M. Neubauer, Space Sci. Rev. **21**, 235–257 (1977)
- L.F. Burlaga, *Interplanetary Magnetohydrodynamics* (Oxford University Press, New York, 1995)
- L.F. Burlaga, R.P. Lepping, J.A. Jones, in *Physics of Magnetic Flux Ropes*, ed. by C.T. Russell, E.R. Priest, L.C. Lee. Geophys. Monogr. Ser., vol. 58 (AGU, Washington, 1990), pp. 373–378.
- L.F. Burlaga, R.M. Skoug, C.W. Smith, D.F. Webb, T.H. Zurbuchen, A. Reinard, J. Geophys. Res. **106**, 20,957–20,978 (2001)
- H.V. Cane, J. Geophys. Res. **93**, 1 (1988)
- B.E. Gordon, M.A. Lee, E. Mobius, K.J. Trattner, J. Geophys. Res. **104**, 28,263–28,277 (1999)
- J.T. Gosling, in *Physics of Magnetic Flux Ropes*, ed. by C.T. Russell, E.R. Priest, L.C. Lee. Geophys. Monogr. Ser., vol. 58 (AGU, Washington, 1990), pp. 343–364.
- J.C. Kasper, W.C. Manchester IV, Astrophys. J. (2007, in press)
- S. Koutchmy et al., Astron. Astrophys. **420**, 709 (2004)
- D.E. Larson, R.P. Lin, J.M. McTiernan, J.P. McFadden, R.E. Ergun, M. McCarthy, H. Reme, T.R. Sanderson, M. Kaiser, R.P. Lepping, J. Mazur, Geophys. Res. Lett. **24**, 1911–1914 (1997)
- M.A. Lee, J. Geophys. Res. **88**, 6109–6119 (1983)
- R.P. Lepping, D.B. Berdichevsky, C.-C. Wu, A. Szabo, T. Narock, F. Mariani, A.J. Lazarus, A.J. Quivers, Ann. Geophysicae **24**, 215–245 (2006)
- G. Li, Q. Hu, G.P. Zank, in *The Physics of Collisionless Shocks*, ed. by G. Li, G.P. Zank, C.T. Russell. AIP Conference Proceedings, vol. 781 (Melville, New York, 2005), pp. 233–239
- D.A. Lohr, L.J. Zanetti, B.J. Anderson, T.A. Potemra, J.R. Hayes, R.E. Gold, R.M. Henshaw, F.F. Mobley, D.B. Holland, M.H. Acuña, J.L. Scheifele, Space Sci. Rev. **82**(1,2), 255–281 (1997)
- J.G. Luhmann et al., Space Sci. Rev. (2007, this issue). doi:[10.1007/s11214-007-9170-x](https://doi.org/10.1007/s11214-007-9170-x)
- J.M.G. Merayo, P. Brauer, F. Primdahl, J.R. Petersen, O.V. Nielsen, Meas. Sci. Tech. **11**, 120–132 (2000)
- R.A. Mewaldt, C.M.S. Cohen, A.W. Labrador, R.A. Leske, G.M. Mason, M.I. Desai, M.D. Looper, J.E. Mazur, R.S. Selesnick, D.K. Haggerty, J. Geophys. Res. **110**, A09–S18 (2005). doi:[10.1029/2005JA011038](https://doi.org/10.1029/2005JA011038)
- T. Mulligan, C.T. Russell, J. Geophys. Res. **10**, 581 (1999)
- T. Mulligan, C.T. Russell, B.J. Anderson, D.A. Lohr, D. Rust, B.A. Toth, L.J. Zanetti, M.H. Acuña, R.P. Lepping, J.T. Gosling, J. Geophys. Res. **104**, 28,217 (1999)
- F.M. Neubauer, M.H. Acuña, L.F. Burlaga, B. Franke, B. Gramkow, J. Phys. E **20**, 714–720 (1987). ISSN 0022-3735
- M. Neugebauer, R. Goldstein, in *Coronal Mass Ejections*, ed. by N. Crooker, J. Joselyn, J. Feynman. AGU Geophys. Mon., vol. 99 (Washington, 1997), p. 245
- D. Odstrcil, P.C. Riley, X.P. Zhao, J. Geophys. Res. **109** (2004). doi:[10.1029/2003JA010135](https://doi.org/10.1029/2003JA010135)
- G. Paschmann, N. Sckopke, S.J. Bame, J.T. Gosling, Geophys. Res. Lett. **9**, 881–884 (1982)
- T.A. Potemra, L.J. Zanetti, M.H. Acuña, IEEE Trans. Geosci. Remote Sens. **GE-23**, 246 (1985)
- I.G. Richardson, H.V. Cane, J. Geophys. Res. **98**, 15,295–15,304 (1993)
- I.G. Richardson, H.V. Cane, Geophys. Res. Lett. **31**, L18804 (2004). doi:[10.1029/2004GL020958](https://doi.org/10.1029/2004GL020958)

- J.D. Richardson, K.I. Paularena, *Geophys. Res. Lett.* **25**, 2097 (1998)
- D.A. Roberts, M.L. Goldstein, L.W. Klein, W.H. Matthaeus, *J. Geophys. Res.* **92**, 12,023–12,035 (1987)
- D.A. Roberts, M.L. Goldstein, W.H. Matthaeus, S. Ghosh, *J. Geophys. Res.* **97**, 17,115–17,130 (1992)
- C.T. Russell, J.T. Gosling, R.D. Zwickl, E.J. Smith, *J. Geophys. Res.* **88**, 9941 (1983)
- T.R. Sanderson, R. Reinhard, P. van Nes, K.P. Wenzel, *J. Geophys. Res.* **90**, 19–27 (1985)
- H. Schwarzs, C.T. Russell, *J. Geophys. Res.* (2007, to be submitted)
- O.C. St.Cyr, J.M. Davila, in *Space Weather*, ed. by P. Song, H.J. Singer, G.L. Siscoe. AGU Geophys. Mon., vol. 125 (Washington, 2001), pp. 205–209
- A. Szabo, *J. Geophys. Res.* **99**, 14,737–14,746 (1994)
- A. Szabo, D.E. Larson, R.P. Lepping, in *Proceedings of Solar Wind Nine*, ed. by S.R. Habbal, R. Esser, J.V. Hollweg, P.A. Isenberg (AIP, Woodbury, 1999), pp. 589–592
- A. Szabo, R.P. Lepping, J. Merka, C.W. Smith, R.M. Skoug, in *Proceedings of “Solar Encounter: The First Solar Orbiter Workshop”*, ed. by E. Marsch, V. Martinez Pillet, B. Fleck, R. Marsden. ESA, vol. SP-493 (Puerto de la Cruz, Tenerife, Spain, 2001), pp. 383–387
- A. Szabo, in *The Physics of Collisionless Shocks*, ed. by G. Li, G.P. Zank, C.T. Russell. AIP CP, vol. 781 (Melville, New York, 2005)
- Thompson et al., *Space Sci. Rev.* (1985, this issue). doi:[10.1007/s11214-007-9249-4](https://doi.org/10.1007/s11214-007-9249-4)
- A.F. Viñas, J.D. Scudder, *J. Geophys. Res.* **91**, 39–58 (1985)
- L.J. Zanetti, T.A. Potemra, R.E. Erlandson, P. Bythrow, B.J. Anderson, A.T.Y. Lui, S. Ohtani, G. Fountain, R. Henshaw, B. Ballard, D. Lohr, J. Hayes, D. Holland, M.H. Acuña, D. Farifield, J. Slavin, W. Baumjohann, M. Engebretson, K.-H. Glassmeier, T. Iijima, H. Luehr, F. Primdahl, *Space Sci. Rev.* **70**, 465–482 (1994)
- G.P. Zank, G. Li, G.M. Webb, J.A. Le Roux, V. Florinski, X. Ao, W.K.M. Rice, in *The Physics of Collisionless Shocks*, ed. by G. Li, G.P. Zank, C.T. Russell. AIP Conference Proceedings, vol. 781 (Melville, New York, 2005), pp. 170–179
- R.D. Zwickl, J.R. Asbridge, S.J. Bame, W.C. Feldman, J.T. Gosling, E.J. Smith, in *Solar Wind Five*, ed. by M. Neugebauer. NASA Conference Publication, vol. 2280 (JPL, 1983), pp. 711–718

The IMPACT Solar Wind Electron Analyzer (SWEA)

J.-A. Sauvaud · D. Larson · C. Aoustin · D. Curtis · J.-L. Médale · A. Fedorov ·
J. Rouzaud · J. Luhmann · T. Moreau · P. Schröder · P. Louarn · I. Dandouras ·
E. Penou

Originally published in the journal Space Science Reviews, Volume 136, Nos 1–4.
DOI: [10.1007/s11214-007-9174-6](https://doi.org/10.1007/s11214-007-9174-6) © Springer Science+Business Media, Inc. 2007

Abstract SWEA, the solar wind electron analyzers that are part of the IMPACT in situ investigation for the STEREO mission, are described. They are identical on each of the two spacecraft. Both are designed to provide detailed measurements of interplanetary electron distribution functions in the energy range $1\sim3000$ eV and in a $120^\circ\times360^\circ$ solid angle sector. This energy range covers the core or thermal solar wind plasma electrons, and the suprathermal halo electrons including the field-aligned heat flux or strahl used to diagnose the interplanetary magnetic field topology. The potential of each analyzer will be varied in order to maintain their energy resolution for spacecraft potentials comparable to the solar wind thermal electron energies. Calibrations have been performed that show the performance of the devices are in good agreement with calculations and will allow precise diagnostics of all of the interplanetary electron populations at the two STEREO spacecraft locations.

Keywords Solar wind · CME · Electrons · Multipoints

1 Introduction

IMPACT (see Luhmann et al., this volume, 2007, for an investigation overview) is one of the STEREO mission's four measurement packages whose principal objective is to understand the origin and consequences of coronal mass ejections (CME's). As one of IMPACT's in situ instruments, the Solar Wind Electron Analyzer, SWEA, measures the distribution function of solar wind core, halo, and strahl electrons from 1 to ~3000 eV with high spectral and angular resolutions. SWEA is specifically designed to provide accurate measurements even for very cold ($T_{\text{elec}} < 1$ eV) core electrons which provide a tracer of ejected cold prominence

J.-A. Sauvaud (✉) · C. Aoustin · J.-L. Médale · A. Fedorov · J. Rouzaud · P. Louarn ·
I. Dandouras · E. Penou
CESR, Centre d'Etude Spatiale des Rayonnements, CNRS-UPS, Toulouse, France
e-mail: sauvaud@cesr.fr

D. Larson · D. Curtis · J. Luhmann · T. Moreau · P. Schröder
SSL, Space Science Laboratory, University of California, Berkeley, USA

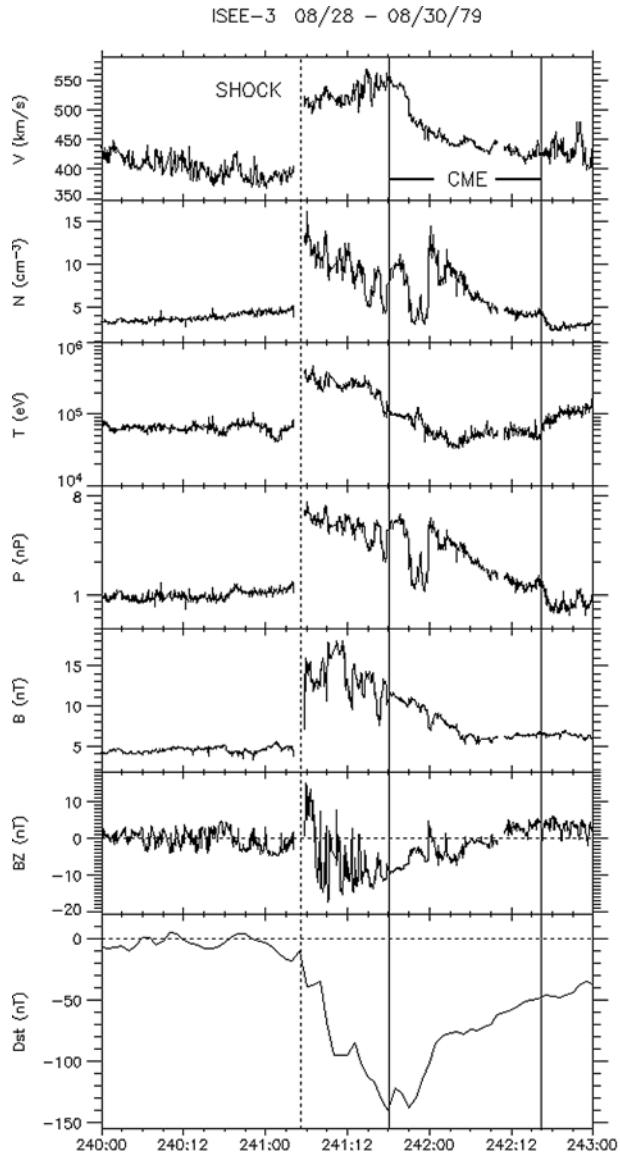
material in Interplanetary Coronal Mass Ejection (ICME) events. It also provides nearly full sky coverage of the directionality of strahl electrons, for determining the magnetic topology of ICMEs even when the interplanetary magnetic field (IMF) rotates far out of the ecliptic. In order to allow such performances, the potential of SWEA is controlled to compensate for the spacecraft potential. This maintains the full energy resolution of SWEA even for electron energies lower than the spacecraft potential. Distribution functions are obtained with a time resolution between 2 s and 30 s.

2 Scientific Objectives

Electron velocity distribution functions in the solar wind contain three different components: a thermal core and a suprothermal halo, which are typically present at all pitch angles, and a suprothermal magnetic field-aligned “strahl” which is usually directed anti-sunward and which carries the solar wind electron heat flux (Montgomery et al. 1968; Feldman et al. 1975; Rosenbauer et al. 1977; Pilipp et al. 1987). At 1 AU, the core has a typical temperature of 10^5 K and represents about 95% of the total electron number density. The halo population has a typical temperature of 7×10^5 K and represents, together with the strahl, the remaining portion of the total electron number density. Furthermore, above ~ 2 keV, a nearly isotropic “superhalo” electron component is present even during the quietest times (Lin et al. 1996). This superhalo typically extends to > 100 keV and its origin is presently unknown. Note that the impulsive acceleration of electrons to ~ 1 to a few hundred keV is the most common solar particle acceleration process. Whereas Coulomb collisions can largely explain the relative isotropy of the core population, the origin of the halo population, and more specifically the origin of its sunward directed part is still debated. Electrons constantly escaping from the Sun are focused into field aligned strahl by conservation of the magnetic moment and transport heat flux away from the Sun. The halo consists of a background population of suprothermal electrons scattered over very large heliospheric distances. Magnetic focusing acts to narrow the strahl, while scattering processes and the interplanetary potential act to broaden it. Competition between these determines the actual strahl width (Rosenbauer et al. 1977; Gosling et al. 2004). Observations of the strahl in the solar wind is evidence of direct magnetic connection to the Sun. On a heliospheric field line that is disconnected from the Sun, one expects to see the strahl disappear and the electron heat flux to be greatly reduced (e.g., Gosling et al. 2005). However, disconnection is not the only cause of heat flux dropouts. The heat flux often drops at and near the IMF sector boundaries (Pilipp et al. 1990; McComas et al. 1989; Fitzenreiter and Ogilvie 1992; Crooker et al. 2003). However, many of these heat flux dropouts are not apparent in higher-energy electrons, suggesting enhanced scattering over disconnection as the cause in many such events (Lin and Kahler 1992; Fitzenreiter and Ogilvie 1992).

Solar electrons from ~ 0.1 to 10^2 keV in the energy range covered by SWEA and STE (see Lin et al., this volume, 2007, for a description of the higher energy electron measurements by IMPACT’s STE sensor), are thus excellent tracers of the structure and topology of IMF lines since they are fast and have very small gyroradii. An ICME/magnetic cloud often has a force-free configuration and may remain magnetically connected to the Sun even beyond 1 AU (e.g. Larson et al. 1997); its plasma composition and characteristics are often very different from the pre-existing solar wind (e.g. Wurz et al. 1998; Wimmer-Schweingruber et al. 1999). Figure 1 shows plasma and magnetic field data for an ICME event observed near 1 AU. Note the forward shock, the compression of the plasma density and magnetic field, and the slow rotation of the magnetic field vector inside the ICME which in this case was

Fig. 1 Plasma and magnetic field data for an ICME event observed near 1 AU and the Dst index. Note the forward shock, the compression of the plasma density and magnetic field, and the slow rotation of the magnetic field vector inside the magnetic cloud (labeled *CME*) itself. Adapted from Gosling and McComas (1987) and Gosling et al. (1990)



a magnetic cloud (e.g., Burlaga 1991). Many questions related to CME/ICME evolution in the solar wind are closely related to the questions of CME origins. For example magnetic clouds often appear to expand as they propagate out through the heliosphere, but the extent of their expansion is likely controlled by the ambient coronal and solar wind conditions as well as their internal structure (e.g. Osherovich and Burlaga 1997; Gosling 1997).

A significant fraction of ICMEs have intervals with very cold electron temperatures T_{ec} (e.g., Montgomery et al. 1974) ranging down to <1 eV, while in non-ICME solar wind, T_{ec} never drops below ~ 6 eV. For such an ICME (e.g., the event shown in Fig. 2), detailed fits to electron distributions show that T_{ec} generally range from ~ 1 to 4.5 eV (Larson et al. 2000). For most of this ICME the halo density was very low (<0.1 cm 3), suggesting magnetic dis-

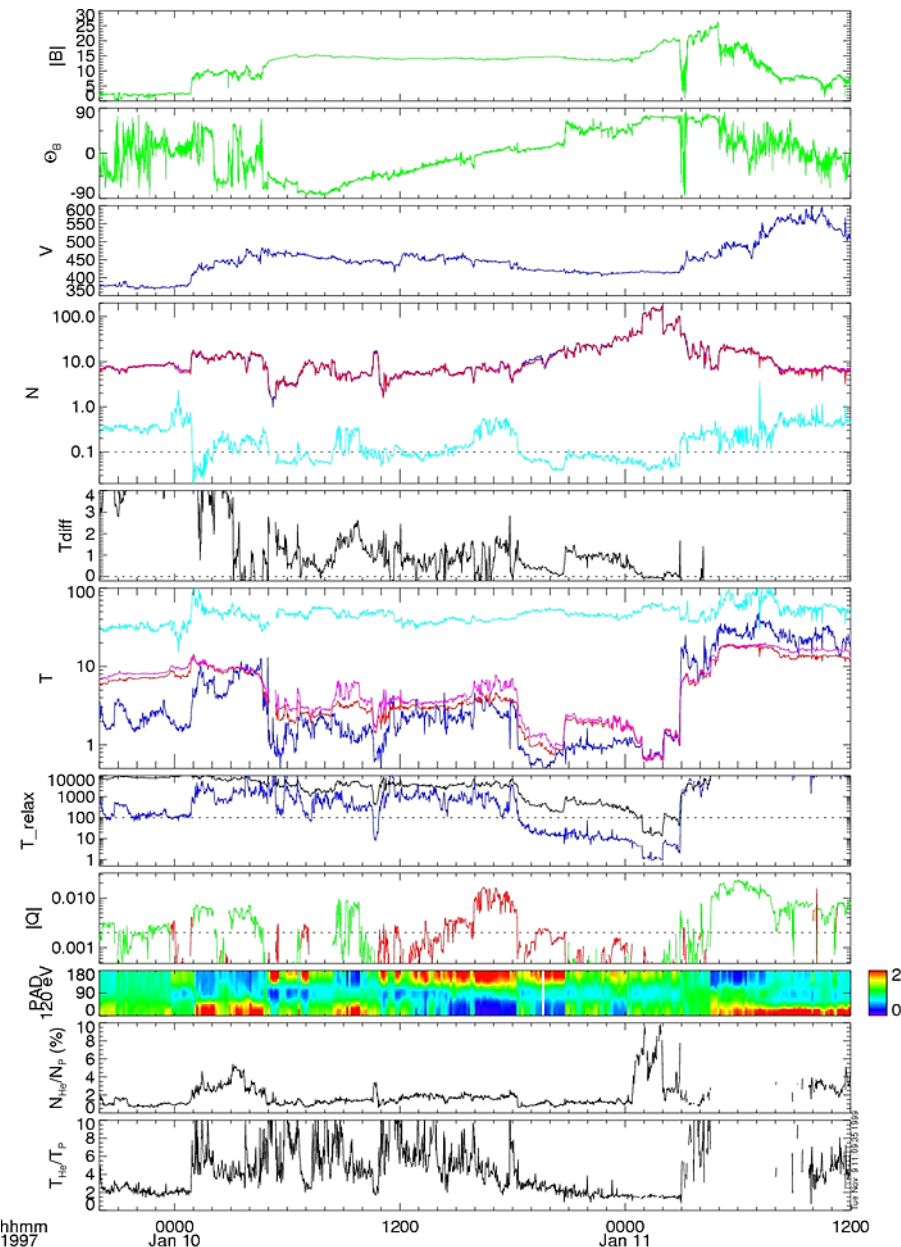


Fig. 2 Summary plot of solar wind parameters: from top to bottom: – 1) magnetic field strength ($|B|$), and – 2) angle out of ecliptic (Θ_B), – 3) plasma bulk speed (V), – 4) density (N) of the electrons (red), protons (blue) and of the halo electrons (light blue), – 5) core electron–proton temperature difference, – 6) temperatures (T) of the protons (blue), electrons (pink), core electrons (red) and halo electrons (light blue), – 7), collisional relaxation time (T_{relax}) for electron–proton (black) and alpha–proton (blue), – 8) electron heat flux parallel to B ($|Q|$), $Q > 0$ in green, – 9) normalized electron flux at 120 eV versus pitch-angle (PAD), – 10) alpha to proton density ratio (N_α/N_p) and – 11) alpha to proton temperature ratio. From Larson et al. 2000

connection from the Sun. Remarkably, during these times the solar wind proton temperature, T_p , is equal to T_{ec} , and shows the same temporal variations. This behavior, which is never observed in the non-ICME solar wind, provides strong evidence that the ICME has evolved through adiabatic cooling as it travel to 1 AU, most likely due to expansion in the radial direction (the solar wind speed decrease through the ICME). In the regions of this ICME where the halo density is at normal levels ($\sim 0.03\text{--}0.5\text{ cm}^{-3}$) T_{ec} increases significantly above T_p , indicating that the core electrons were being heated by the halo. SWEA's precise measurements of very cold core and halo electrons, together with the detailed ion measurements made by the PLASTIC plasma ion composition analyzer on STEREO (see Galvin et al., this volume, 2007), will provide powerful diagnostics of CME/ICME evolution, cooling and heating while the multipoint perspective provided by STEREO measurements and models will illuminate ICME interplanetary evolution and the 3D context of the surrounding solar wind structure.

The magnetosphere of the Earth is driven by the solar wind convection electric field and the solar wind dynamic pressure. While the influence of the first factor is well quantified, the action of the pressure remains less clear and depends on particular situations. Of special importance are large amplitude solar wind pressure enhancements associated with interplanetary shocks and ICMEs. Such pressure jumps significantly move the bow shock and magnetopause earthward, leading to large induced electric fields and to major currents that can couple to the ionosphere and to the ring current and lead to strong ionospheric disturbances. Furthermore, an interplanetary shock can cause large numbers of energetic particles to be injected into the earth's inner magnetosphere, worsening the radiation environment for spacecraft. Heliospheric disturbances are often accompanied by solar energetic particles (SEP) accelerated by interplanetary shocks or solar flares. These high energy particles also interact with the non-magnetized planets Venus and Mars whose upper ionospheric layers are affected by the high solar wind dynamic pressures associated with these heliospheric disturbances. When Venus, Earth and Mars are within the same heliospheric longitudinal sector (e.g. expected in summer 2008), the same ICME may affect all three planets and especially affect their upper atmospheres. Together with the two STEREO spacecraft, the Venus Express (VEX), Mars Global Surveyor (MGS) and Mars Express (MEX) particle and field payloads will be used to track the ICME topology and propagation characteristics in the heliosphere and to assess their effects on the planetary environments.

3 Instrument Overview

The Solar Wind Electron Analyzer – SWEA and the supra-thermal electron detector (STE) are linked together and to the spacecraft command and data handling by the data processing unit. Figure 3 gives the SWEA block diagram and Table 1 summarizes the SWEA measurement parameters and instrument characteristics. Each SWEA consists of an electrostatic analyzer with front-end deflectors to measure electron fluxes from $\sim 1\text{ eV}$ to 3 keV over a solid angle of $360^\circ \times 120^\circ$ with sufficient sensitivity at the extreme flux levels likely to be encountered. To minimize spacecraft potential effects on the low energy electrons and to provide unimpeded fields-of-view, SWEA and STE are mounted antisunward at the end of the IMPACT boom, 4.5 m from the spacecraft and located in its shadow (Fig. 4). Furthermore in order to keep constant the energy resolution of SWEA, even when solar electrons are accelerated by the spacecraft electrostatic potential, the electrostatic analyzer and the deflectors are biased to a commandable voltage, which is used to decelerate the incoming electrons.

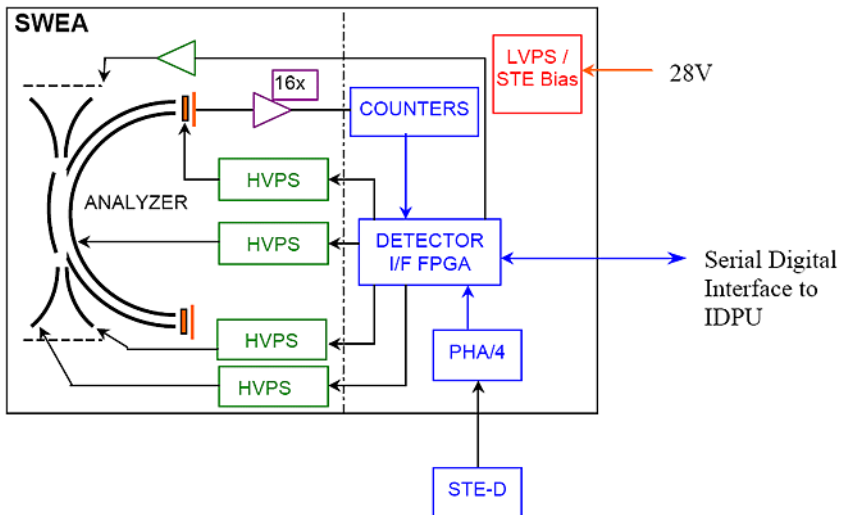


Fig. 3 SWEA block diagram

Table 1 STEREO solar wind electron instrument

A. Measurement parameters

	Electrons energy range	Geometrical factor at 0° elevation ($\text{cm}^2 \cdot \text{sr} \cdot \text{eV}/\text{eV}$)	Field of view (°)	Dynamic range $\text{eV}/(\text{cm}^2 \cdot \text{sr} \cdot \text{eV} \cdot \text{s})$
SWEA	1 eV–3 keV	8.4×10^{-3}	$360 \times 120^\circ$	$\sim 10^8$

B. Instrument characteristics (without the common SWEA/STE-D pedestal electronics)

	Mass, kg	Power, W	Volume, cm^3	Nominal bit rate, bps
SWEA	0.97	0.55	1150	534

Fig. 4 The solar wind electron analyzer at the end of the stowed IMPACT boom and the magnetometer on its shelf. After boom deployment the two instruments are separated by ~ 1 m



To fully utilize the capabilities of SWEA and STE, microprocessors are employed to provide physically meaningful on-board data processing and compression, as well as flexible operation. For example, ten moments of the electron distributions: density, the three components of bulk velocity, the six unique elements of the momentum flux tensor and the energy flux vector are computed onboard following every complete energy and angle scan. In addition, the particles can be sorted by pitch angle and reduced distribution functions computed, using the magnetic field vector obtained directly from the on-board magnetometer. Besides the spacecraft power and command and data handling interfaces, the experiment has interfaces to the magnetometer (see the IMPACT Instrument Data Processing Unit (IDPU) discussion in the paper by Luhmann et al., this volume, 2007).

4 Electrostatic Analyzers and Deflectors

The SWEA electrostatic analyzers and deflectors have been designed for measurements of the interplanetary electron core, halo and strahl electrons ($1 \text{ eV} \leq 6 \text{ keV}$). The quasi-3D distribution of these particles will be sampled as often as every 2 seconds. The geometrical factor of the analyzer can be electrostatically changed, increasing the range of fluxes that can be measured without detector saturation and allowing direct sampling of the core solar wind electron populations as well as high sensitivity measurements of the suprathermal electrons. The analyzer design is a symmetrical spherical section electrostatic analyzer (Carlson et al. 1983; Carlson and McFadden 1998) with a 360° disk-shaped field of view.

The imaging of parallel rays onto the detector plane provides about 1° inherent analyzer resolution in the detection plane. Ultraviolet light (UV) entering the sensor is a potential background source. The analyzer geometry forces at least a 2 bounce light path to the microchannel plate detector and the smooth inner and scalloped outer hemispheres have a gold black coating applied to further reduce scattered light. Very similar analyzers have been flown on the WIND, Interball and Cluster spacecraft and have provided good solar UV rejection. A grid at the analyzer exit prohibits leakage field from the microchannel plates (MCPs) from entering the analyzer section. Electrons are post-accelerated by a +300 V potential applied to the front of the MCPs to increase detection efficiency to about 70%. An aperture cover, together with a one-time opening mechanism, which maintains an internal dry nitrogen environment during integration and launch, sealed the inside of the analyzer prior to launch.

The SWEA electrostatic analyzer has a 360° planar field-of-view (FOV) that is perpendicular to the ecliptic plane and to the boom carrying SWEA, STE and MAG (Fig. 4). The SWEA FOV is electrostatically deflected into a cone up to $\pm 60^\circ$ out of its normal plane by a voltage applied to curved plates placed at the analyzer entrance aperture (Fig. 3). A pair of grids at the outer analyzer collimator minimizes leakage fields from the deflectors.

The SWEA analyzer has an inner plate radius of 3.75 cm and the plate separation is 0.28 cm. The resulting energy resolution is 17%. The total geometric factor is $0.01 \text{ cm}^2 \cdot \text{sr} \cdot \text{eV/eV}$ including an MCP efficiency of about 70% and grid transmission (3 grids), of 73%. SWEA compensates for the effects of spacecraft potential on the lowest energy particles by having an outer hemisphere that can be biased according to the plasma density measured by the PLASTIC solar wind ion instrument. With V_i and V_0 defined as the potentials of the inner and outer hemispheres, the inter sphere potential drop $\delta V = V_0 - V_i$, the pass band energy and the energy resolution can be written: $\langle E \rangle = qV_0 + k_a q \delta V = q \delta V (\alpha + k_a)$ and $\delta E = w k_a q \delta V$. Here k_a and w are characteristics of the geometry of the top hat and we have defined $\alpha = V_0 / \delta V$. For SWEA, $k_a = 10$

and $w \sim 0.17$ (17%). By varying the value of α the relative energy resolution can be varied:

$$\frac{\delta E}{E} = \frac{w}{1 + \alpha/k_a}.$$

Conservation of the phase space volume, $(E dE)d\Omega dA$, provides the following useful result to compute the geometrical factor corresponding to $V_0 \neq 0$:

$$G_\alpha = \frac{G_0}{1 + \alpha k_a},$$

where G_0 is the geometrical factor of the instrument for $\alpha = 0$. The effective geometrical factor ($\text{cm}^2 \cdot \text{sr} \cdot \text{eV}/\text{eV}$) is defined as:

$$g_\alpha = \frac{G_\alpha}{\langle E \rangle} = \frac{g_0}{(1 + \alpha/k_a)^2}.$$

Finally, note that the effect of the retarding potential, V_0 , is to improve the energy resolution by a factor $(1 + \alpha/k_a)$ and to lower the geometrical factor by a factor $(1 + \alpha/k_a)^2$. Although the SWEA detector is strictly for electrons, this scheme can be used for ions as well.

SWEA uses MCP detectors in a chevron pair configuration, which gives an electron multiplication gain of about 2×10^6 and a narrow pulse height distribution. The Photonis MCPs are each 1 mm thick. The plates are processed for high strip current to provide fast counting capability. The microchannel plates are on a polyimide printed board that supports the electrostatic analyser and the MCP stack. 16 collectors of 22.5 degrees each are implemented on the MCP side of the board. On the opposite side are a heating circuit and 16 coupling circuits to the amplifier board. A simulation of the magnetic field generated by the current of the heating system was performed and the routing of the power supply line was optimised in order to minimise the impact of that magnetic field on the trajectory of the electrons inside the analyzer.

Charge pulses produced by the MCPs are collected on the set of discrete anodes and sent to preamplifier-discriminators. The amplifiers are A111F amplifiers from Amptek. On the board a pulse generator is implemented to generate test pulses on the input of each amplifier. The threshold of the amplifiers is adjusted at 45 pC corresponding to a gain of 2.75×10^5 on the MCP. The maximum count rate of the amplifiers is 2×10^6 pulses per second. The output pulses of the amplifiers are provided to sixteen counters situated on the digital board.

The high voltage board generates four positive high voltages (HV) and one negative voltage to compensate the spacecraft potential (V_0). One HV supplies the MCP. The HV converter can deliver 3.2 kV and it is adjustable by analog command. The three other programmable HVs supply the optics of the instrument, one for the electrostatic analyser with a range from 0 to 750 V and the two others for the two deflectors with a range from 0 to 1500 V. These three positive HVs are delivered by three amplifiers. They are controlled by analog commands generated by the digital board of the instrument. A non-regulated HV converter generates the power supplies of the HV amplifiers. The HVs for the electrostatic analyser and for the deflectors are referenced to the V_0 voltage that can be adjusted in the range from 0 to -25 V. The HV amplifiers have a rise time and fall time of 100 μs and a stability better than 1% in the temperature range from -70°C to $+50^\circ\text{C}$. The two HV converters are synchronised at 100 kHz. The SWEA interface provides two digital signals that enable the MCP and the non regulated high voltage supplies. These signals are at zero volts to turn off the supplies and +5 V to turn on the supplies.

5 Calibrations

The calibration of the SWEA sensor has been performed at the CESR Toulouse vacuum facilities and at SSL Berkeley. At CESR, a simple cylindrical electron gun was used as a source of low energy electrons (~ 600 eV). The mechanical setup of the electron gun and of the sensor is shown in Fig. 5. The electron beam current was monitored and stabilized using the total current on the cylinder surrounding the gun. The gun produces a rather narrow beam, so that uniform illumination of the SWEA effective aperture was obtained by scanning the gun in the vertical and horizontal directions. The sensor was mounted on the turntable allowing azimuthal and elevation angles of the electron beam to be set with an accuracy of 0.1° .

The MCP dead-time was measured by illuminating the MCP surface via small pin-holes with electron fluxes of different intensities. Knowing the beam current in each case, and measuring the non-linear profile of the MCP count rate as a function of the beam current, allowed us to determine the dead-time of one micro channel to be 200 ms.

The Energy (eV)/Voltage (V) ratio of the analyzer, k , was found to be nearly independent of the voltage applied to the deflectors and equal to 6.28 for sector “1”. But there is a non-negligible variation of k with azimuth due to the non-concentric inner and outer hemispheres. Figure 6 shows this variation that can be described by:

$$k = 6.26 + 1.17 \cdot 10^{-2} \sin(\phi - 65.1) + 6.8 \cdot 10^{-2} \cos(\phi - 65.1).$$

Here $\phi = 0$ corresponds to the center of sector “1”.

The energy resolution of the analyzer was found to be almost constant for all values of the elevation and azimuth and equal to 0.167. The total geometrical factor G of each of the 16 anodes for a zero elevation angle are given in Table 1. G is in 10^{-4} cm 2 ·sr·eV/eV.

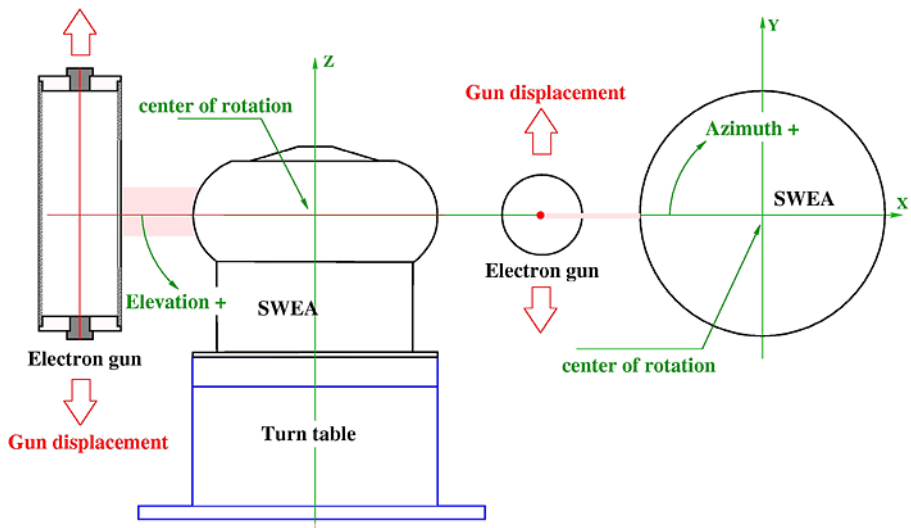


Fig. 5 Mechanical setup of the electron gun and sensor for calibrations

Fig. 6 Variation of the energy/voltage ratio of the analyzer, k , as a function of azimuth for zero degrees elevation. Colors and numbers refer to different sensor sectors

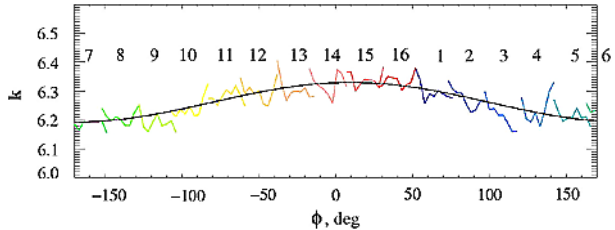


Table 2 Geometrical factors of the 16 anodes for a zero degree elevation

A	1	2	3	4	5	6	7	8	9	10	11	12	13	14	15	16
G	4.8	5.8	5.7	5.2	5.6	6.2	4.3	4.4	5.3	5.8	5.6	4.9	5.3	5.2	5.0	4.8

The energy-angular response of the analyzer depends on the deflection angle of the electrons, defined by the following parameter:

$$D = \frac{U_{\text{defTHV}} - U_{\text{defBHV}}}{E} = \frac{U_{\text{def}}}{E}.$$

Here U_{defTHV} and U_{defBHV} are voltages of the top and bottom electrodes of the deflector.

The variation of the energy-angular response of the analyzer is illustrated in Fig. 7, which shows examples for several values of D compared with simulation results. The top row of panels correspond to $D = -0.59$, the middle row corresponds to $D = 0.03$, and the bottom row corresponds to $D = 0.71$. The measurements of the central elevation angle, θ , as a function of the D -factor gives an excellent, almost linear, relation between θ and D :

$$\theta = -2.9 + 78.3 \times D - 1.22 \times D^2.$$

The geometrical factor of the sensor depends on the elevation angle. Figure 8 shows the variation of the $dG/d\phi$ value corresponding to the center of sector “1” as a function of θ . To obtain the total geometrical factor of the sector this value must be integrated over ϕ . Accurate measurements can be done between -50 and $+50$ degrees of elevation angle (Fig. 8). Beyond these extremes the geometrical factor of the sensor (as well as other parameters) degrades quickly.

6 Digital Electronics

SWEA/STE-D share a common set of digital electronics and a low voltage power supply. Most of the digital electronics is contained in an Actel FPGA, supplemented by Digital to Analog converters to generate control voltages and an Analog to Digital converter to provide housekeeping measurements. The digital electronics includes 16 counters for the preamp-discriminators that are read out to the IMPACT Instrument Data Processing Unit, IDPU, every high voltage step (5.8 ms). The digital electronics also control the analyzer high voltage supplies and V_0 supply from a look-up table loaded by the IDPU. The look-up table contains a full sweep profile for the two deflector supplies, the analyzer supply, and V_0 . The MCP supply is programmed to a fixed value provided by the IDPU. The nominal profile consists of an exponentially decaying analyzer voltage with a 2-second period. The deflector

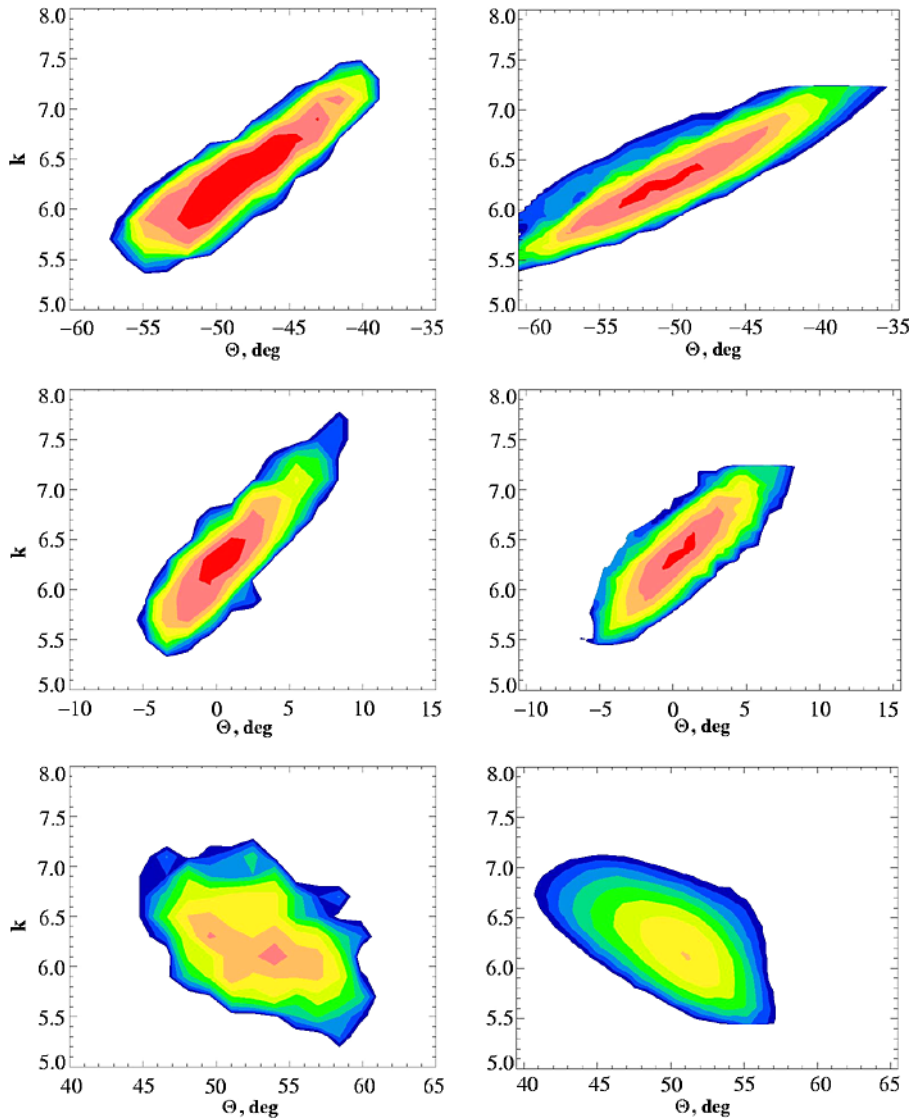
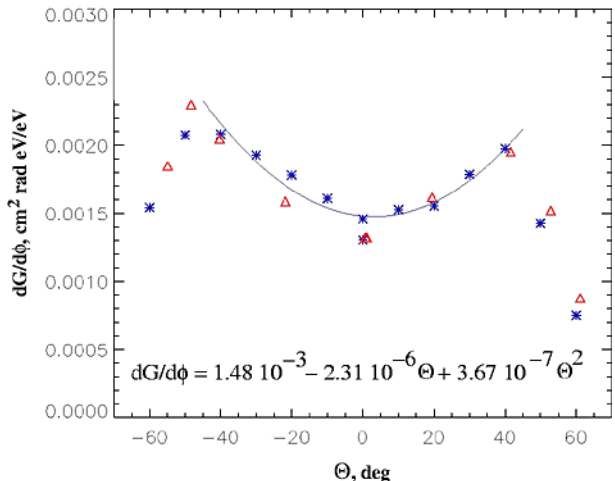


Fig. 7 Energy-angular responses of SWEA. The *left column* corresponds to the measurements, and the *right column* corresponds to numerical simulations. The *top, middle* and *bottom rows* correspond to different deflection angles of the electrons (see text)

supplies ramp up and down 48 times during the sweep to a maximum voltage proportional to the analyzer voltage in order to sample the full range of deflection angles. The counter readout is synchronized to the sweep waveform in order to provide 6 deflection samples (at ~ 22 degree resolution) for each of 48 energy steps. The digital electronics also controls the SWEA operational heater, the SWEA aperture door actuator, and the SWEA test pulser, in addition to STE-D functions. A high voltage enable plug mounted to the digital electronics

Fig. 8 $dG/d\phi$ measured at the center of sector “1” versus the elevation angle



interrupts primary power to the high voltage supplies to render the instrument safe on the ground.

7 Experiment Modes of Operations

SWEA has a single mode of operation, adjusted by a large number of programmable parameters such as MCP voltage and analyzer sweep supply waveform generation parameters. The nominal operational mode causes the instrument to sweep over the full range of deflections and energies every 2 seconds as described in Sect. 6. The data are read out and collected into a matrix corresponding to the measured electron distribution function. These data are sent with full time resolution to the burst memory, and are sampled every 30 seconds for normal (continuous) telemetry. Moments of the distribution function with full time resolution are computed and sent every 2 seconds. A pitch angle distribution is also extracted based on the measured magnetic field direction and sent every 10 seconds. All this processing takes place in the IDPU.

8 Summary

The Solar Wind Electron Analyzers, SWEAs, onboard STEREO are designed to provide precise measurements of the low energy electrons in interplanetary space at 1 AU over a wide range of energies, angles and fluxes. Because of the large amount of data generated by SWEA, substantial data selection and compression are performed. On a routine basis, these instruments provide measurements of the solar wind electron density, temperatures, pitch-angle distributions, heat flux and velocity. The variable potential of the instruments allows valuable measurements to be obtained even when the positive potential of the satellites is of the order of the measured electron energy.

Acknowledgements The realization of the SWEA sensor heads and of their calibrations has been supported by CNES under Contract No. CNES-221. We thank E. Le Comte for his support in the calibration process.

References

- L.F. Burlaga, in *Physics of the Inner Heliosphere*, 2., ed. by R. Schwenn, E. Marsch (Springer, Berlin, 1991), pp. 1–22
- C.W. Carlson, J.P. McFadden, in *Measurements Techniques in Space Plasmas: Particles*, ed. by R.F. Pfaff, J.E. Borovsky, D.S. Young (AGU, Washington, 1998), pp. 125–140
- C.W. Carlson, D.W. Curtis, G. Poschmann, W. Michael, *Adv. Space Res.* **2**, 67 (1983)
- N.U. Crooker, D.E. Larson, S.W. Kahler, S.M. Lamassa, H.E. Spence, *Geophys. Res. Lett.* **30**(12), 1619 (2003). doi:[10.1029/2003GL017036](https://doi.org/10.1029/2003GL017036)
- W.C. Feldman, J.R. Asbridge, S.J. Bame, M.D. Montgomery, S.P. Gary, *J. Geophys. Res.* **80**, 4181–4196 (1975)
- R.J. Fitzzenreiter, K.W. Ogilvie, *J. Geophys. Res.* **97**, 19,213–19,219 (1992)
- Galvin et al. (2007, this volume)
- J.T. Gosling, D.J. McComas, *Geophys. Res. Lett.* **14**, 355 (1987)
- J.T. Gosling, S.J. Bame, D.J. McComas, J.L. Phillips, *Geophys. Res. Lett.* **17**, 901 (1990)
- J.T. Gosling, in *Coronal Mass Ejections*, ed. by N.U. Crooker, J.A. Jocelyn, J. Feyman. American Geophys. Union Monog., vol. 99 (American Geophys. Union, 1997), p. 9
- J.T. Gosling, C.A. de Koning, R.M. Skoug, J.T. Steinberg, D.J. McComas, *J. Geophys. Res.* **109**, A05102 (2004). doi:[10.1029/2003JA010338](https://doi.org/10.1029/2003JA010338)
- J.T. Gosling, R.M. Skoug, D.J. McComas, C.W. Smith, *Geophys. Res. Lett.* **32**, L05105 (2005)
- D.E. Larson et al., *Geophys. Res. Lett.* **24**, 1911 (1997)
- D.E. Larson, R.P. Lin, L. Steinberg, *Geophys. Res. Lett.* **27**(2), 157 (2000)
- R.P. Lin, S.W. Kahler, *J. Geophys. Res.* **97**(A6), 8203–8209 (1992)
- R.P. Lin, D. Larson, J. McFadden, C.W. Carlson, R.E. Ergun, K.A. Anderson, S. Ashford, M. McCarthy, G.K. Parks, H. Reme, J.M. Bosqued, C. d'Uston, T.R. Sanderson, K.-P. Wenzel, *Geophys. Res. Lett.* **23**(10), 1211–1214 (1996)
- R.P. Lin et al. (2007, this volume)
- J.G. Luhmann, D.W. Curtis, P. Schroeder, J. McCauley, R.P. Lin, D.E. Larson et al., *Space Sci. Rev.* (2007, this volume), doi:[10.1007/s11214-007-9170-x](https://doi.org/10.1007/s11214-007-9170-x)
- D.J. McComas, J.T. Gosling, J.L. Phillips, S.J. Bame, *J. Geophys. Res.* **94**, 6907–6916 (1989)
- M.D. Montgomery, S.J. Bame, A.J. Hundhausen, *J. Geophys. Res.* **73**, 4999–5003 (1968)
- M.D. Montgomery, J.R. Asbridge, S.J. Bame, W.C. Feldman, *J. Geophys. Res.* **79**, 3103 (1974)
- V. Osherovich, L.F. Burlaga, in *Coronal Mass Ejections*, ed. by N.U. Crooker, J.A. Jocelyn, J. Feyman. American Geophys. Monog., vol. 99 (American Geophys. Union, 1997), p. 9
- W.G. Pilipp, H. Miggenrieder, M.D. Montgomery, K.-H. Muhlhauser, H. Rosenbauer, R. Schwenn, *J. Geophys. Res.* **92**, 1075 (1987)
- W.G. Pilipp, H. Miggenrieder, K.-H. Mühlhäuser, H. Rosenbauer, R. Schwenn, *J. Geophys. Res.* **95**, 6305–6329 (1990)
- H. Rosenbauer, R. Schwenn, E. Marsch, B. Meyer, H. Miggenrieder, M.D. Montgomery, K.H. Muehlhäuser, W. Pilipp, W. Voges, S.M. Zink, *J. Geophys.* **42**, 561 (1977)
- R.F. Wimmer-Schweingruber, O. Kern, D.C. Hamilton, *Geophys. Res. Lett.* **26**, 3541 (1999)
- P. Wurz et al., *Geophys. Res. Lett.* **25**, 2557 (1998)

The STEREO IMPACT Suprathermal Electron (STE) Instrument

R.P. Lin · D.W. Curtis · D.E. Larson · J.G. Luhmann ·
S.E. McBride · M.R. Maier · T. Moreau · C.S. Tindall ·
P. Turin · Linghua Wang

Originally published in the journal Space Science Reviews, Volume 136, Nos 1–4.
DOI: [10.1007/s11214-008-9330-7](https://doi.org/10.1007/s11214-008-9330-7) © Springer Science+Business Media B.V. 2008

Abstract The Suprathermal Electron (STE) instrument, part of the IMPACT investigation on both spacecraft of NASA’s STEREO mission, is designed to measure electrons from ~ 2 to ~ 100 keV. This is the primary energy range for impulsive electron/ ^3He -rich energetic particle events that are the most frequently occurring transient particle emissions from the Sun, for the electrons that generate solar type III radio emission, for the shock accelerated electrons that produce type II radio emission, and for the superhalo electrons (whose origin is unknown) that are present in the interplanetary medium even during the quietest times. These electrons are ideal for tracing heliospheric magnetic field lines back to their source regions on the Sun and for determining field line lengths, thus probing the structure of interplanetary coronal mass ejections (ICMEs) and of the ambient inner heliosphere. STE utilizes arrays of small, passively cooled thin window silicon semiconductor detectors, coupled to state-of-the-art pulse-reset front-end electronics, to detect electrons down to ~ 2 keV with about 2 orders of magnitude increase in sensitivity over previous sensors at energies below ~ 20 keV. STE provides energy resolution of $\Delta E/E \sim 10\text{--}25\%$ and the angular resolution of $\sim 20^\circ$ over two oppositely directed $\sim 80^\circ \times 80^\circ$ fields of view centered on the nominal Parker spiral field direction.

Keywords Solar energetic particles · Energetic particle detectors · STEREO mission · Suprathermal electrons · Silicon detectors

R.P. Lin (✉) · L. Wang

Physics Department & Space Sciences Laboratory, University of California, Berkeley, CA 94720-7450,
USA

e-mail: rlin@ssl.berkeley.edu

D.W. Curtis · D.E. Larson · J.G. Luhmann · S.E. McBride · T. Moreau · P. Turin
Space Sciences Laboratory, University of California, Berkeley, CA 94720-7450, USA

M.R. Maier · C.S. Tindall
Lawrence Berkeley National Laboratory, Berkeley, CA 94720, USA

1 Introduction

The SupraThermal Electron (STE) instrument is part of the IMPACT (In-situ Measurements of Particles And CME Transients) investigation (see Luhmann et al. 2007, for overview), one of the four instrument packages on both spacecraft of NASA's STEREO (Solar TERrestrial RElations Observatory) mission. STE is designed to measure the \sim 2–100 keV suprathermal “superhalo” electrons (Fig. 18, panels a & b, of Luhmann et al. 2007) that was discovered by Wind spacecraft observations to be present in the interplanetary medium (IPM) near 1 AU, even during the quietest times (Lin 1997). They are the dominant particle species in impulsive solar energetic particle (SEP) events, the most frequently occurring transient solar emissions. These fast electrons with small gyro-diameters are ideal tracers of solar-heliospheric magnetic field connections, since the X-ray and radio emission they generate at the Sun and in the IPM can be detected remotely. Furthermore, they suffer significant energy losses in traversing the corona, so their energy spectra can provide information on their source height. Thus, they are powerful probes of particle acceleration and escape from the Sun, and of solar-heliospheric magnetic structure and connectivity, both for transients (ICMEs) and the quiet heliosphere.

Previously, measurements of particles below \sim 20–30 keV energies were made by electrostatic analyzers (ESAs) with microchannel plate detectors (e.g., the EESA and PESA (electron and proton) detectors of the 3D plasma & Energetic Particles investigation on the Wind spacecraft (Lin et al. 1995) and the SWEA (Solar Wind Electron Analyzer) detector of IMPACT [see Sauvaud et al. 2007]). The fluxes of suprathermal electrons, however, are typically many orders of magnitude lower than the solar wind halo and strahl electrons (see Fig. 18, panels a & b, of Luhmann et al. 2007). STE is designed to provide about 2 orders of magnitude increase in sensitivity over previous measurements in the \sim 2 to 20–30 keV energy range, by extending the range of silicon semiconductor detectors (SSDs) for particle detection down to \sim 2 keV. STE’s sensitivity and resolution in energy and angle enables the detailed study of solar and interplanetary particle acceleration, escape, and propagation; of the structure and solar connectivity of the IPM, in particular, ICMEs; and of the wave-particle processes (together with the STEREO waves (SWAVES) instrument (see Kaiser et al. 2007) that produce solar type III and type II radio bursts.

2 Scientific Objectives

STE measurements will directly address many of the prime objectives of the STEREO mission. It will:

- Probe particle acceleration near the Sun in both impulsive and gradual SEP events.
- Identify the magnetic footpoints and determine the length of field lines of ICMEs.
- Probe the *in situ* acceleration of electrons by ICME shock waves,
- Study the plasma physics of the wave-particle interactions that generate type II and III radio emission.
- Identify the source (presently unknown) of the superhalo (\sim 1–100 keV) electrons that are always present in the interplanetary medium.

Solar impulsive electron events were first observed above \sim 40 keV and later detected down to keV energies (see Lin 1985 for review), and even to \sim 0.1 keV (Gosling et al. 2003). They are almost always accompanied by an interplanetary type III solar radio burst, and often by low-energy, tens of keV to \sim MeV/nucleon ions highly enriched in ^3He (Reames

et al. 1985), forming the class of “impulsive” SEP events. Over \sim 100 events/month occur over the whole Sun near solar maximum above pre-STE detection thresholds, making these the most frequent transient energetic particle emissions from the Sun (Lin 1985).

Using WIND observations, Krucker et al. (1999) found the injection of the >25 keV electrons were often delayed by an order of \sim 10 minutes after the type III radio bursts at the Sun, and suggested the delays may be related to propagation of large-scale coronal transient (EIT or Moreton) waves across the Sun. Haggerty and Roelof (2002) found a median delay of \sim 10 min for 38–315 keV electrons; Simnett et al. (2002) suggested acceleration by shock waves associated with coronal mass ejections (CMEs). Maia and Pick (2004) proposed that these events are related to the coronal magnetic restructuring in the aftermath of CMEs, while Cane and Erickson (2003) argue from radio observations that the delays are due to propagation effects in the IPM. Comparisons to SOHO/LASCO coronagraph and EIT observations indicate the delayed high energy injections may be related to jets or narrow CMEs (Wang et al. 2006b).

More recently, Wang et al. (2006a) was able to derive the injection profile of electrons at the Sun for three extremely scatter-free impulsive electron events. They found two distinct injections: one at low energies (\sim 0.4 to \sim 10 keV) that begins minutes before the type III burst at the Sun and lasts for 50–300 minutes, and one at high energies ($>\sim$ 13 to 300 keV) that is delayed by \sim 10 minutes from the type III burst and lasts for \sim 10–30 minutes. Thus, the source of the type III radio burst can be identified with the low-energy electrons, consistent with the detection of Langmuir waves *in situ* when the \sim 1–10 keV electrons arrive near 1 AU (Ergun et al. 1998).

STE’s extremely high sensitivity for suprathermal electrons will provide many more impulsive solar electron events for study than previous missions. Electron injection profiles, energy spectra, and pitch angle distributions in impulsive and gradual SEP events will be determined from measurements with STE. Simultaneous identical measurements by the two STEREO spacecraft as they move away from each other will provide information on the longitudinal extent of the cone of field lines populated by these events. Comparison of these *in situ* electron observations at \sim 1 AU with RHESSI (Ramaty High Energy Solar Spectroscopic Imager mission, see Lin et al. 2002) measurements of the spectrum, temporal profile, and imaging of the bremsstrahlung X-rays produced by these energy electrons at the Sun will provide detailed information about electron acceleration and escape processes in impulsive and gradual SEP events.

Electrons in impulsive SEP events provide ideal tracers of magnetic field connection from the Sun into the heliosphere. They can be located at the Sun through their bremsstrahlung X-ray emission (imaged by RHESSI), tracked as they travel along the magnetic field lines through the interplanetary medium by the type III radio bursts that they generate (with the triangulation by the SWAVES instruments on the two STEREO spacecraft), and detected *in situ* by the STE instruments on the two spacecraft. By analyzing the velocity dispersion of these impulsively accelerated electrons, the field line length can be obtained in both ICMEs, where the lengths can be several times the typical Parker spiral length at the outer edge of the twisted field of a magnetic flux rope (see Fig. 2 in Luhmann et al. 2007 [from Larson et al. 1997]), and in the quiet interplanetary medium.

These electron diagnostics of ICME magnetic field line properties, obtained from both STEREO spacecraft, can be compared with the stereo imaging of the CME/ICMEs from the SECCHI (Sun Earth Connection Coronal and Heliospheric Investigation) instruments, and to the radio imaging from SWAVES instruments on STEREO. The extremely high sensitivity of STE, coupled with the time resolution (2 sec at 20 keV) with which the anisotropy measurements are made, provides the best opportunity to date to search for the signatures

of the closing down of interplanetary field connections to the Sun, to evaluate the balance between opening and closing flux in ICME transients, and to determine whether the slow solar wind (and by inference, the coronal streamer belt) is an important participant in the flux balance problem.

The SWAVES instrument will track CME-driven shocks and flare electrons as they propagate away from the Sun, using type II and type III radio bursts as a proxy. This tracking, however, depends on the beam pattern of the radio burst, which is specific to the radio emission mechanism. It is believed that plasma waves are generated at f_{pe} , the electron plasma frequency, by suprathermal $\sim 2\text{--}20$ keV electrons escaping from the Sun (see Lin et al. 1986). Wind observes elliptically polarized plasma waves at $1 f_{pe}$ in the source of these bursts, where longitudinally polarized Langmuir waves were expected (Bale et al. 1998). These plasma waves then interact, in a poorly understood way, to produce radio emissions at f_{pe} and $2 f_{pe}$. How the radio emissions depend on the electron distribution and ambient plasma characteristics is unknown. STE will provide electron measurements to compare with SWAVES radio and plasma wave measurements.

Recently, Wind provided the first observation of the Type II electron source *in situ* (Bale et al. 1999). The radio emission is observed to come from near quasi-perpendicular connections to the ICME-driven shock, while the source shock-accelerated electrons show the shock surface is highly structured, giving rise to multiple emission sites. As type II and III radio source regions pass over the two STEREO spacecraft, the IMPACT and SWAVES instruments will make coordinated burst observations of the suprathermal electrons and plasma waves. The exceptional sensitivity, temporal, and energy resolution of STE, when coupled with SWAVES 3 axis electric and 1 axis magnetic waveforms, should lead to advances in the understanding of the type III and type II radio emission processes. Together, SWAVES and STE will further resolve the Type II source nature, allowing us to better infer shock structure from remote particle and radio measurements.

Above ~ 2 keV the “superhalo” electron component (Fig. 18, panels a & b, of Luhmann et al. 2007) that is present even during the quietest times (Lin 1997) typically extends up to >100 keV. Its origin is presently unknown. These electrons could be related to the solar wind acceleration process, or result from continuous acceleration by micro/nanoflares in the solar atmosphere, or come from interplanetary acceleration processes similar to those likely responsible for the suprathermal ions. As mentioned earlier, the impulsive acceleration of electrons to ~ 1 to $>\sim 100$ keV energies is the most common solar particle acceleration process. Detailed high sensitivity measurements by STE of the superhalo, including its spectral, angular, temporal and spatial properties, are needed to determine its origin.

3 Instrument Overview

STE is a new instrument designed to provide geometry factor times observing time product about two orders of magnitude larger than previous detectors (electrostatic analyzers) in the ~ 2 to 20 keV energy range, with much lower background. Electrostatic analyzers such as the very large EESA-H sensor (~ 20 cm diam, ~ 3 kg, ~ 3 W) of the 3D Plasma & Energetic Particle instrument (Lin et al. 1995) on the Wind spacecraft measure one energy band at a time. EESA-H has $\Delta E/E = \sim 0.2$ so ~ 14 contiguous energy steps covered 2–20 keV, a duty cycle of $\sim 7\%$ at a given energy. STE utilizes silicon semiconductor detectors (SSDs) that measure all energies simultaneously (100% duty cycle). Up to now the SSDs used for particle detection have had relatively high capacitance and leakage currents, resulting in electronic noise thresholds of $>\sim 15$ keV, and thick window dead layers that further increase the minimum

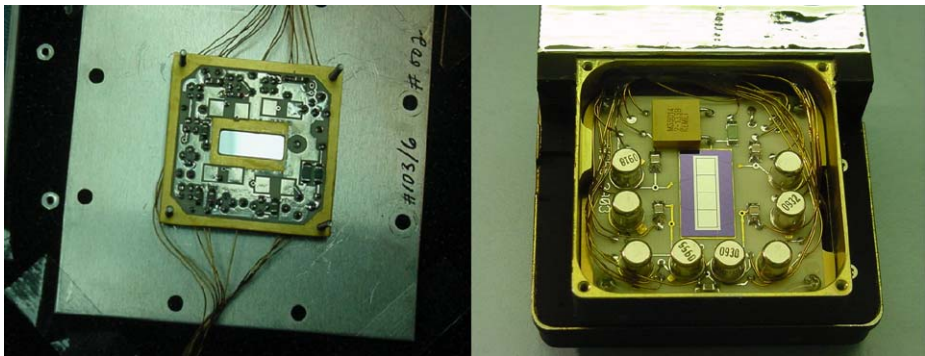
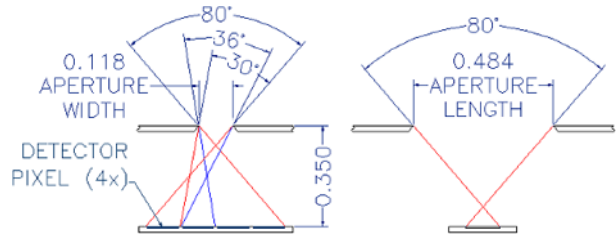


Fig. 1 Detector board front side (*left*) and back side shown in housing (*right*)

Fig. 2 Detector pixel fields of view (FOV), maximum extent, for STE_D; STE_U has a $70^\circ \times 70^\circ$ FOV. The FWHM FOVs are $\sim 20^\circ \times 70^\circ$ for each pixel



energy detectable to $\sim 20\text{--}30$ keV for electrons and ions. STE consists of arrays of small, low capacitance, cooled SSDs (Fig. 1), fabricated with an unusually thin window dead layer (Tindall et al. 2008), so $<\sim 2$ keV electrons can penetrate and be detected. The SSDs are surrounded by a guard ring and passively cooled to ~ -30 to -90°C to minimize leakage current, and coupled to state-of-the-art, cooled FET, pulse-reset preamp-shaping electronics to obtain an electronic threshold of ~ 1.5 keV.

STE consists of two arrays, STE-U and STE-D, each with four SSDs in a row on a single silicon wafer, looking through a rectangular opening (Fig. 2) that provides a $\sim 20^\circ \times \sim 80^\circ$ field of view (FOV) for each SSD (with the $80^\circ (\pm 40^\circ)$ direction perpendicular to the ecliptic). Adjacent FOVs are offset from each other by $\sim 20^\circ$ for pitch angle resolution of $\sim 20^\circ$ FWHM. The two arrays each have total nominal FOV of $\sim 80^\circ \times 80^\circ$ (STE-D), centered on the nominal Parker spiral magnetic field direction, one array facing toward (STE-U) and the other (STE-D) away from the Sun. Since the thin-window SSDs are very sensitive to light, carefully designed sun shades are needed to prevent stray light and glint from the spacecraft and booms from entering the aperture. Table 1 summarizes the measurement parameters and instrument characteristics for STE.

STE has a total geometric factor of $\sim 0.2 \text{ cm}^2 \text{ ster}$ vs 0.05 for Wind/EESA-H, a 100% duty cycle vs 7%, for a factor of ~ 60 gain in effective signal. EESA-H used an anticoincidence shield to reject penetrating high-energy particle background, but even so the count rate above ~ 2 keV at quiet times was ~ 30 c/s, dominated by intrinsic background counts of the very large microchannel plate detector. The primary background at 2–20 keV for the STE detectors is expected to be diffuse sky X-rays (~ 1 c/s per pixel), but this is much lower than the anticipated electron superhalo count rate ($>\sim 5$ c/s per pixel). Penetrating particles such as cosmic rays and high energy SEPs leave more than 200 keV (minimum ionizing) and are rejected.

Table 1 STEREO IMPACT Suprathermal Electron (STE) instrument

A. Measurement parameters

Detector	Particle & energy range ¹	Geometric factor	Field of view ²	Dynamic range
STE-U	2–100 keV electrons	0.08 cm ² ster	70° × 70° centered 45° from Sun	~0.1–10 ⁶ (cm ² ster s) ⁻¹
STE-D	2–100 keV electrons	0.10 cm ² ster	80° × 80° centered 225° from Sun	~0.1–10 ⁶ (cm ² ster s) ⁻¹

¹Energy resolution $\Delta E/E$ is ~1 keV at low energies to $\Delta E/E \sim 0.2$ at high energies

²Each of the four detectors has a $\sim 17^\circ \times 70^\circ$ FWHM FOV with $\sim 18\text{--}19^\circ$ for STE-D spacing between detectors

B. Instrument characteristics

	Mass ³	Power ⁴	Volume	Bit rate
STE-U	0.4 kg	0.5 watts		
STE-D	0.4 kg	0.5 watts		
Total	0.8 kg	1.0 watts		230 bps

³Does not include bias supply and other electronics in IDPU

⁴Does not include part of SWEA or IDPU used for STE, or conversion efficiency

Low energy ions (protons $>\sim 4$ keV, He $>\sim 8$ keV, etc.), however, can penetrate the window and stop. Energetic neutral atoms (ENAs) or molecules, if present, will be detected as ions, since they will be ionized upon passing through the detector window. The STE FOV excludes solar wind ions, but pickup ions will fill a shell in velocity space of radius $\sim V_{sw}$ centered on the solar wind (Mobius et al. 1998). For typical $V_{sw} \sim 400$ km/s, pickup protons will be below threshold, but pickup He are expected to be detected with typical fluxes of $\sim 1\text{--}2 \times 10^3$ (cm² s ster keV)⁻¹, from directions within $\sim 45^\circ$ of the solar wind. The SSD whose FOV is closest to the solar Wind will see He count rates of a few hundred per second (an interesting measurement in itself), while the count rates of the other SSDs should be dominated by superhalo electrons. Of course, at higher V_{sw} more pickup ions will be detected, in more SSDs.

For detection of impulsive electron events (defined somewhat arbitrarily as an 5 sigma increase in 5 minutes), STE should have greater than two orders of magnitude more sensitivity than EESA-H. Thus, far more events will be detected. At the same time STE requires significantly less resources than EESA-H (Table 1).

The STE sensors (including detector, FET, enclosure, door) are 40 g each. The STE-U preamp and enclosure is 360 g. The STE-U electronics card (in the IDPU) is 300 g. STE-U shares the processor (260 g) and LVPS (280 g) of the IDPU. The IDPU chassis is 690 g. The STE-D preamp and electronics is included in the SWEA/STE-D package. The combined SWEA/STE-D electronics, including shared LVPS, shared digital interface, shared chassis, and STE preamp and electronics (but excluding STE-D sensor, SWEA sensor, SWEA preamps and HVPS) weighs 960 g. STE-D also shares the IDPU processor. Thus, a stand-alone STE unit without processor or LVPS would be ~ 700 g.

Each STE unit dissipates <100 mW in the sensor, ~ 200 mW in the preamp, and ~ 290 mW in the remaining electronics (excluding processor and LVPS). So the total for a stand-alone STE is ~ 600 mW, excluding processor and LVPS.

4 Silicon Semiconductor Detectors (SSDs)

STE's SSDs have very thin entrance contacts fabricated through a processing technique that employs a thick, doped polysilicon layer on the wafer backside to getter impurities during the high temperature processing steps. This helps to maintain the material resistivity at values greater than $10\text{ k}\Omega\text{-cm}$ throughout the process and minimizes the incorporation of deep levels within the active area of the device that lead to increased leakage current (Holland 1989). In order to form the thin contact, near the end of the process, the one micron thick gettering layer was removed either by chemical etching or chemical-mechanical polishing (CMP). A 100 to 200 \AA thick, doped polysilicon layer was then deposited on the entrance side of the detectors to form the n+ contact (Holland et al. 1997). Although the SSDs are well shielded from stray light, a 200 \AA thick layer of aluminum was deposited over the doped-poly silicon contact to further reduce the SSDs' sensitivity to light.

For STE, 1×4 linear arrays of $3\text{ mm} \times 3\text{ mm}$ SSDs (Fig. 1) were fabricated on $315\text{ }\mu\text{m}$ thick, high resistivity ($\sim 10\text{ k}\Omega\text{-cm}$), (100) n-type silicon substrates, with a multiple guard ring structure to gradually drop the bias voltage and to take up the surface leakage current. The SSDs are operated fully depleted, so that the electric field extended to the back contact. Leakage currents are typically on the order of a few hundred picoamps per square centimeter at room temperature. The residual impurity level was found to be between $3 \cdot 10^{11}$ and $4 \cdot 10^{11}\text{ cm}^{-3}$. The SSD elements are wirebonded to the input low noise FET of a charge-sensitive preamplifier and connected to amplification, shaping and digitizing electronics.

5 Electronics

The Analog Electronics start with a pulse-reset charge sensitive preamplifier. The lack of feedback resistor means its contribution to the electronic noise is not present—an important source at these noise levels (450–600 eV FWHM). Additionally, it is very effective in removing the charge resulting from an extremely high energy event captured in the detector. Because of the close physical proximity of the four detectors in the array, however, a reset in a single detector will generate a signal in the other three, resulting in a dead time in all four detectors.

The preamplifier input FETs and reset transistors are mounted on a small low leakage printed circuit board very close to the SSDs (Fig. 1) so stray capacitance doesn't add electronic noise to the system, and the FETs are passively cooled along with the SSDs to minimize electronic noise. The FETs are dual gate devices chosen for their superior noise performance. The SSD/FET circuit board is connected to the rest of the preamp electronics through manganin wires to provide adequate thermal isolation. The detector/FET board also includes a thermometer, high voltage filtering, bypassing of the reset circuitry and the feedback capacitors for the charge sensitive amplifiers. A test pulser signal modulates the high voltage on the SSDs to provide stimulus to the detectors for calibration.

The outputs of the preamp go to unipolar shaping amplifiers with a shaping time of approximately $2\text{ }\mu\text{sec}$. These are 5 pole quasi-Gaussian filters and have gated baseline restorers. A simple differentiator and compensation network provide peak detection. The outputs

of the amplifiers go to a set of discriminators whose output allows the digital electronics to control the data acquisition. The digital signals available are Peak Detection (signal active when the unipolar pulse reaches its peak), (LLD) Low Level Discriminator (signal is above a threshold set by the Digital Electronics), (ULD) Upper Level Discriminator (signal is above the acceptable range of the Analog/Digital converter), and Reset (active during a preamp reset). The LLD is also used by the timing logic in the Digital Electronics to provide simple pile-up rejection. Each channel has its own low power Analog/Digital converter (16 bit converter with 12 bits used by the system) controlled by the Digital Electronics.

The STE Digital Electronics takes the ADC signal in the form of converted pulse heights (energy) together with an event strobe and accumulates it, and provides the results to the IMPACT IDPU via a serial interface. The Digital Electronics is implemented in the STE Interface FPGA (SIF) Actel and an SRAM memory. The SIF also runs the SWEA instrument in the case of STE-D. The front end ULD, LLD, and Reset event rates are counted in the SIF. The SIF provides an event threshold energy level to the analog front end chain via a Digital to Analog Converter (DAC). This level is set by the IDPU and is commandable from the ground. These interfaces are replicated for each of the 4 detector segments.

The SIF also provides the test pulser input to the analog electronics for calibration. The test pulser has a fixed event rate and a programmable amplitude which can be set to ramp up smoothly or in 8 discrete levels. The pulser operation is set by the IDPU in response to ground commands.

The SIF controls the STE detector bias voltage over a range of 0–150 V. Each of the 4 STE units has a separately programmed bias voltage (shared by the 4 detectors in the STE unit). The bias voltage is set by the IDPU in response to ground commands.

The SIF controls a protection circuit which identifies an over current event in the analog front end (perhaps due to Single Event Latchup) and powers off the analog front end automatically. The IDPU can reset this circuit in response to a command from the ground.

The SIF also controls the STE door actuators. It applies power to the open or close actuators until either the end of travel sense switch is activated or a pre-programmed timeout occurs (to protect the actuator from over-heating). The door actuation is initiated by the IDPU either in response to a ground command or a spacecraft status change (e.g., a thruster firing warning).

The SIF determines when a valid event has occurred based on information from the analog front end, including the peak detect signal, the ULD, the LLD, and the Reset signals. The scheme is designed to eliminate pile-up and veto ULD events and events that occur during Reset. Once a valid event has been recognized the event is converted by the ADC and binned into an accumulator. The system can only deal with one event at a time, up to ~300,000 events/second combined for all 4 detectors. The system is designed to be non-preferential so that one detector cannot lock out another.

Event binning is based on a programmable look-up table (LUT) that takes a combination of the 12-bit energy amplitude provided by the ADC and the 2-bit detector ID and generates an 8-bin accumulator ID to increment. The standard LUT generates 32 logarithmically spaced energy channels (in $1/\nu$) for each of the 4 detectors (see Table 2). Other LUTs are used for calibration and diagnostics.

The events are accumulated for 2 seconds and then read out to the IDPU. The IDPU passes the 2-second resolution data (both spectra and rate counters) to the burst memory. It also averages the data for a programmable interval (nominally 10 seconds) for the normal telemetry channel, and longer (1 minute) for the beacon telemetry channel.

Table 2 Nominal STE Energy Bins. The energy bins accumulate events from the next energy level below to the energy level indicated; bin “0” counts from the discriminator threshold level to the indicated level

Bin	Energy, keV	Bin	Energy, keV	Bin	Energy, keV	Bin	Energy
0	2.00	8	6.00	16	11.21	24	26.99
1	2.50	9	6.50	17	12.27	25	31.14
2	3.00	10	7.00	18	13.50	26	36.32
3	3.50	11	7.50	19	14.92	27	42.92
4	4.00	12	8.08	20	16.58	28	51.49
5	4.50	13	8.72	21	18.53	29	62.91
6	5.00	14	9.45	22	20.84	30	78.60
7	5.50	15	10.27	23	23.62	31	100.0

6 Mechanical

On each STEREO spacecraft there are separate STE-U and STE-D arrays with FOVs aligned with the nominal Parker spiral magnetic field direction facing toward (45°) and away (225°) from the Sun, respectively. Since the two spacecraft are rotated by 180° about the sun-spacecraft line relative to each other, the STE FOVs are also rotated by 180° between spacecraft. The total field of view (FOV) of the STE-D is $80^\circ \times 80^\circ$, while that of the STE-U is restricted to $70^\circ \times 70^\circ$ for sunshade clearance. The 1×4 linear arrays of $3\text{ mm} \times 3\text{ mm}$ SSDs are mounted on a ceramic circuit board inside an aluminum housing (Fig. 1). A gold-plated BeCu grid (Fig. 3, top) covering the opening serves as a Faraday cage to suppress the electric field of the SSD high voltage. STE has a reclosable door (Fig. 3, top) to protect the SSDs during ground handling, launch, and maneuvers (thruster plumes). Space constraints and the wide temperature range made traditional actuators problematic, so an SMA (Shape Memory Alloy, typically about equal parts Ti and Ni) actuated device was designed instead (Fig. 3, bottom). SMAs contract when heated above their transition temperature, and can be trained to return to their original shape when cooled. For this application, about $10''$ of $0.003''$ dia. Flexinol wire (manufactured by Dynalloy, Inc.) was used as an actuator for each direction. The linear wire contraction is converted into a rotary stroke of 120° by wrapping the free wire ends around tensioners attached to the door shaft. In order to fit this length of wire in the available mechanism volume of $1.6'' \times 2'' \times 38''$ inches, the wire was wrapped around a series of pulleys to fold the required length into the available space.

All moving plastic parts were made from Vespel SP, a MoS_2 impregnated polyimide with a very low coefficient of friction in vacuum. The toroidal door shaft bearings are synthetic sapphire, which is very hard and has a fairly low coefficient of friction when dry. The 303 stainless steel door shaft was coated with Ti nitride and dry lubed using a process called Brycoat. This consists of impregnating the surface with MoS_2 . Knowledge of the door position was provided by custom designed very low actuation force end-of-travel (EOT) switches

To move the door, 9 V is applied to the appropriate SMA wire. The wire resistively dissipates 1.6 W, self-heating it to the transition temperature and contracting the wire, and pulling the door either open or closed. The door is held in the cam detent until enough force is generated in the wire to overcome the overcenter plunger, and the door snaps smartly into the opposite position. As the door begins to move, one EOT switch opens, indicating the beginning of travel, and once it reaches its end of stroke the other EOT switch closes and shuts off the current.

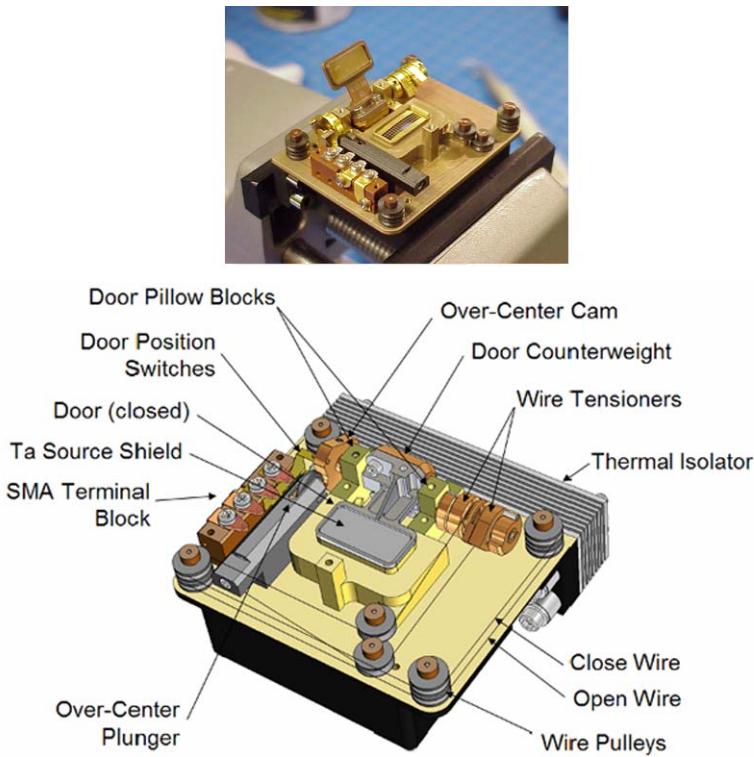


Fig. 3 *Top:* STE detector housing showing door open. *Bottom:* Schematic showing reclosable door mechanism

For the sunward-looking STE-U, a sun shield keeps sunlight and glint from the instrument aperture (Fig. 4). The sun shield has a double-beveled edge so that any glint from the sunward-most edge is blocked from entering the aperture by the second edge, and the second edge is prevented from generating glint by the shadow of the first edge.

The STE SSDs are passively cooled to operate in the range of -30°C to -90°C on orbit to minimize electrical noise. The SSDs and housing (with sun shield) are separated by PEEK thermal isolators (Fig. 3) from the preamp for STE-U, and from the SWEA instrument for STE-D. The other major heat path is through the approximately thirty 30ga. wires. Custom drawn and Teflon coated Manganin ($\text{Cu}86/\text{Mn}12/\text{Ni}2$) wires, with less than half the thermal conductivity of copper, were used for this application. Silver Teflon tape was applied to sunward facing surfaces to reflect sunlight during off-pointing maneuvers, preventing excessive heating of the electronics. As the STE-D instrument is mounted far from the spacecraft and in its shadow, the majority of its outer surface is gold alodine to prevent it from getting too cold. The STE-U is on the sunward side and sitting in direct sunlight, necessitating the thermally isolated sunshade and extensive silver Teflon tape and black paint (Fig. 4). Post-launch the SSDs reached equilibrium temperatures of -63°C and -80°C for STE-D, and -38°C and -51°C for STE-U, for spacecraft A and B, respectively.

The electrostatic cleanliness (ESC) requirements necessitate careful control of outer skin charging by use of conductive materials on most exposed surfaces, particularly those in shadow. The silver Teflon tape used on the STE instruments as well as on the sunward facing spacecraft blankets was ITO (Indium-Tin-Oxide) sputtered to provide a path for draining any



Fig. 4 STE-U sunshield (*left*) and thermal blanketing (*right*)

charge that develops due to photoemission or other effects. The STE-U preamp and SWEA electronics are covered with MLI blankets with conductive black Kapton outer surfaces with a Ge coating for improved thermal properties. To prevent leakage of electric fields from electronics, all mechanical joints in the STE and preamp housings were staggered, and an aperture grid covered the SSDs.

7 Calibration

Calibrations of the STE instruments were performed in the laboratory using radioactive sources and an electron gun. Figure 5 shows a typical spectrum for a STE detector exposed to a ^{55}Fe and a ^{109}Cd radioactive sources simultaneously, taken at room temperature. The $^{55}\text{Mn K}_{\alpha}$ X-ray at 5.9 keV is the largest peak in the spectrum and the 3 keV peak from the daughter isotope ^{109}Ag is clearly evident. The broad peaks centered around 68 keV and 40 keV are due to the 84 and 62 keV ^{109}Cd conversion electrons that have lost energy in the source and detector Windows. A similar $^{109}\text{Cd}/^{55}\text{Fe}$ radioactive source on the inside of the STE reclosable door provides in-orbit calibration of the SSDs.

The primary calibration involves measuring the response of the STE SSDs to incident electrons of known energy from an accelerator. Photo-electrons generated by a UV lamp illuminating a specially coated photo-anode are accelerated through a potential drop to produce a wide (~ 3 cm) parallel mono-energetic electron beam with energy adjustable from 0 to 30 keV. A Helmholtz coil was positioned outside the chamber to nullify the Earth's magnetic field and minimize the curvature of low energy electrons.

In addition, an on-board Test Pulser that runs at ~ 2000 c/s with a ramping amplitude, cycling every 40 seconds, is used to stimulate the preamplifier and downstream electronics chain and verify the stability and linearity of the electronics. It has two modes; smoothly ramping (good for testing ADC DNL), and stepping over 8 linearly spaced discrete amplitudes (for calibrating front end gain and electronic noise).

Figure 6 shows the pulse height distribution of one SSD in the STE instrument for normally incident 4 keV electrons. The largest peak is observed with center energy at the STE ADC channel 18.4, along with an overlying Gaussian fit showing a FWHM of 1.1 keV. The low energy excess below the peak is due to the roughly 5 to 10% of electrons incident upon the SSD that scatter back out of the detector, resulting in partial energy deposition.

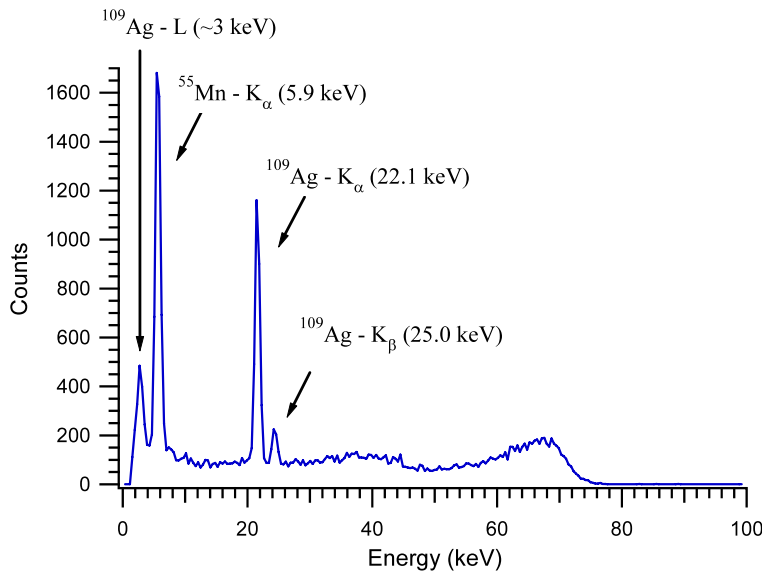


Fig. 5 Spectrum obtained by illuminated a STE detector at ambient temperature with a source of one μCi ^{55}Fe and a one μCi ^{109}Cd simultaneously. The integration time is not sufficient to show the 88 keV gamma emission of the ^{109}Cd . The broad peaks centered around 68 keV and 40 keV are due to the 84 and 62 keV ^{109}Cd conversion electrons that have lost energy in the source and detector Windows. A combination of ^{109}Cd and ^{55}Fe radioactive source to the inside of the door provides in-orbit calibration of the SSDs when door is closed

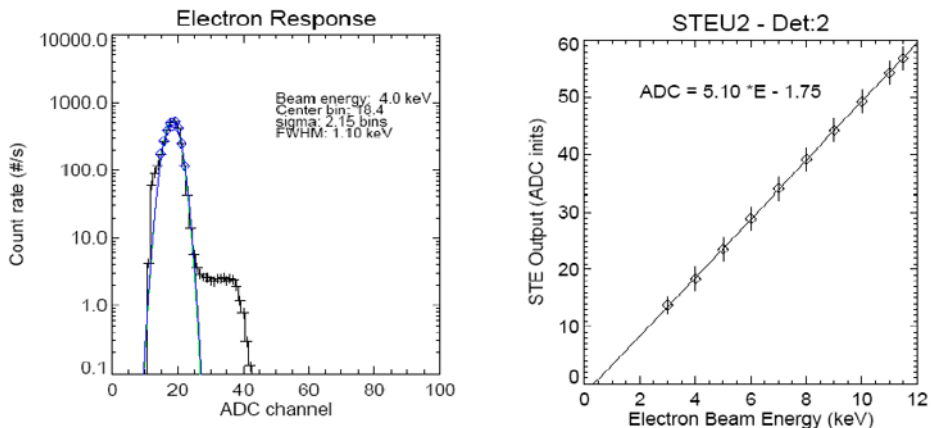


Fig. 6 *Left panel:* Response of a STE detector to a normally incident beam of 4 keV electrons. The fit to the peak gives ~ 1.1 keV FWHM energy resolution. The secondary peak at twice the energy is due to pulse pileup from two electrons striking the detector simultaneously, unusually prominent because the beam is pulsed. *Right panel:* STE ADC channel output for different energy electrons (vertical error bars dominated by FWHM width of the detector response)

The STE sensor was mounted on a 3-axis manipulator to allow the instrument response to be determined as a function of the 2 incident angles and linear position along to the beam

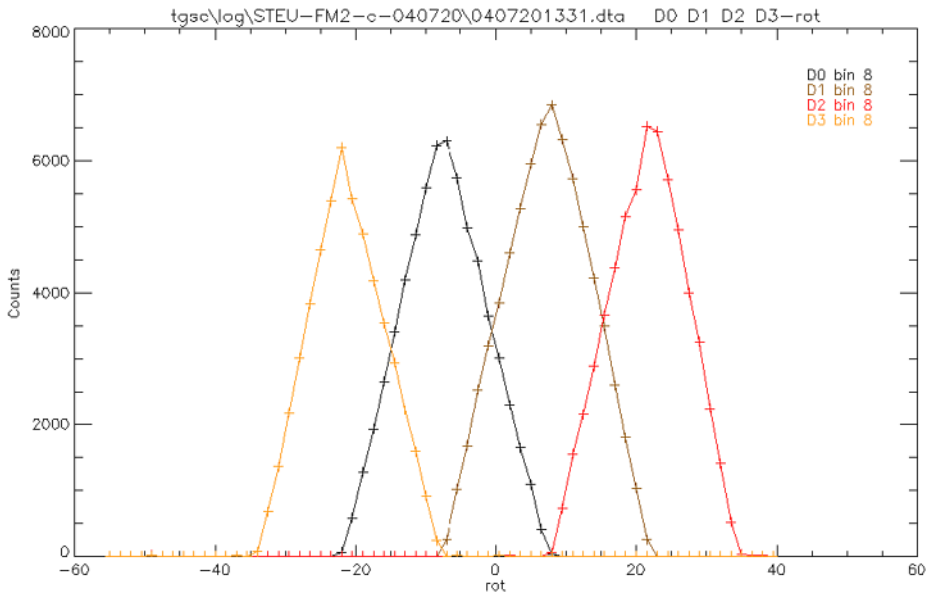


Fig. 7 Angular response in azimuth angle (0° is normal incident to the detector plane) for the four detectors of the STE-U sensor

width. Figure 7 shows the total count rate observed in each of the four pixels of STE-U as a function of the azimuth angle. This measurement was performed while keeping the electron beam energy constant at 10 keV.

For comparison, Fig. 8, left panel, shows preliminary observations of an impulsive solar electron event, and Fig. 8, right panel, the energy spectra for both the pre-event background and for the peak flux at each energy for the event, from STE-D for the B spacecraft. The lowest energy point is at 2 keV, and shows some detector noise as expected. This is an active time when the pre-event background is dominated by solar electron fluxes.

8 Modes of Operation & Data Format

The normal mode of operation for STE is door open, test pulser off, with the energy Look Up Table (LUT) number zero for the nominal case (Table 2) in use, and normal telemetry time resolution set to 10 seconds. The Bias voltage is set to optimize the detector noise performance and the LLD threshold is set to give <10 c/s background in the lowest energy channel. Note that the energy levels in Table 1 are nominal, depending on the gain of the front end.

The STE door will be closed periodically during the mission when the observatory is off-pointing or firing thrusters. Then, the SSDs are exposed to the $^{109}\text{Cd}/^{55}\text{Fe}$ radioactive source for calibration of the detectors and the front end gain and noise characteristics (peak width). The STE door calibration is often used with a special LUT to provide 256 linearly spaced energy bins to a single detector.

The STE Rates packet includes information on the state of the STE door, STE test pulser, accumulation time, and LUT in use. The LUT in use is encoded as the “STE Mode ID”. Values 1–6 are used for various diagnostic modes used with the STE door source and test

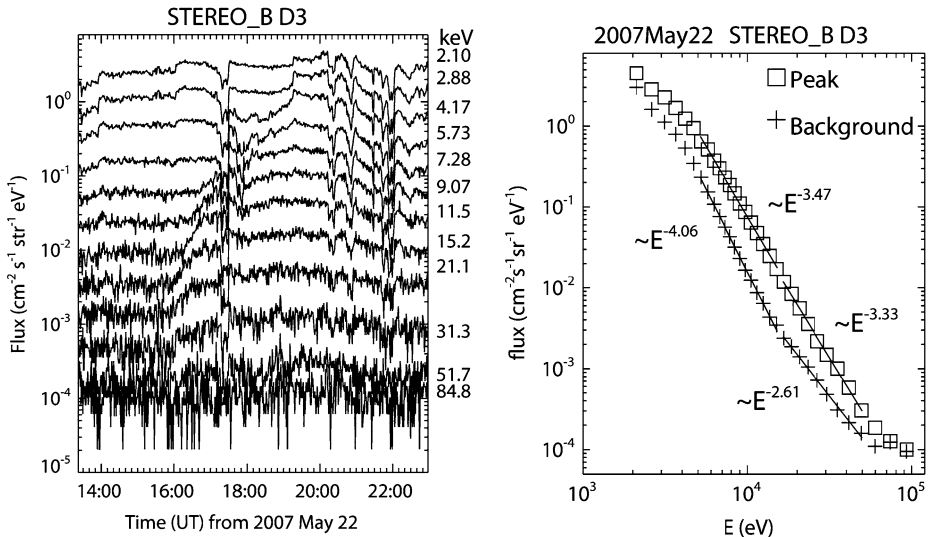


Fig. 8 *Left panel:* One-minute average electron fluxes observed downstream by a single STE detector on 2007 May 22. A solar energetic electron event begins at ~ 1555 UT, with velocity dispersion evident down to ~ 3 keV. *Right panel:* Energy spectra from the same detector. The *squares* indicate the peak fluxes observed in the 32 energy bins, and the *crosses* show the pre-event electron fluxes

pulsar. Other values may be used if new LUT are loaded post-launch. Threshold and detector HV settings are included in the STE parameter table that is transmitted periodically (once an hour).

The STE data is accumulated into telemetry packets. Details of these packets are described in the IMPACT Command and Telemetry database. Spectra packets contain the accumulated spectra data. Each energy bin count is log-compressed to 8-bits. In normal mode, a Spectra packet contains all the accumulated spectra for STE-U and STE-D (32 energies time 4 detectors times two STE units = 256 counters per spectra packet).

Rates packets contain accumulated rate counters. Each counter is log-compressed to 8 bits. Each Rates packet contains 10 samples of LLD, ULD, and Reset counters for 4 detectors for each STE unit. The 10 samples are consecutive measurements at the accumulation time interval (nominally 10 seconds). The Rates packets also contain various detector status information. The format of burst and normal telemetry packets are the same, but with different packet identifiers. The difference is that Burst data has 2-second resolution, while normal telemetry has 10 second resolution. Burst data is being taken continuously. A burst can be triggered by an increase in STE count rate, or by other IMPACT instruments—MAG or SWEA—or by the PLASTIC instrument. When a trigger occurs, five minutes of pre-trigger data is captured and stored, together with five minutes following the trigger.

STE Beacon data is a subset of the IMPACT Boom Suite Beacon packet produced once a minute. It contains 5-energy spectra (obtained by summing the 32-energy normal telemetry spectra into bands). Spectra are summed over detectors into 3 categories: STE-D, STE-U sunward detector, and the rest of STE-U. Beacon data also contains the combined STE-U and STE-D LLD rate. All of this is averaged over a 1-minute interval.

Acknowledgements We acknowledge the support of many colleagues, including B. Ludewigt, M. Colby, P. Berg. This research is supported in part by NASA Contract NAS5-00133 for IMPACT.

References

- S.D. Bale, P.J. Kellogg, K. Goetz, S.J. Monson, Transverse z-mode waves in the terrestrial electron foreshock. *Geophys. Res. Lett.* **25**, 9–12 (1998)
- S.D. Bale, M.J. Reiner, J.-L. Bougeret, M.L. Kaiser, S. Krucker, D.E. Larson, R.P. Lin, The source region of an interplanetary type II radio burst. *Geophys. Res. Lett.* **26**, 1573–1576 (1999)
- H.V. Cane, W.C. Erickson, Energetic particle propagation in the inner heliosphere as deduced from low-frequency (<100 kHz) observations of type III radio bursts. *J. Geophys. Res.* **108**, 1203 (2003)
- R.E. Ergun et al., Wind spacecraft observations of solar impulsive electron events associated with solar type III radio bursts. *Astrophys. J.* **503**, 435–445 (1998)
- J.T. Gosling et al., Solar electron bursts at very low energies: Evidence for acceleration in the high corona? *Geophys. Res. Lett.* **30**(13), 1697–1700 (2003)
- D.K. Haggerty, E.C. Roelof, Impulsive near-relativistic solar electron events: Delayed injection with respect to solar electromagnetic emission. *Astrophys. J.* **579**, 841–853 (2002)
- S. Holland, Fabrication of detectors and transistors on high-resistivity silicon. *Nucl. Instrum. Methods Phys. Res.* **A275**, 537–541 (1989)
- S.E. Holland et al., Development of low noise, back-side illuminated silicon photodiode arrays. *IEEE Trans. Nucl. Sci.* **44**, 443–447 (1997)
- Kaiser et al., The STEREO Mission: An Introduction. *Space Sci. Rev.* (2007, this issue). doi:[10.1007/s11214-007-9277-0](https://doi.org/10.1007/s11214-007-9277-0)
- S. Krucker et al., On the origin of impulsive electron events observed at 1 AU. *Astrophys. J.* **519**, 864–875 (1999)
- D.E. Larson, R.P. Lin et al., Tracing the topology of the October 18–20, 1995, magnetic cloud with ∼0.1–10² keV electrons. *Geophys. Res. Lett.* **24**, 1911 (1997)
- R.P. Lin, Energetic solar electrons in the interplanetary medium. *Sol. Phys.* **100**, 537–561 (1985)
- R.P. Lin, Observations of the 3D distributions of thermal to near-relativistic electrons in the interplanetary medium by the Wind spacecraft, in *Coronal Physics from Radio and Space Observations*, ed. by G. Trotter. Lecture Notes in Physics, vol. 483 (Springer, Berlin, 1997), p. 93
- R.P. Lin, W.K. Levedahl, W. Lotko, D.A. Gurnett, F.L. Scarf, Evidence for nonlinear wave-wave interactions in solar type III radio bursts. *Astrophys. J.* **308**, 954 (1986)
- R.P. Lin et al., A three-dimensional plasma and energetic particle investigation for the wind spacecraft. *Space Sci. Rev.* **71**, 125–153 (1995)
- R.P. Lin et al., Observation of an impulsive solar electron event extending down to ∼0.5 keV energy. *Geophys. Res. Lett.* **23**, 1211–1214 (1996)
- R.P. Lin, B.R. Dennis, G.J. Hurford et al., The Reuven Ramaty High-Energy Solar Spectroscopic Imager (RHESSI). *Sol. Phys.* **210**, 3–32 (2002)
- J.G. Luhmann et al., STEREO IMPACT investigation goals, measurements, and data products overview. *Space Sci. Rev.* (2007, this issue). doi:[10.1007/s11214-007-9170-x](https://doi.org/10.1007/s11214-007-9170-x)
- D. Maia, M. Pick, *Astrophys. J.* **609**, 1082–1097 (2004)
- E. Mobius, D. Rucinski, M.A. Lee, P.A. Isenberg, Decreases in the antisunward flux of interstellar pickup He+ associated with radial interplanetary magnetic field. *J. Geophys. Res.* **10**, 257 (1998)
- D.V. Reames et al., Solar ³He-rich events and nonrelativistic electron events—A new association. *Astrophys. J.* **292**, 716–724 (1985)
- Sauvageot et al., *Space Sci. Rev.* (2007, this issue). doi:[10.1007/s11214-007-9174-6](https://doi.org/10.1007/s11214-007-9174-6)
- G.M. Simnett et al., The acceleration and release of near-relativistic electrons by coronal mass ejections. *Astrophys. J.* **579**, 854–862 (2002)
- C.S. Tindall, N.P. Palaio, B.A. Ludewigt, S.E. Holland, D.E. Larson, D.W. Curtis, S.E. McBride, T. Moreau, R.P. Lin, V. Angelopoulos, Silicon detectors for low energy particle detection. *Trans. Nucl. Sci.* (2008, to be submitted)
- L. Wang, R.P. Lin, S. Krucker, J.T. Gosling, Evidence for double injections in scatter-free solar impulsive electron events. *Geophys. Res. Lett.* **33**, L03106 (2006a). doi:[10.1029/2005GL024434](https://doi.org/10.1029/2005GL024434)
- Y.-M. Wang, M. Pick, G.M. Mason, Coronal holes, jets, and the origin of ³He-rich particle events. *Astrophys. J.* **639**, 495 (2006b)

The Suprathermal Ion Telescope (SIT) for the IMPACT/SEP Investigation

G. M. Mason · A. Korth · P. H. Walpole · M. I. Desai ·
T. T. Von Rosenvinge · S. A. Shuman

Originally published in the journal Space Science Reviews, Volume 136, Nos 1–4.
DOI: [10.1007/s11214-006-9087-9](https://doi.org/10.1007/s11214-006-9087-9) © Springer Science + Business Media B.V. 2007

Abstract The Solar-Terrestrial Relations Observatory (STEREO) mission addresses critical problems of the physics of explosive disturbances in the solar corona, and their propagation and interactions in the interplanetary medium between the Sun and Earth. The In-Situ-Measurements of Particles and CME Transients (IMPACT) investigation observes the consequences of these disturbances and other transients at 1 AU. The generation of energetic particles is a fundamentally important feature of shock-associated Coronal Mass Ejections (CMEs) and other transients in the interplanetary medium. Multiple sensors within the IMPACT suite measure the particle population from energies just above the solar wind up to hundreds of MeV/nucleon. This paper describes a portion of the IMPACT Solar Energetic Particles (SEP) package, the Suprathermal Ion Telescope (SIT) which identifies the heavy ion composition from the suprathermal through the energetic particle range (\sim few 10 s of keV/nucleon to several MeV/nucleon). SIT will trace and identify processes that energize low energy ions, and characterize their transport in the interplanetary medium. SIT is a time-of-flight mass spectrometer with high sensitivity designed to derive detailed multi-species particle spectra with a cadence of 60 s, thereby enabling detailed studies of shock-accelerated and other energetic particle populations observed at 1 AU.

Keywords Solar energetic particles (SEPs) · Cosmic rays · Shock acceleration · CMEs

G. M. Mason (✉)

Johns Hopkins University/Applied Physics Laboratory, Laurel, MD 20723, USA
e-mail: glenn.mason@jhuapl.edu

A. Korth

Max-Planck-Institut für Sonnensystemforschung, Lindau, Germany

P. H. Walpole

University of Maryland, College Park, MD 20742

M. I. Desai

Southwest Research Institute, San Antonio, TX 78238

T. T. Von Rosenvinge · S. A. Shuman

NASA/Goddard Spaceflight Center, Greenbelt, MD 20771

1 Scientific Goals

1.1 Particle Acceleration Near the Sun and in the Heliosphere

The production of energetic particles takes place throughout the heliosphere with multiple processes taking place at different locations and times. In interplanetary space at 1 AU, this wide variety of sources is sketched in Figure 1, which shows a multi-year sum of the O fluence over the energy range <1 keV/nucleon to >100 MeV/nucleon (adapted from Mewaldt *et al.*, 2001). Starting at the low energy end we have the solar wind plasma, whose characteristic flow speed is generally either “slow” (~ 400 km/s) or “fast” (~ 700 km/s). Above the range dominated by the solar wind there is a large decrease in intensity leading to

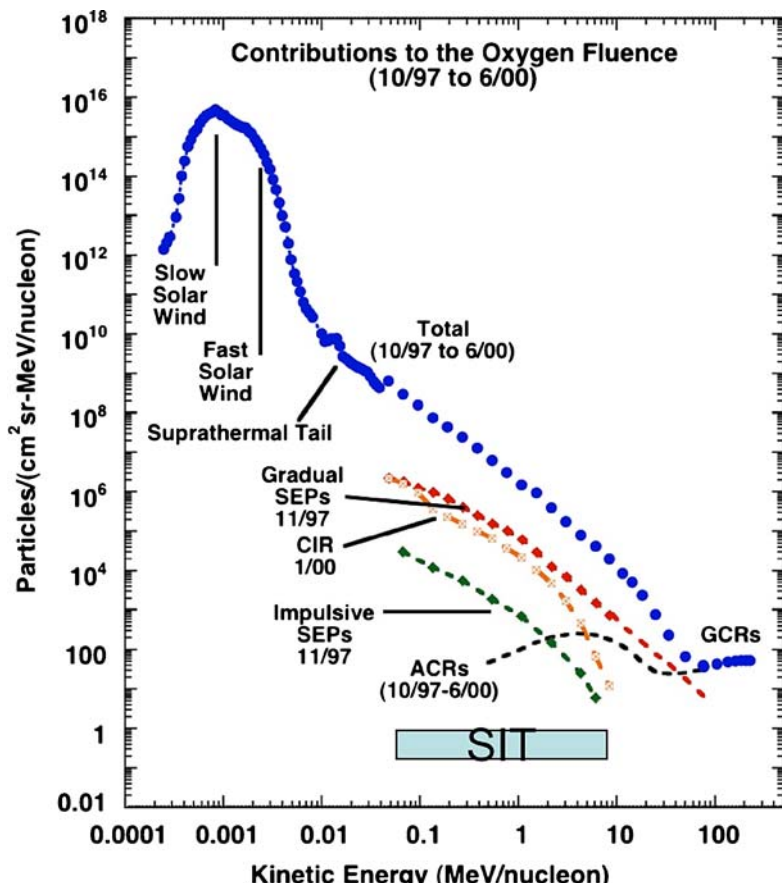


Fig. 1 Long term fluence of O summed from several instruments on the ACE spacecraft from Oct. 1997 through June 2000. In addition to the total fluence (filled blue circles) the figure also shows typical contributions from a Gradual Solar Energetic Particle (SEP) event, a typical Corotating Interaction Region (CIR) event, and a typical Impulsive SEP event. Also shown are the long term average levels of Anomalous Cosmic Rays (ACRs) during quiet periods during the summing interval. At the highest energies, the falling spectrum flattens and rises slowly due to the Galactic Cosmic Rays (GCRs). Shaded box shows the energy coverage of the SIT sensor (figure adapted from Mewaldt *et al.*, 2001)

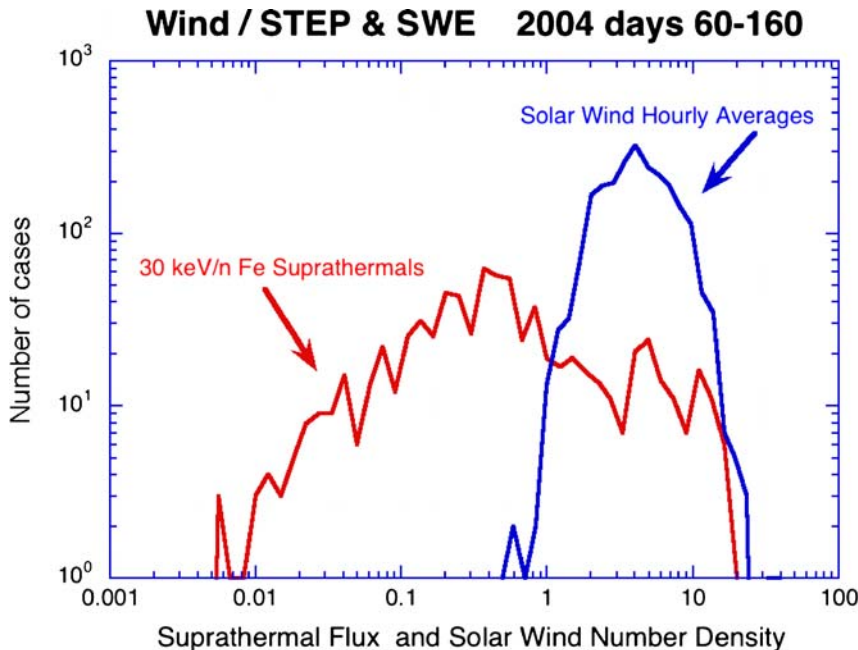


Fig. 2 Hourly average suprathermal (red) and solar wind (blue) flux values for a 100 day period in 2004. While the solar wind shows a factor of 10 variation, the 30 keV/nuc Fe suprathermals show a factor of 1000 variation (from Mason *et al.*, 2005)

a suprathermal tail that extends from several times the solar wind speed to ~ 10 MeV/nucleon, where particle speeds are $\sim 0.15c$, about 100 times the solar wind speed. In this energy range of ~ 0.01 to 10 s of MeV/nucleon, multiple particle sources exist, with each dominating the intensities at one time or another. The largest of these are gradual Solar Energetic Particle (SEP) events, which last for days and occur with a frequency of $\sim 1/\text{month}$ during active periods of the solar cycle. At generally lower intensities are Corotating Interaction Regions (CIRs) which are generally most intense during the declining phase of the sunspot cycle, and whose primary acceleration region and maximum intensities occur at a few AU. At even lower levels are impulsive SEPs, brief events with enhanced electron, ${}^3\text{He}$, and heavy ion abundances (for a recent review, see Reames, 1999). At energies above ~ 10 MeV/nucleon Anomalous Cosmic Rays (ACRs) and Galactic Cosmic Rays (GCRs) dominate the average intensities.

In the last few years it has become apparent that interplanetary suprathermal particles are a key component of the seed population of particles energized in gradual SEP events and by traveling interplanetary shocks (e.g., Mason *et al.*, 1999a, 2005; Desai *et al.*, 2001, 2005, 2006; Tylka *et al.*, 2001, 2003, 2006a; Mewaldt *et al.*, 2006). It can be seen from Figure 1 that this suprathermal tail has many contributors including heated solar wind, material from prior large SEP events, impulsive SEP events, traveling shock events, etc. This leads to a much larger variability than is observed in the solar wind itself. For example, Figure 2 shows the hourly averaged intensities of Fe suprathermals and solar wind over a 100 day period in 2004. Note that while the solar wind shows a factor of ~ 10 variation in density, the suprathermals show a factor of ~ 1000 . Thus, if the seed particles energized by interplanetary shocks are solely suprathermals, then the range of input densities the shocks encounter will be much

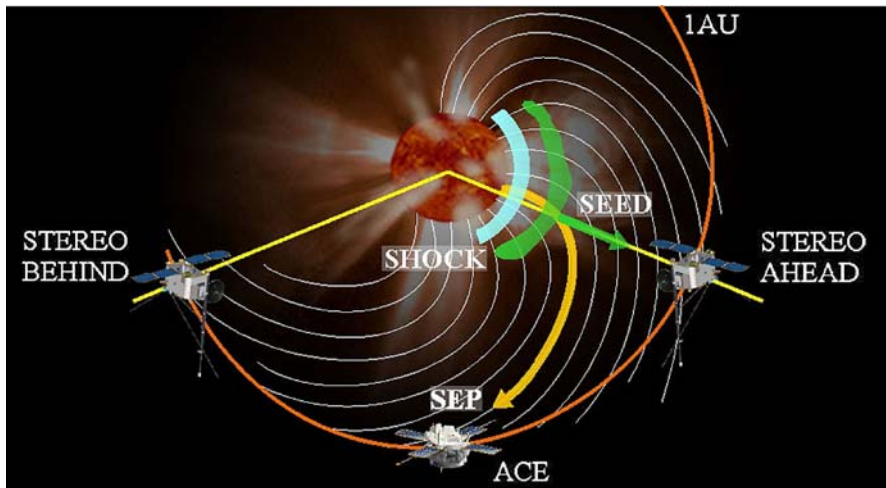


Fig. 3 Sketch of geometry of a western hemisphere shock-associated SEP event. The shock (light blue) accelerates particles out of the seed population (green) in its path. The energetic particles then follow (yellow arrow) the interplanetary magnetic lines that direct them east of the shock. For the geometry shown, STEREO-Ahead and ACE are required to observe both the seed population and the energetic particles; for other shock locations, different pairs of spacecraft would be used

larger than if the seeds were solar wind. In addition, the suprathermals show a much wider range of abundance variation than the solar wind; for example, the Fe/O ratio in SEPs varies by over a factor of ~ 100 , while in the solar wind the variation is closer to a factor of ~ 5 . These considerations will critically affect the abundances of the energized ions, as has been observed for traveling interplanetary shocks (Desai *et al.*, 2003).

In order to explore the relationship between the energetic particle populations and the seed particles, it is important to observe the seed particles associated with energetic particle events. In the case of traveling interplanetary shocks this can be done in an approximate way by measuring suprathermals a day or two upstream of the shock-associated particle enhancements. When this is done, it is found that there is a significant correlation between the suprathermal ion composition and spectra, and the composition and spectra of the energetic particles (Desai *et al.*, 2003). This is an indirect comparison since the upstream suprathermals are not the ones that encounter the shock. However the correlation is apparently preserved since the interplanetary shock is accelerating particles locally, and so the upstream particle properties are correlated, on average, with those accelerated by the shock.

For the case of large SEP events, this correlation no longer holds (Desai *et al.*, 2006a), presumably because the acceleration site is closer to the Sun. Figure 3 sketches the geometry in the case of a western hemisphere shock-associated SEP event. The shock is most effective at accelerating particles close to the nose of the shock front (e.g., Reames, 1999). Once energized, the particles follow the interplanetary magnetic field spiral, and move east of the shock front as shown in Figure 3. Observations at a single point are unable to measure both the seed and energetic particle populations, but the STEREO spacecraft, supplemented by missions at L1 such as ACE and Wind will be able to make the required multi-point measurements. This is just one example of how the STEREO *in-situ* instruments will permit critical new measurements in studies of energetic particles in the interplanetary medium.

1.1.1 Large Solar Particle Events

Large SEP events produce the highest energy particles of any mechanism in the solar system, and their ionizing radiation can disrupt or damage space systems. The shocks in many of the largest events are associated with Coronal Mass Ejections (CMEs) that can be imaged by the two STEREO spacecraft, opening the opportunity to explore the relationship between the CME/shock and energetic particle population. Figure 4 shows fluences of major ions accelerated in the 2003 November 2 event, which was one of several in the so-called “Halloween” series of SEP events (from Mewaldt *et al.*, 2005). The energy spectra show “breaks” or roll-overs that occur at different energies for different species. The location of these spectral breaks may be related to the details of the energetic particle escape from the accelerating shock (Ellison *et al.*, 1985; Li *et al.*, 2005), but it is also possible that diffusion effects in the interplanetary medium play the dominant role (Cohen *et al.*, 2005). Measurements with one of the STEREO spacecraft can trace CMEs moving out from the Sun, while the other

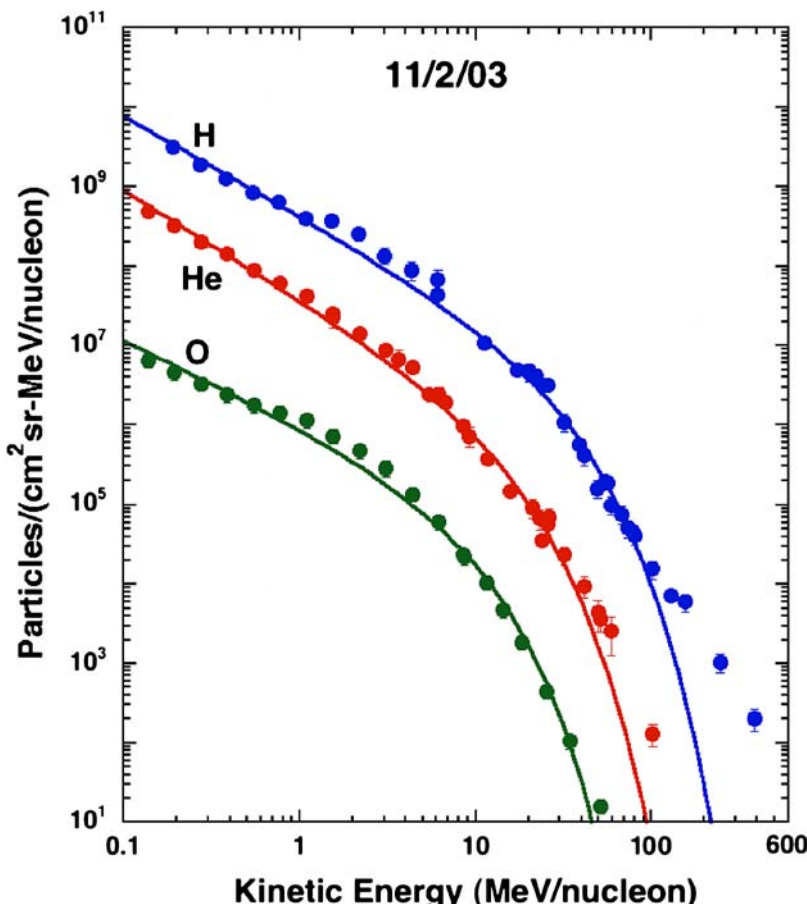


Fig. 4 Fluences of major energetic ion species in the 2003 Nov. 2 event show power law dependence at energies below a few MeV/nucleon, followed by steepening at higher energies. Notice that the spectra steepen at different kinetic energies for different species (from Mewaldt *et al.*, 2005)

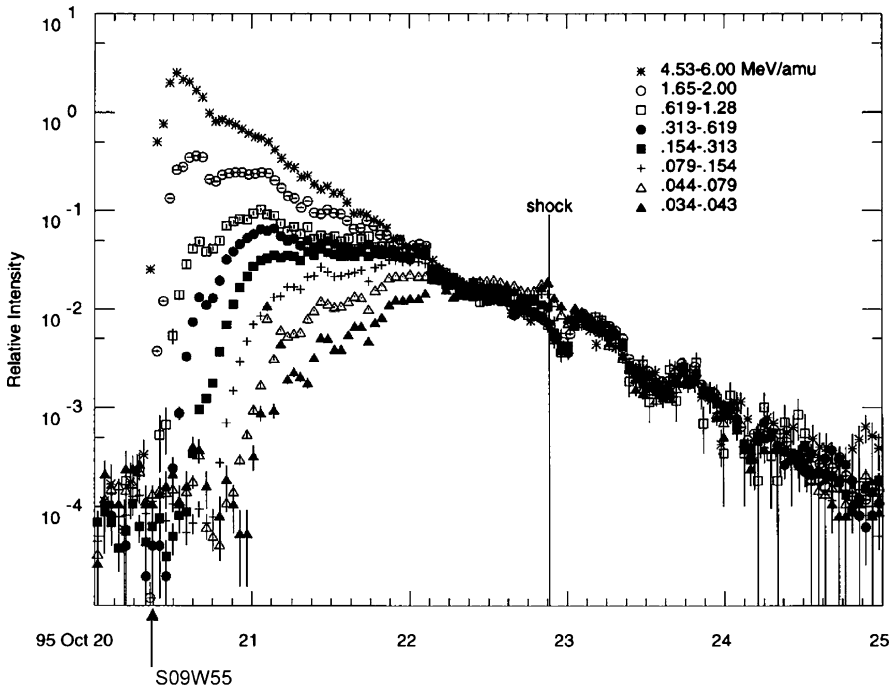


Fig. 5 ${}^4\text{He}$ intensity profiles for the 1995 October 20 event normalized to the decay phase intensities after October 22. Other species showed this same behavior (from Reames *et al.*, 1997a). The parent event at the Sun was a flare of importance OF and X-ray intensity M1

spacecraft will simultaneously observe the energetic particles from the shock in front of the CME, thereby enabling critical studies of the relationship between particle energy spectral slopes and breaks and the initiating CME-driven shocks in large SEP events.

Although the event-integrated fluences shown in Figure 4 from low energies out to a few MeV/nucleon follow a single power law, there are dramatic differences in the time evolution of the particle intensities over this energy range. Figure 5 illustrates this for an event at S09W55 on 1995 October 20 (from Reames *et al.*, 1997a). In this figure, the intensities have been adjusted to the same intensities during the decay phase starting on October 22. Even though the parent event in this case was magnetically well-connected to Earth, the intensity increases at low energies were very slow, with the 34–43 keV/nucleon channel beginning to increase almost 12 hours after the 4.53–6.00 MeV/nucleon channel intensity had peaked. This event had been preceded by an interplanetary shock on October 18 and some of the slow rise at low energies may be due to turbulence associated with the earlier shock. In an event of this kind, however, with the low energy intensity peaks lagging the higher energy onset by 1–2 days, solar corotation may play an important role (Reames *et al.*, 1997a) since at this late period the magnetic field lines are $>20^\circ$ from the shock center which had been sampled by the high energies when the event began. Since acceleration across the shock front is not uniform, corotation will significantly affect the low energy intensity profiles (Reames *et al.*, 1997b). Behind the shock intensities are generally constant, and that may be responsible for the constant decay rates over the broad energy range shown in the figure (Reames *et al.*, 1997b). However, alternate explanations are also possible (e.g., Sollitt *et al.*,

2003; Sollitt, 2004). For example if the SEPs are released from near the Sun and diffuse into a large scattering volume, the decay timescales will depend only on convection and adiabatic deceleration, which may be nearly constant over a significant energy range. This would result in energy and species independent decay time constants as seen in Figure 5. In cases where the scattering free-escape outer boundary is closer to the observer, then particle speed and mean free path can lead to decay time constants that vary with both energy and species (Sollitt *et al.*, 2003; Sollitt, 2004), in contrast to the behavior shown in Figure 5. By probing the properties of these particle populations at widely varying longitudes, these contrasting models can be tested.

1.1.2 Traveling Interplanetary Shocks

In the large SEP event shown in Figure 5, the associated shock passage has virtually no effect on the high energy intensities. For the low energies, however, the situation is quite different; indeed, for the 34–43 keV/n O channel, the intensity for the whole event peaks at the shock passage. At energies above \sim 10 MeV/nucleon intensity peaks at shock passage are only occasionally observed, while at \sim 1 MeV/nucleon peaking at shock passage is observed frequently. As an example, Figure 6 shows low energy ion fluxes associated with an interplanetary shock whose parent activity was a halo CME originating near the solar central meridian at 23:23 on 2000 October 9 (http://cdaw.gsfc.nasa.gov/CME_list/UNIVERSAL/). The figure shows no promptly arriving particles for this event; however, the interplanetary intensities at low energies began to rise above background about 24 hours later, fully \sim 2 days before the shock arrived (see also Desai *et al.*, 2001; Vandegriff *et al.*, 2005). Assuming an average travel speed of \sim 600 km/s, this event was detectable at 1 AU after the shock reached only \sim 0.3 AU. Coordinating this information with optical data from the SECCHI instruments, it will be possible on STEREO to correlate the optical information from well within 1 AU with the particle population observed at 1 AU. In the case of this particular event, at 1 AU energetic O ions were detected up to \sim 1.5 MeV/nucleon, a broad enough range to compute particle energy spectra that could be compared with model calculations. The geometry of the STEREO spacecraft (see Figure 3) will allow studies of this kind to be carried out for a very wide range of separations, with either of the STEREO spacecraft supplying the optical information, and the other the *in-situ* intensities.

The elemental composition and spectral shapes for shock-accelerated energetic particles carry information about the seed population and acceleration mechanism. Examining events where the peak intensities occur close to shock passage at 1 AU, Desai *et al.* (2003, 2004) characterized the average abundance and spectral properties of 72 interplanetary shock events. They found that the average abundances of the shock-accelerated particles had no simple relationship to solar wind abundances, but found instead that they were significantly correlated with the average abundances in the suprathermal ion population upstream of the shock. Indeed, it was found that in some cases the shock-accelerated particles had abundances of the rare isotope ^3He greatly in excess of solar wind values (Desai *et al.*, 2001), which could only be due to acceleration of suprathermals from impulsive SEP events (see below). Figure 7 (*left panel*) shows spectra from the 1999 June 26 event which accelerated particles to several MeV/nucleon (Desai *et al.*, 2004). The spectra are close to power laws at energies below \sim 1 MeV/nucleon, and then roll over at higher energies. The Fe spectrum is steeper than the O spectrum at all energies, causing a systematic decrease in the Fe/O ratio as a function of energy (*right panel*). Desai *et al.* (2004) concluded that the shock acceleration mechanism

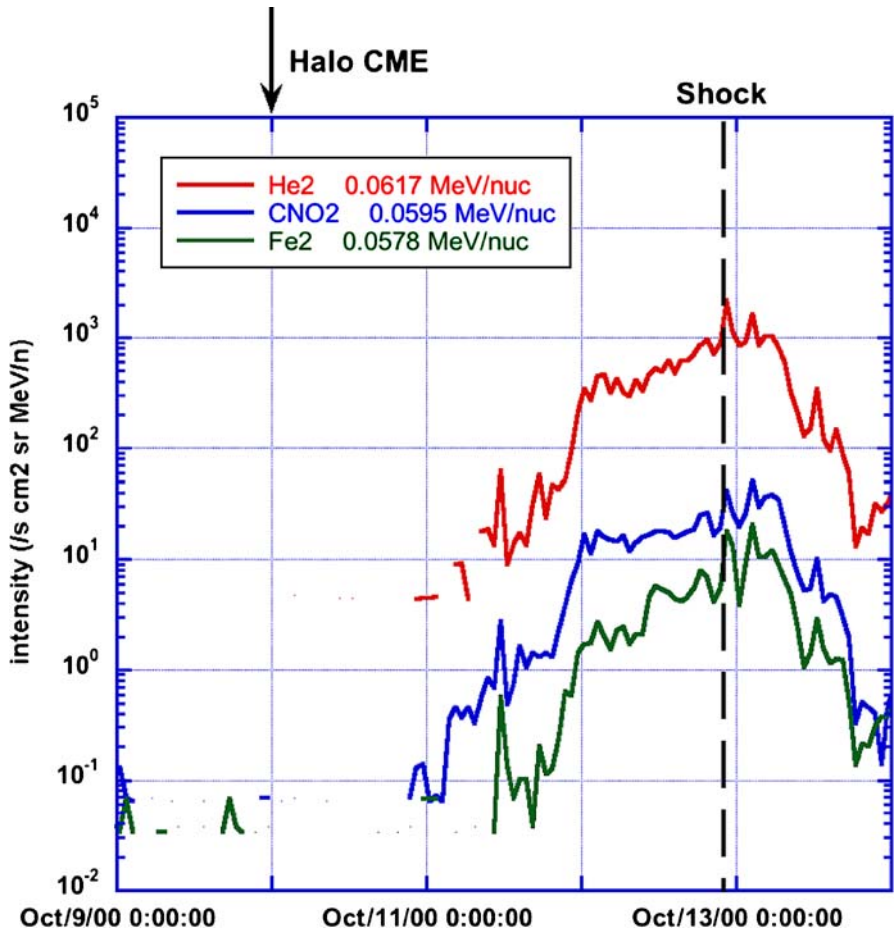


Fig. 6 Hourly average intensities of ~ 60 keV/nucleon He, C+N+O, and Fe from the Wind/STEP instrument for the 2000 October 13 shock. Notice that the interplanetary intensities begin to rise almost 2 days before the shock reaches 1 AU. On STEREO, an event of this kind would allow comparison of *in-situ* particle intensities with optical observations from SECCHI over an extended time interval

was less efficient at accelerating higher rigidity particles, and so Fe, with its higher M/Q ratio than O, was accelerated less efficiently.

1.1.3 Impulsive Solar Flares

In addition to large SEP events, there are “impulsive” SEPs, which are characterized by large enrichments of heavy ions and electrons, and enormous enrichments of the rare isotope ^{3}He as well as ions heavier than Fe (e.g. review by Reames, 1999, 2000; Mason *et al.*, 2004). These events are infrequently associated with CMEs (Kahler *et al.*, 2001). Recently Wang *et al.* (2006) and Pick *et al.* (2006) identified source regions for several impulsive events using energetic particle, optical, and imaging radio data. They found that in essentially every case, the event site was next to a coronal hole containing Earth-directed open field lines. The sites studied by Wang *et al.* (2006) were typically small, flaring active regions of the kind associated

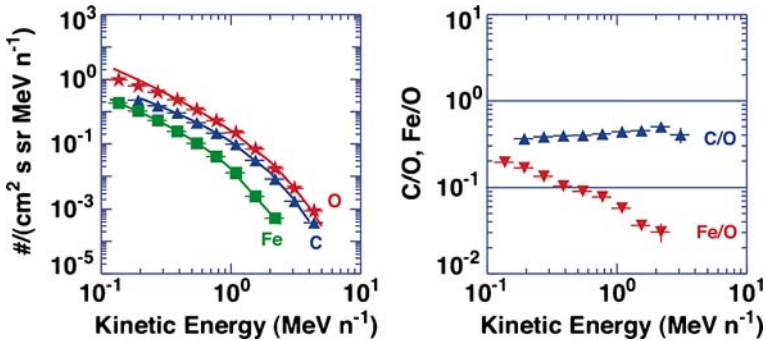


Fig. 7 Energy spectra (left panel) and abundance ratios (right panel) for the 1999 June 26 interplanetary shock event (event #13 from Desai *et al.*, 2004). The decrease of Fe/O with increasing energy is typical, and indicates that the acceleration mechanism is less efficient for higher rigidity ions

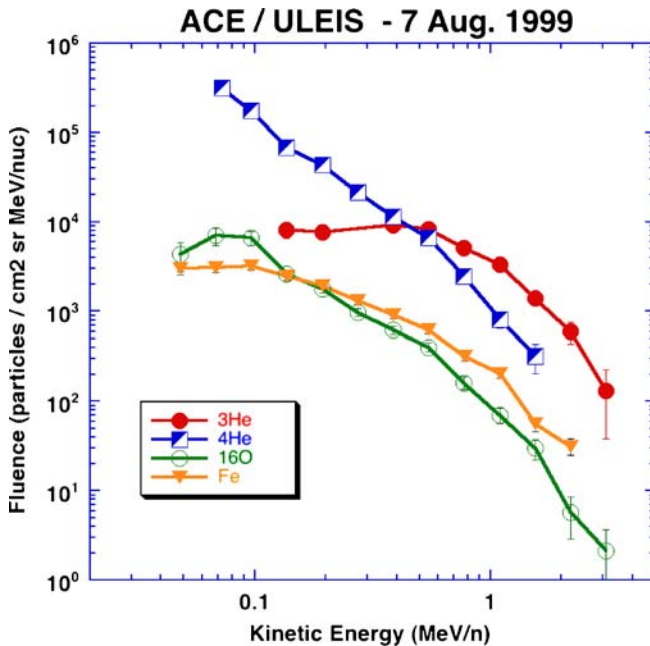


Fig. 8 Energy spectra for the 1999 August 7 impulsive SEP event; notice that the ³He spectral shape is radically different from ⁴He, leading to a strong energy dependence of the ³He:⁴He ratio (from Mason *et al.*, 2000)

with EUV jets. These jets have been studied extensively using Yohkoh observations, and have been interpreted as signatures of magnetic reconnection between open and closed magnetic field lines (e.g., Shimojo *et al.*, 2000).

Figure 8 shows ion spectra from an impulsive ³He-rich event on 1999 August 7 (Mason *et al.*, 2000). This event was associated with an M1.2 X-ray flare at N18W40. Notice that the energy spectra have strikingly different shapes, where the ³He rolls over at lower energies, as does the Fe spectrum, while the ⁴He spectrum is a power law. The ³He:⁴He ratio is a strong

function of energy (see also Möbius *et al.*, 1982). Different spectral forms such as shown in Figure 8 are commonly observed at lower energies; however, some of these events show power-law, or broken power-law spectra as well, with most all the species having similar spectra (Mason *et al.*, 2000; Mason *et al.*, 2002). These different spectral properties indicate that there may be more than one acceleration process at work in impulsive flares (Mason *et al.*, 2002).

There are only a handful of impulsive SEP events that have been observed on multiple spacecraft (e.g., Mason *et al.*, 1989) and these were with instruments with much higher energy thresholds than the STEREO instruments. Thus, STEREO will allow the first systematic studies of impulsive events that probe the longitude dependence on a case-by-case basis. Impulsive events come from rather compact regions and are observed over at most a few 10 s of degrees of longitude. In addition, “drop-outs” observed in impulsive event intensities can be best understood if the source region is small (Mazur *et al.*, 2000). Particle injection timing studies for these events show that if the interplanetary transport is scatter-free, then the ions appear to be injected roughly an hour later than the low energy electrons (Wang *et al.*, 2005). If the ion injection is significantly later than the electrons, this has important implications for the acceleration process or site. STEREO will allow studies of multiple impulsive events whose magnetic connection to the spacecraft will be somewhat different in each case, making it possible to probe the role of scattering versus acceleration in the interpretation of the data at 1 AU.

Due to the common frequency of occurrence of impulsive events during active periods, impulsive event material is present in the interplanetary medium for a substantial fraction of the time (e.g., Wiedenbeck *et al.*, 2003). This material can be accelerated by shocks associated with large solar energetic particle events and detected due to the enrichment of ^3He sometimes seen in Large Solar Energetic Particle (LSEP) events (Mason *et al.*, 1999a). Thus, in interpreting shock-associated acceleration in LSEP events, it is essential to be able to monitor suprathermal particle intensities for the presence of impulsive SEP material, since this material is an important component of the seed particle pool.

1.1.4 Corotating Interaction Regions (CIRs)

Corotating interaction regions (CIRs) are regions of interplanetary space where fast- and slow-solar wind streams interact to form forward and reverse shocks that can accelerate particles to multi-MeV energies (Richardson *et al.*, 1984; Richardson, 1985; review by Mason *et al.*, 1999b). The particle intensities in these events often peak well outside 1 AU, however, in many cases the particles are observed at 1 AU as shown in Figure 9. Since CIRs such as the one shown are in nearly a steady state lasting for multiple solar rotations, the width of the event is a measure of its angular extent (~ 4 days in this case, or $\sim 50^\circ$ of longitude). By measuring CIRs using the two STEREO spacecraft, it will be possible to test the extent to which profiles such as that in the figure are actually unchanging over short periods. In addition, CIRs are important contributors to the interplanetary suprathermal ion pool, since they can last for many solar rotations and reach fairly high intensities for low energy ions. This is shown in Figure 10, which plots the suprathermal Fe/O and C/O ratios over the past solar cycle (Desai *et al.*, 2006b). The figure shows that during the declining phase of the prior cycle (1994–96) the suprathermal ion pool measured during “quiet” days had high C/O and low Fe/O ratios typical of CIRs. As solar activity increased, these ratios systematically changed over to values much closer to SEPs, namely lower C/O and relatively high Fe/O ratios. Since the activity maximum in 1999–2002, they are now returning to the values closer to the prior solar minimum values. Since this suprathermal ion pool is the source of energetic particles accelerated by CME-

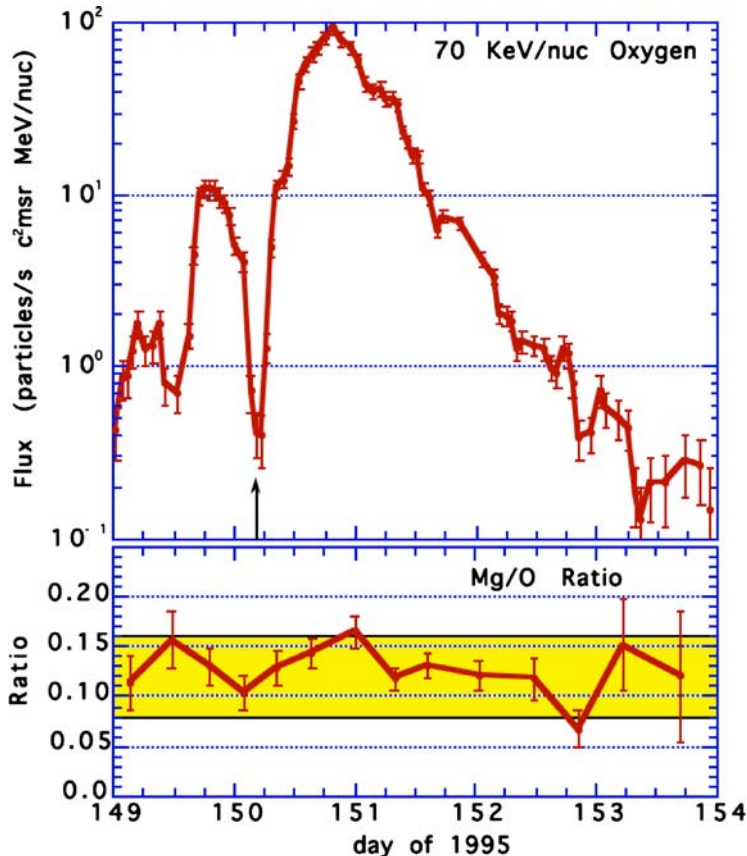


Fig. 9 Top: Intensity of 70 keV/nucleon O ions observed by the Wind/STEP instrument during a CIR in 1995. Arrow marks the strong decrease in intensity associated with the passage of the stream interface. Bottom: ratio of Mg/O during the CIR, compared with solar wind Mg/O value in slow- and fast-solar wind streams (yellow shaded box) (Mason *et al.*, 1997)

driven interplanetary shocks, understanding its composition and temporal variations is key for many STEREO observations. Multiple spacecraft observations will make it possible to put together a much more complete picture than is available now.

2 Design Requirements

The preceding discussion illustrates why measurements of energetic particles on each of the STEREO spacecraft are required to address one of the key mission objectives, namely to discover the mechanisms and sites of energetic particle acceleration in the low corona and interplanetary medium. This requires knowledge of the particle energy spectra, directionality, and intensity, as well as the timing of these quantities compared with other observables at the Sun and in the interplanetary medium.

The Suprathermal Ion Telescope (SIT) for the STEREO mission is one of a coordinated group of sensors designed to give comprehensive coverage of ions and electrons from the energy range just above the solar wind to low energy cosmic rays (see Luhmann *et al.*, 2007).

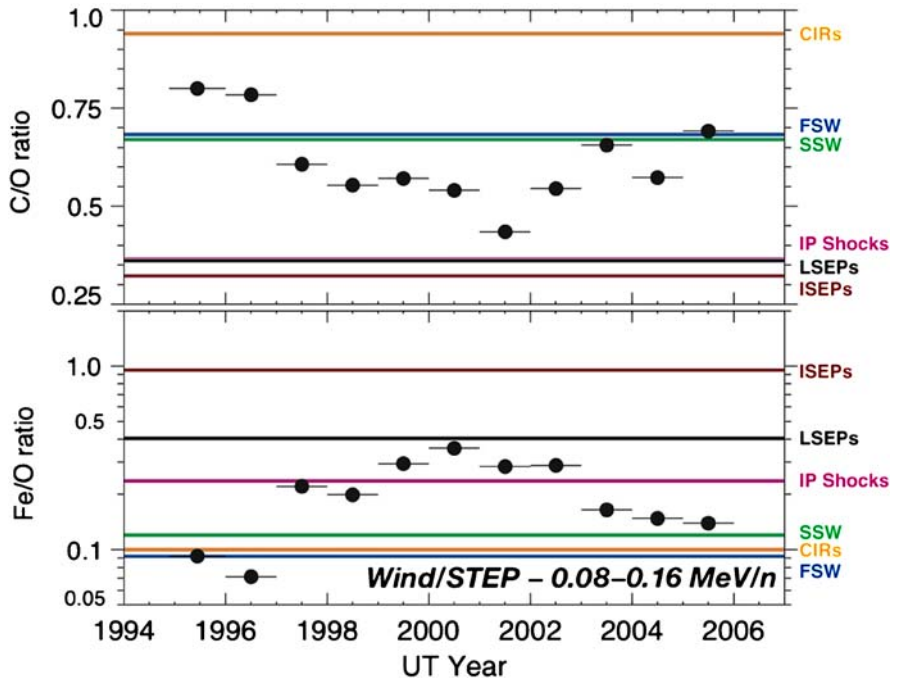


Fig. 10 80–160 keV nucleon $^{-1}$ C/O (upper panel) and Fe/O (lower panel) ratios obtained by Wind/STEP during the quiet-days of each year over a complete solar cycle. Horizontal lines represent average abundances measured in various heliospheric ion populations. Orange: corotating interaction regions (CIRs, Mason *et al.*, 1997); brown: ^3He -rich or impulsive solar energetic particle events (ISEPs; Mason *et al.*, 2002); black: gradual or large solar energetic particle events (LSEPs; Desai *et al.*, 2006a); purple: CME-driven IP shock events (IP shocks; Desai *et al.*, 2003); blue: fast solar wind (FSW); and green: slow solar wind (SSW). Average solar wind values are taken from von Steiger *et al.* (2000)

In addition to SIT, IMPACT includes other sensors optimized to cover the required energy range: the Solar Electron and Proton Telescope (SEPT, Müller-Mellin *et al.*, 2007), the Low Energy Telescope (LET, Mewaldt *et al.*, 2007), and the High Energy Telescope (HET, von Rosenvinge *et al.*, 2007). As shown in Figure 1, this energy range covers a broad range of phenomena central to the studies on STEREO. However, in 1997 when the STEREO science definition team (SDT) defined a model payload for STEREO, the critical role of the suprathermal ion population had not yet been realized since most of the discoveries in this area have come from the ACE mission that was launched only \sim 4 months before the final SDT report. The STEREO model payload therefore made no allocation to cover suprathermal heavy ions. By the time the Announcement of Opportunity for STEREO was released in mid-1999 the role of the suprathermals was becoming increasingly clear to the science community, and the IMPACT science team proposed covering this additional energy range even though it was not in the model payload. In order to keep the cost and spacecraft resource impacts at a minimum, it was decided to use a legacy design, namely the dual-telescope Suprathermal through Energetic Particle (STEP) detector which is part of the EPACT investigation on the Wind mission (von Rosenvinge *et al.*, 1995). While it would have been desirable to increase the solid angle coverage to accommodate the fact that STEREO is a stabilized spacecraft (while Wind is a spinner), resource limitations ruled this out and the team proposed a single SIT sensor for each spacecraft.

Table 1 SIT design goals

	Goal	Science driver
Geometrical factor	0.29 cm ² sr	Adequate counting statistics for <ul style="list-style-type: none"> – weak shock events – impulsive SEPs
Particle species range	$2 \leq Z \leq 28$	– He-Ni covers most abundant material above protons (protons covered by SEPT) – need to distinguish particle populations from: <ul style="list-style-type: none"> – gradual SEP events – impulsive SEP events – corotating interaction regions
Mass resolution	$\sigma_m/m = 0.1$	– resolve ³ He from ⁴ He, C from O
Analysis rates	1/day < $R < 10^5$ /s	– Low background to allow study of impulsive SEPs – Upper limit allows coverage of large SEP events

The overall design goals for SIT are summarized in Table 1. By meeting these goals, SIT will cover the energy range from the suprathermals above the solar wind, up to the energy threshold of the LET sensor (Mewaldt *et al.*, 2007). It will also be able to resolve key species that permit discrimination between the gradual SEP, impulsive SEP, CIR, and other energetic particle populations. Finally, the goals require both low background for small event periods, and high analysis rates for large SEP events so that the particle distribution functions can be measured under all conditions.

3 Instrument Description

3.1 Telescope Cross Section

Figure 11 shows cross sectional views of the SIT telescope, which is a time-of-flight mass spectrometer. Ions enter the telescope chamber through thin Ni foils, and strike a Si solid-state detector mounted a distance $L = 10$ cm behind the foil. When the ions exit the inner Ni foil, secondary electrons are emitted and these are accelerated to ~ 1 kV and directed to a chevron-microchannel plate (MCP) pair that provides a fast “start” pulse for the instrument electronics. If the ions pass through the surface of the Si detector, secondary electrons are also emitted, and these are accelerated and directed to another set of MCPs that provide a fast “stop” signal so that the time-of-flight τ is obtained. The electrostatic acceleration and focusing is done using techniques used in vacuum-tube technology (Harman, 1953) and avoids the use of accelerating grids. The particle is stopped in the solid state detector, where its residual energy E_{SSD} is measured. The mass of the ion is obtained from:

$$m = 2E_{SSD} \left(\frac{\tau}{L} \right)^2. \quad (1)$$

The mass identification in Equation (1) is approximate due to the non-linear response of the solid state detector for very low energy ions (e.g., Ipavich *et al.*, 1978; Galvin, 1982). However, since the main element masses are known this is not a problem since all that is required

Suprathermal Ion Telescope (SIT)

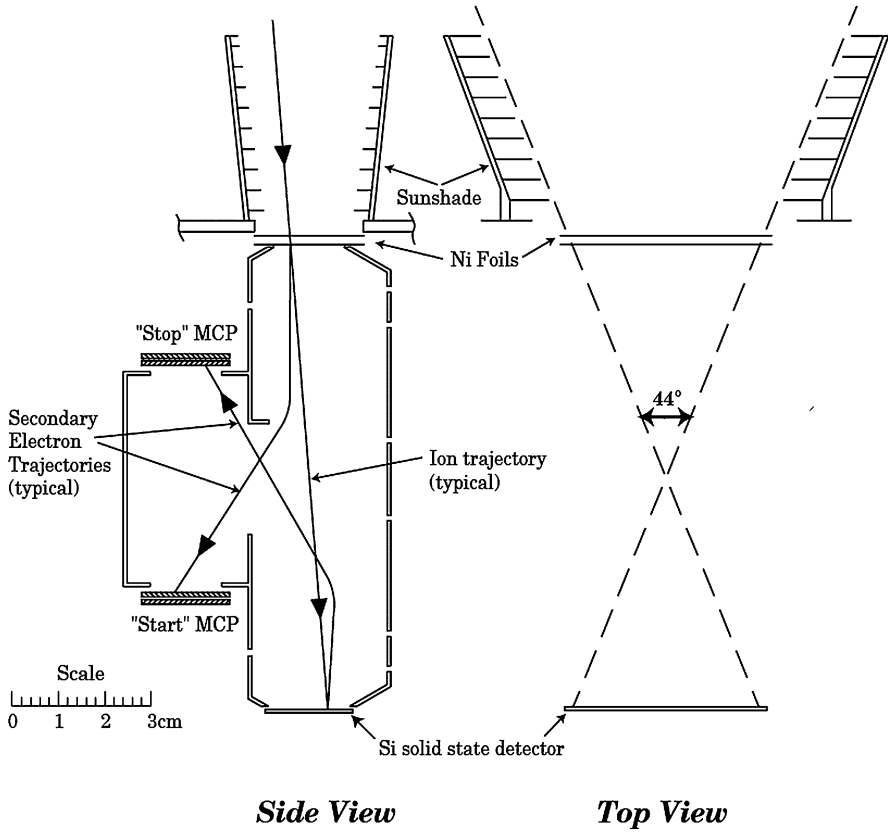


Fig. 11 Schematic cross sections of the Suprathermal Ion Telescope (SIT, see also von Rosenvinge *et al.*, 1995). Acceptance angle for *left* view is 17° . See text for a description of the operating principles

for identification is a separation of different mass ions. The incident energy is determined from the time-of-flight measurement after taking account of the foil thickness and non-linear response of the solid state detector at low energies. At energies below ~ 100 keV/nucleon, non-ionizing collisions in the solid-state detector limit the instrument resolution (Ipavich *et al.*, 1978; Galvin, 1982). At energies above ~ 1 MeV/nucleon, dispersion in the time-of-flight measurement dominates the instrument resolution (for a more complete discussion see Mason *et al.*, 1998). In the range ~ 0.1 – 1.0 MeV/nucleon, the mass resolution is $\sim \sigma_m/m = 0.1$. A summary of detector properties and instrument response and resources is given in Table 2.

In order to keep the solid state detector temperature down, and to prevent solar UV from striking the front foil, there is a sunshade that extends for ~ 3 cm outside the foils and limits the solid angle seen by the front foil. A closable cover (not shown in Figure 11) protects the foils during launch and is opened on orbit. Figure 12 is a photograph of the STEREO/Behind SIT sensor with door open during a pre-launch test. The sunshade is painted black, and the outer foil, mounted on an Au-coated grid, is clearly visible at the back. The cylindrical housing on the bottom of the sunshade contains a TiNi pin-puller that is fired by a spacecraft

Table 2 SIT summary

Item	Technique or details
Objective	Elemental and isotopic composition of interplanetary suprathermal ions from CME-associated solar energetic particle events; impulsive ^3He -rich solar flares, interplanetary shocks, and Corotating Interaction Regions
Technique	Time-of-flight vs. residual energy using microchannel plate detection of secondary electrons and solid state detector; 10 cm ion flight path
Detectors	Window foils: two 40.7×15.5 mm 1000\AA Ni (each) mounted on 90% transparent Au-plated BeCu etched mesh; supplied by LeBow Co., Goleta, CA. Silicon ion implant detector: 15×40 mm active area; thickness 500μ ; active surface metalization 0.1μ Al, junction dead layer $0.35 \pm 0.03 \mu$; noise pulser width 25 keV typical; supplied by Micron Semiconductor Ltd., Lancing, Sussex, England Microchannel plates: chevron, 15×37 mm active area; thickness 1.0 mm each; 25 micron pore size; bias angle 8° ; supplied by Galileo Electro-Optics Corp., Sturbridge, MA
Sensor	One on each STEREO spacecraft
Electronics	Solid state detector energy measurement: 11-bit precision; threshold 240 keV; high gain ramp maximum energy ~ 21 MeV; low gain ramp maximum energy 174 MeV Time of flight measurement: 9-bit precision; range $\sim 2.5\text{--}125$ ns
Geometry	$\Delta\Omega$: $0.29 \text{ cm}^2\text{-sr}$ each unit after correction for foil mesh transparency FOV: $44^\circ \times 17^\circ$ field of view; 44° angle lies in ecliptic plane; 17° angle is perpendicular to ecliptic plane; center line of 44° cone is 60° west of S/C-Sun line
Charge Interval	$2 \leq Z \leq 26$
Energy Intervals for typical elements	He 123 keV/nucleon – 8.1 MeV/n C 68 keV/nucleon – 8.1 MeV/n O 57 keV/nucleon – 8.1 MeV/n Fe 28 keV/nucleon – 3.2 MeV/n 300–800 keV/nucleon
Energy interval for resolving ^3He	$\sigma_m/m = 0.1$ ($\sim 0.1\text{--}1.0$ MeV/nucleon)
Mass resolution	
Resources	
Mass	1.63 kg (including thermal coatings and heaters)
Power	1.65 W (regulated; includes HVPS; solid state detector bias not included)
Bit rate	424 bits/s

signal on orbit to release the spring-operated door (top). A small shade on the left of the sunshade is for additional UV protection. The interior of the sunshade door is coated for thermal control. On the spacecraft, the entire assembly is covered with thermal blankets, and only the telescope opening is visible.

Figure 13 shows the SIT field-of-view (FOV) orientation. The narrower (17° full width) FOV is bisected by the ecliptic plane. The larger (44° full width) FOV is oriented so that its center line is 60° from the spacecraft-Sun line. With this angle of orientation, the first foil is always shadowed by the sunshade. The other obvious constraint on the FOV is that it should look close to the average Parker magnetic field spiral line, a requirement that is met by this geometry.

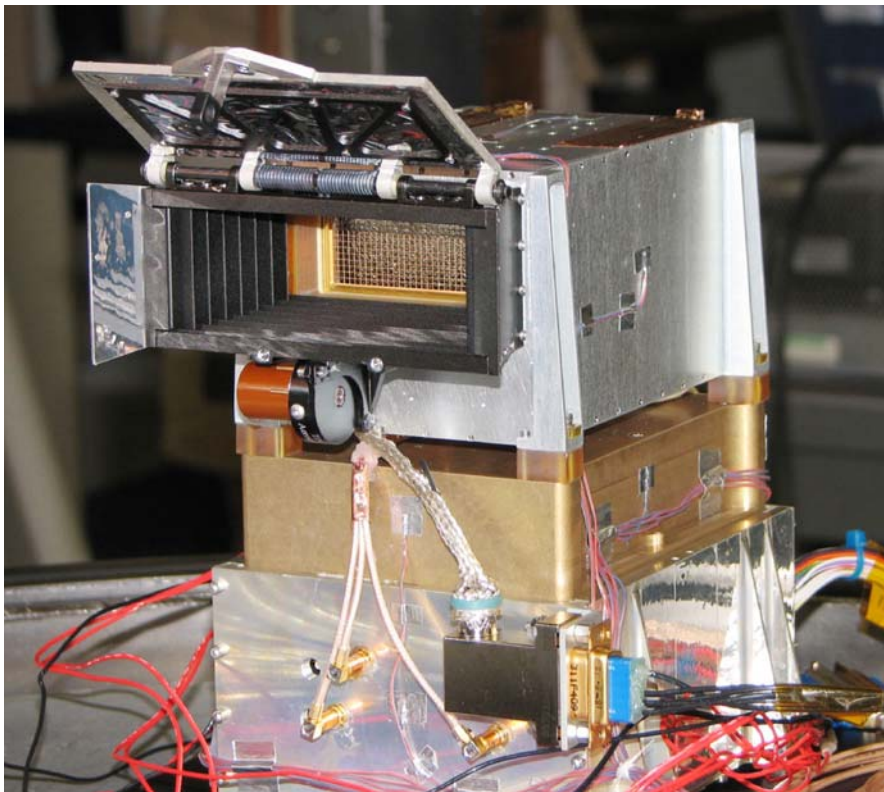


Fig. 12 SIT instrument for the STEREO Behind spacecraft shown in a thermal vacuum chamber after a test of the openable door. The telescope box is Al-colored; underneath it lies the gold-colored high voltage power supply for microchannel plate bias; beneath that is the electronics box that has reflective thermal coatings

3.2 Functional Block Diagrams

3.2.1 Telescope Electronics

Although the SIT telescope mechanical design is essentially identical to the Wind/STEP design, the electronics are a new design in order to take advantage of advances of the past ~ 15 years, and to meet the more stringent quality assurance requirements of the STEREO mission. Figure 14 is a functional block diagram of the SIT instrument. Dashed lines in the figure separate the three components of the instrument, namely the telescope box, high voltage power supply (HVPS) box, and the electronics box (see Figure 12). The HVPS supplies bias to the telescope MCP stacks, and to the sections of the housing that set up the electrostatic field that accelerates and deflects the secondary electrons to the MCPs. The initial operating HV setting of about 3100 V provides 900 V for the secondary electron assembly acceleration and deflection bias, and 930 V bias across each MCP and some additional voltage steps for interplate bias and bias of the collector plate. The design includes provision for raising the HV to compensate for loss of MCP gain; the maximum voltage is about 25% higher than the initial operating voltage, and can be increased in steps of 0.6% each.

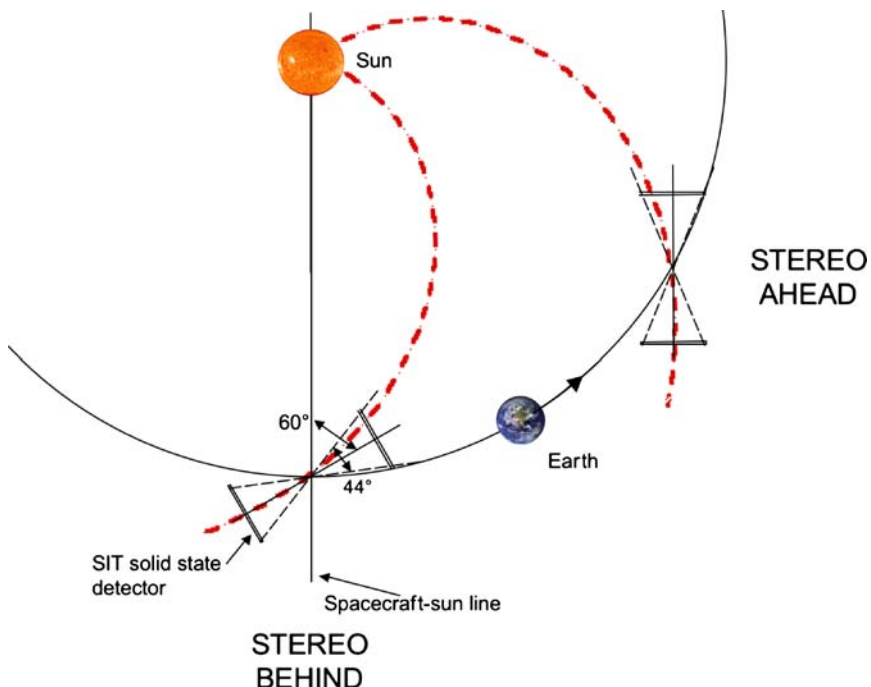


Fig. 13 Orientation of the SIT telescopes with respect to the spacecraft-Sun line. *Dashed red spirals:* typical interplanetary spiral magnetic field lines. The 44° FOV lies in the ecliptic as shown, and the 17° FOV is bisected by the ecliptic. The mounting of the SIT instruments on the AHEAD and BEHIND spacecraft is arranged as to achieve the same IMF look direction for both. *Black arrow* shows direction of Earth's orbital motion

Signals from the START MCP, STOP MCP, and solid state detector are processed in the electronics box. The Analog time-of-flight (TOF) board receives the telescope START and STOP MCP signals that go first to fast amplifiers followed by constant fraction discriminators (CFDs) that remove TOF “walk” arising from different signal amplitudes on the input. The electronics box houses four separate boards that are connected by a backplane motherboard. The CFD output signals are then sent to the Digital TOF board (DTOF, described below).

Solid state detector signals are sent to the Energy board, where they are amplified using Amptek hybrids. Every signal from the solid-state detector is split and then analyzed by both a high- and low-gain amplifier. Both the high- and low-gain signals are digitized and sent to the Logic Board. In addition, a discriminator output from the Si detector is sent to the DTOF for use in forming the event coincidence.

The digital time-of-flight system consists of two main components, a Time-to-Digital Converter (TDC) implemented in an ASIC, and an ACTEL FPGA that contains the necessary support circuitry. The power consumption is small (120 mW at 30 k events/s). Figure 15 shows a functional block diagram of the DTOF board. The CFD START and STOP outputs from the ATOF board are split and sent to the TDC where they are digitized, and also to the DTOF board ACTEL for processing. The output TOF and input control signals are sent on serial lines to minimize connector size, and other signals from the Logic Board are required to check for coincidence between the START-STOP and solid state detector. The time range of the 9-bit TDC output is 0–128 ns.

Suprathermal Ion Telescope (SIT) block diagram

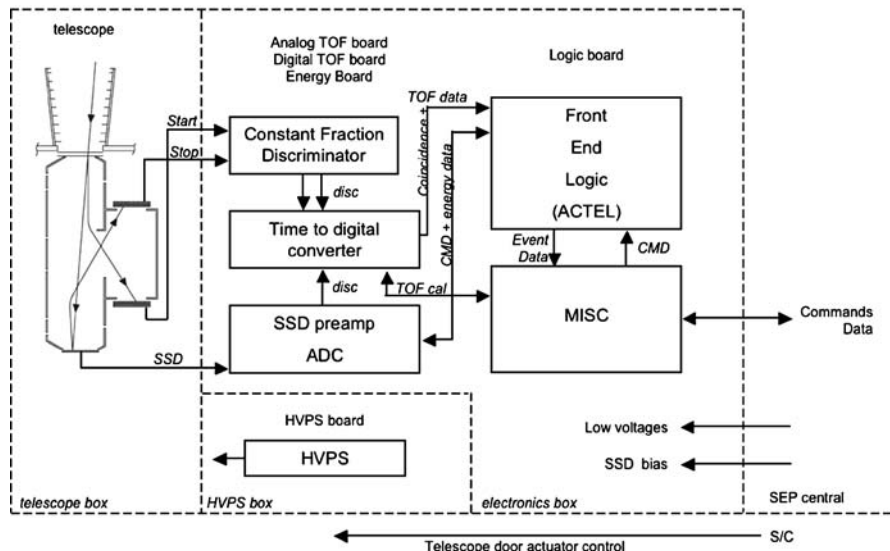


Fig. 14 Functional block diagram of the SIT instrument

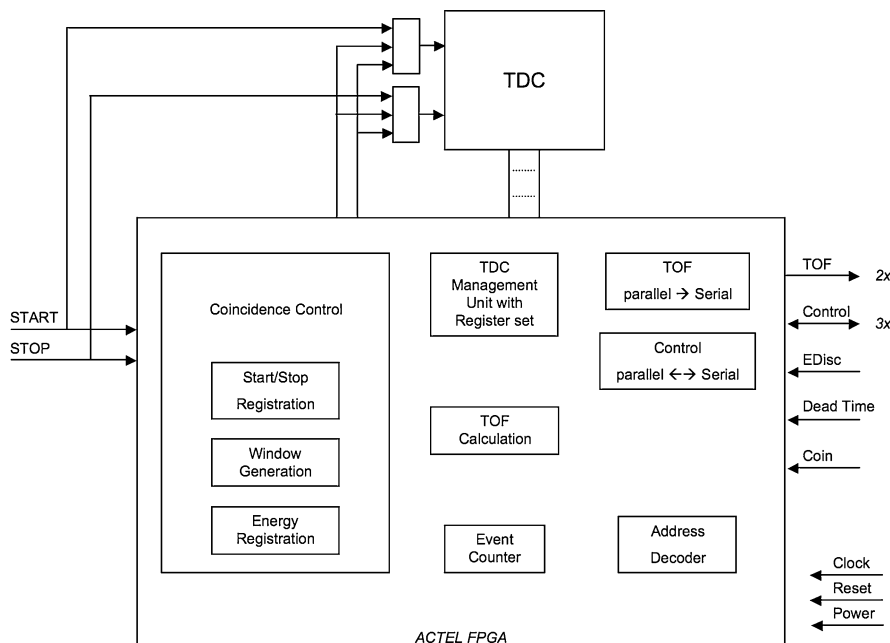


Fig. 15 Functional block diagram of the Digital Time-Of-Flight (DTOF) system

The TOF system calibration is affected by temperature and voltage. It is therefore calibrated once per second by stimulating the TDC at a known fixed interval, and processing the resulting values. The Logic Board initiates the calibration, reads output values and does a short calculation whose results for gain and offset are written into the DTOF system, thus keeping the TOF system calibrated. The TOF gain and offset values are also telemetered in the instrument housekeeping. The TOF system also monitors the occurrence of multiple START or STOP signals for a given event, and sets flags for these conditions for each event. The system also provides count rates for START, STOP, and valid TOF events. The maximum event rate of the system is >200 kHz, a factor of ~ 50 higher than the maximum anticipated event rate. Rate accumulators in the DTOF system are 16-bit counters that read to the MISC once per second where they are accumulated as 24-bit numbers. Rates with the potential to overflow the accumulator (i.e., >65 kHz) are prescaled (see Table 3).

Digitized TOF and solid state detector signals along with timing and coincidence information are sent to the Logic Board, which processes each event. The front-end logic is contained in an ACTEL FPGA, that also contains the Minimum Instruction Set Computer (MISC, Mewaldt *et al.*, 2007). SIT command states are also sent to the Logic Board ACTEL where they control event processing (see below). The output digital event data and count rate data is collected into telemetry packets in the MISC, then sent to the SEP Central Data Processing Unit (see Mewaldt *et al.*, 2007) where it is time tagged. Housekeeping data is digitized in the Logic Board and sent to SEP Central for inclusion in a telemetry packet shared by other sensors in the IMPACT/SEP package. SEP Central also provides SIT with command data, low voltage power, and solid state detector bias.

3.3 Data Outputs

3.3.1 PHA Data

Each ion that triggers a START followed by a single STOP signal within 128 ns is a “VALID STOP” event and is counted (see Table 3). Each “VALID STOP” event that is accompanied by a coincidence with the solid state detector amplifier is a VALID EVENT, and is counted and analyzed by the system (see Table 3). Each valid event is formatted into a 32-bit long Pulse-Height-Analysis event whose contents are shown in Table 4. In addition to the TOF value and silicon detector Energy signal amplitude, each PHA event contains the two-bit TOF FLG from the DTOF analysis (see table notes). The gain of the amplifier used for the Energy signal is determined by the Logic Board, which examines the channel number for the high gain amplifier: if it is saturated (channel 2048, approximately 21 MeV) then the low gain channel number is used (maximum value approximately 174 MeV). The TOFERROR gives the status of one of the command bits (see below). The matrix box number is the result of the matrix rate calculation for this event, and is telemetered to allow verification of the on-board software calculation. There is also a 2-level priority that is stored along with the matrix rate number; this priority level is used to determine priority for telemetering this PHA event (see below).

SIT PHA events are formatted by the MISC; there are 11 PHA packets per minute allocated to SIT (APIDs 606–616), each with 64 PHA events for a total of 704 PHA events/minute. The first 704 events that occur during a minute are stored in a buffer in the MISC. If additional events occur and if their priority = 1 (high), they will be written over existing events starting with the first event. This will continue until the number of events reaches a limit (LIMHI) that is set by ground command. After that no further events are written into the buffer. It should be noted that in the case of high event rates with many high priority events, this scheme will

Table 3 SIT on-board rates: Matrix & beacon rate assignments

Rate	Description
Discriminator rates	
DR1	START singles (prescaled by 8)
DR2	STOP singles
DR3	Valid Stop
DR4	SSD singles
DR5	Valid events (triple coincidence: START + STOP + SSD)
DR6	Dead time counter: fraction of time when instrument was processing events ($\times 32768$)
DR7	Number of artificial STOP counts generated by DTOF to close windows opened with a START pulse but followed by no STOP pulse within 128 ns (prescaled by 8)
DR8	TOF system error count (number of events with either TOF FLG 1 or 2 non-zero)
Matrix rates	
MR1	Priority 0
MR2	Priority 1
MR3	SSD high gain ramp
MR4	SSD low gain ramp
MR5	Discarded events (event FIFO not emptied)
MR6	Out of bounds (no matrix box found)
MR7	Junk (matrix box #7)
MR8–19	H counts for different energy bins
MR20–29	^3He counts (+ some spillover from ^4He) for different energy bins
MR30–45	^4He counts for different energy bins
MR46–62	C counts for different energy bins
MR63–78	O counts for different energy bins
MR79–94	Ne+Mg+Si counts for different energy bins
MR95–108	Fe counts for different energy bins
MR109–114	UH ($m > 80$ amu) counts + background for different energy bins
MR115–116	Background
Beacon rates	
B1–4	He counts
B5–8	C+N+O counts
B9–12	Fe counts

result in the first portion of the 704 PHA event buffer to be exclusively high priority events that had arrival times after the last event in the buffer.

3.3.2 Rates

In addition to the PHA events, SIT collects count-rate data described in Table 3. There are three general types of rates: discriminator rates which are outputs from the Energy and DTOF boards, and both matrix and beacon rates which are calculated in the MISC. The 8 discriminator rates have simple logic and are described in the table. Note that DR1 and DR7 are prescaled by a factor of 8. Once per minute all the rates in the table are compressed from

Table 4 SIT PHA event data

Item	No. of bits	Bit location	Source ^a	Comments
TOF	9	0 (lsb)–8	F	Time of flight channel number
Energy	11	9–19	F	Solid state detector channel number
TOF FLG 1 ^b	1	20	F	TOF error flag 1
TOF FLG 2 ^b	1	21	F	TOF error flag 2
GAIN	1	22	F	SSD energy gain bit (0 = high; 1 = low)
TOFERROR	1	23	C	Command bit state
Matrix box	7	24–30	L	Matrix box number
PRI	1	31 (msb)	L	Priority bit (0 = low; 1 = high)

^a Data source: F = received from front-end logic/ACTEL; C = command state bit; L = Matrix rate lookup table (low order 7 bits)

^b TOF flag encoding (bit 1, bit 2) shows discriminator firings during the TOF measurement period: (0,0) = 1 start, 1 stop (nominal event); (0,1) = n start ($n > 1$), 1 stop; (1,0) = 1 start, n stop; (1,1) = n start, n stop, or Stop occurred before start

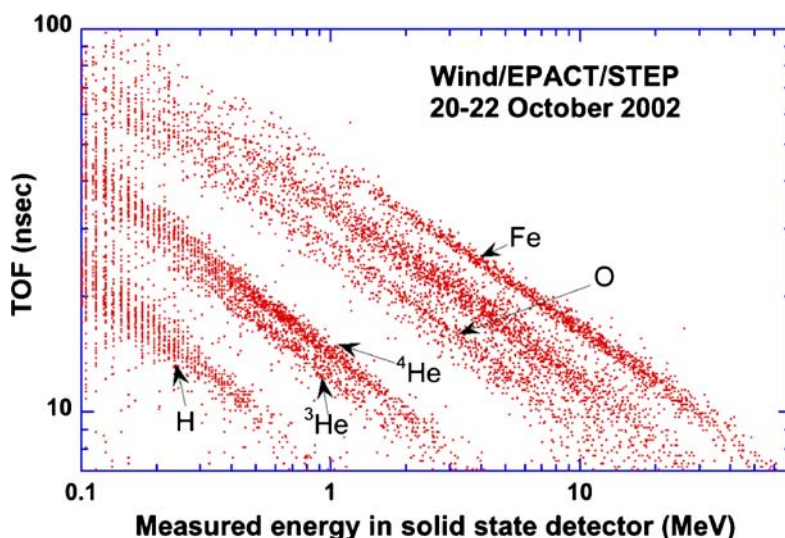


Fig. 16 Sample data from Wind/STEP 20–22 October 2002 ^3He -rich period showing typical time vs. energy data from the telescope. Each dot represents a single ion event analyzed by the telescope

24 to 16 bits (for details, see Mewaldt *et al.*, 2007), packetized in APID 605, and sent to SEP central.

The Matrix Rates and Beacon Rates are calculated in the MISC, and give particle intensities for several species allowing calculation of spectra with 60 s cadence when intensities are high. Figure 16 shows sample data from the Wind/STEP sensor that illustrates the appearance of data to be processed by SIT. The matrix rate calculation in essence picks box-like areas in the matrix, and sums together all the particles in one of these boxes. For example, the ^4He track would be split into a number of sections, and the number of events falling in each of these sections (boxes) would be counted separately. In defining the boxes, it is most convenient to transform the matrix shown in Figure 16 from time vs. energy to axes of mass vs. energy/nucleon, since the matrix boxes are defined in those terms.

For the SIT telescope, the particle mass in AMU is reasonably approximated by:

$$m = 0.021^* E_{\text{SSD}} \tau^2 \quad (2)$$

where E_{SSD} is the solid state detector signal in MeV, and τ is the time of flight in nsec. The incident energy in MeV/nucleon E_{inc} is approximately:

$$E_{\text{inc}} = \frac{1}{0.021 \tau^2} \quad (3)$$

The mass-energy space covered by (2) and (3) is then scaled into a 128×128 matrix that is used for assigning the matrix boxes. The functions $f(m)$ and $f(E)$ that span this space are:

$$f(m) = (\ln m + 1)^*(128/7) \quad (4)$$

and

$$f(E_{\text{inc}}) = (\ln(E_{\text{inc}}) + 5.5)^* 16. \quad (5)$$

If there were no defect or dead layers in the solid state detector, the particle distributions would follow constant $f(m)$ lines in the matrix. However, these effects are present and cause the tracks to sag below the constant $f(m)$ lines at low energies. The matrix box assignments for the different species take this into account, and so for each species the actual matrix boxes assigned deviate from the constant $f(m)$ lines at low energies. This can be seen in Figure 17, which shows a sample matrix of $f(m)$ vs. $f(E)$ with sample data from Wind/STEP (Figure 16) converted using Equations (2–5). Due to differences between the STEP and SIT solid-state detectors, the alignment of species areas and particle tracks is only approximate. The choice of 128 bins for the mass axis is based on the goal of separating C and O over most of the energy range, and for separating ${}^3\text{He}$ and ${}^4\text{He}$ over limited portions of the range. The choice of 128 bins for the energy axis is required to allow reasonably close matching between the nominal energy bins (whose start energies are spaced by a factor of $\sqrt{2}$) and the actual bins available on the $f(E)$ scale.

To carry out the calculations of Equations (2–5) in integer arithmetic, the MISC uses lookup tables that contain the logarithms of the solid state detector energy (MeV) and time-of-flight (nsec) for each channel number. The $(f(m), f(E_{\text{inc}}))$ cell address is used to look up a value in a 128×128 cell array whose contents are the matrix rate number assigned to that cell, the beacon rate number assigned to that cell, and the event priority level for that cell (high or low). Since the tables can be uploaded from the ground, the matrix rate, beacon rate, and priority determination can all be modified post launch if necessary. The colored bands in Figure 17 show sample assignments where matrix rate *purple* cells are H, *light blue* are ${}^3\text{He}$, etc. Each colored band for a species is divided into 10–15 different bands of $f(E_{\text{inc}})$ to give multiple energy points for particle spectra. The lookup tables require approximately 63 kbytes of memory, and the MISC processing algorithm can process events up to at least 4 kHz, considerably higher than the maximum anticipated event rate of ~ 1 kHz. The beacon rates are a subset of 12 rates for He, C+N+O, and Fe over wider energy bins than the matrix

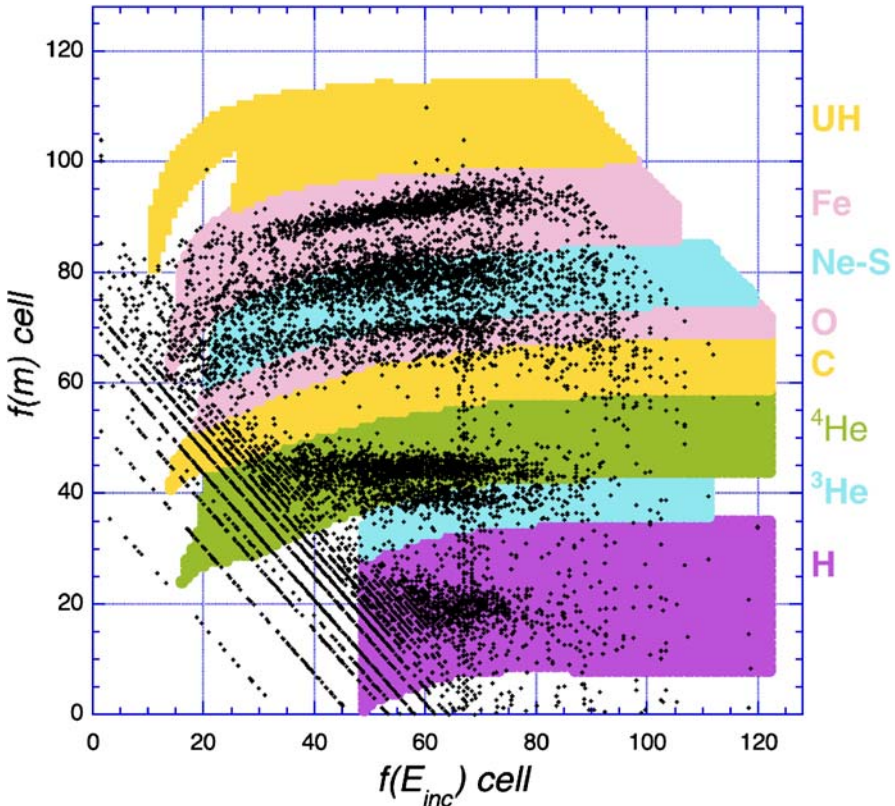


Fig. 17 Wind/STEP data from Figure 16 data converted to artificial mass and energy bins ($f(m)$ and $f(E_{inc})$) using Equations (2–5) and compared to nominal matrix box locations for SIT. Alignment between STEP and SIT data is only approximate. *Species symbols* on right correspond to the same color bands on the figure. Each species band is split into 10–15 energy bins

rates. SIT beacon rates are combined with beacon rates from HET/LET in APID 624 and are part of the STEREO real-time telemetry stream.

Referring to Table 3, there are 116 Matrix Rates and 12 Beacon Rates. MR1–7 tally overall event rates, plus the lookup table rates. Note that MR6 is for events where the algorithm gave a value out of the range 1–128 for either $f(E_{inc})$ or $f(m)$, and MR7 counts events that did not fall into an assigned species and energy bin.

3.3.3 Calculation of Intensities

The design of SIT is such that the detection efficiency for protons is \sim few percent, and for helium \sim 25% (these are the approximate expected initial values post-launch). For heavier ions, the detection efficiency is \sim 1. The omni-directional intensity I_j for a single readout of Matrix Rate j ($= MR_j$) is

$$I_j = \frac{1}{A\Omega \times \varepsilon_j \times \Delta E_j \times 60} MR_j \quad (6)$$

where I_j is in units of particles/($s \text{ cm}^2 \text{ sr MeV/nuc}$), $A\Omega$ is the geometry factor ($\text{cm}^2 \text{ sr}$), ε_j is the efficiency for the species and energy box, ΔE_j is the energy interval covered by rate MR_j , and MR_j is the number of counts in this rate bin for 60 s. The calculation is analogous for the Beacon Rates. Due to the low H and He efficiency, the Wind/STEP data show that the triggering rate of the instrument will rarely exceed a few hundred counts/s, so the live time is $\sim 100\%$.

Intensities may also be calculated for any arbitrary area of the τ vs. E plane (Figure 16) using the PHA data. In this case, it is necessary to use the matrix rates to normalize the number of PHA counts because of the limited number of PHA events that are read out. For any arbitrary area in the τ vs. E plane, let N_{0j} be the number of events with priority 0, and N_{1j} be the number of events with priority 1. Let N_0 and N_1 be the total number of events of priority 0 and 1 in the entire τ vs. E plane. Then for a single 60 s period the intensity for the selected area is:

$$I_j = \frac{1}{A\Omega \times \varepsilon_j \times \Delta E_j \times 60} \left(\frac{N_{0j}\text{MR1}}{N_0} + \frac{N_{1j}\text{MR2}}{N_1} \right) \quad (7)$$

Note that MR1 and MR2 are the number of counts of priority 0 and 1 (Table 3). The values of N_0 and N_1 are obtained from the total group of PHA events transmitted for the same 60 s period as the matrix rate data. Longer time interval intensities are obtained by averaging the 60 s intensities.

3.3.4 Particle Calibration Data & Background Issues

End-to-end testing of the SIT instruments was done by placing the units in vacuum and exposing them to alpha-sources. Figure 18 (left panel) shows a sample run from the AHEAD instrument just before it was mounted on the spacecraft. The mass resolution of $\sigma_m/m = 0.1$ is sufficient to allow identification of impulsive SEP events with ${}^3\text{He}/{}^4\text{He}$ ratios above $\sim 10\%$.

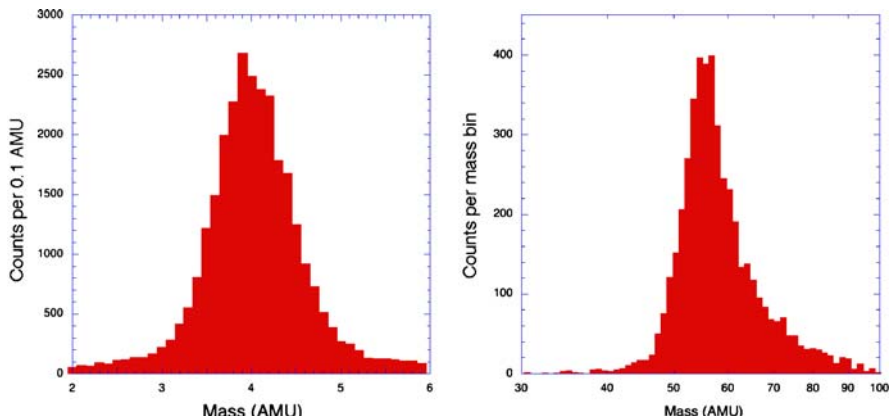


Fig. 18 STEREO/SIT calibration data samples. *Left panel*: alpha source resolution for the AHEAD flight instrument for particles with incident energy 0.7–0.9 MeV/n, showing mass resolution $\sigma_m/m = 0.1$. *Right panel*: Fe peak from engineering model telescope and AHEAD flight electronics for ~ 0.25 –0.5 MeV/nucleon incident energy

The instrument was also taken to an accelerator to test the electronics response for large pulse sizes and high event rates that could not be achieved with alpha sources. Figure 18 (right panel) shows a mass peak for Fe from this test, showing resolution that easily allows identification of e.g., Fe-rich solar particle events.

The sample Wind/STEP flight data shown in Figure 17 shows that background in the instrument is relatively low. The main limit on performance at low energies is caused by broadening of the mass peaks due to decreased accuracy in the solid state detector measurement. At high energies, dispersion of ~ 1 ns in the TOF system leads to mass peak broadening; for example, at the 8 MeV/nucleon, the time of flight is only about 2.5 ns, and so the mass can be measured only approximately. There is no anti-coincidence detector in back of the SIT solid state detector, and so penetrating particles can trigger the system. However, for heavier ions, the penetration energy is so high (e.g. 15 MeV/n for C and higher energy/nucleon for heavier ions) that these events do not form an identifiable component of the background.

4 Flight Operations

SIT requires minimal commanding in flight. Early pointing maneuvers of the two STEREO spacecraft require that the telescope doors be kept closed early in the mission to avoid risk of the telescopes pointing toward the Sun. The door opening on STEREO Ahead is nominally scheduled for day 49 post-launch; for STEREO Behind it is scheduled for day 70 (the final door opening schedule depends on the exact launch date). After initial slow ramp-up of the high voltage SIT is fully operational. Due to the distinctive appearance of particle tracks in the τ vs. E plane, the instrument calibration can be monitored easily, so there is no separate on-board calibration circuitry. It is anticipated that the matrix look-up tables will be adjusted after examining post-launch data; the provision for uploading new tables is included in the design. The only other anticipated commanding is adjustment of the MCP bias to compensate for loss of gain that can occur after extremely intense particle events such as those that occurred in 2000 July or 2003 October/November.

4.1 Commands

Table 5 lists commands used for routine operation of SIT. Additional commands such as turning on the instrument or loading new software or tables, are done through SEP Central and are not listed. Commands are normally executed by the MISC at the beginning of the next minute boundary so that command boundaries will coincide with the start of new rate and PHA accumulation intervals. However, if the command IMMED = 1 has been sent, commands are executed without waiting for the minute boundary.

The command EONLY is a 1-bit command, with normal state 0. If EONLY = 1, then events are analyzed with energy signal only (no TOF required). The command HVENABLE is a 1-bit command with turn on state = 0, normal state = 1 to allow operation of the HV supply. The command HVLEVEL is an 8-bit command that sets the voltage level of the HVPS. The command TOFERROR is a 1-bit command whose normal state is 0, in which case PHA events that have either error flag set will be discarded. If TOFERROR = 1, all PHA events are transmitted, regardless of the error flag values. JUNK is a 1-bit command whose normal state is 0, and in this case PHA events with matrix box = 0 (out of bounds) are not transmitted; if JUNK = 1, all PHA events are transmitted regardless of their matrix box number. LIMHI is a 2-byte command that sets the limit of the number of high-priority PHA events that will be allowed to overwrite earlier events in the 704-event long PHA buffer. The

Table 5 SIT command summary

Item	Description	Command name
Triggering logic		
Coincidence requirement	Enable/disable SSD coincidence	EONLY
Instrument operation		
High Voltage	Enable/disable HVPS	HENABLE
High Voltage setting	Set High Voltage to level x	HLEVEL
Software parameters	Enable/disable events with TOF error flags set	TOFERROR
PHA buffer contents	Enable/disable events with matrix box = 0	JUNK
Priority threshold	Set number of high priority PHA events that will overwrite low priority events in PHA event buffer (LIMHI)	LIMHI
Lookup tables	Read in new lookup tables for calibration and matrix boxes	(Multiple)

default value is LIMHI = 500. The current setting of all these commands is transmitted once per minute in the Rate packet (APID 605).

Acknowledgements We are grateful to the many dedicated individuals whose efforts made possible the successful construction of the SIT instruments. At the University of Maryland Space Physics Group, we thank Tom James who carried out the original mechanical design of the telescope, and who inventoried the residual parts from Wind/STEP and organized the handoff of the mechanical design to GSFC. Scott Lasley ordered and tested the MCPs and provided support for the vacuum systems and testing/qualification for SIT. Joseph Dwyer participated in the early conceptual states of the on-board processing design, and suggested the pseudo-energy and mass scheme that was implemented. Jody Reed ably handled all aspects of the contracting and procurement initiation.

At the Max-Planck-Institut für Sonnensystemforschung (MPS), Lindau, Germany we thank the engineering staff for the construction of the ATOF, and particularly acknowledge the work of Klaus Heerlein on this project. The DTOF board was designed by Christian Dierker of the Institut für Datentechnik und Kommunikationsnetze at the Technische Universität Braunschweig. The flight ATOF and DTOF boards were constructed, and all flight qualifications were carried out by MPS.

Many individuals in the Goddard Space Flight Center Laboratory for High Energy Astrophysics supported the construction and qualification of SIT. The flight software was written by Kristin Wortman and Tom Nolan. George Winkert provided the Logic Board ACTEL FPGA which contained both the front-end logic and MISC. Kristin Wortman also provided critical support during many long hours of vacuum testing and spacecraft testing. Traci Pluchak-Rosnack assembled the flight electronics boards and telescope harness; Bert Nahory tested the solid state detectors; Haydar Teymourlouei supported the test data analysis. We thank John Hawk for the thermal design, and Mario Martins for untiring support of many cycles of thermal balance and thermal vacuum testing.

The Space Sciences Laboratory at the University of California Berkeley played a critical role in the development of SIT. Dave Curtis, IMPACT lead engineer, was actively involved throughout the project, supervising quality assurance and parts approval, and providing excellent tactical advice on innumerable issues. David Berg designed and built the SIT HVPS and housing, which was delivered fully qualified to the University of Maryland.

We thank Chuck Carlson and the operations crew of the Brookhaven Tandem Van de Graaff for their support during the August 2004 calibration of the prototype telescope and flight electronics.

The STEREO project office at Goddard Space Flight Center was unfailingly supportive throughout the project, and we especially thank Nick Chriessimos for his leadership and Steve Wasserzug for energetic help with Goddard product assurance issues. We want to express our great appreciation to the IMPACT instrument manager, Lillian Reichenthal, whose hands-on involvement in support of SIT pre-delivery, and especially post-delivery was absolutely essential to the successful completion of the flight instruments. Finally we thank Richard Fisher, Eric Christian and Madhulika Guhathakurta, at NASA Headquarters for their enthusiastic support of the STEREO project and their dedication to maximizing the scientific returns of the mission.

This work was supported by the NASA STEREO project and in Germany by the Max-Planck-Gesellschaft zur Förderung der Wissenschaften and the Bundesministerium für Bildung und Forschung (BMBF) under grant 50 OC 0006.

References

- C.M.S. Cohen, E.C. Stone, R.A. Mewaldt, M.I. Desai, T.T. von Rosenvinge, M.E. Wiedenbeck, *J. Geophys. Res.* **110**, A09S16 (2005), doi: 10.1029/2005JA011004
- M.I. Desai, G.M. Mason, J.R. Dwyer, J.E. Mazur, R.E. Gold, S.M. Krimigis, *et al.*, *Astrophys. J.* **588**, 1149 (2003)
- M.I. Desai, G.M. Mason, J.R. Dwyer, J.E. Mazur, C.W. Smith, R.M. Skoug, *Astrophys. J. (Lett.)* **553**, L89 (2001)
- M.I. Desai, G.M. Mason, R.E. Gold, S.M. Krimigis, C.M.S. Cohen, R.A. Mewaldt, *et al.*, *Astrophys. J.* **649**, 470 (2006a)
- M.I. Desai, G.M. Mason, J.E. Mazur, J.R. Dwyer, *Astrophys. J. (Lett.)* **645**, L81 (2006b)
- M.I. Desai, G.M. Mason, M.E. Wiedenbeck, C.M.S. Cohen, J.E. Mazur, J.R. Dwyer, *et al.*, *Ap.J.* **611**, 1156 (2004)
- D.C. Ellison, R. Ramaty, *Astrophys. J.* **298**, 400 (1985)
- A.B. Galvin, Ph.D. thesis, Dep't of Physics, University of Maryland (1982)
- W.W. Harman, *Fundamentals of Electronic Motion*, (McGraw Hill, New York, 1953)
- F.M. Ipavich, R.A. Lundgren, B.A. Lambird, G. Gloeckler, *Nuc. Instr. Methods* **154**, 291 (1978)
- S.W. Kahler, D.V. Reames, N.R. Sheeley Jr., *Astrophys. J.* **562**, 558 (2001)
- G. Li, G.P. Zank, W.K.M. Rice, J. *Geophys. Res.* **110**, A06104 (2005), doi: 06110.01029/2004JA010600
- J. Luhmann *et al.*, *Space Sci. Rev.* in press (2007), doi: 10.1007/s11214-007-9170-x
- G.M. Mason, M.I. Desai, J.E. Mazur, J.R. Dwyer, in *The Physics of Collisionless Shocks, Energetic Particles Accelerated in the Heliosphere: What is the Source Material?* ed. by G. Li, G.P. Zank, C.T. Russell (AIP, New York, 2005), pp. 219–226
- G.M. Mason, J.R. Dwyer, J.E. Mazur, *Astrophys. J. (Lett.)* **545**, L157 (2000)
- G.M. Mason, *et al.*, *Space Sci. Rev.* **86**, 409 (1998)
- G.M. Mason, J.E. Mazur, J.R. Dwyer, *Astrophys. J. (Lett.)* **525**, L133 (1999a)
- G.M. Mason, J.E. Mazur, J.R. Dwyer, J.R. Jokipii, R.E. Gold, S.M. Krimigis, *Astrophys. J.* **606**, 555 (2004)
- G.M. Mason, J.E. Mazur, J.R. Dwyer, D.V. Reames, T.T. von Rosenvinge, *Astrophys. J. (Lett.)* **486**, L149 (1997)
- G.M. Mason, C.K. Ng, B. Klecker, G. Green, *Astrophys. J.* **339**, 529 (1989)
- G.M. Mason, T.R. Sanderson, *Space Sci. Rev.* **89**, 77 (1999b)
- G.M. Mason, *et al.*, *Astrophys. J.* **574**, 1039 (2002)
- J.E. Mazur, G.M. Mason, J.R. Dwyer, J. Giacalone, J.R. Jokipii, E.C. Stone, *Astrophys. J. (Lett.)* **532**, L79 (2000)
- R.A. Mewaldt, C.M.S. Cohen, A.W. Labrador, R.A. Leske, G.M. Mason, M.I. Desai, *et al.*, *J. Geophys. Res.* **110**, A09S18 (2005), doi: 10.1029/2005JA011038
- R.A. Mewaldt, C.M.S. Cohen, G.M. Mason, in *Solar Eruptions and Energetic Particles, Geophysical Monograph #165*, ed. by N. Gopalswamy, R.A. Mewaldt, R.B. Torbert (AGU, Washington, 2006), pp. 115–126
- R.A. Mewaldt *et al.*, in *A.I.P. CP #598*, ed. by R.F. Wimmer-Schweingruber (A.I.P., New York, 2001), p. 165
- R.A. Mewaldt, E.C. Stone, R.A. Leske, A.C. Cummings, M.E. Wiedenbeck, T.T. von Rosenvinge, *Space Sci. Rev.* in press (2007)
- E. Möbius, M. Scholer, D. Hovestadt, B. Klecker, G. Gloeckler, *Astrophys. J.* **259**, 397 (1982)
- R. Müller-Mellin, S. Böttcher, J. Falenski, E. Rode, L. Duvet, T.R. Sanderson, *et al.*, *Space Sci. Rev.* in press (2007)
- M. Pick, G.M. Mason, Y.-M. Wang, C. Tan, and L. Wang, *Astrophys. J.* **648**, 1247 (2006)
- D.V. Reames, *Space Sci. Rev.* **90**, 413 (1999)
- D.V. Reames, *Astrophys. J. (Lett.)* **540**, L111 (2000)
- D.V. Reames, L.M. Barbier, T.T. von Rosenvinge, G.M. Mason, J.E. Mazur, J.R. Dwyer, *Astrophys. J.* **483**, 515 (1997a)
- D.V. Reames, S. Kahler, C.K. Ng, *Astrophys. J.* **491**, 414 (1997b)
- I.G. Richardson, *Planet. Space Sci.* **33**, 557 (1985)
- I.G. Richardson, R.D. Zwickl, *Planet. Space Sci.* **32**, 1179 (1984)
- M. Shimjojo, K. Shibata, *Astrophys. J.* **542**, 1100 (2000)
- L. Sollitt, Ph.D. thesis, Dep't. Physics, California Inst. of Tech. (2004)
- L.S. Sollitt, E.C. Stone, R.A. Mewaldt, C.M.S. Cohen, R.A. Leske, M.E. Wiedenbeck, *et al.*, *ICRC* **28**, 3295 (2003)
- A.J. Tylka, C.M.S. Cohen, W.F. Dietrich, M.A. Lee, C.G. MacLennan, R.A. Mewaldt, *et al.*, *Astrophys. J.* **625**, 474 (2005)

- A.J. Tylka, C.M.S. Cohen, W.F. Dietrich, C.G. MacLennan, R.E. McGuire, C.K. Ng, *et al.*, *Astrophys. J. (Lett.)* **558**, L59 (2001)
- A.J. Tylka, M.A. Lee, *Astrophys. J.* **646**, 1319 (2006)
- P. Vandegriff, K. Wagstaff, G.C. Ho, J. Plauger, *Adv. Space Res.* **36**, 2323 (2005)
- T.T. von Rosenvinge *et al.*, *Space Sci. Rev.* in press (2007)
- T.T. von Rosenvinge *et al.*, *Space. Sci. Rev.* **71**, 155 (1995)
- R. von Steiger, N.A. Schwadron, L.A. Fisk, J. Geiss, G. Gloeckler, S. Hefti, *et al.*, *J. Geophys. Res.* **105**, 27217 (2000)
- L. Wang, R.P. Lin, S. Krucker, G.M. Mason, in *Solar Wind 11/SOHO 16, Comparison between Impulsive ^3He -rich Events and Energetic Electron Events* (Whistler, Canada, 2005)
- Y.-M. Wang, M. Pick, G.M. Mason, *Astrophys. J.* **639**, 495 (2006)
- M.E. Wiedenbeck, *et al.*, in *A.I.P. Conf. Proc. #679, How Common are Flare Suprathermals in the Inner Heliosphere?*, ed. by M. Velli, R. Bruno, F. Malara (A.I.P., New York, 2003), p. 652

The Low-Energy Telescope (LET) and SEP Central Electronics for the STEREO Mission

R.A. Mewaldt · C.M.S. Cohen · W.R. Cook · A.C. Cummings · A.J. Davis · S. Geier ·
B. Kecman · J. Klemic · A.W. Labrador · R.A. Leske · H. Miyasaka · V. Nguyen ·
R.C. Ogiore · E.C. Stone · R.G. Radocinski · M.E. Wiedenbeck · J. Hawk ·
S. Shuman · T.T. von Rosenvinge · K. Wortman

Originally published in the journal Space Science Reviews, Volume 136, Nos 1–4.
DOI: [10.1007/s11214-007-9288-x](https://doi.org/10.1007/s11214-007-9288-x) © Springer Science+Business Media B.V. 2007

Abstract The Low-Energy Telescope (LET) is one of four sensors that make up the Solar Energetic Particle (SEP) instrument of the IMPACT investigation for NASA's STEREO mission. The LET is designed to measure the elemental composition, energy spectra, angular distributions, and arrival times of H to Ni ions over the energy range from ~ 3 to ~ 30 MeV/nucleon. It will also identify the rare isotope ^3He and trans-iron nuclei with $30 \leq Z \leq 83$. The SEP measurements from the two STEREO spacecraft will be combined with data from ACE and other 1-AU spacecraft to provide multipoint investigations of the energetic particles that result from interplanetary shocks driven by coronal mass ejections (CMEs) and from solar flare events. The multipoint in situ observations of SEPs and solar-wind plasma will complement STEREO images of CMEs in order to investigate their role in space weather. Each LET instrument includes a sensor system made up of an array of 14 solid-state detectors composed of 54 segments that are individually analyzed by custom Pulse Height Analysis System Integrated Circuits (PHASICs). The signals from four PHASIC chips in each LET are used by a Minimal Instruction Set Computer (MISC) to provide onboard particle identification of a dozen species in ~ 12 energy intervals at event rates of $\sim 1,000$ events/sec. An additional control unit, called SEP Central, gathers data from the four SEP sensors, controls the SEP bias supply, and manages the interfaces to the sensors and the SEP interface to the Instrument Data Processing Unit (IDPU). This article outlines the scientific objectives that LET will address, describes the design and operation of LET and the SEP Central electronics, and discusses the data products that will result.

R.A. Mewaldt (✉) · C.M.S. Cohen · W.R. Cook · A.C. Cummings · A.J. Davis · S. Geier · B. Kecman · J. Klemic · A.W. Labrador · R.A. Leske · H. Miyasaka · V. Nguyen · R.C. Ogiore · E.C. Stone
California Institute of Technology, Pasadena, CA 91125, USA
e-mail: rmewaldt@srl.caltech.edu

R.G. Radocinski · M.E. Wiedenbeck
Jet Propulsion Laboratory, California Institute of Technology, Pasadena, CA 91109, USA

J. Hawk · S. Shuman · T.T. von Rosenvinge · K. Wortman
NASA/Goddard Space Flight Center, Greenbelt, MD 20771, USA

Keywords Space vehicles: instruments · Instrumentation: detectors · Sun: particle emission · Sun: coronal mass ejections · Sun: flares · Acceleration of particles

Acronyms and Abbreviations

ACE	Advanced Composition Explorer
ACR	Anomalous Cosmic Ray
ADC	Analog-to-Digital Converter
ALU	Arithmetic Logic Unit
ApID	Application process Identifier
ASCII	American Standard Code for Information Interchange
ASIC	Application Specific Integrated Circuit
C&DH	Command and Data Handling
CCSDS	Consultative Committee for Space Data Systems
CF	Correction Factor
CIR	Corotating Interaction Region
CME	Coronal Mass Ejection
CMOS	Complementary Metal Oxide Semiconductor
CNO	Carbon, Nitrogen, and Oxygen element group
CPU	Central Processing Unit
CPU24	GSFC version of MISC
CRIS	Cosmic Ray Isotope Spectrometer
CV	Capacitance (C) vs. Voltage (V)
DAC	Digital-to-Analog Converter
DC	Direct Current
DPU	Data Processing Unit
EEPROM	Electronically Erasable Programmable Read-Only Memory
EGSE	Electrical Ground Support Equipment
EM	Engineering Model
EOR	End of Record
EPAM	Electron, Proton, and Alpha Monitor
EPHIN	Electron Proton Helium Instrument (SoHO)
ERH	Event Record Header
ESA	European Space Agency
ESP	Energetic Storm Particles
EUV	Extreme Ultraviolet
E/M	Energy/nucleon
FET	Field Effect Transistor
FM1	Flight Model 1
FM2	Flight Model 2
FOV	Field Of View
FPGA	Field-Programmable Gate Array
FR4	Flame Resistant 4 (printed circuit board material)
F.S.	Full scale
GALEX	Galaxy Evolution Explorer
GCR	Galactic Cosmic Ray
GEANT	Geometry And Tracking (A toolkit for the simulation of particles through matter)
GOES	Geostationary Operational Environmental Satellite
GSE	Ground Support Equipment

GSFC	Goddard Space Flight Center
HAZ	“HAZard” event
HET	High Energy Telescope
HV	High Voltage
HVPS	High Voltage Power Supply
I/F	Interface
I/O	Input/Output
ICD	Interface Control Document
ICME	Interplanetary Coronal Mass Ejection
ID	Identification
IDPU	IMPACT Data Processing Unit
IMF	Interplanetary Magnetic Field
IMP	Interplanetary Monitoring Platform
IMPACT	In situ Measurements of Particles And CME Transients
ISEE-3	International Sun-Earth Explorer 3
ISM	Interstellar Medium
IT	Information Technology
ITAR	International Traffic in Arms Regulations
ITO	Indium Tin Oxide
IV	Leakage current (I) vs. Voltage (V)
JPL	Jet Propulsion Laboratory
LBL	Lawrence Berkeley Laboratory
LEMT	Low Energy Matrix Telescope
LET	Low Energy Telescope
LiBeB	Lithium, Beryllium, and Boron element group
LVPS	Low Voltage Power Supply
MAG	Magnetometer
MISC	Minimal Instruction Set Computer
MRD	Mission Requirements Document
MSU	Michigan State University
NASA	National Aeronautics and Space Administration
NASTRAN	NASA Structural Analysis system
NeMgSi	Neon, Magnesium, and Silicon element group
NOAA	National Oceanic and Atmospheric Administration
NSCL	National Superconducting Cyclotron Laboratory
OGO	Orbiting Geophysical Observatory
PDFE	Particle Detector Front End
PEN	Penetrating event
PHA	Pulse Height Analyzer
PHASIC	Pulse Height Analysis System Integrated Circuit
PLASTIC	Plasma And Suprathermal Ion Composition
PSI	Pounds per Square Inch
RHESSI	Ramaty High Energy Solar Spectroscopic Imager
RISC	Reduced Instruction Set Computer
RTSW	Real-Time Solar Wind
SAMPEX	Solar, Anomalous, and Magnetospheric Particle Explorer
SDO	Solar Dynamics Observatory
SECCHI	Sun Earth Connection Coronal and Heliospheric Investigation
SEP	Solar Energetic Particle

SEPT	Solar Electron Proton Telescope
SEPT-E	Ecliptic-viewing component of SEPT
SEPT-NS	North/South viewing component of SEPT
SIS	Solar Isotope Spectrometer
SIT	Suprathermal Ion Telescope
SOHO	Solar Heliospheric Observatory
SRAM	Static Random Access Memory
SRL	Space Radiation Laboratory
SSD	Solid-State Detector
STEREO	Solar Terrestrial Relations Observatory
STIM	Stimulated (pulser-produced) event
SWAVES	STEREO/WAVES Radio and Plasma Wave Experiment
TCP/IP	Transmission Control Protocol/Internet Protocol
TOF	Time Of Flight
UCB	University of California Berkeley
UH	Ultra-Heavy
ULEIS	Ultra-Low Energy Isotope Spectrometer
UT	Universal Time
VLSI	Very Large Scale Integration

1 Introduction

The Solar Terrestrial Relations Observatory (STEREO) will employ two nearly identical spacecraft in orbit about the Sun (one moving ahead of the Earth, and one moving behind) to provide the first-ever 3-D images of coronal mass ejections (CMEs). These stereo images will be supplemented by multipoint in situ measurements of solar wind and CME plasma and the energetic particles accelerated in association with solar eruptions, and by multipoint observations of radio bursts occurring in these events. The Low Energy Telescope (LET) is one of four solar energetic particle sensors for the IMPACT (In Situ Measurements of Particles and CME Transients) investigation on STEREO. IMPACT provides measurements of solar wind and suprathermal electrons, interplanetary magnetic fields, and solar energetic particles (see Luhmann et al., 2005, 2007). The Solar Energetic Particle (SEP) suite is composed of the Solar Electron Proton Telescope (SEPT; Müller-Mellin et al. 2007), the Suprathermal Ion Telescope (SIT; Mason et al. 2007), the LET, and the High Energy Telescope (HET; von Rosenvinge et al. 2007).

The STEREO Mission Requirements Document (MRD) includes the following science objective that is specifically directed toward energetic particle studies:

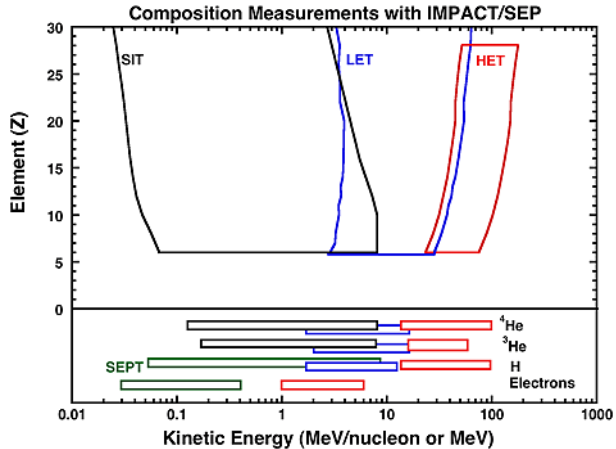
Discover the mechanisms and sites of energetic particle acceleration in the low corona and the interplanetary medium

This leads to two additional, more specific objectives:

- Characterize distribution functions to an accuracy of $\pm 10\%$ for electrons and/or ions with energies typical of solar energetic particle populations.
- Determine the location of particle acceleration in the low corona to within 300,000 km in radius and in interplanetary space to within 20° in total longitude.

The four SEP instruments complement each other in addressing these objectives by providing comprehensive measurements of the composition and energy spectra of energetic nuclei from H to Ni ($1 \leq Z \leq 28$) spanning the energy range from ~ 0.03 to

Fig. 1 Species and energy coverage of the four SEP sensors. The HET coverage is shown in red, the LET coverage in blue, the SIT coverage in black, and the SEPT coverage in green. The SIT and LET sensors can measure trans-iron species with $Z > 30$



>100 MeV/nucleon, as well as electrons from 0.03 to 6 MeV (see Fig. 1). In addition, the SIT and LET instruments will be sensitive to trans-iron nuclei with $30 \leq Z \leq 83$, and SEPT and LET will provide information on the pitch-angle distributions of solar energetic particles.

A block diagram of the SEP system is shown in Fig. 2. The LET, HET, and SIT sensors each include a dedicated microprocessor for onboard data processing and sensor control. An additional control unit, called SEP Central, gathers data from the four SEP sensors, controls the SEP bias supply, and manages the interfaces to the sensors and the SEP interface to the Instrument Data Processing Unit (IDPU). A photo of LET, HET, and SEP Central is shown in Fig. 3.

In this article we describe the LET instrument, including the science objectives, design requirements, measurement capabilities, and data products. The paper documents the features and capabilities of LET, as well as the onboard software and functions that can be altered by command or with new table uploads. There are two identical LET instruments: Flight Model 1 (FM1) is flying on the STEREO Ahead spacecraft, and FM2 is on the Behind spacecraft. Table 1 summarizes key characteristics of the LET instrument, and refers to the sections, figures, and tables where more details can be found. It is intended that sufficient information be provided so that a broad range of users in the solar and space physics community can make use of LET data.

The primary measurement goal of LET is to measure the composition, energy spectra, and time variations of solar energetic particles ranging from H to Ni. The energy range for oxygen extends from ~ 3 to 30 MeV/nucleon (Fig. 1). In this range the intensities can vary by a factor of $\sim 10^6$, as illustrated in Fig. 4, which includes data from 9 years of the 11-year solar cycle. During the last two years of solar minimum (1997–1998) there were not many SEP events, and the daily intensities typically reflect the quiet-time intensities of anomalous cosmic ray (ACR) and galactic cosmic ray (GCR) oxygen nuclei. Typical quiet time energy spectra from the last solar minimum are shown in Fig. 5. Superimposed on the quiet time intensities in Fig. 4 are hundreds of SEP events that typically last a few days. The frequency of large SEP events began to pick up in 1997–1998 and continued through 2005. Based on the >30 MeV proton fluences measured by NOAA's GOES satellites, the two largest events were the July 14, 2000 (Bastille Day), event and the October 28, 2003, event. Figure 5 includes an oxygen spectrum from the January 20, 2005 event, which had a power-law spectrum extending over two decades in energy.

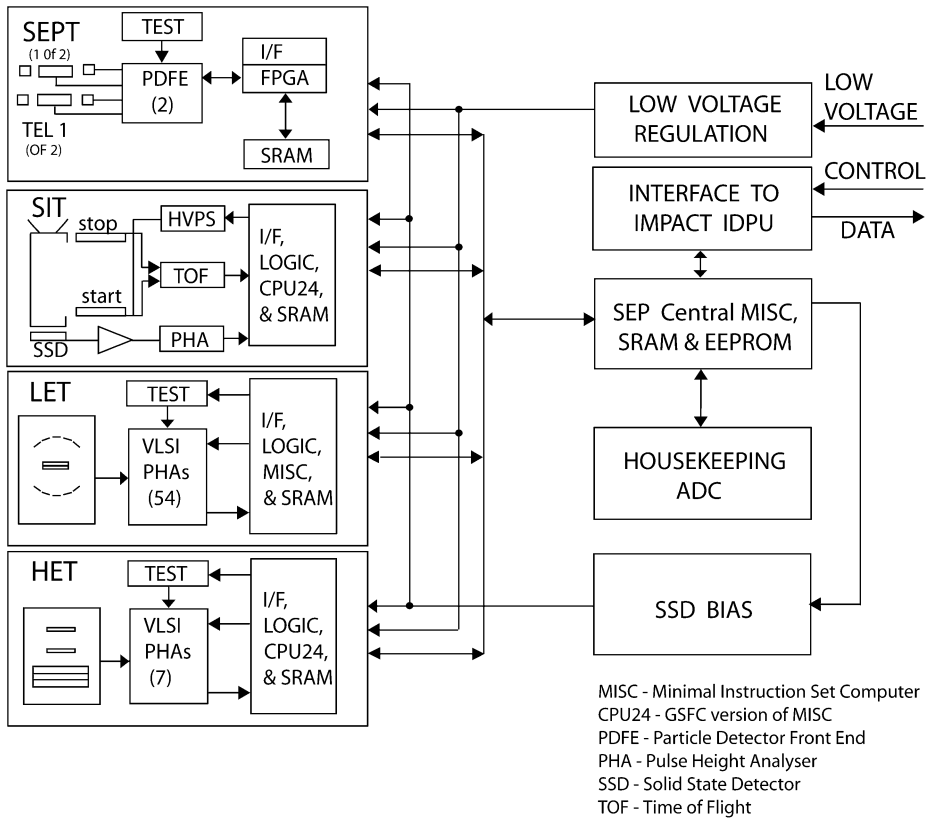


Fig. 2 SEP Sensor Suite block diagram. LET, HET, and SIT each include a dedicated microprocessor. An additional microprocessor, SEP Central, gathers data from the four SEP sensors, controls the SEP bias supply, and manages the interfaces to the sensors and the SEP interface to the Instrument Data Processing Unit (IDPU)

STEREO was launched on October 25, 2006, during the approach to solar minimum, which should be reached sometime in 2007. The frequency of SEP events is expected to begin to increase in 2008.

2 Science Objectives

A key aspect of the STEREO mission is the combination of stereo imaging of solar eruptions and CMEs (see Howard et al. 2007) with multipoint in situ measurements of solar wind and CME plasma (Galvin et al. 2007; Lin et al. 2007) and the energetic particles accelerated in association with these events. There will also be multipoint observations of the radio bursts associated with solar eruptions (Bougeret et al. 2007). In addition, near-Earth instruments will provide a third imaging point of view (RHESSI, SoHO, Hinode, SDO, TRACE, and ground-based observations) as well as a third in situ point of view (ACE, Wind, and SoHO). The paper by Luhmann et al. (2007) discusses some of the questions that can be addressed by new perspectives on solar eruptions. In this paper we focus on objectives that can be addressed with data from the LET.

Fig. 3 Photo of the LET and HET and the SEP Central housing. LET is mounted on a post so as to clear the FOV. HET is mounted on top of the SEP Central housing, with its electronics mounted inside. The SEP Central processor and the low-voltage power supply and bias supply for the four SEP sensors are located in this housing



2.1 SEP Acceleration by CME-Driven Shocks

By 1995 it was well accepted that solar energetic particle (SEP) events generally fell into two distinct categories: “impulsive” and “gradual” (Reames 1995). According to this description, impulsive events are generated by acceleration in solar flares and are characterized by particle intensities generally lasting for hours and confined to narrow ranges of solar longitude, enhanced intensities of ^3He relative to ^4He and Fe relative to O, and enhanced abundances of high charge state ions (e.g., Fe^{20+}) relative to the solar wind. With some notable exceptions, these events are not generally associated with coronal mass ejections (CMEs). In contrast, gradual events are larger in peak intensity, last for days, and have a composition that is variable but generally more similar to the solar wind in elemental abundances and average charge states. Gradual events are a result of shock acceleration by CME-driven shocks in the corona and solar wind.

With the launch of ACE and the subsequent availability of detailed compositional measurements in many SEP events, this simple categorization of SEP events was called into question (e.g., Cohen et al. 1999; Mason et al. 1999; Mewaldt 2000; Mewaldt et al. 2006). Many large events have been observed that have elemental composition similar to that of impulsive events (Fig. 6), while having solar associations (CMEs, long X-ray flare duration) expected of gradual events. The average charge state of >20 MeV/nucleon heavy ions was also measured by SAMPEX, and, in many gradual events, was found to be similar to those of impulsive events (Labrador et al., 2003, 2005). Given the similarity in composition be-

Table 1 Summary of LET characteristics

Characteristic	Value	Details
Measurement objective	Composition, energy spectra, time variations of solar and interplanetary energetic particles	Sects. 2.1–2.5; Figs. 4–18
Measurement technique	Multiple- ΔE vs. residual energy, with corrections for trajectory	Sects. 3.1, 3.3; Figs. 20–22
Sensor system	One double-ended detector stack composed of 14 ion-implanted Si detectors of varying thickness and segmentation	Sects. 3.3, 3.4, Appendix 1; Figs. 19–20
Trajectory measurements	Five segmented apertures on opposite sides arranged in a fan and backed up by a 1-D position-sensitive detector with 10 segments	Sects. 3.3, 3.4, 4.7, Figs. 20, 23, 38
Onboard particle identification	Sixteen species from H to Fe identified within an average of 12 energy intervals	Sects. 3.6.4, Appendixes 2, 3, 4; Figs. 29–31, 41, 42
Charge interval		Sects. 3.6.4, 4.6; Fig. 1
Primary interval	$1 \leq Z \leq 28$	
Extended interval	$1 \leq Z \leq 83$	
Energy interval		Sects. 3.6.4, 4.5, 4.6; Figs. 1, 29, 31, 32, 37
H, He	1.8–15 MeV/nucleon	
O	3.4–33 MeV/nucleon	
Si	4.0–45 MeV/nucleon	
Fe	3.8–59 MeV/nucleon	
Field of view	Two 133° by 29° fans	Sects. 3.3, 4.7; Figs. 20, 38
Geometry factor	$4.0 \text{ cm}^2 \text{ sr}$	Sects. 4.5–4.6; Table 13; Fig. 37
Event yields (large SEP event)	$>10^6$ H & He; $>10^5$ C–Si; $>10^4$ S–Fe	Sect. 4.8; Fig. 39
Element resolution	<0.2 charge units	Sects. 4.2, 4.5; Figs. 22, 35
Mass resolution	Range 2 He: 0.23 amu Range 3 He: 0.20 amu	Sect. 4.5
Resource allocations		
Dimensions (l × w × h)	$16.8 \text{ cm} \times 14.8 \text{ cm} \times 5.8 \text{ cm}$	Fig. 19
Mass	0.855 kg	Sect. 3.10; Table 12
Instrument power	1.18 W (excludes power supply ineffic.)	Sect. 3.10; Table 12
Bit rate	577 bps	Sect. 3.10; Tables 12, 16

Fig. 4 Daily intensity of 7–90 MeV/nucleon oxygen over the period from September 1997 through October 2006. The smoothly varying background is due to anomalous cosmic ray and galactic cosmic ray oxygen, while the spikes are due to large SEP events. The data are from the SIS instrument on ACE

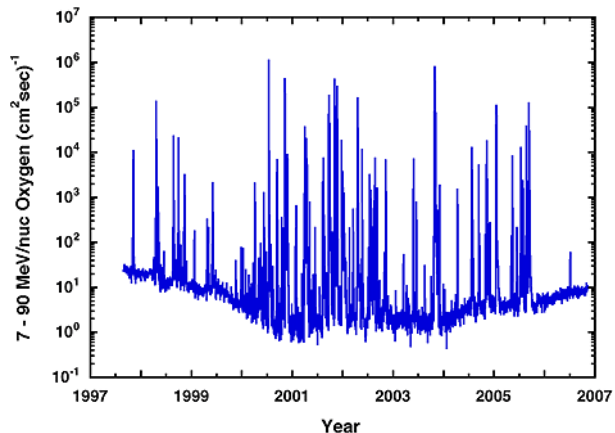
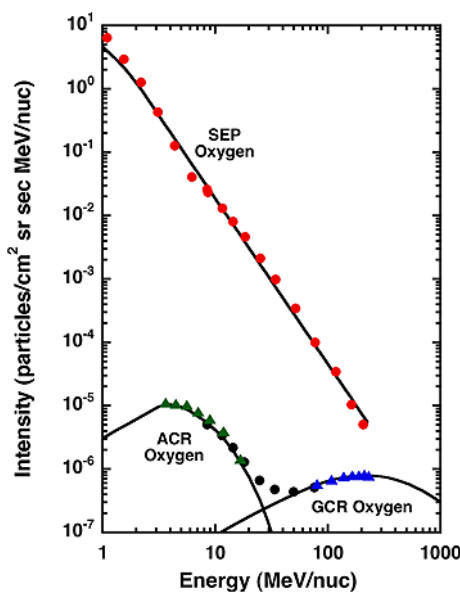


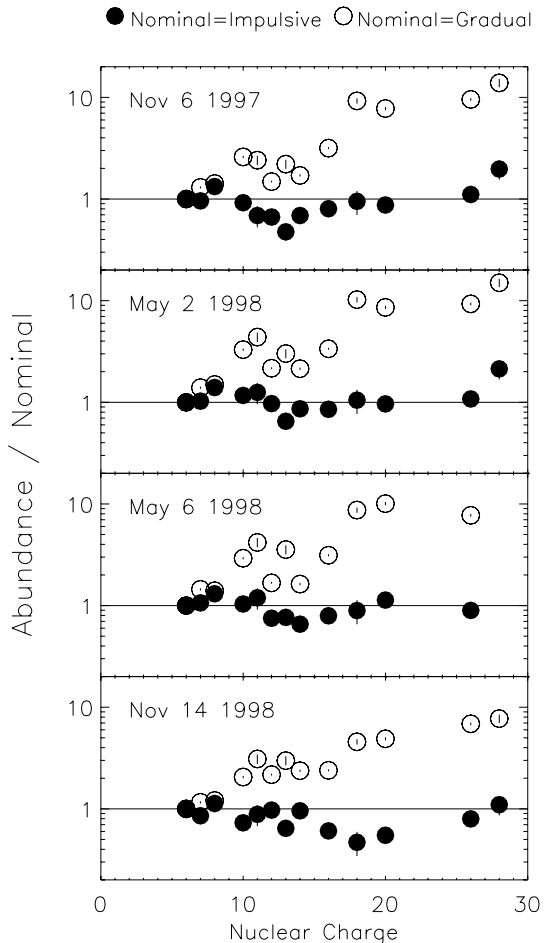
Fig. 5 Quiet-time ACR and GCR spectra for oxygen are shown along with the average intensity of oxygen during the first 34 hours of the January 20, 2005 SEP event. The SEP data are from the SIS and ULEIS instruments on ACE (Mewaldt et al. 2005a). The GCR and ACR data (Leske et al. 2000) are from the CRIS (blue triangles) and SIS (black circles) instruments on ACE and the LEMT instrument (green triangles) on Wind. Note that the ACR spectra are present only during solar minimum while large SEP events occur mainly during solar maximum



tween these “hybrid” events and impulsive events (thought to be accelerated flare material), most proposed explanations for the generation of hybrid events involve mixing flare material with ambient coronal or solar wind material. Table 2 summarizes the characteristics of SEP events according to the two-class picture, and also lists some of the new results from solar cycle 23 that have modified this picture.

The hypothesis by Tylka et al. (2005) suggests that the suprathermal population from which SEP events are accelerated has an energy-dependent composition, moving from more solar-wind-like at lower energies to more flare-like at higher energies (Fig. 7). Under the assumption that perpendicular shocks have a higher injection threshold than parallel shocks, acceleration at perpendicular shocks would result in more flare-like material being accelerated to produce a SEP event with enhanced Fe/O, $^{3}\text{He}/^{4}\text{He}$, and elevated heavy ion charge states. In contrast, parallel shocks would predominantly accelerate suprathermal material with “nominal” composition resulting in typical gradual SEP events. A competing hypoth-

Fig. 6 Composition of four SEP events observed by ACE/SIS as compared to standard abundances for gradual events (open circles) and impulsive events (filled circles). Cohen et al. (1999) found that these and other large SEP events associated with CMEs appeared to have an impulsive composition, including enhancements of ${}^3\text{He}$



esis by Cane et al. (2003, 2006) involves a simpler scenario of flare-accelerated material superimposed on shock-accelerated material to produce a composite SEP event with an energy-dependent composition. The relative intensity of the two components depends on the strength of the shock, the size of the flare and flaring region, and the magnetic connection to the observer.

Energy-dependent composition has also been observed in events that are clearly dominated by shock-accelerated material. The inability of the shock to confine particles to the acceleration region results in “spectral breaks” such as those apparent in Fig. 8. As the turbulence near the shock is the dominant mechanism for returning particles to the shock, one would expect the relative energies of the break points for different ions to be a function of the particles’ mean free paths or rigidity. This was found to be a reasonable approximation for the large SEP events of October/November 2003 (Cohen et al. 2005; Mewaldt et al. 2005b, 2005c), as well as others (Cohen et al. 2007). Modeling of shocks shows that the strength of the shock and its orientation varies along the face of the shock (Fig. 9).

There are several ways in which data from LET can further the understanding of CME-driven shock acceleration and the generation of hybrid events. For the first time since the Helios spacecraft (Schwenn and Marsch 1991), SEP events will be measured simultane-

Table 2 Characteristics of SEP events

Characteristic	Conventional picture (Reames 1999)		New results	
	Impulsive	Gradual	Impulsive	Gradual
$^3\text{He}/^4\text{He}$	~1	~0.0004	>0.01 (a)	~0.001–0.1 (b)
Fe/O	~1	~0.1		~0.01–1 often energy dependent (c)
H/He	~10	~100		
Fe Q-State	~20	~14	~13–20 broad distribution, energy depend (d)	~10–20 can be energy dependent (e)
Electron/Proton	Electron-rich	Proton-rich		
X-rays	Impulsive	Gradual		
Typical duration	Hours	Days		
Longitudinal cone	<30°	~180°		
Radio type	III, V (II)	II, IV		II, IV, III-ℓ (f)
Coronagraph	–	CME 96%	Frequently CMEs, often narrow (g)	Always CME, usually wide/fast (h)
Enhancements of ($Z \geq 33$)/O			up to 10^4 (i)	0.2–20 (j)
Heavy isotope enhancements			up to factors of ~5 (k)	up to factors of ~3 (l)

(a) Ho et al. (2005)

(b) Desai et al. (2006)

(c) Cohen et al. (1999), Cane et al. (2006), Desai et al. (2006), Cohen et al. (2005), Mewaldt et al. (2006)

(d) Klecker et al. (2006)

(e) Labrador et al. (2003), Mazur et al. (1999)

(f) Cane et al. (2002)

(g) Wang et al. (2006a)

(h) Kahler and Vourlidas (2005)

(i) Reames and Ng (2004), Mason et al. (2004), Leske et al. (2007a)

(j) Reames and Ng (2004)

(k) Wiedenbeck et al. (2003), Leske et al. (2003b)

(l) Leske et al. (2007b)

ously at different solar longitudes. In combination with other SEP instruments (e.g., HET and SIT) on STEREO, particle spectra for many heavy ions (H through Fe) will be measured over a large energy range (~0.04 to ~100 MeV/nucleon), something that was not possible with Helios. Such measurements are critical for understanding compositional variations in SEP events. The ability to make multipoint determinations of heavy-ion spectra over a large energy range is a crucial step in differentiating between current theories—the direct flare hypothesis of Cane et al. (2003, 2006), which predicts a longitudinal dependence

Fig. 7 Schematic illustration of the model of Tylka et al. (2005). The higher injection threshold at quasi-perpendicular shocks results in the acceleration of mainly suprathermal ions that are enriched in remnant flare material. At quasi-parallel shocks the injection threshold is assumed to be lower, and a more normal composition is accelerated

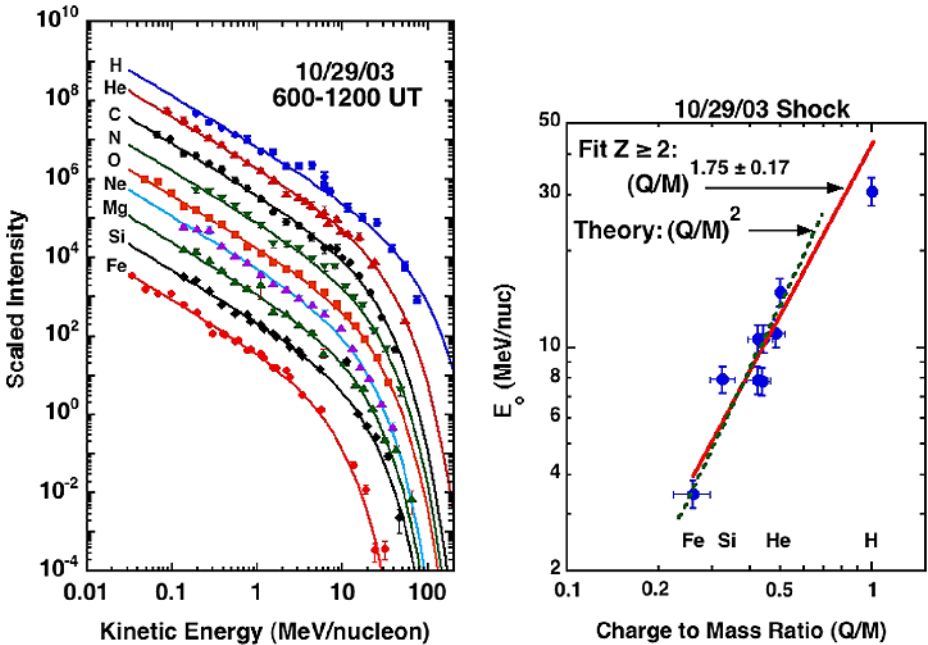
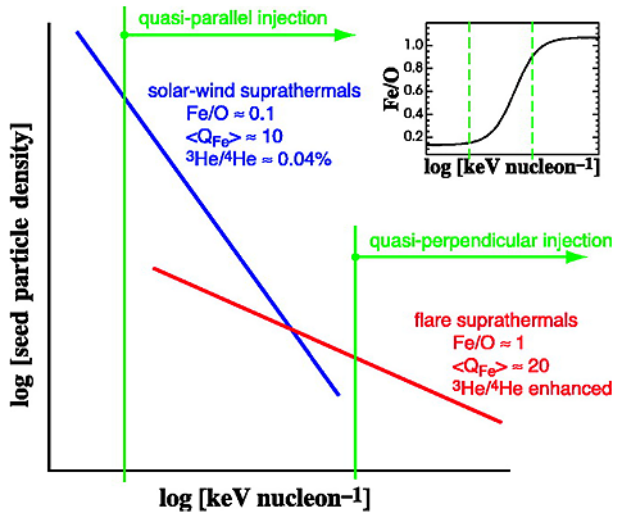


Fig. 8 Example of spectral breaks observed in the October 28, 2003 SEP event following the arrival of the shock at ACE (from Mewaldt et al. 2005c). In the left panel spectra measured by ACE and GOES are fit with a power-law times an exponential form with e-folding energy E_0 . In the right panel the E_0 values are plotted vs. the charge-to-mass ratio (Q/M) measured by SAMPEX (Labrador et al. 2005). The observed slope of 1.75 ± 0.17 is reasonably close to that predicted by the model of Li et al. (2005)

in the presence of flare-like material, and the shock-orientation model of Tylka et al. (2005), which does not, on average, predict a longitudinal dependence. Although the current SEP instrumentation boasts measurements made over a larger energy range with greater sensitivity

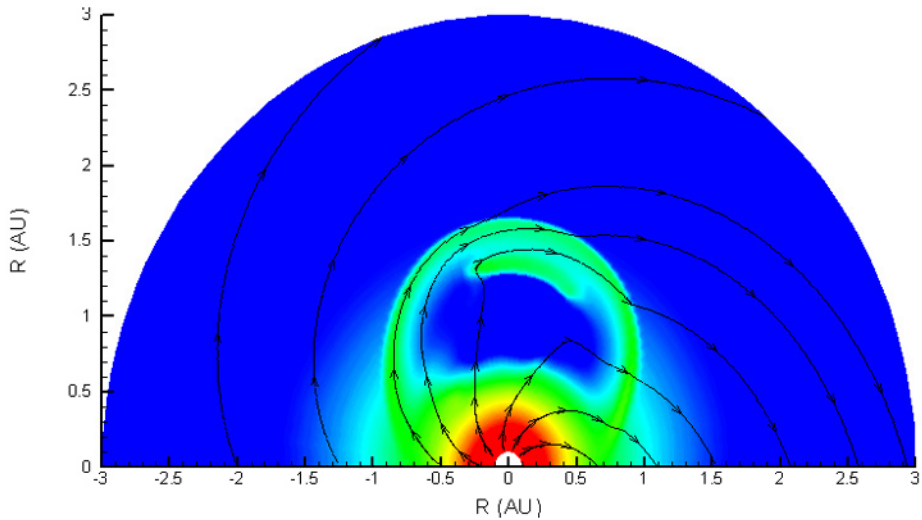
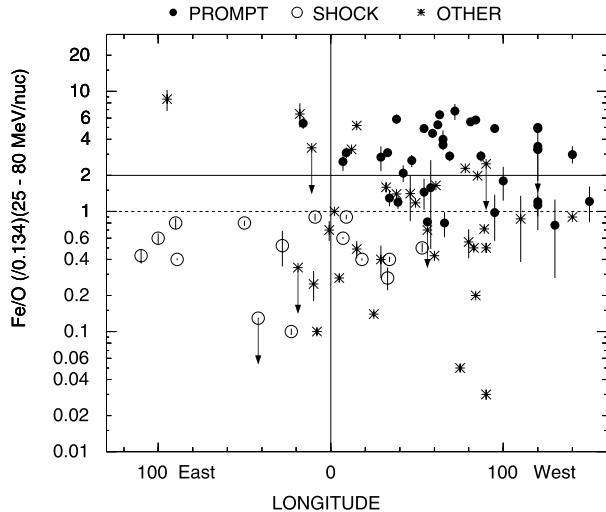


Fig. 9 Results of a shock simulation (see, e.g., Rice et al. 2003) shows density enhancements (color) around an expanding CME. The increases in density indicate the shock region and strength. The orientation of the magnetic field lines (black arrows) changes in relation to the shock normal along the flanks and nose of the shock

Fig. 10 Longitude distribution of Fe/O ratios (divided by 0.134) measured in SEP events (from Cane et al. 2006). The predominance of Fe-rich events in the western hemisphere has been interpreted as evidence for direct contributions of flare accelerated particles in some well-connected events



than previously possible (Stone et al. 1998a), longitudinal studies using such instrumentation (e.g., von Rosenvinge et al. 2001) have not made significant progress over similar research performed decades ago (e.g., Mason et al. 1984) largely because they have been statistical in nature (Fig. 10) and have not involved multipoint measurements. With STEREO other aspects of SEP events, such as the energy of spectral breaks, the spectral index at high and low energies, and the temporal evolution of spectra, intensities, and composition can be examined as a function of longitude within a single SEP event, providing key information for testing models of SEP acceleration and transport.

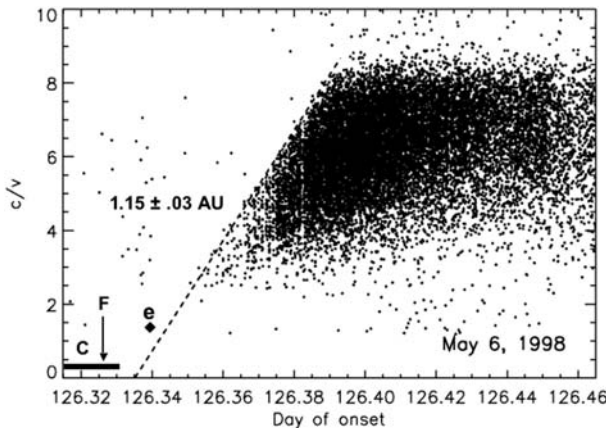


Fig. 11 The measured value of c/v (where c is the speed of light and v is the particle velocity) is plotted vs. arrival time of individual C to Ni ions with > 7 MeV/nucleon observed by ACE/SIS during the May 6, 1998, SEP event (Mewaldt et al. 2003). Also shown is the onset time for near-relativistic electrons (Haggerty and Roelof 2001), the onset of the X-ray flare, and the CME release time (band includes range of two extrapolation approaches). A fit to the onset gives an interplanetary pathlength of 1.15 ± 0.03 AU and a particle release time near the Sun of $8:02 \pm 2$ minutes

The source of the energetic particles can also be examined through timing studies. Using the arrival time and energy of energetic particles, the particle release time near the Sun can be deduced (Fig. 11). This time can then be compared to the height vs. time profiles of CMEs, temporal evolution of flares, and the timing of other solar phenomena. Such studies have been performed with events observed by instruments on ACE, Wind, and SoHO (e.g., Krucker and Lin 2000; Haggerty and Roelof 2002; Mewaldt et al. 2003; Tylka et al. 2003; Klassen et al. 2005) in an effort to determine the likely accelerator (CME-driven shock or flare-related reconnection) of the particles. Although there is statistical evidence for a dependence of SEP onset timing on connection longitude, it is not known if this is due to the time it takes for the shock to reach the field line on which the spacecraft is located, or the time it takes for particles to diffuse to this field line. Multipoint timing studies may be able to decide between these possibilities.

Finally, during SEP events the combination of data from STEREO and ACE (located at the inner Lagrange point) will allow the seed particle population to be studied along with the resulting accelerated population. This cannot be done by a single spacecraft as the seed and accelerated populations travel along different trajectories from the Sun (the seed population taking a more radial path, while the accelerated particles are generally flowing along the Parker spiral). However, with two or more separated spacecraft the composition of the seed and accelerated populations can be measured and compared (see Fig. 12).

2.1.1 Comparison of SEP and CME Kinetic Energies

The particles accelerated by CME-driven shocks derive their energy from the kinetic energy of the CME. It is of interest to compare the total kinetic energy of SEPs in large SEP events to the kinetic energy of the CME measured by coronagraphs in order to evaluate the efficiency of SEP acceleration. This efficiency is known to vary over many orders of magnitude (see, e.g., Kahler and Vourlidas 2005). Figure 13 shows a comparison of the kinetic energy of SEPs vs. the CME kinetic energy for 17 large SEP events from solar cycle 23 (Mewaldt

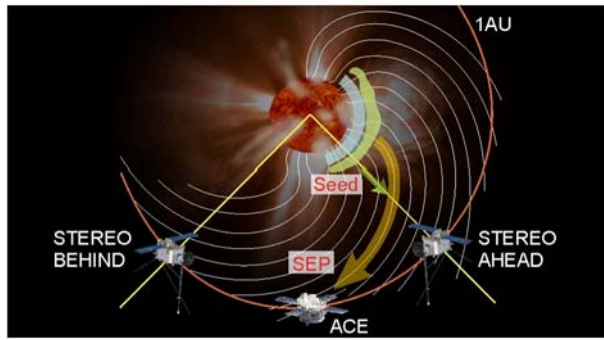
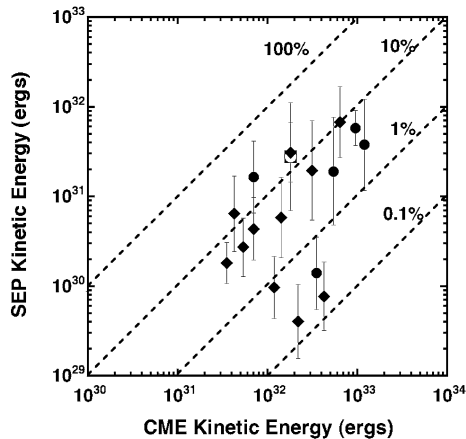


Fig. 12 Schematic of the trajectories of the accelerated and seed particle populations and their relation to the positioning of the STEREO and ACE spacecraft. For CME-driven shocks originating in the western hemisphere of the Sun, the Ahead STEREO spacecraft will be able to measure the seed populations for the accelerated SEPs, which follow the magnetic field lines and will be measured by either ACE or Behind (typically $\sim 50^\circ$ to the west of where they were accelerated, depending on the solar wind velocity). Thermal plasma travels radially, while suprathermal particles will be distributed in longitude when they reach 1 AU, depending on their velocity and on how much they scatter in the inner heliosphere. In the above picture the Behind STEREO spacecraft will also be situated to image the CME as it moves away from the Sun

Fig. 13 Comparison of CME and SEP kinetic energies for 17 large SEP events (from Mewaldt et al. 2005d). The single square is the April 21, 2002 event; the circles are the October–November 2003 events, and the diamonds are other events where CME mass estimates were available



et al. 2005d; Mewaldt 2006). The SEP kinetic energies were obtained by integrating the measured and extrapolated SEP spectra from 0.01 to 100 MeV/nucleon. Note that while there is a wide range of deduced efficiencies, it is not uncommon for the SEP kinetic energy to amount to $\sim 10\%$ of the CME kinetic energy. It is interesting that a similar efficiency is required for the acceleration of galactic cosmic rays by supernova shock waves to sustain the cosmic ray intensity in the Galaxy (Ptuskin 2001).

The data in Fig. 13 are from single-point measurements of SEPs with near-Earth instruments that were corrected for the longitude of the associated flare and CME. This correction is uncertain, and undoubtedly depends on the configuration of the interplanetary magnetic field. With measurements of SEP spectra over a wide energy range from the two STEREO spacecraft and from ACE and GOES near Earth it will be possible to measure directly the longitudinal variation in SEP intensities for many SEP events, thereby increasing the ac-

curacy of the SEP energy estimates. The best estimates of CME kinetic energies are for limb CMEs, while estimates for halo-CMEs are more uncertain (Vourlidas et al. 2000). With STEREO there should be CME images of the events from two or three points of view, thereby providing much more accurate estimates of the CME kinetic energy.

2.2 Impulsive Solar Energetic Particle Events

As noted earlier there exists a second category of solar energetic particle events. These are frequently called “impulsive” events because they tend to occur in association with impulsive solar X-ray events (i.e., events with fast onsets and short durations). A variety of observational characteristics distinguishing impulsive from gradual events have been suggested (see Table 2 and Sect. 2.1), many of which rely on composition signatures. The most distinctive indicator of an impulsive event is a large enhancement of the ${}^3\text{He}/{}^4\text{He}$ ratio, which often can be $>1,000 \times$ the solar wind value of $\sim 4 \times 10^{-4}$. Thus the term “ ${}^3\text{He}$ -rich” is often used as a synonym for impulsive SEP events.

Although it is widely believed that particle acceleration in impulsive events is driven by magnetic reconnection in solar flares, the detailed physical mechanisms are only poorly understood. A variety of resonant processes for heating the background plasma or otherwise extracting the population of particles to be accelerated from it have been proposed. To date, however, none of them has proven capable of accounting for all of the observed characteristics.

Measurements of impulsive SEP events over a relatively broad energy range (Mason et al. 2000, 2002) show that spectral shapes can differ from event to event and among different species in an individual event. Thus, it is not sufficient to characterize impulsive events by their composition derived from observations made over a narrow range of energies. The spectral variability may be responsible for the fact that correlations among various abundance ratios are often relatively weak (Reames et al. 1994). On STEREO the broad energy coverage provided by the combination of SIT, SEPT, LET, and HET will provide the spectral measurements needed to better understand the observed composition. Figure 14 compares the energy coverage and sensitivities of SIT and LET with spectra of key species that have been reported in two impulsive events. The overlap in energy coverage between the various SEP instruments will also help facilitate their intercalibration using particle measurements made in flight.

The heavy-element ($Z \geq 6$) composition observed in most impulsive SEP events follows a pattern of enhancements (relative to solar wind or to gradual SEP composition) that increase approximately monotonically with atomic number (or mass). However, a small number of events have been reported with large deviations from this pattern (Mason et al. 2002; Wiedenbeck et al. 2003). In addition, isotopic composition measurements have shown that impulsive events frequently have strongly enhanced abundances of heavy isotopes (Mason et al. 1994; Dwyer et al. 2001; Wiedenbeck et al. 2003). Observed values of the ${}^{22}\text{Ne}/{}^{20}\text{Ne}$ ratio $>3 \times$ the solar wind value are larger than seen in any but the most extremely fractionated gradual events (Leske et al. 2003a), as illustrated in Fig. 15. Thus far there have been relatively few well-measured examples of impulsive SEP events with extreme elemental and isotopic fractionation patterns. STEREO will search for additional events of this sort, measure their composition over a broad energy range, and provide context information that should help in identifying the features that distinguish these highly fractionated events from the general population of impulsive SEP events.

Recent measurements from Wind/LEMT (Reames and Ng 2004), ACE/ULEIS (Mason et al. 2004), and ACE/SIS (Leske et al. 2007a) show that some impulsive SEP events exhibit

Fig. 14 The average ${}^3\text{He}$ and ${}^4\text{He}$ intensities for two ${}^3\text{He}$ -rich SEP events measured by the ULEIS and SIS instruments on ACE are plotted vs. energy/nucleon. The sensitivity of the SIT and LET instruments for measuring energy spectra of ${}^3\text{He}$ and ${}^4\text{He}$ is also indicated (*solid line*) as the intensity at which one event per 3 hrs would be collected in a given energy bin [using the energy bins in Fig. 30 for LET and in Mason et al. (2007) for SIT]

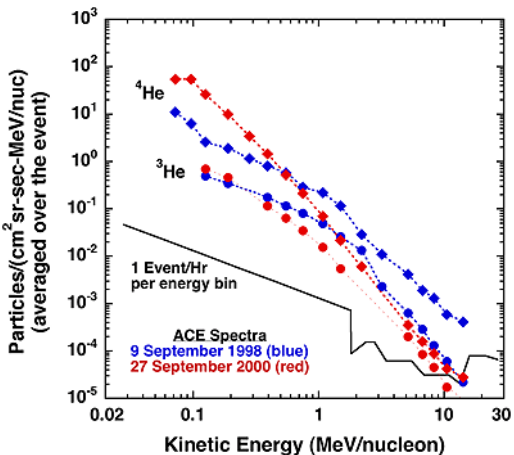
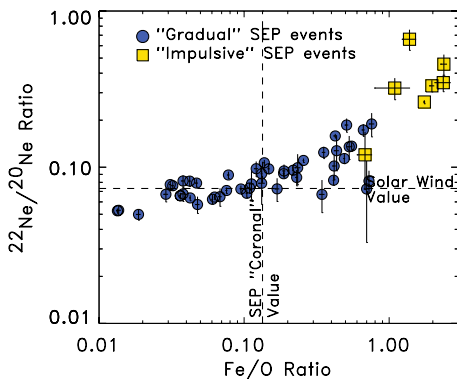


Fig. 15 Plot of the ${}^{22}\text{Ne}/{}^{20}\text{Ne}$ isotope ratio vs. Fe/O for a number of SEP events observed with the ACE/SIS instrument from 1997 through 2005. The impulsive events shown, which are indicated by *yellow squares*, are among the largest ${}^3\text{He}$ -rich events observed by SIS. Note that both elemental and isotopic fractionation tends, on average, to be more extreme in impulsive than in gradual events



large abundance enhancements of ultraheavy (UH, $Z \geq 30$) elements relative to standard solar composition that tend to increase with increasing Z . In some cases these enhancements can be $>10^2\text{--}10^3$, comparable to observed ${}^3\text{He}$ enhancements. These observations provide new constraints on theories of particle acceleration in impulsive SEP events since the UH species occur with a wide range of M/Q ratios and with such low abundances in the background plasma that they behave strictly as test particles. The studies from Wind/LEMNT and ACE/ULEIS only resolved major charge groups, while the higher-resolution ACE/SIS data were restricted to elements with $Z \leq 40$ and had a relatively high energy threshold (>12 MeV/nucleon). The LET instrument, which has a significantly lower energy threshold than SIS and a dynamic range sufficient for measuring elements over the entire periodic table, should provide improved charge resolution for $Z > 40$ in those impulsive events having significant intensities above several MeV/nucleon.

In a significant fraction of impulsive SEP events, particle distributions at 1 AU are observed to be highly anisotropic and appear during their early phases as beams propagating outward from the Sun along the magnetic field. Such events tend to exhibit a dispersive onset, with the time of first arrival of particles of a given velocity, v , increasing linearly with $1/v$. It is often (but not always) the case that the slope of this relation corresponds to the expected ~ 1.2 AU length of a nominal Parker spiral magnetic field line between the Sun and Earth as in Fig. 11. This behavior is taken as indicating nearly scatter-free propa-

gation from the point of release at the Sun to 1 AU. Using the observed dispersion of onset times and/or the time evolution of the anisotropy as constraints, one can model the injection and propagation of SEPs in order to deconvolve the effects of injection and release times of finite duration from those of scattering during propagation (Wang et al. 2006b; Dröge et al. 2006). The LET instrument, with its capability for measuring arrival direction distributions within the ecliptic plane (see Sect. 4.7), will provide data for such studies. LET anisotropy observations will also help in the interpretation of data from the SIT and HET instruments (which make measurements within a limited field of view around the nominal magnetic field direction) when the particle fluxes have significant anisotropies. High velocity particles (e.g., $v/c > 0.15$) are particularly useful for timing studies because they experience less propagation delay and provide more-precise time markers than very low-velocity particles. Although electrons generally yield the most precise timing data, the higher-energy ions measured by LET and HET will be important for understanding differences between the acceleration and release histories of ions and electrons (Krucker and Lin 2000; Mewaldt et al. 2003).

A major impediment to the study of impulsive SEP events has been the fact that such events tend to be associated with relatively small X-ray flares on the Sun. The particle data generally do not provide precise enough timing information to unambiguously distinguish which of many small X-ray events they are associated with. Following seminal work of Reames et al. (1985), considerable progress has recently been made in associating impulsive SEP events with their counterparts on the Sun (Wang et al. 2006a; Nitta et al. 2006). Timing associations between ion events and electron events observed *in situ* near 1 AU and then between the electron events and Type III radio bursts, which are triggered by the streaming of lower-energy electrons near the Sun, have made it possible, in some cases, to pinpoint the solar release time with sufficient accuracy to identify a unique solar-flare counterpart. This association can be checked using EUV or X-ray imaging data in conjunction with a model of the solar magnetic field: if the calculated field line from the imaged flare location through the corona does not correspond to an interplanetary field line that the Parker spiral will ultimately connect to the observer, the association is called into question.

For impulsive SEP events with clear solar flare associations one can then use sequences of EUV and white-light images to investigate dynamical changes in the solar corona associated with the particle release and obtain information about the physics that is involved. Such studies, which are still in their infancy, have provided intriguing evidence that impulsive SEP events originate when flaring loops undergo reconnection with adjacent open field lines and that the particle injections can be accompanied by escaping “jets” or narrow CMEs (Wang et al. 2006a). The STEREO mission will provide the key observations needed for making the sequence of connections essential to these studies: ion and electron measurements from the IMPACT/SEP instruments, radio burst data from SWAVES, EUV and white-light imaging from SECCHI. Measurements from RHESSI, GOES, Hinode, SoHO, ACE, and Wind as well as ground-based solar radio burst observatories will provide valuable supporting data.

Based on investigations that attempted to associate impulsive SEP events with specific solar flares on the Sun (Reames 1993) and multispacecraft studies involving Helios and ISEE-3 (Reames et al. 1991) it has been concluded that impulsive SEPs propagate into a $\sim 10^\circ\text{--}20^\circ$ half-angle cone about the magnetic field line connected to the source region. This narrow spread is attributed to the relatively small spatial region from which the particles are released, in contrast to the very broad region from which the shock-accelerated particles in gradual SEP events originate. However, as noted earlier, flare associations are difficult. It is not clear whether some associations with eastern hemisphere flares actually reflect a highly distorted magnetic connection between the Sun and the observer or some deficiency in our simple picture of impulsive SEP release and transport.

It has been found that there is a maximum fluence of ${}^3\text{He}$ that can be obtained from an impulsive SEP event (Ho et al. 2005). This observation, which indicates that only a limited number of energetic ${}^3\text{He}$ particles can be released from the Sun in such an event, may also be related to the small spatial size of the acceleration region.

In the course of an impulsive SEP event the particle intensity seen at a single spacecraft can exhibit “dropouts” (Mazur et al. 2000). These have been explained in terms of the shredded character of the interplanetary field caused by the random walk of field lines (Giacalone et al. 2000). The related phenomenon of abrupt event onsets with no velocity dispersion is thought to be due to the observer moving into flux tubes already populated with particles.

The two STEREO spacecraft, together with ACE, Wind, and other spacecraft operating near Earth, will obtain measurements of individual impulsive SEP events from different heliolongitudes, thereby probing the longitudinal widths of these events at 1 AU without having to rely on solar-flare associations. If impulsive SEPs do indeed have a narrow longitudinal spread, multispacecraft correlations will mainly be seen in the first one to two years of the STEREO mission. During this solar minimum period the interplanetary field should be relatively undisturbed, but impulsive SEP events may be rather infrequent. Investigation of correlations at larger angular separations and how they depend on solar activity could provide new insights into these events later in the mission. The plasma beta, which may play an important role in organizing the particle transport (Reames et al. 2001), will be available using data from the MAG and PLASTIC instruments.

2.3 Space Weather

2.3.1 An Interplanetary SEP Network

Although CME, X-ray, and radio observations all provide early warning of large solar eruptive events that are a space weather concern, the best way to accurately gauge how large a SEP event will be is with direct particle measurements from a location that is magnetically well connected to the particle acceleration site near the Sun, whether it be a CME-driven shock or a flare. This is illustrated in Fig. 16, which shows typical intensity profiles for SEP events originating at different longitudes. The two STEREO spacecraft ahead and behind Earth, combined with ACE (Stone et al. 1998a) and GOES (Onsager et al. 1996) near Earth, will form a three-point interplanetary network for early detection of large SEP events. It is likely that any large SEP event of concern in the near-Earth environment will be magnetically well connected to at least one of these spacecraft, all of which broadcast SEP intensities in real time. Algorithms now exist that forecast the eventual size of an event based on its onset profile (e.g., Hoff et al. 2003; Neal and Townsend 2005). With this network, alerts for large SEP events can be made sooner and with much greater precision. Real-time data from LET and HET will provide energy spectra of H, He, CNO and Fe from ~ 3 to ~ 100 MeV/nucleon, including the most important energy range for radiation effects on humans or hardware.

With the many spacecraft that are and will be exploring the inner heliosphere during the coming years, the growing set of assets that are exploring Mars, and the expected return of astronauts to the Moon, it is clear that there will be an increasing need for global models, forecasts, and “nowcasts” of space weather throughout the inner heliosphere, and not just along the Earth–Sun line. In particular, there will be a need to model the global longitude distribution of particle intensities from large SEP events as they occur (see, e.g., Turner 2006). SEP data from the three-point network described earlier will build up a statistical database of SEP longitude distributions, and it will provide valuable tests for global models that are driven by imaging and in situ observations.

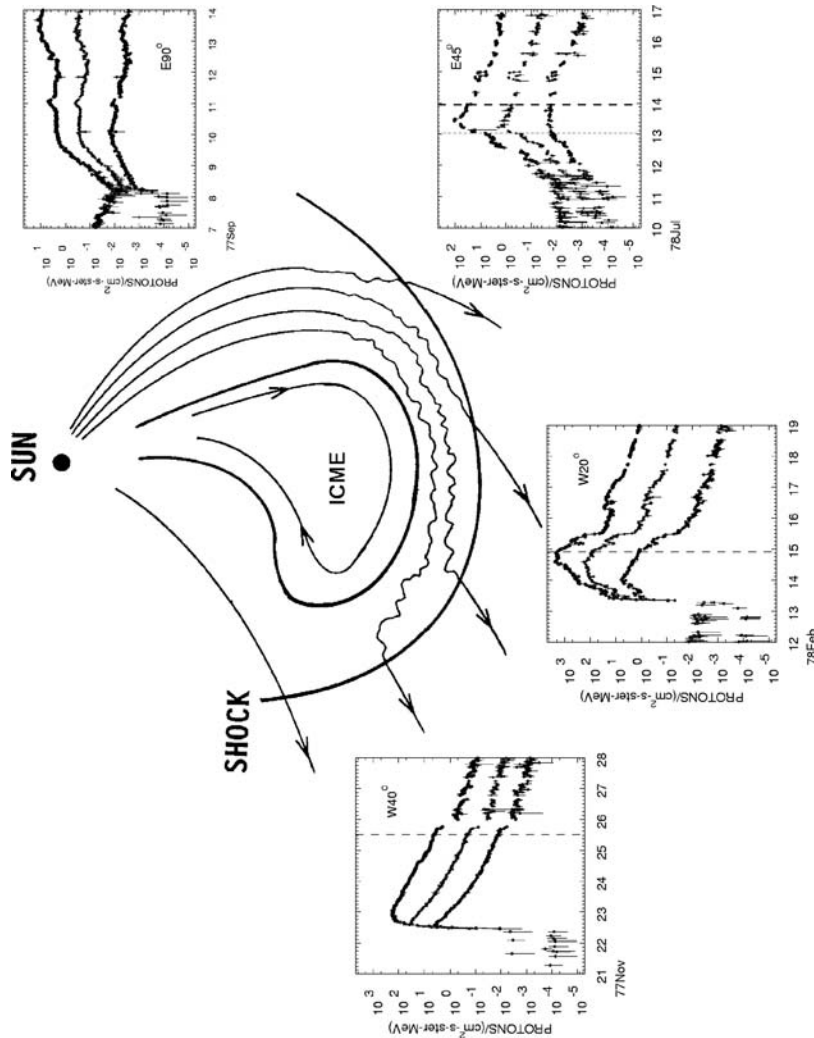


Fig. 16 Illustration of how the time profiles of SEP events depend on the relative longitude of the CME-driven shock and the observer (Cane and Lario 2006). Time intensity profiles are shown in three energy intervals for events observed at four locations with respect to the CME. Observers to the west of the CME see a rapid rise and decay. Observers near the nose of the CME see a maximum intensity when the shock arrives, while those to the east see a much more gradual rise and decay

Interplanetary shocks are currently identified using both magnetic field and plasma instruments on ACE, providing \sim 1-hour warning. However, to extend the warning time, the escaping upstream component of energetic storm particle (ESP, see Sect. 2.4) ion events can be used to provide short-term forecasts of approaching interplanetary shocks. ACE/EPAM data have been used to train an artificial neural network to predict the arrival time of the maximum intensity of an ESP event at Earth (Vandegriff et al. 2005). On STEREO, SIT, SEPT, and LET will all be sensitive to ions escaping upstream from approaching shocks, and it will be possible to have a three-point network to warn of interplanetary shocks.

2.3.2 Characterizing the 1-AU Radiation Environment

Knowledge of the long-term radiation environment is important for evaluating design requirements for spacecraft hardware. Although the intensity of GCRs in a given energy interval varies by at most a factor of 10 over the solar cycle, the intensity of SEPs with, e.g., 10 to 30 MeV/nucleon can vary by a factor of \sim 10⁶ (see Figs. 4 and 5). Indeed, ACE data have shown that the yearly average intensity of >20 MeV/nucleon CNO and Fe during the past solar maximum has been considerably greater than earlier in the space era, with three of the years from 2000 to 2003 exceeding the 90% confidence limits of Tylka et al. (1997) for yearly fluences of 21 to 43 MeV/nucleon CNO and 45 to 95 MeV/nucleon Fe (Mewaldt et al. 2007). These results from ACE indicate that models of the 1-AU radiation environment need to be updated. Data from LET and HET can complement ACE data in developing improved models of the radiation environment. In particular LET and HET provide H and He data in an interval where ACE has incomplete coverage, and where GOES data are often affected by relatively high background and by temporal variations in the geomagnetic cutoff at geosynchronous altitude.

2.4 Acceleration by CIRs and ESP Events

2.4.1 Corotating Interaction Regions

Corotating interaction regions (CIRs) occur when a stream of fast solar wind overtakes a stream of slow solar wind. The compression region that forms at the boundary can strengthen into a shock pair (forward and reverse shocks) and accelerate particles up to \sim 20 MeV/nucleon (see, e.g., Richardson 2004). As long as the two streams are consistently emerging from the Sun, the structure will corotate past fixed points as the Sun rotates, sometimes existing over many solar rotations.

The elemental composition of the accelerated particle population associated with CIRs is still a puzzle. Although some of the elemental ratios (e.g., Fe/O) are similar to those found in the solar wind, other ratios like C/O are significantly enhanced (e.g., Mason et al. 1997). The cause of this remains unknown. Although it has been suggested that the CIR composition anomalies are due to preferential acceleration of seed particles arising from the “inner source” of pickup ions (Gloeckler 1999), measurements of the charge states of CIR-accelerated ions have not found evidence for singly charged C ions (Mazur et al. 2002; Möbius et al. 2002).

With the multispacecraft measurements from STEREO and ACE, it will be possible to examine the energy spectra and abundances of many heavy-ion species over a wide energy range simultaneously at three different spatial points in the CIR structure. The evolution of the spectra at these three points can also be measured as the structure corotates past the spacecraft. Under circumstances where both a forward and a reverse shock are formed by

1 AU, comparing the resulting accelerated particle population using the coincident measurements made in the leading and trailing regions of the CIR will yield valuable information concerning the characteristics and evolution of these two different shocks and the seed particles that are accelerated.

Typically CIR events exhibit inverse velocity dispersion (i.e., the lower energy ions arrive first) due to the fact that the shock strengthens as it moves outwards and so, initially, is only able to accelerate particles to lower energies (Reames et al. 1997). Later, when the shock is strong enough to generate higher energy particles, this dispersion effect is lessened as transport over longer distances affects the low energy ions more. Examining these signatures simultaneously at three different points in the large CIR structure will provide key information regarding the formation and evolution of the reverse shock.

2.4.2 Energetic Storm Particles

Similar to CIR events, energetic storm particle (ESP) events are a result of interplanetary shock acceleration which occurs relatively near the spacecraft (rather than primarily near the Sun, as in SEP events). ESP events provide one of the best opportunities to study shock acceleration of energetic particles since the characteristics of the particle population, as well as the characteristics of the shock, can be measured at the same time. With two well-separated spacecraft, STEREO will be able to examine the spatial extent and characteristics of traveling, interplanetary shocks and will also be able to observe composition differences resulting from differing seed populations. Comparing the measured ESP characteristics over a wide energy range with the magnetic field and plasma properties at several points will provide insight into the structure of the shock and related acceleration conditions.

2.5 Anomalous Cosmic Rays

Anomalous cosmic rays (ACRs) originate from both interstellar and heliospheric sources. The most abundant ACR species are those that have a large neutral component in the ISM, including H, He, N, O, Ne, and Ar (see, e.g., Cummings et al. 2002). Interstellar neutral atoms of these elements drift into the heliosphere, are ionized by solar UV or charge exchange with the solar wind to become pickup-ions, and are then convected into the outer heliosphere where they are accelerated to energies of tens of MeV/nucleon (Fisk et al. 1974). Pesses et al. (1981) first proposed that ACRs are accelerated at the solar-wind termination shock by diffusive shock acceleration, and ACR energy spectra of these elements at 1 AU and in the outer heliosphere out to 70 AU are consistent with those expected from shock acceleration models (Cummings et al. 2002).

Although Voyager 1 did not observe the expected shock-accelerated power-law spectrum in unmodulated form when it crossed the termination shock (Stone et al. 2005; McDonald et al. 2005), Voyager 1 did find a weak shock with a compression ratio of ~ 2.5 (Burlaga et al. 2005). It is possible that ACRs are accelerated at another location on the termination shock (e.g., McComas and Schwadron 2006; Stone et al. 2005), and it has also been suggested that ACRs are accelerated in the heliosheath (e.g., Moraal et al. 2006; Zhang et al. 2006).

Figure 17 shows 1 AU spectra for N, O, Ne, and Ar that were measured by ACE and Wind during the 1997–1998 solar minimum period (Reames 1999; Leske et al. 2000). Also shown are five other species measured at 1 AU, four of which—Mg, C, Si, and S—also exhibited low-energy increases at Voyager (as did Na) (Cummings et al. 2002), but of much lower intensity than the abundant ACR elements. Since species such as Mg, Si, and Fe should be either ionized or locked up in grains in the ISM (e.g., Slavin and Frisch 2002), their origin is unclear but must be from the heliosphere.

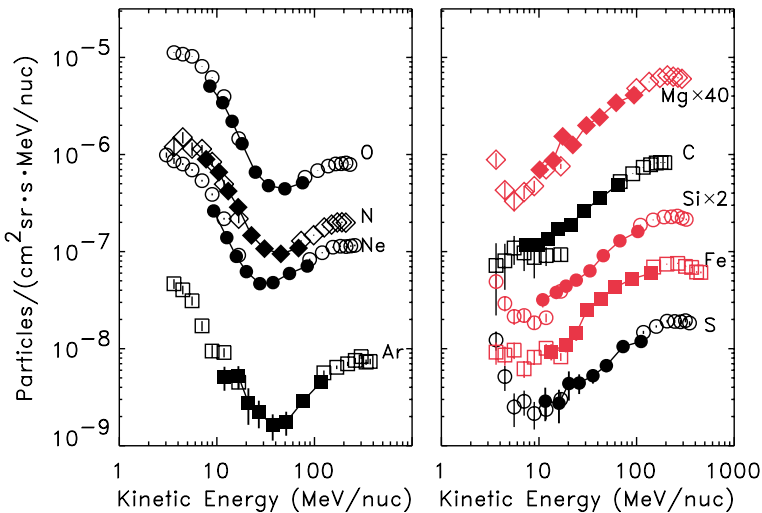
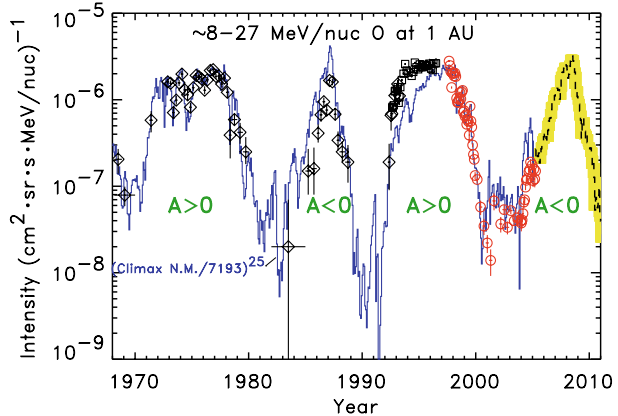


Fig. 17 Solar minimum spectra showing ACR contributions to N, O, Ne, and Ar (*left side*), along with similar, but much smaller contributions to the 1 AU spectra of five other species (*right side*). The data are from ACE and Wind (from Leske et al. 2000)

Fig. 18 Time history of ACR oxygen from 1968 to 2006, based on measurements from OGO-5, IMP-7&8, SAMPEX, and ACE. Also shown is the Climax neutron monitor count rate, scaled to the 25th power. The expected profile for 2007–2010 is shown in yellow



It has been suggested that these additional rare-ACR species could originate from the “inner source” of pickup ions associated with dust grains near the Sun (e.g., Cummings et al. 2002) or from an “outer source” of pickup ions originating in the Kuiper Belt (Schwadron et al. 2002). Cummings et al. (2002) also found that the energy spectra of ACR Mg, Si, and S measured at 1 AU with the Wind spacecraft (Reames 1999) did not fit the modulation model using the same modulation parameters that fit the more abundant ACR elements. This puzzle and the mystery of the origin of the rare ACRs will be addressed during the 2007–2008 solar minimum, when the intensities are expected to reach a maximum (see Fig. 18), using the LET and HET sensors in combination with instruments on ACE. LET and HET complement the SIS and CRIS instruments on ACE by providing coverage that extends to lower energy and by making much better measurements of H and He spectra.

If the minor ACR species (C, Na, Mg, Si, S, and Fe) do originate from pickup ions formed from Kuiper Belt material, then the source of these pickup ions is much more confined to

the ecliptic than are interstellar pickup ions. The difference in the latitude distribution of the Kuiper Belt and interstellar pickup ion sources might be expected to result in a solar-cycle dependence in the ratio of minor-ACR species to major-ACR species, which has, to our knowledge, not yet been modeled.

3 Instrumentation

3.1 Design Requirements

To achieve the objectives discussed in Sect. 2 the LET sensor had to satisfy several design requirements. These were ultimately derived from the STEREO Mission Requirements Document (taking into account allocated resources), which states that the SEP suite shall measure the intensity, composition, energy spectra, and direction of energetic protons from 0.06 to 40 MeV, heavier ions from ~ 0.03 to 40 MeV/nucleon, electrons from ~ 0.03 to 6 MeV, and ^3He -rich solar particle events. The STEREO Level-1 Requirements Document states that:

LET shall measure SEP ion fluxes, spectra, and composition in two oppositely directed 100×30 deg or better FOVs, covering the energy range from 3–25 MeV/nucleon for C to Fe ions, 1.5–13 MeV/nucleon for He, and 1.5–3 MeV for H. The mass resolution shall be better than 0.35 amu for ^3He and ^4He . Time resolution shall be 1 minute for H and He Beacon data, and 15 minutes otherwise. LET shall handle at least 1,000 events/sec.

The above statement has led to the requirements and goals summarized in Table 3, which were used to drive the detailed design of the instrument. Table 3 also shows the present capability of the two LET instruments, which meet or surpass essentially all of these requirements.

3.2 Approach

The LET instrument employs the well-established dE/dx vs. total energy technique to determine the nuclear charge, and in some cases the mass, of detected heavy ions. This particle-identification technique uses the energy loss signal from a detector that the particle fully penetrates (ΔE) and the energy deposited in a following detector in which the particle stops (E'), together with the thickness penetrated in the ΔE detector (L) to obtain an estimate of the particle's charge, Z , as follows (Stone et al. 1998b):

$$Z \cong \left(\frac{k}{L(2 + \varepsilon)^{a-1}} \right)^{1/(a+1)} (E^a - E'^a)^{1/(a+1)}. \quad (1)$$

Here $E = \Delta E + E'$, $2 + \varepsilon$ is the mass-to-charge ratio of the nuclide being considered, and k and a are constants obtained by approximating the range-energy relation for heavy ions in silicon in the form $R \cong k(M/Z^2)(E/M)^a$, where R and M denote the particle range and mass, respectively. In the energy range covered by LET $a \cong 1.55$ and $k \cong 18.6$ when R is expressed in μm of Si and E/M in MeV/nucleon. In the course of data analysis these values are adjusted to fit the observed relationship between ΔE and E' .

Table 3 LET design requirements

Description	Requirement	Goal	Capability
Field of view	2 oppositely directed 100° × 30° fans	2 oppositely directed 130° × 30° fans	2 oppositely directed 133° × 29° fans
Energy range (MeV/nucleon)	H: 1.8–3; He: 1.8–13 O: 4–25; Fe: 4–25	H: 1.4–6; He: 1.4–13 O: 2.5–25; Fe: 2.5–25	H: 1.8–12; He: 1.8–15 O: 4–50; Fe: 4–50
Geometry factor (cm ² sr)	H, He: 0.5 $6 \leq Z \leq 26$: 2	H, He: 0.9 $6 \leq Z \leq 26$: 4.5	H, He: 4.04 $6 \leq Z \leq 26$: 4.04
L1 noise level	<90 keV rms	≤60 keV rms	<30 keV rms for 25 μm thick L1
L1 thickness uniformity	$\sigma_T \leq 0.6 \mu\text{m}$ rms	$\sigma_T \leq 0.3 \mu\text{m}$ rms	$\sigma_T = 0.44 \mu\text{m}$ rms (typical)
Element resolution	Resolve: H, He, C, N, O, Ne, Mg, Si, Fe	Also resolve: Na, Al, Ar, Ca	Resolve: H, He, C, N, O, Ne, Na, Mg, Al, Si, S, Ar, Ca, Fe, Ni
⁴ He mass resolution	≤0.35 amu	≤0.25 amu	L1L2: 0.23–0.33 L1L2L3: 0.13–0.16
Maximum event rate	1,000 per sec	5,000 per sec	1,000–2,000 per sec
Energy binning	6 intervals per species for $Z \geq 2$; 3 for H	8 intervals per species for $Z \geq 2$; 3 for H	~10 intervals per species for H and $Z \geq 2$
Onboard species identification	H, He, C, N, O, Ne, Mg, Si, Fe	Add ³ He, S, Ar, Ca	H, ³ He, ⁴ He, C, N, O, Ne, Na, Mg, Al, Si, S, Ar, Ca, Fe, Ni
Time resolution	H, He: 1 min $Z \geq 6$: 15 min Telemeter 1 event/s	H, He: 1 min $Z \geq 6$: 1 min Telemeter 4 events/sec	H, He: 1 min $Z \geq 6$: 1 min Telemeter 4 events/s
Beacon telemetry	1 min for H, He, $Z \geq 6$	1 min for H, He, $Z \geq 6$	1 min for H, He, $Z \geq 6$

3.3 The LET Sensor System

The sensor system is illustrated with a three-dimensional drawing in Fig. 19 and in cross-section in Fig. 20a. The active elements are all silicon solid-state detectors and include three different detector designs, designated L1, L2, and L3. Table 4 lists the nominal characteristics of each of these detector designs. The geometry used for segmenting the detectors into multiple active elements is illustrated in Fig. 20b.

The instrument has 10 entrance apertures, each occupied by an L1 detector. Five of these are arranged along an arc of a circle that in flight lies in the ecliptic plane and is centered along the direction of the nominal Parker spiral magnetic field, generally toward the Sun. The other five are located 180° from these, centered on the same direction but facing generally away from the Sun. The central area of the instrument contains four additional detectors,

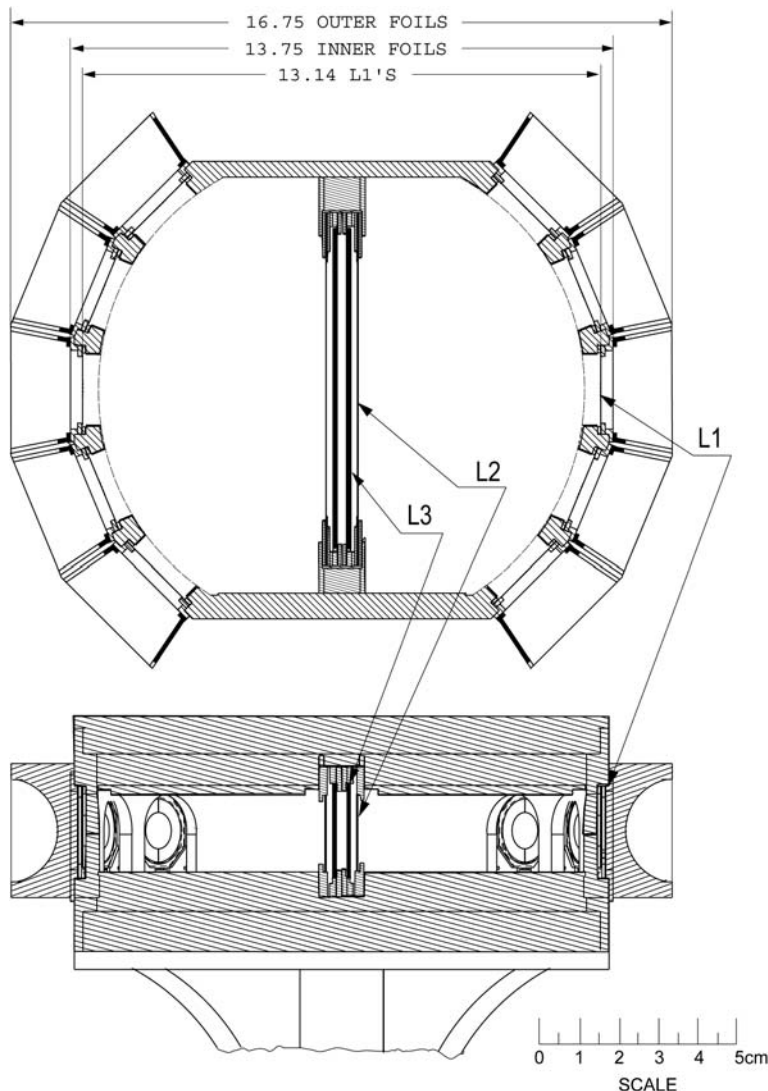


Fig. 19 Two cut-away views of the LET sensor system illustrate the locations of the detectors, entrance foils, and collimators, as well as structural components

including two L2 and two L3 devices. Each detector is segmented into multiple active areas, as indicated in Table 4. This provides some position sensitivity, which is used for determining particle trajectories, as well as for reducing noise and improving instrument performance when exposed to high intensities of incident particles. Each segment of each detector (a total of 54 signal sources) is separately pulse height analyzed to obtain a measure of the energy deposited by the particle in that segment.

The sunward- and antisunward-facing halves of the detector array are designated the "A" and "B" sides of the instrument, respectively. The labels used to designate the various detector segments are shown in Fig. 20. Coincidence between the L1 and L2 detectors defines

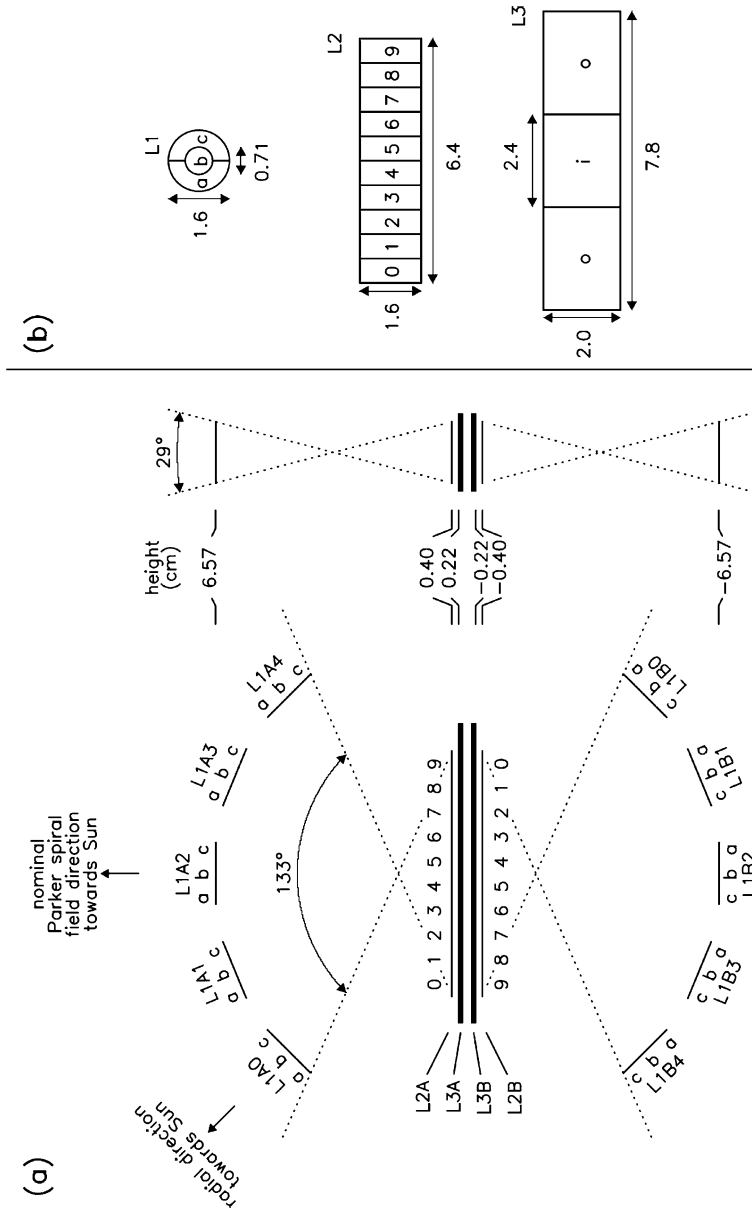


Fig. 20 Panel (a) shows a cross-sectional view of the LET detector system together with the limits of the field of view. The L1A2 detector is oriented generally sunward along the nominal direction of the Parker spiral magnetic field on both spacecraft. On the Ahead spacecraft the L1A0 points radially towards the Sun, as shown in the figure. On the Behind spacecraft L1A4 lies along the radial direction towards the Sun. Panel (b) illustrates the sizes and segmentation of the LET detectors. Each of the three segments on the L1 detectors and the 10 segments on the L2 detectors is individually pulse height analyzed. The L3 detector signals are processed with two pulse height analyzers, one for the inner segment (i) and the other for the combination of the two outer segments (o)

Table 4 Detector design characteristics

Detector designation	Number in LET instrument	Thickness (μm)	Active area (cm^2)	Active segments per detector
L1	10	24	2.0	3
L2	2	50	10.2	10
L3	2	1000	15.6	2*

*The two outer regions of each L3 detector are connected to the same PHA channel

the instrument field of view comprising two approximately fan-shaped regions extending $\pm 14.5^\circ$ normal to the ecliptic and $\pm 66.5^\circ$ about the nominal Parker spiral field direction within the ecliptic plane (Fig. 20). The disk-shaped detector assembly is mounted between the LET electronic boards yielding a compact design that has relatively short signal connections between detectors and front-end electronics and in which the electronic boards and housing provide a degree of shielding against out-of-geometry particles.

Nuclei that enter the instrument through one of the L1 detectors, penetrate into the following L2 detector, and subsequently come to rest in that L2 detector or in one of the two L3 detectors that are the most useful for charge identification. Using the signal from the detector in which the particle stops as E' and the signal from the preceding detector as ΔE one obtains a set of distinct tracks, one for each nuclide, on a plot of ΔE vs. E' . Figure 21 illustrates the nominal response tracks (solid lines) for selected nuclides stopping at various depths in the LET instrument for the case where the particles penetrate the ΔE detector normal to its surface ($\theta = 0^\circ$).

The measured signals will be displaced slightly from the nominal track positions when the particle penetrates the ΔE detector at some larger angle, θ , or at a position where the detector thickness differs from the nominal value, L_0 . Approximate information about the angle of incidence is available since the pulse height data indicate which detector segments the particle passed through. Detector thickness maps derived from laboratory measurements (see Sect. 3.4) or from flight data can be used to better estimate the thickness at the point penetrated. If $f = L/L_0$ is the ratio of the actual thickness penetrated to the nominal detector thickness (combining the effects of both the incidence angle and the detector thickness nonuniformity), then the measured ΔE and E' signals can be scaled so that they lie on the track corresponding to the nominal detector thickness, L_0 , and $\theta = 0^\circ$. Examination of (1) shows that dividing E' and ΔE by $f^{1/a}$ accomplishes the desired transformation (recall that $E = \Delta E + E'$). Figure 22 illustrates this procedure using the results of a Monte Carlo simulation of the LET response to an isotropic distribution of particles having power-law energy spectrum with intensity proportional to E^{-2} . In the upper left panel the uncorrected measurements of ΔE obtained from L1 vs. E' from L2 are shown for particles stopping in L2. These data, corrected for the mean thickness of the penetrated L1 segment and for the mean angle between the hit segments in L1 and L2, are plotted in the upper right panel of Fig. 22. Corresponding uncorrected and corrected plots for particles stopping in L3 are shown in the lower panels. This correction technique is the basis for the onboard particle identification performed by LET.

To obtain energies of the incident particles, corrections must be applied to the sum of the measured ΔE and E' energies to account for unmeasured energy losses in overlying material. This material includes any detectors preceding the ΔE detector as well as a pair of thin windows mounted in front of each L1 detector to keep the sensor assembly light tight and to provide a degree of protection from micrometeorites. The energy losses in the

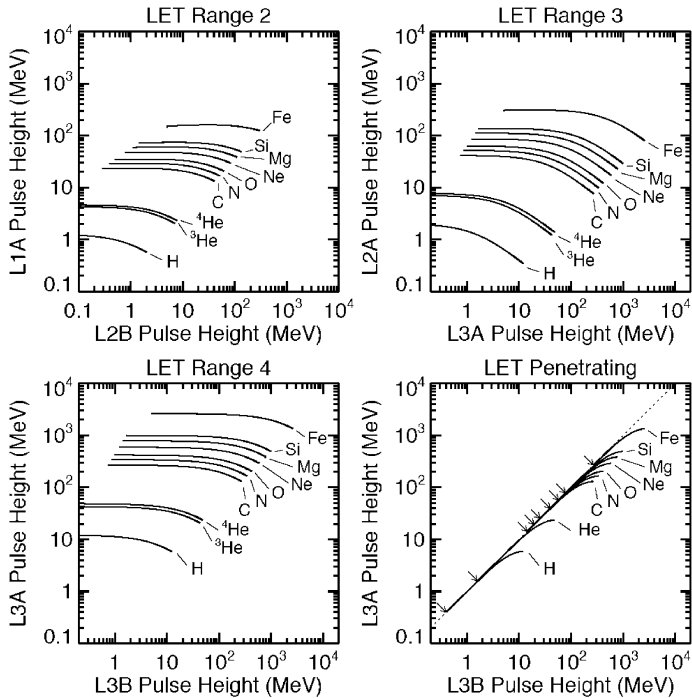


Fig. 21 Ideal response tracks are shown for selected energetic ion species normally incident on a stack of detectors of thicknesses 24 μm (L1A2), 50 μm (L2A), 1,000 μm (L3A), and 1,000 μm (L3B). Ranges 2, 3, and 4 include particles that stop in L2A, L3A, and L3B, respectively. On the “penetrating” panel, which includes particles energetic enough to exit through the back surface of L3B, arrows indicate the high-energy end points of the various element tracks. Note that the tracks that are plotted show the average response and do not include fluctuations due, for example, to energy loss fluctuations or uncorrected variations of incidence angle (see Fig. 22)

detectors preceding the ΔE detector are directly measured, while the energy loss in the windows (consisting of two layers of 8- μm thick Kapton foil, which together contribute an energy loss equivalent to that in $\sim 12 \mu\text{m}$ of Si) is calculated by scaling from the energy loss measured in L1.

Because of the importance of the isotope ${}^3\text{He}$ for identifying material from impulsive solar particle events (see Sect. 2.2), LET is designed to resolve ${}^3\text{He}$ from ${}^4\text{He}$ over much of the measured energy range. Tracks for different isotopes of an element are displaced slightly from one another on a ΔE vs. E' plot, corresponding to the fact that the quantity ε in (1) depends on the particle’s mass-to-charge ratio ($\varepsilon = M/Z - 2$). Figure 21 illustrates the difference in the nominal response tracks for the isotopes ${}^3\text{He}$ and ${}^4\text{He}$. In addition to ${}^3\text{He}$ and ${}^4\text{He}$, a few other key isotope pairs (e.g., ${}^{20}\text{Ne}$ and ${}^{22}\text{Ne}$) should be distinguishable in the upper portion of the LET energy range where the resolution is best.

The response tracks are broadened by the finite resolution of the instrument, which is attributable to a number of different effects (discussed in detail by Stone et al. 1998c). Typically the most significant contributions to the uncertainties in the charge and mass determinations of dE/dx vs. total energy instruments are attributable to the statistical nature of the energy-loss process (Landau fluctuations) and to errors in L , the thickness of material penetrated in the ΔE detector due to uncertainties in the angle of incidence and to uncorrected

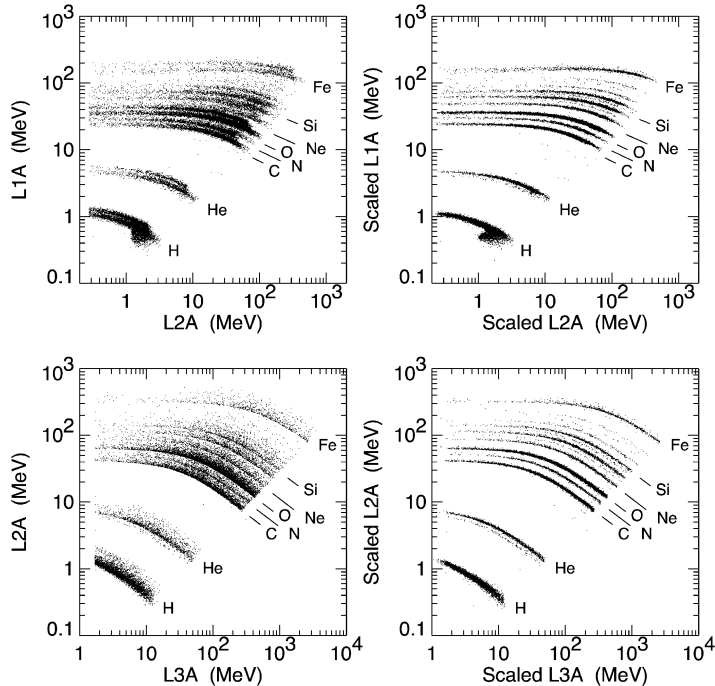


Fig. 22 Monte Carlo simulation of the LET response to particles incident from the A side and stopping in the L2A (upper panels) or L3A (lower panels) detectors. The left-hand panels show the actual energy losses while the right-hand panels show the same events after approximate correction for variations in incidence angle and detector thickness, as described in the text. The simulation includes the effects of incidence angle variations, L1 detector thickness variations (based on the measured detector characteristics for the A-side detectors on the Ahead spacecraft), Bohr/Landau fluctuations in the particle energy losses, and electronic noise. An incident particle population with typical gradual event composition was assumed, except that H and He were suppressed by factors of 5,000 and 500, respectively, and ${}^3\text{He}$ was set to be 10% of ${}^4\text{He}$. The multiple tracks for individual elements in the upper left panel are due to the differences among the thicknesses of the five L1A detectors

nonuniformities in the detector thickness. The charge and mass resolution were determined from a combination of Monte Carlo simulations and accelerator calibrations, which are discussed in Sect. 4.5 and Sect. 4.2, respectively.

3.4 Silicon Detectors

Photographs of the three different detector designs used in LET are shown in Fig. 23. All of the detectors were manufactured by Micron Semiconductor Ltd. starting from high-resistivity float-zone-refined n -type silicon wafers with (100) crystal orientation. These wafers were lapped and polished to the desired detector thicknesses. This mechanical thinning to produce the very thin, fragile wafers needed for the L1 detectors had a relatively poor yield and led to the use of detectors with thicknesses ranging from 22 to 30 μm (average 24 μm , see Table 4 and Appendix 1), somewhat thicker than the original design goal of 20 μm .

Boron ions were implanted on one surface to produce pn junctions in the desired pattern of active elements, as illustrated in Fig. 20b. Around the periphery of the active area, thin

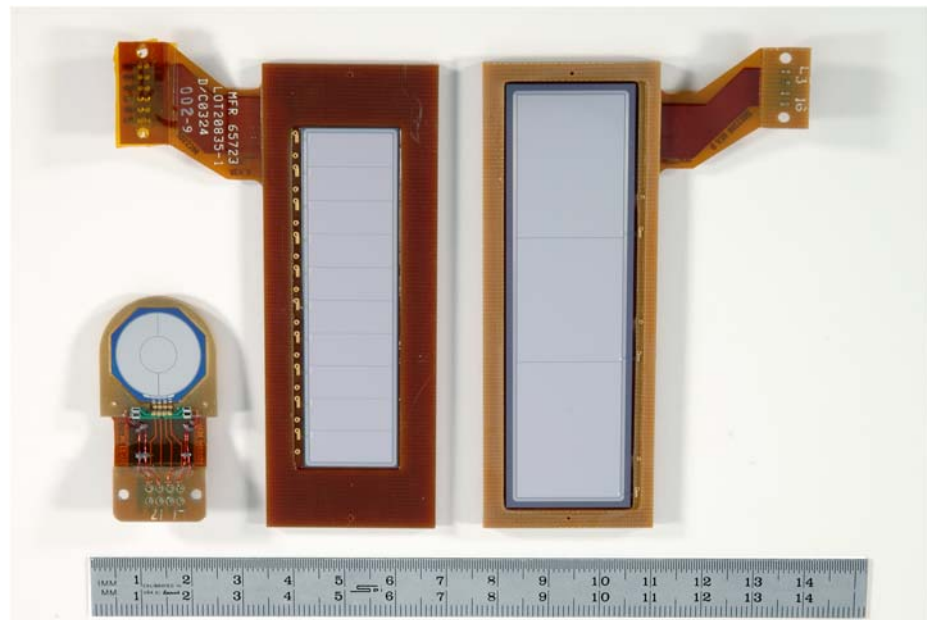


Fig. 23 Photographs showing (from left to right) examples of L1, L2, and L3 detectors. These views from the junction surfaces of the detectors show the segmentation into multiple active areas. The opposite (ohmic) surfaces consist of a single, full-area contact in each detector design. Detectors are installed by the manufacturer in multilayer circuit board mounts with flexible metallized Kapton strips for making electrical connections to the LET bias and pulse height analysis circuitry

guard rings were implanted to help avoid regions of high electric field that could increase the detector noise. On the opposite surface of the detector, phosphorus was implanted to form a single ohmic contact. Aluminum was subsequently evaporated over the implanted areas on each surface. Finally, a thin layer of SiO_2 was deposited over the detector surfaces to protect against surface contamination. This SiO_2 was omitted on the flight L3 detectors because thermal-vacuum tests (discussed later) suggested that it was contributing to a long-term instability of the leakage current in these thicker detectors, which are operated at relatively high bias voltages.

The silicon detector chips were installed in custom-designed detector mounts using a silicone resin (Shin-etsu KJR-9022E). These mounts were fabricated as multilayer FR4 or polyimide circuit boards including a flexible Kapton circuit layer on which the signals are brought out to a connector that could be plugged into the circuit board containing the pulse height analysis electronics (see Sect. 3.5.1). Connections between the active detector elements and the associated pads on the detector mount were made using redundant sets of wirebonds made with 25- μm -diameter aluminum wire. Pull tests were performed to assure good bond quality.

Electrical and environmental tests were performed to qualify individual detectors for flight prior to assembly of the flight instruments. Measurements of detector capacitance vs. bias voltage (CV test) and leakage current vs. bias voltage (IV test) established the voltages at which each detector becomes fully depleted and breaks down, respectively. For the L3 and L2 detectors, maps of pulse height vs. position on the detector were made using a collimated source of 5.8 MeV alpha particles from a ^{244}Cm source. Since the range of the

alpha particles (~ 33 microns of Si) is less than the L2 and L3 detector thicknesses, one should obtain a narrow pulse height distribution that is consistent across the detector when the ionization charge is being collected with high efficiency. With the alpha particles incident on the detector from the ohmic surface these measurements are sensitive to the local depletion characteristics of the detector, which generally vary from point to point because of nonuniformity in the doping of the silicon crystals from which the detectors were fabricated. Response maps made at a series of bias voltages were used to determine the minimum bias at which the detector was fully depleted over its entire area. The depletion voltage determined in this way is consistently higher than the average depletion voltage obtained from the CV test. In flight the detectors are operated at fixed bias voltages of +5 V, +10 V, and +175 V for L1, L2, and L3, respectively.

All of the LET detectors were subjected to a thermal-vacuum stability test in which they were exposed to temperature extremes of -25°C and $+40^{\circ}\text{C}$. During the test the detectors were continuously biased and their leakage current and noise were monitored. The test included an extended period (typically >3 weeks) at the warm temperature extreme, which was intended to uncover latent instabilities in the detectors. These tests demonstrated a long-term leakage current growth in L3 detectors that were made with a protective SiO_2 coating (discussed earlier) and led to the replacement of all of the flight L3 detectors with devices that did not have this coating.

Prior to delivery from the manufacturer the detectors were subjected to a random vibration test as part of their qualification. Because the L1 detectors are very thin ($20\text{--}30\ \mu\text{m}$), microscopic chipping of their edges, which can occur when detectors are sawed out of a larger silicon wafer, can lead to cracks that may propagate into the active area of the device when subjected to mechanical stress. Before the final assembly of the flight instruments the L1 detectors were put through an acoustic screening test to eliminate devices that could subsequently fail in this way.

A precise knowledge of detector thicknesses is needed in order to correct the ΔE and E' signals so that measurements from all combinations of detector segments can be mapped onto a common response track (see Sect. 3.3). For the L1 detectors, thickness maps were made by using a collimated beam of 8.78 MeV alpha particles from a ^{228}Th source. A thick detector placed behind the L1 was used to measure the residual energy of the alpha particles that passed through this thin device at each of 12 points distributed over its surface. These residual energy values were translated into detector thicknesses by comparison with measurements on a set of thin aluminum foils of known thickness. The left-hand panel of Fig. 24 shows a typical L1 thickness map obtained in this way. The right-hand panel shows the measured correlation between the L1 thicknesses obtained from the alpha particle maps and detector capacitances measured with the devices fully depleted. Since the area of each segment is known (Table 4) and capacitance scales inversely with thickness for a simple parallel-plate capacitor, this type of correlation can be used as the basis for estimating the thicknesses of detectors that are too thick to be measured using available alpha particle sources. Appendix 1 summarizes the thickness measurements that were made for all of the flight L1 detectors.

Preliminary measurements of thicknesses for some of the L2 and L3 detectors were derived from data obtained with energetic heavy ions during a cyclotron calibration run (see Sect. 4.2). Such data are not available for all of the flight detectors because some devices were replaced subsequent to the cyclotron run. An initial estimate of the relative thicknesses of the unmapped L2 detector segments was obtained from laboratory measurements of the capacitances of individual detector elements made with the detector fully depleted (cf. Fig. 24 right panel).

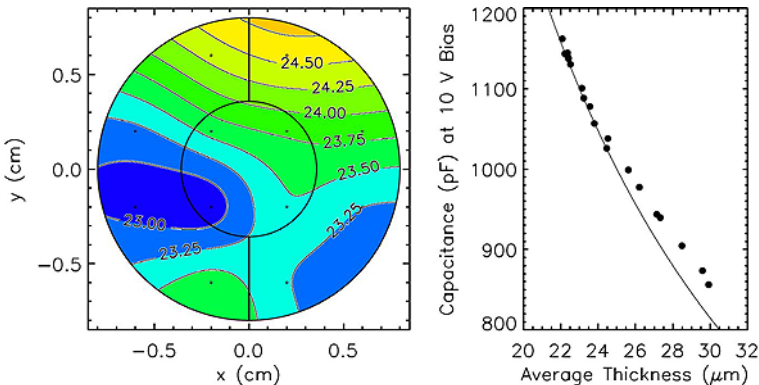


Fig. 24 *Left-hand panel* shows the thickness map of one of the L1 detectors obtained by measuring the residual energy of a collimated beam of alpha particles incident at 12 different locations centered on the positions indicated by the *small circles*. Thickness contours are labeled in μm . *Right-hand panel* shows the measured correlation between average L1 detector thickness and detector capacitance for the 20 flight L1 detectors. For these measurements all three detector segments were combined. The line indicates the ideal capacitance vs. thickness relationship expected from a silicon detector with the 2 cm^2 active area of an L1 device and a thickness equal to the plotted physical thickness minus a total of $3 \mu\text{m}$ dead thickness, which could be due to conductive layers on the two surfaces caused by ion implantation and subsequent diffusion during annealing. The tight correlation between thickness and detector capacitance was used to obtain estimates of the segment-to-segment thickness variation of L2 detectors, which were too thick to be measured with available alpha particle sources

Heavy ion data collected in flight will be used to obtain final thickness values for all of the L2 and L3 detector segments. As is clear in the simulations shown in Fig. 22, H, He, and several of the heavier elements are unambiguously identifiable on a plot of ΔE vs. E' even without applying corrections for incidence angle and detector thicknesses; most of the abundant heavy ions in ranges 3 and 4 become well-resolved when corrected for incidence angle using a nominal detector thickness. To refine the estimate of a detector thickness, (1) is solved for L and evaluated using measured ΔE and E' values in flight data selected for a given species with known Z .

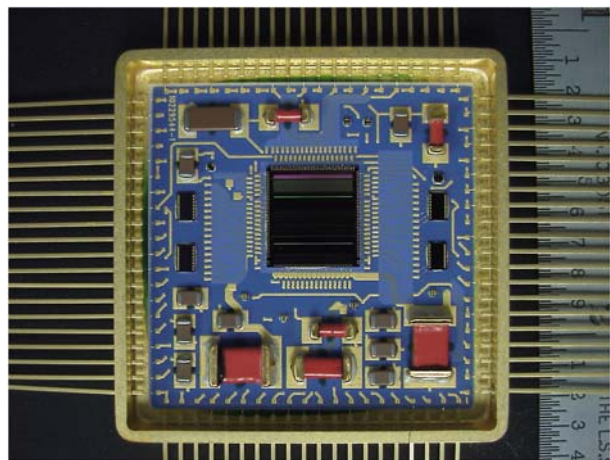
3.5 Electronics

The SEP suite is organized as four distinct instruments serviced by a block of common electronics, “SEP Central”, that includes low voltage and detector bias supplies, as well as a microprocessor that coordinates data and command flow, and provides a single-point interface with the IMPACT DPU (see Fig. 2). Three of the four instruments contain microprocessors in close contact with the detector front-end electronics to support onboard high-speed identification of particle species and energy. Very tight power and mass constraints inspired two innovations: a custom designed pulse height analysis ASIC and a unique FPGA-embedded microprocessor based on the Minimal Instruction Set Computer (MISC) architecture. The custom ASIC, used in both LET and HET, and the unique processors used in LET, HET, SIT, and SEP Central, are discussed in detail in the following sections.

3.5.1 The PHASIC

The silicon detectors in LET are read out using a Pulse Height Analysis System Integrated Circuit (PHASIC). The PHASIC was custom designed for the STEREO mission

Fig. 25 Photo of the PHASIC hybrid. The package dimensions are $31.8 \text{ mm} \times 31.8 \text{ mm}$. The PHASIC chip (located in the center) has dimensions of $7.4 \text{ mm} \times 7.4 \text{ mm}$



and contains 16 identical channels of pulse height analysis (PHA) circuitry. The PHASIC represents an evolution of similar PHA designs which were flight-proven in numerous space instruments over the past 40 years (Halpern et al. 1968; Halpern and Marshall 1968; Harrington and Marshall 1968, 1969; Harrington et al. 1974; Althouse et al. 1978; Cook et al. 1993; Stone et al. 1998b, 1998c). The key technical development is the use of CMOS rather than bipolar technology and the inclusion of all passive components on the ASIC.

Relative to the prior design employed in the SIS and CRIS instruments on ACE (Stone et al. 1998b, 1998c) the PHASIC performance is improved in several areas: (1) board space is reduced by a factor of 16 (see picture in Fig. 25), (2) power consumption is lower by a factor of 4, and (3) dynamic range is larger by a factor of 5. The very wide dynamic range of $\sim 10,000:1$ is achieved with a dual gain approach. Each preamplifier output signal is coupled to two shaping amplifier/offset-gate/peak-detector/Wilkinson-ADC chains that operate in parallel, but with gains that differ by a factor of 20. The separate low and high gain on-chip Wilkinson-ADCs each provide 11-bit resolution and excellent differential linearity. The system is designed for positive-polarity input signals.

The PHASIC supports high rate, low deadtime analysis via bipolar shaping with a primary time constant of $1 \mu\text{s}$, time to peak of $1.9 \mu\text{s}$, and a 32 MHz clock rate for the Wilkinson-ADCs. In addition, on-chip digital circuitry provides sparsified parallel readout of ADC conversion results, and control of the PHAs.

The PHASIC offers a high degree of programmable reconfigurability that allows a single design to accommodate a wide range of different detector capacitances, leakage currents, and signal ranges. Programmable items include: the preamplifier gain (feedback capacitance), the preamplifier input FET transconductance, and the peak detection threshold. The preamplifiers are DC coupled to the detectors and a 10-bit current DAC is provided on-chip at each preamplifier input to aid in balancing and measuring the detector leakage current. A built-in precision test pulser for each dual-gain PHA chain is used for functional test and calibration.

The PHASIC chip was fabricated using American Microdevices Inc.'s $0.5\text{-}\mu\text{m}$ CMOS process (C5N) incorporating high-density linear capacitors and high value resistors suitable for mixed-signal designs. For STEREO applications the chip and supporting passive components are mounted on a ceramic substrate and installed in a standard 80-pin Kovar package to form a "PHASIC" hybrid. Prototype tests place the total dose tolerance at

Table 5 PHASIC chip specifications

Number of dual-gain PHAs	16
Power	9 mW per active PHA* + 30 mW per chip
Dynamic range	10,000 (full-scale/trigger-threshold)
Integral nonlinearity	<0.05% of full scale
Differential nonlinearity	<1%
High/Low gain ratio	20
ADC type	Wilkinson
ADC resolution (both gains)	11 bits, 12th bit overflow
Shaping	Bipolar, 1.9 μ s to peak
Preamp feedback capacitance	5–75 pF, programmable in 5-pF steps
Radiation tolerance	Total dose to \sim 15 krad, latchup-free to at least 80 MeV/(mg/cm ²)
Gain temperature coefficient	<50 ppm/ $^{\circ}$ C
Offset temperature coefficient	<0.1 channel/ $^{\circ}$ C
Operating temperature range	-30 to +50 $^{\circ}$ C
Threshold programmability	up to 6% of F.S. (each gain), 10-bit resolution

* Each dual-gain PHA chain can be separately powered on or off

\sim 15 krad. With use of guard banding, the chip has been found to be latch-up free to at least 80 MeV/(mg/cm²).

Table 5 summarizes key characteristics of the PHASIC chip. In the STEREO application, for a 20- μ m thick detector with 440-pF capacitance, the estimated noise level is 30 keV rms. A photo of the PHASIC hybrid is shown in Fig. 25.

3.5.2 The Minimal Instruction Set Computer (MISC)

The microprocessor used in LET and SEP Central is the P24 MISC (Minimal Instruction Set Computer), designed at Caltech with the aid of Dr. C. H. Ting. The design derives from earlier MISC implementations developed by Chuck Moore (MuP21; see <http://www.ultratechnology.com/mup21.html>) and C. H. Ting (P8 and P16) and is simple enough to fit within a field-programmable gate array (FPGA), yet powerful enough to provide the needed onboard event analysis capability. The microprocessor used in HET and SIT is called the CPU24 and is based on the P24, implemented with some modifications at GSFC to tailor the processor to their applications. Both the P24 and CPU24 designs are implemented in the ACTEL 54SX72-S FPGA, which provides radiation tolerance with its triple-voting architecture.

The MISC employs a RISC-like instruction set with four 6-bit instructions packed into a 24-bit word. Instructions are executed consecutively after a word is fetched from memory. The most significant bit of each instruction designates an I/O buss operation when set. For I/O buss instructions the second most significant bit specifies a write when set, and a read when cleared, while the remaining four bits specify the I/O buss address. For non-I/O buss instructions the most significant bit is cleared and the remaining 5 bits specify 32 possible instructions, 31 of which are implemented.

Following is a list of distinctive features of the P24:

- 24-bit address and data busses
- 6-bit RISC-like CPU instructions

4-deep instruction cache
 24-deep data stack
 24-deep return stack
 Uses about 75% of 54SX72A FPGA registers and logic modules
 Current implementation runs at 6.4 MHz, using <0.25 W.

The MISC has the following registers, all 24 bits wide:

- A Address Register, supplying address for memory read and write
- I Instruction Latch, holding instructions to be executed
- P Program Counter, pointing to the next program word in memory
- R Top of Return Stack
- S Top of Data stack
- T Accumulator for ALU.

The return stack is used to preserve return addresses on subroutine calls. The data stack is used to pass parameters among the nested subroutine calls. With these two stacks in the CPU hardware, the MISC is optimized to support the Forth programming language.

3.6 Onboard Processing

3.6.1 Coincidence Logic

Whenever any detector in the LET instrument is triggered, the coincidence logic decides whether a valid event has occurred. The normal requirement for an event is a coincidence between L1A (logical OR of the 15 L1A segments) and L2A (logical OR of the 10 L2A segments), which gives an A-side event, or “Aevent”, or between L1B and L2B (giving a B-side event, or “Bevent”). However, the requirements for generating an Aevent or a Bevent signal are programmable—either the L1 or L2 requirement can be omitted, or an L3 requirement can be included (see Fig. 26). These options might prove useful if a detector were to fail.

Given an Aevent or a Bevent signal, several other requirements must be met before a valid coincidence signal is generated. These other requirements are also programmable. For instance, if the event is an internally generated calibration or livetime pulse (a STIM event [see Sect. 4.1], in which case `stimtag = TRUE`), and `reqstim` is set to `TRUE`, then only STIM events will generate a valid coincidence. An event is tagged as a “hazard” event if a new trigger occurs $< N \mu\text{s}$ after the coincidence logic is able to accept new events, where N is a commandable value (presently $2.8 \mu\text{s}$). Table 6 lists the state of the programmable inputs to the coincidence logic after LET is booted.

Once the requirements for a valid coincidence have been met, the event data are read out into a buffer and queued for subsequent processing by the LET onboard event processing software. The raw event data include six tag bits that indicate which of the six layers of the LET instrument were triggered. These tag bits are used to sort each event into one of 10 classes (see Appendix 2 for details). The number of events in each class is telemetered each minute (coincidence rates).

3.6.2 Nominal Detector Thresholds

The minimum energy deposit required to trigger a given high-gain PHASIC channel, commonly referred to as the “threshold”, is adjustable by command over a range that extends up to 6.3% of the high-gain full-scale energy, with a resolution of $\sim 0.1\%$ of the maximum threshold setting. In order to maximize the dynamic range of a PHA and to maximize the

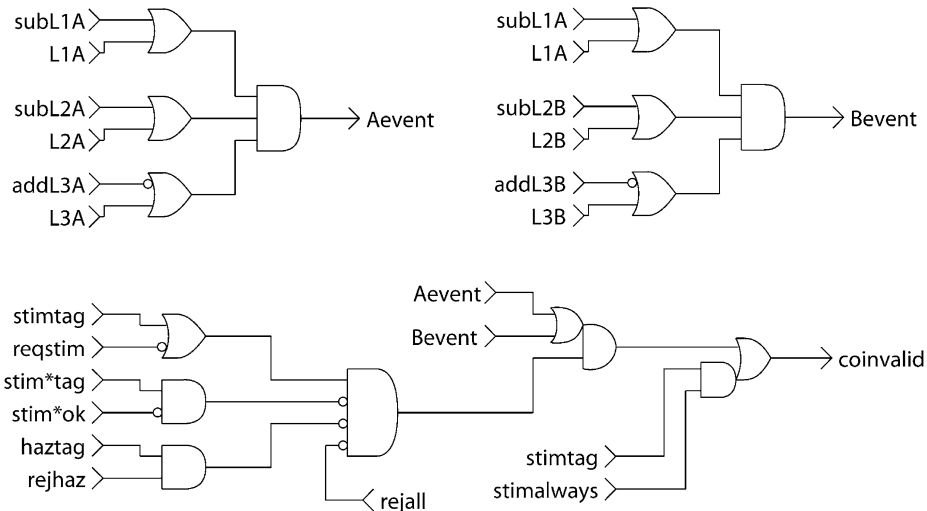


Fig. 26 A diagram of the LET Coincidence Logic. In the *above diagram* Aevent is a signal (from the front-end logic) indicating that the event is an A-side event, Bevent is a signal indicating that the event is a B-side event, stimtag is a signal indicating that the event is a STIM event, stim*tag is a signal that the event is an anti-STIM event (i.e., generated by the negative-going edge of the STIM pulse), hztag is a signal indicating that the event is a hazard event. For other items, refer to Table 6 in Sect. 3.6.1

Table 6 LET coincidence logic programmable inputs

Input	Nominal requirement	Description (effect when true)
subL1A	FALSE	Delete L1A requirement for Aevent
subL2A	FALSE	Delete L2A requirement for Aevent
addL3A	FALSE	Include L3A requirement for Aevent
subL1B	FALSE	Delete L1B requirement for Bevent
subL2B	FALSE	Delete L2B requirement for Bevent
addL3B	FALSE	Include L3B requirement for Bevent
reqstim	FALSE	Require STIM event for valid coincidence
stim*ok	FALSE	Allow anti-STIM events ⁺ to generate valid coincidence
rejhaz	TRUE	Reject events with hazard tags
rejall	FALSE	Reject all events. However, STIM events will still be accepted if stimalways is true.
stimalways	TRUE	Always accept STIM events

⁺An anti-STIM event is one generated by the negative-going edge of the STIM pulse

energy range over which protons can trigger a coincidence, it is desirable to set the high-gain L1 and L2 thresholds as low as possible (without allowing them to trigger excessively on noise). There is also a second consideration—it is important to avoid excessive triggering of L1 and L2 by electrons in order to minimize deadtime due to these triggers, and to avoid electron triggers that might lead to chance coincidences with other single-detector triggers.

Table 7 Nominal low- and high-gain thresholds and full-scale energies

Detector	Nominal high-gain threshold (MeV)	Nominal low-gain threshold (MeV)	Nominal low-gain full scale (MeV)
L1	0.174 (L1 centers), 0.205 (L1 edges) (depending on thickness)	5.4	920
L2	0.29	7	1,534
L3	1.3	18	3,989

For the L1 devices, laboratory measurements showed that the noise levels were generally lower in the center regions than in the edge regions, as expected from their lower capacitance (see Fig. 20b). In order to measure protons to as high an energy as possible with uniform directional response, the prelaunch thresholds of the ten L1 centers in each instrument were adjusted to a constant ratio of 7.05 keV/ μ m (Si), corresponding to the dE/dx of a 12-MeV proton (Janni 1966). The thresholds of the 20 L1 edge segments were adjusted to achieve a constant ratio of 8.3 keV/ μ m (Si), corresponding to the dE/dx of a \sim 10 MeV proton. Note that it is reasonable to set the thresholds of the L1 centers somewhat lower because during large SEP events proton measurements will be restricted to these segments once the “dynamic threshold” system raises the thresholds on the L1 edge segments (see Sect. 3.6.3). Following launch, when noise levels were found to be lower, it was possible to lower these thresholds and extend the proton energy coverage such that the mean keV/ μ m value for the L1 centers corresponds to the dE/dx of a 14.8 MeV proton, while the mean for the L1 edges corresponds to the dE/dx of a 12.3 MeV proton.

The L2 signals are less affected by noise than are the L1 devices. Following launch the L2 thresholds were all adjusted to 0.290 keV, corresponding to the dE/dx of a \sim 16.5 MeV proton. The prelaunch L3 thresholds were set to an average level of 1.7 MeV. Following launch they were lowered to 1.3 MeV. The nominal threshold settings in place in early 2007 are summarized in Table 7, along with the nominal low-gain full-scale energy values.

The electron sensitivity of the L1 and L2 devices was estimated using GEANT and an electron spectrum consistent with that measured in the October 28, 2003 SEP event (Mewaldt et al. 2005b). In addition, an exposure was made to a ^{90}Sr beta source. We expect that 0.5% of SEP electrons with >200 keV will trigger L1 and that $<0.03\%$ with >300 keV will trigger L2. According to the simulations, less than 4×10^{-5} of >500 keV electrons will trigger a coincidence. In flight the electron sensitivity of the L1 and L2 devices will be calibrated based on electron and proton spectra from the SEPT sensor (Müller-Mellin et al. 2007) during the onset of SEP events. If desired, the thresholds can be individually adjusted by command. Threshold changes are implemented via a programmable current source that changes the offset of the pulse height passed to the peak detector in a linear and predictable manner. Any threshold adjustments will therefore require updating the offset table used for the onboard analysis (Appendix 4) as well as modifying ground-based code used for the analysis of telemetered pulse-height events. The required offset change is equal to the threshold change, when measured in energy units.

It is planned that with these settings LET proton measurements will be obtained to high enough energy to overlap with the HET instrument (von Rosenvinge et al. 2007). The stated requirement for measuring protons in LET is 1.8 to 3 MeV (Sect. 3.1). The improvement in the maximum proton energy has been possible because of the better-than-expected noise

performance of the PHASIC chip and the fact that the L1 detectors are somewhat thicker than originally planned.

3.6.3 Dynamic Thresholds

During large SEP events the single-detector count rates can increase by a factor of as much as 10^4 due mostly to low-energy protons. These elevated single-detector count rates create instrument deadtime and also lead to chance coincidence events involving two separate particles. In order to minimize these effects the LET design includes “dynamic thresholds” in which the trigger threshold on selected PHAs are increased during periods when the count rates are high. This action reduces the count rates of selected detectors, minimizing dead-time and effectively reducing the geometry factor for H and He events with minimal effect on the geometry factor for heavy ions with $Z \geq 6$.

The dynamic thresholds are implemented in a three-stage process that is controlled by the summed count rates of those selected detectors that do not participate, as summarized in Table 8 and Fig. 27. In the first stage, the high-gain ADCs on all 20 of the L1 outer segments are disabled. The effective threshold for triggering these devices is thereby raised from ~ 0.25 MeV to the low-gain thresholds, nominally set at 5 MeV (see Table 7). The result is that neither H nor He ions can trigger these higher thresholds except for particles incident at very wide angles (see Fig. 28). As a result, the geometry factor for H and He is reduced by a factor of 5.

In the second stage the high-gain ADCs are disabled on all but the center L1 centers (L1A2 and L1B2), providing a decrease in the effective geometry factor for H and He by a second factor of ~ 5 . At this point LET has reduced angular coverage for H and He ($\sim 90^\circ$ coverage instead of $\sim 130^\circ$), but the angular coverage for $Z \geq 6$ ions is not affected (except at the lowest and highest energies, where the L1 and L2 thresholds have some minor effects).

In the third stage the high-gain thresholds are disabled on all but the center two L2 segments on both the A and B sides (L2A4, L2A5, L2B4, L2B5 remain enabled), as well as the outside L3A and L3B segments. The nominal L2 and L3 low-gain thresholds are ~ 7 MeV and ~ 18 MeV, respectively, in order to be above the maximum energy loss of all but very wide-angle protons (see Fig. 29). This effectively reduces the geometry factor for H and He by an additional factor of ~ 4.5 .

The monitor count rate for this process is the sum of all singles rates that are not affected by these changes (the centers of L1A2 and L1B2; L2A4, L2A5, L2B4, and L2B5; and the centers of L3A and L3B). These monitor-rate trigger levels may be changed by command;

Table 8 Dynamic threshold trigger levels and geometry factors

Affected detectors	Trigger rate (counts/s)	Turn-off rate (counts/s)	H and He geometry factor (cm ⁻² sr)
L1 outsides	1,000	500	0.815
L1 centers except L1A2 and L1B2	5,000	2,500	0.175
All L2s but L2A4, L2A5, L2B4, L2B5; L3 outsides	25,000	12,500	0.0392

Fig. 27 Illustration of the effect of dynamic thresholds on the count rates and event readout from LET during a solar event with the composition and spectra of the July 14, 2000 (Bastille Day), SEP event. As the thresholds of various detector segments are gradually raised in response to the Monitor rate, the measured singles rate (labeled “scaled Singles”) and the H and He event rates are reduced, thereby preserving instrument livetime to record a greater sample of $Z \geq 6$ events

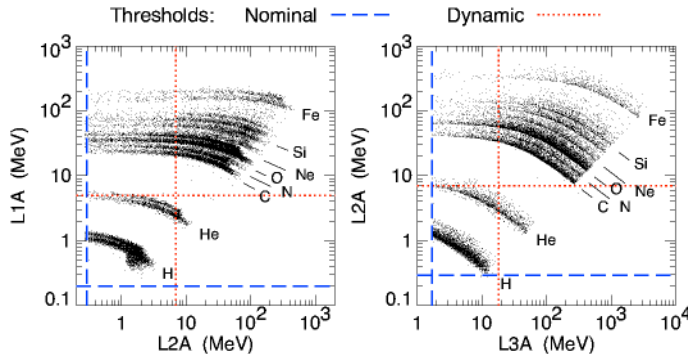
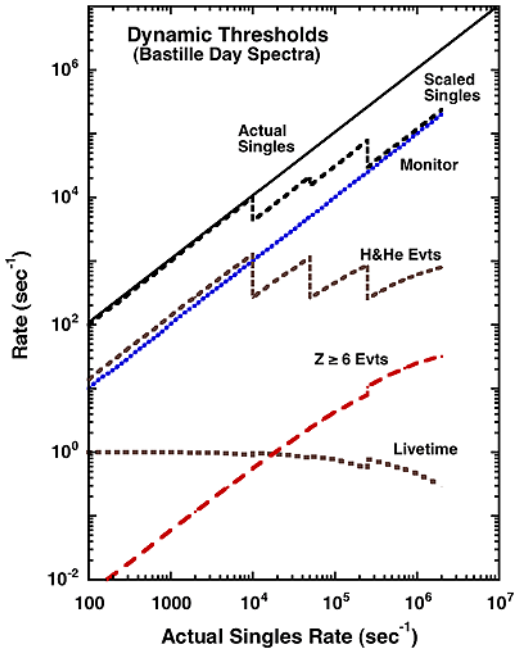
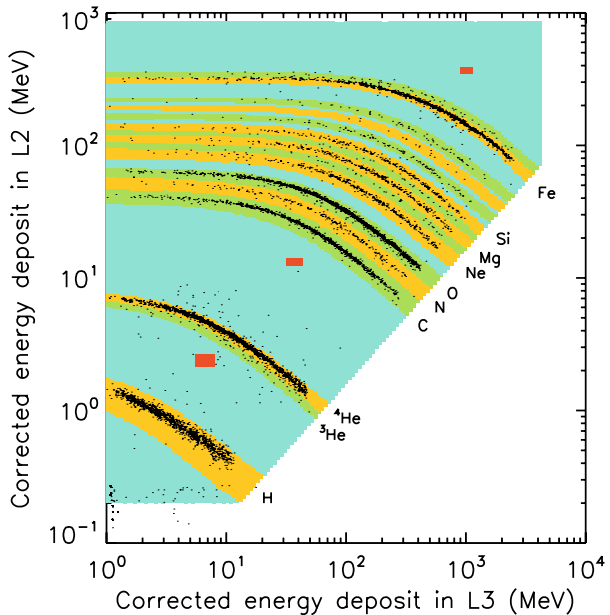


Fig. 28 Illustration of the nominal and dynamic thresholds for L1A•L2A events (left panel) and for L1A•L2A•L3A events (right panel)

the nominal levels are summarized in Table 8. In order to avoid toggling back and forth when the rates are near the trigger levels the dynamic thresholds for a given stage do not return to their nominal level until the count rates drop below the trigger level by some (commandable) factor (nominally = 2; see Turn-off Rate in Table 8). By disabling the high-gain thresholds, the singles rates in large events such as July 14, 2000 (Bastille Day event) and October 28, 2003 will be reduced by a factor of ~ 10 , with a corresponding increase in livetime (see Fig. 27). The state of the dynamic threshold currently implemented is indicated by two of the “miscellaneous bits” (see Table 20, Appendix 3) in the LET Science Data Frame, allowing the variable thresholds to be properly accounted for in calculating the true particle rates.

Fig. 29 The Range 3 (L2 vs. L3, or L2L3) LET matrix. Foreground species are H, ^3He , ^4He , C, N, O, Ne, Na, Mg, Al, Si, S, Ar, Ca, Fe, and Ni, and these are shown in alternating green and yellow bands. Background regions are blue, and live STIM boxes are shown in orange. The data points are from the December 13, 2006, SEP event. Note that only 1 in 100 of the events below C have been plotted



3.6.4 Onboard Particle Identification System

The telemetry bandwidth allocated to LET (576.5 bps) is adequate to telemeter only a fraction of the events recorded by the sensor. The raw data for ~ 4 events/second can be telemetered, while the onboard particle identification system processes up to $\sim 1,000$ events/second. The objective of the onboard event processing software is to analyze the data gathered for each event and assign a species and energy to the particle that generated the event. For certain species–energy combinations, direction of incidence information is also calculated onboard. In addition, the Range is calculated. Range 2 events trigger only an L1 and an L2 on the same side (but not the L3 on that side). Range-3 events trigger an L1, and L2, and L3 on the same side (but not the other L3), and Range 4 events trigger both L3A and L3B (see Table 19).

ADC-calibration events (see Sect. 4.1) are buffered for telemetry but are not assigned a species or energy onboard. For each non-ADC-cal event acquired by the LET sensor, the onboard software performs the following operations:

1. Sort the event into one of 10 classes based on the tag bits in the event data (see Sect. 3.6.1 and Appendix 2). Increment the appropriate coincidence rate counter based on the classification, and decide whether the event is valid for further processing. An event having one or more of the following properties is not valid:
 - a. Classification of ERROR or 2TEL based on the tag bits.
 - b. Events that have multiple hits above a certain threshold in a single detector layer of the instrument.
 - c. Events for which the particle trajectory results in an ambiguity in deciding whether the particle stops in the instrument or escapes out the side.
 - d. Events with pulse-height data from an invalid combination of detector layers (the trajectory is not a straight line).
2. For valid Range 2, 3, or 4 events:

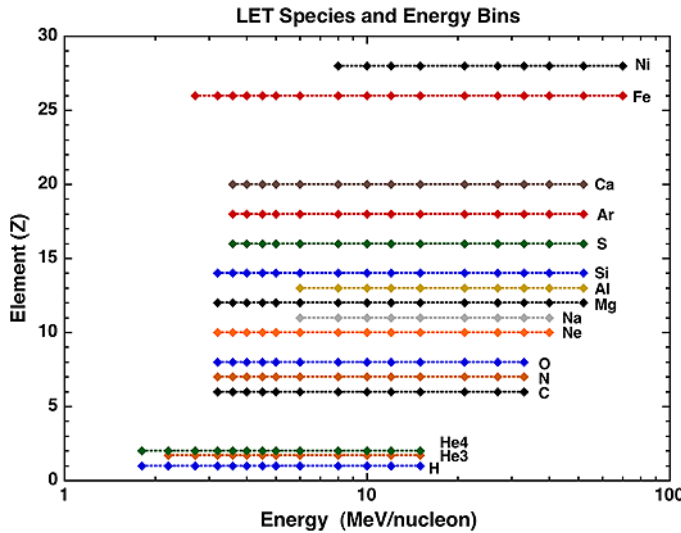


Fig. 30 LET species and energy bins identified in onboard processing

- a. Perform gain, detector thickness, and incident angle corrections on the raw pulse-height data from each detector layer.
 - b. Determine the species (proton, ${}^3\text{He}$, ${}^4\text{He}$, C, etc.) of the particle by mapping corrected ΔE and E' signals into a two-dimensional detector response matrix. The matrix for Range 3 events is shown in Fig. 29.
 - c. Determine the total energy of the particle by summing the energy signals from each detector layer and correcting for energy loss in the entrance window.
 - d. For Range 3 events, treat the particle as an invalid event if the energy in the L2 layer is less than the energy in the L1 layer.
 - e. For Range 3 and 4 events, treat the particle as an invalid event if the L1/L2 energy ratio is below a commandable threshold.
 - f. Map the particle into a species–energy/nucleon bin using the calculated species and total energy, and increment the appropriate rate counter. The species and energy bins into which the onboard software maps particles are shown in Figs. 30 and 31.
 - g. For selected species/energy ranges, determine look-direction (direction of incidence) using the Range 1 and Range 2 detector-combination for the event, and increment the appropriate sectored rate counter (see Sect. 4.7).
3. For invalid events: Sort the event into one of four bins: Range2-LowZ, Range2-HighZ, Range3/4-LowZ, Range3/4-HighZ. The largest signals in each layer are compared with software threshold levels in a simple algorithm to perform this sort.
 4. Prioritize all events for telemetry using the priority scheme described in Sect. 3.6.5.

Some of the operations performed onboard deserve more detailed description:

Detector thickness and incident angle corrections: Section 3.3 describes how the ΔE and E' signals can be scaled so that they lie on the track corresponding to the nominal detector thickness, L_0 , and $\theta = \theta_0$. In the onboard processing, lookup tables are used to provide the appropriate correction factors for each range and $\Delta E-E'$ detector combination.

Treatment of events with multiple hits in a single detector layer: A large signal in one channel of a PHASIC can cause small cross-talk signals in other channels on the same

Species	Z	A	Threshold kinetic energy (MeV/nucleon)																
			1.8	2.2	2.7	3.2	3.6	4	4.5	5	6	8	10	12	15	21	27	33	40
H	1	1	2	2	2	23	23	23	23	3	3	3	3	3	3	34			
³ He	2	3	2	2	2	23	23	23	23	3	3	3	3	3	3				
⁴ He	2	4	2	2	2	23	23	23	3	3	3	3	3	34					
C	6	12				2	2	23	23	23	23	3	3	3	34	34			
N	7	14				2	2	2	23	23	23	3	3	3	34	34			
O	8	16				2	2	2	23	23	23	3	3	3	34				
Ne	10	20				2	2	2	23	23	23	23	3	3	3	34			
Na	11	23							3	3	3	3	3	3	3	3	3	3	
Mg	12	24				2	2	2	2	23	23	23	23	3	3	3	34	34	
Al	13	27								3	3	3	3	3	3	3	3	3	
Si	14	28				2	2	2	2	23	23	23	23	3	3	3	34	34	
S	16	32				2	2	2	2	23	23	23	23	3	3	3	3	3	
Ar	18	36								23	23	23	23	3	3	3	3	3	
Ca	20	40								2	2	23	23	3	3	3	3	3	
Fe	26	56				2	2	2	2	2	23	23	23	3	3	3	34	34	
Ni	28	58									3	3	3	3	3	3	3	3	

Fig. 31. Chart of the species and energy bins identified by onboard processing indicating the detector layers (Ranges) where particles of a given energy/nucleon will stop, taking into account variations in the incidence angle. Thus, a 23 indicates that particles in this energy interval will stop in both Range 2 and Range 3. The energy labels represent the threshold energy of the bins shown in Fig. 30. Some of these bins will be populated only at small angles, and some will be populated only at wide angles of incidence

PHASIC. Bench and accelerator calibration tests show that these cross-talk signals never exceed an amplitude of ~ 20 ADC channels, and that they are not created unless the “real” signal is greater than ~ 750 ADC channels. An algorithm has been implemented in the on-board processing that attempts to identify cross-talk signals in events with multiple hits in a single detector layer. If, after discarding hits that appear to be the result of cross-talk, the event no longer has multiple hits, it is treated as a valid event.

There are a large number of programmable variables and tables used to control features of the onboard real time particle identification system. ADC offsets and gains, thickness and angle correction factors, allowed detector combinations, and other variables can all be changed by command. Various consistency cuts applied to each event can also be enabled/disabled or adjusted, as can the criteria used to identify signals arising from ADC cross-talk. These programmable items are described in Sect. 3.8.

3.6.5 The Priority System

The LET telemetry allocation is normally able to transmit about four complete PHA events/sec in addition to the count rate and housekeeping data (see Sect. 5.3). While this is expected to be adequate to transmit essentially all interesting events during quiet times, it will not be possible to keep up with the $Z \geq 6$ events, let alone the H and He event rate, during SEP events in which the intensity of $Z \geq 6$ ions with $E > 3$ MeV/nucleon is more than $\sim 1/\text{cm}^2 \text{ sr-sec}$. However, it is desirable to transmit as many $Z \geq 6$ events as possible at these times in order to obtain statistically accurate measurements of the abundance of elements not covered by the onboard particle identification system. In addition, it is especially important at these times to telemeter a broad selection of events in order to evaluate the performance of the instrument in an extreme environment. The LET priority system is designed to select a comprehensive sample of events for transmission while at the same time giving preference to those categories of events that are most interesting scientifically.

There are a total of 29 priority buffers, of which 27 are currently in use (see Table 9). Each of these buffers can hold up to eight events at a time. Events identified as belonging to an already full buffer are dropped after being counted. The events to be read out are selected by a “round-robin” system from a list of 240 entries. The “weight” assigned to a given buffer indicates the number of times the buffer appears on the list, so that buffers with heavier weights are read out more often. Thus, for example, every third entry on the list is for buffer number 3 (Range 3 ions with $9 \leq Z \leq 30$).

During solar quiet periods it will be possible to go through this list many times per minute since most buffers will be empty. During a large SEP event it should still be possible to cycle completely through the list once per minute, since many buffers are rarely populated and, on average, four events/second can be telemetered. Thus all 29 buffers will be read out at least once per minute if there are events available, with the oldest event in a given buffer read out first. Events need not be telemetered during the same minute in which they occurred; if an event’s readout is delayed, time bits are set in the event header to provide event latency information (see Latency Tag in Table 22).

The weights were assigned taking into account the scientific priority of the class of events, as well as their expected frequency of occurrence. Thus, since events with $Z \geq 40$ have high scientific priority, they are given five slots even though it is very unlikely that five events will occur in one minute. Range 3 events with $9 \leq Z \leq 30$ are given the greatest weight (occur most often on the list) because they provide the opportunity to measure the spectra and abundances of additional species not covered by the onboard analysis. The assigned weights can be altered by command.

Table 9 LET priority buffers

Buffer	Weight	Description
0	6	ADC-cal
1	5	Range 2, 3, or 4 with $Z \geq 40$
2	5	Range 2, 3, or 4 with $31 \leq Z \leq 39$
3	80	Range 3 with $9 \leq Z \leq 30$
4	40	Range 2 with $9 \leq Z \leq 30$
5	30	Range 3 LiBeB and CNO
6	15	Range 2 LiBeB and CNO
7	8	Range 4 LiBeB, CNO, and $9 \leq Z \leq 30$
8	2	Range 4 or “Range 5” penetrating $Z > 30$
9	8	Matrix-sort Reject events with L3 and $Z \geq 3$
10	4	Matrix-sort Reject events with no L3 and $Z \geq 3$
11	4	Range 3 ^3He
12	3	Range 2 ^3He
13	3	Range 4 or “Range 5” penetrating $3 \leq Z \leq 30$
14	5	Range 3 ^4He and He background
15	1	Range 4 He
16	4	Range 2 ^4He and He background
17	4	Range 3 H
18	1	Range 4 H
19	4	Range 2 H
20	2	Matrix-sort Reject events with L3, $Z < 3$
21	1	Matrix-sort Reject events with No L3, $Z < 3$
22	1	Range 4 or “Range 5 penetrating” H and He
23	1	Range 2, 3, or 4 “Backward” events
24	1	“Clean” Livetime STIM events
25	1	“Poor” Livetime STIM events
26	1	ERROR - Onboard processing of event was aborted due to an error
27	6	Spare
28	5	Spare

3.6.6 Livetime Measurement

The fraction of the time for which the LET front-end electronics are “alive” and able to respond and read out data for incident particle events is measured using a gated counter in the FPGA logic. The counter is enabled only when the front-end electronics are in the “ready” state, awaiting a trigger. Additionally, the livetime is monitored by the periodic creation of artificial “Livetime STIM” events using the PHASIC built-in test pulsers. These events are designed with specific pulse heights and detector trigger combinations to mimic events of each of the three ranges (Range 2, Range 3, and Range 4) at three different pulse height levels in each range, and are processed entirely through the onboard analysis software in the same way as particle-induced events. The Livetime STIM events with pulse heights falling within their expected boxes in the event matrices (Fig. 29 and Appendix 3) are referred to as “clean”, while those falling outside the boxes are “poor” (Table 9). “Poor” Livetime STIM events may appear during high-rate periods such as SEP events when the Livetime STIM

pulse heights are distorted by chance coincidences with real particle events. The known generation rate of these events allows a cross-check on the gated counter livetime measurement.

3.7 LET Data

LET science and housekeeping data are accumulated and transmitted at one-minute intervals. LET is allocated 16 CCSDS packets of science data per minute in telemetry (see Sect. 5.3). The data formatted into these 16 packets constitute a LET Science Frame. The contents of the LET Science Frame are described in Appendix 3. The 11-byte header and 1-byte checksum for each 272-byte CCSDS packet are not included in the LET Science Frame format. Therefore, one minute of LET science data corresponds to $16 \times 260 = 4,160$ bytes, and this defines the length of one LET Science Frame. The LET CCSDS packets are transmitted once every three seconds to SEP Central, with nulled and unused 17th through 20th packets following the 16 Science Data packets. The SEP Central MISC fills in time stamps and checksums in the CCSDS packets before passing them to the IDPU. Due to the 16 CCSDS packet LET telemetry allocation, SEP Central transmits only 16 packets for each LET Science Data Frame and does not transmit the empty 17th through 20th packets. However, the limit is commandable, so that up to 20 packets may be used for data if more bandwidth becomes available to LET later in the mission.

LET generates and sends rate, pulse height, and housekeeping data at intervals of one minute. Data collected during one minute are packaged and transmitted in CCSDS packets over the next minute. Rate and pulse height data are packaged and sent in a LET Science Frame (see Appendix 3). LET housekeeping data are transferred to SEP Central once per minute to be combined with housekeeping data from the other SEP sensors and telemetered in a separate SEP Housekeeping CCSDS packet (see Sect. 5.3). Housekeeping data sent by LET include leakage currents from all detector segments as well as four temperatures measured on the LET electronics board.

3.7.1 LET Beacon Data

STEREO Beacon data are to be broadcast continuously for tracking by NASA, NOAA, and other partners around the world. Much like the Real Time Solar Wind (RTSW) system on ACE (Zwickl et al. 1998), these data are meant to provide a snapshot of interplanetary conditions that can be used for forecasting and nowcasting of space weather. All four SEP sensors contribute to the Beacon data, broadcasting particle intensities on a one-minute time scale. The species and energy coverage provided by the four SEP sensors is illustrated in Fig. 32. During SEP events, it will be possible to construct time-intensity profiles and energy spectra using Beacon data for five key species (or species groups), including H, He, CNO, Fe, and electrons over a reasonably wide energy range. In addition, there is anisotropy (front to back) information available for ions and electrons in a range of energy intervals, and limited information on the ${}^3\text{He}/{}^4\text{He}$ ratio. Compared to the ACE RTSW coverage for energetic particles, STEREO Beacon data provide several times as many items, including, in particular, composition data for He, CNO, and Fe that are not available in ACE RTSW data, as well as much broader energy coverage.

Details of the species and energy coverage provided by LET are summarized in Table 10 [Beacon data from the other SEP instruments are discussed in Müller-Mellin et al. (2007), Mason et al. (2007), and von Rosenvinge et al. (2007)]. Each of the LET items is obtained from the onboard matrices described in Sect. 3.6.4 and Appendix 3. All items but three are summed over all directions of incidence; for one proton and two He intervals the data from

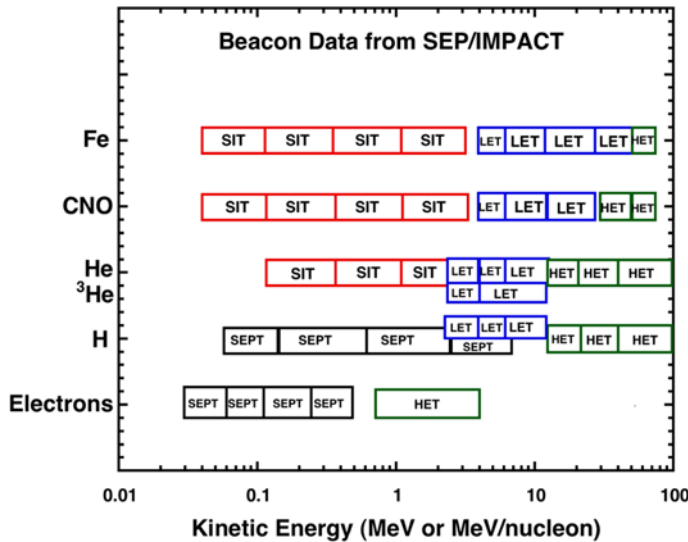


Fig. 32 Species and energy coverage provided in STEREO Beacon data by the four SEP sensors

the A and B sides of LET are separated in order to provide a rough measure of the intensity ratio of particles streaming away from and towards the Sun along the average interplanetary field line. The data from C, N, and O are summed in order to improve the statistical accuracy during quiet times and small SEP events.

Also broadcast in the LET Beacon telemetry stream are several items needed to compute absolute intensities, including the instrument livetime, and the trigger, hazard, and accepted event rates (see Appendix 3). The status of the dynamic threshold system is included so that the effect of disabling the high-gain thresholds for some detector segments can be factored into computing the effective geometry factor during any given minute (this only comes into play in large SEP events, as described in Sect. 3.6.3).

3.8 The Command System

The command system for the SEP suite of instruments is described in detail in Sect. 5. Briefly, SEP Central manages the command interface between LET and the spacecraft. SEP Central receives LET commands from the ground via the IMPACT IDPU as CCSDS telecommand packets (CCSDS 2000). SEP Central unpacks the commands and routes them to LET via a bidirectional serial command interface. Command responses from LET are routed back to the spacecraft via the same path. This section provides a summary of the key commandable functions and parameters in LET

There are a wide range of parameters and functions for the operation of the LET instrument that can be modified by command in order to optimize its performance and to preserve as many as possible of the instrument functions in the event of in-flight component failures or degradation. Table 11 summarizes these commandable functions. In addition, there are a wide variety of commandable parameters that control ADC thresholds, the ADC and live-time STIM pulsers, and in-flight calibration. It is also possible to modify the priority system, the event format, and various software parameters that define the classification and priority of events.

Table 10 LET beacon data

Species or item	Energy range (MeV/nucleon)	Geometry factor (cm ² sr)	Comments
Protons	2.2–4	4.0	Summed over 258°
Protons, A-side	4–6	2.0	A-side 129° sector
Protons, B-side	4–6	2.0	B-side 129° sector
Protons	6–12	4.0	Summed over 258°
⁴ He	2.2–4	4.0	Summed over 258°
⁴ He, A-Side	4–6	2.0	A-side 129° sector
⁴ He, B-Side	4–6	2.0	B-side 129° sector
⁴ He, A-Side	6–12	2.0	A-side 129° sector
⁴ He, B-Side	6–12	2.0	B-side 129° sector
³ He	2.2–4	4.0	Summed over 258°
³ He	4–12	4.0	Summed over 258°
CNO	4–6	4.0	Summed over 258°
CNO	6–12	4.0	Summed over 258°
CNO	12–27	4.0	Summed over 258°
Fe	4–6	4.0	Summed over 258°
Fe	6–12	4.0	Summed over 258°
Fe	12–27	4.0	Summed over 258°
Fe	27–52	4.0	Summed over 258°
Livetime counter			Scaled from 24 to 16 bits
Trigger rate			16-bit compressed
Hazard rate			16-bit compressed
Accepted event rate			16-bit compressed
Mode bits			Dynamic threshold state; Internal code check; Heater duty cycle; state of leakage current balancing.

Other LET commands are possible, but would first need to be qualified on the LET EM unit prior to execution on any flight unit. Commands related to boot-up, HV control, etc. are really SEP Central commands, and are described Sect. 5. A list of variables and tables that control features of the LET onboard real-time particle identification system is given in Appendix 4. The contents of these variables and tables are commandable.

3.9 Mechanical and Thermal Design

3.9.1 Mechanical Design

The mechanical design requirements for SEP included:

- provide clear instrument fields of view along the Parker spiral
- withstand vibration and acoustic environments at launch
- equalize internal and external pressures during launch phase
- provide a purge flow of dry nitrogen to protect detectors from volatile contaminants prior to launch

Table 11 LET command summary

Item	Comments
Instrument operation	
ADC thresholds	Adjust trigger thresholds for all ADCs
Coincidence logic	See Table 6 and Appendix 2
ADC STIM pulsers	Change pulse-rate, amplitudes
Livetime STIM pulsers	Change pulse-rate, amplitudes
Operational heaters	Change heater threshold settings
Dynamic threshold states	Enable/disable, plus the specifications of each state are programmable in detail
Data telemetry rate	The number of LET packets telemetered/minute is programmable. Extra packets would be filled with events.
Software parameters	
ADC offsets	Set low- and high-gain ADC offsets (ADC channels)*
ADC gain corrections	Set low- and high-gain ADC gain corrections*
Detector thickness corrections	Set detector thickness corrections*
L1 window corrections	Set L1 detector window thickness corrections*
Incident angle corrections	Set incident angle corrections for each L1–L2 detector combination*
Included detector combinations	Enable/disable each L1–L2 detector combination for inclusion in onboard processing
Look-direction sectors	Define L1–L2 detector combinations for each look-direction
Priority buffer slots	Define number of telemetry slots for each event priority buffer
Event categories	Define event categories based on combination of LET detector layers
Telemetered event format	Enable/disable telemetry of cross-talk ADC signals
Particle ID consistency cuts	Set max number of ADCs telemetered/event
Raw event integrity	Enable/disable consistency cuts for Range 3 and 4 events
Hi-Z/Lo-Z cuts	Enable/disable onboard checking/fixing of event headers
Crosstalk cuts	Set ΔE and E' levels for prioritizing events
	Set ADC levels for detection of cross-talk signals

*For use in onboard processing only. Settings do not affect telemetered events

- minimize weight
- provide RF shielding and a continuous, grounded electrostatic shield
- prevent light from reaching any of the particle detectors
- make it possible to meet the thermal requirements
- maintain a common design for each spacecraft to the extent possible

The initial proposal for the IMPACT Solar Energetic Particles (SEP) instruments had all the SEP telescopes on each spacecraft mounted together as a single unit. This was in part to meet the weight and power constraints. As the spacecraft design evolved, it became apparent that it was not possible to simultaneously meet the field of view constraints of each of the SEP telescopes and to have them mounted as single units on each spacecraft.

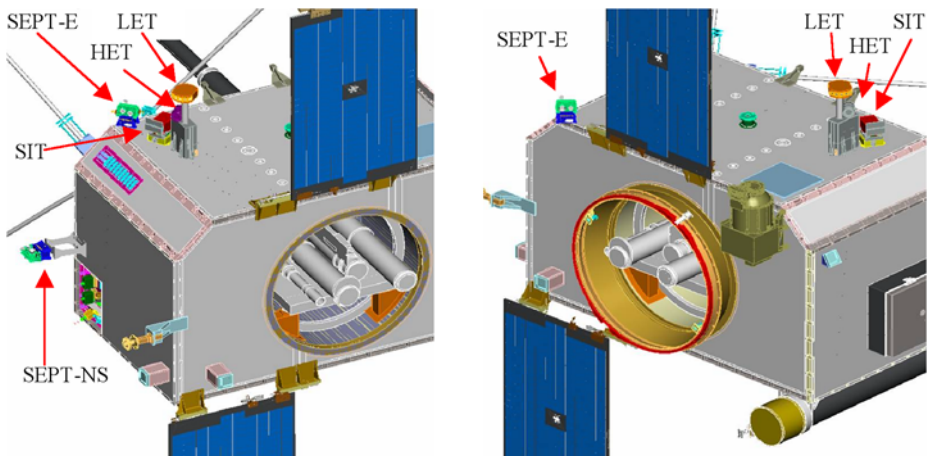


Fig. 33 The IMPACT SEP suite on the body of the Ahead (*left*) and Behind (*right*) spacecraft, including SEPT, SIT, LET, and HET. Note that the Behind spacecraft is shown upside down to indicate the placement of the SEP sensors (which are mounted on the panel facing the south ecliptic pole)

By and large, the Ahead and Behind spacecraft designs are identical. However, the orientation of the interplanetary magnetic field (IMF) at 1 AU affects the location of LET and other SEP sensors. The SEP Fields of View (FOVs) are oriented at 45° to the spacecraft–Sun line so as to look along the nominal Parker spiral direction at 1 AU. The Behind spacecraft is predominantly a copy of the Ahead spacecraft rolled 180° about the spacecraft–Sun line. This points each dish antenna towards the Earth and doesn't disturb the Sun-pointing instruments, but it does mean that the SEP instruments need to be repointed to view along the nominal Parker spiral direction. In order to clear the fields of view with different pointing directions, it was necessary to have different locations for some of the telescopes, including HET and LET, on the two spacecraft. The result is illustrated in Fig. 33. Note that all the SEP instruments on the Ahead spacecraft, with the exception of the SEPT-NS, are on the spacecraft panel that faces the north ecliptic pole, whereas these same instruments on the Behind spacecraft are on the panel facing the south ecliptic pole.

The HET and LET telescopes were kept together with SEP Central, as shown in Fig. 3. Clearing the LET and HET fields of view required raising them fairly high off the spacecraft deck in a direction perpendicular to the launch thrust axis. In particular, LET is mounted on a support tube protruding from the SEP Central enclosure. The support tubes for the Ahead and Behind spacecraft are different, holding the LET telescopes in positions which differ by 90° . Concern about the vibration of this arrangement was allayed initially by NASTRAN analysis of the design and subsequently by actual vibration tests.

Because the LET is located at some distance from SEP Central, the LET electronics are located in the same enclosure that holds the detectors. By contrast, the HET electronics are located inside the SEP Central enclosure. The LET electronics use two multilayer printed circuit boards, one above the detector volume and one below. The board containing the PHASICs, which is less radiation hard than other electronic components, is on the spacecraft-facing side of LET. The two boards are interconnected by a flex-circuit, and the connections between LET and SEP Central are carried by a flex-circuit that passes through the LET support tube. This arrangement minimizes the separation between the PHASIC preamplifier inputs and the detectors.

RF shielding and light-tightness are maintained by using overlapping double 90° edges wherever external covers and walls meet. All metal enclosures are iridized on the outside to maintain electrical continuity of the shield. Internal walls are black-anodized in order to promote thermal equilibrium. Vent holes and the natural gaps between mechanical parts provide venting paths to equalize the internal and external pressures during launch. This is required in part to prevent the rupture of thin foils covering the telescope apertures.

Prior to launch, internal Teflon tubing is used to introduce purge gas near the telescope detectors during ground operation, from whence it passes out through the electronics enclosures and escapes through the vent holes. The vent holes point the escaping gas away from the spacecraft in an effort to also carry away any possible dust. The purge gas is dry nitrogen derived from boil-off of liquid nitrogen. It is provided at 15 PSI and is filtered and restricted by sintered metal filters in the purge lines. The LET and HET purge rates are ~ 5 and ~ 1 liters/hour, respectively. Purging is nearly continuous until just prior to launch.

3.9.2 Thermal Design

The thermal design implementations are somewhat different for the LET/SEP Central units on the two STEREO spacecraft, but the design approach is the same. Since the spacecraft does not provide a well-defined thermal environment, the SEP Central enclosure is isolated from the spacecraft using Ultem bushings, which thermally isolate the mounting bolts from the spacecraft. Ground straps were specifically designed by UC Berkeley to provide electrical grounding of the SEP Central enclosure to the spacecraft while maintaining a minimum thermal conductivity.

The minimum and maximum temperatures are expected to occur in two critical situations. For the cold case, this occurs when the solar radiation is a minimum, the instruments are operating with the lowest heat dissipation in the electronic equipment, and the optical properties of the coatings have not been degraded. For the hot case, this occurs when the solar radiation is at the maximum, the instruments are in operational mode with the highest heat dissipation, and the optical properties of the coatings are degraded. The goal of the SEP/HET/LET thermal design is to manage the heat flow in a way that keeps the temperature of the assemblies within the required ranges of +30°C to -25°C operational and +35°C to -35°C nonoperational. The cooling approach includes passive radiators, which radiates to deep space. One important issue was to define the size and position of the radiators required during periods of high heat dissipation in the electronics and high external thermal loads. Conversely, these areas must not be so large that the temperatures would go below the allowed minimum during periods of low heat loads. The radiators are positioned on the side of the SEP Central electronics and LET housing that "see" deep space and consist of Mylar tape covered with a high-emissivity silver-Teflon coating.

Two types of electrical heaters are employed: operational and survival heaters. Operational heater power is enabled when the instruments are on and survival power is enabled when the instruments are off. The heaters are chip resistors mounted on the instrument circuit boards. The operational heater chip resistors are mounted on the LET circuit board only, whereas the survival chip resistors consist of two zones, one mounted on the LET circuit board and the other on SEP Central's Analog/Post-Regulator circuit board. The resistors are mounted near the board attachments to the housing so heat is conducted to the aluminum housing. The insides of both the LET and SEP Central electronics are black anodized to enhance radiation heat transfer. Radiation heat transfer is also enhanced with the conformal coating on the boards. Heat is radiated and conducted from the aluminum housing to the additional circuit boards and also to the detectors in LET.

The HET sensor is conductively coupled to the SEP Central electronics in order to maintain the desired temperature range. The LET operational heater on the Ahead S/C can supply 1.0 W (0.75 W on the Behind S/C) at 30.5 V and 75% duty cycle. The survival heaters in the Ahead LET/SEP Central can supply 4.3 W (4.75 W on Behind) at 25 V and 100% duty cycle. The operational temperature zone is controlled by a microprocessor that receives feedback from a local thermistor. The operational setpoint can be adjusted remotely via ground commands. At launch it was set at -10°C in both LET units. The survival heaters are controlled by the redundant set of mechanical thermostats that close at -26.1°C and open at -9.4°C . The predicted flight temperatures for the LET detectors are -11°C to $+27^{\circ}\text{C}$ for the Sun-facing side and -21°C to $+11^{\circ}\text{C}$ for the shaded side.

Inside LET/SEP Central there are eight internally read-out thermistors and two that are read out by the spacecraft for independent temperature verification and as the only temperature indicator when SEP power is turned off.

There was particular concern that the sunward staring LET detectors not get too hot. Two thin foils, each one-third mil thick Mylar, cover each LET aperture. The inner foil is a circular foil immediately adjacent to each L1 detector. The outer foil is a single long and narrow foil on each end of the LET telescope, covering five apertures. The foils seen in Fig. 3 have a high infrared emissivity ($\epsilon \sim 0.67$) and low solar absorptivity ($\alpha \sim 0.1$) coating (the so-called Goddard composite coating) facing away from the detectors and a low-infrared emissivity coating (double vacuum deposited aluminum with a combined thickness of $\sim 2.1 \text{ mg/cm}^2$) facing the detectors. The coating facing away from the detectors keeps the foils facing the Sun cool. The low-emissivity coating facing the detectors minimizes radiation heat transfer exchange between the foils and the detectors. In the event that an outer foil breaks the inner foil provides a redundant foil. The two foils in series also help minimize the radiative exchange between the detectors and outer foil. An outer indium tin oxide (ITO) coating, as required to meet the electrostatic cleanliness specification, is present on the outer surface of the outer foil only and only for the end of the telescope that does not see the Sun. This coating was applied on top of the Goddard composite.

All external areas with the exception of the radiators and telescope apertures are covered with multilayer insulation blanket. The total power dissipated by LET/HET/SEP Central is 6.05 watts.

3.10 Resources

The measured mass, power, and allocated data rate, and the heater power for LET and SEP Central, are summarized in Table 12. The LET mass numbers include the electronics, detectors, and the housing. In addition, LET is mounted on a tubular bracket that has a mass of 0.465 kg (see Fig. 3), and the thermal blankets weigh 0.180 kg (average of spacecraft A and B). The thermal blanket for SEP Central weighs 0.192 kg (average). Note that the SEP Central housing also encloses the HET electronics board. This resource is book-kept under the HET sensor.

The SEP Central power values include an efficiency of 56% for the low-voltage power supply (LVPS). The power values are average values. Note that if any sensor draws additional power for whatever reason, the power dissipation by SEP Central increases because of the 56% LVPS efficiency. The maximum power that SEP Central could draw is 4.842 W, which could occur if five separate LET detectors were short-circuited and if all other sensors are drawing their maximum power levels.

The data rate shown in Table 12 includes Science, Housekeeping, and Beacon data.

Table 12 Summary of LET and SEP central resources

Resource	LET	SEP Central
Mass (kg)	0.855	2.196
Power (W) (excluding heaters)	1.18	4.111
Data Rate (bps)	576.5	9.1
Op-heater power (W)	1.0 Ahead, 0.75 Behind	–
Survival heater power (W)	1.3 Ahead, 1.75 Behind	3.0 Ahead, 2.75 Behind

3.11 Electrical GSE

Electrical ground support equipment (EGSE) was developed for communication with SEP Central during development and laboratory testing. This EGSE consists of a pair of computers, one running Windows and the other running Linux. The Windows machine controls the operation of an IDPU Simulator, a custom-designed piece of hardware that has interfaces and functionality equivalent to those of the IMPACT flight IDPU (see Luhmann et al. 2007). Both the IDPU simulator and the software that controls it were supplied by UC Berkeley. The Linux system, which uses a TCP/IP interface to the Windows system, provides the capability to send ASCII commands and do binary uploads to SEP Central and the individual SEP instruments. It collects telemetry data from SEP, logs it to disk, and allows communication with remote computers by means of TCP/IP sockets. This latter feature makes it possible to monitor test data and generate commands from remote sites as well as locally. The Linux system also makes a variety of LET data displays including rates, housekeeping parameters in both raw and engineering units, and information from individual events.

For testing SEP when it is installed on the STEREO spacecraft the Linux system communicates directly with the IMPACT GSE, which provides the interface to the flight IDPU. The EGSE is used during early-orbit operations after launch to provide a real-time display of data collected during the STEREO telemetry pass.

4 Calibrations and Performance

4.1 Electronic Calibrations

Prior to being installed in the instruments, each PHASIC hybrid used in the LET PHA chains was individually tested over a temperature range of -35°C to $+45^{\circ}\text{C}$ in intervals of 20°C (-35°C , -15°C , $+5^{\circ}\text{C}$, $+25^{\circ}\text{C}$, and $+45^{\circ}\text{C}$). Within each assembled LET instrument, there are 54 test pulsers, one for each of the 54 electronics channels. These pulsers are driven by two pulser reference voltages, one for all of the L1 detector segments and one for all of the L2 and L3 segments. Each reference voltage is generated by an eight-bit DAC with two gain states that differ by a factor of 110. All test pulsers may be pulsed independently, or in coincidence, in any combination, although usually preprogrammed patterns of detector combinations are pulsed at a fixed grid of pulse heights.

There are two varieties of pulser-generated events. In order to monitor instrument livetime (see Sect. 3.6.6), “Livetime STIM” events are generated in detector segments L1A2b, L2A4, L3Ai, L1B2b, L2B4, and L3Bi (i.e., those detectors nearest the instrument centerline), simulating Range 2, Range 3, and Range 4 particles at three different pulse height levels each. The pulse height data from these events should fall into the STIM boxes in the

event matrices (Fig. 29 and Appendix 3). To avoid saturating the telemetry with Livetime STIM events, their pulse heights are assigned to low-priority readout buffers (buffers 24 and 25; see Table 9). It is the rates of these events, not their pulse heights, which are required to check the livetime measurement.

In order to check the linearity of the PHA response and routinely monitor the stability of all ADC gains and offsets and the electronic noise, a second type of pulser-produced event, “ADC-calibration” events, are periodically generated by pulsing at most a single detector in each of the six layers at 32 different pulse height levels which span the entire dynamic range. (The location of the thresholds on each PHA channel can also be measured on command with a more finely-spaced grid of pulses limited to smaller pulse heights.) A and B sides of the LET instrument are pulsed simultaneously for ADC-cal events, each of which contains an L1A and L1B detector. An L2 or L3 detector is pulsed along with an L1 segment on each side for 12 of the 15 L1s. Note that this pattern of detector hits, unlike those for the Livetime STIM events, does not mimic that expected for an actual particle event (see Appendix 2). In order to be recognized onboard as a legitimate instrument trigger and undergo pulse height analysis, special provisions were made in the coincidence logic for these ADC-cal events (Sect. 3.6.1 and Fig. 26).

In the default normal mode, 3.5 pulser events are generated every second, however, this rate is programmable on command. Normally 9 seconds out of every 10 are devoted to Livetime STIM events, with 1 second out of every 10 used for ADC-calibration events, some of which get read out each minute (buffer 0; Table 9). The detector configuration and pulse height level is changed at most only once per second. Thus, with 15 different detector configurations (each of which includes one L1A and L1B segment, as described earlier) at 32 different levels being pulsed for one second out of every 10, it normally takes 4,800 seconds (or 80 minutes) to cycle through all 54 ADCs over the entire dynamic range. A commandable mode which disables Livetime STIM and generates only ADC-calibration events may be used to assess the health of all ADCs in only eight minutes, which proved useful during preflight environmental testing.

The ADC-cal events have shown that linearity for all channels is better than $\sim 0.2\%$ even at the largest pulse heights. Furthermore, since the electronic noise of the high-gain L1 channels is dominated by the detector capacitance of the thin (~ 24 micron) L1 detectors, the RMS width of the pulsed events is well-correlated with the detector thickness, as illustrated in Fig. 34. This provides a useful check on detector integrity after environmental tests such as the acoustics and vibration tests.

4.2 Accelerator End-to-End Test and Calibration

An engineering model of LET was tested at the Lawrence Berkeley Laboratory (LBL) 88" Cyclotron in March 2004 using a mixed, “cocktail” beam (McMahan 2005) of heavy ions ranging from ^{10}B ($Z = 5$) to ^{209}Bi ($Z = 83$). Although the low-beam energy (4.5 MeV/nucleon) limited the range of most species to Range 2 events, the test proved that the new LET electronic designs could resolve heavy ions over a wide range of intensities and that the instrument had sensitivity to ions ranging from H up to very heavy ions.

A much more thorough accelerator calibration was performed on both LET flight units at the National Superconducting Cyclotron Laboratory (NSCL) at Michigan State University (MSU) in July 2004 using a beam of 140 MeV/nucleon ^{58}Ni ($Z = 28$). A variable-thickness target upstream of the instrument, consisting of a water-filled bellows aligned with the beam and mounted on a translation stage driven remotely by a stepper motor, allowed the ^{58}Ni beam to be stopped at any desired depth within LET. By continuously varying the thickness

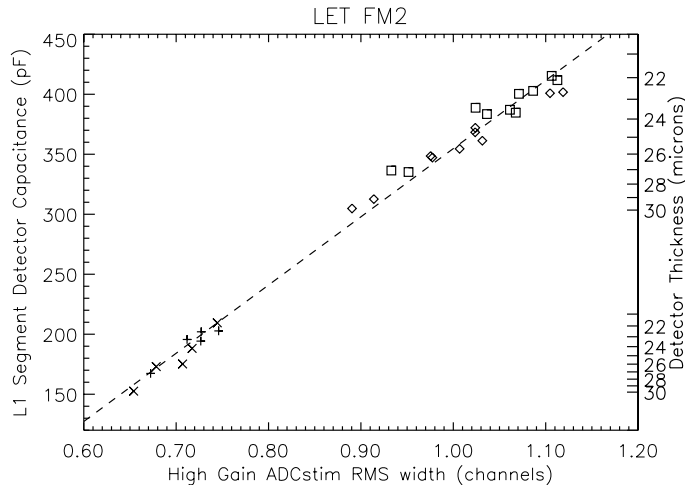


Fig. 34 Calculated L1 segment detector capacitance (based on thicknesses indicated on the right-side axis as determined using alpha particles (see Appendix 1) vs. measured rms width of the high-gain onboard pulser-generated pulseheights. Electronic noise for these thin detectors is dominated by the detector capacitance, which produces a tight correlation and provides a useful tool to check for broken detectors after environmental testing. Crosses and plusses are for circular center segments on sides A and B, respectively, while diamonds and squares are for the larger, semi-annular edge segments on sides A and B

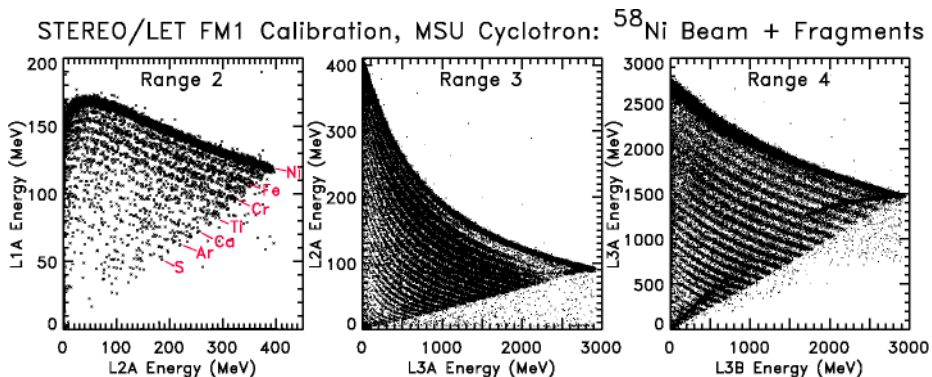


Fig. 35 ^{58}Ni beam and fragment data from the end-to-end test of LET at the MSU cyclotron. Resolution for Ni under the conditions shown is approximately 0.18, 0.17, and 0.07 charge units for Range 2, 3, and 4, respectively

of the water target, complete tracks of Ni at all depths in the instrument were obtained, while by increasing the water thickness in order to stop the Ni beam and serve as a fragmenter, samples of all elements from H to Ni were produced, as illustrated in Fig. 35. These and similar data were collected with LET mounted in a vacuum chamber (to avoid the otherwise substantial amount of dead material that air would introduce between the L1 and L2 detectors). The entire vacuum chamber was mounted on a rotation stage so the beam could enter LET at a variety of incidence angles, all of which were tilted 5° off the horizontal to avoid a primary channeling plane of the (100) silicon detectors.

In addition to mapping the element track locations to better define the onboard matrix boxes, test the accuracy of low-energy heavy-ion range-energy relations, and demonstrate the detector and ADC response with species, energy, and angle, the accelerator tests were used to calibrate and check the performance of a variety of the instrument functions described in Sect. 3.6. These include: (1) the coincidence logic, (2) real-time particle identification, (3) the priority and readout systems, (4) nominal detector thresholds, (5) livetime determination, and (6) dynamic thresholds. Testing some of these features required high beam rates, and a variety of rates from about 0.3 to 18 kHz were employed. Use of a beam of particles of a known species and energy enabled the mapping of segment-to-segment mean thickness variations in the L2 detectors (which were too thick to measure with laboratory alpha sources as was done for the L1 detectors as described in Sect. 3.4), and the relatively large pulse heights of the stopping Ni ions proved useful for refining onboard algorithms designed to deal with electronic cross-talk (Sect. 3.6.4). As is visible in the third panel of Fig. 35, accelerator testing revealed a pronounced broadening of the Range 4 heavy ion tracks, which has been attributed to the L3 detectors being somewhat less than fully depleted at their nominal flight bias. The decreased resolution is minor enough to not impact the achievement of LET science objectives.

4.3 Radioactive Source Tests

Both LET instruments were periodically tested with radioactive sources in order to verify their operation during the integration and test program. Alpha sources (^{228}Th and ^{210}Po) were used to check the aliveness of the 54 individual detector segments as well as the coincidence circuitry before and after the thermal-vacuum, acoustic, and vibration tests, and following any repairs. In addition, a ^{90}Sr beta source was used at times to check the aliveness of all detectors and to verify the response of the L1 and L2 detectors to electrons.

The alpha-particle tests, which were performed at 1 atm. pressure, employed a source holder that mounted five alpha sources (four ^{210}Po and one ^{228}Th) to either the A or B sides of the LET telescope. A 1- μCi ^{228}Th alpha source was mounted in front of the center L1 detector (L1A2 or L1B2) and four ^{210}Po sources (5 mCi each) were mounted in front of the remaining L1A or L1B detectors. Each source was covered by a thin (~8.4 μm) polyethylene foil that was used as a target to produce energetic protons using Rutherford scattering. The ^{210}Po alpha particles did not have sufficient energy to reach the L1 detectors, but the elastically scattered protons produced a count rate of ~5 to 10 counts/minute in the L1 segments. The maximum alpha-particle energy from the thorium source is 8.785 MeV, which yielded protons with energies up to ~5.6 MeV. These protons were able to penetrate the L1 detector and reach all of the L2 and L3 segments on a given side, thereby providing functional tests of the detector response, the coincidence circuitry, and the onboard analysis routines. The ^{210}Po and the ^{228}Th half-lives are 138 day and 1.91 year, respectively. The counts rates were corrected for these half-lives to monitor long-term stability.

4.4 In-Flight Particle Calibrations

In addition to the electronic calibrations discussed in Sect. 4.1, LET will also be calibrated using in-flight particles. The stability of the detectors and electronics will be monitored by checking whether the elements identified onboard remain centered in the bands in the three matrices as a function of time, temperature, and radiation dose (see Sect. 3.6.4). If not, it is possible to upload revised particle identification matrices. Large SEP events provide excellent statistical accuracy over a short time interval. Since the LET response overlaps

with those of all three other SEP sensors (see Fig. 1), comparisons of the count rates, composition, and energy spectra between the four sensors will make it possible to continually intercalibrate the SEP suite.

4.5 Monte Carlo Simulations

Monte Carlo simulations were used in the design and optimization of the LET instrument to calculate geometry factors, to determine charge and mass resolution, to optimize detector threshold settings, and to test onboard particle identification software. Section 4.6 describes Monte Carlo calculations of the LET geometry factor as a function of particle energy and the various L1, L2, and L3 detector-segment combinations. These calculations also determined the results of modifying the response of the LET detectors dynamically during large SEP events in order to optimize the performance. In these calculations a numeric model of LET was exposed to an isotropic flux of particles with a known composition and energy spectrum.

Numerical simulations of the LET response were also used to determine the charge and mass resolution of the instrument. Although LET was tested with accelerator beams of heavy ions, as discussed in Sect. 4.2, it is impractical with a parallel, monoenergetic beam of a single nuclide to collect data over the full range of positions, angles, energies, and species to which LET will be exposed in space. The simulations for evaluating instrument resolution took into account heavy ion range-energy relations (including the energy dependence of the ions' effective charge) and Bohr/Landau fluctuations. They also used the measured mean thickness of each segment of the individual L1 detectors, to which was added a thickness deviation drawn on a particle-by-particle basis from a Gaussian distribution with a standard deviation equal to the measured rms thickness variation of the segment. The deposited energy in each hit detector segment was calculated and then a noise signal was added based on the typical characteristics of the LET PHASIC and the capacitance of the detector and the associated front-end circuit. Finally these signals were compared with the nominal detector thresholds to determine whether the events would satisfy the LET coincidence requirements and which pulse heights would be included in the telemetry stream. The resulting set of pulse heights were then analyzed using the same algorithms that will be applied to flight data.

Figure 22 shows results obtained from the Monte Carlo calculation using input energy spectra in the form of power laws with exponent -2 . Particles were sampled from an isotropic distribution, but only those incident from the A (sunward) side of the instrument were included in the plots. Particle composition used for this calculation was typical of that found in gradual SEP events with the following exceptions: He and H have been suppressed relative to the heavier elements by factors of 500 and 5,000, respectively, in order to avoid saturating the plot with these light elements, and ^3He has been set to 10% of ^4He in order to illustrate capability for identifying ^3He using the onboard analysis. The left-hand panels show the raw pulse heights. For Range 3 (lower left) the element tracks are broadened due to the wide range of angles sampled. For Range 2 (upper right) the angular spread sampled by a given detector is less (because the L1 detectors are arrayed along an arc of a circle) but the range of L1 detector thicknesses sampled is relatively large. The different L1 thicknesses cause the multiple tracks for individual elements in this plot. The two plots on the right-hand side of the figure show how the events can be mapped onto well-separated element tracks based on the scaling procedure that is used onboard to approximately correct for spread in angles and ΔE detector thicknesses, as discussed in Sect. 3.3.

For the subset of events that is telemetered to the ground, one is able to derive particle charge and mass using the full range-energy relation (Stone et al. 1998b; Appendix 1) rather

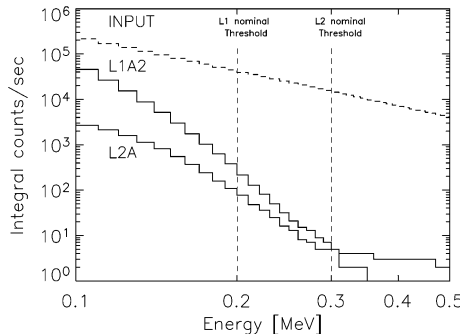


Fig. 36 Monte Carlo simulations of the response of a 25 μm thick L1 detector to electrons. The expected integral count rate of electrons hitting an L1A2 detector (*top solid line*) and penetrating to any L2A detector (*lower solid line*) is shown as a function of the energy deposit in those detectors. The input spectrum (plotted vs. the incident electron energy) is from the large October 28, 2003, SEP event. The *vertical dashed lines* indicate the nominal L1 and L2 threshold energies, respectively. Less than 10^{-5} of the electrons with >0.3 MeV will trigger a coincidence between L1 and L2

than the power-law approximation employed onboard. This should yield somewhat better mass resolution, particularly at low energies where the power law approximations are accurate only over relatively narrow energy intervals. To estimate the LET mass resolution Monte Carlo simulations were run in which the input composition contained equal abundance of ^3He and ^4He or of ^{20}Ne and ^{22}Ne . Histograms of the masses calculated for particles stopping in Ranges 2, 3, and 4 were constructed and the mass resolution was obtained from the standard deviations of Gaussian fits to the central portions of the mass peaks. These values are listed in Table 1. The mass resolution in flight should be slightly degraded from that predicted based on the Monte Carlo simulations because of several effects not included in the calculations (statistical fluctuations of the particles' effective charge, multiple Coulomb scattering in the instrument). In some cases resolution can be further optimized by restricting analysis to those combinations of L1 and L2 detector segments for which the uncertainty in the penetrated ΔE thickness is the smallest.

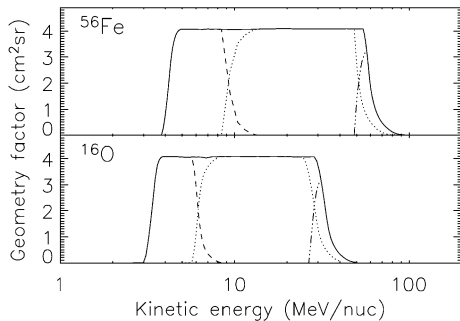
Simulated events obtained from the Monte Carlo simulations also proved useful for developing and testing the particle identification software implemented in the LET MISC.

Monte Carlo simulations were also made using GEANT-4 to optimize the L1 and L2 ADC thresholds. If the thresholds are too low, the high electron intensities during a large SEP event may increase the singles rates of L1 and L2 causing additional deadtime, and possibly increasing the chance coincidence rate. Figure 36 shows the expected integral count rates of a single L1 detector and any L2 detector during the October 28, 2003, event (Mewaldt et al. 2005b). Vertical lines indicate the nominal L1 and L2 threshold energies. Note that the ADC thresholds are adjustable by command, as described in Sects. 3.6.2 and 3.8.

4.6 Energy Range and Collecting Power

The collecting power and energy range of LET was evaluated for a wide range of key ions using Monte Carlo simulations as described in Sect. 4.5. The energy range spanned by nuclei stopping in Range 2, Range 3, and Range 4 is shown in Fig. 1. Figure 37 shows the result of Monte Carlo simulations of the LET geometrical factor (area solid-angle factor) plotted as a function of particle energy for the abundant isotopes ^{16}O and ^{56}Fe . The curves indicate the geometrical factors for particles stopping in Range 2, Range 3, and Range 4, along with

Fig. 37 LET Geometry Factor vs. energy/nucleon for O and Fe. The geometry factor for Range 2, 3, and 4 events are indicated by dashed, dotted, and *dash-dot* lines, respectively. The *solid line* represents the sum of the responses



the sum of these responses. The Range 4 response (for the A-side) has been evaluated only to a depth in L3B of 0.3 mm of Si, in order to avoid confusion with heavy particles that completely penetrate both L3A and L3B (see also the Range 4 particle identification matrix in Appendix 3). Over most of the energy range the total geometry factor is $4.0 \text{ cm}^2 \text{ sr}$.

LET will also measure ultraheavy (UH) ions with $Z \geq 30$ that are sometimes over-abundant by up to a factor >1,000 in impulsive SEP events (Reames and Ng 2004; Mason et al. 2004). During an exposure of the LET engineering unit at the LBL 88-inch cyclotron LET observed UH ions that included ^{65}Cu , ^{86}Kr , ^{136}Xe , and ^{209}Bi . The energy range of the UH response starts at $\sim 4 \text{ MeV/nucleon}$. There are two priority buffers devoted to UH events.

Each of the ten L1 detectors has three segments and when combined with the ten segments of the L2 detectors a total of 300 different directions in the ecliptic plane (150 per side) are defined. Table 13 shows the geometry factor of each of the possible L1•L2 segment combinations evaluated for particles that stop at the endpoint of L2. For example, the geometry factor of a particle trajectory from L1A1a to L2A0 is $0.0244 \text{ cm}^2 \text{ sr}$. Note that Table 13 result does not include the energy dependence visible at the highest and lowest energies in Fig. 37. In Sect. 4.7 these detector combinations are grouped to measure particle anisotropies. Another use of Table 13 is to evaluate the effect of disabling (by command) a noisy detector should this become necessary. Finally, Table 13 includes the summed geometry factors for the H and He response when the dynamic threshold system is employed during large SEP events (see Sect. 3.6.3).

Table 13 indicates that the total geometry factor for forming an L1•L2 coincidence is $4.05 \text{ cm}^2 \text{ sr}$. This is also the geometry factor for events telemetered to the ground. However, the onboard particle identification system ignores the four widest-angle detector combinations (L1A0•L2A9, L1A4•L2A0, L1B0•L2B9, and L1B4•L2B0) because, for example, a fraction of these events may pass through L1A0, L2A0, and L3A and then exit out the side without triggering L3B. These four detector combinations are also excluded in tabulating the sectored rates (Sect. 4.7). The geometry factor for onboard particle identification is $4.0 \text{ cm}^2 \text{ sr}$.

4.7 Anisotropy Measurements

STEREO is a three-axis stabilized spacecraft that always looks at the Sun. As a result, there is no information on the arrival directions of particles except for what is provided by the sensors themselves. As discussed in Sect. 4.6, the various combinations of L1 and L2 segments define a total of 300 different directions in the ecliptic plane (150 per side). These directions have been sorted into 16 sectors, 8 of which are illustrated in Fig. 38. For sectored count rates

Table 13 LET geometry factors

L1AO			L1A1			L1A2		
L1 segment	L2 segment	Geometry factor (cm ² sr)	L1 segment	L2 segment	Geometry factor (cm ² sr)	L1 segment	L2 segment	Geometry factor (cm ² sr)
a	0	0.0328	a	0	0.0244	a	0	0.0157
a	1	0.0267	a	1	0.0240	a	1	0.0173
a	2	0.0212	a	2	0.0225	a	2	0.0186
a	3	0.0168	a	3	0.0206	a	3	0.0193
a	4	0.0133	a	4	0.0184	a	4	0.0196
a	5	0.0106	a	5	0.0159	a	5	0.0193
a	6	0.0084	a	6	0.0137	a	6	0.0183
a	7	0.0068	a	7	0.0115	a	7	0.0168
a	8	0.0055	a	8	0.0096	a	8	0.0150
a	9	0.0044	a	9	0.0081	a	9	0.0128
b	0	0.0164	b	0	0.0114	b	0	0.0074
b	1	0.0136	b	1	0.0116	b	1	0.0082
b	2	0.0111	b	2	0.0111	b	2	0.0090
b	3	0.0090	b	3	0.0103	b	3	0.0095
b	4	0.0072	b	4	0.0095	b	4	0.0098
b	5	0.0058	b	5	0.0083	b	5	0.0098
b	6	0.0046	b	6	0.0073	b	6	0.0095
b	7	0.0038	b	7	0.0062	b	7	0.0090
b	8	0.0031	b	8	0.0053	b	8	0.0082
b	9	0.0025	b	9	0.0044	b	9	0.0074
c	0	0.0275	c	0	0.0158	c	0	0.0128
c	1	0.0264	c	1	0.0214	c	1	0.0150
c	2	0.0224	c	2	0.0216	c	2	0.0168
c	3	0.0185	c	3	0.0207	c	3	0.0183
c	4	0.0151	c	4	0.0191	c	4	0.0193
c	5	0.0124	c	5	0.0172	c	5	0.0196
c	6	0.0100	c	6	0.0152	c	6	0.0193
c	7	0.0081	c	7	0.0131	c	7	0.0186
c	8	0.0067	c	8	0.0113	c	8	0.0173
c	9	0.0056	c	9	0.0096	c	9	0.0157

a segment total = 0.1464

a segment total = 0.1687

a segment total = 0.1728

b segment total = 0.0770

b segment total = 0.0854

b segment total = 0.0876

c segment total = 0.1527

c segment total = 0.1650

c segment total = 0.1728

all segment = 0.3761

all segment = 0.4191

all segment = 0.4333

A or B side total = 2.024

Dynamic thresholds:

Both side total = 4.047

1) Disable all 20 of the L1 outer regions

0.8249 cm² sr2) Disable all L1 except center of L1A2b & L1B2b
0.1752 cm² sr3) Disable L2 segments except L2A4, L2A5; L2B4 and L2B5.
Also disable the L3 segments L3Ao and L3Bo.0.0392 cm² sr

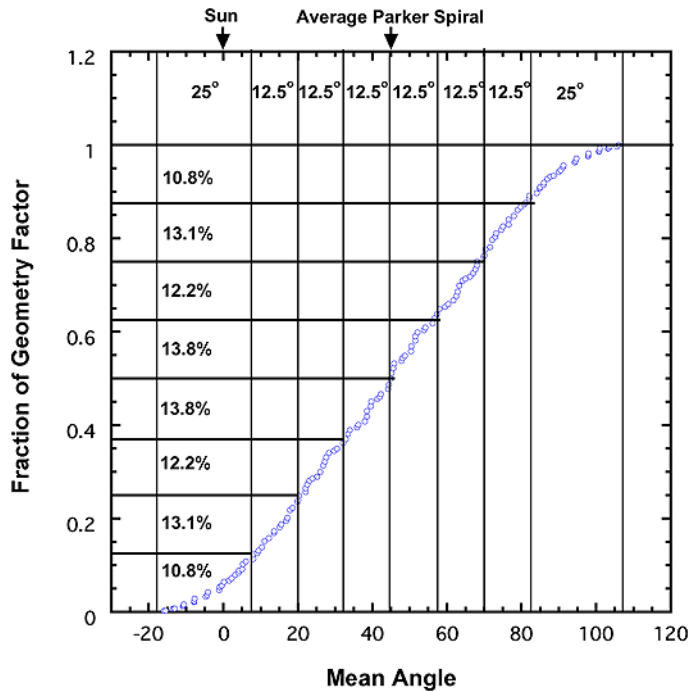


Fig. 38 The LET viewing directions are divided into eight sectors on the A-side and eight on the B-side. Shown here is the fraction of the geometry factor in each sector on the A-side. In this representation particles coming in a straight line from the Sun would arrive at 0° and those arriving along the average Parker Spiral angle would arrive at $\sim 45^\circ$. Note that the central six sectors are 12.5° wide and the width of the two outside sectors is 25° .

Table 14 LET sectored rates

Species	Energy range	Number of sectors	Geometry factor ($\text{cm}^2 \text{ sr}$)
H	4.0–6.0	16	0.039–4.0
${}^3\text{He}$	4.0–6.0	16	0.039–4.0
${}^4\text{He}$	4.0–6.0	16	0.039–4.0
	6.0–12.0	16	0.039–4.0
CNO	4.0–6.0	16	4.0
	6.0–12.0	16	4.0
NeMgSi	4.0–6.0	16	4.0
	6.0–12.0	16	4.0
Fe	4.0–6.0	16	4.0
	6.0–12.0	16	4.0

both the front (A-side) and rear (B-side) include particles from a $129^\circ \times 29^\circ$ Field of View (FOV) with the 129° fan looking along the ecliptic plane. The center of the A-side fan points at an angle that is 45° west of the Sun, along the average Parker Spiral direction at 1 AU.

There are ten 16-sector rates that are read out once per minute (see Table 14). All of these count the particles identified by the onboard particle identification system described

in Sect. 3.6.4. The CNO and NeMgSi rates sum the events along the three tracks in order to achieve improved statistical accuracy. The use of common energy intervals makes it possible to compare the pitch-angle distributions of species with the same velocity, but differing rigidities. There is complementary anisotropy data for ions and electrons provided by the SEPT sensor (Müller-Mellin et al. 2007).

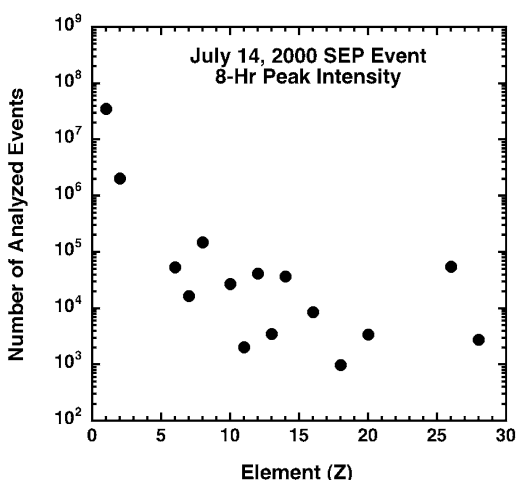
During large SEP events, when the first stage of the dynamic thresholds are imposed (only L1 centers used for H and He; Sect. 3.6.3), the number of sectors that are triggered by H and He events will remain at 16 but the coverage in the forward and rear directions will be 127° wide instead of 129° . During the second stage of the dynamic thresholds (when H and He trigger only the center segments of L1A2 and L1B2), the number of sectors that are triggered by H and He events will be reduced to six per side, and the H and He angular coverage in the ecliptic will be reduced to $\sim 62^\circ$ wide in the front and rear. During the third stage of the dynamic thresholds the angular coverage in the ecliptic for H and He will be only 19° wide in the front and rear.

4.8 Solar Energetic Particle Yields

In order to estimate the yield of energetic ions that would be obtained in a very large SEP event an analysis was done of the performance of LET during the July 14, 2000 (Bastille Day), event when the intensity reached its maximum (10:00–18:00 UT on July 15). Using composite spectra compiled by Tylka et al. (2001), the count rates of H, He, O, and Fe ions incident on the LET telescope were estimated. In addition, the singles rates of all detectors were estimated, including particles that enter through the sides of the telescope. The estimated total singles rate (summed over all detectors) is $\sim 1.6 \times 10^5 \text{ s}^{-1}$, leading to a livetime of 38% during this interval. The rate at which proton events would be analyzed [taking into account the dynamic thresholds (Sect. 3.6.3) and livetime] was estimated to be $\sim 1,200 \text{ s}^{-1}$, and the analysis rate of $Z \geq 6$ heavy ions was estimated at 14 s^{-1} . Figure 39 shows the total number of events that would be expected from Ranges 2, 3, and 4 during this 8-hr period (only those elements for which there is onboard analysis are tabulated). Note that the event numbers are adequate to construct energy spectra for all species.

There will also be pulse-height data for individual heavy ion events telemetered during this period. We expect ~ 3 events/s with $Z \geq 6$ to be telemetered or $\sim 20\%$ of the total that

Fig. 39 Estimated yield of particle events that a LET would have measured during the eight hours when the counting rate from the Bastille Day SEP event was at its maximum. The effects of the dynamic thresholds and the instrument deadtime have been taken into account. Only those species identified by the onboard analysis system are shown



were analyzed. These data can be used to check the onboard analysis and also to analyze the abundance of species not covered by the onboard analysis. Over the course of the entire Bastille Day event we expect the number of analyzed heavy ions to be several times the totals in Fig. 39.

4.9 In-Flight Performance

The twin STEREO spacecraft were launched from Cape Canaveral on the evening of October 25, 2006, and placed into a lunar phasing orbit. The four instruments of the SEP suite on the Behind spacecraft were first powered up on November 13; one day later the SEP suite on the Ahead spacecraft was also turned on. As of late December both LET sensors were operating nominally. The LETs were turned on during the decay of a small energetic particle event which provided a first opportunity to test the onboard particle identification routines and obtain a cross-calibration with other 1 AU instruments. The energy spectra for H and He measured by the LETs on November 14 were in good agreement with spectra measured by the EPAM, ULEIS, and SIS instruments on ACE, and by the EPHIN instrument on SoHO. Several small impulsive SEP events on November 21 and 22 provided further tests of the onboard particle identification system. The highly elliptical STEREO orbit during November and early December made regular transits through Earth's magnetosphere, providing an opportunity to test the "dynamic threshold" function (see Sect. 3.6.3) in an extreme radiation environment.

During early December the recovery to solar minimum conditions was interrupted by four X-class flares and associated CMEs that resulted in two large SEP events. These events populated all of the species and energy bins identified by onboard processing, providing critical in-flight calibration data for adjusting the location of the boxes in Figs. 29, 41, and 42. The observed composition and energy spectra were found to be in good agreement with simultaneous data from ACE.

5 SEP Central

5.1 SEP Central Overview

The LET, HET, and SIT sensors each require a dedicated microprocessor (MISC) for onboard data processing and sensor control. An additional MISC, called SEP Central, gathers data from all the SEP sensors, gathers SEP housekeeping data, controls the SEP SSD bias power supply, manages the SEP interface to the IMPACT IDPU, and manages the interfaces to the sensors. SEP Central also directly controls and manages data from the SEPT-NS and SEPT-E detectors, which do not incorporate dedicated microprocessors.

There are two multiplexed serial interfaces between the LET/HET/SIT sensors and SEP Central. The first interface is bidirectional, for transferring boot-code, commands, and command responses. The second interface is unidirectional, for transferring data from the instruments to SEP Central. The protocol for using these interfaces is defined in Interface Control Documents (ICDs) between each sensor and SEP Central. SEP Central controls and acquires data from SEPT-NS and SEPT-E via a separate multiplexed bidirectional serial interface.

Processed data from the microprocessors associated with LET, HET, and SIT are transmitted by those sensors to SEP Central as CCSDS packets. SEP Central timestamps these packets, recalculates the checksum, and forwards them to the IMPACT IDPU. Raw data from SEPT-NS and SEPT-E are acquired from those sensors by SEP Central. SEP Central

compresses and packetizes these data, and forwards the packets to the IDPU. Figure 2 in Sect. 1 shows a block diagram of the SEP Sensor Suite.

The IMPACT IDPU provides the interface between the STEREO Spacecraft C&DH system and the IMPACT instruments, including the SEP suite. All information transfer between the IMPACT instruments and the Spacecraft/Ground flows through the IDPU, including telemetry, commands, and status. SEP Central communicates with the IDPU over a dedicated serial interface. The SEP sensors and SEP Central are designed to be relatively autonomous. Once their look-up tables have been loaded and their modes and parameters set, they cycle through their data collection and transmission automatically, and provide data to the IDPU without handshaking.

5.2 Power-On and Boot Procedures

After power-on, SEP Central attempts to boot from page 0 of EEPROM. Subsequently, three different discrete reset commands can be sent to SEP. The first causes SEP Central to boot from page 0 of EEPROM. The second causes SEP Central to boot from page 1 of EEPROM, and the third causes SEP Central to accept boot code over the serial link to the IDPU.

The LET, HET, and SIT processors power-on whenever SEP Central powers-on. After power-on, the LET, HET, and SIT processors execute a small boot loader program stored in the processor FPGA. This boot loader manages the reception and execution of boot code received from SEP Central on the serial command link. After SEP Central boots, the process of booting LET, HET, and SIT begins via a command from the ground or the IDPU. After the sensor boot command is received, SEP Central begins the process of transferring boot code from EEPROM to the LET, HET, and SIT processors over the serial command link. All EEPROM resides within SEP Central; the sensors do not have any EEPROM.

5.3 SEP Telemetry Data

Telemetry data generated by the SEP sensor suite fall into five categories: science data, housekeeping data, beacon data, fill data, and command responses.

Except for beacon data, SEP telemetry data are transferred to the IMPACT IDPU as CCSDS telemetry packets. Each packet is 272 bytes in length, including an 11-byte header. An ApID code in the packet header defines the origin and content of these packets. ApID codes allocated to the SEP sensor suite are shown in Table 15 (all numbers are decimal, and all ranges are inclusive). Telemetry allocations for the SEP sensors are summarized in Table 16.

All the sensors have a data accumulation period of one minute (synchronized with each other and with the IMPACT suite). Data accumulated by the LET, HET, and SIT sensors during minute N are packetized by those sensors and transferred to SEP Central during minute $N + 1$. At the beginning of minute $N + 2$, SEP Central combines housekeeping packets from HET, LET, and SIT with housekeeping data gathered from SEPT and from the SEP common electronics (all of the data having been collected during minute N on each sensor) into a common SEP housekeeping CCSDS packet. This packet is also transmitted to the IMPACT IDPU during minute $N + 2$.

Also at the beginning of $N + 2$, SEP Central combines Beacon packets from HET, LET, and SIT with Beacon data gathered from SEPT (all of the data having been collected during minute N on each sensor) into a SEP Beacon message block. The format of this message block is described in Sect. 8.1 of the IMPACT Serial Interface Document. It is not a CCSDS packet. SEP Central transmits this Beacon message to the IMPACT IDPU during minute

Table 15 ApID allocations

Item	ApID
Command response	576
SEP combined housekeeping	577
LET science	580–587
LET housekeeping	588
LET beacon	589
HET science	590–597
HET housekeeping	598
HET beacon	599
SIT science	605–617
SIT housekeeping	618
SIT beacon	619
SEPT science	600, 601
Fill Packet	623
Spares	578–579, 602–606, 620–622

Table 16 SEP telemetry allocations

Data type	HET	LET	SEPT	SIT	SEP Central
Housekeeping (bytes/minute)	41	102	26	36	55
Beacon (bytes/minute)	28	46	44	24	2
Science (packets/minute)	6	16	2	12	0

$N + 2$. The IMPACT IDPU incorporates the SEP Beacon message into the IMPACT Beacon CCSDS packet during the same minute.

Finally, all science packets received by SEP Central from LET, HET, and SIT during minute $N + 1$ are timestamped by SEP Central with the beginning of the data accumulation time (minute N), the packet checksums are recalculated, and the packets are forwarded to the IMPACT IDPU during minute $N + 2$. Also, SEPT science packets containing data gathered by SEP Central from the SEPT sensors during minute N are forwarded to the IMPACT IDPU during minute $N + 2$.

Acknowledgements This research was supported by the National Aeronautics and Space Administration (NASA) at the Space Radiation Laboratory (SRL) of the California Institute of Technology (under Subcontract SA2715-26309 from the University of California at Berkeley (UCB) under NASA contract NASS-03131), the Jet Propulsion Laboratory (JPL), and the Goddard Space Flight Center (GSFC).

The authors thank the many individuals and organizations that contributed to the successful development of LET and SEP Central. Within SRL at Caltech we thank Janet Valenzuela, who procured and kitted electronics parts and was responsible for our documentation control; Norman Lee, who assisted the cognizant engineer in a variety of tasks; Jill Burnham, who laid out the PHASIC chip and provided engineering assistance; Minerva Calderon, who supported us in the computer and IT networks area; and Stacia Rutherford, Caprice Anderson, Pamela Nickson, Christina Davezan, Marjorie Miller, Cheryllinn Rangel, and Donna Jones, who provided administrative assistance. André Jefferson of the Caltech Safety Office assisted us in moving radiation sources around the country. We wish to thank Richard Seligman, Nancy Daneau, and Gaylene Ursua of Caltech's Office of Sponsored Research for assisting us with contract issues. We thank Ray

Yuen, Jose Lopez-Tiana, and Rudy Arvizu for procurement help. Rebekah Sims assisted in developing our Small Business Plan. Richard Paniagua and Joe Haggerty of Caltech's Physics shop assisted in making a variety of parts used in the lab and at accelerator calibrations. We thank Chris Martin and Peter Friedman of the GALEX team for the use of their excellent clean room facility.

Caltech's JPL was instrumental in many areas of the development of LET and SEP Central. Toshiro Hatake and Amin Motiwala were responsible for the fabrication of the Caltech PHASIC hybrid; Patrick Martin, Terry Fisher, and Andy Rose supplied environmental test facilities which were superbly run by technicians Doug Perry, Geoff Laugen, Mike Sachse, Bruce Woodward, and Sandro Torres; Tom Hill provided a bake-out chamber; Dennis Kern, Wan B. Tsoi, Michael O'Connell, and Tim Werner helped with environmental test plans and reports; Charles Cruzan, Chuck Derksen, Don Schatzel, and Reza Ghaffarian assisted with failure analysis and L1 detector rework; James Arnett, David Guarino, Peyton Bates, and Guy Prichard provided management and financial accounting assistance; Pat Dillon, Glenn Anderson, Angel Garnica, Mark Hetzel, and Pat Rodriguez helped us with connector selection and harness fabrication; Gary Bivins provided expert advice for PHASIC hybrid screening; Ed Powell and Kristan Ellis helped with parts; Mark Duran helped with thermal blankets; and Brian Blakkolb assisted with contamination control. Special thanks to the engineers and technicians in the Electronics & Packaging Section: Atul Mehta, Anarosa Arreola, Tran Ngo Lu, Martha Cortez, Yolanda Walters, Hung Truong, and Gerald Gaughen; as well as the people in Instruments & Measurements Lab working under Lothar Kirk. Providing advice on ITAR issues were Edmond Momjian, Ann Bussone, Stephanie Lear, and Kerry Dolan.

Dean Alami of Space Instruments was responsible for the design of the Analog Post-regulator board and the detector bias supplies. Colin Wilburn and his staff at Micron Semiconductor Ltd. fabricated the silicon detectors. Robert Kopp of Dynacs Inc. assisted with quality assurance at Caltech. C. H. Ting consulted on the design of the P24 MISC and provided the Forth operating system used in the LET and SEP Central microprocessors.

We have many to thank at UCB. Janet Luhmann is the IMPACT Principal Investigator and we thank her for her support and encouragement throughout the development period. David Curtis was the IMPACT project manager and provided expert assistance and advice to us on many levels. Peter Berg and Selda Heavner designed and fabricated the low voltage power supplies. Ron Jackson assisted us in the quality assurance area and Trish Dobson and David Weldon provided financial assistance.

The support of many individuals at GSFC was critical in the development process. Russell Harrison assisted us with the thermal vacuum testing. Bert Nahory and Traci Pluchak-Rosnack provided technician assistance. Therese Errigo was responsible for contamination control and was assisted by Kelly Henderson of Swales Aerospace. Also helping us in a variety of areas were Fred Gross, Antonio Reyes, Leslie Cusick, Jong Kadesch, Richard Katz, Mario Martins, Brian Rice, and Haydar Teymourlouei.

We are grateful to the individuals and institutions that provided facilities and assistance during our accelerator calibrations and part irradiation testing. Rocky Koga, Jeff George, and Mark Looper of Aerospace Corp. helped in both areas, providing assistance with the use of their chamber at the 88-in cyclotron at UCB and with ^{60}Co radiation testing at Aerospace. Raman Anantaraman facilitated our accelerator calibration at the Michigan State National Superconducting Cyclotron Lab.

We are grateful to the STEREO Project Office at GSFC for their support. Nick Chrissotimos was the STEREO Project Manager and Mike Delmont was the Deputy Project Manager. We thank them for their guidance. We are especially indebted to the IMPACT Instrument Manager, Lillian Reichenthal, who became a dedicated team member, helping us in every aspect of the development and testing of LET and SEP Central. Also assisting us were Harry Culver, Larry Gibb, Jerry Hengemihle, Shane Hynes, Mike Jones, Michael Kaiser, Diane Kolos, Alexia Lyons, Tabitha Merchant, Kevin Milligan, Robert Palfrey, James Rogers, James Thurber and Steve Wasserzug.

Finally, we thank Eric Christian of NASA Headquarters who not only provided encouragement but also took shifts in monitoring our instrument during thermal vacuum testing.

Appendix 1: L1 Detector Thicknesses

As discussed in Sect. 3.4, detailed thickness maps were made for all of the flight L1 detectors in order to provide the information needed for correcting dE/dx measurements made using these detectors for the actual thickness of the detector segment penetrated. The resulting thicknesses and their rms deviations from this mean are summarized in Table 17. For the individual detector segments these values are based on thicknesses measured at 4 points. The overall values were calculated from the entire set of 12 points, 4 on each of the 3 segments.

Table 17 LET L1 detector thicknesses. [mean \pm rms (μm)]

Detector position	Serial number	Overall thickness	a segment	b segment	c segment
Ahead spacecraft					
L1A0	L1-51	22.22 ± 0.76	22.33 ± 0.41	22.83 ± 0.48	21.50 ± 0.72
L1A1	2250-2-1	28.49 ± 0.55	28.39 ± 0.70	28.65 ± 0.11	28.42 ± 0.75
L1A2	2250-2-2	29.92 ± 0.37	29.59 ± 0.31	30.00 ± 0.21	30.18 ± 0.32
L1A3	L1-12	22.52 ± 0.47	22.71 ± 0.55	22.18 ± 0.17	22.67 ± 0.48
L1A4	L1-59	24.52 ± 0.55	24.22 ± 0.60	24.57 ± 0.61	24.79 ± 0.38
L1B0	L1-22	22.08 ± 0.57	21.72 ± 0.23	21.84 ± 0.35	22.70 ± 0.50
L1B1	L1-28	27.33 ± 0.38	27.15 ± 0.46	27.45 ± 0.39	27.39 ± 0.31
L1B2	L1-58	23.23 ± 0.33	23.43 ± 0.27	22.99 ± 0.27	23.28 ± 0.33
L1B3	L1-49	23.80 ± 0.68	23.64 ± 0.96	23.92 ± 0.63	23.84 ± 0.58
L1B4	L1-06	22.41 ± 0.38	22.73 ± 0.32	22.35 ± 0.31	22.14 ± 0.32
Behind spacecraft					
L1A0	L1-36	22.36 ± 0.76	22.71 ± 0.97	21.73 ± 0.22	22.66 ± 0.55
L1A1	L1-02	26.21 ± 0.47	26.22 ± 0.59	26.31 ± 0.47	26.12 ± 0.44
L1A2	2250-2-3	29.59 ± 0.46	29.85 ± 0.20	29.82 ± 0.17	29.12 ± 0.51
L1A3	L1-08	24.46 ± 0.43	24.47 ± 0.46	24.19 ± 0.30	24.72 ± 0.41
L1A4	L1-24	25.62 ± 0.63	25.68 ± 0.42	25.98 ± 0.65	25.20 ± 0.65
L1B0	L1-05	22.40 ± 0.57	21.92 ± 0.54	22.53 ± 0.27	22.74 ± 0.58
L1B1	L1-35	27.14 ± 0.38	27.16 ± 0.50	27.20 ± 0.39	27.06 ± 0.34
L1B2	L1-37	23.13 ± 0.53	23.74 ± 0.63	22.82 ± 0.17	22.86 ± 0.15
L1B3	L1-19	23.56 ± 0.52	23.74 ± 0.63	23.43 ± 0.40	23.52 ± 0.61
L1B4	2250-3-1	22.39 ± 0.36	22.60 ± 0.28	22.45 ± 0.19	22.11 ± 0.43

Appendix 2: Event Classes and Coincidence Conditions

There are ten different classes of events defined in LET, as summarized in Table 18. These classes are defined by the event tag bits L1A (logical OR of the 15 L1A segments), L2A (logical OR of the ten L2A segments), and L3A (logical OR of the 15 L3A segments), with similar definitions for the L1B, L2B, and L3B tags. In order to resolve whether a PENA? event should be classified as PENA or ERROR, the onboard software examines the L2B hits and decides if they are due to cross-talk from L3B. If they are, then the event is PENA. If not, the event is rejected for onboard processing and sent to priority buffer 26.

Table 19 gives the coincidence conditions that lead to the ten different classes of events. Events are classified based on the pattern of hits in each layer of the LET instrument. A “1” in any cell in the table signifies one or more hits in that layer. The number of events assigned to each class is counted and the totals are telemetered each minute. (These are the coincidence rates.) Note: the ordering of the layers in this table is for human readability. It does not reflect the ordering of the tag bits in the raw event data.

Table 18 LET event classes

Event Class	Definition
L12A	Range 2 A-side events
L123A	Range 3 A-side events
PENA	Range 4 A-side events
L12B	Range 2 B-side events
L123B	Range 3 B-side events
PENB	Range 4 B-side events
2TEL	Coincidence on both sides; rejected for onboard processing
PENA?	Needs subsequent processing to decide if PENA or ERROR event
PENB?	Needs subsequent processing to decide if PENB or ERROR event
ERROR	Rejected for onboard processing; sent to priority buffer 26

Table 19 Onboard classification of PHA events

L1A	L2A	L3A	L3B	L2B	L1B	Class
1	1	0	0	0	0	L12A
1	1	1	0	0	0	L123A
1	1	0	0	0	1	L12A
1	1	1	0	0	1	L123A
1	1	0	0	1	0	L12A
1	1	1	0	1	0	L123A
0	0	0	0	1	1	L12B
1	0	0	0	1	1	L12B
0	1	0	0	1	1	L12B
1	1	0	0	1	1	2TEL
0	0	1	0	1	1	L12B
1	0	1	0	1	1	L12B
0	1	1	0	1	1	L12B
1	1	1	0	1	1	2TEL
1	1	0	1	0	0	L12A
1	1	1	1	0	0	PENA
1	1	0	1	0	1	L12A
1	1	1	1	0	1	PENA
0	0	0	1	1	1	L123B
1	0	0	1	1	1	L123B
0	1	0	1	1	1	L123B
1	1	0	1	1	1	2TEL
0	0	1	1	1	1	PENB
1	0	1	1	1	1	PENB
0	1	1	1	1	1	PENB?
1	1	1	1	1	1	2TEL
All other combinations						ERROR

Appendix 3: Rates, Particle IDs, and Event Data

The LET Science Frame is envisioned as a stream of bytes. Each minute, this stream is formatted into 16 CCSDS packets and telemetered via SEP Central. When data elements span more than one byte, the elements are transmitted in order of high byte to low byte. Both rates and PHA event data are present in the LET Science Frame (see Fig. 40). LET rates data include livetimes, detector singles and coincidence rates, onboard event processing rates, priority buffer counters, science rates, background rates, and look direction rates. The science rates are counts per minute of elements in various energy bins, divided between penetration ranges in the LET instrument. All rates are compressed to 16 bits with a modified biased exponent, hidden one algorithm with a 12-bit mantissa and a 4-bit exponent. Table 20 summarizes the rates and particle PHA event data that are telemetered each minute by LET. The format of the PHA event data is described later in this appendix.

As described in Sect. 3.6.4, valid particle events (e.g., those having straight-trajectory single detector hits in a given detector layer of the instrument) are sorted into penetration ranges (2 through 4) in the instrument. After performing gain, angle, and thickness corrections, the algorithm determines species by mapping ΔE vs. E' signals onto response matrices. The matrix for Range 3 is given in Fig. 29 in Sect. 3.6.4, and the matrices for Range 2 and Range 4 are shown here in Figs. 41 and 42. Each matrix is a 128×400 array logarithmically spanning ΔE vs. E' space. Each array element is an integer identifying an element or helium isotope (1–16) or background or a STIM box (127–139).

Each colored region on the matrix figures represents a particle region (e.g., H, ^3He , ^4He , C, N, O, etc., depending on range), a background region, or a STIM box. The matrices assign a number to each particle species, according to Table 21. Thus, a particle is mapped via ΔE

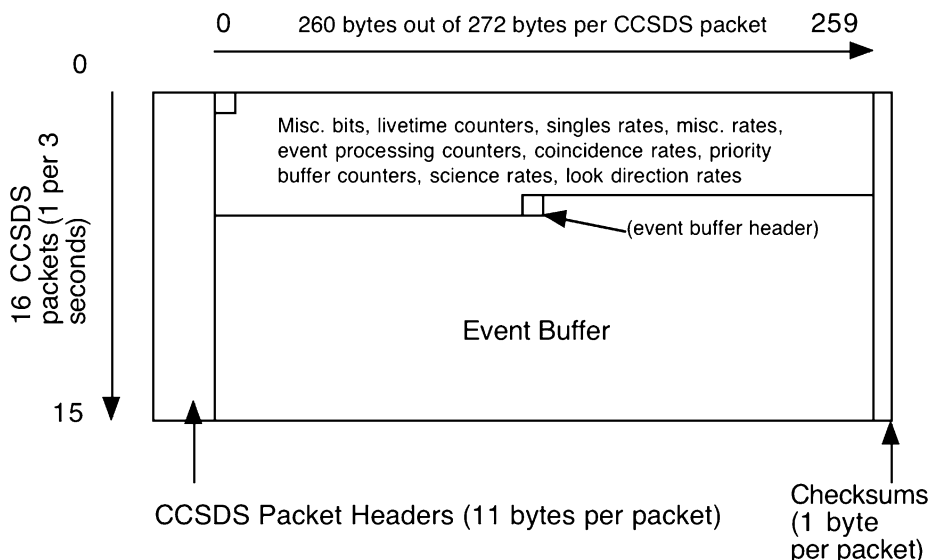
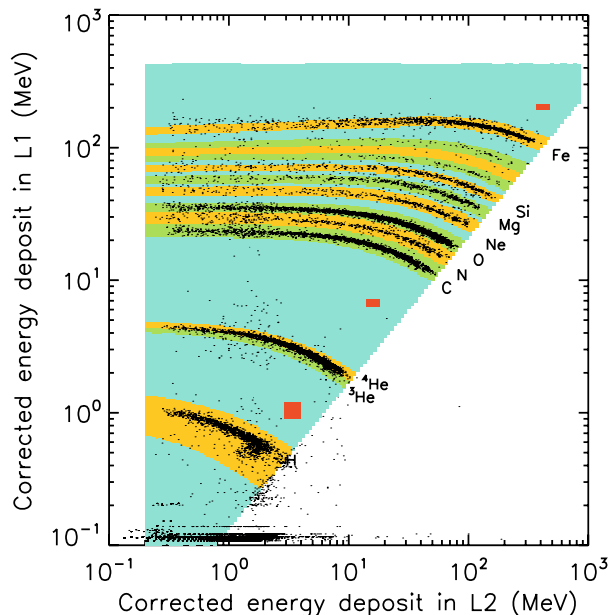


Fig. 40 LET Science Frame Overview, with CCSDS packet headers and checksums. LET Science Frame Header is unlabeled at upper left. (Data elements not to horizontal scale.) LET transmits 16 Science Frame packets to SEP Central, followed by four additional, nulled packets that SEP Central does not forward to telemetry. If more bandwidth is allocated to LET, these additional packets could be added to the LET Science Frame format

Table 20 LET science format summary

Byte #	Description
0–4	Header
5–6	Miscellaneous bits (MISCBITS)
7–24	Livetime counters (ERATES)
25–240	Singles rates (SNGRATES)
241–250	Miscellaneous rates (MISCRATES)
251–282	Event processing counters (EVPRATES)
283–306	Coincidence rates
307–364	Priority buffer rates (BUFRATES)
365–628	Range 2 science rates (L2FGRATES)
629–652	Range 2 background and STIM rates (L2BGRATES)
653–986	Range 3 science rates (L3FGRATES)
987–1,010	Range 3 background and STIM rates (L3BGRATES)
1,011–1,076	Range 4 science rates (PENFGRATES)
1,077–1,106	Range 4 background and STIM rates (PENBGRATES)
1,107–1,426	Look direction (sectored) rates (SECTRATES)
1,427–1,428	Event buffer header
1,429–4,159	Event records buffer

Fig. 41 The Range 2 (L1 vs. L2, or L1L2) LET matrix. Foreground elements are H, ^3He , ^4He , C, N, O, Ne, Mg, Si, S, Ar, Ca, and Fe, and these are shown in alternating green and yellow bands. Background regions are blue, and live STIM boxes are shown in orange. The data points are from the December 13, 2006, SEP event. Note that only 1 in 100 of the events below C have been plotted



vs. E' onto a matrix, and from its location on the matrix file, it is assigned a matrix value (1–16, 128–141). If a particle is identified as a selected element for its penetration range (matrix value 1–16), its energy is calculated from the sum of deposited energies in each detector layer, and its energy/nucleon is calculated from the total energy and assumed mass.

Fig. 42 The Range 4 (L3A vs. L3B, or L3A vs. L3B) LET matrix. Foreground elements are H, ^4He , C, N, O, Ne, Mg, Si, and Fe, and these are shown in alternating green and yellow bands. Background and RNG4 penetrating particle regions are blue, and live STIM boxes are shown in orange. The data points are from the December 13, 2006, SEP event. Note that only 1 in 100 of the events below C have been plotted

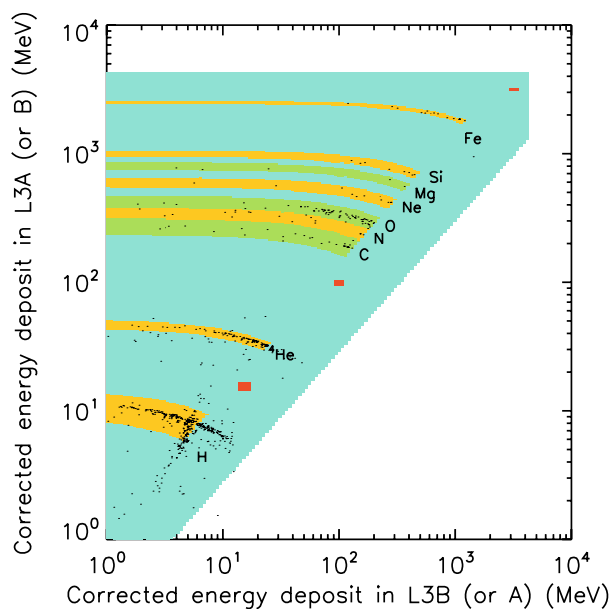


Table 21 Matrix value and particle ID assignments

Element	Matrix value	Range 2 particle IDs	Range 3 particle IDs	Range 4 particle IDs
H	1	0–8	0–10	0–2
^3He	2	9–17	11–19	
^4He	3	18–26	20–30	3–5
C	4	27–35	31–41	6–9
N	5	36–44	42–51	10–13
O	6	45–53	52–61	14–16
Ne	7	54–63	62–71	17–20
Na	8		72–81	
Mg	9	64–74	82–92	21–24
Al	10		93–103	
Si	11	75–85	104–114	25–28
S	12	86–95	115–125	
Ar	13	96–106	126–136	
Ca	14	107–117	137–146	
Fe	15	118–130	147–156	29–31
Ni	16		157–166	
Other (e.g. STIM, background)	128–141	255	255	255

Table 22 Event record header (ERH)

Data	Bit	Note
Particle ID	0–7	= particle ID if the particles are sorted by the LET Matrices as “foreground” particles. (= 255 if the particles are not sorted by the matrices or are identified as background particles). Allows matrices to ID particles by range (matrix), species, and energy. See Appendix 2, Table 18 for lists of Particle IDs.
Priority buffer number	8–12	See Sect. 3.6.5, Table 9 for a list of Priority Buffer Numbers and their descriptions.
L1A tag	13	Indicates an L1A detector contributed to the coincidence trigger.
L2A tag	14	Indicates an L2A detector contributed to the trigger.
L3A tag	15	Indicates an L3A detector contributed to the trigger.
L1B tag	16	Indicates an L1B detector contributed to the trigger.
L2B tag	17	Indicates an L2B detector contributed to the trigger.
L3B tag	18	Indicates an L3B detector contributed to the trigger.
STIM tag	19	Flags a STIM event.
HAZ tag	20	Hazard flag.
Time tag (latency)	21–24	Duplicates the 4 least significant bits of an onboard minutes counter; used to identify event latency.
A/B event tag	25	A = 0, B = 1
# Unread ADCs	26–28	# hit ADCs not included in the Event Record. Saturates at 7.
Extended header flag	29	= 1 if an additional header byte (or set of bytes) is appended to this header.
STIM block flag	30	= 1 if STIM Information Block is included in this event.
Culling flag	31	= 1 if number of ADCs culled from this event is nonzero.

The final particle ID is then determined from species, energy, and range, with separate tables of particle ID values used for each penetration range. Energy bin boundaries are shown in Fig. 30. Particle ID values range from 0 to 166, depending on range. STIM events, events falling into the background regions of the matrices, and invalid events are assigned particle IDs of 255.

LET also transmits pulse height data for a sample of all events processed through the particle identification and priority system; see Sects. 3.6.4 and 3.6.5. These events are packaged in variable-length event records, including an event record header, an optional extended header, an optional STIM information block, and a number of event record ADC fields. The 32-bit event record header summarized in Table 22 contains various tags as well as priority buffer number and particle ID number. The event record header is also shown graphically in Fig. 43a, reflecting the high-byte-first ordering.

The optional 16-bit extended header block contains the location of the event on the event matrices. If the event was not processed through a matrix, its location is 0,0. If the extended header block is included in an event record, it is appended after the ADC fields.

The optional 16-bit STIM information block contains a time counter indicating the time during the accumulation minute at which the STIM event was generated. The block also includes bits indicating the DAC settings for the STIM event, i.e., the DAC levels and which ADCs were stimulated. If included, this block would be appended after the ADC fields or after the optional extended header block.

The rest of an event record is filled with 20-bit ADC fields, one field for each ADC included in the event. The ADC field contents are summarized in Table 23 and Fig. 43b. Gen-

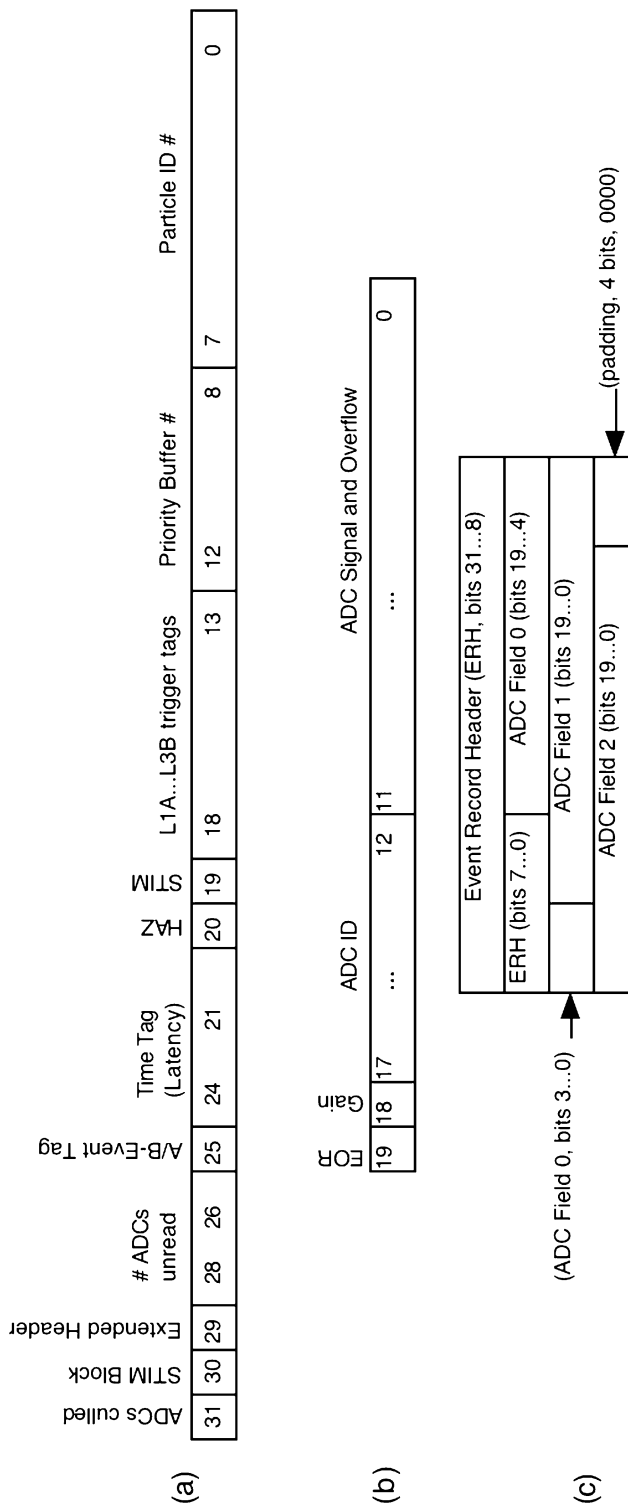


Fig. 43 LET Data Structure Diagrams: (a) LET Event Record Header. (b) LET ADC field. (c) LET Event Record, with three ADC fields and four bits of padding

Table 23 ADC field

Data	Bits	Note
ADC signal	0–11	11 bits signal, 1 bit overflow
ADC/Detector ID	12–17	54 detectors maximum
Low/High gain	18	0 = low gain, 1 = high gain
Last hit flag (End of Record, EOR)	19	Set to 1 for the last ADC in an event, 0 for all other ADCs

erally, the event record contains only those ADC fields corresponding to the pulse heights used by the onboard software to identify the particle. More ADCs may be included for unsorted events, and if large numbers of detectors reported pulse heights, some are dropped and counted only in the event record header. Finally, the LET sensor has a VERBOSE mode in which both low- and high-gain signals from a given detector may be transmitted.

Finally, an event record is padded with additional zero bits as needed to align each event record along byte boundaries in the Science Frame. A sample event record with three ADC fields and without a STIM information block or extended header is shown diagrammatically in Fig. 43c. If a STIM information block and/or an extended header were included, any necessary padding would be appended after these blocks.

Appendix 4: LET Variables

Table 24 defines LET software variables and tables used to control features of the real-time particle identification system described in Sect. 3.6.4. All variables in Table 24 with units of ADC channels are compared with ADC pulse-height data after the onboard software has performed DC offset-subtraction. The values of all variables in the tables may be changed by command.

The following tables used by the real-time particle ID system may also be changed by command.

The index into the following seven tables is the six bits of chip/PHA address contained in each PHA word read in from the PHASIC (two bits chip and four bits pha address). The contents of these tables are different for each Flight Unit.

FSETLOW: LET Low-gain DC offset corrections, in ADC channels.

FSETHIGH: LET high-gain DC offset corrections, in ADC channels.

GAINLOW: LET Low-gain gain correction lookup table. Each entry is (int)(256 * CF), where CF is a multiplicative correction factor that converts an offset-corrected PHA signal to a nominal gain-level. For each entry, CF is scaled so that gain-corrected low-gain signals from L1, L2, and L3 all have the same energy-scale.

GAINHIGH: LET Low-gain gain correction lookup table. Each entry is (int)(256 * CF), where CF is a multiplicative correction factor that converts an offset-corrected PHA signal to a nominal gain-level. For each entry, CF is scaled so that gain-corrected high-gain signals from L1, L2, and L3 all have the same energy scale. Note: the nominal factor of 20 difference between high-gain and low-gain signals is handled separately from these tables.

THICKNES: Each entry is (int)(256 * CF), where CF is a multiplicative correction factor that converts a PHA signal to the signal that would be expected for a detector of nominal thickness. $CF = [L/L_0]^{1/\alpha}$, where α differs for L1, L2, L3 (see the following cosine tables).

WINCORR2, WINCORR3: LET window correction lookup table. Each entry is (int)(256 * CF). Only L1 signals need to be corrected to account for the thickness of the

Table 24 LET onboard event processing tunable variables

Variable name	Default value	Units	Description
REJHAZ	TRUE	Boolean	if TRUE, hazard-tagged events are rejected for onboard processing
FCULL	TRUE	Boolean	If TRUE, cross-talk hits are culled from telemetered events
FNMAX	20	ADCs/event	Max number of ADCs that will be formatted per event, (independent of FCULL)
CHKR3E?	TRUE	Boolean	If TRUE, enables checking of L1 and L2 energies for Range 3 events
CHKL1L2R?	TRUE	Boolean	If TRUE, enables checking of L1/L2 energy ratio for Range 3 and 4 events
L2SHIFT	4	–	sets minimum allowed value of L1/L2 energy ratio: 4 implies min_ratio = 1/16, 3 implies min_r = 1/8, 2 implies min_r = 1/4, etc.
STFSET2	8	Matrix cells	# of cells to shift EPrime IDX if a real event falls in Range 2 STIM box
STFSET3	8	Matrix cells	# of cells to shift EPrime IDX if a real event falls in Range 3 STIM box
STFSET4	22	Matrix cells	# of cells to shift EPrime IDX if a real event falls in Range 4 STIM box
CHKTAGS?	TRUE	Boolean	If TRUE, enables onboard checking of tags generated by front-end logic
FIXTAGS?	TRUE	Boolean	If TRUE, enables onboard fixing of tags generated by front-end logic
REJL3TH		ADC channels	used to test for the presence of an L3 signal in events rejected for onboard processing. If an L3 signal above REJL3TH is present, the event is assigned to priority buffers 9 or 20. If not, the event is assigned to priority buffers 10 or 21.
L2DELOWZLIM		ADC channels	used to test if a Range 2 event is lo-Z or Hi-Z. This is the cut on the L1 (δ_E) signal
L2EPLOWZLIM		ADC channels	used to test if a Range 2 event is lo-Z or Hi-Z. This is the cut on the L2 (Eprime) signal
L3DELOWZLIM		ADC channels	used to test if a Range 3 event is lo-Z or Hi-Z. This is the cut on the L2 (δ_E) signal
L3EPLOZLIM		ADC channels	used to test if a Range 3 event is lo-Z or Hi-Z. This is the cut on the L3 (Eprime) signal
PDELOWZLIM		ADC channels	used to test if a Range 4 event is lo-Z or Hi-Z. This is the cut on the L3 (ΔE) signal

Table 24 (*Continued*)

Variable name	Default value	Units	Description
PEPLOWZLIM		ADC channels	used to test if a Range 4 event is lo-Z or Hi-Z. This is the cut on the L3 (Eprime) signal
XTALKTH12		ADC channels	L1, L2 cross-talk threshold – L1or L2 pulse-heights above this are not cross-talk
XTALKTH3		ADC channels	L3 cross-talk threshold – L3 pulse-heights above this are not cross-talk
CRXTALKTH		ADC channels	threshold above which an ADC is likely to produce cross-talk

LET windows, so the L2 and L3 entries are unused. WINCORR2 is used for Range 2 events. WINCORR3 is used for Range 3 and 4 events.

The index into the following nine tables is $(\text{L1ID} \ll 2) | \text{L2ID}$. So, each entry refers to a particular L1–L2 detector combination.

R2COSINES, R3COSINES, PENCOSINES: Angle correction lookup tables for Range 2, Range 3, and Range 4 (PEN) events. Each entry is $(\text{int})(256 * (\cos(q))^{1/\alpha})$. For Range 2, $\cos\theta$ is the cosine of the angle between the L1-perpendicular and the line between the centers of the L1 and L2 detectors. For Range 3 and 4, $\cos\theta$ is the cosine of the angle between the L2-perpendicular and the line between the centers of the L1 and L2 detectors. α is different for each range: currently 1.36, 1.65, 1.77 for Ranges 2, 3, and 4 respectively.

EXCLUDER2A, EXCLUDER2B: For Range 2 events, if a table entry is set to 1, then that L1–L2 combination will be excluded from onboard processing for A-side (B-side) events.

EXCLUDER3I: For Range 3 events with L3-inner hit, table entries are set to 1 if the L1–L2 combination is inconsistent with an L3-inner hit, or if the event might be a penetrating particle escaping out the side without hitting the R4 (PEN) detector.

EXCLUDER3O: For Range 3 events with L3-outer hit, table entries are set to 1 if the L1–L2 combination is inconsistent with an L3-outer hit, or if the event might be a penetrating particle escaping out the side without hitting the R4 (PEN) detector.

SECTORID: Identifies the sector that any given L1–L2 combination belongs to.

TAGTABLE : This table is indexed by the six tag bits of an ADC word. Each entry is a constant that defines the type of event that the tag bits signify: L12A, L123A, L12B, L123B, PENA, PENB, PENA?, PENB?, 2TEL, ERR.

References

- W.E. Althouse et al., IEEE Trans. Geosci. Electron. **GE-16**, 204 (1978)
- J.-L. Bougeret et al., Space Sci. Rev. (2007, this issue)
- L.F. Burlaga et al., Science **309**, 2027 (2005)
- CCSDS, in *Packet Telemetry Recommendation for Space Data System Standards* (CCSDS, Washington, 2000). 102.0-B-5, Blue Book, Issue5
- H.V. Cane, D. Lario, Space Sci. Rev. (2006). doi:[10.1007/s11214-006-9011-3](https://doi.org/10.1007/s11214-006-9011-3)
- H.V. Cane, W.C. Erickson, N.P. Prestage, J. Geophys. Res. (2002). doi:[10.1029/2001JA000320](https://doi.org/10.1029/2001JA000320)
- H.V. Cane et al., Geophys. Res. Lett. (2003). doi:[10.1029/2002GL016580](https://doi.org/10.1029/2002GL016580)
- H.V. Cane et al., J. Geophys. Res. (2006). doi:[10.1029/2005JA011071](https://doi.org/10.1029/2005JA011071)
- C.M.S. Cohen et al., Geophys. Res. Lett. **26**, 2697 (1999)

- C.M.S. Cohen et al., J. Geophys. Res. (2005). doi:[10.1029/2005JA011004](https://doi.org/10.1029/2005JA011004)
- C.M.S. Cohen et al., Space Sci. Rev. (2007). doi:[10.1007/s11214-007-9218-y](https://doi.org/10.1007/s11214-007-9218-y)
- W.R. Cook et al., Custom analog VLSI for the Advanced Composition Explorer (ACE), small instruments for space physics, in *Proceedings of the Small Instrument Workshop*, held 29–31 March, 1993 in Pasadena, CA, ed. by B.T. Tsurutani (National Aeronautics and Space Division, Washington, 1993), p. 7
- A.C. Cummings, E.C. Stone, C.D. Steenberg, *Astrophys. J.* **578**, 194 (2002)
- M.I. Desai et al., *Astrophys. J.* **649**, 470 (2006)
- W. Dröge et al., *Astrophys. J.* **645**, 1516 (2006)
- J.R. Dwyer et al., *Astrophys. J.* **563**, 403 (2001)
- L.A. Fisk, B. Koslovsky, R. Ramaty, *Astrophys. J. Lett.* **190**, L35 (1974)
- A.B. Galvin et al., Space Sci. Rev. (2007, this issue)
- J. Giacalone, J.R. Jokipii, J.E. Mazur, *Astrophys. J.* **532**, L75 (2000)
- G. Gloeckler, *Space Sci. Rev.* **89**, 91 (1999)
- D.K. Haggerty, E.C. Roelof, in *27th International Cosmic Ray Conference*, ed. by W. Dröge, H. Kunow, M. Scholer (Schaltungsdiest Lange o.H.G., Berlin, 2001), p. 3238
- D.K. Haggerty, E.C. Roelof, *Astrophys. J.* **579**, 841 (2002)
- E. Halpern, J.H. Marshall, *IEEE Trans. Nucl. Sci.* **NS-15**, 242 (1968)
- E. Halpern, J.H. Marshall, D. Weeks, *Nucleonics in Aerospace* (Plenum, New York, 1968), p. 98
- T.M. Harrington, J.H. Marshall, *Rev. Sci. Instrum.* **39**, 184 (1968)
- T.M. Harrington, J.H. Marshall, *IEEE Trans. Nucl. Sci.* **NS-16**, 314 (1969)
- T.M. Harrington et al., *Nucl. Instrum. Methods* **118**, 401 (1974)
- G.C. Ho, E.C. Roelof, G.M. Mason, *Astrophys. J.* **621**, L141 (2005)
- J.L. Hoff, L.W. Townsend, J.W. Hines, *IEEE Trans. Nucl. Sci.* **50**, 2296 (2003)
- R.A. Howard et al., Space Sci. Rev. (2007, this issue)
- J.F. Janni, Technical report No. AFWL-TR-65-150, Air Force Weapons Laboratory, Kirtland Air Force Base, NM, 1966
- S.W. Kahler, A. Vourlidas, J. Geophys. Res. (2005). doi:[10.1029/2006JA011073](https://doi.org/10.1029/2006JA011073)
- A. Klassen et al., J. Geophys. Res. **110** (2005). CiteID A09S04
- B. Klecker et al., *Adv. Space Res.* **38**, 493 (2006)
- S. Krucker, R.P. Lin, *Astrophys. J.* **542**, L61 (2000)
- A.W. Labrador et al., in *28th International Cosmic Ray Conference*, ed. by T. Kajta, Y. Asaoka, A. Kawachi, Y. Matsubara, M. Sasaki (Universal Academy Press, Inc., Tokyo, 2003), p. 3269
- A.W. Labrador et al., in *29th International Cosmic Ray Conference*, vol. 1, ed. by B. Sripathi et al. (Tata Institute of Fundamental Research, Mumbai, 2005), p. 99
- R.A. Leske et al., in *Acceleration and Transport of Energetic Particles Observed in the Heliosphere*, ed. by R.A. Mewaldt et al. (AIP, Melville, 2000), p. 293
- R.A. Leske et al., in *Connecting Sun and Heliosphere*, ed. by B. Fleck, T.H. Zurbuchen, H. Lacoste (ESA, Whistler, 2003a), p. 616
- R.A. Leske et al., in *28th International Cosmic Ray Conference*, ed. by T. Kajta, Y. Asaoka, A. Kawachi, Y. Matsubara, M. Sasaki (Universal Academy Press, Inc., Tokyo, 2003b), p. 3253
- R.A. Leske et al., *Space Sci. Rev.* (2007a). doi:[10.1007/s11214-007-9191-5](https://doi.org/10.1007/s11214-007-9191-5)
- R.A. Leske et al., *Space Sci. Rev.* (2007b). doi:[10.1007/s11214-007-9185-3](https://doi.org/10.1007/s11214-007-9185-3)
- G. Li, G.P. Zank, W.K.M. Rice, J. Geophys. Res. (2005). doi:[10.1029/2004JA010600](https://doi.org/10.1029/2004JA010600)
- R.P. Lin et al., *Space Sci. Rev.* (2007, this issue)
- J.G. Luhmann et al., *Adv. Space Res.* **36**, 1534 (2005)
- J.G. Luhmann et al., *Space Sci. Rev.* (2007, this issue). doi:[10.1007/s11214-007-9170-x](https://doi.org/10.1007/s11214-007-9170-x)
- G.M. Mason, G. Gloeckler, D. Hovestadt, *Astrophys. J.* **280**, 902 (1984)
- G.M. Mason, J.E. Mazur, D.C. Hamilton, *Astrophys. J.* **425**, 843 (1994)
- G.M. Mason et al., *Astrophys. J.* **486**, L149 (1997)
- G.M. Mason et al., *Geophys. Res. Lett.* **26**, 141 (1999)
- G.M. Mason, J.R. Dwyer, J.E. Mazur, *Astrophys. J.* **545**, L157 (2000)
- G.M. Mason et al., *Astrophys. J.* **574**, 1039 (2002)
- G.M. Mason, J.E. Mazur, J.R. Dwyer, *Astrophys. J.* **565**, L51 (2002)
- G.M. Mason et al., *Astrophys. J.* **606**, 555 (2004)
- G.M. Mason et al., *Space Sci. Rev.* (2007, this issue). doi:[10.1007/s11214-006-9087-9](https://doi.org/10.1007/s11214-006-9087-9)
- J.E. Mazur et al., *Geophys. Res. Lett.* **26**, 173 (1999)
- J.E. Mazur et al., *Astrophys. J.* **532**, L79 (2000)
- J.E. Mazur, G.M. Mason, R.A. Mewaldt, *Astrophys. J.* **566**, 555 (2002)
- F.B. McDonald et al., in *29th International Cosmic Ray Conference*, vol. 2, ed. by B. Sripathi Acharya et al. (Tata Institute of Fundamental Research, Mumbai, 2005), p. 35
- D.J. McComas, N.A. Schwadron, *Geophys. Res. Lett.* (2006). doi:[10.1029/2005GL025437](https://doi.org/10.1029/2005GL025437)

- M.A. McMahan, Nucl. Instr. Methods Phys. Res. **B241**, 409 (2005)
- R.A. Mewaldt, in *26th International Cosmic Ray Conference, Invited, Rapporteur, and Highlight Papers*, ed. by B.L. Dingus, D.B. Kieda, M.H. Salamon (AIP, Melville, 2000), p. 265
- R.A. Mewaldt et al., in *28th International Cosmic Ray Conference*, ed. by T. Kajita, Y. Asaoka, A. Kawachi, Y. Matsubara, M. Sasaki (Universal Academy Press, Inc., Tokyo, 2003), p. 3313
- R.A. Mewaldt et al., in *Proc. 29th International Cosmic Ray Conf.*, vol. 1, ed. by B. Sripathi Acharya et al. (Tata Institute of Fundamental Research, Mumbai, 2005a), p. 57
- R.A. Mewaldt et al., J. Geophys. Res. (2005b). doi:[10.1029/2005JA011038](https://doi.org/10.1029/2005JA011038)
- R.A. Mewaldt et al., in *The Physics of Collisionless Shocks*, ed. by G. Li, G.P. Zank, C.T. Russell (AIP, Melville, 2005c), p. 227
- R.A. Mewaldt et al., in *Connecting Sun and Heliosphere*, ed. by B. Fleck, T.H. Zurbuchen, H. Lacoste (ESA, Whistler, 2005d), p. 67
- R.A. Mewaldt, C.M.S. Cohen, G.M. Mason, in *Solar Eruptions and Energetic Particles*, ed. by N. Gopalswamy, R.A. Mewaldt, J. Torsti (AGU, Washington, 2006), p. 115
- R.A. Mewaldt, Space Sci. Rev. (2006). doi:[10.1007/s11214-006-9091-0](https://doi.org/10.1007/s11214-006-9091-0)
- R.A. Mewaldt et al., Space Sci. Rev. (2007). doi:[10.1007/s11214-007-9200-8](https://doi.org/10.1007/s11214-007-9200-8)
- E. Möbius et al., Geophys. Res. Lett. (2002). doi:[10.1029/2001GL013410](https://doi.org/10.1029/2001GL013410)
- H. Moraal et al., in *Physics of the Heliosheath*, ed. by J. Heerikhuisen, V. Florinski, G.P. Zank, N.V. Pogorelov (AIP, Melville, 2006), p. 219
- R. Müller-Mellin et al., Space Sci. Rev. (2007, this issue). doi:[10.1007/s11214-007-9204-4](https://doi.org/10.1007/s11214-007-9204-4)
- J.S. Neal, L.W. Townsend, Radiat. Prot. Dosim. **115**, 38 (2005)
- N.V. Nitta et al., Astrophys. J. (2006). doi:[10.1086/507442](https://doi.org/10.1086/507442)
- T.G. Onsager et al., in *GOES-8 and Beyond, SPIE Conference Proceedings*, ed. by E.R. Washwell (SPIE, Bellingham, 1996), pp. 281–290
- M.E. Pesses, J.R. Jokipii, D. Eichler, Astrophys. J. Lett. **246**, L85 (1981)
- V.S. Ptuskin, Space Sci. Rev. **99**, 281 (2001)
- D.V. Reames, Adv. Space Res. **13**, 331 (1993)
- D.V. Reames, Adv. Space Res. **15**, 41 (1995)
- D.V. Reames, Space Sci. Rev. **90**, 413 (1999)
- D.V. Reames, C.K. Ng, Astrophys. J. **610**, 510 (2004)
- D.V. Reames, T.T. von Rosenvinge, R.P. Lin, Astrophys. J. **292**, 716 (1985)
- D.V. Reames, R.G. Stone, M.-B. Kallenrode, Astrophys. J. **380**, 287 (1991)
- D.V. Reames, J.-P. Meyer, T.T. von Rosenvinge, Astrophys. J. Suppl. **90**, 649 (1994)
- D.V. Reames et al., Geophys. Res. Lett. **24**, 2917 (1997)
- D.V. Reames, C.K. Ng, D. Berdichevsky, Astrophys. J. **550**, 1064 (2001)
- W.K.M. Rice, G.P. Zank, G. Li, J. Geophys. Res. (2003). doi:[10.1029/2002JA009756](https://doi.org/10.1029/2002JA009756)
- I.G. Richardson, Space Sci. Rev. **111**, 267 (2004)
- N.A. Schwadron et al., Geophys. Res. Lett. (2002). doi:[10.1029/2002GL015829](https://doi.org/10.1029/2002GL015829)
- R. Schwenn, E. Marsch, *Physics of the Inner Heliosphere I and II* (Springer, Berlin, 1991)
- J.D. Slavin, P.C. Frisch, Astrophys. J. **565**, 364 (2002)
- E.C. Stone et al., Space Sci. Rev. **86**, 1 (1998a)
- E.C. Stone et al., Space Sci. Rev. **86**, 357 (1998b)
- E.C. Stone et al., Space Sci. Rev. **86**, 285 (1998c)
- E.C. Stone et al., Science **309**, 2017 (2005)
- R.E. Turner, in *Solar Eruptions and Energetic Particles*, ed. by N. Gopalswamy, A. Mewaldt, J. Torsti (AGU, Washington, 2006), p. 367
- A.J. Tylka, W.F. Dietrich, P.R. Boberg, IEEE Trans. Nucl. Sci. **44**, 2140 (1997)
- A.J. Tylka et al., Astrophys. J. **558**, L59 (2001)
- A.J. Tylka et al., in *28th International Cosmic Ray Conference*, ed. by T. Kajita, Y. Asaoka, A. Kawachi, Y. Matsubara, M. Sasaki (Universal Academy Press, Inc., Tokyo, 2003), p. 3305
- A.J. Tylka et al., Astrophys. J. **625**, 474 (2005)
- J. Vandegrift et al., Adv. Space Res. **36**, 2323 (2005)
- T.T. von Rosenvinge et al., in *Solar and Galactic Composition*, ed. by R.F. Wimmerschweingruber (AIP, Melville, 2001), p. 343
- T.T. von Rosenvinge et al., Space Sci. Rev. (2007, this issue)
- A. Vourlidas et al., Astrophys. J. **534**, 456 (2000)
- Y.-M. Wang, M. Pick, G.M. Mason, Astrophys. J. **639**, 495 (2006a)
- L. Wang et al., Geophys. Res. Lett. (2006b). doi:[10.1029/2005GL024434](https://doi.org/10.1029/2005GL024434)
- M.E. Wiedenbeck et al., in *28th International Cosmic Ray Conference*, ed. by T. Kajita, Y. Asaoka, A. Kawachi, Y. Matsubara, M. Sasaki (Universal Academy Press, Inc., Tokyo, 2003), p. 3245
- M. Zhang et al., in *Physics of the Heliosheath*, ed. by J. Heerikhuisen, V. Florinski, G.P. Zank, N.V. Pogorelov (AIP, Melville, 2006), p. 226
- R.D. Zwickl et al., Space Sci. Rev. **86**, 633 (1998)

The Solar Electron and Proton Telescope for the STEREO Mission

R. Müller-Mellin · S. Böttcher · J. Falenski · E. Rode ·
L. Duvet · T. Sanderson · B. Butler · B. Johlander ·
H. Smit

Originally published in the journal Space Science Reviews, Volume 136, Nos 1–4.
DOI: [10.1007/s11214-007-9204-4](https://doi.org/10.1007/s11214-007-9204-4) © Springer Science+Business Media B.V. 2007

Abstract The Solar Electron and Proton Telescope (SEPT), one of four instruments of the Solar Energetic Particle (SEP) suite for the IMPACT investigation, is designed to provide the three-dimensional distribution of energetic electrons and protons with good energy and time resolution. This knowledge is essential for characterizing the dynamic behaviour of CME associated and solar flare associated events. SEPT consists of two dual double-ended magnet/foil particle telescopes which cleanly separate and measure electrons in the energy range from 30–400 keV and protons from 60–7 000 keV. Anisotropy information on a non-spinning spacecraft is provided by the two separate telescopes: SEPT-E looking in the ecliptic plane along the Parker spiral magnetic field both towards and away from the Sun, and SEPT-NS looking vertical to the ecliptic plane towards North and South. The dual set-up refers to two adjacent sensor apertures for each of the four view directions: one for protons, one for electrons. The double-ended set-up refers to the detector stack with view cones in two opposite directions: one side (electron side) is covered by a thin foil, the other side (proton side) is surrounded by a magnet. The thin foil leaves the electron spectrum essentially unchanged but stops low energy protons. The magnet sweeps away electrons but lets ions pass. The total geometry factor for electrons and protons is $0.52 \text{ cm}^2 \text{ sr}$ and $0.68 \text{ cm}^2 \text{ sr}$, respectively. This paper describes the design and calibration of SEPT as well as the scientific objectives that the instrument will address.

Keywords Solar energetic particles · CME · Acceleration · Propagation · Instrumentation

1 Introduction

The twin observatories of the STEREO mission will perform comprehensive studies of Coronal Mass Ejections (CMEs) directed towards Earth from two vantage points which

R. Müller-Mellin (✉) · S. Böttcher · J. Falenski · E. Rode
Universität Kiel, 24118 Kiel, Germany
e-mail: muller-mellin@physik.uni-kiel.de

L. Duvet · T. Sanderson · B. Butler · B. Johlander · H. Smit
ESA/ESTEC, 2200 Noordwijk, The Netherlands

allow stereoscopic remote observations of CMEs and multi-point in-situ measurements of their interplanetary counterparts (ICMEs). The angle STEREO-A–Sun–STEREO-B increases at a rate of 44 degrees per year. As the observatories separate, larger ICME structures are revealed by the particles and field instruments of the IMPACT investigation. When the Sun transforms stored magnetic energy into electromagnetic radiation and kinetic energy of coronal matter (increased bulk motion of plasma as well as acceleration of energetic particles) the solar energetic particles (SEPs) bear the imprint of the various physical processes at work and of the regions through which they have travelled. Examples of these processes are stochastic acceleration, involving resonant wave–particle interactions that transfer energy from waves to particles or shock acceleration where resonant wave generation by particles traps them near the shock increasing the efficiency of their acceleration to higher energies. Electrons and protons are a major contributor to the energy balance and dynamics of the interplanetary medium. They outnumber by far the remaining constituents of the particle population. A considerable amount of the total energy release during a CME can be imparted to energetic particles in the energy interval 10 keV to 1 GeV, whereof up to 80% can be accounted for by protons and up to 18% by electrons (Mewaldt et al. 2005). Their greatly differing mass can uniquely reveal the details of acceleration and propagation mechanisms. Solar flare or shock accelerated electrons reach the Earth rapidly compared to protons assuming a simultaneous release at the Sun (Klein and Posner 2005). Their energy spectra will be useful as predictors of the severity of terrestrial effects.

The Solar Electron and Proton Telescope (SEPT) is one of seven instruments of the IMPACT investigation and is designed to cleanly separate and measure electrons in the energy range from 30–400 keV and protons from 60–7 000 keV. The electron measurements will cover the gap with some overlap between suprathermal electrons measured by STE (Luhmann et al. 2007) and high energy electrons measured by HET (von Rosenvinge et al. 2007). The proton measurements fill in without completely covering the gap between solar wind energies (PLASTIC SWS; Galvin et al. 2007) and higher energy measurements of LET (2–13 MeV; Mewaldt et al. 2007) as well as HET (13–100 MeV). The four SEPT instruments for the twin STEREO mission are shown in Fig. 1, their essential features are summarized in Table 1. A discussion of the scientific objectives is presented in Sect. 2, while details of the design and calibration can be found in Sects. 3 and 4.

2 Science Objectives

2.1 SEP Acceleration

Energetic processes on the Sun are known to occasionally accelerate protons to GeV and electrons to tens of MeV energies. First evidence of high-energy particles from the Sun was obtained 60 years ago when Forbush studied the large solar events of February and March of 1942 (Forbush 1946). Since then extensive knowledge of energy spectra, abundance variations, intensity-time profiles, and spatial distributions has been gathered leading in the 1980s to the classification of solar energetic particle events into gradual events—accelerated by shock waves driven outward by coronal mass ejections—and impulsive events originating from a stochastic acceleration process in the flare site (Cane et al. 1986; Reames 1995). However, in recent years several studies have challenged this classification. In a refinement of the two-class picture (Cliver 1996) it was suggested that gradual events possess an impulsive “core” in which similar acceleration processes as in impulsive flares operate, and from which particles can escape into the interplanetary medium where they can be observed

Fig. 1 SEPT-E (*in front*) and SEPT-NS (*on bracket*). SEPT for Ahead S/C with doors closed (*right*), and for Behind S/C with doors open (*left*)



Table 1 Summary of SEPT characteristics

Characteristic	Value	Details
Measurement objective	Clean separation of electrons and protons and measurement of their energy spectra and angular distribution	Sect. 2
Measurement technique	Total energy measurement in magnet/foil particle telescope	Sect. 3.1.2
Sensor system	Ion-implanted Si detectors (300 μm thick) in anti-coincidence configuration. Rare-Earth magnets (remanence 0.5 tesla in the air gap) to deflect electrons. Parylene foil (4.95 μm thick) to stop protons.	Sects. 3.1.3, 3.1.4, 3.1.5
Energy interval		Sect. 4
Electrons	30–400 keV	
Protons	60–7 000 keV	
Field of view		Sect. 3.1.2
Electrons	$4 \times 52.8^\circ$ conical	
Protons	$4 \times 52.0^\circ$ conical	
Geometrical factor		Sect. 3.1.2
Electrons	$4 \times 0.13 \text{ cm}^2 \text{ sr}$	
Protons	$4 \times 0.17 \text{ cm}^2 \text{ sr}$	
Resources	SEPT-E	SEPT-NS with bracket
Dimensions	$99 \times 156 \times 147 \text{ mm}^3$	$100 \times 175 \times 312 \text{ mm}^3$
Mass	795 g	1175 g
Power (worst case)	600 (765) mW	600 (765) mW
Bit rate (beacon)	40 (3) bit/s	40 (3) bit/s

together with particles accelerated by a CME-driven shock (for a review see Reames 1999; Kallenrode 2003). The existence of these “hybrid” cases poses a challenge to the observer to characterize and identify “pure” events which best allow studies of the two acceleration mechanisms.

SEPT will use near-relativistic electrons as time markers for injection of solar particles. The onset times of these escaping electrons can be compared to electromagnetic radiation signatures of interacting particles and dispersion-dependent arrival times of escaping protons. Time variations, energy spectra and angular distributions will be studied to answer important questions like:

- (1) Are particles which are accelerated in the low and middle corona prevented from travelling to Earth either by the CME shock (Kahler 1996) or because they are supposedly trapped in the coronal magnetic fields (Reames 2002)?
- (2) If these particles contribute to CME-associated SEP events, is their escape energy-dependent?
- (3) Are there different acceleration sites for interacting and escaping particles?
- (4) While the shock wave may continue to accelerate particles all the way from the solar corona to beyond 1 AU, are there identifiable contributions from particles well behind the front of the CME at the time of acceleration (Klein and Posner 2005)?
- (5) Representing the measured electron and proton spectra by a power law modulated by an exponential, can we distinguish whether the spectra are dominated by acceleration effects or transport effects?
- (6) Can we distinguish signatures of solar injection from in-situ acceleration processes?

2.2 Comparing Gradual and Impulsive SEP Events

Historically the terms impulsive and gradual were introduced to describe soft X-ray events on the Sun to which SEP events could later be associated. While the X-ray time scales “impulsive vs. gradual” only poorly resolve the acceleration mechanism, impulsive particle events can be distinguished from gradual events by their elemental and isotope abundances, ionization states, energy spectra, angular distributions and time behaviour (Reames 1999). They are electron rich, and their proton to helium ratio is low (Mueller-Mellin et al. 1993), their Fe charge state is high (Luhn et al. 1987; Tylka et al. 1995), and they are rich in ^3He and enhanced in heavy elements up to Fe (Reames 1988). Table 2 summarizes these particle characteristics which reflect the paradigm as of the early 1990’s. As stated in Sect. 2.1, refined measurement techniques have been applied in solar cycle 23 which modify this picture. Thus, most gradual events include ^3He in excess of the solar wind ratio (Cohen et al. 1999; Mason et al. 1999). Also the Fe charge states and the Fe/O ratio can vary considerably from event to event in both impulsive and gradual events, and the Fe charge state is found to be energy dependent, ranging from ~ 10 to 20 (Moebius et al. 2003; Klecker et al. 2006). The scheme in Table 2 serves to classify the particle signatures in comparison to electromagnetic properties of Table 3 even if SEPT cannot contribute to charge state or composition measurements other than electron/proton ratios and even if mixed events are known to be a common feature.

Solar energetic electron and ion observations often correlate with solar radio and optical observations. The properties of electromagnetic radiation of impulsive and gradual flares which can be associated with SEP events are given in Table 3. The complement of remote and in-situ instrumentation onboard STEREO will greatly support correlation studies with SEPT data to understand the physical processes of the active Sun and in the disturbed interplanetary medium.

Table 2 Classes of solar particle events

	Gradual	Impulsive
Particles	Proton rich	Electron rich
$^3\text{He}/^4\text{He}$	~0.0005	~1
Fe/O	~0.15	~1.2
H/He	~100	~10
Q_{Fe}	~14	~20
Duration	Days	Hours
Longitude distribution	$\leq 180^\circ$	$< 30^\circ$
Solar wind signature	Interplanetary shock	–
Event rate	~10 per year	1000 per year

Table 3 Electromagnetic properties of gradual and impulsive flares (Kallenrode 2003)

	Gradual	Impulsive
Duration in soft X-rays	> 1 h	< 1 h
Decay in soft X-rays	> 10 min	< 10 min
Duration in hard X-rays	> 10 min	< 10 min
Duration in microwaves	> 5 min	< 5 min
Metric type II	Always	75%
Metric type III	50%	Always
Metric type IV	Always	Rare
Chromospheric H α size	Large	Small
Height in corona	$\sim 5 \times 10^4$ km	$\leq 10^4$ km
Volume	$10^{28} \text{--} 10^{29}$ cm 3	$10^{26} \text{--} 10^{27}$ cm 3
Energy density	Low	High
Coronal mass ejections	Always	Rare

2.3 ICME Topology

Magnetic clouds are often embedded in ICMEs (interplanetary evolution of a CME). It is known that electrons of 100 eV to 1 keV streaming out from the hot tail of the coronal thermal distribution become bidirectional if they enter magnetic clouds where both ends intercept the corona (Gosling et al. 1987). But also electrons and ions in the SEPT energy range can lend support in outlining the ICME topology when their counterstreaming is observed. Anisotropy information on the non-spinning STEREO spacecraft is provided by the two separate telescopes: SEPT-E looking in the ecliptic plane along the Parker spiral magnetic field both towards and away from the Sun, and SEPT-NS looking vertical to the ecliptic plane towards North and South. The answers to questions of how the field lines are routed inside an ICME or whether the field lines in an ICME are still connected to the Sun as opposed to a detached plasmoid can find further corroboration by measurements of the angular distribution.

2.4 Space Weather

Electrons from SEP events reach the Earth rapidly, carrying significant information about the source region. In particular, electrons from flare sites produce hard spectra which almost

never produce effects on the Earth's magnetosphere and atmosphere. Conversely, shock accelerated electrons are associated with proton-rich SEP events signalling the arrival of stormy conditions with the power to imperil satellites, take down power grids, disrupt communications, pose a radiation hazard to astronauts, or produce colourful aurorae. However, there are statistical studies (Oakley et al. 2003) which claim a correlation of radio type II bursts with hard electron spectra. When properly understood, electron spectra and the electron to proton ratio will be useful as predictors of the severity of terrestrial effects. SEPT data are included in the IMPACT beacon mode data set for continuous transmission to the ground stations. Four energy bands for electrons and four energy bands for protons are provided with a time resolution of one minute. The lowest and highest energy bands are sectorized in four directions.

3 Instrument Description

3.1 Approach

3.1.1 Design Requirements

Providing the three-dimensional distribution of energetic electrons and protons with good energy resolution poses several instrumental challenges: as singly charged particles in the energy range from some 10 keV to several MeV deposit only small amounts of energy in a solid state detector, the requirements on noise suppression are more stringent than they would be for heavier ions. Furthermore, separating electrons from protons in this energy range is complicated by the fact that the well-proven $dE/dx - E$ approach is not viable as it is for higher energies because one cannot afford to have two measurements in separate detectors: either the dE/dx detector would stop all the low energy particles before they reach the E detector or the dE/dx detector would have to be made so thin as to render the signal of a penetrating singly-charged particle indiscernible from detector noise. In addition the spectra of solar energetic particles have a steep spectral slope, i.e. an instrument has to cope with very high fluxes at low energies. Also, as the spacecraft is not spinning, special efforts must be made to acquire anisotropy information. Finally, the secondary particles generated by solar and galactic cosmic rays in the surrounding matter of the spacecraft constitute a background against which good discrimination is mandatory. The following discussion will document how these requirements were met.

3.1.2 The Detector System

Each double-ended telescope has two solid state detectors (SSDs) which are operated in anti-coincidence. One SSD looks through an absorption foil and its partner through the air gap of a magnet system. The foil leaves the electron spectrum essentially unchanged but stops protons of energy up to the energy of electrons (~ 400 keV) which penetrate the SSD. The magnet is designed to sweep away electrons below 400 keV, but leaves ions unaffected. In the absence of > 400 keV ions, the foil SSD only detects electrons, and the magnet SSD only detects ions. Ions from 400 keV to 7 MeV will stop in the magnet SSD and their fluxes will be cleanly measured. The contribution of > 400 keV ions to the foil SSD can then be computed and subtracted to obtain the electron fluxes. The SEPT sensor schematics are shown in Fig. 2. Some SEPT sensor characteristics are given in Table 4.

Table 4 SEPT sensor characteristics

Channel (anti) coinc.	Particle species	Geometrical factor	View cone	Boresight ahead S/C	Accum. time
D0 D1 G0 G1	electrons 30–480 keV	0.13 cm ² sr	52.8°	ecliptic 135°	60 s
D1 D0 G0 G1	protons 70–6 500 keV	0.17 cm ² sr	52.0°	ecliptic 315°	60 s
D2 D3 G2 G3	electrons 30–480 keV	0.13 cm ² sr	52.8°	ecliptic 315°	60 s
D3 D2 G2 G3	protons 70–6 500 keV	0.17 cm ² sr	52.0°	ecliptic 135°	60 s
D4 D5 G4 G5	electrons 30–480 keV	0.13 cm ² sr	52.8°	north	60 s
D5 D4 G4 G5	protons 70–6 500 keV	0.17 cm ² sr	52.0°	south	60 s
D6 D7 G6 G7	electrons 30–480 keV	0.13 cm ² sr	52.8°	south	60 s
D7 D6 G6 G7	protons 70–6 500 keV	0.17 cm ² sr	52.0°	north	60 s

Note: Channels of SEPT-E and -NS on Behind S/C with reversed boresight

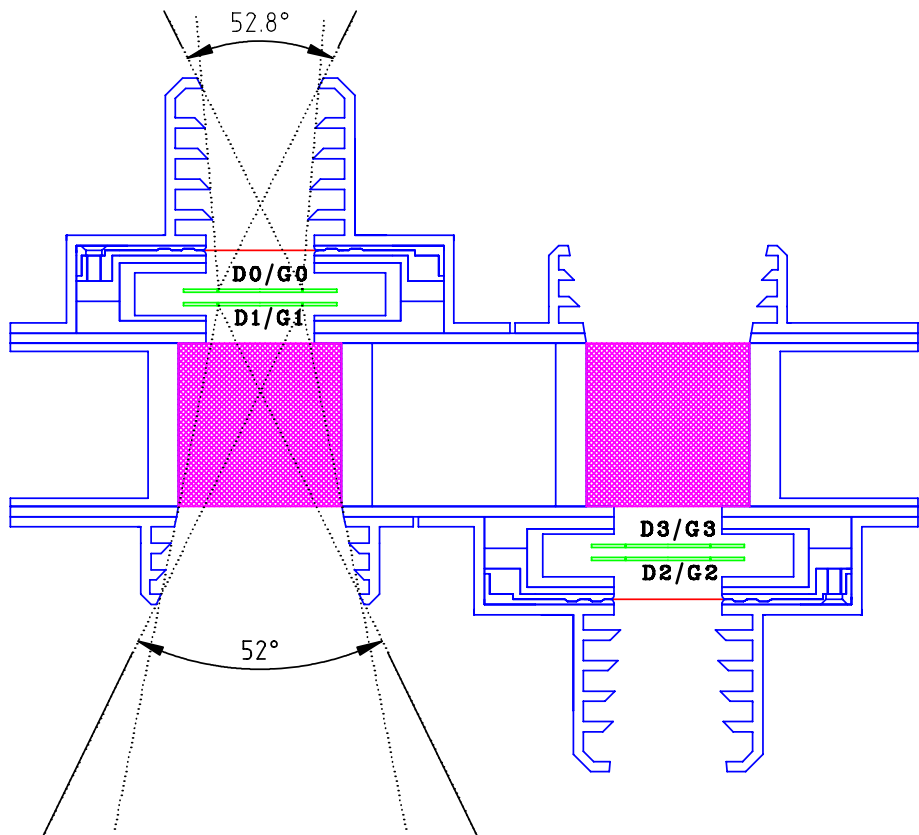


Fig. 2 SEPT sensor schematics. Detection elements are silicon detectors (D0, ..., D3, green) with guard rings (G0, ..., G3), Parylene foils (red), and magnetic fields perpendicular to the drawing plane (magenta)

Anisotropy information is acquired in four look directions: SEPT-E observes in the ecliptic plane along the nominal Parker spiral magnetic field direction both forward and backward, SEPT-N/S observes out of the ecliptic plane perpendicular to the magnetic field both

Table 5 PIPS specification

Detector active area	center: 53 mm ² , ring 58 mm ²
Detector diameter	center: 8.2 mm, ring: 12 mm crosstalk ring: 8.4 mm
Chip dimensions	flat to flat: 15.15 mm on diagonal: 16.4 mm
Chip thickness	300 ± 25 µm
Depletion depth (min./max.)	285/325 µm
Contact to junction	wire bonding
Contact to ohmic side	wire bonding
Junction window thickness	<1 500 nm
Ohmic window thickness	<350 nm
Detector capacitance	center: 20 pF, ring 21 pF
Nominal operating voltage	40 V
Actual operating voltage	80 V
Current at 20°C at 5 000 lux	typ. 15 nA, max. 60 nA

North and South. Thus, SEPT partially complements the viewing directions for ions of the Low Energy Telescope (LET, see Mewaldt et al. 2007) the multiple look directions of which are all in the ecliptic. To warrant unobstructed fields of view, the full angle of the viewing cones is limited to 52 degrees and SEPT-N/S is mounted on its own mounting bracket. The geometrical factor for each of the four magnet telescopes is 0.17 cm² sr and for each of the four foil telescopes 0.13 cm² sr.

3.1.3 The Solid State Detectors

The SSDs are of the Passivated Ion-implanted Planar Silicon (PIPS) type. Each SSD is surrounded by an active guard ring on the same Si wafer and closely stacked with its partner at 1 mm separation. To achieve low background, the output of each center segment is operated in anti-coincidence with its own guard ring and with its partner and the partner's guard ring to reject penetrating particles or secondary particles from outside the viewing cone. A special feature is the implementation of a 100 µm wide crosstalk ring between center segment and guard ring to prevent a veto by crosstalk for large pulses. The detector specifications are given in Table 5. Figure 3 shows the detector layout with three solder pads for center segment, guard ring, and crosstalk ring. As some detectors will see stray light from minor impingements of antennas and solar panels in their fields of view, all detectors are mounted with their ohmic side facing outward, which is treated with a 170 nm aluminium layer for light tightness. Each detector is biased at least 50 V beyond its depletion voltage to account for radiation dose effects towards the end of mission life time. The PIPS detectors are manufactured by Eurisys Canberra, Belgium.

3.1.4 The Magnet System

The magnet system consists of four rare-earth permanent magnets of type VACODYM VD745HR which offer highest remanence values and thus energy densities currently available. The excellent magnetic properties of this material group can be traced to the strongly magnetic matrix phase Nd₂Fe₁₄B featuring very high saturation polarization and high magnetic anisotropy. Each two of the four magnets are facing each other leaving an air gap with

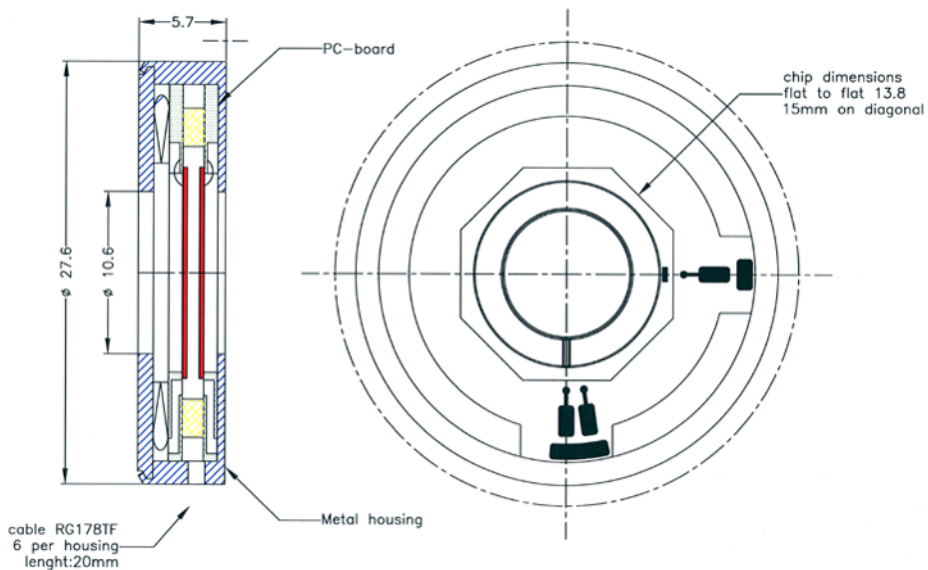


Fig. 3 Passivated ion-implanted planar silicon (PIPS) detector layout (Canberra, Belgium)

the necessary magnetic induction to deflect the electrons. Two yokes, made of the iron–cobalt alloy VACOFLUX 50, combine the two sets intensifying the magnetic induction. The long-range field is attenuated by having two oppositely polarized magnetic dipoles at close distance. Thus, the two air gaps provided by the magnet system serve two sensor systems simultaneously with anti-parallel viewing directions at minimum weight penalty while satisfying the stringent requirements on magnetic cleanliness.

A number of design options were investigated for the magnet system the most significant of which were an evaluation of the magnetic field strength and homogeneity in the air gaps. Both finite-element field calculations and an analytical approximation yield a maximum magnetic induction of 500 mT in the center of the air gap decaying to 170 mT towards the edges. A large number of magnets were fabricated and precisely measured to allow selection of individual magnets according to minimum differences in remanence and polarization vector. Thus the magnet manufacturer (Vacuumschmelze, Germany) could reduce the mismatch to better than 0.5%. The far-field as measured with the magnetometer of the MAG instrument onboard STEREO amounted to 1.8 nT at a distance of 3 m.

3.1.5 The Absorption Foil

The requirements on the absorber are demanding: while ultrathin, it must feature thermal stability over a large temperature range, a high physical strength against pressure differential and micrometeoroid impact, low sensitivity to thermal cycling and creep, high stability against exposure to UV and particle radiation, and low outgassing characteristics. The material of choice is Parylene N, a thin polymer film membrane which will stop about 400 keV protons with a corresponding range of 5.7×10^{-4} g/cm² in plastic. While the exact foil thickness is not critical, the homogeneity is. The Parylene N pellicle with a specific gravity of 1.12 g/cm³ has a measured uniform thickness of 4.95 µm with an amazingly small variation of ±0.2 µm over the diameter of 3 cm. A 100 nm Al coating is evaporated on both sides of the pellicles.

3.2 The Onboard Electronics

Two identical electronics units are mounted close to their respective telescopes. Each electronics unit analyses the signals of four SSDs and four associated guard rings. One Particle Detector Front End (PDFE) integrated circuit is used to analyze the charge pulse from detector D1, using its guard ring in anti-coincidence. A second PDFE is used to analyze the signal from D2 in anti-coincidence with its guard ring. Furthermore, anti-coincidence signals between D1 and D2 ensure that an “exclusive OR” function is performed, i.e. only stopping particles are analyzed. In a special calibration mode, this exclusive OR is inhibited in order to use minimum ionizing particles for on-station calibration. The signals from the detector pairs D3/D4 through D7/D8 are treated in an identical fashion.

Additional 10 housekeeping signals are sampled, digitized, and transferred to the SEP-Central processor to monitor SEPT health and status. A specific test pulse generator permits a functional check-out of the instrument in flight and during ground testing. The low-level operation of SEPT electronics is controlled by a specific FPGA. The high level operation of SEPT is controlled by the SEP-Central processor by way of commands sent on the serial interface. The same serial interface is used to transfer all scientific, calibration and house-keeping data from SEPT to the SEP-Central processor. The block diagram in Fig. 4 shows in some more detail the front-end electronics for one of the two SEPT telescopes, together with the accumulation logic. Figure 5 shows top and bottom views of the electronics package.

3.2.1 PDFE

The Particle Detector Front End (PDFE) is a custom design Application Specific Integrated Circuit (ASIC) using a standard 0.7 µm CMOS process suited for charged particle spectroscopy applications which has been developed for the European Space Agency (ESA) by KU Leuven/Belgium and IMEC-Invomec/Belgium (Wouters et al. 2000). A block diagram is shown in Fig. 6. It contains two analog charge-amplifying channels. The first channel is the main one; the second channel is used for coincidence or gating purposes. The coincidence detection can also be done externally via a digital input. Eight-bit-programmable discriminators are provided for both channels. For the main channel, after peak detection, an 8-bit analog to digital conversion is performed. It can be cascaded together with more PDFEs to control a multiple detector telescope. The operation of the PDFE is controlled via pins and a serial interface which permits also uploading of parameters. The PDFE features are given in Table 6.

3.2.2 FPGA

The Field Programmable Gate Array (FPGA) controls operations of the SEPT electronics. It steers the operation of the four PDFEs, reads their conversion results, applies logarithmic binning (selectable) to the data, reads, increments, and stores counter contents kept in the SRAM. It handles the communication interface with the SEP-Central processor, i.e. data transmission, command receipt and command interpretation. It controls the test generator and housekeeping multiplexer.

Upon detection of a valid event, the PDFE notifies the FPGA which reads the parallel output of the PDFE. Dependent on mode selection the address compressor either does a quasi-logarithmic or linear binning. The result is used as an address in the SRAM where the corresponding 24-bit counter is incremented. A timing command from the SEP-Central processor causes the FPGA to transfer the accumulated data: either 8 histograms with 32 bins of 24-bit

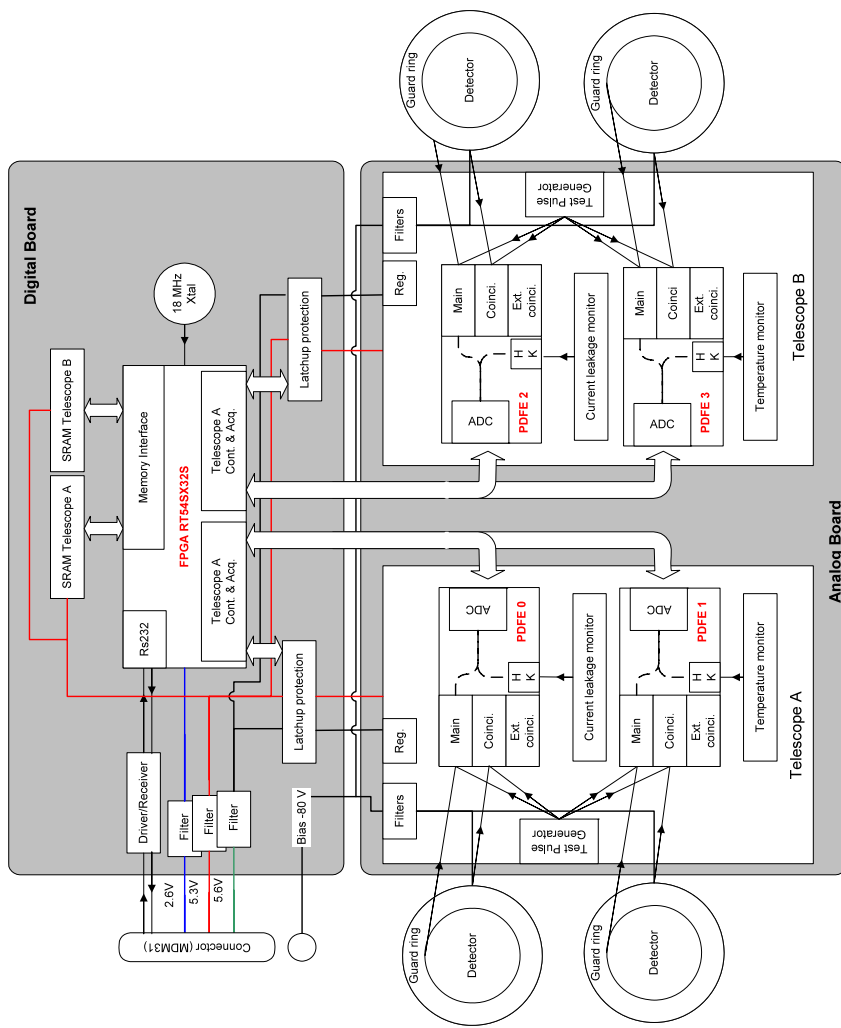


Fig. 4 SEPT electronics block diagram

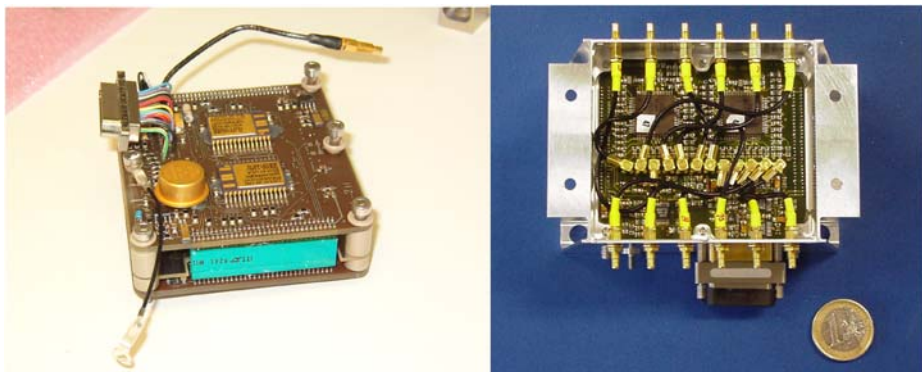


Fig. 5 Electronics board stack (*left*) and top view of analog board (*right*)

Table 6 PDFE specifications

Charge amplifying channels	1. main channel with shaper, baseline restorer, peak detector sample/hold 2. (anti-) coincidence channel for gating
Discriminators	1. 8-bit programmable for main channel 2. 8-bit programmable for coin. channel
Analog-to-digital converter	Linear 8-bit ADC
Operation	Completely event-driven
Radiation protection	All internal registers SEE (single event effects) protected
Package	64 pin CQFP (Ceramic Quad Flat pack)
Maximum detector capacitance	100 pF
Minimum/maximum detection charge	0.37/100 fC (8.8 keV / 2.3 MeV)
Conversion gain	30 mV/fC
Conversion gain adjustment	±5%
Noise	
at 0 pF detector capacitance	740 e_{rms} or 6.3 keV FWHM (measured)
at 120 pF	1160 e_{rms} or 9.8 keV FWHM (measured)
Noise slope	4.2 e_{rms} /pF (30 eV/pF)
Peaking time	1 μ s
Maximum counting rate at	
maximum detection charge	25 kSamples/s
maximum detection charge/40	250 kSamples/s
Maximum pulse amplitude at analog output	3 V

depth (logarithmic binning) or 8 histograms with 256 bins of 24-bit depth (linear binning). Linear binning is only used on unit level during ground checkout. After the transfer, the counters are reset.

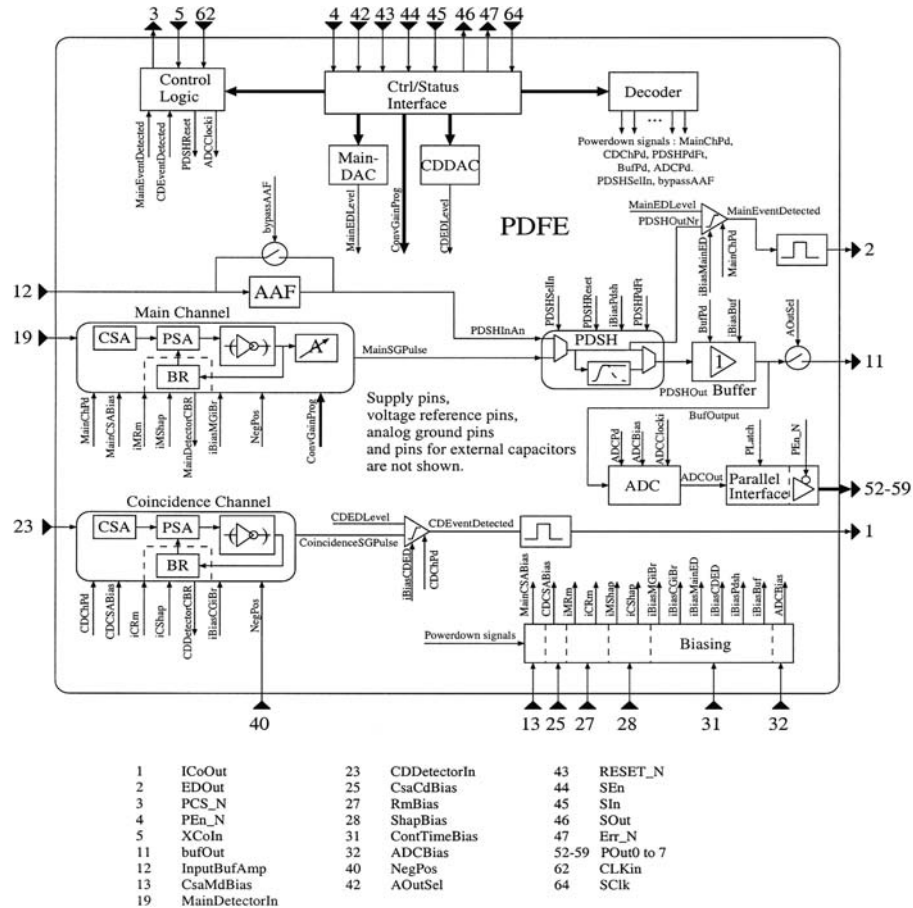


Fig. 6 PDFE block diagram

On command the FPGA can start the test pulse generator which feeds pulses of 4 different amplitudes to the 8 test inputs of the 4 PDFEs. A 4-bit mask defines the set of inputs for coincidence/anti-coincidence verification. Upon completion the generator is automatically switched off returning SEPT into nominal operation mode. Also on command, the FPGA can transfer to the SEP-Central processor the 10 housekeeping channels (2 temperatures and 8 detector leakage currents), which were converted by the PDFE internal ADC.

As the PDFE may develop latch-ups, the supply lines for the PDFE need to be current limited and—in case of a latch-up trigger—to be power cycled. This is to remove the latch-up condition from the chip. When sensing over-current conditions on the analog or digital supply lines, the latch-up monitor automatically switches off the corresponding telescope. A 900 μ s built-in timer is used to filter spurious signals. When power is reapplied normal operation can be resumed.

The ACTEL RT54SX32S FPGA is fed by an 18 MHz crystal oscillator from which the core 4.5 MHz clock is derived as well as a hybrid 4 MHz clock used for each PDFE. The verification of the FPGA design has been performed using the initial register transfer level

VHDL model and dedicated test benches. The FPGA design and verification was carried out by Gaisler Research (Sweden) under ESA contract.

3.2.3 Coincidence Logic

The coincidence logic is partly implemented in the PDFE and partly in the FPGA. The FPGA receives the four discriminator output signals and returns a separate coincidence signal to each PDFE. The PDFE can be configured to either ignore this external signal and use the discriminator output of its guard channel instead, or use the external coincidence signal requiring either coincidence or anti-coincidence. Table 7 summarizes the subset of useful combinations.

3.3 SEPT Telemetry Products

The scientific data from the two telescopes SEPT-E and SEPT-NS are comprised in a total of 8 histograms with 32 bins each. Four electron histograms (one for each of four directions) cover the electron energy range from 30 keV to 400 keV with quasi-logarithmic binning. Four proton histograms (one for each of four directions) cover the proton energy range from 60 keV to 2 MeV with quasi-logarithmic binning and a single bin for ions from 2–7 MeV/n. All histogram data are logarithmically compressed using a 24-bit to 14-bit compression scheme. Table 8 gives a summary.

Table 7 Coincidence filter configurations

FPGA filter mode (2 bit)	PDFE filter mode (3 bit)	Description	Operational mode
0	don't care	Disabled: no event is propagated	
1	4	Independent: no correlation with pair detector or guard	
2	4	Anti-coincidence with guard and pair and pair guard	Nominal observation
2	5	Coincidence with guard or pair or pair guard	
3	4	Anti-coincidence with pair	
3	5	Coincidence with pair	Calibration

Table 8 SEPT bit rate requirement

Data item	Number of channels	Bits per channel	Total number of bits	Time resolution
Histogram	8×32	14	3 584	60 s
Single rate	16/8	24	48	8×60 s
Leakage current	16	8	128	60 s
Temperature	4	8	32	60 s
Status	2	168	336	60 s
Lookup table	2	96	192	60 s
Total			4 320	

Table 9 SEPT beacon mode data

Species	Energy window [keV]		Geom. factor [cm ² sr]
Electrons	35	65	4×0.13
Electrons	65	125	0.52
Electrons	125	255	0.52
Electrons	255	485	4×0.13
Ions (mostly protons)	75	137	4×0.17
Ions (mostly protons)	137	623	0.68
Ions (mostly protons)	623	2224	0.68
Ions (mostly protons)	2224	6500	4×0.17

To evaluate the detector health, 16 single detector rates (8 center disks, 8 guard rings, subcommutated by factor 8) and 16 bias leakage currents are monitored along with four telescope temperatures.

The total SEPT bit rate requirement including header and checksum but excluding analog housekeeping is 4 352 bits per 60 seconds (2 science telemetry packets of length 272 bytes each) corresponding to 72.53 bits/s. Leakage currents and temperatures are included as a subset in the SEP housekeeping packets.

3.4 SEPT Beacon Mode Data

SEPT will provide electron and proton rates in four energy channels for each species for continuous transmission of beacon mode data to the ground station. The lowest and highest energy channels are sectorized in the four look directions while the two mid-range rates are summed over the four look directions. This results in a total of 20 rates shown in Table 9, which are compressed using a 24-to-16 bit compression scheme for transmission. The time resolution is 60 seconds.

3.5 SEPT Commands

The SEPT-E and -NS instruments are completely independent. They do not have their own command processors. Commanding for SEPT is received and executed by the SEP-Central processor. The command language is FORTH. The two instruments are powered on whenever the SEP-suite of instruments is commanded on. However, detector bias may be commanded off or on separately. Also, the two anti-parallel viewing telescopes within one instrument may be switched off separately to recover from a catastrophic failure. High level commands change the operational mode of the instruments. Low level commands change operational parameters. Some parameters can be changed only by variable assignment. Variable and command names given in Tables 10 and 11, respectively, are all uppercase. Lower-case letters in the tables denote: s = 1, 2 (S/C), i = E, N (instrument), p = 0, 1, 2, 3 (PDPE).

3.6 Mission Operations

The main concern for the SEPT sensors is solar heat input when the STEREO spacecraft is in off-nominal attitude. During the transfer trajectory phase, when the spacecraft is in a highly elliptical orbit (HEO), there is the possibility that the SEPT apertures will view

Table 10 SEPT variables

Variable	Default	Description	Related to
ACC-TIME	15 256	Accumulation time in 1/256 sec	
GAINp-i	\$80	PDFE mode and gain	SPFMs
MLEVp-i	15	PDFE main threshold	MLEV-i!
CLEVp-i	20	PDFE guard threshold	CLEV-i!
ELEC-BINn	1, 4, 8, 13, 18	Beacon electron energy bins, $n = 1, \dots, 5$	
ION-BINn	1, 7, 20, 31, 32	Beacon proton energy bins, $n = 1, \dots, 5$	
SPiCAL-N	\$AA	Coincidence filter mode, nominal	
SPiCAL-C	\$FF	Coincidence filter mode, calibration	SPiCALM
SPi-SEQL	40	Duration of test runs in minutes	SPiCALM, SPiTTEST
SPi-PAGE	0	Memory page	
SPi-TGOAL	152	Op-heater temperature goal, degC + 166	SPi-HAUTF
SPi-TPARM	256	Op-heater scaling parameter	SPi-HAUTF
SPi-HAUTF	-1	Op-heater regulator enable flag	
SPi-TPREF	0	Preferred temperature sensor (0 = A, 1 = B)	SPi-HAUTF
SPiAT-EN	-1	Enable use of temperature sensor A	SPi-TPREF
SPiBT-EN	-1	Enable use of temperature sensor B	SPi-TPREF
SPi-SHLVL	2	Heater level while no temps available	
SPi-MHLVL	0	Manual heater level, 0, ..., 10	SPi-HAUTF
SPFMs-INI	array[24]	S/C-s PDFE configuration table	SPFMs
SING-NORM	0, 4, 1, 5, 2, 6, 3, 7	Nominal single counter address table	
SING-TEST	array[40]	Test mode single counter address table	SPiTTEST
CALCONF	array[40]	Test pulser configuration table	SPiTTEST
FLTRMODE	array[40]	Test mode coincidence filter modes	SPiTTEST
PDFEMODE	array[40]	Test mode PDFE mode and gain	SPiTTEST

the Sun for periods of about 20 minutes. The thermal input is a hazard to the solid state detectors, to the magnet, and to the foil. Owing to the low energy thresholds no aperture foils are built in for the proton telescopes, and the foil thickness of the electron telescopes is exactly determined in terms of stopping power for protons and cannot be adjusted for optimum thermal control. Hence, in space, direct sunlight as well as specular straylight must be avoided and diffuse straylight minimized to guarantee flawless detector performance. All four telescope apertures are equipped with doors which will be opened by one-shot cover release mechanisms once HEO phase is passed on mission day 54 and 89 for Behind and Ahead spacecraft, respectively.

Initial turn-on in space will occur 19 days after launch to allow for outgassing. Commissioning will take place following the cover release. Thereafter SEPT will operate autonomously without the need for ground intervention except for occasional (every few months) commanding into calibration mode. Discriminator thresholds will be adjusted by table upload if deemed necessary after commissioning. Further table uploads or change of

Table 11 SEPT commands

Command	Parameter	Description	Related to
SPiNORM		Nominal mode	
SPiAONLY		Telescope A only	
SPiBONLY		Telescope B only	
n SPiCALM	n: number of acquisitions	Calibration mode	
n SPiTEST	n: number of acquisitions	Test pulse mode	
SPiOFF		Turn off	
SAUTO-ON		Automatic latchup mode	
SAUTO-OFF		Automatic latchup mode off	
SPFM!		Load default PDFE configuration	SPFM-INI
SP-GO		Turn on Bias, nominal mode	
SPFM-GO		SPFM! SP-GO	
n MLEV-i!	n: threshold	Load all main thresholds	MLEVp-i
n CLEV-i!	n: threshold	Load all guard thresholds	CLEVp-i
SP-SAVE		Save all main thresholds	MLEVp-i
SP-RESTORE		Restore main thresholds	SP-SAVE

coincidence filter configuration will only be commanded to compensate for noisy detectors or other anomalies.

3.7 Mechanical and Thermal Design

The sensor and electronics box housing are using a weight-saving design with a wall thickness of 1 mm aluminium. An Alodine 1200 protective coating, also known as Iridite or Chromate Conversion, is applied for desired electrical resistance characteristics. The detector stacks are mounted in their own Ni-plated Al housings with Delrin spacers and glued on FR4 frames with EPO-TEK electrically conductive adhesive with matching thermal expansion coefficients. Contact to ohmic and junction sides is made by wire-bonding.

The instruments will be mostly covered by MLI thermal blankets except for the apertures and doors. Once open in space, the doors will be illuminated by sunlight. To mitigate heat input into the telescopes, the doors, hinges and hinge-bolts are made of titanium for its lower heat conductance. The titanium parts received an anodizing treatment with Teflon impregnation to prevent fretting or cold welding.

Those parts of the collimators which receive sunlight are covered with Goddard Composite. The sides of the electronics box facing away from the Sun are covered with silver-coated Teflon to create radiator surfaces. The instruments are mounted on the spacecraft thermally isolated via Ultem bushings. Both operational and survival heaters are provided for thermal control. The nominal internal operating temperature is in the range -10 to $+20^{\circ}\text{C}$. Black anodizing is used on inside surfaces for better radiative coupling. Chemglaze Z306 on the magnets and magnet mount will absorb any stray-light.

The two doors on each side share a Shape Memory Alloy (SMA) activated pin-puller developed under NASA contract. A titanium rod attached to the pin-puller shaft transmits the pin-puller action to the door clevises.

SEPT uses a simple purging system to allow dry nitrogen purge of the SSDs during ground operations and storage until some time into the launch campaign. The purge inlet

is integrated into the side support of the sensor and consists of a purge barb with a flow restrictor. A light-tight purge path is machined into the detector housing, detector mounting frame, and magnet mount to allow free diffusion of the purge gas. No outlet is necessary, the proton aperture is essentially open as the doors are not hermetically sealing. The electronics box is not purged, but evacuation vents are designed in for launch.

3.8 Electrical GSE

The SEPT EGSE consists of a power controller box and a core software running on a dedicated desktop, both connected via RS232 interface. One EGSE can provide the voltage rails (2.6 volt digital, 5.3 volt digital, 5.6 volt analog and -80 volt bias) for two SEPT units. The control software on the desktop was written in visual C/C++, it features a graphical interface for configuration and data display as well as data logging and scripting capabilities (Vbscript) used extensively during environmental tests. The EGSE was developed in a collaboration between the KTH Alfven Laboratory (Sweden) and ESA/ESTEC.

4 Calibrations and Performance

4.1 Electronic Calibration

The SEPT electronics was tested without detectors in order to establish an intercalibration of all analog channels with an external precision pulse generator, to map out the discriminator thresholds, to measure the differential non-linearity (DNL), and to calibrate the leakage current monitor. Figure 7 shows an example revealing a 2^4 pattern in DNL. SEPT data plots with full 256 channel resolution in the following sections were corrected for the effects of DNL. These measurements were performed on all SEPT flight instruments and the flight spare.

4.2 Source Tests

The 16 detectors making up the eight stacks of the four SEPT instruments were selected from a total of 30 SSD devices supplied by the detector manufacturer. Each individual detector was calibrated with conversion electrons from radioactive sources ^{109}Cd , ^{133}Ba , and ^{207}Bi .

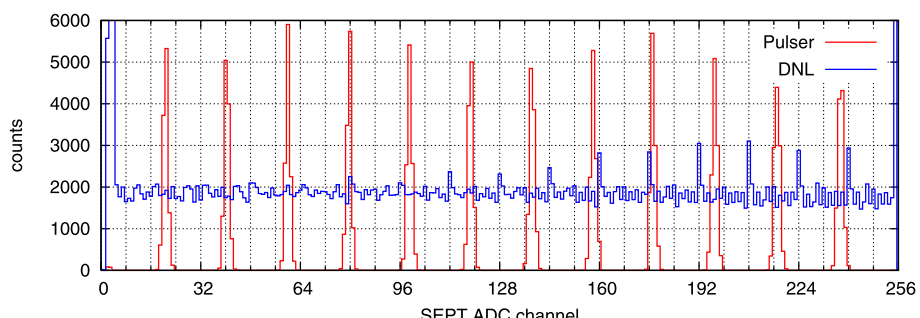


Fig. 7 Electronics calibration with an external precision pulse generator. *Red:* intercalibration with reproducible pulse amplitudes. *Blue:* linear amplitude ramp for differential non-linearity (DNL) measurement

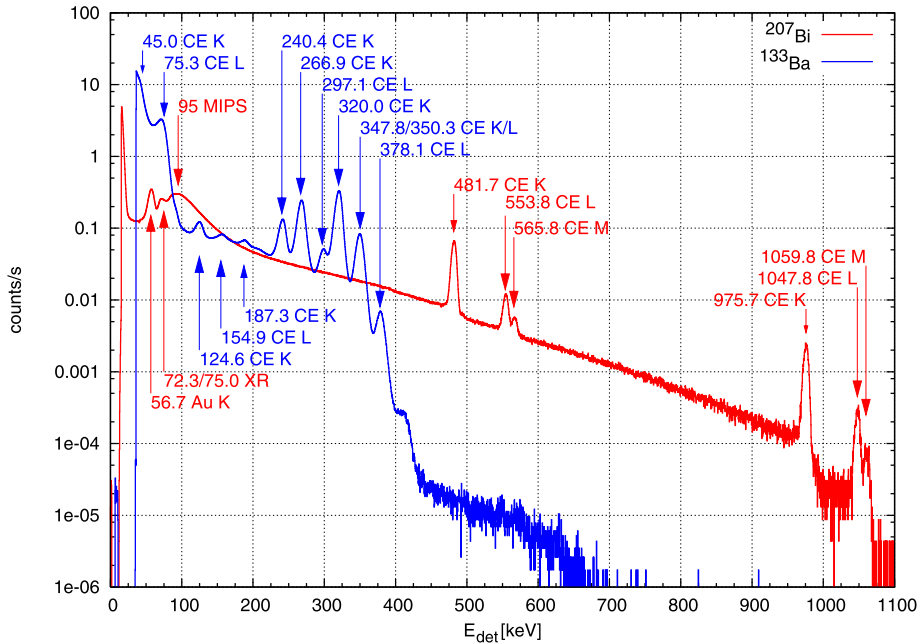


Fig. 8 Silicon detector response to conversion electrons (CE) from ²⁰⁷Bi (red) and ¹³³Ba (blue) sources, measured with laboratory electronics. K, L, and M shell energies can be resolved

The sample spectra of ¹³³Ba and ²⁰⁷Bi in Fig. 8 were measured in vacuum with laboratory electronics, demonstrating an energy resolution of the detectors of 7 keV FWHM.

Measurements with the integrated telescopes using the onboard electronics in linear mode (256 channels, see Fig. 9) give an energy resolution of 25 keV FWHM. Note that the onboard quasi-logarithmic binning which was introduced to conserve bitrate will further reduce the energy resolution above 100 keV. These measurements were performed in air, but energy loss through ionisation in the source (¹³³Ba sealed between plastic foils 0.1 mm and 0.015 mm thick, ²⁰⁷Bi sealed between Mylar foils 0.9 mg/cm² thick) and in 2 cm air have been appropriately taken into account.

The blue graph in Fig. 9 is the direct signal of the conversion electrons in the electron detector, measured in anti-coincidence mode. The orange graph is the signal from penetrating electrons in the pair proton detector, measured in coincidence. The black graph is the Compton scattering signal from gamma-radiation lines in the neighbouring telescope, which is shielded from the electron radiation by the sensor housing. The magenta graph shows a measurement with the source placed in front of a proton telescope aperture, where the conversion electron signal is reduced and the 482 keV lines are not visible at all due to the deflection in the magnetic field. Finally, the red graph is the SEPT response to atmospheric muons from cosmic radiation. Both the top and bottom x-axis show the energy in keV, but the tic marks on the top show the telemetry data binning in 32 bins.

The dominant electron lines from the ²⁰⁷Bi source, at 481 and 975 keV, were used to measure the end-to-end gain of all electron telescopes. Figure 10 shows a measurement with a ¹³³Ba source, which provides an additional calibration point in the lower energy range. The best estimate of the offset of the ADC, being 10 keV at the center of ADC channel zero, was derived from this measurement. The external pulser measurements from Fig. 7 were used to

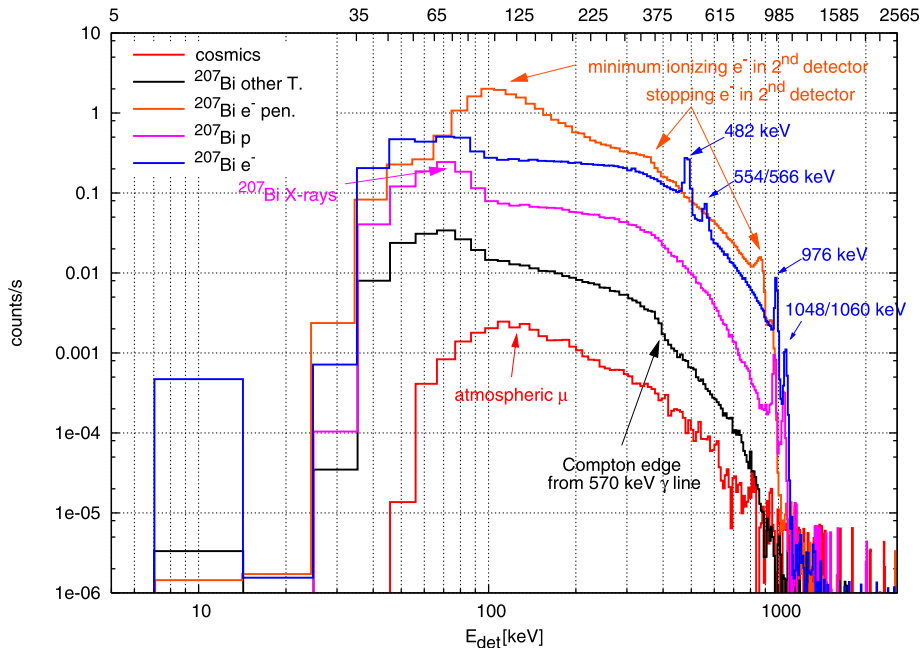


Fig. 9 SEPT response to the radiation field of a ^{207}Bi source placed in front of an electron (blue) and a proton (magenta) telescope. See text for details

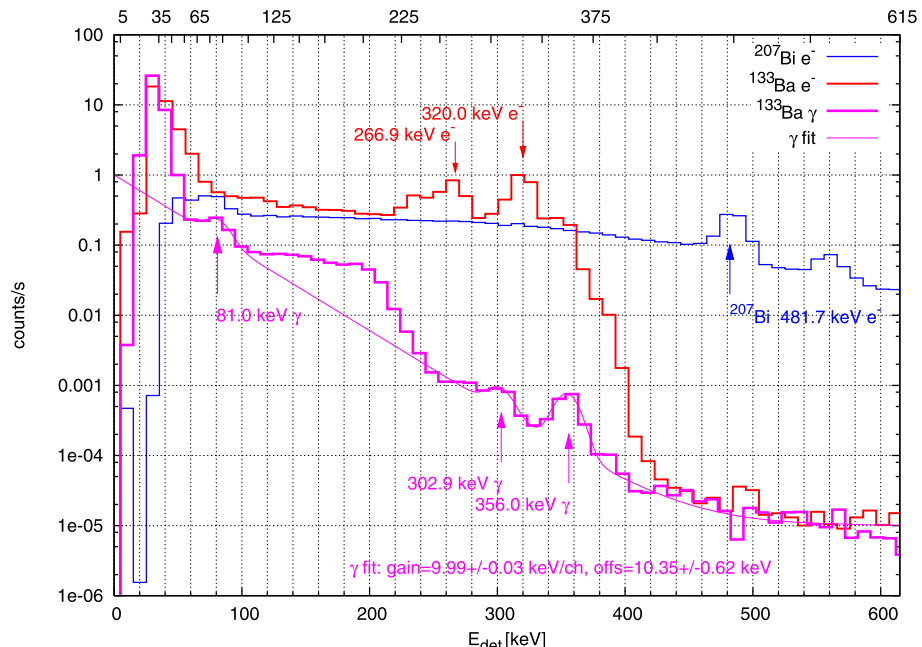


Fig. 10 SEPT response to conversion electrons (red) and γ -ray lines (magenta) from a ^{133}Ba source

intercalibrate all telescopes. From these results a set of gain correction factors is derived to adjust each telescope to a gain of 10 keV/ADC channel. These corrections will be included in the SEP-Central flight software tables and loaded into the PDFE registers before each data acquisition cycle.

4.3 Accelerator Calibration

The SEPT flight spare was calibrated at the Physikalisch-Technische Bundesanstalt (PTB) in Braunschweig, Germany, in February, 2006 with proton and alpha particles from the 3.75 MV Van-de-Graaff accelerator and from the 17 MeV cyclotron TCC-CV28 at various beam energies. These measurements were used to calibrate and check the performance of several instrument functions, including: detector thresholds, detection efficiency, coincidence/anti-coincidence logic, ADC response, counting rates, saturation effects in a high rate environment, accuracy of the range-energy relation for the absorption foil, dead layer, and front detector. Only the flight spare was calibrated at the accelerators, but the spare telescope is representative enough that the results are applicable also to the flight units. In these calibrations, the flight spare was mounted in a vacuum chamber to avoid beam degradation in air at low energies. The particle beams were injected along the boresight direction of both the electron and the proton apertures.

The telescope response for protons is shown in Fig. 11 and for alphas in Fig. 12.

Plotting the detected energy in the telescope on a scale determined by the conversion electron measurements versus the beam energy determined by the accelerator facility's calibration magnets, we can see the effects of detector dead layers affecting the ions at low energies, see Fig. 13.

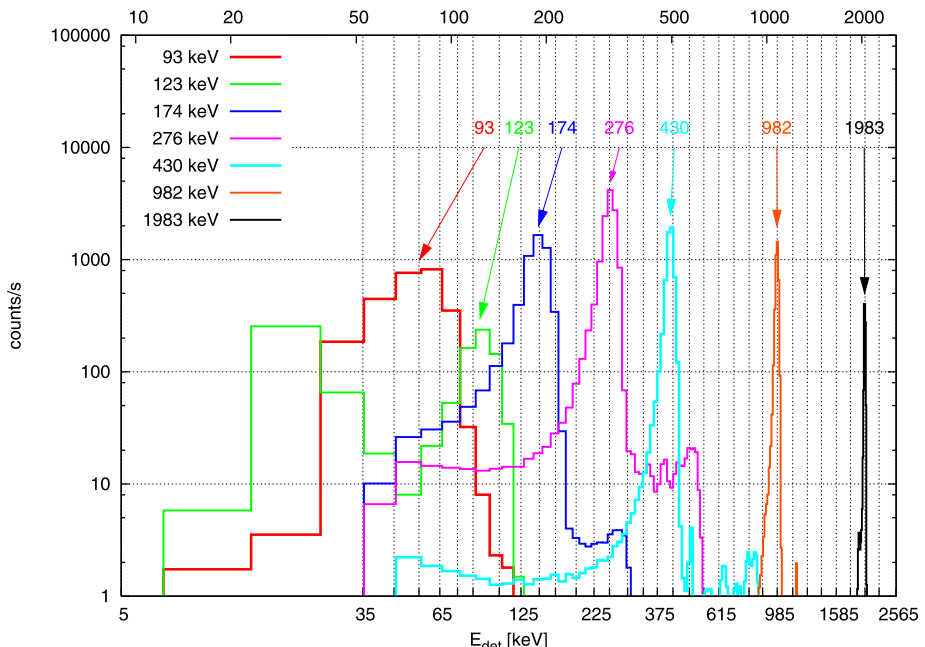


Fig. 11 SEPT response to monoenergetic proton beams at PTB. The bottom x-axis tic marks show the telemetry binning

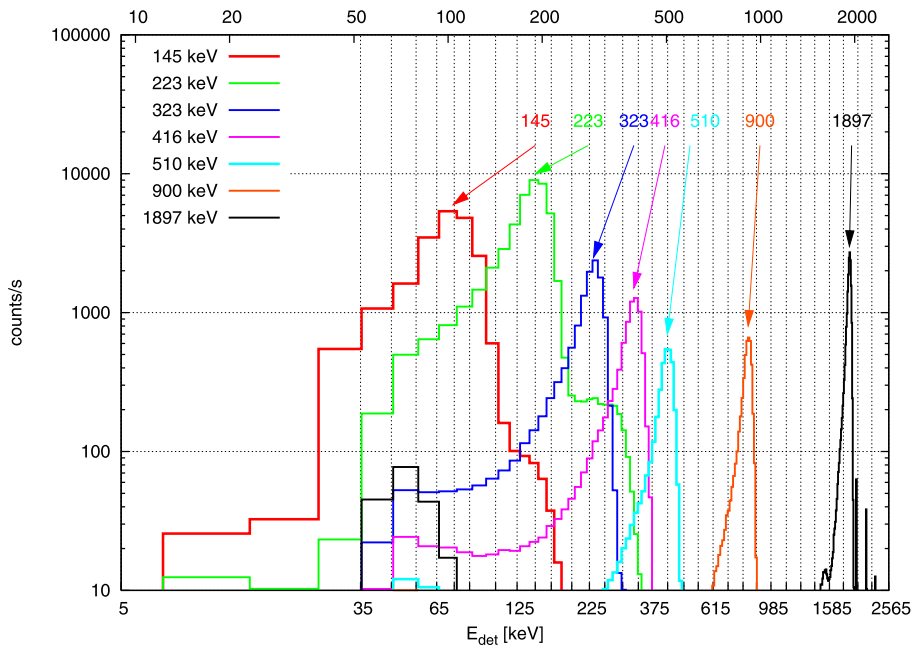


Fig. 12 SEPT response to monoenergetic alpha particle beams at PTB. The *bottom x-axis* tic marks show the telemetry binning

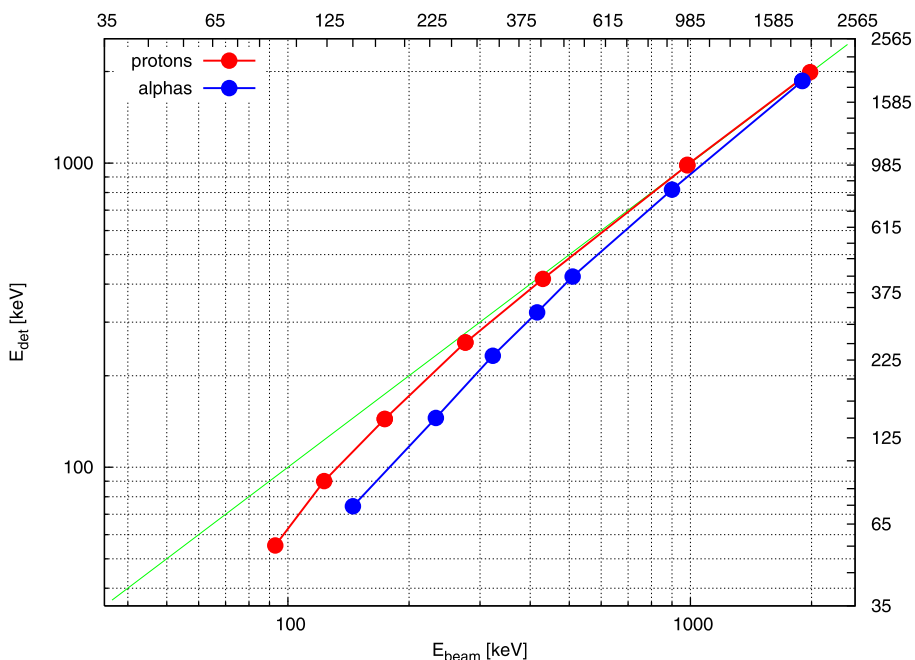


Fig. 13 Proton and alpha particle calibration on the electron energy scale

Table 12 SEPT energy bins for electrons, protons and alpha particles (values are upper boundaries of energy bins)

Bin	ADC	Electrons	Protons	Alphas
0	2	35 keV	75 keV	96 keV
1	3	45 keV	84 keV	108 keV
2	4	55 keV	93 keV	121 keV
3	5	65 keV	101 keV	133 keV
4	6	75 keV	110 keV	146 keV
5	7	85 keV	119 keV	158 keV
6	9	105 keV	137 keV	183 keV
7	11	125 keV	156 keV	208 keV
8	13	145 keV	175 keV	233 keV
9	15	165 keV	193 keV	253 keV
10	18	195 keV	220 keV	284 keV
11	21	225 keV	246 keV	315 keV
12	24	255 keV	273 keV	346 keV
13	28	295 keV	312 keV	387 keV
14	32	335 keV	351 keV	427 keV
15	36	375 keV	390 keV	464 keV
16	41	425 keV	438 keV	511 keV
17	47	485 keV	496 keV	570 keV
18	53	545 keV	555 keV	629 keV
19	60	615 keV	623 keV	698 keV
20	68	695 keV	701 keV	777 keV
21	77	785 keV	788 keV	866 keV
22	86	875 keV	876 keV	953 keV
23	97	985 keV	983 keV	1058 keV
24	110	1115 keV	1112 keV	1183 keV
25	124	1255 keV	1251 keV	1316 keV
26	139	1405 keV	1400 keV	1459 keV
27	157	1585 keV	1578 keV	1631 keV
28	176	1775 keV	1767 keV	1812 keV
29	198	1995 keV	1985 keV	2022 keV
30	222	2235 keV	2224 keV	2251 keV

The accelerator measurements, together with the adjusted electron gains, lead to the SEPT energy bin table shown in Table 12. The table lists the upper boundary of the energy bins. The first bin (bin 0) will be dominated by background counts. The programmable discriminator thresholds will be set in-flight by telecommand to achieve a tolerable background level. Hence the detection efficiency of the first bin will be less than 100% making this bin useful only when count rates are high. The last bin (bin 31) is not shown, it registers all ions above 2.25 MeV which stop in the front detector, mainly protons up to 6.5 MeV and alphas up to 26 MeV total energy. Due to limitations of storage capacity in the FPGA, only one binning table for the quasi-logarithmic binning could be made available for both elec-

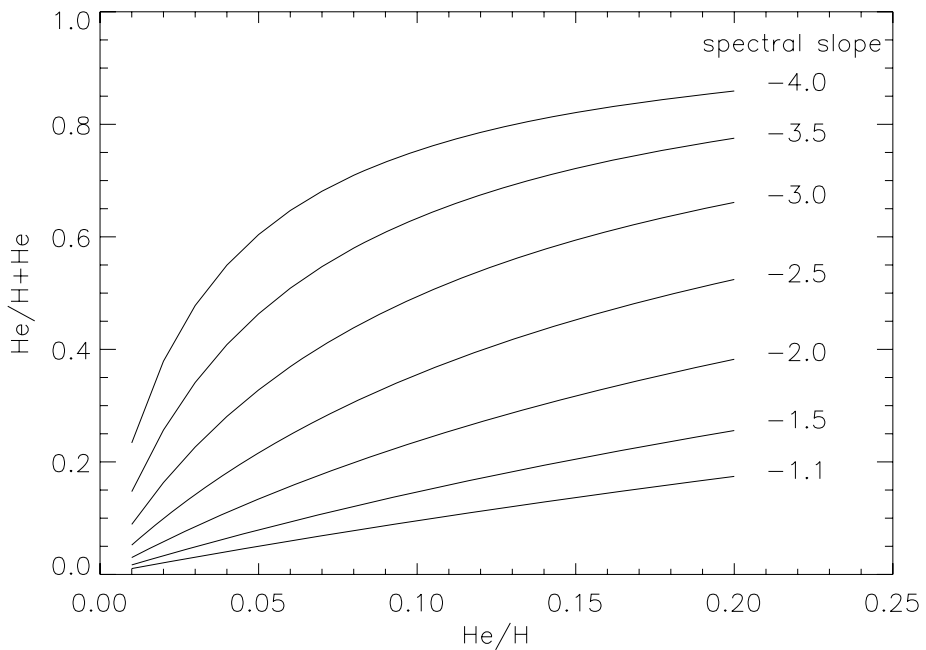


Fig. 14 Helium contribution to SEPT ion channels as a function of the helium to proton ratio typically observed in SEP events with spectral slopes as parameters

tron and proton energy measurements. Hence electron energies from 35 through 485 keV are mapped to histogram bins 1 through 17 only.

4.4 Response to Alpha Particles

In telescopes such as SEPT that measure the total energy of the ion, but not its nuclear charge, most of the response is usually due to protons, with smaller contributions due to helium and negligible contributions due to heavier nuclei. In most cases this is a good approximation, and the term “electron and proton telescope” is appropriate because helium and heavier ions can be safely neglected. However, in events where the spectra are steep or when the ratio He/H is enhanced, helium can account for a sizable amount of the ions against which SEPT cannot discriminate.

In order to derive the helium content in the ion channels we used the calibration results from Table 12, integrated over Bins 1 to 30, and plotted the He/(H + He) ratio versus the He/H ratio in a range typically observed for solar energetic particle events. Figure 14 shows the results with the spectral slopes as parameters assuming that H and He have the same spectral slope. While the He content is only 8% for a gradual event with a hard energy spectrum $\sim E^{-1.5}$ and low He/H ratio of 0.05, it can amount to 50% for an impulsive event with a steep spectrum ($\sim E^{-3}$) and large He/H ratio of 0.1.

4.5 In-Flight Test and Calibration

A simple in-flight test pulse generator provides an electronic stimulation with four different pulse amplitudes at the charge sensitive amplifier inputs in order to check the

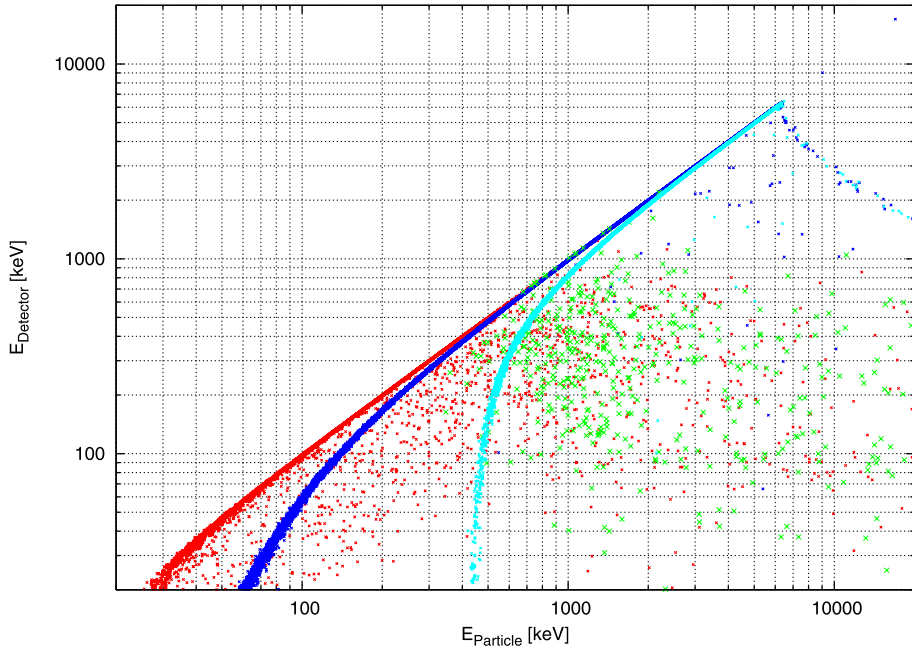


Fig. 15 SEPT response matrix from Geant4 Monte Carlo simulations. *Red* are electrons detected by the electron telescope. *Blue* are protons detected by the proton telescope. *Cyan* are protons detected as electrons, and *green* are electrons detected as protons

coincidence/anti-coincidence functionality and a coarse ADC response. Upon completion the generator is automatically switched off returning SEPT into nominal operation mode. While its accuracy is not sufficient to achieve an electronic calibration, SEPT can be calibrated using in-flight particles. To this end, the anti-coincidence condition between the two paired detectors can be commanded into coincidence to detect penetrating particles. The signals of minimum ionizing particles form a peak in the lower energy bins which can be used for on-station calibration.

4.6 Monte Carlo Simulation

A preliminary Monte Carlo model of the SEPT instrument was used to verify the design principle and to guide some design decisions, like the impact of a thicker detector window to guard against stray-light, and the choice of the foil material and thickness to stop protons.

Figure 15 shows the response matrix of the SEPT design, without taking into account detector and electronics noise. Shown on the y-axis is the energy deposited in the silicon detector volume versus the primary particle energy on the x-axis. A sharp threshold of 20 keV is assumed on the primary and all anti-coincidence detectors. While only a few electrons can mimic protons, the protons in a narrow energy range from 450 to 650 keV can mimic electrons and will have to be subtracted on ground knowing the well-measured proton spectrum in the neighbouring telescope.

Figure 16 shows the same data projected to the x-axis, scaled such that it will yield the geometry factor as a function of particle energy.

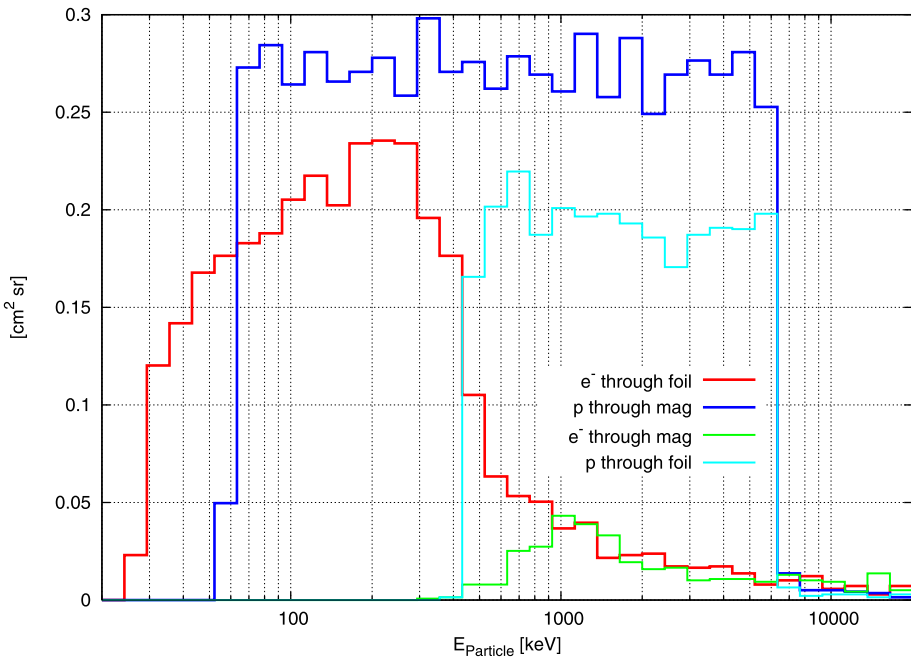


Fig. 16 SEPT geometry factor from Geant4 Monte Carlo simulations. Red are electrons detected by the electron telescope. Blue are protons detected by the proton telescope. Cyan are protons detected as electrons, and green are electrons detected as protons

Acknowledgements The efforts of R. Lin on the sensor design and of D. Curtis on the host of engineering issues during the development, manufacturing, test, and integration phases are gratefully acknowledged. We appreciate the professional workmanship of the contributions from all members of the IMPACT team. We acknowledge the support by P. Falkner on the electronics design and by S. Habinc on the FPGA design and manufacturing. Ion-implanted detectors were provided by Canberra Eurisys, special thanks to M. Keters and P. Burger. The magnet system was provided by Vacuumschmelze, special thanks to F. Jurisch. We also wish to express sincere thanks to all members of the teams in our home institutions who supported design and fabrication of the instruments, in particular in the areas of electrical and mechanical workmanship and engineering as well as administration. This work was partly supported by ‘Deutsches Zentrum für Luft- und Raumfahrt (DLR)’ under grant 50 OC 0004.

References

- H.V. Cane, R.E. McGuire, T.T. von Rosenvinge, *Astrophys. J.* **301**, 448 (1986)
 E.W. Cliver, in *High Energy Solar Physics*, ed. by R. Ramaty, N. Mandzhavidze, X.-M. Hua. American Institute of Physics Conf. Proc., vol. 374 (1996), p. 45
 C.M.S. Cohen et al., *Geophys. Res. Lett.* **26**, 2697 (1999)
 S.E. Forbush, *Phys. Rev.* **70**, 771 (1946)
 A. Galvin et al., *Space Sci. Rev.* (2007), this volume
 J.T. Gosling, D.N. Baker, S.J. Bame, W.C. Feldman, R.D. Zwickl, *J. Geophys. Res.* **92**, 8519 (1987)
 S.W. Kahler, in *High Energy Solar Physics*, ed. by R. Ramaty, N. Mandzhavidze, X.-M. Hua. American Institute of Physics Conf. Proc., vol. 374 (1996), p. 61
 M.-B. Kallenrode, *J. Phys. G Nucl. Phys.* **29**, 965 (2003)
 K.-L. Klein, A. Posner, *Astron. Astrophys.* **438**, 1029 (2005)
 B. Klecker et al., *Adv. Space Res.* (2006, in press)
 J. Luhmann et al. (2007), this volume, doi:[10.1007/s11214-007-9170-x](https://doi.org/10.1007/s11214-007-9170-x)

- A. Luhn, B. Klecker, D. Hovestadt, E. Moebius, *Astrophys. J.* **317**, 951 (1987)
G.M. Mason, J.E. Mazur, J.R. Dwyer, *Astrophys. J. Lett.* **525**, L133 (1999)
R.A. Mewaldt et al., *J. Geophys. Res.* **110**, A09S18 (2005)
R.A. Mewaldt et al. (2007), this volume
E. Moebius et al., *28th Internat. Cosmic Ray Conf.*, vol. 6 (2003), p. 3273
R. Mueller-Mellin, B. Heber, M.-B. Kallenrode, H. Kunow, G. Wibberenz, *Adv. Space Res.* **13**(6), 85 (1993)
P. Oakley, S. Krucker, R.P. Lin, *American Astron. Society, SPD meeting #34*, #16.7 (2003)
D.V. Reames, *Astrophys. J.* **330**, L71 (1988)
D.V. Reames, *Rev. Geophys. Suppl.* **585** (1995)
D.V. Reames, *Space Sci. Rev.* **90**, 413 (1999)
D.V. Reames, *Astrophys. J.* **571**, L63 (2002)
A.J. Tylka, P.R. Boberg, J.H. Adams Jr., L.P. Beahm, W.F. Dietrich, T. Kleis, *Astrophys. J.* **444**, L109 (1995)
T.T. von Rosenvinge et al. (2007), this volume
J. Wouters, S. Redant, K. Marent, C. Das, S. Habinc, B. Johlander, T. Sanderson, in *Proc. of the European Space Components Conferences ESCCON 2000*, 21–23 March 2000, ESTEC, Noordwijk, The Netherlands, ed. by B. Schürmann. European Space Agency, ESA-SP, vol. 439 (2000), p. 247

The High Energy Telescope for STEREO

T.T. von Rosenvinge · D.V. Reames · R. Baker · J. Hawk · J.T. Nolan · L. Ryan ·
S. Shuman · K.A. Wortman · R.A. Mewaldt · A.C. Cummings · W.R. Cook ·
A.W. Labrador · R.A. Leske · M.E. Wiedenbeck

Originally published in the journal Space Science Reviews, Volume 136, Nos 1–4.
DOI: [10.1007/s11214-007-9300-5](https://doi.org/10.1007/s11214-007-9300-5) © Springer Science+Business Media B.V. 2008

Abstract The IMPACT investigation for the STEREO Mission includes a complement of Solar Energetic Particle instruments on each of the two STEREO spacecraft. Of these instruments, the High Energy Telescopes (HETs) provide the highest energy measurements. This paper describes the HETs in detail, including the scientific objectives, the sensors, the overall mechanical and electrical design, and the on-board software. The HETs are designed to measure the abundances and energy spectra of electrons, protons, He, and heavier nuclei up to Fe in interplanetary space. For protons and He that stop in the HET, the kinetic energy range corresponds to \sim 13 to 40 MeV/n. Protons that do not stop in the telescope (referred to as penetrating protons) are measured up to \sim 100 MeV/n, as are penetrating He. For stopping He, the individual isotopes 3 He and 4 He can be distinguished. Stopping electrons are measured in the energy range \sim 0.7–6 MeV.

Keywords Space instrumentation · STEREO mission · Energetic particles · Coronal mass ejections · Particle acceleration

PACS 96.50.Pw · 96.50.Vg · 96.60.ph

Abbreviations

2-D	Two dimensional
ACE	Advanced Composition Explorer
ACRs	Anomalous Cosmic Rays
ADC	Analog to Digital Converter

T.T. von Rosenvinge (✉) · D.V. Reames · R. Baker · J. Hawk · J.T. Nolan · L. Ryan · S. Shuman ·
K.A. Wortman
NASA/Goddard Space Flight Center, Greenbelt, MD 20771, USA
e-mail: Tycho.T.vonRosenvinge@nasa.gov

R.A. Mewaldt · A.C. Cummings · W.R. Cook · A.W. Labrador · R.A. Leske
California Institute of Technology, Pasadena, CA 91125, USA

M.E. Wiedenbeck
Jet Propulsion Laboratory, California Institute of Technology, Pasadena, CA 91109, USA

ApID	Application Identifier; used to identify specific CCSDS packets
APL	The Applied Physics Laboratory of Johns Hopkins University
Calstim	Calibration stimulus event
Caltech	California Institute of Technology
CCSDS	Consultative Committee for Space Data Systems
CME	Coronal Mass Ejection
CPU	Central Processor Unit
CPU24	GSFC-specific version of MISC
DAC	Digital-to-Analog Converter
EEPROM	Electronically Erasable Programmable Read-Only Memory
EPAM	Electron, Proton, and Alpha Monitor (on the ACE spacecraft)
ETU	Engineering Test Unit (prototype)
FIFO	First In First Out (event queues)
FM1	Flight Model 1 (Ahead spacecraft)
FM2	Flight Model 2 (Behind spacecraft)
FPGA	Field Programmable Gate Array
GCRs	Galactic Cosmic Rays
GEANT	Geometry ANd Tracking toolkit for the simulation of particle instruments
GOES	Geostationary Operational Environmental Satellite (NOAA)
GOR	gated OR of binary signals
GSFC	Goddard Space Flight Center
HET	High Energy Telescope
HVPS	High Voltage Power Supply
I/F	Interface
I/O	Input/Output
ICD	Interface Control Document
IDPU	Instrument Data Processing Unit
IMP-8	Interplanetary Monitoring Platform number 8
IMPACT	In situ Measurements of Particles and CME Transients (title of the STEREO investigation to which HET belongs)
JPL	Jet Propulsion Laboratory
LET	Low Energy Telescope
MISC	Minimal Instruction Set Computer
MOC	Mission Operations Center
MRD	Mission Requirements Document
MSU	Michigan State University
MSb	Most Significant bit
NASA	National Aeronautics and Space Administration
NOAA	National Oceanic and Atmospheric Administration
NSCL	National Superconducting Cyclotron Laboratory
OSO	Orbiting Solar Observatory
PDFE	Particle Detector Front End
PH	Pulse Height
PHA	Pulse Height Analyzer
PHASIC	Pulse Height Analysis System Integrated Circuit
POC	Payload Operations Center
PREOUT	analog output of a PHASIC preamplifier selected by command
RNDN	Signal that is high during the run-down of a Wilkinson pulse-height converter
SAMPEX	Solar, Anomalous, and Magnetospheric Particle Explorer

SEPs	Solar Energetic Particles
SEPT	Solar Electron Proton Telescope
SEU	Single Event Upset (flipping of a bit by a highly ionizing particle)
SIT	Suprathermal Ion Telescope
SoHO	Solar and Heliospheric Observatory
SRAM	Static Random Access Memory
SSC	STEREO Science Center
SSD	Solid-State Detector
STEREO	Solar–TErrestrial RElations Observatory
stim	electronically stimulated event
TOF	Time of Flight
UART	Universal Asynchronous Receiver/Transmitter
UCB	University of California at Berkeley
UK	United Kingdom (England)
VDA	Vacuum-Deposited Aluminum
VLSI	Very Large Scale Integration

1 Introduction

1.1 STEREO/IMPACT/SEP/HET

NASA's Solar Terrestrial Relations Observatory (STEREO) comprises two nearly identical observatories in orbit about the Sun (one gradually moving ahead of Earth, called the Ahead spacecraft, and the second gradually moving behind, called the Behind spacecraft). STEREO will provide the first 3-D images of the solar corona and of coronal mass ejections (CMEs). These stereo images will be supplemented by multi-point *in situ* measurements of solar wind and CME plasma and of the energetic particles accelerated in association with CME-driven shocks and solar flares. The High Energy Telescope (HET) is one of four instruments in the Solar Energetic Particle (SEP) subsystem that is part of the IMPACT (In-Situ Measurements of Particles and CME Transients) investigation on STEREO. IMPACT is providing measurements of solar wind and suprathermal electrons, interplanetary magnetic fields, and solar energetic particles (Luhmann et al. 2007, 2005). The SEP suite is composed of the Solar Electron Proton Telescope (SEPT; Müller-Mellin et al. 2007), the Suprathermal Ion Telescope (SIT; Mason et al. 2007), the Low-Energy Telescope (LET; Mewaldt et al. 2007b), and the HET.

The STEREO Mission Requirements Document (MRD) includes the following Science Objective that is specifically directed toward energetic particle studies:

Discover the mechanisms and sites of energetic particle acceleration in the low corona and the interplanetary medium.

The four SEP instruments address this objective by providing complementary measurements of the composition and energy spectra of energetic nuclei from H to Fe ($1 \leq Z \leq 26$) that span the energy range from ~ 0.03 to > 100 MeV/n, as well as measurements of electrons from 0.03 to 6 MeV (see Fig. 1). Note that the HET is responsible for measuring the highest energy particles observed by these four sensors. STEREO will also make an important contribution to space weather forecasting efforts by continuously broadcasting Beacon data that include low-resolution coronal and CME images, solar wind and interplanetary magnetic field parameters, and a fairly complete survey of SEP intensities and composition, including protons from HET in the critical energy range from 14 to > 100 MeV.

Fig. 1 Energy coverage by IMPACT/SEP for different species

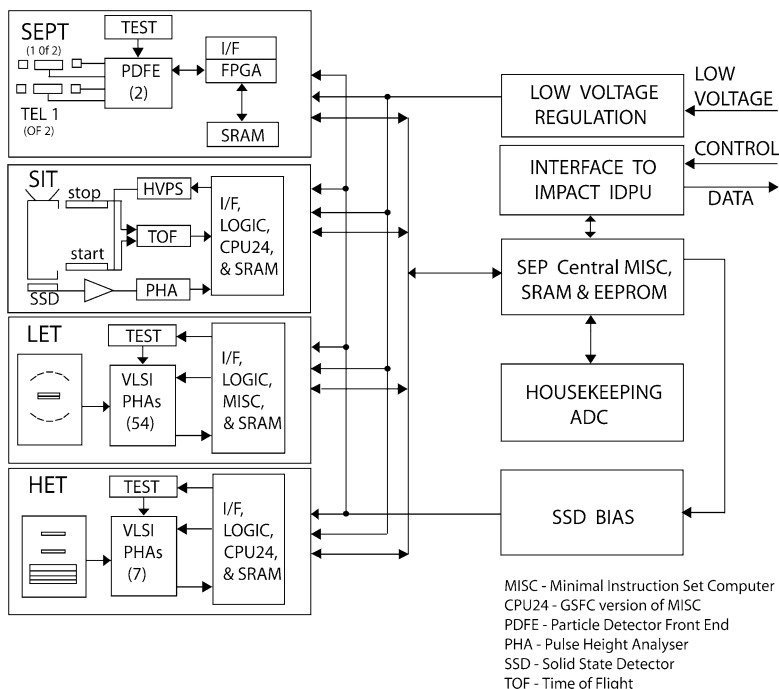
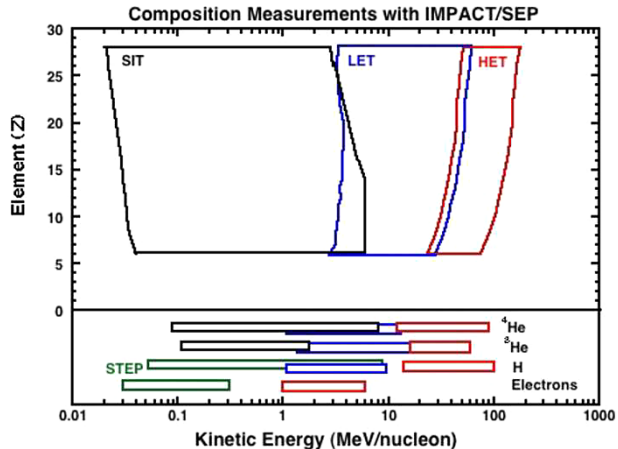


Fig. 2 Block diagram of IMPACT/SEP

A block diagram of the SEP system is shown in Fig. 2. The LET, HET, and SIT sensors each include a dedicated microprocessor for onboard data processing and sensor control. There is an additional control unit called SEP Central (Mewaldt et al. 2007b) that gathers data from the four SEP sensors, controls the SEP bias supply, and manages the interfaces to the sensors and the SEP interface to the Instrument Data Processing Unit (IDPU). The IDPU is described in Luhmann et al. (2007). A photo of HET, LET, and SEP Central is shown in Fig. 3.

Fig. 3 Photograph of LET (*top center*), HET (*center left*) and SEP Central (*enclosure at bottom*). Overall height is approximately 43.4 cm. The bottom of SEP Central is elevated $\frac{3}{4}''$ (1.9 cm) above the spacecraft deck due to thermal isolators



This article describes the HET instrument, along with the science objectives, design requirements, measurement capabilities, and data products. Also described are the onboard software and functions that can be altered by command or with new table uploads. There are two identical HET instruments: Flight Model 1 (FM1) is flying on the STEREO Ahead spacecraft, and FM2 is on the Behind spacecraft. Table 1 summarizes key characteristics of the HET instrument and refers to the sections, figures, and tables where additional details can be obtained. The mounting of HET on each of the two spacecraft is shown in Figs. 4a and 4b.

The primary measurement goal of HET is to measure the energy spectra and time variations of solar energetic particles, including H and He ions with 13 to 100 MeV/n and electrons with 0.7 to 6 MeV. In addition, HET will provide measurements of individual ions ranging from C to Fe with \sim 30 to \sim 150 MeV/n (depending on species; see Fig. 1). During solar quiet times HET will also measure the composition and energy spectra of anomalous cosmic ray (ACR) and galactic cosmic ray (GCR) nuclei.

1.2 Scientific Goals

The scientific goals of the STEREO mission are centered on better understanding Coronal Mass Ejections (CMEs): what triggers their eruption, what is their role in accelerating energetic particles, how do they affect the transport of particles from the Sun to 1 AU, and how do they contribute to magnetospheric storms at Earth? The first CME was observed in

Table 1 Summary of HET characteristics

Characteristic	Value	Details*
Measurement objective	Composition, energy spectra, and time variations of solar and interplanetary ions and electrons	§1.1 F1-1–1-2
Measurement technique	Multiple- ΔE vs. residual energy	§2
Sensor system		
Energy-loss measurements	A single detector stack composed of 9 ion-implanted Si detectors, each 1 mm in thickness	§2.1, 2.1.1, 2.1.2, 2.2; F2.2–F2.6
On-board particle identification	9 species from H to Fe with an average of 9 energy intervals. Electrons in 3 energy intervals	§3.4; A; F1.1, F2.1, F3.1–3.3, T3.3
Charge interval	Ions with $1 \leq Z \leq 26$; electrons	§2.4; F1.1, F2.1, F3.2
Energy interval (MeV/n)		§2.4; F1.1, F2.1
Electrons	0.7–6	
H, He	13–100	
O	28–89	
Si	38–124	
Fe	49–167	
Field of view	55° cone (full angle)	F2.6
Geometry factor	0.61 cm ² sr	§2.4
Event yields (large SEP event)	$>10^5$ H & He	§5.3
Element resolution	<0.2 charge units	§5.3
Mass resolution	0.2 amu for ³ He and ⁴ He	§5.3
Resource allocation		§4
Dimensions (l × w × h)	Envelope: 172 mm × 95 mm × 206 mm Telescope: 82 mm long × 68.5 mm diam	

* Sections (\$), figures (F), tables (T) and appendices (A) containing additional details

1971 from OSO-7 (Tousey 1973), and they were subsequently observed by Skylab (1973–1974), Solwind (1979–1985) and Solar Maximum Mission (1980–1989). These early missions made good observations of individual events, but long-term surveys suffered from low sensitivity, small fields of view that didn't encompass the whole Sun, and low data cadence. The Solar and Heliospheric Observatory (SoHO), launched in 1995, began a systematic study of CMEs, which continues to the present. SoHO makes excellent observations of CMEs for events that originate near the limbs of the Sun. The image projected onto the sky shows clear structure and the radial expansion velocity can be readily measured. By contrast, CMEs that are headed towards Earth appear as ‘halo CMEs’, with little discernible

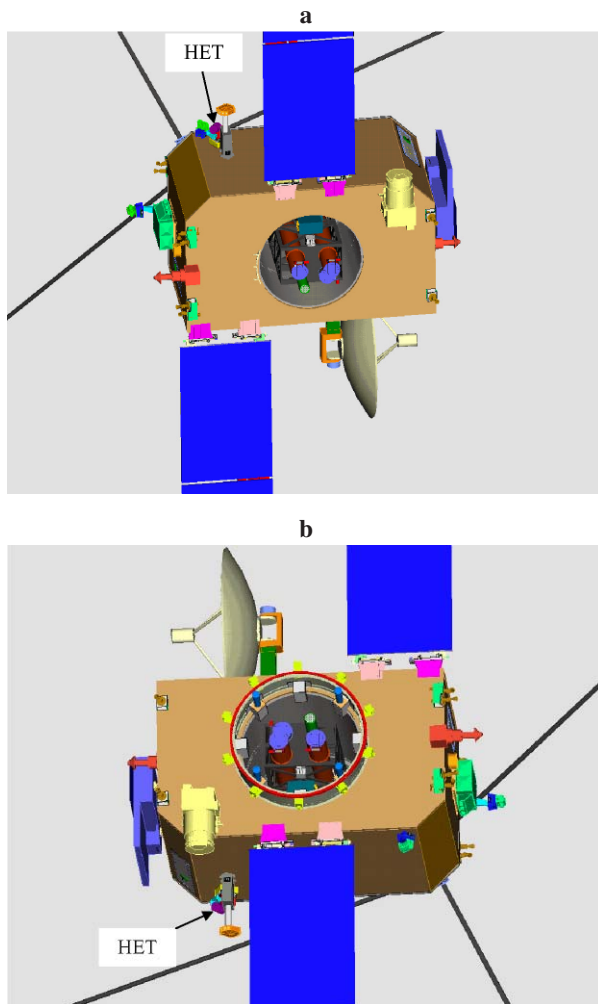
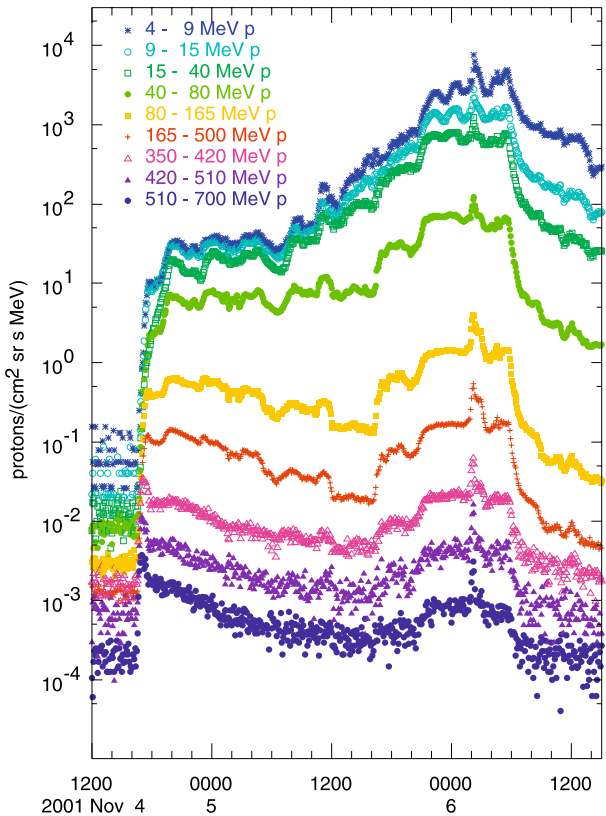


Fig. 4 **a** The Ahead spacecraft viewed from somewhat above the ecliptic plane (SEP Central, with HET and LET mounted on top, is on the top of the spacecraft to the left and behind the solar panel). **b** The Behind spacecraft viewed from somewhat below the ecliptic plane (SEP Central is mounted on the underneath side of the spacecraft). Note the deployed dish antennas looking towards Earth in each case (Earth is approximately midway between the two spacecraft). Both HETs look along the nominal Parker spiral towards the Sun

structure. In addition, it is very difficult to determine radial expansion velocities. Of course these are the events that have the most impact on Earth. STEREO observations, made from two spacecraft on opposite sides of the Earth–Sun line, will be able to circumvent many of these problems.

Interplanetary shock waves driven by CMEs have been observed in plasma and magnetic field data for a long time, and it has long been known that low energy particles (e.g., <40 MeV protons) are often seen in association with passing shocks (e.g., Bryant et al. 1962; Cohen 2006). The first set of spacecraft to be able to make long-term, multi-point observations of energetic particles at ≤ 1 AU consisted of Helios 1 and 2 (launched into solar orbit

Fig. 5 Shows proton intensities versus time for the SEP event of 4 November 2001 as observed by the NOAA/GOES satellites. The corresponding energies are provided in the figure

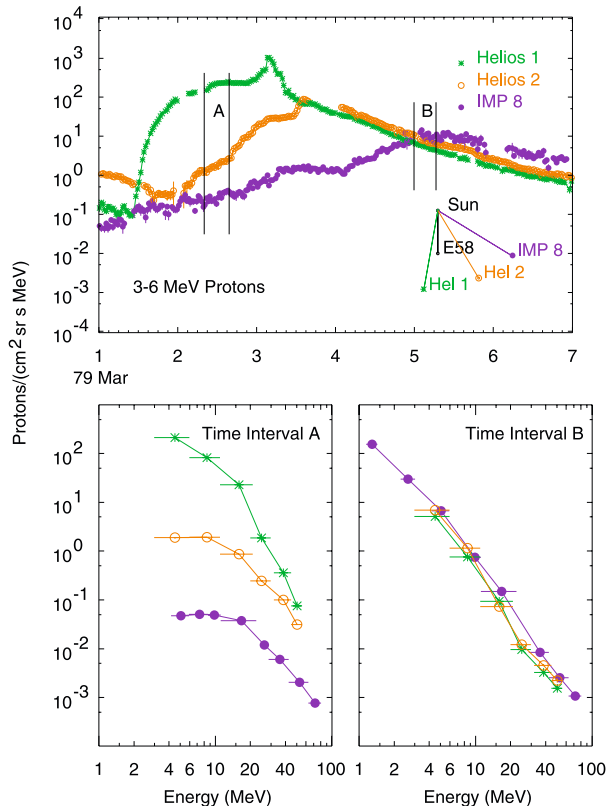


in 1974 and 1976) together with IMP-8 at Earth. Unfortunately, there were essentially no CME observations associated with particle events observed by these spacecraft. The advent of STEREO will dramatically change this situation.

Recent reviews of our understanding of solar energetic particles include Reames (1999) and von Rosenvinge and Cane (2006). Reames has made extensive arguments to support the idea that all large, CME-associated solar energetic particle (SEP) events are accelerated by the associated CME-driven shock. Although others have argued that some high energy particles originate in the associated flare, there can be no doubt that acceleration by the CME-driven shock is a dominant effect at low energies and, on occasion, this effect is clearly observed at energies above 1 GeV. A striking example is shown in Fig. 5, which shows proton intensities for the event of 4 November 2001: there is a sharp peak at the shock (around 02:00 on 6 November 2001) at all energies shown, including the highest energy interval for which proton data is available, 510–700 MeV. It is also apparent that the increases shown for energies from 15 MeV to >350 MeV, starting at ~17:00 on 5 November and ending at ~07:00 on 6 November (a total period of 15 hours) are closely associated with the shock. No doubt all the particles seen in this event have this same origin.

Many other observations also emphasize the importance of shock acceleration in SEP events. For example, the observations of streaming-limited proton intensities in SEP events has been shown to originate with the generation of waves by protons in the vicinity of the shock (Reames and Ng 1998). Cohen et al. (2005) and Mewaldt et al. (2005) have reported on spectral breaks that they interpret as being due to rigidity-dependent escape from shocks

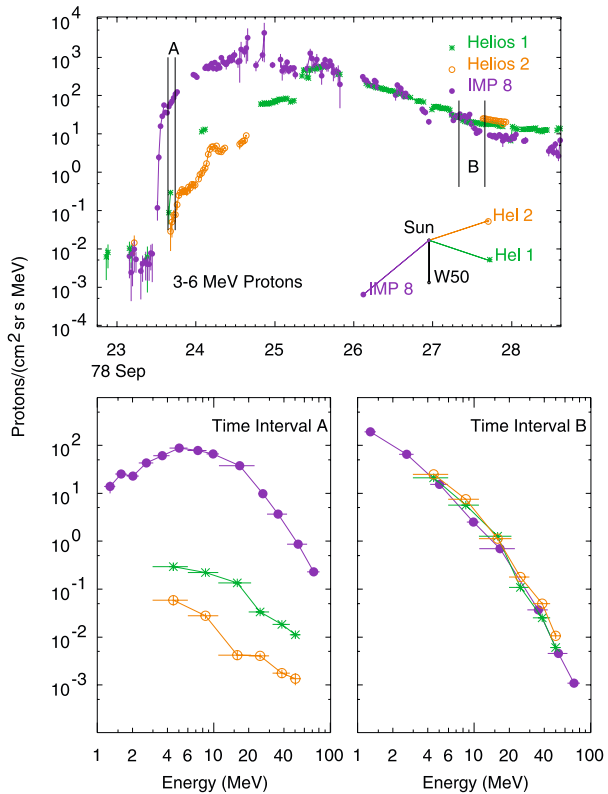
Fig. 6a Example of simultaneous SEP observations at different solar longitudes. Note the substantial differences in intensity profiles even though the spacecraft are not widely separated in longitude. From Reames et al. (1997)



accelerating the observed particles. They find that H, He, and O spectra “resemble double power laws, with a break in the spectral index between ~ 5 and ~ 50 MeV/nucleon which appears to depend on the charge-to-mass ratio of the species.” Since the HET has a strong overlap with these energies, HET will be vital for observing spectral breaks in SEP spectra.

Simultaneous observations of energetic particles at different solar longitudes are shown in Figs. 6a and 6b. These observations were made by Helios 1 and 2 and IMP-8 (Reames et al. 1997). In each figure there is an inset that shows the relative positions of the 3 spacecraft. The longitude of the corresponding active region is given by the black line in each figure. We see in the first figure substantial initial differences in intensity profiles even though the spacecraft are not widely separated in longitude. Somewhat more than 3 days after the first particles were seen, the decay profiles at all three spacecraft are essentially identical, suggesting that after that they are inside a region with fairly uniform and decaying particle intensity. We see much the same behavior in the second figure. The differences are (1) in the second figure, the spacecraft are separated considerably more in longitude, and (2) the initial differences are actually smaller in the second event than they were in the first. The different features in these two events are most likely associated with differences in the associated CMEs. With STEREO (and with WIND and ACE near Earth) we will have the opportunity to investigate such effects with a greatly expanded data set. If flare particles are sometimes a major contributor to SEP events, we might expect to see them more clearly at one spacecraft than another due to different connections being made to the flare region. Tylka and Lee (2006) have suggested that enhancements of heavy nuclei abundances in SEP events may

Fig. 6b Another example of simultaneous SEP observations at different solar longitudes. Note how similar the intensity profiles are after \sim mid-day of 25 September despite the large differences in solar longitude. From Reames et al. (1997)



originate at the flanks of CMEs where the shocks are more likely to be quasi-perpendicular. This too might be discernible by multiple spacecraft as a longitudinal variation of observed abundances. At the time of the older missions like Helios 1 and 2, access to data from different instruments was fairly restricted. We now have the advantage that data from all the different instruments on STEREO are readily available.

Within the past two years NASA has decided to send astronauts back to the Moon for extended periods of time, with the goal of eventually sending humans to Mars and back. Although there has been a continuous human presence in space over the past decade on MIR and the International Space Station, these missions were carried out within the protective cover of Earth's magnetosphere, which shields against most galactic cosmic rays and solar energetic particles over much of the orbit. Once astronauts leave Earth orbit, they will be subject to increased radiation risks due to cosmic rays and large SEP events. The same applies to the electronic instrumentation that they will depend on. This has focused increased attention on the need to characterize the highly variable SEP radiation environment, with a goal of providing improved forecasts of the intensity and timing of the largest events. Spectral roll-overs will determine the severity of exposure to the most penetrating particles. The electrons observed by HET generally will arrive at earth before the ions by roughly 45 minutes, providing some advanced warning of impending high ion intensities. Warnings of the highest intensity ions, which occur at shocks, will be provided pre-shock by observing streaming-limited proton intensities (Reames 2001).

It takes a minimum of \sim 10 MeV for a proton to penetrate a space suit; for electrons the corresponding energy is \sim 1 MeV. Inside a pressure vessel the minimum proton energy

is increased to ~ 30 MeV. Thus, the response of HET is well matched to monitoring SEP protons, He, and electrons in the critical energy range where they pose a radiation risk to humans. The multi-point Beacon measurements (selected data broadcast to the ground continuously) provided by STEREO, supplemented by data from near-Earth spacecraft, will provide improved warning of the largest SEP events. In addition, STEREO studies using the full data set will lead to increased understanding of (1) which CMEs accelerate particles to high energies; (2) how SEPs are distributed in longitude; and (3) how interplanetary conditions govern particle transport in the inner heliosphere.

1.3 Design Requirements

The HET sensor must satisfy a number of design requirements to achieve the objectives in Sect. 2 and to support a range of studies that will be carried out by the SEP, IMPACT, and STEREO teams (see, e.g., Luhmann et al. 2007; Mewaldt et al. 2007b; Mason et al. 2007; and Müller-Mellin et al. 2007). These requirements were ultimately derived from the STEREO Missions Requirement Document, which states that the SEP suite shall measure the intensity, composition, energy spectra, and direction of energetic protons from 0.06 to 40 MeV, heavier ions from ~ 0.03 to 40 MeV/n, electrons from ~ 0.03 to 6 MeV, and ^3He -rich solar particle events. The STEREO Level-1 Mission Requirements Document states that:

HET shall measure SEP ion fluxes, spectra, and composition covering the energy range from 30–80 MeV/n for C to Fe ions, 13 to 40 MeV/n for H and He, and 1 to 6 MeV for electrons. The mass resolution shall be better than 0.3 amu for ^3He and ^4He . Time resolution shall be 1 minute for H and He Beacon data, and 15 minutes otherwise. Shall handle at least 1000 events/sec.

The above statement has led to the requirements and goals summarized in Table 2, which were the basis for the detailed design of the HET. Table 2 also shows the capability of the two HET instruments, which meet or surpass all of the requirements.

2 Instrument Description

The HET telescope uses the classic $\Delta E \times E - \Delta E$ method of particle identification for particles that stop in the telescope. The method is extended to include particles that penetrate the telescope, thereby extending the observed energy range of protons and He in particular. Here ΔE refers to the energy loss of a particle with incident kinetic energy E as it traverses a thin detector with thickness Δx , and $E - \Delta E$ (also denoted by E') is the residual energy after passing through the ΔE detector. In a plot of ΔE versus E' , particles with different charge Z and mass A are separated into different tracks. The location on each track depends upon the incident energy. A sample such plot based upon a Monte Carlo simulation of HET is shown in Fig. 7. Note the separation of ^3He and ^4He .

2.1 HET Detectors

The HET detectors are ion-implanted Si detectors provided by Micron Semiconductor, Ltd. in the UK. This type of detector is well known for its excellent linearity of energy loss response and ruggedness. The HET detectors are all nominally 1 mm thick and are operated with a bias voltage of 175 volts. Estimates of the detector thicknesses were obtained by averaging the thicknesses of wafer samples adjacent to where each detector was cut out from its wafer. For example, for FM1 these estimates ranged from 989–1015 μm .

Table 2 HET design requirements

Description	Requirement	Goal	Capability
Field of view	$\geq 50^\circ$ cone	60° cone	55° cone
Energy range (MeV/n)	H, He: 13–40; ^3He : 16–40; $6 \leq Z \leq 14$: ~30–80	H, He: 13–100; ^3He : 16–50; $6 \leq Z \leq 14$: ~30–80	H, He: 13–100; ^3He : 17–47; $Z = 6$: 27–74 $Z = 26$: 52–163
Geometry factor ($\text{cm}^2 \text{sr}$)	H, He: 0.1–0.5; $6 \leq Z \leq 26$: 0.5	H, He: 0.15–0.7; $6 \leq Z \leq 26$: 0.7	H, He: 0.10–0.61; $6 \leq Z \leq 26$: 0.61
H1 detector noise level	<40 keV rms	≤ 30 keV rms	<30 keV rms
Element resolution	$\delta Z \leq 0.2$ charge units for $1 \leq Z \leq 14$	$\delta Z \leq 0.3$ charge units for $16 \leq Z \leq 26$	$\delta Z \leq 0.2$ for $1 \leq Z \leq 14$; $\delta Z \leq 0.3$ for $16 \leq Z \leq 26$
^4He mass resolution	≤ 0.3 amu rms	≤ 0.2 amu rms	≤ 0.2 amu rms
Maximum event rate	1000 per sec	5000 per sec	~4000 per sec
Energy binning	6 intervals per species	8 intervals per species	10 intervals per species for H and $Z \geq 2$
Onboard species identification	H, ^3He , ^4He , electrons, $6 \leq Z \leq 14$	Also identify $16 \leq Z \leq 26$	H, ^3He , ^4He C, O, Ne, Mg, Si, Fe, electrons
Time resolution	15 min; Telemeter 0.3 prioritized event/sec	15 min; Telemeter 1 prioritized event/sec	15 min; Telemeter ~2 prioritized events/sec
Beacon telemetry	1 min for H, He, electrons	1 min for H, He, electrons	1-min for H, He, C, O; Fe, electrons

2.1.1 H1, H2 Detectors

The H1 detectors were made using planar, polygonal Si disks, 1 mm thick, that are mounted in a mechanical mount constructed using printed circuit board/flex-circuit technology. Figure 8a is a picture of the junction side of an H1 detector; Fig. 8b is a picture of the ohmic side. Gold-plated copper pads on the mount are used to make redundant wire-bond connections between the detector electrode surfaces and copper traces that run through the mount and flex-circuit to a connector that plugs into the flight electronics board. The H1 detector has two separate sensitive areas on the junction side that are defined by ion implanting 2 separate p–n junctions. The inner sensitive area is a circle, 0.8 cm in diameter. The outer sensitive area is a concentric ring, with outer diameter 2 cm, around the inner circular area. The outer area is separated from the inner area by a circular gap that is 60 μm wide. In addition, the outer ring has a narrow (130 μm wide) radial area cut-out through which passes a narrow extension of the central area that terminates in a small pad (one mm by 0.28 mm) located

Fig. 7 Simulated response of HET telescope to incident electrons, hydrogen (protons), ^3He , ^4He , C, O, Ne, Mg, Si, and Fe. Electrons are not well-modeled in this figure

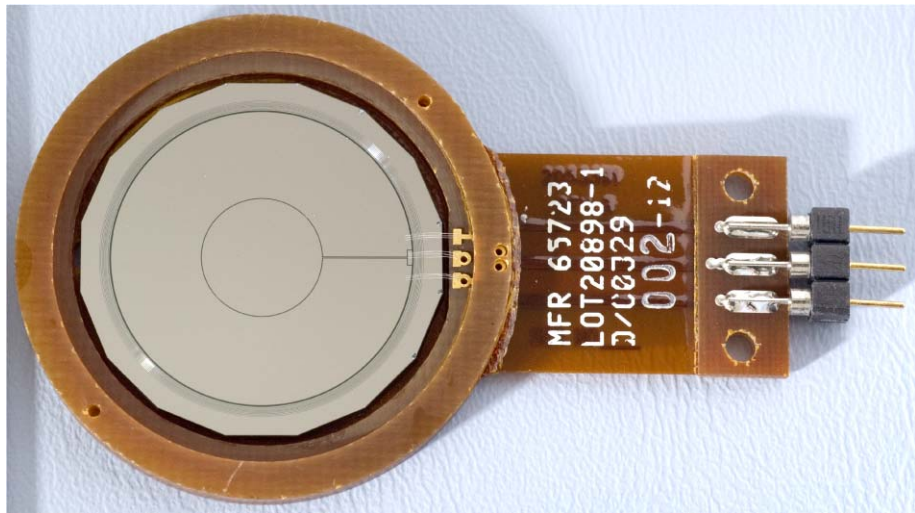
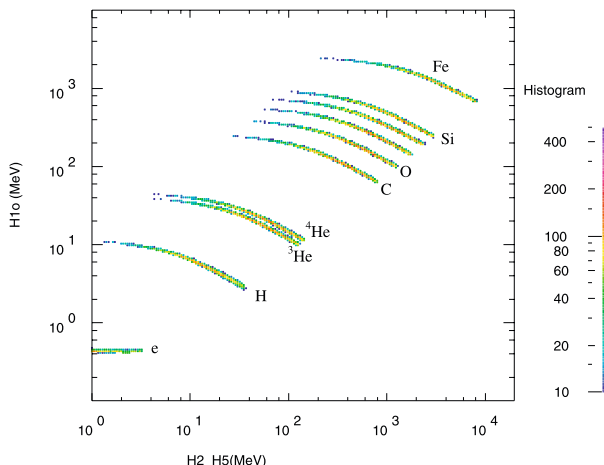


Fig. 8a Shows the junction side of an H1 detector

just inside of the outer circular ring. There is only a single, circular charge collection surface on the ohmic side. Surrounding the outer sensitive area on the junction side is a stepped guard intended to reduce excess detector leakage current. The stepped guard consists of a sequence of separate, narrow metalized rings that are allowed to float electrically.

In effect, the H1 detector consists of two detectors, one inner circular detector and one outer ring detector. These are designated H1i and H1o, respectively.

The H2 detector is identical to the H1 detector but it has the two separate areas on the junction side electrically shorted together external to the detector mount. In effect, the H2 detector acts as a circular detector 2 cm in diameter by 1 mm thick.

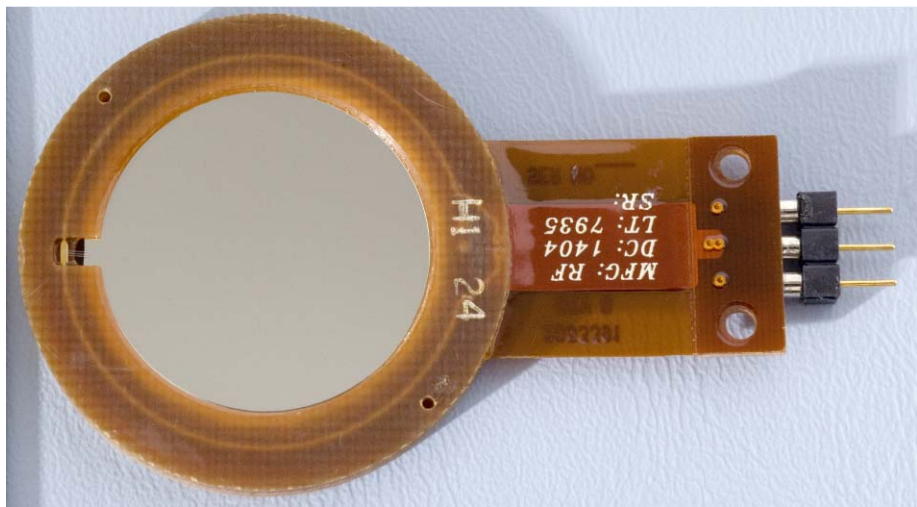


Fig. 8b Shows the ohmic side of an H1 detector

2.1.2 HET Stack Detectors

The remainder of the HET telescope is constructed using a second detector type that is similar to the H1 detector except that it only has a single circular p–n junction with diameter 4 cm. One of these detectors, which we will refer to as a stack detector, is shown in Fig. 9.

2.1.3 Detector Testing

Detector quality checking was performed at three different locations: initially Micron Semiconductor, Ltd. did thermal cycling at ambient pressure, thickness measurements on wafer samples, and vibration testing prior to shipment of the detectors to Caltech. Caltech inspected the detectors for scratches and photographed the bond wires prior to shipment to GSFC. GSFC then made the following measurements:

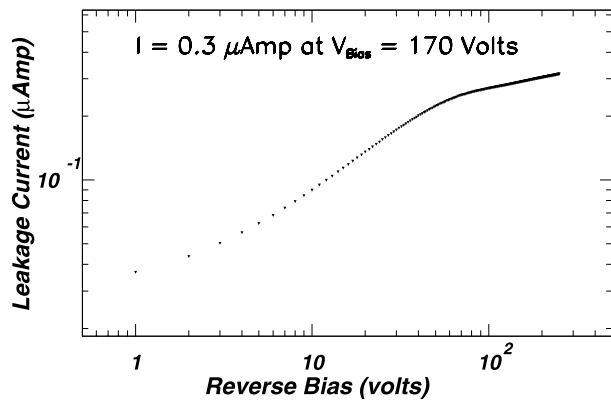
1. Detector leakage current versus bias voltage at ambient pressure and temperature with a maximum test bias voltage of 250 V.
2. Detector capacitance versus bias voltage at ambient pressure and temperature.
3. ^{241}Am alpha particle exposures in vacuum through both the junction and ohmic detector sides at different bias voltages, including the flight operating bias of 175 V. We positioned the uncollimated source at 1.5 detector diameters from the center of the detector and looked for the alpha peak to be at ~ 5.48 MeV with similar width for both front and back exposures. In at least one case the flight detector (H2 on the Behind spacecraft) did not quite live up to this requirement, but the schedule didn't permit a late substitution.
4. So-called lifetest, where up to 20 detectors were operated at $+40^\circ\text{C}$ over an extended period in vacuum (a few times 10^{-6} Torr or less), typically 3 weeks, with a single cycle of \sim two days to -25°C . Detector leakage current and noise were monitored continuously during lifetest.

Sample test results for test types 1 and 2 are shown in Figs. 10 and 11. The intent of test 1 is to look for evidence that a detector might be operating too close to reverse bias breakdown.



Fig. 9 Shows a HET stack detector (junction side)

Fig. 10 Shows detector leakage current versus bias voltage for a sample H3 detector



The voltage above which the capacitance saturates in test type 2 gives an indication of the voltages at which the detectors are fully-depleted. Test type 3 gives a separate measure of detector depletion, and in general full-depletion is only observed at higher voltages than are indicated by test type 2.

We initially received detectors that had a double passivation layer that was intended to make the detectors more resistant to attack by chemical vapors in the air. We observed that most of the initial detectors might behave well for awhile in lifetest, but eventually their leakage currents would start to grow without check. In the end we flew only detectors with a

Fig. 11 Shows the detector capacitance versus bias voltage curve for a sample H3 detector

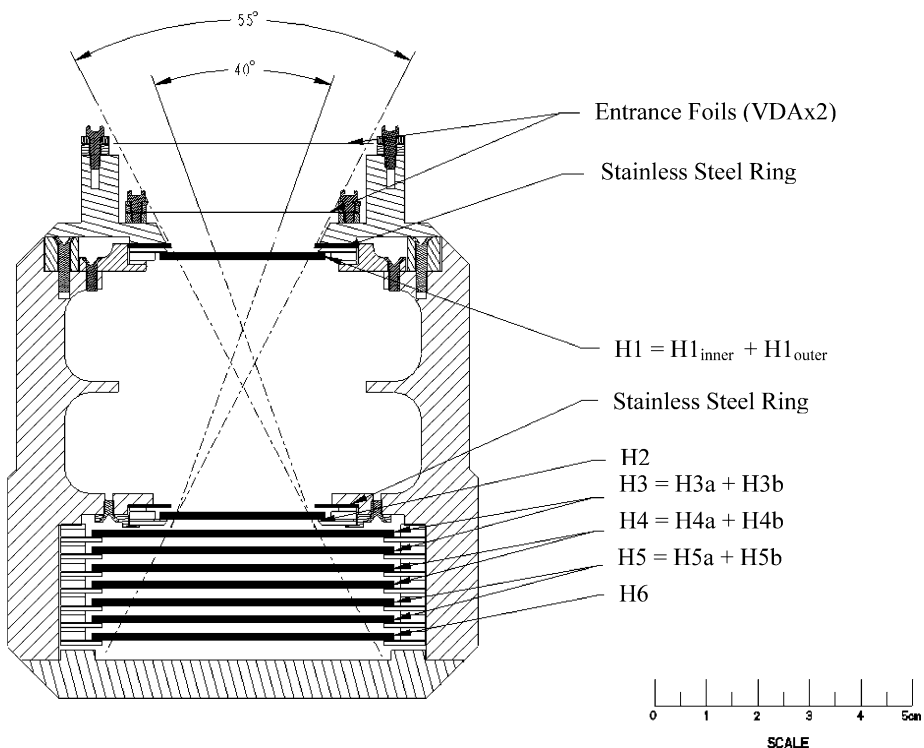
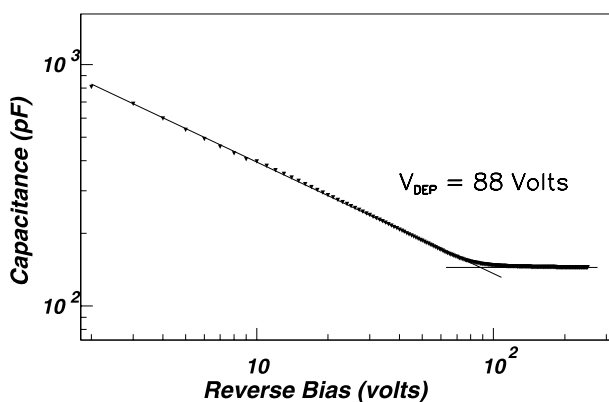


Fig. 12 Shows a schematic cross-section of a HET telescope

single passivation layer. These detectors rarely had problems with steadily growing leakage currents, and the few that did have such problems were rejected.

2.2 HET Telescope

Figure 12 shows a cross-sectional view of an assembled HET telescope. The spacing between the bottom of the H1 detector and the top of the H2 detector is 3.68 cm. The spacing

between the remaining detectors is nominally 0.15 cm. Note that the outputs of detectors H3a and H3b are summed into a single pulse height analyzer. This detector pair is referred to as H3. Similarly, H4 and H5 each consist of 2 detectors summed together. The acceptance angles for particles stopping in the telescope are defined by H1o and H1i and H2. H6 is a single detector that determines whether or not a particle stops in the preceding detectors: ‘stopping particles’ enter the telescope through the H1 detector but don’t reach the H6 detector; ‘penetrating particles’ traverse H1 and reach H6. Most penetrating particles penetrate H6 as well.

The telescope body is designed to prevent external light from reaching any detector surface. The front end of the telescope is blocked by two separate Kapton foils, each 0.005" thick and coated front and back with vapor deposited aluminum (VDA). The double foil design (as contrasted with a single foil of double the thickness) is intended to decrease the effects of pin-holes in the VDA and also to provide better protection from incident micrometeors. The body of the telescope is also designed to reduce the numbers of low energy particles that can reach any of detectors H2 through H6 without passing through H1 first. In particular, 0.5 mm thick stainless steel rings with inner diameter of 21.0 mm are included in the body in front of H1 and H2 (see Fig. 12). Further details of the mechanical and thermal design of the combined LET/HET/SEP Central package may be found in Mewaldt et al. (2007b).

2.3 HET Electronics

2.3.1 Introduction

Figure 2 shows a block diagram of the IMPACT Solar Energetic Particles suite, including the HET and SEP Central. SEP Central includes a low-voltage power supply for all of IMPACT/SEP, a bias supply for all the solid-state detectors, EEPROM for storing on-board code, response tables, and boot-up command states, and a central Minimal Instruction Set Computer (MISC). The SEP Central MISC performs the following functions:

1. It receives commands from the IMPACT IDPU (see Luhmann et al. 2007) and forwards them to the appropriate subsystem (in our case, HET); it also receives command echoes from each subsystem and assembles them into telemetry packets, which are then passed back to the IDPU.
2. It time-tags HET telemetry packets with Universal Time and transmits them to the IDPU.
3. It assembles housekeeping data and so-called Beacon data from each subsystem into telemetry packets, which it then sends to the IDPU.
4. It receives and stores in EEPROM the on-board code and tables for LET and HET as well as for SEPT, SIT, and the SEP Central MISC. It also transmits this information to the appropriate subsystem when the latter is booted up.

SEP Central is described more fully in the LET paper in the present volume (Mewaldt et al. 2007b). Note that, due to the central low-voltage power supply, all of SEP is either turned ON or OFF. For example, HET cannot be powered down without powering down all of the rest of SEP. Similarly, a common bias voltage (175 volts) is used for the 1 mm thick detectors in HET and LET.

Figure 13 shows a block diagram of the HET. The HET electronics board is housed in the same enclosure as SEP Central. It consists of a single printed circuit board with two PHASICs (Pulse Height Analysis System Integrated Circuits) supplied by Caltech, an ACTEL FPGA (Field Programmable Gate Array, part number RT54SX72S), three SRAM

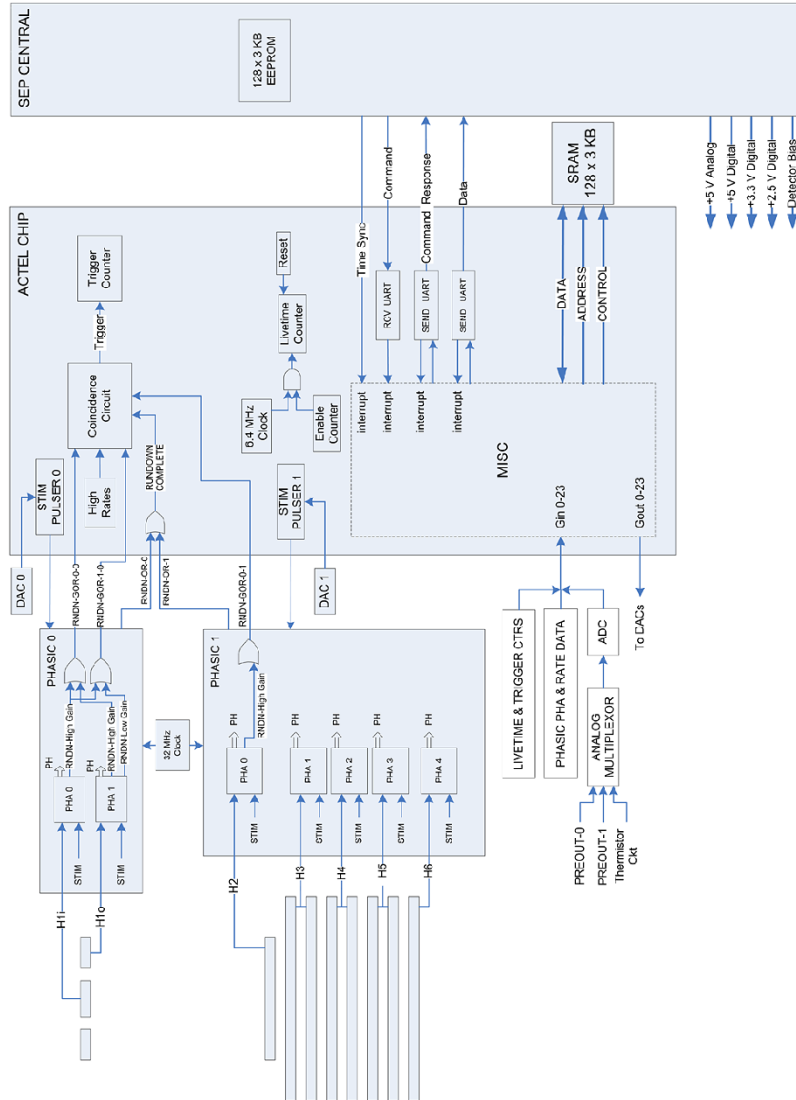


Fig. 13 Simplified block diagram of the HET electronics. Note that HET receives low voltages and detector bias from SEP Central. EEPROM in SEP Central contains all of the HET software and tables. The HET tables are stored in EEPROM in a compressed format which is expanded when it is transferred to SRAM. HET commands are received from SEP Central and HET telemetry is transmitted to SEP Central. Details such as the filters for analog voltages on the HET electronics board are not shown

chips, and power-conditioning filters. The SRAM chips (Honeywell HLX6228) each have $128\text{ K} \times 8$ bits, for a total of $128\text{ K} \times 24$ bits for program and data storage.

Additional circuitry is provided for on-board pulsers that can stimulate each PHA channel, and to measure the leakage currents of each detector (or, in the case of H3, H4, and H5, pairs of detectors). Pulse height events that are created by the on-board pulsers will be referred to as “stim events”.

The HETs and LETs are mounted differently with respect to SEP Central on each of the two STEREO spacecraft. This was shown earlier in Fig. 4. A single HET electronics board design permits the HET telescope to be mounted in either one orientation for the Ahead spacecraft or at 90° to this orientation for the Behind spacecraft. The resultant look-direction for each HET in flight is towards the Sun along the nominal Parker spiral interplanetary magnetic field. Figure 14 shows pictures of a HET and its electronics board.

2.3.2 PHASICs

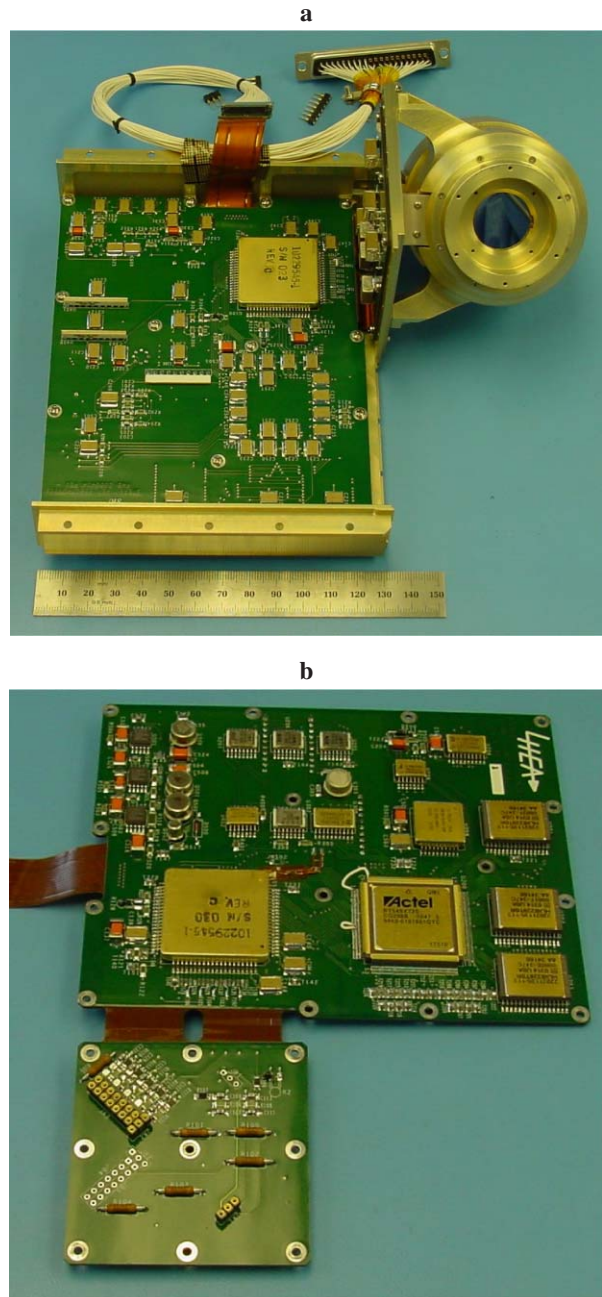
Charge pulses due to particles losing energy in the HET detectors are digitized by pulse height analyzers contained in an integrated circuit known as a PHASIC, designed by Rick Cook of Caltech (Cook 2002). A detailed description of the PHASIC is provided in Mewaldt et al. (2007b), so only a brief description will be provided here. A PHASIC contains 16 separate, large-dynamic-range pulse height analyzers (PHAs). Each of these separate PHAs has a charge-sensitive preamplifier with commandable gain. Each preamplifier output signal is coupled to two shaping amplifier/offset-gate/peak-detector/Wilkinson-ADC chains that operate in parallel, but with gains that differ by a factor of 20. A variety of parameters of each separate PHA can be set by sending a single 108-byte serial command to the PHASIC. For example, individual unused PHA channels in a PHASIC can be powered down, the high-gain and low-gain sections of each PHA can be disabled, and various test points internal to the chip can be steered to an output pin to be examined by an oscilloscope. Two different types of data may be extracted from the PHASIC: pulse height data outputs and the number of times high or low gain thresholds of each PHA have been triggered since reset (rate counter outputs). In flight we sample the rate counter outputs for each PHA channel every minute. A count is extracted as a 24-bit word. The pulse height data are also read out as 24 bits (we shall call this a raw pulse height). A raw pulse height includes the chip address, PHA address, gain, and overflow bits as well as the pulse height value. In addition, there are several read-out modes for pulse heights: in terse readout mode, which is the dominant mode used for flight, only the high gain pulse height is read out for each PHA that triggered unless the high-gain pulse height counter overflowed (i.e. went over 2047 counts); in the latter case only the low-gain pulse height is read out. The other readout mode is called the verbose mode. In this mode, both the high and low gain pulse heights are read out if both were triggered. The verbose mode is primarily for engineering diagnostics, however we also use it during high-rate mode (described later). Each PHA channel can be independently set to either terse or to verbose mode.

The format of PHASIC pulse height readouts is described in Table 3.

The token bit is set to 1 for the last pulse height read in a serial sequence of pulse heights being read out of the PHASICs. The stim bit has to be set by the MISC.

Note that HET uses two PHASICs. There are in principle more than enough PHA channels in a single PHASIC to service all the detectors in a HET. However, at the time of the initial telescope design, the first PHASICs were not available. There was some concern that there might be cross-talk within a single PHASIC, which could create artificial coincidences between the H1 and H2 detector channels. Two PHASICs were used to circumvent that possibility.

Fig. 14 **a** Photograph of a HET telescope mated to its electronics board. The white cable is a ‘connector-saver’. **b** Photograph showing the other side of the HET electronics board

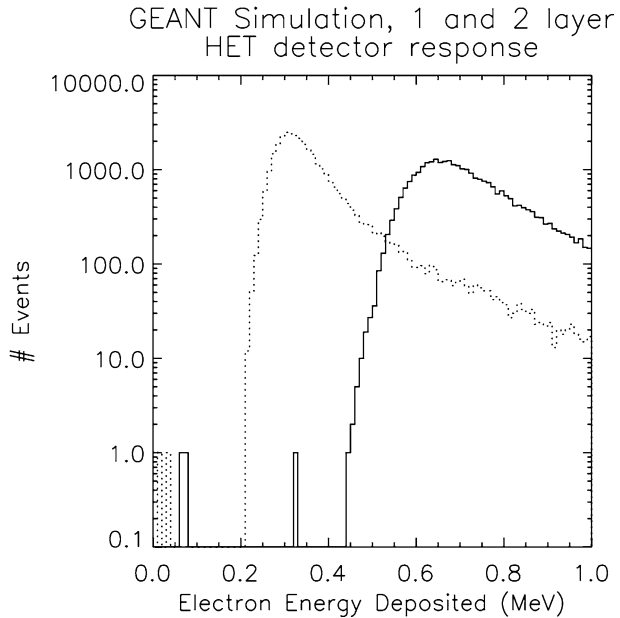


The dynamic range of the PHASICs is very large ($\sim 10,000$), but the needs of the HET are somewhat larger. GEANT simulations of electrons (e.g., see Fig. 15) showed that, in order for minimum-ionizing electrons to remain above threshold in the H1, H2, and H6 detectors, the corresponding electronic thresholds needed to be set at no higher than 0.2 MeV.

Table 3 Raw event format (23 bits)

23	22-20	19	18-15	14	13-12	11	10-0
Token bit	Chip address	Stim bit	PHA address	High gain bit	Reserved	Overflow bit	Pulse height

Fig. 15 GEANT 3.21 Simulation of 1 mm and 2 mm HET detector responses to minimum ionizing electrons at normal incidence



An Fe nucleus incident at an angle of 30° from the normal to an H1 detector can lose as much as about 2800 MeV, leading to a total dynamic range of $2800/0.2 \sim 14,000$. Since Fe is by far the most abundant element in SEPs above Ca ($Z = 20$), we have limited Fe pulse heights to a maximum value (e.g., see Fig. 19a).

Finally, we note that for each PHA channel in a PHASIC, the thresholds for both high and low gain pulses are adjustable by command up to $\sim 6\%$ of full-scale. This feature is not entirely intuitive because the PHA offset channel also changes when the threshold is changed. By offset channel, we mean the PHA channel versus input energy curve extrapolated to 0 MeV. Because pulse heights are offset-corrected on-board, it is essential that the offset channel stored on-board is changed at the same time that any change is made in the corresponding threshold. This is facilitated by changing the threshold setting, noting the shift in an on-board pulser peak, and then changing the offset to restore the peak channel position. The threshold values and offset channels are routinely reported in telemetry.

Tables 4a and 4b provide the key parameters for each detector channel for the HETs onboard the Ahead (Table 4a) and Behind (Table 4b) spacecraft as they were configured at launch.

2.3.3 Cross-Talk

Cross-talk occurs when a large signal in one signal channel couples into another, producing an unintended signal in the second channel. During the first of two visits to the National Su-

Table 4a PHASIC parameters for the HET on the Ahead spacecraft

Detector channel	Gain	Threshold (MeV)	Offset channel	MeV/channel
H1i	High	0.21	47.8	0.0524
	Low	4.0	50.1	1.063
H1o	High	0.2	47.4	0.0531
	Low	21.0	33.0	1.066
H2	High	0.19	47.4	0.0524
	Low	4.0	48.0	1.072
H3	High	0.38	46.7	0.1043
	Low	9.0	47.3	2.087
H4	High	0.34	47.0	0.1044
	Low	9.0	47.7	2.111
H5	High	0.34	46.7	0.1043
	Low	9.0	47.7	2.099
H6	High	0.2	47.1	0.0520
	Low	4.0	47.9	1.057

Table 4b PHASIC parameters for the HET on the Behind spacecraft

Detector channel	Gain	Threshold (MeV)	Offset channel	MeV/channel
H1i	High	0.2	47.6	0.0526
	Low	4.0	49.4	1.050
H1o	High	0.2	46.5	0.0523
	Low	23.0	30.0	1.054
H2	High	0.2	49.5	0.0521
	Low	4.0	50.8	1.061
H3	High	0.33	49.3	0.105
	Low	9.0	50.5	2.107
H4	High	0.33	49.0	0.105
	Low	9.0	50.1	2.097
H5	High	0.36	48.8	0.104
	Low	9.0	50.0	2.097
H6	High	0.2	47.9	0.0525
	Low	4.0	49.9	1.058

perconducting Cyclotron Laboratory at Michigan State University (July 2004) we exposed the two flight HETs to a 160 MeV/n Ni beam. Ni was not a particularly good choice for HET because Ni saturates at least one PHA channel, but a variable length water target/absorber

was put in the beam to create lower Z fragments. The lower Z fragments produce smaller energy losses and hence smaller cross-talk signals. With the large signals from the Ni beam, we quickly discovered two different forms of crosstalk. The first of these was cross-talk between H1i and H1o that is due to stray capacitance between H1i and H1o. Normally, events with pulses in both H1i and H1o are rejected as events where the particle trajectory traversed both H1i and H1o. The cross-talk is only about one part in 400, so the key point is to not reject events in which one of two H1 pulse heights is due to cross-talk.

The second type of cross-talk occurs between channels inside of PHASIC 1. Cross-talk in PHASIC 1 is negligible with regard to obtaining residual energy losses in the stack (H2–H5 or H3–H5). The critical part is to determine whether a signal in H6 is due to cross-talk or not so that stopping particles with large energy losses in the stack don't get erroneously put in the penetrating particle queue. If the H6 pulse height is small, one must unpack the raw pulse heights and gain bits of H2–H5 in order to determine whether the H6 pulse height is real or is just due to cross-talk. It is to be emphasized that the on-board software identifies both types of cross-talk and eliminates their effects.

2.3.4 MISC and Front-End Logic

The MISC, HET front-end logic, and UARTS for communicating with SEP Central are contained in the Actel FPGA. The HET design is similar to the LET design, but the implementation was different. In particular, the layout at Caltech was performed by manual graphical schematic entry. The HET design was implemented using Verilog (a high-level language for describing electronic circuits) and computer-automated layout. The HET MISC has been named the CPU24, to distinguish it from the Caltech MISC (named the P24).

CPU24 is a 24-bit processor with a dual-stack architecture chosen to be optimal for using the Forth kernel (see Mewaldt et al. 2007b). For HET, programming was done using the 32 native MISC instructions rather than Forth. The processor design is sufficiently simple to allow implementation within an Actel RT54SX72S FPGA.

CPU24 employs a reduced instruction set with four 6-bit instructions packed into 24-bit words. The most significant bit (MSb) of each instruction designates an I/O bus operation when set. For I/O bus instructions (the I/O bus will be referred to as the G bus) the second MSb specifies a write when set and a read when cleared. The remaining 4 bits specify one of 16 G bus addresses. For non-G-bus instructions, the MSb is cleared and the remaining 5 bits specify one of 32 possible instructions.

Following is a list of CPU24 features:

- 24-bit address and data buses
- 6-bit RISC-like CPU instructions
- 4-deep instruction cache
- 17-deep data stack
- 33-deep return stack
- 11 prioritized interrupts
- stack underflow/overflow detection
- clock gating, ability to turn off processor clock during idle time
- stack register clocks individually generated for power saving
- Boot ROM, executes on power up or reset, loads program via UART
- Instruction rate of 6.4 million instructions per second
- Instruction types:
 - arithmetic and logical
 - memory access

- register and stack
- program control
- input/output.

Details of CPU24 are specified in “CPU24 Microprocessor User’s Manual for STEREO HET” (Baker 2003). There are several functional differences between the CPU24 and the P24. The most important of these is stack underflow/overflow detection in the CPU24. This was found to be very useful for finding bugs in the flight software.

The Actel also contains two UARTs. The first is for receiving commands and sending command echoes from/to SEP Central. The second UART (transmit only) is for sending science data to SEP Central. The UARTs all run at 57.6K baud.

The Actel also contains

- PHASIC read/write control registers
- a counter that counts valid coincidence pulses
- a front-end livetime counter
- ADC and DAC input/output control signals
- Two extra general purpose input/output registers.

The HET pulse-height controller flow is illustrated in Fig. 16. This figure shows, among other things, how the front-end livetime counter is implemented. This counter measures the time that the PHASICs are enabled to accept a new event (5 μ s ticks).

MISC tasks will be enumerated and discussed in Sect. 3.

2.4 Geometry Factors

2.4.1 Stopping Particles

The geometry factors are essentially independent of kinetic energy and particle type. The geometry factor for particles that pass through H1o or H1i into detector H2 and don’t enter H6 is 0.61 cm²-steradian. The geometry factor for particles that pass through H1i into H2 and don’t enter H6 is 0.10 cm²-steradian. Note that during high-rates mode (described in Sect. 3.6.1), particles with $Z > 2$ that pass through either H1i or H1o are accepted for analysis, whereas particles with $Z \leq 2$ are only accepted if they pass through H1i.

2.4.2 Penetrating Particles

The geometry factor for penetrating particles that pass through H1i+H1o and exit through H6 is 0.61 cm²-steradian. The geometry factor for penetrating particles that pass through H1i and exit through H6 is 0.10 cm²-steradian. Similar to the stopping particles, penetrating particles with $Z \leq 2$ in high-rates mode are only accepted if they pass through H1i. Figure 17 shows a simulation of forwards and backwards protons and He between 40 and 100 MeV/n. This figure shows that the forwards and backwards particles are essentially separated below 100 MeV/n. Above 100 MeV/n the tracks rapidly merge.

3 Onboard Software

3.1 Introduction

The onboard software performs the following tasks:

- supports the PHASICs (establishes their logic state; reads pulse heights and singles rates and transfers them to the MISC; controls logic terms that define valid coincidences; and controls the on-board pulsers)
- processes pulse height events to bin them into predefined particle and energy bins
- processes all commands
- controls housekeeping measurements such as detector leakage currents and temperatures, and
- formats data into telemetry packets at the end of each major frame and transmits them to SEP Central.

Fig. 16 Illustrates the controller which controls the processing of pulse height events. It also shows how the front-end livetime counter is implemented

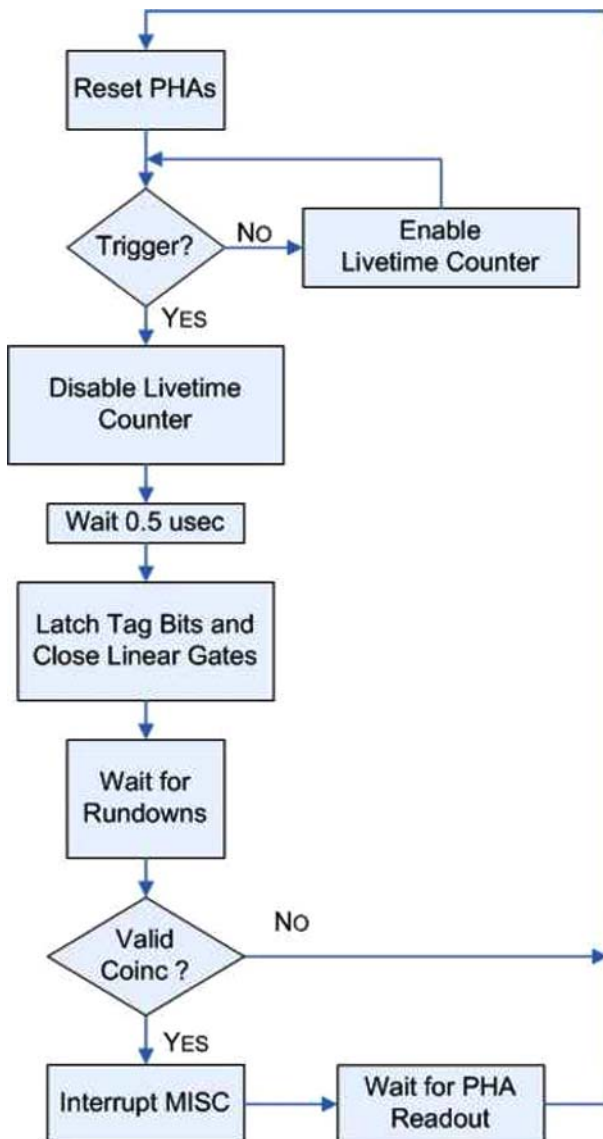
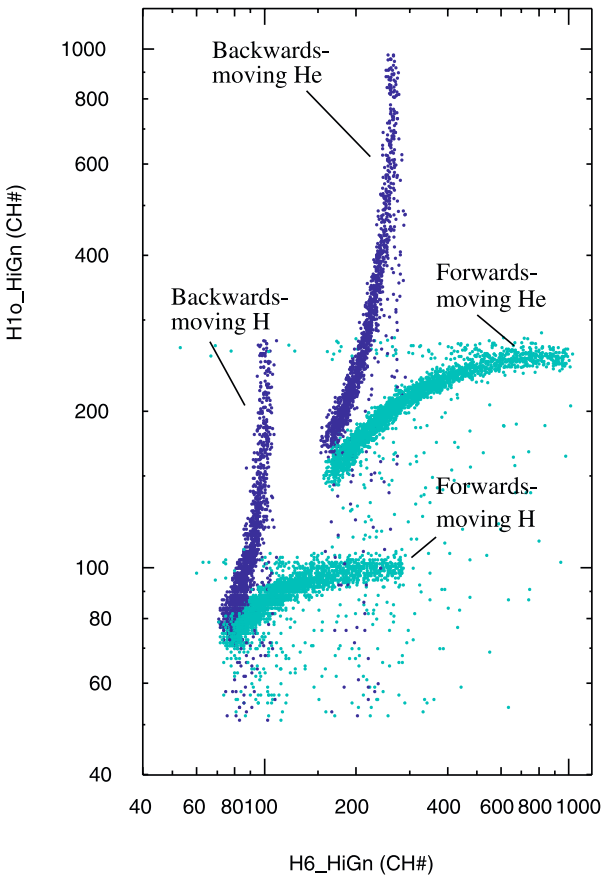


Fig. 17 Simulation of forwards (light blue) and backwards (dark blue) protons and He between 40 and 100 MeV/nucleon. This figure shows that the forwards and backwards particles are essentially separated below 100 MeV/nucleon. Above 100 MeV/nucleon (not shown) the tracks rapidly merge



3.2 Flight Software Architecture

The HET flight software operates in a background loop with interrupt service routines to respond to external events. On power-up, a one-time bootup section executes before interrupts are enabled and the background loop begins executing. The bootup code loads the remaining on-board code and all the on-board tables from EEPROM in SEP Central, sets up communication buffers, initializes the PHASICs and other hardware, and then enables interrupts and transfers control to the background routine.

The HET software uses the first 8 of 11 prioritized interrupts supported by the CPU24 design. Table 5 lists the interrupt assignments.

Interrupts 0, 1, and 2 signal that the corresponding communications tasks are complete. Interrupt 6 is used during code development but is disabled during flight.

Major frames start on one-minute boundaries. HET telemetry packets are transmitted to SEP Central at assigned seconds so as not to conflict with other subsystems that also transmit telemetry to SEP Central.

3.3 Flight Software Development Environment

The decision was made to program the MISC using its native commands rather than Forth, the language used by the LET and SEP Central MISCs. For this a MISC compiler was

Table 5 CPU24 interrupts

int 0	UART #1 (command) receiver data ready
int 1	UART #1 (command) transmitter buffer empty
int 2	UART #2 (telemetry) transmitter buffer empty
int 3	Event interrupt
int 4	One second interrupt
int 5	One minute interrupt
int 6	Stack problem
int 7	Timer

Table 6 Compressed event header (16 bits)

Category	High Rate Mode bit	Stim bit	SWCtr #	# of PHs in the event
15-13	12	11	10-3	2-0

written. In addition, a MISC emulator was created in software that allows the programmer to step through the on-board code and, for example, be able to examine the stack contents at any step. In addition, connection of the instrument via ground support electronics to the Internet was enabled early on. In this way it didn't matter whether the instrument was sitting on a bench next to us, was at Caltech on the other side of the country, or was in integration and test at some remote location.

3.4 Onboard Particle Processing

To transmit the pulse heights of a single HET particle event to the ground can require up to 16 bytes whereas a count of tens of thousands of events can be transmitted using only two bytes. Due to the limited telemetry allocation for HET it is not possible to send a large number of pulse height events to the ground. For this reason it is important to analyze individual particle events on board and bin the particles into software counters that count the numbers of particles of each type in different kinetic energy intervals. These different software counters for HET are listed in the [Appendix](#). Note that some of these counters are counting background events and events from the on-board pulser. The latter are intended to determine live times and will be discussed further later. The primary purpose of transmitting pulse height events to the ground is to verify that the on-board analysis is being done correctly. In addition, particle types without software counters can be studied to some degree.

The on-board algorithm for stopping particles uses the classic $dE/dx \times E'$ method of particle identification. Penetrating particles are also accepted and analyzed by a separate algorithm in order to extend the energy range. The expected locations of particle tracks were calculated by a Monte Carlo program that uses energy loss algorithms based on scaling proton range-energy formulae given by Andersen and Ziegler ([1977](#)).

HET pulse height events in telemetry are compressed from 3 bytes to only 2 bytes per pulse height and include an event header. The event header has the format as shown in Table 6.

The categories referred to in Table 6 are presented in Table 7.

The category values correspond to different readout queues (see also Figs. [18a](#), [18b](#)). Note that the coincidence logic can be set to accept H1 only events as well as events that require an H1 and H2 coincidence. To date, H1 only events have not been accepted on-board.

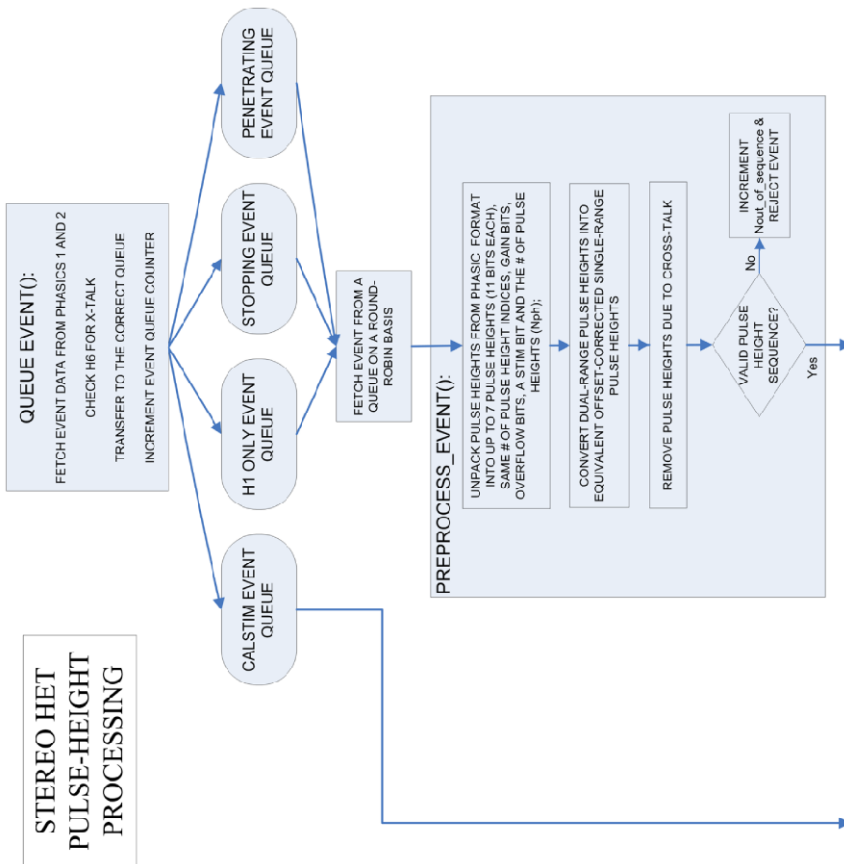


Fig. 18a Shows the processing flow of the on-board particle identification algorithm (part a.)

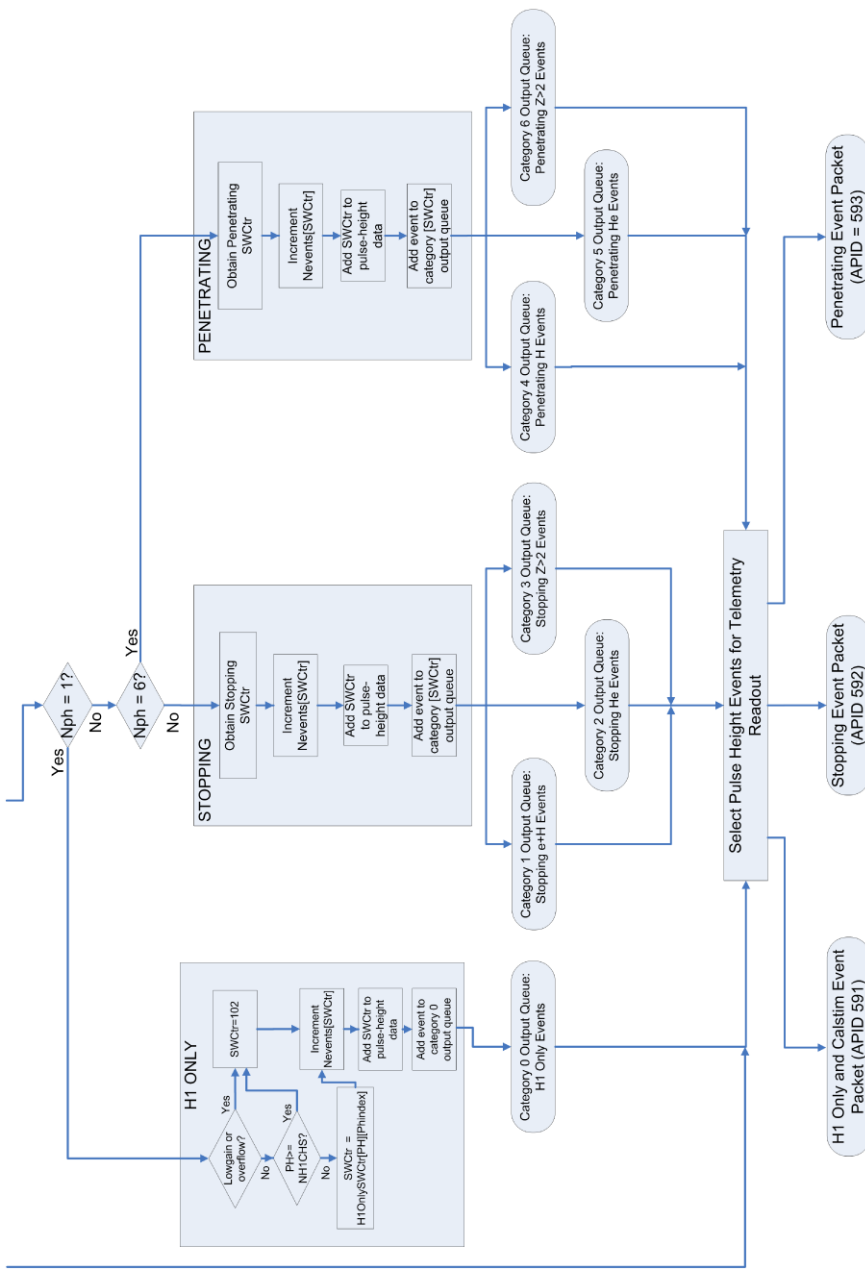


Fig. 18b Shows the processing flow of the on-board particle identification algorithm (part b).

Table 7 Event Categories

Category	Description
0	H1 only
1	Stopping protons and electrons
2	Stopping He
3	Stopping particles with $Z > 2$
4	Penetrating protons
5	Penetrating He
6	Penetrating particles with $Z > 2$

Table 8 Compressed event PH format (16 bits)

15-13	12	11	10-0
PHA index	High gain bit	Overflow bit	Pulse height

The compressed format of individual pulse heights is presented in Table 8, where PHA Index has the values: 0 for H1i, 1 for H1o, 2 for H2, 3 for H3, 4 for H4, 5 for H5, 6 for H6, and 7 for Invalid, and the High Gain bit is 0 for Low Gain.

Note that one can transform the compressed event data back into the raw data format as well as obtain additional information for each event (category, high-rates mode bit, stim bit, and the software counter number assigned on board).

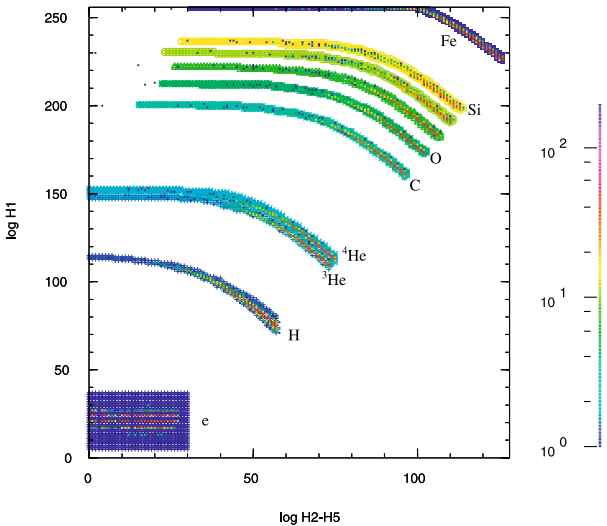
The overall on-board processing flow is illustrated in Figs. 18a and 18b. When the front-end logic issues a valid coincidence interrupt, the MISC reads the event from the PHASICs and the process queue_event() is initiated. queue_event's task is to queue the incoming event into one of 4 different input queues (FIFOs) as well as capture the value of the stim bit and the number of pulse heights in the event.

Calstim events are calibration events that are generated at a low rate (<1/second) by triggering all 7 on-board pulsers simultaneously. For these events, the pulser DACs are increased by one step per minute during minutes 0–8 out of every 15 minutes. The resultant events are used to verify the linearity and overall performance of the PHASICs. These are placed in the Calstim event queue (256 3-byte words deep).

If the event is not a Calstim event, then the pulse height index values are determined from the Chip Address and PHA Address values and examined. If there is an H6 pulse height it is checked for cross-talk and the event is correspondingly queued as a stopping event or as a penetrating event. Each queue slot holds the number of pulse heights in the event and the event itself in raw format. The H1 only queue, the stopping queue and the penetrating event queue can each hold 256 events. The Calstim event queue can hold up to 32 events.

The next step in the event processing is to fetch an event from one of the input queues (other than the Calstim event queue) on a round-robin basis. The event is then handed to the routine preprocess_event(), which performs the sequence illustrated in Fig. 18a. The event will be rejected if the pulse heights are not in H1 (either H1i, H1o, or possibly H1i followed by H1o), H2, H3, H4, H5, H6 order. This sequence check is intended to eliminate events for which there are more than two incident particles or possibly events with cross-talk. If accepted, the processing continues as shown in Fig. 18b. The task of the blocks marked H1 only, Stopping, and Penetrating is to determine the proper software counter number, increment this counter by one, and add the event to one of 7 different output queues together with the software counter number. This is also shown in Fig. 18b. The queues for categories 3–6 can each hold up to 64 events. The category 1 and 2 queues can each hold up to 128

Fig. 19a A 2-D histogram of simulated stopping particles is shown overlaid on top of the stopping particle response table. The response table is plotted with a different color for each stopping particle type



events. At the end of the major frame, events will be selected from these queues on a round-robin basis and read out into telemetry.

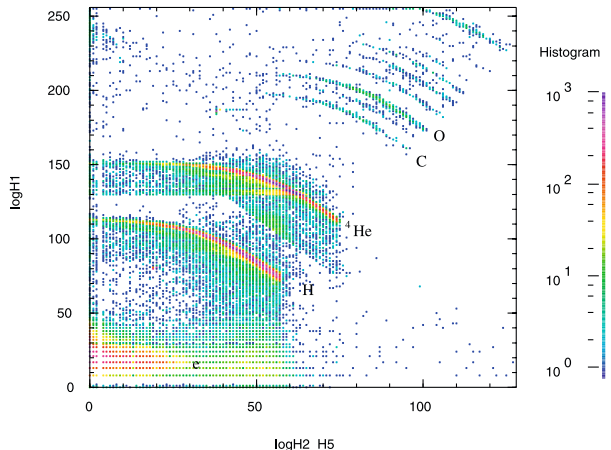
Determination of the stopping software counter number is as follows. Up to 4 logarithmic indices are obtained from the pulse heights by table lookup: $\log H_1$ (0–255), $\log H_2$ (0–255), $\log H_2\text{--}H_5$ (0–127), and $\log H_3\text{--}H_5$ (0–127). Here $\log H_2\text{--}H_5$ denotes the index for the logarithm of the sum of offset- and gain-corrected pulse heights H_2 through H_5 . There are two corresponding response tables with dimensions 256×128 . The first is for the software counter ($\text{SWCtr} = \text{stopSWCtr}[\log H_1][\log H_2\text{--}H_5]$) and the second is for the stopping particle type ($\text{stopParticleType}[\log H_1][\log H_2\text{--}H_5]$). The table size is definitely sufficient for identifying particle types. Quantization of the residual E due to log conversion ($\log H_2\text{--}H_5$) means that the energy intervals for each particle type are not quite as well matched as one might like. We are considering altering the on-board software to do this binning in linear space to improve this part of the HET performance.

If the software counter does not correspond to a particle track it is assigned a background counter number (0 for the category 1 output queue, i.e. for electrons and protons; 1 for the category 2 output queue, i.e. for He; and 2 for the category 3 output queue, i.e. for $Z > 2$) or a livetime stim pulser event counter number (103, 104, or 105). Otherwise, if there is an H_3 pulse height then a consistency check can be made to see if $\text{stopParticleType}[\log H_1][\log H_2\text{--}H_5]$ is the same as $\text{stopParticleType}[\log H_2][\log H_3\text{--}H_5]$. If not, the event software counter is assigned the appropriate background counter. This amounts to the dE/dx vs E' method being applied first with H_1 as the dE/dx detector and then with H_2 as the dE/dx detector. The same table can be used for each since the Δx detector is 1 mm thick Si in each case and because the gains have been matched.

The stopping response tables are illustrated in Figs. 19a and 19b. Figure 19a shows a 2-D histogram derived from simulated particle events overlaid on top of the stopping particle response table $\text{stopPrtc1Type}[\log H_1][\log H_2\text{--}H_5]$. Figure 19b shows a sample histogram of stopping particles from the SEP event of 13 December 2006 (see Sect. 5).

Analysis of penetrating events is similar. This multi-dimensional problem has been reduced to two 2-dimensional response planes: the first of these is the $\log H_1$ versus $\log H_6$ plane (128 by 128 logarithmic channels for protons and He), and the second is the $\log H_2$ versus $\log H_3\text{--}H_5$ plane (also 128 by 128 logarithmic channels). No accelerator tests were

Fig. 19b Shows a 2-D histogram of stopping particles in the logH1 versus logH2_H5 plane observed during the event of 2006 December 13



performed with penetrating protons and He, so the current tables are solely based upon the simulated response. An additional complication is that, due to the relatively shallow stack, the forward and backwards tracks merge at a fairly low energy. It is intended to refine the response tables using solar event data.

3.5 Command Processing

The default command state, on-board tables, and software for HET are all contained in EEPROM in SEP Central and are loaded into HET at boot up. Changes to the EEPROM contents can be made by transmitting a complete HET EEPROM image to the spacecraft. This takes approximately 10 minutes of commanding. Alternatively, a paging scheme is available that uploads only pages that have changed. The remainder of this section addresses commands that may be used to make changes in HET RAM and in the PHASICs. These changes will of course be lost if HET is turned OFF or is rebooted. Command bits in the PHASICs are refreshed once per major frame by the HET software. The reason for this is that the RAM chips used by the MISC are much more resistant to single-event upsets (SEUs) than the PHASICs.

The command interface between HET and the spacecraft is managed by SEP Central. HET commands transmitted from the ground as CCSDS telecommand packets (CCSDS 2000; see also STEREO MOC to POC and to SSC ICD 2002) are received by the IMPACT IDPU, which in turn forwards them to SEP Central. SEP Central unpacks the commands and routes them to the HET sensor via a bi-directional serial command interface. Command echoes from the HET sensor are routed back to SEP Central and then to the spacecraft via the same path.

Commands can be received by the HET sensor at any time during a major frame. There are two modes for command execution by the HET software: immediate and non-immediate. In immediate execution mode, commands are executed immediately instead of waiting for a major frame boundary. In non-immediate mode, the commands are executed at the major frame boundary. Non-immediate mode is the default command execution configuration used for the HET software. The non-immediate mode strategy preserves the integrity of the data for each major frame (i.e. the command state is the same throughout the major frame).

A command that is sent to SEP Central for execution by the HET sensor is preceded by an identifier that informs SEP Central to forward the command to HET, and indicates whether

the command is ASCII or binary (see below). These command keywords “HET-CMD” and “HET-BIN” are used to identify the HET sensor and precede any sequence of commands routed through SEP Central. These keywords are interpreted by SEP Central and not passed through to the HET sensor.

The HET response for each command is essentially an ASCII command echo. If the keyword in the command received by the HET sensor is not recognized by the software, the response will contain the keyword echo followed by a question mark. The absence of a question mark in the command response signifies confirmation that the command was received and is queued for execution. Immediate execution is indicated in the command echo by an asterisk. SEP Central collects the HET command responses and multiplexes them into packets and transmits them as part of its telemetry stream.

ASCII commands are used to set parameters in the software and to configure the HET front-end electronics and the PHASICs. Different commandable functions for the PHASICs were cited in Sect. 2.3.2. Binary commands are used in conjunction with ASCII commands to load large particle look up tables into the HET MISC RAM.

Binary commands are used to specify the starting memory location in RAM and the number of words to load, followed by the data. The HET software accepts the binary data as a byte stream, buffering it in memory with no interpretation. Once the binary data have been transmitted, a subsequent ASCII command is necessary to interpret and activate the loading of the data. A subsequent ASCII command causes the HET software to copy the buffered byte stream, according to the specified decompression scheme, to a specified memory address.

If the computed checksum matches the received checksum, the OK echo is sent in the command response. The command response consists of the ASCII keyword “binary” followed by the relative address “A:” where the binary command load was placed in memory, and the number of bytes “N:” in the command load. Additionally, if an error occurred, “ck-err” is present followed by the received and computed checksums.

3.6 High-Rate Strategy

3.6.1 High-Rate Mode

Historically speaking, particle telescopes have frequently saturated during the largest solar particle events. In order to increase HET’s capability to make measurements during intense events, the front detector on HET has been segmented into a small central detector (H1 inner, denoted as H1i) surrounded by a circular ring (H1 outer, denoted by H1o). The normal mode is the low-rates mode, where both H1i and H1o are fully enabled. In this mode, electrons, protons and He are detected and processed by either H1i or H1o through their high-gain PHA channels. When the H1i singles rate exceeds a (commandable) level, the MISC automatically switches the instrument to high-rates mode. This switching occurs at a major frame boundary and involves disabling the H1o high-gain PHA channel. Higher Z particles that pass through the H1o detector continue to trigger the H1o low-gain PHA channel. After launch we discovered that low energy stopping He, which normally is processed by the H1o high-gain PHA channel, will be accepted and processed by the low gain channel when the high-gain channel is disabled. High energy stopping He, however, is unable to trigger the low-gain channel. This complicates the He high-rates analysis, because He now has two different geometry factors, depending on the He energy. We could raise the H1o low-gain threshold and eliminate this effect, but so far we have elected to not do so. When the H1i singles rate falls below a certain (commandable) count rate, normally half the rate that causes

HET to go into high-rate mode, the MISC re-enables the low-rate mode. To date the H1i rate at which the high-rate mode begins has been set at 400 counts per second, a rather low value.

There are some draw-backs to the high-rate mode, but we don't consider them serious. One is that in low-rates mode, the H1i and H1o detectors act as guards for particles that pass through both detectors. In high-rate mode, the H1o threshold is raised too high to detect low Z particles that intersect both H1i and H1o. In particular, ${}^4\text{He}$ that passes through the H1i edge can fall down into the ${}^3\text{He}$ region of the H1 versus H2_H5 SWCt matrix. On the other hand, the stopping-particle consistency check described in Sect. 3.4 can help to eliminate these ${}^4\text{He}$ from being misidentified as ${}^3\text{He}$. One reason that this is not really a serious problem is that ${}^3\text{He}$ -rich events are generally small events, ones that are too small to trigger the high-rate mode.

3.6.2 *Livetimes*

The front-end livetime is measured by counting pulses from a clock running at 2×10^5 pulses per second in a counter that is gated off when the MISC is not available to accept new events (see Fig. 16).

It was mentioned in Sect. 3.4 that Calstim events are generated during minutes 0–8 out of every 15 minutes. During minutes 9–14, the pulsers are set to generate events that correspond in turn to each of the different event categories 0–5 (see Sect. 3.4) at a rate of 600 per minute. These events are processed on-board as if they were due to particles. They are counted in software counter numbers 103–108. These counters are located in low-background regions of their respective categories. The number that get counted in a given minute is a measure of the livetime for on-board processing events in the corresponding category. This overall sequence of pulsing (minutes 0–14) can be disabled by command. These events have been chosen so that their counting rate is unaffected by the high-rate mode. Category 6 does not have a livetime counter.

The livetime counters measure the total livetimes for categories 0–5. These livetimes are in general shorter than the front-end livetime because, at high rates, the MISC may not be able to obtain the software counter number for every pulse height event that it receives. Figure 20 shows the front-end livetime and the 3 stopping event category livetimes during the large event of 13 December 2006. It can be seen that the front-end livetime is only slightly longer than the other livetimes, and also that the livetimes were reasonably high, even at the peak of the event.

3.7 Telemetry Formatting

3.7.1 *Packet Strategy*

The telemetry output of the STEREO IMPACT HET telescope contains CCSDS packets in 8 different data formats:

- A. Rate packets
- B. Status and single PH packets
- C. Stopping particle PH packets
- D. Penetrating particle PH packets
- E. Table status dump
- F. Beacon packets

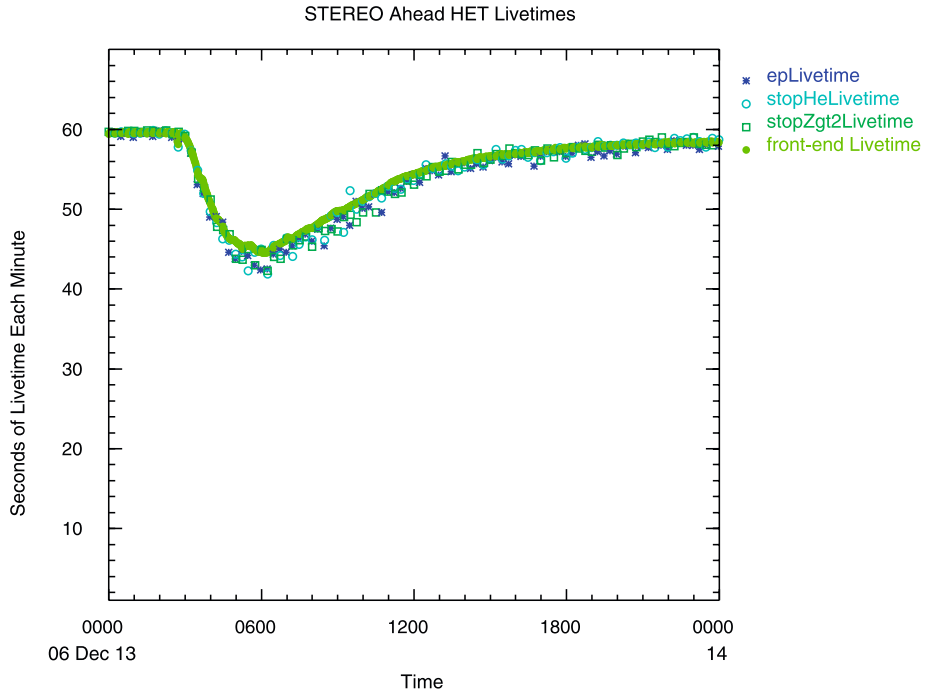


Fig. 20 Plots the front-end livetime and the stim event livetimes versus time during the ground level event which started on December 12, 2006. Note that the livetimes measured by the stim pulser are only slightly below the front-end livetime at the peak of the event (minimum livetime)

G. Housekeeping data packets

H. Raw event packets (non-flight).

Each CCSDS packet is 272 bytes long and begins with an 11-byte CCSDS header. The quantities of primary interest in the CCSDS header are the ApID, which identifies the specific packet type, and Universal Time in seconds since 1 January 1958 00:00:00. Packet types A.–E. have ApIDs 590–594; Packets F. and G. are sent to SEP Central with ApIDs of 599 and 598, respectively; Packet H has ApID 597.

After individual particle pulse height (PH) events are recorded by HET, the onboard processing algorithm identifies particle species and energies and bins the particles in “software rate counters”, as distinguished from hardware counters in the front-end electronics. The identification of these counters is given in the [Appendix](#). In addition to binning all the particles, samples of the raw PH events are selected in 8 categories (including the Calstim events) for inclusion in the telemetry stream. Note that PH events can vary in length from 2 to 16 bytes (always even).

All rates are log compressed from 24-bit to 16-bit quantities for telemetry (5 bits for the characteristic, and 11 bits for the mantissa with leading 1 suppressed; integers up through 4096 are recovered exactly). Quantities longer than one byte are written into the packets least significant byte first with the exception of the CCSDS header, which is most significant byte first.

In normal operation, HET generates 6 primary packets during a one-minute frame; these might be formatted as follows: one A packet, one B packet, three C packets, and one D

Table 9 HET Beacon data

Electrons 0.7–6 MeV—sum of SWCtrs 6–8
Protons 13–21 MeV—sum of SWCtrs 9–12
Protons 21–40 MeV—sum of SWCtrs 13–18
Protons 40–100 MeV—sum of SWCtrs 81–82
He 13–21 MeV/n—sum of SWCtrs 24–27
He 21–40 MeV/n—sum of SWCtrs 28–33
He 40–100 MeV/n—sum of SWCtrs 86–87
C+O 30–52 MeV/n—sum of SWCtrs 35–39, 42–46
C+O 52–74 MeV/n—sum of SWCtrs 40–41, 47–48
Fe 52–74 MeV/n—sum of SWCtrs 73–74
Livetime (log compressed)
High-rates mode bit

packet. E packets are multiplexed out at a rate that can be selected by command. In flight, typically, E packets replace a PH packet once every 15 minutes to produce a complete dump every \sim 7 days. F and G packets contribute the HET portions of the SEP Beacon and housekeeping data, respectively, i.e. they are sent to SEP Central, which in turn combines them with data from other IMPACT SEP instruments to create combined Beacon (ApID 624) and housekeeping packets (ApID 577). Command echoes are in packet 576. Sample PHs to fill the stopping particle PH packets are obtained by a round-robin sampling of the three stopping-event queues (categories 1–3). Similarly, sample PHs to fill the penetrating particle PH packets are obtained by a round-robin sampling of the three penetrating event queues (categories 4–6).

Each HET packet ends with a checksum as the last byte. The checksum is calculated such that if all 272 bytes of the packet are added together the lowest order byte is hex 00.

3.7.2 Beacon Packet

STEREO broadcasts Beacon data continuously to be used by NOAA and others to monitor and forecast interplanetary space weather (see, e.g., Luhmann et al. 2007). Included are both imaging and *in situ* data. HET Beacon data are transmitted to SEP Central to be incorporated into a single telemetry packet (ApID 624 decimal) that contains Beacon data for the entire IMPACT SEP suite. SEP Central time tags the data to correspond to the start of the data accumulation time. The HET Beacon data include the quantities presented in Table 9.

3.7.3 Housekeeping Packet

HET housekeeping data are transmitted to SEP Central to be incorporated into a single telemetry packet for the entire IMPACT SEP suite. HET housekeeping includes 2 temperatures, subcommutated threshold settings, digitized preamplifier DC output values (the preamplifiers are selected by commands), leakage current data, 2 bytes of command error flags, a checksum for all the tables taken together, the major frame number, the number of invalid triggers, and the software version number.

4 HET Resources

The HET uses the following resources:

Weight: 595 g

Power: 359 mW average, 498 mW maximum (excluding power supply inefficiency)

Bit-rate: 218 bits/s.

The HET weight reported here includes the telescope plus the electronics board. It does not include the portion of the SEP Central walls to which HET is mounted (see Fig. 14a). These walls will be referred to as the HET electronics enclosure. The HET telescope is 82 mm long and has a maximum diameter of 68.5 mm. The overall height, measured from the top of the telescope to the bottom of the electronics enclosure, is 206 mm. The electronics enclosure has maximum dimensions 133 mm high, 172 mm wide, and 95 mm deep.

The bit-rate includes HET's shares of the housekeeping and Beacon packets.

The HET does not require any heaters.

5 System Level Tests

5.1 Bench Tests

The HET electronics performance was tested at -20°C , 0°C , $+20^{\circ}\text{C}$, and $+40^{\circ}\text{C}$. Pulse height thresholds, offsets and analyzer linearity curves were measured using an Ortec 448 Research Pulser. The results are reported in Tables 4a, 4b. Particle response performance was measured using pulsers (including the on-board stim pulsers), a ^{106}Ru electron source, and muon runs.

5.2 Accelerator Runs

As mentioned earlier, accelerator runs were made at the National Superconducting Cyclotron Laboratory at Michigan State University in East Lansing. The initial runs were marred by unexpected cross-talk. The flight units were no longer available for our second trip to MSU in May 2006, so we did runs with the engineering test unit. The on-board tables were modified by replacing the Fe response with the expected Ca response (the test beam was ^{40}Ca at 140 MeV/n). Air between H1 and H2 was included in the response calculations since the telescope was not placed in a vacuum for these tests. The ETU tests showed that the overall design, including the on-board software, was performing reasonably well. Particle tracks were populated using fragments from the primary beam. Some changes were made to the flight software as a result of the ETU tests. For the purpose of demonstrating the performance of the two flight units, rather than presenting the ETU accelerator data, we will present flight data for the two flight units. In particular, in the next section we present results from a perigee pass and from an SEP event in December 2006.

5.3 Post-Launch Data

After launch by a single rocket, the two STEREO spacecraft were placed in elliptical orbits with apogees at the lunar distance. Subsequently the Ahead spacecraft did a lunar swing-by that injected it into its current orbit around the Sun with an aphelion slightly less than 1 AU. The Behind spacecraft performed two lunar swing-bys that injected it into a solar orbit with aphelion slightly greater than 1 AU. As a consequence, the Ahead spacecraft will drift ahead of the Earth by about 22.5° per year, and the Behind spacecraft will drift behind the Earth at the same rate.

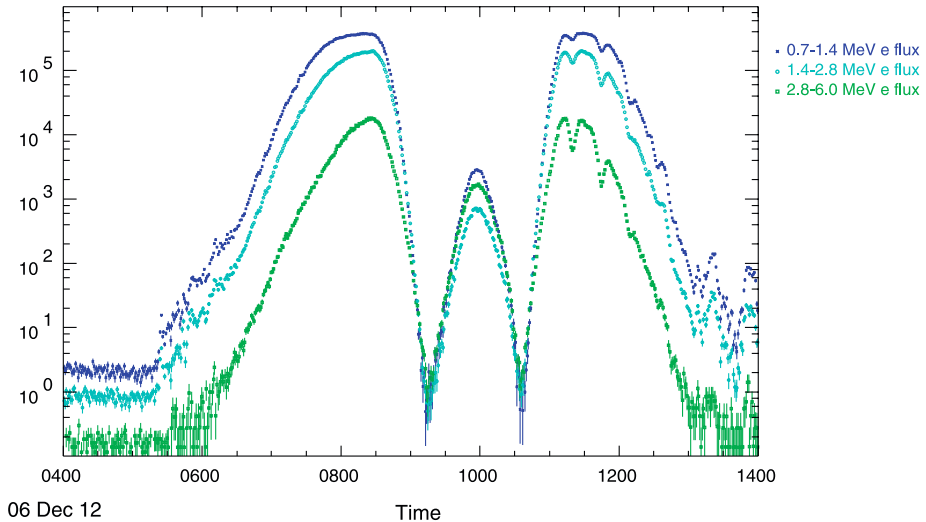


Fig. 21 Shows electron intensities (#/cm²-sr-sec-MeV) for 3 different energy intervals during a perigee pass of the Behind spacecraft

The early post-launch data from both the Ahead and Behind HETs are essentially identical, so in what follows different figures will be chosen for a random spacecraft and will not be shown for both spacecraft.

Figure 21 shows electron intensities in three energy intervals as measured by the Behind spacecraft during the perigee pass on 12 December 2006. The apparent lack of count-rate saturation demonstrates the ability of the HET to perform at high counting rates.

Since launch the Sun has been at the minimum of the 11-year solar activity cycle as measured by sunspot number. Hence it was quite surprising when several large SEP events occurred in December of 2006. The event of 13 December was a Ground Level Event (i.e. it was detected by neutron monitors at sea level). It occurred at a solar longitude of W23. At the peak of this event, HET was processing almost 4000 particles per second. Between 13 December 02:40 and 14 December 14:00, the Ahead HET processed 3×10^6 H and 2.6×10^5 He.

Figure 22 shows two histograms: the first is for Z-values estimated for stopping H and He pulse height events that were sent to the ground. These estimates were based on the H2 and H3–H5 energy losses for each event (Stone et al. 1998). Inspection of the first figure shows that the required charge resolution of <0.2 charge units is being met for H and He. The second histogram is for similar estimates of the particle masses. Again, inspection of the figure shows that the desired mass resolution of <0.2 mass units is being met for ⁴He.

Figure 23 shows the measured intensity-time profiles for electrons (0.7–1.4 MeV), H (20.8–23.8 MeV), and He (21.1–24.4 MeV/n) for the event of 13 December. Figure 24 shows similar data for two previous solar events from the same active region that produced the event of 13 December. Note how different the time profiles are as compared to those of Fig. 23. One of the objectives of STEREO is to better understand how such different profiles occur. Figure 25 shows a comparison of proton energy spectra measured by ACE/EPAM, SAMPEX, STEREO/IMPACT/LET, and HET. And finally, Fig. 26 shows a 2-D histogram of H and He that penetrated the HET telescope, either forwards or backwards. Collectively

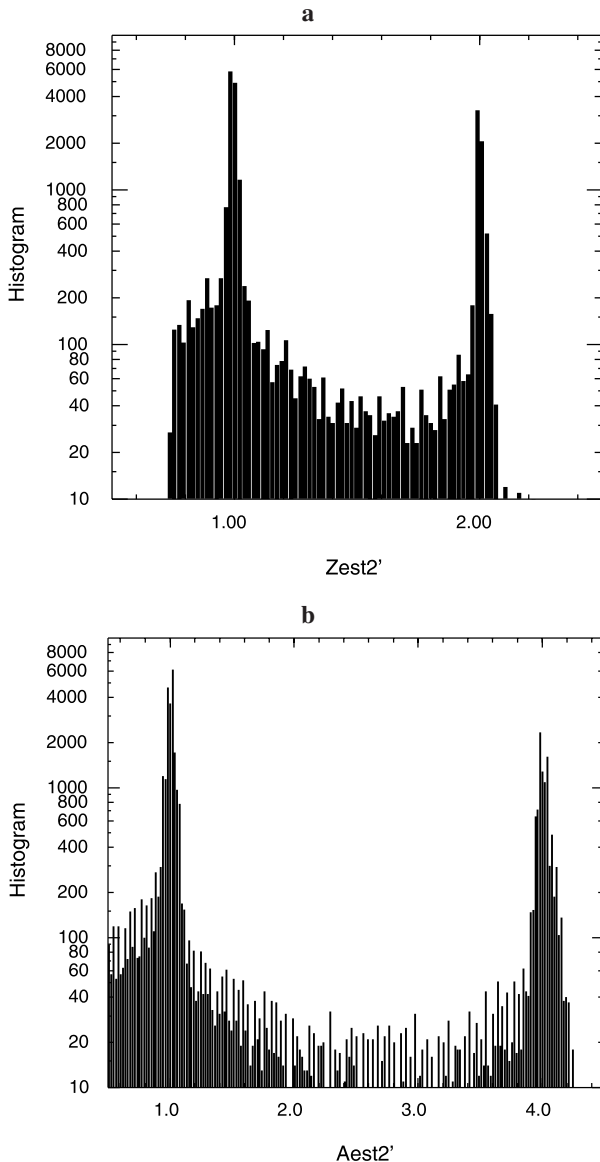


Fig. 22 Histograms of estimated Z -values and A -values for H and He observed during the event of 2006 December 13th

these figures illustrate that the HETs are working well, even in solar events that have very high intensities.

Acknowledgements This research was supported by the National Aeronautics and Space Administration at the Goddard Space Flight Center (GSFC). The design, building, and testing of the HETs was only possible with the assistance of a large number of people, whom we wish to acknowledge here. Branislav Kecman at Caltech provided many of the HET electronic parts, in particular the fully tested PHASICs. The many individuals who contributed to the PHASICs are acknowledged in Mewaldt et al. (2007b). Other parts were

Fig. 23 Shows the measured intensity-time profiles for electrons (0.7–1.4 MeV), H (20.8–23.8 MeV), and He (21.1–24.4 MeV/n) for the event of 2006 December 13

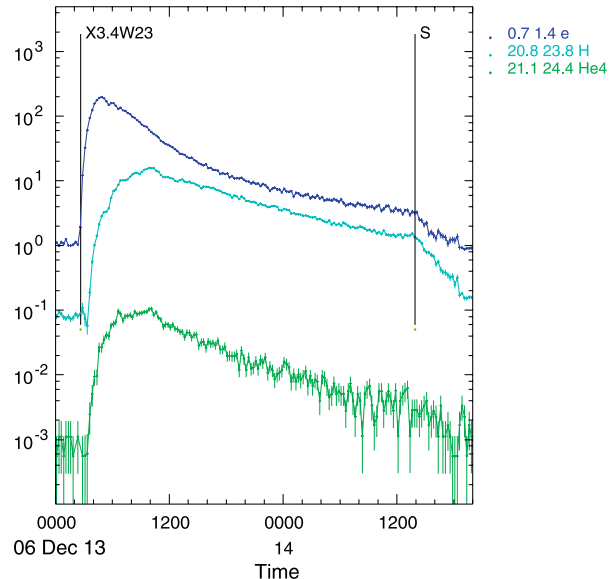
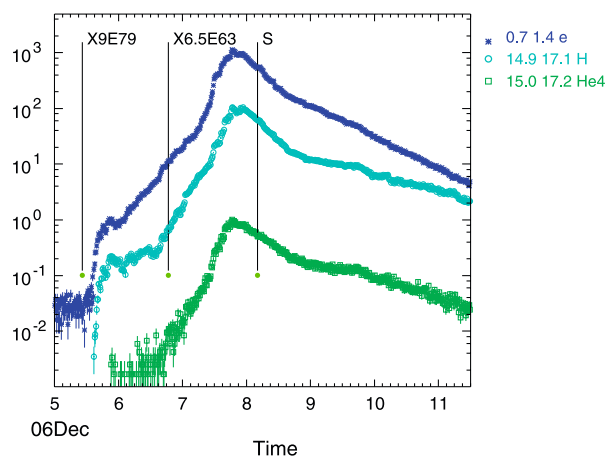


Fig. 24 Shows the time-intensity profiles of 0.7–1.4 MeV electrons, 14.9–17.1 MeV H, and 15.0–17.2 MeV/n He for the time period 2006 Dec 5–11. Note the very different time profiles as compared to the previous figure



procured by Maxine Windhausen at GSFC. Marci Holzapfel performed the board layout for the HET electronics. Traci Pluchak-Rosnack populated the electronic boards and supervised staking and conformal coating of the boards. Bert Nahory and John Krizmanic performed the detector tests at GSFC. Environmental testing and spacecraft-level testing of the HETs was done together with LET and SEP Central under the guidance of Branislav Kecman, with software support from Bob Radocinski, and other support from personnel at JPL and Caltech. Janet Cunningham was the technician in charge of thermal blanketing of HET/LET/SEP Central. The HET front foils were coated by George Harris. Colin Wilburn of Micron Semiconductor worked with us until significant problems with HET detector leakage currents were resolved. Mechanical modeling of HET/LET/SEP Central was performed by Terry Fan of Swales, Inc. Software support at GSFC was provided by Haydar Teymourlouei.

Accelerator calibrations and performance tests were performed on the HET flight units and subsequently on the HET engineering test unit at the National Superconducting Cyclotron Laboratory (NSCL) at Michigan State University in East Lansing, Michigan. We thank Raman Anantaraman and his support staff at NSCL for their prompt and very professional support. We also thank Sven Geier and Hiromasa Miyasaka at Caltech for their support of the accelerator tests.

Fig. 25 Shows a comparison of proton intensities measured by ACE/EPAM, SAMPEX, STEREO/IMPACT/LET, and HET. The figure is taken from R.A. Mewaldt et al. (2007a)

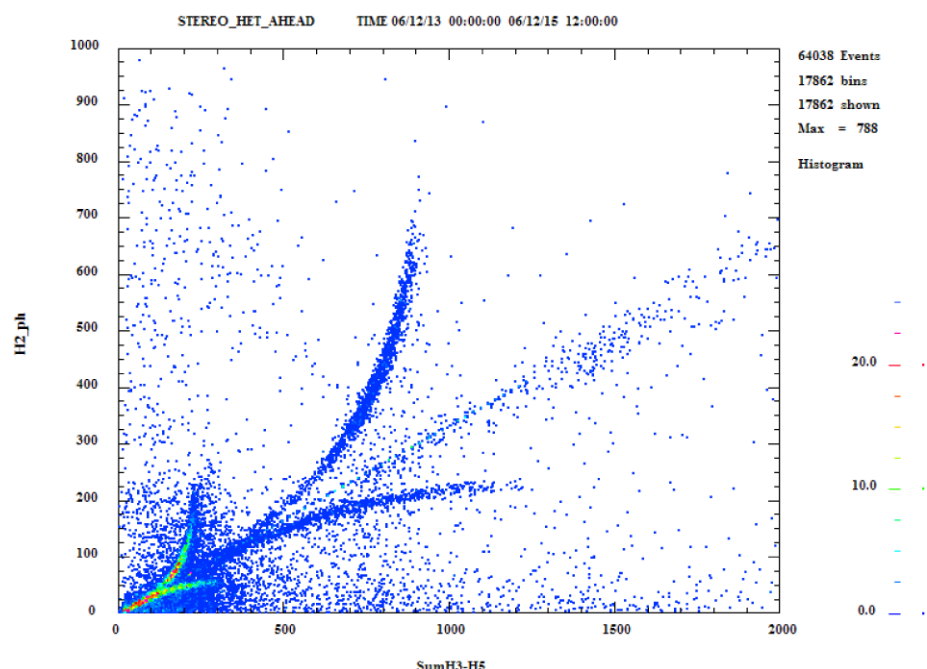
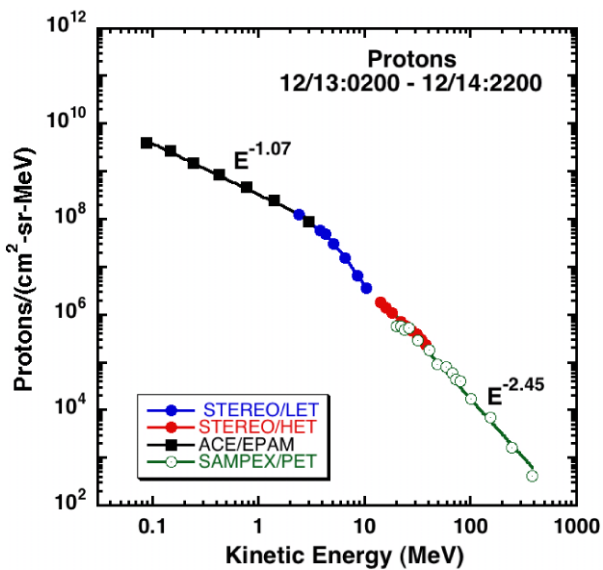


Fig. 26 Shows the HET response for penetrating H and He. This figure is a 2-D histogram formed from penetrating particle pulse height events transmitted to the ground. The offset-corrected H₂ pulse height is binned and plotted on the y-axis and the sum of the offset corrected pulse heights H₃-H₅ is binned and plotted on the x-axis. The number of events in each x-y bin is plotted as a color. The upper tracks are for backwards-moving particles, while the lower two tracks are for forward-moving particles (see Fig. 17)

We wish to thank the STEREO Mission Project Office at GSFC for their extensive support. Haydee Maldonado was the initial STEREO Project Manager, a role subsequently passed to Nick Chrissotimos. Mike Delmont was the Deputy Project Manager. Joe Davila was the initial STEREO Project Scientist, followed by Mike Kaiser. We thank each of them for their support. We especially wish to acknowledge Lillian Reichenthal, the STEREO Project Instrument Manager for IMPACT, who was a staunch supporter and active member of our team. She prodded us to look at the big picture (schedule, schedule, schedule!) when we were mired in details, and assisted us on a daily basis. Other support from the Project Office was provided by Harry Culver, Therese Errigo, Larry Gibb, Fred Gross, Jerry Hengermihle, Shane Hynes, Mike Jones, Diane Kolos, Tabitha Merchant, Bobby Power, Antonio Reyes, and Steve Wasserzug.

We also wish to thank many individuals at the Johns Hopkins Applied Physics Laboratory (APL), some of them unknown to us, for their support as the spacecraft contractor. In particular, we wish to thank Andy Dreisman, the Deputy Project Manager at APL, and Dave Myers, the primary APL contact for IMPACT. Possible detector contamination by low-level volatile fumes was a constant issue that APL handled effectively.

We wish to thank various individuals at the University of California at Berkeley (UCB). Janet Luhmann is the IMPACT Principal Investigator and we thank her for her active encouragement and support. David Curtis was the IMPACT project manager at UCB. His long professional experience, his easy-going manner under fire, and his ability to keep on top of many different complex issues all at the same time were invaluable to us. Other support has been provided by Peter Berg, Selda Heavner, Ron Jackson, and Peter Schroeder.

Finally, we thank Eric Christian, the STEREO Program Scientist at NASA Headquarters, both for his administrative support and encouragement, but also for his willingness to take night shifts for spacecraft-level thermal vacuum testing which required 24 hours per day/7 days per week coverage for approximately a month.

Appendix: Nominal HET software counters

SW Ctr #	Z	A	KEmin (MeV/n)	KEmax (MeV/n)	Particle type	Cat.
0					–	1
1					–	2
2					–	3
3					–	4
4					–	5
5					–	6
6	–1	–	0.7	1.4	1	1
7	–1	–	1.4	2.8	1	1
8	–1	–	2.8	~6	1	1
9	1	1	13.3	15.0	2	1
10	1	1	15.0	17.0	2	1
11	1	1	17.0	19.0	2	1
12	1	1	19.0	21.0	2	1
13	1	1	21.0	24.0	2	1
14	1	1	24.0	27.0	2	1
15	1	1	27.0	30.0	2	1
16	1	1	30.0	33.0	2	1
17	1	1	33.0	36.0	2	1
18	1	1	36.0	40.0	2	1
19	2	3	17.0	21.0	3	2
20	2	3	21.0	27.0	3	2

SW Ctr #	Z	A	KEmin (MeV/n)	KEmax (MeV/n)	Particle type	Cat.
21	-2	3	27.0	33.0	3	2
22	-2	3	33.0	40.0	3	2
23	-2	3	40.0	47.0	3	2
24	-2	4	13.3	15.0	4	2
25	-2	4	15.0	17.0	4	2
26	-2	4	17.0	19.0	4	2
27	-2	4	19.0	21.0	4	2
28	-2	4	21.0	24.0	4	2
29	-2	4	24.0	27.0	4	2
30	-2	4	27.0	30.0	4	2
31	-2	4	30.0	33.0	4	2
32	-2	4	33.0	36.0	4	2
33	-2	4	36.0	40.0	4	2
34	-6	12	26.4	30.0	6	3
35	-6	12	30.0	33.0	6	3
36	-6	12	33.0	36.0	6	3
37	-6	12	36.0	40.0	6	3
38	-6	12	40.0	45.0	6	3
39	-6	12	45.0	52.0	6	3
40	-6	12	52.0	62.0	6	3
41	-6	12	62.0	74.0	6	3
42	-8	16	30.0	33.0	8	3
43	8	16	33.0	36.0	8	3
44	8	16	36.0	40.0	8	3
45	8	16	40.0	45.0	8	3
46	8	16	45.0	52.0	8	3
47	8	16	52.0	62.0	8	3
48	8	16	62.0	74.0	8	3
49	8	16	74.0	87.0	8	3
50	10	20	33.0	36.0	10	3
51	10	20	36.0	40.0	10	3
52	10	20	40.0	45.0	10	3
53	10	20	45.0	52.0	10	3
54	10	20	52.0	62.0	10	3
55	10	20	62.0	74.0	10	3
56	10	20	74.0	87.0	10	3
57	10	20	87.0	98.0	10	3
58	12	24	40.0	45.0	12	3
59	12	24	45.0	52.0	12	3
60	12	24	52.0	62.0	12	3
61	12	24	62.0	74.0	12	3
62	12	24	74.0	87.0	12	3
63	12	24	87.0	98.0	12	3

SW Ctr #	Z	A	Kemin (MeV/n)	KEmax (MeV/n)	Particle type	Cat.
64	12	24	98.0	109.0	12	3
65	14	28	40.0	45.0	14	3
66	14	28	45.0	52.0	14	3
67	14	28	52.0	62.0	14	3
68	14	28	62.0	74.0	14	3
69	14	28	74.0	87.0	14	3
70	14	28	87.0	98.0	14	3
71	14	28	98.0	109.0	14	3
72	14	28	109.0	119.0	14	3
73	26	56	52.0	62.0	26	3
74	26	56	62.0	74.0	26	3
75	26	56	74.0	87.0	26	3
76	26	56	87.0	98.0	26	3
77	26	56	98.0	109.0	26	3
78	26	56	109.0	119.0	26	3
79	26	56	119.0	140.0	26	3
80	26	56	140.0	163.0	26	3
; penetrating particles:						
81	1	1	40.0	60.0	2	4
82	1	1	60.0	100.0	2	4
83	1	1	100.0	200.0	2	4
84	1	1	200.0	400.0	2	4
85	1	1	400.0	2000.0	2	4
86	2	4	40.0	60.0	4	5
87	2	4	60.0	100.0	4	5
88	2	4	100.0	200.0	4	5
; H1-stopping:						
89	1	1	4.1	6.0	2	0
90	1	1	6.0	8.0	2	0
91	1	1	8.0	10.0	2	0
92	1	1	10.0	12.0	2	0
93	1	1	12.0	14.0	2	0
94	1	1	14.0	16.0	2	0
95	2	4	5.5	7.0	4	0
96	2	4	7.0	8.0	4	0
97	2	4	8.0	9.0	0	0
98	2	4	9.0	10.0	4	0
99	2	4	10.0	11.0	4	0
100	2	4	11.0	12.0	4	0
101	2	4	12.0	13.0	4	0
102	-	-	>13.0	-	-	0

SW Ctr #	Z	A	KEmin (MeV/n)	KEmax (MeV/n)	Particle type	Cat.
; livetime counters						
103	“stopping”	stim events	in category 1	(stopping e + H)		
104	“stopping”	stim events	in category 2	(stopping He)		
105	“stopping”	stim events	in category 3	(stopping Z > 2)		
106	“penetrating”	stim events	in category 4	(penetrating H)		
107	“penetrating”	stim events	in category 5	(penetrating He)		
108	“H1Only”	stim events	in category 0	for H1only	livetime	

References

- H.H. Andersen, J.F. Ziegler, *Hydrogen Stopping Powers and Ranges in All Elements* (Pergamon, New York, 1977)
- R. Baker, CPU24 Microprocessor User’s Manual, GSFC internal document, 2003
- D.A. Bryant, T.L. Cline, U.D. Desai, F.B. McDonald, *J. Geophys. Res.* **67**, 4983 (1962)
- CCSDS Packet Telemetry Recommendation for Space Data System Standards, 102.0-B-5, Blue Book, Issue 5 (CCSDS, Washington, DC, 2000)
- C.M.S. Cohen, in *Solar Eruptions and Energetic Particles*, ed. by N. Gopalswamy, R.A. Mewaldt, J. Torsti. AGU Geophysical Monograph, vol. 165 (2006), p. 275
- C.M.S. Cohen et al., *J. Geophys. Res.* (2005). doi:[10.1029/2005JA011004](https://doi.org/10.1029/2005JA011004)
- W.R. Cook, STEREO PHASIC User’s Manual, Caltech internal document, 2002
- J. Luhmann et al., *Adv. Space Res.* **36**, 1534 (2005)
- J. Luhmann et al., *Space Sci. Rev.* (2007, this issue). doi:[10.1007/s11214-007-9170-x](https://doi.org/10.1007/s11214-007-9170-x)
- G.M. Mason et al., *Space Sci. Rev.* (2007, this issue). doi:[10.1007/s-11214-006-9087-9](https://doi.org/10.1007/s-11214-006-9087-9)
- R.A. Mewaldt et al., 30th Int. Cosmic Ray Conf., Mérida, México (2007a)
- R.A. Mewaldt et al., *Space Sci. Rev.* (2007b, this issue). doi:[10.1007/s-11214-007-9288-x](https://doi.org/10.1007/s-11214-007-9288-x)
- R.A. Mewaldt et al., *J. Geophys. Res.* (2005). doi:[10.1029/2005JA011038](https://doi.org/10.1029/2005JA011038)
- R. Müller-Mellin et al., *Space Sci. Rev.* (2007, this issue). doi:[10.1007/s11214-007-9204-4](https://doi.org/10.1007/s11214-007-9204-4)
- D.V. Reames, *Space Sci. Rev.* **90**, 413 (1999)
- D.V. Reames, in *Space Weather*, ed. by P. Song, H.J. Singer, G. Siscoe. AGU Geophysical Monograph, vol. 125 (2001), p. 101
- D.V. Reames, C.K. Ng, *Astrophys. J.* **504**, 1002 (1998)
- D.V. Reames, S.W. Kahler, C.K. Ng, *Astrophys. J.* **491**, 414 (1997)
- STEREO Mission Operations Center (MOC) to Payload Operations Center (POC) and to STEREO Science Center (SSC) Interface Control Document (ICD), Applied Physics Laboratory internal document 7381-9045A (2002)
- E.C. Stone et al., *Space Sci. Rev.* **86**, 357 (1998)
- R. Tousey, in *Space Research XIII*, ed. by M.J. Rycroft, S.K. Runcorn (Akademie-Verlag, Berlin, 1973), p. 713
- A.J. Tylka, M.A. Lee, *Astrophys. J.* **646**, 1319 (2006)
- T.T. von Rosenvinge, H.V. Cane, in *Solar Eruptions and Energetic Particles*, ed. by N. Gopalswamy, R.A. Mewaldt, J. Torsti. AGU Geophysical Monograph, vol. 165 (2006), p. 103

The Plasma and Suprathermal Ion Composition (PLASTIC) Investigation on the STEREO Observatories

A.B. Galvin · L.M. Kistler · M.A. Popecki · C.J. Farrugia · K.D.C. Simunac · L. Ellis · E. Möbius · M.A. Lee · M. Boehm · J. Carroll · A. Crawshaw · M. Conti · P. Demaine · S. Ellis · J.A. Gaidos · J. Googins · M. Granoff · A. Gustafson · D. Heirtzler · B. King · U. Knauss · J. Levasseur · S. Longworth · K. Singer · S. Turco · P. Vachon · M. Vosbury · M. Widholm · L.M. Blush · R. Karrer · P. Bochsler · H. Daoudi · A. Etter · J. Fischer · J. Jost · A. Opitz · M. Sigrist · P. Wurz · B. Klecker · M. Ertl · E. Seidenschwang · R.F. Wimmer-Schweingruber · M. Koeten · B. Thompson · D. Steinfeld

Originally published in the journal Space Science Reviews, Volume 136, Nos 1–4.
DOI: [10.1007/s11214-007-9296-x](https://doi.org/10.1007/s11214-007-9296-x) © Springer Science+Business Media B.V. 2008

Abstract The Plasma and Suprathermal Ion Composition (PLASTIC) investigation provides the in situ solar wind and low energy heliospheric ion measurements for the NASA Solar Terrestrial Relations Observatory Mission, which consists of two spacecraft (STEREO-A, STEREO-B). PLASTIC-A and PLASTIC-B are identical. Each PLASTIC is a time-of-flight/energy mass spectrometer designed to determine the elemental composition, ionic

A.B. Galvin (✉) · L.M. Kistler · M.A. Popecki · C.J. Farrugia · K.D.C. Simunac · L. Ellis · E. Möbius · M.A. Lee · M. Boehm · J. Carroll · A. Crawshaw · M. Conti · P. Demaine · S. Ellis · J.A. Gaidos · J. Googins · M. Granoff · A. Gustafson · D. Heirtzler · B. King · U. Knauss · J. Levasseur · S. Longworth · K. Singer · S. Turco · P. Vachon · M. Vosbury · M. Widholm
Institute for the Study of Earth, Oceans and Space, University of New Hampshire, SSC Morse Hall, Durham, NH 03824, USA
e-mail: toni.galvin@unh.edu

A.B. Galvin · L.M. Kistler · C.J. Farrugia · K.D.C. Simunac · E. Möbius · M.A. Lee
Department of Physics, University of New Hampshire, SSC Morse Hall, Durham, NH 03824, USA

L.M. Blush · R. Karrer · P. Bochsler · H. Daoudi · A. Etter · J. Fischer · J. Jost · A. Opitz · M. Sigrist · P. Wurz
Physikalisches Institut, University of Bern, Sidlerstrasse 5, 3012 Bern, Switzerland

B. Klecker · M. Ertl · E. Seidenschwang
Max-Planck-Institut fuer extraterrestrische Physik, Postfach 1312, 85741 Garching, Germany

R.F. Wimmer-Schweingruber · M. Koeten
Extraterrestrial Physics, Institute for Experimental and Applied Physics, Christian-Albrechts-University Kiel, Leibnizstr. 11, 24098 Kiel, Germany

B. Thompson
National Aeronautics and Space Administration, Goddard Space Flight Center, Greenbelt, MD 20771, USA

D. Steinfeld
Orbital Sciences Corporation, 7500 Greenway Center Drive, Suite 700, Greenbelt, MD 20770, USA

charge states, and bulk flow parameters of major solar wind ions in the mass range from hydrogen to iron. PLASTIC has nearly complete angular coverage in the ecliptic plane and an energy range from ~ 0.3 to 80 keV/e, from which the distribution functions of suprathermal ions, including those ions created in pick-up and local shock acceleration processes, are also provided.

Keywords STEREO · Solar wind · Plasma · Suprathermal · Composition · Time-of-flight spectrometer · Coronal mass ejections · Multipoint spacecraft observations

1 Introduction

The Solar TErrestrial RElations Observatory (STEREO) is the third strategic mission in NASA's Solar Terrestrial Probes (STP) Program and consists of two spacecraft that are drifting apart in solar longitude by 45° per year. The primary science goal for the STEREO mission is to understand the origin and consequences of Coronal Mass Ejections (CMEs), including their interplanetary manifestations (ICMEs). The specific scientific objectives (Kaiser et al. 2007) are to:

- Understand the causes and mechanisms of CME initiation,
- Characterize the propagation of ICMEs through the inner heliosphere to 1 AU,
- Discover the mechanisms and sites of solar energetic particle (SEP) acceleration, in the low corona and in the interplanetary medium, and
- Develop a three-dimensional, time-dependent model of the magnetic topology and plasma temperature, density and velocity structure of the ambient solar wind.

As a secondary objective, STEREO will

- Provide a continuous, low rate data stream ("Beacon Mode") for the purposes of space weather specification and possible prediction of geomagnetic storms.

A science payload consisting of four investigations is on each observatory. Two remote imaging investigations (SECCHI, SWAVES) are used for continuous viewing of solar features and to track transients such as CMEs and shocks traveling toward Earth's orbit. Two in situ investigations (IMPACT, PLASTIC) continuously sample the particles and magnetic fields of associated heliospheric structures and phenomena (including CIRs, ICMEs and SEPs) as they pass by the spacecraft near 1 AU. The SECCHI instrument suite is described by Howard et al. (2007), the SWAVES instrument by Bougeret et al. (2007), and the IMPACT instrument suite by Luhmann et al. (2007). The PLASTIC instrument is described herein. These experiments, combined with the unique vantage points afforded by the STEREO spacecraft drifting orbits, are designed to meet the mission science objectives.

The STEREO mission timeline can be roughly divided into two operational stages, ordered by their orbits and payload status. The "phasing orbit stage" took place during the first three months after launch (late October 2006 through January 2007). The leading (in heliocentric orbit) spacecraft is denoted as "STEREO-A" (AHEAD) and the lagging spacecraft as "STEREO-B" (BEHIND). The observatories, while in the phasing stage, were in geocentric orbits that included one (A) or two (B) gravity-assist lunar swing-bys. Most spacecraft and instrument commissioning activities took place during this near-Earth stage. Thereafter began the primary data or "science orbit stage" where both observatories had attained their respective heliocentric orbits, drawing away from each other and from the Earth. The spacecraft are currently at ~ 1 AU, drifting away from the Earth-Sun line at a rate of $\sim 22.5^\circ$ per

year. Using these drifting orbits, the two observatories combine measurements in the ecliptic plane from two different vantage points in solar longitude. This unique orbit configuration allows the STEREO spacecraft to image the Sun in a three dimensional perspective.

The Plasma and Suprathermal Ion Composition (PLASTIC) investigation team on STEREO includes participants from the University of New Hampshire (USA), the University of Bern (Switzerland), the Max-Planck-Institute for extraterrestrial Physics (Germany), the Christian-Albrechts-University Kiel (Germany), and NASA Goddard Space Flight Center (USA). Instrument Data Processing Unit (IDPU) functions for PLASTIC, as well as the PLASTIC LVC and its EM Interference Filter, were provided by the IMPACT investigation (Luhmann et al. 2007). Specific contributions from these institutions are further summarized in the acknowledgements.

2 STEREO PLASTIC Scientific Objectives

The Plasma and Suprathermal Ion Composition (PLASTIC) instrument on STEREO is designed to study in situ the bulk properties of solar wind (SW) protons and the composition and properties of solar wind minor ions. PLASTIC also measures the composition, spectra, and anisotropy of heliospheric suprathermal (ST) ions in the energy-per-charge range from ~ 0.3 to 80 keV/e. (See Table 1 for additional details.) With these measurements, PLASTIC is the primary sensor on STEREO for studying the link between coronal and solar wind ion processes, and between solar wind and heliospheric processes, as discussed below.

2.1 Solar Processes and Solar Wind Studies

The elemental and isotopic composition of the solar wind observed at 1 AU is determined in the low solar atmosphere and in the corona. Deviations from photospheric abundances indicate that various fractionation processes are involved in the solar material that is fed into the corona and in the subsequent extraction of some portion of this material into the solar wind (Wimmer-Schweingruber 2002, and references therein). The solar wind composition provides in essence a “DNA sample” of its origin, which survives even situations where the solar wind kinetic properties have been dramatically altered, such in corotating or stream interaction regions.

Charge state distributions of minor species in the solar wind can be related (via models) to coronal electron temperature-, electron density-, and ion velocity-profiles obtained from optical observations along the solar wind flow tube and particularly from the region where the charge states effectively freeze-in (e.g., Aelrigg et al. 1997; Ko et al. 1998). Such observations are used, for example, to assess the role of suprathermal electrons and electron anisotropies in the freezing-in process (Ko et al. 1996). Solar wind compositional signatures can also be used to infer small-scale changes (on the order of the supergranulation) in the corona. Thus, composition measurements give detailed knowledge of the coronal structure in the formation region of the solar wind.

Compositional signatures, such as abundance variations related to the first ionization potential (FIP) or first ionization time (FIT) effects, seem to be temporally and spatially related to the charge-state composition of minor species and to dynamic properties of the ambient solar wind flow. The details of this link are still not understood. The processes affecting coronal/solar wind elemental abundances and charge state distributions operate at very different sites between the solar surface and 1 AU, yet they seem to be closely correlated. Observing optically the conditions off the solar limb and comparing them to in

situ measurements of particles and magnetic fields will provide useful clues on the nature of such correlations. It is especially advantageous to carry out these studies over a series of transitions from slow to fast or fast to slow solar wind during the early phase of the STEREO mission (which coincides with solar activity minimum).

The origin of the slow solar wind is still a controversial issue. The in-depth case study presented by Ko et al. (2006) illustrates both the importance and the complexity of relating in situ solar wind elemental and charge state measurements, models, and solar limb spectroscopic observations to resolve this issue. Limb measurements of solar features (such as streamers, active regions, and coronal holes) that are potential sources of the solar wind are taken about seven days before or after that feature passes central meridian. Since the solar wind travels in a radial direction outward from the Sun, in-situ composition measurements are restricted to solar wind originating from near the disk's center (from the perspective of the spacecraft). This leads to a significant temporal offset in the corresponding optical and in-situ measurements. There have been a limited number of quadrature measurements between Ulysses and near-Earth solar observatories (e.g. Poletto et al. 2001). Ulysses carries a sophisticated solar wind composition spectrometer that has provided major new solar wind discoveries (Gloeckler et al. 1992). However, Ulysses limb passages are restricted to two per year and correlations can be affected by uncertainties in estimating the solar originating longitudes, introduced by the long solar wind transit distances to the Ulysses orbit. Solar wind and optical correlations are further hampered by optical ambiguities, notably line-of-sight affects. The twin STEREO spacecraft will advance our understanding of the sources of the solar wind by removing some of these ambiguities. For the first time it is possible to relate variations in the solar wind properties, including composition, with the relevant temporal variations of features observed in the chromosphere and the corona.

The importance of such correlations is further illustrated, for example, by the observation of O⁺⁵ in situ (Wimmer-Schweingruber et al. 1998). A SOHO/UVCS observation of this ion in the corona implies that the O⁺⁵ outflow velocity enhancement relative to protons must decrease with increasing radius (Cranmer et al. 1999). With STEREO, velocity profiles and velocity distributions of species obtained in the inner corona by means of the Doppler dimming technique can be matched with the corresponding velocity distributions of such species in situ—thus allowing a better match of all types of solar wind and coronal conditions than previously achieved.

STEREO PLASTIC measures all major solar wind ion species under all conditions. It has an exceptional directional geometrical factor (active area) for ions of nuclear charge state $Z > 2$, and it determines the flow direction for selected $Z > 2$ ions. With STEREO, we will be able to draw substantial new conclusions for the slow and fast solar wind as well as for transient phenomena.

2.2 Interplanetary Manifestations of Coronal Mass Ejections (ICME)

One of the anticipated achievements of STEREO will be the ability to remotely observe the launch of a CME and the propagation of it and its shock from the Sun out to 1 AU with the remote imagers (SECCHI and SWAVES) from one STEREO observatory, and then subsequently measuring its interplanetary properties with the in situ instruments (IMPACT and PLASTIC) as the ICME passes the other STEREO observatory. In combination with modelling and theory (Aschwanden et al. 2007; Forbes et al. 2006), this unique configuration will allow us to causally relate the solar and interplanetary phenomena.

Although much is known about CMEs and ICMEs, many fundamental questions remain regarding their origin, evolution and propagation. The reader is referred to the AGU monograph (Geophysical Monograph 99: Coronal Mass Ejections, 1997) and the more recent

Space Science Reviews special issue (March 2006) for extensive reviews on our current state of knowledge on ICMEs. Some of the outstanding questions have been summarized by Wimmer-Schweingruber (2006). The reader is also referred to Luhmann et al. (2007). Here we highlight a few of the open questions that STEREO will strive to answer.

2.2.1 CME Structure on the Sun and Related In Situ Signatures

A “three-part structure” is often observed in white light coronagraph images of eruptive prominence-associated CMEs: a leading bright shell, followed by a dark region, and finally a dense bright core. These are believed to correspond to, respectively, the pre-eruption dome of the helmet streamer that overlies the prominence, the cavity surrounding the prominence in its quiet state, and the embedded quiescent prominence (e.g., Hundhausen 1988; Low 1994). The material blown into space would thus originate from the low corona or chromosphere. If ICMEs involve and retain closed magnetic topologies, this will be reflected in the magnetic field and electron structures observed in situ by IMPACT. Bulk properties, composition, and ionization state of the solar wind ions will be measured by PLASTIC.

ICMEs exhibit a tremendous variability in their internal structure and composition, as described by Galvin (1997) and illustrated in the study of 41 ICMEs by Neukomm (1998). Elevated charge states are often observed (e.g., Galvin et al. 1987, 1993; Galvin 1997; Lepri et al. 2001; Lepri and Zurbuchen 2004; Richardson and Cane 2004a), as well as unusual elemental composition (e.g., Richardson and Cane 2004a). As discussed by Wimmer-Schweingruber et al. (2006), the frozen-in ionic charge states of the solar wind plasma appear to provide a direct link to the CME initiation process on the Sun, while the elemental composition provides information on the solar atmosphere prior to the CME initiation. With the quadrature measurements of STEREO, remote imaging of the Sun (both prior to and during the CME initiation) can be linked with the in situ sampling of the associated ICME.

There have been some reported cases of ICME-related solar wind containing singly charged He, with observed $\text{He}^+/\text{He}^{+2}$ ranging from less than 1% to as much as 30% (see review by Bame 1983), and other low charge state observations for minor ions (e.g., Gloeckler et al. 1999). Are these low charge states and unusual composition a tag for chromospheric material? Or are they rather associated with a reconnection process at the Sun, as suggested by Riley et al. (2002)? The combined observations by the remote imagers and the in situ investigations may provide the opportunity to delineate the origin of these unusual compositional features.

2.2.2 ICME Boundaries

As described, for example, by Galvin (1997) and more extensively by Zurbuchen and Richardson (2006), there are several in situ signatures used to identify ICMEs in interplanetary space; however, not all signatures are normally seen for a given event, and some signatures are not even unique to ICMEs (see also Neugebauer and Goldstein 1997). In addition, the boundaries associated with ICMEs can be ambiguous, and different boundaries are often observed for different signatures (see case study by Galvin et al. 1987, and discussion by Wimmer-Schweingruber et al. 2006). Multiple magnetic field discontinuities (some supporting waves), magnetic holes, and other substructures may be involved (Crooker et al. 1990; Farrugia et al. 2001; Janoo et al. 1998; Vasquez et al. 2001). Multi-spacecraft observations of a given ICME provide spatial and temporal tracking of these boundaries, and help to distinguish cases of merged (coalescing) ICMEs. This type of study requires a full constellation of spacecraft, such as ACE, Wind, STEREO, SOHO and Ulysses.

2.2.3 The Evolution of ICMEs in the Inner Heliosphere

One of the scientific objectives of STEREO is to follow the evolution of ICMEs from the Sun to 1 AU. Of perhaps special interest in the early phase of the mission is the subset of ICMEs known as magnetic clouds (MCs). ICMEs occurring near solar minimum have been statistically associated with MCs (Richardson and Cane 2004b), and in all stages of the solar cycle they form a substantial fraction of observed ICMEs.

Magnetic clouds (MC) are defined as a mesoscale structure characterized by a strong magnetic field executing a large rotation in plasma of low proton beta (Burlaga et al. 1981). They have been modelled as cylindrically symmetric, force-free configurations; i.e., as solutions of $\nabla \times \mathbf{B} = \alpha(\mathbf{r}) \mathbf{B}$ (Goldstein 1983; Marubashi 1986). The case for $\alpha(\mathbf{r})$ equals a constant was proposed by Burlaga (1988), and the magnetic field components can be written in terms of Bessel functions of zeroth and first order (Lundquist 1950). Fitting of in situ data as a force-free magnetic flux tube has become a standard approach to provide a cylindrical geometry solution for the cloud. From this solution, one may infer the magnetic helicity (or handedness) of the field, the orientation of the axis, the maximum field on the axis, and the closest distance the spacecraft passes from the axis. More recent approaches include reconstruction of the magnetic field, flux tube orientation, etc., based on the Grad-Shafranov equation (Hu and Sonnerup 2002), and using kinematic expansions of the clouds (Riley and Crooker 2004). These recent modelling efforts suggest deviations from a circular cross-section.

When in situ data are available from a constellation of spacecraft at different locations, these modelled reconstructions can be used as a “probe” on the cloud’s internal structure, with a direct comparison to spatial and temporal variations in plasma properties observed within the cloud (Farrugia et al. 2005a; Leitner et al. 2007). This is an ideal situation for the STEREO, ACE, and Wind constellation. The wide spacecraft separation may allow an investigation of the spatial structure and coherence lengths of ICME parameters over longitudinal separations of ten’s of degrees. Earlier studies (Farrugia et al. 2005b, 2005c) have provided cross-correlating parameters of magnetic clouds using the largest separations (a few 100 Re) attained between the Wind and ACE spacecraft—both along, and orthogonal to, the bulk solar wind flow vector. These studies may now be extended to larger spatial scales.

2.3 Injection and Acceleration of Ions at CME-Driven Shocks

With the PLASTIC and IMPACT investigations, each STEREO covers an extensive particle energy range (\sim few eV to \sim 100 MeV). The combined composition measurements, in particular the ability of PLASTIC to measure charge states and distinguish pickup ions, are ideally suited to study the 3-dimensional evolution of suprathermal and energetic particles into the heliosphere, including the injection, acceleration, and elemental fractionation processes. The suprathermal range of PLASTIC (up to 80 keV/e) covers injection and the standard power law of stationary planar shock acceleration, while the energy range of IMPACT SEP (up to 100 MeV) covers the signatures of ion escape from the shock, which in turn provide information on shock structure near the Sun.

Generally two classes of solar energetic particle (SEP) events are distinguished (Reames 1999). Impulsive events are typically characterized by low intensity, narrow angular spread, short duration, and enrichment in ^3He , heavy ions, and electrons. These events are associated with solar flares and type III radio bursts. Gradual events are higher intensity, long-lived, proton rich, and show a broad angular spread. This class is associated with fast CMEs and type II radio bursts.

CME/ICMEs are the most likely origin of large “gradual” SEP events that occur ~ 10 times per year during solar maximum. The correlation between fast CMEs and these SEPs is over 95% (Kahler et al. 1984). Fast ICMEs drive shock waves into the solar wind, which strengthen as the Alfvén speed decreases with increasing heliocentric radial distance. The resulting shock wave can accelerate solar wind ions, pickup ions, or SEPs from previous gradual or impulsive events, up to energies occasionally in excess of 1 GeV/n. A fraction of the higher energy ions continually escape the shock and propagate to the orbit of Earth, where their composition and energy spectra provide information on the conditions at the ICME and shock when they are closer to the Sun (for a recent summary on the characteristics of SEPs related to CMEs and ICMEs see Klecker et al. 2006). SEPs and the associated shock waves have important effects on Earth’s space environment, and SEPs can pose radiation hazards for astronauts.

This two-class picture of impulsive and gradual events is oversimplified, as evident from recent results from instruments with improved collecting power and resolution onboard the Wind, SAMPEX, SOHO and ACE spacecraft (for a recent summary see von Rosenvinge and Cane 2006, and references therein). The new composition and ionic charge measurements indicate that some solar particles have their origin in a dense plasma low in the corona, even in events otherwise classified as “gradual” (Möbius et al. 1999; Popecki 2006, and references therein); that enrichments in ^3He are also common in interplanetary shock accelerated populations (Desai et al. 2001); and that enrichments in heavy ions are often observed in large events at high energies (Cane et al. 2003). It is heavily debated whether these new findings are best explained by a suprathermal seed population leftover from previous “impulsive” events (Mason et al. 1999); by the interplay of shock geometry and different seed populations such as solar wind and flare suprathermals (Tylka et al. 2005); or by direct injection from the flare acceleration process (e.g. Klein and Trottet 2001, and references therein; Cane et al. 2003) with or without further acceleration by a coronal shock.

Simulations indicate that locally accelerated solar wind protons and alphas are a likely source population for suprathermal ion distribution functions associated with interplanetary shock events observed by Ulysses (Baring et al. 1997). Indeed, both solar wind and pickup ions accelerated by various types of shocks (interplanetary and bow shocks) appear to contribute to the suprathermal populations as observed in the outer heliosphere by Ulysses (Gloeckler et al. 2005a). A crucial test for the various SEP acceleration models will consist of a detailed comparison of the suprathermal seed population with the characteristics of the more energetic particles. With its high time resolution and ability to observe ions both before and after injection, PLASTIC will be able to determine ion injection rates when the shock passes the two spacecraft, as functions of the magnetic field orientation and shock strength at each spacecraft. The temporal resolution of the ions and magnetic field fluctuations in the turbulent sheath will provide a good test of wave-particle interactions taking place in this region.

Recent observations from ACE have provided evidence of simultaneous changes in the Fe charge states in the solar wind and SEP populations during an ICME event (Popecki et al. 2000; Farrugia et al. 2002). Because the ICME structure in this event was connected to an active region on the Sun with ongoing activity, it has been difficult to determine (from the one observational point afforded by ACE) as to whether the high charge component of the energetic ions is accelerated out of the solar wind, or stems from an impulsive event. PLASTIC will extend such measurements down to the suprathermal region (just above solar wind energies). The two STEREO spacecraft will make it possible to distinguish between these two possible sources.

2.4 Heliospheric Studies

Among the primary science objectives for STEREO is an enhanced understanding of the origins, properties, and evolution of heliospheric structures and phenomena. Phenomena of interest are not just magnetic clouds and other ICME-related structures, but also include stream interfaces, sector boundaries, co-rotating interaction regions (CIR events), and pickup ions.

2.4.1 Stream Interaction Regions and Heliospheric Current Sheet

During the last solar minimum in 1996, the Whole Sun Month campaign (Galvin and Kohl 1999) provided an unprecedented opportunity for observers and modelers to connect the global corona to structures seen in the solar wind (Gibson 2001). STEREO has been launched near the minimum activity phase of the current solar cycle and will contribute to a new, enhanced global perspective of the solar minimum heliosphere.

The large-scale corona at this time is mostly defined by long-lived coronal holes (including the polar holes) and the equatorial streamer belt. These coronal structures are reflected within the global heliosphere as a relatively stable pattern of high-speed streams and interstream (“slow”) solar wind that interact dynamically as the Sun rotates. The evolution of these large-scale structures, known as stream interaction regions or CIRs, is of primary interest to both heliospheric studies and space weather prediction. A recent review by Riley (2007) gives an overview of the current state of observations and models of the evolution of CIRs from the Sun to 1 AU. The two sets of STEREO in situ measurements, combined with those at the Earth solar longitude, allow for *the first time* a determination of the *temporal evolution* of these corotating structures and an investigation of their structure in the longitudinal direction (i.e., along the Earth’s orbital direction). Any changes can then be directly compared with the solar observations of temporal changes in the corresponding solar wind source longitude.

Stream interfaces mark the boundary of high-speed streams and the slow, interstream, solar wind. Stream interfaces are often embedded in the leading edge of CIRs. Identification of the stream interface is important for many heliospheric studies, including the study of recurrent particle events and current sheet dynamics. While stream interfaces are often identified by a change in entropy, this signal can, in some cases, be misleading. The safest identification includes the compositional signatures of the solar wind (Wimmer-Schweingruber et al. 1997, 1999).

2.4.2 Particle Acceleration at Corotating Interaction Regions

The launch of STEREO during the approach to solar minimum provides an opportunity to study the recurrent ion events associated with corotating interaction regions (CIRs). These CIR-related events are known to be an important source of the low-energy interplanetary particle populations during periods of low solar activity (Reames 1999, and references therein). CIRs continue to develop beyond the orbit of the Earth; and, indeed, it is typically beyond 1 AU that a forward and reverse shock pair forms. Observations with many spacecraft have shown that the strongest particle acceleration occurs at the reverse shock (e.g. review by Mason et al. 1999); that there is strong cross-field transport in intense events (Dwyer et al. 1997); and that the contribution of singly charged ions (C, O, Ne, Mg, or Fe) to the source population of CIRs is at most a few per cent (Mazur et al. 2002; Möbius et al. 2002).

These observations suggest the solar wind as a possible source; however, compositional peculiarities observed for He, C, and Ne in CIRs are not entirely consistent with this scenario, or at least suggest that more than one seed population is involved. Pickup He^+ has been observed as accelerated suprathermals at a CIR reverse shock at >2 AU (Gloeckler et al. 2005b), and in CIR compression regions at 1 AU (Chotoo et al. 2000). The C/O-ratio has been found to be different from both solar wind and solar energetic particle abundances, and to vary systematically with solar wind speed (Mason et al. 1997). A small, but noticeable Ne^+ contribution has been measured, indicating that efficient pickup ion acceleration of heavies can occur, even if it is not a dominant source population at 1 AU (Möbius et al. 2002). STEREO, by providing complete compositional and spectral information extending from solar wind and suprathermal energies (PLASTIC) to energies of several MeV/amu (IMPACT), is ideally suited for the in-situ study of these events and their source populations. Furthermore, by making use of multi-spacecraft measurements, a detailed analysis of spatial and temporal variations and anisotropies will be possible.

2.4.3 Pickup Ions

As seen in the “first light” section at the end of this paper, the compositional, angular, energy and flux coverage of PLASTIC is well-suited for the study of pickup ions, whether of interstellar or local origin. Pickup ions are of interest in their own right, and as a potential seed population.

Pickup ions originate from neutral atoms that become freshly ionized due to various mechanisms, and are “picked up” by the interplanetary magnetic field (e.g., Thomas 1978; Möbius et al. 1985; Gloeckler and Geiss 1998). Because the pickup process generates speeds up to twice the solar wind speed (in the spacecraft frame), these ions can be easily injected into acceleration mechanisms. As indicated earlier, pickup ions have been observed as a source population for particle acceleration at shocks and perhaps compression regions (Gloeckler et al. 2005b; Chotoo et al. 2000; Kucharek et al. 2003).

Studies of pickup ions have shown that their fluxes are controlled not just by ionization rates, but also by transport effects that vary with the interplanetary magnetic field and solar wind conditions (e.g., Möbius et al. 1998; Saul et al. 2007). Another observable effect on the flux of the interstellar pickup ions is the gravitational focusing cone that is formed on the downwind side of the Sun, seen from the Earth’s perspective each December. Untangling spatial from temporal variations requires a three-dimensional constellation of heliospheric spacecraft. STEREO provides two additional simultaneous in-ecliptic measurements separated in solar longitude. These will be combined with near-Earth in-ecliptic observations (for example, by ACE and the future IBEX) and out-of-ecliptic measurements (Ulysses).

2.5 Space Weather

Part of the STEREO mission includes the real-time, continuous transmission of a limited number of space weather related products, called Beacon Mode (see Biesecker et al. 2007).

STEREO provides a test of the ability of in situ experiments at solar longitudes different than that of the Earth to issue real-time space weather warnings. In situ data from satellites along the Sun-Earth line at L1 are in a better position to issue warnings that an interplanetary CME is in a direct path to impact the Earth. However, the off-angle, 1 AU orbits of the STEREO observatories provide a complementary aspect to space weather forecasting, particularly for recurrent high-speed streams, and the associated CIRs, prevalent during solar minimum conditions. They also provide a warning for transient flows that last for several days, but not for multiple solar rotations (Burlaga 1995).

CIR-related storms have been associated with elevated spacecraft potentials, with subsequent effects on instrument performance (Denton et al. 2006). Using the lagging STEREO B spacecraft in situ measurements, STEREO is able to provide considerable advance notice and much more accurate estimates of the time and possible geo-effectiveness of these structures than can currently be issued by using only L1 satellites. (For example, an Earth–Sun–STEREO B angle of 20° corresponds to 36 hours of solar rotation and additional advance notice.) With the STEREO spacecraft slowly drifting apart from Earth, STEREO will allow us to estimate the optimal spacecraft longitude for this type of forecast in planning future operational missions. In addition, CMEs launched while corotating streams are present have a tendency to be caught in the structure, thus affecting the CME propagation through space. In this context, knowledge of high-speed stream structures obtained by *both* STEREO spacecraft provides important information for space weather forecasting.

3 Instrument Description

3.1 Overview

The PLASTIC sensor (Fig. 1) is comprised of three structural elements: Entrance System (Energy/charge Analyzer), Time-of-Flight/Energy (TOF/E) Chamber and its Housing, and the Electronics Box (EBox). The Entrance System selects incident particles for subsequent analysis by their incoming direction and by their energy-per-charge (E/Q) value. The Time-of-Flight/Energy Chamber contains the ion optics, detectors, detector electronics, and the signal processing board. The Electronics Box contains all of the digital electronics, the remaining analog electronics, the low and high voltage power supplies, and the connections to spacecraft power and to the IMPACT/PLASTIC Instrument Data Processing Unit (IDPU).

To accommodate measurements of both plasma and suprathermal populations within a single instrument package on a 3-axis stabilized platform, the PLASTIC sensor incorporates three distinct fields of view (FOV) and geometrical factors (GF). Each FOV/GF is combined with an instrument ion optics section optimized for a particular type of ion population. A summary of the PLASTIC instrument sections is given below, and their basic measurements are provided in Table 1.

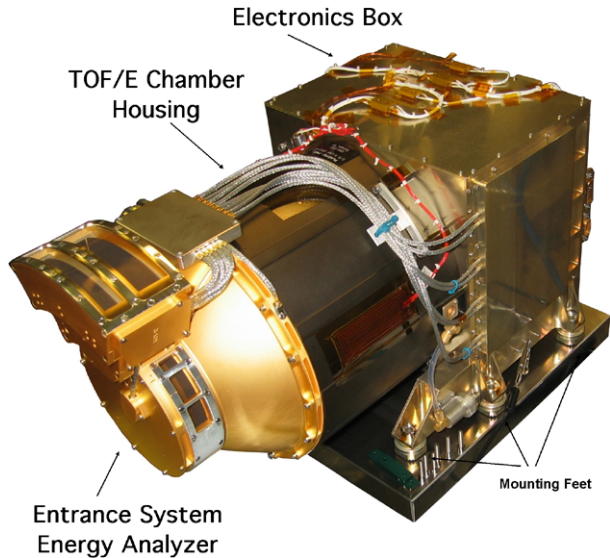
The PLASTIC *Solar Wind Sector* (SWS) provides a 45° field of view in the azimuth (nominally ecliptic) plane, centered on the Sun–spacecraft line, and ±20° in elevation (nominally polar) direction through the use of electrostatic deflectors. The SWS has two channels with different geometrical factors suited to the high flux solar wind protons and the low intensity solar wind minor ions, respectively.

- The *Solar Wind Sector* (SWS) *Small Channel* measures the distribution functions of solar wind protons (H^+) and alphas (He^{+2}), providing proton density (n), velocity (V_{sw}), thermal speed (v_{th}), and alpha to proton (He^{+2}/H^+) ratios.
- The *Solar Wind Sector* (SWS) *Main Channel* measures the elemental composition, ionic charge state distribution, and bulk and thermal speeds of the more abundant solar wind minor ions (e.g., C, O, Mg, Si, and Fe).

The *Suprathermal Ions Wide-Angle Partition Sector* (WAP) covers 210° (B) and 225° (A) fields of view in the remaining unobstructed off-Sun azimuth directions, and <10° in the polar (centered on the ecliptic plane) direction. The WAP has a larger geometrical factor but less directional information than either of the two SWS channels.

The SWS and WAP share a common 360° toroidal top-hat electrostatic analyzer with its azimuth entrance in the ecliptic plane. At the detector level, this full circular geometry is

Fig. 1 Photograph of PLASTIC Flight Model, showing the three structural elements comprising the instrument: the Entrance System (domelike, gold color, with the Solar Wind Sector deflectors facing upwards), the Time-of-Flight/Energy Chamber and its Housing (cylindrical center section), and the Electronics Box. Cables running from beneath the SWS of the Entrance System down to the side of the EBox are the connections to the various high voltage power supplies for the Entrance System. Red and white cabling on the top of the EBox are attached to survival heaters



subdivided into four 90° quadrants (designated Q0, Q1, Q2, and Q3, see insert of Fig. 2). Each quadrant has its own 90° annular Micro-channel Plate (MCP). Different geometrical factors, viewing angles, measurement techniques, event logic conditions, and data products are used depending upon which sector and quadrant the incident particle traverses.

3.2 Principles of Operation

The PLASTIC sensor combines a top-hat 360° electrostatic (energy-per-charge) analyzer (ESA) with instantaneous full aperture (in-ecliptic) coverage, followed by post-acceleration (PAC), a time-of-flight (TOF) system, and an energy (E) measurement by solid state detectors (SSD) in selected portions (Fig. 2). The detector area is divided into four 90-degree quadrants (Q0–Q3). The Entrance System is divided into a 45° sunward-centered solar wind sector (SWS) with polar deflectors and the remaining wide-angle partition (WAP) sector without polar deflectors. There are three geometrical factors employed in the Entrance System. The electrostatic deflectors enable solar wind angular coverage outside of the ESA aperture plane, up to 20° elevation above and below the ecliptic plane for the three-axis-stabilized STEREO spacecraft. Discrete anodes (coarse angular resolution, 22.5° , used in quadrants Q1, Q2, Q3) or a resistive anode (fine angular resolution, $2-5^\circ$, used in quadrant Q0) provide measurement of the azimuthal entry angle.

Combining the energy-per-charge (E/Q), post-acceleration voltage (PAC), and time-of-flight (τ) measurements allows the determination of the mass-per-charge (M/Q) of the incoming ion according to:

$$M/Q = 2 \cdot (E/Q + |PAC|) \cdot \alpha \cdot (\tau/d)^2,$$

where d is the length of the time-of-flight path in the TOF/E Section and $\alpha(E, M)$ denotes the energy and species-dependent energy loss in the carbon foil. The mass (M) of the ion is determined from the residual energy E_{ssd} and the time-of-flight (τ) measurement:

$$M = 2 \cdot E_{\text{ssd}} / \beta \cdot (\tau/d)^2,$$

Table 1 Summary of PLASTIC section characteristics and basic measurements

Instrument section	Primary measurement	Energy range (E/Q)	FOV	Eff*Area (SW) or Eff*G (ST)	Time
SWS	Solar wind proton	0.3–10.6* keV/e	Centered on Sun–Earth line	$4 \times 10^{-4} \text{ cm}^2$	1 min
Small Channel	bulk parameters	(* upper limit) 6.3% FWHM	$45^\circ \times 20^\circ$	(single coincidence)	
	• n				
	• V_p	5% Step spacing	(Dynamic)		
	• v_{th}		$45^\circ \times 0.4^\circ$	$2 \times 10^{-4} \text{ cm}^2$	1 min
	Moments		(Instantaneous)	(double coincidence)	
SWS	Solar wind minor ions	0.3*–80 keV/e (* lower limit)	Centered on Sun–Earth line	0.4 cm^2	1 min
Main Channel	• Species	6.3% FWHM	$45^\circ \times 20^\circ$	(single coincidence)	
	($M, M/Q$)	5% Step spacing	(Dynamic)		
	He to Fe		$45^\circ \times 2^\circ$	0.1 cm^2	1–5 min
	• Abundances		(Instantaneous)	(double coincidence)	
	• Speeds				
	• Direction				
ST WAP (w/SSD)	Suprathermals	0.3–80 keV/e	$50^\circ \times 6^\circ$	$1 \times 10^{-3} \text{ cm}^2\text{-eV/eV-sr}$	1 min
	• Species	7.0% FWHM		(single coincidence)	
	($M, M/Q$)	5% Step spacing			
	H to Fe				
	• Flux			$5 \times 10^{-4} \text{ cm}^2\text{-eV/eV-sr}$	5–10 min
	• Direction			(double coincidence)	
ST WAP (noSSD)	Suprathermals	0.3–80 keV/e	$160^\circ \text{ (B)}/175^\circ \text{ (A)} \times 6^\circ$	$3 \times 10^{-3} \text{ cm}^2\text{-eV/eV-sr}$	1 min
	• Species	7.0% FWHM		(single coincidence)	
	(M/Q)	5% Step spacing			
	H to Fe				
	• Flux			$2 \times 10^{-3} \text{ cm}^2\text{-eV/eV-sr}$	5–10 min
	• Direction			(double coincidence)	

The instrument cycles through 128 E/Q voltage steps in a one-minute cadence

Values provided for detection efficiency times the energy-geometric factor or detection efficiency times the active area are representative values based a 2 keV/e He⁺ beam calibration with PAC set at 18–20 kV and MCP bias set to 3000 V

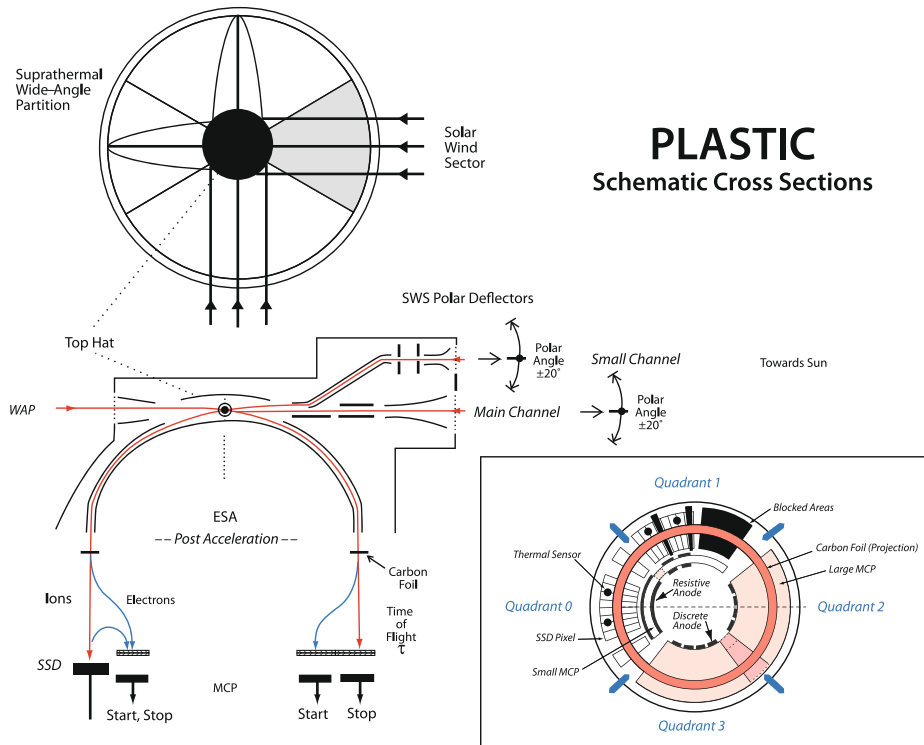


Fig. 2 PLASTIC Principle of Operation. (Top) View of sample ion trajectories through the ESA, looking down onto the entrance plane of the top-hat electrostatic analyzer (ESA). (Bottom) Cross-sectional schematic of the basic layout for the TOF (M/Q) and TOF/E (M/Q and M) measurement (described in the text). (Insert) Schematic view, looking down into the TOF Chamber from the exit of the ESA, defining the four quadrants Q0, Q1, Q2, Q3 at the detector levels

where $\beta(E, M)$ is a function of the pulse height deficit in the SSD over the incident particle energy. This deficit is velocity and species dependent. Pre-flight calibrations and simulations determine the α and β functions. This TOF plus E mass spectrometer technique has been successfully used by solar wind composition instruments flown on Ulysses (Gloeckler et al. 1992), on SOHO (Hovestadt et al. 1995), and on ACE (Gloeckler et al. 1998).

The following sections describe the details of the PLASTIC measurement components shown in the operational schematic (Fig. 2), as encountered by an incident particle.

3.3 Entrance System / Energy Analyzer (E/Q , Elevation Angle, and GF)

3.3.1 Entrance System / Energy Analyzer Overview

The PLASTIC instrument measures solar wind and suprathermal ion distributions spanning a wide range of ion fluxes. By employing ion collection apertures with three different geometric factors (GF), the main solar wind distribution (protons and alphas), the less abundant solar wind heavy ion distributions, and selected types of suprathermal ion distributions can be measured within one instrument. An electrostatic deflection system called the Entrance System / Energy Analyzer (Allegrini 2002; Blush et al. 2005;

Karrer 2007) selects solar wind ions for out-of-ecliptic angles of incidence and filters the solar wind and suprathermal ions by energy-per-charge (E/Q) before the ions pass into the Time-Of-Flight/Energy (TOF/E) section of the instrument.

The Entrance System steers and filters ions utilizing the electrode configurations shown in Fig. 3. The sun-centered solar wind sector (SWS) spans a 45° in-ecliptic FOV. The instantaneous polar angle acceptances are 0.4° and 2° FWHM for SWS Small and Main Channels, respectively, and up to $\pm 20^\circ$ out-of-ecliptic dynamic FOV is attained with the use of deflectors. The Small Channel (proton-alpha) and the Main Channel (heavy ion), positioned one above the other in the SWS (Fig. 1), collect the main distribution of solar wind ions.

The Wide-Angle Partition (WAP) spans the remainder of the 360° in-ecliptic FOV (with the exclusion of spacecraft and instrument blockages). The WAP entrance aperture accepts ions in the polar direction with a FWHM of 3° for a given E/Q , or about 6° FOV over the entire E/Q bandwidth.

Ions collected through all entrance apertures are filtered by E/Q with an electrode pair of toroidal domes that are used as an electrostatic analyzer (Ewald and Liebl 1955; Wollnik et al. 1972; Young et al. 1988). The ESA is cylindrically symmetric about the instrument azimuth, permitting the simultaneous collection of solar wind ions in the SWS and suprathermal ions in the WAP. The E/Q bandwidth is $\sim 6\%$ in the full E/Q dynamic range, for all entrance apertures (Tables 2, 3 and 4).

The outer and inner domes of the ESA are connected, respectively, to the positive and negative high voltage power supplies SWEEP ESA_plus and SWEEP ESA_minus (Sect. 3.7.2). The voltages of both domes are matched and set simultaneously to one of 128 output settings (SWPE = 0–127). These voltage settings are logarithmically spaced from ± 6000 V down to ± 10 V, in order to cover the full E/Q range from ~ 80 to 0.3 keV/e.

The nominal energy-per-charge response of the ESA is given by

$$ESA_E/Q \text{ [keV/e]} = 0.2 \times 1.04895^{(127-SWPE)}.$$

There is a non-linear response in the power supplies at the lowest voltages, bringing the lowest ESA_E/Q closer to 0.3 keV/e rather than the nominal value of 0.2 keV/e. The voltage settings are loaded into a table for implementation. These table entries can be changed by ground command.

During a 60-second collection cycle, comprised of 128 ESA steps, the ESA voltages are stepped and held every 435.6 ms, which entails a 26 ms interval for HV settling followed by 409.6 ms of data accumulation. At each step of the ESA voltages, the polar angle deflectors in the SWS are ramped through a pre-defined set of voltages provided by the deflector high voltage power supplies (SWEEP DEFL1, SWEEP DEFL2), providing 32 deflection bins per ESA step, with an accumulation time of 12.8 ms per deflection bin. The voltages of the deflectors are matched to each set of ESA voltages in order to collect incident ions up to $\pm 20^\circ$ in elevation, with each DEFL bin nominally corresponding to about 1.25° in polar angle. After the ESA cycle has been completed (~ 56 sec), the remaining time in the 60-second cadence is used for sampling housekeeping, data transfer, resetting registers, implementing commands, and setting up the SWEEP high voltages for the start of the next collection cycle.

The Solar Wind Sector Main and Small Channels are activated sequentially, with the switching between channels commanded by the IDPU based upon a monitored rate count. The less-abundant solar wind ion species (typically $< 1\%$ of the solar wind) are collected in the initial part of the ESA stepping cycle though the Main Channel, which has a large energy-geometric factor ($G_{(45^\circ)} \sim 2.5\text{--}3.2 \times 10^{-3}$ cm 2 sr eV/eV per 45° , active area

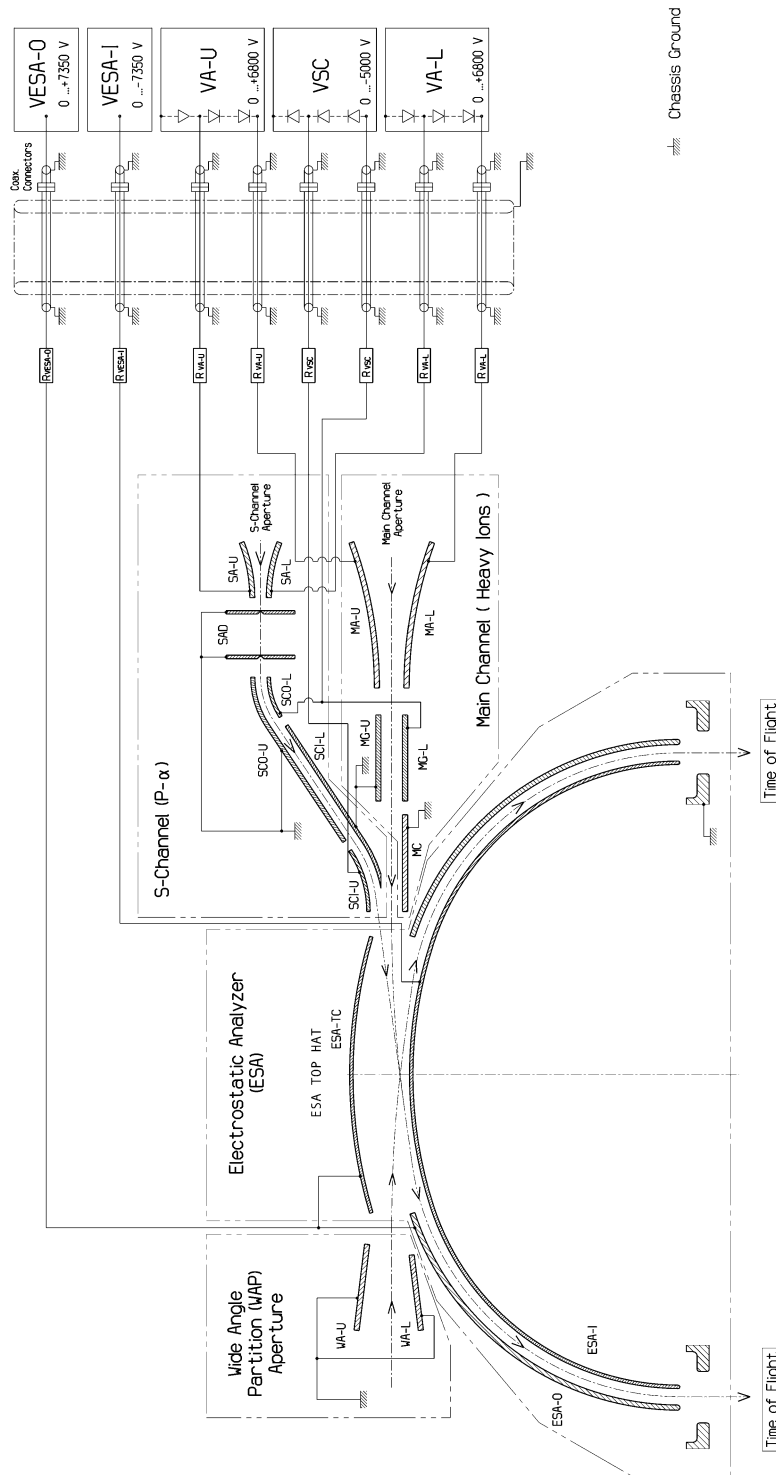


Fig. 3 The electrical specifications schematic shows the internal electrode system of the Entrance System. The Small and Main Channel entrance apertures select ions for out-of-ecliptic angle (SA-U, SA-L, MA-U, MA-L). An electrostatic gate disables the Main Channel by deflecting ions in the Main Channel with the MG-L electrode. Simultaneously the Small Channel is enabled with the SCO-L and SCI-L steering electrodes. Ions passing through an entrance aperture enter the E/Q analyzer domes (ESA-I and ESA-O) before being passed to the TOF/E section. Grounded elements include the WAP (WA-U, WA-L), the 25-35 micron with Small Channel slits (SAD, and other Channel components (MC, MG-U, SCO-U, SCI-L))

$A_{act} \sim 0.8 \text{ cm}^2$). As the ESA voltage decreases, the incident ion flux increases as the solar wind alpha particle (typically $\sim 4\%$ in number density) and then proton (typically $\sim 96\%$ in number density) portions of the distribution are sampled. At a predetermined (commandable) count rate set point, the SWEEP SCHN high voltage is enabled and applied to the steering electrodes (SCO-L, SCI-U), allowing ions to pass through this channel into the ESA. These SCHN voltages must be appropriately tuned to the ESA settings. Simultaneously, an electrostatic deflection gate (Main Gate, MG) located past the Main Channel entrance aperture disables ion collection through the Main Channel. This effectively switches the geometrical factor to the smaller active area Small Channel ($G_{(45^\circ)} \sim 6 \times 10^{-7} \text{ cm}^2 \text{ sr eV/eV}$, $A_{act} \sim 1.5 \times 10^{-3} \text{ cm}^2$). This GF switching is necessary to prevent saturation of the detector electronics and to limit the lifetime fluence on the SSD and MCP detectors.

In addition to the instrument ion measurement properties, the Entrance System suppresses solar UV radiation. All electrode surfaces are blackened with copper-sulfide and many surfaces are serrated. The instrument is designed to minimize direct exposure of internal components to solar photospheric UV radiation; pre-launch measurements give a UV suppression factor exceeding 1×10^8 . The serrated surfaces in the Entrance System also inhibit scattered particles from reaching the TOF/E Chamber.

3.3.2 Characterization of the Entrance System / Energy Analyzer

As a major subsystem of the PLASTIC instrument, the Entrance System has undergone extensive design, prototype testing, and flight model calibrations prior to integration. Considering the complex ion optical system of the PLASTIC instrument, calibration and simulation of the sub-system responses are important for understanding the overall instrument behavior. The calibration results herein summarized are details of the final Flight Model (FM-A, FM-B) calibrations, which are fully presented in Karrer (2007). Karrer (2007) also presents details of the Flight Spare Entrance System (not flown).

The Entrance System ion optical calibration measurements were performed in the CASYMS ion beam facility at the University of Bern (Ghielmetti et al. 1983; Steinacher et al. 1995). CASYMS provides a broad parallel beam of an area of $\sim 250 \text{ cm}^2$ of uniform flux. CASYMS delivers ions of many different species and charge states in an energy range from 5 eV/e to 60 keV/e, with an energy spread of $\sim 0.1\%$ ($< 1\%$ for very low E/Q) and a beam divergence of $\sim 0.3^\circ$. Ar^+ and He^+ beams in an energy range from 0.1 keV/e to 60 keV/e were used for the Entrance System calibration. The systems were mounted on a turning table with elevation and azimuth angle articulation. (Note that the CASYMS elevation angle corresponds to the solar wind out-of-ecliptic angle.) Ions passing through the ESEA were counted by micro-channel plates in chevron configuration with a position-sensing anode (Lampton and Carlson 1979). Variation in detection efficiency due to particle energy was accounted for in the results (see Allegri 2002; Karrer 2007).

The energy acceptance and the analyzer constants were determined using different beam energies and ion species. The analyzer constants give the relation between the applied electrode voltage and the collected ion energy per charge, E/Q :

$$k_{\text{electrode}} = E/Q / V_{\text{electrode}}.$$

The measured values given in Table 2 are quoted in terms of eV/e per volt, reflecting the energy-per-charge units (eV/e) normally used in describing an ESA response. The analyzer constant given for the Small Channel differs slightly from the rest, because ions passing

Table 2 Overview of entrance system analyzer constants

Entrance system channel	Electrode identifier	ES/ESA-FM A		ES/ESA-FM B	
		Analyzer constant (eV/e V ⁻¹)	FWHM	Analyzer constant (eV/e V ⁻¹)	FWHM
Small	SCO-L	3.23(1)	10.40%	3.25(1)	10.64%
	SCI-U	3.68(1)	13.20%	3.64(1)	10.75%
	ESA	8.46(1)	6.35%	8.46(2)	6.26%
Main	ESA	8.26(1)	6.12%	8.26(2)	6.48%
WAP	ESA	8.25(4)	6.77%	8.26(1)	7.30%

Table 3 Overview of deflection constants and angular acceptance

Entrance system channel	ES/ESA-FM A		ES/ESA-FM B	
	Deflection constant (deg-keV/e V ⁻¹)	Angular FWHM (deg)	Deflection constant (deg-keV/e V ⁻¹)	Angular FWHM (deg)
Small	0.117(1)	0.37	0.114(1)	0.27
Main	0.128(3)	1.9	0.127(3)	1.8
WAP	–	3.2	–	3.1

through the Small Channel enter the ESA at a slight angle ($\sim 0.2^\circ$) from above the instrument plane (Fig. 3), thereby lowering the voltage required to collect an ion of a given energy. The energy acceptance is given by the FWHM of the energy distribution as measured by varying the ESA voltage for a given beam energy.

The angular acceptance and deflection constants for the deflection plates were determined using different energies and elevation angles (see Table 3). The deflection constants give the relation between applied electrode voltage and the ion incident angle:

$$k_{\text{deflection}} = \Theta \cdot E/Q / V_{\text{electrode}}$$

where Θ is the polar (elevation) angle, E/Q is the beam energy per charge, and $V_{\text{electrode}}$ is the voltage of the deflection electrode. The angular acceptance is given by the FWHM of the angular distribution measured by varying the elevation angle for a given beam energy.

To determine the geometric factor, the instrument electrodes were tuned for a specific beam energy after which the active areas, A_{act} , were measured for different beam energies and elevation angles:

$$A_{act} = n_{\text{detector}} (\Phi t \eta_{\text{detector}})^{-1}$$

where n_{detector} is the counts on the detector during the accumulation time t , Φ is the beam flux per unit area, and η_{detector} is the detection efficiency of the particle detector. The results are plotted in Fig. 4 in terms of the angular and energy acceptance for the three different entrance apertures of FM A and FM B. The respective geometric factors G (similar to the energy-geometric factor G_E as defined by Young et al. 1989), were calculated from the

Table 4 Active areas and geometrical factors for the FM-A and FM-B Entrance System Apertures

Entrance system channel	Azimuth position (deg)	FM A		FM B	
		Active area (cm ²)	Geometrical factor G (cm ² eV/eV sr per 45° sector)	Active area (cm ²)	Geometrical factor G (cm ² eV/eV sr per 45° sector)
Small	0	1.41(4) × 10 ⁻³	6.0(5) × 10 ⁻⁷	1.50(4) × 10 ⁻³	6.3(4) × 10 ⁻⁷
Main	0	8.9(7) × 10 ⁻¹	3.15(4) × 10 ⁻³	7.5(5) × 10 ⁻¹	2.52(4) × 10 ⁻³
WAP	-90	8.2(3) × 10 ⁻¹	8.35(6) × 10 ⁻³	-	-
	-180	1.12(8)	6.82(7) × 10 ⁻³	9.4(4) × 10 ⁻¹	6.44(6) × 10 ⁻³
	-38.5	4.7(2) × 10 ⁻¹	3.19(3) × 10 ⁻³	-	-

discrete measurements using the approximation:

$$G_{(45^\circ)} \approx \alpha_{SWS} \cdot \sum_i \sum_j \Delta\theta_i (\Delta E_j / E_j) (A_{act})_{ij}$$

where α_{SWS} is an integrated (over 45°) azimuth angle parameter, $\Delta\theta_i$ is the elevation angle step size for step i , E_j and ΔE_j energy and energy step size for step j , and $(A_{act})_{ij}$ is the active area of step i, j .

The discrete-sums approximation for calculating the geometric factor as applied to the PLASTIC entrance system is discussed by Allegrini (2002) and by Karrer (2007). The α_{SWS} parameter incorporates a full integration in azimuth over 45°, under the assumption of uniform response and cylindrical symmetry. The measured active areas and geometric factors for each entrance system and its apertures are provided in Table 4. The active area, sometimes called the directional geometric factor, is defined for a parallel beam, and is useful for solar wind applications. Note that the geometrical factors in Table 4 appear different from those provided in Table 1. The entries specified in Table 1 were obtained from the integrated instruments, and include the effects of transmission in the TOF/E Chamber, the efficiency of the detectors (Sect. 3.4.3), and the full FOV of the respective channel.

For the Small Channel of both flight models, a complete elevation versus azimuth angle scan of the system response was performed (Fig. 5a,b). An azimuth angle scan for one elevation angle was made for the Main Channel and WAP (Fig. 5c,d). For these measurements all electrodes were tuned for an incident beam energy $E/Q = 3$ keV/e.

Entrance System calibration and testing (including a full set of environmental tests) has ensured optimal ion optical functionality after integration with the full PLASTIC. Detailed knowledge of the response functions, especially the analyzer and deflection constant relations between applied voltage and measured ion properties, are critical for setting in-flight operational tables for the ESA, Channels, and Deflectors (“SWEEP”) high voltage system, and ultimately for the interpretation of the resulting solar wind data.

3.4 Time-of-Flight Measurement System

3.4.1 TOF/E Chamber Overview

An ion exiting the ESA is accelerated through a -15 kV to -25 kV voltage drop (PAC voltage, commandable) just before entering the TOF/E chamber (refer to Fig. 2). The ion

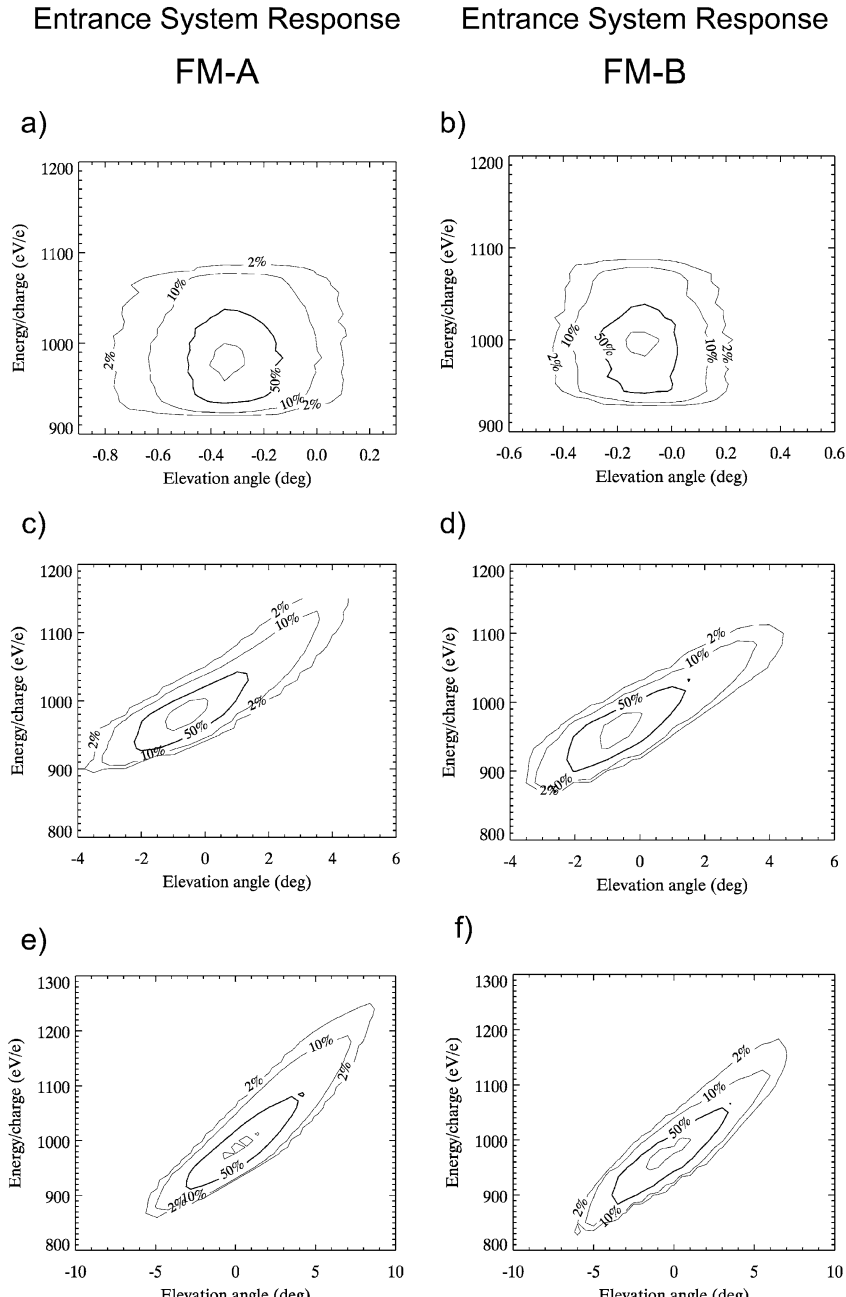


Fig. 4 Contours of relative geometrical factors. (a, b) Small Channel on the FM-A and FM-B Entrance Systems as a function of beam energy and elevation angle (all normalized to 1 keV/e). For FM-A, the ion beam used was 5 keV/e He⁺. For FM-B, 5 keV/e Ar⁺ was used. (c, d) Main Channel on the FM-A and FM-B Entrance Systems as a function of beam energy and elevation angle (all normalized to 1 keV/e). For FM-A, the beam was 5 keV/e Ar⁺. For FM-B, 3 keV/e Ar⁺ was used. (e, f) WAP Channel on the FM-A and FM-B Entrance Systems as a function of beam energy and elevation angle (all normalized to 1 keV/e). For FM-A, the beam used was 5 keV/e Ar⁺. For FM-B, 3 keV/e Ar⁺ was used

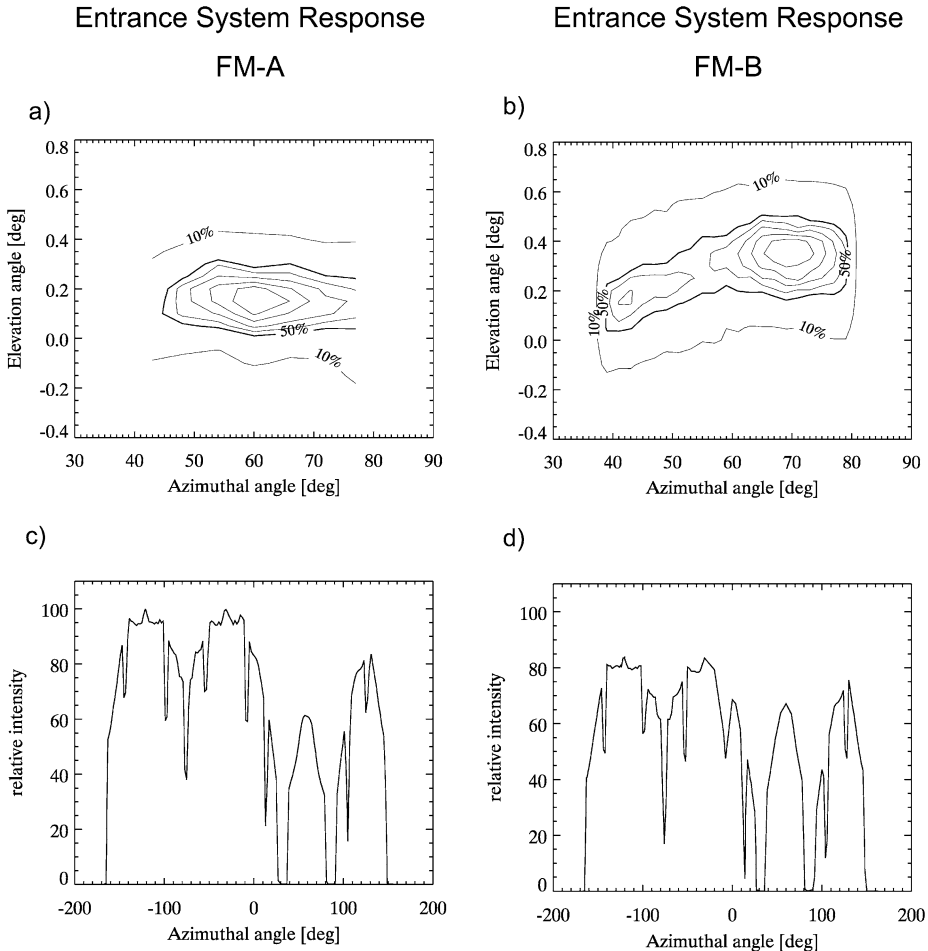


Fig. 5 Azimuth angle scans. Center of SWS in the calibration coordinate system is at 60° . (a, b) Azimuth response as a function of elevation angle for the Small Channel, for Entrance Systems FM-A and FM-B, respectively. (c, d) Azimuth response for the Main Channel and the WAP at a single elevation angle: -0.5 deg for FM-A and 0 deg for FM-B. Intensity differences are due to different beam settings used between FM-A and FM-B

then traverses a thin ($\approx 3.5 \mu\text{g}/\text{cm}^2$) carbon foil located at the entrance to the chamber. The carbon foil is deposited on a supporting nickel grid that, together with an associated overlying field control grid (for suppression of backscattered electrons), is 83% transparent to the incident particles. Grid transmission was measured optically as well as with an ion beam (Lüthi 2003).

The carbon foil emits secondary electrons (Meckbach et al. 1975) that are subsequently accelerated and steered by guiding electrodes onto a micro-channel plate (MCP) chevron pair to trigger the “START” timing signal. The cascade (output) electrons at the exit of the MCPs are accelerated from the negative PAC voltage of the TOF/E Chamber to the signal board at ground potential. A fast “START” signal is read from an 80% transmission grid, and the “START” position is read from anodes located below the grid.

After the ion traverses the carbon foil, it continues its passage through the TOF/E chamber and reaches the detector level, where it impacts either a solid state detector (SSD) or the “STOP” portion of a large MCP. The nominal (without scattering) travel distance is 8.0 cm on the SSD level, and 5.8 cm on the “Large” MCP detector level.

In the SSD section, the penetrating particle causes the emission of backscattered secondary electrons from the detector surface. These electrons are steered onto a “Small” MCP. The cascade electrons at the exit of the MCP are accelerated from the negative PAC voltage of the TOF/E Chamber to the signal board at ground potential. The fast “STOP” signal is provided from a solid anode located on the signal board.

In portions of the WAP sector where there are no SSDs, the incident particle directly impacts the “Large” MCP, thereby triggering its “STOP” timing signal directly.

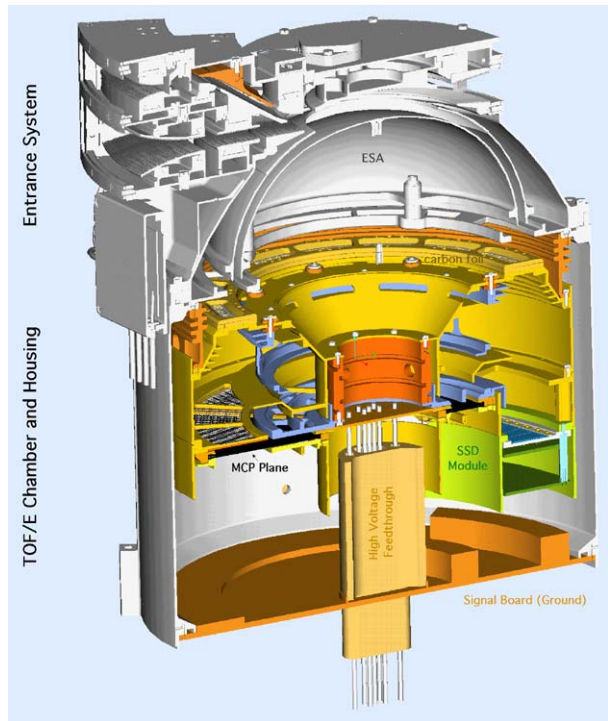
The START and STOP signals of the SSD and non-SSD sections of PLASTIC are fed into two independent time-to-amplitude converter (TAC) boards. Rate information is provided from the START, STOP, and Coincidence (START with STOP) elements of the two sections, as is a measurement of the flight time τ of the ions. The time signals are processed in a 10-bit time-to-amplitude converter. The τ range \sim 4 to 250 ns is converted to TOF channel range 0–1023; and the TOF value is subsequently transferred to the event selection logic for further processing (see Sect. 3.7). These two boards (designated TAC0 and TAC2) also provide in-flight test and calibration capabilities by adjustable internal stimulation circuitry. The electronic resolution of the time measurement is <0.2 ns. The total time-of-flight dispersion is also affected by the angular spread and energy straggling of the ion passage through the carbon foil.

3.4.2 Design of the TOF/E Chamber

A cutaway representation of the PLASTIC Entrance System and TOF/E Chamber is shown in Fig. 6. The TOF with energy measurement system is shown on the right half of the TOF/E Chamber, and the TOF-only measurement system on the left side of the cutaway. The TOF/E chamber dimensions and the applied electrode voltages were designed using the electrostatic ion optics analysis and design program SIMION 3D version 7.0 (Dahl 1995). This program calculates ion and electron trajectories, time-of-flight, kinetic energy, angles of incidence, and electric potential field arrays. The program output was used in designing the SSD, MCP, and anode detector dimensions and their respective placement in the TOF/E Chamber, in order to maximize the probability of hitting the targeted detector (i.e., optimization of the geometrical factor). Simulations were also used in assigning the voltages applied to the steering and focusing electrodes and to the electron acceleration grids. Electrode and grid parameters were varied until the output response was optimized to minimize the dispersion in the time-of-flight (species resolution) and in the angle (position integrity and resolution). The fidelity of the simulation relies on appropriate initial inputs. User inputs include the initial particle distributions (species, energy, position, elevation and azimuth angles) for: (1) ions exiting the carbon foil; (2) secondary electrons from the carbon foil and from the SSD; and (3) cascade (MCP output) electrons for start and stop signals.

The method used in generating the test file for ions exiting the carbon foil is fully described by Allegrini (2002). The standard run assumed nominal solar wind element abundances and charge state distributions (1.5 MK freeze-in temperature) for O, Ne, Mg, Si, Ar, and Fe, representing a range of solar wind $Z > 2$ species; a bulk speed of 440 km/s with nominal thermal spread; post acceleration of -25 kV; and carbon foil charge exchange, energy loss, and angle dispersion. The carbon foil energy loss and angular straggling functions were measured by Lüthi (2003) for the same $3.5 \mu\text{g}/\text{cm}^2$ carbon foils and supporting grid

Fig. 6 Cutaway view of the PLASTIC Entrance System and TOF/E Chamber



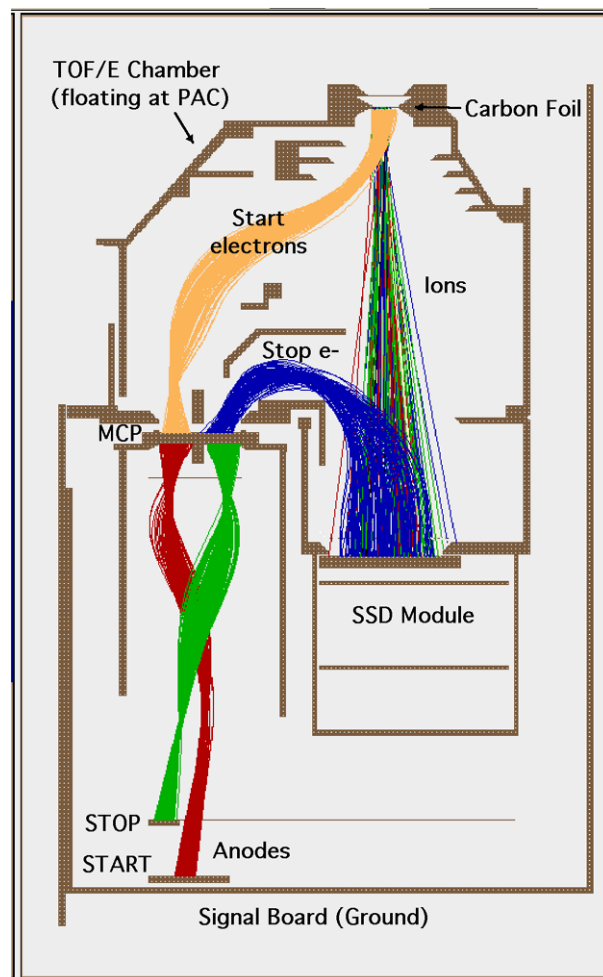
system as those used in PLASTIC. Charge exchange within the foil is expected to alter the ion's ionic charge state, and the results of Gonin et al. (1995) were used for determining the post-foil charge fractions. Separate simulation runs were executed for singly charged species, as would represent solar wind protons or oxygen pickup ions.

Secondary electrons emitted from solids typically have an energy distribution with a maximum (most probable energy) of $\sim 2\text{--}3$ eV, with a long energy tail, and a cosine angular distribution relative to the surface normal (e.g., Wehner 1966; Kawata et al. 1991; Ritzau and Baragiola 1998). This general distribution shape was used in generating the simulated test electrons exiting from the carbon foil and from the SSD surface. For the simulated cascade (MCP output) electrons, the energy distribution was derived from Koshida and Hosobuchi (1985), with the initial electron angular dispersion centered at the MCP channel angle (19° for the large MCP, 13° for the small MCP).

Figure 7 illustrates the simulated trajectories for the Solar Wind Sector side of the TOF/E Chamber using these input distributions. Ions are shown exiting the carbon foil and hitting the solid state detector; start electrons are steered from the carbon foil to the small micro-channel plate; stop electrons emitted from the front surface of the SSD are steered to the small micro-channel plate; and the MCP-generated cascade electrons are accelerated to their respective anodes located on the signal board. Combined target efficiency for nominal operational voltages was estimated (through these simulations) to be $>92\%$.

Simulations were also employed to verify that any backscattered electrons, created either by ions or electrons hitting internal structures other than their intended detectors, would not accidentally be steered onto an MCP, where it could trigger false event counts (creating a background population).

Fig. 7 Ion and electron trajectories from a SIMION 3D simulation for the TOF/E chamber on the Solar Wind Sector side (with SSDs)



Prototype testing was performed using the UNH ion gun facility (0–40 keV/e, singly charged ions) to verify the simulation results and to determine any modifications that were needed (e.g., for fringe field effects). An over-sized square MCP with a position-sensing anode (Lampton and Carlson 1979) was used in the prototype tests to verify geometries and placements chosen for the various detectors. The laboratory MCP could be rotated in the detector plane (i.e., in azimuth) to determine relative detection efficiencies as a function of position. Laboratory power supplies were used to determine the fine adjustment of various steering and grid voltages on the prototype. End-to-end performance testing was performed on the integrated engineering and flight models.

Some typical species resolution for the fully integrated PLASTIC Flight Model is illustrated in Fig. 8a. These calibration data for protons and heavy ions were taken at the CASYMS facility.

Fig. 8a TOF distributions obtained for H^+ , He^+ , and Ne^{+4} ions at 1 and 60 keV/e CASYMS (UBe) beam energies. TOF resolution is a function of the species and total energy of the ion. Higher charge states for a given species will have higher energies, and hence improved resolution, as seen in the response for the Ne^{+4} ions

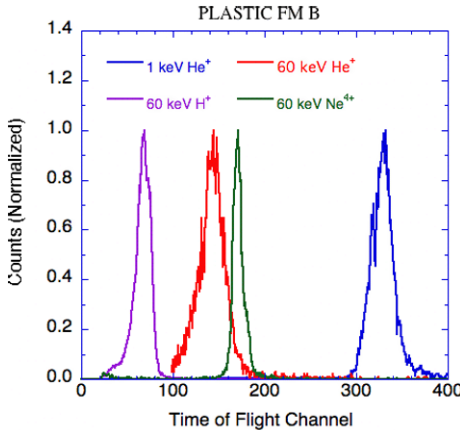
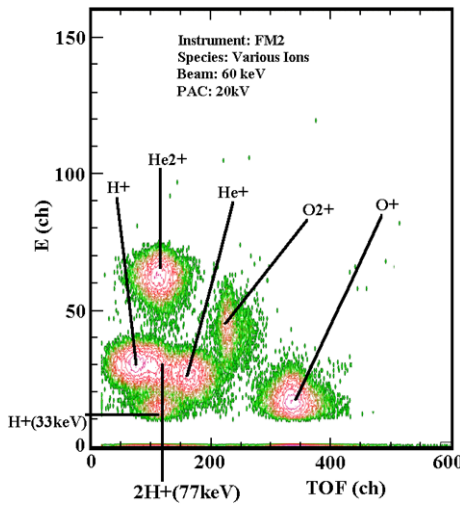


Fig. 8b A composite of Energy vs. TOF obtained for various ions, illustrating resolution for different species

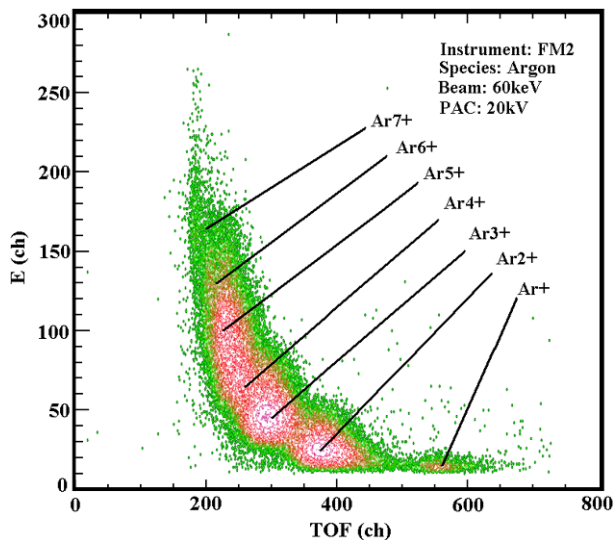


3.4.3 TOF Detection Efficiency

The total efficiency for measuring the particular ion in the TOF/E system is affected by three separate contributions: the efficiency for getting a “START” signal, the efficiency for getting a “STOP” signal, and the efficiency for getting a “VALID EVENT”.

The START efficiency is a function of the number of secondary electrons emitted from the carbon foil; the effectiveness of focusing these electrons onto the START MCP; the MCP detection efficiency; and the anode detection efficiency and signal threshold. On the “small” MCP side, the STOP efficiency is a function of the scattering of the ion in the carbon foil (that is, the number of ions successfully hitting the active area of the SSDs); the yield of electrons emitted from the SSD; the focusing of these electrons onto the STOP side of the MCP; the MCP detection efficiency; and the corresponding anode detection efficiency and signal threshold. On the “large” MCP side, the STOP efficiency has similar inputs, except the ion itself triggers the STOP MCP. The VALID EVENT efficiency depends on the logic conditions imposed on the event selection. These typically include the requirement for a

Fig. 8c Energy vs. TOF for an argon beam with various ionic charge states, illustrating the charge state resolution within a single species



START signal and a coincident STOP signal (thereby providing a double coincident TOF), and may include conditions on energy and position coincidences.

The yield of secondary electrons forward emitted from the carbon foil or backward emitted from the SSD surface is a function of the incident ion's mass and velocity. The yield is typically larger for forward emission than backward emission, with smaller yields for protons than for heavier ions at a given velocity (Meckbach et al. 1975; Ritzau and Baragiola 1998).

The effectiveness of the focusing of the secondary (and the cascade) electrons were simulated and then tested with a prototype, as discussed previously. The simulations also included the measured effect of carbon foil straggling (Lüthi 2003).

The detection efficiency of MCPs is a strong function of its gain, which in turn depends upon its dimensions (active area, plate thickness and channel diameter), bias voltage, and the type, energy and angle of the primary radiation or particle being detected (Hellsing et al. 1985; Photonis, private communication). The annular, long-life micro-channel plates (MCP) used in PLASTIC were custom made by Photonis, and were provided as matched (in resistance) chevron pairs. The channel bias angle for the “small” MCPs was set at 13° with an azimuth orientation. This angle was chosen to optimize the gain for incident electrons (which in this case are used for both the START and the STOP signals), while limiting the likelihood of ion feedback. For the “large” MCP, the START particles are secondary electrons, while the STOP particle is the incident ion itself. For this configuration, the channel bias angle was set to 19°, with a radial orientation. (The expected angles of incidence and the angular spread for the particles impacting the MCP were determined from the TOF/E Chamber simulations.) The gain and pulse height distribution as a function of bias voltage was established for each MCP chevron pair using an americium-241 alpha source and a nickel-63 beta source. These measurements were taken at the UBe KAFKA facility, and the results were used to make the flight unit selections.

The UNH ion gun and the UBe CASYMS ion beam calibration facilities were used to determine the final (end-to-end) efficiencies of the integrated instruments. The calibrations were achieved in two steps. First, the relative efficiency was measured for selected ion species as a function of the MCP bias. Second, using the optimum MCP voltage, the effi-

iciencies for selected species were measured as a function of energy and position. Calibration data were obtained for beams of H^+ , H_2^+ , $He^{+1,+2}$, N^+ , $O^{+1,+2}$, and $Ar^{+1,+2,+3,+4,+5,+6}$. Figure 9 illustrates the START, STOP, and VALID EVENT efficiencies measured for Neon and Argon in quadrant Q0 of the PLASTIC FM2/B. In Fig. 10, proton STOP efficiencies by quadrant are shown. The proton STOP efficiency is typically the worst scenario for the instrument, as protons produce the lowest yield of backward emitted secondary electrons (Ritzau and Baragiola 1998).

3.5 Energy Measurement System

Sixteen solid state detector (SSD) pixels are located at the end of the time-of-flight path in quadrants Q0 and Q1 of the TOF/E chamber. The SSDs provide two functions: (1) measurement of the residual energy (after pulse height defect) of the incident ion, and (2) emission of secondary electrons, which are used to trigger the stop signal for the coincident time of flight measurement.

The SSDs chosen for PLASTIC are custom made Canberra passivated implanted planar silicon (PIPS) detectors with an equivalent entrance window of 25 nm silicon. Eighteen SSD pixels are mounted on two macor silver–platinum metallized frames. Two of the pixels are obstructed by supporting structures and are not used in analysis. Table 5 provides the physical characteristics of the SSD pixels.

The energy measurement response function of silicon PIPS detectors includes the detector nonlinearity (pulse height defect as a function of incident particle species and velocity) and the shape and width of the response function (noise), including broadening effects from channeling (Collier et al. 1988; Oetliker 1993; Steinbauer et al. 1994). The silicon crystal 7° off-axis orientation was specified to minimize channeling by normal incidence particles. Pulse height defect and noise response of the PLASTIC flight detectors were calibrated pre-launch at the MEFISTO beam facility (UBe). Measurements were made of ions H, C, O, N, and Ar in the energy range 10–600 keV. The calibration results are described in Blush et al. (2005).

The SSD Module for PLASTIC consists of the mounted solid state detectors and three electronic circuit boards. Two of the boards (SSD-A, SSD-B) are stacked directly behind the detector arrays, and are referenced to the PAC voltage. The remaining board (SSD-C) is located on the Signal Board, and is referenced to ground. Optical links using infrared emitter

Table 5 PLASTIC solid state detector characteristics

Manufacturer	Canberra Industries
Type	Custom PIPS
Pixel shape	Trapezoid
Pixel active area (nominal)	95 mm ²
Number of pixels	18 (16 used)
Batch chip thickness, fully depleted	502 microns
Batch resistivity	13200 ohm-cm
Silicon wafer crystal orientation	(111) 7° off axis
Equivalent entrance window thickness	25 nm
Operating voltage	80–120 V (95 V in instrument)
FM1 serial numbers (quad 0, 1)	S8, A5
FM2 serial numbers (quad 0, 1)	S3, A1

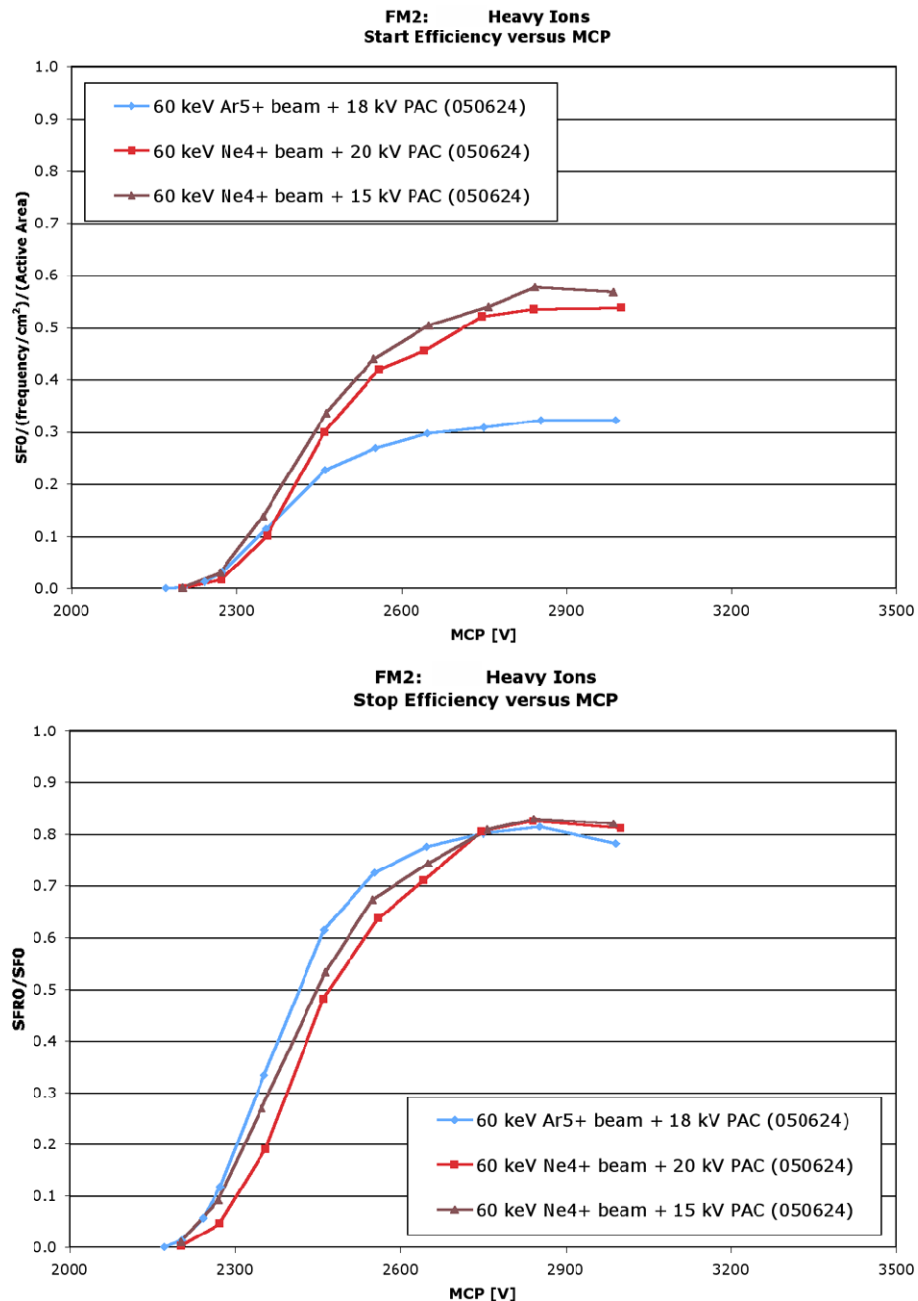


Fig. 9 (Top to bottom) START, STOP and VALID EVENT efficiencies for neon and argon in FM2/B, as a function of bias applied to the MCP detector system. (a) START efficiency is given by the start trigger (“start flag”, SF) rate normalized to the calibration beam monitor flux (counts/s-cm²) and illuminated area (cm²). (b) The STOP efficiency is derived from the ratio of the TOF coincidence rate (“start flag reset”, SFR) to the start trigger rate (SF). (c) The VALID EVENT required coincident TOF and Energy signals, and its efficiency is derived from the ratio of its respective rate to the start trigger (SF). Data was obtained at the UBe CASYMS beam facility

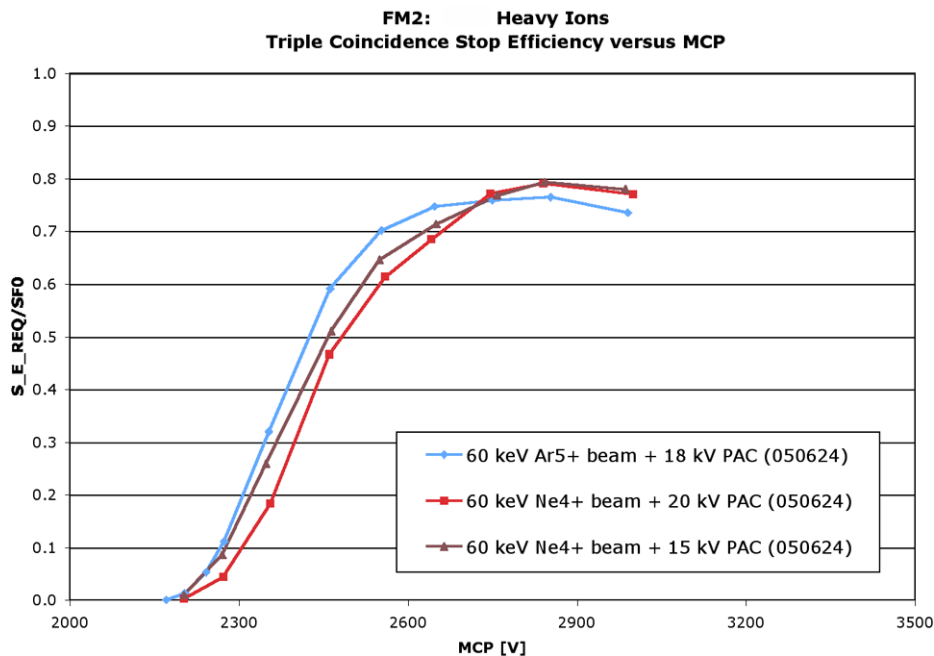
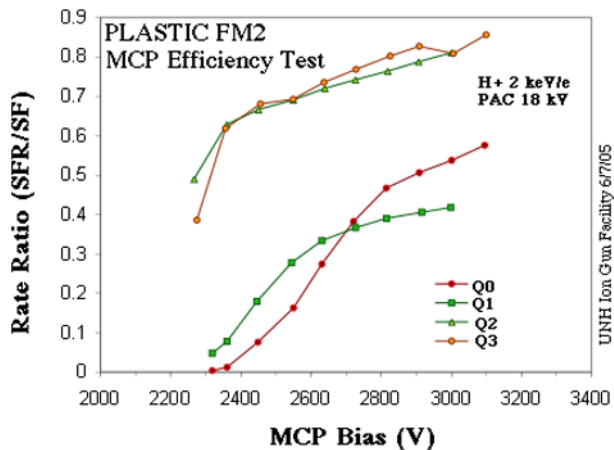


Fig. 9 (Continued)

Fig. 10 FM2/B STOP efficiencies (given as the ratio SFR/SF) for 20 keV total energy protons as a function of MCP bias, for quadrants Q0–Q3. Data was obtained at the UNH ion gun facility



and diode detector pairs transfer signals across the PAC-to-Ground potential vacuum gap, that is, from the SSD-B to the SSD-C boards, and vice versa. These signals include uplinking of commands to an application-specific integrated circuit (ASIC) and downlinking of energy pulse height analysis (Energy PHA) values, rates, and housekeeping data.

The SSD-A board services the signals from the SSD pixels and includes an ASIC built by Ideas ASA (Norway). The Ideas XA16_HR was customized specifically for use with the PLASTIC SSD electronics and provides a high rate, 16-channel charge sensitive amplifier array, featuring low-noise buffered preamplifiers, shaping with peak and hold, individual

channel threshold discriminators (commandable 8-bit DAC threshold settings), and internal calibration stimulation. Channels can be enabled/disabled individually in case a particular SSD pixel becomes noisy. The full-scale energy range is 15 to 2000 keV. Measured energies are converted to 10-bit (1024 bins) energy pulse height value with a nominal gain of 2 keV per bin. The ASIC device was chosen over discrete electronics because of its low power consumption and small space requirements. As the PLASTIC ASIC represented new flight technology, the flight lot was tested for latch up susceptibility using heavy ion (Ar, Cu, Kr, Xe) beams at the Texas A&M Single Event Effect Test Facility. Each flight ASIC's response at various temperatures was also calibrated within its respective SSD Module using the gamma and X-ray lines of radioactive cobalt (^{57}Co) and americium (^{241}Am) sources.

3.6 Azimuth Position Measurement System

The ESA and TOF/E optics are designed such that the original azimuth position information for the incident ion is maintained by the secondary electrons. Therefore, the entrance position of the ions can be determined from the position of the “START” pulse generated in the TOF System. PLASTIC measures the azimuth of incoming ions by using either discrete or continuous position detectors.

3.6.1 Position by Discrete Anodes

In quadrants Q1, Q2, and Q3, the azimuth is reported through ten discrete anodes. Each of these discrete anodes spans 22.5° of azimuth and is plated directly onto the signal board. The charge accumulated on these anodes is detected by ten fast amplifiers and is reported if it exceeds threshold.

3.6.2 Position by the Resistive Anode

In quadrant Q0, which includes the solar wind sector, the azimuth is reported by a resistive anode (RA) position detector. The resistive anode offers better azimuth resolution than the discrete anodes. A photo of the signal board with the discrete and resistive anode position detectors is shown in Fig. 11.

The custom designed resistive anode is composed of a 25-micron thick resistive film layer deposited on an arc-shaped substrate with a mean radius of 45 mm. The film is DuPont QS874, and the substrate is a 1 mm thick layer of 96% alumina. Contacts at each end are made of DuPont QS170 silver. The contacts were first bonded to the ceramic, and then the resistive film was deposited on top. The end-to-end resistance is approximately 50 kohms. The anode is placed on a 3.5 mm thick Ultem 1000 baseplate. This minimized the potential for damage from handling, and provided a durable connection point for a charge amplifier at each end.

A schematic of the resistive anode is shown in Fig. 12. The arc-shaped anode is shown with an MCP charge pulse deposited near the center. The deposited charge diffuses outward and is collected by charge amplifiers at each end of the anode. The location of the charge shower is calculated by collecting charge Q_A and Q_B from each end and entering this information into a lookup table held in EEPROM (Electrically Erasable Programmable Read-Only Memory) in the digital electronics. The axes of the table are values of Q_A and Q_B . The content of the table is the distance from one end of the anode (A) to the point of charge deposition. The distances are calculated by:

$$\text{Azimuth position} = Q_B / (Q_A + Q_B) \times \text{mean arc length}.$$

Fig. 11 A photo of the signal board is shown. The screens collect MCP showers from “start” electrons. The opaque panels collect MCP showers from “stop” electrons or ions. The black resistive anode can be seen below the solar wind sector screen in the foreground

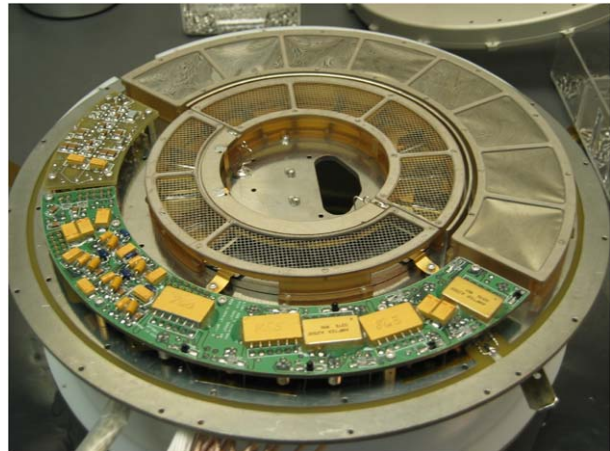
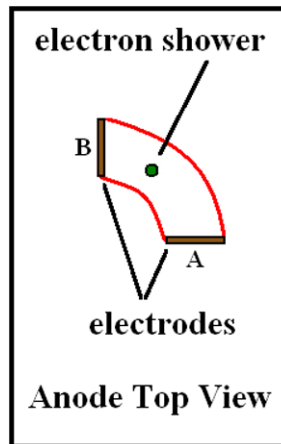


Fig. 12 A schematic of the resistive anode is shown. The location of the charge shower is calculated by collecting a charge Q from each end and entering a lookup table. The contents of the table are distances from one end of the anode (A) to the point of charge deposition



The use of a table simplifies and speeds up the position calculation. It also permits compensation for any gain imbalance between the two charge amplifiers.

The resistive anode position electronics include a charge amplifier for each end of the anode and a trigger for event counting. The trigger is set if the combined charge $Q_A + Q_B$ exceeds a threshold of 50 fC. The amplifiers have a gain of 5 mV/fC.

An inherent challenge for the anode circuit is the accommodation of a wide range of MCP pulse heights. These pulses may reach ~ 5 pC, depending on the MCP voltage. The resistive anode amplifiers may therefore saturate on MCP pulses from some ions. The circuit is designed to allow a delayed conversion, in which the position is acquired just after the amplifiers come out of saturation. The trigger pulse width is approximately 600 ns for non-saturated cases, and approximately 2.8 μ s for saturated pulses. A deadtime of approximately 2 μ s has been derived from high rate tests. These results evidently include a mixture of saturated and non-saturated pulses. This design provides a fast counter with a wide dynamic range for high rate solar wind protons.

3.6.3 Resistive Anode Measurements

The response of the resistive anode as a function of incoming beam angle is shown in Fig. 13. The mapping is unique over the central solar wind sector covering $\pm(3\text{--}19^\circ)$. The extreme position ($>20^\circ$) response is relatively flat. This is in part because the anode is much longer than it is wide, and therefore the azimuth resolution is best near the center, where it is most critical for the science requirements. The sections beyond $\pm20^\circ$ are located in the Suprathermal Wide Angle Partition (WAP) section, used for pickup and suprathermal ions. This section needs only 22.5° azimuth resolution.

The position mapping in the center of the solar wind sector is double-valued in the $\pm 3^\circ$ range. This is caused by a structural support for the carbon foils. The support tends to electrostatically steer carbon foil knock-off electrons away from the center. In flight, the solar wind is expected to lie typically to one side of center, due to the aberration resulting from the speed of the spacecraft relative to that of the solar wind.

Resistive anode position distributions are shown in Fig. 14 for eight incoming ion beams used in pre-launch calibration. The beams entered the instrument azimuthally at angles between $+1^\circ$ and -6° , measured from the center of the solar wind sector. The FWHM of the distributions in this particular example is $\sim 8^\circ$. The behavior of the position distribution for incoming azimuths of 3° or less is shown. The distributions make a jump transition across the center of the solar wind sector in the $\pm 1^\circ$ range. Ions entering directly in the center of the solar wind sector are largely obstructed by carbon foil support structures.

At high rates, pulse pileup causes the deposited charge from several ions to be summed, in which case the circuit reports their average azimuth. This is acceptable in the solar wind, as only the bulk direction of the high flux solar wind protons is required.

In circumstances where a large quantity of charge is accumulated, the A/C coupling of the amplifiers may broaden the position distribution. This may happen in cases where the rate is high, or MCP pulses are large for other reasons. This effect is observed, for example, when the MCP bias is high and heavy ions are detected. The broadening develops as the signal baseline drops below ground. A constant is therefore subtracted from the charge accumulated at each end of the anode. This tends to shift the calculated position away from the centroid.

Figure 15 shows the azimuth position reported for an increasingly high rate calibration beam of He ions from a single azimuth. The position peak channel decreases by approxi-

Fig. 13 An azimuth scan is shown in which the instrument is rotated past a fixed calibration beam. Plotted is the azimuth bin channel reported by the resistive anode vs. the incoming beam azimuth. The reported azimuth bin is uniquely related to the incoming azimuth from $\sim -19^\circ$ to $+19^\circ$. In the suprathermal sections beyond $\pm 29^\circ$, the anode reports a single value, corresponding to the 22.5° resolution required for the WAP section

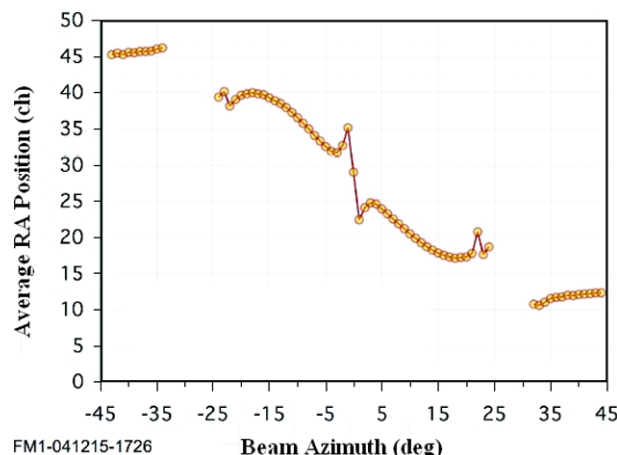


Fig. 14 The resistive anode output is shown for eight incoming ion beams during pre-launch calibration. Beam azimuths were +1 to -6 degrees from the center of the solar wind sector

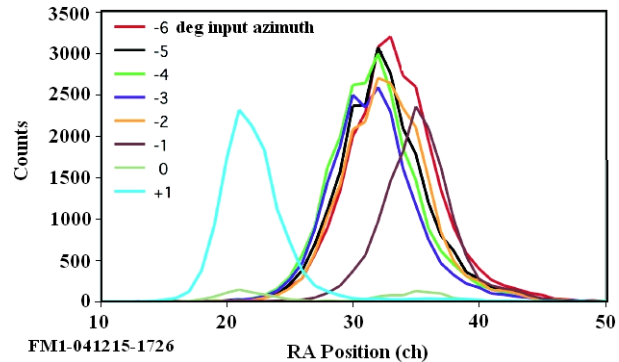
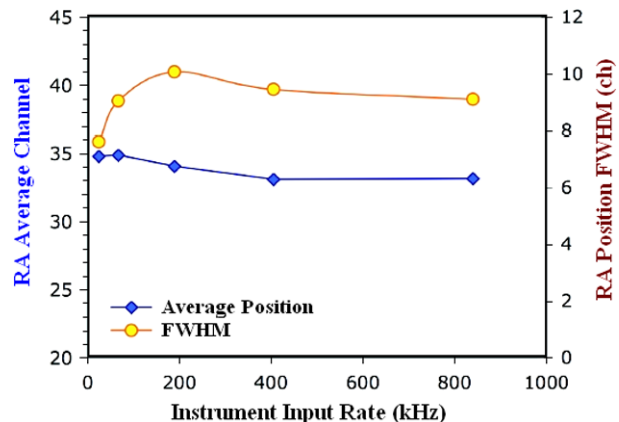


Fig. 15 The average and FWHM of the position reported by the RA is shown for a single calibration beam azimuth at increasing rates. Each RA channel corresponds to an angle bin of $\sim 1.3^\circ$ width



mately 2 channels as the rates increase (each channel represents a 1.3° bin). The position distribution widens somewhat as well.

The uncertainty in the average azimuth depends on the number of ions collected in a single deflection step. For example, an input of 4×10^8 protons/s-cm 2 to the Small-channel aperture would reduce to ~ 600 kHz on the resistive anode. The reported rate with dead time would be ~ 100 kHz. A sampling duration of 12.8 msec at each deflection step would then collect ~ 1400 events. The resulting uncertainty in the average azimuth would be $\sim 0.25^\circ$.

3.7 Analog and Digital Electronics

3.7.1 Functional Overview

The instrument electronics are contained on more than thirty circuit boards, with components that include seven Actel complementary metal-oxide-semiconductor (CMOS) field programmable gate arrays (FPGAs), five electrically erasable programmable read-only memories (EEPROMs), and an application-specific integrated circuit (ASIC) device. Some of the signal-processing electronics have been previously described under the corresponding measurement description section.

The functions of the sensor electronics include:

- Providing the sensor interface to the IDPU for information transfer (commands and time ticks, data requests received from the IDPU; PHA events, rates and housekeeping data transmitted to the IDPU);
- Providing low voltage conversion and EMI filtering from the spacecraft 28 V power input;
- Controlling the sensor's operating mode;
- Controlling voltage sequences in the Entrance System, such as setting the sweeping voltages for the polar deflectors, enabling/disabling the Main Channel Gating, and stepping of the ESA high voltages;
- Providing, controlling, and distributing high voltages;
- Processing detector signals;
- Implementing logic selection criteria for the validation of events;
- Controlling information flow within the sensor, including the transfer of products forming the pulse height analysis (PHA) word;
- Building up the PHA word for each validated event and providing real time, high-speed, PHA event classification using table look-up techniques;
- Collecting Matrix Rates from the PHA classification, for transmission to IDPU;
- Collecting and selecting PHA events, for transmission to IDPU;
- Collecting Monitor Rates at predetermined intervals, for transmission to IDPU;
- Collecting sensor analog and digital housekeeping (HK), for transmission to IDPU;
- Providing internal stimulation for pre-flight and onboard functional tests; and
- Monitoring and responding to latch up conditions.

A simplified functional diagram for the analog and digital electronics is given in Fig. 16. Most of the circuits are referenced to ground and primarily reside either on the Signal Board (located in TOF Housing at ground) or else within the Electronics Box. Portions of the SSD Module and the MCP/SSD power supplies float relative to the PAC voltage (0 to $-25\,000$ V).

3.7.2 Power Supplies (PS)

There are a total of eight power supplies incorporated into the PLASTIC sensor:

- The low voltage power converter LVC (Luhmann et al. 2007);
- Four dynamic high voltage (HV) power supplies (together called the “SWEEP” supplies), which apply a pre-determined sequence of voltage settings (obtained from EEPROM tables) to the Entrance System’s Main Channel polar deflectors (DEFL1, DEFL2, 0 to $+6$ kV), with taps for the Small Channel polar deflectors; the two electrostatic analyzer voltages (ESA_{plus}, $+10$ V to $+6$ kV; ESA_{minus}, -10 V to -6 kV), and the Small-channel steerage (SCHN, 0 to -4 kV), with taps for Small Channel tuning and for the Main Gate. A customized high-voltage, radiation-tolerant optocoupler was developed to control the voltage ramp for each of the SWEEPS. The ESA $+/$ $-$ cadence is 128 logarithmic steps in less than 60 seconds. The DEFL1 and DEFL2 power supplies are synchronously either held or ramped through appropriate voltages matched to a given set of ESA voltages;
- Three static power supplies incorporated into the TOF HV supply: the post acceleration PAC (0 to -25 kV), the MCP detector voltage (0 to 4 kV), and the SSD detector and electronics bias (~ 100 V). The MCP and SSD power supplies float at the PAC voltage.

3.7.3 Onboard Classification and Data Handling (Sensor)

The PLASTIC digital electronics generates three types of data information: (1) identification and signal pulse height information from each ion event (“Pulse Height Analysis Words” and

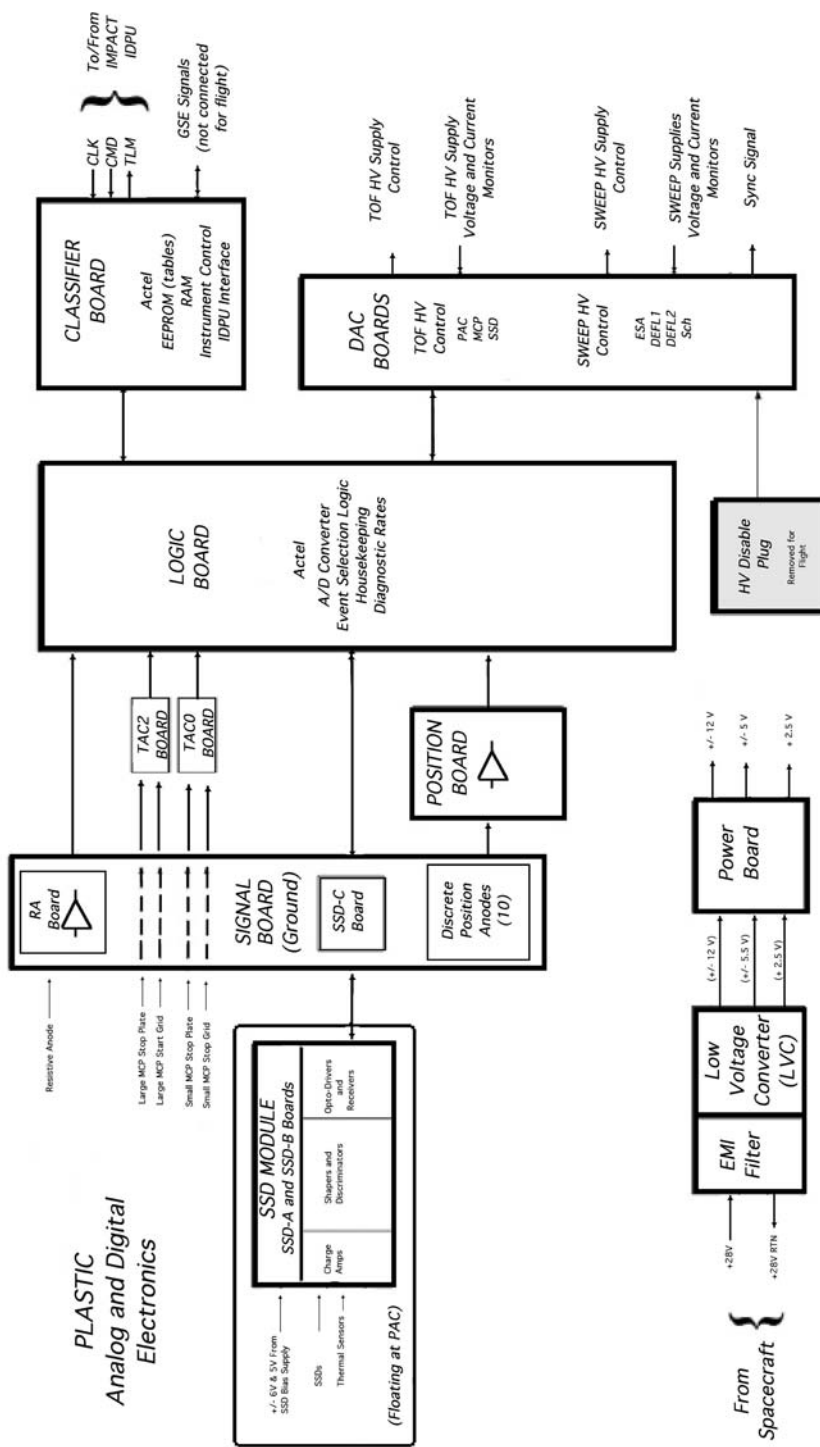


Fig. 16 Top-level block diagram of the PLASTIC analog and digital electronics

“Classified Matrix Rates”); (2) counts of various detector diagnostic “Monitor Rates” within specific time interval (each deflector step, 12.8 ms); and (3) various instrument “Housekeeping and Status” information. Data types (2) and (3) are sent directly to the IDPU. The PHA Words are sent to the “classifier board”, where they are further analyzed, as described below.

3.7.3.1 PHA Word An incident ion that satisfies the (commandable) event selection logic conditions is assigned a 48-bit pulse height analysis (PHA) word that contains the following information: The ESA voltage step (SWPE, 0–127) during which the event occurred; SWS polar deflection step (SWPD, 0–31); quadrant of triggered anode (QUAD, 0–3); measured energy in the SSD (SSDE, 10-bit channel number, 2 keV/chn); identification of the SSD pixel triggered (SSD_ID, 0–15; or if no SSD was triggered, set to 0); time-of-flight (TOF, 10-bit channel number, 0.25 ns/chn); azimuth angle within given quadrant (POS, 64 bins in Q0; 2 bins in Q1; 4 bins each in Q2, Q3); section of instrument triggered (SWS-Main, SWS-Schn, WAP-SSD, WAP-noSSD, SECTION assignment is 0–3, respectively); and priority range assignment for PHA normalization (PRIORITY, 0–3). The priority determination is based on the event classification described next.

The digital electronics use the assigned priority to select a sample of 512 PHA events during each ESA step for transmission to the IMPACT/PLASTIC IDPU. These direct PHA events provide the most detailed and self-contained information possible for any event.

3.7.3.2 Event Species Classification Every PHA word is classified by mass and mass-per-charge through an onboard determination. Event classification by the digital electronics employs fast look-up table techniques that establish a direct correspondence between the SWPE, SSDE, TOF, and QUAD parameters provided in the PHA word to bin assignments from the Mass Tables (Nm) and M/Q Tables (Nq) stored in EEPROM (see Fig. 17, and Table 6). The classification algorithm used to generate the look-up tables is based on the basic relationships presented previously under the principle-of-operation section. The algorithm incorporates the calibrated instrument response function for the energy loss in the carbon foil, the pulse height defect in the solid-state detectors, the TOF signal-to-channel conversions, and the measured energy signal to channel conversions. The algorithm depends on commandable instrument parameters, such as the voltage (hence energy-per-charge) assigned to a given SWPE value, and the PAC voltage value (0 to –25 000 V). These look-up tables are not calculated onboard by the IDPU as done on previous missions (e.g., Gloeckler et al. 1992; Hovestadt et al. 1995), but are rather commanded as table loads directly into EEPROMS in the PLASTIC electronics. It is an important consequence to post-launch flight operations that the tables associated with species classification match any changes made to the ESA table assignments or to the commanded PAC voltage. Otherwise, an event may not be assigned to its appropriate Priority or Matrix Rate.

3.7.3.3 Matrixs Rates Data “Matrix Rates” correspond to the accumulated counts over a pre-defined accumulation time of selected ion species or groups of species (see Fig. 18). Matrix Rate “species box” definitions are based on assignments in a logarithmic Mass vs. M/Q space as represented by the Nm, Nq binning as defined in Table 6.

The Nm, Nq rate assignments are up-loaded into the EEPROM “Classification Bin Tables” by ground command, and thus can be reconfigured if desired during the mission.

“Priority Rates” are Matrix Rates that correspond to large scale (coarse species groupings) M vs. M/Q “species boxes” that are used in assigning a priority value to each PHA event. The priority rate accumulators are incremented for each and every PHA event whose calculated location in (Nm, Nq) space matches the assigned (Nm, Nq) priority bin table entry. The calculated priority value (0–3) is then inserted into each PHA word. Priority Rates

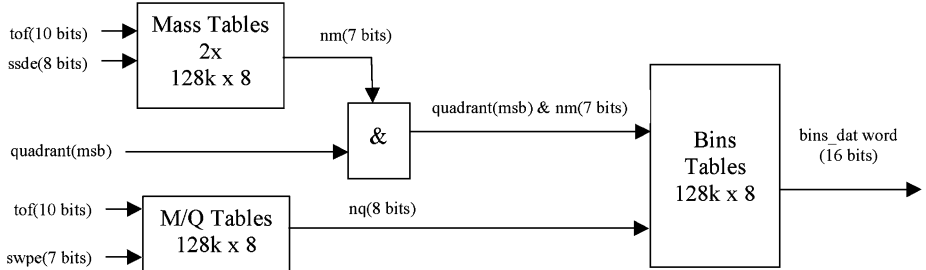


Fig. 17 Matrix Rate generation table look-up flow chart using table lookups from four $128k \times 8$ EEPROMs

Table 6 Mass and mass-per-charge binning

Nm	Nq
Formula:	Formula:
$\text{Mass range} = M_{\min} \text{ to } M_{\max}$	$\text{Mass/charge range} = MQ_{\min} \text{ to } MQ_{\max}$
$N_M \text{ range} = 1 \text{ to } N_{MAX}$	$N_Q \text{ range} = 1 \text{ to } NQ_{MAX}$
$M \text{ (lower bound of } N_M) = M_{\min} \cdot k_M^{(N_M - 1)}$	$M/Q \text{ (lower bound of } N_Q) = MQ_{\min} \cdot k_Q^{(N_Q - 1)}$
$k_M = (M_{\max}/M_{\min})^{1/N_{MAX}}$	$k_Q = (MQ_{\max}/MQ_{\min})^{1/NQ_{MAX}}$
Parameters at launch:	Parameters at launch:
$M_{\min} = 0.5 \text{ amu}$	$MQ_{\min} = 0.5 \text{ amu/e}$
$M_{\max} = 95.0 \text{ amu}$	$MQ_{\max} = 60.0 \text{ amu/e}$
$N_{MAX} = 90$	$NQ_{MAX} = 254$
$k_M = 1.06$	$k_Q = 1.02$

are used for the normalization of the PHA words for ground analysis of flux determinations. There are four classification priorities for the Solar Wind Sector and two priorities for the Suprathermal WAP Sectors. The solar wind priorities are illustrated in Fig. 18 as blue outlined boundaries in M vs. M/Q matrix space.

There are a total of 47 Matrix (including Priority) Rates divided between the SWS and Suprathermal WAP Sectors. Some of these retain full polar, azimuth, and ESA stepping information ($32 \times 32 \times 128$) as they are transmitted to the IDPU. Others are summed, resulting in coarser directional resolution. The “Matrix” Rates products, constituting 13 Kbytes, are sent to the IDPU every ESA step, where they are further processed to create the final data products that fit into the PLASTIC telemetry allocation of 3 kbps.

3.8 Spacecraft Accommodation

The STEREO observatories are three-axis stabilized and sunward-pointing. The PLASTIC-A and PLASTIC-B instruments are identically mounted on the sunward-facing $+X$ panels of the STEREO-A and -B spacecraft, overhanging the respective spacecraft $+Y$ panels (Fig. 19). There are minor differences in the two spacecraft mountings in the thermal control features and in the extent and location of external obstructions in the FOVs. Instrument physical resource requirements are provided in Table 7.

The FOV for the solar wind sector is $\pm 20^\circ$ in the polar (nominally centered on the ecliptic plane) direction, and is sun-centered 45° in the azimuth (in-ecliptic) direction for both

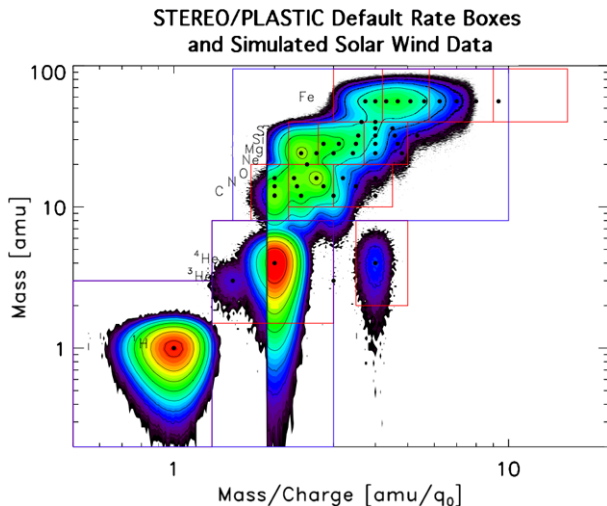


Fig. 18 Default Matrix (red) and Priority (blue) rate “boxes” in logarithmic Mass and M/Q space as defined for the Solar Wind Sector. Rate boundary definitions can be changed by command, and need not consist of contiguous boxes. Superimposed on the M vs. M/Q space are contour plots of a simulated ion population corresponding to a coronal charge state temperature of 1.7 MK (Mazzotta et al. 1998) and nominal solar wind-like abundances. The singly charged helium illustrates a different source population, such as pick up ions. The “ridge” seen just above $M/Q > 2$ and the suppressed counts at He^{+2} , C^{+6} and H^+ illustrate the simulated switching in the Solar Wind Sector entrance from the Main Channel geometrical factor to the Small Channel geometrical factor

the Small and Main Channels. The FOVs in the solar wind sector are unobstructed. For the suprathermal ions wide-angle-partition (WAP) sector, a polar FOV of $\pm 7^\circ$ and azimuth FOV of 305° were originally requested. However, practical accommodations with spacecraft structures (solar panel arrays, SA tie downs and snubbers, the spacecraft bus and thermal blanket) and with the required location (for facing the Parker spiral direction) for the IMPACT SEP packages created impingements in both FOV directions (Fig. 20). These blocked areas were in some instances utilized within the instrument as the locations for internal structural supports.

Each PLASTIC sensor is thermally isolated from the respective spacecraft deck through the use of six mounting feet isolators (which also served to dampen vibration at launch). Thermal blankets, radiator surfaces, and two survival heater circuits are used for thermal control. The survival heaters are controlled by mechanical thermostats and by spacecraft monitoring. One heater (4 W) is located on the starboard radiator of the Electronics Box. Two 2 W heaters are placed on the TOF/E Chamber Housing. The multi-layer insulation (MLI) thermal blanket material on STEREO is made of perforated ITO Silver Teflon. This material meets the spacecraft electrostatic cleanliness requirements. On STEREO-A, which has the higher solar heat input as a result of its closer heliocentric orbit, an exterior auxiliary radiator that is mounted on the $+Y$ deck provides additional heat sinking for PLASTIC. The primary thermal concern is the regulation of the micro-channel plates (MCP) and solid state detectors (SSD) to temperature ranges of -25°C to $+25^\circ\text{C}$ and -20°C to 35°C , respectively. Pre-launch thermal design incorporated radiation models created in Thermal Synthesizer System (TSS) and temperature analysis using SINDA, and then predictions were compared with instrument and spacecraft thermal vacuum.

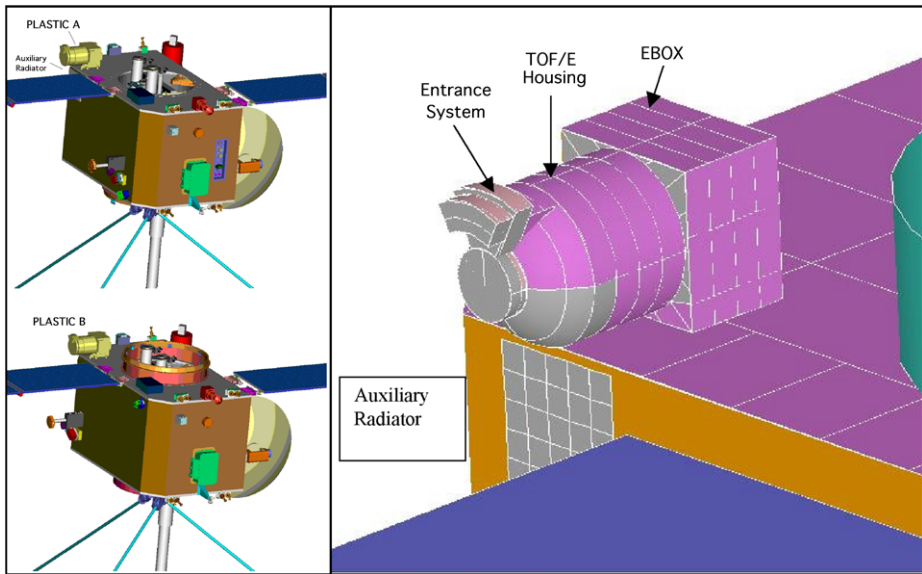


Fig. 19 (a) The mounting location of the PLASTIC sensor on the top deck (sunward facing) of the STEREO-A (top) and STEREO-B (bottom) spacecraft. (b) Schematic view of the PLASTIC sensor. The corner overhang on the spacecraft deck provides the field of view for the WAP sector. Auxiliary radiator is on the A spacecraft, only

4 Instrument Data Products

The IDPU receives from the sensor interface the classifier data (Matrix Rate count accumulators, prioritized PHA), data from the Monitor Rate accumulators, Housekeeping data, and instrument status. The DPU formats the various data products into a data stream that fits into the telemetry allocation of 3 kilobits/sec.

Housekeeping products are sampled once per minute during normal (science) operations. There are in excess of 300 housekeeping and status products, including those status products relating to IDPU operations.

Monitor Rate data consist of raw counts from individual 16-bit counters corresponding to 32 diagnostic rates. These are sent to the IDPU every 12.8 msec (every deflection bin).

Matrix Rate data consists of raw counts from individual 16-bit counters that correspond to 47 selected species boxes. These are sent to the IDPU every 435.6 msec (every ESA step). Prioritized PHA events are also sent to the IDPU every ESA step.

The IDPU compresses the accumulator counts from a 16-bit to an 8-bit representation, and performs sums on various Matrix and Monitor rates in terms of angle bins, energy bins, and/or time resolution, in order to further reduce the required telemetry rate. In addition, the IDPU down-selects the prioritized PHA data. The IDPU PHA down-selection is designed such that the final transmitted selection covers the full range of energies, but emphasizes the heavy ion data.

The data-related tasks performed by the IDPU include creating moments from the solar wind proton distribution, finding the peaks in the solar wind proton and alpha distributions, and creating reduced data products that contain the distribution surrounding these peaks.

The PLASTIC data transmission utilizes three possible telemetry modes: Science Mode (S), Proton Mode (P), and Engineering Mode (E). Only one telemetry mode is enabled by

Table 7 PLASTIC spacecraft resources

Resource	Value	Comments
Size ($L \times W \times H$)	$479 \times 243 \times 265 \text{ mm}^3$	Sensor only
	$202 \times 202 \times 1.5 \text{ mm}^3$	Exterior Auxiliary Radiator (STEREO-A)
Mass	11.4 kg	Sensor and mounting feet, does not include external thermal components (blanket, ext. radiator) nor IDPU harness
Power	12 W	Sensor, 28v
	8 W	Survival Heaters, 100% duty cycle
Telemetry		
Assigned APID	200	IMPACT/PLASTIC Combined HK
Ranges (hex)	300–36F	PLASTIC Data (Science, Engineering)
	370–37F	PLASTIC Beacon
Average Rate	3.2 kbps	Nominal Real Time Allocation
Field of view		
SWS Proton		SWS is Sunward centered in azimuth, polar
Sweeping	$45^\circ \times 40^\circ (E/Q < 10 \text{ keV/e})$	centered on ecliptic plane
Instantaneous	$45^\circ \times 0.3^\circ (\text{FWHM})$	
SWS Main		
Sweeping	$45^\circ \times 40^\circ (E/Q < 40 \text{ keV/e})$	
Instantaneous	$45^\circ \times 2^\circ (\text{FWHM})$	
WAP-STEREO-A	$50/175^\circ \times 3^\circ (\text{FWHM})$	WAP is non-sunward in azimuth, polar centered on
WAP-STEREO-B	$50/160^\circ \times 3^\circ (\text{FWHM})$	ecliptic plane. Azimuth shown as SSD/noSSD

the IDPU at a given time. This mode is selected by ground command. Level 0 data products for all PLASTIC modes are listed in Table 8.

In Science Mode (normal science operations), the science products in the solar wind sector (SWS) consist of on-board computed moments for the solar wind protons, distributions of the solar wind protons and alphas surrounding the peak energy and angle, PHA events, and a number of Matrix Rates covering a variety of the heavy ion species. (Figure 18 illustrates a mass *vs.* mass-per-charge PHA data representation with the default Matrix Rate “species boxes” for the SWS.) The WAP science products also include PHA events and Matrix Rates, including proton, alpha, and heavy ion rates. All science rate definitions are commandable, and may change after launch.

In Proton Mode (P), the entire energy *vs.* angle array for solar wind protons is included in the telemetry. The primary purpose of this mode is for occasional in-flight verification of the proton moment determinations. In order to make room for this data product in the telemetry, there are no heavy ion Matrix Rates included, only the Priority Rates. In this mode, the heavy ion analysis can only be done using the PHA data.

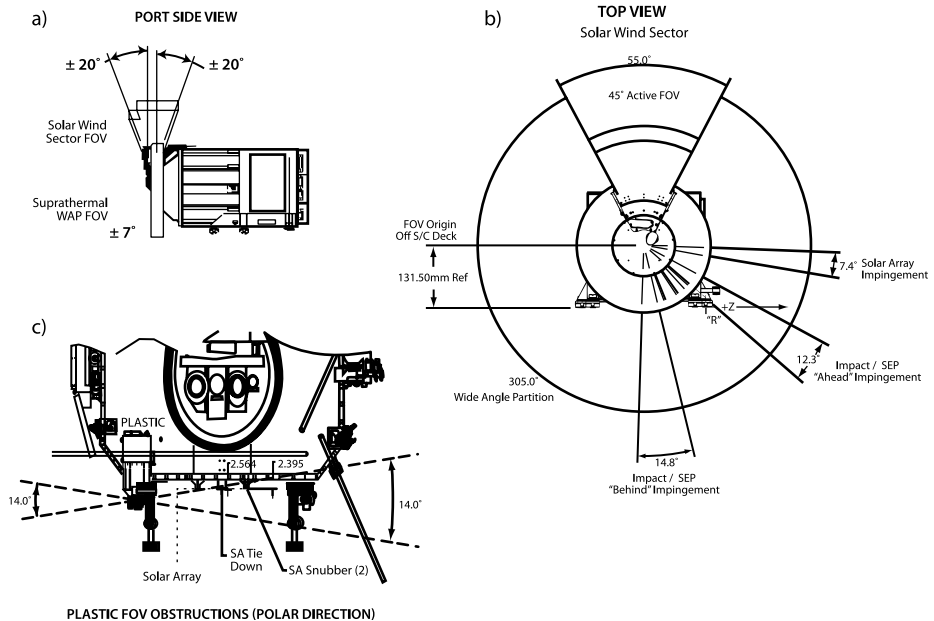


Fig. 20 (a) Port side view of the instrument, indicating the polar FOV for the SWS and the WAP. (b) Top view of the azimuth (in-ecliptic) FOV, indicating locations of azimuth impingements for the mounted instrument. (c) Schematic front view of instrument mounted on the spacecraft, indicating polar impingements to the FOV

In Engineering Mode (E), the diagnostic Monitor Rates are transmitted with full time resolution. There are no science products in this mode, and it is primarily meant for commissioning and trouble-shooting.

In addition to the normal science products, the STEREO mission allocates a small amount of realtime telemetry to Beacon Mode (B) data products. These data products are provided for the purpose of space weather forecasting (Biesecker et al. 2007). For PLASTIC, these products include the solar wind proton density, bulk speed, kinetic temperature, and representative composition information.

5 First Light

STEREO was successfully launched on October 26, 2006, and PLASTIC commissioning began in late November. We report here some initial observations, taken during the commissioning phase, which illustrate the three science functions of the instrument.

5.1 Solar Wind Proton Distributions

Shown in Fig. 21 is a 7-day time-series stack plot of the intensities of solar wind protons observed on STEREO A. The horizontal axis corresponds to E/Q , from which the bulk speed is derived. Intensity is represented by the height of the distribution. During this seven-day period, there is a transition from slow to fast solar wind, with a weak CIR-associated forward shock. The fast solar wind originates from the central meridian passage of a coronal hole.

Table 8 PLASTIC Level 0 Data

Apid	Data product	Mode availability
200	Analog Housekeeping (also includes IMPACT data)	S, E, P
313	Digital Housekeeping	S, E, P
315	PHA Data	S, P
316	Normal Monitor Rates	S, E
317	Full Resolution Monitor Rates	S, E
318	'Trickle-Down' Memory Dump	S
319	Meta-data for Heavy Ions (number of packets summed)	S
31A	SW Z > 2 – High: Class 0	S
31B	SW Z > 2 – High: Class 1	S
31C	SW Z > 2 – Low: Classes 2–9	S
31D	SW Z > 2 – Low: Classes 10–14	S
31E	WAP-SSD-TCR	S
31F	WAP-SSD-DCR	S
320	WAP-noSSD-DCR	S
321	SW Priority Rates	S, P
322	WAP Priority SSD	S, P
323	WAP Priority no-SSD	S, P
324	SW-All H-Alpha Reduced Distribution	S
325	SW-H (Doubles) H+Peak Reduced Distribution & Proton Moments	S, P
326	SW-Alpha (Doubles) He ⁺⁺ Peak Reduced Distribution	S
327	SW-Alpha (Triples) He ⁺⁺ TCR Reduced Distribution	S, P
328	Compressed Classifier Data (Proton Mode)	P
329	Uncompressed Classifier Data (Proton Mode)	P
370	Beacon Data	B

Each horizontal trace represents a single sweep in E/Q through the solar wind velocity range. There are 1440 sweeps per day (cadence 1 minute). Seen to the right of the stack plot are selected one-minute snapshots of the full resolution rate. The protons were measured in the Small Channel of the Solar Wind Sector, the alphas and trace elements in the Main Channel.

5.2 Solar Wind Minor Species

Figure 22 illustrates the switching from the Main Channel (large geometrical factor) to the Small Channel (small geometrical factor) that allows the measurement of both minor species and the more abundant protons and alphas with one common ESA system. At the lower ESA Step (higher E/Q) values, the Solar Wind Sector is open in the Main channel, providing excellent statistics for minor species, such as pickup helium, solar wind iron and oxygen. In this selected time interval, the IDPU onboard control ordered the Main channel closed (electrostatically) at about ESA step number 76, and the Small channel was enabled. To the right of this ESA step, the suppressed solar wind helium and some oxygen can still be seen in the Energy determination. The protons are seen at about ESA step number 96 in the top figure. Only a small percentage of the protons have sufficient energy to trip the SSD threshold, but they are readily observed in the TOF pulse height.

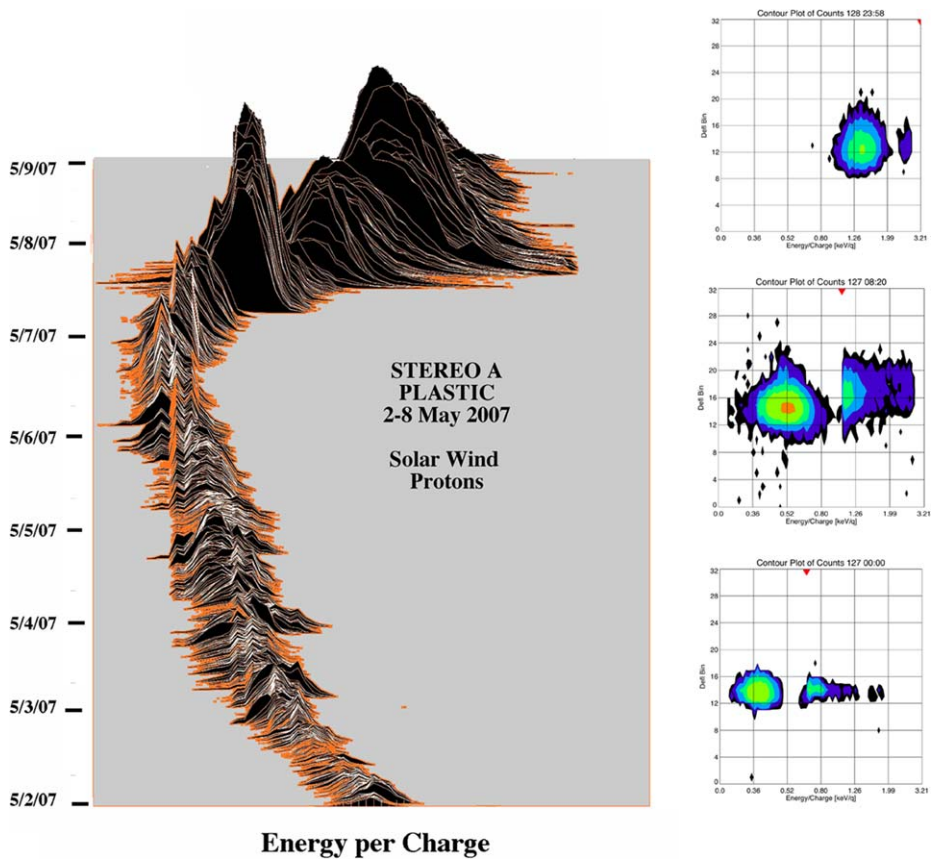


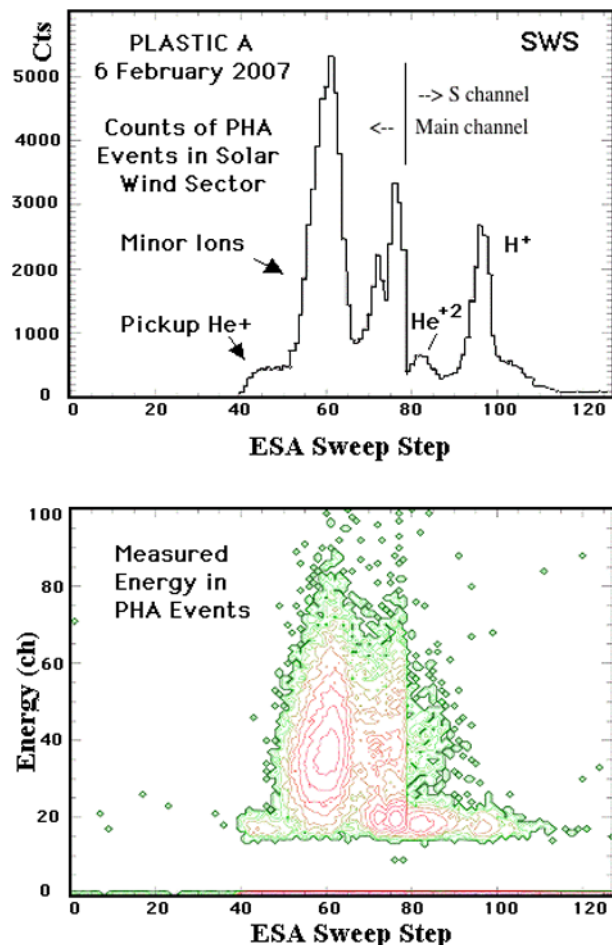
Fig. 21 *Left:* Seven-day time series stack plot of solar wind proton distributions observed by the Small Channel of the solar wind sector, summed over polar and azimuth directions (PLASTIC on STEREO A). The distributions can be used to yield proton bulk parameters, such as speed, density and kinetic temperature. *Right (bottom to top):* One-minute snapshots of the full resolution monitor rate for a slow, shocked, and high-speed solar wind during this time period. Data shows intensity (color contour) plotted against E/Q (horizontal axis) and polar deflection (vertical axis). A red arrow at the top of each panel denotes the switch between the Main (minor ions) and Small (proton) Channels

Species tracks in energy versus TOF in the Solar Wind Sector Main Channel are shown in Fig. 23 for PLASTIC B. Each element has its own track in E-T space. An ion's position on its track depends on the incident energy and the PAC value. Higher energy particles of a given species move up in measured energy and to the left in time-of-flight. If the E/Q information from the ESA step number is included, individual charge states can be distinguished. The helium track shown here contains both He^{+2} and He^+ .

5.3 Suprathermal Ion Populations

One of the suprathermal heliospheric ion populations of interest for STEREO is interstellar pickup ions and their accelerated component at interplanetary shocks. The M/Q histogram in Fig. 24a shows helium observed by PLASTIC-A over a two-hour interval during a high-speed ($\sim 620 \text{ km/s}$, or $\sim 2 \text{ keV/nuc}$) solar wind stream. Pickup helium (He^+) is a prominent

Fig. 22 Two hours of accumulated pulse height data (PHA) events taken from PLASTIC A. Data are not normalized by priority. (*Top*) PHA event frequency against ESA Step. All PHA have at least a TOF signature, but an Energy measurement is not required. (*Bottom*) Contour of Energy measurements against ESA step for the same time period



constituent during this period, and is easily distinguished from solar wind He^{+2} . When the frequency of the identified He^+ is plotted against the incident E/Q (Fig. 24b), the characteristic pickup ion cutoff energy is easily observed. (In the spacecraft frame, the cutoff energy is approximately four times the solar wind energy; in this instance corresponding to $\sim 8 \text{ keV/nuc}$, or $\sim 32 \text{ keV/e}$ for He^+).

The source of the helium pickup ions are likely interstellar neutral atoms that pass through the heliosphere, become ionized, and are subsequently “picked up” and accelerated by the interplanetary magnetic field (a process first directly observed by Möbius et al. 1985 and described therein). The interstellar neutrals are gravitationally focused into a conical region on the opposing side of the sun from the direction of entry as the heliosphere travels through the local interstellar medium. The Earth passes through this focus cone in December of each year. One of the science opportunities for STEREO, as the observatories move away from Earth, will be able to provide direct in situ measurements of the focusing cone at alternative times of the year, for direct comparison with near-Earth (ACE, IBEX) or out-of-ecliptic (Ulysses) measurements.

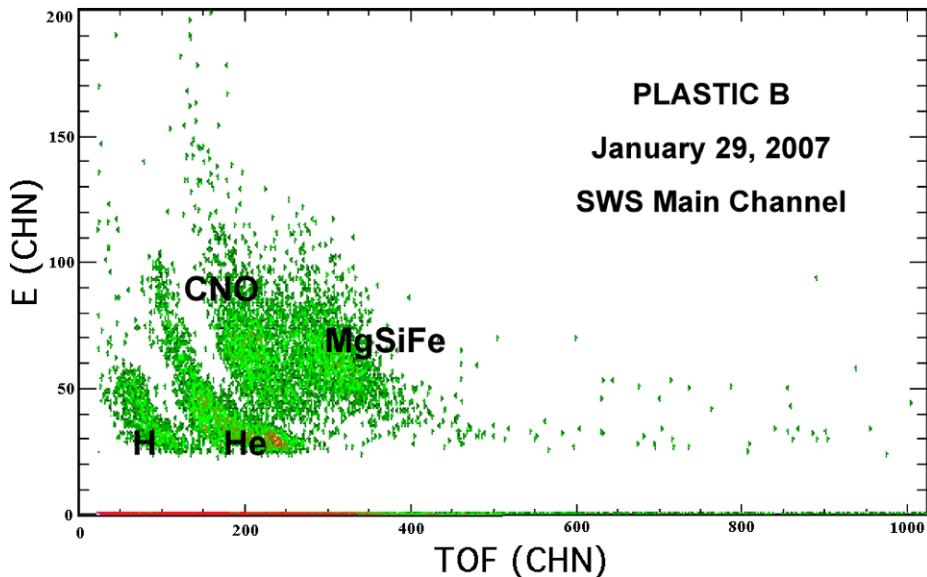


Fig. 23 One hour of composition data taken from the Main Channel on PLASTIC B. Data illustrates the species separation in mass resolution

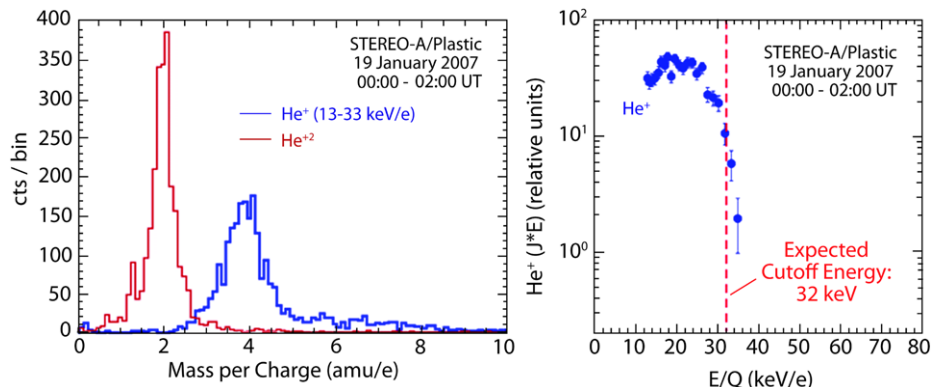


Fig. 24 (a) Mass per charge spectrum for helium, showing separation of the two charge states. (b) Two-hour accumulation count spectrum for pickup He^+ , showing the expected cutoff at twice the solar wind speed (four times the solar wind energy)

These and other initial measurements by the STEREO observatories indicate that the PLASTIC instruments are meeting all functional requirements to address the science objectives.

Acknowledgements The PLASTIC investigation is an international (USA, Switzerland, Germany) effort involving the University of New Hampshire, the University of Bern, the Max-Planck-Institute for extraterrestrial Physics, Christian-Albrecht-University Kiel, NASA/Goddard Space Flight Center, and the University of California, Berkeley (for the shared IMPACT IDPU and LVC). The specific contributions and responsibilities from these institutions are detailed in Table 9.

Table 9 PLASTIC institutional contributors

Institution	Contributions
University of New Hampshire (UNH)	PLASTIC Principal Investigator (PI) institution. Overall PLASTIC management (except for LVC/IDPU). Time-of-Flight/Energy Chamber and Housing (ion optics), Electronics Box, Digital Electronics, Solid State Detector (SSD) Frames and SSD Module Electronics, High Voltage Power Supplies, Position Anodes and Signal Electronics, Auxiliary Radiator, Damper modifications, Thermal, Electronic Ground Support Equipment (EGSE), Mechanical Ground Support Equipment (MGSE), Data System, PLASTIC Operations Center (POC) and Flight Operations, Data Analysis, and Education/Public Outreach (EPO).
University of Bern (UBe)	PLASTIC Co-Investigator (Co-I) institution. Entrance System (Energy/charge Analyzer), Solid State Detectors (SSD), Microchannel Plates (MCP), SSD & MCP Detector Testing, UV and Ion Beam Calibration Facilities and Support, Data Analysis.
Max Planck Institute for extraterrestrial Physics (MPE)	PLASTIC Co-Investigator (Co-I) institution. Time-Amplitude-Converter (TAC) Electronics, Carbon Foils, Dampers, design for Position (POS) Board, Test Support, Data Analysis.
Christian-Albrecht-University Kiel (CAU)	PLASTIC Co-Investigator (Co-I) institution. Electronics Box Panels, MGSE, Test Support, Data Analysis.
NASA Goddard Space Flight Center (GSFC)	PLASTIC Co-Investigator (Co-I) institution. Calibration and Test Facilities, Test Support, Data Analysis.
University of California, Berkeley (UCB)	IMPACT PI institution. Manages and provides shared IMPACT/PLASTIC IDPU, PLASTIC LVC/EMI Filter, and IDPU-PLASTIC Instrument Harness.

During the seven years constituting Phase A through D, many other individuals made substantial contributions to the design, development, fabrication, testing, calibration, and data definition of the PLASTIC instruments. At the University of New Hampshire: our best wishes to our colleague K. Crocker, who retired early for health reasons, and we remember the surviving family of our colleague F. Di Donna. Specific thanks to A. Ames, A. Anderson, S. Battel, E. Coutre, K. Crocker, F. Di Donna, R. DiFabio, T. Enrigo, R. Kearney, and J. Vandiver. We thank D. Curtis of the IMPACT team and S. Judy, J. Hengemihle, and W. Mocarsky for PLASTIC-related IDPU s/w development. UNH administrative support was provided by S. Asselin, L. Belaidi, J. Davis, P. Eckard, K. Giberson, S. Roy, D. Thibault, C. Williams and R. Williams. C. Kustra and K. Donahue provided meeting support; web support by J. Heirtzler. The PI particularly thanks our four frequent flyers who handled the instrument operations at APL, GSFC, Astrotech, and on the launch pad at the Cape—M. Popecki, K. Singer, J. Gaidos, and S. Ellis. The University of Bern acknowledges their technical support staff. Special thanks to F. Allegri for the extensive Entrance System/Energy Analyzer prototype calibrations and design simulations. Thanks to Contraves Space AG STEREO/PLASTIC team for construction of the Entrance System/Energy Analyzer.

The entire PLASTIC team extends thanks to M. Ketters of Canberra Semiconductor NV for extensive design discussions and construction of the PLASTIC solid-state detector wafers. Our sincere gratitude to the entire APL STEREO Spacecraft Team for their support during instrument level environmental testing and spacecraft I&T, especially during the instrument integrations, including Ed Reynolds, M. Stevens, A. Driesman. We are grateful to the NASA STEREO Project Office at Goddard Spaceflight Center for their support, including but not limited to: N. Chriissotimos, M. Delmont, R.P. Buchanan, A. Jacques, M. Jones, S. Hynes, J. Cerullo, and A. Reyes. The STEREO mission was only possible through the unfailing support at NASA Headquarters, including R. Fisher, M. Guhathakurta, and E. Christian.

The PLASTIC investigation at UNH is funded by NASA through contract NAS5-00132. The work at the University of Bern has been supported by the Swiss National Fund and PRODEX Grant C90119.

References

- M.R. Aellig, H. Grünwaldt, P. Bochsler, S. Hefti, P. Wurz, R. Kallenbach, F.M. Ipavich, A.B. Galvin, R. Bodmer, D. Hovestadt, M. Hilchenbach et al., Solar wind minor ion charge states observed with high time resolution with SOHO/ CELIAS/ CTOF, in *Correlated Phenomena at the Sun, in the Heliosphere and in Geospace*. ESA SP-415, 27–31 (1997)
- F. Allegrini, The PLASTIC sensor on STEREO: Design of the entrance system/energy analyzer and numerical simulations of solar wind measurements. Ph.d. thesis, University of Bern, Switzerland, 2002
- M.J. Aschwanden et al., Theoretical modeling for the STEREO mission. *Space Sci. Rev.* (2007, this issue). doi:[10.1007/s11214-006-9027-8](https://doi.org/10.1007/s11214-006-9027-8)
- S.J. Bame, Solar wind minor ions—recent observations, in *Solar Wind Five, NASA Conf. Publ. CP-2280*, ed. by M. Neugebauer (NASA Scientific and Technical Information Branch, 1983), p. 573
- M.G. Baring, K.W. Ogilvie, D.C. Ellison, R.J. Forsyth, Acceleration of solar wind ions by nearby interplanetary shocks: Comparison of Monte Carlo simulations with Ulysses observations. *Astrophys. J.* **476**, 889–902 (1997)
- D. Biesecker, D.F. Webb, O.C.St. Cyr, STEREO space weather and the space weather Beacon. *Space Sci. Rev.* (2007, this issue). doi:[10.1007/s11214-007-9165-7](https://doi.org/10.1007/s11214-007-9165-7)
- L.M. Blush, F. Allegrini, P. Bochsler, H. Daoudi, A. Galvin, R. Karrer, L. Kistler, B. Klecker, E. Moebius, A. Optiz, M. Popecki, B. Thompson, R.F. Wimmer-Schweingruber, P. Wurz, Development and calibration of major components for the STEREO/PLASTIC (plasma and suprathermal ion composition) instrument. *Adv. Space Res.* **36**, 1544–1556 (2005)
- L.F. Burlaga, E. Sittler, F. Mariani, R. Schwenn, Magnetic loop behind an interplanetary shock: Voyager, Helios and IMP 8 observations. *J. Geophys. Res.* **86**, 6673–6684 (1981)
- L.F. Burlaga, Magnetic clouds: Constant alpha force-free configurations. *J. Geophys. Res.* **93**, 7217 (1988)
- L.F. Burlaga, Large scale fluctuations, in *Interplanetary Magnetohydrodynamics* (Oxford University Press, New York, 1995), pp. 169–200
- J.-L. Bougeret, K. Goetz, M.L. Kaiser et al., S/WAVES: The radio and plasma wave investigation on the STEREO mission. *Space Sci. Rev.* (2007, this issue)
- H.V. Cane, T.T. von Rosenvinge, C.M.S. Cohen, R.A. Mewaldt, Two components in major solar particle events. *Geophys. Res. Lett.* **30**(12), SEP 5-1 (2003)
- K. Chotoo, N.A. Schwadron, G.M. Mason, T.H. Zurbuchen, G. Gloeckler, A. Posner, L.A. Fisk, A.B. Galvin, D.C. Hamilton, M.R. Collier, The suprathermal seed population for corotating interaction regions at 1 AU deduced from composition and spectra of H+, He++, and He+ observed on Wind. *J. Geophys. Res.* **105**, 23107–23122 (2000)
- M.R. Collier, R.A. Lundgren, D.C. Hamilton, Channeling in ion implanted silicon solid-state detectors, University of Maryland Technical Report, PP 89-001, Dept. of Physics and Astronomy, and the Institute for Physical Science and Technology, University of Maryland, 1988
- N. Crooker, J.T. Gosling, E.J. Smith, C.T. Russell, A bubblelike coronal mass ejection flux rope in the solar wind, in *Physics of Magnetic Flux Ropes*, ed. by C.T. Russell, E.R. Priest, L.C. Lee. *Geophys. Monogr. Ser.*, vol. 58 (AGU, Washington, 1990), pp. 365
- S.R. Cranmer et al., An empirical model of a polar coronal hole at solar minimum. *Astrophys. J.* **511**, 481–501 (1999)
- D.A. Dahl, *SIMION 3D Version 6.0 User's Manual* (Ion Source Software, Idaho National Engineering Laboratory, 1995)
- M.H. Denton, J.E. Borovsky, R.M. Skoug, M.F. Thomsen, B. Lavraud, M.G. Henderson, R.L. McPherron, J.C. Zhang, M.W. Liemohn, Geomagnetic storms driven by ICME- and CIR-dominated solar wind. *J. Geophys. Res.* **111**, A07S07 (2006). doi:[10.1029/2005JA011436](https://doi.org/10.1029/2005JA011436)
- M.I. Desai, G.M. Mason, J.R. Dwyer, J.E. Mazur, C.W. Smith, R.M. Skoug, Acceleration of ^3He nuclei at interplanetary shocks. *Astrophys. J.* **553**(1), L89–L92 (2001)
- J.R. Dwyer, G.M. Mason, J.E. Mazur, J.R. Jokipii, T.T. von Rosenvinge, R.P. Lepping, Perpendicular transport of low energy corotating interaction region-associated nuclei. *Astrophys. J.* **490**, L115–L118 (1997)
- H. Ewald, H. Liebl, Der Astigmatismus des Toroidkondensators. *Z. Naturforschung* **10a**, 872–876 (1955)
- C.J. Farrugia et al., A reconnection layer associated with a magnetic cloud. *Adv. Space Res.* **28**(5), 759 (2001)
- C.J. Farrugia et al., Wind and ACE observations during the great flow of 1–4 May 1998: Relation to solar activity and implications for the magnetosphere. *J. Geophys. Res.* **107**(A9), SSH 3–1 (2002). doi:[10.1029/2001JA000188](https://doi.org/10.1029/2001JA000188)
- C.J. Farrugia et al., Evolution of magnetic clouds from 0.3 AU to 1 AU: A joint Helios-Wind Investigation. *Sol. Wind* **11**, 723–726 (2005a)
- C.J. Farrugia et al., Cross-correlation of interplanetary parameters for large (~ 450 Re) separation: Dependence on interplanetary structure. *Sol. Wind* **11**, 719 (2005b)

- C.J. Farrugia et al., Interplanetary coronal mass ejection and ambient interplanetary magnetic field correlations during the Sun–Earth connection events of October–November 2003. *J. Geophys. Res.* **110** (2005c). doi:[10.1029/2004JA10968](https://doi.org/10.1029/2004JA10968)
- T.G. Forbes et al., CME theory and models. *Space Sci. Rev.* **123**, 251–302 (2006)
- A.B. Galvin, F.M. Ipavich, G. Gloeckler, D. Hovestadt, S. Bame, B. Klecker, M. Scholer, B.T. Tsurutani, Solar wind iron charge states preceding a driver plasma. *J. Geophys. Res.* **92**(A11), 12069–12081 (1987)
- A.B. Galvin, G. Gloeckler, F.M. Ipavich, C.M. Shafer, J. Geiss, K. Ogilvie, Solar wind composition measurements by the Ulysses SWICS experiment during transient solar wind flows. *Adv. Space Res.* **13**(6), 75–78 (1993)
- A.B. Galvin, Minor ion composition in CME-related solar wind, in *Coronal Mass Ejections, Geophysical Monograph* 99, ed. by N. Crooker, J.A. Joselyn, J. Feynman (American Geophysical Union, 1997), pp. 253–260
- A.B. Galvin, J.L. Kohl, Whole Sun Month at solar minimum: An introduction. *J. Geophys. Res.* **104**(A5), 9673–9678 (1999). doi:[10.1029/1999JA900008](https://doi.org/10.1029/1999JA900008)
- A.G. Ghielmetti, H. Balsiger, R. Baenninger, P. Eberhardt, J. Geiss, D.T. Young, Calibration system for satellite and rocket-borne ion mass spectrometers in the energy range from 5 eV/charge to 100 keV/charge. *Rev. Sci. Instrum.* **54**(4), 425–436 (1983)
- S.E. Gibson, Global solar wind structure from solar minimum to solar maximum: Sources and evolution. *Space Sci. Rev.* **97**(1/4), 69 (2001)
- G. Gloeckler, J. Geiss, H. Balsiger, P. Bedini, J.C. Cain, J. Fischer, L. Fisk, A.B. Galvin, F. Gliem, D.C. Hamilton, J.V. Hollweg, F.M. Ipavich, R. Joos, S. Livi, R. Lundgren, J.F. McKenzie, U. Mall, K.W. Ogilvie, F. Ottens, W. Rieck, E.O. Tums, R. von Steiger, W. Weiss, B. Wilken, The solar wind ion composition spectrometer. *Astron. Astrophys. Suppl. Ser.* **92**, 267 (1992)
- G. Gloeckler et al., The solar wind and suprathermal ion composition investigation on the WIND spacecraft. *Space Sci. Rev.* **71**, 79–124 (1995)
- G. Gloeckler, J. Geiss, Interstellar and inner source pickup ions observed by SWICS on Ulysses. *Space Sci. Rev.* **86**, 127 (1998)
- G. Gloeckler, P. Bedini, P. Bochsler, L.A. Fisk, J. Geiss, F.M. Ipavich, J. Cain, J. Fischer, R. Kallenbach, J. Miller, O. Tums, R. Wimmer, Investigation of the composition of solar and interstellar matter using solar wind and pickup ion measurements with SWICS and SWIMS on the ACE spacecraft. *Space Sci. Rev.* **86**, 497 (1998)
- G. Gloeckler et al., Unusual composition of the solar wind in the 2–3 May 1998 CME observed with SWICS on ACE. *Geophys. Res. Lett.* **26**(2), 157 (1999)
- G. Gloeckler, L.A. Fisk, L.J. Lanzerotti, Acceleration of solar wind and pickup ions by shocks, in *Proceedings of the Solar Wind 11 / SOHO 16, “Connecting Sun and Heliosphere” Conference* (ESA SP-592), published on CDROM, 17, 2005a
- G. Gloeckler, L.A. Fisk, L.J. Lanzerotti, Pickup ions upstream and downstream of shocks. *AIP Conf. Proc.* **781**, 252–260 (2005b). doi:[10.1063/1.2032705](https://doi.org/10.1063/1.2032705)
- H. Goldstein, On the field configuration in magnetic clouds, in *Solar Wind Five*. NASA Conf. Publ. 2280, 1983, p. 731
- M. Gonin, R. Kallenbach, P. Bochsler, A. Buergi, Charge exchange of low energy particles passing through thin carbon foils: Dependence on foil thickness and charge state yields of Mg, Ca, Ti, Cr and Ni. *Nucl. Instr. Methods B* **101**, 313–320 (1995)
- M. Hellsing, L. Karlsson, H.-O. Andren, H. Norden, Performance of a microchannel plate ion detector in the energy range 3–25 keV. *J. Phys. E.: Sci. Instrum.* **18**, 920–925 (1985)
- D. Hovestadt, M. Hilchenbach, A. Buergi, B. Klecker, P. Laeverenz, M. Scholer, H. Gruenwaldt, W.I. Axford, S. Livi, E. Marsch, B. Wilken, H.P. Winterhoff, F.M. Ipavich, P. Bedini, M.A. Coplan, A.B. Galvin, G. Gloeckler, P. Bochsler, H. Balsiger, J. Fischer, J. Geiss, R. Kallenbach, P. Wurz, K.-U. Reiche, F. Gliem, D.L. Judge, H.S. Ogawa, K.C. Hsieh, E. Moebius, M.A. Lee, G.G. Managadze, M.I. Verigin, M. Neugebauer, CELIAS: The charge, element, and isotope analysis system for SOHO. *Sol. Phys.* **162**, 441 (1995)
- R. Howard et al., Sun Earth Connection Coronal and Heliospheric Investigation (SECCHI) (2007, this issue)
- Q. Hu, B.U.O. Sonnerup, Reconstruction of magnetic clouds in the solar wind: Orientation and configuration. *J. Geophys. Res.* **107** (2002). doi:[10.1029/2001JA000293](https://doi.org/10.1029/2001JA000293)
- A.J. Hundhausen, The origin and propagation of coronal mass ejections, in *Proc. 6th Int'l. Solar Wind Conf.*, ed. by V.J. Pizzo, T.E. Holzer, D.G. Sime (NCAR Technical Note NCAR/TN-306+Proc.), 1988, 1, 131
- L. Janoo, C.J. Farrugia, R.B. Torbert, J.M. Quinn et al., Field and flow perturbations in the October 18–19, 1995, magnetic cloud. *J. Geophys. Res.* **103**, 17249 (1998)
- S.W. Kahler, N.R. Sheeley Jr., R.A. Howard, D.J. Michels, M.J. Koomen, R.E. McGuire, T.T. von Rosenvinge, D.V. Reames, Associations between coronal mass ejections and solar energetic proton events. *J. Geophys. Res.* **89**, 9683–9693 (1984)

- M. Kaiser, T.A. Kucera, J.M. Davila, O.C. St. Cyr, The STEREO mission: An overview. *Space Sci. Rev.* **(2007, this issue)**. doi:[10.1007/s11214-007-9277-0](https://doi.org/10.1007/s11214-007-9277-0)
- R. Karrer, Ion-Optical Calibration of STEREO/PLASTIC, Ph.D. Dissertation, University of Bern, 2007
- J. Kawata, K. Ohya, I. Mori, A Monte Carlo simulation of ion-induced kinetic electron emission with a stochastic excitation of electrons in solids. *Jpn. J. Appl. Phys.* **30**, 3510–3515 (1991), doi:[10.1143/JJAP.30.3510](https://doi.org/10.1143/JJAP.30.3510)
- B. Klecker et al., Energetic particle observations. *Space Sci. Rev.* **123**, 217–250 (2006). doi:[10.1007/s11214-006-9018-9](https://doi.org/10.1007/s11214-006-9018-9)
- K.-L. Klein, G. Trottet, The origin of solar energetic particle events: Coronal acceleration versus shock wave acceleration. *Space Sci. Rev.* **95**, 215–225 (2001)
- Y.-K. Ko, L.A. Fisk, G. Gloeckler, J. Geiss, Limitations on suprathermal tails of electrons in the lower solar corona. *Geophys. Res. Lett.* **23**, 2785–2788 (1996)
- Y.-K. Ko, J. Geiss, G. Gloeckler, On the differential ion velocity in the inner solar corona and the observed solar wind ionic charge states. *J. Geophys. Res.* **103**(A7), 14539–14546 (1998). doi:[10.1029/98JA00763](https://doi.org/10.1029/98JA00763)
- Y.-K. Ko, J.C. Raymond, T.H. Zurbuchen, P. Riley, J.M. Raines, L. Strachan, Abundance variation at the vicinity of an active region and the coronal origin of the slow solar wind. *Astrophys. J.* **646**, 1275–1287 (2006)
- N. Koshida, M. Hosobuchi, Energy distribution of output electrons from a microchannel plate. *Rev. Sci. Instrum.* **56**(7), 1329–1331 (1985)
- H. Kucharek, E. Möbius, W. Li, C.F. Farrugia, M.A. Popecki, A.B. Galvin, B. Klecker, M. Hilchenbach, P. Bochsler, On the source and acceleration of energetic He+: A long-term observation with ACE/SEPICA. *J. Geophys. Res.* **108**(A10), 8040 (2003). doi:[10.1029/2003JA009938](https://doi.org/10.1029/2003JA009938)
- M. Lampton, C.W. Carlson, Low-distortion resistive anodes for two-dimensional position-sensitive MCP systems. *Rev. Sci. Instrum.* **50**(9), 1093–1097 (1979)
- M. Leitner, C.J. Farrugia, C. Möstl, K.W. Ogilvie, A.B. Galvin, R. Schwenn, H.K. Biernat, Consequences of the force-free model of magnetic clouds for their heliospheric evolution. *J. Geophys. Res.* **112**, A06113 (2007). doi:[10.1029/2006JA011940](https://doi.org/10.1029/2006JA011940)
- S.T. Lepri et al., Iron charge distribution as an identifier of interplanetary coronal mass ejections. *J. Geophys. Res.* **106**(A12), 29231–29238 (2001)
- S.T. Lepri, T. Zurbuchen, Iron charge state distributions as an indicator of hot ICMEs: Possible sources and temporal and spatial variation during solar maximum. *J. Geophys. Res.* **109**(A1), A01112 (2004)
- B.C. Low, Coronal mass ejections and magnetic helicity, in *Proc. of the Third SOHO Workshop—Solar Dynamic Phenomena and Solar Wind Consequences*. ESA SP-373, 1994, p. 123
- B.S. Lüthi, Angular scattering of ions in thin carbon foils, simulations, measurements, and predictions for the PLASTIC instrument on STEREO, Diplomarbeit, University of Bern, 2003
- J.G. Luhmann et al., STEREO IMPACT investigation goals, measurements, and observations overview. *Space Sci. Rev.* (2007, this issue). doi:[10.11007/s11214-007-9170-x](https://doi.org/10.11007/s11214-007-9170-x)
- S. Lundquist, Magneto-hydrostatic fields. *Arkiv fuor fysik* **2**, 361–365 (1950)
- K. Marubashi, Structure of interplanetary magnetic clouds and their solar origins. *Adv. Space Res.* **6**(6) 335–338 (1986). doi:[10.1016/0273-1177\(86\)90172-9](https://doi.org/10.1016/0273-1177(86)90172-9)
- G. Mason, J.E. Mazur, J.R. Dwyer, New spectral and abundance features of interplanetary heavy ions in corotating interaction regions. *Astrophys. J.* **486**, L149–L152 (1997)
- G.M. Mason et al., Origin, injection and acceleration of CIR particles: observations. *Space Sci. Rev.* **89**, 327–367 (1999a)
- G.M. Mason, J.E. Mazur, J.R. Dwyer, 3He enhancements in large solar energetic particle events. *Astrophys. J.* **525**(2), L133–L136 (1999b)
- J.R. Mazur, G.M. Mason, R.A. Mewaldt, Charge states of energetic particles from corotating interaction regions as constraints on their source. *Astrophys. J.* **566**, 555–561 (2002). doi:[10.1086/337989](https://doi.org/10.1086/337989)
- P. Mazzotta, G. Mazzitelli, S. Colafrancesco, N. Vittorio, Ionization balance for optically thin plasmas: rate coefficients for all atoms and ions of the elements H to NI. *Astron. Astrophys. Suppl. Ser.* **133**, 403–409 (1998)
- W. Meckbach, G. Braunstein, N. Arista, Secondary-electron emission in the backward and forward directions from thin carbon foils traversed by 25–250 keV proton beams. *J. Phys. B: At. Mol. Phys.* **8**, L344–L349 (1975)
- E. Möbius, D. Hovestadt, B. Klecker, M. Scholer, G. Gloeckler, F.M. Ipavich, Direct observation of He+ pick-up ions of interstellar origin in the solar wind. *Nature* **318**, 426 (1985)
- E. Möbius, D. Rucinski, M.A. Lee, P. Isenberg, Decreases in the antisunward flux of interstellar pickup He+ associated with radial interplanetary magnetic field. *J. Geophys. Res.* **103**, 257 (1998)
- E. Möbius, M. Popecki, B. Klecker, L.M. Kistler, A. Bogdanov, A.B. Galvin et al., Energy dependence of the ionic charge state distribution during the November 1997 solar energetic particle event. *Geophys. Res. Lett.* **26**, 145–148 (1999)

- E. Möbius, D. Morris, M.A. Popecki, B. Klecker, L.M. Kistler, A.B. Galvin, Charge states of energetic (~ 0.5 MeV/n) ions in corotating interaction regions at 1 AU and implications on source populations. *Geophys. Res. Lett.* **29**(2), (2002). doi:[10.1029/2001GL013410](https://doi.org/10.1029/2001GL013410)
- M. Neugebauer, R. Goldstein, Particle and field signatures of coronal mass ejections in the solar wind, in *Coronal Mass Ejections, Geophysical Monograph 99*, ed. by N. Crooker, J.A. Joselyn, J. Feynman (American Geophysical Union, 1997), pp. 245–251
- R.O. Neukomm, Composition of coronal mass ejections derived with SWICS/Ulysses, Ph.D. dissertation, University of Bern, 1998
- M. Oetliker, Response of a passivated implanted planar silicon (PIPS) detector for heavy ions with energies between 25 and 360 keV. *Nucl. Instrum. Methods Phys. Res. A* **337**, 145–148 (1993)
- G. Poletto, S.T. Suess, D.A. Biesecker, R. Esser, G. Gloeckler, Y.-K. Ko, T.H. Zurbuchen, Low-latitude solar wind during the fall 1998 SOHO-Ulysses quadrature. *J. Geophys. Res.* **107**(A10), 1300 (2001). doi:[10.1029/2001JA000275](https://doi.org/10.1029/2001JA000275)
- M.A. Popecki, T.H. Zurbuchen, R.M. Skoug, C.W. Smith, A.B. Galvin, M. Lee, E. Möbius, A.T. Bogdanov, G. Gloeckler, S. Hefti, L.M. Kistler, B. Klecker, N.A. Schwadron, Simultaneous high Fe charge state measurements by solar energetic particle and solar wind instruments, AIP Conference Proceedings, September 15, 2000, vol. 528, *Acceleration and Transport of Energetic Particles Observed in the Heliosphere: ACE 2000 Symposium*, 2000, pp. 139–142
- M.A. Popecki, Observations of energy-dependent charge states of solar energetic particles. *Geophys. Monogr. Ser.* **165**, 127–135 (2006)
- D.V. Reames, Particle acceleration at the sun and in the heliosphere. *Space Sci. Rev.* **90**, 413–491 (1999)
- P. Riley et al., Evidence of post-eruption reconnection associated with coronal mass ejections in the solar wind. *Astrophys. J.* **578** (2002)
- P. Riley, N.U. Crooker, Kinematic treatment of coronal mass ejection evolution in the solar wind. *Astrophys. J.* **600**, 1035–1042 (2004)
- P. Riley, Modeling corotating interaction regions: from the Sun to 1 AU. *J. Atmospheric Sol.-Terr. Phys.* **69**, 32–42 (2007). doi:[10.1016/j.jastp.2006.06.008](https://doi.org/10.1016/j.jastp.2006.06.008)
- I.G. Richardson, H.V. Cane, Identification of interplanetary coronal mass ejections at 1 AU using multiple solar wind plasma composition anomalies. *J. Geophys. Res.* **109**, A09104 (2004a). doi:[10.1029/2004JA010598](https://doi.org/10.1029/2004JA010598)
- I.G. Richardson, H.V. Cane, The fraction of interplanetary coronal mass ejections that are magnetic clouds: Evidence for a solar cycle variation. *Geophys. Res. Lett.* **31**, L18804 (2004b). doi:[10.1029/2004GL020958](https://doi.org/10.1029/2004GL020958)
- S.M. Ritzau, R.A. Baragiola, Electron emission from carbon foils induced by keV ions. *Phys. Rev. B* **58**, 2529–2538 (1998)
- L. Saul, E. Möbius, P. Isenberg, P. Bochsler, On pitch-angle scattering rates of interstellar pickup ions as determined by in situ measurement of velocity distributions. *Astrophys. J.* **655**, 672–677 (2007)
- M. Steinacher, F. Jost, U. Schwab, A modern and fully automated calibration system for space ion mass spectrometers. *Rev. Sci. Instrum.* **66**(8), 4180–4187 (1995)
- E. Steinbauer, P. Bauer, M. Geretschlaeger, G. Bortels, J.P. Biersack, P. Burger, Energy resolution of silicon detectors—approaching the physical limit. *Nucl. Instrum. Methods in Phys. Res. B* **85**, 642–649 (1994)
- G.E. Thomas, The interstellar wind and its influence on the interplanetary environment. *Ann. Rev. Earth Planet. Sci.* **6**, 173 (1978)
- A.J. Tylka et al., Shock geometry, seed populations, and the origin of variable elemental composition at high energies in large gradual solar particle events. *Astrophys. J.* **625**, 474–495 (2005)
- B.J. Vasquez, C.J. Farrugia et al., The nature of fluctuations on directional discontinuities inside solar ejecta: Wind observations and theoretical interpretation. *J. Geophys. Res.* **106**, 29283 (2001)
- T.T. von Rosenvinge, H.V. Cane, Solar energetic particles: An overview, in *Solar Eruptions and Energetic Particles*, ed. by N. Gopalswamy, R.A. Mewaldt, J. Torsti. AGU Monogr. Ser. **165**, 103–114 (2006)
- G. Wehner, [De]Energieverteilung der von 2, 5, 10 und 15 keV He- und Ar-Ionen an Molybdaen asugeloesten electronen. *Z. Physik A Hadrons Nucl.*, 439–442 (1966). doi:[10.1007/BF01326441](https://doi.org/10.1007/BF01326441)
- R.F. Wimmer-Schweingruber, R. von Steiger, R. Paerli, Solar wind stream interfaces in corotating interaction regions: SWICS/Ulysses results. *Geophys. Res.* **102**, 17407–17417 (1997)
- R.F. Wimmer-Schweingruber, R. v. Steiger, J. Geiss, G. Gloeckler, F.M. Ipavich, B. Wilken, O⁵⁺ in the high-speed streams: SWICS/Ulysses results. *Space Sci. Rev.* **85**, 387–396 (1998)
- R.F. Wimmer-Schweingruber, R. v. Steiger, R. Paerli, Solar wind stream interfaces in corotating interaction regions: New SWICS/Ulysses results. *Geophys. Res.* **104**, 9933–9945 (1999)
- R.F. Wimmer-Schweingruber, The composition of the solar wind. *Adv. Space Res.* **3**(0), 23–32 (2002)
- R.F. Wimmer-Schweingruber, Coronal mass ejections, a personal workshop summary. *Space Sci. Rev.* **123**, 471–480 (2006)

- R.F. Wimmer-Schweingruber et al., Understanding interplanetary coronal mass ejection signatures. *Space Sci. Rev.* **123**, 177–216 (2006)
- H. Wollnik, T. Matsuo, H. Matsuda, The electrostatic potential in a toroidal condenser. *Nucl. Instrum. Methods* **102**, 13–17 (1972)
- D.T. Young, S.J. Bame, M.F. Thomsen, R.H. Martin, J.L. Burch, J.A. Marshall, B. Reinhard, 2π -radian field-of-view toroidal electrostatic analyzer. *Rev. Sci. Instrum.* **59**(5), 743–751 (1988)
- D.T. Young, J.A. Marshall, J.L. Burch, S.J. Bame, R.H. Martin, A 360° field-of-view toroidal ion composition analyzer using time-of-flight, in *Yosemite Conference on Outstanding Problems in Solar System Plasma Physics: Theory and Instrumentation*, 1989, pp. 171–176
- T.H. Zurbuchen, I.G. Richardson, In-situ solar wind and magnetic field signatures of interplanetary coronal mass ejections. *Space Sci. Rev.* **123**, 31–43 (2006)

S/WAVES: The Radio and Plasma Wave Investigation on the STEREO Mission

J.L. Bougeret · K. Goetz · M.L. Kaiser · S.D. Bale · P.J. Kellogg · M. Maksimovic · N. Monge · S.J. Monson · P.L. Astier · S. Davy · M. Dekkali · J.J. Hinze · R.E. Manning · E. Aguilar-Rodriguez · X. Bonnin · C. Briand · I.H. Cairns · C.A. Cattell · B. Cecconi · J. Eastwood · R.E. Ergun · J. Fainberg · S. Hoang · K.E.J. Huttunen · S. Krucker · A. Lecacheux · R.J. MacDowall · W. Macher · A. Mangeney · C.A. Meetre · X. Moussas · Q.N. Nguyen · T.H. Oswald · M. Pulupa · M.J. Reiner · P.A. Robinson · H. Rucker · C. Salem · O. Santolik · J.M. Silvis · R. Ullrich · P. Zarka · I. Zouganelis

Originally published in the journal Space Science Reviews, Volume 136, Nos 1–4.
DOI: [10.1007/s11214-007-9298-8](https://doi.org/10.1007/s11214-007-9298-8) © Springer Science+Business Media B.V. 2008

J.L. Bougeret · M. Maksimovic (✉) · N. Monge · P.L. Astier · S. Davy · M. Dekkali · R.E. Manning (deceased in 2002) · X. Bonnin · C. Briand · B. Cecconi · S. Hoang · A. Lecacheux · A. Mangeney · Q.N. Nguyen · P. Zarka · I. Zouganelis
LESIA, UMR CNRS 8109, Observatoire de Paris, 92195 Meudon, France
e-mail: milan.maksimovic@obspm.fr

K. Goetz · P.J. Kellogg · S.J. Monson · J.J. Hinze · C.A. Cattell · J.M. Silvis
School of Physics and Astronomy, University of Minnesota, Minneapolis, USA

M.L. Kaiser · J. Fainberg · R.J. MacDowall · C.A. Meetre · M.J. Reiner
NASA, Goddard Space Flight Center, Greenbelt, MD, USA

S.D. Bale · E. Aguilar-Rodriguez · J. Eastwood · K.E.J. Huttunen · S. Krucker · M. Pulupa · C. Salem · R. Ullrich
Space Sciences Laboratory, University of California, Berkeley, USA

S.D. Bale · M. Pulupa
Physics Department, University of California, Berkeley, USA

I.H. Cairns · P.A. Robinson
School of Physics, University of Sydney, Sydney, NSW 2006, Australia

R.E. Ergun
Laboratory for Atmospheric and Space Physics, University of Colorado, Boulder, USA

W. Macher · T.H. Oswald · H. Rucker
Space Research Institute, Austrian Academy of Sciences, Graz, Austria

X. Moussas
Section of Astrophysics, Astronomy and Mechanics, Department of Physics, University of Athens, Athens, Greece

M.J. Reiner
The Catholic University of America, Washington, DC, USA

Abstract This paper introduces and describes the radio and plasma wave investigation on the STEREO Mission: STEREO/WAVES or S/WAVES. The S/WAVES instrument includes a suite of state-of-the-art experiments that provide comprehensive measurements of the three components of the fluctuating electric field from a fraction of a hertz up to 16 MHz, plus a single frequency channel near 30 MHz. The instrument has a direction finding or goniopolarimetry capability to perform 3D localization and tracking of radio emissions associated with streams of energetic electrons and shock waves associated with Coronal Mass Ejections (CMEs). The scientific objectives include: (i) remote observation and measurement of radio waves excited by energetic particles throughout the 3D heliosphere that are associated with the CMEs and with solar flare phenomena, and (ii) in-situ measurement of the properties of CMEs and interplanetary shocks, such as their electron density and temperature and the associated plasma waves near 1 Astronomical Unit (AU). Two companion papers provide details on specific aspects of the S/WAVES instrument, namely the electric antenna system (Bale et al., Space Sci. Rev., 2007) and the direction finding technique (Cecconi et al., Space Sci. Rev., 2007).

Keywords Solar radioastronomy · Space instrumentation

1 Introduction

The measurement of fluctuating electric fields at a spacecraft in interplanetary space using simple monopole or dipole antenna systems gives access to both remotely produced electromagnetic waves (radio astronomy) as well as electromagnetic and electrostatic waves produced in the vicinity of the spacecraft.

Long wavelength radio astronomy covers the range of decametric, hectometric and kilometric wavelengths (or radio frequencies below roughly 30 MHz), which are usually not well detected from ground-based radio observatories without perturbations due to the reflection of radiation from Earth's ionosphere. At these wavelengths, a rich variety of radio bursts of solar origin are observed that trace particles produced by energetic phenomena through the solar corona and interplanetary medium. Since the late 1960's, these radio emissions have been observed and studied, primarily by numerous single spacecraft missions. These radio emissions are produced by non-thermal radiation mechanisms that are still incompletely understood. The STEREO mission will provide the first dedicated stereoscopic observations of remotely generated solar radio emissions to elucidate their origin.

In-situ observation of waves can yield valuable information on processes occurring throughout the heliosphere. Of special importance are processes which include the generation of radio waves, cascade of plasma turbulence, reconnection at flux-tube boundaries, etcetera.

The accurate measurement of the weak noise spectrum near the local plasma frequency (plasma line) can yield a robust measurement of the electron density and temperature, e.g., when a Coronal Mass Ejection (hereafter CME) crosses the spacecraft. This measurement

O. Santolik

Faculty of Mathematics and Physics, Charles University, Prague, Czech Republic

O. Santolik

IAP/CAS, Prague, Czech Republic

technique, called Quasi-thermal noise spectroscopy (Meyer-Vernet and Perche 1989), is independent of the spacecraft potential even when the spacecraft environment is disturbed by the passage of a CME.

Radio and plasma wave investigations are currently part of the payload of several spacecraft in the earth environment and of interplanetary or planetary probes. They provide unique information that is complementary to particle and other in-situ measurements. In particular, the Ulysses, WIND, and CASSINI spacecraft are carrying similar instruments, portions of which have been designed and built by the same institutions as S/WAVES (Stone et al. 1992; Bougeret et al. 1995; Gurnett et al. 2004). Both Ulysses and WIND are spinning spacecraft, while CASSINI and STEREO are three-axis stabilized. The instruments on the latter two spacecraft use similar techniques to determine source direction, though the S/WAVES measurement techniques are more sophisticated. These methods of analysis are described in more detail in a companion paper devoted to direction finding of radio sources from three-axis stabilized spacecraft, such as STEREO (Cecconi et al. 2007). The STEREO antenna system used for making these measurements is described in the companion paper by Bale et al. (2007). The implications of these radio and plasma wave measurements for theoretical studies and modeling are summarized in the paper by Aschwanden et al. (2006).

In Sect. 2, we summarize the S/WAVES scientific objectives and provide the scientific background relevant for the radio stereoscopic observations that will be made during the STEREO mission. In Sect. 3, we give a brief summary of the direction-finding method as well as the quasi-thermal noise spectroscopy method. The S/WAVES suite of instruments is described in detail in Sect. 4 and specific technical aspects, including Electro-Magnetic Cleanliness, inter-communication with other STEREO instruments and calibration, are presented in Sect. 5. Scientific operations are outlined in Sect. 6 and the Education and Public Outreach plan is summarized in Sect. 7. Finally, Sect. 8 provides an overall summary and conclusion.

2 Scientific Objectives

2.1 Summary of S/WAVES Science Objectives

The primary S/WAVES science goals are to:

- Remotely track and probe CME-driven shocks and flare electrons at high frequency and time resolution from their genesis in the low corona to their interaction with the terrestrial magnetosphere, to establish the link between the EUV and coronagraph images and the in-situ CME and particle observations.
- Measure the spatial extent and structure of CME-driven shocks and flare- and CME-associated electron beams.
- Make remote and in-situ measurements of solar radio sources that may provide a deeper and more comprehensive understanding of the mechanisms that generate type II (CME) and type III (flare) radio bursts.
- Measure solar wind electron plasma density and temperature in regions of cold, dense plasma within CME-associated magnetic clouds using quasi-thermal noise techniques.
- Study the role of plasma microphysics in CME-driven shocks.

2.2 Remote Sensing of Type II (CME-Associated) and Type III (Flare-Associated) Solar Radio Emissions

CMEs, once ejected from the Sun (after, for example, large filament eruptions) propagate through the corona and interplanetary medium. When directed towards the Earth, they can affect the space weather environment in two ways: by accelerating solar energetic particles (SEPs) near the Sun and later by the direct encounter of the CME material and its associated driven shock with the Earth's magnetosphere. Since radio emissions are often generated at CME-driven shocks, these radio observations provide an important means of tracking CMEs through the corona and the interplanetary medium, a crucial capability for space weather forecasting, as discussed in Sect. 6.2 (Gopalswamy et al. 2001b; Schwenn et al. 2005).

Radio emissions associated with the propagation of a CME are called *type II radio bursts or emissions*. The mechanism responsible for the generation of these radio emissions at the fundamental and harmonic of the local plasma frequency and the relevant in-situ observations are described in Sects. 2.3 and 2.4. Because the interplanetary density decreases with increasing heliocentric distance, the type II emissions decrease in frequency as the CME/shock propagates through the corona and the interplanetary medium. An example of such frequency drift is shown on the dynamic spectrum of Fig. 1a.

Remote measurements of the frequency drift of these type II emissions provide a frequency-time track of the CME/shock through interplanetary space. In the example displayed in Fig. 1, which was an Earth-directed (halo) CME event, the diffuse radio emissions were continuously observed as the CME propagated from the solar corona to Earth. Once a heliospheric density model is assumed, this frequency-time track can be converted

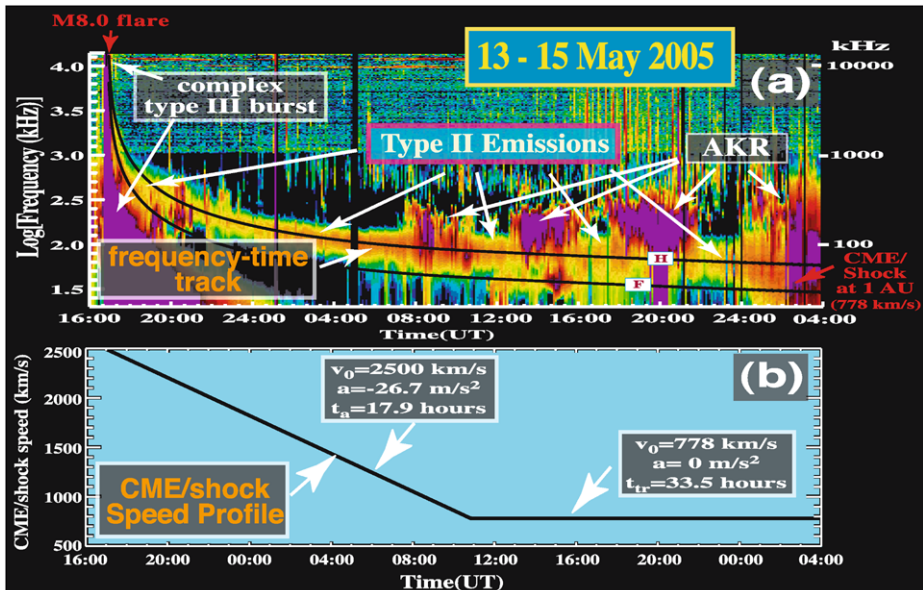


Fig. 1 (a) Dynamic spectrum from WIND/WAVES showing the frequency-drifting type II radio emissions generated by a halo CME as it propagated from the Sun to Earth between May 13 and 15, 2005. The *black curves* are the frequency-time tracks of the frequency-drifting type II radiation, generated at the fundamental and harmonic of the plasma frequency. (b) Speed profile of the corresponding CME derived from the frequency-time track in (a), assuming a $1/r^2$ falloff of the interplanetary plasma density

into a distance–time track that describes the spatial progress of the propagating CME. The CME/shock speed profile, such as shown in Fig. 1b, can then be derived directly from this distance–time track, showing that the CME initially decelerated at a rate of 27 m/s^2 in this particular case.

Until the recent advent of heliospheric imagers, this model-dependent approach has been the most efficient way for indirectly tracking CMEs. This method has been used to reconstruct the speed and distance–time profiles describing the spatial progress of CMEs through interplanetary space (Reiner et al. 1998a, 2001a, 2007b; Dulk et al. 1999). On STEREO, such remote radio observations will provide overlapping coverage with the SECCHI white-light images of CMEs, including in the critical spatial region between 60 and 100 solar radii (Rs) where significant changes in CME dynamics are expected as the CME moves from the solar corona to the interplanetary solar wind.

A shortcoming of remote frequency–time tracking is that the coronal and interplanetary density profiles, required to convert to spatial information, are dynamic and typically not known *a priori*. S/WAVES, however, can overcome this difficulty by exploiting the direction finding capabilities on both spacecraft. The 3D spatial location of a given radio source can be directly deduced using radio triangulation, i.e. from the intersection of the measured lines of sight from the two STEREO spacecraft, without any assumptions for the interplanetary density profile (see Sects. 3.3 and 3.4 for details). The two spacecraft triangulations, measured at a series of consecutive frequencies, allow direct spatial tracking of a given solar radio source and, in the case of a type II burst, of the associated CME/shock.

Comparison of the 3D locations of the radio sources with the corresponding white-light CME, provided by SECCHI on STEREO (Howard et al. 2008) and SOHO LASCO (Brueckner et al. 1995), will provide new information about the spatial relationship between the CME and its associated driven shock, and about conditions favorable to the generation of these radio emissions (Reiner et al. 1998b, 2005).

The S/WAVES radio observations will provide a better understanding of the complex features commonly observed for type II radio emissions. In addition to the more continuous and diffuse emissions shown in Fig. 1, type II radiation consisting of intermittent, narrow bands of emissions that can often be nearly as intense as the radiation from solar type III emissions, have often been reported. Some of the intense, complex type II emission features represent signatures of interactions between two propagating CMEs (Gopalswamy et al. 2001a; Reiner et al. 2001b). An example of enhanced radio emissions resulting from such interactions is shown in Fig. 2. The ability of S/WAVES to view these emissions from two vantage points and to triangulate the actual radio source spatial locations, which can then be directly compared with the stereo views of the associated white-light CME, will provide a better understanding of the origin and nature of these unusual type II radiation features. Analysis of the STEREO observations will also provide important new information on the beaming patterns of the type II emissions and on the propagation characteristics of radiation through the interplanetary plasma. The analysis and interpretation of these observations will be greatly facilitated by complementary modeling efforts (Knock and Cairns 2005; Aschwanden et al. 2006). Finally, these STEREO observations of the type II radio signatures may provide new insights into the origin and nature of solar energetic particles (SEPs) (Gopalswamy et al. 2002, 2005).

Although the same plasma emission mechanism that generates type II radio emissions also generates type III radio bursts, the origin of these latter bursts is quite different. Type III radio bursts are produced by streams of suprothermal electrons ejected onto open magnetic field lines during solar flares. These electrons, due to their small gyroradii, are constrained to follow the Parker spiral magnetic field lines through interplanetary space, generating intense

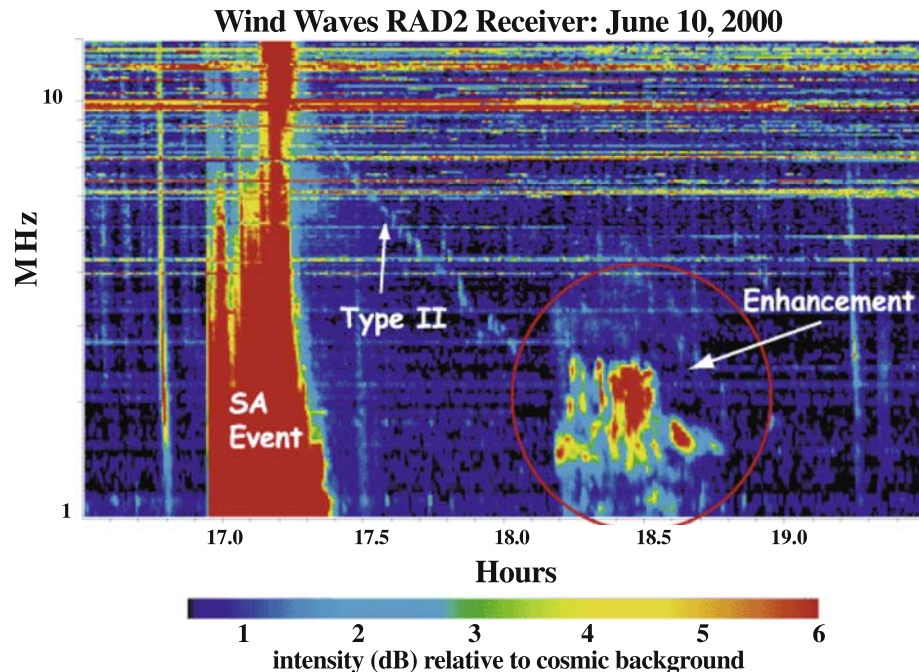
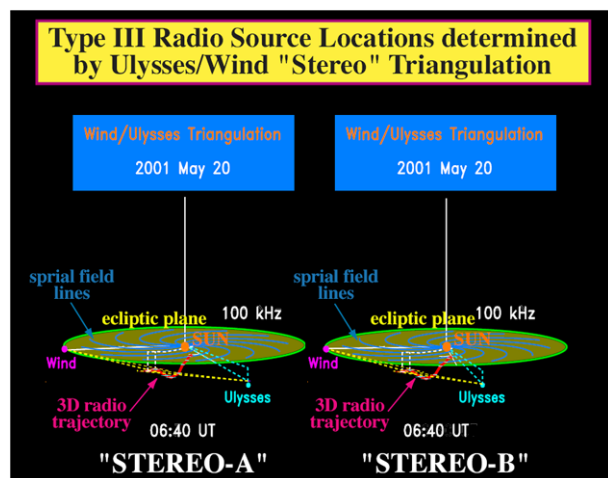


Fig. 2 Enhanced type II radiation due to the interactions between two CMEs

Fig. 3 (Color online) Stereo image of a type III burst trajectory deduced by triangulation from the WIND and Ulysses spacecraft for a solar type III event observed on May 20, 2001 at about 06:40 UT. The yellow dashed lines are the lines of sight to the radio source from the Ulysses and WIND spacecraft, whose intersection gives the 3D location of the radio source at each observing frequency. (To view the 3D stereo image, relax the eyes (by focusing at a distant object through the page) and allow the two images to merge into a third image at the center of the page, which will be seen in 3D)



radio emissions with their passage. The locations of the radio sources for the type III bursts at different frequencies, therefore, trace the global structure of the interplanetary magnetic field. An example of a 3D trajectory obtained from two spacecraft triangulation for a type III radio burst is shown in Fig. 3.

The orbital geometry of STEREO is ideal for routinely performing such triangulation measurements. The triangulation is expected to work best when the angular separation of the STEREO spacecraft is between about 40 and 60 degrees. The stereo views, as shown in Fig. 3, provide an opportunity to measure the beaming patterns of the type III radiation, to deduce the intrinsic characteristics of the type III radio sources and to study the effects of propagation and scattering of the radiation in the interplanetary medium (Hoang et al. 1997; Reiner et al. 1998c). These observations are important for providing a deeper understanding of the emission mechanism, as discussed in Sect. 2.4.

STEREO/WAVES observations will also provide a new understanding of the *complex type III-like bursts* (formerly called SA events) that are nearly always associated with major flare events involving CMEs (Cane et al. 1981; Bougeret et al. 1998; Reiner et al. 2000). Reiner and Kaiser (1999) pointed out the unusual fine-structure characteristics of these complex type III-like emissions below about 10 MHz, such as shown in Figs. 1 and 2. The STEREO observations, performed simultaneously from different spatial viewpoints, will give a better understanding of the nature and origin of these unusual radiation characteristics.

Solar *type III radio storms*, which originate in quasi-stable active regions, are long-lasting, quasi-continuous events consisting of thousands of weak type III radio bursts per day. Single spacecraft observations of these type III storms have used dynamic parallax to deduce the 3D locations of the radio sources (Bougeret et al. 1984). STEREO independently determines the source locations with two spacecraft triangulation. Information on the propagation and scattering effects of the interplanetary plasma on the type III radiation are obtained from the comparison of the type III source locations using these two complementary techniques. It has recently been discovered that type III radio storms are weakly circularly polarized (Reiner et al. 2007a). These observations were used to deduce the radial dependence of the solar magnetic fields along the path of electron beams. By simultaneously providing the corresponding 3D beam trajectory, the STEREO observations may identify the interplanetary plasma structure associated with the magnetic field profile by revealing the corresponding density profile.

2.3 Observation of In-Situ Type II and III Source Regions

As discussed above, type II and type III radio bursts are generated by the “plasma” emission process. As shock- or flare-accelerated energetic electrons propagate in the interplanetary medium, they form beam-like (positive slope) features in phase space. These beams are thought to form by simple advection, the fast electrons running ahead of the slower ones. As this beam feature moves toward lower energies, it becomes more and more “dense” until the growth rate, which is related to the positive slope of the electron distribution function, is sufficient to excite Langmuir waves. Eventually, the beam feature falls below the solar wind thermal/suprathermal electron population. Electrons with energies between $\sim 1\text{--}10$ keV are thought to be responsible for generating the Langmuir waves, which eventually couple to propagating electromagnetic radiation. This region of unstable electron beams and Langmuir wave growth is often called the “source region” of the radio burst.

The theoretical understanding of the radiation from beams of suprathermal electrons in the solar atmosphere is based on comprehensive observations from space including both radio and in-situ observations and on energetic particle and plasma measurements (Lin et al. 1981; Robinson et al. 1993; Cairns and Robinson 1997, 1998, 1999). Type III source regions were encountered by the ISEE-3 (for, e.g., Lin et al. 1981) and WIND (for, e.g., Ergun et al. 1998) spacecraft. These earlier studies have left several questions unanswered:

- (1) What is the mechanism of coupling between Langmuir waves and radio waves?
- (2) How does the electron beam remain “unstable” over 1 AU of transit?
- (3) What are the spatial dimensions of the source and the fraction of the source volume actually emitting radiation (the so-called filling factor)?
- (4) What is the role of density fluctuations in the radio emission process?

S/WAVES observations, with 3-axis wave measurements, will allow us to take the next step in addressing these questions. The S/WAVES Time Domain Sampler (TDS) will measure the polarization state of Langmuir waves, their location within density structures (with the Low Rate Science (LRS) and Antenna Potential Monitor (APM) measurements), and their statistical properties (with the Langmuir Wave Statistics (LWS) measurements). Coordination with the IMPACT/STE instrument on STEREO (Luhmann et al. 2007) will provide important new measurements of the properties of electron beams associated with waves. In addition, combined with WIND (Bougeret et al. 1995) and ACE (Stone et al. 1998 and references therein) measurements, STEREO may provide the first spatial measurements of the source region. In its first month in orbit, STEREO has already observed at least one in-situ type III burst.

Type II radio bursts are generated upstream of fast CME-driven IP shocks. The radio emission process is fundamentally the same as for type III bursts, but beam speeds are probably lower (500 eV–1.5 keV). Type II bursts are often observed to be patchy in nature, with radio emission apparently coming from multiple sites near the shock front. However, only a few type II radio sources have been observed in-situ (Bale et al. 1999; Pulupa and Bale 2006). The first published event (Bale et al. 1999) showed a highly structured shock with radio emission coming from within a “bay” on the shock front. The STEREO spacecraft, together with WIND and ACE, will allow for the first multi-spacecraft studies of in-situ type II bursts.

2.4 Contribution of STEREO to the Theory of Radio Emission in the Interplanetary Medium

The STEREO data will constrain theories for interplanetary radio emissions using both remote observations (Aschwanden et al. 2006) and in-situ detection of plasma waves, density fluctuations, particle distributions, shock waves and other source characteristics responsible for producing the radiation. One unique aspect is the ability of S/WAVES to triangulate remote radio sources with near simultaneous Low Frequency Receiver (LFR), High Frequency Receiver (HFR) and Fixed Frequency Receiver (FFR) data from both STEREO spacecraft.

In the past decade or so, the theory of radio wave generation set out by Ginzberg and Zheleznyakov (1958), as modified by Melrose (1982), Cairns (1988) and others, has been challenged by several different mechanism. The original theory treated the conversion of electrostatic waves to electromagnetic waves by scattering from electron polarization clouds around ions, while the modified theory involves decay processes involving ion acoustic waves (Melrose 1982; Cairns 1988; Robinson and Cairns 1998a). Alternatively Kellogg (1986) pointed out that the Langmuir waves should be subject to reflection and trapping by density fluctuations, providing an alternative source of scattered Langmuir waves than non-linear processes. Finally, Field (1956) introduced the idea that conversion of electrostatic waves could take place at major density gradients, and more recently, a series of papers have considered this process for the strong density fluctuations in the solar wind (Hinkel-Lipsker et al. 1992; Yin et al. 1999; Willes and Cairns 2001). The simultaneous detection of three-axis electric waveforms of Langmuir waves and low frequency fluctuations using the Time

Domain Sampler (TDS) and Low-Rate Science (LRS) experiments will provide constraints on these processes, as described in the subsections below.

2.4.1 Low Frequency Receiver (LFR), High Frequency Receiver (HFR) and FFR Receiver Science

S/WAVES is expected to make four primary contributions to the theory of type II and III bursts using remote observations:

- (1) S/WAVES will use LFR, HFR and FFR data to test theoretical predictions for the dynamic spectra, fluxes, brightness temperatures, polarization and time-varying source locations of type II and III bursts. Increasingly sophisticated theories (Robinson and Cairns 1998a, 1998b; Knock and Cairns 2005; Cairns and Knock 2006; Aschwanden et al. 2006) were motivated by the anticipated solar wind data available from STEREO/IMPACT, S/WAVES thermal noise spectroscopy (Sect. 3.5), and other spacecraft.
- (2) FFR, LFR and FFR direction finding and triangulation analyses, combined with theory-data comparisons, will allow the role of scattering by density irregularities to be disentangled from intrinsic directivity patterns (Steinberg et al. 1984; Thejappa and MacDowall 2005). Establishing whether the directions and source sizes inferred from each spacecraft's data independently are consistent with the triangulation solution and correlating 3D information on the source (e.g., location, size, and time variations) are key to this analysis.
- (3) The relationship of burst “hotspots” to CMEs, shocks, interactions between several CMEs and solar wind structures (cf. Reiner et al. 1998a; Gopalswamy et al. 2001a; Knock and Cairns 2005) will be firmly established and quantified using S/WAVES direction-finding capabilities and data-driven solar wind models and will provide a means of testing current theories on the relationship.
- (4) Radio sources like Earth’s auroral kilometric radiation (AKR) and similar radiation from Jupiter and Saturn, which have known locations and independently measured spectra and intensity, will undergo changes in direction, angular size and intensity that provide independent constraints on scattering by density irregularities (Hess and MacDowall 2003) along multiple lines of sight to the two STEREO spacecraft, both in heliocentric longitude (for Earth) and distance (for Jupiter and Saturn).

2.4.2 Time Domain Sampler (TDS)

TDS observations of local Langmuir waves in type II and III events and comparisons with associated IMPACT and PLASTIC data will strongly constrain theories for type II and III bursts. Three major coupled questions need to be answered (Cairns and Kaiser 2002; Kellogg 2003): (i) why are the waves bursty, (ii) what is the origin of the localized wave packets that are sometimes observed, and (iii) what are the roles of linear and nonlinear processes in the evolution of Langmuir waves and the production of type II and III radiation?

In addition to these major studies, simultaneous high time resolution ($\approx 1 \mu\text{s}$) TDS data on 3 electric antennas will allow detailed comparison with stochastic growth theory (SGT) (Robinson 1992, 1995; Robinson et al. 1993; Cairns and Robinson 1999; Robinson and Cairns 2001), together with frequency-domain and correlation analyses of nonlinear product waves (Bale et al. 1998), and investigation of the reflection and linear mode conversion of Langmuir waves by density irregularities (Hinkel-Lipsker et al. 1992;

Bale et al. 1998; Yin et al. 1999; Willes and Cairns 2001). In addition, localized Langmuir wavepackets will be compared with the predictions of strong turbulence “wave collapse” (Robinson 1997). Continuous provision of TDS and LFR amplitude statistics on the timescale of a few minutes, another unique aspect of S/WAVES will allow a connection between amplitude distributions on timescales of a wave packet and the timescale of ≈ 1 minute.

The TDS will also observe ion acoustic and other low-frequency waves in the solar wind, for instance in corotating interaction regions and shocks. The field distributions and high-resolution time series, especially coupled with “burst” IMPACT and PLASTIC data, will constrain theories for the generation of these waves. New theoretical constraints will result from the time series of high temporal resolution electric field measurements provided by TDS and data from IMPACT and PLASTIC in their burst modes.

An additional goal of the S/WAVES TDS is the study of harmonic generation in Langmuir waves. Electromagnetic radiation at twice the plasma frequency is usually observed with the fundamental radiation near the plasma frequency, and even higher (but weaker) harmonics are observed (Cairns 1986). If Langmuir waves are converted to electromagnetic radiation on density ramps, then the mechanism for generation of the harmonic becomes a problem. Reflection on density ramps provides a convenient source of oppositely directed Langmuir waves to generate the harmonic by the traditional process of nonlinear interaction of such pairs of waves. It is, however, important to consider the harmonic content of the primary Langmuir waves, especially as electron trapping occurs only in the positive potential peaks of the waves and will lead to a second harmonic component. Whereas the earlier Wind-Waves TDS experiment had a non-linear A/D converter which made the study of harmonic generation difficult, the A/D converter used in the S/WAVES TDS is accurately linear, and will allow a definitive study of harmonics.

The TDS system also supplies signals to a part of S/WAVES, the Langmuir Waves Statistics (LWS) subsystem, which periodically provides a distribution of wave amplitudes. An earlier experiment on WIND, the WAVES instrument (Bougeret et al. 1995), provided much useful information on large amplitude Langmuir waves. As discussed in the science section, because small amplitudes are more common and may represent appreciable energy, we also need the distribution of Langmuir wave amplitudes to compare various theories with observations. Theories of conversion to electromagnetic modes and the Stochastic Growth Theory require this comparison. The Langmuir Wave Statistics (LWS) subsystem will provide a histogram of the distribution of wave amplitudes based on the largest signal detected by the TDS in a (commandable) period of about 20 msec. This histogram will be collected and telemetered about once per minute. Separate wave amplitude histograms are made simultaneously for each of the four TDS channels.

2.4.3 Low Rate Science (LRS)

This part of the instrument is designed to investigate:

- (1) conversion of Langmuir waves into the electromagnetic signals of type II and type III solar radio bursts; and
- (2) turbulent processes which are an important part of the behavior of the solar wind, particularly how it is heated and altered at 1 AU.

To carry out these objectives, the LRS will measure density fluctuations and electric fields, especially in the frequency range which would resonate with ions. Comparison of the observed density fluctuations with observations of Langmuir waves by the Time Domain Sampler (TDS) and radio parts of the experiment will determine whether conversion of Langmuir waves on density ramps is important in the production of radio bursts.

The three DC-coupled APW channels provide rapid measurements of plasma density, using a method similar to that described by Pedersen (1995), but modified because the antennas are not biased to float at the plasma potential. This method is based on the fact that the floating potential of a conducting body in a plasma depends on a competition between photoelectron emission, which is essentially constant, and ambient electron pickup, which depends on electron density and temperature. The floating potential also depends on the geometry of the photo-emitting and electron pickup surfaces, and is expected to be different, and to depend differently on density and temperature, for the antennas and spacecraft. There is no adequate theoretical basis to calculate *a priori* the relation between density and potential difference so this density measurement will be calibrated using density measurements by PLASTIC and IMPACT. When possible, measurements of the quasi-thermal plasma line will be used, in preference to the density measurement of the plasma instruments. Because the antennas are so short, the quasi-thermal plasma line is expected to be observable only during times when the halo part of the electron distribution is relatively large (i.e. at times of low total density). When it can be observed, however, it provides a more accurate measure of electron density as described below. The electric field measurements will be calibrated using the lower frequency $\mathbf{V}_{sw} \times \mathbf{B}$ field from PLASTIC and IMPACT.

2.5 Solar Wind Physics: Electric Field and Density Fluctuations

At periods longer than a few seconds, three dimensional electric fields in the solar wind have not been measured. As a result, little is known except for the expectation and measurement of a convection field $\mathbf{E} = -\mathbf{v} \times \mathbf{B}$. Kellogg and Lin (1997) pointed out that solar wind electric fields in the frequency range which would resonate with the cyclotron frequency of the ions had never been measured, and that such fields could act as collisions and have a determining effect on the particle distributions of the solar wind. This range, which is Doppler shifted to about one hertz, is very difficult to measure on a spinning satellite because photoelectric voltages are much larger and in the same frequency range.

Several efforts have been made to measure electric fields in this frequency range in the solar wind. Our first attempt was with the URAP experiment on Ulysses (Stone et al. 1992). The Ulysses spin axis is always pointed at the Earth, which reduces photoelectric variations when the axis is also pointed near the sun. However, leakage from the photoelectric variations was too large in the 1 Hz range, though frequencies above 10 Hz were measurable because a hardware filter eliminated the spin frequency (Lin et al. 2003). The next attempt was with the experiment RPWS on Cassini (Kellogg et al. 2001, 2003). Cassini is 3-axis stabilized, but an instability on the wake caused interference which prevented good measurements.

More recently, a successful attempt using the EFW experiment on the Cluster satellites has been made (Bale et al. 2005; Kellogg et al. 2006). Kellogg et al. (2006) showed that the electric fields are indeed strong, and that their effect on the ions is larger than the effect of magnetic field fluctuations. The Cluster spacecraft spin but use electric field probes which are designed to minimize photoelectron variations. As discussed more fully in Bale et al. (2005) and Kellogg et al. (2006), it is unclear whether the measurements at the high frequency end of the plateau are reliable. It is one of the objectives of the Low Rate Science system to settle this question. Cluster is not in the solar wind very much of the time, and is in the free solar wind (i.e. not connected to the Earth's bow shock or magnetosphere) even less often. Hence, having shown that electric fields in the ion cyclotron range are important, we will use the 3-axis stabilized STEREO spacecraft for studies of the occurrence and amplitude, correlation with other phenomena, etc. of these low frequency electric fields.

The measurement of rapid density fluctuations is an essential part of our efforts to understand the mechanism of generation of type II and type III radio bursts. In addition to being a part of solar wind turbulence which has been neglected in favor of studies of magnetic field and velocity turbulence, it has been suggested (Field 1956; Kellogg 1986; Bale et al. 1998; Willes and Cairns 2001) that density changes play an essential role in the conversion of Langmuir waves to electromagnetic radiation. It has been argued that density fluctuations account for the long, exponentially decaying tail of fundamental emission in type III solar radio bursts, via multiple scattering of the emitted radiation, and the non-integer fundamental to harmonic frequency ratio via mode conversion back to Langmuir waves (Kellogg 1986; Robinson and Cairns 1998a).

Sufficiently accurate and rapid measurements of density have been difficult to do with plasma instruments. Typical density fluctuations amount to one or a very few percent—of the same order as typical plasma instrument counting statistics when samples are made rapidly. Early measurements on Ogo 5 (Unti et al. 1973) and on ISEE (Celnikier et al. 1983, 1987) have determined these amplitudes using other techniques, as well as a spectrum which is close to, but not exactly, a descending power law.

3 Required Measurements

Figure 4 shows the overall instrument sensitivity that is required to fulfill the S/WAVES scientific objectives. Superimposed is the sensitivity actually obtained with S/WAVES. The shot noise on this curve corresponds to the noise induced by solar wind electrons and protons impacting on the antennas.

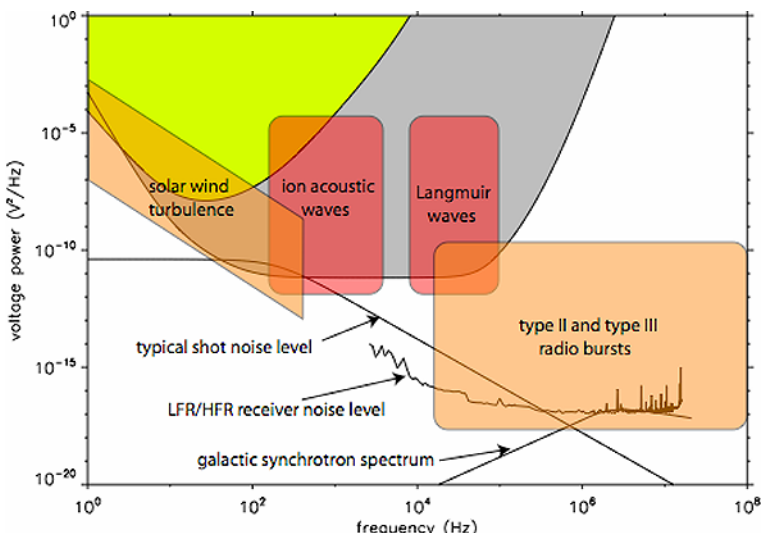


Fig. 4 (Color online) Required and known sensitivity as a function of frequency. Typical levels of solar wind electric field turbulence, ion acoustic, and Langmuir wave power are shown, as well as IP radio burst levels. The galactic nonthermal continuum level and the expected shot noise levels will determine the actual measurement background. The *green area* shows the expected sensitivity of the LRS burst measurement, while the *grey area* shows the expected TDS sensitivity. Measured LFR and HFR noise levels are also shown

Table 1 S/WAVES frequency domain parameters

	LFR	HFR	FFR
Frequency coverage	2.5–160 kHz	125–16.025 MHz	30.025 or 32.025 MHz
Bandwidth	2-octave	25 kHz	25 kHz
Frequency resolution	$\Delta F/F_0 = 8.66\%$	≥ 50 kHz	N/A
Sensitivity	$6 \text{ nV/Hz}^{1/2}$	$6 \text{ nV/Hz}^{1/2}$	$40 \text{ nV/Hz}^{1/2}$
Dynamic range	120 dB	80 dB	50 dB

3.1 Frequency Domain Measurements

In order to carry out this scientific program, the remote-sensing part of S/WAVES consists of:

- the Fixed Frequency Receiver (FFR) for connection with ground based measurements
- the High Frequency Receivers (HFR) for spectral analysis and direction finding of radio noise generated from a few solar radii (16 MHz) to about half an Astronomical Unit (125 kHz)
- the Low Frequency Receiver (LFR) for spectral analysis and direction finding from about half an Astronomical Unit (160 kHz) to one AU (2.5 kHz).

Table 1 lists the measurement requirements for these receivers, described in more detail in the experiment description section.

3.2 Time Series Measurements

In order to carry out this scientific program, the in-situ part of S/WAVES consists of:

- The Time Domain Sampler (TDS) and its associated Langmuir Wave Statistics system (LWS) for measurement of the Langmuir waves which are the first stage of solar radio radiation. The TDS measurements will also measure density fluctuations on a time scale appropriate for their interaction with the Langmuir waves.
- The Low Rate Science (LRS) system for measurement of density fluctuations and of electric fields in the frequency range around the ion plasma frequency (0.03 to 32 Hz).
- The Antenna Potential Monitor (APM), for slow monitoring of plasma density changes.

These instruments will be described in more detail in the experiment description section.

3.3 Direction Finding capabilities of S/WAVES

Based on the Cassini/RPWS experiment (Gurnett et al. 2004), the S/WAVES radio receiver also has the capability for radio direction finding (also known as goniopolarimetry). From these measurements it is possible to ascertain the direction of arrival of an incoming electromagnetic wave (represented by two angles: the colatitude θ and azimuth ϕ), its flux density (S), its polarization state (three Stokes parameters: Q and U , the linear polarization degrees, and V the circular polarization degree) and possibly the typical angular extension of the source (γ). The basic measurement obtained by S/WAVES is a set of four instantaneous measurements on a pair of electrical antennas: one autocorrelation on each of the two antennas and the complex cross-correlation between them.

For complete direction finding, there are seven unknowns (θ , ϕ , S , Q , U , V and γ) but only 4 measurements (two autocorrelations and a complex cross correlation) in a single measurement cycle, so a single S/WAVES measurement does not contain enough independent

information with which to solve the system without assumptions on the wave parameters. To overcome this difficulty, two specialized direction finding modes allow making two or three basic measurements quasi-instantaneously. This is done by switching the antenna configuration at the receiver input as often as every measurement. With two successive measurements on two different pairs of antennas, we obtain seven independent measurements (three autocorrelations and two complex cross-correlations). For three successive measurements on three different pairs of antennas, there are nine independent measurements (three autocorrelations and three complex cross-correlations). The measurements must be inverted to solve for the source parameters.

The details of these inversions are discussed in Cecconi et al. (2007) which contains a more complete presentation of the direction finding capabilities of the S/WAVES experiment, as well as an insight into the kind of results that will be obtained based on the example of Cassini/RPWS observations of solar radio bursts.

3.4 Triangulation and Stereoscopic Measurements

To achieve the science goals discussed above, the S/WAVES investigation will make use of the full 2D radio direction finding measurements from the separate STEREO spacecraft. Combining S/WAVES observations from the two spacecraft will lead to three dimensional source location of radio emissions (triangulation) and stereoscopic measurements of their properties.

3.4.1 Radio Triangulation

Radio triangulation can be performed at each sampled frequency by two different means, using 2D direction finding and the time of arrival of the radiation on each spacecraft.

- (1) Triangulation with the directions of arrival of the radiation observed on the two spacecraft.
- (2) Triangulation with the direction D of arrival of the radiation on one spacecraft together with the difference Δt of the arrival times measured at both spacecraft. This method assumes radio propagation in free space at the speed of light and the 3D location of the radio emission source will then be given by the intersection between D and the hyperboloid of revolution where Δt is constant.

Performed on a large statistical basis as a function of direction and using a combination of the two methods, comparison of these 3D source locations will provide insights into propagation effects at work, as shown previously in stereoscopic case studies by Steinberg et al. (1984) on the ISEE-3 and Voyager spacecraft and by Hoang et al. (1998) and Reiner et al. (1998c) on Ulysses and WIND.

In this way, the reliability of the determination of the radio source positions can be checked and the accuracy estimated. This is a crucial element in tracking interplanetary CME driven shocks that emit type II radio bursts. Another important advantage of direct radio triangulation is avoiding the use of a heliospheric density models (e.g., Saito et al. 1977; Leblanc et al. 1998) or simple $1/r^2$ density variation to convert the frequency scale to a distance scale.

3.4.2 Stereoscopic Measurements of Radio Emission Properties

Stereoscopic direction finding measurements from both spacecraft with increasing viewing angles, made on large data sets, will allow derivation of statistical characteristics of the radio emission as a function of observing direction. The emission directivity, or beam pattern,

together with the source size and frequency drift rate, yields information on the emission mechanism, the radiation mode and on the propagation medium. From Ulysses-ARTEMIS observations of solar kilometric type III bursts, Poquerusse et al. (1996) and Hoang et al. (1997) reported the average radiation pattern of interplanetary type III bursts to be shifted significantly East of the radial direction. S/WAVES can study this important effect, as well as the directivity of the type II emission associated with interplanetary CME shocks.

3.5 Thermal Noise Spectroscopy in Solar Filamentary Material

Many CMEs originate in coronal prominences that are ejected violently from the sun by a mechanism that is not yet fully understood and which may include magnetic reconnection in some cases. These CMEs propagate in the interplanetary medium, carrying the magnetic field pattern from their parent prominence. The physical properties of these magnetic field structures, known as magnetic clouds, are not well known because of a lack of adequate observations. However we know they are fundamentally different from the ambient solar wind.

In magnetic clouds, electron distributions can be very dense and extremely cold (Larson et al. 2000). Traditional electrostatic analyzers have difficulty measuring electrons in this regime, as the illuminated spacecraft floats at several volts positive, making measurements at a few eV quite difficult.

Since particles and electrostatic waves are so closely coupled in a plasma, particle properties can often be determined by measuring waves. In a stable plasma, the particle thermal motions produce electrostatic fluctuations which are completely determined by the velocity distributions (and the static magnetic field). Hence, measurement of this quasi-thermal noise provides information on the density, temperature and relative numbers of core and halo electrons.

The technique of quasi-thermal noise spectroscopy (Meyer-Vernet and Perche 1989) can be used in the regime where the Debye length is small compared with the electric antenna length. This technique, which is based on the analysis of the wave spectrum measured by electric antennas, is not affected by the spacecraft potential. It is thus more accurate in this regime than traditional analyzers and can be used for absolute calibration.

In the solar wind, the electron gyrofrequency f_{ce} is much smaller than the plasma frequency f_p . In this case, the electron thermal motions excite Langmuir waves, so that the quasi-equilibrium spectrum is cut-off at f_p , with a peak just above it (see Fig. 5). In addition, electrons passing within a Debye length, L_D , of the antenna induce voltage pulses on it,

Fig. 5 Spectrogram measured by the WIND spacecraft on April 08, 2003. This spectrogram represents, as a function of time, the radio power spectral density in the frequency range between 16 to 256 kHz. One can clearly see the plasma peak varying on that day between roughly 25 and 90 kHz. This corresponds to density variations between roughly 8 and 100 cm⁻³

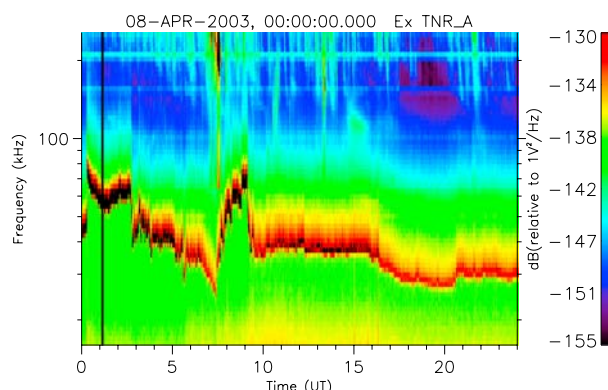
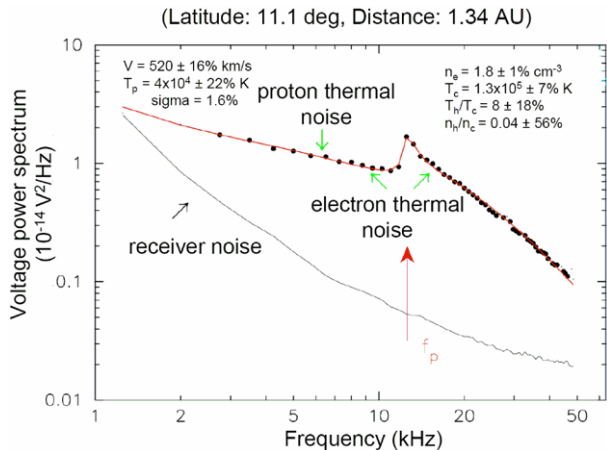


Fig. 6 Typical spectrum measured on Ulysses. The solid line is the theoretical Quasi-thermal noise spectrum which best fits the data (points) within 1.6% of the standard deviation



producing a plateau in the wave spectrum below f_p and a decreasing level above f_p . Since L_D is mainly determined by the bulk (core) electrons, the spectrum above f_p gives information about the core population. In contrast, since the Langmuir wave phase velocity becomes infinite at f_p , the fine shape of the f_p peak is determined by the fast (halo) electrons. Hence the quasi-thermal spectrum gives information on the whole electron distribution as well as giving an accurate measure of the total electron density.

When $f_{ce} \ll f_p$, measuring the thermal noise spectrum allows a precise determination of the electron density and bulk temperature (using respectively the cut-off at f_p and the spectrum level and shape around it), whereas the detailed shape of the peak itself reveals the suprathermal electrons (Meyer-Vernet and Perche 1989; Meyer-Vernet et al. 1998). This method has yielded routine measurements of the solar wind electron plasma parameters for space missions such as Ulysses (Maksimovic et al. 1995; Hoang et al. 1996; Issautier et al. 1998) and WIND (Maksimovic et al. 1998). It has also been used in both magnetized and unmagnetized environments, for example, planetary magnetospheres (Moncuquet et al. 1995) and a cometary plasma tail (Meyer-Vernet et al. 1986).

Figures 5 and 6 show examples of quasi-thermal noise (QTN) observations in the solar wind. Figure 5 is a spectrogram measured by the WIND spacecraft on 8 April, 2003, plotting the power spectral density in the frequency range between 16 to 256 kHz as a function of time. One can clearly see the plasma peak varying on that day between roughly 25 and 90 kHz. This corresponds to density variations between roughly 8 and 100 cm^{-3} . Figure 6, adapted from Issautier et al. (2001a), shows a typical plasma spectrum on Ulysses, obtained in the solar wind, with an intense peak just above the local plasma frequency f_p . The spectral analysis yields the electron density and thermal temperature with a good accuracy, in addition to the solar wind speed (due to the Doppler-shifted thermal fluctuations of the ions), and suprathermal parameters (Issautier et al. 1999). Note that the density measurement is independent of any calibration gain determination, since it relies directly on a frequency determination that is usually very accurate.

QTN spectroscopy is almost immune to the limitations due to spacecraft charging due to the fact that, close to the local plasma frequency, the antenna is sensitive to Langmuir waves with very large wavelengths. At the plasma frequency peak the antenna samples an average over a large plasma volume. Therefore TN spectroscopy has been used to calibrate the density and temperature obtained by the electron analyzers, which are usually perturbed by spacecraft charging effects.

Maksimovic et al. (1995) and Issautier et al. (2001b) performed detailed comparisons between the two kind of instruments on Ulysses and emphasized that the TN spectroscopy method is a complementary tool to cross-check other techniques for determining electron densities. Moreover, it is important to note that, using QTN electron densities, it is possible to improve the determination of the spacecraft potential, and thus to correct the electron parameters determined by particle spectrometers (Maksimovic et al. 1998; Salem et al. 2001).

4 Instrument Description

4.1 Introduction

The S/WAVES instrument is shown schematically in Fig. 7. There are a number of related subsystems which are described in detail in the following sections. On the left are the antennas and their deployment units. Within the antenna assembly is a preamplifier enclosure which houses all of the preamplifiers. The amplified signals from the preamplifier connect to a number of receivers. The Low Frequency Receiver (LFR), a spectrum analysis receiver, and the High Frequency Receiver (HFR), a super-heterodyne swept frequency receiver connect to a dedicated Digital Signal Processor unit. A Fixed Frequency Receiver (FFR) at about 32 MHz provides in-flight measurements which can be compared to ground observations. The signals also feed the time series receivers: the Time Domain Sampler (TDS) which includes the Langmuir Waves Statistics histogram, and the Low Rate Science (LRS) subsystem. All of the data then flows into the Data Processing Unit (DPU) and then to the spacecraft data handling system.

4.2 Antennas/Sensors

S/WAVES measures the fluctuation electric field present on three orthogonal monopole antennas mounted on the back (anti-sunward) surface of the spacecraft. Each monopole antenna unit is a 6 m long Beryllium-Copper (BeCu) “stacer” spring. The three units deploy from a common baseplate that also accommodates the preamplifier housing (see Fig. 8). The 6 m length was chosen to put the antenna quarter-wave resonance near the top of the S/WAVES HFR2 frequency band. The details of the antenna design are reported in a separate paper (Bale et al. 2007).

4.3 Preamplifiers

The three electric monopoles are connected to low noise and high impedance preamplifiers located close to the base of the deployment mechanism. This is required to minimize the effect of the base capacity, which can severely limit the sensitivity of the receiver. As shown in Fig. 9, below, each preamplifier channel has a single FET (field effect transistor) at its input and provides three outputs: one with AC coupling for the frequency domain analyzers (LFR and HFR), another with AC coupling for the time domain analyzer (TDS) and one with DC coupling for antenna and spacecraft potential monitoring. This path also provides a path from the antenna elements to the spacecraft ground (through a large resistance) to avoid having the elements become highly charged. Three additional preamplifiers are specifically dedicated to the Fixed Frequency Receiver (FFR). The FFR preamplifiers are connected to the three monopoles, allowing the FFR to be connected to one of three pseudo-dipole combinations Ex/Ey , Ey/Ez or Ex/Ez .

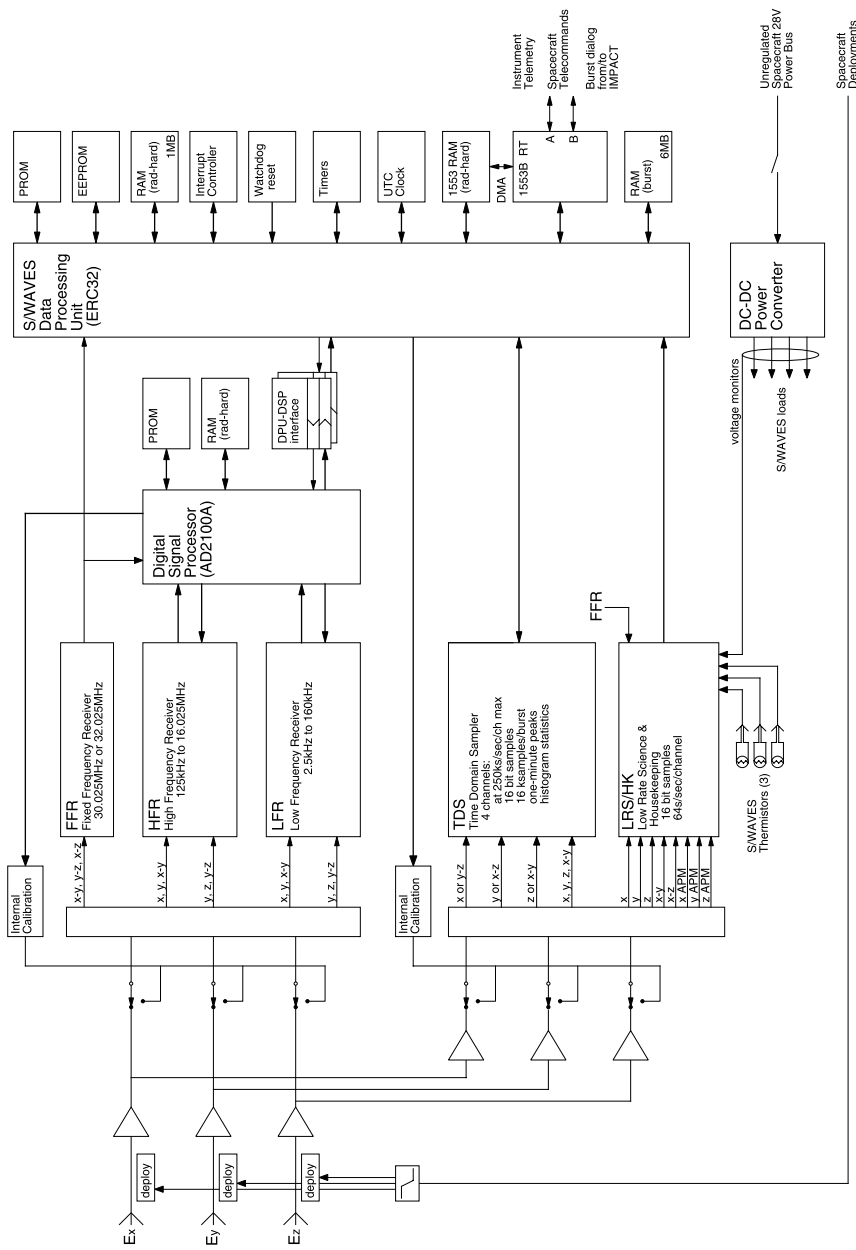


Fig. 7 The overall block diagram of the S/WAVES instrument

Fig. 8 The S/WAVES antenna assembly with three mutually orthogonal antenna elements (stowed and protected with retaining covers) and preamplifier enclosure

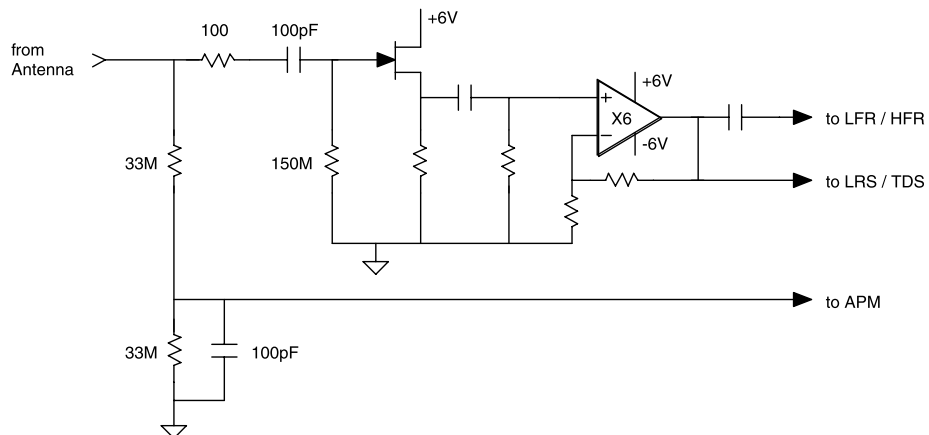
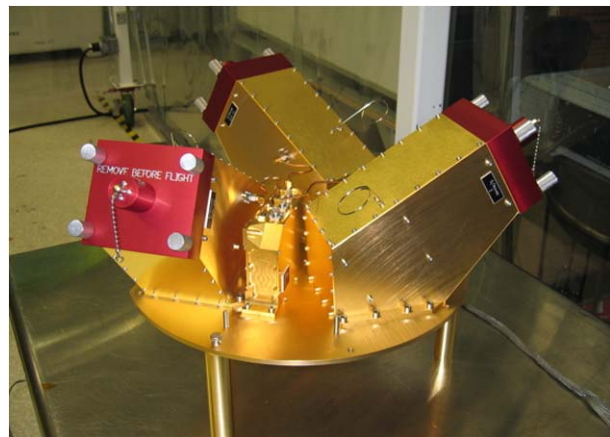


Fig. 9 A typical preamplifier circuit

4.4 The Low Frequency Receivers (LFR)

The LFR is a direct conversion receiver for spectral processing from 2.5 kHz up to 160 kHz. This frequency range is divided into three 2-octave bands with sharp anti-aliasing analog filters. Except for band A (2.5–10 kHz), the LFR front end has two channels which are essential for the processing of the cross correlation used in direction finding. In normal operation, each 2-octave band is sequentially connected to the antennas and simultaneously sampled on both channels. The LFR block diagram is shown in Fig. 10.

Using a wavelet-like transform, the digital spectral analysis is processed in each 2-octave band with 16 logarithmically-spaced frequencies, leading to a 8.66% spectral resolution. This results in a total of 48 log-spaced frequencies (Table 2).

The LFR is intended to cover a broad dynamic range with a constant amplitude resolution over the whole range. This implies that the receiver is able to adjust its gain according to the input level. An Automatic Gain Control (AGC) determines the receiver gain on a logarithmic scale as a function of the input level. The LFR analog front end normalizes the signal amplitude with an allowable gain variation of 80 dB. Combined with 12-bit analog to

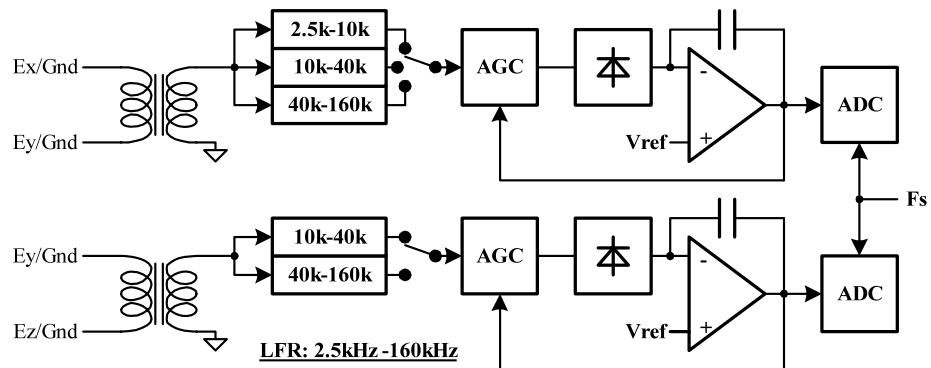


Fig. 10 LFR block diagram

Table 2 LFR frequency coverage

Band	Frequency coverage (kHz)	Channels	Frequencies
A	2.5–10	1 channel	16 log-spaced
B	10–40	2 channels	16 log-spaced
C	40–160	2 channels	16 log-spaced

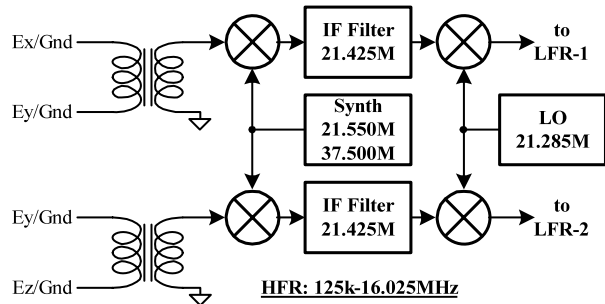
Table 3 LFR/HFR antenna combinations

Band	Channel 1	Channel 2
A	Off	X
	E_x	X
	E_y	X
	E_y/E_x	X
B, C & HF	Off	Off
	E_x	E_y
	E_x	E_z
	E_y	E_z
	E_x	E_y/E_z
	E_y/E_x	E_z

digital converters, the LFR provides a total dynamic range of 120 dB. The LFR sensitivity is $6 \text{ nV/Hz}^{1/2}$ at the preamplifier input. These characteristics are indispensable to accurate plasma wave measurements over a large dynamic range.

Various antenna configurations are available by command. The LFR can be switched to use either pseudo-dipoles (E_y/E_x or E_y/E_z) or monopoles (E_x , E_y or E_z). Table 3 gives the possible antennas combinations.

The two channel receiver allows the production of auto-correlations as well as complex cross-correlations. These measurements can be made between any of the antenna combinations mentioned above. This is especially important for direction finding processing which can be performed in two different modes. The first mode consists of a two step analysis,

Fig. 11 HFR block diagram

combining dipoles and monopoles ($Ex/Ey-Ez$ and $Ex-Ez/Ey$). The second mode is a three-step sequence combining the three monopoles ($Ex-Ey$, $Ey-Ez$ and $Ex-Ez$).

4.5 The High Frequency Receivers (HFR)

The HFR is a dual sweeping receiver operating in the frequency range 125 kHz–16.025 MHz. Using a super-heterodyne technique, the signal from the selected antenna is down-converted using mixers and a programmable synthesizer. The synthesizer produces frequencies at odd multiples of 25 kHz. This intermediate frequency signal is then sharply filtered such that a comb filter across the HF band is the result. The rejection of noise at even multiples of 25 kHz is 62 dB. This filtering scheme allows S/WAVES to sample between lines of noise that may be produced by power supply harmonics at multiples of 50 kHz (even multiples of 25 kHz). The odd/even “picket fence” technique allows for the coexistence of a very sensitive radio receiver and sometimes noisy spacecraft power supplies. Frequency shifted down, the finished signal is handled by the same LFR digitization and analysis hardware (described above) at a comparatively low digitization sample rate. The HFR provides a total dynamic range of 80 dB and its sensitivity at the preamplifier input is $6 \text{ nV/Hz}^{1/2}$. The HFR block diagram is shown in Fig. 11.

The receiving frequency is determined by a programmable synthesizer which covers the HFR spectrum from 125 kHz to 16.025 MHz with 50 kHz increments. Thus, the highest spectral resolution is 50 kHz and can be configured to multiples of 50 kHz by command. The time resolution is also adjustable depending on the integration time.

In a manner similar to the LFR, the antennas are configurable as monopoles or dipoles (see Table 3). The direction finding is performed using the same modes as the LFR.

4.5.1 Digital Signal Processing Unit

To support the in-flight signal processing and data stream, the LFR and HFR front ends are connected to a digital signal processing unit. The conditioned analog signals are simultaneously digitized with 12-bit resolution on both channels. The time series sampling rate is selected to be appropriate to the selected band as listed in Table 5.

Digital filtering and the correlation calculation are the core of the signal processing. The digital filters are of the Finite Impulse Response (FIR) type and their coefficients have been determined by an optimization program. Their maximum length is 341 taps for the LFR and 191 taps for the HFR. This results in a bandwidth of 8.66% of the corresponding LFR frequency, and 12.5 kHz for the whole HFR frequency range. The digital filtering gives an out-of-band rejection greater than 70 dB, determined by the 12-bit digitization. Table 4 gives the digital filtering characteristics.

Table 4 Digital filtering characteristics

Band A		Band B		Band C		Band HF	
$F_s = 40.625$ kHz	$\Delta F_{(-3 \text{ dB})}/F_o = 8.66\%$	$F_s = 162.500$ kHz	$\Delta F_{(-3 \text{ dB})}/F_o = 8.66\%$	$F_s = 464.286$ kHz	$\Delta F_{(-3 \text{ dB})}/F_o = 8.66\%$	$F_s = 464.286$ kHz	$\Delta F_{(-3 \text{ dB})} = 12.5$ kHz
F_o (kHz)	# taps	F_o (kHz)	# taps	F_o (kHz)	# taps	F_o (kHz)	# taps
2.61	341	10.45	341	41.81	245	140	191
2.85	313	11.40	313	45.59	225		
3.11	287	12.43	287	49.72	207		
3.39	263	13.56	263	54.22	189		
3.70	241	14.78	241	59.13	173		
4.03	221	16.12	221	64.48	159		
4.40	203	17.58	203	70.32	145		
4.79	185	19.17	185	76.68	133		
5.23	169	20.91	169	83.62	121		
5.70	155	22.78	155	91.19	111		
6.22	143	24.86	143	99.44	103		
6.78	131	27.11	131	108.44	93		
7.39	119	29.56	119	118.26	85		
8.06	109	32.24	109	128.96	79		
8.79	101	35.16	101	140.63	71		
9.59	91	38.34	91	153.36	65		

Auto-correlations and complex cross-correlations are calculated for the 16 frequencies of each LFR band. The resulting calculations are compressed into 12-bit words and sent to the DPU in a compressed floating point format through a parallel interface. The auto-correlations are coded using a 5-bit exponent and a 7-bit mantissa while the cross-correlation requires a sign-bit with a 5-bit exponent and a 6-bit mantissa.

The measurement cycles are defined by the integration time which is set to produce acceptable statistical variations. The time needed for a block acquisition is inversely proportional to the frequency band of interest. This directly affects the temporal resolution which increases almost linearly with the integration time, as shown in Table 5.

4.6 The Fixed Frequency Receiver (FFR)

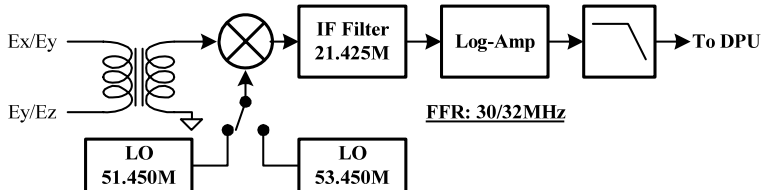
The S/WAVES package includes a fixed frequency receiver which consists of a single channel super-heterodyne receiver operating around 31 MHz. Depending on the response after launch, the frequency will be switched to either of two frequencies, 30.025 MHz or 32.025 MHz.

The FFR detects the incoming signal to produce a slowly varying voltage which is logarithmically proportional to the input level. Its sensitivity is about $40 \text{ nV}/\text{Hz}^{1/2}$ with a dynamic range of about 50 dB. The FFR block diagram is shown in Fig. 12.

The DC voltage is sampled directly by the DPU at 64 samples per second. To reduce noise the resulting time series is filtered with a variable length median filter to a few samples per second before transmission to the ground.

Table 5 DSP integration time parameters

Band	Sampling rate (kHz)	Effective period (ms)	Number of blocks	Integration time (ms)	Time res. (ms)
A 2.5–10 kHz	40.625	2.988	42	125/ 1	406 ± 1
			84	250/ 1	800 ± 1
			168	500/ 1	1590 ± 1
			336	1000/ 1	3180 ± 1
B 10–40 kHz	162.500	0.747	42	125/ 4	182 ± 1
			84	250/ 4	356 ± 1
			168	500/ 4	704 ± 1
			336	1000/ 4	1420 ± 1
C 40–160 kHz	464.286	0.188	42	125/ 16	96 ± 1
			84	250/ 16	184 ± 1
			168	500/ 16	364 ± 1
			336	1000/ 16	748 ± 1
HF 125–16 MHz	464.286	0.085	29	2.5	36 ± 1
			58	5	63 ± 1
			116	10	117 ± 1
			232	20	224 ± 1

**Fig. 12** FFR block diagram

4.7 The Time Domain Sampler (TDS)

The Time Domain Sampler makes rapid samples of waveforms and is intended primarily for the study of Langmuir waves, waves at the plasma frequency and the precursors of type II and III radio bursts. Other wave modes, such as ion acoustic waves, can also be studied. The rapid simultaneous sampling of three orthogonal antennas as well as a pseudo-dipole channel obtained by taking the difference of any two monopoles allows the study of waveforms, their distortions, and, through ground-based Fourier analysis, a frequency determination which is far more accurate than any possible on-board filter analysis system.

Analysis of data from the TDS of WIND/WAVES (Bougeret et al. 1995) provided major contributions to our understanding of Langmuir waves in the solar wind. The TDS of S/WAVES is a similar, but improved instrument.

The TDS (Time Domain Sampler) provides for rapid sampling of transient events in the time domain. Its objective is to make very fast samples while also making effective use of the telemetry downlink. The maximum continuous sampling speed of the TDS is 16 million

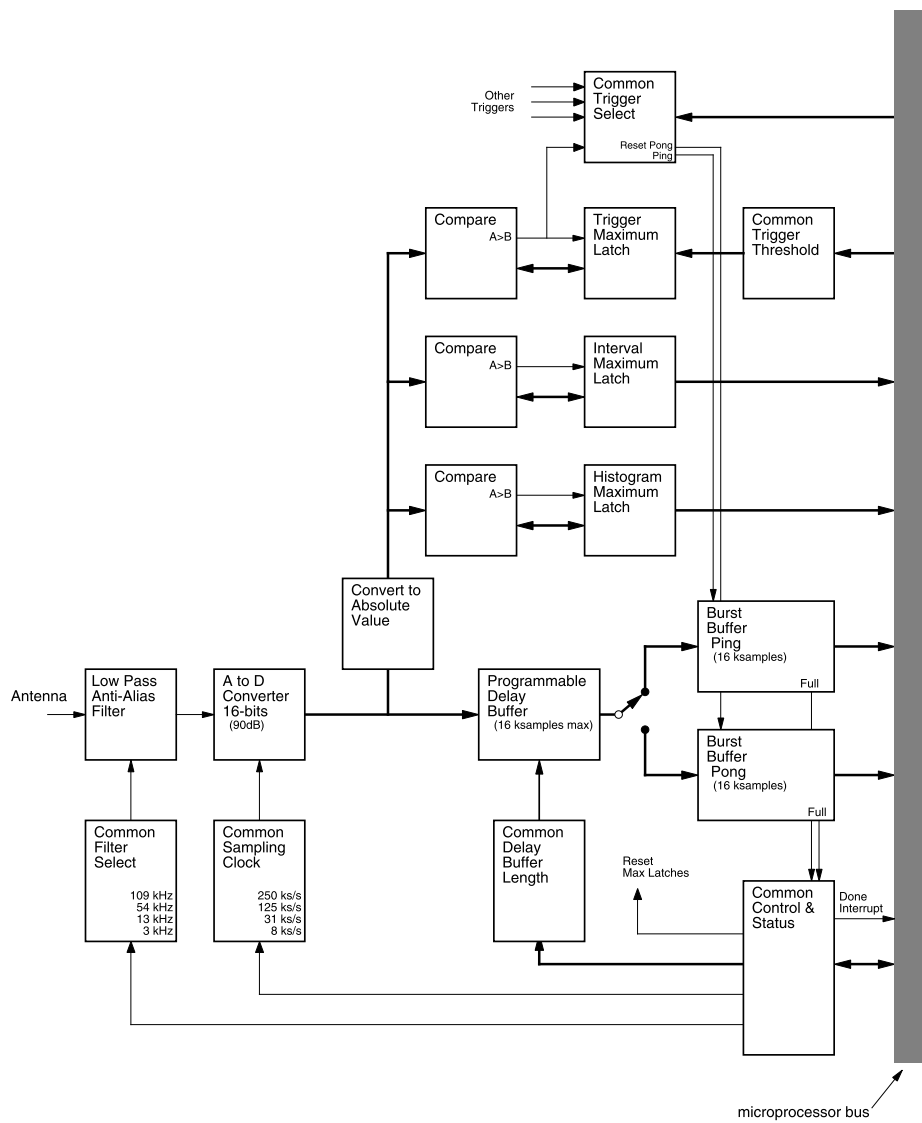


Fig. 13 A block diagram of one (of four) TDS channel

bits per second. The typical TDS share of the S/WAVES downlink rate is only about 500 bits per second. The TDS achieves that large reduction in bit-rate while maintaining high scientific return by choosing events for transmission to the ground intelligently.

The TDS functions like a modern digital oscilloscope. It samples the voltage on the S/WAVES antennas quickly and continuously. When the sampled amplitude exceeds a commandable threshold (as described below), a triggering system takes a snapshot with the largest part of the signal at the center of the time series. A typical event from one channel is shown in Fig. 14.

Fig. 14 A typical Langmuir wave packet from the TDS

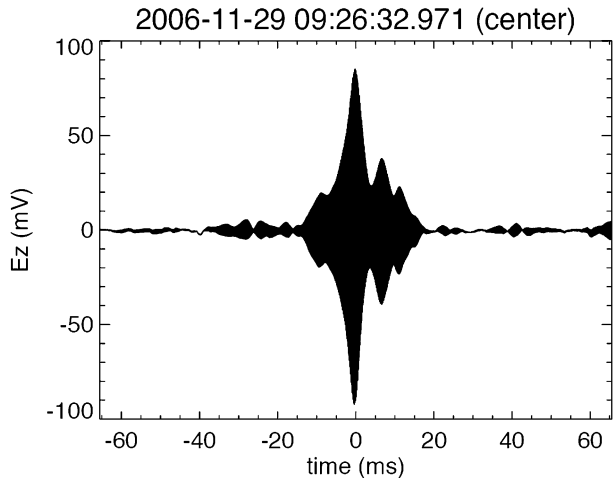


Table 6 TDS characteristics

	Sample speed (s/s)	Low pass filter (kHz)	Maximum duration (ms)
A	250,000	108	66
B	125,000	54	131
C	31,250	13.5	524
D	7,812.5	3.375	2,097

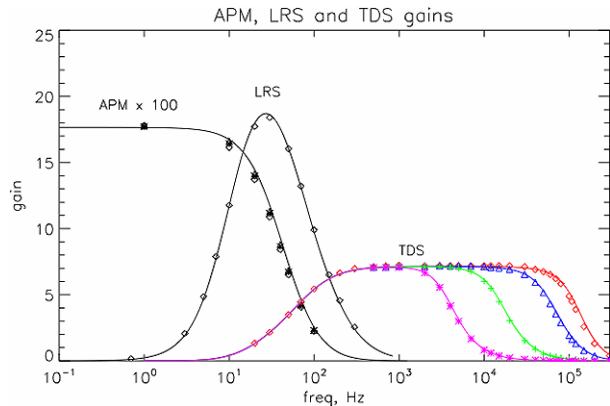
The TDS gathers events on four channels simultaneously. The commandable sampling times are listed in Table 6 with 250,000 samples per second the fastest sampling speed. This gives a Nyquist frequency of 125 kHz. Events can be as long as 16,384 samples, giving a maximum event duration of about 2 seconds. This gives a lower frequency bound of 0.5 Hz. The DPU's 6 MB burst memory provides storage for about 40 full events, each of which has 4 channels. Software criteria determine the effective quality of each event and, in general, the events with the highest quality are selected for transmission to the ground.

The TDS has four input channels connected to commandable combinations of the S/WAVES antenna system. Its nominal mode of operation is to have the three S/WAVES monopole antennas connected to each of three input channels while the fourth channel is connected to a pseudo-dipole obtained from the analog difference between two monopoles. The commandable switching network allows for full capability even with a failure of one channel.

Figure 13 is a block diagram of one of the four TDS acquisition channels. The selected analog signal is first filtered with a commandable bank of low pass filters to avoid aliasing. In general, the low pass filter (as shown in Table 6) is selected to match the current sampling speed. The effects of these simple filters are shown in Fig. 15 which gives the complete frequency response of the TDS including the four selectable low pass filters.

After filtering, the analog signals are digitized. Each of the four channels is digitized simultaneously by one of four analog to digital converters (ADC). The ADCs used here provide 16 bits of dynamic range and are quite linear over the range. The digitized signals are then made available to a number of parts of S/WAVES. While these commercial parts are acceptable in their tolerance of total radiation dose, it is possible they could latch-up in

Fig. 15 The gain of the time domain parts of S/WAVES. *Discrete points* represent measurements. *Lines* represent theory. The negative APM gain (i.e. gain less than unity) is multiplied by 100 for visibility. Different TDS curves reflect selectable low pass filters



the presence of energetic particles. To prevent permanent damage, the ADCs are protected by a circuit breaker which shuts off power when high current is detected, allowing parasitic currents within the device to dissipate. The S/WAVES DPU normally turns the converters back on after a programmable cooling-off period (nominally 5 seconds).

For the TDS itself, the outputs of each of the four ADCs enter digital comparators. Each comparator examines the incoming stream of digital samples, searching for a new input value that is arithmetically larger than the value currently latched in its memory. Upon finding a larger value, the new value is latched for later comparisons and a trigger pulse is produced. One of the four trigger pulses is used to reset or clear the TDS hardware burst buffers. At initialization and after the collection of each full event, the comparator memories are initially set to a commandable threshold value. Setting the threshold to a value just above the noise level can be used to limit the number of “small” or uninteresting events acquired by the system. While each of the four channels has trigger generation logic, one is commanded as the trigger source for all TDS channels at any given time.

The digitized signals are also sent into a digital delay buffer. The delay buffer is simply a first-in-first-out memory which provides for a commandable delay time. The memory can provide delays of from one to 16,383 samples. Setting the delay time allows the peak value of an event to appear anywhere in the event. The delay buffer length is typically set to half the length of the event itself giving an event with a peak in its center.

After a programmable delay, the digital values emerge from the delay buffers and enter the burst buffers. Each burst buffer is another first-in-first-out memory in which 16,384 samples are obtained from the output of the digital delay buffer. As these buffers are being filled, they are reset by one of the digital comparators as larger signals are obtained. At the start of an event, the resets occur rapidly but as the comparator obtains increasingly large values, the resets stop. Shortly thereafter, the burst buffer becomes full, indicating that a complete event has been acquired on all four channels.

When a burst buffer is full, the DPU copies the completed event from the burst buffers to TDS burst memory. While the DPU is reading out the contents of the burst buffer, the burst buffer is unable to begin storing a new event. To prevent a reduction in the acquisition of possibly good events during the comparatively long copying period, there are dual or ping-pong burst buffers which alternate such that one burst buffer can be acquiring a new event while the previous event in the other buffer is being emptied by the DPU. After the event has been completely copied by the DPU, a new event can begin filling the burst buffer.

When a new event is acquired, the DPU time-stamps the new event and begins the process of copying it from the burst buffer to burst memory, which is a large part of the DPU memory

dedicated to storing about 40 4-channel TDS events for eventual transmission to the ground. Once the event has been copied, the DPU invokes a process to determine the “quality” of the new event. With changes in flight software, the quality determination could be any arithmetic evaluation of the event. In this way, the “best” events are sent to the ground.

When a new event is ready to be copied from the burst buffer to burst memory, the DPU discards the existing event with lowest quality to make room for the new event. An event’s quality assignment is also used when space becomes available in the telemetry stream for a new TDS event. At that time, the DPU examines the pool of events in the burst memory and sends the event with the highest quality to the ground. This quality information can also be used (as described below in Sect. 5.3) to trigger simultaneous bursts with the IMPACT instrument and vice-versa.

In addition to sending events with high quality to the telemetry stream, the TDS also maintains a separate stream of events which are selected at random, without regard to their quality. The relative proportion of such “honest” events to “quality” events can be changed by command. This prevents having the TDS send “good” events to the exclusion of other, perhaps still interesting events with small quality values (e.g., smaller amplitude).

While the sensitivity of the TDS depends on frequency, in practice the noise level for each channel is less than $10 \mu\text{V}$ RMS (at about 10 kHz) at the input to the preamplifier. The largest signal obtained before saturation is about 125 mV RMS. To relate observations to actual observed electric field strength depends both on the frequency (as shown in Fig. 15) and the effective antenna length (see Bale et al. 2007).

4.8 Langmuir Waves Statistics (LWS)

As described above in Sect. 4.7, the TDS part of S/WAVES gathers data continuously at a high sampling rate. It examines the stream of data and sends “interesting” events to the ground. This often results in clusters of events where all the events of a cluster are acquired in a few minutes. These clusters, which based on WIND observations will usually be Langmuir waves (but could have other causes), are often separated by many hours.

The Langmuir Waves Statistics (LWS) subsystem is intended to fill in the gaps between clusters of TDS events. This subsystem uses the stream of digitized signals as described in Sect. 4.7 above. After low pass filtering, the TDS produces four continuous streams of digital data sampled at a commandable sampling rate defined in Table 6. In addition to flowing to the TDS, these streams flow to a set of digital comparators for the LWS subsystem as shown in Fig. 13.

Each comparator examines the incoming stream of digital samples. Each new value is compared to a value previously saved in the comparator. When the new value is arithmetically larger than the value currently latched in the comparator’s memory, the new value is retained for future comparisons. Under software control, the S/WAVES DPU examines the saved contents of the comparator at a programmable interval. Each time the DPU examines the saved value, the saved value is reset (set to zero) such that a new search for a peak amplitude value begins.

In this way, the LWS comparators always contain the largest amplitude values observed during the preceding collection interval. Under software control, the DPU typically obtains the peak value from an LWS comparator once every 5,000 TDS samples. The number of samples for this interval can be changed by command and gives a time period of 20 ms at the highest TDS sampling speed. The LWS software uses the most significant 8 bits of the digital peak value as an address to one bin of a 256 bin histogram and increments the addressed location by one. The number of TDS channels used, the number of histogram bins

(i.e. the number of bits used) and the use of sign bits are characteristics that are determined by flight software and may be changed and optimized at some future time based on flight experience.

After a commandable number of collection intervals, the LWS software closes the finished histogram and formats it for telemetry. The number of collection intervals is 500 by default but can be commanded to give much longer collection periods and nearly 100% coverage of TDS samples. The resulting histogram(s) of peak amplitude distribution give a statistical view of peak wave amplitudes during the period regardless of the number or size of TDS events in the same period.

4.9 Low Rate Science (LRS)

The Low Rate Science (LRS) system is intended to make electric field and density measurements at a rate which encompasses the ion cyclotron frequency and other characteristic low frequencies of the plasma. It samples 8 channels at a rate of 64 samples per second. The characteristics of these channels are shown in Table 7. The gains of the various components are shown in Fig. 15. The discrete points are measured values of the gain, made by applying known sine waves to the preamplifier inputs. The solid lines are the theoretical magnitudes of the complex gains calculated from the circuit diagram. In Fig. 15, the negative gain (i.e. the gain is less than one) of the APM has been multiplied by 100 so that it will be readable.

After filtering, the analog signals from the antenna preamplifiers are digitized. Each of the eight LRS channels is digitized in series by a single analog to digital converter (ADC) with a network of multiplexers to switch amongst the analog inputs. In addition to the eight LRS channels, a number of other housekeeping values are multiplexed and sampled at the same cadence.

The sampling rate for the LRS channels is 64 samples per second. This rate was chosen to be exactly twice the sampling rate of the IMPACT magnetometer (see Acuña et al. 2007) to allow good correspondence between the two sets of data. Although there is only one ADC, an effort was made to sample the eight LRS channels at nearly the same time and with minimal jitter in the acquisition time. In order to prevent software-induced jitter in the acquisition times, a hardware acquisition system was developed to acquire the samples under hardware control. A hardware acquisition sequence is started 64 times per second. Within a sequence, each sample of the set of LRS values is acquired only 122 microseconds ($=1/8192$ seconds) after one sampled before it (as defined in Table 7).

The ADC used here provides 16 bits of dynamic range and is quite linear over the range. As with the TDS (described above), this commercial part could latch-up in the presence of

Table 7 LRS characteristics

Channel number	Channel name	Frequency response
1	E_x APM	DC
2	E_y APM	DC
3	E_z APM	DC
4	E_x LRS	>0.03 Hz
5	E_y LRS	>0.03 Hz
6	E_z LRS	>0.03 Hz
7	$E_x - E_y$ LRS	>0.03 Hz
8	$E_x - E_z$ LRS	>0.03 Hz

energetic particles and is protected by a circuit breaker which shuts off power when a high current is detected.

While the sensitivity of the LRS depends on frequency, in practice the noise level for the five AC-coupled LRS channels is less than 10 μV RMS (at about 10 Hz) at the input to the preamplifier. The largest signal obtained before saturation is about 70 mV RMS. The three DC-coupled APM channels have a range of ± 7 V DC and are accurate to about ± 1 mV. To relate observations to actual observed electric field intensity depends both on the frequency (shown in Fig. 15) and the effective antenna length (see Bale et al. 2007).

4.9.1 Low Rate Science Housekeeping

To give a broad and continuous picture of the DC antenna potentials and the other LRS quantities, they are included in the S/WAVES housekeeping telemetry. Once each minute, the DPU gathers the diverse information of the instrument housekeeping. This includes an instantaneous sample of the most recently acquired LRS values.

4.9.2 Low Rate Science Bursts

To allow more direct comparisons with both the TDS and particle measurements, the eight channels of LRS data are also saved in a ring buffer in the DPU memory. The buffer is filled at 64 samples per second, the normal acquisition rate of the LRS. The ring holds 8,192 continuous samples from each of the 8 LRS channels. When the instrument triggers, it causes an LRS burst snapshot be taken. A commandable number of samples is then formatted for telemetry from each of the eight LRS channels. The number of samples in a channel's burst is typically 2,048 (although events can be shorter or as long as 8,192) which corresponds to 32 seconds of LRS time series data.

The default triggering mechanism for these bursts is simply to take a snapshot whenever the telemetry stream has room for an LRS burst. It is also possible to generate a burst using a telecommand as the trigger or using information from the IMPACT instrument (see Sect. 5.3). It is planned that other triggering modes will be developed.

4.10 Data Processing Unit (DPU)

The heart of the S/WAVES instrument is its Data Processing Unit (DPU). The DPU is based on an ERC32 microprocessor developed by and for the European Space Agency at ESTEC. The RISC processor is an implementation of the SPARC V7 architecture. The commercial part is radiation hard and is produced by Atmel as the TSC695. The processor is a modern processor with 32 bit address and data busses.

As shown in Fig. 7, the DPU's processor is equipped with a 32 kB boot PROM, 512 kB of electrically erasable memory (EEPROM) and 1 MB of radiation-hard RAM. In addition to the rad-hard RAM, another 6 MB of radiation-tolerant RAM are dedicated to TDS and LRS bursts. This memory is larger but also slightly more susceptible to upsets but is used only for temporary data storage and not for instrument operation. A number of peripheral devices such as an interrupt controller, timers and counters are implemented in an FPGA connected to the processor.

The DPU communicates to the spacecraft using a MIL-STD 1553 communications bus. This interface is memory mapped into the processor's address space and uses direct memory access (DMA) as well as interrupts to communicate with the processor. The DPU receives telecommands and sends telemetry using this interface. The DPU also sends and receives

status messages and communicates with the IMPACT instrument with this interface. One of the status messages from the spacecraft provides the DPU with the current UTC time once each second.

The DPU also has a number of memory mapped devices which connect to the various S/WAVES science subsystems. A combination serial/parallel interface allows communication with the Digital Signal Processor (the HFR and LFR). The TDS and LRS subsystems are simply direct memory mapped interfaces.

With the application of power (or by command or watchdog time-out), the DPU's processor boots from reliable rad-hard PROM. Boot loader software burned into PROM before launch executes a simple boot loader program. The boot loader examines the contents of certain memory locations in RAM and in EEPROM in search of a valid block of executable flight software. In normal circumstances, a valid block is located in one of two banks of EEPROM memory. The boot loader copies the valid block of software into RAM and, after verifying the integrity of the block, transfer control to the flight software in RAM.

In normal circumstances, one copy of flight software is kept in the prime EEPROM bank and another version is kept in the backup location. This allows for reliable and safe operation even at times when the flight software in one EEPROM bank is being replaced by ground command. Once per hour during the mission, the EEPROM banks are checked for continued validity with the results reported in instrument housekeeping.

The S/WAVES DPU runs the RTEMS real-time operating system. RTEMS is a pre-emptive multi-tasking operating system which supports the various pieces of flight software. At the time of launch, the flight software had about 30 processes running and communicating using the RTEMS system.

4.11 Power Supply

The S/WAVES instrument includes a low voltage power supply. The STEREO spacecraft supplies S/WAVES with a single unregulated power service ranging from 22 to 36 volts. In order to produce a number of isolated but well regulated power services for the S/WAVES subsystems, the converter is built with a two stage design. The first stage uses a pulse width modulation technique to produce an intermediate voltage of 12 volts. This intermediate voltage is carefully controlled and provides the stability of most of the final output supplies. The second stages are also PWM converters but because their supply is the carefully controlled 12 volt intermediate voltage, they are tuned to run at the optimal 50/50 (flat out) conversion rate. Separate outputs with isolated grounds are provided for several loads. The various grounds are then connected to chassis at appropriate locations in order to minimize instrument noise. Eight analog voltage levels are included in the S/WAVES housekeeping stream.

Using the MIL-STD-1553 communications interface for spacecraft communications was an unfortunate choice which causes enormous fluctuations of the power services in synchronization with the spacecraft bus schedule. Despite considerable built-in capacitive support, the secondary voltages sag when the S/WAVES 1553 transceiver drives the bus (e.g. when S/WAVES telemetry is sent from the instrument to the spacecraft command and data handling system). Although the negative effects were minimized, it would be an improvement to avoid this noisy interface bus on future missions.

In sensitive scientific instruments of this kind, the power supply is an important element. The S/WAVES power supply achieved reasonable efficiency (70% end to end). The crystal controlled two stage design coupled with the isolation of outputs and grounds resulted in very good self compatibility within the S/WAVES instrument.

4.12 Resources, Mass, Power and Bits

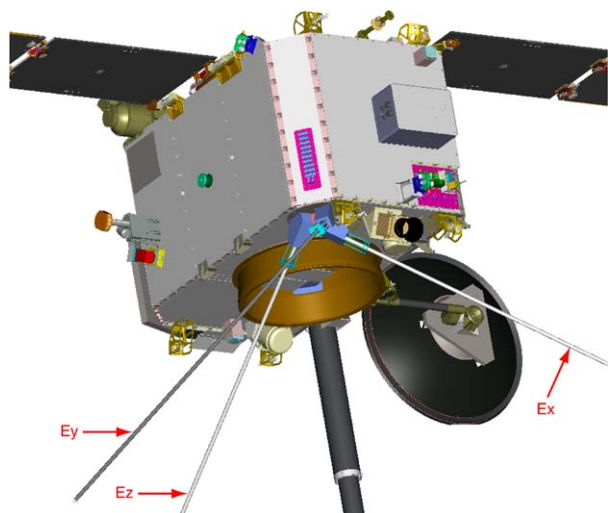
The mass of the S/WAVES antenna assembly, including three monopole antennas, preamplifier and mounting plate, was 7.080 kg. The electronics box, including all receivers, power supply and DPU had a mass of 5.750 kg. Including the harness and thermal blankets (for the antenna assembly), the total S/WAVES mass was 13.230 kg. S/WAVES has one nominal operating mode at turn-on and a wide variety of commandable options which do not affect instrument power consumption or bit-rate usage. The instrument has one spacecraft power interface which has a nominal primary load of about 15.4 W. The nominal allocation of spacecraft telemetry for S/WAVES is 2176 bits per second. This rate includes science data, instrument housekeeping, packet overhead and space weather data. Using a telecommand, it is possible to increase the actual bit-rate by as much as a factor of two.

5 Implementation/Integration

5.1 Accommodation on Spacecraft

The S/WAVES instrument, identical on the two STEREO spacecraft, was composed of two major pieces. The three mutually orthogonal antennas and preamplifier form one assembly and was attached to the rear face of the spacecraft, away from the sun (see Fig. 16). When deployed, the antennas extended into the sunlight. The S/WAVES receivers, power supply and data processing unit were assembled as a separate electronics box and was attached to the interior of the spacecraft structure. A cable harness connected the main electronics box to the preamplifier. S/WAVES had a single interface to the spacecraft power system and dual (for redundancy) 1553 interfaces to the spacecraft command and data handling system. Since, for safety reasons, the spacecraft was responsible for deploying the three antennas, each antenna had a simple filtered interface to the spacecraft deployment bus.

Fig. 16 The S/WAVES antennas (indicated by arrows) as they appear on the anti-sunward side of the spacecraft



5.2 Electromagnetic Compatibility

Many of the S/WAVES scientific objectives are based on the measurement of low-level radio-frequency signals for which maximum sensitivity and minimum noise are required. S/WAVES measurement goals are to provide sensitivity at or below ~ 7 nV/m/Hz $^{1/2}$. To make measurements of such small signal levels, several steps were implemented on STEREO. Efforts were made at the spacecraft, subsystem and instrument levels to produce observatories with minimal conducted and radiated electromagnetic interference. EMC tests were performed on each subsystem and instrument as part of its acceptance testing. A complete EMC survey was performed on each of the observatories before they were delivered to the launch site. As a result, the STEREO spacecraft were remarkably clean in ground tests and have proven acceptably clean on orbit.

Early in the Project, an EMC Board was formed to provide advice and direction in terms of electromagnetic compatibility. The NASA Project office, the spacecraft and the instrument teams all participated as members of the board's monthly meetings. In the beginning, the board laid out guidelines and requirements. The board provided advice on topics such as power supply design, shielding and grounding. The board held peer reviews of all detailed designs. As the subsystems and instruments completed their qualification and testing, the board reviewed EMC test results and suggested remedial action in cases thresholds were exceeded. The board also covered related areas such as electro-static cleanliness and magnetic cleanliness.

The following steps, which were implemented from the beginning of the project under the direction of the Project EMC Committee, produced excellent EMC results with a minimum investment in resources as well as minimum risk of problems in development or flight.

5.2.1 *Electrostatic Shielding*

The spacecraft body should form a Faraday cage to prevent stray electric field emissions from reaching the exterior and the S/WAVES antennas. Electronics boxes of spacecraft subsystems or instruments should also be well sealed. At points where instruments or harnesses penetrate from the interior to the exterior of the spacecraft structure, gaps must be sealed with conductive gaskets or tape.

5.2.2 *Electrical Bonding*

All electronics enclosures and especially those on the exterior of the spacecraft structure should be well grounded to the spacecraft structure. Electrical bonding should be maintained at all mechanical interfaces.

5.2.3 *Grounding*

Whenever possible, signal grounds should be connected to chassis grounds, in each electronics box. Primary power grounds must be isolated at all end users.

5.2.4 *Harnessing*

All harnesses should have an overall shield, connected to chassis ground at all ends. Within the bundles clock and other "noisy" signals must be shielded individually or in groups, with the shields connected to the signal ground at the source end or, when possible, at both ends of the cable. Primary power will be distributed as twisted shielded pairs or quads.

5.2.5 Frequency Control

The switching frequency of all DC/DC power converters must be stabilized at 50 kHz or harmonics thereof, with a preference for higher frequencies. Frequency control of at least one part in 10,000 is required and can be accomplished with synchronization or, as was done on STEREO, crystal controlled power supplies. Other major frequencies (clocks, oscillators, drive frequencies, etc.) used within the spacecraft should be recorded.

5.2.6 Solar Arrays

Capacitive filtering will be required for the leads from the solar array panels to the spacecraft power system in order to prevent noise from the power bus getting on to the panels.

5.2.7 Frequency Controlled Power Supplies: The Picket Fence Approach

One of the key approaches to this low-impact EMC plan is the use of frequency controlled power supplies throughout the spacecraft. In building electronic systems for use in space, it is recognized that some noise is unavoidable. DC to DC power converters usually require a chopping frequency and modern supplies using pulse width modulation produce switching transient noise at their conversion frequency and its harmonics. In recognition that some noise is inevitable, STEREO implemented a “picket fence” approach to power supplies and other sources of noise. All power converters were required to switch at 50 kHz or higher multiples. The frequency of conversion was also required to be very stable (typically using crystal control).

This combination results in a “picket fence” of noise at the power supply conversion frequencies and their harmonics (e.g., exactly 50 kHz, 100 kHz, 150 kHz and so on). As illustrated in Fig. 17, this picket fence of high order harmonics often extends across the entire S/WAVES band. Because the noisy frequencies are carefully controlled, the picket fence of noise has noise-free areas in the spectrum. The S/WAVES HFR receiver (described above) was built to take advantage of these noise free areas by making observations at odd multiples of 25 kHz (e.g., 125 kHz, 175 kHz, 225 kHz and so on across the spectrum) with a sharp comb filter. As a result, STEREO was not required to be very clean across the spectrum but only at odd multiples of 25 kHz. This approach, combining a safe design with a complete testing program made it possible to achieve S/WAVES scientific goals without an onerous EMC requirement or unverifiable testing limits.

5.3 Inter-Instrument Communication

To help coordinate in-situ observations made on STEREO, the S/WAVES and IMPACT teams established an inter-instrument communication path. This path is implemented using the spacecraft 1553 communication bus, the bus also used for instrument telemetry and telecommand. Once each second a message passes from S/WAVES to IMPACT and another message goes from IMPACT to S/WAVES.

The quality of a TDS event is first determined with an arithmetic calculation by the DPU. The quality value that is assigned can be altered. Messages S/WAVES receives from IMPACT contain information about burst activity within the IMPACT instrument. Upon receiving news that IMPACT is observing substantial activity, corresponding S/WAVES TDS events can be amended to increase their quality score and ensure they are sent to the ground. This produces simultaneous S/WAVES and IMPACT burst events for correlative study.

S/WAVES can also use information in the message from IMPACT to trigger LRS bursts. The LRS sampling period is exactly half that of the IMPACT magnetometer, allowing direct comparison of low frequency wave activity with magnetic field activity.

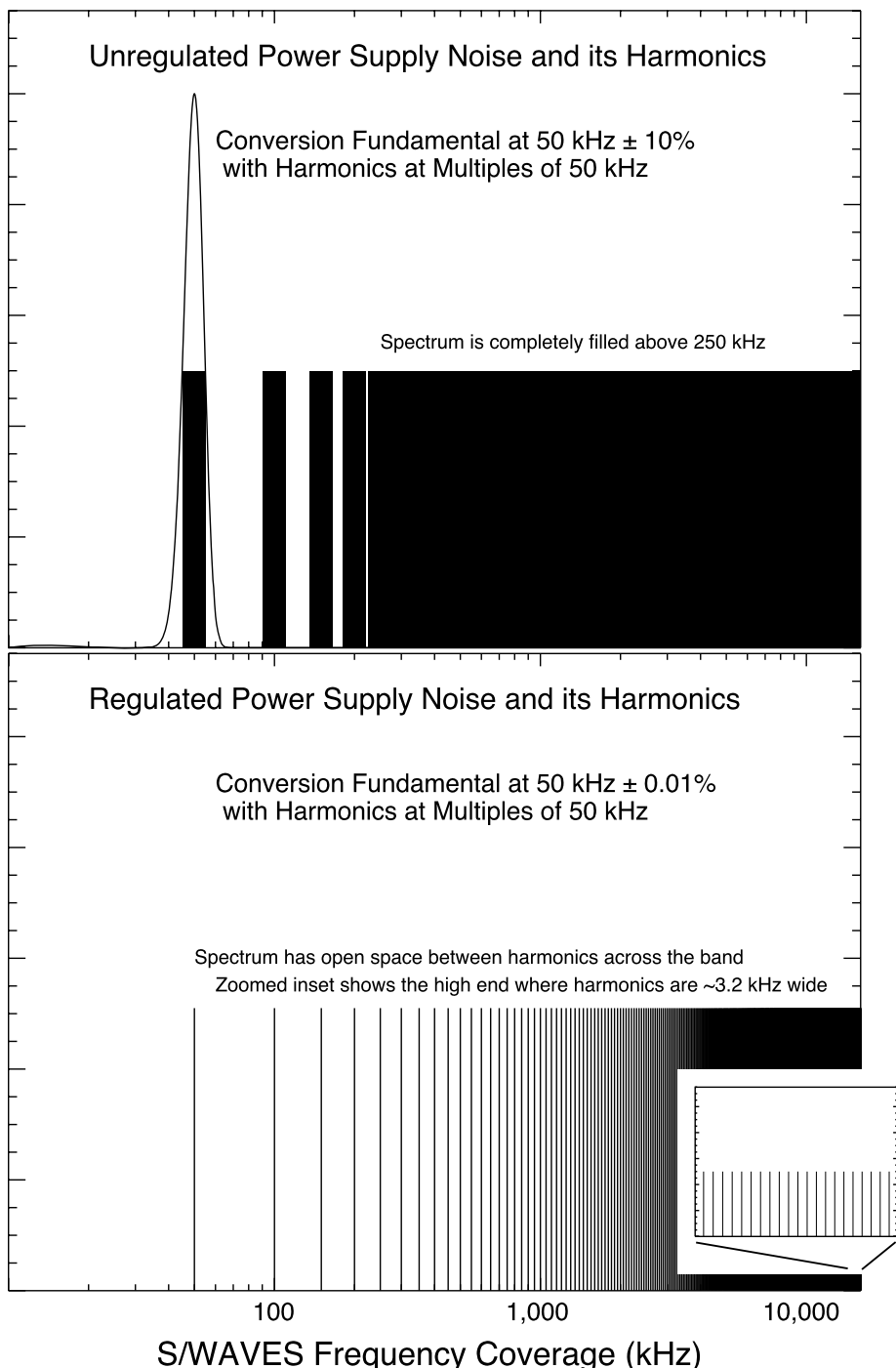


Fig. 17 The “picket fence” made possible by strict control of power supply switching transients. The *top* panel shows an unregulated spectrum of power supply noise, covering the entire band above 200 kHz. The *bottom* panel shows the quiet gaps in the band made possible when power supplies have good frequency control

5.4 Calibrations

5.4.1 Calibrations of the LFR, HFR and FFR

The calibrations for the LFR, HFR and FFR yield the receivers' responses and are used to convert binary telemetry data received on the ground into the physical parameters measured by the sensors. Complete calibrations were done in the laboratory before launch (ground calibrations) and are verified during the mission (in-flight calibration, described below).

5.4.1.1 Ground Calibrations Sophisticated and precise test equipment was designed and built for testing the instruments on the ground. Sine wave and white noise sources are provided. This test equipment is used for three kinds of test: gain curve measurements ("log law"), frequency bandwidth measurement and phase measurements.

For the receivers' gain curve measurements, a noise generator feeds a signal to the instrument through a variable programmable attenuator and a fixed attenuator. The programmable attenuator can step from 0 to 128 dB of attenuation with a programmable number of steps and step size. The response of the instrument is measured on all channels (1 for LFR band A, 2 for LFR bands B and C and the HFR). Channel 1 is connected to the antenna input $-Ex$ and channel 2 to $-Ez$. The input $-Ey$ is connected to the ground.

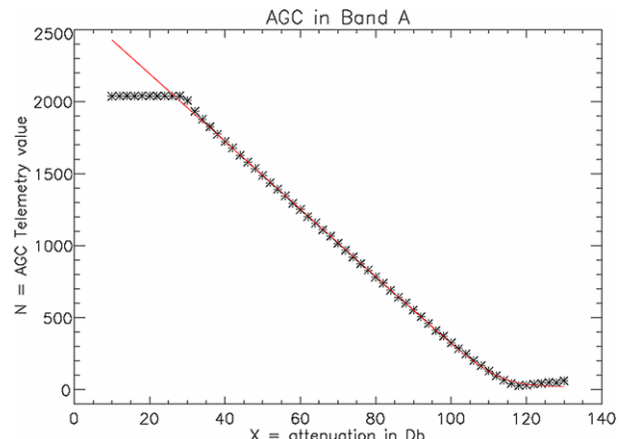
Figure 18 represents a typical gain curve obtained as a function of the attenuation for band A for the LFR. Nearly linear dependence between the input voltage and the continuous AGC output in telemetry points can be seen. For large signals (small attenuation) the AGC saturates, while for small signals, the receiver noise dominates.

This gain curve can be modeled by the following "log law" formula:

$$N = A_2 \cdot \log_{10} \left\{ \left[10^{\frac{(A_1 - x)}{10}} + 10^{\frac{A_4}{10}} \right]^{1/4} - 1 \right\} + A_3,$$

where N is the telemetry level (between 0 and 2047) and x represents the attenuation of the input signal in dB. The parameters A_1 , A_2 , A_3 and A_4 have a physical significance in the AGC circuitry. They represent the receiver's gain, the offsets and the internal and external noise, respectively. These parameters are computed by numerical fitting and then used for the computation of physical data values. The red line on Fig. 18 represents the result of such a fit.

Fig. 18 Typical analog output obtained as a function of attenuation in the case of LFR band A



5.4.1.2 In Flight Calibrations For in flight verification of the instrument calibration, an internal noise generator provides eight attenuation levels (in 10 dB steps), applied successively to the receiver inputs at a point after the preamplifier. This calibration sequence allows a verification of the long-term stability of the receivers' gain and phase shift as functions of amplitude and frequency throughout the course of the mission. If a drift in gain is observed, the calibration parameters used in data analysis can be corrected. The calibration cycle is initiated by telecommand and will be performed at regular intervals (e.g., every 48 hours).

5.4.2 Inter Calibration between STEREO and Wind

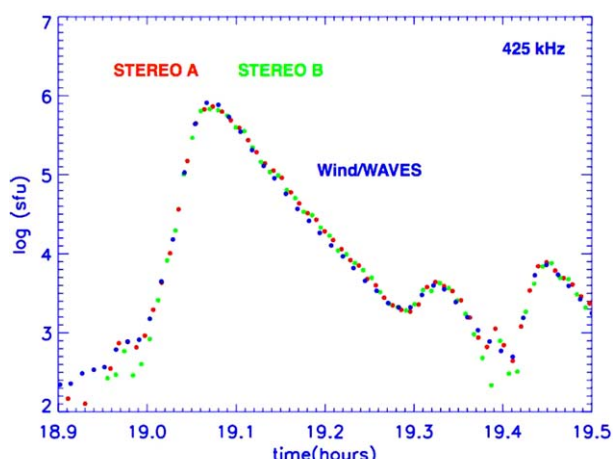
During the early phases of the STEREO mission, the STEREO spacecraft are together in Earth orbit and, therefore, also near WIND, which has a very well calibrated radio receiver (WAVES) and accurate direction-finding capability. This provides a unique opportunity to inter-calibrate the STEREO radio receivers using WIND/WAVES as the calibration standard. Because of their high intensity and their particularly smooth, long-duration intensity profiles, solar type III bursts provide an excellent calibration source for all three spacecraft.

We have measured the maximum flux density for a number of type III radio bursts to establish the relationship between the flux measurements at WIND and STEREO. By providing an absolute calibration for the STEREO data, we can directly compare the profile of a type III burst at each spacecraft. Preliminary results of a comparison of a type III radio burst, derived using this inter-calibration procedure, are shown in Fig. 19. The type III profiles observed at STEREO A (red dots), STEREO B (green dots) and WIND/WAVES (blue dots) are seen to match very well. This inter-calibration technique will provide three identically calibrated spacecraft that will enable us to correctly interpret any differences in the radio burst profiles that may be observed when the STEREO spacecraft are well separated from each other and from WIND.

5.4.3 Calibration of the TDS

The various time domain systems (4 TDS channels and 8 LRS channels) were calibrated before launch by applying known sine waves to the preamplifier inputs. For the LRS (8 channels including the APM), the complex gains were also calculated from the circuit diagram.

Fig. 19 The log of the radio flux density (in Solar Flux Units or sfu) of a type III radio burst observed simultaneously by STEREO A and B and by WIND/WAVES on December 7, 2006 at 425 kHz, as a function of the time in hours of the day



The magnitude of the calculated gains are shown as solid lines in Fig. 15 while the measured points are shown as discrete symbols. Knowledge of the complex gains is necessary to correct the sampled time sequences, which have been somewhat distorted by variations of gain with frequency, to give the true input waveform. The effects of the anti-aliasing filters have been included in the calibrations, and are shown in the figure.

5.4.4 Antenna Calibrations

The S/WAVES antenna reception properties have been analyzed by means of rheometry (electrolytic tank measurements) and numerical computer simulations (Bale et al. 2007; Macher 2005; Macher et al. 2006; Oswald et al. 2006a, 2006b; Rucker et al. 2005). The main focus is on the determination of the effective length vectors of the three antenna elements, since these are the quantities of interest for the evaluation of WAVES data (for wave direction finding and polarimetry). As an intermediate step, the simple antenna capacitances were measured as well.

A transfer matrix formalism (Macher 2005) was applied to take account of the coupling between the antennas, which is partly represented by the mutual capacitances. The aim was to determine the mentioned quantities for the quasi-static frequency range, where the wavelength is much greater than the antenna dimension. A frequency limit was sought below which the quasi-static parameters are applicable. For that purpose the frequency dependence of the effective length vectors over the whole frequency range of the S/WAVES receivers was calculated by wire-grid modeling. The obtained variation with frequency indicates that the sought limit is at about 1 MHz when the maximum achievable accuracy is required for each direction of wave incidence. The limit lies at about 2 MHz when it is sufficient to obtain this accuracy level on average over all directions of incidence. The details of these studies are described in Macher et al. (2006).

6 Scientific Operations

6.1 Space Weather forecasting with S/WAVES

The S/WAVES space weather beacon data (Biesecker et al. 2007) consists of receiver intensities from alternate channels of the HF band once per minute. This normally gives frequency resolution of 100 kHz from 125 kHz to 16 MHz, which corresponds to solar bursts occurring in the altitude range of 1–2 solar radii to as high as 80 solar radii. With this level of resolution in both time and frequency, solar bursts are easily detected, permitting estimates of the speed of CME-driven shocks and monitoring of the activity level associated with flares.

6.2 Archiving

6.2.1 Data Archiving at the STEREO Science Center

The STEREO Science Center (SSC) at NASA Goddard Space Flight Center (see Eichstedt et al. 2007) is responsible for archiving the STEREO data during the life of the mission after which they will transfer the archives to the US National Space Science Data Center for permanent storage. For S/WAVES, the archive will include the level-0 telemetry files, the space weather beacon products (data and daily plots), and processed data such as daily summary plots, one-minute averages, tables of events, limited direction of arrival data, etc.

6.2.2 The Archiving at the CDPP Centre

The S/WAVES data are also archived at the CDPP (Centre de Données de Physique des Plasma). This archiving activity is a usual commitment when CNES (Centre National d'Etudes Spatiales, the French space agency) is contributing to a French hardware experiment. Calibrated power spectral data are archived in both full resolution and 1-minute averaged resolution. Daily summary plots are also available. The data is accessible through the CDPP web site (<http://cdpp.cesr.fr>).

6.3 Ancillary Radio Data

Several radio observatories will contribute ancillary data at frequencies higher than the upper frequency limit of S/WAVES, corresponding to radio phenomena in the lower levels of the solar corona and yielding information on the origin of particles and shock waves. In particular, the Nançay Radio Heliograph will bring support to both SECCHI and S/WAVES. Other instruments include the Nançay Decametric Array, the Gauribidanur Radio Heliograph in India, the BIRS radio spectrograph in Tasmania, the ARTEMIS spectrograph in Greece, and the Ondrejov spectrograph.

7 Education and Public Outreach

The S/WAVES team is committed to participating significantly in public outreach for the STEREO mission. The first outreach component will be an outreach web site, dedicated to making the S/WAVES data and results available to the public. The emphasis will be on a clear and interesting presentation for the scientifically oriented public. Appropriate links to the S/WAVES education site will be included. To convey the excitement of the scientific process, the S/WAVES data appear on the Web in a timely manner.

To promote the STEREO mission at science museums and similar locations, the S/WAVES team will participate in the development of one or more traveling exhibits, designed to explain STEREO and contributions to understanding the Sun-Earth Connection and space weather. Opportunities will be used in connection with the organization of the International Heliophysical Year 2007–2008, a celebration of the 50th anniversary of the International Geophysical Year in 1957–58, which was the starting point of space exploration and space physics.

The S/WAVES education plan and web presence will be based primarily on the triangulation and tracking of solar radio bursts from flares and CME-driven shocks. To this end, we are developing a number of components, to be made available on the web page <http://swaves.gsfc.nasa.gov/>, which explain the scientific background, the spacecraft instrumentation and data analysis techniques, and the grade level appropriate, hands on projects that one can do to understand S/WAVES science and data analysis. One of our themes will be the “invisible universe”, because S/WAVES measures a section of the electromagnetic spectrum that is not visible to the human eye, but radio waves are a concept that people feel they understand. The ultimate web-based EPO component, towards which we are working, is user-oriented, interactive triangulation of radio bursts observed by S/WAVES, with radio-frequency correlated sonification. (Sonification makes good sense for radio waves, since they possess both frequency and intensity (volume). All that needs to be explained to the student/public is that we shift the radio frequencies to range of audible sound waves and, possibly, change the timescale.) Radio waves, radio receivers, and radio-stereoscopy provide a simple, understandable scientific perspective into the realm of space that we cannot “see”.

In parallel with the data and web-based activities, we are developing several classroom-oriented, S/WAVES radio models. The simplest version is used to demonstrate the directionality of radio waves and how this permits triangulation of the sources. Two of these simple models can be built for a minimal sum. With these models, we can explain that:

- A simple spacecraft model with one monopole antenna demonstrates *directionality* of (AM) radio waves, and two models can convey triangulation *measurement concepts* (kindergarten–fourth grade).
- A spacecraft model with a triad antenna (3 orthogonal antennas, like the S/WAVES antennas) permits discussion of a realistic spacecraft system; measurement of angles leads to investigation of basic *geometry & trigonometry* (fifth–eighth grade).
- The triad antenna equations provide motivation for *spherical trigonometry* and more advanced *algebraic equation solving* (ninth–twelfth grade).

More sophisticated S/WAVES models are in development; they will use more advanced electronics to approximate the performance of a S/WAVES radio receiver system. With audio output or analog output to an oscilloscope, it will be easier for students and others to understand how S/WAVES works. Eventually, digital output to a computer could be examined and analyzed in a manner similar to data from the on-orbit S/WAVES data.

8 Summary and Conclusions

The S/WAVES investigation on the STEREO spacecraft has the following main scientific objectives:

- Remotely track and probe CME-driven shocks and flare electrons, at high frequency and time resolution, from their genesis in the low corona to their interaction with the terrestrial magnetosphere, thereby creating the link between the EUV and coronagraph images and the in-situ CME and particle observations.
- Measure in-situ the spatial extent and structure of CME-driven shocks and flare and CME-associated electron beams.
- Make remote and in-situ measurements of solar radio sources that may provide a deeper and more comprehensive understanding of the mechanisms that generate type II (CME) and type III (flare) radio bursts.
- Measure solar wind electron plasma density and temperature in regions of cold, dense plasma within CME-associated magnetic clouds using quasi-thermal noise methodologies.
- Study the role of plasma microphysics in CME-driven shocks.

To achieve these objectives the S/WAVES instrument consists of a set of radio receivers and analyzers covering the frequency range from a fraction of a hertz to 16 MHz plus a single frequency channel near 30 MHz.

The instrument is fully operational and meets its specifications on the two STEREO spacecraft on which the level of electromagnetic interference is generally lower than specified.

The stereoscopic radio technique will allow new studies of energetic particle phenomena associated with CMEs relevant to space weather studies. The S/WAVES measurements will be enhanced by similar investigations on the Ulysses, WIND, and Cassini spacecraft, and by an extensive support from ground-based observations at higher frequencies. The prospects are excellent to attain major progress for a comprehensive understanding of radio

phenomena associated with CMEs and active phenomena in the inner heliosphere leading, in particular, to a significant validation of radio diagnostics as a major tool for the prediction of the impact of solar activity in the heliosphere.

Acknowledgements The authors would like to thank many individuals who contributed to making STEREO and S/WAVES a success. Some from the University of Minnesota are: Allen Knutson, Ron Bystrom, Sharon Barthel, Joshua Lynch, Ev Olcott, John Schilling and Doug Rowland. From the Observatoire de Paris: Daniel Carrière, Cécile Guériaud, Liam Friel, René Knoll and Léon Ly. From the Centre de Données en Physique des Plasmas: Christian Jacquay. From the University of California at Berkeley: Jeremy McCauley, Kate Harps and Ken McKee. From NASA/GSFC: Harry Culver, Lillian Reichenthal, Paul Buchanan, Antonio Reyes, Kevin Milligan, Steve Wasserzug, Shane Hynes, Jerry Hengemehle, Rick Mason, Rich Katz, Rod Barto, Therese Errigo, Lisa Bartusek, Mitch Davis, Julie Janus, Mike Delmont, Jim Adams, Nick Christimos and Haydée Maldonado. Some of our spacecraft partners at the Johns Hopkins University Applied Physics Laboratory are: Dave Myers, Andy Driesman, Carl Herrmann, Jim Roberts, Stuart Hill, Luke Becker, Jennifer Fischer, Marie Stevens, Ted Mueller, Ed Reynolds, Ron Dennison, Annette Dolbow and, of course, Elliot Rodberg.

At the Observatoire de Paris, this work was performed with the support of both CNES and CNRS. We wish to thank Jean-Yves Prado for his support concerning the CNES tracking antenna facility. At Minnesota and Berkeley, this work was performed with the support of NASA contract: NAS5-03076. I. Zouganelis acknowledges the European Marie Curie Fellowship SOPHYSM for financial support.

References

- M.H. Acuña et al., Space Sci. Rev. (2007, this issue). doi:[10.1007/s11214-007-9259-2](https://doi.org/10.1007/s11214-007-9259-2)
- M.J. Aschwanden, L.F. Burlaga, M.L. Kaiser et al., Space Sci. Rev. (2006). doi:[10.1007/s11214-006-9027-8](https://doi.org/10.1007/s11214-006-9027-8)
- S.D. Bale, P.J. Kellogg, D.E. Larson et al., Geophys. Res. Lett. **25**, 2929 (1998)
- S.D. Bale, M.J. Reiner, J.-L. Bougeret et al., Geophys. Res. Lett. **26**(11), 1573 (1999)
- S.D. Bale, P.J. Kellogg, F.S. Mozer, T.S. Horbury, H. Reme, Phys. Rev. Lett. **94**(21), 2150021 (2005)
- S.D. Bale, R. Ullrich, K. Goetz et al., Space Sci. Rev. (2007, this issue). doi:[10.1007/s11214-007-9251-x](https://doi.org/10.1007/s11214-007-9251-x)
- D.A. Biesecker, D.F. Webb, O.C. St. Cyr, Space Sci. Rev. (2007, this issue). doi:[10.1007/s11214-007-9165-7](https://doi.org/10.1007/s11214-007-9165-7)
- J.-L. Bougeret, J. Fainberg, R.G. Stone, Astron. Astrophys. **141**, 17 (1984)
- J.-L. Bougeret, M.L. Kaiser, P.J. Kellogg et al., Space Sci. Rev. **71**, 231 (1995)
- J.-L. Bougeret, P. Zarka, C. Caroubalos et al., Geophys. Res. Lett. **25**, 2513 (1998)
- G.E. Brueckner, R.A. Howard, M.J. Koomen et al., Sol. Phys. **162**, 357 (1995)
- I.H. Cairns, J. Geophys. Res. **91**, 2975 (1986)
- I.H. Cairns, J. Geophys. Res. **93**, 3958 (1988)
- I.H. Cairns, M.L. Kaiser, in *The Review of Radio Science: 1999–2002*, ed. by W.R. Stone (IEEE Press, 2002), p. 749
- I.H. Cairns, S.A. Knock, in *Planetary Radio Emissions VI*, ed. by H. Rucker, W.S. Kurth, G. Mann (2006), p. 499
- I.H. Cairns, P.A. Robinson, Geophys. Res. Lett. **24**, 369 (1997)
- I.H. Cairns, P.A. Robinson, Astrophys. J. **509**, 471 (1998)
- I.H. Cairns, P.A. Robinson, Phys. Rev. Lett. **82**(15), 3066 (1999)
- H.V. Cane, R.G. Stone, J. Fainberg et al., Geophys. Res. Lett. **12**, 1285 (1981)
- B. Cecconi, X. Bonnin, S. Hoang et al., Space Sci. Rev. (2007, this issue). doi:[10.1007/s11214-007-9255-6](https://doi.org/10.1007/s11214-007-9255-6)
- L.M. Celnikier, C.C. Harvey, R. Jegou, P. Moricet, M. Kemp, Astron. Astrophys. **126**(2), 293 (1983)
- L.M. Celnikier, L. Muschietti, M.V. Goldman, Astron. Astrophys. **181**(1), 138 (1987)
- G.A. Dulk, Y. Leblanc, J.-L. Bougeret, Geophys. Res. Lett. **26**, 2331 (1999)
- J. Eichstedt, W.T. Thompson, O.C. St. Cyr, Space Sci. Rev. (2007, this issue). doi:[10.1007/s11214-007-9249-4](https://doi.org/10.1007/s11214-007-9249-4)
- R.E. Ergun, D. Larson, R.P. Lin et al., Astrophys. J. **503**, 435 (1998)
- G.B. Field, Astrophys. J. **124**, 555 (1956)
- V.L. Ginzberg, V.V. Zheleznyakov, Soviet Astron. **2**, 653 (1958)
- N. Gopalswamy, S. Yashiro, M.L. Kaiser, R.A. Howard, J.-L. Bougeret, Astrophys. J. **548**, L91 (2001a)
- N. Gopalswamy, A. Lara, S. Yashiro, M.L. Kaiser, R.A. Howard, J. Geophys. Res. **106**, 29207 (2001b)
- N. Gopalswamy, S. Yashiro, G. Michalek et al., Astrophys. J. **572**, L103 (2002)
- N. Gopalswamy, E. Aguilar-Rodriguez, S. Yashiro et al., J. Geophys. Res. **110**(A12) (2005). CiteID12S07
- D.A. Gurnett, W.S. Kurth, D.L. Kirchner et al., Space Sci. Rev. **114**, 395 (2004)

- R.A. Hess, R.J. MacDowall, J. Geophys. Res. **108**(A8) (2003). CiteID 1313
 D.E. Hinkel-Lipsker, B.D. Fried, G.J. Morales, Phys. Fluids B **4**, 559 (1992)
 S. Hoang, N. Meyer-Vernet, K. Issautier, M. Maksimovic, M. Moncuquet, Astron. Astrophys. **316**, 430 (1996)
 S. Hoang, M. Poquerusse, J.-L. Bougeret, Sol. Phys. **172**, 307 (1997)
 S. Hoang, M. Maksimovic, J.-L. Bougeret, M.J. Reiner, M.L. Kaiser, Geophys. Res. Lett. **25**(14), 2497 (1998)
 Howard et al., SECCHI paper., Space Sci. Rev. (2008, this issue)
 K. Issautier, N. Meyer-Vernet, M. Moncuquet, S. Hoang, J. Geophys. Res. **103**, 1969 (1998)
 K. Issautier, N. Meyer-Vernet, M. Moncuquet, S. Hoang, D.J. McComas, J. Geophys. Res. **104**, 6691 (1999)
 K. Issautier, M. Moncuquet, N. Meyer-Vernet, S. Hoang, R. Manning, Astrophys. Space Sci. **277**, 309 (2001a)
 K. Issautier, R.M. Skoug, J.T. Gosling, S.P. Gary, D.J. McComas, J. Geophys. Res. **106**, 15665 (2001b)
 P.J. Kellogg, Astron. Astrophys. **169**, 329 (1986)
 P.J. Kellogg, Planet. Space Sci. **51**, 681 (2003)
 P.J. Kellogg, N. Lin, *The 31st ESLAB Symposium, Correlated Phenomena at the Sun, the Heliosphere and in Geospace*, ed. by A. Wilson, SP-415 (ESTEC, Noordwijk, 1997)
 P.J. Kellogg, D.A. Gurnett, G.B. Hospodarsky, W.S. Kurth, Geophys. Res. Lett. **28**, 87 (2001)
 P.J. Kellogg, D.A. Gurnett, G.B. Hospodarsky et al., J. Geophys. Res. **108**(A1) (2003). CiteID 1045
 P.J. Kellogg, S.D. Bale, F.S. Mozer, T.S. Horbury, H. Reme, Astrophys. J. **645**, 704 (2006)
 S.A. Knock, I.H. Cairns, J. Geophys. Res. **10**(A1) (2005). CiteID A01101
 D.E. Larson, R.P. Lin, J. Steinberg, Geophys. Res. Lett. **27**, 157 (2000)
 Y. Leblanc, G.A. Dulc, J.-L. Bougeret, Sol. Phys. **183**, 165 (1998)
 R.P. Lin, D.W. Potter, D.A. Gurnett, F.L. Scarf, Astrophys. J. **251**, 364 (1981)
 N. Lin, P.J. Kellogg, R.J. MacDowall et al., Geophys. Res. Lett. **30**(19), 8029 (2003). doi:[10.1029/2003GL017244](https://doi.org/10.1029/2003GL017244)
 J.G. Luhmann, D.W. Curtis, P. Schroeder et al., Space Sci. Rev. (2007, this issue). doi:[10.1007/s11214-007-9170-x](https://doi.org/10.1007/s11214-007-9170-x)
 M. Maksimovic, S. Hoang, N. Meyer-Vernet et al., J. Geophys. Res. **100**(A10), 19881 (1995)
 M. Maksimovic, J.-L. Bougeret, C. Perche et al., Geophys. Res. Lett. **25**(8), 1265 (1998)
 W. Macher, Transfer matrix description of multi-port antennas and its application to the Mars Express/MARSIS radar. Doctoral Thesis, University of Technology, Graz, 2005
 W. Macher, T.H. Oswald, H.O. Rucker, G. Fischer, STEREO-WAVES antennas: Reception properties in the quasi-static frequency range. Technical Report of the Space Research Institute of the Austrian Academy of Sciences, IWF-178, 2006
 D.B. Melrose, Sol. Phys. **79**, 173 (1982)
 N. Meyer-Vernet, C. Perche, J. Geophys. Res. **94**, 2405 (1989)
 N. Meyer-Vernet, P. Couturier, S. Hoang, C. Perche, J.-L. Steinberg, Geophys. Res. Lett. **13**, 279 (1986)
 N. Meyer-Vernet, P. Couturier, S. Hoang, C. Perche, J.-L. Steinberg, *AGU Monograph on Measurements Techniques in Space Plasmas*. Geophysical Monograph, vol. 103 (1998), p. 205
 M. Moncuquet, N. Meyer-Vernet, S. Hoang, J. Geophys. Res. **100**, 21697 (1995)
 T.H. Oswald, W. Macher, H.O. Rucker et al., Adv. Space Res. (2006a, submitted)
 T.H. Oswald, W. Macher, G. Fischer et al., in *Planetary Radio Emissions VI*, ed. by H.O. Rucker, W.S. Kurth, G. Mann (Austrian Academy of Sciences Press, Vienna, 2006b), p. 475
 A. Pedersen, Ann. Geophys. **13**, 118 (1995)
 M. Poquerusse, S. Hoang, J.-L. Bougeret, M. Moncuquet, AIP Conf. Proc. **382**, 62 (1996)
 M. Pulupa, S.D. Bale, American Geophysical Union, Fall Meeting 2006, abstract #SM13A-0349 (2006)
 M.J. Reiner, M.L. Kaiser, Geophys. Res. Lett. **26**(3), 397 (1999)
 M.J. Reiner, M.L. Kaiser, J. Fainberg, R.G. Stone, J. Geophys. Res. **103**, 29651 (1998a)
 M.J. Reiner, M.L. Kaiser, J. Fainberg, J.-L. Bougeret, R.G. Stone, Geophys. Res. Lett. **25**, 2493 (1998b)
 M.J. Reiner, M.L. Kaiser, J. Fainberg, R.G. Stone, J. Geophys. Res. **103**, 1923 (1998c)
 M.J. Reiner, M. Karlicky, K. Jiricka et al., Astrophys. J. **530**, 1049 (2000)
 M.J. Reiner, M.L. Kaiser, M. Karlicky, K. Jiricka, J.-L. Bougeret, Sol. Phys. **204**, 123 (2001a)
 M.J. Reiner, M.L. Kaiser, J.-L. Bougeret, J. Geophys. Res. **106**, 29989 (2001b)
 M.J. Reiner, B.V. Jackson, D.F. Webb et al., J. Geophys. Res. **100**(A9) (2005). CiteID 109814
 M.J. Reiner, J. Fainberg, M.L. Kaiser, J.-L. Bougeret, Sol. Phys. **241**(2), 351 (2007a)
 M.J. Reiner, M.L. Kaiser, J.-L. Bougeret, Astrophys. J. **663**(2), 1369 (2007b)
 P.A. Robinson, Sol. Phys. **139**, 147 (1992)
 P.A. Robinson, I.H. Cairns, D.A. Gurnett, Astrophys. J. **407**, 790 (1993)
 P.A. Robinson, Phys. Plasmas **2**, 1466 (1995)
 P.A. Robinson, Rev. Mod. Phys. **69**, 507 (1997)
 P.A. Robinson, I.H. Cairns, Sol. Phys. **181**, 363 (1998a)

- P.A. Robinson, I.H. Cairns, Sol. Phys. **181**, 395 (1998b)
P.A. Robinson, I.H. Cairns, Phys. Plasmas **8**, 2394 (2001)
H.O. Rucker, W. Macher, G. Fischer et al., Adv. Space Res. **36**, 1530–1533 (2005)
C. Salem, J.-M. Bosqued, D.E. Larson et al., J. Geophys. Res. **106**, 21701 (2001)
K. Saito, A.J. Poland, R.H. Munro, Sol. Phys. **55**, 121 (1977)
R. Schwenn, A. Dal Lago, E. Huttunen, W.D. Gonzalez, Ann. Geophys. **23**, 1033 (2005)
J.-L. Steinberg, S. Hoang, A. Lecacheux, M.G. Aubier, G.A. Dulik, Astron. Astrophys. **140**, 39 (1984)
R.G. Stone, J.-L. Bougeret, J. Caldwell et al., Astron. Astrophys. Suppl. Ser. **92**, 291 (1992)
E.C. Stone, A.M. Frandsen, R.A. Mewaldt et al., Space Sci. Rev. **86**, 1 (1998)
G. Thejappa, R.J. MacDowall, Bull. Am. Astron. Soc. **37**, 1502 (2005)
T.W. Unti, M. Neugebauer, B.E. Golstein, Astrophys. J. **180**, 591 (1973)
A.J. Willes, I.H. Cairns, Publ. Astron. Soc. Aust. **18**, 355 (2001)
L. Yin, M. Ashour-Abdalla, R.L. Richard, L.A. Frank, W.R. Paterson, J. Geophys. Res. **104**, 12415 (1999)

The Electric Antennas for the STEREO/WAVES Experiment

S.D. Bale · R. Ullrich · K. Goetz · N. Alster · B. Cecconi ·
M. Dekkali · N.R. Lingner · W. Macher · R.E. Manning ·
J. McCauley · S.J. Monson · T.H. Oswald · M. Pulupa

Originally published in the journal Space Science Reviews, Volume 136, Nos 1–4.
DOI: [10.1007/s11214-007-9251-x](https://doi.org/10.1007/s11214-007-9251-x) © Springer Science+Business Media B.V. 2007

Abstract The STEREO/WAVES experiment is designed to measure the electric component of radio emission from interplanetary radio bursts and in situ plasma waves and fluctuations in the solar wind. Interplanetary radio bursts are generated from electron beams at interplanetary shocks and solar flares and are observed from near the Sun to 1 AU, corresponding to frequencies of approximately 16 MHz to 10 kHz. In situ plasma waves occur in a range of wavelengths larger than the Debye length in the solar wind plasma $\lambda_D \approx 10$ m and appear Doppler-shifted into the frequency regime down to a fraction of a Hertz. These phenomena are measured by STEREO/WAVES with a set of three orthogonal electric monopole antennas. This paper describes the electrical and mechanical design of the antenna system and discusses efforts to model the antenna pattern and response and methods for in-flight calibration.

Keywords Sun: magnetic field · Sun: flares · Sun: coronal mass ejections

1 Introduction

The STEREO mission has as its primary science goal the study of the generation, evolution, and propagation of Coronal Mass Ejections (CMEs). CMEs that propagate into the

S.D. Bale · N. Alster · N.R. Lingner · M. Pulupa
Physics Department, University of California, Berkeley, USA

S.D. Bale (✉) · R. Ullrich · J. McCauley · M. Pulupa
Space Sciences Laboratory, University of California, Berkeley, USA
e-mail: bale@ssl.berkeley.edu

K. Goetz · S.J. Monson
School of Physics and Astronomy, University of Minnesota, Minneapolis, USA

B. Cecconi · M. Dekkali · R.E. Manning
LESIA, Observatoire de Paris, Meudon, France

W. Macher · T.H. Oswald
Space Research Institute, Austrian Academy of Sciences, Graz, Austria

heliosphere are called Interplanetary Coronal Mass Ejections (ICMEs) and are known to drive strong interplanetary (IP) shocks as they propagate through the heliosphere and often contain magnetic flux ropes (or “magnetic clouds”) carrying plasma thought to be remnants of solar filaments and loops.

As ICME-driven IP shocks propagate, they accelerate electrons by a fast-Fermi process (Wu 1984; Leroy and Mangeney 1984); the efficiency of fast-Fermi acceleration is thought to be a strong function of shock tangent angle, being most efficient at nearly perpendicular shocks (e.g. Krauss-Varban and Burgess 1991). The electrons accelerated at the shock front stream into the solar wind and form beam-like features, due to advection (Fitzenreiter et al. 1984; Bale et al. 1999). These beams are unstable to the growth of Langmuir waves and Langmuir waves propagating in the inhomogeneous solar wind may mode-convert by linear (Kellogg 1986; Bale et al. 1998) and/or nonlinear (Cairns and Melrose 1985; Goldman 1984) processes into freely propagating o -mode radiation at the electron plasma frequency $f_{pe}(r) = \sqrt{4\pi n(r)e^2/m_e}$ and its harmonic $2f_{pe}$, where $n(r)$ is the heliospheric plasma density at a distance r from the Sun.

These radio emissions, from CME-driven IP shocks, are known as “IP type II bursts” and are observed to drift in time from high to low frequencies. Since the emission frequencies are related to the local plasma density, IP type II bursts can be used to track CMEs from near to the Sun to 1 AU. For typical heliospheric density profiles, this corresponds to frequencies of 20 MHz (near the Sun) to 20 kHz (near 1 AU). IP type II bursts exhibit fine structure that may be related to shock structure (Bale et al. 1999), an important consideration for theories of energetic particle acceleration at shocks. The primary measurement goal of the STEREO/WAVES (S/WAVES) experiment is to resolve these IP type II bursts in frequency and time, to measure their direction of arrival (e.g. Fainberg et al. 1972), and use these measurements to infer CME speed and acceleration, shock structure, and heliospheric density. S/WAVES will also measure the fast-drifting radio emission from solar flare electrons, called “type III” radio bursts. Type II and III radio emission are observed at 1 AU to have intensities from approximately 10^{12} Jy (10^{-14} W/m² Hz) for very large events and down to the level of the galactic synchrotron spectrum at a few MHz (approximately 10^6 Jy or 10^{-20} W/m² Hz) (Novaco and Brown 1978), which defines the instrument noise level requirement.

Another science goal for STEREO/WAVES is the measurement *in situ* of the plasma waves involved in the plasma radiation process and collisionless shock physics. Langmuir waves are driven unstable by shock-accelerated electron beams and mode-convert to the observed radio emission. The mechanism of mode-conversion from Langmuir to radio waves is still poorly understood and polarization measurements from S/WAVES are essential. Langmuir waves in IP radio bursts and the terrestrial foreshock are observed to have amplitudes from above the thermal noise level to approximately 100 mV/m (e.g. Bale et al. 1997) at the local plasma frequency f_{pe} (10–40 kHz at 1 AU). Electric field noise at collisionless shocks is observed to have similar amplitudes and is primarily Doppler-shifted $f \approx v_{sw}/\lambda_D$, where λ_D is the local Debye length; this corresponds to measured frequencies up to a few kHz at 1 AU.

Some secondary science goals are the measurements of low-frequency electric field and density fluctuations (Bale et al. 2005; Kellogg et al. 2006) probably associated with the Alfvénic turbulent cascade and the measurement of the plasma thermal noise spectrum in CME filament material (Meyer-Vernet and Perche 1989; Larson et al. 2000). Although these measurements are scientifically very compelling (indeed perhaps more fundamental than the primary science!), they do not drive S/WAVES instrument requirements (next section). The overall STEREO/WAVES experiment is described in a companion paper (Bougeret et al. 2007).

Table 1 Antenna science requirements

Science objective	Antenna requirement
Radio direction finding	$L < 9$ m
Radio sensitivity	$C_B < 150$ pF and maximum L

2 Antenna Science Requirements

The primary S/WAVES science requires the measurement of the electric field component of radio emission from 16 MHz down to approximately 20 kHz, corresponding to free-space wavelengths of 18.75 m to >15 km. The need to do direction-of-arrival analysis requires an electrically short antenna ($2L \ll \lambda/2$) to minimize sidelobes and phase perturbations near the antenna quarter-wave resonance. The desire to observe the galactic synchrotron spectrum (as the instrument background), however, argues for more sensitivity and therefore longer antennas. The in situ plasma wave measurement goals also benefit from longer antenna elements. These requirements are summarized in Table 1.

At radio frequencies, the voltage gain of the antenna system goes as $G \sim C_A/(C_A + C_{\text{stray}})$, where C_A is the antenna capacitance and C_{stray} is the stray capacitance; C_{stray} includes the “base” capacitance C_B of the antenna with respect to the enclosure as well as cable and preamp input capacitance and is discussed more in Sect. 5. Therefore to maximize system sensitivity, the base capacitance must be minimized. Previous experience from the Wind, Ulysses, ISEE, and Cassini radio instruments suggested that C_B must be less than 150 pF (requirement) with a desired goal of $C_B < 100$ pF. A simple expression for the reactance of a monopole antenna (of length L , radius a , and wavenumber k) above an infinite ground plane (Balanis 1997) gives the antenna free-space capacitance

$$C_A \approx \frac{2\pi\epsilon_0}{(\log(L/a) - 1)} \frac{\tan(kL)}{k} \quad (1)$$

which takes a value of approximately 63 pF for a single $L = 6$ m monopole (with a 2.3 cm average diameter) at long wavelengths $kL \ll 1$. A preliminary measurement of the antenna base capacitance, done in the lab on an engineering model, gave a value of about 50 pF. Further measurements of base capacitance are described in Sect. 5. The above values imply a gain of $G \sim 1/2$ at radio frequencies, which is considered to be quite good.

The secondary science goals of measuring low frequency (to DC) electric fields would be better carried out with a “double-probe” antenna system similar to that on the Polar, Cluster, and FAST satellites (e.g. Harvey et al. 1995). A double-probe uses a current-biased probe extended on a boom (or wire) away from the spacecraft (see Pedersen et al. 1998).

3 Sensor Electrical Design

The S/WAVES antennas measure both the electric fields of freely propagating radio emission at frequencies above f_{pe} and in situ plasma waves and DC fields. In addition, the antenna floating voltage is sensitive to the ambient electron density, as discussed in the following.

Electric fields in the plasma couple to the antenna both resistively and capacitively (Fig. 1 illustrates this). In sunlight, the antennas emit photoelectrons with a characteristic (e-folding) energy of a few volts (e.g. Grard 1973). The antennas therefore charge positively with respect to the plasma and draw a return current from the thermal electron and the emitted photoelectron population. An electron sheath forms around the antenna with a thickness

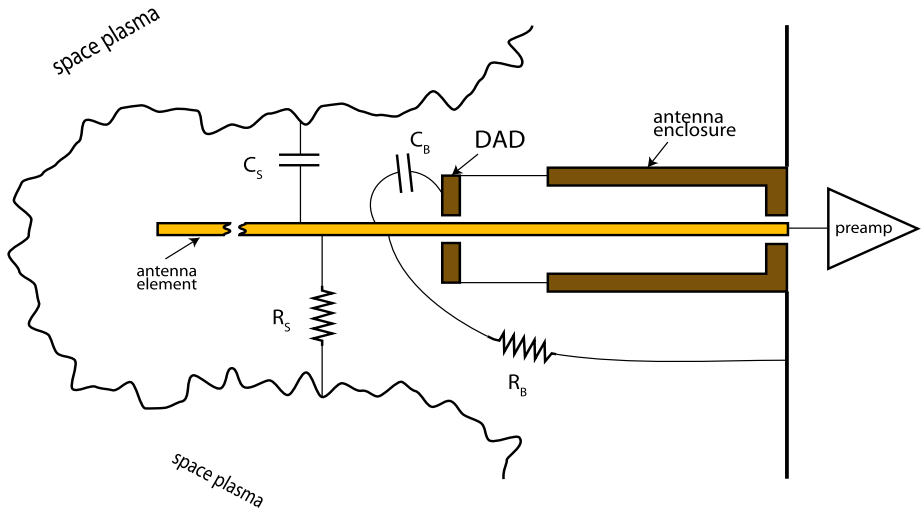


Fig. 1 A cartoon of the electrical design of an S/WAVES antenna. The antenna element is coupled both resistively and capacitively to the plasma, as well as being coupled to the antenna enclosure and spacecraft, as discussed in the text. At radio frequencies ($f \gg f_{pe}$), the antenna capacitance is effectively that of a monopole in vacuum and the coupling is purely capacitive

given approximately by the Debye length of the photoelectrons λ_p (e.g. Gurnett 1998 and references therein).

At DC and very low frequencies (typically less than a few hundred Hz), the antenna–plasma coupling is primarily resistive with the “sheath” resistance being given by the slope of the current–voltage curve (which of course depends on the thermal electron flux in the plasma). For an unbiased antenna in sunlight, this is approximately $R_s \approx V_p/I_e$, where V_p is the photoelectron energy (typically a few volts) and $I_e = A n_e e v_{the}$ is the thermal electron current on the antenna (of area A). In the solar wind at 1 AU, we would expect values like $R_s \approx 0.75 \text{ M}\Omega$.

Photoelectrons that leave one surface and are collected on another can be a source of current that flows between the antenna and the ground surfaces (antenna enclosure, spacecraft, solar panels, etc.). This is a short circuit to the measurement and is represented by a “base” resistance R_B . From Fig. 2, it can be seen that the antenna gain at low frequencies is approximately $G \sim R_B/(R_B + R_s)$. Since the sheath resistance R_s can be a strong function of the plasma thermal current (which varies), it is desired to make the base resistance R_B as large as possible. Ideally, this is accomplished by having very long booms (wire or rigid) to hold the sensor far from any ground surfaces. Insulating coatings and/or voltage-biased surfaces may also be used to erect a barrier between the probes and the spacecraft ground. For S/WAVES, no such accommodations have been made, since DC/LF measurements are not a primary science goal. Kellogg and Bale (2001) measured the base resistance on the Wind spacecraft, which uses long, thin wire antennas in the spin plane and short rigid antennas along the spin axis. They found a base resistance (for the wire antennas) that varies weakly with electron flux ($R_B \approx A + B/\text{flux}$, where A and B are constants) and takes values from 50 M Ω to 300 M Ω , depending on whether the antenna base is shadowed or in sunlight. Scaling those results to the S/WAVES antenna diameters (with shaded bases) gives a base resistance between 1–10 M Ω .

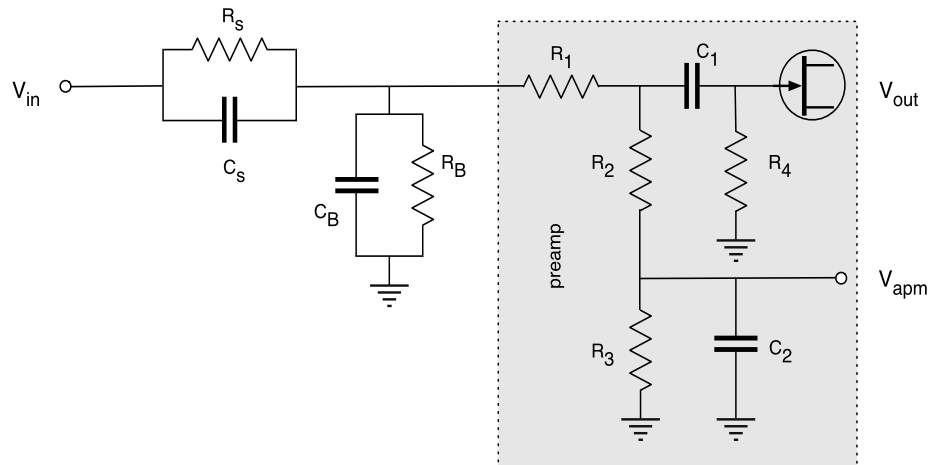


Fig. 2 Schematic of the electrical design of an S/WAVES antenna and preamp. The antenna impedance and base impedance have both resistive and capacitive components (see Fig. 1). Circuit elements in the gray box are real components within the preamplifier and have the values given in Table 2. Waveform and spectral measurements are high-pass filtered into a high-impedance FET (V_{out}). The antenna floating voltage is also produced at V_{apm}

Table 2 Values for circuit elements in Fig. 2

	Component	Value
Sheath resistance	R_s	$\sim 0.75 \text{ M}\Omega$
Antenna capacitance	C_s	$\sim 40 \text{ pF}$
Base resistance	R_b	$\sim 1\text{--}10 \text{ M}\Omega$
Base capacitance	C_B	$\sim 60 \text{ pF}$
	C_1	100 pF
	C_2	100 pF
	R_1	100 Ω
	R_2	33 $\text{M}\Omega$
	R_3	33 $\text{M}\Omega$
	R_4	150 $\text{M}\Omega$

At high frequencies ($f \gg f_{pe}$), the electric field of a radio wave is only coupled to the plasma very weakly. In this case, we can ignore the plasma and consider the antenna to be in a vacuum. As discussed in Sect. 2, the antenna gain is then given by $G \sim C_A/(C_A + C_B)$ and the design goal is to minimize the stray or “base” capacitance C_B between the antenna elements and any conducting structure (discussed in Sect. 5). For S/WAVES this was achieved by paying special attention to overall design and materials; for example, the roller surfaces which are in contact with the antenna element were anodized and isolated on insulating axes.

The basic design of the S/WAVES antenna system is a set of three orthogonal monopoles. Ideally, one would use three orthogonal dipole antennas, however mass and accommodation constraints did not permit this. While a monopole extended normal to an infinite ground-plane will behave as a dipole, the spacecraft is *not* an infinite groundplane and the final antenna pattern is different from that of a dipole. This effect is discussed in Sect. 5.

4 Antenna Mechanical Design

Each antenna assembly consists of a 6 m long Beryllium–Copper (BeCu) “stacer” element installed in a magnesium and aluminum housing that provides launch storage, deployment means, and support at the proper orientation. Figure 3 shows a CAD drawing of an antenna unit with the external covers removed. The basic components of a unit are the stacer antenna element, a flyweight brake mechanism, a deployment assist device (DAD), and a release mechanism (SMAR) to deploy the sensor. These components are described in the following. Figure 4 is a photograph of a deployed antenna unit.

Each spacecraft has three antenna assemblies mounted to a single interface plate which is integrated to the anti-sun side ($-X$ deck) of the spacecraft. When deployed, the three antennas form a mutually orthogonal pattern, equi-angular from the spacecraft deck. As shown in Fig. 5, the antenna elements deploy to form three edges of a cube whose corner touches the spacecraft. Projected onto the $-X$ deck of the spacecraft, the antennas are separated by 120° clock angle. Although not shown in Fig. 5, the “Z” antenna passes closest to the IMPACT instrument boom Luhmann et al. 2007.

A transformation matrix

$$\mathbf{M}_1 = \begin{pmatrix} -\frac{1}{\sqrt{3}} & -\frac{1}{\sqrt{3}} & -\frac{1}{\sqrt{3}} \\ -\frac{1}{\sqrt{2}} & \frac{1}{\sqrt{2}} & 0 \\ \frac{1}{\sqrt{6}} & \frac{1}{\sqrt{6}} & -\sqrt{\frac{2}{3}} \end{pmatrix} \quad (2)$$

takes a vector from the antenna coordinate system to the spacecraft coordinate system $\vec{x}_{sc} = \mathbf{M}_1 \cdot \vec{x}_{ant}$. This transformation does *not* include the perturbations of the antenna pattern due to electrical coupling with spacecraft structure (i.e. the “effective” antenna vectors); that effect is discussed in Sect. 5.

4.1 Stacer Antenna Elements

A stacer is a rolled, constant helical pitch, fixed diameter flat spring. The strip width, thickness, roll diameter, and helical pitch are selectable, allowing a stacer to be tailored for optimum properties for each application. Stacers range in size from 1–10 meters in length, from 4–55 mm in diameter at the tip, and can provide extensive force from almost nothing to >200 N. Trade studies can balance mass versus length, force, stiffness, etc. In the

Fig. 3 CAD drawing of an antenna unit, without covers, showing the flyweight brake, stacer antenna element, and the deployment assist device (DAD)

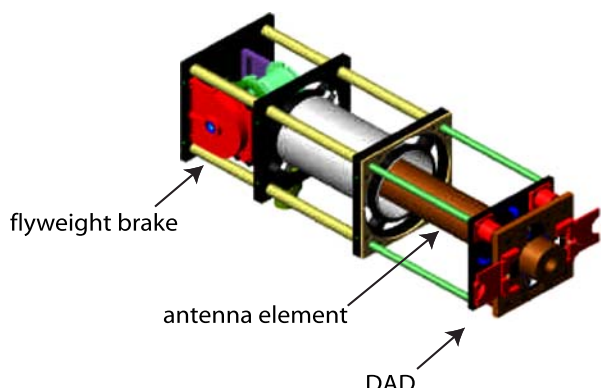


Fig. 4 A complete deployed antenna unit. The external housing is designed to point the deployed antenna

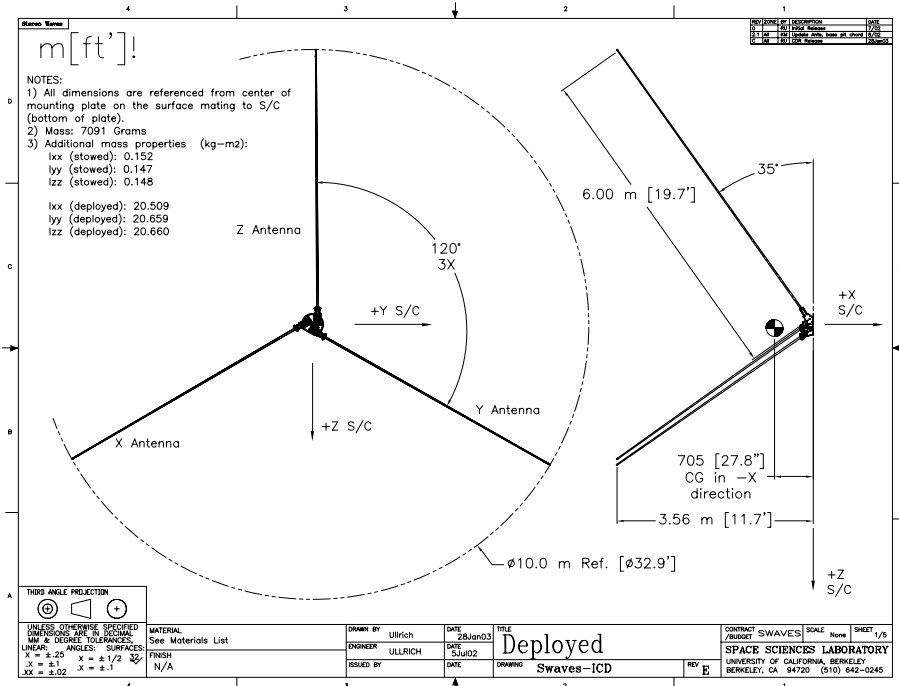
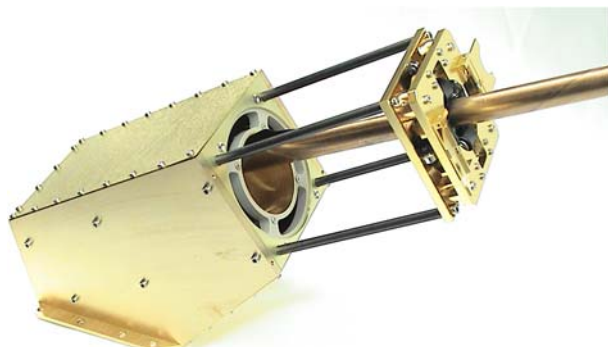


Fig. 5 The deployed configuration of the S/WAVES antennas. The deployed antennas form vertices meeting at the corner of a cube. The antennas are labeled X, Y, and Z and the spacecraft coordinate system is defined with $+X_{S/C}$, $+Y_{S/C}$, and $+Z_{S/C}$

last 30 years, more than 650 units have been used in aerospace applications, from sounding rocket sensors to gravity gradient booms with large masses on the end. Most applications use the stacer as a boom with the sensor(s) mounted directly on it; for the S/WAVES antennas the stacer itself is the antenna element. For this program, the selected spring material was the traditional beryllium copper (Be-Cu). This alloy (CDA172, XHMS temper) has a modulus (E) of ~ 131 GPa and a yield strength of $\sim 1,200$ MPa. To ensure repeatability of deployment, the hidden edge of the strip is coated with PermaSlik RMAC: molybdenum



Fig. 6 Beryllium copper stacer antenna element. The aspect ratio is exaggerated here for display purposes

disulfide in an epoxy binder. To minimize the optical intrusions of the stacer antennas for the other instruments on the spacecraft, the natural matte copper-colored surface was selected.

At deployment, the formation of the stacer starts with the initial coil winding inward from the (larger diameter) storage canister onto a cylindrical tip piece, which is slightly larger than the free-coil diameter of the stacer. Thus the stacer grabs the tip piece tightly, and as the tip deploys, the subsequent coils stack up on the prior, producing the characteristic spiral appearance. The typical helix angle provides for significant overlap, such that a section taken at any point along the stacer would yield at least two thicknesses of strip material. Since the outer layer of strip is rolled to the same diameter as the inner layer, the outer grips the inner with a force normal to the surface. Thus between layers significant inter-coil friction exists and prevents inter-coil slipping for small disturbances. This gives the stacer one of its more useful properties: it behaves as a thin-walled tube for small displacements, with similar bending strength and stiffness. If a larger displacement occurs, the coils slip, dissipating the strain energy, serving as a friction damper. The damping ratio value is typically 5–15% for the non-slipping regime, and can reach 30–40% with the slipping. Of course, the displacement limit is buckling, as any tube would experience when the material is taken beyond its yielding strength.

The motive force for the deployment is the stored strain energy that is input to the system when the stacer is stowed. The strip is flexed against the inner wall of the canister, laying each coil inside its predecessor, and expanded tightly against the inside of the can.

When deployed, the S/WAVES stacer antenna elements are approximately 6 m long with a tip diameter of 15.2 mm and a base diameter of 32 mm; this gives a surface area of about 0.45 m^2 . The mass of each stacer element is approximately 1 kg.

When compressed (stowed) it is a very compact package: the 6 m element fits in a cylinder 53×106 mm long. When released, this stored strain energy is reclaimed, giving the motive effort needed to extend the stacer along its path. The stacer generates a higher force at the beginning of stroke which drops off at the end of stroke. When stowed, the stacer is in a “meta-stable” state. If left unconstrained, it could deploy in either direction, therefore a back plate on the canister is required to ensure the correct deployment direction. To ensure that it deploys properly, with a well-formed helix gripping tightly on the tip piece, a deployment assist device (DAD) is incorporated.

4.2 Deployment Assist Device (DAD)

The Deployment Assist Device (DAD) guides the stacer element from its stowed configuration and also acts to provide effective rigidity to the deployed element by securing it at a second point.

As mentioned, a stacer when stowed in its canister is in a meta-stable configuration. It is wound out against the inner wall of the canister, and does not immediately develop a large force in the deployment direction. At initial motion, the stacer moves slowly in the axial

Fig. 7 Deployment assist device (DAD). The *upper panel* shows the DAD before antenna deployment, with the antenna tip piece held by trap doors. In the *lower panel*, the fully deployed antenna is held by roller nozzles, electrically isolated from the DAD itself



direction as the first coil pivots to grip the tip piece. The coils then form one at a time in the center of the can, pushing the previously formed coils outward along the deployment axis. It has been seen through many years of development that the stiffness and repeatability of the formed stacer can be enhanced by the use of an initiator that gives the first couple of coils a velocity boost. This is achieved by incorporating a spring-driven set of rods that are temporarily connected to the tip piece via trap doors. These springs pull the stacer out of the canister with ~ 90 N force, giving a strong initial impulse to the deployment. By the time the DAD reaches end of its 100 mm stroke and stops, the stacer has reached full velocity and the flyweight brake is spun up to speed. The stacer, continuing to deploy, pops the doors open, allowing it to continue deploying to full length unobstructed.

At this time the second feature of the DAD becomes functional: the roller nozzle is in contact with the outer surface of the stacer, giving strong radial support with low longitudinal drag. As the diameter of the stacer increases, the roller nozzle expands to accommodate it. The roller nozzle incorporates a set of four radially symmetric roller bearings that are mounted into a bell crank mechanism. The upper and lower plates of the nozzle are joined via springs, and supply the centering force for the rollers. The stiffness of the nozzle is set by the spring value, and is tailored for each application. As the stacer deploys and its diameter increases, the rollers are forced apart, compressing the springs, centering the stacer. Any offset from center lowers the force on the side away from the offset, and increases by a similar amount the side in the offset direction, giving a double centering force. Axial drag is typically less than 2 N while the centering force is ~ 50 N. The DAD is shown in Fig. 7.

4.3 Shape Memory Alloy Release (SMAR)

Deployment is initiated when the Shape Memory Alloy Release (SMAR) is triggered. The SMAR uses the interesting phase change properties of a 50% titanium–50% nickel alloy

Fig. 8 SMAR and filter board



(trade named Nitinol initially) to provide the actuation of each of the S/WAVES antenna elements. This device, pioneered by TiNi Aerospace in cooperation with UCB-SSL, takes advantage of the ~4% dimensional change in the drawn alloy wire when heated above its transformation temperature. This lengthening allows a ball detent mechanism to release a spring-loaded retracting pin. Since there was a low design load requirement (@ 50 Gs), a standard P10-605-4.5RS with roller tip providing 45 N of retraction force was selected. When an electric current is passed through the Ti–Ni wire, it heats up, changes phase, elongates, and releases the pin, which retracts, allowing the stacer to deploy. The main benefit of using an SMAR, aside from increased safety as no explosives are incorporated, is that the flight unit can be tested over and over again (hundreds of cycles), and can be simply reset using a hand tool, with no temperature- or time-dependent constraints. A filter circuit was inserted in line with the SMAR trigger wires to remove any noise from the spacecraft firing circuits that could be conducted into the antennas. The SMAR and filter are shown in Fig. 8.

4.4 Flyweight Brake

After the SMAR has been triggered, kick springs push the DAD rods out of the tubes giving the stacer a good initial velocity. The stacer continues to recover the stored strain energy as it uncoils during extension, so the deployment velocity would continue to accelerate unless/until a balance between drag and push is achieved. This balance is never reached by the bare stacer, so the deployment velocity unchecked can reach a run-away condition, with the possible issues of rivet shearing, strip tearing and resultant separation from the assembly or other damage as consequences. As with every stacer, a means to limit deployment velocity (or travel) is incorporated. For the S/WAVES Antennas, a flyweight brake mechanism is used to govern the stacer velocity. Similar to the device found on dial telephones that regulates the rotation rate, the flyweight brake supplies braking force proportional to the rotational speed of its weight assembly. At the beginning of deployment, the FWB is not up to speed, and provides no resistive drag as the brake shoes are not touching the brake drum. Once the DAD has completed its stroke, the FWB is up to speed and the shoes are engaged. If the force (speed) increases, the flying brake shoes are centripetally accelerated against the brake drum harder, increasing the braking force and slowing the rotational velocity. As the speed

Fig. 9 Flyweight brake (without the Dacron string)



then decreases, the centripetal acceleration of the shoes decreases, allowing the deployment speed to stabilize. Over a wide range of forces, the brake typically can control the speed to $\pm 10\%$. For S/WAVES, a deployment velocity of ~ 2 m/s was chosen. This allows a strong momentum to build, but is slow enough to be controlled, preventing damage to the stacer at the end of travel. The stacer tip piece is connected to the brake assembly by a woven Dacron (parachute “shock”) cord. To dissipate the final momentum at the end of the stroke, the Dacron cord stretches, absorbing the shock from the stacer coming to a sudden halt. The flyweight brake mechanism is shown in Fig. 9.

4.5 Mechanism Operation and Safety

When the SMAR is triggered, the restraint pin pulls out of the tail of the stacer tip piece. The deployment assist device (DAD) gives the stacer an initial kick for the first 100 mm of travel. By this time, the initial coils of the stacer are fully formed around the tip piece, and the flyweight brake has been spun up to speed, limiting the speed of deployment to ~ 2 m/s, giving a total deployment time of ~ 3 s.

The stacer is *not* retractable once deployed. Re-stowing is achieved by removal from the spacecraft, and hand retraction whereby the stacer is compressed into its canister and the lanyard and flyweight brake are rewound. Finally, the SMAR is reset, reinstalled, and the spool lock is set.

The primary method for retaining the stacer is the SMAR. It has a stainless steel pin that is inserted into the tail of the stacer tip piece. It retracts only upon spacecraft command, and is the method for deployment on orbit. A safety pin inserts into the rear part of the tip piece to provide a redundant method of keeping the stacer from deploying at undesired times. This pin is a red-tag item, meaning it must be removed prior to launch. It can be removed from the exterior of the unit. Additionally, an RF tight test cap incorporating a method of attaching to the antenna to provide input for instrument verification and calibration, has the ability to capture a released stacer, should there be an unexpected deployment event when the safety pin is removed. The test cap is also a red-tag item. This three-tier approach gives the antennas excellent defense from unexpected deployment and potential contact with support personnel.

4.6 Verification

The S/WAVES qualification activities were based on GEVS SE, as modified by JHU-APL for mission-specific needs. The test regime selected for the STEREO mission was Protoflight, meaning new (unflown or non-heritage) hardware is tested with a combination of prototype (EM) levels (i.e. temperature or vibration) with flight (FM) durations. This method is typically used to shorten development times by eliminating the engineering/qualification model fabrication and test period. However, the S/WAVES Team did build up an engineering model, and tested it to the protoflight levels. The main changes and additions to the testing regimen: Level 300 cleanliness, UV + Visible light inspection, no silicones used for fabrication, and testing for silicone residuals. Vibration levels were taken from the Delta II users manual modified by APL analysis for the stacked configuration.

Validation of deployables must balance the desire to prove beyond question that the mechanism will deploy in space with the requirement to avoid wear and damage to the device. This breaks down to: How many times? GEVS provides a minimum number, and each program defines how many additional operations are required. There is a concern regarding wear margin, too. The design must show that it is sufficiently robust to survive testing and flight without degradation. The EM served this purpose, getting many deployments more than the FMs did. After inspection of the EM, a test plan was developed, reviewed, and implemented. The EM was deployed more than 15 times throughout the program while the FM units were deployed 4 times: 2 in ambient conditions and 2 in thermal vacuum.

Testing large deployables in a simulated space environment is difficult, and ensuring that the test actually verifies functionality is critical. Deploying the antennas horizontally was chosen as it is easy to develop a 6 m long test rig that rests on stands, and can be used in thermal vacuum deployment tests. This consisted of an aluminum track, with a low-friction trolley to guide the tip piece down its length. A 6 m long \times 210 mm diameter tube was attached to an existing thermal vacuum chamber allowing the deployment track to be installed inside for thermal vacuum deployments. The length measurements and deployment times are more accurate horizontally than if deployed vertically as the stacer behaves more uniformly when not subjected to an axial gravity load. Each antenna assembly was subjected to seven hot/cold cycles at high vacuum (10^{-6} Torr). At the final temperature cycle, each unit was deployed once hot and once cold.

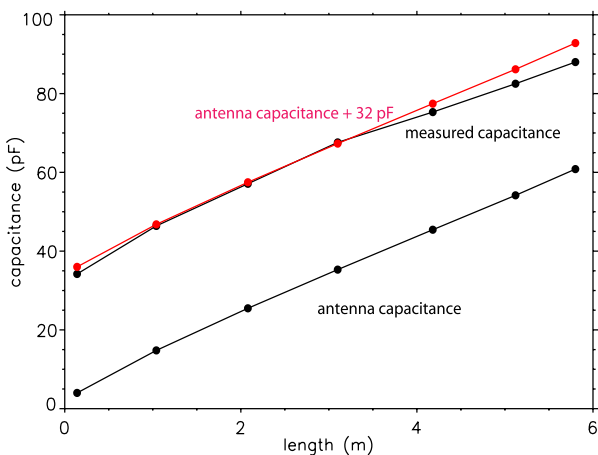
The first natural (cantilever) frequency of each antenna element was measured using a small accelerometer, after the second ambient deployment. Measurements of the cantilever frequency f_0 and damping ratio showed a family of values clustering around $f_0 \approx 0.6$ Hz and an average damping ratio of 5.2%.

5 Base Capacitance Measurements

As discussed in Sect. 2, the gain of the antenna system at high frequencies is determined by the level of stray capacitance. In this context, sources of stray capacitance are the “base” capacitance, capacitance in the semi-rigid coax cables between the antennas and preamps, and the input capacitance of the preamps. Cable and preamp-input capacitance are measured easily in the lab: for S/WAVES, cable capacitance is approximately $C_C \approx 13$ pF and the measured input capacitance of the preamps is $C_{PA} \approx 22$ pF.

The base capacitance is more difficult to measure, since an accurate measurement requires that the antenna be deployed and it is measured in parallel with the antenna free-space capacitance C_A (1).

Fig. 10 Measurements of the capacitance of an S/WAVES antenna. The upper black points are measured capacitances vs antenna length. The lower black points are the theoretical expectation C_A for a monopole against a ground plane (1). The red points are C_A plus 32 pF, which represents the base capacitance



To understand the base capacitance, an S/WAVES flight spare unit was deployed in the high bay at the Space Sciences Laboratory at UC Berkeley. The unit was mounted to deploy normal to a 1 m \times 1 m horizontal conducting plane and suspended from the tip by a 2 m nonconducting string from a crane. The exterior of the antenna unit was connected to the ground plane. The capacitance was measured at the SMA connector on the antenna box using a BK Precision 878 LCR meter (operating at 1 kHz). Following this measurement, the antenna was lowered, 1 m of stacer was cut from the end, the length and diameter were measured, and it was suspended and tested again. This process was repeated until only 14 cm of the stacer antenna extended beyond the base of the deployment unit.

The results of these measurements are shown in Fig. 10. The upper set of black dots shows the measured capacitance as a function of antenna length. The lower black dots show the theoretical free-space antenna capacitance C_A (1) as a function of length (and radius, which varied at the antenna length was cut). The set of red dots shows the free-space capacitance C_A plus 32 pF, which agrees well with the measured values. For antenna lengths greater than 4 m, the theoretical curve overestimates the measured capacitance. This is because (1) is valid for an infinite groundplane and this approximation becomes weaker with longer antenna lengths.

These measurements suggest a value of $C_B \approx 32$ pF for the base capacitance. Then the total stray capacitance of an antenna unit is $C_{\text{stray}} \approx C_B + C_C + C_{PA} \approx 32$ pF + 13 pF + 22 pF = 67 pF, which gives an antenna gain of approximately $G \approx C_A / (C_A + C_{\text{stray}}) \approx 1/2$.

6 Modeling of the S/WAVES Antennas

The three monopole antenna elements are used by S/WAVES to sense the electric field of radio waves. Due to radiation coupling between each other and with the spacecraft body and appendages the reception properties of the antennas differ from what one would expect from the respective “stand-alone” monopoles. In the present context the so-called effective length vector \vec{h} is most suitable to represent the reception properties. It comprises the electrically effective length and direction of an antenna, thereby representing the relation $V = \vec{h} \cdot \vec{E}$ between the voltage V received from an electromagnetic wave and its electric field \vec{E} . For the mentioned reasons the effective length vectors \vec{h}_X , \vec{h}_Y and \vec{h}_Z of the S/WAVES antennas

X , Y , and Z deviate considerably from the respective mechanical elements. Several methods are applied to determine these vectors as well as the antenna capacitances. The focus is on the quasi-static frequency range, where the wavelength is much greater than the dimension of the antenna-spacecraft system. In this range, the effective length vectors are real and constant quantities, therefore in-flight calibration is feasible (whereas at higher frequencies, the antenna pattern is complicated and modified by spacecraft structure—this makes in-flight calibration very difficult).

6.1 Simulations and Rheometry Measurements

Computer simulations and rheometry measurements are performed, providing completely independent approaches. The computer simulations are based on wire-grid modeling, where the whole spacecraft structure is represented by a mesh of wires covering the spacecraft surface. Several smaller features which show no significant influence on the results were omitted in the final modeling. The main features which affect the reception properties most are the solar panels, the high-gain antenna and the IMPACT boom (Fig. 11). For the rheometry measurements, a more detailed model is devised (Fig. 12). Rheometry is an electrolytic tank measurement adapted to antenna analysis, which was developed at the Observatoire de Paris-Meudon in the early 1970s. It proved very suitable for the determination of effective length vectors of many spaceborne antenna systems. For the measurement of the S/WAVES antennas a similar set-up was used as for the Cassini/RPWS antennas (Rucker et al. 1996) at Graz and a new rheometry facility was built at UC Berkeley. Both rheometry models were 1/30 scale.

The results of the numerical and the experimental approach agree within the inherent inaccuracy of the methods. The table in Fig. 14 shows the averages of the effective length vectors as obtained by the two methods, from both Graz and Berkeley. The Berkeley results include only rheometry results, as no wire grid simulations were done at Berkeley. The accuracy is about 5–6 degrees for directions and 5% for the effective lengths. The mechanical antenna elements are also shown for comparison. The spacecraft coordinate axes are defined as follows: The X -axis is directed opposite to the boom, the Y -axis parallel to the axes of the solar panels and directed as shown in Fig. 10, the Z -axis completes the right-handed triad. The antenna axes are given in spherical coordinates with regard to the reference frame ($-Z$,

Fig. 11 Wire-grid model of STEREO spacecraft with S/WAVES antennas (red). The components which affect the antenna reception properties most are the solar panels (blue), the high gain antenna (gray), and the IMPACT boom (tapered vertical rod)

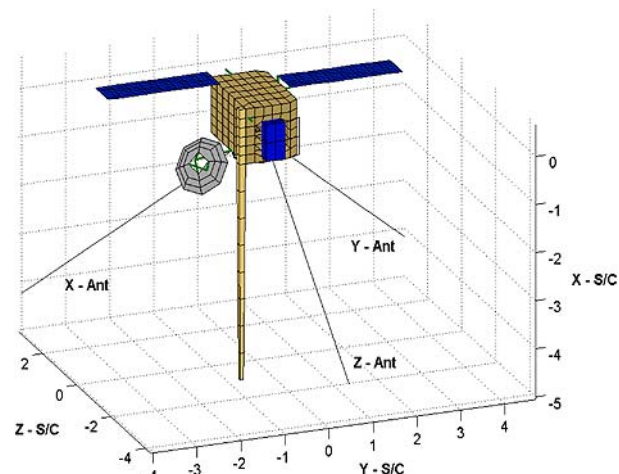


Fig. 12 STEREO spacecraft model used for the rheometry measurements in Graz. Only two of the S/WAVES antennas are visible

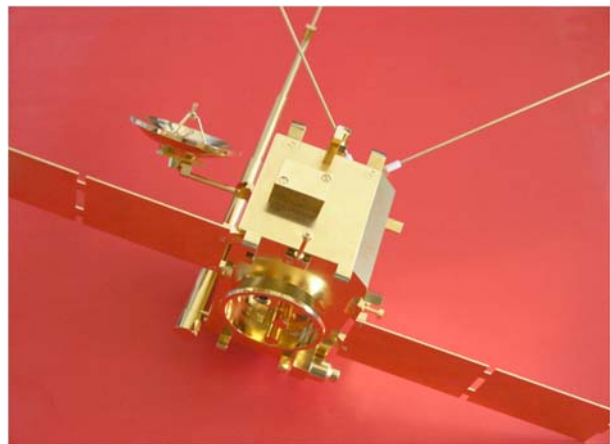
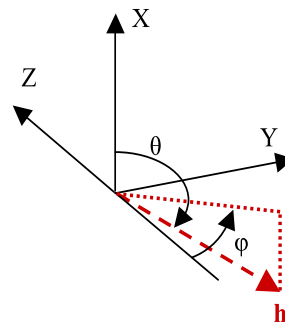


Fig. 13 Definition of spherical coordinates θ and ϕ in the spacecraft-fixed reference frame for the representation of effective and mechanical antenna axes (in the latter case the origin is identified with the respective antenna feed)



Y, X), i.e. colatitude θ from $+X$ and azimuth ϕ from $-Z$ towards Y (Fig. 13). The Graz results are also given for open and loaded antenna ports. In this context the loads are the base capacitances C_B of the respective antennas, consisting of receiver input capacitances, cable, and mounting capacitances. Measurements of the individual capacitances gave the same total $C_B = 90$ pF for each antenna, which was implemented in both methods. The results show clearly that the effective lengths for open ports are about half of the respective mechanical antenna lengths, which is a well-known result for the ideal dipole. However, the effective axes significantly differ from the respective mechanical ones. One also can clearly see that the base capacitances further reduce the effective lengths dramatically, and even cause an offset of the effective antenna directions. This effect is due to the radiation coupling between the antennas (directly or via the spacecraft body) and confirms the importance of the base capacitances. A detailed study of the antenna system including the dependence of the reception properties on various spacecraft features (e.g. the rotation angle of the high gain antenna which gradually changes in the course of the mission) will be published in a separate paper.

To transform from measured voltages V_X, V_Y, V_Z on the antennas (where X, Y, Z subscripts denote the antenna coordinate system) into an “electric field” in the spacecraft coordinate system, a transformation

		h [m]	θ [deg]	ϕ [deg]
Physical antennas	X	6.00	125.3	-120.0
	Y	6.00	125.3	120.0
	Z	6.00	125.3	0.0
Open feeds (Graz)	$\mathbf{h}_{X,0}$	2.98	126.0	-141.2
	$\mathbf{h}_{Y,0}$	3.85	118.8	128.7
	$\mathbf{h}_{Z,0}$	2.34	133.0	21.5
Open feeds (UC Berkeley)	$\mathbf{h}_{X,0}$	3.04	127.0	-148.0
	$\mathbf{h}_{Y,0}$	3.95	120.8	123.6
	$\mathbf{h}_{Z,0}$	2.45	132.6	22.6
w/base caps (Graz)	\mathbf{h}_X	1.17	120.2	-135.0
	\mathbf{h}_Y	1.44	114.5	127.1
	\mathbf{h}_Z	0.97	124.5	15.5

Fig. 14 Mechanical antenna lengths and directions of S/WAVES antennas X , Y , and Z compared with the effective length vectors for open feeds and for a load (base capacitance) of 90 pF at each antenna. The given results are averages of rheometry measurements and wire-grid simulations, with the exception of the Berkeley results, which include only rheometry measurements

$$\begin{pmatrix} E_x \\ E_y \\ E_z \end{pmatrix}_{\text{SC}} = \mathbf{M}_2 \cdot \begin{pmatrix} V_X \\ V_Y \\ V_Z \end{pmatrix}_{\text{ANT}},$$

where

$$\mathbf{M}_2^{-1} = \begin{pmatrix} h_X \cos \theta_X & h_X \sin \theta_X \sin \varphi_X & -h_X \sin \theta_X \cos \varphi_X \\ h_Y \cos \theta_Y & h_Y \sin \theta_Y \sin \varphi_Y & -h_Y \sin \theta_Y \cos \varphi_Y \\ h_Z \cos \theta_Z & h_Z \sin \theta_Z \sin \varphi_Z & -h_Z \sin \theta_Z \cos \varphi_Z \end{pmatrix}$$

can be applied using the effective lengths and angles from the table in Fig. 14.

6.2 Anechoic Chamber Measurements at High Frequencies

S/WAVES measurements also include the Fixed Frequency Receiver (FFR) which operates at high frequencies above the antenna resonance. For the FFR, two monopoles are used as a dipole and any combination is selectable (i.e. dipole $X-Y$, $Y-Z$, or $X-Z$); these dipoles will have an electrical resonance around 25 MHz while the FFR operates at 30.025 or 32.025 MHz. Furthermore, at these frequencies it is no longer possible to neglect the influence of the spacecraft and its appendages. These effects may give rise to unexpected secondary lobes and cause lower gains in the primary lobes.

To understand these effects, an electrical model of the STEREO spacecraft was built at 1/10th scale and antenna patterns were measured in an anechoic chamber at the CNES facility in Toulouse, France. In order to keep the same ratio of the wavelength to spacecraft dimension, the testing frequencies are multiplied by 10. The testing campaign consisted of measurements on the three dipoles at various frequencies (300, 320, 340 and 360 MHz) and various orientations of the scale model. Facilities consist of an anechoic chamber including

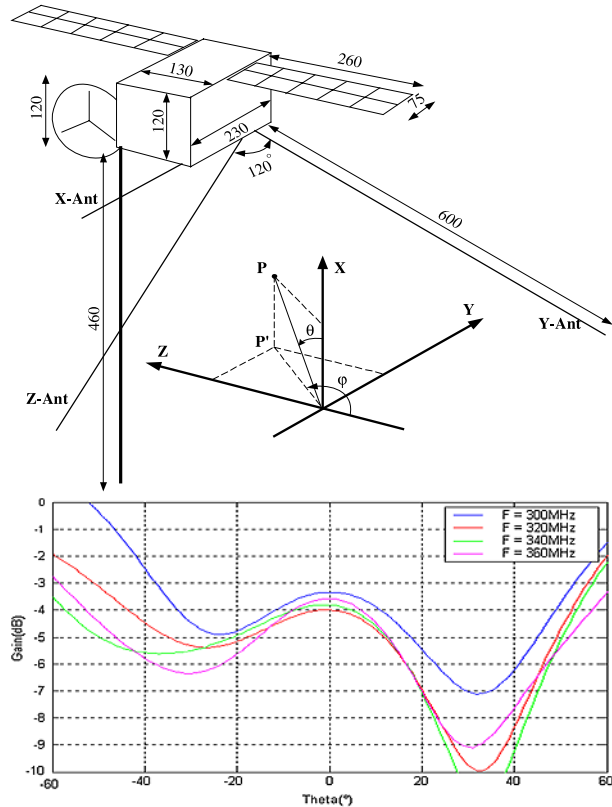


Fig. 15 Antenna gain at high frequencies from anechoic chamber measurements with a scale model. The coordinate system is shown in the spacecraft schematic (*upper panel*)

a large parabolic reflector providing a plane wave. Both components of the electric field were measured in the horizontal and vertical position (E_h and E_v), which are associated using (2):

$$E_{dB} = 10 \log(E_h^2 + E_v^2) \quad (3)$$

with E_h and E_v in V/m. Finally, the absolute gain was determined and calibrated by comparison to a reference antenna. As an example, the Fig. 15 shows the resulting radiation patterns of the dipole 1–2. This is plotted in a Cartesian representation, where the X -axis is the θ angle from -60° to $+60^\circ$ and the Y -axis is the antennas gain for a given orientation. More specifically we are interested in the antenna gain in direction of the sun (i.e. for θ neighboring 0°). Taking into account the localization of the antennas on the (backside of the) spacecraft, it is clear that their gain is not optimal in direction of the Sun. For $\theta = 0^\circ$, the gain disparities are about 2 dB depending on the frequency. The gain is between -2 dB and -4 dB for dipoles 1–2 and 1–3, and slightly weaker for the dipole 2–3 which is in the shadow of the solar panels. Since the gain at the frequencies 300 MHz and 320 MHz are less disturbed by the spacecraft configuration (especially true for dipole 2–3), the corresponding frequencies (30.025 and 32.025 MHz) were chosen for the design of the FFR.

7 In-Flight Antenna Calibration

In order to calibrate the STEREO/WAVES electrical antenna system, in-flight antenna calibration is necessary. In-flight calibration includes the characterization of the equivalent effective dipole antenna directions and the calibration of the antenna system gain (antenna capacitance, base capacitance and antenna effective lengths). The antenna gain and the antenna and base capacitances are inferred using the galactic background radiation, as was done for the Cassini/RPWS electrical antenna system (Zarka et al. 2004). The effective antenna directions are calibrated with spacecraft rolls. The methodology of this calibration is described in Vogl et al. (2004). The reference radio source used for calibration is the Earth auroral kilometric radiation (AKR). The spacecraft rolls have been programmed at about $120 R_E$ (Earth radii) from the Earth, so that the spacecraft is far enough from the Earth to be able to assume that the AKR sources are in the Earth direction, and that the signal to noise ratio (SNR) is high enough to get an accurate result. We assume that the position of the source is known and that the emissions are purely circularly polarized (Kaiser et al. 1978). It is then possible to invert the direction finding measurements and obtain the antenna directions and relative lengths. As described by Vogl et al. (2004), the “effective” antenna vector should ideally point towards the selected radio source twice per roll in order to perform the calibration. This ideal geometrical configuration could not be met in the case of the STEREO/WAVES antenna calibration sequences because of spacecraft pointing requirements. However, as shown by Cecconi and Zarka (2005), the data has to be carefully selected in order to get accurate calibration results. The two critical criteria are the SNR and the angular distance between the antennas and the reference radio source direction. We define α_i , the angular distance between the i th antenna and the direction of the radio source, and β_{ij} , the angular elevation of the source over the plane defined by the i th and j th antennas. It has been shown by Cecconi and Zarka (2005) that the data selection for accurate antenna parameters calibration are: (a) $15^\circ < \alpha_i < 45^\circ$, $\beta_{ij} > 10^\circ$ and $\text{SNR} \geq 20 \text{ dB}$ in the case of the i th antenna direction calibration (using measurements on antenna i and j), (b) $\alpha_i > 20^\circ$, $\alpha_j > 20^\circ$ and $\text{SNR} \geq 20 \text{ dB}$, when calibrating the h_i/h_j antenna length ratio. These data selections are compatible with the spacecrafts rolls programmed for the in-flight antenna calibration of the STEREO/WAVES electrical antenna system.

8 Summary and Early Results

The S/WAVES antennas completed qualification and acceptance verification for use in flight for the NASA STEREO mission and were integrated onto the spacecraft in early 2005. STEREO launched on October 25, 2006, and the S/WAVES instrument was powered up on October 27. The S/WAVES antennas were deployed successfully on the Ahead spacecraft on October 27, 2006, at approximately 16:42, 17:00, and 17:24 UT (X , Y , and Z respectively). Shortly after deployment, spacecraft controllers noted a slight ($\sim 10^{-5}$ radians amplitude) spacecraft wobble at the antenna cantilever frequency (approximately 0.6 Hz); the spacecraft attitude control system has been adjusted to correct for this motion. On October 29, 2006, the Behind spacecraft antennas were deployed successfully (at 21:24, 21:59, and 22:22 UT for X , Y , and Z). Early data confirm that the S/WAVES antennas work well.

Acknowledgements S/WAVES antenna design and fabrication was funded at UC Berkeley under NASA contract NAS5-03076. Several people at UC Berkeley helped to develop the S/WAVES antennas, chief among them are Paul Turin, Ken McKee, David Pankow, and Kate Harps. We thank Paul Buchanan, Therese Erigo, and Steve Wasserzug from NASA/GSFC.

Part of the S/WAVES antenna modeling program was financed by the Austrian Research Promotion Agency (FFG) in the framework of the Austrian Space Applications Program (ASAP) under contract FFG 811682. The Graz rheometry model was manufactured by H. Reiterer, Prototypenbau Meister. We thank H.O. Rucker and G. Fischer for valuable support and discussions on the antenna analyses.

References

- C.A. Balanis, *Antenna Theory* (Wiley, New York, 1997)
- S.D. Bale, D. Burgess, P.J. Kellogg, K. Goetz, S.J. Monson, *J. Geophys. Res.* **102**, 11–281 (1997)
- S.D. Bale, P.J. Kellogg, K. Goetz, S.J. Monson, *Geophys. Res. Lett.* **25**, 9 (1998)
- S.D. Bale, M.J. Reiner, J.-L. Bougeret, M.L. Kaiser, S. Krucker, D.E. Larson, R.P. Lin, *Geophys. Res. Lett.* **26**, 1573 (1999)
- S.D. Bale, P.J. Kellogg, F.S. Mozer, T.S. Horbury, H. Reme, *Phys. Rev. Lett.* **94**, 215002 (2005)
- J.-L. Bougeret et al., *Space Sci. Rev.* (2007, this issue)
- I.H. Cairns, D.B. Melrose, *J. Geophys. Res.* **90**, 6637 (1985)
- B. Cecconi, P. Zarka, *Radio Sci.* **40**, RS3003 (2005). doi:[10.1029/2004RS003070](https://doi.org/10.1029/2004RS003070)
- J. Fainberg, L.G. Evans, R.G. Stone, *Science* **178**, 743 (1972)
- R.J. Fitzenreiter, A.J. Klimas, J.D. Scudder, *Geophys. Res. Lett.* **5**, 496 (1984)
- M.V. Goldman, *Rev. Mod. Phys.* **56**, 709 (1984)
- R.J.L. Grard, *J. Geophys. Res.* **78**, 2885 (1973)
- D.A. Gurnett, *Principles of Space Plasma Wave Instrument Design*. AGU Geophysical Monograph, vol. 103 (1998), p. 121
- P. Harvey, F.S. Mozer, D. Pankow, J. Wygant, N.C. Maynard, H. Singer, W. Sullivan, P.B. Anderson, R. Pfaff, T. Aggson, A. Pedersen, C.-G. Falthammar, P. Tanskannen, *Space Sci. Rev.* **71**, 583 (1995)
- M.L. Kaiser, J.K. Alexander, A.C. Riddle, J.B. Pearce, J.W. Warwick, *Geophys. Res. Lett.* **5**, 857 (1978)
- P.J. Kellogg, *Astron. Astrophys.* **169**, 329 (1986)
- P.J. Kellogg, S.D. Bale, *J. Geophys. Res.* **106**(18), 721 (2001)
- P.J. Kellogg, S.D. Bale, F.S. Mozer, T.S. Horbury, H. Reme, *Astrophys. J.* **645**, 704 (2006)
- D. Krauss-Varban, D. Burgess, *J. Geophys. Res.* **96**, 143 (1991)
- D.E. Larson, R.P. Lin, J. Steinberg, *Geophys. Res. Lett.* **27**, 157 (2000)
- M.M. Leroy, A. Mangeney, *Ann. Geophys.* **2**, 449 (1984)
- J.G. Luhmann et al., *Space Sci. Rev.* (2007, this issue). doi:[10.1007/s11214-007-9170-x](https://doi.org/10.1007/s11214-007-9170-x)
- N. Meyer-Vernet, C. Perche, *J. Geophys. Res.* **94**, 2405 (1989)
- J.C. Novaco, L.W. Brown, *Astrophys. J.* **221**, 114 (1978)
- A. Pedersen, F. Mozer, G. Gustafsson, *Electric Field Measurements in a Tenuous Plasma with Spherical Double Probes*. AGU Geophysical Monograph, vol. 103 (1998)
- H.O. Rucker, W. Macher, R. Manning, H.P. Ladreiter, *Radio Sci.* **31**, 1299 (1996)
- D. Vogl, B. Cecconi, W. Macher, P. Zarka, H.P. Ladreiter, P. Fedou, A. Lecacheux, T. Averkamp, G. Fischer, H.O. Rucker, D.A. Gurnett, W.S. Kurth, G.B. Hospodarsky, *J. Geophys. Res.* **109**, A09S17 (2004). doi:[10.1029/2003JA010261](https://doi.org/10.1029/2003JA010261)
- C.S. Wu, *J. Geophys. Res.* **89**, 8857 (1984)
- P. Zarka, B. Cecconi, W.S. Kurth, *J. Geophys. Res.* **109**, A09S15 (2004). doi:[10.1029/2003JA010260](https://doi.org/10.1029/2003JA010260)

STEREO/Waves Goniopolarimetry

B. Cecconi · X. Bonnin · S. Hoang · M. Maksimovic · S.D. Bale · J.-L. Bougeret ·
K. Goetz · A. Lecacheux · M.J. Reiner · H.O. Rucker · P. Zarka

Originally published in the journal Space Science Reviews, Volume 136, Nos 1–4.
DOI: [10.1007/s11214-007-9255-6](https://doi.org/10.1007/s11214-007-9255-6) © Springer Science+Business Media B.V. 2007

Abstract The STEREO/Waves experiment is dedicated to the study of inner heliosphere radio emissions. This experiment is composed of a set of two identical receivers placed on each of the two STEREO spacecraft. The STEREO/Waves receivers have instantaneous Goniopolarimetric (GP) capabilities (also referred to as direction-finding capabilities). This means that it is possible to retrieve the direction of arrival of an incoming electromagnetic radio wave, its flux and its polarization. We review the state of the art of GP-capable radio receivers and available GP techniques. We then present the GP capabilities of the STEREO/Waves experiment. We finally show some GP results on solar Type III radio bursts, using data recorded with the Cassini/RPWS/HFR, which are very similar to the STEREO/Waves data.

Keywords STEREO/Waves · Goniopolarimetry (direction finding) · Sun: solar type III bursts

1 Introduction

The STEREO (Solar TERrestrial RElations Observatory) mission (Kaiser 2005) is dedicated to the study of the sun and the inner heliosphere. It is composed of two three-axis stabi-

B. Cecconi (✉) · X. Bonnin · S. Hoang · M. Maksimovic · J.-L. Bougeret · A. Lecacheux · P. Zarka
LESIA, UMR CNRS 8109, Observatoire de Paris, 92195 Meudon, France
e-mail: baptiste.cecconi@obspm.fr

S.D. Bale
Space Sciences Laboratory, Univ. of California, Berkeley, CA 94720, USA

K. Goetz
Dept. of Physics and Astronomy, Univ. of Minnesota, Minneapolis, MN 55455, USA

M.J. Reiner
Hughes STX, Lanham, MD 20706, USA

H.O. Rucker
Space Research Institute, Austrian Academy of Sciences, 8010 Graz, Austria

lized spacecraft orbiting the sun close to the orbit of Earth. The STEREO-A (for “Ahead”) spacecraft leads the Earth whereas the STEREO-B (for “Behind”) spacecraft trails. The solar longitudinal separation of the two spacecraft is increasing during the mission, as well as their respective distance from the Earth along its orbit. The STEREO/Waves experiment (Bougeret et al. 2007, [this issue](#)) is a set of two identical radio receivers placed onboard the two STEREO spacecraft. Both receivers have been developed to fulfill the STEREO mission science objectives and particularly the study of the solar and heliospheric radio emissions: interplanetary (IP) type II radio emission sources, IP shock topology (Hoang et al. 1998; Reiner et al. 1998a); IP type III radio emission sources (Fainberg and Stone 1974); solar wind (SW) radio emission propagation physics (Steinberg et al. 1984; Kellogg 1986).

Inheriting from the High Frequency Receiver of the Radio and Plasma Waves Science (HFR/RPWS) receiver experiment onboard Cassini (Gurnett et al. 2004), the STEREO/Waves receivers have goniopolarimetric (GP) capabilities (also referred to as direction-finding capabilities). That is, the direction of arrival, the polarization state and the flux of the observed electromagnetic wave can be retrieved quasi-instantaneously. As the experiment is deployed on two spacecraft, the localization of the inner heliosphere radio sources through stereoscopic analysis of the GP results is enabled. We will, however, concentrate on the GP capabilities of each receiver independently. The stereoscopic analysis capabilities of the STEREO mission are discussed by Bougeret et al. (2007, [this issue](#)).

We review the different GP methods available in the literature in Sect. 2. We then present the GP instrumentation of the STEREO/Waves experiment in Sect. 3. We finally give an insight of the STEREO/Waves capabilities using Cassini/RPWS/HFR data recorded in August 1999, during the Earth flyby.

2 Space-Borne Radio Receivers Goniopolarimetry

Space-borne radio receivers are connected to antennas fulfilling the constraints on size and mass of space missions: i.e., monopole or dipole antennas. These antennas have no intrinsic angular resolution, defined as λ/L , where λ is the wavelength (1 km to 10 m) and L the antenna effective length (typically a few meters); we then have $\lambda/L \sim 1$. A more useful description is their beaming pattern defined as the antenna gain for each direction.

The antenna beaming pattern of a short dipole ($L \ll \lambda$, typically $L \leq 10\lambda$) is proportional to $\sin^2 \theta$, where θ is the angular distance from the dipole to the source direction. The frequency range where the antenna is considered as a short dipole is called the quasi-static range or short dipole range. The antenna pattern shows a sharp null in the antenna direction, whereas the maximum gain is obtained for directions perpendicular to the antenna direction. The signal strength measured by a receiver connected to such antennas will thus depend on the orientation of the antenna with respect to the direction of the source. The shape of the beaming pattern implies that it is more efficient to determine the minimum gain than the maximum one. However, the antenna pattern equator can also be detected as the apparent polarization is reversed when crossing this limit. In case of short monopoles (as for Cassini/RPWS or STEREO/Waves), the beaming pattern can be approximated by that of a short dipole. The antenna calibration process provides the effective dipole length and direction equivalent to the system composed of the monopole and the conducting surface of the spacecraft. The antennas used with the STEREO/Waves experiment are described by Bale et al. (2007, [this issue](#)).

2.1 Antenna Calibration

The antenna calibration is necessary to get accurate GP results. This calibration provides the length and orientation of the effective electrical dipole equivalent to the electrical system composed of the monopole (or dipole), the antenna mounts and feeds (represented by the antenna and base impedances) (Manning and Fainberg 1980), and the spacecraft body. Three calibration methods are available and complementary: rheometry, electromagnetic simulation and in-flight calibration.

The rheometric analysis is conducted with a scale model of the spacecraft immersed in a tank filled with a dielectric liquid. A low-frequency electric field is applied across the tank and we measure the voltage at the antenna tips while the model spacecraft is slowly rotating (Rucker et al. 1996).

The electromagnetic simulation consists of a computer simulation including a wire grid model of the spacecraft (Fischer et al. 2001; Rucker et al. 2005; Oswald et al. 2006).

In-flight calibrations are conducted using a radio source with known parameters: the jovian HOM (hectometric) emissions has been used to calibrate the effective directions of the Cassini/RPWS antennas, during the Jupiter flyby of Cassini (Vogl et al. 2004; Cecconi and Zarka 2005). The Cassini/RPWS antenna lengths and antenna system gain were calibrated using the galactic background and the system noise data acquired in flight before the antenna deployment (Zarka et al. 2004). The antenna calibrations used for the STEREO/Waves antennas are described thoroughly by Bale et al. (2007, *this issue*).

2.2 Goniopolarimetric Measurement Expressions

In the quasi-static frequency range, the voltage induced by an incoming electromagnetic wave is $V = \vec{h} \cdot \vec{E}$ where \vec{h} is the effective antenna vector and $\vec{E} = \vec{E}_0 e^{i\omega t}$ is the electric field of the wave. A GP radio receiver then measures a series of correlation values:

$$P_{ij} = \langle V_i V_j^* \rangle, \quad (1)$$

where V_i is the complex voltage measured on the i th antenna, V_j^* is the complex conjugate of the voltage measured on the j th antenna, and $\langle \dots \rangle$ denotes an average over an integration time longer than the wave period. In the case of an electromagnetic plane wave (i.e., emitted by a point radio source at infinity) characterized by its Stokes parameters (Kraus 1966) (S the flux, Q , U , the linear polarization degrees, and V the circular polarization degree), the voltage correlation can be written as (Cecconi and Zarka 2005):

$$P_{ij} = \frac{Z_0 G h_i h_j S}{2} [(1 + Q) \Omega_i \Omega_j + (U - iV) \Omega_i \Psi_j + (U + iV) \Omega_j \Psi_i (1 - Q) \Psi_i \Psi_j], \quad (2)$$

where we have explicitly included the impedance of free space Z_0 and the gain of the antenna system $G h_i h_j$ (Manning and Fainberg 1980); and Ω_i and Ψ_i are the projection of the antenna vector \vec{h}_i on the wave plane axes. When $i = j$, P_{ii} is the autocorrelation of the voltage at the i th antenna outputs, hence a power. When $i \neq j$, P_{ij} is the voltage cross-correlation between the antenna i and j .

Another formalism, proposed by Lecacheux (1978), describes the correlation antenna response with the wave coherence matrix:

$$P_{ij} = {}^t [h_i] \cdot [S] \cdot [h_j]^*, \quad (3)$$

where $[S]$ is the normalized wave coherence matrix that depends on the four Stokes parameters (Lecacheux 1978), $'[h_i]$ is the transpose of $[h_i]$ and $[h_j]^*$ is the complex conjugate of $[h_j]$ ($[h_i]$ and $[h_j]$ being the effective antenna vectors).

As the antenna are measuring the electric field of passing electromagnetic waves in the vicinity of the spacecraft, GP techniques can measure only the direction of the local wave vector. Any propagation effect (such as refraction or diffusion effects) is not taken into account. The directions of arrival obtained with GP techniques only provide apparent sources positions. One should then be particularly careful when analyzing data close to the local plasma frequency where strong refraction can occur on radio waves.

The GP capabilities of a radio receiver depend on the receiver design and especially on the number of independent analysis channels, i.e., the number of simultaneous correlation measurements. For single channel receivers, only one autocorrelation is measured whereas for dual channel receivers (thus connected to two antennas), up to two auto-correlations (one on each antenna) and a complex cross-correlation may be measured. In order to increase the capabilities of the radio receivers (with one or two analysis channels), successive measurements with antenna switching can be performed quasi-instantaneously.

GP techniques are often referred to as direction-finding techniques in the literature. This latter expression does not reflect the fact that these techniques provide both direction and polarization, which are not retrievable independently.

There are two possible ways to achieve GP on space-borne radio receivers: spin demodulation GP (on a spinning spacecraft, like Wind and Ulysses) and instantaneous GP (on three-axis stabilized spacecraft, like Cassini and STEREO). Both of these GP techniques may provide the direction of arrival of the wave, flux, polarization and the angular size of the source. At the time of writing of this paper, inversions providing the size of the source exist for spin demodulation GP, but not for instantaneous GP.

2.3 Spin Demodulation Goniopolarimetry

On a spinning spacecraft, the measured correlation is modulated by the antenna spin. The minimum signal is obtained when the antenna is pointing closest to the source direction. The result of the demodulation is a plane containing the spacecraft spin axis and the source position. This simple method has been used to perform GP analysis of terrestrial Auroral Kilometric Radiation (AKR; Kurth et al. 1975) using the Hawkeye and IMP 8 spacecraft radio data, and of solar type III bursts (Gurnett et al. 1978) using Helios 2, IMP 8 and Hawkeye radio data. The radio receivers used on these spacecraft were single-antenna receivers.

To obtain additional independent measurements, single-channel receivers with antenna switching capabilities were developed for ISEE-3, Wind and Ulysses. These receivers provide series of autocorrelation measurements with different antennas (or antenna combinations) for a given sampling set up (central frequency, integration time, frequency bandwidth).

Lecacheux (1978) proposed GP inversions in the case of (i) one antenna (inclined to the spin axis) and (ii) two antennas (one parallel and one perpendicular to the spin axis). These GP inversions are adapted to the three spacecraft mentioned earlier. GP techniques, including the size of the source, are also available for such receivers (Manning and Fainberg 1980; Fainberg et al. 1985). The techniques developed in these two papers were used to derive the source location of solar radio emissions using (i) ISEE-3 radio data only (Steinberg et al. 1984; Dulk et al. 1986), (ii) Ulysses/URAP data only (Hoang et al. 1994; Reiner et al. 2006), (iii) Wind/Waves data only (Reiner et al. 1998a, 2005) and (iv) Wind/Waves and Ulysses/URAP data performing GP analysis on each data set and then applying triangulation techniques (Hoang et al. 1998; Reiner et al. 1998b, 1998c). These observations are essential to put constraints on the solar radio burst emission mechanism and radio wave propagation.

The GP techniques, as described earlier, have also been applied to the jovian radio emissions observed by Ulysses/URAP during its Jupiter flyby in February 1992 (Reiner et al. 1993; Ladreiter et al. 1994).

The POLRAD experiment on the Interball spacecraft (Hanasz et al. 1998a, 1998b) is a nine-channel receiver connected to three orthogonal electrical dipoles. Each channel of this receiver is outputting a combination of antenna signals (with or without quadrature phase shifts). The full set of GP measurement is thus recorded. GP inversions have been built and used on these data to characterize the AKR (Hanasz et al. 2003; Panchenko 2004).

2.4 Instantaneous Goniopolarimetry

On a spinning spacecraft, no meaningful GP result can be obtained on timescales shorter than the spacecraft spin period. This requires that the wave parameters are fixed over the spin period. Instantaneous measurements require several antennas and multi-channel receivers such as those developed for Cassini/RPWS/HFR and STEREO/Waves. Such receivers provide four independent measurements that can be retrieved instantaneously and seven to nine quasi-instantaneously (Gurnett et al. 2004; Cecconi 2004; Cecconi and Zarka 2005).

For dual-channel receivers, two successive measurements with antenna switching are necessary to obtain the full set of GP unknown (S , Q , U , V , θ and ϕ). We thus have seven independent measurements: P_{ii} , P_{jj} , P_{kk} , $\mathcal{R}e(P_{ij})$, $\mathcal{R}e(P_{ik})$, $\mathcal{I}m(P_{ij})$, $\mathcal{I}m(P_{ik})$ (see (2) for correlation expressions). In case of switching between three antennas, one has nine independent measurements: the seven ones mentioned above plus $\mathcal{R}e(P_{jk})$ and $\mathcal{I}m(P_{jk})$.

The ideal case of an orthogonal triad of antennas was studied by Lecacheux (1978) who showed that measurements on three antennas (i.e., seven or nine measurements) are sufficient to obtain the six wave parameters. It was also mentioned that instantaneous measurements on one pair of antennas (i.e., four measurements) suffice to derive either the source polarization (if the source location is known) or its location (if assumptions on the wave polarization are made).

Due to both geometrical configuration and electromagnetic interaction between the conducting spacecraft body and the antennas, the effective directions of the antennas mounted on spacecraft are generally not orthogonal one to another. GP inversion taking into account a real antenna triad geometry was first proposed by Ladreiter et al. (1995). The proposed GP technique involves a least-square model fitting through singular value decomposition (SVD). A GP inversion using a Powell minimization algorithm was also described by Vogl et al. (2004). Although these methods provide useful estimates on the GP result error, they do not ensure that the provided solution is unique. Another drawback is the computing time needed to invert the data, which is not adequate for long term or large scale automatic processing. In order to overcome these limitations, Cecconi and Zarka (2005) provided analytical inversions to be used on GP data obtained with three antennas.

Ladreiter et al. (1995), Vogl et al. (2004) and Cecconi and Zarka (2005) proposed inversions to perform the antenna calibration needed for accurate GP. In the case of Cassini, the calibration was performed using the Cassini flyby of Jupiter. In the case of S/Waves, spacecraft rolls have been planned at a distance from Earth when AKR can be used as a reference source to calibrate the effective antenna directions.

2.5 Error Sources and Order of Magnitudes

Several sources of error may alter or bias the GP measurements and results. Complete discussions on these sources of error may be found in the papers by Lecacheux (1978), Ladreiter et al. (1995), Cecconi and Zarka (2005) and Cecconi (2007). The different sources of error are the following:

1. *Signal-to-noise ratio.* The signal-to-noise ratio (SNR) is inherent to any measurement. The noise level theoretically depends on the analysis bandwidth b and integration time τ : the signal fluctuations are equal to $S_n/\sqrt{b\tau}$, where S_n is the background level (receiver noise level, interference level, galactic background ...) In theory, this noise interferes only when the signal amplitude is comparable to the noise amplitude. In practice, a SNR larger than 20 to 30 dB is necessary to obtain accurate GP results (Cecconi and Zarka 2005).
2. *Galactic radio background.* In the studied frequency range from <1 MHz to >30 MHz (Dulk et al. 2001), the sky radio background is bright. This background level has to be subtracted from the data before any analysis of GP measurements. The background level has to be determined over a long period of time (Zarka et al. 2004).
3. *Receiver noise.* The receiver noise (mainly from the preamplifier electronics) may be dominant in the low-frequency range (<1 MHz for Cassini). The precise noise level has to be measured onboard the spacecraft, with the receiver power on but before the antenna deployments.
4. *Digitization noise.* When data are digitized as in the case of Cassini or STEREO receivers, they are converted into floating point words of 8 or 12 bits, respectively. Contrary to the SNR fluctuations, which depend on the integration time and frequency bandwidth of observation, the digitization noise is proportional to the signal amplitude (see Fig. 1). The 8 bits digitization superimposes ± 0.17 dB (V^2/Hz) fluctuations on the digitized signal whereas the 12 bits digitization ± 0.04 dB (V^2/Hz) only (Cecconi and Zarka 2005).
5. *Geometrical configuration.* Within the short antenna frequency range, the beaming pattern of an antenna has sharp nulls in the effective antenna direction. This implies that the signal measured on an antenna pointing to the source will be low compared to the case when it is perpendicular to the direction of the source. The SNR of measurements done

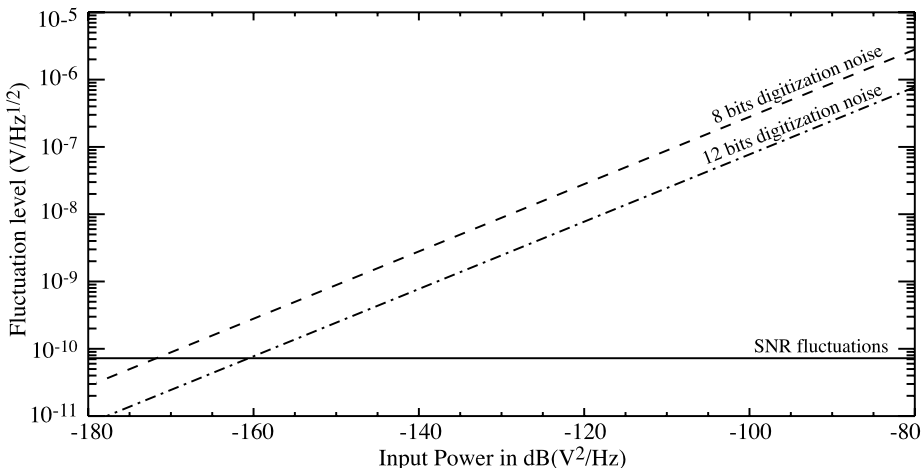


Fig. 1 Simulated noise levels (in $nV \cdot Hz^{-1/2}$) with respect to input power. Plain line: SNR fluctuation level, which is the product of the background level (here fixed to a receiver noise level of $7 nV \cdot Hz^{-1/2}$) and the $1/\sqrt{b\tau}$ factor (here fixed to 0.1); dashed line: digitization noise (8 bits); mixed line: digitization noise (12 bits). For each input power, the upper line has to be taken into account to determine the level of noise. The receiver noise level is thus predominant up to input powers of the order of -171 dB (V^2/Hz) for 8 bits digitization (-161 dB (V^2/Hz) for 12 bits)

- in such an ill-defined geometrical configuration will then be low. However, as the null is sharp, the direction of arrival of the wave may be obtained accurately (if the antenna system is accurately calibrated), contrary to the flux and polarization measurement.
6. *Inversion indetermination.* Depending on the GP inversion used, series of directions in space or polarization values may not be solved accurately (Cecconi and Zarka 2005). For instance, no valid GP result can be obtained if $V = 0$ in the case of the general GP inversion proposed by Cecconi and Zarka (2005). In that case, another GP inversion was provided.
 7. *Calibration indetermination.* Accurate antenna calibration is needed to obtain accurate GP results. Any bias on effective antenna directions will induce offsets on the source location, on the flux and on the polarization degrees obtained with GP inversions (Vogl et al. 2004; Cecconi and Zarka 2005). Two kinds of indetermination may occur: effective antenna length and direction indetermination and misfit to an ideal dipole antenna pattern (especially the warping of the electrical equator for monopole antenna measurements). Current analytical inversions cannot take into account the latter. However, it could be possible to correct for this effect with least square fitting methods.
 8. *Intrinsic source variability.* When GP measurements are not recorded simultaneously, source parameters may have changed between two successive measurements. In the case of solar and planetary radio emissions, the flux and the source location are most likely to vary. This source of error is more critical in the case of a spinning spacecraft but it should also be considered on three-axis stabilized spacecraft, when measuring GP samples with antenna switching.
 9. *Multiple sources.* The GP inversions proposed in the literature usually suppose a point source or an extended source, but do not take into account the case when several sources are emitting within the antenna pattern at the same frequency. If this happens, the measured power is the sum of the powers induced by each source. If one source dominates by a few orders of magnitude, the GP results will be mainly related to that source. If no source dominates, one should either consider solving the measurement as an extended source (see next point), or develop GP inversions assuming several sources at a time.
 10. *Intrinsic size of the source.* When using point source inversions, the case of an extended source (i.e., a resolved source) gives erroneous GP results if the disk-equivalent radius of the source is $>5^\circ$ (Cecconi 2007).

As already mentioned, the direction of arrival provided with GP techniques do not take into account propagation effects that affected the observed radio wave. However, the displacement of the apparent source position due to these propagations effects is not considered to be an indetermination of the GP techniques as there is no way to modify the GP techniques to correct for the distortion of the path of the radio waves between emission and detection.

In order to obtain a typical accuracy of the order of 1° for directions, 10% for polarization degrees, and 1 dB for flux, typical data criteria are: $\text{SNR} > 23 \text{ dB}$ and $\beta_{ij} > 20^\circ$, where β_{ij} is the elevation of the source direction above the plane defined by the i th and j th pair of antennas (Cecconi and Zarka 2005). In practice $\text{SNR} > 33 \text{ dB}$ is necessary to get accurate GP results with the Cassini data. These numbers are valid if the source extension is $<5^\circ$ as seen from the spacecraft (Cecconi 2007). The selection thresholds should be lowered with the S/Waves data, as the digitization noise is there of one order of magnitude smaller.

3 STEREO/Waves Goniopolarimetric Instrumentation

The radio remote sensing part of the experiment consists of three receivers: the Low Frequency Receiver (LFR) covering the 2.5–160 kHz range, the High Frequency Receiver

(HFR) covering the 125 kHz–16 MHz range and the Fixed Frequency Receiver (FFR) providing measurements at 30 or 32 MHz. The high-frequency part of the LFR (10–160 kHz) and the HFR have two simultaneous analysis channels, whereas the low-frequency part of the LFR (2.5–10 kHz) and the FFR have only one. The sensors are a set of three 6 m long electric monopole antennas (Bale et al. 2007, *this issue*). Each analysis channel can be connected to one of the three antennas (monopole configuration) or to an electrical combination of two of the three antennas (dipole configuration). The antenna connections at the receiver inputs are set by the instrument operating mode. In addition, the operating mode defines the bandwidth and integration time of each measurement as well as the frequency resolution for each receiver. The operating mode (hence the connected antennas) can be changed in-flight as often as necessary.

3.1 Goniopolarimetric Data Samples

Thanks to their two analysis channels, both the LFR (above 10 kHz) and HFR provide GP measurements. The instantaneous measurement used to form the GP data samples consist of a set of four measurements acquired simultaneously using the two connected antennas: two autocorrelations and one complex cross-correlation. This set of four real measurements is called a GP0 data sample. A GP data sample can be composed of a set of either one, two or three GP0 data samples, obtained with antenna switching at the receiver inputs between successive GP0 measurements.

A GP1 data sample is composed of eight measurements (two successive GP0 data samples with antenna switching). We then obtain four auto-correlations and two complex cross-correlations. As one of the two antennas remain the same during the antenna switching two of the four autocorrelations are measured on the same antenna. Although we keep these two redundant autocorrelations as a check for emission stationarity, we actually get seven independent measurements.

A GP2 data sample is composed of 12 measurements (three successive GP0 data samples with antenna switching). Each of the GP0 measurements is made with a different pair of antenna. We obtain six auto-correlations (with redundancy: two autocorrelations on each antenna, i.e. only three independent measurements) and three complex cross-correlations. The three redundant auto-correlations are kept for emission stationarity check. We thus get nine independent measurements.

The GP unknowns are the wave direction of arrival (opposite to the direction of the wave vector \vec{k} and usually represented using two angles: the colatitude θ and the azimuth ϕ), the wave flux and polarization state (usually represented by the four wave Stokes parameters: the intensity S , the degree of circular polarization V and the two linear polarization degrees U and Q), and the source size [represented by its disk-equivalent radius γ (Cecconi 2007)]. We then have seven unknowns. The correlation measurements can be expressed in terms of these GP unknowns and of the antenna parameters: three parameters for each antenna (effective length, colatitude and azimuth of the antenna direction). The set of equations linking the four (GP0), seven (GP1) or nine (GP2) independent measurements to the GP unknowns and antenna parameters is called the GP system of equations. As mentioned by Cecconi and Zarka (2005), there is an intrinsic indetermination within the GP system of equations: two waves with opposite direction of arrival and opposite circular polarization degree will give the exact same response on the antenna. This means that the GP system of equations is degenerate and that the GP1 data samples do not provide enough independent measurements to solve for the seven GP unknowns. The GP2 data samples will provide enough measurements to achieve the inversion for the whole set of GP unknowns. The GP1

data samples may still be used to obtain part of the GP unknowns, assuming some of them to be known.

3.2 Adapted Goniopolarimetric Equations

In the case of type II and III solar bursts, we can assume that the emission is not polarized in the S/Waves frequency range and that source is extended. We can then set Q , U and V to zero and solve for the four remaining unknowns (S , θ , ϕ , γ). According to (33) in Cecconi (2007), the measurement expression is then:

$$P_{ij} = \frac{Z_0 G h_i h_j S}{4} \left[(A_i A_j + B_i B_j) \left(\Gamma_1 + \frac{\Gamma_1 + \Gamma_3}{4} \right) + 2C_i C_j \left(\Gamma_1 - \frac{\Gamma_1 + \Gamma_3}{4} \right) \right], \quad (4)$$

where Z_0 is the impedance of free space, $G h_i h_j$ the gain of the antenna system (Manning and Fainberg 1980), S the flux density,

$$A_i = -\sin \theta_i \cos \theta_c \cos(\phi_c - \phi_i) + \cos \theta_i \sin \theta_c, \quad (5)$$

$$B_i = -\sin \theta_i \sin(\phi_c - \phi_i), \quad (6)$$

$$C_i = \sin \theta_i \sin \theta_c \cos(\phi_c - \phi_i) + \cos \theta_i \cos \theta_c \quad (7)$$

with (θ_c, ϕ_c) the direction of the source centroid, and (θ_i, ϕ_i) the direction of the i th antenna, and Γ_k are the coefficients depending on the brightness distribution and the size of the source. In case of an uniform source, we have $\Gamma_1 = 1$ and $\Gamma_3 = \frac{4}{3}(1 + \cos \gamma + \cos^2 \gamma) - 1$, with γ the disk-equivalent radius of the source (Cecconi 2007). As the source is assumed unpolarized, the imaginary part of the cross-correlation is zero. A GP0 data set provides then only three measurements, which is not enough to solve for the four remaining unknowns.

4 Application of Goniopolarimetry to the Study of Solar Type III Radio Bursts

As mentioned earlier, the GP capabilities of the S/Waves receivers are very similar to those from the Cassini/RPWS/HFR experiment, although only GP0 and GP1 data samples are available with Cassini. We present here an illustration of GP results for a type III solar radio bursts observed during the Cassini Earth flyby in August–September 1999. These results give an overall view of what we expect to measure with the S/Waves radio instrument. Simultaneous GP results obtained with the Wind radio receiver are also shown for comparison.

Cassini GP results were obtained using a direct inversion method applied to GP0 data with Stokes parameters Q , U set to zero (these assumptions do not affect type III burst GP results since type III bursts are known to be linearly unpolarized below 20 MHz due to propagation effects). This allows us to retrieve the remaining unknowns (S , V , θ , ϕ) for each measurements (Cecconi and Zarka 2005). GP measurements taking into account a finite angular radius γ of the source are not illustrated here, but they will be considered with upcoming S/Waves data (Cecconi 2007).

Solar type III radio bursts are produced by beams of suprathermal electrons ($v \sim 0.03$ to $0.3c$) accelerated from active regions (AR) and traveling outward along open magnetic field lines to lower densities n_e in the interplanetary medium (IPM). Along their path in the IPM, these electrons trigger intense Langmuir waves which are partly converted into radio emission at the fundamental (F) and/or second harmonic (H) of the local plasma frequency f_p . Since $f_p \propto \sqrt{n_e}$ and $n_e \propto 1/r^2$ (n_e is the plasma density and r the distance to sun),

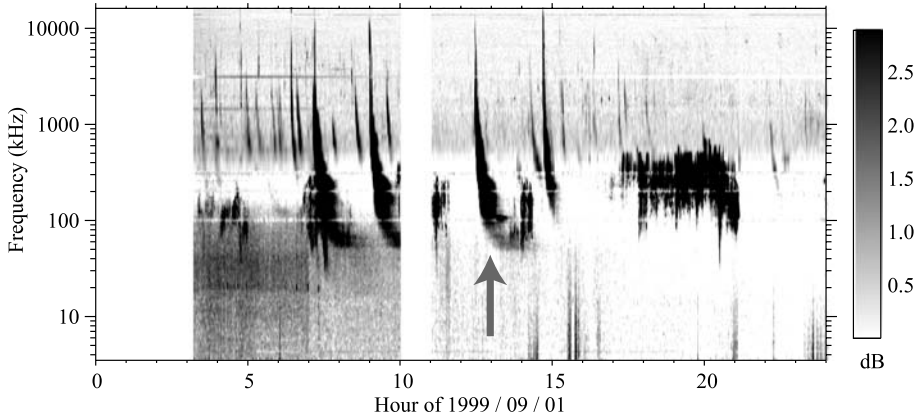


Fig. 2 Cassini/RPWS dynamic spectrum on September 1, 1999. Several type III bursts are visible as well as AKR. The selected event was observed between $\sim 12:25$ and $\sim 14:30$ UT (marked by the grey arrow). The event becomes noisy below ~ 100 kHz due to possible pollution from AKR

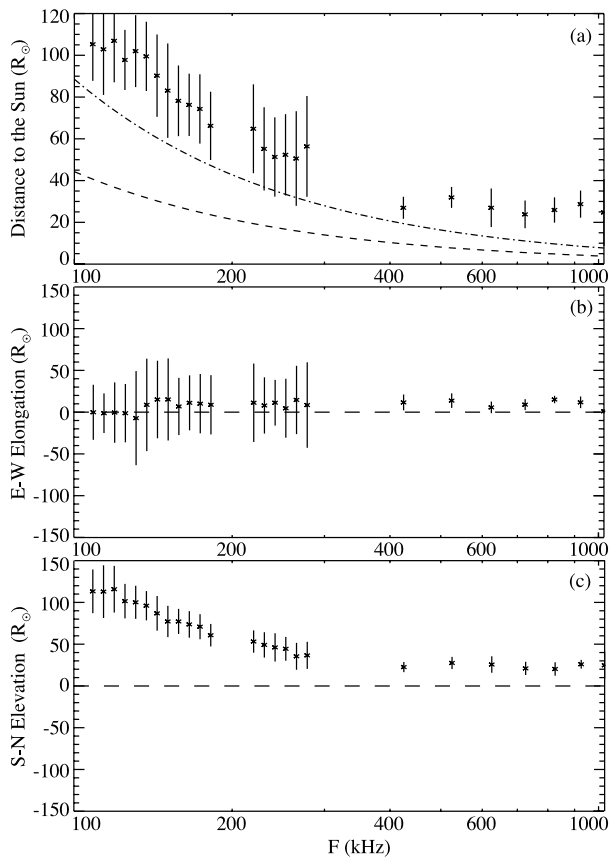
$f_p \propto 1/r$. The heliocentric distances of the type III radio sources thus increase as their frequency decreases.

To illustrate the GP capabilities onboard a three-axis stabilized spacecraft, we have chosen an isolated type III burst observed by Cassini during the Earth flyby. Figure 2 displays a Cassini/RPWS/HFR dynamic spectrum on September 1, 1999. Cassini was at ~ 1.13 AU from the Sun. Its Heliocentric Earth Ecliptic (HEE) latitude and longitude were, respectively, $\sim +1^\circ\text{N}$ and $\sim +1^\circ\text{W}$. Several type III bursts were observed this day. The selected type III burst occurred between 12:25 UT (at $f \sim 10$ MHz) and 14:30 UT (at $f \sim 40$ kHz). It was associated with NOAA AR 8681 observed at HEE coordinates ($+25^\circ\text{N}$, $+28^\circ\text{W}$) using Nancay Radioheliograph observations at 327 and 164 MHz (obtained from the <http://secchirh.obspm.frserver>). No flare was observed at this time, however. Data points with SNR above 20 dB and in the frequency range [100–1025 kHz] have been selected. The signal is noisy below 100 kHz due to possible pollution from AKR. Some data points have also been removed due to interference lines.

The GP results corresponding to the selected burst are shown in Fig. 3. Plot (a) represents the average distance in units of a solar radius (R_\odot) from the Sun to the source centroid direction as referred to the Sun–Cassini line as a function of frequency. The plot clearly shows that the distance increases with decreasing frequencies, which means that the type III source moves away from the sun with time. Plots (b) and (c) represent, respectively, the average E–W elongation and S–N elevation in solar radius of the source direction relative to the Sun–spacecraft line as functions of frequency. We can see the type III source moving north (from $\sim 20 R_\odot$ at 1,000 kHz to $\sim 120 R_\odot$ at 100 kHz), with an elongation close to the Sun–spacecraft direction. The standard deviation of the measured distribution are given on the plots. The error bars are noticeably larger at low frequencies. This is due to the fact that the low-frequency range (<320 kHz) is sampled with a theoretical normalized noise $(B\tau)^{-1/2} = 0.066$ whereas the high-frequency range (>320 kHz) with $(B\tau)^{-1/2} = 0.035$, where B and τ are, respectively, the effective bandwidth and integration time of the measurements.

According to the AR’s location, these GP results are compatible with a type III electron beam moving along Archimedean spiral-like magnetic field lines. However we can formulate two remarks: (i) this event is atypical since the type III sources follow open magnetic

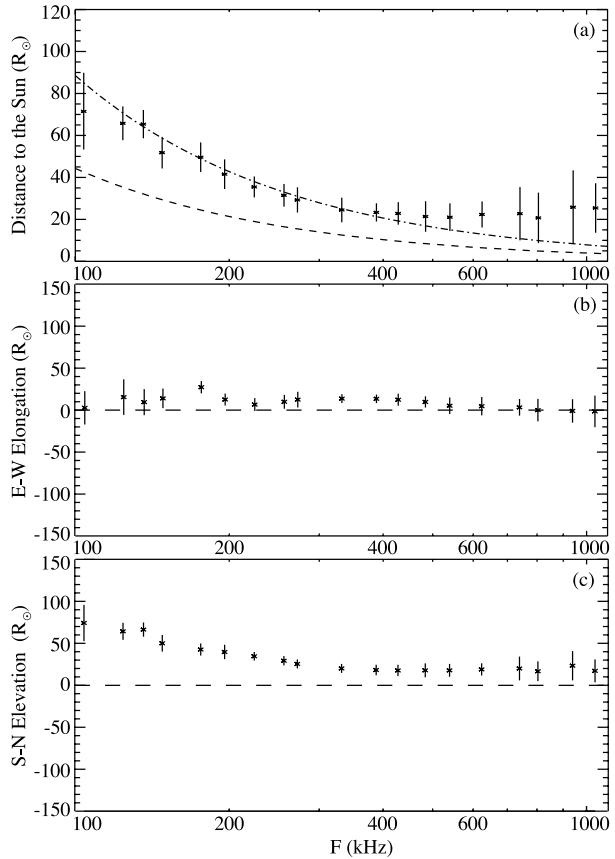
Fig. 3 RPWS/HFR GP results of solar type III radio burst observed by Cassini between 12:25 and 14:30 UT on September 1, 1999. Plot (a) represents distance r in solar radius (R_\odot) between the center of the Sun and apparent source direction as seen from the spacecraft (i.e., $r = r_c \sin \alpha$, where $r_c = 1$ AU $\sim 214 R_\odot$ and α is the angular distance from the Sun to the source location as seen from the spacecraft). The dashed and mixed lines give the distance from the sun deduced from a simple density model for the F and H components, respectively. Plots (b) and (c) represent, respectively, source elongation and elevation in solar radius in the coordinate system centered on the spacecraft and aligned with the spacecraft–Sun direction



field lines which are more usually localized around the solar equatorial plane. (ii) Using a simple IPM density model where the electron density decreases approximately as $\sim 1/r^2$, and assuming fundamental (F) emission at f_p , we expect to measure the burst position at $\sim 4 R_\odot$ at 1,000 kHz and at $\sim 40 R_\odot$ at 100 kHz. This means that the burst position measured by GP is about two to five times farther than the location inferred from a simple density model. There are two possible explanations for this effect. On the one hand, we may observe the second harmonic component which radiates at $2f_p$, or also a mix of both, F and H, components (for more details see Dulk et al. 1984). For instance, the emission measured at 100 kHz should come, in this case, from a location where $f_p \sim 50$ kHz which corresponds to a distance of $\sim 84 R_\odot$, as suggested by the curves in Fig. 3a and Fig. 4a. On the other hand, important scattering effects exist in the IPM and may strongly affect the radio emissions propagation especially close to the source at the fundamental (Steinberg et al. 1984). In all the cases, the only knowledge of the GP measurements is not sufficient to solve this issue. It requires more thorough investigations about the propagation effects and the F/H components determination which is not the purpose of this paper.

The same event was simultaneously observed by the Wind/Waves/RAD2 and RAD1 receivers. At this time, Wind was at ~ 1 AU beyond the Earth's bow shock. The angular elongation distance between the two spacecraft was $\sim 1^\circ$ as seen from the Sun. This does not allow event localization using triangulation methods. GP measurements available on WAVES/RAD1 (20–1,040 kHz) were obtained using a non-linear sweeping

Fig. 4 Waves/RAD1 GP results of solar type III radio burst observed by Wind between 12:25 and 14:30 UT on September 1, 1999. Plot (a) represents distance r in units of solar radii (R_\odot) between the center of the Sun and apparent source direction as seen from the spacecraft (i.e., $r = r_c \sin \alpha$, where $r_c = 1 \text{ AU} \sim 214 R_\odot$ and α is the angular distance from the Sun to the source location as seen from the spacecraft). The dashed and mixed lines give the distance from the Sun deduced from a simple density model, respectively, for the F and H components. Plots (b) and (c) represent respectively source elongation and elevation in units of solar radii in the coordinate system frame centered on the spacecraft and aligned with the spacecraft–Sun direction



mode which is well suited to type III observations. In this mode, 32 frequency channels are selected among the 256 possibilities in such a way that sampling rate increases with frequency. At each frequency, the signal is sampled during about one spin period (~ 3 sec), and it takes about three minutes to obtain a complete 32-frequency sweep. The unknowns (θ, ϕ, γ) are then deduced from GP analysis (Manning and Fainberg 1980; Fainberg et al. 1985).

Figure 4 shows GP measurements for the same type III burst observed by Wind. Assuming that each GP direction of arrival result (θ, ϕ) is the centroid of a Gaussian source distribution, plots (a), (b) and (c) are equivalent to those for Cassini. Figure 5 summarizes the GP observations by the two spacecraft. This figure clearly emphasizes that the GP results from both spacecraft are consistent. Figure 6 represents the average angular radius of the source as a function of the frequency. This latter plot shows that apparent source size increases significantly with decreasing frequency ($\lesssim 20^\circ$ at 1 MHz to $> 50^\circ$ at 100 kHz).

As the Cassini data have been treated with a point source GP inversion, the GP results are biases. We simulated the GP results that would output the Cassini radio receiver with an extended source having the parameters found by the Wind at the lower frequency channel (E–W elongation $\sim 0 R_\odot$, N–S elevation $\sim 70 R_\odot$ with a angular extension of 50°). We obtain an apparent source shifted northward by $\sim 11^\circ$, which gives an N–S elevation of the order of $110 R_\odot$, which is exactly what we get with Cassini on the real data. So, despite a wide source extension implying strong biases on the Cassini results, the GP results on both

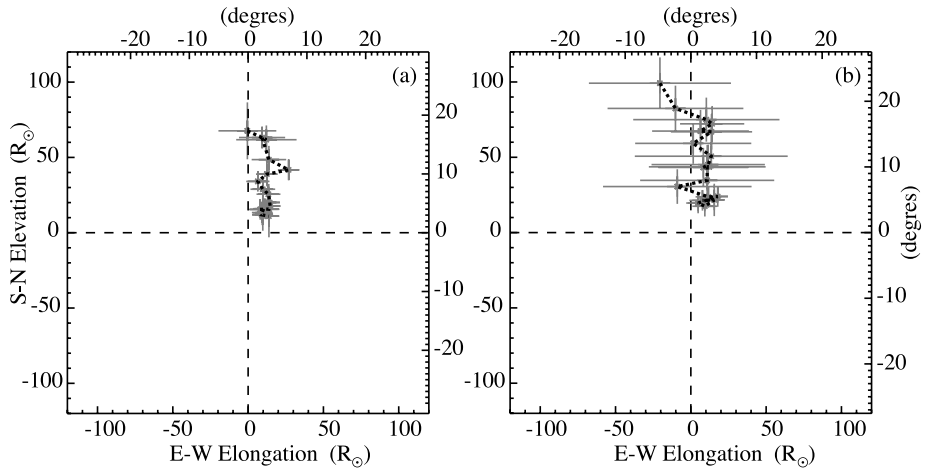
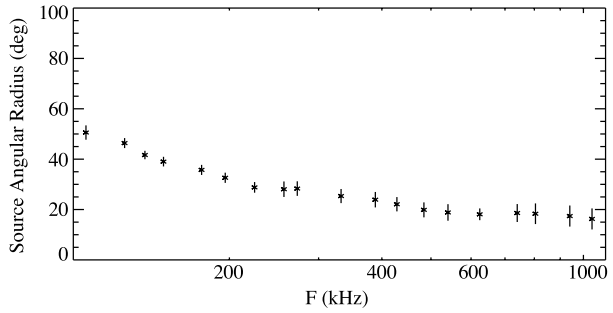


Fig. 5 Waves/RAD1 **(a)** and Cassini/RPWS/HFR **(b)** GP results of a solar type III radio burst observed simultaneously by the two spacecraft between 12:25 and 14:30 UT on September 1, 1999. The plots show the source positions as a function of elongation and elevation (in units of degrees and solar radii). The results are in good agreement with the type III source moving along northern Archimedean spiral-like magnetic field lines, consistent with the AR's location on the Sun

Fig. 6 Waves/RAD1 GP results of type III solar radio burst observed by Wind between 12:25 and 14:30 UT on September 1, 1999. The plot represents angular radius of the apparent source in degree as a function of frequency. Since the type III burst apparent source is extended, GP measurements which take account of the angular radius γ of the source will also be applied to S/Waves data



spacecraft are in good agreement. Moreover, we can check that above 200 kHz the Cassini and Wind goniopolarimetric results are giving the same direction of arrival.

5 Summary and Concluding Remarks

This paper has presented the different GP inversions available for space-borne radio receivers. Both spinning and stabilized spacecraft have been discussed. The GP specifics of the S/Waves instrument were presented in Sect. 3. We did not explicitly provide GP inversions or calibration inversions in this paper, but they are available in the various referenced papers. The GP inversion including the size of the source as a GP unknown is currently being developed and is the subject of a future paper.

In Sect. 4, we analyzed a type III burst observed with the Cassini and Wind radio receivers. We showed that both receivers provided the same source characteristics. However, as the Wind spacecraft is a spinning spacecraft, one spacecraft rotation (i.e., 3 sec) is necessary to obtain GP measurements. This also implies that the emission must remain constant

over a spacecraft spin. The GP measurement on the Cassini and STEREO receivers are only limited by the receiver integration time which is of the order of a few tens of milliseconds, depending on the instrument operating mode. When operating in an antenna switching mode (i.e., GP1 or GP2 modes), the time coherence of the source has to be greater than the time needed to switch antenna between successive GP0 measurements, which is a few tens of milliseconds. The S/Waves instrument is less sensitive than the Wind radio receivers to temporal variations of the observed signal. However, as Cassini and STEREO GP measurements include a smaller number of measurements than the Wind ones, the Cassini and STEREO GP results are then more sensitive to SNR errors.

The data coding used for S/Waves data is a significant improvement compared to the one used with the Cassini radio receiver. The S/Waves data are coded with 12-bit words, whereas the Cassini/RPWS/HFR data with 8 bits only. It has been showed that the digitization noise induced by 8-bit coding was the most important source of noise in the case of Cassini (Cecconi 2004; Cecconi and Zarka 2005). The new 12-bit coding reduces the digitization noise by a factor of ~ 16 (i.e., the expected order of magnitude as $2^{12}/2^8 = 16$).

The error bars displayed for the GP results obtained from Cassini show that the choice of the instrument operating mode (integration time and frequency bandwidth, which are determining the measurement noise level) is essential to obtain the desired accuracy. As the S/Waves receivers include a more efficient data coding (12 bits instead of 8 bits), the recorded data will eventually be more accurate than Cassini/RPWS even with the same bandwidth and integration time.

Another improvement on STEREO, with respect to the Cassini radio receiver, is the shorter antenna used. This allows pushing up the high-frequency limit of quasi-static frequency range defined as $L \leq 10\lambda$. The monopoles are physically shorter (6 m for STEREO, 10 m for Cassini), but the effective lengths are also shorter in the case of STEREO: preliminary results from electromagnetic wire-grid simulations (Rucker et al. 2005; Oswald et al. 2006) give effective lengths of the order of 1.5 m, whereas the effective antenna length obtained for Cassini/RPWS/HFR is 1.68 m for the monopole antennas. The effective antenna length shall however be calibrated in-flight using the radio galactic background as a calibrated source.

Regarding type III observations, GP measurements provided by the new generation of receivers onboard stabilized spacecraft like Cassini or STEREO, offer great opportunities to study solar radio bursts with the best accuracy. It is then possible to retrieve radio source trajectories in the corona and the solar wind as well as to obtain the size and the possible polarization of the radio emissions.

Furthermore, in order to get accurate radio source locations in the corona and IPM, triangulation will be performed on GP measurements from the STEREO-A and -B spacecraft. This allows one to trace out Coronal Mass Ejections (CMEs) which drive shocks emitting type II radio bursts, as well as solar energetic electrons responsible for type III bursts. Propagation effects are both the main issues in solar radio burst studies, and their study will provide great a tool for sounding IPM properties. GP measurements applied on S/Waves will bring essential observational constraints on these propagation effects: joint observations of visible CMEs by the Sun Earth Connection Coronal Heliospheric Observatory (SECCHI; see Howard et al. 2007, [this issue](#)) and of associated type II radio burst emissions by S/Waves will provide, for the first time, CME trajectories in the IPM and comparison between optical observations and radio observations based on GP measurements.

Acknowledgements The authors wish to thank P.-L. Astier and M. Dekkali (LESIA, Observatoire de Paris, France) for their helpful comments and discussions. The Austrian team, lead by H.-O. Rucker (Austrian Academy of Sciences, Space Research Institute, Graz, Austria) is also thanked for its work on antenna modelling. They finally also thank Q.-N. Nguyen for her deep involvement in the processing of the S/Waves data.

References

- S. Bale et al., Space Sci. Rev. (2007, this issue). doi:[10.1007/s11214-007-9251-x](https://doi.org/10.1007/s11214-007-9251-x)
- J.-L. Bougeret et al., Space Sci. Rev. (2007, this issue)
- B. Cecconi, PhD thesis, Observatoire de Paris-Université Paris 7, Meudon, France, 2004
- B. Cecconi, Radio Sci. **42**, RS2003 (2007)
- B. Cecconi, P. Zarka, Radio Sci. **40**, RS3003 (2005)
- G.A. Dulk, J.-L. Steinberg, S. Hoang, Astron. Astrophys. **141**, 30 (1984)
- G.A. Dulk, J.-L. Steinberg, S. Hoang, A. Lecacheux, in *The Sun and the Heliosphere in Three Dimensions*, ed. by R.G. Marsden, ASSL, vol. 123 (1986), p. 229
- G.A. Dulk, W.C. Erickson, R. Manning, J.-L. Bougeret, Astrophys. J. **365**, 294 (2001)
- J. Fainberg, R.G. Stone, Space Sci. Rev. **16**, 145 (1974)
- J. Fainberg, S. Hoang, R. Manning, Astron. Astrophys. **153**, 145 (1985)
- G. Fischer et al., in *Planetary Radio Emissions V*, ed. by H.O. Rucker, M.L. Kaiser, Y. Leblanc (Austrian Acad. of Sci. Press, Vienna, 2001), p. 347
- D.A. Gurnett, M.M. Baumback, J. Rosenbauer, J. Geophys. Res. **83**, 616 (1978)
- D.A. Gurnett et al., Space Sci. Rev. **114**, 395 (2004)
- J. Hanasz, R. Schreiber, H. de Feraudy, M.M. Mogilevsky, T.V. Romantsova, Ann. Geophys. **16**, 1097 (1998a)
- J. Hanasz et al., Cosm. Res. **36**, 575 (1998b)
- J. Hanasz et al., J. Geophys. Res. **108**, 1408 (2003)
- S. Hoang, G.A. Dulk, Y. Leblanc, Astron. Astrophys. **289**, 957 (1994)
- S. Hoang, M. Maksimovic, J.-L. Bougeret, M.J. Reiner, M.L. Kaiser, Geophys. Res. Lett. **25**, 2497 (1998)
- S. Howard et al., Space Sci. Rev. (2007, this issue)
- M.L. Kaiser, Adv. Space Res. **36**, 1483 (2005)
- P.J. Kellogg, Astron. Astrophys. **169**, 329 (1986)
- J.D. Kraus, *Radio Astronomy* (McGraw-Hill, New York, 1966)
- W.S. Kurth, M.M. Baumback, D.A. Gurnett, J. Geophys. Res. **80**, 2764 (1975)
- H.P. Ladreiter, P. Zarka, A. Lecacheux, Planet. Space Sci. **42**, 919 (1994)
- H.P. Ladreiter, P. Zarka, A. Lecacheux, W. Macher, H.O. Rucker, R. Manning, D.A. Gurnett, W.S. Kurth, Radio Sci. **30**, 1699 (1995)
- A. Lecacheux, Astron. Astrophys. **70**, 701 (1978)
- R. Manning, J. Fainberg, Space Sci. Inst. **5**, 161 (1980)
- T. Oswald et al., in *Planetary Radio Emissions VI*, ed. by H.O. Rucker, W.S. Kurth, G. Mann (Austrian Acad. Sci. Press, Vienna, 2006), p. 475
- M. Panchenko, Radio Sci. **39**, 6010 (2004)
- M.J. Reiner, J. Fainberg, R.G. Stone, J. Geophys. Res. **98**, 18767 (1993)
- M.J. Reiner, M.L. Kaiser, J. Fainberg, J.-L. Bougeret, R.G. Stone, Geophys. Res. Lett. **25**, 2493 (1998a)
- M.J. Reiner, J. Fainberg, M.L. Kaiser, R.G. Stone, J. Geophys. Res. **103**, 1923 (1998b)
- M.J. Reiner, M.L. Kaiser, J. Fainberg, R.G. Stone, J. Geophys. Res. **103**, 29651 (1998c)
- M.J. Reiner, B.V. Jackson, D.F. Webb, D.R. Mizuno, M.L. Kaiser, J.-L. Bougeret, J. Geophys. Res. **110**, A09S14 (2005)
- M.J. Reiner, M.L. Kaiser, J. Fainberg, J.-L. Bougeret, Sol. Phys. **234**, 301 (2006)
- H.O. Rucker, W. Macher, R. Manning, H.P. Ladreiter, Radio Sci. **31**, 1299 (1996)
- H.O. Rucker, W. Macher, G. Fischer, T. Oswald, J.-L. Bougeret, M.L. Kaiser, K. Goetz, Adv. Space Res. **36**, 1530 (2005)
- J.-L. Steinberg, G.A. Dulk, S. Hoang, A. Lecacheux, M.G. Aubier, Astron. Astrophys. **140**, 39 (1984)
- D.F. Vogl et al., J. Geophys. Res. **109**, A09S17 (2004)
- P. Zarka, B. Cecconi, W.S. Kurth, J. Geophys. Res. **109**, A09S15 (2004)

Theoretical Modeling for the STEREO Mission

**Markus J. Aschwanden · L. F. Burlaga · M. L. Kaiser ·
C. K. Ng · D. V. Reames · M. J. Reiner · T. I. Gombosi ·
N. Lugaz · W. Manchester IV · I. I. Roussev ·
T. H. Zurbuchen · C. J. Farrugia · A. B. Galvin ·
M. A. Lee · J. A. Linker · Z. Mikić · P. Riley ·
D. Alexander · A. W. Sandman · J. W. Cook ·
R. A. Howard · D. Odstrčil · V. J. Pizzo · J. Kóta ·
P. C. Liwer · J. G. Luhmann · B. Inhester ·
R. W. Schwenn · S. K. Solanki · V. M. Vasylunas ·
T. Wiegelmans · L. Blush · P. Bochsler · I. H. Cairns ·
P. A. Robinson · V. Bothmer · K. Kecskemeti ·
A. Llebaria · M. Maksimovic · M. Scholer ·
R. F. Wimmer-Schweingruber**

Originally published in the journal Space Science Reviews, Volume 136, Nos 1–4.
DOI: [10.1007/s11214-006-9027-8](https://doi.org/10.1007/s11214-006-9027-8) © Springer Science + Business Media B.V. 2007

Abstract We summarize the theory and modeling efforts for the STEREO mission, which will be used to interpret the data of both the remote-sensing (SECCHI, SWAVES) and in-situ

M. J. Aschwanden (✉)
Solar & Astrophysics Lab., Lockheed Martin ATC, 3251 Hanover St., Palo Alto, CA 94304, USA
e-mail: aschwanden@lmsal.com

L. F. Burlaga · M. L. Kaiser · C. K. Ng · D. V. Reames · M. J. Reiner
NASA/Goddard Space Flight Center, Greenbelt, MD 20771, USA

T. I. Gombosi · N. Lugaz · W. Manchester IV · I. I. Roussev · T. H. Zurbuchen
University of Michigan, 1141 Space Research Bldg., Ann Arbor, MI 48109, USA

C. J. Farrugia · A. B. Galvin · M. A. Lee
University of New Hampshire, EOS SSC Morse Hall, Durham, NH 03824, USA

J. A. Linker · Z. Mikić · P. Riley
SAIC, 10260 Campus Point Dr., San Diego, CA 92121, USA

D. Alexander · A. W. Sandman
Dept. Physics & Astronomy, Rice University, PO Box 1892, Houston, TX 77251, USA

J. W. Cook · R. A. Howard
Naval Research Laboratory, Code 7660, 4555 Overlook Ave. SW, Washington DC, 20375, USA

D. Odstrčil · V. J. Pizzo
NOAA/SEC, Code R/E/SE, 325 Broadway, Boulder, CO 80303, USA

J. Kóta
University of Arizona, Lunar and Planetary Laboratory, Tucson, AZ 85721-0092, USA

instruments (IMPACT, PLASTIC). The modeling includes the coronal plasma, in both open and closed magnetic structures, and the solar wind and its expansion outwards from the Sun, which defines the heliosphere. Particular emphasis is given to modeling of dynamic phenomena associated with the initiation and propagation of coronal mass ejections (CMEs). The modeling of the CME initiation includes magnetic shearing, kink instability, filament eruption, and magnetic reconnection in the flaring lower corona. The modeling of CME propagation entails interplanetary shocks, interplanetary particle beams, solar energetic particles (SEPs), geoeffective connections, and space weather. This review describes mostly existing models of groups that have committed their work to the STEREO mission, but is by no means exhaustive or comprehensive regarding alternative theoretical approaches.

Keywords STEREO mission · Solar corona · Solar wind · Coronal mass ejection (CME) · Solar filaments · Heliosphere · Interplanetary shocks · Interplanetary particle beams · Solar energetic particle events (SEP) · Solar flares · Space weather · Stereoscopy · 3D reconstruction techniques · White-light emission · EUV emission · Interplanetary radio emission

P. C. Liewer
Jet Propulsion Laboratory, Mail Stop 169-506, Pasadena, CA 91109, USA

J. G. Luhmann
University of Berkeley, Space Sciences Lab., 7 Gauss Way #7450, Berkeley, CA 94720, USA

B. Inhester · R. W. Schwenn · S. K. Solanki · V. M. Vasyliunas · T. Wiegelmann
Max-Planck Institut für Sonnensystemforschung, Max-Planck Str.2, D-37191, Katlenburg-Lindau,
Germany

L. Blush · P. Bochsler
Physikalischs Institut, University of Bern, Sidlerstrasse 5, CH-3012 Bern, Switzerland

I. H. Cairns · P. A. Robinson
University of Sydney, School of Physics, Sydney, NSW 2006, Australia

V. Bothmer
Universität Göttingen, Institut für Astrophysik, Friedrich-Hund-Platz 1, 37077 Göttingen, Germany

K. Kecskemeti
KFKI RMKI, POB 49, H-1525, Budapest, Hungary

A. Llebaria
Laboratoire d'Astronomie Spatiale, C.N.R.S., BP8, 13376 12, Marseille Cedex, France

M. Maksimovic
CNRS & LESIA, Observatoire de Paris-Meudon, F-92195 Meudon Cedex, France

M. Scholer
Center for Interdisciplinary Plasma Science, Max-Planck-Institute for Extraterrestrial Physics,
85740 Garching, Munich, Germany

R. F. Wimmer-Schweingruber
Extraterr, Physics IEAP, University of Kiel, Leibnizstr. 11, Kiel, 24118 Germany

1 Introduction

Theoretical modeling is of particular importance for the *Solar TERrestrial RElations Observatory (STEREO)* mission because we obtain for the first time mission-dedicated 3-dimensional (3D) information of solar-terrestrial phenomena. Some 3D modeling has been accomplished before, of course, e.g., by means of solar-rotation tomography, combined imaging and Doppler-spectroscopy, or multiple in-situ spacecraft observations of the solar wind (such as with CLUSTER), but STEREO is the first mission dedicated to study the 3D evolution of CMEs and the solar wind from stereoscopic vantage points. Realistic models of the 3D structure and dynamics of solar/heliospheric plasma and particles are needed to fully exploit the science return of the data, for our exploration of the unknown physical processes whose outcome we are observing, as envisioned in a number of anticipatory pre-launch papers (Grigoryev, 1993; Pizzo *et al.*, 1994; Davila *et al.*, 1996; Schmidt and Bothmer, 1996; Socker *et al.*, 1996, 2000; Rust *et al.*, 1997; Socker, 1998; Liewer *et al.*, 1998; Howard *et al.*, 2002; Davila and St. Cyr 2002; Mueller *et al.*, 2003). Table 1 gives an overview of what the four instrument suites of the two STEREO spacecraft will yield: SECCHI/EUVI will image the solar corona, eruptive filaments, flares, and coronal mass ejections (CMEs) in the lower corona at EUV wavelengths. SECCHI/COR and HI will image the CME phenomena that propagate to the outer corona in white light. SWAVES will triangulate the radio emission generated by CMEs and interplanetary shocks and particle beams. The IMPACT and PLASTIC instruments are in-situ particle detectors that measure particle distribution functions and elemental abundances at 1 AU in the solar wind or in passing CMEs, interplanetary shocks, particle beams, or in *solar energetic particle (SEP)* events. The theoretical modeling of all these processes includes both *magneto-hydrodynamic (MHD)* and kinetic theories. A great potential, but also challenge, is the unprecedented computer power that supports these theoretical and numerical modeling efforts today, never available to such a large extent in previous missions.

We organize this review in the following order: First we describe theoretical modeling of the solar/heliospheric background plasma (solar corona in Section 2, solar

Table 1 Metrics of modeled solar/heliospheric phenomena versus detecting STEREO instruments

	SECCHI EUVI, COR /HI	SWAVES	IMPACT ^a	PLASTIC
Background plasma				
Solar corona (Section 2)	EUV, WL
Solar wind (Section 3)	...	Waves	Particles	Particles
CME Initiation				
Filament eruption (Section 4)	EUV, WL
Coronal mass ejection launch (Section 5)	EUV, WL	Radio, waves
CME Propagation				
Interplanetary shocks (Section 6)	WL	Radio, waves	Particles	Particles
Interplanetary particle beams (Section 7)	...	Radio, waves	Particles	Particles
Solar energetic particle events (Section 8)	Particles	Particles
Geo-connected space weather (Section 9)	Particles	Particles

^aIMPACT will also be able to make in-situ measurements of the magnetic field at 1 AU

wind in Section 3), then processes of CME initiation (filament eruption in Section 4, CME launch in Section 5), and finally processes of interplanetary CME propagation (interplanetary shocks in Section 6, interplanetary particle beams and radio emission in Section 7, solar energetic particles in Section 8, geoeffective events and space weather in Section 9).

2 Modeling of the Solar Corona

2.1 Physical 3D-Modeling of the Global Corona

The quantitative analysis of stereoscopic EUV images requires full 3D models of the electron density $n_e(x, y, z)$ and electron temperature $T_e(x, y, z)$ of the coronal plasma, so that emission measure images $EM(x, y)$ can be self-consistently produced by integrating the *differential emission measure (DEM)* distribution, i.e., $dEM(x, y, T)/dT = \int n_e^2(x, y, z, T)dz$, along each stereoscopic line-of-sight direction z . In addition, the DEM depends also on assumptions on elemental abundances and ionization equilibrium (see Section 5.2 for more details and references). The most detailed state-of-the-art models represent the inhomogeneous 3D solar corona with up to $\approx 10^5$ coronal loop structures, each one calculated based on a physical model (e.g., Schrijver *et al.*, 2004). A key observable input is a (synoptic) full-Sun magnetogram of the photospheric magnetic field as a boundary condition, which can be extrapolated into the 3D corona by means of a potential field (source surface) model or a nonlinear force-free field model. An energy input into the corona has to be assumed, which could be a function of the local magnetic field strength $B(x, y)$ at the footpoint and the loop length $L(x, y)$, yielding a local Poynting flux (or heating rate) of $E_H(x, y) \propto B^a(x, y)L^b(x, y)$ at position (x, y) . The physical model of a coronal loop can then be specified by a hydrostatic equilibrium solution, where the heating rate is balanced by the conductive and radiative losses, e.g., the RTV solutions known for uniform heating and constant pressure (Rosner *et al.*, 1978), the RTVS solutions corrected for non-uniform heating and gravitation (Serio *et al.*, 1981), or empirical scaling laws inferred from Yohkoh observations (Kano and Tsuneta, 1995). The latest TRACE studies imply deviations from the equilibrium scaling laws because of the asymmetric heating functions caused by flows (Winebarger *et al.*, 2002). The emission measures $dEM(x, y, z, T)/dT$ of the physical loops can then be filled into a datacube (x, y, z) aligned with a (stereoscopic) direction z and integrated along this line-of-sight. Full-Sun visualizations based on such physical models have been simulated for soft X-ray and EUV instruments (Figure 1). The input parameters (such as the magnetic field model or the heating scaling law) can then be varied until the simulated images show the best match (quantified by a χ^2 -value) with an observed soft X-ray or EUV image. Fitting two stereoscopic EUV images from SECCHI/EUVI simultaneously with the same physical 3D model obviously represents a very powerful method to constrain the heating function, a key observable in the *coronal heating problem*.

The 3D reconstructions of the magnetic field and electron density of the global corona have been attempted for decades (e.g., Altschuler, 1979): from line-of-sight inversions of the white-light polarization (e.g., Van de Hulst, 1950; Lamy *et al.*, 1997; Llebaria *et al.*, 1999; Quémérais and Lamy, 2002), from synoptic maps combined with magnetic field extrapolations (Liewer *et al.*, 2001), from stereoscopic image pairs in soft X-rays (Batchelor, 1994), from stereoscopic or multi-frequency images in radio (Aschwanden and Bastian, 1994a,b; Aschwanden *et al.*, 1995, 2004; Aschwanden, 1995), from tomographic multi-image sequences in soft X-rays or EUV (Hurlburt *et al.*, 1994; Davila, 1994; Zidowitz *et al.*, 1996;

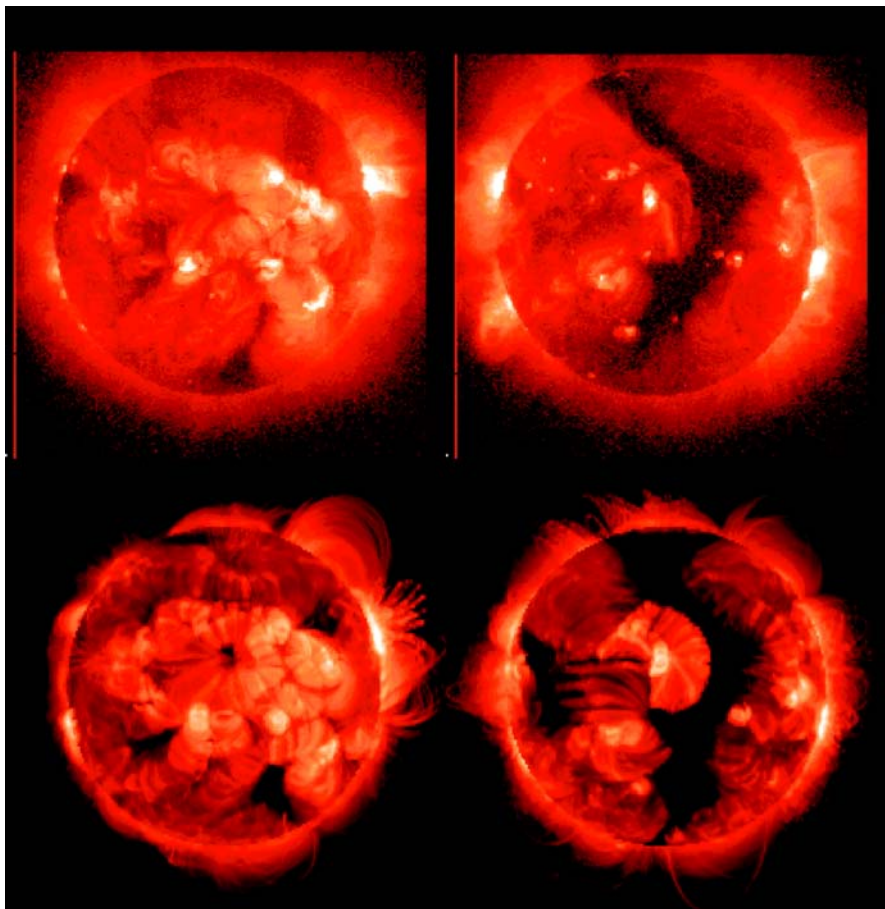


Fig. 1 Full-Sun visualization of stereoscopic corona modeling: soft X-ray images from Yohkoh/SXT from two different aspect angles (top row), and simulated 3D corona images (bottom row), both shown on a logarithmic scale with a total range of 4 orders of magnitude in brightness. The theoretical 3D model is based on the observed magnetic field on the solar surface, a potential magnetic field model, a heating function, hydrostatic solutions of $\approx 50,000$ individual coronal loops, and convolution with the filter response functions (Schrijver *et al.*, 2004)

Zidowitz, 1997, 1999; Frazin and Kamalabadi, 2005), or from DEM-tomographic multi-filter images (Frazin, 2000; Frazin and Janzen, 2002; Frazin *et al.*, 2005). However, these reconstructions of the 3D density $n_e(x, y, z)$ of the global corona have only been demonstrated with a resolution of $\gtrsim 15^\circ$ in longitude, mostly limited by the time variability over the time-span of substantial rotation. Such approaches can characterize the smooth 3D density of the background corona, but cannot be used to reconstruct elementary coronal loop structures (which require a spatial resolution of $\lesssim 1''$). However, some numerical simulation studies have zoomed into partial views of the 3D corona, rendering active regions on the level of elementary loops, based on hydrodynamic loop models (Gary, 1997; Alexander *et al.*, 1998) or full-scale MHD simulations with realistic plasma heating from photospheric drivers (Gudiksen and Nordlund, 2002, 2005a,b; Mok *et al.*, 2005).

2.2 Stereoscopic 3D-Reconstruction of Coronal Loops

Although stereoscopic observations with two spacecraft provide only limited constraints for 3D modeling of the global corona, the 3D reconstruction of a single elementary loop structure should be much better constrained, if we succeed to isolate a single loop by appropriate subtraction of the background corona, which consists of myriads of other competing loop structures. 3D reconstructions of elementary loop structures are of fundamental importance for studying the physical plasma properties, their (MHD) dynamics, the associated (non-potential) magnetic field and electric currents (e.g., Aschwanden, 2004, Sections 3–8). The mathematical determination of the 3D geometry of a single loop has been formulated for planar loops (Loughhead *et al.*, 1983) as well as for non-planar loops (Bertone and Sakurai, 1985). The determination of the 3D position of a point-like feature, such as the loop centroid in a particular viewing plane, is essentially a triangulation method in *epipolar planes* (Portier-Fozzani and Inhester, 2001, 2002), also called *tiepoint method* (Figure 2) in some applications to solar stereoscopy (Liewer *et al.*, 2000; Hall *et al.*, 2004).

Such stereoscopic 3D reconstructions of single loops have been attempted in the past by using the solar rotation to mimic two different viewing angles, which of course works only for stationary loops. 3D reconstructions of single coronal structures (threads, rays,

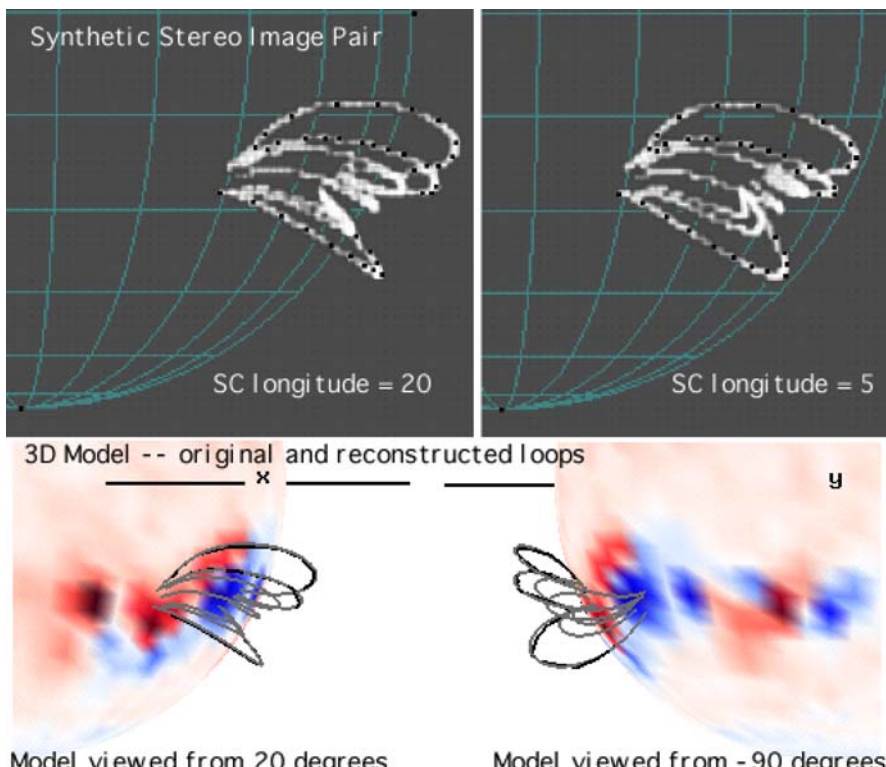


Fig. 2 Stereoscopic 3D reconstruction of individual loops in EUV images using the tie-point method. Two corresponding loop structures have to be identified in a pair of images, pinpointed with tiepoints for triangulation of their 3D geometry (courtesy of Eric DeJong and Paulett Liewer)

streamers) aligned with individual coronal magnetic field lines have been achieved from white-light images taken 1–3 h apart (Koutchmy and Molodensky, 1992; Vedenov *et al.*, 2000). In order to make solar-rotation stereoscopy more general, the concept of *dynamic stereoscopy* has been developed for the 3D reconstruction of coronal loops, which relies more on static magnetic fields, rather than on static brightness maps (Aschwanden *et al.*, 1999, 2000). Alternative 3D reconstructions of magnetic field lines combine theoretical 3D magnetic field models with the observed 2D projection of a coronal loop from an EUV image (Gary and Alexander, 1999; Wiegelmans and Neukirch, 2002; Wiegelmans and Inhester, 2003; Wiegelmans *et al.*, 2005), which can be even more strongly constrained by two simultaneous projections from two STEREO spacecraft (Wiegelmans and Inhester, 2006). Forward-fitting techniques using some *a priori* constraints are expected to be superior to straightforward backprojection techniques (Gary *et al.*, 1998). The efficiency of stereoscopic correlations can be considerably enhanced with automated detection of loops, e.g., with the *oriented-connectivity method* (Lee *et al.*, 2005; Aschwanden, 2005), with help of extrapolated magnetic field lines (Wiegelmans *et al.*, 2005), or even by constraining the heating input with subsurface (magnetoconvection) dynamics (Hurlburt *et al.*, 2002). Stereoscopy of coronal loops is expected to be most suitable at small separation angles ($\lesssim 30^\circ$), which has to take place in the initial phase (during the first year) of the STEREO mission.

3 Modeling of the Solar Wind

In order to understand the propagation of CMEs and energetic particles from the corona through the heliosphere, detailed time-dependent models of the background plasma and solar wind are required. Solar wind models can be subdivided depending on their boundary conditions, either given by the magnetic field in the lower corona (Section 3.1), or by heliospheric conditions (Section 3.2). Recent space weather models involve the fully connected Sun-to-Earth system by coupling in with magnetospheric and ionospheric models, such as in the *Community Coordinated Modeling Center (CCMC)*, and these will provide the most comprehensive context for STEREO data.

3.1 Coronal Solar Wind Models

An approximate description of the global coronal magnetic field close to the Sun is given by the so-called *potential field source surface (PFSS)* model, constrained by the lower boundary condition of the photospheric magnetic field and an upper artificial boundary condition at $r \approx 1.6\text{--}3.25 R_\odot$, where the magnetic field is assumed to be current-free ($\nabla \times \mathbf{B} = 0$). There exist a number of numerical codes based on such PFSS models, initially developed by Altschuler and Newkirk (1969) and Schatten *et al.* (1969), later refined by Hoeksema (1984) and Wang and Sheeley (1992), and recently used with input from Wilcox Solar Observatory magnetograms (at CCMC), or from *Michelson Doppler Imager (MDI)* magnetograms onboard the *Solar and Heliospheric Observatory (SoHO)* (Schrijver and DeRosa, 2003). These codes are extremely useful to map out open magnetic field regions that connect not only from coronal holes but also from some parts of active regions out into the heliosphere (Figure 3), outlining escape paths for high-energetic particles.

The *Magnetohydrodynamics Around a Sphere (MAS)* model is developed by the *Science Applications International Corporation (SAIC)* group, which is an MHD model of the solar corona extending over a domain of 1–30 solar radii. The input of the model is (1) the radial

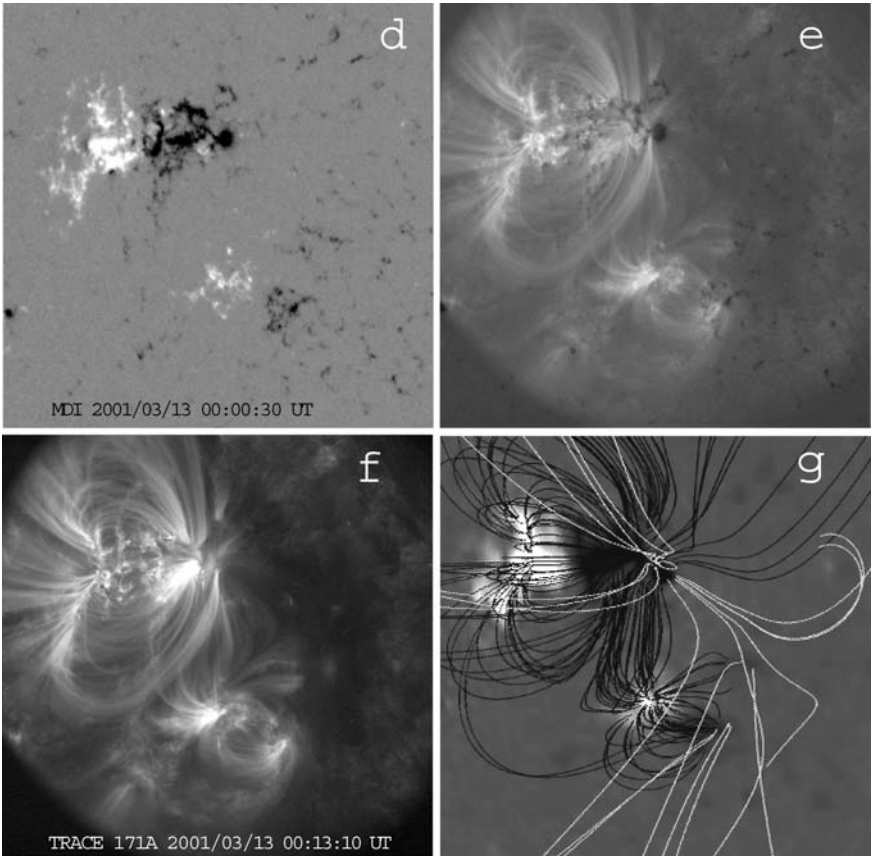


Fig. 3 (Panel *d*) MDI magnetogram; (Panel *e*) MDI magnetogram overlayed with TRACE 171 Å; (Panel *f*) TRACE 171 Å image of 2001-Mar-13, 00:13 UT; (Panel *g*) Potential field extrapolation using a source-surface model. Closed field lines of active regions are indicated with black color, the open field lines that connect to interplanetary space with white color (Schrijver and DeRosa, 2003)

magnetic field $B_r(\vartheta, \phi)$ as a function of co-latitude ϑ and longitude ϕ from a (full-Sun) synoptic magnetogram (e.g., from *Kitt Peak National Observatory, KPNO*) that is slightly smoothed, and (2) the temperature $T_e(\vartheta, \phi)$ and density $n_e(\vartheta, \phi)$ at the coronal base. The model computes a stationary solution of the resistive MHD equations and provides as output the plasma temperature $T_e(r, \vartheta, \phi)$, pressure $p(r, \vartheta, \phi)$, density $n_e(r, \vartheta, \phi)$, solar wind velocity $v(r, \vartheta, \phi)$, and magnetic field $B(r, \vartheta, \phi)$ as a function of the distance, in the range of $1 < r < 30 R_\odot$. The initial condition employs a transonic solution for the gas-dynamic variables with a polytropic index of $\gamma = 1.05$, which avoids the complications of the heating, thermal conduction, and radiative loss terms in the energy equation. An example of such a 3D model is shown in Figure 4. The MAS model has been used to simulate 3D coronal streamers (Linker *et al.*, 1990) and the solar corona during the *whole-Sun month* (Linker *et al.*, 1999). Given an (approximate) 3D model of the coronal density, stereoscopic images in white-light can be integrated straightforwardly and compared with observed images from SECCHI/COR and HI.

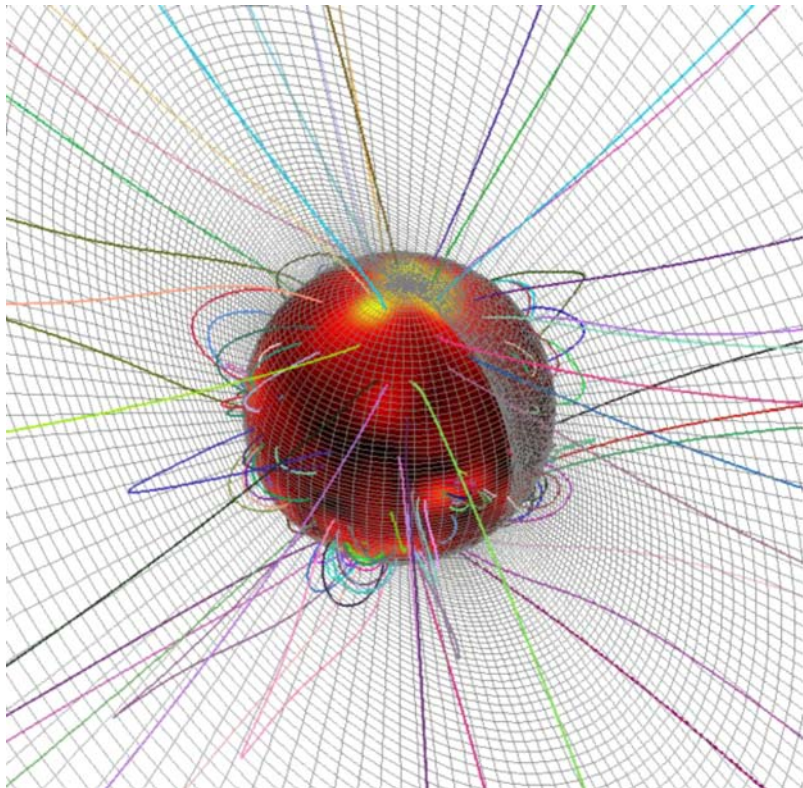


Fig. 4 A 3D numerical computation of the solar corona with $101 \times 75 \times 64$ (non-uniform) meshpoints (r, ϑ, ϕ) , (courtesy of SAIC group)

3.2 Heliospheric Solar Wind Models

Recent numerical codes that simulate or reconstruct the solar wind in the heliosphere (e.g., Schwenn and Marsch, 1991a,b; Neugebauer, 2001; Balogh *et al.*, 2001) include *MAS-IP* (Riley *et al.*, 2001a,b), *ENLIL* (developed by D. Odstrčil), *heliospheric tomography* (developed by B. Jackson and P. Hick), and the *exospheric solar wind model* (developed by H. Lamy and V. Pierrard), all part of the space weather modeling effort coordinated by CCMC. The aim of these codes is to provide components for “end-to-end models” (e.g., CISM, UMich, and CCMC) that link the coronal and solar wind physics and geometry – which is just what the STEREO combined imaging and in-situ experiments are trying to do.

In the past we have had many separate coronal/imaging studies and on the other side in-situ studies. But linking them demands combined data sets and coupled corona/solar-wind models with realistic characteristics. For example, the magnetic field models tell us for a particular photospheric boundary condition where open field regions (hence solar wind sources) should be located, and which ones connect to specific points in space, e.g., to the STEREO spacecraft or to the Earth (within the uncertainty of the chosen magnetic field model, of course). So we may associate a particular coronal hole seen in an EUV image with a solar wind stream we detect on the spacecraft or at Earth.

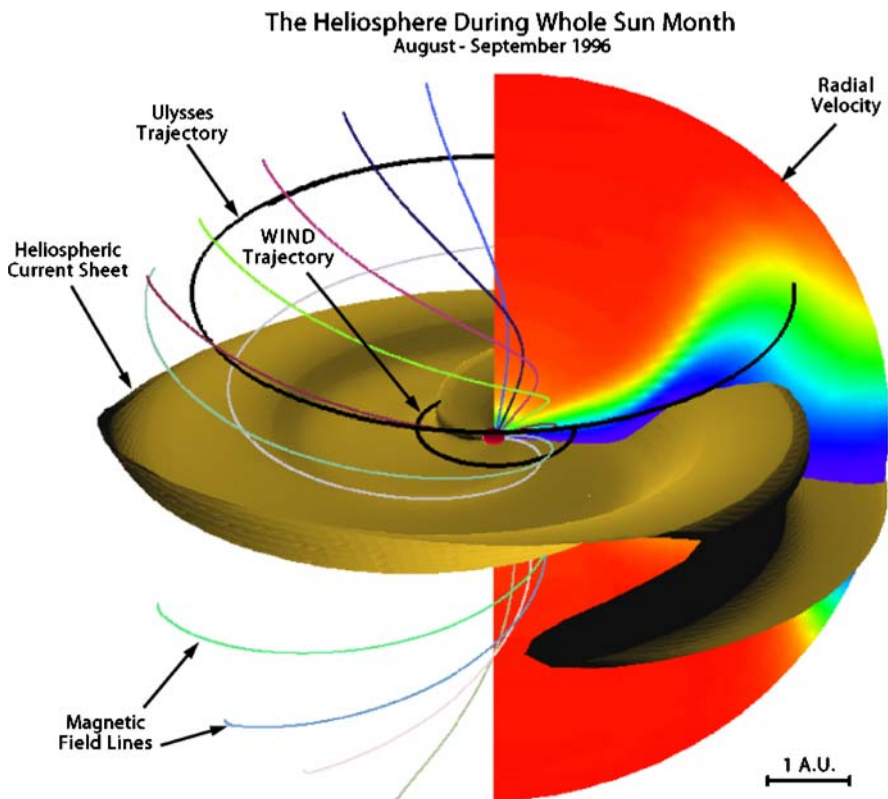


Fig. 5 Model solution for Carrington rotations (CR) 1912–1913. The heliospheric current sheet (inferred from the isosurface $B_r = 0$) is displayed out to 5 AU. The central sphere marks the inner boundary at $30 R_\odot$. A meridional slice of the radial velocity is shown at an arbitrary longitude. Red corresponds to fastest speeds ($\approx 750 \text{ km s}^{-1}$) and blue to the slowest speeds ($\approx 350 \text{ km s}^{-1}$). Superimposed is a selection of interplanetary magnetic field lines originating from different latitudes. Finally, the trajectories of the Wind and Ulysses spacecraft are marked (Riley *et al.*, 2001b)

The solar physics group at SAIC has developed a 3D MHD model of the solar corona and heliosphere (Riley *et al.*, 2001a,b). They split the modeling region into two distinct parts: the solar corona ($1\text{--}30 R_\odot$) and the inner heliosphere ($30 R_\odot - 5 \text{ AU}$). The combined model is driven solely by the observed line-of-sight photospheric magnetic field and can thus provide a realistic global picture of the corona and heliosphere for specific time periods of interest. Figure 5 summarizes the global structure of the inner heliosphere for the interval coinciding with Carrington rotation CR 1913 (1996 August 22–1996 September 18), which occurred near solar minimum and overlapped the first “Whole Sun Month” campaign. Comparisons of Ulysses and Wind observations with the simulation results for a variety of time periods (e.g., Riley *et al.*, 2003a) show that the model can reproduce the overall features of observations. In a subsequent study, the SAIC team employed this model to explore the evolution of the *heliospheric current sheet* (HCS) during the course of the solar cycle (Riley *et al.*, 2002a). They compared their results with a simple “constant-speed” approach for mapping the HCS outward into the solar wind, demonstrating that dynamic effects can substantially deform the HCS in the inner heliosphere ($\lesssim 5 \text{ AU}$). They also noted that while the HCS may almost

always be topologically equivalent to a “ballerina skirt”, more complicated shapes were possible. One example was an interval approaching the maximum of solar cycle 23 (CR 1960 and 1961) when the shape would be better described as “conch shell”-like.

The NOAA/SEC heliospheric model (ENLIL) solves the time-dependent MHD equations in a spherical geometry using either the *Flux-Corrected-Transport* or *Total-Variation-Diminishing* schemes (e.g., Odstrčil, 1994; Toth and Odstrčil, 1996, 2003; Odstrčil *et al.*, 2002). These high-resolution schemes produce second-order accuracy away from discontinuities, while simultaneously providing the stability that ensures non-oscillatory solutions. The inner radial boundary is located beyond the sonic point ($\approx 21.5\text{--}30 R_\odot$), provided, e.g., by the MAS or *Wang-Sheeley-Arge* (WSA) code. The outer radial boundary can be adjusted to 1–10 AU, and the latitudinal extent covers $\approx \pm 60^\circ$ north and south of the ecliptic.

In support of the STEREO mission, the CCMC is running a series of solar and heliospheric models (by coupling the MAS and ENLIL code) and is saving model input/output on a daily basis. Driven by synoptic magnetogram data obtained by ground-based solar observatories, the solar coronal potential field source surface (PFSS) model represents the approximate coronal magnetic field within $2.5 R_\odot$. The ENLIL solar wind is driven by the WSA model (Arge and Pizzo, 2000) which extends a PFSS magnetic field to $21.5 R_\odot$ past the sonic point (where the plasma velocity starts to exceed the sound speed) using a heliospheric current sheet model and a slow and high speed solar wind distribution depending on the location of coronal holes. ENLIL covers the radial distance between the WSA boundary of $21.5 R_\odot$ and 1.6 AU in the inner heliosphere, between $\pm 58^\circ$ degrees heliographic latitude (which brackets the streamer regions).

In both the PFSS and ENLIL models the time stamp of each file refers to the end time of the solar rotation period covered by the magnetogram data. Typically this date lies about 2 days in the future, as magnetic fields on the solar disc can be measured fairly reliably up to 30 degrees of heliographic longitude away from the disk center (Carrington longitude of the Earth).

The *heliospheric tomography model* makes use of *interplanetary scintillation* (IPS) data to tomographically reconstruct the global structure of the solar wind, provided by earlier IPS observations from STELab in Nagoya, Japan. The model output yields solar wind density and velocity throughout the inner heliosphere, and is able to make real-time heliospheric 3D reconstructions (Jackson and Hick, 2002). For a review of solar wind properties from IPS observations, see, e.g., Kojima *et al.* (2004). Since January 2003, the *Solar Mass Ejection Imager Mission* (SMEI) has been providing data for the IPS Thomson scattering modeling of the all-sky heliospheric solar wind and CMEs (Figure 6).

The 1-D *exospheric solar wind model* (Lamy *et al.*, 2003), also part of the CCMC end-to-end model chain, is developed for coronal holes over a radial range of $\approx 2\text{--}30 R_\odot$, including protons and electrons, modeled with a nonmonotonic total potential for the protons, and with a Lorentzian (kappa) velocity distribution function for the electrons. The exospheric kinetic model assumes that there is a critical height where there is a transition from a collision-dominated to a collisionless regime (at $\approx 1.1\text{--}5.0 R_\odot$, called the *exobase*). An overview of the main differences between the exospheric and fluid/MHD approaches is given in Cranmer (2002).

In addition to the CCMC effort, numeric codes to simulate the steady-state solar wind with helmet-type streamer belt have been developed by the MHD modeling group at the University of Michigan. An example of such a 3D MHD simulation is shown in Roussev *et al.* (2003a), designed to reproduce the global structure of the solar corona and wind under realistic conditions. The magnetic field in the model is split into a potential, \mathbf{B}_0 ,

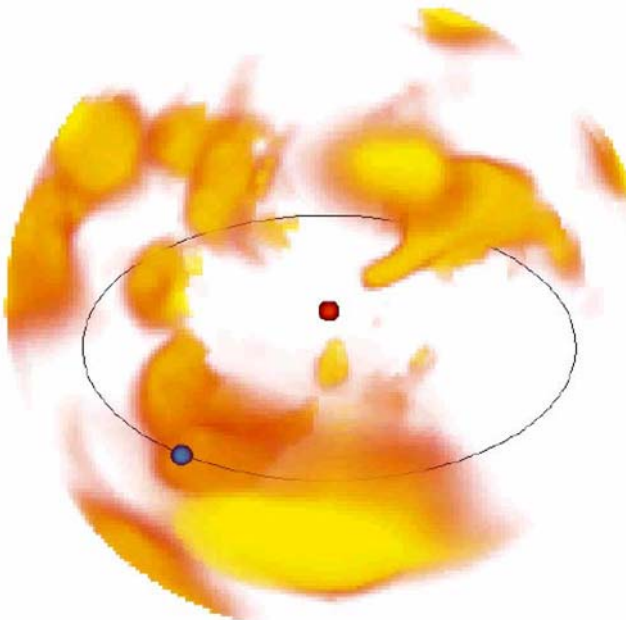


Fig. 6 Time-dependent tomographic reconstruction of the solar wind using SMEI data during the 2003 May 28 CME (courtesy of Bernie Jackson)

and a non-potential, \mathbf{B}_1 , part: $\mathbf{B} = \mathbf{B}_0 + \mathbf{B}_1$, where $\nabla \times \mathbf{B}_0 = 0$. To obtain the bulk solar magnetic field, $\mathbf{B}_0 = -\nabla\psi$, the PFSS method by Altschuler *et al.* (1977) is used. In this method, the magnetic scalar potential, ψ , is evaluated as a series of spherical harmonics. The coefficients in the series are chosen to fit real magnetogram data obtained from the Wilcox Solar Observatory, and most recently from SoHO/MDI. The MHD solution in the model is evolved from a static, potential initial configuration to a steady-state, non-potential solution with a non-zero induced field, \mathbf{B}_1 . The solar wind is powered (heated and accelerated) by the energy interchange between the solar plasma and large-scale MHD turbulence, assuming that the additional energy is stored in the “turbulent” internal degrees of freedom. Note that close to the Sun, an additional amount of energy is stored in waves and turbulent fluctuations, hence the specific heat ratio, γ , of the solar plasma is close to 1 (e.g., Steinolfson and Hundhausen, 1988). The lower values of γ near the Sun are assumed to be associated with those “turbulent” internal degrees of freedom. It is assumed that $n = n_0 + n_{\text{turb}}(R)$, where the number of “turbulent” degrees of freedom near the Sun is $n_{\text{turb}}(R_\odot) \approx 10$, while at larger distances it drops to zero, i.e., $n_{\text{turb}}(\infty) \approx 0$, similar to the approach described in Zeldovich and Raizer (2002) for partially ionized plasmas. Specifically, $n_{\text{turb}}(R) = 10(R_\odot/R)^m$, with $m = 1$ is assumed in the original work by Roussev *et al.* (2003a). Thus the full energy equation is employed in the computations, with a polytropic index $\gamma(R) = [n(R) + 2]/n(R)$ that is now a function of radius describing the additional energy density associated with turbulent motions. This technique is an empirical one inspired by the “hidden internal” degrees of freedom. The physical motivation is to bridge a polytrope, which is nearly isothermal, to a fully fledged energy equation.

The 3D models of the corona and solar wind described above will help to link IMPACT solar wind measurements to the Sun by allowing observations of specific electron populations,

magnetic fields, and solar flare particle events to be mapped back to their source regions. The seven instruments of IMPACT will sample the 3D distribution of solar wind plasma electrons and the local vector magnetic field.

PLASTIC is a prime sensor on STEREO for studying coronal/solar-wind and solar-wind/heliospheric processes. It measures the distributions of density, velocity, and kinetic temperature (and its anisotropy), solar wind protons (H) and alphas (He), the elemental composition, charge state distribution, kinetic temperature, and velocity of the more abundant solar wind heavy ions (C, O, Ne, Mg, Si, Fe), as well as the distribution functions of suprathermal ions (H through Fe). The PLASTIC measurements at two different heliospheric positions will constrain better the relations between variations of the elemental composition (including the FIP effect) in the solar wind and their coronal origin, by having two spatial checkpoints at 1 AU for theoretical time-dependent 3D models of the heliospheric solar wind. The hope is to understand the acceleration of the solar wind, for instance how the slow solar wind originates near coronal streamer boundaries, or how the recurrent ion events originate near *corotating interaction regions (CIRs)*.

4 Modeling of Eruptive Filaments

4.1 MHD Models of Eruptive Filaments

The trigger of a flare or CME is often the (magnetic) destabilization and subsequent eruption of a *filament* (called a *prominence* if seen over the solar limb), which is initially suspended over a highly-sheared neutral line. The destabilization of the filament can be caused either by the kink instability, during a process of increased twisting, or by some other equilibrium-loss process. It can be initiated by continued shearing of the magnetic field, by increasing currents, by converging motion of magnetic footpoints, by buoyancy with subsequent ballooning, or through new magnetic flux emergence. The physical understanding of the origin of a CME has now evolved from sketchy cartoons inspired by observations to full-scale numerical 3D MHD simulations constrained by observed magnetic fields; for recent reviews see, e.g., Forbes (2000), Klimchuk (2001), Zhang and Low (2005), and Roussev and Sokolov (2005). Let us mention a few of the most recent 3D MHD simulations that seem to be most relevant for modeling of STEREO data.

The eruption of a filament or a *magnetic flux rope* in a gravitationally confined helmet streamer cavity (in the form of cool, dense prominence material) could be initiated after draining of the prominence material. The buoyancy force causes the rise and eruption of the flux rope, pushing aside the helmet streamer field lines (Low, 1996). A time-dependent 3D (ideal) MHD simulation of this CME eruption model was realized by Gibson and Low (1998), and the 3D structure viewed from different (stereoscopic) aspect angles is discussed in Gibson and Low (2000). Recent 3D MHD simulations of the *Gibson-Low model* of a buoyantly emerging magnetic flux rope were performed by Manchester *et al.* (2004a). The steady-state coronal field in the MHD model is generated from a prescribed dipole field that progressively is opened up by the solar wind at high latitudes. Then a *Gibson-Low type flux rope* is inserted inside a closed magnetic loop. To initiate the filament eruption, about 20% of the balancing mass is removed from the flux rope, which produces an unbalanced pressure that brings the flux rope out of equilibrium. Future models will incorporate self-consistent arcade eruptions, based on the new insight that the magnetic field and shear velocity are not independent (Manchester, 2003; Manchester *et al.*, 2004b).

Another line of CME initiation models is based on the analytical model of Titov and Démoulin (1999), which contains a flux rope that is suspended in the corona by a balance between magnetic compression and tension forces. In the 2D models, the flux rope with current I has two possible equilibrium positions, provided that the current is not too large: The lower position is stable, while the upper position is unstable. Above a critical current there are no equilibria, and a small outward displacement leads to eruption of the flux rope. In a modified version of the Titov and Démoulin (1999) model developed by Roussev, Sokolov, and Forbes, the flux rope has a poloidal force-free field produced by a (toroidal) ring current and a toroidal force-free field produced by azimuthal currents. An example of such a 3D MHD simulation of an erupting flux rope is shown in Roussev *et al.* (2003b), with the initial configuration illustrated in Figure 7. A special application of this CME model is illustrated in Roussev *et al.*, 2004 (Figure 8): The fully 3D numerical model of a solar eruption incorporates solar magnetogram data and a loss-of-equilibrium mechanism. The study was inspired by the CME event that took place on May 2, 1998, in NOAA AR 8210 and is one of the SHINE Campaign Events. The CME model has demonstrated that a CME-driven shock wave can develop close to the Sun ($\sim 3R_\odot$), and is sufficiently strong to account for the prompt appearance of high-energy solar protons (~ 1 GeV) at the Earth. Using this CME model, Sokolov *et al.* (2004) have carried out a numerical investigation in which they quantified the diffusive acceleration and transport of solar protons at the shock wave from the MHD calculations. The coupled CME-SEP simulation has demonstrated that the theory of diffusive shock acceleration alone can account for the production of GeV protons during solar eruptions.

A further line of CME initiation models focuses on the kink instability of a twisted flux rope. The force-free coronal loop model by Titov and Démoulin (1999) is found to be

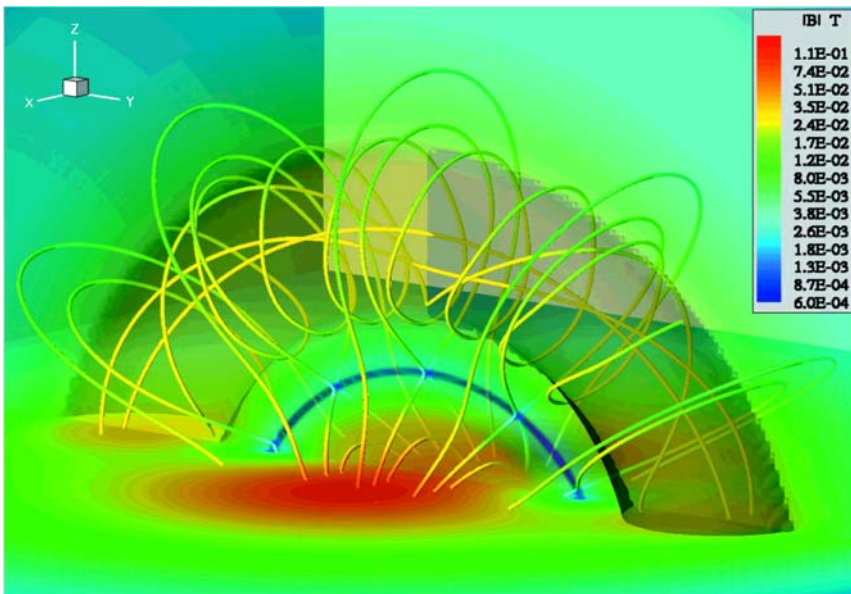


Fig. 7 Initial configuration of the 3D magnetic field of a flux rope prone to loss of equilibrium and subsequent eruption. The solid lines are magnetic field lines, where the false-color code visualizes the magnetic field strength in units of Testa. The surface shaded in gray is an isosurface at $B_z = 0$ (Roussev *et al.*, 2003b)

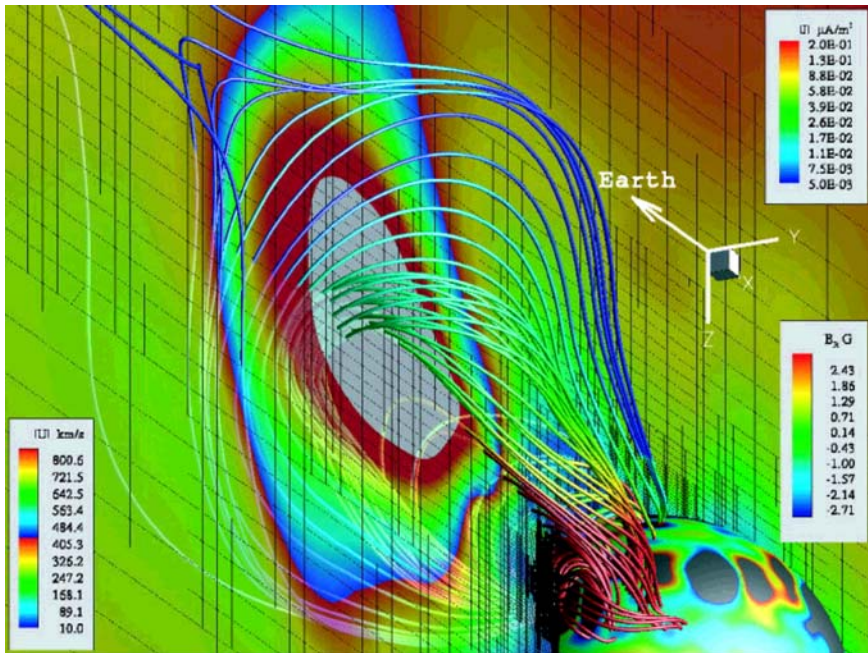


Fig. 8 Three-dimensional view of the modeled CME from May 2, 1998, at 1.1 h after the initiation (from Roussev *et al.*, 2004). The solid lines are magnetic field lines and the false color shows the magnitude of the current density in units of $\mu\text{A m}^{-2}$ (see color legend at top right). The magnitude of flow velocity, in units of km s^{-1} , is shown on a translucent plane (see color legend to the left). Values in excess of $1,000 \text{ km s}^{-1}$ are blanked and shown in light grey. The grid-structure on this plane is also shown as the black frame. The inner sphere corresponds to $R = R_\odot$. The color shows the distribution of radial magnetic field in units of Gauss (see color legend at bottom right). Regions with field strength greater than 3 G are blanked and appear in grey (Roussev *et al.*, 2004)

unstable with respect to the ideal kink mode, which suggests this instability as a mechanism for the initiation of flares, once the average twist of $\Phi \lesssim 3.5\pi$ is exceeded (Török and Kliem, 2003; Török *et al.*, 2003; Kliem *et al.*, 2004; Rust and LaBonte, 2005). A particularly fitting simulation of a kinking filament that becomes unstable is shown in Figure 9, where a close resemblance with EUV images from TRACE 195 Å is demonstrated (Török and Kliem, 2004). The magnetic field decrease with height above the filament is critical whether a confined eruption or a full (unconfined) eruption occurs. Because this model predicts a fairly accurate evolution of the 3D geometry of the kinking filament, a time-dependent 3D reconstruction with two STEREO spacecraft using EUVI images promises very stringent tests of this theoretical model.

More complex CME initiation models involve multiple magnetic flux systems, such as in the *magnetic break-out model* (Antiochos *et al.*, 1999). In this model, reconnection removes unstressed magnetic flux that overlies the highly stressed core field and this way allows the core field to erupt. The magnetic break-out model involves specific 3D nullpoints and separatrices. A multi-polar configuration was also included in the updated *catastrophe model* (Lin and Forbes, 2000; Lin and van Ballegooijen, 2005), which contrasts the *magnetic break-out model*. Such more complex magnetic configurations are difficult to disentangle, but two independent views with the STEREO/EUVI imagers provide a more promising capability to test the 3D magnetic field configuration than previous single-spacecraft observations.

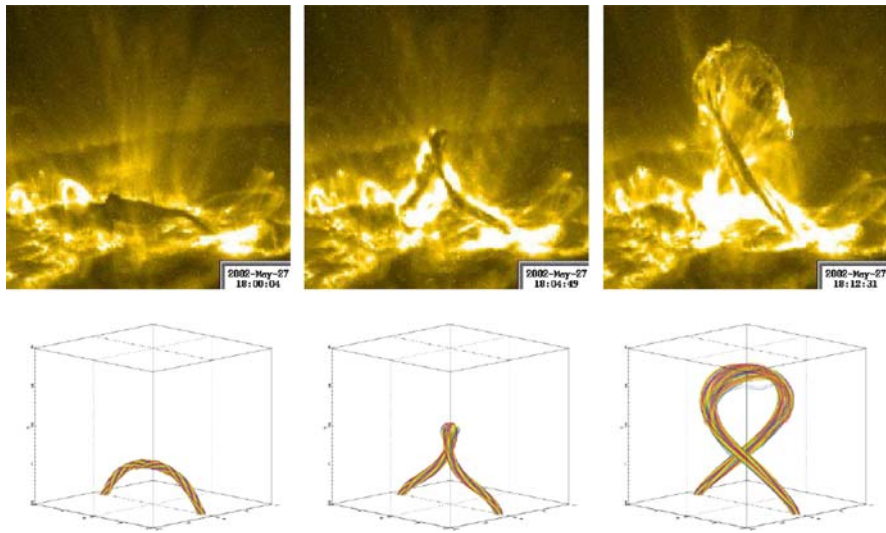


Fig. 9 **Top:** TRACE 195 Å images of the confined filament eruption on 2002 May 27. The right image shows the filament after it has reached its maximum height. **Bottom:** magnetic field lines outlining the kink-unstable flux rope reproduced with 3D MHD simulations (Török and Kliem, 2004)

4.2 Modeling of EUV and White-Light Emission

While most theoretical models of eruptive filaments are formulated in terms of the 3D magnetic field, quantitative tests with observations require the magnetic field lines to be filled with plasma, so that emission measures and line-of-sight integrated images can be simulated and compared with observed images, e.g., in white-light for SECCHI/COR and HI, or in EUV for SECCHI/EUVI.

Previous comparisons of theoretical models with observed images of eruptive filaments showed evidence for the helical geometry of magnetic flux ropes (Rust and Kumar, 1996; Chen *et al.*, 1997, 2000; Dere *et al.*, 1999; Wood *et al.*, 1999; Ciaravella *et al.*, 2000; Gary and Moore, 2004, Figure 10 here), evident in EUV images in the lower corona as well as in white-light images in the outer corona. There is a strong connection between the magnetic structure of interplanetary magnetic flux ropes (or magnetic clouds) and that of the associated coronal fields at the site of erupting filaments/prominences (Bothmer and Schwenn, 1998; Bothmer, 2003; Cremades and Bothmer, 2004). Some synthetic white-light images have been simulated for a flux rope model by Chen *et al.* (2000), but an unambiguous test of the 3D geometry requires at least two views with different aspect angles, as SECCHI/COR and HI will provide.

The eruption of a filament or launch of a CME can also be tracked at the base of the solar corona: (1) where a dimming occurs in EUV (Hudson *et al.*, 1998) due to a temporary deficit of evacuated coronal plasma, (2) by detecting the formation of post-eruption arcades in EUV and white-light (Tripathi *et al.*, 2004), or (3) in the form of EIT waves. (Thompson *et al.*, 1999), which concentrically propagate over the entire solar surface, caused by the “*pressure implosion*” at the epicenter of the erupted filament. The propagation of EIT waves has been theoretically simulated in terms of fast-mode MHD waves (Wang, 2000; Chen *et al.*, 2002; Wu *et al.*, 2001), which helped to reconcile the observed speed of propagating EIT waves with

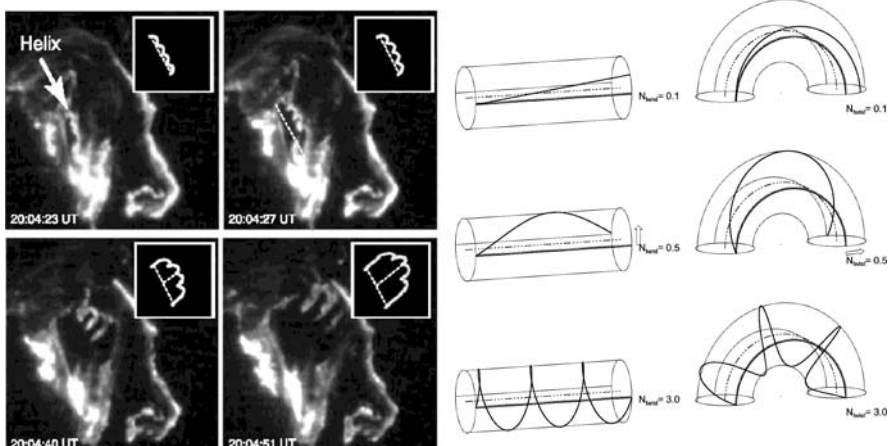


Fig. 10 **Left:** TRACE 1600 Å images in CIV of the GOES-class X3 flare on 2002-Jul-15, 20:04 UT. The inserts illustrate the geometry of the helical structure, exhibiting 3–4 turns. Note that the helical structure expands, rises, and unwinds during the eruption (Gary and Moore, 2004); **Right:** Geometrical models of helical fluxtubes with different twists (0.1, 0.5, 3.0 turns), projected onto straight and curved cylinders

the theoretically expected speeds of (fast-mode MHD) magnetoacoustic waves (Figure 11). STEREO/EUVI images enable us to determine the average local density $n_e(\mathbf{x})$ and temperature $T_e(\mathbf{x})$ (in the range of $T_e \approx 0.7$ –2.7 MK) of the coronal plasma, while photospheric magnetograms provide input for extrapolation of the coronal magnetic field $B(\mathbf{x})$, and this way the local Alfvén speed $v_A(\mathbf{x})$ and sound speed $c_S(\mathbf{x})$ can approximately be computed for every location \mathbf{x} in the global corona. This allows us then to predict the (fast-mode MHD) magnetoacoustic wave speed, which in turn can be compared with the observed propagation speed of EIT waves. The SECCHI images will therefore provide powerful constraints for the 3D propagation of global waves in the corona.

The data search, the objectivity of morphological characterization, and the modeling efficiency can considerably be enhanced by automated detection algorithms, as it has already been facilitated by automated filament detection (Ipson *et al.*, 2005; Zharkova and Schetinin, 2005), by automated detection of EIT waves and dimming (Podladchikova and Berghmans, 2005), by automated CME detection (Robbrecht and Berghmans, 2004), and by automated detection and 3D reconstruction of EUV prominences (Foullon, 2003). In summary, powerful tools for automated feature detection, theoretical 3D models of erupting filaments, and simulations of the corresponding EUV and white-light images have been developed over the last decade, but the feedback algorithms that vary the free parameters in theoretical models and control the forward-fitting to observed images (as we expect from STEREO) are still lacking.

5 Modeling Coronal Mass Ejections

5.1 MHD Simulations of CMEs

Some key questions of the STEREO mission address the 3D structure and evolution of CMEs from the solar corona to interplanetary space, in particular the physical understanding

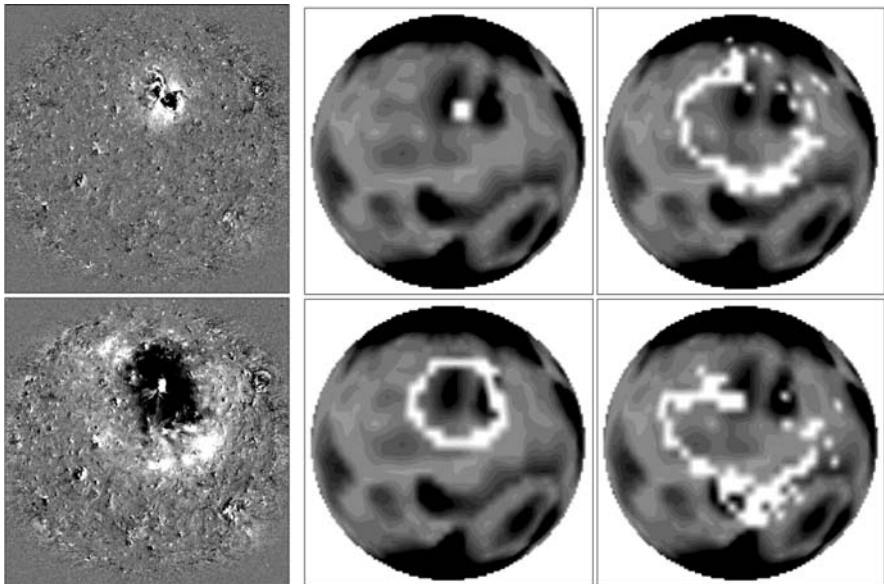


Fig. 11 **Left:** Two running-difference SoHO/EIT 195 Å images of an EIT wave observed 16 and 30 min after launch of the CME on 1997-May-12, 04:34 UT. **Right:** Simulation of an EIT wave by a ray-tracing method of fast-mode MHD waves. The color range indicates wave speeds $v > 500 \text{ km s}^{-1}$ (black) and lower speeds (white). The four simulated images correspond to 2, 15 min (middle column), and 30, 45 min (right column) after launch of the CME (Wang, 2000)

of the forces involved in various acceleration and deceleration phases of propagating CMEs. These questions can only be answered by 3D MHD simulations of CMEs constrained by 3D observations such as those from STEREO. Powerful numerical 3D MHD codes have now become available that are capable of performing the required simulations, such as the coupled MAS/ENLIL code used by the SAIC and NOAA Team (see also Section 3.1), or the BATS-R-US code used by a University of Michigan Team.

As with the ambient solar wind model described in Sections 3.1 and 3.2, SAIC and NOAA/SEC have coupled their models to study the eruption and evolution of CMEs through the corona and into the solar wind. The details of the algorithm used to advance the equations of the SAIC coronal models (MAS) are given elsewhere (Mikić and Linker, 1994; Lionello *et al.*, 1998; Mikić *et al.*, 1999). Briefly, the equations are solved on a spherical (r, ϑ, φ) grid, which permits non-uniform spacing of mesh points in both r and ϑ , thus providing better resolution of narrow structures, such as current sheets. Staggered meshes are employed, which has the effect of preserving $\nabla \cdot \mathbf{B} = 0$ to within round-off errors for the duration of the simulation.

Figure 12 illustrates how CME initiation can be modeled self-consistently. The configuration of the solar corona prior to the emergence of the flux rope is summarized in the two left most panels. This type of equilibrium solution has been discussed in more detail by Linker *et al.* (1999). Contours of the magnetic flux function (fiduciaries of magnetic field lines in two dimensions) are shown by the solid lines and shaded contours (Figure 12, top). The system consists of a single streamer belt displaced by $\approx 10^\circ$ below the heliographic equator. The first column shows the state of the corona after the system has reached equilibrium. The second column shows how this configuration is modified by energization of the magnetic field via photospheric shear (Linker and Mikić, 1995). At this point, the system is still in equilibrium.

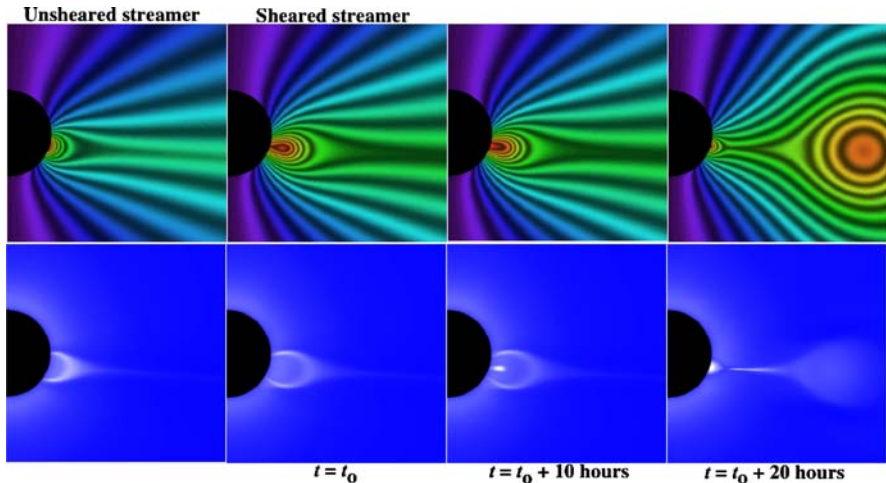


Fig. 12 Evolution of a sheared helmet streamer via flux cancellation. The top panels show contours of the magnetic flux function, which in two dimensions are equivalent to the magnetic field. The bottom panels show the simulated polarized brightness. The four columns summarize: (1) the state of the unsheared corona; (2) the sheared corona; (3) the eruption of the flux rope after 10 h; and (4) the eruption of the flux rope after 20 h, respectively (Riley *et al.*, 2003b)

The polarized brightness (pB) is shown in the Figure 12 bottom panels, constructed by integrating the product of the number density with the scattering function (Billings, 1966) along the line-of-sight (see Section 5.3). The resulting image bears some generic resemblance to SoHO/LASCO white-light images taken near solar minimum (although the model does not reproduce details such as the often observed twisted field lines and bright pre-CME central cores seen in white light images). The remaining panels of Figure 12 summarize the launch of a flux rope following the cancellation of flux. As can be seen, the origins of the flux rope lie in the closed magnetic field lines embedded within the streamer belt. As the flux rope erupts into the solar corona, overlying field lines, which are still connected back to the Sun at both ends, are brought together under the flux rope. As they reconnect with each other, they contribute both to the flux of the evolving flux rope to the right of the reconnection site and to the re-growth of the streamer belt to the left. Note that the flux rope has developed an elliptical shape, with its major axis approximately in the ecliptic plane. Note also that the reconnection site underneath the erupting flux rope is visible in the simulated pB image at $t = 20$ h. This density enhancement was produced by the vertical (i.e., approximately parallel to the solar surface) flow of plasma into the reconnection region and has been observed in white light images (Webb *et al.*, 2003). With regard to the simulated polarized brightness images, we also remark that they bear a strong resemblance to the classic three-part structure of CMEs observed in white light: the bright front, dark cavity, and dense core.

The BATS-R-US solves a set of (ideal) MHD equations using the *Block Adaptive Tree Solar Wind Roe-type Upwind Scheme (BATS-R-US)* code (Powell *et al.*, 1999; Groth *et al.*, 2000), in combination with the *Artificial Wind approximate Riemann (AWR)* solver (Sokolov *et al.*, 2002). This is a conservative finite-volume method with shock-capturing total variation diminishing schemes, explicit/implicit time stepping, a block-adaptive mesh refinement scheme, that runs on massively parallel computers. The energy equation is simplified to the kinetic and gravitational terms (neglecting radiative losses, heat conduction, background heating, and dissipative effects due to viscosity and electric resistivity). A series of BATS-R-US

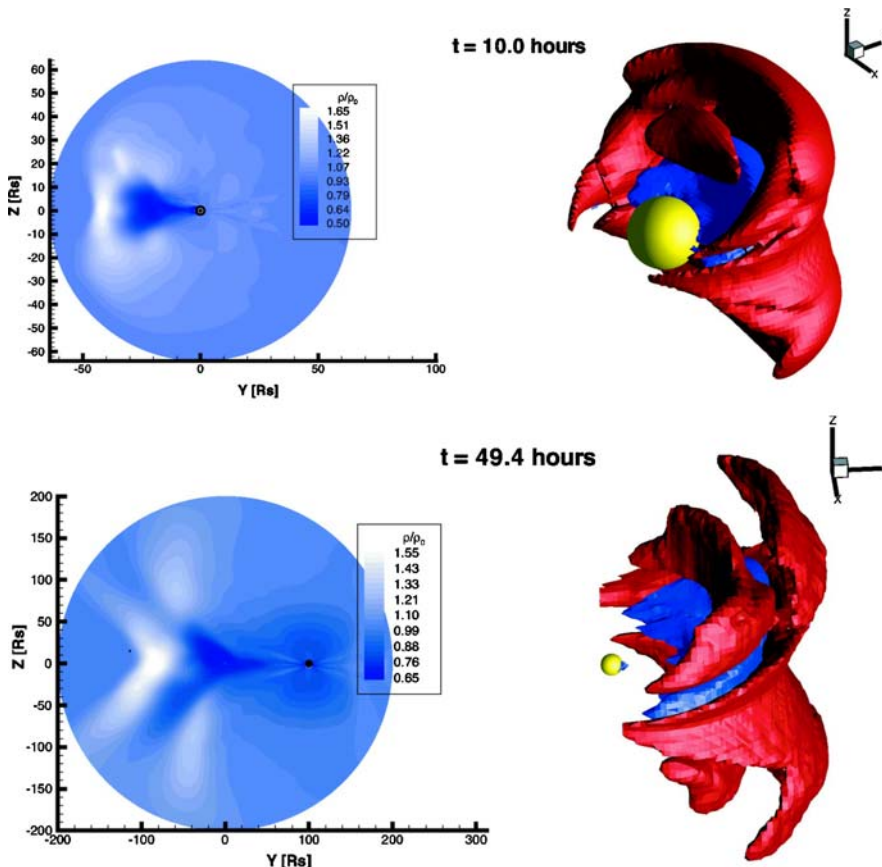


Fig. 13 **Top left:** Line-of-sight image of a CME simulated with the BATS-R-US code, 10 h after its launch, as seen from a coronagraph looking at the limb CME with a field of view of $64 R_\odot$ centered at the Sun. The black disk, corresponding to $2 R_\odot$, shows the occulting disk of the coronagraph. **Top right:** Two isosurfaces showing the density increase by 30% (red) and a density decrease of 20% (blue) over the pre-event density structure, 10 h after launch of the CME. The yellow sphere is positioned at the Sun and has a radius of $10 R_\odot$. **Bottom left:** Line-of-sight image of the CME, 49.6 h after launch, with a field-of-view of $200 R_\odot$. **Bottom right:** Similar representation as top right, at 49.6 h after launch (Lugaz *et al.*, 2005)

runs simulate the launch of a CME by loss of equilibrium of a flux rope anchored on the solar surface (Roussev *et al.*, 2003b), shock formation at a distance of $5 R_\odot$ (Roussev *et al.*, 2004), and the evolution of the CME density structure during propagation out to $100 R_\odot$, with simulations of stereoscopic views in white-light (Figure 13) as it will be seen by STEREO/HI-2 (Lugaz *et al.*, 2005).

The ENLIL code, described in the foregoing section on the solar wind (Section 3.2), is a heliospheric code developed by the NOAA Team (Odstrčil *et al.*, 2002) and covers the range from $30 R_\odot$ to 1–5 AU, using input at the lower boundary from the MAS model that extends from 1 to $30 R_\odot$. The heliospheric code is somewhat simpler than the coronal code (which requires to solve the resistive MHD equations), because the ambient solar wind is everywhere super-critical and the ideal MHD equations can be used. This heliospheric code (Odstrčil *et al.*, 1996; Toth 1996; Odstrčil and Pizzo, 1999a,b) solves the ideal MHD equations with an explicit finite-difference scheme, uses an adiabatic constant of $\gamma = 5/3$ to describe the

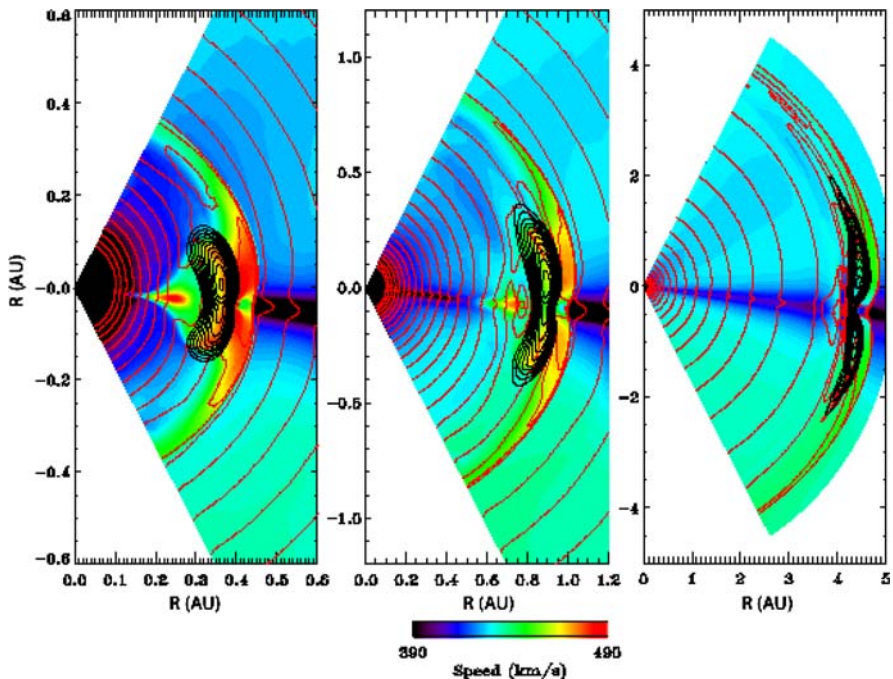


Fig. 14 Evolution of a flux rope through the inner heliosphere. The panels extend $\pm 60^\circ$ in latitude and from left to right, extend in heliospheric distance from the Sun to 0.6 AU, 1.2 AU, and 5 AU. The contours denote: radial velocity (color); density (red lines); and magnetic field (black lines) (Riley *et al.*, 2003b)

fully-ionized solar wind plasma, and produces accurate shock strengths. This code simulates the distortion of the interplanetary magnetic field by the 3D propagation of a CME in a structured solar wind (Odstrčil and Pizzo 1999a), the 3D propagation of a CME launched within (Odstrčil and Pizzo, 1999b) and adjacent to a streamer belt (Odstrčil and Pizzo, 1999c) out to 5 AU. These runs have shown that the disentangling of merged CME and CIR shocks require multi-spacecraft observations such as STEREO will provide. Simulations of the 12 May 1997 *interplanetary coronal mass ejection (ICME)* event have enabled us to predict the arrival of the shock and ejecta at Earth (Odstrčil *et al.*, 2004a). Stereoscopic white-light images simulated from these 3D MHD outputs are expected to allow for discrimination between different event scenarios (Odstrčil *et al.*, 2005).

The most comprehensive end-to-end approach of modeling CMEs has been started at the *Center for Integrated Space Weather Modeling (CISM)*, led by Boston University (Principal Investigator: W. J. Hughes). The goal is to simulate the full Sun-to-Earth system by coupling state-of-the-art codes (Luhmann *et al.*, 2004), modeling the solar corona (MAS code), the solar wind (ENLIL code), the magnetosphere, and the upper atmosphere/ionosphere. The propagation of a CME in a coupled coronal (MAS) and heliospheric (ENLIL) MHD code is described in Odstrčil *et al.* (2004b).

Figure 14 summarizes the evolution of a flux rope and its associated disturbances between the Sun and 5 AU at 3 times. The displayed speeds have been restricted to $390\text{--}490 \text{ km s}^{-1}$ to emphasize flows associated with the disturbance. Note how the ejecta become progressively more distorted with increasing heliocentric distance. By ≈ 5 AU it has been squeezed so much at low latitudes that it has evolved into two lobes, connected by a thin band of compressed

field. Surprisingly, much of this distortion can be described by kinematic effects (Riley and Crooker, 2004). More importantly, even under such idealized conditions, the flux rope develops considerable structure, suggesting that interpreting and de-convolving STEREO observations of the same ICME will be a challenge. We also note the presence of outflow associated with post-eruption reconnection underneath the flux rope, which has remained intact within the expansion wave (rarefaction region) behind the flux rope; It has a limited latitudinal extent ($\pm 15^\circ$) and trails the ejecta by $\approx 35 R_\odot$ at 1 AU (middle panel). This aspect of the simulation is discussed in more detail by Riley *et al.* (2002b).

A comparison of different techniques that fit the magnetic structure of an ICME to force-free and non-force free flux ropes was performed by Riley *et al.* (2004). Such end-to-end models of the Sun-to-Earth system are of course extremely important to provide a self-consistent context for modeling the STEREO multipoint images and multipoint in-situ SEP measurements.

5.2 Modeling the EUV Emission of CMEs

The field of view of the SECCHI/EUVI imager extends to about $1.7 R_\odot$, so EUV emission of CMEs can only be imaged in the corona during the first few minutes after their launch, while the propagation further out can be tracked in white light with SECCHI/COR (COR1: 1.1–3.0 R_\odot ; COR2: 2–15 R_\odot) and SECCHI/HI (12–318 R_\odot). The 3D reconstruction of CMEs in EUV can be approached in two different ways: either with forward-fitting using a parameterized 3D density model $n_e(x, y, z, t, T_e)$ as a function of space (x, y, z), time t , and electron temperature (T_e), or by “tomographic” inversion (e.g., using a back-projection method). The first method can be very computing-intensive if there is a large number of free parameters involved, while the second method suffers from extreme undersampling in the case of two spacecraft only (though an additional third view might be available from the SoHO/EIT telescope).

Although no efficient method has been published yet for the 3D reconstruction of CMEs from stereoscopic EUV images, we expect that some iterative forward-fitting method will be developed in near future that has a feedback between the goodness of the fit and the variation of the free model parameters. Once a geometric density model is specified for a given time t , i.e., $n_e(x, y, z, T_e)$, the EUV intensity for an optically thin spectral line of wavelength λ_{ij} (for transition from atomic energy level ε_j to a lower level ε_i) for a given line-of-sight in direction z is then

$$I(\lambda_{ij}) = A_X \int C(T_e, \lambda_{ij}, n_e) n_e n_H dz, \quad (1)$$

where $A_X = N(X)/N(H)$ is the abundance factor of element X to hydrogen H , n_e the electron density, n_H the hydrogen density, and $C(T_e, \lambda_{ij}, n_e)$ is the *contribution function*,

$$C(T_e, \lambda_{ij}, n_e) = \frac{h\nu_{ij}}{4\pi} \frac{A_{ji}}{n_e} \frac{N_j(X^{+m})}{N(X^{+m})} \frac{N(X^{+m})}{N(X)} \quad (\text{erg cm}^{-2}\text{s}^{-1}\text{ster}^{-1}), \quad (2)$$

with $N_j(X^{+m})$ the population number of the ionization state $+m$. Since the corona is fully ionized, we can use the so-called *coronal approximation* by setting the hydrogen density equal to the electron density, $n_H \approx n_e$ (neglecting the helium electrons), which demonstrates that the (optically thin) EUV emission is essentially proportional to the squared electron density, $I \propto n_e^2$, for a given electron temperature. [The electron temperature T_e determines the

ionization equilibrium, collision rates, and EUV contribution function.] For the calculation of the contribution function $C(T_e, \lambda_{ij}, n_e)$, there are now codes available in the solar community, e.g., the CHIANTI code (Dere *et al.*, 1997, 2001; Young *et al.*, 1998; Landi *et al.*, 1999; see also URL site in Table 2). The total density function at any point in a CME can then be obtained (at time t) by integrating over all temperatures, $n_e(x, y, z, t) = \int n_e(x, y, z, t, T_e) dT$. We need to derive an approximate (timedependent) density model $n_e(x, y, z, t)$ from modeling the stereoscopic EUV images, either by forward-fitting or by inversion, in order to facilitate quantitative comparisons and tests of dynamic CME models simulated with 3D MHD codes (Section 5.1).

5.3 Modeling the White-Light Emission of CMEs

The SECCHI/COR1, COR2, and HI instruments will track CMEs in white light over a range from $1.1 R_\odot$ to $328 R_\odot$ (≈ 1.5 AU), so they are the primary imagers for 3D reconstruction of propagating CMEs. 3D reconstruction and visualization of CMEs in white light is mostly led by the *Naval Research Laboratory (NRL)* and *Max Planck Institut für Sonnenforschung (MPS)* Teams. The goal is to reconstruct the 3D density distribution $n_e(x, y, z, t)$ in the solar K-corona, such as polar plumes, equatorial streamers, CMEs, and the coronal volume inbetween. Information is available in total *brightness* (B) images as well as in *polarized brightness* (pB) images. Standard tomographic methods are not suitable for only two projections. Maximum entropy and pixon methods (Puetter, 1995, 1996, 1997; Puetter and Yahil, 1999) are considered as more viable, currently investigated by the NRL Team. Current tests with a pixon code require relatively long computing times, but demonstrate successful reconstructions of simple CME geometries (e.g., cones or semi-shells).

In order to reconstruct the electron density from the image of the K-corona captured by the spacecraft, we have to integrate the *Thomson-scattered* light from all directions that are incident on the spacecraft. The scattered radiation can be separated into tangentially and radially polarized light (Billings, 1966), where the *tangential emission coefficient* I_t may be written as

$$I_t(\mathbf{r}) = \frac{\pi I_0 \sigma}{2} n_e(\mathbf{r}) \Sigma_A \quad (\text{photons s}^{-1}), \quad (3)$$

and the *radial emission coefficient* I_r may be written as

$$I_r(\mathbf{r}) = \frac{\pi I_0 \sigma}{2} n_e(\mathbf{r}) [\Sigma_B \cos^2(\chi_s) + \Sigma_C] \quad (\text{photons s}^{-1}). \quad (4)$$

I_0 is the solar intensity at disk center, R is the solar radius, r is the distance of the scattering point from Sun center, σ is the Thomson scattering cross section, χ_s is the scattering angle, and Σ_A , Σ_B , and Σ_C , are functions of r/R which account for the non-zero radius of a limb-darkened Sun (Billings, 1966; Minnaert, 1930; Milne, 1921; Neckel and Labs, 1994). The polarized (pB) and unpolarized brightness B are given by

$$pB = I_t - I_r \quad (5)$$

and

$$B = 2I_r \quad (6)$$

Recent applications of the proper treatment of Thomson-scattered emission of CMEs observed over a large range of elongations angles are given in Vourlidas and Howard (2006).

Note that there are two important differences to EUV imaging: (1) white light emission is proportional to the total density, while EUV emission is proportional to the squared density, and (2) white light sees the total density summed over all temperatures, while EUV images see only the density in the temperature range of a particular filter. Simulations of white-light images from model 3D density distributions are visualized in Lugaz *et al.* (2005) and in Pizzo and Biesecker (2004). The latter study demonstrates a robust triangulation method to obtain the centroid location, approximate shape, and velocity of CMEs, using a sequence of stereoscopic white-light images. Some new insight about the 3D configuration of CME shapes is also obtained from a recent data analysis study by Cremades and Bothmer (2004), which shows that CMEs arise in a self-similar manner from pre-existing smallscale loop systems, overlying regions of opposite magnetic polarities, which can be exploited to predict some geometric properties based on the relative orientation of the underlying neutral line in each hemisphere.

Based on the density determination of CMEs from white-light images, the total mass and velocity of a CME can be quantified during propagation, which allows to study the energetic balance between potential, kinetic, and magnetic energy, whose sum is found to be approximately conserved based on LASCO data (Vourlidas *et al.*, 2000). However, the thermal energy generated by cumulative heating during its evolution can add a comparable amount to the energy budget of CMEs (Akmal *et al.*, 2001).

A complementary method of 3D reconstruction of CMEs in white light is the method of 3D polarimetric imaging (Moran and Davila, 2004; Dere *et al.*, 2005). The underlying assumption in this method is that the polarized brightness increases for Thomson scattering with $I_p \propto \sin^2 \chi$, while the unpolarized brightness decreases with increasing $\sin^2 \chi$. This information can be used to distribute the mass $n_e(x, y, z)$ along each line-of-sight z in such a way that it matches both the polarized brightness $pB(x, y)$ and unpolarized brightness $B(x, y)$. Although this method can be used for a single white light imager (e.g., as demonstrated for SoHO/LASCO), it promises an even better constrained 3D reconstruction for two stereoscopic spacecraft, and thus will provide a very useful test for alternative reconstruction methods (such as pixon).

Further out in the heliosphere, the 3D density distribution of CMEs can be reconstructed tomographically either from polarized brightness data or from interplanetary scintillation (IPS) data (Jackson and Froehling, 1995; Jackson and Hick, 2002, 2004), as mentioned in Section 3.2 (Figure 6).

5.4 Modeling Radio Emission of CMEs

Although there is no radio imaging capability onboard the STEREO spacecraft, we emphasize that ground-based radio imaging can provide a very useful complement for 3D reconstructions of CMEs. In the CME event of 1998-Apr-20 it was demonstrated for the first time that an expanding CME can be imaged directly at (metric) radio wavelengths, based on the nonthermal synchrotron emission from electrons with energies of $\approx 0.5\text{--}5$ MeV (Bastian *et al.*, 2001). CMEs might even be imaged in radio wavelengths based on their thermal free-free emission (Gopalswamy and Kundu, 1993; Bastian and Gary, 1997), which would help to constrain their 3D density and temperature distribution. Joint radio imaging (with the Nançay radioheliograph) and SoHO/LASCO observations of a CME indicate also successive magnetic reconnection events at the CME leading edge that are responsible for multiple injections of electrons into interplanetary space (Pick *et al.*, 1998).

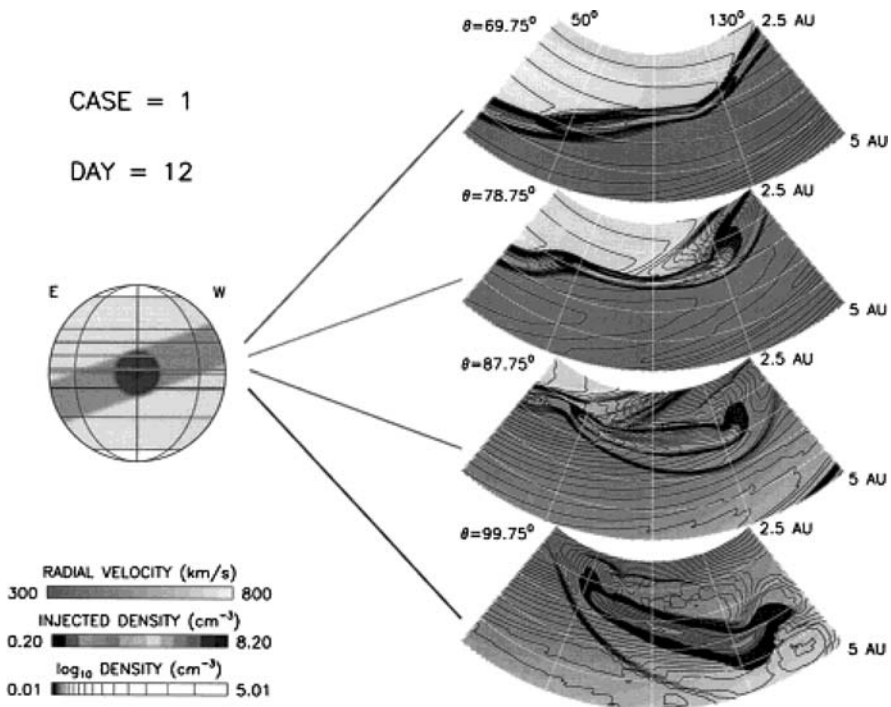


Fig. 15 Numerical MHD simulations of a CME shock wave moving through the ambient solar wind. The CME is injected in the center of the heliospheric current sheet streamer belt (left), which is tilted to the solar axis. The propagating CME is shown at slices in heliographic longitudes and at a distance of 2.5–5 AU from the Sun 12 days after launch. The slices are 4 different heliographic latitudes and show how the CME's shape, pressure and speed vary depending on the ambient solar wind conditions (Courtesy of Victor Pizzo)

6 Modeling Interplanetary Shocks

6.1 MHD Modeling of Interplanetary Shocks

CMEs have typical propagation speeds of $v \approx 300\text{--}400 \text{ km s}^{-1}$, but fast CMEs have been measured in excess of $v = 2000 \text{ km s}^{-1}$. The fast solar wind has a typical speed of $v \approx 800 \text{ km s}^{-1}$. The fast-mode speed dictates whether a fast-mode shock will form, leading to CME driven transient interplanetary shocks. Numerical simulations with HD or MHD codes (e.g., Figure 15), have been able to reproduce the observed speeds and pressure profiles of shocks and CME events out to large distances from the Sun. In such simulations, a pressure pulse is initiated in the lower corona. As the front of a fast CME overtakes the slower solar wind, a strong gradient develops and pressure waves steepen into a forward shock propagating into the ambient wind ahead, and occasionally a reverse shock propagates back through the CME towards the Sun. Numerical simulations of CMEs propagating from the corona (Mikić and Linker, 1994; Linker and Mikić, 1995; Linker *et al.*, 2001) through the heliosphere can be found in Odstrčil *et al.* (1996, 2002), Odstrčil and Pizzo (1999a, b, c), and Odstrčil *et al.* (2005). The shock strength as well as the stand-off distance between the shock front and the CME driver gas can vary considerably across the structure, depending where compression or rarefaction occurs between the slow solar wind in the streamer belt and the fast solar wind

in coronal holes (Odstrčil and Pizzo, 1999b,c). The predicted arrival time of CME shocks at 1 AU depends critically on the modeling of the background solar wind, which controls the shock propagation speed (Odstrčil *et al.*, 2005).

There are a number of complications that can occur, such as the fact that a faster CME can catch up with a slower CME and interact (Gopalswamy *et al.*, 2001). Such interactions form compound streams in the inner heliosphere.

These systems continually evolve further and merge with other CMEs and shocks as they move outward. In the outer heliosphere, beyond 5 AU, such structures form *Global Merged Interaction Regions (GMIRs)*, which become so extensive that they encircle the Sun like a distant belt. Such regions block and modulate galactic cosmic rays (i.e., the flux of high-energy particles that continuously streams into the heliosphere). Finally, a forward interplanetary shock wave that passes the Earth's magnetosphere may cause a sudden commencement of a *magnetic storm* or *substorm* at the Earth and change the electrical and magnetic connection of the interplanetary magnetic field with the Earth's magnetic field.

6.2 Detection of Interplanetary Shocks by STEREO

The kinematic 3D reconstruction of a CME leading edge with SECCHI/COR and HI will provide the true 3D velocity $\mathbf{v}(\mathbf{r})$ of the propagating CME front, while previous measurements with a single spacecraft (e.g., with SoHO/LASCO) yielded only the velocity component projected in the plane-of-sky, and thus only a lower limit. A large number of CMEs will therefore reveal a higher propagation speed than previously reported values, which may also give a systematic correction from subsonic to supersonic propagation speeds. Triangulation measurements with SECCHI will therefore be an important diagnostic of the true Mach number of interplanetary shocks.

The double-spacecraft configuration of STEREO will also provide situations where a CME shock passes one spacecraft, while the other can observe the CME shock from the side. This provides a unique opportunity to relate the in-situ measurements of shock-accelerated or shock-trapped particles at one spacecraft to the density and velocity diagnostic from the other spacecraft. Specific modeling of such situations has not been published so far, but we anticipate that such data analysis will provide insights into shock acceleration, the primary shock structure, its interactions with corotating streams, interaction regions (CIRs), secondary interplanetary shocks, and transient (solar wind) flows. Detection of radio waves from shock-associated particle beams and energetic particles (SEPs) will be discussed in more detail in the next two Sections (Sections 7, 8).

7 Modeling of Interplanetary Particle Beams and Radio Emission

7.1 Modeling for STEREO/WAVES

Interplanetary radio bursts provide a rich diagnostic on the acceleration and propagation of energetic particles and shock waves (Figure 16). Radio bursts with plasma frequencies $\lesssim 20$ MHz (above the Earth's ionospheric cutoff frequency) can be observed with ground-based radio telescopes. These radio bursts extend only out to about 1–2 solar radii, while all interplanetary radio bursts further out have lower plasma frequencies and require space-based radio detectors such as STEREO/SWAVES. Previous stereoscopic radio experiments (STEREO-1) with a single spacecraft and a ground-based instrument were able to map out the directivity pattern of type III bursts (Caroubalos and Steinberg, 1974; Caroubalos *et al.*,

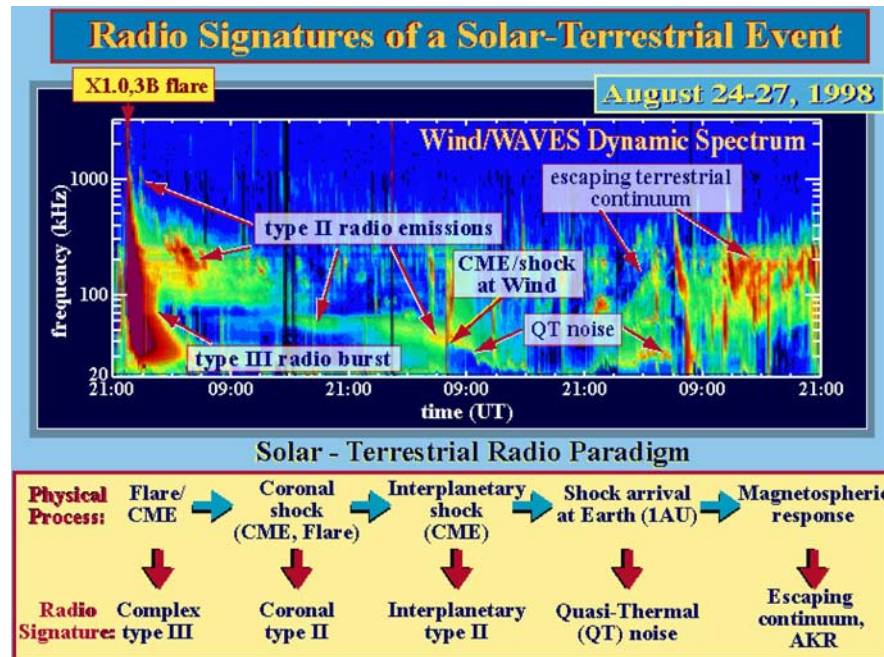


Fig. 16 Overview of physical processes and corresponding radio signatures produced by a flare/CME event. The radio dynamic spectrum is observed by the WIND spacecraft for the 1998 Aug 24–27 geoeffective event (SWAVES website)

1974; Reiner and Stone, 1986, 1988, 1989), while a combination of three spacecraft was able to resolve the 3D trajectory of type III bursts and to demonstrate harmonic emission (Gurnett *et al.*, 1978; Reiner *et al.*, 1998b; Dulk *et al.*, 1985).

The STEREO/WAVES (SWAVES) instruments will have two vantage points in space, and can also be combined with a third viewpoint from ground (at least for frequencies $\lesssim 20$ MHz). SWAVES will be able to triangulate type II and type III radio emission and can observe them remotely as well as in situ together with associated plasma waves, while IMPACT and PLASTIC instruments can detect radio-associated nonthermal particles in situ. The two-point wave measurements by the two identical SWAVES instruments (combined with the particle detections by IMPACT and PLASTIC) can map out the acceleration efficiency and conversion efficiency into radio waves at two geometrically different parts of a shock, for instance in parallel shock regions (at the CME front) and in perpendicular shock regions (in the flanks of a CME), for large stereoscopic separation angles later in the mission. Previous measurements showed that type II emission upstream of a strong CME-driven interplanetary shock is strongest in quasi-perpendicular shock regions (Bale *et al.*, 1999). The triangulation of the strongest radio type II source as a function of time will track the location of the most efficient particle acceleration and conversion into radio emission within a propagating shock front. The triangulation of multiple radio sources will reveal the detailed shock structure (e.g., foreshock regions). Furthermore, since SWAVES can triangulate the absolute position of plasma emission sources, the plasma frequency and related electron density $n_e(\mathbf{r})$ can be determined directly without using heliospheric density models. The triangulated radio source will also yield the direct radial speed $v(\mathbf{r})$ of the CME-driven shock from the Sun to 1 AU, providing real-time predictions of the shock arrival at Earth.

7.2 Particle Beams and Radio Type III Emission

Particle beams, i.e., nonthermal particles with an anisotropic velocity distribution concentrated in a direction parallel to the magnetic field, reveal flare-associated or CME-associated acceleration processes. Flares can produce interplanetary particle beams if the coronal magnetic reconnection site is connected with interplanetary space via open magnetic field lines. Alternatively, interplanetary particle beams might be generated *in situ* in interplanetary super-Alfvénic CME shock waves. So, the localization and tracking of these dual sources of interplanetary particle beams will be a fitting task for the STEREO mission.

Since the plasma in interplanetary space is nearly collisionless, suprathermal and high-energy particles can propagate through interplanetary space and form particle beams (e.g., electron beams or ion beams). The velocity dispersion causes the higher energy electrons to stream ahead of the lower energy electrons, creating a transient bump-in-tail instability. The free (kinetic) beam energy is converted into Langmuir waves via the Landau resonance, and some Langmuir wave energy is converted into radio waves at the fundamental or harmonic local plasma frequency (e.g., McLean and Labrum 1985). Thus, beam-driven type III-like radio bursts are common in interplanetary space. The spatial size of interplanetary radio bursts can be very large, since the extent of the radio source grows with distance from the Sun. A quantitative model of interplanetary type III emission, which incorporates large-angle scattering and reabsorption of fundamental emission amid ambient density fluctuations, called *stochastic growth theory*, accounts for anomalous harmonic ratios, the exponential decay constant of bursts, burst rise times, and the directivity of type III emission (Robinson and Cairns, 1998a,b,c), which is suitable for comparisons with SWAVES and IMPACT measurements.

7.3 Shock Waves and Radio Type II Emission

Classic radio diagnostics of propagating shock fronts are type II bursts, which are characteristic of plasma emission at the fundamental and harmonic plasma frequency generated in coronal and interplanetary shocks, appearing as slowly-drifting pair bands in radio dynamic spectra. Type II bursts are interpreted in terms of shock waves, either CME-driven or blast waves, that accelerate electrons and produce radio emission near the electron plasma frequency f_{pe} and near $2f_{pe}$ in the upstream region (Wild *et al.*, 1963; Nelson and Melrose, 1985; Bale *et al.*, 1999; Cairns and Kaiser, 2002; Warmuth and Mann, 2005). However, there is no one-to-one correspondence between the existence of shocks and type II bursts. Slowly-drifting type II bursts mark the passage of a shock, but not all shocks produce radio bursts. Furthermore, type II bursts do not outline the entire shock front, but occur only where a shock wave intersects preexisting structures (Stewart, 1984; Reiner and Kaiser, 1999). However, interplanetary type II bursts were all found to be associated with fast CMEs, with shock transit speeds $\gtrsim 500 \text{ km s}^{-1}$ (Cane *et al.*, 1987).

Dynamic spectra of both coronal and interplanetary type II bursts routinely show multiple emission bands that appear and disappear, have different frequencies and frequency drift rates, and time varying intensities (e.g., Reiner *et al.*, 1998a; Cane and Erickson, 2005). One goal of the two STEREO/SWAVES instruments is to remotely track type II bursts and interpret the varying frequency fine structures in terms of emission from spatially distinct regions of the shock as they move through the inhomogeneous solar wind. This inversion requires detailed theoretical modelling of type II emission. Recent MHD simulations of CME shocks show also that a single flare/CME event can generate coronal disturbances observed as two separate type II radio bursts (Odstrčil and Karlický, 2000).

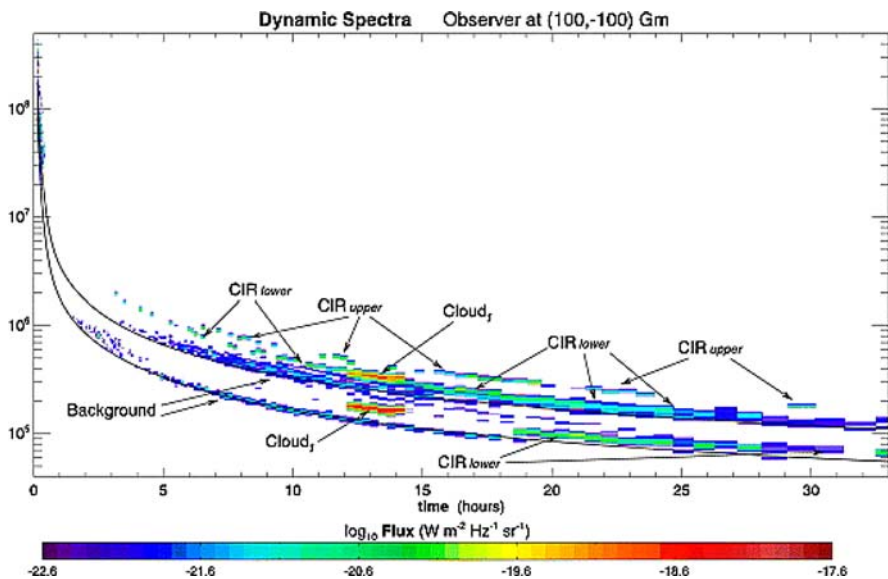


Fig. 17 Dynamic spectrum of a modeled type II burst. The two solid curves are the fundamental and harmonic frequency drift rate of the shock's leading edge. The structures responsible for various spectral features are indicated (Knock and Cairns, 2005)

A semi-quantitative theory exists for type II bursts (Knock *et al.*, 2001, 2003a,b; Knock and Cairns, 2005), which combines (i) “magnetic mirror” reflection and acceleration of upstream electrons incident on the shock, using magnetic moment conservation in the de Hoffmann-Teller frame, (ii) formation of foreshock electron beams by “time-of-flight” effects, using Liouville’s theorem, (iii) estimation of the net energy flow Langmuir waves driven by the electron beams, using quasilinear relaxation and stochastic growth theory, (iv) conversion of Langmuir energy into radiation near f_{pe} and $2f_{pe}$, using nonlinear Langmuir wave processes with known conversion efficiencies, with shock propagation through an inhomogeneous solar wind. Figure 17 shows the dynamic spectrum predicted for a shock moving through an MHD Parker-model solar wind with two corotating interaction regions (CIRs), two magnetic clouds (e.g., associated with CMEs), and random small-scale inhomogeneities in plasma quantities like density, flow speed, and vector magnetic field (Knock and Cairns, 2005). Features associated with the shock’s interactions with specific CIRs and clouds are identified (cf., Reiner and Kaiser 1999; Gopalswamy *et al.*, 2001), while the smaller time scale variations are due to the random solar wind turbulence leading to enhanced or decreased emission from localized regions of the shock. Moreover, predictions for multiple observers show considerable differences interpretable in terms of proximity and frequency-blocking effects, directly relevant to future interpretations of STEREO data. The type II burst model of Knock and Cairns (2005) reproduces a number of observed features that can be used for more detailed diagnostic of the underlying shocks. For instance, the intensity of type II bursts is strongly diminished near a peak in the heliospheric Alfvén speed profile. Other features observed in dynamic spectra of type II bursts, such as multiple-lane effects, variations in the frequency-time drift rate dv/dt , onsets and turn-offs of emission, narrowband and broadband emission, can be reproduced with this type II model by inserting local structures in the coronal or interplanetary plasma.

It is envisaged that the microscopic physics of this and other theories will be tested and improved using future IMPACT and SWAVES data, extended to include macroscopic shock and solar wind models and directivity effects, and used to interpret STEREO white light and radio data in terms of CMEs, shocks, and other interplanetary structures. For a full understanding of the link between CMEs and type II bursts, knowledge of strong interplanetary shocks, the macroscopic and microscopic structure of CME-driven shocks, the generation mechanism of radio emission, and the radiation beaming pattern are required.

8 Modeling of Solar Energetic Particles (SEPs)

Solar energetic particle (SEP) events refer to accelerated high-energy particles detected in the heliosphere. Some originate in solar flares, while others are accelerated in transient interplanetary shocks, as they are produced by fast CMEs. The acceleration mechanisms can be DC electric fields, stochastic wave-particle interactions, or shock acceleration mechanisms. Solar energetic particle events are classified into two types, *gradual* and *impulsive* SEP events, depending on their energy versus time profile. *Gradual SEP events* occur with a rate of $\approx 10/\text{year}$ during the maximum of the solar cycle, each one can last several days, and they are likely to be accelerated directly in interplanetary shocks rather than by flares in the corona. *Impulsive SEP events* occur more frequently, with a rate of $\approx 100/\text{year}$ during the maximum of the solar cycle, they last only a few hours, and they are much weaker than gradual SEP events. Since they originate along magnetic field lines connected to coronal flare sites, their acceleration could be governed by the same magnetic reconnection process that governs the associated flare. So, charged particles can be used to trace the interplanetary field topology (Kahler, 1997).

Because the ${}^3\text{He}/{}^4\text{He}$ ratio of some SEPs is much higher than in the normal solar wind, they are also called ${}^3\text{He}$ -rich events. Interplanetary particles can also be accelerated in the electric fields that are generated at corotating interaction regions (CIR) between high-speed and low-speed streams. The location where acceleration of interplanetary particles takes place can approximately be determined from the velocity dispersion (i.e., time-of-flight effects), $t_{\text{prop}} = L/v$, of particles arriving at Earth. Multi-spacecraft observations help us to map the spatial distributions of the accelerated particles that flow out into the heliosphere from the evolving CME shock or those that remain trapped behind it (Reames, 1997). Particularly advantageous opportunities are in-situ particle observations in CME fronts that are observed in *Earth-STEREO-Sun quadrature configuration* (Figure 18), i.e., when the CME is observed from the side (rather than head-on as with SoHO previously). Such quadrature observations should reveal the shock profile more clearly than at other viewing angles.

8.1 Theoretical Modeling of SEP Acceleration

The most recent theoretical modeling of SEP acceleration includes coupled hydromagnetic wave excitation and ion acceleration in an evolving coronal/interplanetary shock (Lee, 2005), the injection problem at a CME-driven shock (Zank and Li, 2004), or SEP acceleration in solar wind compression regions associated with CIRs (Giacalone *et al.*, 2002). The acceleration of solar energetic particles (SEPs) at an evolving coronal/interplanetary CME-driven shock is the most promising theory for the origin of SEPs observed in the large gradual events associated with CMEs (Lee, 2005). This calculation includes the essential features of the

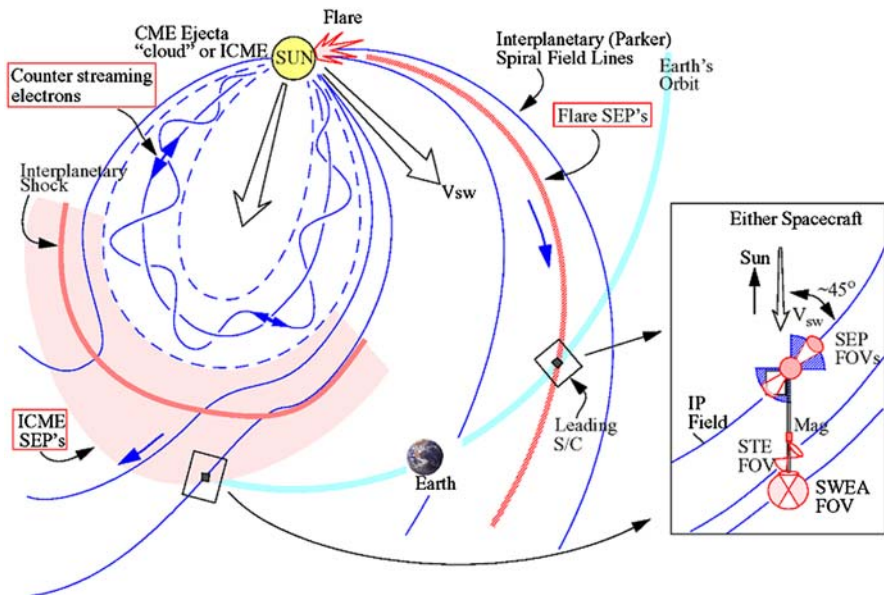


Fig. 18 Possible STEREO/IMPACT observations of SEPs at two magnetically disconnected locations in the heliosphere: STEREO-A is located on an open magnetic field line that is connected to the coronal flare region and will probe flare-accelerated particles, while STEREO-B probes SEPs in-situ in a CME-driven shock in interplanetary space at 1 AU (IMPACT website)

process: diffusive shock acceleration, proton-excited waves upstream of the shock, and escape of particles upstream of the shock by magnetic focusing. The wave spectra and particle distributions predicted are in general agreement with observations but improvement is needed including the form of the excited wave spectrum, which affects ion fractionation and the form of the high-energy cutoff, and a more general velocity distribution for the injected seed population. The seed populations for quasi-perpendicular and quasi-parallel shocks are subjects of current debates. One thought is that quasi-parallel shocks generally draw their seeds from solar-wind suprathermals, while quasi-perpendicular shocks—requiring a higher initial speed for effective injection—preferentially accelerate seed particles from flares. These different origins of seed populations can explain the observed differences in the composition of high-energy SEPs (Tylka *et al.*, 2005).

Numerical modeling of SEP acceleration is now approached by combining MHD fluid codes with kinetic codes, to obtain a self-consistent description of CME shocks and SEP acceleration. In a recent study SEP particles are accelerated in a CME-driven shock at $5 R_{\odot}$ when the shock exceeds a fast-mode Mach number of $\lesssim 4$, producing solar energetic protons with energies below 10 GeV, for which a cutoff energy of ≈ 10 GeV would be predicted by diffusive shock acceleration (Sokolov *et al.*, 2004; Roussev *et al.*, 2004).

8.2 Modeling of SEP for STEREO/IMPACT

STEREO/IMPACT will sample the 3D distributions of SEP ions and electrons, as well as the local magnetic field (Figure 18). SEP modeling with specific relevance for IMPACT is described in Ng *et al.* (1999, 2003). This line of SEP modeling focuses separately on SEP

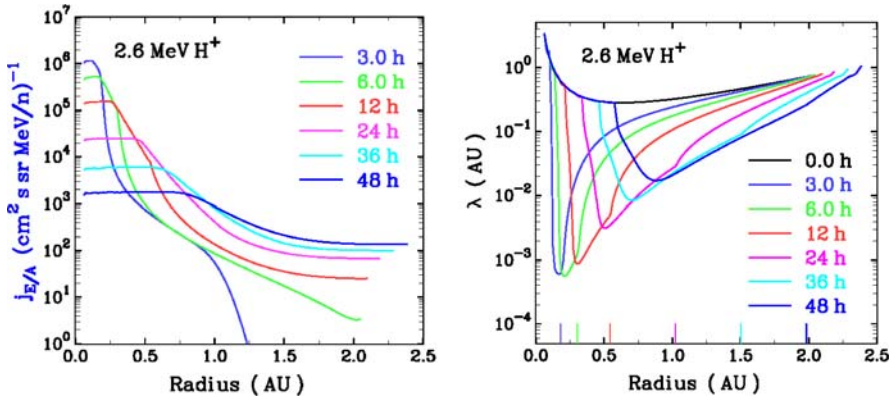


Fig. 19 Coupled evolution of 2.6 MeV proton intensity (left) and mean free path (right) versus radius (Ng *et al.*, 2003)

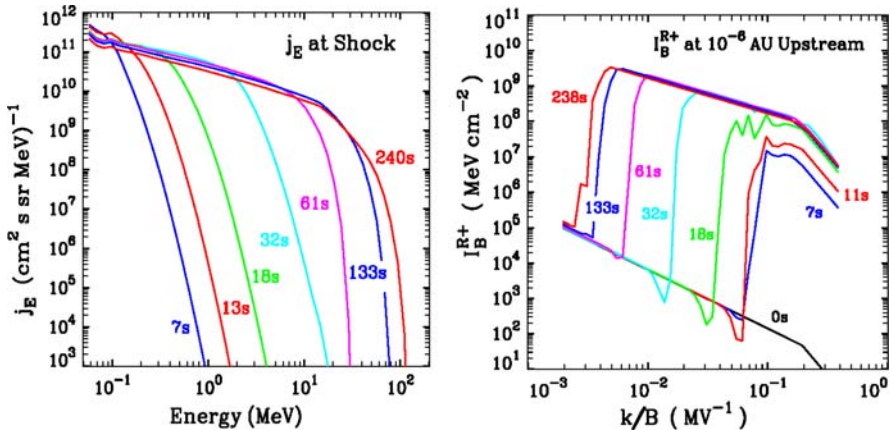


Fig. 20 Proton acceleration (left) and Alfvén wave growth (right) upstream of a moving shock at ~ 3.7 solar radii (Courtesy of Chee Ng and Don Reames)

transport over several AU and their extension to fast acceleration by a coronal shock on fine time and spatial scales. Both efforts study the coupled nonlinear evolution of SEPs and Alfvén waves in inhomogeneous plasma and magnetic field, featuring self-consistent quasilinear wave-particle interaction with full pitch-angle dependence. Both models include focusing, convection, adiabatic deceleration, and scattering (by Alfvén waves) for SEPs, and wave transport and amplification (by SEPs) for the Alfvén waves. The acceleration model treats, in addition, first-order Fermi acceleration and wave transmission/reflection at the shock. The results reveal that, contrary to common assumption, wave amplification strongly impacts SEP acceleration and transport. This transport model predicts the self-throttling of proton transport through wave excitation (Ng *et al.*, 2003), as shown by the evolution of the radial profiles of SEP intensity j_E and mean free path λ (Figure 19). Wave growth also explains the observed complex time variations of SEP elemental abundances (Tylka *et al.*, 1999). The shock acceleration model predicts proton intensity and Alfvén wave spectra evolving in tandem upstream of a 1800 km/s shock traveling from 3.7 to 4.3 solar radii (Figure 20).

Acceleration of 1 MeV (70 MeV) protons “ignites” at 18 s (130 s), when wave growth drives the respective λ down from 0.5 AU (1 AU) to below 10^{-4} AU. Future work will attempt to integrate the shock acceleration and interplanetary transport models and to generalize it so that it can accept arbitrary input of plasma and shock parameters from other CME and shock models.

Attempts are being made to add SEPs to the Sun-to-Earth end-to-end MHD models at CCMC, CISIM, and University of Michigan, which simulate SEP acceleration in realistic CME environments (e.g., Roussev *et al.*, 2004). The STEREO multipoint measurements and multiple viewpoints of the SEP sources will be combined with the models to answer outstanding questions like the relative contribution of flare versus IP shock-generated SEPs in major events. Both the Michigan group and the CISIM group are attempting these end-to-end system models, and CCMC has the role of a model component provider to STEREO and the larger community.

9 Modeling of Geoeffective Events and Space Weather

A key requirement in evaluating geoeffective events and space weather is the determination of CME trajectories towards Earth, with the goal to establish magnetic connectivity and to predict the timing and impact of CME-induced geomagnetic disturbances. While previous single-spacecraft observations (e.g., with SoHO/LASCO) have difficulty in reconstructing the directionality of CMEs, in particular for *frontside halo CMEs*, the dual vantage point of the two STEREO spacecraft will provide less ambiguous directionality measurements and better arrival forecasts (in real time) from the true 3D vector $\mathbf{r}(t)$ and velocity $\mathbf{v}(t)$ reconstructions by the SECCHI/HI imagers. Once the Sun-Earth connectivity of the CME path is established, we further want to know whether the CME hits the Earth directly, grazes it, or misses it, what the longitudinal extent and cross-section of a CME is, and what the southward magnetic field component B_z is (which determines the geoeffectiveness).

Current modeling efforts of space weather are coordinated by Dave Webb (see chapter on Space Weather and Beacon mode) and by Jim Klimchuk at NRL. MHD Modeling for the ESA Space Weather Initiative is coordinated by David Berghmans. An effort to model the geoeffectiveness of CMEs is planned by the 3D reconstruction group led by Volker Bothmer. Modeling of the magnetic field that connects the subphotospheric domain with the coronal magnetic field during CME initiation is also addressed by the *Solar Multidisciplinary University Research Initiative (SOLAR/MURI)* at the *University of California, Berkeley (UCB)*. Particular efforts to model space weather by end-to-end simulations of CMEs and SEPs are ongoing at the *Center for Integrated Space Weather Modeling (CISM)* at the *University of California at Berkeley (UCB)*, and at the *Center for Space Environment Modeling (CSEM)* at the University of Michigan, which we partly described in Section 3.2 on heliospheric solar wind models. Their *Space Weather Modeling Framework (SWMF)* aims to come up with a self-consistent framework of models that starts from the CME initiation in the solar corona, follows the CME propagation and SEP acceleration through interplanetary space, and predicts the consequences in the Earth’s magnetosphere. Part of their space weather modeling includes also predictions of fluxes and arrival times of high-energy protons at spacecraft locations, which produce a real radiation hazards for manned and unmanned spacecraft. More information of the activities of various groups that perform space weather modeling relevant for the STEREO mission can also be found from the URLs given in Table 2.

Table 2 Acronyms and URLs of webpages relevant to modeling of STEREO data

Acronym	Full Name \leftrightarrow Website URL
CACTUS	Computer Aided CME Tracking \leftrightarrow http://sidc.oma.be/cactus/
CCMC	The Community Coordinated Modeling Center \leftrightarrow http://ccmc.gsfc.nasa.gov/
CHIANTI	Atomic Database for Spectroscopic Diagnostics of Astrophysical Plasmas \leftrightarrow http://wwwsolar.nrl.navy.mil/chianti.html/
CISM	Center for Integrated Space Weather Modeling \leftrightarrow http://www.bu.edu/cism/
CSEM	Center for Space Environment Modeling \leftrightarrow http://csem.engin.umich.edu/
IMPACT	In-situ Measurements of Particles and CME Transients \leftrightarrow http://sprg.ssl.berkeley.edu/impact/
PLASTIC	PLastic And Supra Thermal Ion Composition investigation \leftrightarrow http://stereo.sr.unh.edu/
SECCHI	Sun Earth Connection Coronal and Heliospheric Investigation \leftrightarrow http://stereo.nrl.navy.mil/
SECCHI/MPS	The SECCHI website at Max Planck Institut für Sonnenforschung \leftrightarrow http://star.mppae.gwdg.de/secchi/
SMEI/UCSD	Solar Mass Ejection Imager, University California San Diego \leftrightarrow http://cassfoss02.ucsd.edu/solar/
SOHO	SOlar and Heliospheric Observatory \leftrightarrow http://sohowww.nascom.nasa.gov/
SOLAR-B	SOLAR-B mission website \leftrightarrow http://www.nasa.gov/mission-pages/solar-b/
SOLAR/MURI	Solar Multidisciplinary University Research Initiative at UCB \leftrightarrow http://solarmuri.ssl.berkeley.edu/
STEREO	The Solar TErrestrial RElations Observatory (STEREO) \leftrightarrow http://stereo.gsfc.nasa.gov/
STEREO/SW	The STEREO Space Weather Group \leftrightarrow http://stereo.nrl.navy.mil/swx/swindex.html
SWAVES	The STEREO Waves Instrument \leftrightarrow http://www-lep.gsfc.nasa.gov/swaves/swaves.html
TRACE	Transition Region And Coronal Explorer \leftrightarrow http://sunland.gsfc.nasa.gov/smex/trace/

10 Conclusive Remarks

In this review we described some theoretical tools that already exist or are being prepared by groups that are committed to the STEREO mission and space weather effort in general, which mostly includes models that try to reproduce transient events in the solar wind and the evolution of coronal mass ejections, but it should not be considered as a complete and exhaustive compilation of relevant theoretical models. There exist a number of alternative solar wind models that explore the physical processes driving the solar wind that are not covered here. Since new observations always challenge existing theories and require new approaches of data modeling we hope that the STEREO mission, once it is launched and produces science data, will stimulate the development of new models and discriminatory tests by data fitting in the future. The anticipated STEREO data base will be an extremely rich database and enable us to model the heliospheric magnetic field and

propagation of CMEs in unprecedented detail, constrained by true 3D information from stereoscopic vantage points, yielding the 3D kinematics of MHD processes as well as kinetic processes associated with the solar wind, CMEs, and particles accelerated in interplanetary shocks. Since the STEREO mission is our first extensive multi-spacecraft 3D exploration of our heliosphere, its importance might be compared with the first determination of the true 3D geometry of our Earth globe by Thales of Milet and Pythagoras around 600 BC.

Acknowledgements We gratefully acknowledge the useful and complementary comments of the two anonymous referees, which helped to improve the readability and accuracy of this paper. Part of the work was supported by NASA contract N00173-01-C-6001 and N00173-02-C-2035 to NRL (SECCHI project).

References

- A. Akmal, J.C. Raymond, A. Vourlidas, B. Thompson, A. Ciaravella, Y. Ko, *et al.*, ApJ **553**, 922 (2001)
- D. Alexander, G.A. Gary, B.J. Thompson, in *Three-Dimensional Structure of Solar Active Regions*, ed. by C. Alissandrakis, B. Schmieder, Proc. 2nd Advances in Solar Physics Euroconference, vol. 155 (Astronomical Society of the Pacific (ASP), San Francisco, ASP Conference Series, 1998), p. 100
- M.D. Altschuler, G. Newkirk Jr., Solar Phys. **9**, 131 (1969)
- M.D. Altschuler, R.H. Levine, M. Stix, J. Harvey, Solar Phys. **51**, 345 (1977)
- M.D. Altschuler, in *Image Reconstruction from Projections*, ed. by G.T. Herman (Springer, Berlin, 1979), p. 105
- S.K. Antiochos, C.R. DeVore, J.A. Klimchuk, ApJ **5**(10), 485 (1999)
- C.N. Arge, V.J. Pizzo, JGR **105/A5**, 10, 465 (2000)
- M.J. Aschwanden, T.S. Bastian, ApJ **426**, 425 (1994a)
- M.J. Aschwanden, T.S. Bastian, ApJ **426**, 434 (1994b)
- M.J. Aschwanden, J. Lim, D.K. Gary, J.A. Klimchuk, ApJ **454**, 512 (1995)
- M.J. Aschwanden, Lecture Notes in Phys. **444**, 13 (1995)
- M.J. Aschwanden, J.S. Newmark, J.P. Delaboudiniere, W.M. Neupert, J.A. Klimchuk, G.A. Gary, *et al.*, ApJ **515**, 842 (1999)
- M.J. Aschwanden, D. Alexander, N. Hurlburt, J.S. Newmark, W.M. Neupert, J.A. Klimchuk, *et al.*, ApJ **531**, 1129 (2000)
- M.J. Aschwanden, *Physics of the Solar Corona – An Introduction* (Praxis Publishing Ltd., Chichester, UK, and Springer, New York, 2004, ISBN 3-540-22321-5), p. 842
- M.J. Aschwanden, D. Alexander, M. DeRosa, in *Solar and Space Weather Radiophysics*, ed. by D.E. Gary, C.O. Keller. Astrophysics and Space Science Library, vol. 314 (Kluwer Academic Publishers, Dordrecht, The Netherlands, 2004), p. 243
- M.J. Aschwanden, Solar Phys. **228**, 341 (2005)
- S.D. Bale, M.J. Reiner, J.-L. Bougeret, M.L. Kaiser, S. Krucker, D.E. Larson, *et al.*, GRL **26/11**, 1573 (1999)
- A. Balogh, R.G. Marsden, E.J. Smith (eds.), *The Heliosphere Near Solar Minimum – The Ulysses Perspective* (Springer-Praxis Books in Astrophysics and Astronomy, Praxis, Chichester, UK, and Springer, New York, 2001)
- T.S. Bastian, D.E. Gary, JGR **102/A7**, 14,031 (1997)
- T.S. Bastian, M. Pick, A. Kerdraon, D. Maia, A. Vourlidas, ApJ **558**, L65 (2001)
- D.A. Batchelor, Solar Phys. **155**, 57 (1994)
- R. Berton, T. Sakurai, Solar Phys. **96**, 93 (1985)
- D.E. Billings, *A Guide to the Solar Corona* (Academic Press, New York, 1966)
- V. Bothmer, R. Schwenn, Ann. Geophysicae **16**, 1 (1998)
- V. Bothmer, Sources of Magnetic Helicity Over the Solar Cycle, Proc. ISCS 2003 Symposium *Solar Variability as an Input to the Earth's Environment* (Tatranska Lomnica, Slovakia, 23–28 June 2003), ESA SP-535, p. 419
- I.H. Cairns, M.L. Kaiser, in *The Review of Radio Science 1999–2002*, ed. by W.R. Stone (IEEE Press, 2002), p. 749
- H.V. Cane, N.R. Sheeley Jr., R.A. Howard, JGR **92**, 9869 (1987)
- H.V. Cane, W.C. Erickson, ApJ **623**, 1180 (2005)
- C. Caroubalos, J.-L. Steinberg, A&A **32**, 245 (1974)

- C. Caroubalos, M. Poquerusse, J.-L. Steinberg, A&A **32**, 255 (1974)
- J. Chen, R.A. Howard, G.E. Brueckner, R. Santoro, J. Krall, S.E. Paswaters, *et al.*, ApJ **409**, L191 (1997)
- J. Chen, R.A. Santoro, J. Krall, R.A. Howard, R. Duffin, J.D. Moses, *et al.*, ApJ **533**, 481 (2000)
- P.F. Chen, S.T. Wu, K. Shibata, C. Fang, ApJ **572**, L99 (2002)
- A. Ciaravella, J.C. Raymond, B.J. Thompson, A. Van Ballegooijen, L. Strachan, L. Gardner, *et al.*, ApJ **529**, 575 (2001)
- S.R. Cranmer, Space Sci. Rev. **101/3**, 229 (2002)
- H. Cremades, V. Bothmer, A&A **422**, 307 (2004)
- J.M. Davila, ApJ **423**, 871 (1994)
- J.M. Davila, D.M. Rust, V.J. Pizzo, C. Paulett, in *Solar Terrestrial Relations Observatory (STEREO)*, ed. by D. M. Rust. SPIE Proc. Missions to the Sun, vol. 2804 (SPIE, 1996), p. 34
- J.M. Davila, O. St. Cyr, *Science Prospects for the STEREO Mission*, in *Proc. 34th COSPAR Scientific Assembly, The Second World Space Congress* (Houston, Texas, Oct 10–19, 2002), p. 478
- K.P. Dere, E. Landi, H.E. Mason, B.C. Monsignori-Fossi, P.R. Young, A&A **125**, 149 (1997)
- K.P. Dere, E. Landi, P.R. Young, G. Del Zanna, ApJS **134**, 331 (2001)
- K.P. Dere, G.E. Brueckner, R.A. Howard, D.J. Michels, J.P. Delaboudiniere, ApJ **516**, 465 (1999)
- G.A. Dulc, J.L. Steinberg, A. Lecacheux, S. Hoang, R.J. MacDowall, A&A **150**, L28 (1985)
- T.G. Forbes, JGR **105/A10**, 23,153 (2000)
- C. Foullon, in *Proc. ISCS Symposium on Solar Variability ans an Input to the Earth's Environment*, vol. 535, ed. by A. Wilson (ESA, ESTEC Noordwijk, The Netherlands, ESA-SP, 2003), p. 477
- R.A. Frazin, ApJ **530**, 1026 (2000)
- R.A. Frazin, P. Janzen, ApJ **570**, 408 (2002)
- R.A. Frazin, F. Kamalabadi, M.A. Weber, ApJ **628**, 1070 (2005)
- R.A. Frazin, F. Kamalabadi, ApJ **628**, 1061 (2005)
- A. Gary, Solar Phys. **174**, 241 (1997)
- A. Gary, J.M. Davis, R. Moore, Solar Phys. **183**, 45 (1998)
- A. Gary, D. Alexander, Solar Phys. **186**, 123 (1999)
- A. Gary, R.L. Moore, ApJ **611**, 545 (2004)
- J. Giacalone, J.R. Jokipii, J. Kóta, ApJ **573**, 845 (2002)
- S.E. Gibson, B.C. Low, ApJ **493**, 460 (1998)
- S.E. Gibson, B.C. Low, JGR **105/A8**, 18,187 (2000)
- N. Gopalswamy, M.R. Kundu, Solar Phys. **143**, 327 (1993)
- N. Gopalswamy, S. Yashiro, M.L. Kaiser, R.A. Howard, and J.-L.H. Bougeret, ApJ **548**, L91 (2001)
- V.M. Grigoryev, Solar Phys. **148**, 389 (1993)
- C.P.T. Groth, D.L. DeZeeuw, T.I. Gombosi, K.G. Powell, JGR **105**, 25,053 (2000)
- B.V. Gudiksen, A. Nordlund, ApJ **572**, L113 (2002)
- B.V. Gudiksen, A. Nordlund, ApJ **618**, 1020 (2005a)
- B.V. Gudiksen, A. Nordlund, ApJ **618**, 1031 (2005b)
- D.A. Gurnett, M.M. Baumback, H. Rosenbauer, JGR **83**, 616 (1978)
- J.R. Hall, P. Sheth, E. DeJong, J. Lorre, P. Liewer, *3D Sun Loop Tracer: A Tool for Stereoscopy of Coronal Loops for NASA's STEREO Mission* (American Geophysical Union, Fall Meeting 2004, abstract #SH21B, 2004)
- R.A. Howard, J.D. Moses, D.G. Socker, The SECCHI Consortium, Adv. Space Res. **29**, 2017 (2002)
- J.T. Hoeksema, Structure and evolution of the large scale solar and heliospheric magnetic fields, PhD Thesis (Stanford University, California, 1984)
- H.S. Hudson, J.R. Lemen, O.C. St.Cyr, A.C. Sterling, D.F. Webb, GRL **25**, 2481 (1998)
- N.E. Hurlburt, P.C.H. Martens, G.L. Slater, S.M. Jaffey, in *Solar Active Region Evolution: Comparing Models with Observations*, ed. by K.S. Balasubramaniam, G.W. Simon, 14th Internat. Summer NSO Workshop, vol. 68 (Astronomical Society of the Pacific (ASP), San Francisco, ASP Conference Series, 1994), p. 30
- N.E. Hurlburt, D. Alexander, A.M. Rucklidge, ApJ **577**, 993 (2002)
- S.S. Ipson, V.V. Zharkova, S. Zharkov, A.K. Benkhailil, J. Abourdarham, N. Fuller, Solar Phys. **228**, 399 (2005)
- B.V. Jackson, H.R. Froehling, A&A **299**, 885 (1995)
- B.V. Jackson, P.P. Hick, Solar Phys. **211**, 345 (2002)
- B.V. Jackson, P.P. Hick, in *Solar and Space Weather Radiophysics*, ed. by D.E. Gary, C.O. Keller, Astrophysics and Space Science Library, vol. 314 (Kluwer Academic Publishers, Dordrecht, The Netherlands, 2004), p. 355
- S.W. Kahler, in *Coronal Mass Ejections*, ed. by N. Crooker, J. Joselyn, J. Feynman, Proc. Chapman Conference, Geophysical Monograph Series, vol. 99 (American Geophysical Union (AGU), Washington, DC, 1997), p. 197
- R. Kano, S. Tsuneta, ApJ **454**, 934 (1995)

- B. Kliem, V.S. Titov, T. Török, A&A **413**, L23 (2004)
- J.A. Klimchuk, in *Space Weather*, ed. by P. Song, H.J. Singer, G.L. Siscoe, American Geophysical Union, Geophysical Monograph Series, vol. 125, Proc. Chapman Conference on Space Weather, Clearwater, Florida, 2000 Mar 20–24 (AGU, Washington DC, 2001), p. 143
- S.A. Knock, I.H. Cairns, P.A. Robinson, Z. Kuncic, JGR **106/A11**, 25,041 (2001)
- S.A. Knock, I.H. Cairns, P.A. Robinson, JGR **108/A10**, SSH 2-1 CiteID 1361, DOI 10.1029/2003JA009960 (2003a)
- S.A. Knock, I.H. Cairns, P.A. Robinson, Z. Kuncic, JGR **108/A3**, SSH 6-1 CiteID 1126, DOI 10.1029/2002JA009508 (2003b)
- S.A. Knock, I.H. Cairns, JGR **110/A1** (2005), CiteID A01101, DOI 10.1029/2004JA010452
- M. Kojima, K.-I. Fujiki, M. Hirano, M. Tokumaru, T. Ohmi, K. Hakamada, in *The Sun and the Heliosphere as an Integrated System*, ed. by P. Poletto, S.T. Suess, Astrophysics and Space Science Library, vol. 317 (Kluwer Academic Publishers, Dordrecht, The Netherlands, 2004), p. 147
- S. Koutchmy, M.M. Molodensky, Nature **360**, 717 (1992)
- H. Lamy, V. Pierrard, M. Maksimovic, J.F. Lemaire, JGR **108**, 1047, pp. SSH 13-1 (2003), CiteID 1047, DOI 10.1029/2002JA009487
- P.L. Lamy, E. Quemerais, A. Llebaria, M. Bout, R. Howard, R. Schwenn, *et al.*, ESA-SP **404**, 491 (1997)
- E. Landi, M. Landini, K.P. Dere, P.R. Young, H.E. Mason, A&AS **135**, 339 (1999)
- J.K. Lee, T.S. Newman, G.A. Gary, *Oriented Connectivity-Based Method for Segmenting Solar Loops*, Proc. 17th Internat Conf., Pattern Recognition, vol. 4 (Journal, Elsevier, 2005), p. 315
- M.A. Lee, ApJS **158**, 38 (2005)
- P.C. Liewer, J.M. Davis, E.M. DeJong, G.A. Gary, J.A. Klimchuk, R.P. Reinert, SPIE **3442**, 53 (1998)
- P.C. Liewer, E.M. DeJong, J.R. Hall, J. Lorre, EOS **81/48** (November 28, 2000 issue), p. F971
- P.C. Liewer, J.R. Hall, M. DeJong, D.G. Socker, R.A. Howard, P.C. Crane, *et al.*, JGR **106/A8**, 15,903 (2001)
- J. Lin, T.G. Forbes, JGR **105/A2**, 2375 (2000)
- J. Lin, A.A. van Ballegooijen, ApJ **629**, 582 (2005)
- J.A. Linker, G. VanHoven, D.D. Schnack, GRL **17/12**, 2282 (1990)
- J.A. Linker, Z. Mikić, ApJ **438**, L45 (1995)
- J.A. Linker, Z. Mikić, D.A. Biesecker, R.J. Forsyth, S.E. Gibson, D. Biesecker, *et al.*, JGR **104/A5**, 9809 (1999)
- J.A. Linker, R. Lionello, Z. Mikić, T. Amari, JGR **106/A11**, 25,165 (2001)
- R. Lionello, M. Velli, G. Einaudi, Z. Mikić, ApJ **494**, 840 (1998)
- A. Llebaria, P.L. Lamy, S. Koutchmy, ESA-SP **446**, 441 (1999)
- R.E. Loughhead, J.L. Wang, G. Blows, ApJ **274**, 883 (1983)
- B.C. Low, Solar Phys. **167**, 217 (1996)
- N. Lugaz, W.B. Manchester IV, T.I. Gombosi, ApJ **627**, 1019 (2005)
- J.G. Luhmann, S.C. Solomon, J.A. Linker, J.G. Lyon, Z. Mikić, D. Odstrčil, *et al.*, J. Atmos. Solar-Terr. Phys. **66/15–16**, 1243 (2004)
- D.J. McLean, N.R. Labrum (eds.), *Solar Radiophysics* (Cambridge University Press, Cambridge, 1985)
- W. Manchester IV, JGR **108/A4**, 1162, SSH 10-1 (2003), DOI 10.1029/2002JA009252
- W. Manchester IV, T.I. Gombosi, I. Roussev, D.L. DeZeeuw, I.V. Sokolov, K.G. Powell, *et al.*, JGR **109/A1**, A01102 (2004a)
- W. Manchester IV, T. Gombosi, D. DeZeeuw, Y. Fan, ApJ **610**, 588 (2004b)
- Z. Mikić, J.A. Linker, ApJ **430**, 898 (1994)
- Z. Mikić, J.A. Linker, D.D. Schnack, R. Lionello, A. Tarditi, Phys. Plasmas **6/No.5**, 2217 (1999)
- E.A. Milne, MNRAS **81**, 361 (1921)
- M. Minnaert, Zeitschrift für Astrophysik **1**, 209 (1930)
- Y. Mok, Z. Mikić, R. Lionello, J.A. Linker, ApJ **621**, 1098 (2005)
- T.G. Moran, J.M. Davila, Science **305**, 66 (2004)
- J.T. Mueller, H. Maldonado, A.S. Driesman, Acta Astronautica **53**, 729 (2003)
- N. Neckel, D. Labs, Solar Phys. **153**, 91 (1994)
- G.J. Nelson, D.B. Melrose, in *Solar Radiophysics*, ed. by D.J. McLean, N.R. Labrum (Cambridge University Press, Cambridge, 1985), p. 333
- C.K. Ng, D.V. Reames, A.J. Tylka, GRL **26**, 2145 (1999)
- C.K. Ng, D.V. Reames, A.J. Tylka, ApJ **591**, 461 (2003)
- M. Neugebauer, in *The Heliosphere Near Solar Minimum – The Ulysses Perspective*, ed. by A. Balogh, R.G. Marsden, E.J. Smith (Springer-Praxis Books in Astrophysics and Astronomy, 2001), p. 43
- D. Odstrčil, JGR **99/A9**, 17,653 (1994)
- D. Odstrčil, M. Dryer, Z. Smith, JGR **101**, 19,973 (1996)
- D. Odstrčil, V.J. Pizzo, JGR **104/A12**, 28,225 (1999a)

- D. Odstrčil, V.J. Pizzo, JGR **104/A1**, 483 (1999b)
 D. Odstrčil, V.J. Pizzo, JGR **104/A1**, 493 (1999c)
 D. Odstrčil, M. Karlický, A&A **359**, 766 (2000)
 D. Odstrčil, J.A. Linker, R. Lionello, Z. Mikić, P. Riley, V.J. Pizzo, *et al.*, JGR **107/A12**, SSH 14-1 (2002), CiteID 1493, DOI 10.1029/2002JA009334
 D. Odstrčil, Adv. Space Res. **32/4**, 497 (2003)
 D. Odstrčil, P. Riley, X.P. Zhao, JGR, **109/A2** (2004a), CiteID A02116, DOI 10.1029/2003JA010135
 D. Odstrčil, V.J. Pizzo, J.A. Linker, P. Riley, R. Lionello, Z. Mikić, J. Atmos. Solar-Terr. Phys. **66**, 1311 (2004b)
 D. Odstrčil, V.J. Pizzo, C.N. Arge, JGR (Space Phys.) **110**, 2106 (2005), CiteID A02106, DOI 10.1029/2004JA010745
 M. Pick, D. Maia, A. Kerdraon, R.A. Howard, G.E. Brueckner, D.J. Michels, *et al.*, Solar. Phys. **181**, 455 (1998)
 V.J. Pizzo (ed.), *The Findings of the SPINS Science Workshop*, SEL Workshop Report January 1994, *SPINS: Special Perspectives Investigations*, NOAA/SEL, Boulder, Colorado, on November 3–5, (1993)
 V.J. Pizzo, D.A. Biesecker, GRL **31**, 21,802 (2004)
 O.V. Podladchikova, D. Berghmans, Solar Phys. **228**, 265 (2005)
 F. Portier-Fozzani, B. Inhester, Space Sci. Rev. **97**, (1/4), 51 (2001)
 F. Portier-Fozzani, B. Inhester, in *Magnetic Coupling of the Solar Atmosphere*, Proc. Euroconference and IAU Colloquium 188, vol. 505 (ESA, ESTEC Noordwijk, The Netherlands, ESA-SP, 2002), p. 545
 K.G. Powell, P.L. Roe, T.J. Linde, T.I. Gombosi, D.L. deZeeuw, J. Comp. Phys. **154**, 284 (1999)
 R.C. Puetter, Int. J. Image Sys. Tech. **6**, 314 (1995)
 R.C. Puetter, SPIE **2827**, 12 (1996)
 R.C. Puetter, in *Instrumentation for Large Telescopes*, ed. by J.M. Rodriguez Espinosa, A. Herrero, F. Sanchez (Cambridge University Press, New York, 1997), p. 75
 R.C. Puetter, A. Yahil, in *Astronomical Data Analysis Software and Systems VIII*, ASP Conference Series, vol. 172, ed. by D.M. Mehringer, R.L. Plante, D.A. Roberts (1999), p. 307
 E. Qué merais, P. Lamy, A&A **393** 295 (2002)
 D.V. Reames, in *Coronal Mass Ejections*, ed. by N. Crooker, J. Joselyn, J. Feynman, Proc. Chapman Conference, Geophysical Monograph Series, vol. 99 (American Geophysical Union (AGU), Washington, DC, 1997), p. 217
 M.J. Reiner, R.G. Stone, Solar Phys. **100**, 397 (1986)
 M.J. Reiner, R.G. Stone, A&A **206**, 316 (1988)
 M.J. Reiner, R.G. Stone, A&A **217**, 251 (1989)
 M.J. Reiner, M.L. Kaiser, J. Fainberg, J.-L. Bougeret, R.G. Stone, GRL **25/14**, 2493 (1998a)
 M.J. Reiner, J. Fainberg, M.L. Kaiser, R.G. Stone, JGR **103**, 1923 (1998b)
 M.J. Reiner, M.L. Kaiser, JGR **104/A8**, 16,979 (1999)
 P. Riley, J.A. Linker, Z. Mikić, JGR **106/A8**, 15,889 (2001a)
 P. Riley, J.A. Linker, Z. Mikić, R. Lionello, in *Space Weather*, Geophysical Monograph Series, vol. 125, ed. by P. Song, H.J. Singer, G.L. Siscoe (2001b), p. 159
 P. Riley, J.A. Linker, Z. Mikić, JGR **107/A7** (2002a), DOI 10.1029/2001JA000299
 P. Riley, J.A. Linker, Z. Mikić, D. Odstrčil, V.J. Pizzo, D.F. Webb, ApJ **578**, 972 (2002b)
 P. Riley, Z. Mikić, J.A. Linker, Ann. Geophys. J. **21**, 1347 (2003a)
 P. Riley, J.A. Linker, Z. Mikić, D. Odstrčil, T.H. Zurbuchen, D. Lario, *et al.*, JGR **108/A7**, SSH 2-1 (2003b), CiteID 1272, DOI 10.1029/2002JA009760
 P. Riley, J.A. Linker, R. Lionello, Z. Mikić, D. Odstrčil, M.A. Hidalgo, Q. Hu, R.P. Lepping, B.J. Lynch, A. Rees, J. Atmos. Solar-Terr. Phys. **66**, 1321 (2004)
 P. Riley, N.U. Crooker, ApJ **600**, 1035 (2004)
 P.A. Robinson, I.H. Cairns, Solar Phys. **181**, 363 (1998a)
 P.A. Robinson, I.H. Cairns, Solar Phys. **181**, 395 (1998b)
 P.A. Robinson, I.H. Cairns, Solar Phys. **181**, 429 (1998c)
 E. Robbrecht, D. Berghmans, A&A **425**, 1097 (2004)
 R. Rosner, W.H. Tucker, G.S. Vaiana, ApJ **220**, 643 (1978)
 I.I. Roussev, T.I. Gombosi, I.V. Sokolov, M. Velli, W. Manchester, D.L. DeZeeuw, *et al.*, ApJ **595**, L57 (2003a)
 I.I. Roussev, T.G. Forbes, T.I. Gombosi, I.V. Sokolov, D.L. DeZeeuw, J. Birn, ApJ **588**, L45 (2003b)
 I.I. Roussev, I.V. Sokolov, T.G. Forbes, T.I. Gombosi, M.A. Lee, J.I. Sakai, ApJ **605**, L73 (2004)
 I.I. Roussev, I.V. Sokolov, in *Solar Eruptions and Energetic Particles*, Chapman Conf., Turku, Finland, 2–6 Aug 2004, Geophysical Monograph Series, ed. by N. Gopalswamy, R. Mewaldt, J. Torsti (AGU, Washington, DC, 2005, in press)
 D.M. Rust, A. Kumar, ApJ **464**, L199 (1996)

- D.M. Rust, *et al.* (eds.), The sun and heliosphere in three dimensions, Report of the NASA Science Definition Team for the STEREO Mission (edited and published at John Hopkins Univ. Applied Physics Lab., Laurel, Maryland, 1997 Dec 1)
- D.M. Rust, B. LaBonte, ApJ **622**, L69 (2005)
- K.H. Schatten, J.M. Wilcox, N.F. Ness, Solar Phys. **6**, 442 (1969)
- W.K.H. Schmidt, V. Bothmer, Adv. Space Res. **17**, 369 (1996)
- C.J. Schrijver, M.L. DeRosa, Solar Phys. **212**, 165 (2003)
- C.J. Schrijver, A.W. Sandman, M.J. Aschwanden, M.L. DeRosa, ApJ **615**, 512 (2004)
- R. Schwenn, E. Marsch (eds.), *Physics of the Inner Heliosphere. I. Large-Scale Phenomena* (Springer-Verlag, Berlin, 1991a), P. 282
- R. Schwenn, E. Marsch, (eds.), *Physics of the Inner Heliosphere. II. Particles, Waves and Turbulence*, (Springer-Verlag Berlin, 1996) P. 352
- S. Serio, G. Peres, G.S. Vaiana, L. Golub, R. Rosner, ApJ **243**, 288 (1981)
- D.G. Socker, *et al.*, SPIE **2804**, 50 (1996)
- D.G. Socker, SPIE **3442**, 44 (1998)
- D.G. Socker, *et al.*: SPIE **4139**, 284 (2000)
- I.V. Sokolov, E.V. Timofeev, J.I. Sakai, K. Takayama, J. Comp. Phys. **181**, 354 (2002)
- I.V. Sokolov, I.I. Roussev, T.I. Gombosi, M.A. Lee, J. Kóta, T.G. Forbes, *et al.*, ApJ **616**, L171 (2004)
- R.S. Steinolfson, A.J. Hundhausen, JGR **93**, 14,269 (1988)
- R.T. Stewart, Solar Phys. **94**, 379 (1984)
- B.J. Thompson, J.B. Gurman, W.M. Neupert, J.S. Newmark, J.P. Delaboudiniere, O.C. St.Cyr, *et al.*, ApJ **517**, L151 (1999)
- V.S. Titov, P. Démoulin, A&A **351**, 707 (1999)
- T. Török, B. Kliem, A&A **406**, 1043 (2003)
- T. Török, B. Kliem, V.S. Titov, A&A **413**, L27 (2003)
- T. Török, B. Kliem, in *Coronal Heating*, SOHO-15 Workshop, vol. 575 (ESA, ESTEC Noordwijk, The Netherlands, ESA-SP, 2004), p. 56
- G. Toth, Astrophys. Lett. Comm. **34**, 245 (1996)
- G. Toth, D. Odstrčil, J. Comput. Phys. **182**, 82 (1996)
- D. Tripathi, V. Bothmer, H. Cremades, A&A **422**, 337 (2004)
- A.J. Tylka, D.V. Reames, C.K. Ng, GRL **26/14**, 2141 (1999)
- A.J. Tylka, C.M.S. Cohen, W.F. Dietrich, M.A. Lee, C.G. MacLennan, R.A. Mewaldt, *et al.*, ApJ **625**, 474 (2005)
- H.C. Van de Hulst, Bull. Astron. Inst. Neth. **11**, 135 (1950)
- A.A. Vedenov, V.A. Koutvitsky, S. Koutchmy, M.M. Molodensky, V.N. Oraevsky, Astronomy Reports **44/2**, 112 (2000)
- A. Vourlidas, P. Subramanian, K.P. Dere, R.A. Howard, ApJ **534**, 456 (2000)
- A. Vourlidas, R.A. Howard, ApJ **642**, 1216 (2006)
- Y.M. Wang, N.R. Sheeley Jr., ApJ **392**, 310 (1992)
- Y.M. Wang, ApJ **543**, L89 (2000)
- A. Warmuth, G. Mann, A&A **435**, 1123 (2005)
- D.F. Webb, J. Burkepile, T.G. Forbes, P. Riley, JGR **108/A12**, SSH 6-1 (2003), CiteID 1440, DOI 10.1029/2003JA009923
- T. Wiegelmann, T. Neukirch, Solar Phys. **208**, 233 (2002)
- T. Wiegelmann, B. Inhester, Solar Phys. **214**, 287 (2003)
- T. Wiegelmann, A. Lagg, S.K. Solanki, B. Inhester, J. Woch, A&A **433**, 701 (2005)
- T. Wiegelmann, B. Inhester, A. Lagg, S. Solanki, Solar Phys. **228**, 67 (2005)
- T. Wiegelmann, B. Inhester, Solar Phys. (2006, in press)
- J.P. Wild, S.F. Smerd, A.A. Weiss, Annu. Rev. Astron. Astrophys. **1**, 291 (1963)
- A.R. Winebarger, H. Warren, A. VanBallegooijen, E. DeLuca, L. Golub, ApJ **567**, L89 (2002)
- B.E. Wood, M. Karovska, J. Chen, G.E. Brueckner, J.W. Cook, R.A. Howard, ApJ **512**, 484 (1999)
- S.T. Wu, H. Zheng, S. Wang, B.J. Thompson, S.P. Plunkett, X.P. Zhao, *et al.*, JGR **106**, 25,089 (2001)
- P.R. Young, E. Landi, R.J. Thomas, A&A **329**, 391 (1998)
- G.P. Zank, G. Li, Particle acceleration at CME-driven shocks: why the injection problem is important, in Proc. 35th COSPAR Scientific Assembly, 18–25 July 2004, Paris, France, p. 295
- Ya.B. Zeldovich, Yu.P. Raizer, *Physics of Shock Waves and High-Temperature Hydrodynamic Phenomena*, ed. by W.D. Hayes, R.F. Probstein (Mineola, Dover, 2002)
- M. Zhang, B.C. Low, Annu. Rev. Astron. Astrophys. **43**, 103 (2005)
- V.V. Zharkova, V. Schetinin, Solar Phys. **228**, 137 (2005)

-
- S. Zidowitz, B. Inhester, A. Epple, in *Solar Wind Eight*, ed. by D. Winterhalter, J.T. Gosling, S.R. Habbal, W.S. Kurth, M. Neugebauer, Internat, Solar Wind Conference, American Institute of Physics Conference Proceedings AIP-CP, vol. 382 (AIP Press, New York, 1996), p. 165
 - S. Zidowitz, in, *The Corona and Solar Wind Near Minimum Activity*, ed. by A. Wilson, Proc. 5th SoHO Workshop, vol. 404 (European Space Agency, ESTEC Noordwijk, The Netherlands, ESA-SP, 1997), p. 757
 - S. Zidowitz, JGR **104/A5**, 9727 (1999)

STEREO Ground Segment, Science Operations, and Data Archive

J. Eichstedt · W.T. Thompson · O.C. St. Cyr

Originally published in the journal Space Science Reviews, Volume 136, Nos 1–4.
DOI: [10.1007/s11214-007-9249-4](https://doi.org/10.1007/s11214-007-9249-4) © Springer Science+Business Media B.V. 2007

Abstract Vitally important to the success of any mission is the ground support system used for commanding the spacecraft, receiving the telemetry, and processing the results. We describe the ground system used for the STEREO mission, consisting of the Mission Operations Center, the individual Payload Operations Centers for each instrument, and the STEREO Science Center, together with mission support from the Flight Dynamics Facility, Deep Space Mission System, and the Space Environment Center. The mission planning process is described, as is the data flow from spacecraft telemetry to processed science data to long-term archive. We describe the online resources that researchers will be able to use to access STEREO planning resources, science data, and analysis software. The STEREO Joint Observations Program system is described, with instructions on how observers can participate. Finally, we describe the near-real-time processing of the “space weather beacon” telemetry, which is a low telemetry rate quicklook product available close to 24 hours a day, with the intended use of space weather forecasting.

Keywords STEREO · Space weather · Science operations · Data archive · Solar observations

1 Introduction

The STEREO ground system provides the means for planning the STEREO mission, communicating the plans to the STEREO observatories, assessing and maintaining the health and safety of the observatories, and providing detailed data products from these processes to the

J. Eichstedt

Applied Physics Laboratory, Johns Hopkins University, Laurel, MD 20723, USA

W.T. Thompson (✉)

Adnet Systems Inc., NASA Goddard Space Flight Center, Code 671, Greenbelt, MD 20771, USA

e-mail: William.T.Thompson.1@gsfc.nasa.gov

O.C. St. Cyr

NASA Goddard Space Flight Center, Greenbelt, MD, USA

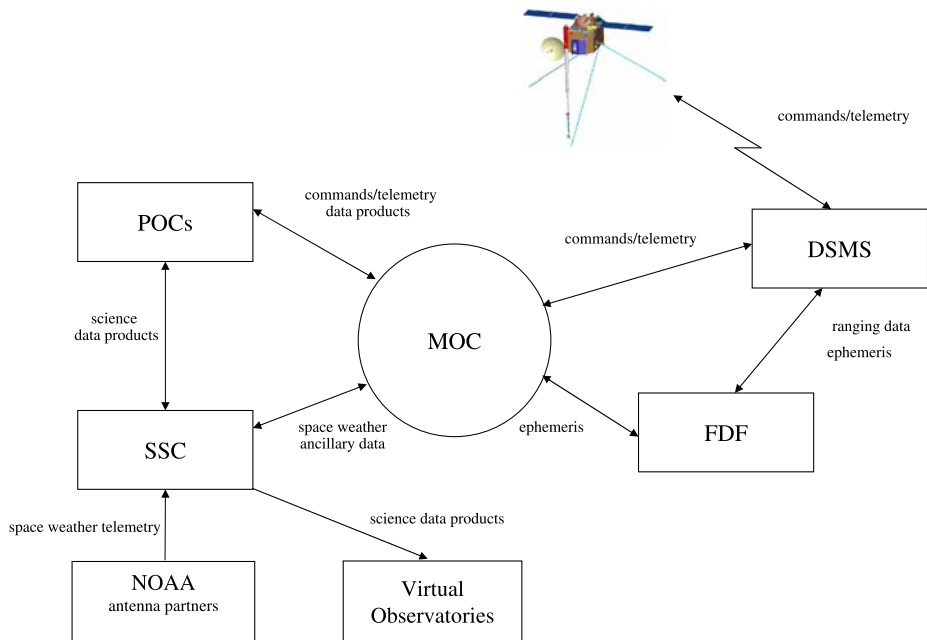


Fig. 1 STEREO ground segment teams and interfaces

STEREO community. Of primary interest to the community are the science data collected, which are brought down from the observatories daily and ultimately reside at the STEREO Science Center for retrieval by the international science community and the general public.

The STEREO ground system consists of several operations centers which each play a role in the STEREO science mission. These operations centers are distributed across the world and consist of the Mission Operations Center (MOC), four Payload Operations Centers (POCs), the STEREO Science Center (SSC), the Flight Dynamics Facility (FDF), and the Deep Space Mission System (DSMS) which operates the Deep Space Network (DSN). The STEREO ground segment provides the means for these operations centers to perform their individual tasks as well as to communicate necessary data products between centers and the observatories. Figure 1 depicts the STEREO ground segment teams and interfaces. The STEREO Mission Operations Center is located at the Johns Hopkins University/Applied Physics Laboratory in Laurel, MD, and is the center that operates the observatory bus and serves as the collection and distribution point for the instrument commands and telemetry. The Payload Operation Centers are the instrument operations centers that generate the commands for each of the four STEREO instrument suites and monitor instrument health and safety. These centers are located at the Naval Research Laboratory in Washington, DC; the University of California–Berkeley in Berkeley, CA; the University of Minnesota in Minneapolis, MN; and the University of New Hampshire in Durham, NH. These are the home bases for the instrument POCs, but they are able to operate remotely when necessary and also maintain a presence at the MOC. The SSC, located at the Goddard Space Flight Center in Greenbelt, MD, provides science coordination and serves as the STEREO archive. Also located at GSFC is the FDF, which performs STEREO navigation services. The DSMS is operated by the Jet Propulsion Laboratory in Pasadena, CA, with ground stations in California, Madrid, Spain, and Canberra, Australia.

1.1 Mission Requirements and the Ground System Design

The top-level requirements levied on the STEREO ground system which influenced the ground system design can be broken down into four major components:

- All instrument operations will be decoupled from the spacecraft bus operations. The instruments and the spacecraft bus will be operated almost entirely independent of each other. The same can be said about the ground elements (the POCs and the MOC).
- The ground system will support subsystem development, observatory integration, and mission operations.
- The spacecraft and ground system will be designed to deliver an average of 5 Gbits of science data per day per observatory to the instrument POCs and the SSC.
- The MOC will provide the data products to the SSC and instrument Payload Operations Centers (POCs). These data products consist of Level 0 telemetry data and Mission Support Data.

Decoupled instrument operations has the effect of greatly simplifying mission operations and the ground planning tools. The STEREO mission is ideal for implementing this separation of spacecraft and instrument operations as there are essentially no shared resources. The spacecraft continually points at the Sun and therefore no coordination is required for encounters and enough power is available to support all instrument operations at all times. In addition, the SSR is portioned such that each instrument (or instrument suite) has its own partitions for recording science data and each POC is responsible for managing its partitions. There are some events that require spacecraft and instrument coordination, such as calibration maneuvers and software loads, but these are coordinated individually and occur infrequently.

The STEREO ground system has evolved over time to support the mission as it is developed. The early system consists of “mini-MOCs”, which are single workstations that support subsystem development. Each mini-MOC contains the same command and control system which is built up into the I&T MOC and the MOC. The mini-MOC contains its own archive within the workstation, while the I&T and Flight MOC is more distributed with an archive and tools specific to I&T and Mission Operations. This concept has been used at APL for many past missions and simplifies spacecraft and operations development.

The data return requirement of 5 Gbits per day on average primarily determines the duration of the DSN tracks and hence is the largest factor in the DSN scheduling process. Throughout the STEREO mission, the track durations are increased as the supported data rates are reduced. The daily track times planned for STEREO take into account data from past deep space missions such as the number of missed tracks, delayed acquisitions, and safe mode demotions. Enough additional track time has been scheduled and the SSR is large enough to support daily downlink of “extra” data such that the yearly daily average should be realized.

There are many data products produced by the STEREO MOC which fulfill the requirements and desires of the mission and instrument teams. These products are produced through the planning, control, and assessment processes and are distributed through an ftp server in the STEREO MOC.

1.2 Spacecraft and Mission Operations

1.2.1 *STEREO Spacecraft*

Each of the two STEREO spacecraft are nearly identical with selective redundancy. The spacecraft bus was built by JHU/APL with NASA Goddard Space Flight Center (GSFC)

procuring the instruments. The entire spacecraft was integrated at JHU/APL. The spacecraft design is described more fully in Driesman and Hynes (2007), but a short summary is given here to lead into the discussion of operations.

The spacecraft bus consists of six operational subsystems supporting a payload suite of four instruments. The spacecraft bus is designed around an Integrated Electronics Module (IEM). The IEM is a single box that contains the Command & Data Handling (C&DH), Guidance and Control (G&C), and Solid State Recorder (SSR) on plug-in cards. A MIL-STD-1553 bus architecture is used for command and telemetry between the IEM and the instrument Data Processing Units (DPU), Guidance and Control (G&C) processor, Transponder, Star Tracker, Inertial Measurement Unit (IMU), and Power subsystem.

The C&DH subsystem provides real-time, timetagged, macro, and autonomy command capabilities. It uses a Rad 6000, 25 MHz, 32-bit processor that formats all spacecraft bus telemetry into CCSDS compliant packets. An 8.5 Gbit RAM Solid State Recorder (SSR) is used for data storage of all science and engineering data. An Oven Controlled Crystal Oscillator (OCXO) is used for time reference.

The RF Communications subsystem provides simultaneous X-Band (XB) uplink, downlink, and navigation data using one High Gain Antenna (HGA) and two Low Gain Antennas (LGA). The LGAs provide communications from launch through the phasing orbits and is used for emergency communications when the spacecraft is in Earth Acquisition mode. The HGA consists of a gimballed, 1.2 meter, parabolic dish with a 180-degree gimbal travel. It will be used when the spacecraft range is greater than 0.2 AU. There are five XB uplink rates, 125, 500, 1,000, and 2,000 bps for normal operations and 7.8125 bps for emergency operations. The RF Communications subsystem is designed to use the DSMS 34-meter Beam Wave Guide (BWG) antennas, although any 34 m or 70 m antenna with XB uplink and downlink can be used.

The G&C subsystem provides three-axis attitude control of the spacecraft and also controls the pointing of the HGA. Nominal orientation of the spacecraft will have the $+X$ -axis of the spacecraft pointed at the Sun within 0.1° and the HGA, near the Z -axis, will be pointed at the Earth within $\pm 0.35^\circ$. The G&C subsystem consists of one Rad 6000 processor, the Attitude Interface Electronics (AIE)/1553 Board, three attitude sensors, an Inertial Measurement Unit (IMU), Star Tracker, and Digital Solar Attitude Detectors (DSAD), and two control actuators, Reaction Wheel Assemblies (RWA) and the Propulsion subsystem.

The AIE/1553 Board provides the 1553 digital interface between the analog G&C components, i.e., DSADs, RWA, HGA gimbal, and thrusters, and the C&DH subsystem. It consists of an electronics board in the Power Distribution Unit (PDU).

During a serious spacecraft emergency (processor reboot, hardware Low Voltage Sense (LVS), or command loss timeout) the spacecraft will go through a system reset and enter Earth Acquisition (EA) mode. Both processors will reboot and the C&DH/EA processor will come up using the EA application. The EA application combines the functionality of the C&DH application along with basic G&C functionality, i.e., using measured data only it will maintain attitude control (inertial knowledge will not be known). The G&C processor will reboot and reload the G&C application; however, it will essentially be idling since it will not be receiving G&C sensor data nor have control over the G&C actuators. The EA application will point the $+X$ axis of the spacecraft at the Sun, switch to the summed LGAs, reduce the downlink and uplink rates to a minimum, and go into a $5^\circ/\text{min}$ roll about the X -axis.

The IMU (redundant) provides spacecraft rate and acceleration data using Ring Laser Gyros and accelerometers. The Star Tracker can autonomously identify up to nine stars,

using a $16.4^\circ \times 16.4^\circ$ field of view (FOV), with brightness between +0.1 to +5.5 magnitude. There are five DSADs each with a $\pm 64^\circ$ FOV to determine the Sun location with an accuracy of 0.5° .

Four RWA provide pointing control. As system momentum builds in the RWAs, it will be dumped, approximately every 13 days, using the thrusters in the Propulsion subsystem. While the G&C can autonomously perform momentum dumps, they are expected to be planned and controlled by mission operations so as to avoid any interference with science data collection.

The Propulsion subsystem consists of two hydrazine propellant tanks, one transducer, three high-pressure latch valves, and 12 4.5 N m thrusters. There will be sufficient propellant to dump momentum for five years with a 10% leakage allowance.

The Power subsystem employs two fixed GaAs/Ge solar arrays (SA). Power is managed by a Peak Power Tracker (PPT) to provide an unregulated 22 to 35 V DC bus. A 23 ampere-hour NiH₂ battery provides power from launch to SA deployment and for Low Voltage Sense (LVS) conditions.

The Thermal subsystem is a passive design using blankets, radiators, and thermostatically controlled heaters. All instruments are thermally isolated from the spacecraft structure

1.2.2 STEREO Mission Operations

The STEREO mission consists of continually pointing at the Sun as the observatories move away from the Earth at 22 deg/year while remaining approximately the same distance from the Sun throughout the mission. In this orbit, the solar array input power is sufficient to cover any instrument mode and the observatory remains thermally stable. Each instrument has its own partitions to use on the SSR which are typically set by Mission Operations to an overwrite mode. This leaves the spacecraft and instruments with no power, thermal, or SSR constraints other than managing the amount of data being placed in their SSR partitions. However, there are two resources that are shared between the instruments which must be managed. These are the downlink during the phasing orbits, and the Stored Command Buffer (SCB) in the C&DH. The SCB is 20 kbits in size and must be managed so as not to overload it. This space is primarily used by the SWAVES instrument, but is also available to PLASTIC and IMPACT. The SSC will be managing these two resources by negotiating between the instruments for the available downlink during early operations and by coordinating the use of the SCB during the mission.

Telemetry is received from the observatory by the DSN during daily tracks. During most of the track, the SSR is played back and collected by the DSN Central Data Recorder while the real-time telemetry is flowed directly to the MOC. These real-time data are made available to the POCs through a socket connection to the MOC. The real-time data can also be “played back” from the MOC archive via a socket connection. The Central Data Recorder will ftp the full data set from the track (both real-time and SSR playback) in 30-minute files. Once all these files are collected by the MOC, they will be processed into level 0 data for each instrument and the SSC and be made available to the instrument POCs and the SSC within 24 hours after receipt of all the data from the DSN via ftp from the STEREO Data Server in the MOC.

Also during each track, commands will be uplinked to the spacecraft beginning early in the track. Following the upload of spacecraft commands, instrument command queues will be opened and commands that have been forwarded to the MOC in advance will be uplinked in a round-robin fashion for each POC. Following this command uplink, the POC command queues may be opened to allow real-time commanding by the instrument POCs.

The POCs will maintain the health and safety of their instruments from review of the telemetry data received and commanding in the process just described. In addition to this, autonomy is onboard the observatory which can power off the instruments at their request or when the spacecraft requires for health and safety purposes.

1.3 Telemetry and Data Processing

Figure 2 illustrates conceptual flow of command and telemetry data between the ground-based observatory bus and instrument operations elements and the on-orbit STEREO spacecraft. The “outer-loop” depicts instrument operations. Using a decoupled instrument operations approach, all instruments will be operated by the instrument operations teams at their home POC. In Fig. 2, begin at the POC Planning, on the far right, where instrument commands are produced. The command messages, which will be packetized along with some additional information needed by the MOC, are transmitted to the MOC via the Internet. At the MOC (MOC Authorize and Route) there is some checking performed, then these commands are queued for eventual uplink to the instrument. Along with the command packets, the POCs will append timing information that indicates the time span (earliest and latest times) over which the command packet may be uplinked to the spacecraft instrument. Real-time command packets, when uplinked to the spacecraft, are immediately routed by the spacecraft bus to the appropriate instrument and time tagged command packets are stored in the instrument’s stored command buffer in the observatory bus Command and Data Handling (C&DH) system. Conceptually, the command packet goes “directly” from the POC to the instrument, since the MOC, ground station and spacecraft bus are merely the delivery system. This delivery system notifies the POC of the delivery status of the command message.

Whereas the POCs produce instrument commands, the MOC produces spacecraft bus commands. This is depicted in the “inner-loop” on the data flow diagram (Fig. 2). Starting at the MOC Planning process, the Mission Operations Team (MOT) prepares command messages to the spacecraft bus to operate it during the next day. These command messages are queued for uplink (MOC Authorize and Route) just like the instrument commands, only they go to a different destination (via the C&DH Routing Service). Real-time commands are immediately routed, by the C&DH processor, to the appropriate spacecraft subsystem and timetagged and macro commands are stored in the C&DH processor. The MOC receives delivery status of the command packets just as the POCs do.

The onboard instruments produce science and engineering data (Instrument Data Collection) in response to the uplinked command messages. The data produced by the instruments are sent to the spacecraft data system in the form of CCSDS telemetry packets. Similarly, engineering data produced by the spacecraft bus are also formatted into CCSDS packets. These packets produced by the instruments and the spacecraft bus and conveyed to the spacecraft data system (C&DH Combine) are stored on the Solid State Recorder (SSR) within the spacecraft data system (C&DH Recording). During a ground track with the spacecraft, the contents of the SSR are transmitted to the MOC (C&DH Frame Packaging).

On the ground (Ground System Telemetry Routing), real-time data are forwarded to the MOC and POCs, while all recorded data are sent to the STEREO Data Server (SDS). All instrument data will be processed into level 0 data files and sent to the POCs for further processing and analysis, and to the STEREO Science Center for mission archival. The cycle repeats, with the POCs preparing instrument commands for still another day in space. Spacecraft bus data are routed to the MOC (MOC Assessment) where an assessment function is performed. The MOC spacecraft bus planning process then repeats.

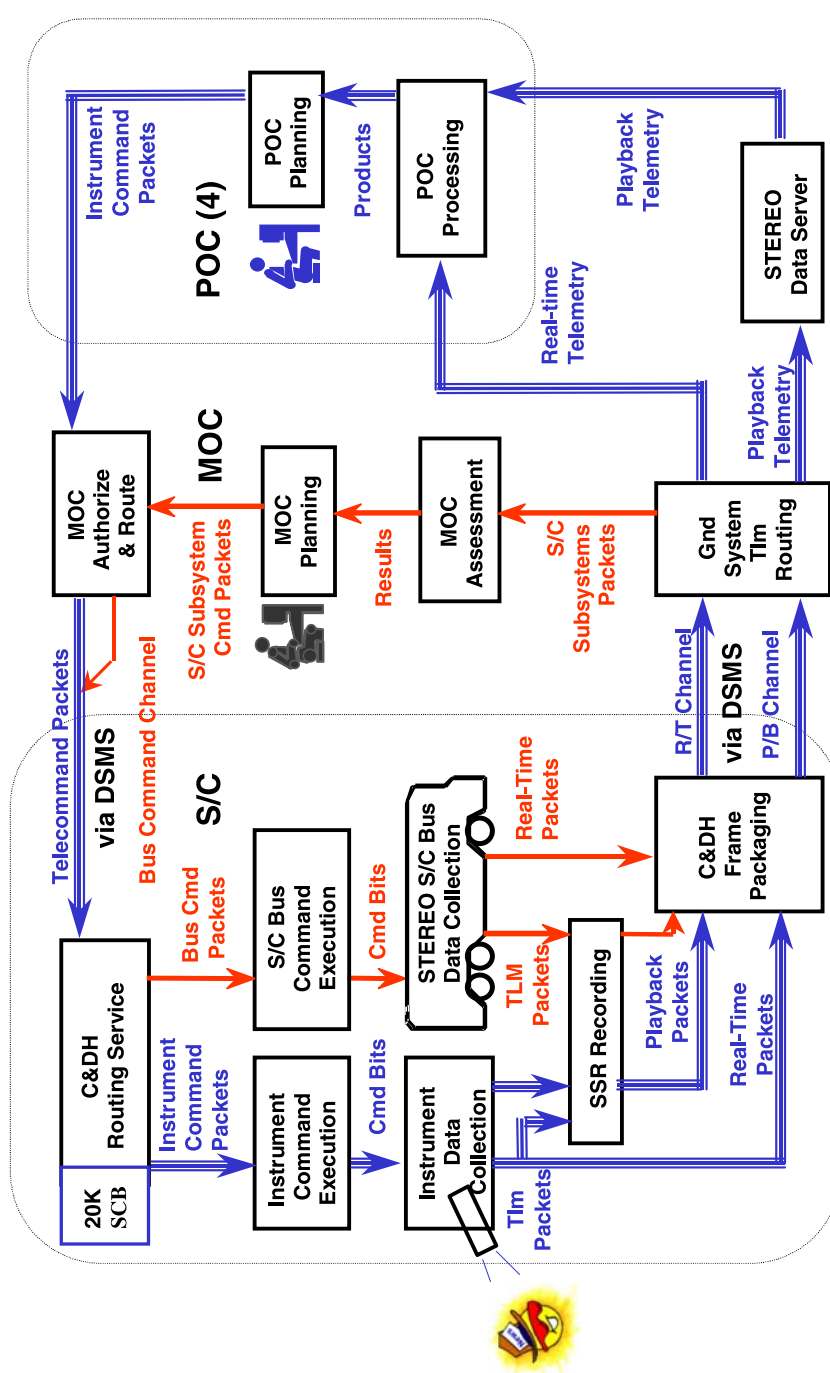


Fig. 2 Decoupled instrument operations data flow

2 STEREO Mission Operations Center

The MOC has the primary responsibility of management of the spacecraft bus including the development of command messages and the uplink to the spacecraft by way of the DSN. Recovery of spacecraft bus engineering (state-of-health) telemetry and the performance analysis based on this telemetry is also performed at the MOC. The MOC receives instrument command messages from the POCs and, after verification that the command APIIDs are appropriate for the POC they came from, queues these for uplink to the spacecraft based on start and expiration times appended to the command messages by the POC. The MOC does not directly verify any instrument commands and does not decommute or analyze any instrument telemetry aside from currents and temperatures observed from the spacecraft side of the instruments. Each POC is individually responsible for the health and safety of its instrument. The MOC does control the instrument power service and can power off an instrument at the request of the POC. In addition, an instrument can autonomously request to be powered down through the spacecraft fault protection system.

2.1 Local Area Network Architecture

Figure 3 illustrates the MOC and the supporting network architecture including interfaces to other mission operations elements. Restricted IONet communication lines connect the MOC primary and backup command workstations to the DSN through a firewall. PCs running Memory Allocation Examiner (MAX) are the only other computers on the Prime Restricted IONet network. These workstations are connected to the Ops “Demilitarized Zone” (DMZ) network through another firewall. The Ops DMZ network houses the assessment workstations and a series of X-Terminals which can display real-time and playback telemetry data to the spacecraft engineering team within the MOC. The Ops DMZ also contains the STEREO Planning system software, real-time telemetry servers, the POC command acceptor, the STEREO Data Server, the second-level archive which stores decommutated spacecraft telemetry for trending, and the Spacecraft Hardware in the Loop Simulators. The Ops DMZ Network is in turn connected to the Internet via a third firewall. The SSC, POCs, and the FDF connect to the Ops DMZ via the Internet to retrieve STEREO Data Products from the SDS and to deliver instrument commands via the POC Command Acceptor. Should the Internet be inaccessible to the POCs or SSC, the Ops DMZ can be accessed through a modem pool. Two additional STEREO workstations will be housed in the APL Multi-Mission MOC which is an Operations facility located in a different building within the APL campus. These workstations are for emergency state-of-health command and telemetry and would be used should a disaster consume the STEREO MOC. These machines are maintained with current files and software for this purpose.

2.1.1 STEREO Telemetry Flow

Real-time telemetry from each STEREO spacecraft will flow from the spacecraft into the DSN and be routed through the Restricted IONet to APL on a low-latency delivery path with complete data delivery not guaranteed. These data are flowed to the Ops DMZ network where they can be viewed in real-time by the spacecraft engineering team or the POCs either locally or remotely. The data are stored for several days on the data servers where they can be played back via instant replay in the MOC or across the Internet at the request of the POCs. The SSR playback data are recorded at the Central Data Recorder (CDR) at JPL where they are sent to the MOC in half-hour segment Intermediate Data Record (IDR) files over the

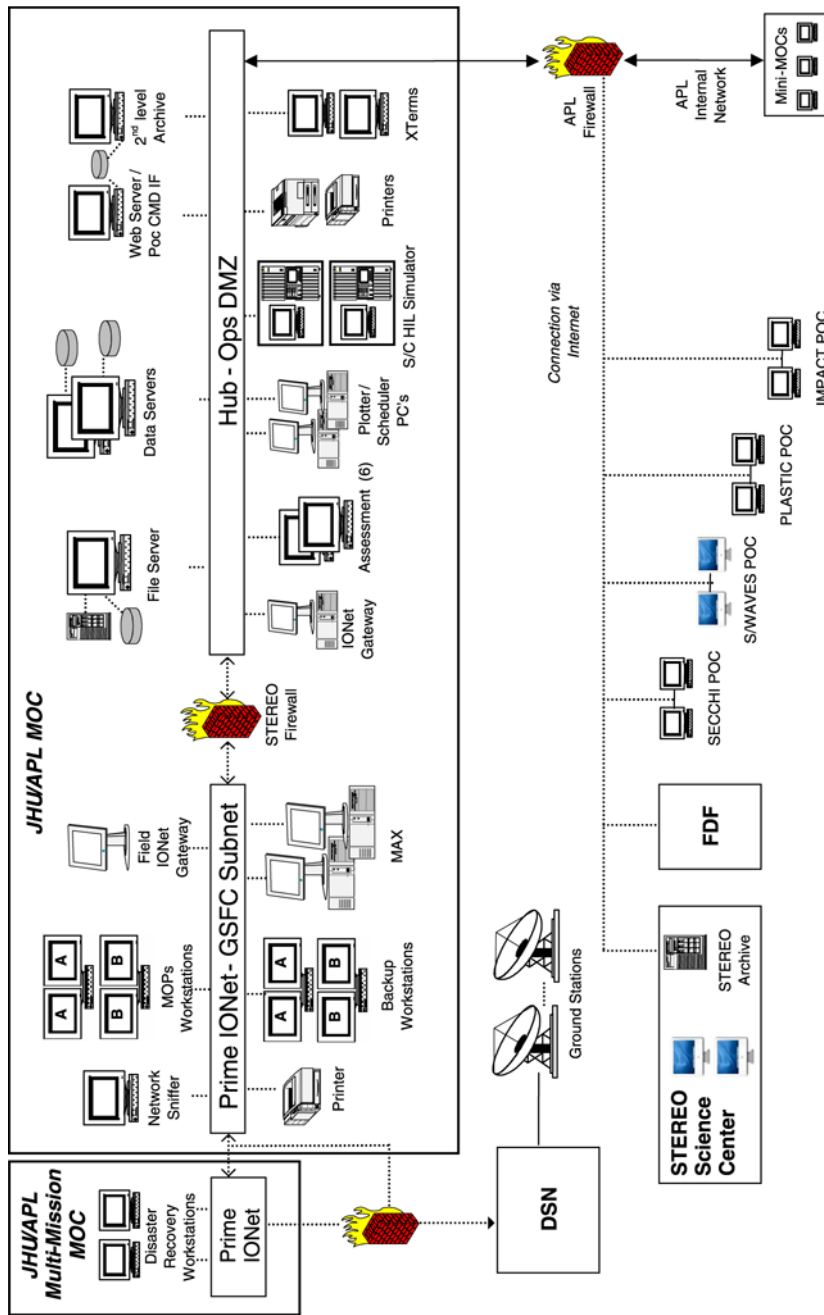


Fig. 3 MOC network architecture

Internet. These data are guaranteed complete and are the data that will be used to populate the raw archive and generate level 0 data. Daily, and upon complete playback of the SSR and MOC receipt of all the IDR files from the CDR, level 0 data are processed for each of the instrument POCs and the spacecraft housekeeping data. Level 0 data are time ordered with duplicates removed. Each day level 0 files are produced for the previous day, the preceding day, the day before that, and for 30 days earlier. This allows for the delivery of data that may have resided on the SSR for a few days and it is expected that the file from 30 days ago will be the final delivery with the complete data for that day. Due to the volume of data in the SECCHI POC partitions, each of these level 0 files are produced in 4-hour segments where all the other level 0 files are produced for a 24-hour period. Once generated, the level 0 files are placed on the STEREO Data Server (within 24 hours from receipt of the IDR files from the DSN) where they can be retrieved by the POCs and SSC. These files are maintained on the SDS for 30 days when they can be removed after receipt of the Archive Products List from the SSC indicating that they have retrieved the data.

2.1.2 STEREO Command Flow

The IMPACT, PLASTIC, SECCHI, and SWAVES POCs will send to the MOC Command Messages that contain the information needed to configure and control their instruments. These command messages will be sent to the MOC at least eight hours prior to the start of the track that they are scheduled for uplink. The MOC shall authenticate and perform minimal syntax checks on the command messages, and sends an Authorization Return Receipt message back to the POCs facility indicating the message status. If the POCs want to delete previously transmitted command messages prior to their upload, the POC verbally sends the MOC a command flush request. Based on the command delivery time information included in the command message header, the MOC shall forward the validated queued command messages to the Deep Space Mission System (DSMS) interface for transfer to the spacecraft in a round-robin format between the POCs. Finally, the Command and Data Handling (C&DH) process on the spacecraft shall forward the commands to the 1553 bus for instrument retrieval. Actual command execution success or failure will be indicated in instrument telemetry telltales. In addition to verification of instrument commands through instrument telemetry, the As Run Track Plan and the Command and Packet History data products are sent out to assist in tracking instrument commands.

During instrument commissioning, instrument special events such as software loads, and during instrument emergencies, real-time commanding by the instrument POC is also available. In this case, the commands flow directly from the POC, through the POC Command Acceptor in the MOC where they are transferred to the Restricted IONet and flowed directly to the DSMS and up to the spacecraft. The MOC can control which POCs will be commanding in real-time and during emergencies, instrument commissioning, and software loads, will restrict realtime commanding to a single POC.

Within the C&DH subsystem on the spacecraft there is also an Instrument Stored Command Buffer. The SWAVES, IMPACT, and PLASTIC POCs may use this Stored Command Buffer to load time tagged commands for their respective instruments. This 20 k buffer will store instrument packets until the UTC time associated with the command packet when it will then forward it to the instrument. The POCs and SSC manage this buffer such that it is not overfilled and following each track the MOC will produce a Stored Command Buffer report indicating the command packets within the buffer to assist in managing it. The Stored Command Buffer on the spacecraft can also be flushed of instrument commands by the MOC, at the request of each POC.

2.2 MOC Personnel

The STEREO Mission Operations Team at APL will launch with 14 team members. This 14-member team will be reduced to 12 by the end of the phasing orbits. The launch team organization consists of:

- 1 Mission Operations Manager
- 4 Real-time controllers
- 8 Spacecraft Specialists
- 1 Anomaly Officer.

Following the phasing orbits the team will operate without the Anomaly Officer and with the Mission Operations Manager also serving as a Spacecraft Specialist. At launch +6 months the team will transition to unattended tracks and will reduce to eight Spacecraft Specialists. At Heliocentric Orbit +1 year the team is expected to reduce again to six Spacecraft Specialists for the remainder of the mission.

Each of the above positions will have the following responsibilities:

- **Mission Operations Manager (MOM):** The Mission Operations Manager will be responsible for verifying the readiness of the ground system for launch. The MOM will also be the primary maneuver planner during the phasing orbits, prepare the weekly status report for the MOC, and serve on the post launch Configuration Control Board. Following completion of all spacecraft maneuvers, the MOM will also serve as one of the Spacecraft Specialists.
- **Real-Time Controller:** The real-time controllers will be the primary interface with the DSN for each real-time track. They will configure the ground system, verify readiness for each track with the DSN Station, and handle ground system contingencies.
- **Spacecraft Specialist:** The Spacecraft Specialists will serve as the Planners, real-time spacecraft evaluators during DSN tracks, and perform spacecraft assessment. The Spacecraft Specialist team will rotate through these roles on a weekly basis.
- **Anomaly Officer:** The Anomaly Officer is unique to early operations. This role will consist of organizing the larger team (Mission Operations and Spacecraft Engineers) to solve anomalies early after launch. The Anomaly Officer will be intimately familiar with the Contingency Handbook and will be able to effectively lead the team in resolving anomalies.

2.3 Other Ground Segment Elements

2.3.1 Deep Space Mission System

The Deep Space Mission System (DSMS) will be used to provide communications to both spacecraft from launch to end of life (EOL). The use of all three DSMS antenna facilities, Goldstone, Madrid, and Canberra, are required to determine the elevation component for the navigation of each spacecraft. Nominally, one 3.5- to 5-hour track, depending on spacecraft range, centered every 24 hours per spacecraft will be conducted using the 34-meter BWG subnet.

The MOC is connected to the DSMS via Restricted IONet links. Commands will be flowed to the DSN using the standard Space Link Extension Service over the Restricted IONet and real-time telemetry will be flowed from the DSN to the MOC over the Restricted IONet using legacy UDP service. Playback data received at the DSN station will be flowed to the Central Data Recorder at JPL where they will in turn be flowed in half-hour increments

to the MOC via FTP as IDR files. Orbit data for each spacecraft will be provided to DSMS from the FDF for acquisition and ranging data will be distributed from the DSMS to the FDF for orbit determination purposes over the Restricted IONet.

2.3.2 Flight Dynamics Facility

The Flight Dynamics Facility (FDF) at Goddard Space Flight Center determines the orbits of the observatory from tracking data provided by the DSN ground stations, and generates predicted DSN station contact periods and predicted and definitive orbit data products. The FDF also generates orbital ephemeris data in support of orbit maneuvers that satisfy science and mission requirements and transfers this information to the STEREO MOC via the FDF Products Center.

Locally, Delta launch and ascent support will be provided by the FDF Expendable Launch Vehicle (ELV) Support Team, whose role it is to provide the following: (1) launch vehicle acquisition data delivered to tracking sites supporting the ascent, and (2) an orbital insertion state vector based on Delta internal guidance telemetry. The orbital insertion state vector obtained in this way provides the first indication of the status of the achieved orbit. The orbital insertion state vector will be delivered by the ELV team to the FDF STEREO orbit determination team and to the APL Mission Design Team for evaluation. At the FDF, the insertion vector may also be used to update tracker acquisition data and to become a “seed” vector for the orbit determination process. Once the two spacecraft have been acquired by two DSN stations, tracking data for each will begin to flow to the FDF. The FDF will perform orbit determination operations on a daily basis, obtaining and delivering to APL a state vector solution at least once per day. Ephemeris files based on these solutions will also be generated and delivered to APL and JPL.

The FDF will continue collecting tracking data during all tracking passes in the early orbit phase, and Orbit Determination (OD) solutions will be updated at intervals following sufficiently extended orbital solution arcs. However, after the first 24 hours these updates are expected to occur at least once daily leading up to the first apogee (A1). OD updates will be computed daily starting seven days in advance of maneuvers to support timely maneuver planning at APL. For all maneuvers, OD updates will be obtained with an epoch just prior to maneuver ignition and again at an epoch just after maneuver burnout. These OD updates will support maneuver reconstruction and calibration activities by the APL Mission Design Team. The FDF will also support maneuvers by measuring the observed component of delta-V along the station line-of-sight to the spacecraft, where applicable. This radial delta-V observation will be communicated to the APL Mission Design Team for use in maneuver calibration activities.

The phase of the mission between the first apogee of the phasing loops and the lunar swingbys will continue to be operationally intense. The FDF will continue collecting tracking data according to the daily support schedule. By definition, this phase of the mission extends to two weeks after the lunar swingbys that propel the spacecraft into heliocentric orbit. The FDF OD team will expect the possibility of orbit maneuvers around the time of every perigee and apogee. For STEREO-A, there is also a likelihood of a trim maneuver(s) following the first lunar swingby to re-target the second swingby. The APL Mission Design Team will keep the FDF apprised of updates to the mission timeline and provide predicted burn details as needed. The FDF will in turn model maneuvers into ephemeris files in cases where the span includes maneuver epochs.

During heliocentric orbit, the mission will settle into a routine phase starting immediately after the lunar swingbys, with no more orbit maneuvers expected for the duration of the

mission. The tracking schedule changes as the observatories move further from the Earth with increased contact time as the data rates are lowered. The FDF will continue to collect the DSN tracking data on this schedule and will evaluate the tracking data as necessary.

2.3.3 NOAA

During the periods that the STEREO observatories are not in DSN contact, each will be broadcasting a low-rate “space weather beacon” telemetry stream. The National Oceanographic and Atmospheric Administration Space Environment Center (NOAA/SEC) has taken on the responsibility of coordinating ground stations at various locations around the world to collect this telemetry and transmit it to the SSC. This process is described in more detail in Sect. 5.3.

3 STEREO Science Center

The STEREO Science Center (SSC)—located at the NASA Goddard Space Flight Center in Greenbelt, MD—serves four main functions for the STEREO mission. First, it is the prime archive of STEREO telemetry and data, and serves that data to the international science community and to the general public, both through its own Web site, and through interaction with virtual observatories (see Sect. 5.5.1). It is also the collection site, processing center, and distribution point for STEREO space weather beacon data. Science coordination between the STEREO instruments, and between STEREO and other observatories, is performed through the SSC. Finally, the SSC is the focal point for education and public outreach activities.

The heritage of the SSC arises from experience acquired in operating earlier solar physics payloads: NASA’s Solar Maximum Mission (SMM) (Bohlin et al. 1980), and the NASA/ESA Solar and Heliospheric Observatory (SOHO) (St. Cyr et al. 1995). In particular, we are building on the experience of the Solar Data Analysis Center (SDAC), which grew out of the earlier SMM Data Analysis Center to support many other missions, including SOHO.

The task of the SSC is not exactly the same as that of the SMM or SOHO Experiment Operations Facilities (EOF). In many ways, it’s much simpler, because the SSC has no direct role in instrument commanding. However, the other major roles of the SOHO EOF—science coordination, data archiving, and public outreach—are duplicated in the SSC. In addition, the SSC has the completely new responsibility of collecting and processing space weather beacon data, as discussed in Sect. 5.3.

3.1 Local Area Network Architecture

A major design objective of the SSC was to build as much as possible on existing facilities within the NASA GSFC Solar Physics Laboratory. Not only does this result in a considerable cost savings, but it also gives us a major leap forward in expertise to draw on. The primary STEREO archive will be co-located with the Solar Data Analysis Center (SDAC) which currently serves the SOHO archive, among others.

The STEREO archive will be stored on a series of external RAID storage systems, connected to servers through high-speed fiber optic switches. RAID systems provide high levels of reliability and data integrity. The use of a fiber optic switch allows several servers to all share the same data archive. Other servers will also be able to access the data through the

network, using one of the fiber-connected nodes as an NFS server. Tasks will be split between servers for load balancing and reliability. There will also be sufficient redundancy in case one or more of the servers fails. The servers will be essentially interchangeable, so that tasks can be easily redistributed to better optimize the system.

A secondary archive will be maintained in a separate building at Goddard, where the Solar Physics Laboratory is housed. This separate (and potentially smaller) archive will provide several functions. First, it will ease access to the data for SSC personnel and others in the Solar Physics Laboratory. Second, it will provide some redundancy in case the primary archive becomes unavailable. Finally, it allows Web traffic to be split up. Under nominal conditions, general information about the mission will be served from the secondary archive, while data access will be from the primary archive. The primary and secondary archives will be on completely separate networks, so one of the two archives will still be available even if the entire other network is down.

STEREO news releases, and other public affairs materials, will be served from a separate NASA-wide portal site, which will further split Web traffic. When Web traffic increases due to high-profile news stories, very little of that traffic should impact the primary archive Web server.

Data on the primary archive site will be backed up internally within the SDAC, and also delivered on a regular basis to the NASA National Space Science Data Center (NSSDC) for disaster recovery and final archive. Data on the secondary archive will be mirrored from the primary archive, and not backed up independently. Frequent backups will be made of all Web pages and software directories on both the prime and secondary server.

3.2 SSC Personnel

The STEREO Science Center is under the direct management of the STEREO Project Scientist and Deputy Project Scientist. Day-to-day operations are managed by a Chief Observer, who is primarily responsible for the science coordination aspect of the mission, and also oversees all the other SSC activities. Hardware and operating system maintenance is provided by a System Administrator, while two Senior Programmers provide general software development and maintenance. A Data Scientist assists the international science community to use the data from the mission, and assists with the science coordination. Science analysis and science planning activities will also be assisted by post-doctoral scientist during mission operations. Education and public outreach activities are assisted by a Web Designer/Graphics Artist, and a Media Specialist.

Many of the technical positions will be shared with the SDAC, while the education and outreach personnel will be shared with SOHO and Living With a Star. This provides us not only with cost savings, but also expedites the coordination and sharing of expertise.

4 Science Operations Concept

4.1 Science Planning Cycle

The STEREO science planning strategy is based on the successful system used for the SOHO mission (St. Cyr et al. 1995). SOHO started out with a series of planning meetings, beginning with quarterly long-range planning meetings, and being further refined through monthly, weekly, and finally daily meetings. STEREO will use the same basic concept; however, since the level of instrument commanding will be far less than on SOHO, the smallest increment of regular meetings during regular operations will be weekly.

4.1.1 *Science Working Group Meetings*

The STEREO Science Working Group (SWG), consisting of the STEREO Program Scientists, Project Scientist, Deputy Project Scientist, and the Principal Investigators and designated members of each of the instrument teams, will set the overall science policy and direction for mission operations, set priorities, resolve conflicts and disputes, and consider observing proposals. During STEREO science operations, the SWG will meet several times a year to consider the long-term period starting in one month's time and form a general scientific plan. If any non-routine operations are required—such as non-standard telemetry allocations—the requests must be formulated at this SWG meeting. Calibration activities, such as spacecraft rolls, will be defined.

4.1.2 *Monthly Teleconferences*

The long-term plan will be refined during monthly planning teleconference calls of the Science Operations Working Group (SOWG), composed of the PIs or their team members, together with a representative of the SSC. These teleconferences will assess progress in achieving the scientific goals of the planned investigations, and to discuss the objectives for operations starting in a month's time. This gives time for coordinated observations to be set up, and any deficiencies in observing sequences to be identified. Inputs to the monthly meeting are made by each instrument team and common objectives are identified. The output of this meeting is a schedule showing when each instrument will be operating, whether joint or individual observations are being made, ground observatory support, and a backup plan if these conditions are not met. Requirements for telemetry rate switching should be identified together with any spacecraft operations which may affect the observations, for example, momentum dumping. Conflicts between instruments for resources are resolved, and disturbances are identified.

4.1.3 *Weekly Optimization*

A weekly “virtual meeting” of the SOWG considers the week starting in approximately three days time, and this is when the detailed plans for all the STEREO instruments are synchronized. It will be convened by the SSC, and will be either a teleconference or computerized communication, depending on the complexity of that week's operations. The intention is to lay out a definitive plan with timings, flag status, disturbances, etc. This meeting will have the conflict-free DSN schedule available.

Any conflicts in the planned use of the spacecraft command buffers will be resolved during the weekly optimization meeting.

The weekly meeting will also be the forum for instrument teams to give advance notice of any special operations or changes to the plan for future weeks. The DSN forecast schedule will be available for the week commencing in 10 days time and the strawman proposal will be available for the week following that.

While the Project Scientist will be responsible for the implementation of the scientific operations plan, execution of the plan will be carried out by the SOWG, led by the SSC.

4.2 Routine Weekly Schedule

The weekly planning process is illustrated in Fig. 4. Operational weeks are defined to run from Monday to Sunday. The planning process starts two weeks ahead (marked “Plan W”)

Weekly Planning Timeline

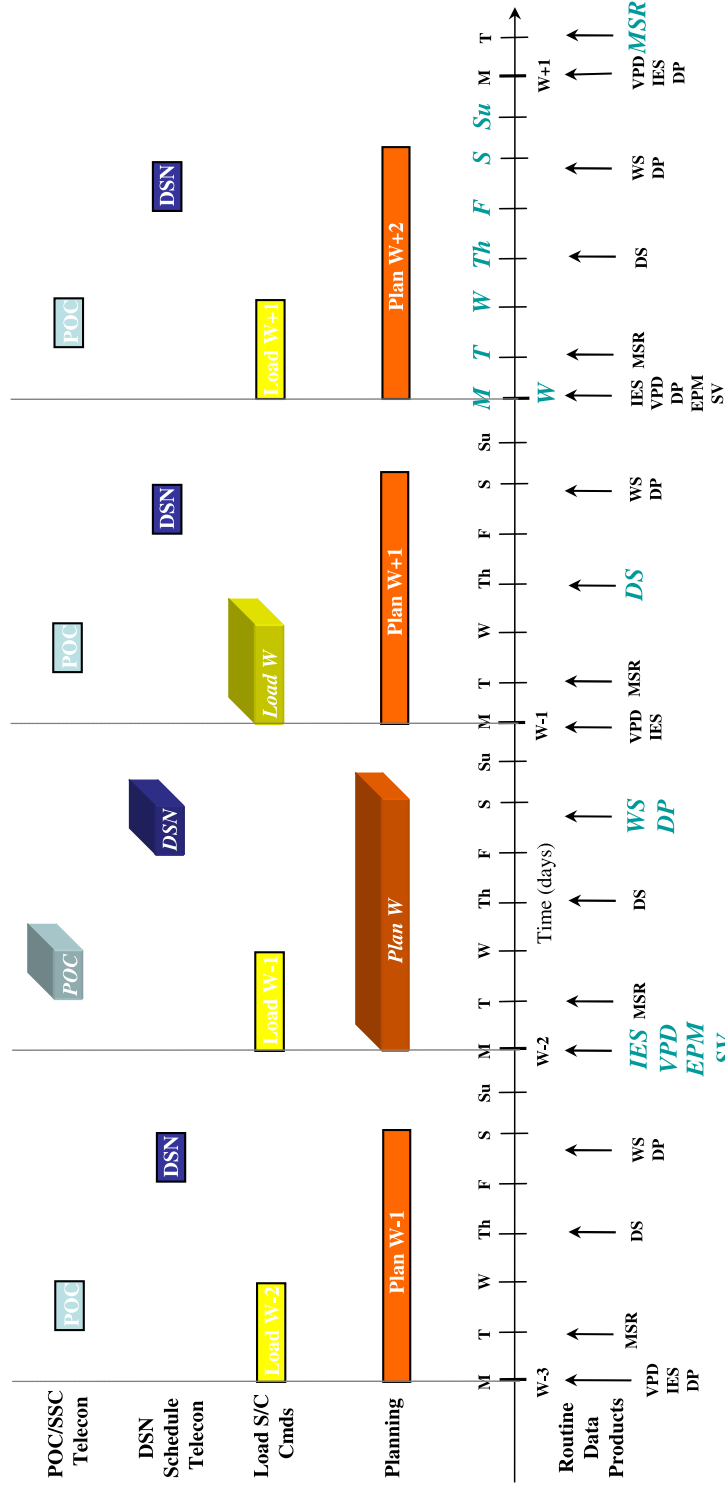


Fig. 4 Weekly planning timeline. The week being planned is at the far right, and the highlighted boxes represent the planning and commanding activities for that week. The acronyms along the bottom represent the availability of various ancillary data products

in the diagram). At that time the relevant ephemeris products (EPM and SV), Viewperiod files (VPD), DSN Schedule (DS), Momentum Dump Predictions (DP), and Instrument Event Schedules (IES) are delivered to the MOC and distributed to the instrument teams. The MOC Status Report (MSR) covering the previous week is also generated. A weekly teleconference is held between the MOC, SSC, and instrument teams to coordinate shared resources and events, such as telemetry rates and instrument rolls. A separate weekly teleconference is held between the MOC and DSN to determine the daily pass schedule. Command loads are verified using a software simulator, and a Weekly Schedule (WS) is published. The uplink of the verified command load occurs in the week prior to the week being planned.

On a daily basis an assessment is made of telemetry data from the previous day, to review any alarms, plots of selected telemetry points, and the as-run track plan. Commands are checked through the software simulator to verify the command load, constraints, and C&DH memory states. A two-person check is made of each command load.

Under normal operations, each observatory will have one pass per day. An effort will be made to have these passes occur during normal east coast work hours whenever possible. The passes for two observatories are planned to be consecutive, although some overlap is possible.

4.3 Infrastructure for Campaign Coordination

4.3.1 *Network Exchange of Information and Data*

The primary mode for campaign collaborators to access information about the STEREO science schedule will be through the World Wide Web. The STEREO schedule will be distributed on the Web in both text and graphical formats.

Information will also be passed through e-mail lists, using a list server program such as Majordomo. Sufficient protections will be put on the lists to keep spam mail off the list, and to keep outsiders from learning the e-mail addresses of users.

4.3.2 *Telephone and Fax*

Besides the network interfaces, the SSC will also have phone and fax facilities available for information transfer to and from campaign collaborators. Conference call facilities are also available.

4.3.3 *STEREO Data Archive*

The STEREO data archive at the SSC, described more completely in the following, will play an important role in campaign coordination. As well as being the site where observers will retrieve the most recent schedules, the latest observational data will be available to assist in planning.

4.4 Planning for Collaborative Observations

STEREO will participate in the successful Joint Observation Program (JOP) system used by SOHO and several other missions. Having a combined JOP system facilitates the sharing of information between missions, as well as providing a unified interface to researchers. Observers who wish to make collaborative observations with STEREO should first write up a draft summary of their plans, including science goals, dates, observing plans, and collaborating observatories. Detailed information about how to write up the JOP description is

given on the SSC Web site at stereo-ssc.nascom.nasa.gov/resources.shtml. Observers who are unfamiliar with the instrument capabilities should contact the instrument teams first to make sure that the instrument is capable of the planned observations. Once the JOP write-up is ready, it should be sent via e-mail to stereo-ssc@listserv.gsfc.nasa.gov. The SSC will forward copies of the message to the relevant instrument teams, but the authors are welcome to contact key members in the teams directly, so long as they keep the SSC informed as well.

To determine how much advance notice is required, one should refer to the STEREO planning cycle described earlier. The initial notification is recommended before the Science Working Group meeting, but that won't always be possible. At the very least the request should come in at least one to two months before the proposed observations, to make sure that it can be discussed at the monthly teleconference. Detailed plans for the observation should be in hand at least two weeks ahead of time to fit within the STEREO planning process.

Most of the STEREO observations are made in a synoptic mode. JOPs should be considered to cover not only the cases where special observations are requested, but also when the normal synoptic observations from STEREO are essential to an observing program. The JOP write-up will ensure that the instrument teams are aware of the collaborative observations, so that other activities such as calibrations do not interfere. The JOP also serves as a mechanism for organizing the collaborative analysis of data from multiple sources.

5 STEREO Data Products, Archiving, and Access

5.1 Telemetry

The MOC stores telemetry packets from the two STEREO spacecraft for 30 days, during which these data are accessed by the instrument teams for processing, and mirrored over to the SSC for permanent storage. A socket interface allows the instrument teams and the SSC to copy packets in real time, and to play back earlier periods still stored at the MOC. The final telemetry are distributed as a secure file transfer.

5.2 Science Processed Data

Each instrument team processes at their home institutions their own telemetry into higher level data files, which are then copied to the SSC for permanent archiving and serving to the community. This process is illustrated in Fig. 5. The SSC is also working with various organizations, such as the Rutherford Appleton Laboratory (RAL) in England, and the Multi-Experiment Data and Operation Centre (MEDOC) in France, to act as mirror sites for the STEREO data.

SECCHI images, and S/WAVES radio data, will be available in detector units, with software available to convert to a higher level of calibration (see Sect. 5.5.3).

Data from the IMPACT and PLASTIC instruments will have calibrations applied to them, to convert from detector units into physical quantities. This process is expected to take about two months. Besides the full-resolution data, lower-resolution summary data will be generated, and the IMPACT and PLASTIC data will be merged to produce higher-level products (e.g., shock identifications and characterizations). These higher level products will be available from the Space Science Center of the University of California at Los Angeles.

Together with the science data files, each team will produce summary images or plots, and will process their data to generate event lists.

Data Flow/SSC Block Diagram

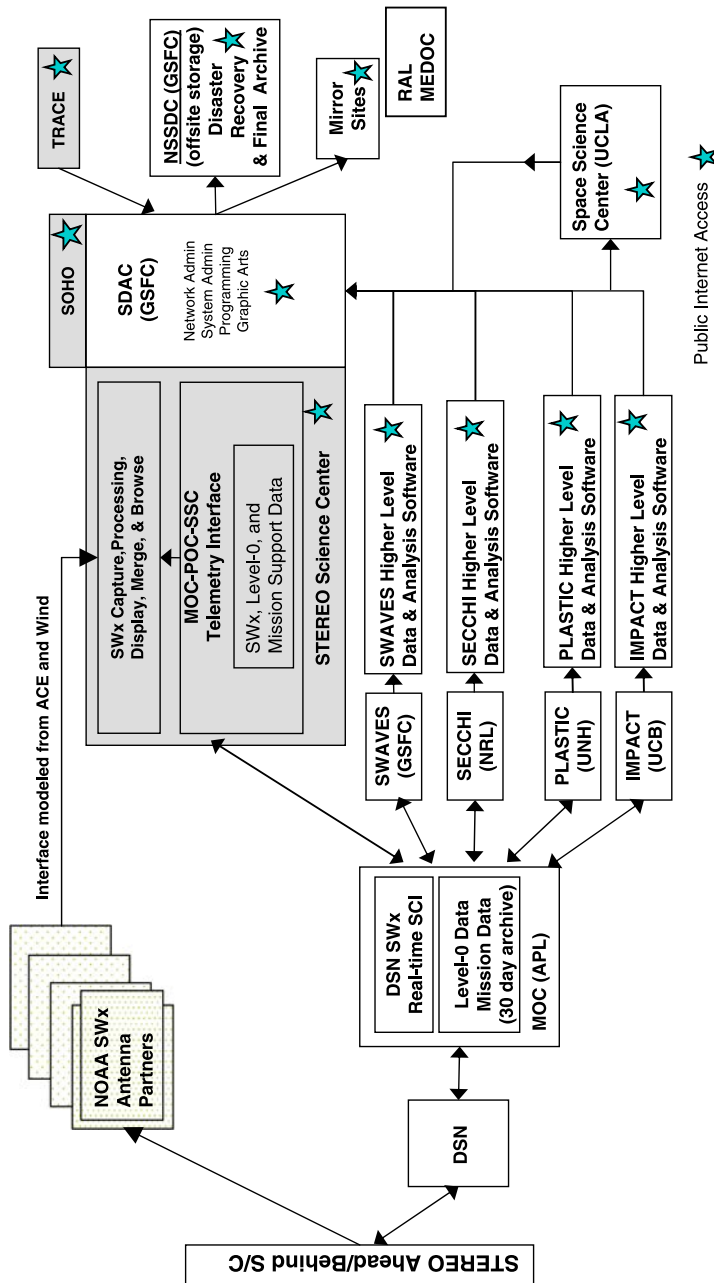


Fig. 5 Data processing flow diagram. Spacecraft telemetry is processed by the instrument teams into higher level products, which are transferred to the STEREO Science Center for distribution and archive. Data are also available from the instrument teams home institutions

Space Weather Beacon Processing

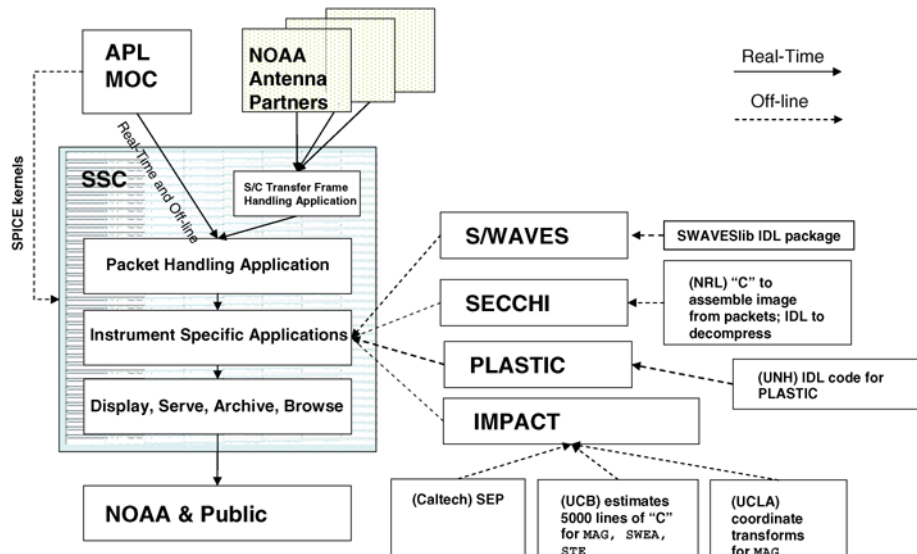


Fig. 6 Beacon processing flow diagram. Real-time telemetry packets, and interim beacon frames from NOAA Antenna Partners, are merged together into a combined telemetry stream, and processed using software provided by the instrument teams

5.3 Space Weather Beacon Data

Along with the normal science telemetry, the instruments on the two STEREO spacecraft will generate a special low-rate telemetry stream, known as the space weather beacon. Outside of DSN contacts, this space weather beacon stream will continue to be broadcast at a rate of approximately 633 bits per second. Various antenna partners around the world, coordinated by the National Oceanographic and Atmospheric Administration (NOAA), will collect this telemetry and pass it on to the SSC in near-real-time via a socket connection over the open Internet. The SSC will collate these data from the antenna partners, sort the packets together into time-order, and run software provided by the instrument teams to process this telemetry into data files. These data will be put on the SSC Web site at stereo-ssc.nascom.nasa.gov in near-real-time, within five minutes of receipt of all needed telemetry. The space weather beacon data flow is shown in Fig. 6.

5.4 Ancillary Data

As well as the level-0 telemetry files, the STEREO Data Server at the MOC will make other data products available for mission planning purposes. These products include ephemeris files and other DSN products, observatory and instrument schedules, telemetry dictionaries, status reports, log files, and converted spacecraft housekeeping files. The most current files will be available from the STEREO Data Server, while the STEREO Science Center will serve as the long-term archive.

5.4.1 SPICE Ephemeris Products

The STEREO orbit and attitude data are provided as “SPICE kernels.” SPICE (for Spacecraft, Planet, Instrument, Camera-matrix, and Events) is a software package provided by the Jet Propulsion Laboratory Navigation and Ancillary Information Facility, and is used by the Flight Dynamics Facility to track the two STEREO spacecraft’s orbits and attitudes. The SPICE package is available for Fortran, C, and IDL on a wide variety of computer platforms. Simple software calls are able to retrieve the spacecraft orbital position and pointing attitude in most standard heliospheric coordinate systems.

5.5 STEREO Data Archive

The STEREO Science Center will serve as the long-term archive for STEREO data during the mission. At the end of the active life of the data, all relevant mission data will be transferred from the SSC to the NSSDC for permanent archive. Data archived at the SSC will include:

- Level-0 telemetry files
- Ancillary data files from the STEREO Data Server
- Science processed data delivered by the instrument teams
- Space Weather Beacon products.

The archive is stored on a series of RAID-5 file systems mounted via fiber-channel and NFS on the SSC workstations. The file systems are backed up with nightly increments to external portable RAID systems, which are swapped monthly with offsite spares.

Access to the data files is through the SSC Web site at stereo-ssc.nascom.nasa.gov. A small subset of the ancillary data files, in particular the telemetry dictionaries, are archived but not made available on the Web. Otherwise, the bulk of the ancillary files are presented in the same directory structure as they appear on the STEREO Data Server. Level-0 telemetry files are served separately, organized into directories by observatory (Ahead or Behind), instrument, year, and month. The same organization is used for the space weather beacon products. Processed science data from each instrument is maintained in the same directory structure as it was delivered to the SSC.

5.5.1 Interaction with Virtual Observatories

The STEREO archive will be completely integrated with the Virtual Solar Observatory (VSO) (Gurman and Davey 2004). The entire design of the archive and data access system is being developed in parallel with the VSO design effort, and we are sharing personnel with the VSO.

In addition, STEREO will interact with the Virtual Heliospheric Observatory (VHO). Interacting with both virtual observatories is a complementary approach: the VSO interface will emphasize the imaging data, while the VHO interface will emphasize the in situ data. Personnel on the STEREO/IMPACT team are also involved with VHO.

Interactions with other virtual observatory efforts—for example the European Grid for Solar Observations, or the Virtual Space Physics Observatory—will be handled through one or the other of the two virtual observatories described above.

Web access to the VSO is through virtualsolar.org, and to the VHO through vho.nasa.gov.

5.5.2 Uniform Data Format

Data from the STEREO instruments will be available in one of two standard file formats. Image data from the SECCHI instrument will be provided in the Flexible Image Transport System (FITS) format (Hanisch et al. 2001), while data from IMPACT, PLASTIC, and S/WAVES will be provided in the Common Data Format (CDF) (Goucher et al. 1994). Use of standardized formats simplifies the data analysis, and opens the data to a wide range of software tools. Conversion programs between the CDF and FITS formats are available.

5.5.3 Data Analysis Software

During the planning for the SOHO mission, it was realized that there were a number of useful data analysis packages that had been developed for previous missions, and that it would be highly advantageous to collect all these packages into a single system. This led to the development of the Solar Software Library (Freeland and Handy 1998), also known as SolarSoft or SSW. STEREO software, both for the mission as a whole, and for the individual instruments, will also be delivered as part of the SolarSoft package. Thus, users will have a single unified way of downloading software for each of the STEREO instruments, as well as for other solar missions.

Another advantage of being part of the SolarSoft library is the rich collection of software already existing in the library, which is available both to the software developers of each instrument team, as well as to the individual scientist.

Within the SolarSoft library will be a separate directory tree for STEREO software. Beneath this top-level STEREO directory will be separate directories for each of the four STEREO instruments, for the SSC, plus a generic (“gen”) STEREO-wide directory. The main concentration will be on IDL software, but the SolarSoft system can also be used to distribute software written in other languages, such as Fortran or C source code.

Acknowledgements The authors thank Joseph Gurman and Peter Schroeder for helpful discussions on the interaction between the STEREO Science Center and the Virtual Observatories.

References

- J.D. Bohlin, K.J. Frost, P.T. Burr, A.K. Guha, G.L. Withbroe, Sol. Phys. **65**, 5–14 (1980)
- A. Driesman, S. Hynes, *Space Sci. Rev.* (2007, this volume)
- S.L. Freeland, B.N. Handy, Sol. Phys. **182**, 497–500 (1998)
- G. Goucher, J. Love, H. Leckner, in *Solar-Terrestrial Energy Program. The Initial Results from STEP Facilities and Theory Campaigns*. Proceedings of the 1992 STEP Symposium/5th COSPAR Colloquium, 1994, p. 691
- J.B. Gurman, A.R. Davey, in *Proceedings of the SOHO 15 Workshop: Coronal Heating*, 2004, pp. 583–586
- R.J. Hanisch, A. Farris, E.W. Greisen, W.D. Pence, B.M. Schlesinger, P.J. Teuben, R.W. Thompson, A. Warnock III, Astron. Astrophys. **376**, 359–380 (2001)
- O.C. St. Cyr, L. Sánchez-Duarte, P.C.H. Martens, J.B. Gurman, E. Larduinat, SOHO Ground Segment, Science Operations, and Data Products. Sol. Phys. **162**, 39–59 (1995)

The Solar Terrestrial Relations Observatory (STEREO) Education and Outreach (E/PO) Program

L.M. Peticolas · N. Craig · T. Kucera · D.J. Michels ·
J. Gerulskis · R.J. MacDowall · K. Beisser ·
C. Chrissotimos · J.G. Luhmann · A.B. Galvin ·
L. Ratta · E. Drobnes · B.J. Méndez · S. Hill ·
K. Marren · R. Howard

Originally published in the journal Space Science Reviews, Volume 136, Nos 1–4.
DOI: [10.1007/s11214-007-9287-y](https://doi.org/10.1007/s11214-007-9287-y) © Springer Science+Business Media B.V. 2007

Abstract The STEREO mission's Education and Outreach (E/PO) program began early enough its team benefited from many lessons learned as NASA's E/PO profession matured. Originally made up of discrete programs, by launch the STEREO E/PO program had developed into a quality suite containing all the program elements now considered standard:

L.M. Peticolas (✉) · N. Craig · J.G. Luhmann · B.J. Méndez
Space Sciences Laboratory, University of California at Berkeley, 7 Gauss Way, Berkeley,
CA 94720-7450, USA
e-mail: laura@ssl.berkeley.edu

T. Kucera · R.J. MacDowall
NASA Goddard Space Flight Center, Code 682, Greenbelt, MD 20771, USA

D.J. Michels · R. Howard
Center for Space Research, Naval Research Laboratory, Washington, DC 20375-5320, USA

J. Gerulskis
Christa McAuliffe Planetarium, 3 Institute Drive, Concord, NH 03301, USA

K. Beisser · K. Marren
Applied Physics Laboratory, Johns Hopkins University, 11100 Johns Hopkins Rd., Laurel, MD 20723,
USA

C. Chrissotimos
Science Systems and Applications, Inc., 3 Cedar Brook Drive, Cranbury, NJ 08512, USA

A.B. Galvin
Space Science Center, University of New Hampshire, Morse Hall, Durham, NH 03824, USA

L. Ratta
Integrated Communications Technology, Inc., Greenbelt, MD 20770, USA

E. Drobnes
ADNET Systems, Inc., Rockville, MD 20852, USA

S. Hill
RS Information Systems, Greenbelt, MD 20771, USA

education workshops, teacher/student guides, national and international collaboration, etc. The benefit of bringing so many unique programs together is the resulting diverse portfolio, with scientists, E/PO professionals, and their education partners all of whom can focus on excellent smaller programs. The drawback is a less cohesive program nearly impossible to evaluate in its entirety with the given funding. When individual components were evaluated, we found our programs mostly made positive impact. In this paper, we elaborate on the programs, hoping that others will effectively use or improve upon them. When possible, we indicate the programs' effects on their target audiences.

Keywords Education · Outreach · Sun: coronal mass ejections (CMEs) · Sun: magnetic fields · Sun: particle emission · Sun: solar-terrestrial relations

PACS 01.00.00 · 01.30.La · 01.30.Lb · 01.30.Os · 01.40.-d · 01.40.Di · 01.40.E- · 01.40.Ek · 01.40.G- · 01.40.Gb · 01.40.J- · 01.40.Jc · 01.40.Jh · 01.50.-i · 01.50.F- · 01.50.Fh · 01.50.H- · 94.05.-a · 94.05.Sd · 95.55.Ev · 95.55.Fw · 96.50.Bh · 96.50.Ci · 96.50.Pw · 96.50.Vg · 96.50.Wx · 96.60.Hv · 96.60.Ph

1 Introduction

While the STEREO spacecrafts and instruments were being built and tested for launch and operation, the STEREO Education and Public Outreach (E/PO) program was preparing future teachers, in-service teachers, students, science centers, and the general public for the launch and subsequent science coming from STEREO. This article describes these prelaunch E/PO activities and provides a section of a much larger paper in this issue of *Space Sciences Review* describing the STEREO Mission and Science. Reflecting on these activities, we hope to provide scientists who have not participated in E/PO activities with an understanding of E/PO, to share with future E/PO professionals some of the paths to the final product or program, and to let solar and space scientists and E/PO professionals know what E/PO resources are available from the STEREO mission.

1.1 Education and Public Outreach at NASA's Science Mission Directorate

NASA's role in education is often under discussion and review. In 1996 the NASA office, then known as the Office of Space Science (OSS), brought together scientists and educators and developed a plan to implement a bold and innovative approach to education and public outreach (E/PO) (OSS-SSAC E/PO Task Force Report 1996). This approach operated on the premise that:

...achieving genuine success in affecting the quality of science, technology, engineering, and mathematics education in America will not be won through short-term activities with immediate results, but rather through a long-term commitment requiring a sustained effort in education and public outreach (SSAC E/PO Task Force Report 2003).

The idea was “to more effectively engage and involve the space science community in support of the nation’s future interests and needs in science education” (Cooper et al. 2004). Since then, NASA has required that each satellite mission use a small percentage (around 1%) of the mission budget, excluding launch costs, for E/PO projects.

In order to help these OSS E/PO projects focus on customer needs (i.e., the needs of teachers, students, and the public), Morrow (2000) published a short report on the categorization of E/PO activities and materials. These three categories are: formal education, informal education, and public outreach. Formal education seeks to reach grades K-14 teachers and students in relation to the classroom. Informal education seeks to engage the public in science education settings—such as after school programs, scouting organizations, and science centers. Public outreach is meant to reach the public in their own environment, such as through educational television shows, games, web pages, or radio shows. Morrow (2000) pointed out that many scientists do not understand the distinction between public relations (PR) and E/PO public outreach. The difference is mostly in the intent: E/PO public outreach aims to educate the public further about science, whereas PR conveys the work done at NASA.

Part of effective E/PO is ensuring the scientists are able to connect their work and research with educators and the public. NASA's mandate that a small percentage of space science mission budgets fund formal, informal, and public outreach E/PO opportunities—closely tied to the NASA satellite missions—is one way to ensure that scientists are more directly involved in educating students, teachers, and the public. A poll of scientists in 2001 found that 42% engaged in no public outreach (NSB Report 2004). More scientist participation in public outreach can ensure that the “customers” of the E/PO program (such as teachers or the public attending science centers) receive correct scientific information based on the most current data and learn about the most recent NASA science discoveries. In 2002, the Solar and Space Physics Survey Committee of the National Research Council found that “NASA-funded E/PO projects encourage and permit researchers to collaborate with educators on a wide variety of educational activities related to solar and space physics, many of which have a substantial impact on public awareness of issues in solar and space physics and their link to broader science and technology concerns.” (SSPSC/NRC 2002). This indicates that, in general, having scientists work with educators in NASA's space science programs is a successful model.

Accurate space science information and inspirational discoveries also potentially help ameliorate the predicted upcoming crisis in providing a scientifically and technically literate workforce for the twenty-first century. In 2004, the National Science Foundation (NSF) reported “US 12th graders recently performed below the international average for 21 countries on a test of general knowledge in mathematics and science” (NSB Report 2004). NSF also reported “in 1999, only 41% of US 8th grade students received instruction from a mathematics teacher who specialized in mathematics; considerably lower than the international average of 71%” (NSB Report 2004). This science literacy crisis has alarmed so many scientists, educators, and technologically dependent companies that senators of the Committee on Energy and Natural Resources and representatives of the House Committee on Science asked the National Academies for a report on a strategy to enhance the science and technology enterprise so the U.S. can successfully compete, prosper, and be secure in the global community of the twenty-first century (NAS Report 2005).

The NSB Report (2004) furthermore examined the public understanding and support for science and technology (S&T). The report's findings help us to understand what the public needs in terms of science education, as well as how the public continues to learn about science outside of school. The report provided the following information.

- Although Americans express strong support for S&T, they are not very well informed about these subjects.
- The popularity of science museums and books suggests that people are interested in science even though they may not be following science-related news.

- The Internet is the preferred source for people seeking information about specific scientific issues.

This NSB Report (2004) underscores the needs facing the nation and provides some guidance on how NASA E/PO programs can help both students and the public.

The 2006 review criteria for most NASA E/PO proposals were adapted to address some of the needs of students and public mentioned in the NSF report. Proposals must focus on the needs of the audience associated with the educational activities or products. Partnerships must be developed with other education institutions in order to leverage the small amount of money NASA provides for E/PO programs, as well as to ensure that the developed activities and products are sustained after the NASA funding is gone. Partnerships also allow for a broader dissemination of the work done by the scientists and E/PO specialists. Furthermore, all proposed efforts must describe how they will be evaluated to determine if the goals of the proposal have been met. Demonstrable goals include how NASA content, people, or facilities will be used; how the proposed activities and products will attract diverse populations to careers in science, technology, engineering, and mathematics (STEM); and how the proposed program will involve underserved and/or underutilized groups in STEM. STEREO E/PO was not reviewed under these criteria, but as the STEREO E/PO program has matured with the NASA E/PO profession, several of the STEREO E/PO programs made an effort to meet these criteria.

1.2 STEREO Education and Public Outreach Program

In 1999, each STEREO instrument team—In-situ Measurements of Particles and CME Transients (IMPACT), Plasma and Supra-Thermal Ion Composition (PLASTIC), Sun Earth Connection Coronal and Heliospheric Investigation (SECCHI), and STEREO Waves (SWAVES)—submitted an E/PO proposal for 1% of the respective instrument budget. These instrument teams, together with the STEREO project office at Goddard and E/PO efforts of the spacecraft team at the Advanced Plasma Laboratory (APL), make up the STEREO E/PO program. Because of the array of groups in this program, many different types of programs and resources have been developed. However, until close to launch these groups operated completely independently. Near and after launch, the various STEREO E/PO groups began to share their products and programs, enhancing the independent programs developed by each group. This paper will reflect on this “loose federation,” while providing an overall view of the program.

After reviewing the intent and evolution of these different programs, it is clear that the STEREO E/PO program had several goals for the E/PO activities in Phases B, C, and D before launch:

1. In formal education, we aimed to educate teachers and students nationally about the science of the Sun, space science technologies, and mathematical tools used in space weather research.
2. In informal education, we aimed to inspire science center and planetarium attendees and artists to learn more about solar science and STEREO.
3. In public outreach, we aimed to share the STEREO mission and its science with the public, primarily through the Internet and radio.
4. We aimed to inspire a variety of underserved groups, in particular girls, Hispanics, and African Americans, to learn more about solar science and magnetism.

STEREO scientists, engineers, and E/PO specialists have been directly involved all of the STEREO activities and products. Details of the programs designed to meet these goals are

described in the following. Program evaluations results are shared when available. (Note that the URLs for websites referenced throughout this paper can be found in Sect. 4.)

2 Formal Education Activities

From discussions with teachers and written feedback from educators in our formal education activities, it is clear that we are providing some needed content in physics, using the Sun as inspiration. Many of these teachers are not trained specifically in science, and even fewer in physics. As mentioned earlier, the U.S. is well behind the rest of the world in STEM education. We cannot claim to have solved this huge problem, but we have helped by directly providing more than 1,000 pre- and in-service teachers and hundreds of students with content and hands-on lessons to enhance their teaching and learning about the Sun, magnetism, gravity, the electromagnetic spectrum, atoms, orbits, and engineering. We have done this through: (1) a one-semester undergraduate, pre-service teacher class about physics using the Sun as the focus of the classes, held once a year for four years; (2) four years of in-service teacher professional development (PD) workshops, which varied in length from one-hour to two-day workshops; (3) STEREO-developed middle school, high school, and undergraduate lessons, and (4) special events for middle and high school students and their teachers.

2.1 Pre-service Teacher Professional Development Workshops

Two simultaneous events resulted in the creation of the Teachers of Physical Science (TOPS!) program, a physics course designed to teach pre-service teachers basic physics concepts using NASA research on the Sun as inspiration: (1) The education department at the Catholic University of America (CUA) in Washington, D.C., needed a course on physical science for their pre-service teachers. (2) After talking with teachers at a variety of education and outreach workshops, the STEREO team at the nearby Naval Research Laboratory (NRL) realized that teachers needed more background knowledge about physics than they got in the short teacher professional development (PD) workshops. Through a connection between these institutions, TOPS! was born. It was designed to produce top teachers of physical science by leveraging a collaboration between the departments of Education and Physics at the CUA, the NRL, and the NASA Goddard Space Flight Center. Together, these partners developed a basic physical science course in the Physics Department at CUA to meet the specific needs of undergraduate, pre-service teachers majoring in Early Childhood and Elementary Education.

The course, called “Sun and Earth: Concepts and Connections,” is a four-credit physics course in which the wonders of Sun–Earth Connection physics serve as a vehicle for teaching a limited number of the fundamental principles of physical science. Hands-on experiments, computer simulations, analysis of real NASA data, and vigorous seminar discussions are blended in an inquiry-driven curriculum to instill confident understanding of basic science and modern, effective methods for teaching it. (See the course outline in Fig. 1). Three faculty members from physics, education, and research teach the course simultaneously to provide students with perspectives from all three realms.

Both course content and the pedagogic techniques reflect and specifically reference the *National Science Education Standards* (NSES) (NRC 1996) and the *Benchmarks for Science Literacy* (AAAS 1993). Through Internet connections and the participation of space scientists in classroom discussions, future teachers work with real data from NASA satellites to understand how key scientific concepts are expressed on local, global, and astronomical scales. Applying these principles to various aspects of Sun–Earth Connection physics

Fig. 1 Course Outline for the TOPS! 4 credit physics course

<p>Magnetism and Gravity: Force Fields—Mass and electrical charge distort space and shape the universe.</p> <p>Our Star, the Sun: Anatomy of the Sun—Sunspots, solar magnetism, solar layers</p> <p>Sun–Earth gravitational interaction maintains Earth in its orbit: <i>1. Newton's conquest: the universal gravitational force</i>—forces and motion, Newton's laws. <i>2. The solar system was formed by and is ruled by gravity</i>—gravitational condensation, atoms, stars, rotations, and orbits in the solar system</p> <p>Electromagnetic radiation transports energy from the Sun to the Earth: <i>1. Electromagnetism: Triumph of 19th century science</i>—charge, currents, circuits, bar magnets, electromagnet. <i>2. Waves of energy: heat, light, and color. Maxwell's rainbow</i></p> <p>Geology and Geography—Earth as we know it, and what we make of it: <i>1. Earth in the solar system</i>—rotation (day and night) and orbital motion (seasons and years). <i>2. Structure of our planet</i>—core, mantle and lithosphere; oceans and continents; tectonic motions and disruptions; magnetic footprints on the ocean floor. <i>3. Pressure and temperature</i>—the atmosphere, ionosphere, and “empty” space. <i>4. Earth’s magnetic field</i>—Gilbert’s <i>De Magnete</i>: a masterpiece of analysis</p> <p>Swimming in the Sun—the solar wind showers Earth with electrons and protons—<i>1. How big is the Sun really?</i> Gravity and our place in the galaxy. <i>2. How hot is the Sun and how hot is that???</i>—our star’s vast atmosphere, solar storms, aurorae, and geomagnetic storms.</p>
--

Fig. 2 TOPS! future K-8 teachers learn design and characteristics of a simple telescope and how to use it for direct observations and projection of solar images



illustrates how a genuine understanding of even the simplest of physical principles can illuminate and integrate our vision of the world around us. In Fig. 2, teachers literally change their view of the world around them, using simple solar telescopes. After four years, this one-semester course is now required for all incoming General Education majors at CUA, leading to a course that will be sustained for years to come.

The program exposes these nonscience students to the excitement and satisfaction of research, with enough emotional impact and sufficient contextual skill that most are enabled to inspire and inform the next generation of students. One teacher, who took the course

Fig. 3 Teacher comments from workshop evaluations

“I learned a tremendous amount of science and also some great teaching tools.”
“I like the different displays to demonstrate the magnetic fields.”
“It was one of the best workshops I have ever attended.”
“Thank you for the CD and other materials.”
“What are the practical uses for students—especially for inner city kids?”
“I would have loved an electronic copy of the PowerPoint presentations.”
“Just needed more time for me to understand it enough to teach it well.”
“I am glad I attended this (workshop) a second time. I feel like I have a much better grasp now.”

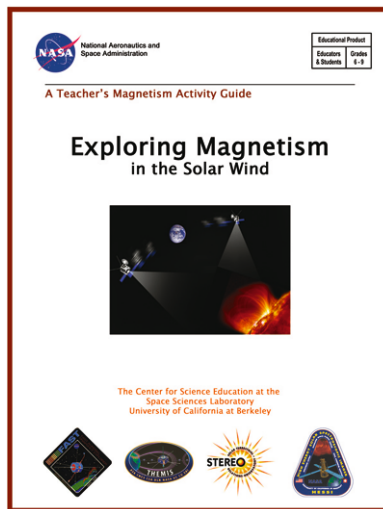
in spring 2005, says what she learned in the course proved invaluable when she did her student teaching in fall 2006, at a public charter school in the Columbia Heights section of Northwest Washington, DC. Another teacher claimed in an interview after she graduated, “Without a doubt, Sun and Earth changed the way I see science.” Several teachers have contacted the TOPS! program to ask for additional STEREO and NASA materials to use in their classrooms.

The STEREO team at NRL aims to expand the TOPS! program to a broader collaboration in the Washington, DC, area teacher preparation community through partnerships with other universities. This team also plans to develop a *Classroom Teacher’s Guide to the Sun*, a manual for teaching the Sun at K-8 levels and companion to the TOPS! teacher education course. The SECCHI E/PO program at the Naval Research Laboratory (NRL) led this endeavor.

2.2 In-Service Teacher Professional Development Workshops

The STEREO E/PO program at the University of California, Berkeley (UCB) has partnered with several other NASA mission E/PO programs and the Sun-Earth Connection Education Forum (SECEF) to hold teacher professional development (PD) workshops around the country. In the STEREO prelaunch years, 1,220 teachers participated in classroom lessons and science content on magnetism, the Sun, geospace, and the STEREO mission in 29 in-service PD workshops. These workshops were either part of national or state science teacher conferences, such as the National Science Teacher’s Association (NSTA) conference, or part of an ongoing effort to train teachers who come to the Space Sciences Laboratory (SSL) at UCB. The PD workshops varied from one-hour workshops to two-day workshops for graduate credit from California State University East Bay. In most of these workshops, the teachers modeled selected activities from the IMPACT E/PO teacher guides described in Sect. 2.3. Evaluation questionnaires indicated that more than half of these teachers had large populations of Hispanic and African-American students in their classrooms. The evaluations, developed with the help of professional evaluators, also indicated that more than 70% of participants in all of the workshops indicated they were “very likely” or “certain” to use the presented materials in their classrooms. However, 50% of the teachers indicated that lack of money to buy magnets, compasses, batteries, and circuits would be a difficult barrier to implementing the magnetism lessons in their classroom. A sampling of some of the teacher feedback demonstrates the successes and challenges of these workshops, as shown in Fig. 3. These types of teacher workshops will continue throughout the life of the STEREO mission and will continue to be improved using the teacher feedback. Information on when and where these workshops will be held can be found on the IMPACT E/PO website.

Fig. 4 Exploring Magnetism in the Solar Wind Teacher's Guide cover



2.3 Development of Classroom Materials

The STEREO E/PO team has developed and created various products for the classroom: teacher guides and classroom activities, web pages for use in the classroom, CD-ROMs and a 3-D poster with STEREO science and mission content, STEREO satellite cut-out design booklets, and STEREO flyers. The CD-ROMs, poster, satellite booklets, and flyers are also meant for the public and are described in Sect. 4.2 for the Public Outreach programs. Materials were also developed and created for the Space Academy and the Space Weather Challenge mentioned in Sect. 2.4. The team felt the creation of these products was important to the STEREO E/PO in order to bring the latest science and mission information into the classroom. Teachers have told STEREO E/PO scientists that students are more engaged in science when they know they are being taught the most up-to-date science and feel that they are part of a NASA mission.

The STEREO E/PO team at the University of California, Berkeley (UCB) created two guides for middle school teachers, “Exploring Magnetism” and “Exploring Magnetism in the Solar Wind,” which are sequential. The cover of the latter is shown in Fig. 4. The goal of the activities is that, through inquiry-based activities, students develop a deeper understanding of electromagnetism and engineering processes related to STEREO. In these guides, students map magnetic field lines around bar magnets, build circuits to map magnetic field lines around coils and explore the effects of increasing current and coil turns relevant to magnetic field strength, learn about the Sun–Earth connection through lecture, brainstorm a design to measure the Sun’s magnetic field, and report on their design to their classmates.

These guides were in part developed using the concept of “backward design” (Wiggins and McTighe 1998). In backward design, assessment drives instruction, leading to a lesson with a built-in way to determine whether a student has actually learned these ideas. The lessons were tested in several classrooms and are tied to the NSES (NRC 1996). A panel of teachers and scientists reviewed these teacher guides as part of the NASA Education Product Review conducted by the Institute for Global Environmental Strategies (IGES). The guides were rated “Excellent” and were thus modeled with 41 NASA’s teacher-educators in the Aerospace Education Services Program (AESP), Education Resource Center (ERC) educators, and broker/facilitators in November 2004. The AESP educators conduct teacher

professional development around the country, so this opportunity allowed for a wide dissemination of these guides. The guides were also modeled and disseminated in the many teacher PD workshops discussed in Sect. 2.2. The IMPACT E/PO group led the development and printing of these guides. The printing of the guides was possible through a collaboration of several NASA mission E/POs. The full guides and activities are available online on the IMPACT E/PO web site (the URL is given in Sect. 4).

The STEREO/WAVES (S/WAVES) E/PO program has developed a series of classroom-oriented S/WAVES radio models. The simplest version is used to demonstrate the directionality of radio waves and how this permits triangulation of the sources. Using these models, teachers can help students learn about the following concepts in the given grade levels:

- (5–8) monopoles or linear dipoles: demonstrate *directionality* of (AM) radio waves, *triangulation measurement concepts*.
- (5–8) triad antenna (three orthogonal antennas, like the S/WAVES antennas) shows realistic spacecraft system; measurement of angles leads to investigation of basic *geometry & trigonometry*.
- (9–12) Model plus triad antenna equations provide motivation for *spherical trigonometry* and more advanced *algebraic equation solving*.

The STEREO project office E/PO at the Goddard Space Flight Center (GSFC) collaborated with the Living With a Star (LWS) E/PO Program to develop and implement classroom activities designed to educate middle school and high school students about STEREO and Sun–Earth Connection (SEC) Science and Engineering. These activities were designed as a science challenge for high school students and an engineering challenge for middle school students for the Fall 2005 semester. For the middle school engineering project, students constructed and balanced a model of the STEREO spacecraft, which was specifically developed by senior engineers for this E/PO activity. The science project challenged high school students to submit answers to challenging engineering questions. The final challenge included space weather and STEREO information and used resources created especially for this project. One hundred forty-six middle school and 28 high school groups registered for the challenge. Participants included 14 public and three private schools from the east coast and six public schools in Puerto Rico. Student groups submitted a final overview, detailing their successes and challenges with the project. The overview indicated that these students and their teachers now have a better understanding of STEREO SEC science and that they were eagerly awaiting the launch of STEREO and the resulting research to generate further classroom discussion. The LWS program facilitated the challenge information and resources, available through the LWS program office web site. (See Sect. 4.1 for the URL for this web site.)

2.4 Student-Focused Events

Students with their teachers from the metropolitan Washington, DC, area elementary and middle schools participated in a Space Weather Day on November 29, 2005, with more than 100 attendees. The day included hands-on activities by E/PO specialists and presentations by scientists. Students were taught about spectrometers, space radiation, and the effects of UV radiation. The activities were not only educational—evaluations indicated that it was also fun for the participants and provided them a unique NASA-based understanding of space weather. This Space Weather Day was a collaborative effort between the STP/LWS E/PO Program office, the STEREO program E/PO at the Goddard Space Flight Center (GSFC), Solar Dynamics Observatory (SDO), Space Environment Testbeds (SET), George Mason University, and the GSFC Visitor Center.

Fig. 5 Students and their teachers visiting the APL Academy



A similar but separate program, Space Academy, gives middle school students a behind-the-scenes look at actual space missions, such as STEREO, and introduces them to engineers and scientists working on NASA projects. Space Academy is held twice a year at the Advanced Plasma Laboratory (APL) in Laurel, Maryland with hands-on, minds-on experiences designed to inspire both students and teachers. Weeks before the event, students learn about a specific mission, its science theme, and space-related careers through classroom activities and videos developed by Discovery Networks and APL. The Space Academy program web site showcases these events and student activities. This web site can be found from the APL STEREO E/PO web site URL given in Sect. 4.

In October 2004, more than 100 Maryland middle school students and their teachers from four schools in three counties (Charles County, Harford County, and Montgomery County) participated in a daylong STEREO Space Academy. A photograph of the participants is shown in Fig. 5. The day included a student press conference, where the students—like real reporters in a real NASA press conference—posed questions to a panel of STEREO team members from NASA and APL. Students also had discussions with scientists and engineers at lunchtime and in hands-on science demonstrations. They toured APL's space facilities, where they saw the twin STEREO spacecraft under construction, and visited labs where the spacecraft were tested prior to launch.

Three lesson plans used as pre- and post-visit activities were created for this event and can be accessed from the APL STEREO E/PO web site. The STEREO Mission activity explains how the unique new data from the two STEREO spacecraft will be used to study the nature of coronal mass ejections (CMEs). This activity addresses the effect these powerful solar eruptions can have on Earth and on the lives of humans in space, and even on global climate over the long term. The Make your Own Stereograms activity has students use a camera to make their own set of stereograms that can be used to create a 3-D image with the homemade stereoscope. This activity also includes instructions for constructing a stereoscope. The Fact Finding, Discussion, and Analysis activity guides students through the APL STEREO web site to investigate more about the STEREO mission. APL, Comcast Cable, and the Discovery Channel sponsor the Space Academy series and STEREO E/PO at APL leveraged this series.

3 Informal Education Activities

The STEREO E/PO team's goal for informal education was to inspire science center and planetarium attendees, musicians, artists, and science enthusiasts to learn more about solar

science and about STEREO in general. We set out to meet this goal by: (1) working with a small planetarium in New Hampshire to reach rural planetarium attendees, (2) working with the Sun–Earth Connection Education Forum during eclipses to bring STEREO mission engineering and science to museums across the country, and (3) inspiring and teaching musicians, artists, and science enthusiasts about STEREO and solar physics by changing silent data and graphs into interesting sounds.

3.1 STEREO in Science Centers and Planetariums

The goal of an in-depth partnership with the Christa McAuliffe Planetarium is creating public awareness and understanding of solar science, and to inspire and encourage young people to pursue careers in science and engineering. Through this partnership, the STEREO team at the University of New Hampshire (UNH) has created two planetarium shows, *Living with a Star* and *Breathing Space*, and helped to hold several events for the public. During the development of both shows, the planetarium gathered a focus group of teachers to find out what they thought was important for the students to learn. They also convened a focus group of high school students to find out what they thought would be important to know, and how they would like the science delivered (types of humor and ways of keeping their interest). In addition to these focus groups, the planetarium gathered questions from their patrons about the Sun. These needs assessments then informed the design of the two shows.

The *Living with a Star* planetarium show is a multimedia show, geared to grades 3–12 and general audiences, on solar science by way of a rocket ship flying into the heart of the Sun. In this show, the audience calls STEREO scientists and talks with them. Students indicated that interacting with the local scientists increased their own confidence in doing science. *Living with a Star* was complemented by *Sunbeams*, an exhibit on the spectrum and solar energy. The *Sunbeams* exhibit includes a model of the STEREO B spacecraft as an example of how spacecraft design includes solar panels as a power source. For the smaller children who cannot read, it was important to have someone available to help explain the spectrum and solar energy hands-on activities. *Living with a Star* showed for about five years to about 50,000 people per year.

The *Breathing Space* planetarium show is also a multimedia show. It is geared to grades 4–12 and general audiences on climate change throughout the solar system. The planetarium show explores the effects of the Sun on climate and endemic, external, and human-caused factors that tend to make climates stabilize or change. Teenagers changed the script in order to make it appeal to their peers. Not surprisingly, they added some “gas” jokes. This collaboration with teenagers has helped reach the teenage audience at large. About 100,000 people have seen the *Breathing Space* show. *Breathing Space* was created through several partnerships including PLASTIC E/PO, Plymouth State University, and the New England Science Center Collaborative.

Two space days have been developed at the planetarium in collaboration with the PLASTIC E/PO program, Spacetacular Saturday and Super Stellar Friday. The Spacetacular Saturday is an aerospace festival, part of the national celebration of Astronomy Day. The events during this annual celebration are also possible due to partnerships with the NH Space Grant Consortium, the Plymouth State University, the NH Army National Guard, and aerospace companies. In 2004 and 2005, more than 500 participants enjoyed exhibits, planetarium shows, demonstrations, booths, programs, and activities offered by educators, scientists, and engineers. Figure 6 shows solar telescopes placed outside for the public to observe sunspots and other solar features. The events focused on space science, astronomy, and aviation. The STEREO E/PO team at UNH ensured that items and information provided by NASA STEREO E/PO were distributed. In addition, U.S. Space and Rocket camp scholarships were awarded to youth.

Fig. 6 Solar viewing at Spacetacular Saturday



The Super Stellar Fridays occurred for 50 Friday nights per year for two years. During these nights, STEREO E/PO activities at the Planetarium included a program series geared toward teens, families, and adults. The activities included sky observation, lectures and multimedia shows in the theater, hands-on workshops, immersive activities for families, and a monthly teens-only immersive workshop and show. Common expressions from the teenagers who attended these nights were: "That was awesome, Teen night is awesome!" and "It is a lot of fun to get together with people who know about space and to eat pizza." One scientist who gave a presentation to this teenage night was amazed that they could get so many teens out for this talk and was impressed by their questions, both the quantity and quality. Attendance exceeded 1,200 people per year. The STEREO PLASTIC E/PO led the efforts with the Christa McAuliffe Planetarium.

To reach an even larger audience and one that is national in scope in 2001 and 2006 the Sun-Earth Education Forum (SECEF) worked with the Exploratorium to provide a live web cast of the total solar eclipses in Africa (2001) and in Turkey (2006). STEREO was featured in both of these huge public events, and most of the E/PO teams took part in events around the country. For the 2001 eclipse, the STEREO E/PO team at UCB coordinated video interviews of the STEREO scientists. The scientists spoke about their roles in the STEREO mission and their views of the solar eclipse. The Exploratorium has a web site where these interviews have been woven together with solar science content and footage of the eclipse, accessible from both the Exploratorium and IMPACT E/PO web sites. The IMPACT E/PO web site URL is located in Sect. 4. For the 2006 live web cast of the eclipse on March 29, the Exploratorium interviewed a STEREO scientist representing the STEREO mission about solar storms. Both of these events reached hundreds of thousands of people in science centers around the country, who watched the broadcast of the live web cast. Archived data can be accessed on the web site for later viewing. The 2006 live web cast received excellent coverage in all 50 states and at least 37 countries. MSNBC, which provided simultaneous web cast, had 23,162 unique users, with a record 1,576,624 streams downloaded in one day. The Exploratorium Eclipse web site reported 627,901 unique visitors from March 2006 until June 2006. Thousands of other people participated via museum events, amateur astronomer events, and teacher's lessons in the classroom.

3.2 Musicians, Artists, and Solar Data

The STEREO E/PO group at UCB worked with graduate student musicians, Roberto Morales and David Bithell, at the Center for New Music and Auditory Technologies (CN-MAT) to create three software programs that would allow users to listen to data through a

process known as sonification. This project was designed to help the public, musicians, and artists engage in the nonvisual STEREO data. One of the programs, called “Incandescence,” targets musicians and artists and allows them to creatively explore sound using solar data as a rich generative material. This program uses Helios 1 and 2 solar energetic particle (SEP) events. A second program, called “Stereo Spectro,” is designed for science enthusiasts and scientists who want to listen to three-dimensional color graphs of solar particle and radio wave data. This program’s interface is shown in Fig. 7. A third program, called “Beginning Application,” was created to help students and the public to learn how the data are plotted and pitches are changed according to the value of the data. While working on incandescence, R. Morales composed a symphony called “Turning Point.” He included a section in the symphony piece inspired by SEP events, as detected by satellites Helios 1 and 2. The piece was performed in Mexico in 2004. This project inspired several magazine articles in “Seed” and “California Magazine,” a radio interview (St. Louis, KMOX Radio 1120 AM), and part of a STEREO exhibit at a science museum (Science Museum in London, UK). The programs and samples of the sounds created by the programs can be found on the IMPACT E/PO web site. IMPACT E/PO led this effort with the STEREO/WAVES (S/WAVES) E/PO, which is also taking part in sonification to help bring alive the “invisible universe” of radio waves.

4 Public Outreach

Through our public outreach efforts, we seek to address the needs of the public such as: “Although Americans express strong support for science and technology (S&T), they are not very well informed about these subjects” and “The Internet is having a major impact on how the public gets information about S&T” (NSB Report 2004). We aimed to share the STEREO science and mission with the public by: (1) creating web pages explaining the STEREO science and mission, (2) providing data such as 3-D images of the Sun to the public, and (3) creating multimedia, paper, and other types of products for dissemination to the public and for use in the media, public events, teacher PD workshops, science centers, and planetariums.

4.1 Reaching the Public via the Internet

The Internet is a incredibly rich resource of information, and almost all of the STEREO E/PO efforts are documented on the web or have web components. The projects and activities described in this paper can be found on the web sites in Table 1. The NASA STEREO web site is the official “portal” and all the web sites in Table 1 can be found through the STEREO web site, even if indirectly. This portal links to the mission and instrument suite web sites, which then link to the education programs associated with the mission and instrument suite websites. The Goddard Space Flight Center web site (STEREO Mission) has links to almost all of the other websites listed in the table. Most of these web sites explain at a public level the scientific background, the spacecraft instrumentation, and data analysis techniques. Many also have grade-level appropriate, hands-on projects that one can do to understand the various instrument, satellite, and project science.

4.1.1 Data Availability to the Public

Space mission data can and has been effectively used in classroom activities and lesson plans (e.g., NASA’s Student Observation Network) by museums and science centers. The data can

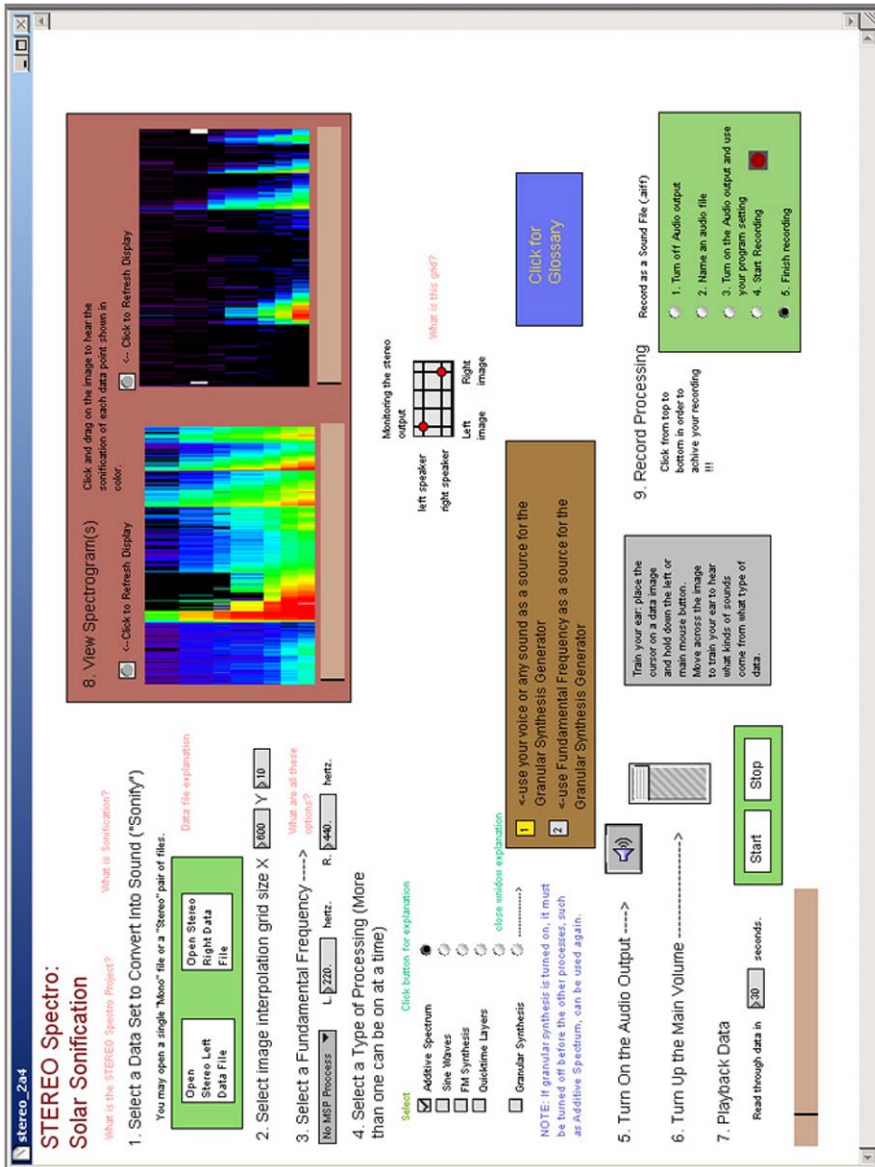


Fig. 7 Interface of the Stereo Spectro software program

Table 1 Relevant STEREO E/PO web sites

Website Name	URL	Brief description and web statistics when available
NASA STEREO	http://www.nasa.gov/stereo/	Information, news and media 556,046 page views for 2006
STEREO Mission	http://stereo.gsfc.nasa.gov/	Public site with educational information 73,779 page views in 2006
IMPACT E/PO	http://cse.ssl.berkeley.edu/impact	E/PO information on magnetism and solar particles 106,007 page views in 2006
Christa McAuliffe Planetarium	http://www.starhop.com/	Information about outreach events (PLASTIC supported)
APL spacecraft E/PO	http://stereo.jhuapl.edu	E/PO information on spacecraft and engineering
STP/LWS	http://stargazer.gsfc.nasa.gov/	The space weather challenge web site

At these web sites, one can find more information about each of the E/PO programs including the products developed by the STEREO E/PO team. Several of the web sites also describe the instrument suites and/or the STEREO mission at an appropriate level for the public.

also be accessed directly by the public. Connection with the data brings the excitement of involvement in a NASA mission to students, teachers, and the public in general. Because of the importance of data to the public, STEREO science data are available in public-friendly formats through the STEREO mission web site and through several of the E/PO sites. Along with the STEREO data, the web sites provide the necessary background information and mission details to put everything into context and enable visitors to understand the big picture. For example, the S/WAVES E/PO data will be accompanied by information on the triangulation and tracking of solar radio bursts from flares and CME-driven shocks.

The completely new, three-dimensional (3-D) aspect of SECCHI imagery provides both an opportunity and a major challenge for exploiting the educational potential of the STEREO Mission. 3-D images can be accessed from the NASA STEREO portal and the STEREO mission web sites. The STEREO E/PO program is using the 3-D rendered images to communicate important themes related to the *Benchmarks for Science Literacy* (AAAS 1993) as key ideas that should be understood by all scientifically literate Americans. Examples of such themes are:

- The Sun, with its hot, layered atmosphere and constant evolution of a solar wind that pervades heliospheric space, washing over the Earth and the other planets.
- The constantly changing aspects of the magnetic Sun: 11/22-year sunspot cycle, sunspots, active regions, flares, coronal mass ejections (CMEs), solar storms and geomagnetic storms, and space weather.
- Geomagnetic effects and the rapidly increasing vulnerability of technological systems to solar activity.
- Implications of solar activity and space storms for humans in space and extended space exploration such as the recently adopted Moon–Mars exploration initiative.

Fig. 8 Cover of the APL Mission DVD



STEREO data are available for incorporation into other existing efforts such as the NASA Sun–Earth Viewer and the Student Observation Network, allowing for a much broader dissemination.

4.2 STEREO Products for the Public and General Educational Use

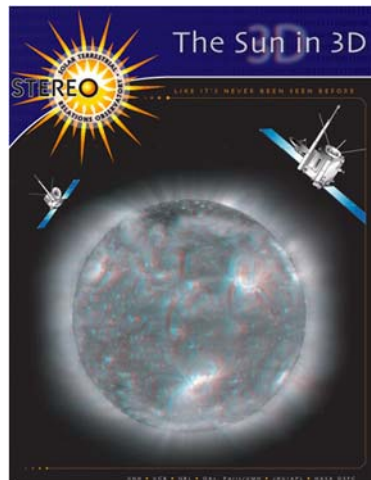
Many different products have been created for the public and general educational use: (1) a CD-ROM with images, media, and other STEREO science and mission content for general educational use; (2) a DVD with a video and also images, media, and other STEREO-related content; (3) a STEREO E/PO poster and a STEREO mission poster; (4) STEREO flyers; (5) educational booklets; (6) satellite cut-outs; (7) a STEREO lenticular; and (8) bookmarks, pins, pens, and decals. Many of the E/PO programs have taken instrument and satellite photographs and placed them on their web sites with appropriate captions. We'll describe several of these products in more detail.

The STEREO mission CD created by the STEREO project office is a comprehensive educational outreach product that helps to explain the STEREO mission and solar science, both to a middle school audiences and to the general public. A primary goal of the CD is to present the information by explaining concepts through simple animations, video, interviews, hands-on demonstrations, and activities as well as articles. This provides easy access to images, media, and other content so that educators can incorporate it into their teaching curriculum or used solely as a resource for students and general users.

In the STEREO project's CD, an example of how the Sun impacts our everyday lives is described and then used to explain the necessity for STEREO's satellite research. Throughout the CD, interactive animations are available to explain STEREO's satellite specifications and its different instruments. The Mission FAQ section features video interviews of members of the STEREO team and allows the user to find answers to questions concerning CMEs, solar science, STEREO, and space research. Hands-on demonstrations have also been video recorded to help teachers, students, and science center personnel in performing the demonstrations. STEREO outreach products and resource material are also provided including a glossary, acronym list, and links to STEREO and Sun related articles.

APL created a DVD with images and mission content as well as video that focus on the unique aspects of designing spacecraft to study the Sun in 3-D. Figure 8 shows the DVD cover. The primary target audience is students and museums/science centers, with the media as a secondary audience. The video addresses the following questions: "Ever wonder why two spacecraft are needed to study the sun or how you build them to operate in the extreme conditions they'll experience in space?" "How do you launch two spacecraft on one

Fig. 9 Front of the STEREO E/PO poster



rocket?" This six-minute video, "Solar News Network: NASA Gets a Double Dose of the Sun," uses a broadcast news approach to help answer these questions. This project included the production of on-camera interviews, animation, footage of milestone events, ranging from integration and test through launch. On this DVD are also four sets of animations titled: "Preparing for Flight: Closing the Launch Vehicle's Fairing," "Placing STEREO into Orbit," "Twin STEREO Observatories in their Orbits," and "Seeing with STEREO." In addition to the DVD and the web site, these animations were used on NASA TV, and as supporting imagery for broadcast media. APL created an educational booklet detailing a behind-the-scenes look at the engineering and technology factors associated with the twin STEREO spacecraft, and the trajectory needed to place them in orbit for their 3-D views of the Sun. This guide complements the DVD by providing a more in-depth overview. It also acts as a stand-alone booklet for general educational use.

The STEREO E/PO 3-D Poster is an educational poster produced by the STEREO project office and intended for a middle- and high-school level audience. The main focal point of the front of the poster is a large red/blue 3-D image of the Sun, to be viewed using the accompanying red/blue 3-D glasses, as shown in Fig. 9. The back of the poster contains a brief overview of the STEREO mission and science to be performed, as well as two activities easily performed in a classroom setting. This poster was evaluated by the NASA education review as excellent and the STEREO team has experienced hundreds if not thousands of "Ahhhh!"s when children see it with the red-blue glasses.

Three distinct flyers were created by the IMPACT, SECCHI, and APL E/PO teams. The IMPACT E/PO flyer describes the IMPACT goals and the E/PO efforts with the Mapping a Magnetic Field activity from the *Exploring Magnetism Teacher's Guide* discussed in Sect. 2.3. It was evaluated through the NASA space science review and updated with the comments from the review committee. The SECCHI flyer is a brochure on CMEs, how coronagraphs work, EUV disk imagery, a history of coronagraphy and coronal observations, sungrazing comets discovered by space coronagraphs, and how the Sun itself works. The APL flyer is an educational fact sheet, which tells about the two STEREO spacecraft. All of these flyers are available in hard copy and placed on web sites to be downloaded. In addition to the educational community, these handouts serve the media and general public.

APL, SECCHI, and IMPACT E/POs have all worked with photographs and images for general education consumption. APL has managed the collection and captioning of the

STEREO photographs. This collection was separated into the following sections: Assembly and Testing of the Twin Observatories; Shipping the Observatories; Prelaunch Environmental Testing; and Artist Concepts. The IMPACT E/PO team also has a multimedia section with IMPACT photographs available to the public with captions. The SECCHI team has created graphic and narrative presentation of the SECCHI instrument design and operational concepts, and the preparation and test activities necessary to assure full functionality on orbit. SECCHI has also created combinations of graphics and real data presentations to convey the three-dimensional and dynamical nature of CME/storm disturbances as reconstructed from STEREO-A and STEREO-B.

Most of these products can be found on the web sites in Table 1. Besides access via the web sites, these products have been and will continue to be disseminated at: (1) the preservice courses discussed in Sect. 2.1; (2) educational workshops such as NSTA, as discussed in Sect. 2.2; (3) pre- and post-launch activities, for example, a total of 25,000 copies of the IMPACT E/PO flyer were included in the 2005 and 2006 SECEF Sun–Earth Day packets; (4) scientist/engineer guest events for students, as discussed in Sect. 2.4; (5) various other such outreach events, such as the planetarium days discussed in Sect. 3.1; and (6) to other E/PO professionals at conferences such as the American Geophysical Union (AGU). Over 100,000 products in total have been disseminated across the country to students, teachers, and the general public.

5 Conclusions

As described in Sect. 1, there is great need in the United States to help increase the scientific knowledge of students and teachers, to inspire students to become scientists and engineers, and to share with the public information about specific scientific programs. Over four years, the STEREO E/PO program has striven and succeeded in meeting some of the need for physics and space science content knowledge and lessons. Thousands of teachers indicated they would use in their classrooms the information and lessons given at in-depth preservice college courses and in one-hour to two-day long in-service teacher professional development workshops about the Sun and the physics of the Sun. The STEREO E/PO program has taught students directly about space science, being or becoming a scientist or engineer, and the science of the STEREO mission through large student events. And the STEREO E/PO program has aimed to meet the needs of the public for information about current science missions. STEREO E/PO has also excited and inspired teens and the general public through several science center activities, including the Breathing Space Planetarium show in New Hampshire, the Sun–Earth day eclipse web casts shown around the world, and through programs that turn data into sounds.

Because of limited funding for NASA E/PO, it is vital to work with partners who can help leverage small programs to increase their impact, to sustain programs, and to disseminate materials. The STEREO E/PO program has done this and more with each of its programs. Most of the programs described here have a diversity of partnerships. For example, the preservice teacher program leverages from a collaboration between the departments of Education and Physics at the Catholic University of America, NRL, and the NASA Goddard Space Flight Center. The in-service teacher PD workshops leverage SECEF and several other NASA mission E/PO programs. The printing of the magnetism teacher guides was also leveraged from other NASA mission E/PO programs. The science center education programs would not be possible without the partnership of the NH Christa McAuliffe Planetarium and the annual Sun–Earth Day put on by SECEF. Partnering with musicians created

an interesting product for the sonification project. All of these partners have put in-kind work and brought their unique expertise, which the STEREO E/PO program needed to succeed. Most of these partnerships will work to ensure that these programs continue long after the STEREO E/PO funding is gone. The partnership with Sun-Earth Day and other NASA E/PO programs have helped to share the STEREO mission and its science and disseminate the STEREO E/PO products with thousands of members of the public and teachers around the country.

One of the benefits of E/PO programs from NASA is the inspiring content and the contact with working scientists and engineers. The STEREO E/PO program is made much more effective because all of the Principal Investigators associated with the suite of instruments are deeply committed to E/PO and have played an active role in the programs. In addition, the education specialists who work with these programs are scientists themselves, and are able to bridge the gap between the science world and the education world. All of the programs have directly involved a scientist working with the STEREO E/PO program. And all of the programs have been developed around the STEREO science content of the dynamic sun. The many products that have been created for the STEREO E/PO program all contribute toward explaining the science of the Sun and the STEREO mission.

Because the United States is so diverse in population, it is crucial to try and reach all types of people through E/PO programs. The STEREO E/PO program has emphasized women scientist role models and mentors. It has also worked with many teachers who teach mostly Hispanic and African American students. In these ways, this program tries to reach out to those not typically represented in the science community—especially in space science.

To really discover if STEREO E/PO has made long-term changes in people's knowledge and attitude about science, the Sun, and careers in science, would take more funding than is typically available through NASA E/PO programs. However, some of the STEREO E/PO program elements were evaluated to determine how useful they were to their audience. These formative evaluations were used to guide the program's development, such as the planetarium shows and the teacher classes and workshops. A couple of the programs had summative evaluations, such as the NASA-reviewed teacher guides and poster. Most programs used internal evaluation to produce their own questionnaires, collect data, and act on these data. An outside evaluator, Cornerstone Associates Inc., LCC, was leveraged from another NASA E/PO program to help evaluate several of the in-service teacher PD workshops. The STEREO E/PO program evaluations have shown that the STEREO E/PO program is educating teachers in a meaningful way, producing classroom materials which will be and are being used in the classroom, providing exciting events for students, and reaching many people across the country, mostly on the East and West coasts. We have also learned some of the challenges teachers face in using our materials (such as not having the funding resources to obtain magnets and compasses for the classroom). However, no outside evaluator has considered the discrete elements as a whole program, therefore there are no STEREO E/PO evaluation reports. Furthermore not all the elements in the overall program have been evaluated. Future E/PO programs, including the ongoing STEREO E/PO program, should plan for a well-defined evaluation strategy with a single outside evaluator looking at the impact of the entire program. The evaluator should be included at the beginning of each program to determine what type of overall impact the program has had.

Perhaps the biggest challenge of the STEREO E/PO team experienced was coordinating and sharing each other's projects and materials, with the exception of the more public outreach materials such as the STEREO poster. The STEREO E/PO program is incredibly diverse with a number of different people working on different programs. Each team (the four instrument teams, the spacecraft bus team, and the management team) developed their

own programs separately. In 2004, Dr. Kucera was appointed to coordinate the groups, and this paper is one result of this organization. A benefit of having so many different people involved is that the STEREO E/PO prelaunch program as a whole has been diverse and national. However, one of the lessons learned regarding E/PO of large NASA space science missions is that it is imperative to the cohesiveness of the E/PO programs to have an E/PO lead overseeing the E/PO programs from the beginning of the mission planning.

The STEREO E/PO program will continue after the STEREO satellites are in space. In addition to the continuation of the teacher classes and workshops, the sustained efforts will focus on dissemination and evaluation of the E/PO products, programs, and including STEREO data in the E/PO activities. The STEREO data will be shared with the public both as solar images, as described in Sect. 4.1.1, and as sound, as described in Sect. 3.2. Through this continued effort, we hope to share with students, teachers, and the public, the many exciting discoveries we expect from the STEREO science mission. And we hope to find out if this program, as we believe, has had an overall positive impact on students, teachers, and the general public.

Acknowledgements The IMPACT E/PO team thanks Dr. Stuart Bale, Co-I of the SWAVES team, and Dr. Chris StCyr, Living with a Star Senior Project Scientist for financial support of the STEREO sonification software program. We would also like to thank Drs. R. M. Morales and D. Bithell at the Center for New Music and Audio Technologies, University of California, Berkeley for their excellent work on the sonification software. L. Peticolas thanks Karin Hauck for final editing.

References

- American Association for the Advancement of Science (AAAS), *Benchmarks for Science Literacy* (AAAS, Washington, 1993). ISBN: 0-19-508986-3. <http://www.project2061.org/publications/bsl/online/bolintro.htm>
- L.P. Cooper, C.A. Morrow, R.A. Pertzborn, J. Rosendhal, P. Sakimoto, An explanatory guide to NASA office of space science education and public outreach evaluation criteria (2004). <http://science.hq.nasa.gov/research/guide.pdf>
- C. Morrow, A framework for planning education and public outreach programs associated with scientific research programs, Space Sciences Institute (2000). <http://www.spacescience.org>
- National Academy of Sciences (NAS) Report, *Rising Above The Gathering Storm: Energizing and Employing America for a Brighter Economic Future, Committee on Prospering in the Global Economy of the 21st Century: An Agenda for American Science and Technology*. Committee on Science, Engineering, and Public Policy (2005). ISBN: 0-309-65463-7. <http://www.nap.edu/catalog/11463.html>
- National Research Council (NRC), *National Science Education Standards* (National Academy Press, Washington, 1996). ISBN: 0-309-05326-9
- National Science Board (NSB), *Science and Engineering Indicators (NSB 04-01)* (National Science Foundation, Arlington, 2004), Chaps. 1 and 7
- Office of Space Science-Space Science Advisory Committee Education/Public Outreach (OSS-SSAC E/PO) Task Force Report, *Office of Space Science Education Implementation Plan* (1996). <http://science.hq.nasa.gov/research/EPO.htm>
- Space Science Advisory Committee Education and Public Outreach (SSAC E/PO) Task Force Report, *Implementing the Office of Space Science Education/Public Outreach Strategy: A critical Evaluation at the Six-Year Mark* (2003). <http://science.hq.nasa.gov/research/EPO.htm>
- Solar and Space Physics Survey Committee, National Research Council (SSPSC/NRC), *The Sun to the Earth and Beyond: A Decadal Research Strategy in Solar and Space Physics* (The National Academies Press, Washington, 2002). ISBN: 0-309-50800-2
- G. Wiggins, J. McTighe, *Understanding by Design, Association for Supervision and Curriculum Development* (ASA, Alexandria, 1998). ISBN: 0-87120-313-8